



3rd International Students Science Congress

03-04 MAY 2019

Proceedings / Bildiriler Kitabı

www.sciencecon.org

 fenkongre@gmail.com



3rd International Students Science Congress Proceedings

3. Uluslararası Öğrenciler Fen Bilimleri Kongresi Bildiriler Kitabı

Editor-in-Chief / Sorumlu Editör

Mehmet Çevik

Co-editors / Yardımcı Editörler

Sinan Yıldırım

Ahmet Aykaç

Furkan Emrem



İzmir Kâtip Çelebi Üniversitesi Yayın No: 12

Bu eserin, İzmir Kâtip Çelebi Üniversitesi Yönetim Kurulu'nun 10.09.2019 tarih ve 2019/29 sayılı toplantısında alınan 04 numaralı kararı uyarınca, elektronik kitap olarak yayımlanmasına karar verilmiştir.

Her hakkı saklıdır.

© İzmir Kâtip Çelebi Üniversitesi Yayınları
Eylül 2019

Sertifika No: 23705

Editör : Mehmet ÇEVİK
Yardımcı Editörler : Sinan YILDIRIM
Furkan EMREM
Ahmet AYKAÇ

E-ISBN: 978-605-81050-1-0

International Students Science Congress (3rd : İzmir : 2019)

3rd International Students Science Congress: Proceedings, 03-04 May 2019 =
3. Uluslararası Öğrenciler Fen Bilimleri Kongresi: Bildiriler Kitabı, 03-04 Mayıs 2019 /
Sorumlu editör: Mehmet Çevik; Yardımcı editörler: Sinan Yıldırım, Ahmet Aykaç, Furkan
Emrem.—İzmir : İzmir Kâtip Çelebi Üniversitesi, 2019.

Çevrimiçi (XIII, 613 Sayfa ; 26 cm.). -- (İzmir Kâtip Çelebi Üniversitesi ; Yayın No: 12)
ISBN: 978-605-81050-1-0

1.Fen Bilimleri – Kongreler 2.Öğrenciler – Kongreler

I.Çevik, Mehmet – II.Yıldırım, Sinan – III.Aykaç, Ahmet – IV.Emrem, Furkan

Adres : İzmir Kâtip Çelebi Üniversitesi Rektörlüğü, Balatçık Yerleşkesi, 35620 Çiğli
İzmir, Türkiye

Telefon : +90 232 329 3535 / 1255

E-posta : ykb@ikc.edu.tr

Belge-geçer : +90 232 386 0888

Web : ykb.ikc.edu.tr

Eserin hukuki ve etik sorumluluğu yazarlara aittir. Tüm hakları saklıdır. Bu kitabın yayın hakkı İzmir Kâtip Çelebi Üniversitesi'ne aittir. İzinsiz kopyalanamaz ve çoğaltılamaz.

All rights reserved © İzmir Kâtip Çelebi University Press, 2019. No part of this book may be reproduced in any form or by any electronic or mechanical means including information storage systems without permission in writing from the publisher, except by a reviewer who may quote brief passages in a review.

Preface

Dear Participants, Colleagues, and International Students,

It is with deep satisfaction that I write this preface to the Proceedings Book of the 3rd International Students Science Congress held in İzmir Kâtip Çelebi University, Turkey, May 03 - 04, 2019.

In the last two years we organized two congresses in order to bring together young international researchers working in various science areas and this has really motivated all of us; and thus, this year we have accomplished the third congress again with great enthusiasm.

Over two hundred and twenty young researchers from more than thirty countries gathered for this congress and one hundred twenty papers were presented in 24 sessions. In addition to the contributed papers, three intriguing invited presentations were given: by Prof. Dr. Yusuf Baran, Rector of İzmir Institute of Technology, who spoke about Science Diplomacy, by Prof. Dr. Şule Erten Ela, Director of Institute of Solar Energy at Ege University, who spoke about New Trends in Solar Cells; and by Prof. Dr. Aydoğın Savran, the Dean of Faculty of Engineering and Architecture at İzmir Kâtip Çelebi University, who spoke about Artificial Intelligence, Robots and Autonomous Systems. The audience followed these three presentations with deep interest.

The congress particularly encouraged the interaction of international research students and developing academics with the more established academic community in an informal setting to present and to discuss new and current work. Their contributions helped to make the Congress as outstanding as it has been. The Congress provided a setting for discussing recent developments in a wide variety of topics including Agricultural Engineering, Architecture, Biology and Bioengineering, Chemistry and Chemical Engineering, Civil Engineering, Computer Science and Engineering, Electrical, Electronics and Communication Engineering, Geomatics Engineering, Food Engineering, Geology Engineering, Mechanical Engineering, Mathematics, Materials Science, Metallurgical and Materials Engineering, Nanotechnology, Renewable Energy, Urban and Regional Planning.

We would like to thank all participants for their contributions to the Congress program and for their contributions to these Abstract Proceedings. Many thanks go as well to the Presidency for Turks Abroad and Related Communities (YTB) for their financial support, which allowed a more pleasant event. It is our pleasant duty to acknowledge the support from İzmir Kâtip Çelebi University, Federation of International Student Associations (UDEFA) and İzmir International Guest Student Association.

I would like to express my sincere gratitude and appreciation to our organizing committee and all the students who worked voluntarily during the event.

The continuing success of this congress series means that planning can now proceed with confidence for the 4th International Students Science Congress to be held in 2020.

We thank all authors, participants, and volunteers for their contributions.

Prof. Dr. Mehmet Çevik
Congress Chair

Önsöz

Değerli Katılımcılar, Meslektaşlarım ve Uluslararası Öğrenciler,

03 - 04 Mayıs 2019 tarihlerinde İzmir Kâtip Çelebi Üniversitesi'nde gerçekleştirmiş olduğumuz 3. Uluslararası Öğrenciler Fen Bilimleri Kongresi Bildiriler Kitabı'na bu satırları yazmanın derin memnuniyeti içindeyim.

Geçtiğimiz iki yıl fen bilimleri alanlarında çalışan uluslararası genç araştırmacıları bir araya getirmek için düzenlediğimiz iki kongre hepimizi gerçekten motive etti ve bu yıl üçüncüsünü büyük bir hevesle gerçekleştirdik.

Kongremizde 30 ülkeden 220'den fazla katılımcı, iki gün içinde toplam 24 oturumda 120 tane bildiri sundu. Bildirilere ek olarak, üç davetli konuşmacımız tarafından gerçekten ilgi çekici sunumlar yapıldı: İzmir Yüksek Teknoloji Enstitüsü Rektörü Prof. Dr. Yusuf Baran bilim diplomasisi hakkında konuştu; Ege Üniversitesi Güneş Enerjisi Enstitüsü Müdürü Prof. Dr. Şule Erten Ela güneş hücrelerindeki yeni trendlerden bahsetti ve İzmir Kâtip Çelebi Üniversitesi Mühendislik ve Mimarlık Fakültesi Dekanı Prof. Dr. Aydoğın Savran yapay zeka, robotlar ve otonom sistemlerden bahsetti. Bu üç sunum da izleyiciler tarafından büyük ilgiyle takip edildi.

Kongre, özellikle fen bilimleri alanında eğitimlerine devam eden uluslararası öğrencilerin ve genç akademisyenlerin önlerindeki akademik camia ile etkileşimlerini gayet samimi bir ortam sunarak teşvik ederken, yeni ve güncel çalışmalarını sunmaları ve tartışmaları için de güzel bir fırsat sağlamış oldu. Onların katkıları sayesinde Kongre olabildiğince seçkin ve nitelikli bir düzeye ulaşmış oldu. Kongre, Ziraat Mühendisliği, Mimarlık, Biyoloji ve Biyomühendislik, Kimya ve Kimya Mühendisliği, İnşaat Mühendisliği, Bilgisayar Bilimi ve Mühendisliği, Elektrik, Elektronik ve Haberleşme Mühendisliği, Harita Mühendisliği, Gıda Mühendisliği, Jeoloji Mühendisliği, Makine Mühendisliği, Matematik, Malzeme Bilimi, Metalurji ve Malzeme Mühendisliği, Nanoteknoloji, Yenilenebilir Enerji, Kentsel ve Bölgesel Planlama, vb. çok çeşitli konulardaki son gelişmeleri tartışmak için keyifli bir ortam sağladı.

Tüm katılımcılara kongre programımıza ve dolayısıyla bildiri özetleri kitabımıza yaptıkları katkılardan dolayı teşekkür ederiz. Sunduğu maddi destek ile etkinliğimizin daha keyifli geçmesini sağlayan Yurtdışı Türkler ve Akraba Topluluklar Başkanlığı'na (YTB) da çok teşekkür ederiz. Ayrıca verdikleri destek ile bu kongrenin gerçekleşmesini sağlayan İzmir Kâtip Çelebi Üniversitesi'ne, Uluslararası Öğrenci Dernekleri Federasyonu'na (UDEF) ve İzmir Uluslararası Misafir Öğrenci Derneği'ne teşekkürlerimizi arz ederiz.

Organizasyon komitemize ve etkinlikte gönüllü olarak çalışan tüm öğrencilerimize içten teşekkürlerimi ve minnettarlığımı ifade etmek isterim.

Bu kongre dizisinin başarı ile devam etmesi, 2020'de düzenlemeyi düşündüğümüz 4. Uluslararası Öğrenciler Fen Bilim Kongresi'nin organizasyonu için bize güven veriyor.

Katkıları için tüm yazarlara, katılımcılara ve gönüllülere teşekkür ederiz.

Prof. Dr. Mehmet Çevik
Kongre Başkanı

Organizing Committee / Düzenleme Kurulu

Mehmet Çevik

Ahmet Aykaç

Fethullah Güneş

Sinan Yıldırım

Abdirahman Ahmed Omar

Furkan Emrem

Miftaudeen Abdul Rahman

Mustafa Abshir Mohamed

Mustafa Öncül

Scientific Committee / Bilim Kurulu

- Prof. Dr. Abdelraouf A. Elmanama** (Islamic University-Gaza)
Prof. Dr. Adnan Kaya (İzmir Kâtip Çelebi University, Turkey)
Prof. Dr. Ahmed Hussein Kamel Ahmed Elshafie (University of Malaya, Malaysia)
Prof. Dr. Ahmet Türk (Manisa Celal Bayar University, Turkey)
Prof. Dr. Akeel H. Ali Al-Assie (Tikrit University, Iraq)
Prof. Dr. Ali Çelik (Manisa Celal Bayar University, Turkey)
Prof. Dr. Ali Mutlu (Manisa Celal Bayar University, Turkey)
Prof. Dr. Amin Solaiman Badawy (University of Tikrit, Iraq)
Prof. Dr. Antonio Vargas-Berenguel (Universidad de Almería, Spain)
Prof. Dr. Aydın Akan (İzmir Kâtip Çelebi University, Turkey)
Prof. Dr. Aydoğan Savran (Ege University, Turkey)
Prof. Dr. Bayram Şahin (Ege University, Turkey)
Prof. Dr. Buket Okutan Baba (İzmir Kâtip Çelebi University, Turkey)
Prof. Dr. Enver Atik (Manisa Celal Bayar University, Turkey)
Prof. Dr. Erdal Çelik (Dokuz Eylül University, Turkey)
Prof. Dr. Md. Ashraful Hoque (Islamic University of Technology, Bangladesh)
Prof. Dr. Mehmet Ali Yurdusev (Manisa Celal Bayar University, Turkey)
Prof. Dr. Mehmet Sezer (Manisa Celal Bayar University, Turkey)
Prof. Dr. Musa Alcı (Ege University, Turkey)
Prof. Dr. Nazar Mohammad Halim (Kabul University, Afghanistan)
Prof. Dr. Nihat Sami Çetin (İzmir Kâtip Çelebi University, Turkey)
Prof. Dr. Nilgül Çetin (İzmir Kâtip Çelebi University, Turkey)
Prof. Dr. Nurcan Baykuş Savaşaneril (Dokuz Eylül University, Turkey)
Prof. Dr. Ramazan Karakuzu (Dokuz Eylül University, Turkey)
Prof. Dr. Sahib Jumaa Abdurrahman (Tikrit University, Iraq)
Prof. Dr. Şerafettin Demic (İzmir Kâtip Çelebi University, Turkey)
Prof. Dr. Roberta Katlen Fusco Marra (Universidade Salgado de Oliveira, Brazil)
- Assoc. Prof. Dr. Ali Konuralp** (Manisa Celal Bayar University, Turkey)
Assoc. Prof. Dr. Ayşegül Alaybeyoğlu (İzmir Kâtip Çelebi University, Turkey)
Assoc. Prof. Dr. Aytuğ Onan (Manisa Celal Bayar University, Turkey)
Assoc. Prof. Dr. Duygu Dönmez Demir (Manisa Celal Bayar University, Turkey)
Assoc. Prof. Dr. Erkan Doğan (Manisa Celal Bayar University, Turkey)
Assoc. Prof. Dr. Ersin Aslan (Manisa Celal Bayar University, Turkey)
Assoc. Prof. Dr. Fabienne Anne Chantal Dumoulin (Gebze Technical University, Turkey)
Assoc. Prof. Dr. Fatih Erdoğan Sevilgen (Gebze Technical University, Turkey)
Assoc. Prof. Dr. Fethullah Güneş (İzmir Kâtip Çelebi University, Turkey)
Assoc. Prof. Dr. Femin Yalçın (İzmir Kâtip Çelebi University, Turkey)
Assoc. Prof. Dr. Gökçen Bombar (İzmir Kâtip Çelebi University, Turkey)
Assoc. Prof. Dr. Gültekin Sınır (Manisa Celal Bayar University, Turkey)
Assoc. Prof. Dr. Hubert Chapuis (Université de Lorraine, France)
Assoc. Prof. Dr. Levent Çetin (İzmir Kâtip Çelebi University, Turkey)
Assoc. Prof. Dr. Mehmet Çevik (İzmir Kâtip Çelebi University, Turkey)
Assoc. Prof. Dr. Merih Palandöken (İzmir Kâtip Çelebi University, Turkey)
Assoc. Prof. Dr. Mücahit Sütçü (İzmir Kâtip Çelebi University, Turkey)
Assoc. Prof. Dr. Muhammad Mukhlisin (Politeknik Negeri Semarang, Indonesia)
Assoc. Prof. Dr. Mustafa Can (İzmir Kâtip Çelebi University, Turkey)
Assoc. Prof. Dr. Neritan Shkodrani (Polytechnic University of Tirana, Albania)
Assoc. Prof. Dr. Ümit İşci (Gebze Technical University, Turkey)

- Assist. Prof. Dr. Abdulfetah Shobole** (Istanbul Sabahattin Zaim University, Turkey)
Assist. Prof. Dr. Adil Ali Haydir Hassan (University of Kirkuk, Iraq)
Assist. Prof. Dr. Ahmet Aykaç (İzmir Kâtip Çelebi University, Turkey)
Assist. Prof. Dr. Ali Yurddaş (Manisa Celal Bayar University, Turkey)
Assist. Prof. Dr. Ali Ettehadî (İzmir Kâtip Çelebi University, Turkey)
Assist. Prof. Dr. Ayşe Kalaycı Önaç (İzmir Kâtip Çelebi University, Turkey)
Assist. Prof. Dr. Aytunga Bağdatlı (Manisa Celal Bayar University, Turkey)
Assist. Prof. Dr. Ceyhun Araz (Manisa Celal Bayar University, Turkey)
Assist. Prof. Dr. Derya Doğan Durgun (Manisa Celal Bayar University, Turkey)
Assist. Prof. Dr. Ebubekir Atan (İzmir Kâtip Çelebi University, Turkey)
Assist. Prof. Dr. Faruk Özger (İzmir Kâtip Çelebi University, Turkey)
Assist. Prof. Dr. Fatih Cemal Can (İzmir Kâtip Çelebi University, Turkey)
Assist. Prof. Dr. İlker Polatoğlu (Manisa Celal Bayar University, Turkey)
Assist. Prof. Dr. Levent Aydın (İzmir Kâtip Çelebi Üniversitesi, Türkiye)
Assist. Prof. Dr. Mohammed Wadi (Istanbul Sabahattin Zaim University, Turkey)
Assist. Prof. Dr. Muhammad Imran Shakir (King Saud University, Saudi Arabia)
Assist. Prof. Dr. Muhammad Shahid (The Islamia University of Bahawalpur, Pakistan)
Assist. Prof. Dr. Mustafa Erol (Dokuz Eylül University, İzmir, Turkey)
Assist. Prof. Dr. Mustafa Erkan Turan (Manisa Celal Bayar University, Turkey)
Assist. Prof. Dr. Nesrin Horzum Polat (İzmir Kâtip Çelebi University, Turkey)
Assist. Prof. Dr. Nihad A. Jafar (Tikrit University, Iraq)
Assist. Prof. Dr. Onur Ertuğrul (İzmir Kâtip Çelebi University, Turkey)
Assist. Prof. Dr. Ozan Karaman (İzmir Kâtip Çelebi University, Turkey)
Assist. Prof. Dr. Ömer Öztürkoğlu (Yaşar University, Turkey)
Assist. Prof. Dr. Özgün Yücel (İzmir Kâtip Çelebi University, Turkey)
Assist. Prof. Dr. Özlem Çağındı (Manisa Celal Bayar University, Turkey)
Assist. Prof. Dr. Saim Kural (Manisa Celal Bayar University, Turkey)
Assist. Prof. Dr. Sedat Yalçinkaya (İzmir Kâtip Çelebi University, Turkey)
Assist. Prof. Dr. Sercan Acarer (İzmir Kâtip Çelebi Üniversitesi, Türkiye)
Assist. Prof. Dr. Simge Öztunç (Manisa Celal Bayar University, Turkey)
Assist. Prof. Dr. Süleyman Murat Bağdatlı (Manisa Celal Bayar University, Turkey)
Assist. Prof. Dr. Şeyma Aykaç (Ege University, Turkey)
Assist. Prof. Dr. Umut Ceyhan (İzmir Kâtip Çelebi University, Turkey)
Assist. Prof. Dr. Utku Kürşat Ercan (İzmir Kâtip Çelebi University, Turkey)
Assist. Prof. Dr. Violeta Rodriguez-Ruiz (The University of Cergy-Pontoise, France)
Assist. Prof. Dr. Walid Sharmoukh Ahmed Moustafa (National Research Centre, Egypt)
Assist. Prof. Dr. Yiğit Aksoy (Manisa Celal Bayar University, Turkey)
Assist. Prof. Dr. Z. Haktan Karadeniz (İzmir Kâtip Çelebi Üniversitesi, Turkey)

- Dr. Amir Shirzadi** (University of Cambridge, United Kingdom)
Dr. Ayşe Kurt Bahşı (İzmir Kâtip Çelebi University, Turkey)
Dr. Hiba Yahyaoui (University of Tunis, Tunisia)
Dr. Juan Manuel Casas-Solvas (University of Almeria, Spain)
Dr. Sivarama Krishna Lakkaboyana (Universiti Teknologi Malaysia, Malaysia)
Dr. Tarkan Akderya (Manisa Celal Bayar University, Turkey)
Dr. Zoltán Fülöp (Budapest, Hungary)

Invited Speakers / Davetli Konuşmacılar



Science Diplomacy: From Past to Future

Prof. Dr. Yusuf Baran, Rector at İzmir Institute of Technology



New Trends in Solar Cells

Prof. Dr. Şule Erten Ela, Director of Institute of Solar Energy at Ege University



Artificial Intelligence, Robots and Autonomous Systems

Prof. Dr. Aydoğın Savran, Dean of Faculty of Engineering and Architecture at
İzmir Kâtip Çelebi University

Table of Contents

Preface.....	iv
Önsöz.....	v
Organizing Committee / Düzenleme Kurulu.....	vi
Scientific Committee / Bilim Kurulu	vii
Invited Speakers / Davetli Konuşmacılar	ix
Invited Speeches / Davetli Konuşmalar	1
New Trends in Organic Solar Cells.....	2
Agricultural Engineering / Ziraat Mühendisliği	6
Physiological and Growth Responses of Cubana Kordes Roses to Cd Stress and Plant Growing Parameters	7
Growth Responses of Pepita kordes Roses to Ni Stress and Ni Accumulation Characteristics.....	12
Somaliland Livestock Export: Historical Review	17
Benin'in Kanatlı Hayvan Üretimi Sektöründe Girişimcilik Fırsatı.....	24
Nijer Tarımının Karakteristik Özellikleri.....	31
Architecture / Mimarlık.....	38
Methodological Review for the Sensational Design and Measurements	39
Biology / Biyoloji.....	44
Remediation of Antimony from Aqueous Solutions Using Pomegranate Peels Residue Accessing to Zero Residue Level (ZRL)	45
Animal Zoonoses: Will Africa Ever Win the Fight?.....	55
Biotechnology / Biyoteknoloji	66
Screening for the Production of Secondary Metabolite (s) by Endophytic Fungi Isolated from Punica granatum in Small Scale Solid State Fermentation	67
Chemistry / Kimya	72
Optimizing Column Chromatography Conditions for Isolation of Resveratrol Using Different Column Fillers.....	73
Best Solvent System for Rapid Determination of Resveratrol Using Thin Layer Chromatography.	82
Urban and Regional Planning / Şehir ve Bölge Planlama	89
A Study on the Limitation of Motorcycle as City Transportation Case study: Bandung, Indonesia	90
Re-assessment of Plan Decisions by Measurement of Recreation Potentials: Case Study of Manisa Keçiliköy District	95
Space Syntax Yöntemi ile Kentsel Açık Yeşil Alanların Erişilebilirliğinin Belirlenmesi; Bornova Büyük Park ve Âşık Veysel Rekreasyon Alanı Örneği.....	103
Civil Engineering / İnşaat Mühendisliği.....	115
Betonarme Bina Kolonları için Sünme ve Büzülme Parametrelerinin İncelenmesi.....	116
Determination of Mixing and Compaction Temperatures of Polymer Modified Bitumen through High Shear Rate Method	122
Comparative Study of Marshall and Superpave Asphalt Pavement Design Methods.....	128

3rd International Students Science Congress
3-4 May 2019, İzmir - Turkey

Review of the Implementation of the Mechanistic-Empirical Pavement Design Guide.....	138
Public Bus Network Evaluation: A Guide for Benchmarking	154
Sonlu Elemanlar Yöntemi ile Modellenen Tekerlek Paletlerinin Kıyaslanması.....	162
Bitümlü Bağlayıcılarda Dinamik Kesme Reometresi ve Çoklu Gerilmeli Sünme Geri Dönme Deneylerinin Karşılaştırılması.....	168
An Experimental Study on the Scour around Two in Line Circular Bridge Piers with Different Diameters	172
Aynı Hizadaki İki Dairesel Kesitli Köprü Ayağının Etrafında Oluşan Oyulma Üzerine Deneysel Bir Çalışma.....	180
Review of the Relationship between Resilient Modulus and Dynamic Modulus	186
Computer Science and Engineering / Bilgisayar Bilimi ve Mühendisliği.....	193
Deep Learning Approaches in Medical Imaging.....	194
Experiments on the Fire Detection System Using a Multi-hop WSN.....	199
The Average Binding Number of Trees	208
Environmental Engineering / Çevre Mühendisliği.....	214
Geospatial Distribution Analysis and Investigation of Hydrochemical Groundwater Quality for Irrigation Purposes Using GIS and Suitability Indices: Case study of Altınova-Turkey	215
Management of Non-Revenue Water (NRW) in Municipal Water Distribution Networks: Antalya- Turkey Case Study	223
Smart Water Management for Smart Cities	229
Food Engineering / Gıda Mühendisliği	235
Effects of Storage Time and Different Storage Conditions on Some Quality Characteristics of Chicken Eggs.....	236
Chemical Interesterification of Palm Olein, Palm Stearin, Palm Mid Fraction, Sunflower oil and Soybean Oil Blends and its Effects on Melting Point, Solid Fat Content and Triglycerides	243
Geological Engineering / Jeoloji Mühendisliği.....	252
Land Use/Land Cover Classification of a Sentinel 2 Image: Forecariah, Guinea Case Study.....	253
Industrial Engineering / Endüstri Mühendisliği	259
Markov Decision Processes in Inventory Management: Finding Optimal Production Scheduling of Limestones in Trakya.....	260
Mathematics / Matematik.....	267
A Rational Parametrization of Cubic Bezier-Like Spiral Curve and its Applications	268
A Reliable Numerical Approximation to Physical Pendulum Equation using Dickson Polynomials	273
Pell Matrix Collocation Method for Solving Damped Wave Equation.....	281
Bernoulli Series Approach for a Class of Fredholm-type Integro-Differential Equations with Proportional Delays.....	290
A Numerical Technique Based on Boole Polynomials for Solving Fredholm Integro-Differential Equations	299
Stirling Matrix-Collocation Method to Solve Systems of Functional Differential Equations with Deviating Argument	309

Numerical Solutions of Fredholm Type Integro-Differential Equations Mixed Delays by Means of Bell Matrix-Collocation Method	317
Gegenbauer-Taylor Matrix Technique for Neutral Type Second Order Functional Integro-Differential Equations with Variable Bounds	326
Boubaker Collocation Method for Neutral Functional-Differential Equations with Proportional Delays.....	335
On Kannan Type Mappings in Near Soft Metric Spaces	344
New Results in Near Soft Metric Spaces	349
On Kannan Type Mappings in Steinhaus Transform Soft Metric Spaces.....	354
Some Remarks on Steinhaus Transform Soft Metric Spaces	360
Remarks on Rectangular Soft Metric Spaces	366
Aspects on Fixed Point Theorems in Rectangular Soft Metric Spaces	372
Domination Parameters in Graph Theory.....	380
An Euler Matrix Technique for Solving Nonlinear Duffing Differential Equation by Using Euler Polynomials.....	386
Euler-Taylor Matrix Technique for Solving a Class of High Order Delay Differential Equations with Nonlinear Terms.....	394
q-Homotopy Analysis Transform Method for Differential Equations having Quadratic Nonlinearity	402
Recent Results on Topologic and Geometric Properties of Fractional Difference Sequence Spaces	409
Some Recent Results on Compactness Conditions of Fractional Difference Sequence Spaces	412
Freud Polynomial Solutions of Linear First Order Generalized Pantograph Differential Equations	415
Sea Surface Temperature Prediction Model for Indonesian Waters	424
Mechanical Engineering / Makina Mühendisliği	431
Kompozit ve Çelik Güçlendirme Halkalarının Depolama Tankının Burkulma Yüküne Etkisi	432
Punch Shear and Low Velocity Impact Behaviours of Laminated Composites.....	438
Drop Weight Impact Response of Laminated Composites	444
Omuz Ekleminde Farklı Kas Gruplarının Sonlu Elemanlar Metodu ile Analizi ve Değerlendirilmesi	451
Low Velocity Impact Response of Thermoplastic Composites Reinforced with Metal Turnings..	458
Silindirik Buzdolabı Tasarımı	464
Low Velocity Impact Response of Aluminum Honeycomb/Glass Fiber Reinforced Sandwich Structures.....	469
PID Algoritması ile Çizgi İzleyen Robot Kontrolü.....	475
Analysis of Complex Thermodynamic Steam and Gas Turbine Cycles Using Cycle Pad	479
Free Vibration Analysis of Axially Exponentially Functionally Graded Beams by Differential Quadrature Method.....	491
Deniz Suyu Desalinasyon Teknikleri Konusundaki Son Gelişmeler	497

3rd International Students Science Congress
3-4 May 2019, İzmir - Turkey

Tavuk Tüyü Fiber/PLA Biyokompozitin Mekanik Özelliklerine Uzun Süreli Yaşlandırmanın Etkisinin İncelenmesi	505
Simfizis Pubis Ayrılmasının Plak ile Tespitinin Sonlu Elemanlar Yöntemi İle Analizi	510
Finite Element Stress Analysis of a Functionally Graded Plate	517
Studying the Condition Based Maintenance Dataset of Naval Propulsion Plants Using Regression ANN	524
Mechatronics Engineering / Mekatronik Mühendisliği	532
Synchronization of Diffusionless Lorenz Chaotic System for Masking Data	533
Development of a Multi Degrees of Freedom Redundant Reconfigurable Planar Parallel Manipulator with 2 DOF Planar Detachable Serial Dyad	540
Material Science and Engineering / Malzeme Bilimi ve Mühendisliği	548
Optimization of ZnO Nanowires via Hydrothermal Growth	549
Anotlama Parametrelerinin Ti ₆ Al ₄ V Alaşımı Üzerinde Oluşturulan TiO ₂ Nanoyapıların Yüzey Özelliklerine Etkisi	552
Preparation and Characterization of Graphene Synthesized by Different Methods	556
Investigation of Mechanical Properties of Al/SiC/nano-FeB Hybrid Composites	564
Nanotechnology / Nanoteknoloji	568
A Study on Improvement of Mechanical Properties of Bone Cement with ZnO Functionalized Carbon Fiber Derivatives	569
Development of Glucose Biosensor from Hierarchical Graphene/ α -Fe ₂ O ₃ Nanocomposites	573
Işığa Duyarlı İlaçların Taşınmasında Kullanılacak PLGA Temeli Polimerik Nanoparçacıkların Sentezi ve Karakterizasyonu	577
Petroleum and Natural Gas Engineering / Petrol ve Doğalgaz Mühendisliği	583
Practical Application of Cased Hole Logs in Fluid Movement Detection	584
Physical Therapy and Rehabilitation / Fizyoterapi ve Rehabilitasyon	591
Using Force-Sensing Resistor – 0.6 Inch Diameter Circle- PI- 1696 to Determine In-Situ Force of Patella	592
Congress Photograph Gallery / Kongre Fotoğraf Galerisi	598

Invited Speeches / Davetli Konuşmalar

New Trends in Organic Solar Cells

Şule Erten Ela

Ege University, Solar Energy Institute, 35100 Bornova-İzmir, Turkey

suleerten@yahoo.com, sule.erten@ege.edu.tr

Keywords: Inverted bulk heterojunction solar cells, ZnO cathode layer, energy, Poly (3-hexylthiophene), C₆₀

Abstract

Inverted bulk heterojunction solar cells are great of interest in recent years because of their stability and lifetime according to normal type bulk heterojunction solar cells. In this paper, solution processed P3HT:C₆₀ blend were prepared in different ratios. Solution processable ZnO cathode layer is used as electron collecting electrode. And bulk heterojunction solar cells were tested in two different ZnO cathode layer. Single and double layered ZnO cathode layers were prepared two methods. One of them, nanoporous single layer ZnO that prepared from Zn²⁺ and HO⁻ solution system. And the other one was double layered ZnO cathode layer that prepared from Zn²⁺ and HO⁻ solution onto ZnO backing layer system. All processes were carried out using spin coating techniques. Bulk heterojunction solar cells were characterized using different blend ratios (2:0.5 and 2:1) of P3HT and C₆₀. Nanostructured morphologies of ZnO cathode layers and P3HT:C₆₀ films were investigated by means of Atomic Force Microscopy, which are correlated with device performance. Better device performance is observed in a double-layered ZnO cathode electrode layer/P3HT:C₆₀/Gold device configuration with the 2:0.5 blend ratio of P3HT:C₆₀ film.

1. Introduction

Energy is a problem of our era because of the greenhouse effect of fossil fuels. Recent problems on energies and environments request a new system for providing an environment friendly and safe energy source. For this reason, new trends for solar cells goes to fabrication of organic solar cells have attracted global attention as its promising candidate [1, 2]. Bulk heterojunction solar cells have attracted considerable attention in the past years owing to their inexpensive, lightweight and flexible fabrication [3-6]. The device structures almost consisted of glass/ indium tin oxide (ITO)/ poly(3,4-ethylenedioxythiophene) (PEDOT):poly(styrene sulfonate) (PSS)/ p-conjugated polymer: fullerene derivative/ lower work functional electrode (Al) which are called normal type solar cells. However, their stability and longevity compared to inorganic solar cells have been the major drawback for faster commercialization. Normal type bulk heterojunction solar cells suffer from degradation of the top electrode, which is normally made of a low work function metal that is reactive and oxidized easily in air. Inverted type solar cells have a reversed device structure against normal type solar cells and photogenerated electrons flow through external circuit from ITO electrode to higher work functional electrode in this type device. The inverted bulk heterojunction devices are attractive concept to improve stability because it only uses electrode and interface materials with a higher work function and significantly improved longevity [7, 11]. That's reason, inverted structure has received much attention as a new device structure to get high efficiency as well as good stability. In the present study, we have focused on optimizing the inverted bulk heterojunction devices using P3HT:C₆₀ active layer. Different blend ratios for P3HT:C₆₀ active layer have been used. Here, it is reported the inverted bulk heterojunction solar cell device efficiency for P3HT:C₆₀ active layer. C₆₀ material is more stable than PCBM material and solution processed active layers were prepared for P3HT:C₆₀ material.

. Experimental

2.1. Materials

P3HT is supplied from Rieke Metals, Inc. Experimental parts are carried out using high pure grade materials.

2.2. Synthesis of Single and Double ZnO Layers and XRD characterization of Porous ZnO Layer

2.2.1 Preparation of Double ZnO Layer

a) ZnO Backing Interlayer by spincoating process

The preparation of backing layer is described in our previous paper [12]. All ZnO interlayer preparations are carried out in air. The thicknesses of all ZnO interlayers are kept constant as 100 nm for comparison of their performances in inverted bulk heterojunction solar cells. Thicknesses of ZnO interlayers are measured using profilometer.

b) Porous ZnO Interlayer onto ZnO Backing Interlayer by spincoating process (Double Layer ZnO)

FTO glass is spincoated with ZnO backing interlayer and calcined at 450 °C, then the solution of zinc acetate (0.04 M) and sodium hydroxide (0.4 M) at 80 °C is spincoated on ZnO backing interlayer. After the deposition of ZnO interlayers, the samples are calcined at 450 °C.

The nanomaterials are characterized using scanning electron microscopy Phillips Analytical XRD 45kV 40mA, with Cu-K- α radiation (1.540 Armstrong) and powder X-ray diffraction (Philips XL-30S FEG).

2.3. Inverted Type Bulk Heterojunction Device Fabrication and Characterization

Inverted bulk heterojunction solar cells are fabricated in a FTO/ZnO (Single or double layer)/P3HT:C60 (different blend ratios)/Au device configuration. Devices are prepared in the following procedures. FTO glasses are cut into square plates (2.5x2.5 cm). Fluorine-doped tin oxide (FTO) is patterned by etching with an acid mixture of HCl and Zinc dust. All FTO glasses are cleaned with acetone and isopropyl alcohol for 20 minutes in ultrasonic bath then, Helmanex soap and distilled water are used for cleaning, afterwards ethanol is used and finally dried by N₂ purging. ZnO backing layer is spin coated at 2000 rpm onto FTO coated glass substrate. Then the substrate is annealed for 30 min at 450 °C. The thickness of flat ZnO backing Layer is measured as 200 nm using profilometer. Then ZnO porous layer were spincoated on dense ZnO backing layer. Then, the films are sintered at 450 °C for 30 min. The blend ratios of P3HT:C60 is prepared with 2:1 and 2:0.5 by weight, respectively. P3HT:C60 active layers are dissolved in chlorobenzene solvent and stirred overnight. The solution composed of P3HT:C60 with 2:1 and 2:0.5 blend ratios are then covered on the top of the ZnO electron collecting layers. The last process is thermal evaporation of metal contact in the glove box. 60 nm of Au anode is thermally evaporated through shadow mask.

2.4. Inverted type Bulk Heterojunction Solar Cell Device Characterization

The current density versus voltage (J-V) characteristics of the devices are measured with a Keithley 2400 source measurement unit. The device performances are characterized under AM 1.5 G condition with an illumination intensity of 100 mW/cm² using a solar simulator. J-V curves are measured both in dark and under illumination.

3. Results and Discussion

3.1. Evaluation of Inverted Bulk Heterojunction Solar Cell

In this paper, the performances of inverted type bulk heterojunction solar cells are reported using a noncorrosive Au metal as a hole collecting electrode, and a transparent conducting oxide (TCO)/n-type semiconductor electrode, zinc oxide (ZnO) as an electron collecting electrode. In device structure (Fig. 1), electrons can transport to FTO electrode through ZnO cathode electrode easily. Moreover, the valance band of ZnO cathode electrode layer is efficient to prevent back electron or hole transfer with its high energy barrier.

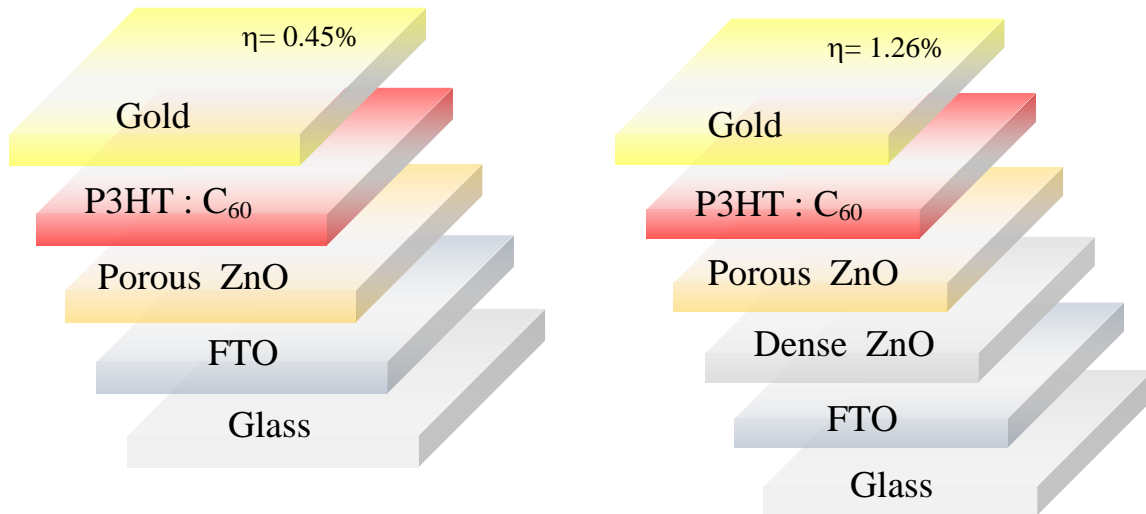


Figure 1. Schematic illustration of inverted bulk heterojunction solar cells

Atomic force microscopy (AFM) is a powerful means to observe film surface morphology. AFM images of single ZnO cathode electrode layer in noncontact mode are shown in Fig 2. Fig. 3(a) exhibits a surface structure of double ZnO layer. Fig.4 shows J-V curve of devices.

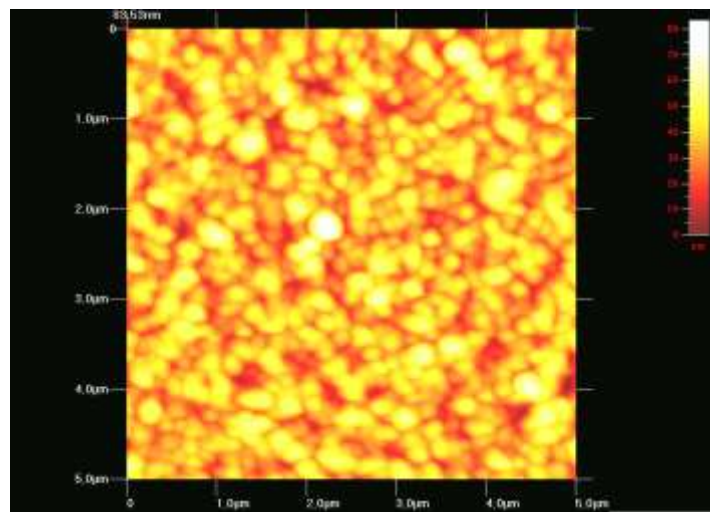


Figure 2. AFM image of Single layer ZnO electrode

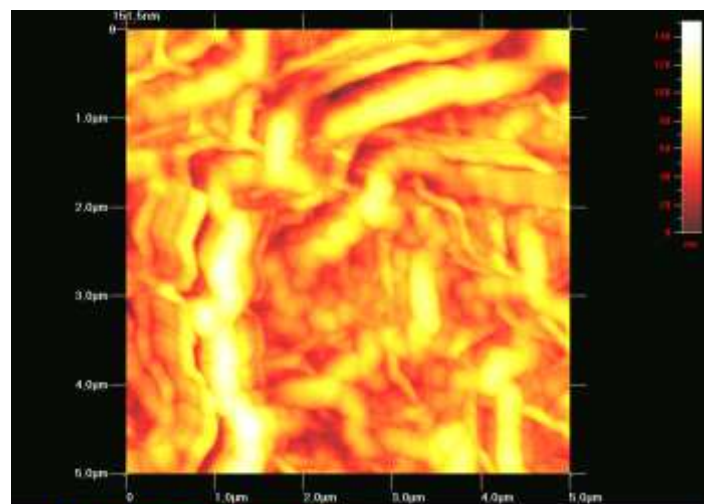


Figure 3. AFM image of Double Layer ZnO electrode

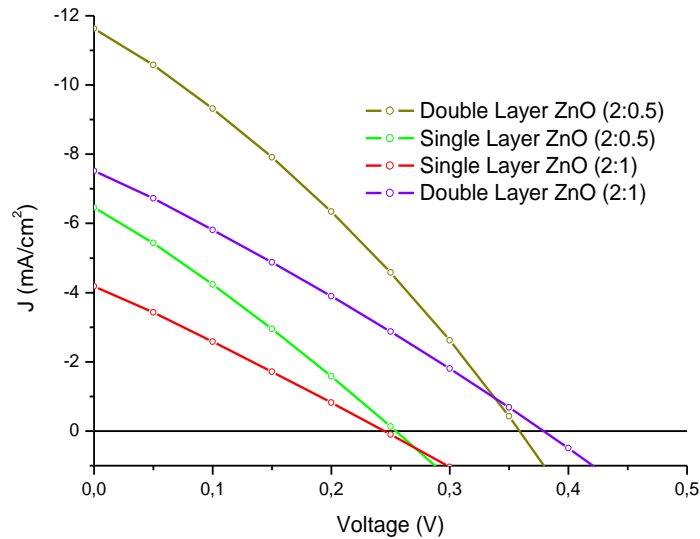


Figure 4. J-V curve of FTO/ZnO (single or double layer)/P3HT:C₆₀/Gold device

4. Conclusion

Inverted-type bulk heterojunction solar cell devices have been paid more and more research attention because of their high stabilities and long lifetimes according to conventional normal-type cell structures. This paper reports the photovoltaic device characterization for the performance evaluation of the inverted type organic solar cells consisting of ZnO cathode electrode layer and P3HT:C₆₀ active layers. Also, results show that ZnO cathode electrode plays an important role as the electron collecting layer and the hole blocking layer.

Acknowledgement

We acknowledge the Project support funds of Alexander von Humboldt Foundation and Scientific Research Council of Turkey (TUBITAK).

References

- [1] Tang CW (1986) Two-Layer Organic Photovoltaic Cell, *Appl. Phys. Lett.*, 48:183-85.
- [2] Sariciftci NS, Smilowitz L, Heeger AJ, Wudl F, (1992) *Science* 258 (5087) 1474.
- [3] Kippelen B, Bredas JL, (2009) *Energy Environ. Sci.* 2 251–261.
- [4] Bekci DR, Erten-Ela S, (2012) *Renewable Energy*, Volume 43, pp.378-382
- [5] Shaheen SE, White MS, Olson DC, Kopidakis N, Ginley NS (2007) Inverted bulk heterojunction plastic solar cells, *SPIE/Newsroom*, doi:10.1117/2.1200704.0756.
- [6] Erten-Ela S, Villegas C, Delgado JL, Martin N (2015) *New Journal of Chemistry (RSC)*, 39, 1477-1482.
- [7] Liao HH, Chen LM, Xu Z, Li G, Yang Y (2008) *Appl. Phys. Lett.* 92, 173303-1-3.
- [8] Steim R, Choulis SA, Schilinsky P, Brabec CJ (2008) *Appl. Phys. Lett.* 92: 093303-1-3.
- [9] Gaynor W, Lee JY, Peumans P (2009) *ACS Nano.* 4, 30–34.
- [10] Jorgensen M, Norrman K, Krebs FC (2008) *Sol. Energy Mater. Sol. Cells* 92: 686–714.
- [11] Hsieh CH, Cheng YJ, Li PJ, Chen CH, Duboscq M, Liang RM, Hsu CS, *Am J* (2010) *Chem. Soc.* 132 4887–4893.
- [12] Erten-Ela S, Cogal S, Turkmen G, Icli S (2010) Hybrid Solar Cells Using Nanorod Zinc Oxide Electrodes and Perylene Monoimide-Monoanhydride Dyes. *Current Appl. Physics* 10(1): 187-192.

Agricultural Engineering / Ziraat Mühendisliği

Physiological and Growth Responses of Cubana Kordes Roses to Cd Stress and Plant Growing Parameters

Haya Abusalih*, Ayşen Akay

Selçuk Univ., Dept. of Soil Science and Plant Nutrition, Alaaddin Keykubat Campus, Konya, Türkiye

*Corresponding author: hayaabusaleh7@gmail.com

Keywords: heavy metals, cadmium, bioavailability, uptake, rose

Discipline: Agricultural Engineering

Abstract

Cadmium is a non-essential metal, but because of its potential toxicity to a human being, and the relative mobility in the soil-plant system it has attention at many studies. Widespread distribution and high mobility of cadmium make it a potential contaminant in many natural environments. Phytoremediation is an in situ, cost-effective potential strategy for cleanup of sites contaminated with trace metals. Selection of plant variety is an important factor for successful field phytoremediation. This study was carried out in order to follow the development of *Cubana kordes* rose, which is an ornamental plant used in environmental regulation studies, at Cd polluted environment. For this purpose, a pot experiment was carried out. Cadmium submitted to five concentrations (0, 25, 50, 100, 200 mg Cd/kg) and applied on *Cubana kordes* roses at greenhouse condition. In addition, different amounts of leonardite (0%, 3%, 6%) were applied to the plant growing medium. The plant height, number of branches and chlorophyll content exhibited no considerable adverse effect indicating the plants' tolerance towards heavy metals during the trial.

Introduction

Cadmium is one of heavy metals that have toxic effects even in small amount, for many years, it has emitted to the environment and it is found in soil, water, fish, and food [1]. When Itai- Itai disease appear in Japan, Cd was consider as a most series metal contaminant [2]. On the other hand, it is not degradable in natural because of its solubility in water and it can be easily bio-accumulate [3]. Increasing Cd concentration in soil over time is evident. The sources of increasing Cd concentration in soils are predominantly through fertilizers, soil amendments, manures, and sewage bio-solids [4].

Cadmium is one of the most dangerous heavy metals due to its high mobility, and affects plants in small concentration [5]. The uptake of Cd by plant increases proportionally to increasing soil Cd when the soil contains substantial concentration of Cd⁺² salts [6]. Some researchers reported that, the iron uptake by the plant can be suppressed when the plant growing medium has a high cadmium content [7]. In other research, Cd toxicity appeared to induce phosphorous deficiency or reduce manganese transport problems [8]. In general, Cd has been shown to interfere with the uptake, transport and use of several elements (Ca, Mg, P and K) and water by plants [9]. In many plant species, cadmium toxicity can decrease with increasing temperature, and usually when soil acidity decreasing plant death rate increased [5].

Cadmium is a highly mobility in the soil and is easily transported in the plant and then distributed to all plant organs and this metal is taken up from soil through plant roots. The normal limits of Cd content in plants were between 0.2-0.8 mg kg⁻¹ and the toxic concentrations of Cd were defined as 5-30 mg kg⁻¹ [10-12]. Plants grown in soil containing high levels of Cd show chlorosis, growth inhibition, leaf roll, browning of the root ends, damage of photosynthetic machinery, reduction in chlorophyll synthesis, and visible signs of death, which finally reflected in death [11; 13-19]. Cadmium has different toxic effects in plant physiological processes. One of the processes inhibited by Cd is Nitrogen-metabolism. Cadmium inhibit the nitrate reductase activity in the shoots, because of the absorption of nitrate, in this situation, it's reduce transport from roots to shoots[20].

Phytoremediation uses to decrease the toxic effect of Cd in the environment without carried any damage to environment. Phytoremediation define as the use of green plants to remove pollutants [13; 21]. For these processes, we have to use hyper-accumulator plants, and some study's shows that some of ornamental plants play as a hyper-accumulator according to its ability to uptake heavy metals from soil and accumulate in there plant parts.

This study conducted as a preliminary experiment, we wanted to research the growth responses of *Cubana kordes* roses to a high concentration of cadmium by knowing its effect on chlorophyll content, number of shoots and the plant height. In addition to, we want to study the ability of this rose's species to accumulate Cd in their plant parts without a high effecting on plant metabolism.

Material and Methods

A experiment conducted to study the effect of cadmium concentration and leonardite on growth and physiological response of *Cubana Kordes* roses. This experiment was done in the greenhouse of Agricultural Faculty/Selcuk University. The soil and *Cubana Kordes* rose seedlings for greenhouse experiments took from Directorate of Parks and Gardens/Selcuklu Municipality. The soil was sieved through a 4 mm sieve, weighed and mixed with three different leonardite doses (0%, 3%, 6%). The pots were filled with this mixture (6 kg/pot). The leonardite obtained from a special company. Some features of the leonardite used in the experiment are presented in Table 1. The trial was experimented in a total of 75 pots as 5 replications. The experiment was arranged according to the random factorial trial design. Macro and micronutrient requirements of the plants were calculated and plants were regularly treated with Hoagland solution.

In addition, the experiment subject Cd given to the pots in the following doses, (0, 25, 50, 100, 200 mg Cd kg⁻¹) in the form of 3CdSO₄.8H₂O (Figure 1).

LEO. 0%				
0 Cd	25 Cd	50 Cd	100 Cd	200 Cd
LEO. 3%				
0 Cd	25 Cd	50 Cd	100 Cd	200 Cd
LEO. 6%				
0 Cd	25 Cd	50 Cd	100 Cd	200 Cd

Figure 1. Experiment plan

We performed the planting of roses in December. The Hoagland fertilizer solution applied with irrigation water. The solution content is as follows: Fe-EDTA, H₃BO₄, MnSO₄, CuSO₄.5H₂O, Zn-EDTA, (NH₄)₆Mo₇O₂₄.4H₂O, CaNO₃, KH₂PO₄, KNO₃, MgSO₄ (16.50, 2.86, 1.29, 0.393, 1.333, 0.018, 590, 219.5, 443.5, 492 mg/L), respectively.

The experiment soil was analyzed. pH and EC of soil and leonardite were measured in H₂O (1:2.5 soil: water), CaCO₃ content (using Scheibler calcimeter) [22]. Organic matter was determined using a modified Walkley-Black procedure [23] (Table 1).

Property	Soil	Leonardite
pH	8.28	3.58
EC (μS/cm)	75	1385
Organic Matter (%)	0.12	-
CaCO ₃ (%)	0.98	-
Moisture (%)	20.92	16.94

The water needs of the plants were met by taking into account the soil moisture condition and the need of the plant. When the plants developments were completed at the end of 135 days, chlorophyll SPAD measurement was determined with Minolta 502. Plant height and shoot numbers were determined. The results obtained from the greenhouse experiment were compared by using the variance analysis and Tukey tests by using MINITAB package programs.

Results and Discussion

In the experiment; there was no statistically significant difference between chlorophyll content of rose petals. The mean chlorophyll content varied between 52.09-55.78 (Figure 2); although the application of leonardite does not make a significant difference statistically, it has a positive effect on plant chlorophyll synthesis in general.

The number of branches of Cubana cordes roses was not affected by high doses of cadmium. Similarly, between leonardite applications was found no statistical difference at the number of branches of roses. However, the together effect of leonardite * Cd was statistically significant ($P < 0.05$). The average values are between 3.75-8.00 pcs / plant (Figure 3).

According to results; plant height was not affected by cadmium applications;but, statistically significant differences were found between leonardite applications ($P < 0.05$). Plant height values ranged from 20.13 to 28.47 (Figure 4).

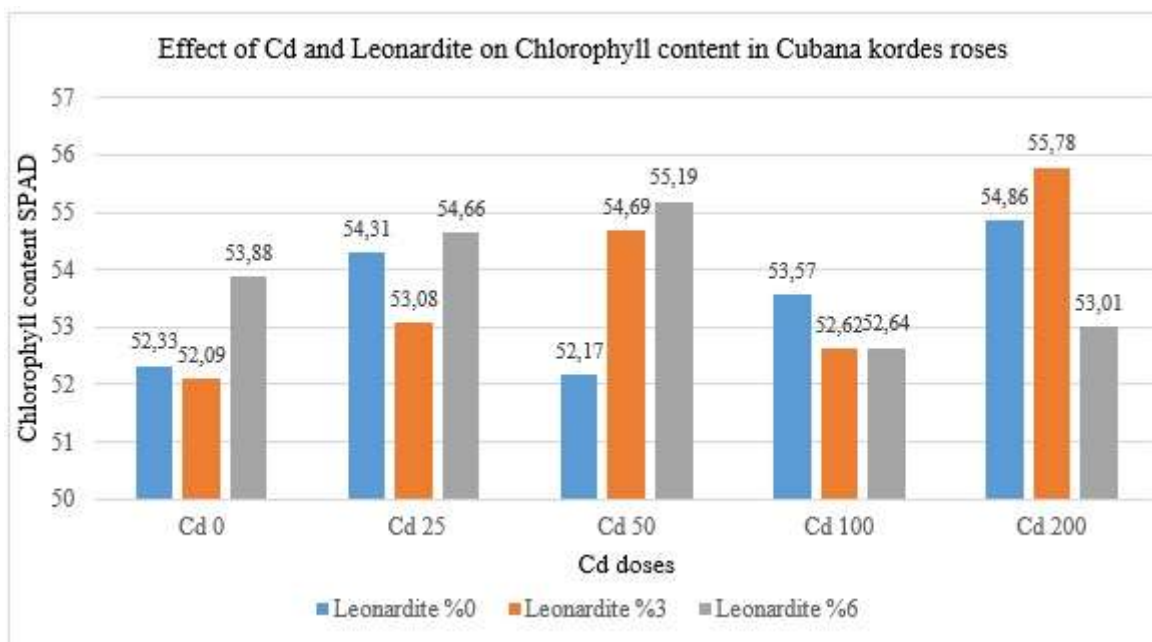


Figure 2. Effect of Cd and Leonardite application on Chlorophyll content in *Cubana kordes* roses

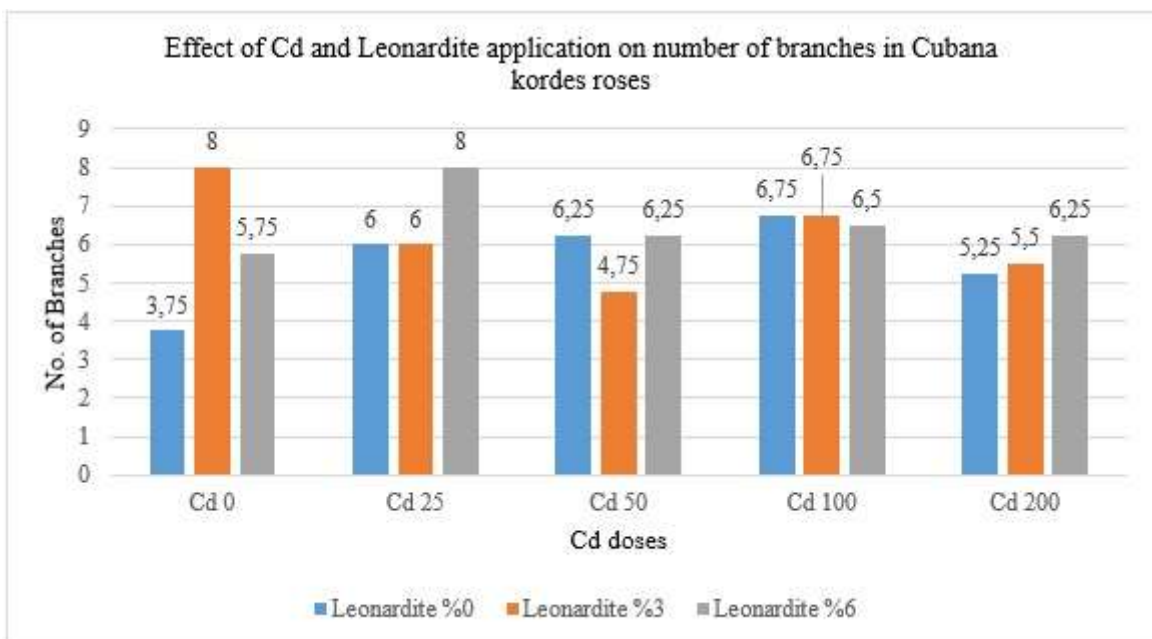


Figure 3. Effect of Cd and Leonardite application on number of branches in *Cubana kordes* roses

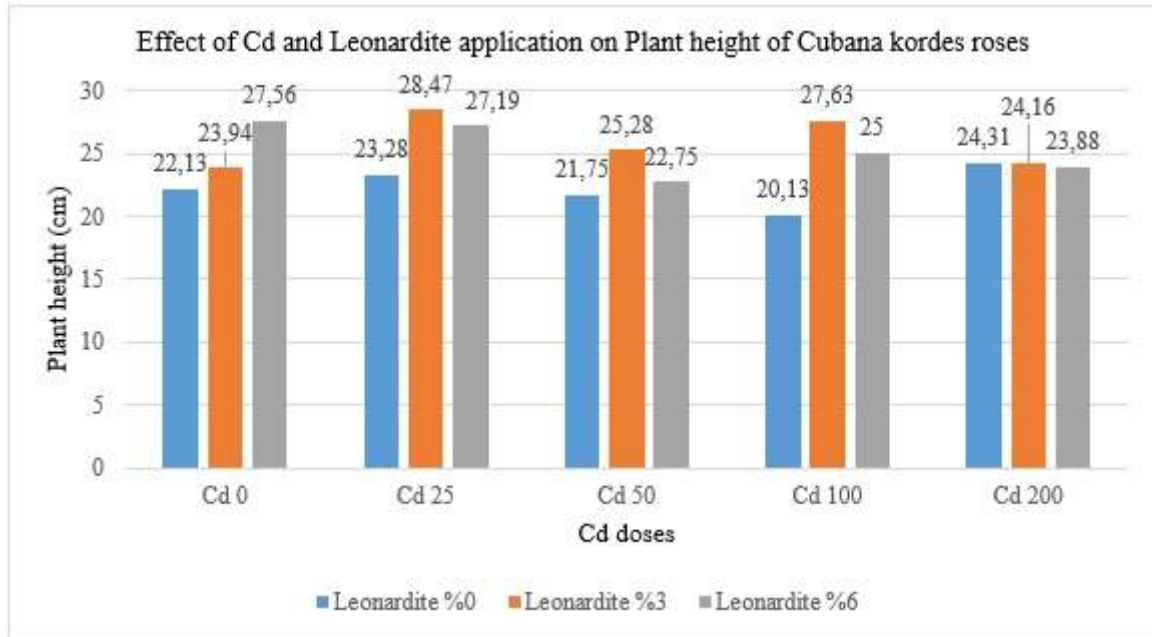


Figure 4. Effect of Cd and Leonardite application on Plant height of *Cubana kordes* roses

Acknowledgment

This work is derived from the current master's thesis, we would like to thank Selçuk University BAP for its financial support in this study.

References

- [1] Tierney DR (1980) Status assessment of toxic chemicals : cadmium. Environmental Protection Agency, Office of Research and Development [Office of Environmental Engineering and Technology], Industrial Environmental Research Laboratory.
- [2] Kobayashi J (1978) Pollution by cadmium and the Itai-itai disease in Japan. In 'Toxicity of Heavy Metals in the Environment, Part 1'(Ed FW Oehme) pp. 199-260. Marcel Dekker Inc.: New York and Basel
- [3] Sharma A, Sachdeva S (2015) Cadmium toxicity and its phytoremediation: A review. International Journal of Scientific and Engineering Research 6:395-405
- [4] McLaughlin MJ, Tiller K, Naidu R, Stevens D (1996) The behaviour and environmental impact of contaminants in fertilizers. Soil Research 34:1-54
- [5] Das P, Samantaray S, Rout GR. (1997) Studies on cadmium toxicity in plants: A review. Environmental Pollution 98:29-36
- [6] Smolders E. (2001) Cadmium uptake by plants. International Journal Of Occupational Medicine and Environmental Health 14:177-83
- [7] Haghiri F. (1973) Cadmium Uptake by Plants 1. Journal of Environmental Quality 2:93-5
- [8] Godbold D, Hüttermann A (1985) Effect of zinc, cadmium and mercury on root elongation of *Picea abies* (Karst.) seedlings, and the significance of these metals to forest die-back. Environmental Pollution Series A, Ecological and Biological 38:375-81
- [9] Sharma A, Mukherjee A, Talukder G (1985) Modification of cadmium toxicity in biological systems by other metals. Current Science:539-49
- [10] Gruenhage L, Jager I (1985) Effect of heavy metals on growth and heavy metals content of *Allium Porrum* and *Pisum sativum*. Angew Bot 59:11-28
- [11] Kabata-Pendias A (2010) Trace elements in soils and plants. CRC press
- [12] Schulze E, Beck E, Müller-Hohenstein K (2005) Plant Ecology. Vol. 12. Springer, Berlin-Heidelberg

**3rd International Students Science Congress
3-4 May 2019, İzmir - Turkey**

- [13] Salt DE, Blaylock M, Kumar NP, Dushenkov V, Ensley BD, et al. (1995) Phytoremediation: a novel strategy for the removal of toxic metals from the environment using plants. *Nature biotechnology* 13:468
- [14] Di Toppi LS, Gabrielli R (1999) Response to cadmium in higher plants. *Environmental and experimental botany* 41:105-30
- [15] Wojcik M, Tukiendorf A (2004) Phytochelatin synthesis and cadmium localization in wild type of *Arabidopsis thaliana*. *Plant Growth Regulation* 44:71-80
- [16] Mohanpuria P, Rana NK, Yadav SK (2007) Cadmium induced oxidative stress influence on glutathione metabolic genes of *Camellia sinensis* (L.) O. Kuntze. *Environmental Toxicology: An International Journal* 22:368-74
- [17] Das P, Samantaray S, Rout G (1997) Studies on cadmium toxicity in plants: a review. *Environmental pollution* 98:29-36
- [18] Alcántara E, Romera FJ, Cañete M, De la Guardia MD (1994) Effects of heavy metals on both induction and function of root Fe (III) reductase in Fe-deficient cucumber (*Cucumis sativus* L.) plants. *Journal of Experimental Botany* 45:1893-8
- [19] Hegedüs A, Erdei S, Horváth G (2001) Comparative studies of H₂O₂ detoxifying enzymes in green and greening barley seedlings under cadmium stress. *Plant Science* 160:1085-93
- [20] Hernandez L, Carpena-Ruiz R, Garate A (1996) Alterations in the mineral nutrition of pea seedlings exposed to cadmium. *Journal of Plant Nutrition* 19:1581-98
- [21] Salt DE, Smith R, Raskin I (1998) Phytoremediation. *Annual review of plant biology* 49:643-68
- [22] Jackson M (1969) *Soil Chemical Analysis-Advanced Course: A Manual of Methods Useful for Instruction and Research in Soil Chemistry, Physical Chemistry of soils, Soil Fertility and Soil Genesis.*
- [23] Walkley A, Black IA (1934) An examination of the Degtjareff method for determining soil organic matter, and a proposed modification of the chromic acid titration method. *Soil Science* 37(1):29-38.

Growth Responses of *Pepita kordes* Roses to Ni Stress and Ni Accumulation Characteristics

Ayşen Akay, Haya Abusalih*

Selçuk Univ., Dept. of Soil Science and Plant Nutrition, Alaaddin Keykubat Campus, Konya, Türkiye

*Corresponding author: hayaabusaleh7@gmail.com

Keywords: contaminated soil, heavy metals, ornamental plant, phytoremediation

Discipline: Agricultural Engineering

Abstract

Nowadays one of the most environmental pollution reason is contamination of heavy metals. As a known, the concentration of heavy metals increase due to some factors; like industrial activities, traffic emissions and domestic waste. Most of the heavy metals are come from petrol, diesel oil and there emitted by vehicle exhaust. Soil and water contaminated with heavy metals are one of the most serious causes of people, plant, and animal health problems; like affects the liver, kidneys, and the nervous system. In this study, we take eight samples for *pepita kordes* roses and there soils from the middle refuges of the highway in Konya city. These samples were taken from 4 km distance in that way with 500 m intervals. Then these plants were divided to flower, stem, and leaves and do the requisite analysis for plant and soil. The result of the analysis showed that Ni concentration in leaves is between 0.76-2.13 mg/kg, in flowers 1.65-3.39 mg/kg, and in stems 0.50-2.15 mg/kg. The Ni concentration can be taken from soils by the plant is between 0.319-0.633 mg/kg. These values are below the limit values for soil and plant.

Introduction

Heavy metals are increasing rapidly in soil and water by weathering of rocks and anthropogenic activities and are now emerging as a major health hazard to humans and plants. Among them, Nickel (Ni^{+2}) is a controversial element because of debate on its essentiality or non-essentiality in plants [1]. According to some researchers, the plant for normal growth requires Ni in very low amounts (0.01 to 5 $\mu\text{g/g}$ dry weight) [2]. Nickel content in most plants is range from 0.05 to 5 mg kg^{-1} dry weight [3]. Due to human activities such as mining works, emission of smelters, burning of coal and oil, adding sewage sludge on soil, phosphate fertilizers and pesticides in some area Ni^{+2} concentration is increasing [4]. Several enzyme systems in bacteria and lower plants require Ni. Examples include NiFe-hydrogenase, carbon monoxide dehydrogenase, acetyl-CoA decarbonylase synthase, methyl-coenzyme M reductase, superoxide dismutase, Ni-dependent glyoxylase, aci-reductone dioxygenase, and methylene ureas [5-7]. It is the activation of urease, to date, that is the most commonly recognized function of Ni in higher plants [5]. Ni can also replace Zn or Fe, and other transition metal ions, in certain other metalloenzymes of lower plants [6], and can probably do so to some degree in higher plants and animals. Ni^{+2} deficiency is also found associated with the reduced symbiotic hydrogenase activity in *Rhizobium leguminosarum* that may directly affect the symbiotic N_2 fixation [8]. Thus, Ni^{+2} is an essential micronutrient for N_2 metabolism in plants. Excess Ni adversely affects germination process and seedling growth traits of plants by hampering the activity of the enzymes such as amylase and protease as well as disrupting the hydrolyzation of storage food in germinating seeds [9]. Several studies in plants including maize [10] and cowpea [11] have confirmed that Ni toxicity can result in inhibited lateral root formation and subsequent development.

Plants grown in high Ni^{+2} containing soil showed impairment of nutrient balance and resulted in the disorder of cell membrane functions. Thus, Ni^{+2} affected the lipid composition and H-ATPase activity of the plasma membrane as reported in *Oryza sativa* shoots [12]. Other symptoms observed in Ni^{+2} treated plants were related with changes in water balance. High uptake of Ni^{+2} induced a decline in water content of dicot and monocot plant species. The decrease in water uptake is used as an indicator of the progression of Ni^{+2} toxicity in plants [13].

Nickel uptake from the soil is as absorption by plant roots. Nickel is usually absorbed from the soil or from solution culture in ionic form (Ni^{+2}) [14]. Many studies reported that plants when supplied as ionic form Ni it will easily to be absorbed, but it cannot when supplied in the chelates form [15]. Some

of the environmental factors that effects on Ni uptake by the plant are soil acidity, CEC, organic and lime contents, moisture potential, and the concentration of macro and micronutrients.

One of the most important factors is soil pH. When soil pH values decrease (increasing in soil acidity) the exchangeable Ni content increase [16]. The Ni concentration in plant and its absorption enhanced by increasing the phosphate content in soils, organic matter present in soil inhibits Ni uptake by plants to some extent, and fertilizers decrease the total absorption of Ni [17]. Nevertheless, in some studies show that in wheat plants and other food plants if phosphorus fertilizers were dominate than the accumulation of Ni in plants will decrease. As well as Ni uptake will be enhance when N-fertilizers was a dominated [14]. Because of high mobility of Ni, it can be accumulated in vegetative and the reproductive parts of the plant, most of Ni translocate and accumulate in leaves during vegetative growth, but when leaves become age most of Ni transported from leaves to seeds [15]. Ni accumulation increase in fruit parts during the growing period [18].

Nickel effect on various physiological processes of the plant, and its starting from the effect on enzyme activities. Heavy metals may directly inhibit enzymes by interacting with protein SH-groups. Because of that, enzymes are inactivated. In the presence of Ni, the contents of mineral nutrients in plant organs may increase, decrease, or stay even. As well as, increasing in Ni concentration that affects negatively on transpiration and water content in plants by decreasing the leaf area and stomata numbers per unit of leaf area, therefore, transpiration may decrease [2].

In this study, nickel uptake and deposition of *pepita kordes* roses, which is one of the most commonly used ornamental plants and is grown on pollutants on roads with high traffic density, was investigated.

Material and Methods

In our studies, we take samples from *Pepita Kordes* Rose, which is a rose miniature special with flowers grouped created by W. Kordes & Sons in Germany in the year 2004. The delicate flowers of a strong pink with double petals, slightly fragrant. It blooms in trusses of 6 to 8 flowers, every 45-55 petals. At maturity, reach a height of 50 cm and a width of 40 cm. It blooms repeatedly from May until late fall. This rose holds seven medals (gold and silver) won in the contests international [19].

In this study, eight samples of *Pepita kordes* roses and there soils from the middle refuges of the highway in Konya city were taken on October 1, 2018. The study site was in Turkish Stars Park, the first sample was taken from (37°58'21.7'N 32°34'38.5'E), the final sample was taken from (37°57'51.1'N 32°34'05.6'E) and other samples were taken with 500 m intervals from 4 km distance (Figure 1).

Soil samples were also taken from the points where the plant samples were taken. The plant and soil samples for analysis were prepared in the laboratory of Soil Science and Plant Nutrition Department/Selcuk University. After taken plant samples from the site, we washed plants and waited for dried on the oven, then divided plants for flowers, leaves, and stem as shown in Figure 2. After that, the plant sample was dissolved in HNO₃ on a hot plate. The samples filtered and analyzed for Ni content in plants by Atomic Absorption Spectrophotometer (AAS-Perkin Elmer Analyst 700 Model). In this study, all of the results expressed on a dry weight basis. By the way, Atomic Absorption Spectrophotometer (AAS-Perkin Elmer Analyst 700 Model) respectively determined available Ni concentration of soil and total Ni, after extracted with DTPA (Wong et al., 2002) and with HNO₃-HClO₄. The Atomic Absorption Spectrophotometer readings of Ni were made at the Soil Laboratory of East Mediterranean Transitional Zone Agricultural Research of Institute / Kahramanmaraş.

The soils of *Pepita kordes* roses were analyzed. Soil pH and EC were measured in H₂O (1:2.5 soil: water), CaCO₃ content (using Scheibler calcimeter) [20]. Organic matter was determined using a modified Walkley-Black procedure [21]. Laboratory analyzes of soil and plant samples were done with two replications.



Figure 1. The point of first, final, and other samples in our study



Figure 2. The plant parts divided to flower, leaves and stems of *Pepita kordes* roses

Results

The chemical properties of soils are shown in Table 1. The soils contain medium and high organic substance percentage. The soils are generally medium alkaline and salt-free, little salty and very lime. The total Ni content in the soils were between 22.01 and 34.82 mg/kg. These values is below the limit values as Kabata-Pendias and Pendias (1984), Topbaş et al.(1998) and the Soil Pollution Control Regulation of our Country [22; 22]. Total Ni concentrations in these soils are below to compare with the normal soil, which range from 5 to 500 mg kg⁻¹ [23]. The available Ni concentrations of soils are between 0.320 and 0.452 mg/kg. According to results of soil and plant analysis, *Pepita kordes* rose could not took the high concentrations Ni from soil. At this way the inhibition of Ni uptake, it could be because of the effect of high soil pH values. Some study's reported that the favorable pH for plants to absorption Ni from soil is below 5.6 [12; 13], but the pH of our research soils were not below that value, even these values of pH are too high.

Table 1. The results of chemical properties, total and available Ni concentrations of resources soils

Sample No.	Ni concentration in soil (mg/kg)	DTPA Ni (mg/kg)	Soil pH	Soil EC ($\mu\text{mhos/cm}$)	%CaCO ₃	Organic Matter
Sample 1	32.89	0.444	8.26	256.5	31.72	2.47
Sample 2	25.09	0.633	8.27	303.5	29.59	3.85
Sample 3	25.06	0.337	8.02	1646.0	34.04	2.95
Sample 4	29.82	0.363	8.47	552.5	32.76	2.11
Sample 5	34.82	0.452	8.54	327.5	31.25	2.60
Sample 6	26.63	0.322	8.45	418.5	32.51	2.76
Sample 7	26.68	0.394	8.48	343.5	30.37	3.06
Sample 8	22.01	0.320	8.45	597.0	31.24	3.36

Nickel concentrations of different parts of *Pepita kordes* rose samples taken from different points, where is observed traffic density, are presented in Figure 3. The examination figure showed that, Ni content of the leaves changes between 0.76-2.13 mg kg⁻¹, Ni content of the flowers changes between 1.65-3.39 mg kg⁻¹ and Ni content of the stems changes between 0.50-2.15 mg kg⁻¹. These values are generally below the critical toxicity limit for nickel (10-50 $\mu\text{g/g}$) [24]. Compared to the available Ni concentration in the soil especially, the nickel content of flower and leaf is higher than the stem.

According to these results, nickel concentrations of *pepita kordes* rose are very low. This plant is not a nickel hyperaccumulator. However, it is thought that more detailed studies should be carried out on other heavy metals intake and accumulation. In spite of a high density of traffic, heavy metal content, dust, and exhaust fumes, the plants can easily develop and show no signs of toxicity. These plants can also withstand these negative conditions. We can said that, *pepita kordes* rose may be a hyperaccumulator for another heavy metal. In addition, the nickel contents of the soil samples taken from the root zone soil of the plant were found below the limit values given in the regulations.

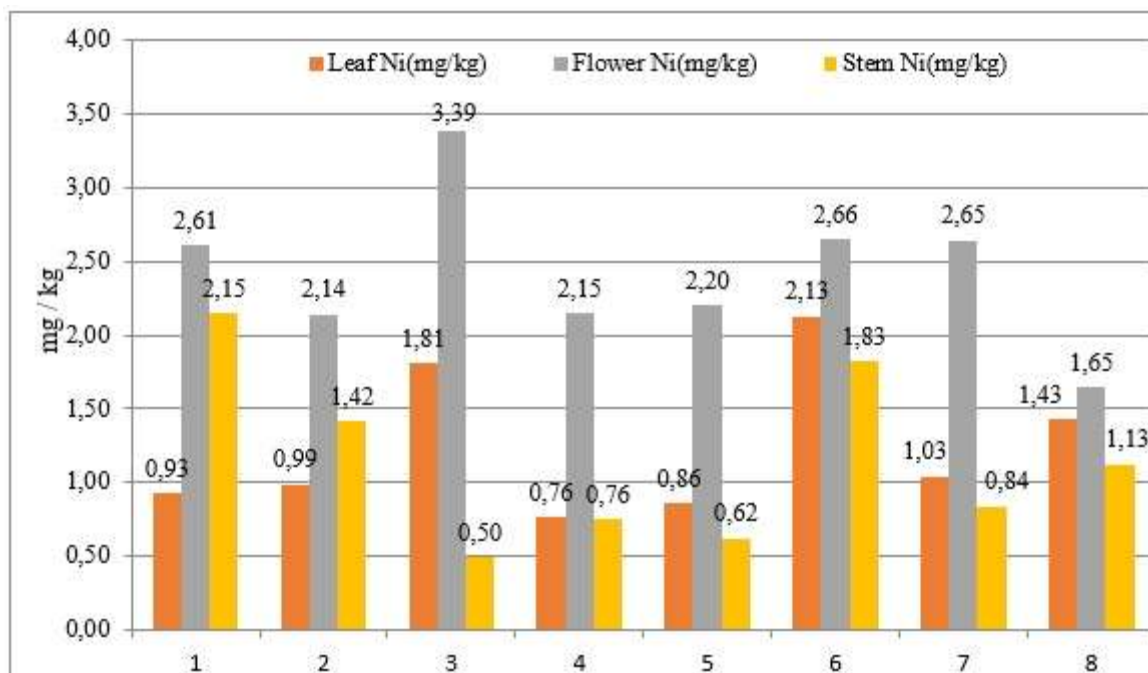


Figure 3. Ni concentration in leaves, flower, and stem of *Pepita kordes* plants.

Acknowledgment

We would express our special thanks to Konya-Selçuklu Municipality Park and Gardens Directorate for their help in this study.

References

- [1] Sachan P, Lal N. (2017) An overview of nickel (Ni²⁺) essentiality, toxicity and tolerance strategies in plants. *Asian Journal of Biology*:1-15
- [2] Seregin IV, Kozhevnikova AD. (2006) Physiological role of nickel and its toxic effects on higher plants. *Russian Journal of Plant Physiology* 53:257-77
- [3] Vanselow AP. (1966) Nickel. *Diagnostic Criteria for Plants and Soils*:302-9
- [4] Gimeno-García E, Andreu V, Boluda R. (1996) Heavy metals incidence in the application of inorganic fertilizers and pesticides to rice farming soils. *Environmental pollution* 92:19-25
- [5] Gerendas J, Sattelmacher B. (1997) Significance of Ni supply for growth, urease activity and the concentrations of urea, amino acids and mineral nutrients of urea-grown plants. *Plant and Soil* 190:153-62
- [6] Mulrooney SB, Hausinger RP. (2003) Nickel uptake and utilization by microorganisms. *Fems Microbiol Rev* 27:239-61
- [7] Walsh CT, Ormejohnson WH. (1987) Nickel Enzymes. *Biochemistry-Us* 26:4901-6
- [8] Ureta AC, Imperial J, Ruiz-Argueso T, Palacios JM. (2005) Rhizobium leguminosarum biovar viciae symbiotic hydrogenase activity and processing are limited by the level of nickel in agricultural soils. *Appl Environ Microb* 71:7603-6.
- [9] Aydinalp C, Marinova S. (2009) The Effects of Heavy Metals on Seed Germination and Plant Growth on Alfalfa Plant (Medicago Sativa). *Bulg J Agric Sci* 15:348-51.
- [10] Seregin IV, Kozhevnikova AD, Kazyumina EM, Ivanov VB. (2003) Nickel toxicity and distribution in maize roots. *Russian Journal of Plant Physiology* 50:711-7
- [11] Kopittke PM, Dart PJ, Menzies NW. (2007) Toxic effects of low concentrations of Cu on nodulation of cowpea (Vigna unguiculata). *Environmental Pollution* 145:309-15
- [12] Ros R, Cooke DT, Martinezcortina C, Picazo I. (1992) Nickel and Cadmium-Related Changes in Growth, Plasma-Membrane Lipid-Composition, Atpase Hydrolytic Activity and Proton-Pumping of Rice (Oryza-Sativa L Cv Bahia) Shoots. *Journal of Experimental Botany* 43:1475-81
- [13] Gajewska E, Sklodowska M, Slaba M, Mazur J. (2006) Effect of nickel on antioxidative enzyme activities, proline and chlorophyll contents in wheat shoots. *Biologia Plantarum* 50:653-9.
- [14] Mishra D, Kar M. (1974) Nickel in plant growth and metabolism. *The botanical review* 40:395-452.
- [15] Sengar R, Gupta S, Gautam M, Sharma A, Sengar K. (2008) Occurrence, uptake, accumulation and physiological responses of nickel in plants and its effects on environment. *Research Journal of Phytochemistry, Deira* 2:44-60
- [16] Mizuno N. (1968) Interaction between iron and nickel and copper and nickel in various plant species. *Nature* 219:1271
- [17] Halstead R, Finn B, MacLean A. (1969) Extractability of nickel added to soils and its concentration in plants. *Canadian Journal of Soil Science* 49:335-42.
- [18] Stewart D, Ross R. (1969) Nickel residues in apple fruit and foliage following a foliar spray of nickel chloride. *Canadian Journal of Plant Science* 49:375-7
- [19] Anonymous. 2019. <https://www.famousroses.eu/>
- [20] Jackson M. (1969) Soil Chemical analysis-advanced course: A manual of methods useful for instruction and research in soil chemistry, physical chemistry of soils, soil fertility and soil genesis.
- [21] Walkley A, Black IA. (1934) An examination of the Degtjareff method for determining soil organic matter, and a proposed modification of the chromic acid titration method. *Soil science* 37:29-38
- [22] Alina K-P, Henryk P. (1984) Trace elements in soils and plants. Boca Raton: CRC.
- [23] Willard LL. (1979) Chemical equilibria in soils. Chichester, UK: John Wiley & Sons
- [24] Krämer U. (2010) Metal hyperaccumulation in plants. *Annual review of plant biology* 61:517-34

Somaliland Livestock Export: Historical Review

Jamal Abdirahman Bulale

*Ege University, Faculty of Agriculture, Dept. of Animal Breeding, 35100 Bornova, İzmir, Turkey
jbulale@gmail.com*

Keywords: livestock, export, Somaliland, historical review, Berbera
Discipline: Agriculture

Abstract

Somaliland is an autonomous self-declared republic formerly known as Somaliland British protectorate in the past. Somaliland profoundly relies on livestock export as other Somali people in The Horn of Africa do and it exported almost fifty million heads of animals in the last three decades. This huge amount of export contributes to national GDP, foreign cash income and also in people's income in different ways. Somaliland has been facing a lot of livestock export challenges since 1991 and for many times it has been harshly hit by embargoes imposed by Arabian countries in the Gulf region. These embargoes have had a direct effect on the number of animals exported during ban periods while they have also affected every aspect of widely livestock dependent market in Somaliland; increasing local shilling prices and causing inflation. In this paper, we will review livestock export through Berbera port from 1991 to 2018 in statistical figures where sheep and goats form the most according to the kind of animals during that period. We will give the real statistical data about Somaliland livestock export of 28 years. This will be fruitful source for interested researchers. It is hoped that this paper will help economic experts and other people interested in Somaliland's livestock for gaining valuable information in this sector.

Introduction

The Republic of Somaliland, the breakaway autonomous region from Somalia has a good profile in livestock rearing and exporting. Livestock is the source of pastoral livelihoods, contributes to government revenues and provides employment to a wide range of professionals and other service providers. Somaliland has had a long history of live animal export to the Arabian Gulf states through the Berbera port. Berbera port was once the major source of meat for British colonial troops in Aden, taking the nickname "Aden's butcher's shop" [1]. Livestock has been the backbone for Somaliland's economy for many centuries involving with every aspect of the life of people. The livestock sector is largest in Somaliland employing a large number of people in the chain between breeding and exporting. It contributes around 28% of the national income and 85% of foreign export earnings where about 65% of the population depends either directly or indirectly on livestock and livestock products for their livelihood [2]. According to Somaliland Ministry of Planning & development, (2015) there are an estimated 9.088 million goats, 9.202 million sheep, 1.739 million camels, and 419,000 cattle [3]. Nonetheless, the livestock trade market is vulnerable to external forces, as can be seen from the two embargoes of Somali livestock imports, by Somaliland's trade partners in the Arabian Peninsula in 1997 and 2000 respectively [4]. These series embargos due to suspicions of diseases like Rift Valley Fever, Peste des Petits Ruminants (PPR) and suspected presence of rinderpest have adversely affected the income and livelihoods of pastoralist families and the national economy in general [5].

In this study we will review livestock export from Berbera port since Somaliland's break away from the rest of Somalia in May 1991 in graspable figures, presenting challenges that confront Somaliland livestock to compete with its market partners in the Horn of Africa, opportunities and the financial contribution of livestock export to Somaliland economy. In the study, we will focus on the economic loss of livestock export ban from The Gulf States to both national level as well as on the private sector.

This paper contributes to filling the periodic gap in the published papers concerning Somaliland livestock export and it will be a helpful statistical reference for the next researchers interested in this field of livestock economy.

Livestock Export in Somaliland

The livestock sector makes a significant contribution to the national economy and a majority of Somalilanders rely on this sector and related activities. Camels, cattle, and sheep/goats are the primary species in the pastoral and agro-pastoral livelihood areas. Most of the country's hard currency is generated through the export of livestock. The livestock market in Burao is Somaliland's largest livestock (Figure 1). A total of 3,089,592 livestock head were exported from January to December 2014. 98% of this were sheep/ goats [3]. According to the Somaliland ministry of trade's report, 75% of livestock export from Berbera comes from Sanaag, Sool and Togdheer regions (the three southern regions in Somaliland).



Figure 1. Largest livestock market in Burao, Somaliland.

In this section, we will review the number of animals exported from Berbera in the period between 1991 up to 2018 taking from the referable sources mainly from Berbera Port authority (Figure 2), the ministry of livestock resources and ministry of national planning.

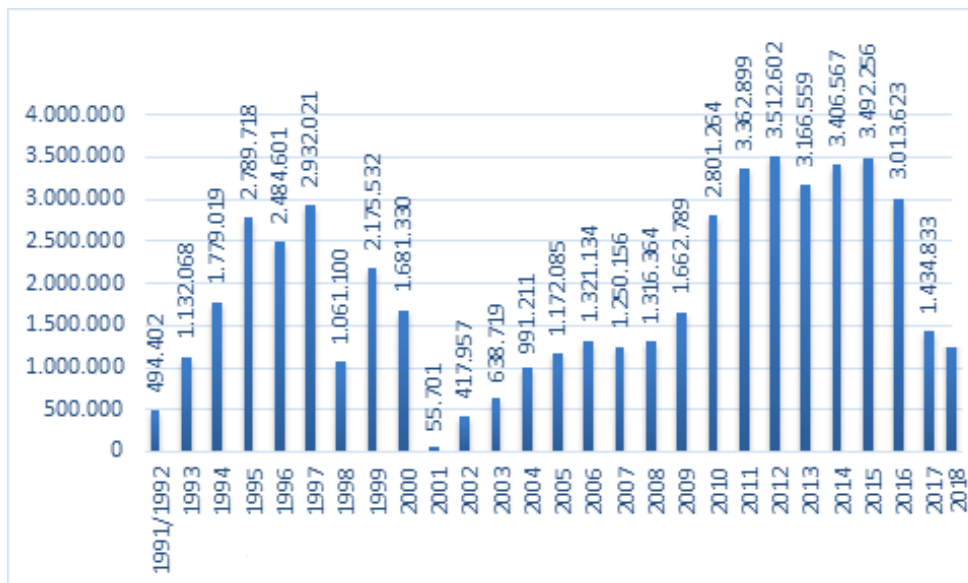


Figure 2. Livestock export from Berbera 1991-2018

3rd International Students Science Congress
3-4 May 2019, İzmir - Turkey

Table 1 demonstrates the number of each kind contributing the total number of exported livestock yearly. (Shoats: sheep and goats)

Table 1. Trends in total livestock exports from Berbera port, 1991-2018 [6]

Years	Camels	Cattle	Shoats	Total
1991/1992	102	11,792	482,508	494,402
1993	14,824	80,861	1,027,383	1,123,068
1994	38,025	55,729	1,685,265	1,779,019
1995	21,993	75,128	2,692,597	2,789,718
1996	42,828	65,127	2,376,646	2,484,601
1997	50,587	66,939	2,814,495	2,932,021
1998	11,663	92,213	957,224	1,061,100
1999	37,430	89,966	2,048,136	2,175,532
2000	16,984	63,263	1,601,083	1,681,330
2001	3513	14,522	37,666	55,701
2002	20,623	36,475	360,859	417,957
2003	19,470	74,764	544,485	638,719
2004	8,579	122,505	860,127	991,211
2005	4,741	145,945	1,021,399	1,172,085
2006	23,512	97,333	1,200,289	1,321,134
2007	15,117	83,978	1,151,061	1,250,156
2008	25,792	81,668	1,208,904	1,316,364
2009	20,414	88,048	1,554,327	1,662,789
2010	92,651	165,659	2,542,954	2,801,264
2011	107,281	150,934	3,104,684	3,362,899
2012	102,664	190,354	3,219,584	3,512,602
2013	75,728	201,879	2,888,955	3,166,559
2014	64,578	252,397	3,089,592	3,406,567
2015	61,475	160,395	3,270,386	3,492,256
2016 ^[7]	55,723	151,288	2,806,612	3,013,623
2017	38	107,610	1,327,185	1,434,833
2018	787	103,577	1,285,306	1,390,030
Total				50,927,540

Somaliland has exported a total livestock of 50,927,540 since its declaration of regaining its independence from Southern Somalia in 1991. After the Saudi Arabian ban on Somaliland's livestock was lifted in 2009, exports in Somaliland grew rapidly in the following years. For example, between 2009 and 2011 livestock exports more than doubled. In the meantime, livestock exports have fluctuated between 3 and 3.5 million animals exported each year.

One plausible explanation of this increase is the internationally accepted certification system set up within the quarantine stations which has led to rapid increase in the number of livestock exported through Berbera from just above 1.6 million in 2009 to about 2.58 million in 2010 and 3.37 million in 2011. Exports in 2012 were promising. In the first five months of 2012, a total number of animals exported is just above 770,000 heads, representing a 33% and 26% increase during the same period in 2010 and 2011 respectively.

It was expected that the investment in quarantine stations will not only expand but stabilize Somaliland livestock exports. The tidings will even be better with the opening of the third quarantine station being constructed by the SEIVQMC (Saudi-Emirates International Veterinary Quarantine Management Company). This new quarantine is expected to be able to hold more than 1.5 million heads of livestock [8].

Somaliland's livestock market is disproportionately affected by the policies of key export markets such as the Kingdom of Saudi Arabia which it exports to for the busy Hajj season. In 2016, the Kingdom banned livestock exports from both Somalia and Somaliland due to an unknown illness among livestock. However, in July 2017, Saudi Arabia lifted the ban and Somaliland was able to resume exporting millions of sheep and goats for the busy Hajj season in Saudi Arabia.

Contribution of Livestock Export to the Economy

Over two decades, Somaliland has built a successful market economy, with GDP rising to \$350 per capita – higher than Tanzania (\$280), Eritrea (\$190) and Ethiopia (\$100). Somaliland's private sector has enjoyed sustained growth, catalyzed by low levels of regulation and a comparatively small government bureaucracy [9]. Livestock is the backbone of Somaliland's growing economy with a contribution of 60% to the GDP where it also employs 70% of the population in different ways, extending from herders, truck owners, brokers, and exporters as can be seen in Table 2 [2,3,5]. It also forms 85% of the foreign export earnings in Somaliland. Apart from revenues gained from livestock export, Somaliland receives significant remittances from the Diaspora, valued at about \$800 million annually [9].

Table 2. Primary sector of work

	Adults (%)		Wage employees (%)	
	Rural	Urban	Rural	Urban
Agriculture and livestock	40.4	5.4	5.1	3.7
Mining and extraction	0.5	0.2	0.4	0.2
Manufacturing	1.4	4.7	1.4	4.3
Construction	2.8	8.4	8.0	11.6
Services	48.9	67.8	67.3	71.4

Livestock export contributes direct cash estimated about millions of dollars to Somaliland's economy. Somaliland's export markets had achieved unprecedented growth: 2.8 million head valued at US\$120 million were exported from Berbera port in 1997. Between September 2000 and November 2002, however, less than 500,000 head were exported. Extrapolating average exports from 1995-1997, represents more than 5 million head in lost exports and several hundred million dollars of foreign exchange not earned [10].

Somaliland's major livestock exports are sheep and goats, accounting for 91% of all animal exports. In 2010 a total of 2.352 million shoats were exported through the Berbera port (including from Ethiopian sources). Of this total, 1.612 million (69%) were exported between September and November for the Hajj festivities. Assuming an average export price of US\$70, the estimated total value would be over US\$160 million. With government taxes at around US\$3.60 per head, this means tax revenue of around US\$8.5 million or 10% of the Somaliland government's total revenue [11].

Livestock plays a crucial role among rural communities in Somaliland. In rural areas, livestock still serves as the primary exchange market where sheep, camels, and cows are bartered. Livestock export market fluctuations and export bans have a clear impact on markets and prices. There have been two noticeable trends in markets and prices during the export ban: a dramatic depreciation in the Somaliland shilling, and local-currency inflation of imported commodities. The dollar exchange rate of the Somaliland shilling dropped from SSh 3,487 at the time when the ban was imposed in September 2000 to SSh 6,200 in December 2002. The prices of imported goods such as petrol, rice, sugar, and wheat flour, while remaining steady in dollar terms, have risen considerably in the local currency due to depreciation, adversely affecting the purchasing power of Somaliland pastoralists [12].

Somaliland has been suffering from high levels of inflation and currency depreciation for the last few years. This has meant that although the amount of livestock exported has remained relatively constant, export earnings are estimated to have fallen due to the depreciation of the Somaliland shilling against the dollar. For example, if we take livestock prices from the Food Security and Nutrition Analysis Unit (FSNAU) for the month of the Hajj in each year, we have estimated that dollar earnings

from livestock exports through Berbera Port peaked in 2014 at around USD 375 million but fell to around USD 280 million in 2015. This fall in livestock export earnings may indicate falling demand due to changing consumer preferences and/or the condition of Somaliland livestock [13].

Livestock exports are often accompanied by its byproducts (i.e. hides and skins); in 2011, approximately 13.6 million pieces were exported as seen in Figure 3 [14].



Figure 3. Yearly export of hides and skin pieces through Berbera port: 2011-2015

In 2016, the Kingdom banned livestock exports from both Somalia and Somaliland and 2017 livestock export through Berbera port was the lowest in the last decade. This ban of livestock export and closing of markets has resulted in millions of dollars lost, but this ban was lifted in July 2017 and livestock export continues and 862,231 heads were exported from Berbera only in August 2018 [15]. Livestock export has backed the utmost to Somali people in many centuries but still they did not manage the transformation of the livestock trade as being forward going as in case many countries.

Assuming a worst-case scenario in which livestock sales stopped completely, the outcome would be catastrophic for poorer pastoralists. Even in a situation where markets still remained open but livestock prices fell, it is possible that poorer herders get displaced by medium wealth and wealthy sellers. This is because, during an export ban, the large volumes of relative high-quality livestock which were destined for the export market are re-directed to domestic markets, and these animals usually belong to wealthier households. During the 1998 ban, it was estimated that the price of sheep and cattle fell by 55% and 65% respectively in the Somali Region. The same scenario is seen in Somaliland during livestock export bans, specifically for the last embargo imposed by Saudi Arabia in 2017 [16].

Somaliland livestock export destination markets

Saudi Arabia is the main destination of Somaliland livestock export. As Table 3 [6] conveys, during times when there is no livestock export ban, one of the most striking features of Somaliland's livestock exports has been its dependence on a single destination market: Saudi Arabia. Approximately 95% of all livestock exported by Somaliland in 2000 was destined for markets within Saudi Arabia. Roughly 98% of all sheep and goats and 85% of all camels went to Saudi Arabia. Yemen imported 93% of Somaliland's cattle exports, reflecting the effect of the cattle embargo imposed by Saudi Arabia in 1983. However, it is well known that many of the cattle exported to Yemen end up in Saudi Arabian markets via "back door" channels, or are exported to other Peninsula countries, including primarily Oman and the United Arab Emirates. These markets are insignificant, accounting for less than 6% of all livestock exports [13].

Table 3. Export destination markets (%)

Markets	Sheep/Goats	Camels	Cattle	All livestock
Saudi Arabia	98.1	84.7	1.5	94.4
Yemen	1.7	10.7	93.0	5.2
United Arab Emirates	0.2	4.6	5.5	0.4
Total	100	100	100	100

Why Saudi Arabia is the Main Market for Somaliland Livestock Export?

Saudi Arabia's religious events like the annual pilgrimage to Mecca and the feast of Al-Fitr rises a huge demand of meat consumption as millions of Muslims from around the world gather to perform Umra and Hajj (pilgrimage). Livestock must be imported alive, so they can be blessed and slaughtered according to Islamic law prior to consumption. Livestock exports are highly cyclical with their peak falling during the 70-day period between Eid al-Fitr, and the start of the Haj, or Eid al-Adha. The unique annual pilgrimage to Mecca in Saudi Arabia guarantees annual peak demand for live animals. Additionally, the Saudi port of Jizan is close to Berbera, making it an ideal destination for the export of live animals [13].

In summary, Somaliland's traditional dependency on a single sector (livestock exports) and market (Saudi Arabia) has proven a liability. For now, pastoralist households – many of them supported by remittances from family-members in the diaspora – have enough resources and coping options to manage. As the livestock ban continues, however, its effects will increasingly heighten the vulnerability of Somaliland pastoralists to other shocks [12].

Discussion

Livestock export contributes the greatest to Somaliland's revenue while the government allocates a huge budget to non-productive sectors. Somaliland needs to improve its exporting capacity so that it can compete with its sector partners in the Horn of Africa as well as in the Somali Peninsula. According to a series of stakeholder's workshops held in Hargeisa, Somaliland in 2003 - 2006, identified main constraints affecting the livestock sector in Somaliland under four clusters namely natural constraints, institutional weaknesses, lack of infrastructure and financial constraints [5].

Berbera Port is strategically located on the southern coast of the Gulf of Aden and well connected to the capital Hargeisa as well as to other regions of Somaliland. In 2017, UAE-based DP World agreed to invest \$422 million to upgrade and modernize Berbera Port as well as create the long-fabled "Berbera Corridor". Analysts now expect this move will strengthen Somaliland's livestock sector as exports will increase exponentially as the investment will mean that Somaliland's Berbera Port will be able to significantly increase operations.

Somaliland's livestock market is disproportionately affected by the policies of key export markets such as the Kingdom of Saudi Arabia which it exports to for the busy Hajj season. Three bans imposed by Saudi Arabia on Somaliland in the last three decades has affected Somaliland's economy seriously leaving an impact on prices and markets, causing youth migration into urban areas, increasing problems of urban poverty and unemployment as well as inflation. Livestock export ban also affected the environment because many teenagers in rural areas started burning trees to sell them as charcoal in urban areas leading to deforestation of rangeland in many areas.

Most of the pastoral cattle graze on free-range low-quality forage and non-supplementary feeding which is provided. Fodder scarcity is understood to have had a direct impact on livestock production in terms of the last few cases of droughts.

Livestock export has political and economic aspects affecting it. These factors need to be assessed sensibly by intellectuals and those who are in charge. Lack of investment is among the factors hindering livestock export and according to World Bank report, 2014 Somaliland has very low levels of investment, ranked approximately 180th in the World for gross fixed capital formation as a percentage of GDP.

Furthermore, Somaliland has very low employment-to-population ratios, with 28% for males and 17% for females (15-24 year-olds in Borama, Hargeisa, and Burao) [17].

Conclusion and Recommendations

Somaliland has exported a total livestock of nearly 50 million heads since its self-declaration of independence from Southern Somalia in 1991. According to the kind of animals exported through Berbera, shoats are the majority. This is because shoats are the largest in number compared to the other kinds of animals. After the Saudi Arabian ban on Somaliland's livestock was lifted in 2009, exports in Somaliland grew rapidly in the following years. For example, between 2009 and 2011 livestock exports more than doubled. One plausible reason for this was the establishment of certified highly equipped quarantines in the coastal city of Berbera, but Somaliland's livestock export is not exclusively dependent on the certification and policies towards exporting a healthy animal. In many times, it was affected by outbreaks in other parts of the Somali peninsula as well as the horn of Africa.

There are many challenges facing Somaliland's livestock export in the near future. One of these is the environmental devastation caused by recurrent droughts in Somaliland as well as the massive deforestation of grazing pastures to establish new villages and cutting of trees for charcoal purposes. Climate changes and primary dependence of rainfall also play role in main challenges ahead Somaliland's livestock breeding. Rainfall is not as well as before, so it needs policies to move pastoralists from the old nomadic systems into the agro-pastoral sedentary system of rearing livestock.

Decreasing dependence on one major market is also important for Somaliland's future economy politics because it will decrease threats coming from the fast-changing Arabian Gulf politics that can use livestock ban as a tool for political pressure. A broad national policy has not yet been set up and the private sector is the only sponsor that is active in livestock trade and Somaliland government is not planning a good stake of the national budget to livestock breeding and development of resettling programs from nomadic rearing system into modern rearing methods. Finally, livestock in Somaliland needs for stable policies that can increase both international and local investment so that it can attract foreign traders and local investors much better.

Acknowledgement

This study was supported by the Presidency for Turks Abroad and Related Communities (YTB) within "International Student Academy" Project.

References

- [1] Tran, M. (2012). Berbera port and pastoralism prove livestock's worth in Somaliland, Guardian.
- [2] Somaliland Ministry of National Planning (2016), Department of Statistics.
- [3] Somaliland statistical bulletin (2015), Somaliland Ministry of Planning & Development.
- [4] Gaani, M. X., 2002. Regulating the livestock economy of Somaliland. Academy for Peace and Development.
- [5] Ministry of Livestock (2006), National Policy for Livestock.
- [6] Berbera port authority, republic of Somaliland
- [7] 2016-2018 is retrieved from (www.Somalilandchamber.com).
- [8] Retrieved from (<http://www.somalilandchamber.com/?p=595>), 2018 Somaliland Chamber of Commerce, Industry and Agriculture.
- [9] Retrieved from (<http://somalilandgov.com/>)
- [10] Retrieved from (<http://www.somalilandtrade.net/sectors/livestock-sector/>)
- [11] Somaliland ministry of trade, (2018).
- [12] Holleman CF (2002). The Socio-economic Implications of the Livestock Ban in Somaliland. Famine Early Warn Syst Netw.;Task Order.
- [13] Retrieved from (<http://www.somalilandbiz.com/sector-guides/livestock/>).
- [14] Ministry of National Planning and Development, (2015); Muhumed, (2018), The Future of Somaliland Livestock Exports : Examining the Sustainability of Livestock Trade, 5(8), 678–692.
- [15] Somaliland Chamber of Commerce, Industry and Agriculture, (2018).
- [16] Aklilu, Y., Catley, A. (2009). Livestock exports from the Horn of Africa: An analysis of benefits by pastoralist wealth group and policy implications. Medford: Feinstein Int. Center Tufts Univ.
- [17] New World Bank GDP and Poverty Estimates for Somaliland. (December 6, 2015). <http://www.worldbank.org/en/news/press-release/2014/01/29/new-world-bank-gdp-and-poverty-estimates-for-somaliland>.

Benin'in Kanatlı Hayvan Üretimi Sektöründe Girişimcilik Fırsatı

*Foudehou Issaka Ibrahima**, Ege Üniversitesi, Fen Bilimleri Enstitüsü, Zootekni Anabilim Dalı, İzmir, Türkiye

Figen Kırkpınar, Ege Üniversitesi, Ziraat Fakültesi, Zootekni Bölümü, İzmir, Türkiye

*İletişimden sorumlu yazar: ifoudehou@hotmail.fr

Anahtar Kelimeler: Benin, kanatlı hayvan eti, et tüketimi, et ithalatı, girişimcilik

Disiplin: Ziraat / Zootekni

Özet

Bu makalede, Benin'in kanatlı hayvan eti üretimi sektöründeki girişimcilik fırsatlarının değerlendirilmesi için kanatlı hayvan etinin üretim ve tüketim değerleri ele alınmıştır. Ayrıca ülkeye yıllık ithal edilen et ve ekonomik değeri de incelenmiştir. Bu amaçla, Benin Ulusal İstatistik ve Ekonomik Analiz Enstitüsü (INSAE), Tarım ve Hayvancılık Bakanlığı (MAEP) ve Birleşmiş Milletler Gıda ve Tarım Örgütü (FAO) raporları değerlendirilmiştir. Ayrıca daha önce yapılmış benzer makalelerden de bazı veriler kullanılmıştır.

Bu makalenin sonucunda, kişi başına gelirin büyümesi ve gıda seçeneklerinin genişletilmesi sayesinde gıda ürünleri ve tüketim modellerinin değişmekte olduğu söylenebilmektedir. Benin'de 2013 (sonraki yıllara ait veri bulunmamaktadır) yılında kişi başına et tüketimi 25,2 kg' a ulaşmıştır. Ancak dünya ortalaması (43,22 kg/kişi/yıl) dikkate alındığında et tüketiminin oldukça düşük olduğu görülmektedir. Benin'de ulusal üretilen etlerin % 21'i kanatlı hayvan etinden oluşmaktadır. Ulusal kanatlı hayvan eti üretimi ise yükselen et talebini karşılayamamaktadır. Yerel üretimin tüketimdeki payı 2005'ten 2013'e kadar oldukça düşmüştür (%21'den %6'ya). Benin'e ithal edilen toplam et miktarının %98'i kanatlı hayvan etidir (tavuk ve hindi eti) ve 2010-2016 yılları arasında yıllık ithal edilen kanatlı hayvan eti değeri ortalama 216,358 milyon dolar olarak gerçekleşmiştir. Bu durum döviz kaybına neden olmaktadır.

Mevcut veriler değerlendirildiğinde Benin'de kanatlı hayvan üretimine yönelik yatırım fırsatları değerlendirilmelidir. Ayrıca gıda güvenliği alanında önemli eksiklikler bulunmakta ve bu alanda ihtiyaçların karşılanması ve geliştirilmesi de girişimcilik fırsatlarını içermektedir.

Keywords: Benin, meat consumption, meat import, poultry meat

Abstract

In this article, the production and consumption values of poultry meat are discussed in order to evaluate the entrepreneurial opportunities in the poultry meat production sector of Benin. In addition, the annual import of meat and its economic value were also examined. For this purpose, The National Institute of Statistics and Economic Analysis (INSAE) of Benin, Ministry of Agriculture and Livestock (MAEP) and The Food and Agriculture Organization of the United Nations (FAO) reports were reviewed. In addition, some data from similar articles published on this subject have been used.

As a result of this review, it can be said that food products and consumption patterns are changing due to the per capita income growth and the expansion of food options. In Benin, food products and consumption patterns are changing due to the growth of income and the expansion of food choice options. Therefore, per capita meat consumption increased and reached 25.2 kg in 2013. However, according to the average of the world meat consumption in 2013 (43.22 kg / person / year) this amount is very low. In general, 21% of the meat produced in Benin consists of poultry meat. National poultry breeding does not meet the rising demand for meat. The part of local production in consumption decreased significantly from 2005 to 2013 (from 21% to 6%). 98% of the total meat imported to Benin is composed by poultry meat (chicken and turkey meat). From 2010 to 2016, the average of imported poultry meat value is \$ 216,358 million and this situation causes loss of currency.

Considering the available data, investment opportunities for poultry production in Benin should be evaluated. In addition, there are significant shortcomings in the field of food safety and the provision. The development of the needs in this sector includes entrepreneurship opportunities.

Giriş

Benin Batı Afrika'da bulunan 114 763 km²lik [1], [2] ve 11,5 milyon civarında nüfusa sahip bir ülkedir [2], [3]. Tarım sektörü, Benin ekonomisini güçlendirmek için büyük önem taşımaktadır; çünkü GSYİH'ya ortalama % 32,7, ihracat kazançlarına % 75 ve devlet gelirlerine % 15 katkıda bulunmaktadır [4].

Benin Ulusal İstatistik ve Ekonomik Analiz Enstitüsü'nün (INSAE) tahminlerine göre 2018'den 2030'a kadar Benin nüfusu 11.362.269'dan 16.581.108'e varacaktır [2], [3]. Başka bir deyişle gelecek 12 yılda Benin nüfusu % 45,93 artış gösterecektir. Bu bakımdan, ülkenin gıda güvenliği için ziraatçıların (araştırmacı ve çiftçiler) görevinin daha yüksek bir seviyeye gelmesi gerekmektedir. Nitekim nüfus arttıkça, azalan arazide daha çok gıda üretebilmek demektir.

Birleşmiş Milletler Gıda ve Tarım Örgütüne (FAO) göre Benin gibi gelişmekte olan ülkelerde nüfusun tükettiği gıdada bitkisel kaynakların oranı gitgide azalıp hayvansal ürünlerin oranı yükselmektedir [5], [6]. Fakat bu ülkelerde, şimdilik tahminlere göre kişi başına yılda ortalama 34 kg'dan az et tüketmekte olup gelişmiş ülkelerinkinden (80 kg/kişi/yıl) oldukça düşüktür [7]. Şimdi olduğu gibi 2030'lu yıllarda da bu ülkelerde kanatlı hayvan etinin tüketilmesi öteki hayvanlarınkinden daha çok hızlı yükselecektir [8]. Zira 2017'den 2030'lu yıllara kadar kanatlı hayvan sektörü, dünyadaki en büyük et üretimi kaynağı olacak (2025'te 131,3 Milyon ton) ve Afrika genelinde büyüyen nüfusun et talebini karşılamak için kanatlı eti ithalatının artması beklenmektedir [8]. Ayrıca öteki çiftlik hayvanlara göre kısa bir zamanda ucuz bir fiyatla elde edilebildiğinden gelişmekte olan ülkelerde beslenme kalitesini arttırmak ve yoksullukla mücadele stratejilerinde öne çıkmaktadır [1], [8]. Benin'deki yükselen et ihtiyaçları kanatlı hayvan eti üretim ve ithalatıyla karşılanmaya çalışılmaktadır. Örneğin 2013'te Benin'deki toplam tüketilen etin % 80'i kanatlı hayvan etinden oluşmuştur [2], [9].

Bu çalışmada, kanatlı hayvan sektörünün Benin ekonomisindeki yerinin değerlendirilmesi amaçlanmıştır. İthal edilen ete değinmeden önce Benin'de kişi başına toplam et tüketimi, kanatlı hayvanların Benin ekonomisindeki değeri, kanatlı hayvan etinin üretimi ve tüketimi gözden geçirilmiştir.

Materyal ve Yöntem

Bu çalışmayı gerçekleştirmek için daha önce yapılmış benzer makalelerin yanı sıra; Benin hayvancılık sektörü yöneticileri (Tarım ve Hayvancılık Bakanlığı (MAEP) ve Hayvancılık Genel Müdürlüğü (DE)), Ticaret ve Sanayi Bakanlığı, INSAE ve FAO gibi uluslararası örgütlerin raporlarına başvurulmuştur.

Toplanan ham verilerin düzenlenmesi ve analizi sonucunda bu rapor hazırlanmıştır. Ancak güncel verilerin bulunmaması nedeniyle, bulunan verilere uymaya özen gösterilmiştir.

Benin'de Toplam Et Tüketimi

Küresel ölçekte olduğu gibi, Benin'de de gelirin büyümesi ve gıda seçeneklerinin genişletilmesi sayesinde gıda ürünleri ve tüketim modelleri değişmektedir. Yükselen gelirler ve kentleşme olayı yaşam tarzlarını değiştirmektedir. Tüketiciler geleneksel gıdalar (tahıl ve yumru) değil, artık meyve ve sebze, hayvansal protein ve işlenmiş gıda ürünlerini tercih etmektedirler [10].

Tablo 1'de görüldüğü gibi 2003'ten 2007'e kadar kişi başına yılda et tüketimi 18,2 kg'dan 13,1 kg'a düşmüştür. Benin'de kırmızı etin pahalı¹ olması nedeniyle [1], ayrıca, çoğunluğu fakir olan nüfus yalnızca kanatlı eti tükettiği için (tüketilen etin yaklaşık % 80'i kanatlı hayvandan oluşmakta) bu azalışın üç temel sebebi olduğu bildirilmiştir [11, 12]:

- 2003 yılında kanatlı çiftliklere zarar veren Gumboro krizinin etkileri,
- 2003'ten itibaren, Güney Afrika gibi ülkelerden dondurulmuş yumurtaların (düşük fiyatlarla) ithal edilmesinin et tüketimine olumsuz etkileri,
- 2004'teki mısır krizinin (mısır fiyatındaki artış) kanatlı çiftliklerine olumsuz etkileri.

İzleyen yıllarda çok değişkenlik göstererek 2013'de 25,2 kg'a ulaşmıştır. Fakat dünyanın 2013'te et tüketiminin ortalamasına (43,22 kg/kişi/yıl) göre bu miktar çok düşüktür [7], [13]. Gelecek yıllarda

¹ 1kg kırmızı et fiyatı yaklaşık 2kg reform tavuğu fiyatının eşdeğeridir.

büyüyen nüfusun (2030'lu yıllarına kadar % 45,93 artış beklenmektedir [2]) et talebini karşılamak için kanatlı hayvan eti ithalatının artması beklenmektedir [8]. Bu nedenle, kanatlı hayvanların Benin ekonomisindeki yeri değerlendirilmelidir.

Tablo 1. Benin'de kişi başına yılda toplam et tüketimi [9]

Yıl	Miktar kg/kişi/yıl	Değişim %
2002	17,8	
2003	18,2	2,25
2004	14,3	-21,43
2005	13,2	-7,69
2006	13,1	-0,76
2007	13,1	0,00
2008	17,5	33,59
2009	16,2	-7,43
2010	14,1	-12,96
2011	23,5	66,67
2012	25,9	10,21
2013	25,2	-2,70

Benin Ekonomisindeki Kanatlı Hayvanların Yeri

Benin ekonomisinin büyük bir payı tarım ve hayvancılığa dayanmaktadır. Aktif nüfusunun % 70'i tarımla (hayvancılık dâhil) uğraşmaktadır. Tarım, Benin GSYH'nin % 37'sini oluşturmaktadır. Hayvancılık sektörü ise, ulusal GSYH'nin % 6'sına katkıda bulunmaktadır [14], [15]. Ulusal hayvansal üretimde, kanatlı hayvan sektörü et kaynağı açısından sığırlardan sonra ikinci sırada gelmektedir (kanatlılar % 21; sığırlar % 58) [16]. Fanou [16], Union Economique et Monétaire Ouest Africaine (UEMOA) verilerine atfen, Benin tavukçuluğunun ulusal tarım cirolarına % 2,4 oranında, yumurta ise % 1,4 oranında katkıda bulunduğu rapor etmiştir.

Benin'de kanatlı hayvan eti ithalat değerlerine bakıldığında, 2000 milyon dolarlık civarında ulusal bütçesi olan bir ülkeye göre, bu değerlerin çok yüksek olduğu söylenebilmektedir. Bu rakamlar, Tablo 2'de görüldüğü gibi, 2008 ve 2011 yıllarında bir önceki yılların değerlerine göre hemen hemen iki kat artmıştır. Ayrıca 2010'dan 2016'ye kadar, bu değerlerin ortalaması \$216,358 milyon olup Benin ulusal bütçesinin 2016'da tarıma (hayvancılık dâhil) ayırdığı masraftan (\$181,68 milyon) daha fazladır¹.

Tablo 2. Benin'deki et ithalatının değeri [9]

Yıl	Et ithalatının değeri (bin dolar)				Kanatlı hayvan eti payı (%)
	Toplam	İndeks	Kanatlı hayvan eti	İndeks	
2005	49 018		47 960		98
2006	50 041	+0,02	48 699	+0,02	97
2007	65 516	+0,31	64 640	+0,33	99
2008	125 700	+0,92	124 440	+0,93	99
2009	147 555	+0,17	145 578	+0,17	99
2010	141 178	-0,04	139 279	-0,04	99
2011	295 578	+1,09	287 623	+1,07	97
2012	224 333	-0,24	218 760	-0,24	98
2013	235 035	+0,05	231 240	+0,06	98
2014	248 376	+0,06	243 624	+0,05	98
2015	229 631	-0,08	226 199	-0,07	99
2016	170 502	-0,26	167 782	-0,26	98

¹ Benin ulusal bütçesinden 2016'da tarıma ayrılan para miktarı şimdiye (2019) kadar bir rekor olmaktadır.

Bu bakış açısında, kanatlı hayvan eti ithalatı, Benin halkına iyi bir protein kaynağı ve çok düşük fiyatlara almaya imkân sağlasa da iyi bir yöntem olduğu kabul edilmemelidir. Zira hem yerel üretim ile rekabet etmekte hem de ülkeye büyük miktarda döviz kaybettirmektedir. Ayrıca Benin hayvancılık sektörünün gelişimini engellemektedir [12]. Devletin gıda güvenliği için yerel üretime önem ve destek verilmelidir.

Benin’de Kanatlı Hayvan Eti Üretimi ve Tüketimi

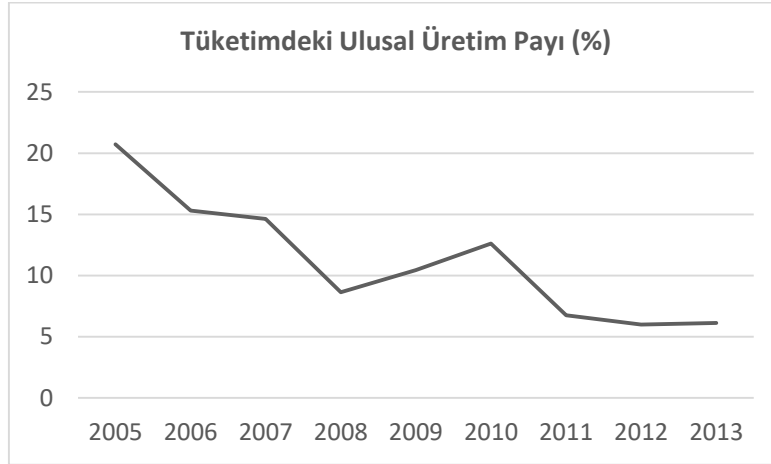
Benin tarım sektörünün son teşhis raporu, küçük çiftliklerin dominant olduğunu göstermiştir. Çoğunlukla polikültür odaklı küçük aile çiftliklerinden oluşmaktadır. Bu tip çiftliklerde ortalama 3-10 tane sığır, 3-6 tane küçükbaş hayvan, 2-5 tane domuz ve 5-10 kanatlı hayvan bulunmaktadır [1].

Kanatlı hayvan üretimi iki sistemde yapılmaktadır: yaygın hayvan yetiştiriciliği (Ekstansif) ve modern hayvan yetiştiriciliği (Entansif). Benin modern hayvan yetiştiriciliği konusunda geri kalmış bir ülkedir. Kanatlı hayvan sektöründe; entansif sistem ancak 1980 yılından itibaren giderek önem kazanmaya başlamıştır [11], [17]. Bu sistemde kullanılan günlük civcivlerin kaynakları Avrupa (Fransa, Belçika ve Hollanda) ve Batı Afrika’dır (Nijerya ve Gana) [17].

Benin’de, daha önce belirtildiği gibi ulusal üretilen etlerin % 21’i kanatlı hayvan etinden oluşmaktadır. Tablo 3, Benin’de kanatlı hayvan eti üretimi ve tüketimini göstermektedir. Şekil 1 ise yerel üretimin tüketimdeki karşılayabildiği payı vermektedir. Bu verilere göre yerel üretimin tüketimdeki payı 2005’ten 2013’e kadar oldukça düşmüştür (%21’den % 6’ye kadar). Örneğin 2013 yılında Benin’deki toplam tüketilen kanatlı hayvan etinin sadece % 6,12’si üretilmiştir. Geri kalan % 93,88 ithalat yoluyla karşılanmıştır. Başka bir söyleyişle Benin nüfusunun artan ihtiyaçlarının büyük bir kısmı sadece ithalat yoluyla karşılanmaktadır. Gıda güvenliği için ulusal kanatlı hayvan eti üretiminde daha fazla yatırım yapılması gerekmektedir.

Tablo 3. 2005’ten 2016’ya kadar Benin’de kanatlı et üretimi ve tüketimi [9]

Yıl	Kanatlı hayvan				
	Sayısı (bin baş)	Eti üretimi (ton)	İndeks	Eti tüketimi (ton)	İndeks
2005	27 432	13 255	–	64000	–
2006	25 700	9 940	-0,25	65000	+0,02
2007	26 519	10 525	+0,06	72000	+0,11
2008	15 525	9 750	-0,07	113000	+0,57
2009	15 999	10 009	+0,03	96000	-0,15
2010	16 550	10 335	+0,03	82000	-0,15
2011	17 087	11 677	+0,13	173000	+1,11
2012	17 634	12 051	+0,03	201000	+0,16
2013	18 198	12 436	+0,03	203000	+0,01
2014	18 779	12 834	+0,03		
2015	19 380	13 245	+0,03		
2016	20 002	13 670	+0,03		



Şekil 1. Benin’de kanatlı hayvan eti tüketiminde ulusal üretimin karşılayabildiği pay

Benin’de Kanatlı Hayvan Eti Fiyatının Varyasyonu

Benin’de kırmızı etin kilosu \$5 ve üzerindeyken [1] Tablo 4’te görüldüğü gibi 2010 yılı dışında kanatlı hayvan etinin kilosu \$2,75 ± 0,12’ye satılmaktadır [17]. Karma yem hammadde maliyetlerinin yüksek olmasından dolayı 2010 yılında bu fiyat \$3,21’e ulaşmıştır. Bu düşük fiyatlar sayesinde kanatlı hayvan eti daha fazla tercih edilmektedir. Fakat ithalat etlerinden sebep olup yerel üretime rekabet etmektedir.

Tablo 4. Benin’de kanatlı hayvan eti fiyatı (2001 - 2011) [17]

Yıl	Fiyat (\$ / kg)	İndeks
2001	2,41	–
2002	2,68	+0,11
2003	2,86	+0,07
2004	2,86	+0,00
2005	2,86	+0,00
2007	2,68	-0,06
2008	2,86	+0,07
2009	2,86	+0,00
2010	3,21	+0,13
2011	2,68	-0,17

Benin’de Kanatlı Hayvan Eti İthalatı

Nispeten küçük miktarlarda olsa da, Benin çok uzun zamandır et ithal etmektedir (1960’lı yıllarda ~100 ton/yıl) [18]. Bu ithalat Brezilya, Güney Afrika ve Avrupa Birliği ülkelerinden gelip Benin’deki büyük şirketler (Cajaf Comon, CDPA, SACOGIE ve Africa Gell) tarafından gerçekleştirilmektedir. Daha önce belirtildiği gibi, ithal edilen etin büyük kısmı (% 98) kanatlı hayvan etinden ibarettir. Genel olarak, Benin’e ithal edilen kanatlı hayvan eti tavuk ve hindi etinden oluşup, yerli üretilen kanatlı hayvan etine göre daha ucuza satılmaktadır. Hindi eti parçalanmış (hindi kanatları) halinde, tavuk eti ise soyulup temizlenmiş fakat parçalanmamış halde ithal edilmektedir.

Tablo 5. Benin'deki toplam et ithalatı ve kanatlı hayvan etinin payı

Yıl	Et ithalat (ton)			İndeks	Kanatlı hayvan eti payı (%)
	Toplam	İndeks	Kanatlı hayvan eti		
2001	58 536		51 999		89
2002	86 535	+0,48	72 328	+0,39	84
2003	88 107	+0,02	71 104	-0,02	81
2004	56 972	-0,35	56 589	-0,20	99
2005	49 833	-0,13	49 048	-0,13	98
2006	49 713	+0,00	49 066	+0,00	99
2007	57 872	+0,16	57 209	+0,17	99
2008	95 053	+0,64	94 084	+0,64	99
2009	116 174	+0,22	114 550	+0,22	99
2010	118 223	+0,02	116 836	+0,02	99
2011	155 430	+0,31	152 102	+0,30	98
2012	183 723	+0,18	180 110	+0,18	98
2013	187 556	+0,02	185 236	+0,03	99
2014	200 903	+0,07	197 625	+0,07	98
2015	187 627	-0,07	184 757	-0,07	98
2016	130 820	-0,30	128 758	-0,30	98

Kaynak: INSAE (2014, 2015c, 2016c, 2016d) [2,3] ve Atlas Mondiale des Données (2019) [9]

Tablo 5'te Benin'deki 2001'den 2016'ya kadar toplam et ithalatı ve kanatlı hayvan etinin payı gösterilmektedir. 2003 yılına kadar, ithal edilmiş kanatlı hayvan eti miktarının 71 104 tona ulaştığı ve sonra 2006 yılında 49 066 tona düştüğü görülmektedir. O yıldan itibaren 2014 yılına kadar önemli bir düzeyde artış göstererek 197 625 tona yükselmiştir (2014'teki ulusal kanatlı hayvan eti üretiminin yaklaşık on beş (15) katı, Tablo 3'e bkz.). Bu önemli artış, Benin'e ithal edilen etin yeniden Nijerya'ya ihraç edilmesiyle açıklanmıştır [18]. Fakat 2016 yılında Nijerya ile yeniden ihracatta karşılaşılan engeller [18] nedeniyle bu ithalat 128 758 tona gerilemiştir.

Sonuç ve Öneriler

Benin'de kanatlı hayvan eti tüketimi gittikçe yükselmektedir. Ancak kanatlı hayvan yetiştiriciliği son yıllarda daha dinamik hale gelmesine rağmen bu yükselen et talebini karşılayamamaktadır. Bu açığı kapatmak için yapılan ithalat ülkeye döviz kaybı nedeni olmaktadır. Ayrıca bazı faktörler, içsel (çiftçilerin düşük teknik seviyeleri ve yeni tekniklerin yetersiz yayılması) veya dışsal (ithalattan kaynaklanan rekabet), bu sektörün gelişmesine engel olmaktadır.

Mevcut veriler değerlendirildiğinde Benin'de kanatlı hayvan üretimine yönelik yatırım fırsatları değerlendirilmelidir. Ayrıca gıda güvenliği alanında önemli eksiklikler bulunmakta ve bu alanda ihtiyaçların karşılanması ve geliştirilmesi de girişimcilik fırsatlarını içermektedir. Bunun için:

- Çiftçilere eğitim (geliştirilmiş üretme teknikleri ve işletme yönetimi) verilmelidir.
- Devletçe çiftçilere destek verilmeli, Araştırma-geliştirme faaliyetlerine önem verilmelidir.
- Gençlerin hayvancılıkta girişimcilik yapması teşvik edilip desteklenmelidir.
- Tarımsal kredi sistemi uygulanmalıdır.
- Yerel tarım ürünlerinin (et, yumurta vb.) tüketim politikası uygulanmalıdır.
- Yerel üretimin ithal edilen et ürünlerin rekabetinde bulunması için kanunlar hazırlanmalıdır.
- Yerel üretiminin verimliliğini arttırmak için ıslah araştırmalarına önem ve destek verilmelidir.

Teşekkür

Bu çalışma Yurtdışı Türkler ve Akraba Topluluklar Başkanlığı'nın (YTB) "Uluslararası Öğrenci Akademisi" Projesi kapsamında desteklenmiştir.

Kaynakça

- [1] Codjia V (2016) Revue des filières bétail/viande & lait et des politiques qui les influencent au Bénin.
- [2] INSAE, "Population - Bénin", 2019. [Çevrimiçi]. Available at: <https://www.insae-bj.org/statistiques/indicateurs-recents/43-population>. [Erişim: 18-Mar-2019].
- [3] INSAE, Principaux indicateurs socio démographiques et économiques (RGPH-4, 2013), Cotonou .
- [4] MAEP ve DPP, Rapport de Performance du Secteur Agricole, Gestion 2013.
- [5] FAO (2009) La Situation Mondiale De L'Alimentation Et De L'Agriculture: Le point sur l'élevage.
- [6] S. Henning ve C. Pius, "Perspective mondiale, Rapport sur l'élevage", 2006.
- [7] Planetoscope, "Statistiques: Consommation mondiale de viande", 2019. [Çevrimiçi]. <https://www.planetoscope.com/elevage-viande/1235-consommation-mondiale-de-viande.html>.
- [8] ITAVI, "Situation de la production et du marché des volailles de chair Bilan 2016", ITAVI (Service Econ., ss. 1-11, 2017.
- [9] Atlas Mondial des Données, "Agriculture - Bénin", knoema.com, 2019. <https://knoema.fr/atlas/Bénin/topics/Agriculture#Production-dorigine-animale-Animaux-délevage>.
- [10] BAD (Banque Africaine de Développement) ve FAO, Croissance Agricole en Afrique de l' Ouest, Facteurs déterminants de marché et de politique. Rome: BAD 2015.
- [11] P. Onibon ve H. Sodegla, "Étude de la sous-filière « aviculture moderne » au Benin", 2006.
- [12] Agoli-Agbo E, Lacroix P, Geay F, Guézodjé L (2005) Chronique d'une organisation de producteurs pour la défense, la promotion et la modernisation de l'aviculture béninoise", Assoc. Natl. des Avic. du Bénin, 7(202) 1-6.
- [13] PRB, "Fiche de données sur la population mondiale", 2013.
- [14] MAEP, Rapport Annuel d'activités 2016 (Projet d'appui à la production vivrière et de renforcement de la résilience dans les départements de l'Alibori, du Borgou et des collines), 2017.
- [15] Youssao Karim Abdou I (2015) Programme National d' Amélioration Génétique.
- [16] U. Fanou, "Bénin Revue du secteur avicole", 2006.
- [17] FAO, Secteur Avicole. Rome: FAO (www.fao.org/publications), 2015.
- [18] Dognon SR, Salifou CFA, Dognon J, Dahouda M, Scippo M.-L, Youssao AKI (2018) Production, importation et qualité des viandes consommées au Bénin", J. Appl. Biosci. J. Appl. Biosci., 124: 12476-12487, 2018.

Nijer Tarımının Karakteristik Özellikleri

*Moustapha Maman Mounirou**, Ankara Üniversitesi, Ziraat Fakültesi, Toprak Bilimi ve Bitki Besleme Bölümü,
Dışkapı, Ankara, Türkiye

*İletişimden sorumlu yazar: mounirhalifamoustapha@gmail.com

Anahtar Kelimeler: Nijer, toprak verimliliği, bitki besleme sorunları

Disiplin: Ziraat / Toprak Bilimi ve Bitki Besleme

Özet

Nijer Batı Afrika'da yer alan geniş bir ülkedir. Yüzölçümü 1.267.000 km²'dir. Yapılan 2016 nüfus sayımına göre ülkenin nüfusu 19.865.068 olarak açıklanmıştır. Nijer nüfusunun %80'den fazlası tarım, hayvancılık, ormancılık ve balıkçılık ile geçimini sağlamaktadır. Geniş yüzölçümüne sahip olmasına rağmen tarıma elverişli araziler oldukça azdır. Topraklarının büyük bir kısmı çöl olmasına karşın ekonomisinde 1. sırayı yine tarım almaktadır.

Hem kurak hem detropikal iklime sahip olan Nijer'de yağış sezonu Mayıs ile Eylül ayları arasındadır. Yerleşik tarımın yapılabildiği Nijer Nehri'nin etkilediği Nijer'in güneybatısının haricindeki bölgelerde arazi kuraktır. Ülke yüzölçümünün sadece %12'si tarıma uygundur. Ülkenin sadece %1'i ormanlık alandır. Nijer'de 4 farklı iklim bulunmaktadır. Çöl (sahra) iklimi, karasal (sahel) iklim, sahra-sahel iklimi ve tropikal (sahel-sudan ve sudan) iklim görülmektedir.

Giriş

Darı ve sorgum Nijer'in başlıca tahıl ürünleridir. Fao verilerine göre 2016-2017 arasında Nijer dünyanın en büyük 2. darı üreticisidir [2]. Mısır yetiştiriciliği daha küçük ölçekli olarak yapılmaktadır. Çeltik geleneksel olarak nehir kıyılarında yetiştirilmesine rağmen, Asya'dan ithal edilen pirinçle rekabet edemediğinden ekim alanları azalmaya başlamıştır. Kuraklığa dayanıklı olması ve komşu ülkelere büyük miktarlarda ihraç edilmesi nedeniyle, bürülce üretimine ayrılan alanlar 1980'lerden itibaren çok hızlı artmıştır. Bölgesel pazarlara ihraç edilmek üzere soğanın da üretimi artmıştır. Benin, Mali ve Burkina Faso'nun aksine kurak iklim nedeniyle Nijer'de pamuk üretimi yok denecek kadar azdır. Tarıma elverişli alanların çoğu Nijer Irmağı kıyısındadır. Nijer'de yaklaşık 30 bitki türünde sulanabilir tarım uygulanmaktadır. Bunlardan en önemlileri soğan, lahanası, marul, biber, domates, kabak, patlıcan, havuç, sarımsak, çeltik, buğday, pamuk ve tütündür. Sulu tarım en çok tercih edilendir.

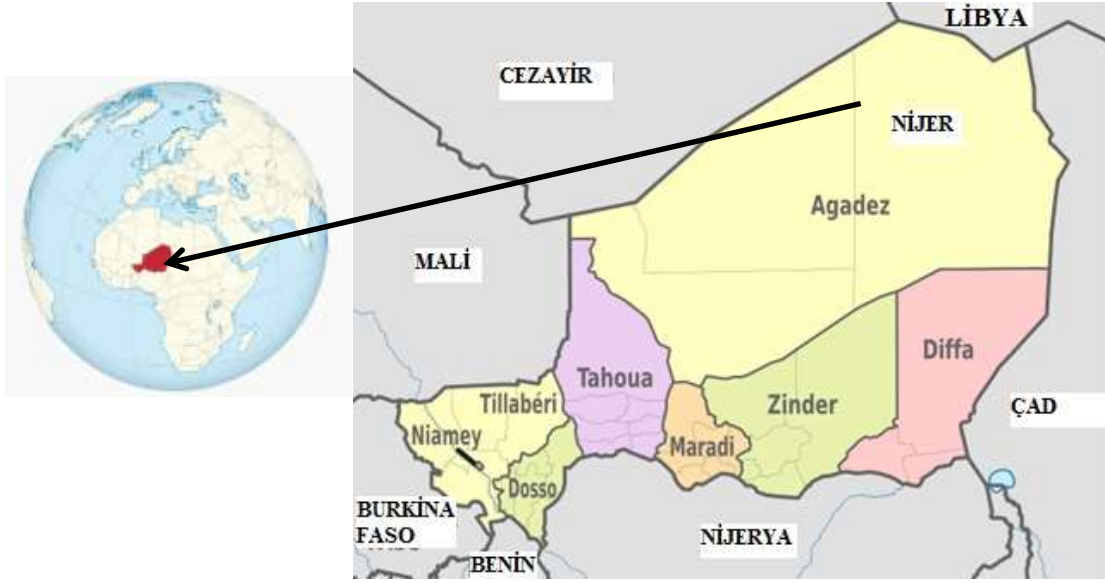
Canlı sığır, uranyumdan sonra en çok döviz getiren ihracat kalemidir. Ulaşım altyapısının yetersizliği ve mezbahaların sınırlı olması nedeniyle et, süt, post ve deri gibi daha yüksek katma değerle elde edilen ürünlerin ihracatından yararlanılamamaktadır.

Nijer tarımının temel olumlu yönleri geniş araziler ile bolca bulunan güneş, rüzgâr, insan enerjisi ve hidroelektrik enerjidir. Tarım alanları ve hayvansal üretim açısından Nijer önemli bir potansiyele sahiptir. Ancak tarımsal potansiyeli yüksek olan Nijer'de, 10 milyon hektar tarım arazisinin etkin bir şekilde kullanılmaması ve birçok ürünün ithal edilmesi, yanlış politikaların sonucu ortaya çıkan önemli bir sorundur. Tarımsal üretimde verim birçok üründe çok düşüktür. Nijer'de tarımsal üretimi ve dolayısıyla verimliliği olumlu ve olumsuz yönlerde; ekolojik koşullar, sosyo-ekonomik yapı, üretim ve teknik gelmektedir.

Araştırmalara göre Nijer topraklarında görülen bitki besin elementi noksanlıkları, meraların ve kültür bitkilerinin verimliliğini sınırlandırmaktadır. Topraklar da çok farklı fiziksel, kimyasal ve biyolojik özelliklere sahiptir.

Nijer'in Coğrafyası ve İklimsel Özellikleri

Nijer Cumhuriyeti, Batı Afrika'nın yüzölçümü (1.267.000 km²) bakımından en büyük devletidir. Güneyde Nijerya ile Benin, batıda Burkina Faso ile Mali, kuzeyde Libya ile Cezayir, doğuda Çad ile sınırları bulunmaktadır. İdari bakımından, Nijer; Agadez, Maradi, Dosso, Diffa, Tillabery, Tahua, Zinder, Niamey başkenti ekleyerek tam sekiz bölge ve 36 il'e ayrılmıştır (Şekil 1). Genel olarak Nijer'de geçim kaynağı tarım ve hayvancılıktan sağlanmaktadır.



Şekil 1. Nijer haritası

Ülke büyük bir Afrika nehrinin adını taşımaktadır. Mali'den gelen Nijer Nehri, ülkeyi 595 kilometrelik bir mesafede kat ederek Nijerya topraklarına girer (Şekil 2). Tarıma elverişli alanların çoğu Nijer nehri kıyısındadır. Ülkenin güneydoğusunda Çad Gölü yer alır [3].

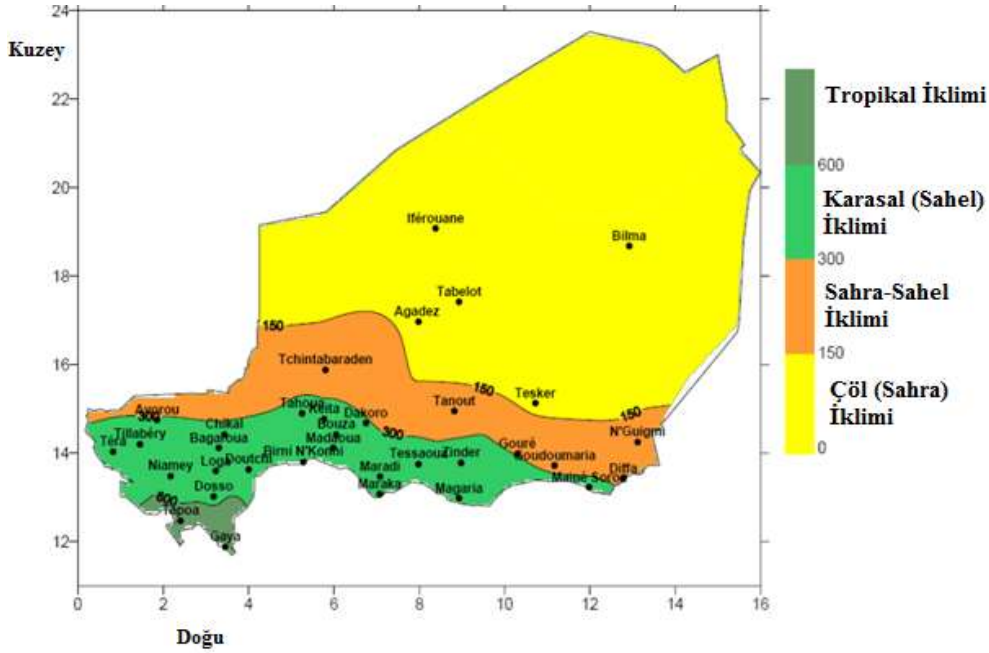


Şekil 2. Nijer nehri

Nijer'de 4 farklı iklim bulunmaktadır. Çöl (sahra) iklimi, karasal (sahel) iklim, sahra-sahel iklimi ve tropikal (sahel-sudan ve sudan) iklim görülmektedir. Güneyden kuzey gidildikçe iklim kuraklaşır, sıcaklık artar. Nijer agro-iklim bölgeleri Şekil 3'de verilmiştir [4].

Yağış

- Çöl (Sahra) bölgesi (<150 mm yıl⁻¹): Toprakların %65'ini oluşturmaktadır.
- Sahra-Sahel bölgesi (150 - 300 mm): Toprakların %12'sini oluşturmaktadır.
- Sahel bölgesi (300-600 mm): Toprakların %12'sini oluşturmaktadır. Bu bölgede genel olarak tahıl yetiştiriciliği yapılmaktadır.
- Sahel-Sudan bölgesi (600 mm): Toprakların %10'unu oluşturmaktadır. Darı, sorgum, fasulye, yer fıstığı yetiştiriciliği için uygun araziler burada bulunmaktadır.
- Sudan bölgesi (>600 mm): Toprakların %1'ini oluşturmaktadır. Nijer'de yetiştiriciliği yapılan tüm bitkiler için en elverişli alanı oluşturmaktadır.



Şekil 3. Nijer agro-iklim bölgeleri

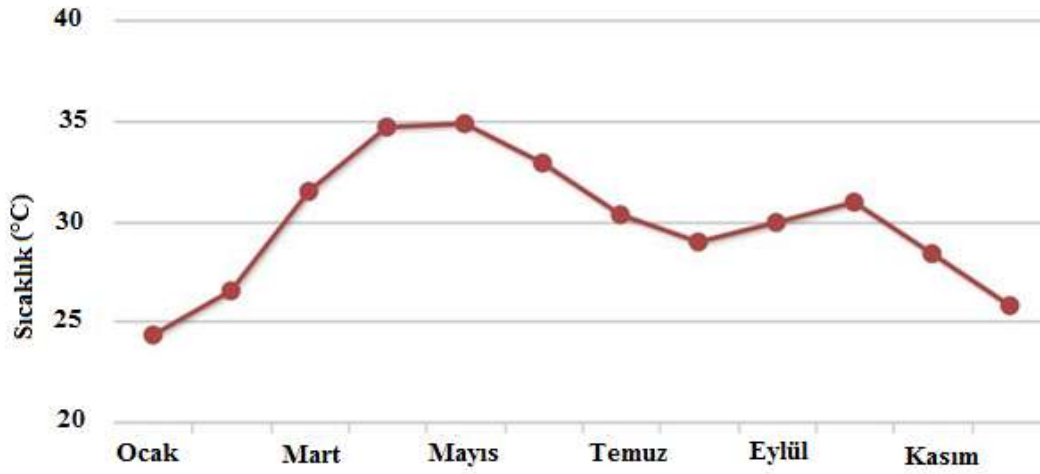
Kuraklığın bütün yılı kapladığı ve yıllık yağış miktarının ancak ($<150 \text{ mm yıl}^{-1}$) olduğu kuzey kesimlerinde yerleşik hayat yoktur. Burada sadece göçebe Tuaregler yaşar. Güneyde nemli tropikal iklim hüküm sürer. Bu iklim tipinde Ekim'den Haziran'a kadar devam eden bir kurak dönemle ve Temmuz'dan Ekim'e kadar yağış alan bir dönem ($600-800 \text{ mm}$) dikkat çeker.

Sıcaklık

Nijer genel olarak sıcak bir ülkedir. Mayıs aylarında sıcaklık $45 \text{ }^\circ\text{C}$ 'ye ulaşmakta ve Aralık-Ocak aylarında $0 \text{ }^\circ\text{C}$ 'ye kadar düşmektedir [5]. Nijer'i ziyaret etmek için en uygun dönem, hava sıcaklıklarının düşük olduğu ve yağış görülmeyen Aralık, Ocak ve Şubat aylarıdır. Kuzey ve Güney Nijer bölgelerinin 1990-2012 yılları arasında aylara göre ortalama sıcaklık dağılımı Şekil 4 ve Şekil 5'de verilmiştir [6].



Şekil 4. Kuzey Nijer bölgesi ortalama aylık sıcaklık değerleri



Şekil 5. Güney Nijer bölgesi ortalama aylık sıcaklık değerleri

Buna göre Kuzey ve Güney Nijer bölgeleri sıcaklık bakımından birbirleri ile oldukça farklılık göstermektedir. Güney Nijer’de en yüksek sıcaklık değeri 35 °C iken Kuzey Nijer’de 45 °C’ye kadar çıkmaktadır.

Nijer’de Yetiştirilen Önemli Kültür Bitkileri

Nijer’de yetiştirilen bazı önemli kültür bitkileri Tablo 1’de verilmiştir.

Tablo 1. Nijer’de yetiştirilen önemli bitkiler

Hububat Ürünleri	Darı, sorgum, çeltik, mısır, buğday, fonio, arpa
Baklagiller	Fasulye, yer fıstığı, voandzou
Yumrulu bitkiler	Manyok, tatlı patates, patates
Diğer Yağmur Suyu ile Beslenen	Susam, topalak, şeker kamışı, tütün, pamuk, bamya
Sebzeler	Soğan, sarımsak, domates, biber, patlıcan, kavun, karpuz, kabak, lahana, marul, havuç
Meyveler	Narenciye, mango, hurma, guava, muz, papaya
Süs Bahçe Bitkileri	Çiçek, çim

Nijer’de yaklaşık 30 bitki türünde sulanabilir tarım uygulanmaktadır. Bunlardan en önemlileri soğan, lahana, marul, biber, domates, kabak, patlıcan, havuç, sarımsak, çeltik, buğday, pamuk ve tütündür. Sulu tarım en çok tercih edilendir.

Nijer Vadisi’nin özellikle Tillabery bölgesinde pirinç, bataklık alanların kenar kesimlerinde mısır, Air ve Ader bölgelerinde buğday, hurma, manyok ve patates ekimi yapılır. Doğuda ve güneyde yer fıstığı, pamuk, şeker kamışı ve sebze tarımı yapılır. Nijer’de yetiştirilen bazı kültür bitkilerinin yıllara göre üretim miktarları ton olarak Tablo 2’de görülmektedir [7].

Tablo 2. Nijer’de değişik bitkilerin yıllara göre üretim miktarları (ton)

Üretim	2013	2014	2015	2016	2017
Darı	2.921.982	3.321.752	3.404.813	3.886.079	3.790.028
Sorgum	1.320.250	1.425.982	1.918.330	1.808.263	1.945.136
Çeltik	87.106	103.941	90.831	104.392	112.632
Mayıs	17.813	56.597	35.387	38.022	38.345
Buğday	5.666	1.802	8.090	8.234	6.003
Susam	55.607	55.186	34.111	66.722	49.263
Kuru soğan	736.271	783.134	837.852	1.011.577	1.159.035
Yeşil soğan	711.963	738.095	584.576	585.933	670.213
Toplam	5.856.658	6.486.489	6.913.990	7.509.222	7.770.655

Fao verilerine göre Nijer’in (8 bitkileri) 2013-2017 yılları arasında toplam üretimine oranla dikkate değer bir artış göstermiştir. 2016-2017 en fazla üretim miktarlarına sahip yıllardır.

Nijer Tarımının Olumlu ve Olumsuz Yönleri

Tarımsal alanlar, beslenmede temel gereksinim olan önemli ürünlerin üretildiği alandır. Tarımın bütün toplumlar için en hayati ekonomik faaliyet alanı olmasının iki temel nedeni bulunmaktadır. Birincisi, insanların en temel sorunu olan beslenme ihtiyacını doğrudan karşılayan sektör olması; ikincisi ise, çağımızda her toplum için zorunlu bir amaç haline gelen ekonomik kalkınmayı sürükleyici kaynakları sağlamasıdır.

Nijer tarımının temel olumlu yönleri geniş araziler ile bolca bulunan güneş, rüzgâr, insan enerjisi ve hidroelektrik enerjidir. Tarım alanları ve hayvansal üretim açısından Nijer önemli bir potansiyele sahiptir. Ancak tarımsal potansiyeli yüksek olan Nijer’de, 10 milyon hektar tarım arazisinin etkin bir şekilde kullanılmaması ve birçok ürünün ithal edilmesi, yanlış politikaların sonucu ortaya çıkan önemli bir sorundur.

Tarımsal üretimde verim birçok üründe çok düşüktür. Nijer’de tarımsal üretimi ve dolayısıyla verimliliği olumlu ve olumsuz yönlerde etkileyen etkenlerin başında;

- Ekolojik koşullar
- Üretim
- Teknik,
- Soyso-ekonomik yapı ve
- Eğitim gelmektedir.

Ekolojik koşullara bakıldığında, tarımı etkileyen unsurların başında su, toprak ve hava kirliliği ile erozyon ve çölleşme gelir. Nijer’in yıl boyunca çok az yağış alması nedeniyle, tarımında en büyük sorun susuzluktur. Tarımda sulama ihtiyacının en fazla olduğu bölge kuzey ve orta Nijer bölgeleri iken bu sorunun en az olduğu bölge güney Nijer özellikle Nijer Nehri bölgesidir. Toprakların çoğunda organik madde, N ve P düzeyi düşüktür. Nijer’de toprak erozyonu ciddi bir problemdir. Özellikle kurak, yarı kurak ve az nemli alanlarda iklim değişiklikleri ve insan aktivitelerinin de dahil olduğu çeşitli etmenlerin sonucunda erozyon meydana gelmektedir. Erozyon ve çölleşmede doğal etmenler toprak aşınması, topraktaki bitki besin elementlerinin uzaklaştırılması ve iklimsel değişimler olarak bilinir. Araziyi erozyon ve çölleşmeye yönlendiren teknik nedenler olarak, arazinin uygun biçimde kullanılmaması, doğal bitki örtüsünün yok edilmesi, ormanların yok edilmesi, meraların düzensiz, kontrolsüz ve zamansız kullanılması, kültürel ve fiziksel toprak koruma önlemlerinin yeterince alınmaması sayılabilir.

Nijer’de üretimle ilgili temel sorunlar arasında tarımsal mücadele ve gübreleme problemi öne çıkmaktadır. Üretimde verimliliğin artırılması ve elde edilen ürün kalitesinin yükseltilmesi için üretimi olumsuz yönde etkileyen hastalık ve zararlılara karşı mücadele önem taşımaktadır. Nijer’de çeşitli bitki

hastalık ve zararlıları (kuşlar, kemirciler, böcekler, mantar, bakteri, virüs neden olduğu hastalıkları, yabancı otlar, parazit bitkileri) nedeniyle ürün meydana gelmektedir. Kimyasal gübre üretimi yeterli olmadığı için gübreler yurtdışından ithal (Nijerya, Cezayir ve Avrupa ülkelerinden) edilmektedir. Bu da maliyeti artırdığından çiftçiler yeterince gübre kullanamamaktadır.

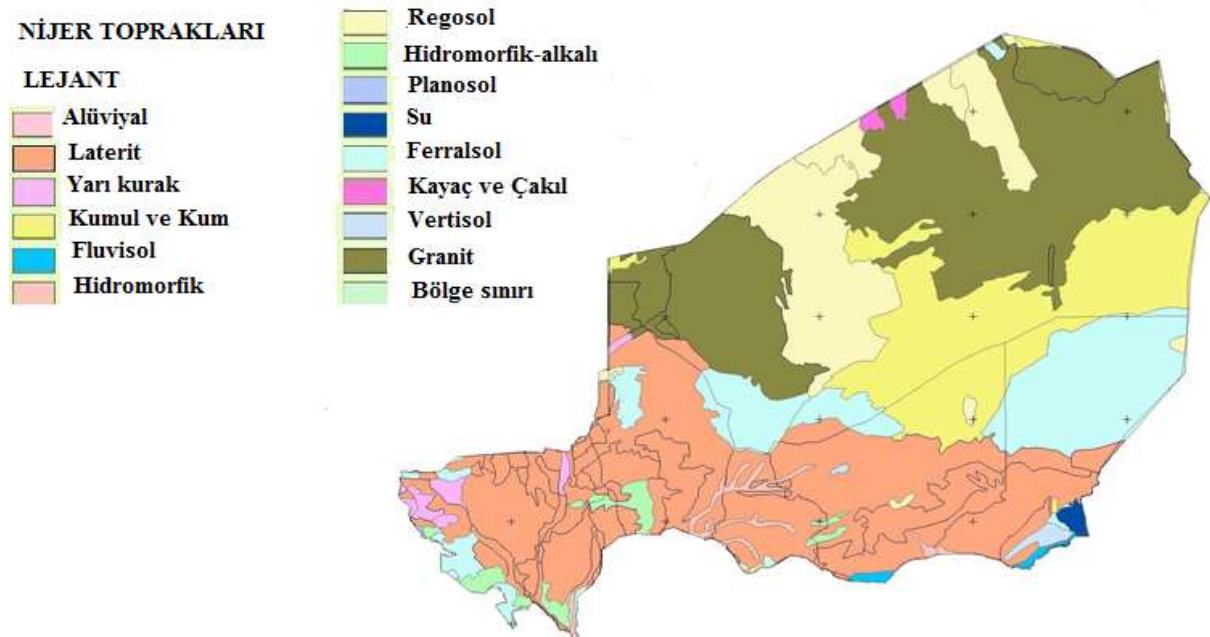
Nijer tarımında teknik ve sosyo-ekonomik sorunların başında, üretimde kullanılan araçlarının düşük performans göstermesi, bazı risk ve belirsizlikler, kredi ve mali kaynakların yetersiz oluşu, kurumsal yapılaşmanın yeterli olmaması, pazarlama sorunu, masrafların yüksek ve gelirin düşük olması, yetersiz bilgi ve eğitim gelmektedir.

Nijer’de Görülen Toprak Çeşitleri

Günümüzde toprağın “Yeryüzünü çevreleyen, bitkilere zemin oluşturan ve besin kaynağı olan, çevreye bağımlı özelliklerini iklim ve yaşayan organizmaların ana materyale etkisiyle çok uzun bir zaman sürecinde kazanmış bulunan doğal varlıklar topluluğudur” şeklindeki tanımı yaygın olarak kabul görmektedir.

Öte yandan, toprak, bitki örtüsünün beslediği kaynakların ana deposudur. Toprağın üst tabakası insanların ve diğer canlıların beslenmesinde temel kaynak teşkil etmektedir. Toprağın kökeni yer kabuğudur. Bir gram toprağın içerisinde milyonlarca canlı bulunmakta ve ekosistemin devamı için bunların hepsinin ayrı önemi bulunmaktadır. Toprağın verimliliğini sağlayan ve humusça zengin olan toprağın 10 cm’lik üst tabakasıdır.

Genel olarak, Nijer’de görülen toprak tiplerinin Şekil 6’da bulunmaktadır [8].



Şekil 6. Nijer toprak haritası

Nijer toprak çeşitliliği yönünden zengin bir ülkedir. Çünkü değişik bölgelerinde farklı iklim tipleri etkilidir. Nijer topraklarının oluşumu, yeryüzünün diğer yerlerindeki toprakların oluşumundan farklı değildir. Topraklar, iklim, topoğrafya, bitki örtüsü gibi etkenlere bağlı olarak kısa mesafelerde farklı özellikler gösterirler. Bunun için Nijer’in coğrafi bölgelerinde hatta aynı bölge içindeki yörelerde bile farklı topraklar oluşmuş durumdadır. Toprakların çoğu hakkında yeterli çalışma bulunmamaktadır.

Toprakların sınıflandırması, toprak özelliklerinin belirli bir amaca yönelik olarak sistemleştirilmesidir. Böylece tarım alanlarındaki topraklarla, ormancılık yapılan alanlardaki topraklar ve otlaklardaki topraklar için ayrı kullanım amaçları ve ayrı sınıflandırma kriterleri ortaya çıkmaktadır. Öte yandan bölgesel iklim etkileri sadece toprak özelliklerini değil, aynı zamanda o bölgedeki tarım, ormancılık ve hayvancılık yöntemlerini ile amaçlarını da önemle etkilemektedir. Nijer’in coğrafi bölgeleri arasındaki farklar, toprakların sınıflandırmaları için farklı amaçlara göre çalışmayı

gerektirmektedir. Tarımsal üretime yönelik olan bu sınıflandırmalar ekolojik toprak sınıflandırmaları olarak adlandırılmaktadır.

Sonuç

Sürdürülebilir toprak verimliliği ve iyi bir tarım için tüm toprak, bitki, iklim koşulları ve insan faktörünün birbirlerine uyumlu olması gerekir. Bu denge ve düzen ne kadar iyi kurulursa, bitki o kadar iyi gelişmekte, verim o ölçüde artmakta, kazanç o kadar fazla olmaktadır. Bu etkenler arasındaki denge ve düzen, birbirlerinin aleyhine bozulduğu anda, toprak verimliliği ve sonuçta ürün verimi olumsuz yönde etkilenmektedir.

Toprak ve bitki analizleri, toprak verimlilik programının başarısını gösterir ve bitkinin beslenme sorunlarının teşhis edilmesini sağlar. Toprak analiz değerlerinde yeterli miktarda besin elementleri ölçülmesine rağmen bitki tarafından besin elementleri topraktan yeterli miktarda alınamıyorsa, toprakların pH, tuz, kireç ve organik madde içeriklerinin meydana getirdiği problemler tespit edilmeli ve ilk önce ıslah yoluna gidilmelidir.

Toprak analizi ve bitki analizi sonuçları birbirlerini doğrular nitelikte olmalıdır. Toprak analiz sonuçları uygun olmasına karşın bitkide beslenme sorunları teşhis edilmişse, bitkinin topraktan kullanılabilir düzeydeki elementlerinin alımını engelleyen sorunların, ideal verimli topraklarda olduğu şekle getirilmesi sağlanmalıdır.

Referanslar

- [1] INS (2019 April 14) Institut National de la Statistique du Niger, Tableau de Bord Social. http://www.stat-niger.org/statistique/file/DSEDS/TBS_2018.pdf
- [2] FAO (2019) Principaux produits agricoles et alimentaires. Division de la Statistique. Organisation des Nations Unies pour l'alimentation et l'agriculture. Rome. <http://www.fao.org/faostat/fr/#data/QC>. (15 Nisan 2019'da ulaşılmıştır).
- [3] Tahirou K (2015) Republic of Nijer. Recherche d'ordre generale, 41p.
- [4] DMN (2005) Direction de la Météorologie Nationale
- [5] Toudou A (2012) Grands Traits de l'Agriculture Nijerienne. Cours de Master 2 Phytotechnie
- [6] Faculté d'Agronomie Université Abdou Moumouni Niamey/Nijer.
- [7] Anonymous (2016) <http://sdwebx.worldbank.org/climateportal/index.cfm>
- [8] FAO (2019) Principaux produits agricoles et alimentaires. Division de la Statistique. Organisation des Nations Unies pour l'alimentation et l'agriculture. Rome. <http://www.fao.org/faostat/fr/#data/QC>. (15 Nisan 2019'da ulaşılmıştır).
- [9] Moussa S (2013) Situation des Sols au Nijer : Contraintes et Besoins. http://www.fao.org/fileadmin/user_upload/GSP/docs/West_africa_partner/SITUATION_DES_SOLS_AU_NIGER_CONTRAINTEES_ET_BESOINS.pdf.

Architecture / Mimarlık

Methodological Review for the Sensational Design and Measurements

*Pınar Orman**, İzmir Kâtip Çelebi Üniv., Dept. of Architecture, Çiğli Main Campus, İzmir, Türkiye
Gökçe Gönüllü Sütçüoğlu, İzmir Kâtip Çelebi Üniv., Inst. of Science, Dept. of Urban Regeneration, Çiğli Main Campus, İzmir, Türkiye
Ahenk Karcı Demirkol, İzmir Kâtip Çelebi Üniv., Inst. of Science, Dept. of Urban Regeneration, Çiğli Main Campus, İzmir, Türkiye
Ayşe Kalaycı Önaç, İzmir Kâtip Çelebi Üniv., Dept. of City and Regional Planning, Çiğli Main Campus, İzmir, Türkiye

*Corresponding author: pınar.orman@asu.edu

Keywords: sensational design, physiological response, methodologies for sensing

Discipline: Architecture

Abstract

The environmental features affect the user perception and experience in the space. The perceived environment has the role on our mood, stress, anxiety, feeling, and relaxation according to the literature in architectural, psychological, neuroscientific, environmental and planning sciences. Many of research have been conducted in the last decades to find out the correlation between senses, perception and space, and how body response to surroundings.

Research to figure out the human perception of outer world evolves around the human senses and feelings that are how they echo our inner world and how we respond to them either emotionally or physically. It is important that these research inform designers to consider environmental factors, features of perceptual and materialistic elements that they would use in their designs to create better and memorable experiences.

The aim of the present study is to review methodologies used in the literature to put forward the relationship between the senses and perceptions of users, space, and environment. In addition to the such subjective methodologies as interviews, surveys, ethnographic observations, the evidence based research methods are developing thanks to the new technologies to conduct objective measurements in spatial experiments.

Although there are many research methods to study physiological and psychological responses of human body to their environments, in this work we reviewed the related literature and form five measurement methods to be taken into consideration for the future design studies also to inspire future research methods to be developed. The methods we analyze in this work are; measuring blood pressure, measuring electroencephalographic (EEG), measuring heart rate variability (HRV), measuring electromyographic (EMG) and regional cerebral blood flow (rCBF). These methods indicated the physical responses to environmental stimuli.

Introduction

The reciprocal interaction between the environment and people have been proven and focused by theorists and researchers in the last decades. While people effect their environment, the environment effects people as well. Various disciplines involve researching the issue such as architectural, psychological, neuroscientific, environmental and planning. In the design disciplines, ‘creating built environments for the best experience’ and ‘optimum function to fulfill users’ needs’ have been the prominent aspects of a good design. Developing technologies and methods in science allow designers to know better how human body reacts to some specific environments, colors, lightings, materials, thermal comfort, etc. According to the many research in literature the environments designed with this in mind create experiences which influence and improve health, wellness, positive moods, motivation, attention and productivity and more.

Research explores the relationship of brain, body and environment work with neuroscience, psychology and psychophysiological domains using different methodologies. In this study, we put together five different measurement methods relevant to design studies to observe body response to different environments. These methods are measuring blood pressure, electroencephalographic (EEG), heart rate variability (HRV), electromyographic EMG, and regional cerebral blood flow (rCBF) in different environmental exposures.

**3rd International Students Science Congress
3-4 May 2019, İzmir - Turkey**

Electrical and chemical signals incoming from sensory organs are analyzed and stored and responded by brain. External environments such as sound, touch, light, smell, temperature, position to gravity and internal parameters such as chemical concentrations, blood pressure, oxygen tension, body temperature are affective determinant on the body response. Generated chemical and motor responses are adaptive to environment to survive and tend to create consciousness and memory by meaningful experiences. Neuroscience discipline researches on the extent of these input signals and physiological body responses, conscious and unconscious thoughts, as well as emotional and aesthetic responses [1]. Thus, it is important for the disciplines in design field to keep informed of the latest developments in related neuroscientific research and also collaborate.

Methods

In this study we reviewed the psychophysiological and neuroscientific methods involve in design studies to see the affects and arousal changes in body at different environments. There are numerous new and powerful techniques to measure the reactions of subject in the perceived space. These methods help to gather data and important information on stress, attention, learning, mental and emotional state etc. via the audio, visual and physical inputs from the experiment environments.

Because the perceptual experiments are done for multiple or large environment with a lot of raters it would be appropriate to use color pictures, slides, or some virtual environment techniques (VR). Otherwise it would be difficult, expensive and time consuming. These would be appropriate methods, since the studies show a general overlap in results between the on and off-site ratings. These kind of objective measurement studies focuses on organism-environment transactions are important because they validate the observation and self-report techniques such as rating and surveys. The objectivity of the measured outputs is especially important feature to make inferences on design studies [2].

Psychological states are often related with physiological events. As Cacioppo and Tassinary [3] note when the psychophysiological relationship is considered it need to be lowered to one to one and one to many relationships. So, it would be possible to make inferences. Parsons et al. [2] give an example of reducing from one to many relationships to one to one relationship. It is showed in Figure 1 that orienting, startle and defense responses in psychological state matching with the elements in physiological state such as phasic skin conductance responding (SCR, a measure of moment to moment differences in sweat gland activity) and heart rate (HR). In the second phase figure shows that, the results give more distinguished relationship when include the pattern of physiological response: orienting response match with increased SCR and decelerating HR, startle and defense responses match with the increased SCR and accelerating HR. In the third phase when introducing the temporal differentiation SCR increases and rate of HR being abrupt for startle ad lingering for defense. By using this kind of methods to reduce it to a one to one relationship it would be possible to make inference preferences and emotional responses to environments and potential health benefit, affect arousal states (mood and arousal) [2].

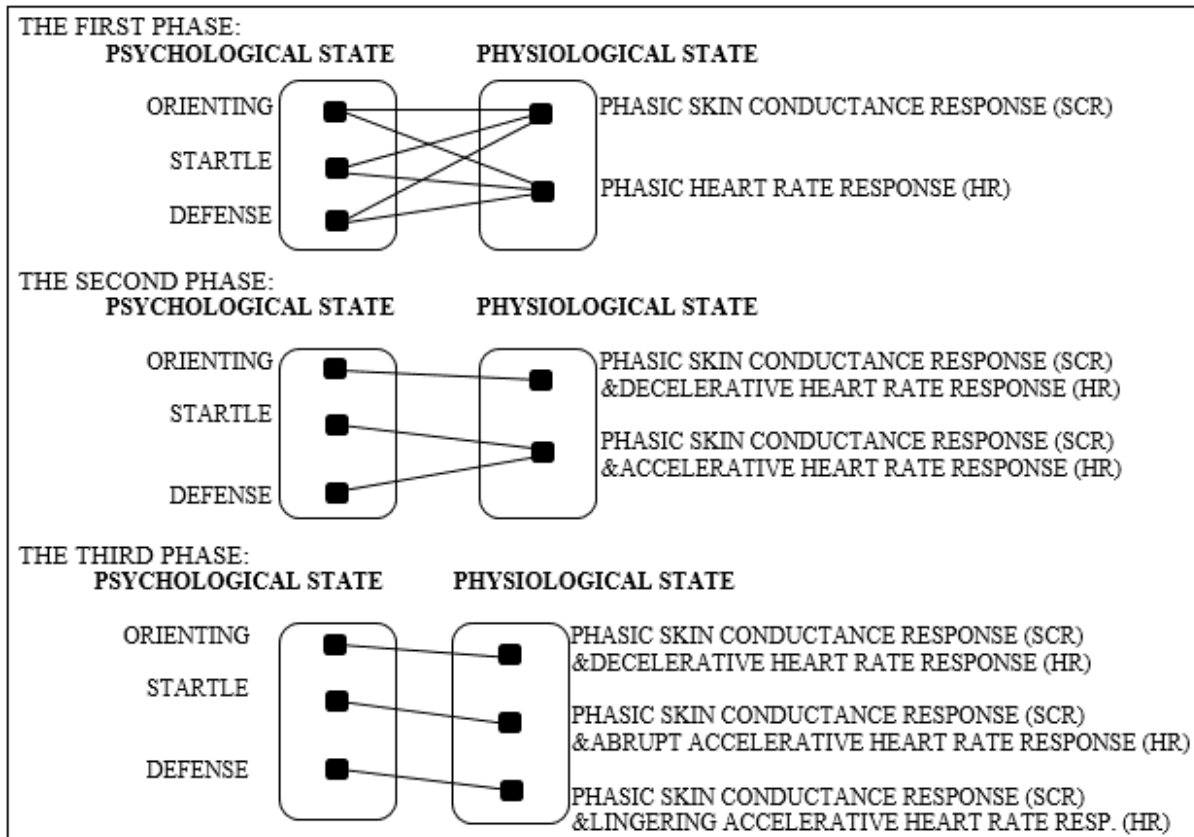


Figure 1. Reducing many to one relationship example: Psychological states are often related with physiological events. Retrieved and modified from Parsons et al. [2].

Discussions

Electromyographic (EMG)

This measurement technique associates the physiological response to emotional state measuring three facial muscles corrugator supercillii (frowning and knitting of the brow), zygomaticus major (mouth up and back eg. smile) and orbicularis oris associates with mouth movements and used to check with activity recorded from zygomaticus major). Dias et al. [4] explains that by electrodermal activity (EDA) and electromyography (EMG) it had been possible for them to objectively measure positive, negative emotions, and neutral condition on subjects in architectural environment in VR.

Trapanotto et al. [5] used the electromyographic (EMG) method to measure the behavioral reactions of infants to the different levels of noise exposure in the Paediatric Intensive Care Unit (PICU). They took EMG records of corrugator supercillii muscle before, after and during the stimulation. The results show that high-intensity noise caused behavioural and physiological (EMG) effects on infants.

Heart Rate Variability (HRV)

The heart rate variability is another measurement method to observe physical reactions to environment. In a study conducted to observe the effects of different color light exposures on memory task performance. The heart rate variability (HRV) showed quite difference after brief exposures to bright white, red and dark condition [6].

Another work aimed to analyze human thermal comfort in built environment the researchers measured heart rate variability (HRV) at the different thermal comfort levels to see mechanism of thermodynamics of human body. Under temperatures of 21, 24, 26, 28, 29, and 30°C, the subjects' electrocardiogram are observed for 5 minutes. The analyzed HRV (the ratio of absolute powers in low- and high-frequency bands, LF/HF ratio) showed that HRV at discomfort level has significantly higher value comparing to comfort level, eventhough same thermal sensation. The study results illustrated that there is an important correlation between subjects' thermal discomfort and sympathetic activity. Researchers also suggested that, LF/HF ratio could be the pointer of physiological thermal comfort [7].

Noguchi and Sakaguchi [8] conducted a study to investigate the effects of illuminance and color temperature of illumination on autonomic nervous system and central nervous system measuring the heart rate variability (HRV) and alpha attenuation coefficient (AAC) and mean frequency of EEG. Subjective evaluation of drowsiness also evaluated during the experiment. The results showed no effect on HRV from illumination. However, values for AAC, mean frequency in the theta-beta EEG and subjective drowsiness suggested that low color temperature lowers the central nervous system activity. Thus, the study suggested to use low color temperature illumination in bedrooms and resting environments.

Electroencephalographic (EEG)

On wayfinding strategies and orienting in architectural space, a research conducted by Edelstein et al. [9] to gain further insight on designing user friendly spaces. Brain activity of the subjects were recorded when they move in the realistic human scale 3D virtual reality (VR) environments. The brain dynamics showed the difference in independent components' (ICs) event related spectral perturbation which stem from independent component analysis (ICA) of the two situations which are 'recognizing orientation' and 'being lost'. High density electroencephalographic (HDEEG) to measure the neural responses on wayfinding gives insight to researchers and designers to consider these clues on the spatial movement and spatial organization.

Another study investigating the physiological impacts of colors measuring blood pressure and electroencephalogram (EEG) put forward that blue color elicits stronger arousal than red color as expressed by the results of alpha attenuation coefficient (AAC) and the mean power of the alpha band [10].

Blood Pressure

The diastolic blood pressure is also another indicator of body reactions to environmental conditions. Kobayashi and Sato [11] revealed the correlation between color temperature of room lighting and blood pressure. The experiment conducted with four subjects under nine different lighting environments while they are performing 95 minutes calculation task. Blood pressure was measured every 30 minutes during the task. Results showed that the diastolic blood pressure was highly effected by the color temperature level and increased under 7500°K.

It is claimed in a study by Grangaard [12] light and color affect learning and blood pressure. The results indicated 24% decrease on off-task behaviour and 9% on blood pressure compared to 'modified color and light' setting classroom and 'normal' one.

Regional Cerebral Blood Flow (rCBF)

This measurement method helps to observe the prefrontal brain activities when subjects are exposed to environmental experiments. In a study aimed to see the impact of visual surrounding in daily living environment, two actual size living room having distinct interior design features were created. The subjects had been spent 90 minutes in those rooms while their pulse rate, blood pressure and cerebral blood flow (rCBF) were being measured. They also were asked to do subjective evaluations. The results of the subjective evaluations did not present significant difference. However, their pulse rate, blood pressure and cerebral blood flow (rCBF) measures revealed different physiological responses. The subjects presented a calm and relaxed state in the ordinary designed room, while they showed an active and aroused state in the room with wooden posts and beams [13].

In a research conducted to clarify stimulative effects of design elements in mental activity, Baba and Watanabe [14] examined the brain activity of subject with wearable optical topography. The subjects worked on memory tasks in different size and color study booths: a large yellow booth, large white booth, small white booth, and small yellow booth. The brain activity in the prefrontal cortex were measured during memory tasks in these booths. The results indicated that the booth size and color impacts the information processing activity. The size of the booth influences the physiological state. Activation of brain activity effects the correct answers' percentage and affected reaction rate. It is also found that among the booths in this study the large and yellow one activated the brain activity in the most.

Another study investigated to find out effects of different interior plant foliage on subjective emotions, visual attention and cerebral activity, subjects observed five variety of Hedera helix plant in 60 seconds randomly. Eye movements and cerebral activity were measured during the experiment. Subjective evaluations also recorded by a semantic differential scale. The study results suggested that

green-yellow and bright green-coloured plants associates with comfort and calmness; red and dark green plants improve energy; while the green-white plants stimulate mostly negative emotions [15].

Conclusion

The developments of physiological measurement techniques and improvements in virtual reality (VR) provide a huge ease on implication of experiments and yields important data for researches to have more information and knowledge about body environment transactions. The possibility of recording physiological and neurological responses to different inner and outer stimulations consolidates and verifies or invalidates the psychological and/or subjective evaluations in researches.

The measurement technologies and methodologies reveal the effects, influences and impacts of design elements on people in built environments, also constitutes the basis of the evidence based design. Design decisions become stronger, and meaningful when architects practice upon evidence based design implications. The collaboration of the neuroscience, architecture, psychology and many other disciplines promotes creating better experiences in built environments while sustaining and flourish health and wellness, which must the ultimate goals of designers.

References

- [1] Edelstein EA, Macagno E. (2012) Form follows function: bridging neuroscience and architecture. In Sustainable environmental design in architecture (pp. 27-41). Springer, New York, NY.
- [2] Parsons R, Ulrich RS, Tassinari LG (1994) Experimental approaches to the study of people-plant relationships. *Journal of Home & Consumer Horticulture*, 1(4): 347-372
- [3] Cacioppo JT, Tassinari LG (1990) Inferring psychological significance from physiological signals. *American Psychologist*, 45(1): 16-28.
- [4] Dias MS, Eloy S, Carreiro M, Proenca P, Moural A, Pedro T, Freitas J, Vilar E, D'alpuim J, Azevedo AS (2014) Designing better spaces for people- Virtual reality and biometric sensing as tools to evaluate space use. *CAADRIA 2014, Hong Kong* 739-748.
- [5] Trapanotto M, Benini F, Farina M, Gobber D, Magnavita V, Zacchello F. (2004) Behavioural and physiological reactivity to noise in the newborn. *Journal of Paediatrics & Child Health* 40:275-281.
- [6] Edelstein EA, Robert JE, Sollers IIIJ, Thayer JF (2007) The effects of lighting on autonomic control of the heart. *Proc. Society for Psychophysiological Research Proceedings*, October, 17-21.
- [7] Liu, W., Lian, Z., & Liu, Y. (2008). Heart rate variability at different thermal comfort levels. *European Journal of Applied Physiology*, 103(3): 361-366. doi:10.1007/s00421-008-0718-6
- [8] Noguchi, H., Sakaguchi, T. (1999) Effect of illuminance and color temperature on lowering of physiological activity. *Applied Human Science:Journal of Physiological Anthropology* 18:117-23.
- [9] Edelstein E A, Gramann K, Schulze J, Shamlo NB, van Erp E, Vankov A, ... Macagno E. (2008). Neural responses during navigation in the virtual aided design laboratory: Brain dynamics of orientation in architecturally ambiguous space. *Movement and Orientation in Built Environments: Evaluating Design Rationale and User Cognition*, 35, 35-41.
- [10] Yoto, A., Katsuura, T., Iwanaga, K., & Shimomura, Y. (2007). Effects of object color stimuli on human brain activities in perception and attention referred to EEG alpha band response. *Journal of Physiological Anthropology*, 26(3): 373-9.
- [11] Kobayashi, H., & Sato, M. (1992). Physiological responses to illuminance and color temperature of lighting. *The Annals of physiological anthropology* 11(1): 45-49.
- [12] Grangaard, E. M. (1995). Color and light effects on learning. (ERIC Document Reproduction Service No. ED382381)
- [13] Tsunetsugu, Y., Miyazaki, Y., & Sato, H. (2005). Visual effects of interior design in actual-size living rooms on physiological responses. *Building and Environment*, 40(10), 1341-1346.
- [14] Baba T, Watanabe A. (2017) Effects of Color and Size in Generating Intellectual Activity in Booth Spaces. *Journal of Asian Architecture and Building Engineering*, 16(3), 551-558.
- [15] Elsadek, M., Sun, M., & Fujii, E. (2017). Psycho-physiological responses to plant variegation as measured through eye movement, self-reported emotion and cerebral activity. *Indoor and Built Environment*, 26(6), 758–770. <https://doi.org/10.1177/1420326X16638711>

Biology / Biyoloji

Remediation of Antimony from Aqueous Solutions Using Pomegranate Peels Residue Accessing to Zero Residue Level (ZRL)

Mohammed Nsaif Abbas, Mustansiriyah Univ., Environmental Engineering Dept., Iraq

Zaidun Naji Abudi, Mustansiriyah Univ., Environmental Engineering Dept., Iraq

Suadat Mustafa Mohammed Al-Hermizy, Tikrit Univ., Dept. of Biology, Iraq

Batool Ahmed Saleem, Mustansiriyah Univ., Environmental Engineering Dept., Iraq

Mohammed Abbas, Mustansiriyah Univ., Environmental Engineering Dept., Iraq

Shadman T. Sadiq, Ege University, Dept. of Industrial and Fundamental Microbiology, İzmir, Turkey*

**Corresponding Author: shadmantsm@gmail.com*

Keywords: adsorption, antimony, pomegranate peel, zero residue level

Discipline: Biology, Ecology, Botany, Biochemistry

Abstract

This paper is related to study the ability of Pomegranate Peel (*Punica granatum*) Residues as low cost agro-adsorbent for treating simulated synthesis aqueous solutions (SSAS) contaminated with antimony at various operating conditions using adsorption technique in batch mode unit. Results exhibit that the maximum remediation efficiency of antimony was 85.72% and the efficiency was decreased with increasing of initial concentration and temperature while the removal efficiency increased with increasing pH, agitation speed, dose of adsorbent material and contact time. The isotherm of antimony adsorption was conducted using the famous two models which were Langmuir and Freundlich models. The results show that the Langmuir isotherm was more suitable than Freundlich equation to describe the experimental results obtained. It was also concluding that the adsorption process obeys the second order kinetic model. By this way it can obtain various benefits which were: remediate the antimony ions from polluted solution and in the same time, get rid of agricultural waste pomegranate peel residue. More type of waste can be removed by a benefit, non-cost and eco-friendly ways accessing to zero residue level (ZRL).

Introduction

Antimony is one of a well-known chemical element since ancient times and it is a semi-metallic element belongs to a group of elements called (chalcophile) [1]. In nature, antimony comprises 0.00002% of the earth's crust and it is found with two types the first one is metallic form of gleaming, silvery, harsh and brittle appearance and the other form is non-metallic of gray powder feature [2]. This metal is usually obtained from ore's mining which are stibnite (Sb_2S_3) and valentinite (Sb_2O_3) and China guides the production of antimony by nearly 90% of world production [1]. Antimony is considered as one of the most important minerals in the global economy where the high purity of it used for manufacturing of special types of semiconductors, diodes and infrared indicators flame retardants, catalysts for plastics synthesis, and alloys for ammunition. It is used in the preparation of high-interest lead alloys, which are used in the manufacture of high hardness and mechanical resistance batteries [3]. This element is used in the hardening of antimony-low content alloys, which are used in the produce of some devices pipes' and also used in the manufacture of low-friction alloys (Babbitt alloy) [4]. On the other hand, some compounds of antimony are used for production of anti-fire materials, dyeing elaboration, glass making, pottery preparation, enameled ceramic and writing metal, as well as for packaging of electrical cables, as well as in bullets and lead shot and in pewter [5]. In addition to that, it is used in the preparation of lead-free welding with antimony 5%. As well as the above, antimony is considered as one of the substances involved in the preparation of antimony potassium tartrate hydrate which is used in schistosomiasis treatment [6]. Because of what is antimony or most of its component characterized, it is used as a raw material in many other industries. Although the wide use of this metal, however, antimony and its compounds is considered as a global priority contaminant [7]. The high concentration of antimony in wastewater disposed from natural or industrial processes is a global concern. On this basis, particular attention is focused on the potential toxicity and damages that may be caused to the environment as a result of water pollution by this element [8]. In addition, the antimony is considered as heavy metals due to its density of 6.79 g/cm³ at 20°C [9]. Therefore, for all the above effects, antimony and its compounds must be removed from wastewater and aquatic environments to

maintain human health and environment. Various conventional methods for treating wastewater contaminated with heavy metals has been used and is still being used such as chemical deposition, electrolysis, ion exchange, solvent extraction, membranes and reverse osmosis [10]. These methods have many disadvantages and technical impediments or economic trammels, e.g. incomplete removal, high energy requirements, and production of huge toxic sludge that may generate additional problems in how to safely dispose of them [11,12]. The adsorption technology has been identified using activated carbon as a possible alternative to previous technologies and is the most common and effective way of treating waste water. It is a trend in green chemistry to reduce the use of toxic and carcinogenic solvents in wastewater treatment processes. However, although adsorption by activated carbon is highly efficient, but the problems related to regeneration and reuse, as well as increased operating costs, have made contaminated water treatment and pollutant removal less useable and have many limitations and constraints [13]. For this reason, there are ongoing researches on low-cost, high-efficiency adsorbents to be alternatives for activated carbon to remove various types of pollutants, particularly heavy metal ions such as antimony. Recently, great attention has been paid to the adsorbent materials of natural basis, such as rice husk [13], banana peel [14], pomegranate peels [15], lemon peel watermelon rinds... etc., which can be used as adsorbents for many pollutants such as heavy metals, dyes, pesticides, inorganic toxics and radioactive substances [12,15]. Pomegranate peels can be used as natural adsorbents, thus reducing the cost of wastewater treatment and polluted water to a large extent and is a useful and practical way of disposing of the remains of an agricultural waste and toxic substances together [15]. The purpose of this paper is to evaluate and determine the efficiency of pomegranate peels residue to remove antimony (Sb^{+5}) ions from simulated synthetic aqueous solutions (SSAS) and to get rid of more than one type of wastes together in a useful, economical and eco-friendly method reaching to Zero Residue Level (ZRL) concept.

Methodology

Preparation of Adsorbent Media (Pomegranate Peels)

Pomegranate peels residue was freely acquired by the domestic usage. The amassed pomegranate peels were washing with redundant deionized water to strip filth, dust, impurities, fine dirt may be stuck on the surface of it. The washed pomegranate peels were dried overnight at 105°C. The pomegranate peels were used for adsorption of antimony (Sb^{+5}) ions directly with its original size and without any further treatment.

Preparation of Antimony (Sb^{+5}) ions Stock Solutions

In order to avoid interference with other elements that may be found in the ordinary wastewater, the antimony (V) ions remediation experiments were carried out using simulated synthesis aqueous solutions (SSAS) of antimony (Sb^{+5}) ions. A quantity of 2.1590 g of potassium hexahydroxoantimonate (V) salt $KSb(OH)_6$ is poured in 1 liter of deionized water for preparing 1000 mg/l stock solution of Sb^{+5} ions. In any subsequent experiment, the desired concentration was prepared by diluting the exact volume of stock solution in distilled water. The concentrations of antimonate ion were measured using spectrophotometric method by atomic absorption spectrometry (AAS).

Calibration Curve

The calibration curve of antimonate ion was carried out using multiple solutions of different concentrations. Absorbance at its maximum wavelength was measured using atomic absorption spectrophotometer (AAS) shimadzu AA-7000, Japan. The installed was performed according to the instructions of manufacturers with corresponding to antimonite ion wavelength. The calibration curve of antimonate ions was determined via absorbance at $\lambda_{max}= 217.6$ nm. Figure 2 showed the absorbance and calibration curves of antimony (V) ions.

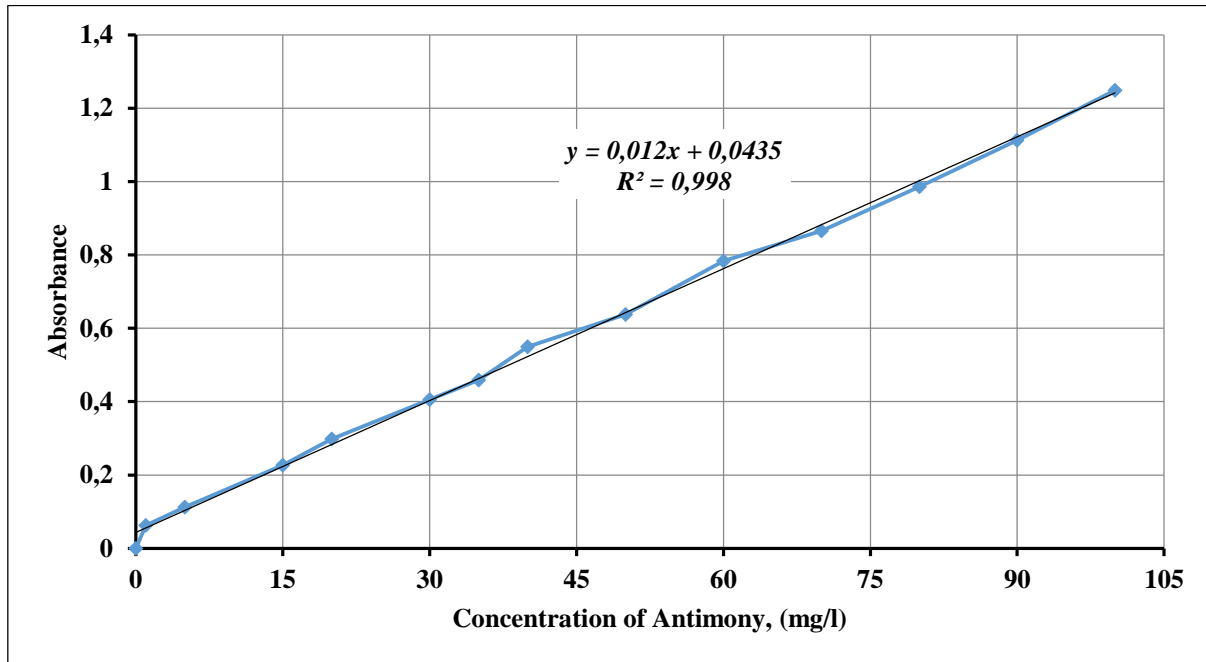


Figure 2. Calibration curve of antimony (V)

Adsorption Experiments in Batch Mode Unit

The removal process of antimonate (Sb^{+5}) ions were achieved using pomegranate peels as low cost adsorption media residue by adsorption technique in orbital shaker and at different operating conditions. The initial concentration of antimonate Sb^{+5} ions, agitation speed, contact time, temperature and pH of SSAS solution were varied from **1-100 mg/l**, **100-500 rpm**, **10-180 minutes**, **20-50 °C** and **1-12** respectively. All experiments performed triplicated and the mean value was taken. The value of pH was controlled using acidic solution of 0.1 N HCl and basic solution of 0.1 N NaOH using Mettler Toledo pH meter Instrument. To detect the antimony concentration removed from the SSAS, samples were taken periodically, filtered, centrifuged and the concentrations of antimonate (Sb^{+5}) ions after treatment with adsorbent media were measured using AAS at $\lambda_{\text{max}} = 217.6 \text{ nm}$ and prepared calibration curve.

Results and Discussion

Initial Concentration Influence:

The results obtained demonstrate that using pomegranate peels residue as an adsorbent media, the percentage removal of antimonate ions from simulated synthesis aqueous solution (SSAS) was increased when the initial concentration of antimonate (Sb^{+5}) ions was decreased at keeping other variables are constants at optimum conditions as shown in Figure 3. This can be elucidated by the actuality that the initial concentration of antimonate ions had a finite influence on the remediation capacity; simultaneously the adsorbent media has a fixed number of active positions, which would have become filled with a certain concentration of Sb^{+5} ions. This gave a rise to increase in the number of Sb^{+5} ions competing for the available function sites on the surface of the adsorbent media. Since the SSAS of lower concentration has small molecules of antimonate ions than the solution of higher concentration of it. Therefore, the percentage efficiency of removal was increased with decreasing the initial concentration of antimonate (Sb^{+5}) ions. The higher percentage removal of Sb^{+5} ions was 85.72% and 24.36%, at initial antimonate (Sb^{+5}) ions concentration of 1 and 100 mg/l respectively. Thus, pomegranate peels were found to be efficient for removing polluted antimony ions from aqueous solutions.

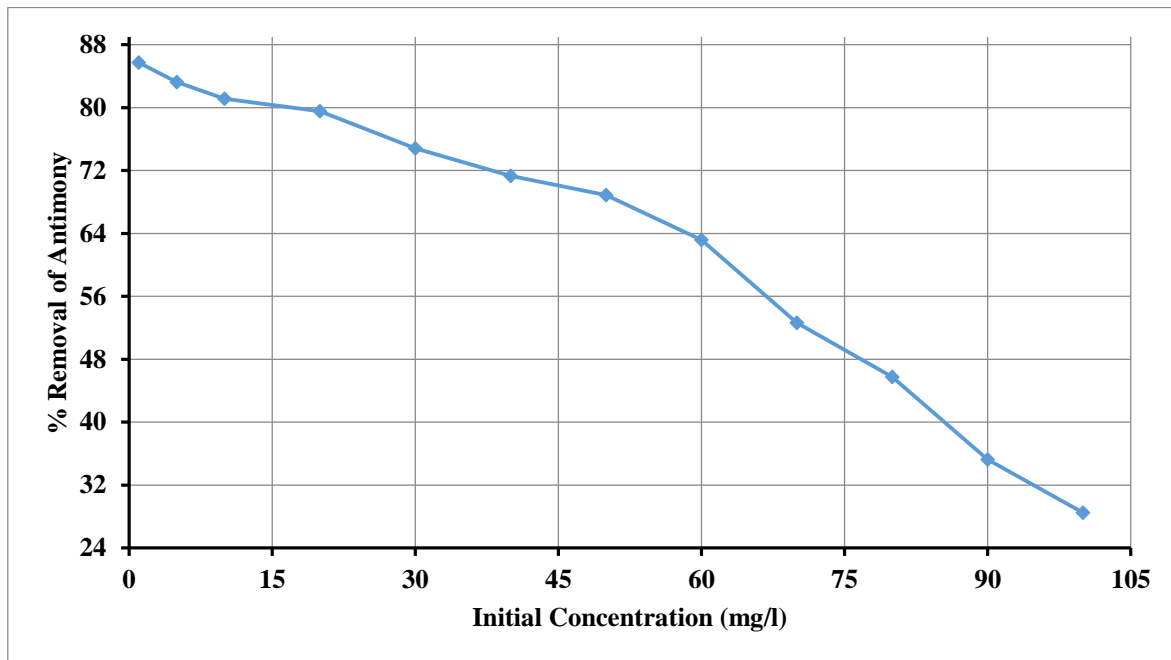


Figure 3. Influence of Initial Concentration on the Percentage Removal of (Sb^{+5}) ions

pH Influence:

It's obvious from Figure 4 that using pomegranate peels residue as an adsorbent media, the removal efficiency of antimonate (Sb^{+5}) ion was decreased when the pH of SSAS was decreased too after reaching to 5 while the efficiency was increased before pH of 5 at constant other variables at optimum values. Usually, due to the certainty that the pH of the solution is an important parameter in adsorption process and the process governed by it is and the pH value had a considerable action on the adsorption removal efficiency. To illustrate the relationship between increasing the adsorption of antimonate and pH increase there are two explanations. The first explanation assumes that the increase in adsorption results from a steady and consistent increase in pH, While the other explanation indicates that the process of adsorption of the antimony ion from the aqueous solutions occurs consistently when moving from the acidic conditions to the neutral conditions which represent the turning point as the adsorption will increase in the base of the solution. This result is agreement with [13]. The adsorption of Sb^{+5} ions can be explained by ion-exchange mechanism of adsorption in which the important role is played by functional groups that have cation exchange properties. For this case at lower pH values, antimonate removal was inhibited, possibly as a result of the competition between hydrogen and Sb^{+5} on the adsorption sites, with an apparent preponderance of hydrogen ions, which restricts the approach of Sb^{+5} ion as in consequence of the repulsive force. As the pH increased, the ligand functional groups in adsorbent media pomegranate peels would be exposed, decreasing the negative charge density on the adsorbent material surface, decreasing the attraction of Sb^{+5} ions with negative charge and preventing the adsorption onto adsorbent material surface.

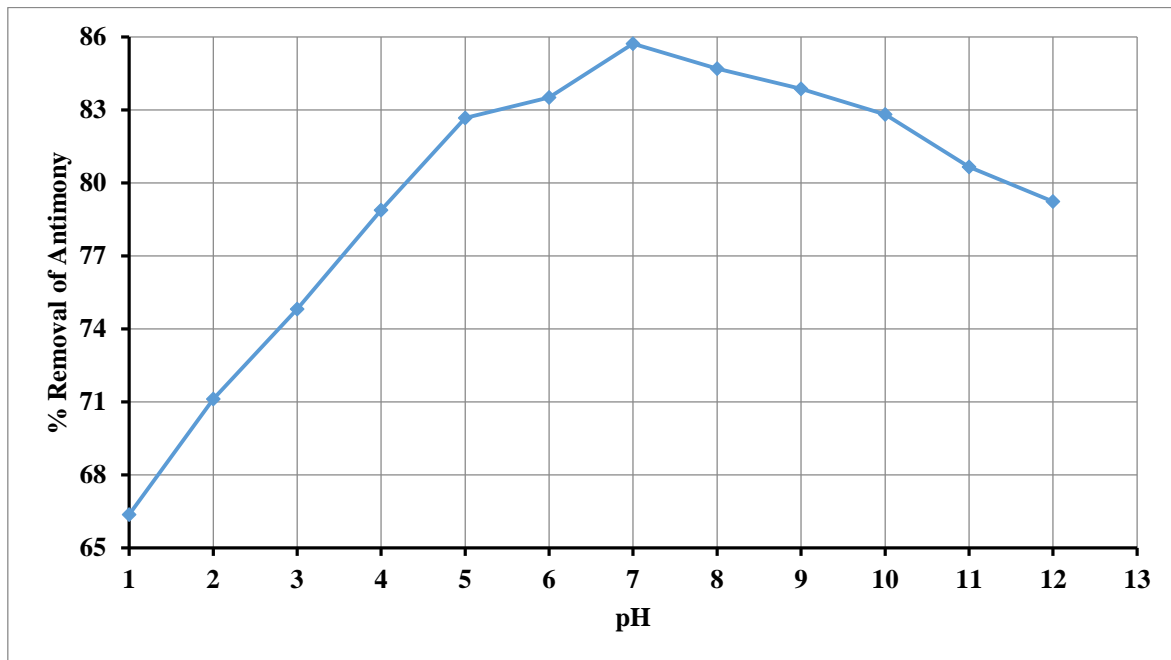


Figure 4. Influence of pH on the Percentage Removal of (Sb^{+5}) ions

Influence of agitation speed:

The effect of agitation speed on adsorption removal efficiency of antimonate (Sb^{+5}) ions is presented in Figure 5. As can be seen from the figure, the removal efficiency of Sb^{+5} ions from SSAS is raised up with increasing agitation speed (i.e. proportional relation). This is due to two facts the first one is the raise up of agitation speed, improves the diffusion of (Sb^{+5}) ions from the SSAS towards the pomegranate peels particles, which have empty pore and can attached the antimonate ions by the functional groups on its surfaces. The other fact that with increased the turbulence, the thickness of boundary layer around the particles of adsorbent media is decrease. It is also obvious from the same figure that the maximum adsorption capacity of pomegranate peels was reach at 350 rpm, but beyond this value there is no further increase in the adsorption efficiency of the antimonate ions. This means that for adsorption process using pomegranate peels residue the optimum agitation speed is 350 rpm.

Contact Time Influence:

The contact time effect on the remediation of antimonate ions from SSAS is shown in Figure 6 at constant other variables at optimum values. The results demonstrated that when the contact time of an antimonate ion in SSAS water was increased, the remediation efficiency of this ion was increased too. This may be due to when the time of (Sb^{+5}) ions treatment in polluted solution was increasing and the agitation velocity of SSAS in shaker with the adsorbent material was remaining constant, the antimonate solution spend longer time in contact with adsorbent media than that it spend when the time of treatment decreased, so the adsorbent material uptake more amount of antimonate ions from SSAS feed, therefore the percent removal of (Sb^{+5}) ions from solution was increased.

Temperature Influence:

The results explained that increasing the temperature of adsorption unit leads to raise up the removal efficiency of antimonate as shown in Figure 7. In general, the movement of positive ions in aqueous solutions is increased by increasing the temperature of the solution. On the other hand, increasing the temperature leads to swelling the internal structure of the adsorbent media, which enables the antimonate ions to penetrate the distant internal pores and in turn to provide additional surface areas through which the adsorption of more particles. The antimonate ions adsorption capacity increased with increasing the temperature from 20 to 50°C. This result is in agreement with the study of Abbas M. N. [15].

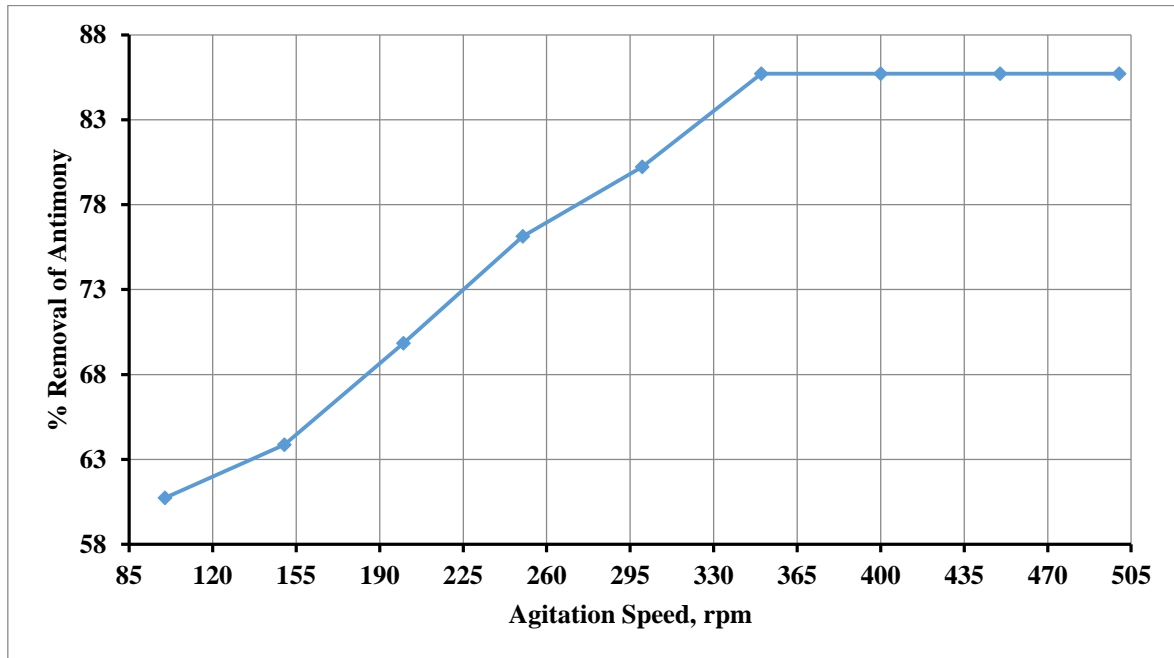


Figure 5. Influence of Agitation Speed on the Percentage Removal of (Sb⁺⁵) ions

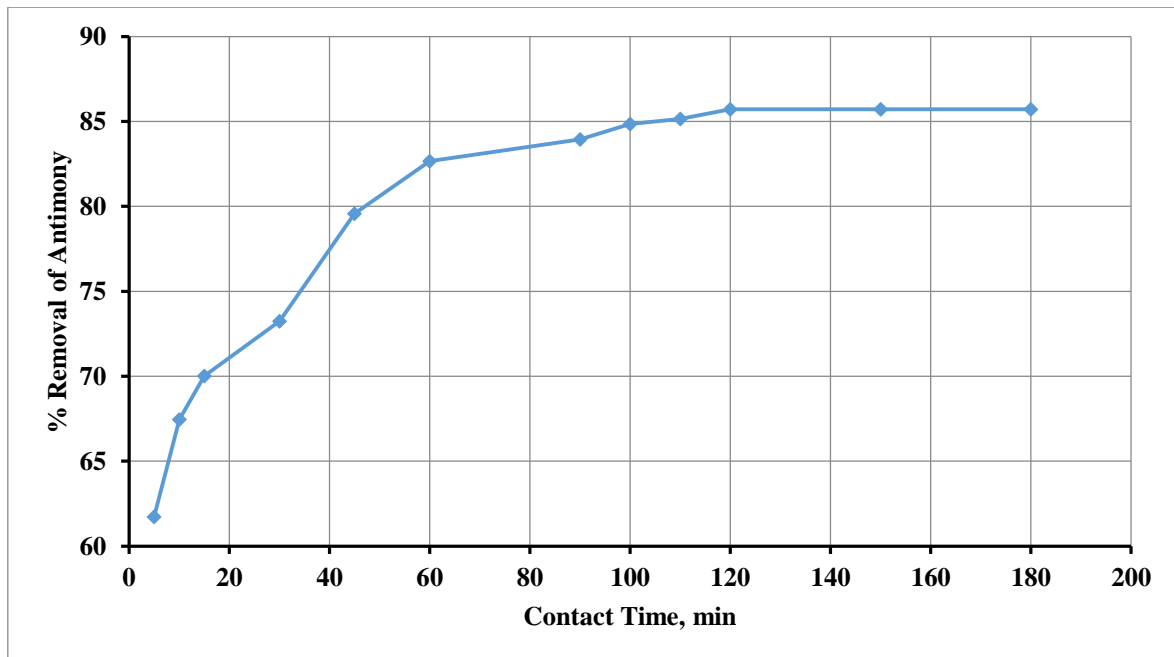


Figure 6. Influence of Contact Time on the Percentage Removal of (Sb⁺⁵) ions

Adsorbent Media Dose Influence:

The results illustrate that at increasing the adsorbent media dose the removal efficiency of antimonate ions from SSAS was increasing too, as depicted in Figure 8, when all other operators are keeping without change at optimum values. The increase in the adsorbent dose inside the adsorption unit lead to increasing the number of active sites that will be adsorbed the antimonate ions from SSAS; as a result, the availability of bonding sites for adsorbing has increased. Consequently, the removal of antimonate ions on the surface of the active sites will be also increased. This will increase the portability of pomegranate peels to adsorb more amounts of antimonate ions from SSAS at various initial concentrations; eventually the percentage removal of antimonate from aqueous solutions will be increased.

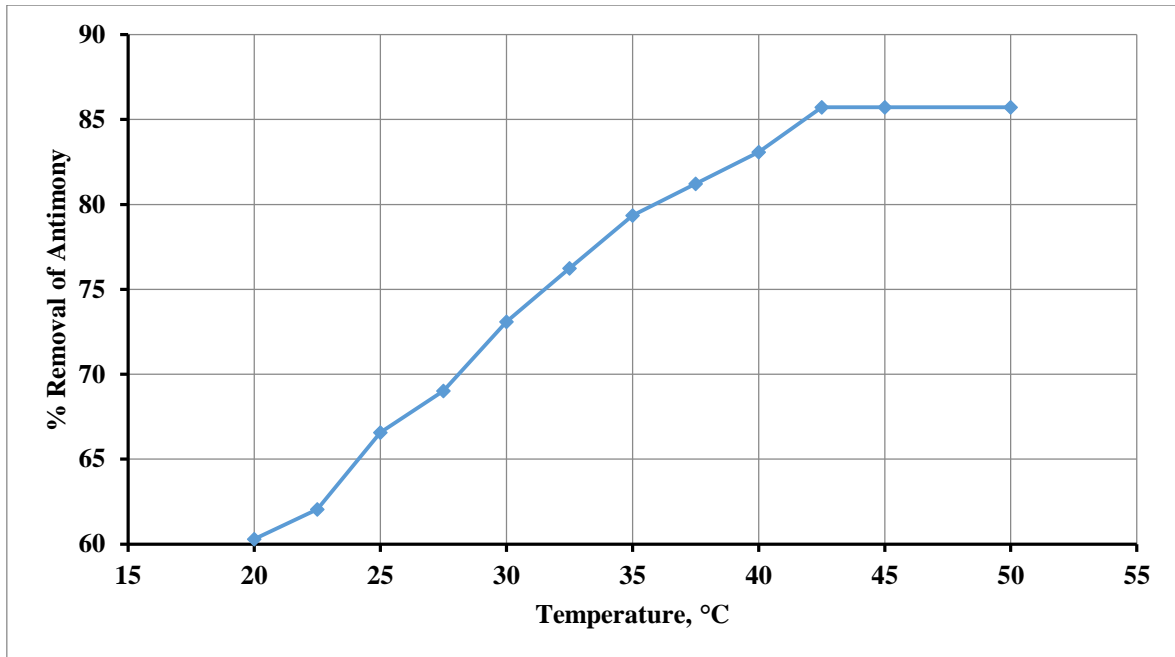


Figure 7. Influence of Temperature on the Percentage Removal of (Sb⁺⁵) ions

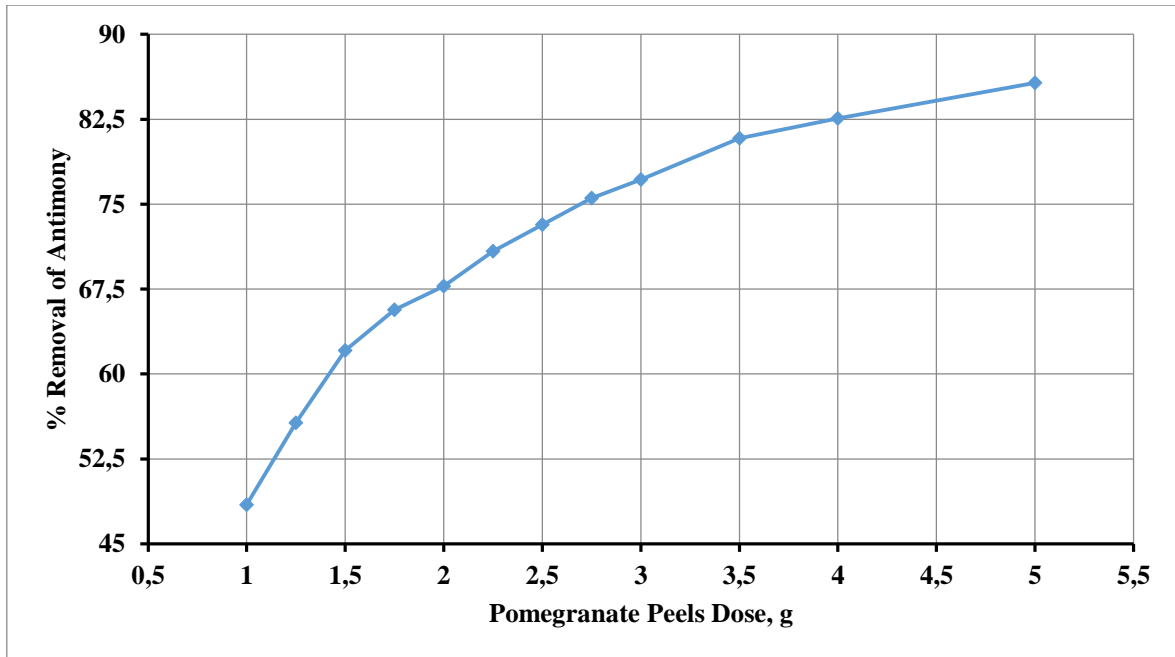


Figure 8. Influence of Dose on the Percentage Removal of (Sb⁺⁵) ions

Adsorption Isotherm

Langmuir and Freundlich models are used to describe the adsorption isotherm behavior in the present study.

Langmuir isotherm model: The Langmuir adsorption isotherm model supposes the adsorption surface is monolayer, homogeneous and the adsorption sites have similar adsorbate ability and each side in the adsorption surface independent on the adsorption in the neighboring sites. Langmuir isotherm model can be described by equation (1):

$$q_{eq} = \frac{q_m \cdot K_L \cdot C_{eq}}{1 + K_L \cdot C_{eq}} \quad \dots (1)$$

where: q_{eq} : is the antimonate ion quantity adsorbate per unit mass of adsorbent at equilibrium concentration C_{eq} , C_{eq} : is the adsorbate concentration in the solution at equilibrium, q_m : is the amount of solute adsorbed per unit mass of adsorbent in forming a complete monolayer on the adsorbent surface and K_L : is a constant related to the energy or net enthalpy of adsorption (1/mg).

For very small amount of adsorption, when $K_L C_{eq} \ll 1$ it yields a linear adsorption isotherm: $q_{eq} = q_m K_L C_{eq}$. For large amount of adsorption, when $K_L C_{eq} \gg 1$ it will be equal: $q_{eq} = q_m$. Thus, the Langmuir isotherms model can be represented by linear form as:

$$\frac{C_{eq}}{q_{eq}} = \frac{1}{K_L q_m} + \frac{1}{q_m} C_{eq} \quad \dots (2)$$

Plotting of $\frac{C_{eq}}{q_{eq}}$ against C_{eq} will give a straight line, has an intercept of $\left(\frac{1}{K_L q_m}\right)$ and the slop is $\left(\frac{1}{q_m}\right)$.

Freundlich isotherm model: The Freundlich adsorption isotherm model is an empirical equation and has been widely used for long time ago. This model depicts the equilibrium on heterogeneous surfaces and assumes multilayer capacity. Usually, for moderate concentrations, Freundlich model is completely concurred with Langmuir model and the experimental data, but in contrast, this isotherm model cannot represent a linear form in very low concentrations as in Langmuir adsorption isotherm model. However, Freundlich isotherm model can be described by equation (3) bellow:

$$q_{eq} = K_F C_{eq}^{\frac{1}{n}} \quad \dots (3)$$

where n and K_F are the Freundlich isotherm constants.

Equation (3) can be rearranging to obtain the linear form of Freundlich adsorption model. The Freundlich isotherm model can be represented by linear form as:

$$\log \log q_{eq} = \log \log K_F + \frac{1}{n} \log \log C_{eq} \quad \dots (4)$$

The calculation of n and K_F values can be performed via plotting $\log \log q_{eq}$ vs. $\log \log C_{eq}$ where the intercept is $\log \log K_F$ and the slop is $1/n$

Adsorption isotherms calculations: The adsorption isotherm constants were calculated from the slopes and intercepts of (Langmuir isotherm) and (Freundlich isotherm) and presented in Table 1. The values of calculated correlation coefficients R^2 were higher for Langmuir isotherm than the Freundlich isotherm; that means Langmuir isotherm model represented the adsorption process well than Freundlich isotherm model.

The maximum capacity of pomegranate peels residue for antimonate ion removal Sb^{+5} was calculated in the range of 15.228 mg/g at constant temperature that indicated the best adsorbing capacity.

Table 1. Values of Langmuir and Freundlich isotherm constants for the adsorption of antimonate using pomegranate peels residue

Langmuir Isotherm Model				Freundlich Isotherm Model		
q_m	K_L	R_L	R^2	K_F	$1/n$	R^2
2.248	0.0256	0.6150	0.9992	0.719	0.7995	0.8827

Adsorption Kinetics

In this paper, the adsorption kinetics is studied due to the important of it's to determine the physical and chemical behavior of the adsorbent media and also to predict the mechanism of adsorption process occurred. Two kinetic models are proposed to investigate the experimental data obtained from the adsorption of antimonate ions using pomegranate peels. These kinetic models are pseudo first order model and pseudo second order model.

1. Pseudo-first order model: This model is depended on the capacity of solid adsorbate. It is assumed that adsorption between liquid and solid occurred on one layer on the adsorption surface (adsorbate). The mathematical expression of this model is described by Equation (7):

$$q_{eq} - q = e^{-k_1 t} \quad \dots (7)$$

where: q_{eq} : is the antimonate ion quantity adsorbate per unit mass of adsorbent at equilibrium (mg/g), q : is the antimonate ion quantity adsorbate per unit mass of adsorbent at any time (mg/g), t : is the time and (k_1): is the first order rate constants (min^{-1}). The linear form of this model can be represented by equation (8):

$$\ln \ln (q_{eq} - q) = \ln \ln q_{eq} - k_1 t \quad \dots (8)$$

So from the plot of $\ln \ln (q_{eq} - q)$ vs. t it can be calculating the rate constant k_1 which appears as the slop of the equation, while the intercept is equal to $\ln \ln q_{eq}$.

2. Pseudo-second order model: Ordinarily it is the best model for expressing the kinetic model of adsorption process. It is assumed that adsorption between adsorbent (solid phase) and adsorbent (liquid phase) performed on two layer on the adsorption surface (adsorbate). This model is described by Equation (9):

$$q = \frac{q_{eq}^2 k_2 t}{1 + q_{eq}^2 k_2 t} \quad \dots (9)$$

where: q_{eq} : is the antimonate ion quantity adsorbate per unit mass of adsorbent at equilibrium (mg/g), q : is the antimonate ion quantity adsorbate per unit mass of adsorbent at any time (mg/g), t : is the time (min) and (k_2): is the first second order rate constants ($\text{g} \cdot \text{mg}^{-1} \cdot \text{min}^{-1}$). The linear form of this model can be represented by equation (10):

$$\frac{t}{q} = \frac{1}{q_{eq}^2 k_2} + \frac{1}{q_{eq}} t \quad \dots (10)$$

From linearized form it is clear when plotting (t/q) against t the slop of equation 10 is $(1/q_{eq})$ while the intercept is $(1/q_{eq}^2 k_2)$

Adsorption kinetic calculations: The adsorption kinetic constants and correlation coefficients of three models used in this study were calculated and given in Table 2. Good correlation coefficients R^2 were observed for the antimonate ions Sb^{+5} uptake process and can be approximated with the pseudo second order kinetics model. Constants k_1 and k_2 for all kinetics models tested have been calculated and summarized in Table 2. Thus, the pseudo second order kinetics was pathway to reach the equilibrium.

Table 2. Values of pseudo first order and pseudo second order for the adsorption of antimonate on pomegranate peels residue

Pseudo first order			Pseudo second order			Experimental
q_{eq}	k_1	R^2	q_{eq}	k_2	R^2	q_{eq}
4.192	1.85×10^{-4}	0.7254	2.1211	1.957×10^{-5}	0.9902	2.0966

Conclusions

The following conclusions can be drawn from the current results:

1. Pomegranate Peels Residue exhibit a good ability to remove antimony ions from SSAS and the maximum percentage removal was 85.72% at 50°C temperature and initial concentration, pH, dose, contact time and agitation speed equal to, 1 mg/l, 5, 4 g, 120 min and 350 rpm respectively.
2. The percentage removal of antimony ions using pomegranate peels residue was increased with increasing pH, contact time, temperature, agitation speed and dose of adsorbent media while it is increasing with decreasing initial concentration.
3. The adsorption process obeys Langmuir isotherm model by correlation coefficient of 0.9992, rather than Freundlich isotherm model of $R^2 = 0.8827$. The adsorption kinetic of antimonate ions is pseudo second order.
4. By this way it can dispose more than one type of waste in benefit, non-cost and eco-friendly method accessing to zero residue level (ZRL).

Acknowledgment

The authors would like to thank the Iraqi universities which were Mustansiriyah University (www.uomustansiriyah.edu.iq) Baghdad – Iraq and Tikrit University (<http://tu.edu.iq>) Tikrit– Iraq for its support in the present work.

References

- [1] Deng RJ, Jin CS, Ren BZ, Hou BL and Hursthouse AS (2017) The Potential for the Treatment of Antimony-Containing Wastewater by Iron-Based Adsorbents. *Water* 9(794):2-18. doi:10.3390/w9100794.
- [2] Johnson CA, Moench H, Wersin P, Kugler P, Wenger C (2005) Solubility of antimony and other elements in samples taken from shooting ranges. *Journal of Environmental Quality* 34:248–254.
- [3] Liu R, Xu W, He Z, Lan H, Liu H, Qua J, Prasai T (2015) Adsorption of antimony(V) onto Mn(II)-enriched surfaces of manganese-oxide and FeAMn binary oxide. *Chemosphere* 138:616–624. <http://dx.doi.org/10.1016/j.chemosphere.2015.07.039>
- [4] Barloková D, Ilavský J, Munka K (2017) Removal of Antimony from Water Using GEH Sorption Material at Different Filter Bed Volumes. “Environmental Engineering” 10th International Conference Vilnius Gediminas Technical University Lithuania, 27–28 April. Article ID: enviro.2017.069. DOI: <https://doi.org/10.3846/enviro.2017.069>.
- [5] Mubarak H, Chai L-Y, Mirza N, Yang Z-H, Pervez A, Tariq M, Shaheen S, Mahmood Q (2015) Antimony (Sb) – pollution and removal techniques – critical assessment of technologies, *Toxicological & Environmental Chemistry*, 97:10, 1296-1318, DOI: 10.1080/02772248.2015.1095549
- [6] Coura JR, Conceição MJ (2010) Specific schistosomiasis treatment as a strategy for disease control. *Mem Inst Oswaldo Cruz, Rio de Janeiro*, Vol. 105(4): 598-603, July
- [7] Nguyen V K, Lee J-U (2015) Antimony-Oxidizing Bacteria Isolated from Antimony-Contaminated Sediment–A Phylogenetic Study. *Geomicrobiology Journal* 32, 50–58. DOI: 10.1080/01490451.2014.925009
- [8] Anjum A., Datta M. (2012) Adsorptive Removal of Antimony (III) Using Modified Montmorillonite: A Study on Sorption Kinetics. *Journal of Analytical Sciences, Methods and Instrumentation*, 2: 167-175. <http://dx.doi.org/10.4236/jasmi.2012.23027>
- [9] Van Nostrand’s Scientific Encyclopedia, (2005) John Wiley & Sons, Inc.
- [10] Barakat M. A., (2011), “New trends in removing heavy metals from industrial wastewater”, *Arabian Journal of Chemistry*, Volume 4, pp:361–377, doi:10.1016/j.arabjc.2010.07.019
- [11] Siddiquee S., Rovina K., Al Azad S., Naher L., Suryani S. and Chaikaew P., (2015), “Heavy Metal Contaminants Removal from Wastewater Using the Potential Filamentous Fungi Biomass: A Review”, *Microbial & Biochemical Technology*, Volume 7, Issue 6, pp: 384-39, doi:10.4172/1948-5948.1000243
- [12] Ibrahim. T. A., Abbas, M. N. and Abbas, F. S., (2016), “Detoxification of Pesticides Wastewater by Adsorption Technique Feasibility of Agricultural Waste Utilization”, LAMBERT Academic Publishing, ISBN-10: 3659411434; ISBN-13: 9783659-832347
- [13] Abbas M. N. and Abbas F. S., (2013), “Iraqi Rice Husk Potency to Eliminate Toxic Metals from Aqueous Solutions and Utilization from Process Residues”, *Advances in Environmental Biology*, Volume 7, Number 2, pp: 308-319, ISSN 1995-0756.
- [14] Abbas M. N., (2014), “Converting Banana Peels from Agricultural Residues to Advantageous Substances”, *Scholars Journal of Engineering and Technology*; Volume 2, Issue 5A, pp: 719-726.
- [15] Abbas M. N., (2014), “Pomegranate Peels: Source of Antioxidants Extraction and Natural Dentifrices Preparation”, *European Academic Research*, Volume II, Issue 3/ June, ISSN 2286-4822. www.euacademic.org

Animal Zoonoses: Will Africa Ever Win the Fight?

Abibu Wasiu Ayodele*

Federal University of Agriculture, Dept. of Microbiology, Abeokuta, Nigeria
Dokuz Eylül University, Graduate School of Natural and Applied Sciences, Dept. of Biotechnology, İzmir,
Turkey

Yunusa Umar Muazu, Dokuz Eylül University, Graduate School of Natural and Applied Sciences, Biochemistry
Unit, İzmir, Turkey

Bamigbade Gafar Babatunde, Federal University of Agriculture, Dept. of Microbiology, Abeokuta, Nigeria
Olayinka Habeeb Olakunle, University of Ibadan, Dept. of Teachers Education, Ibadan, Nigeria

*Corresponding author: abibu@funaab.edu.ng

Keywords: zoonosis, Ebola, Lassa, Africa

Discipline: Biology

Abstract

Studies have shown how domestic animals such as cats, rabies, dogs, chickens etc. constitute important reservoir of deadly human microbial pathogens and spread a disease known as zoonosis. This article reviewed the causes and re-occurrence of zoonotic outbreaks in Africa and provided plausible explanation on ways to ameliorate these problems. A systematic literature search has shown tourism, bush meat trade, practicing intensive agriculture, get in contact with affected animals as the main causes of zoonotic diseases outbreak in Africa. This study also documented how climate change cascade caused by natural and artificial factors; lack of knowledge regarding the consequences of the epidemic by the people; lack experience and specific knowledge to detect cases, treat patients by health practitioners; in ability of the government to enforce relevant laws and implementation of public health measures to prevent further spread; as the main factors for the reoccurrence and escalating rate of zoonosis in Africa. Government should establish more research institutes on these zoonotic diseases, equip existing research centers with state-of-the-art facilities, enforce relevant laws, and the same time enlighten populace through campaign on the consequences of zoonosis.

Introduction

Animals are widely known to be natural reservoir of deadly human microbial pathogen. Frequent contact of human with animals in public settings (e.g., fairs, educational farms, petting zoos, and schools) and the consumption of animals predisposes man to infection from these animals. The World Health Organization expert committee on zoonoses defines zoonoses as those diseases and infections naturally transmitted between vertebrate animals and humans [1]. The causes of the diseases as described by Atawodi et al. [2] can be bacteria, viruses, parasites, fungi and some unconventional agents such as prions. A conceptual framework for understanding a reservoir of infection has been established through various studies that have emphasized different aspects of zoonotic diseases [3, 4]. However, empirical characterization of reservoirs often remains controversial and challenging. The most applicable and accepted way to investigate and define a reservoir emphasizes the annotation of a target group, which is an explicitly defined population of interest in a dynamic and heterogeneous landscape (for example, humans at the livestock–wildlife–human interface) [5].

Since the 1940s, the majority of emerging infectious diseases (EIDs) have originated from animal species [6]. Over half of the new infectious disease events from 1996 to 2009 began in Africa [7]. The spillover of EIDs into wider populations has been linked to host shifts and anthropomorphic driven change, ranging from globalization, urbanization, trade, climate and land use change to habitat fragmentation and loss of biodiversity [8-10]. The West African (Figure 1) outbreak of Ebola virus disease in 2013–2016 was characterized by sustained human-to-human transmission on an unprecedented scale. This outbreak, which caused a massive death toll and societal impact, may have resulted from a single bat-to-human spill-over event [11].

Domesticated animals used as food sources, companion animals or in the workforce are able to act as bridges for viral transmission between wildlife (including bats) and people [12]. Such animals link ‘the field’ and ‘the home’ often having closer physical contact with both wildlife and people than wildlife and people typically have with one another. Yang et al. [13] reported how a 3-year old child in

China, whose parents ran a pig farm, developed influenza-like symptoms in 2010; a European origin avian-like porcine strain was deemed responsible for the episode.

Practicing intensive agriculture, in which livestock are held in large, dense and highly connected populations, provides an ideal opportunity for viral amplification, thereby increasing the risk of otherwise improbable spill-over events to people, as well as causing significant economic and animal health costs [14]. The present study reviewed the causes and re-occurrence of zoonotic outbreaks in Africa and provided plausible explanation on ways to ameliorate these problems.

Zoonoses and Tourism

Advancement in transportation expands global mobility of people and animals. However, pathogens are not left behind in this migration opportunity. Transportation improves economy and results in explosive growth of tourism. Over the century, people are travelling to rural and remote areas in Africa where there are unique and concentrated collections of wildlife. However, travel to zoos and parks could result in a life-threatening problem due to exposure to pathogens not common in the traveler's home location and the worst situation is when infected traveler returns to his/her home country harboring an exotic pathogen, thus, initiating an epidemic [15, 16]. Failure of the traveler to identify and disclose those situations can greatly complicate disease diagnoses when the pathogens involved may not exist in the geographic area where medical assistance is sought. The above truly revealed the successful landing of Ebola virus in Nigeria.

According to the World Health Organization, Ebola virus was introduced into Nigeria on 20 July 2014 when an infected Liberian man arrived by aeroplane into Lagos, Africa's most populous city. The man, who died in hospital 5 days later, set off a chain of transmission that infected a total of 19 people, of whom 7 died. Nigeria was immediately placed on Ebola affected countries (Figure 2) in Africa coupled with developed nations warning their citizens from travelling into Nigeria. According to WHO recommendations, the end of an Ebola virus disease outbreak in a country can be declared once 42 days have passed and no new cases have been detected. The 42 days represents twice the maximum incubation period for Ebola (21 days). This 42-day period starts from the last day that any person in the country had contact with a confirmed or probable Ebola case. Thanks to assistance from international bodies such as WHO, United States Center for Disease Control and Prevention (CDC), Médecins Sans Frontières (MSF), UNICEF etc. Nigeria was considered Ebola free by WHO on October 20th, 2014 [17].



Figure 1. Map of West African states often visited by tourists annually [18]

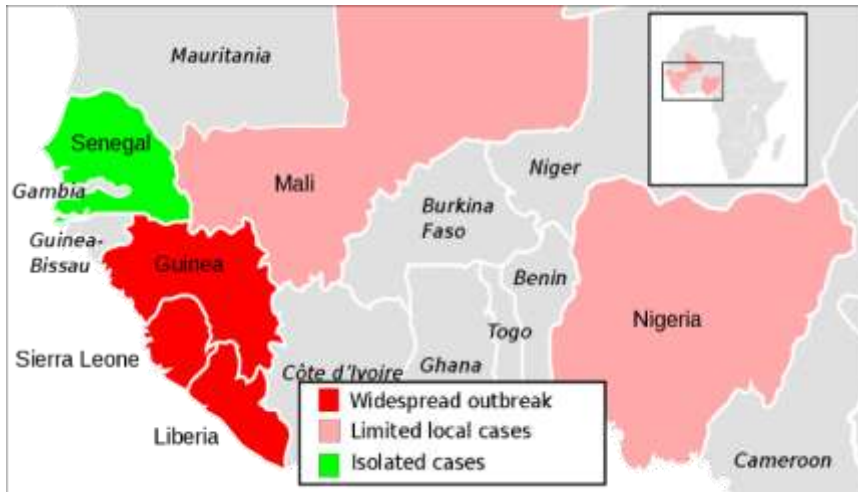


Figure 2. Map of West African states with reported cases of Ebola virus [19]

Widmar *et al.* [20] opined that tourists often get infected with common cold and flu viruses as a result of close contact with people when they are on tour. It is worth establishing that many of the West Africa countries faced with re-occurring zoonotic outbreaks are those deriving much of their income from tourism. In the end, the host country is challenged in terms of health and safety of tourists visiting it and its own citizens [21].

Apart from getting zoonotic diseases in zoos and fairs, human can get infected with it from household pets. These pets are vehicle for transmitting zoonotic infections. In Africa, the dangers associated with keeping pets are more than the accompanying benefits. Presently, there is an increasing number of exotic pets in African countries and their quarantine and clearance at the port of entry is unknown [22]. Additionally, tourists in Africa were seen playing with pets in the localities of area visited while some of them travel along with infected pets. An infected pet coming into the country may not easily be noticed as a result of weak quarantine services at African countries airports. Only few pet owners know the importance of vaccination and other disease prevention methods. They can be colonized or infected with a wide variety of microbes which are pathogenic to animals and people [23].

Several studies have showed how domestic animals such as cats, dogs, sheep, goats, pigs, rabbits, horses, donkeys, ducks, chickens etc. constitute important reservoir of human dermatophytic infections in Nigeria [24, 25]. For example, dogs are frequently infected with intestinal parasites and are causative agents of protozoonoses such as *Entamoeba histolytica* and *Giardia intestinalis* [23]. Other common enteric parasites of dogs are *Ancylostoma caninum*, *Taenia hydatigena*, *Echinococcus spp*, *Diphylidium caninum*, *Trichuris vulpis*, *Giardia spp*, *Cryptosporidium spp* and *Cystoisospora cana* [26, 27]. In comparison with dog bites, which is approximately 80% of all reported animal bites [28], cat bites are more likely to develop wound infection due to the puncture lesions caused by the cat's sharper teeth. It has been estimated that 20-80% of cat bite wounds become infected while infection rates for dog bites are as low as 3-18% [29].

An important question is "could killing of animal reservoirs during outbreak end the spread of diseases?" More often than not, the cheapest and most effective strategy for dealing with zoonotic diseases is to control infection in the animal population [30]. Vaccination programme, routine screening of livestock and changing behavior and practices of animal owners within the community is also a good approach [31]. In addition, African countries can venture into classical and molecular research to identify prevalent genotypes of these microbes affecting both human and animal populations [32].

West African Bush Meat Trade

The 21st century is still challenged by food borne diseases and illnesses particularly in infants and children in most countries irrespective of their wealth index. According to Kun *et al.* [33], food-borne illnesses as a significant contributor to the global disease burden affecting millions of people annually as a result of pathogens of microbial origin. These pathogens use food as vehicle for their transfer from animals to humans and can generate secondary transmissions between humans [34]. This results into

significant morbidities, ranging from mild to severe, and in some cases resulting in mortality [35]. The West Africa bush meat trade is not an exemption to this resulting into thousands of deaths annually.

Milner-Gulland and Bennett [36] described “bush meat” as meat derived from wild animals for human consumption. This includes a wide range of animals, such as invertebrates, amphibians, insects, reptiles, birds, and mammals [37]. In rural areas of east and West Africa inhabitants consume bush meat as a major source of protein, trade it to generate incomes and also serves as business opportunities for most of the unemployed [38]. In some cities, bush meat served as a luxury item and usually commands a premium price and an active market has grown up to supply the needs of urban dwellers [39].

Although, there is no definitive list, almost all wild animals are potential candidate for bush meat. Local factors determine the preferred choice such as market preferences and availability [38]. However, animals mostly consumed in west Africa as bush meats include rodents such as cane rat (grass cutter), great rat, squirrels, flying squirrels, and porcupines; primates such as gorillas, chimpanzees, bonobos and crowned monkeys.

Researchers are of the opinion that any wildlife species harvested for bush meat could be a potential source of food-borne and zoonotic disease that can spillover during the hunting, butchering, and preparation process [40, 41]. In addition, most hunters in Africa hunt using unvaccinated dogs to catch bush meats and games. This is a major problem aiding the spread of zoonoses. They are dressed and sold to people without any veterinary inspection. As bush meat animals are likely to be contaminated with those organisms commonly found in the gut, such as *Salmonella*, *Campylobacter*, *E. coli* and *Shigella* resulting in nerve damage, organ damage, sepsis, stillbirths, haemolytic uremic syndrome, resistant strains and sometimes death [42].

Climatic Change Contribution To Zoonotic Diseases Emergences

Climate change, defined by significant variations of regional or global climates over long periods, includes major changes in average and peak temperature, humidity, atmospheric pressure, precipitations, wind patterns and water salinity, as well as a decrease in the size of mountain and polar glaciers [43]. Several researchers have documented effect of climate change, human and natural factors on zoonotic diseases emergences. Sergon *et al.* [44] showed how an epidemic of chikungunya virus erupted in Lamu, Kenya (East Africa), where an estimated 75% of the population were infected. Climate analysis showed that unseasonably warm and dry conditions, especially over coastal Kenya, occurred during May 2004 [45]. Such conditions may have both led to unsafe domestic water storage practices and infrequent changing of water storage and also, a hastened viral development in the *Aedes* mosquito.

In 2005, Voss *et al.* [46] documented one of the first cases of pig-farming related methicillin-resistant *Staphylococcus aureus* (MRSA) in the Netherlands. These porcine ST398 strains are non-typeable by conventional methods and are spreading throughout Europe. Due to climatic changes farming is now considered a risk factor for livestock associated MRSA (LaMRSA). Antibiotics used in livestock farming to improve growth and treat infection apply selective pressure leading to the emergence of antimicrobial resistant strains in livestock and poultry [47].

The butchering of carcasses in forests in some east African countries had also led to high-risk transmission of airborne, droplet and contact spread zoonoses [48]. Rift valley fever outbreaks were reported exclusively from sub-Saharan Africa in 1977–78, when 18,000 persons were infected and 598 deaths were reported in Egypt [49]. In the desert southwestern United States, plague bacterial levels in rodents have been found to increase in the wake of wet climate conditions following El Niño and Pacific Decadal Oscillation–driven wet weather conditions [50].

Purse *et al.* [51] in their research title “Climate change and the recent emergence of bluetongue in Europe” documented how warming temperatures in the Europe have allowed enhanced survival of bluetongue disease spread by *Culicoides spp* (midges) virus. Another disease enhanced by effects climate variability and change is malaria. Malaria kills between 700,000 and 2.7 million persons each year, mostly children in sub-Saharan Africa. Malaria incidence varies seasonally in highly endemic areas, and its transmission has been associated with temperature anomalies in some African highland areas [52]. A warming trend from 1950 to 2002 was documented in the East African highlands, coinciding with increases in malaria incidence [53]. Patz *et al.* [50] postulated that at just half a degree centigrade increase in temperature trend can translate into a 30% to 100% increase in mosquito abundance, demonstrating a “biologic amplification” of temperature effects.

How Far is Africa Prepared for Reoccurring Zoonotic Diseases?

Zoonotic diseases have high frequency of reoccurrence. The reoccurrence of most of these diseases had been managed in Europe and some Asian countries, while in Africa it is still persisted. According to the United Nations report [54], there should be an enhanced preparation for Nipah outbreaks to avoid a similar unexpected but preventable situation of Ebola pan-epidemics in West Africa which gulped over 11,000 lives as a result of the unavailability of adequate healthcare systems. This signaled a warning to other Africa nations with unrecorded experience to sit tight in terms of needed preparedness measures.

Sazzad *et al.* [55] linked the Ebola virus and the Nipah virus together due to the fact that they occur in healthcare facilities, including infection of health workers, and at burials from an infected corpse and also highlighted the preparedness measures against future Nipah outbreaks to include heightened surveillance, coordinated rapid diagnostic testing, training exercises including the use of and sufficient supplies of personal protective equipment (PPE), detailed isolation and quarantine protocols, clinical management protocols, and discussion of research protocols and their ethics for use of investigative therapies and vaccines. Africa nations should also learn from the reports of Rahman and Husain [56] on Bangladesh (a nation with reoccurring cases of Nipah virus) move by providing a detailed protocol on national guidelines for management, prevention and control of Nipah virus infection.

Another reoccurrence and re-emerging infectious zoonotic diseases affecting the poor and communities lacking access to health services is rift valley fever (RVF). For its managing, Chengula *et al.* [57] suggested the need to increase sensitization of nomadic through community meetings and the involvement of extension workers. Also, herders should be taught how to recognize signs and symptoms of RVF in animals to aid timely reporting as it has been discovered that the lack of education among farmers in reporting deaths among new born animals aids the disease spread thus affecting humans. Anyamba *et al.* [58] gave a report documenting a prediction of RVF outbreak in animals and humans using knowledge of previous RVF outbreaks in the horn of Africa. The prediction established the fact that satellite monitoring and mapping of key climate conditions and land surface ecological dynamics could help prevent future outbreaks.

According to Bass *et al.* [59], lack of reliable surveillance has raised the level of monkey pox disease coupled with the fact that affected countries lack experience and specific knowledge to detect cases, treat patients, and implementation of public health measures to prevent further spread of the virus. Reynolds *et al.* [60] also revealed that Monkeypox cases frequently occur in forested rural areas, which often have limited access to health services. The provision of supportive clinical care and treatment for complications such as ocular and secondary infections is challenging because of resource and specialized care limitations. Also, it is the opinion of the writers of this review that veterinary councils in each African state should rise to their task of local animal surveillance for diseases due to the increasing number of exotic breeds of animals most especially in Nigerian homes. Otherwise, this may lead to another zoonotic episode.

For example, in İzmir (Turkey) which is developed country, cats are usually tattooed in the ear and all dogs are tagged making inhabitants of the city believe that the appropriate animal authority in the municipality have adequate information on those animals. The tags are issued by the veterinary authority within the state and contains information on their vaccination status. However, this is hardly seen in Africa; animals are untagged, even animal owners have little knowledge regarding vaccination, animals are only taken to a veterinarian when sick, and these animals get their daily foods in dumpsites. Some are even found around decomposing human corpses. It is thus a risk playing with stray dogs in the African streets. Figure 3 and 4 shows pictures of stray dogs in Lagos (Nigeria) and İzmir (Turkey) respectively. It is clearly observable that İzmir's dog is tagged in the ear while the Nigeria ones are not.



Figure 3. Examples of stray dogs in the street of Lagos, Nigeria



Figure 4. Examples of stray dog in the street of İzmir, Turkey

Another example is how on 21st January, 2019, the Nigeria Center for Disease Control (NCDC) declared an outbreak of Lassa fever following an increase in the number of cases [61]. The Lassa fever has remained a virus unwilling to leave Nigeria. It kept reoccurring on yearly basis with an increasing number of cases and spreading its map to new localities initially unmapped. Despite the infrastructure and architectural surveillance of the Federal Ministry of Health (FMoH) in Nigeria, it keeps reoccurring. The worst of it is that only 3 hospitals can diagnose Lassa fever in Nigeria.

Presently, the ministries of health of Guinea, Liberia, Sierra Leone, other West African states, WHO, the office of United States foreign disaster assistance, the United Nations, and other partners are working hand in hand to establish the Mano River Union Lassa Fever Network. The programme will supports these countries in developing national prevention strategies and enhancing laboratory diagnostics for Lassa fever and other dangerous diseases. Training in laboratory diagnosis, clinical management, and environmental control is also included [62]. Figure 5 is a map of Lassa fever outbreak in Nigeria while Figure 6 is a map indicating geographic distribution of Lassa fever in West African states.

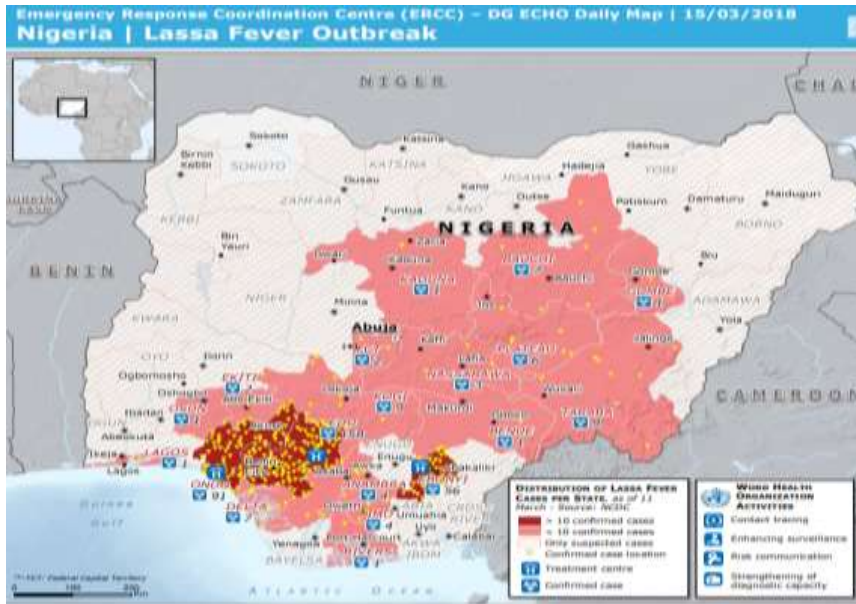


Figure 5. Map of Lassa fever outbreak in Nigeria [63]



Figure 6. Geographic distribution of Lassa fever in West Africa Countries, 1969-2018 [64]

Conclusion and Recommendations

Data gathered in the current review showed that, outbreak of zoonotic diseases in Africa is as a result of lack of knowledge regarding the consequences of the epidemic by people and lack of government support in enlightening the populace and enforcing relevant laws. In addition, global warming, human and natural activities are among several components speeding the reoccurrence of zoonotic diseases.

Government should venture into research and development by establishing more research institutes on these zoonotic diseases and equipping existing research centers with state-of-the-art facilities. The government should not limit its prevention measures to only areas where outbreak occurs but also to areas without issues as these diseases' outbreaks are unpredictable. This is the major problem with Nigeria's fight against Lassa fever as the number of affected areas increases annually. In the same vein, the West African bush meat trade must be greatly looked into. Animals considered zoonotic must never be displayed for sale as foods. The use of unvaccinated dogs and hyenas for hunting should be discouraged.

Acknowledgement

This study was supported by the Presidency for Turks Abroad and Related Communities (YTB) within "International Student Academy" Project.

References

- [1] World Health Organization. (2010). World Health Organization Health Topics: Zoonoses. Available at: <https://www.who.int/topics/zoonoses/en/>. [Accessed: February 9, 2019].
- [2] Atawodi JC, Dzikwi AA, Odoba MB, Dagai DD (2013) Animals as reservoir of some human diseases. *Electronic Journal of Biology* 9(2): 24-28.
- [3] Viana, M., Mancy, R., Biek, R., Cleaveland, S., Cross, P. C., Lloyd-Smith, J. O., & Haydon, D. T. (2014). Assembling evidence for identifying reservoirs of infection. *Trends in Ecology and Evolution*. <https://doi.org/10.1016/j.tree.2014.03.002>
- [4] Drexler, J. F., Corman, V. M., Müller, M. A., Maganga, G. D., Vallo, P., Binger, T., Drosten, C. (2012). Bats host major mammalian paramyxoviruses. *Nature Communications*. <https://doi.org/10.1038/ncomms1796>
- [5] Hallmaier-Wacker, LK, Munster VJ, Knauf, S (2017) Disease reservoirs: From conceptual frameworks to applicable criteria. *Emerging Microbes and Infections*. <https://doi.org/10.1038/emi.2017.65>
- [6] Heffernan C. (2018). Climate change and multiple emerging infectious diseases. *Veterinary Journal*. <https://doi.org/10.1016/j.tvjl.2017.12.021>
- [7] Wood JLN, Leach M, Waldman L, MacGregor H, Fooks AR, Jones KE, Cunningham AA (2012) A framework for the study of zoonotic disease emergence and its drivers: Spillover of bat pathogens as a case study. *Philosophical Transactions of the Royal Society B: Biological Sciences*. <https://doi.org/10.1098/rstb.2012.0228>
- [8] Antia R, Regoes RR, Koella JC, Bergstrom CT (2003) The role of evolution in the emergence of infectious diseases. *Nature*. <https://doi.org/10.1038/nature02104>.
- [9] Woolhouse M, Scott F, Hudson Z, Howey R, Chase-Topping M (2012) Human viruses: discovery and emergence. *Philosophical Transactions of the Royal Society of London* 367, <https://doi.org/10.1098/rstb.2011.0354>
- [10] Daszak P, Zambrana-Torrel C, Bogich TL, Fernandez M, Epstein J H, Murray KA, Hamilton H (2013) Interdisciplinary approaches to understanding disease emergence: The past, present, and future drivers of Nipah virus emergence. *Proceedings of the National Academy of Sciences*. <https://doi.org/10.1073/pnas.1201243109>
- [11] Spengler, J. R., Ervin, E. D., Towner, J. S., Rollin, P. E., & Nichol, S. T. (2016). Perspectives on West Africa Ebola virus disease outbreak, 2013–2016. *Emerging Infectious Diseases*. <https://doi.org/10.32032/eid2206.160021>
- [12] Reperant, L. A., Brown, I. H., Haenen, O. L., de Jong, M. D., Osterhaus, A. D. M. E., Papa, A., ... Kuiken, T. (2016). Companion Animals as a Source of Viruses for Human Beings and Food Production Animals. *Journal of Comparative Pathology*. <https://doi.org/10.1016/j.jcpa.2016.07.006>
- [13] Yang, H., Qiao, C., Tang, X., Chen, Y., Xin, X., & Chen, H. (2012). Human infection from avian-like influenza A (H1N1) viruses in pigs, China. *Emerging infectious diseases*. <https://doi.org/10.3201/eid1807.120009>
- [14] Emma, E.G., Olivier, R., Silke, R.S., Romain, G., Andrew, A.C., et al., 2018. Domesticated animals as hosts of henipaviruses and filoviruses: A systematic review. *The Veterinary Journal*. <https://doi.org/10.1016/j.tvjl.2017.12.024>
- [15] Wilson, M.E., 2003. The traveler and emerging infections: sentinel, courier, transmitter. *Journal of Applied Microbiology*. <https://doi.org/10.1046/j.1365-2672.94.s1.1.x>
- [16] Sejvar, J., Bancroft, E., Winthrop, K., Bettinger, J., Bajani, M., Bragg, S., ... Rosenstein, N. (2003). Leptospirosis in “Eco-Challenge” athletes, Malaysian Borneo, 2000. *Emerging Infectious Diseases*. <https://doi.org/10.3201/eid0906.020751>
- [17] World Health Organization. (2014). WHO | WHO declares end of Ebola outbreak in Nigeria. <https://doi.org/entity/mediacentre/news/statements/2014/nigeria-ends-ebola/en/index.html> [Accessed: February 9, 2019].
- [18] WikiTravel (2011). https://wikitravel.org/en/File:West_Africa_regions_map.png#file
- [19] Wikipedia. https://en.wikipedia.org/wiki/West_African_Ebola_virus_epidemic

**3rd International Students Science Congress
3-4 May 2019, İzmir - Turkey**

- [20] Widmar, N. J. O., Dominick, S. R., Ruple, A., & Tyner, W. E. (2017). The influence of health concern on travel plans with focus on the Zika virus in 2016. *Preventive Medicine Reports*. <https://doi.org/10.1016/j.pmedr.2017.02.023>
- [21] Rupprecht, C. E., & Burgess, G. W. (2015). Viral and vector zoonotic exploitation of a homosome memetic complex. *Clinical Microbiology and Infection*. <https://doi.org/10.1016/j.cmi.2015.02.032>
- [22] Armstrong, D., 2001. Zoonoses. *International Journal of Infectious Diseases* 5(3), 117-118.
- [23] Damborg, P., Broens, E. M., Chomel, B. B., Guenther, S., Pasmans, F., Wagenaar, J. A., ... Guardabassi, L. (2016). Bacterial zoonoses transmitted by household pets: state-of-the-art and future perspectives for targeted research and policy actions. *Journal of Comparative Pathology*. <https://doi.org/10.1016/j.jcpa.2015.03.004>
- [24] Ameh, I.G., Okolo, R.U., (2009). Dermatophytosis among School children: domestic animals as predisposing factor in Sokoto, Nigeria. *Pakistan Journal of Biological Sciences*. <https://doi.org/10.3923/pjbs.2004.1109.1112>
- [25] Nweze, E. I. (2017). Dermatophytoses in domesticated animals. *Revista Do Instituto de Medicina Tropical de São Paulo*. <https://doi.org/10.1590/s0036-46652011000200007>
- [26] Palmer, C. S., Thompson, R. C. A., Traub, R. J., Rees, R., & Robertson, I. D. (2008). National study of the gastrointestinal parasites of dogs and cats in Australia. *Veterinary Parasitology*. <https://doi.org/10.1016/j.vetpar.2007.10.015>
- [27] Khante, G. S., Khan, L. A., Bodkhe, A. M., Suryawanshi, P. R., Majed, M. A., Suradkar, U. S., & Gaikwad, S. S. (2009). Epidemiological survey of gastro-intestinal parasites of non-descript dogs in Nagpur City. *Veterinary World*. <https://doi.org/10.5455/vetworld.2009.22-23>
- [28] Patronek, G.J., Slavinski, S.A., 2009. Animal bites. *Journal of the American Veterinary Medical Association*. <https://doi.org/10.2460/javma.234.3.336>
- [29] Talan, D.A., Citron, D.M., Abrahamian, F.M., Moran, G.J., & Goldstein, E.J. (1999). Bacteriologic analysis of infected dog and cat bites. *New England Journal of Medicine*. <https://doi.org/10.1056/NEJM199901143400202>
- [30] Maudlin, I., Eisler, M. C., & Welburn, S. C. (2009). Neglected and endemic zoonoses. *Philosophical Transactions of the Royal Society B: Biological Sciences*. <https://doi.org/10.1098/rstb.2009.0067>
- [31] Welburn, S. C., Beange, I., Ducrotoy, M. J., & Okello, A. L. (2015). The neglected zoonoses-the case for integrated control and advocacy. *Clinical Microbiology and Infection*. <https://doi.org/10.1016/j.cmi.2015.04.011>
- [32] Adebisi, A. I., & Oluwayelu, D. O. (2017). Zoonotic fungal diseases and animal ownership in Nigeria. *Alexandria Journal of Medicine*. <https://doi.org/10.1016/j.ajme.2017.11.007>
- [33] Hu, K., Renly, S., Edlund, S., Davis, M., & Kaufman, J. (2016). A modeling framework to accelerate food-borne outbreak investigations. *Food Control*. <https://doi.org/10.1016/j.foodcont.2015.05.017>
- [34] Abat, C., Rolain, J. M., & Colson, P. (2018). Investigations by the Institut Hospitalo-Universitaire Méditerranée Infection of food and food-borne infections in the Mediterranean Basin and in sub-Saharan Africa. *New Microbes and New Infections*. <https://doi.org/10.1016/j.nmni.2018.08.019>
- [35] Tefera, T., Tysnes, K. R., Utaaker, K. S., & Robertson, L. J. (2018). Parasite contamination of berries: Risk, occurrence, and approaches for mitigation. *Food and Waterborne Parasitology*. <https://doi.org/10.1016/j.fawpar.2018.04.002>
- [36] Milner-Gulland, E. J., Bennett, E. L., Abernethy, K., Bakarr, M., Bennett, E., Bodmer, R., ... Wilkie, D. (2003). Wild meat: The bigger picture. *Trends in Ecology and Evolution*. [https://doi.org/10.1016/S0169-5347\(03\)00123-X](https://doi.org/10.1016/S0169-5347(03)00123-X)
- [37] Nellemann, C., Redmond, I., Refisch, J., United Nations Environment Programme, & GRID--Arendal. (2010). The Last Stand of the Gorilla: Environmental Crime and Conflict in the Congo basin. *Twentieth Century British History*. <https://doi.org/10.1093/tcbh/hwl005>
- [38] ACMSF, 2005. Review of Possible Microbiological Hazards that may be Associated with the Illegal Importation of Bush meat. Advisory Committee on the Microbiological Safety of Food discussion paper; 1-36 acm/741.

**3rd International Students Science Congress
3-4 May 2019, İzmir - Turkey**

- [39] Bowen-Jones, E., Brown, D., & Robson, E. (2002). Assessment of the solution orientated research needed to promote a more sustainable bush meat trade in Central and West Africa. Report commissioned by Wildlife and Countryside Directorate of DEFRA. Page 1-127.
- [40] Karesh, W.B., & Noble, E., (2009). The Bush meat Trade: Increased opportunities for transmission of zoonotic disease. *Mt Sinai J Med.* <https://doi.org/10.1002/msj.20139>
- [41] Kurpiers, L. A., Schulte-Herbrüggen, B., Ejotre, I., & Reeder, D. A. M. (2015). Bushmeat and emerging infectious diseases: Lessons from Africa. In *Problematic Wildlife: A Cross-Disciplinary Approach.* https://doi.org/10.1007/978-3-319-22246-2_24
- [42] ILSI, 2016. Food Safety for Nutritionists and other Health Professionals. International Life Science Institute Workshop, Federal University of Agriculture, Abeokuta, Nigeria (ILSI-UG-FUNAAAB).
- [43] McMichael, A. J. (2013). Globalization, Climate Change, and Human Health. *New England Journal of Medicine.* <https://doi.org/10.1056/NEJMra1109341>
- [44] Sergon, K., Njuguna, C., Kalani, R., Ofula, V., Onyango, C., Konongoi, L. S., ... Breiman, R. F. (2008). Seroprevalence of Chikungunya virus (CHIKV) infection on Lamu Island, Kenya, October 2004. *American Journal of Tropical Medicine and Hygiene*, 78(2): 333–337.
- [45] Chretien, J. P., Anyamba, A., Bedno, S. A., Breiman, R. F., Sang, R., Sergon, K., ... Linthicum, K. J. (2007). Drought-associated chikungunya emergence along coastal East Africa. *American Journal of Tropical Medicine and Hygiene*. 76(3), 405–407.
- [46] Voss, A., Loeffen, F., Bakker, J., Klaassen, C., & Wulf, M. (2005). Methicillin-resistant *Staphylococcus aureus* in Pig Farming. *Emerging Infectious Diseases.* <https://doi.org/10.3201/eid1112.050428>
- [47] Schlundt, J., Toyofuku, H., Jansen, J., & Herbst, S. A. (2016). Emerging food-borne zoonoses. *Revue Scientifique et Technique de l'OIE.* <https://doi.org/10.20506/rst.23.2.1506>
- [48] Naicker, P. R. (2011). The impact of climate change and other factors on zoonotic diseases. *Archives of Clinical Microbiology.* <https://doi.org/10.3823/226>
- [49] Patz, J., Confalonieri, U. E. C., Amerasinghe, F. P., Chua, K. B., Daszak, P., Hyatt, a. D., ... Whiteman, C. (2005). Human health: ecosystem regulation of infectious diseases. In *Ecosystems and Human Well-being.* <https://doi.org/10.1289/ehp.6877>
- [50] Patz, J. A., Olson, S. H., Uejio, C. K., & Gibbs, H. K. (2008). Disease Emergence from Global Climate and Land Use Change. *Medical Clinics of North America.* <https://doi.org/10.1016/j.mcna.2008.07.007>
- [51] Purse, B. V., Mellor, P. S., Rogers, D. J., Samuel, A. R., Mertens, P. P. C., & Baylis, M. (2005). Climate change and the recent emergence of bluetongue in Europe. *Nature Reviews Microbiology.* <https://doi.org/10.1038/nrmicro1090>
- [52] Zhou, G., Minakawa, N., Githeko, A. K., & Yan, G. (2005). Climate variability and malaria epidemics in the highlands of East Africa. *Trends in Parasitology.* <https://doi.org/10.1016/j.pt.2004.11.002>
- [53] Pascual, M., Ahumada, J. A., Chaves, L. F., Rodo, X., & Bouma, M. (2006). Malaria resurgence in the East African highlands: Temperature trends revisited. *Proceedings of the National Academy of Sciences.* <https://doi.org/10.1073/pnas.0508929103>
- [54] United Nations, 2016. Protecting Humanity from Future Health: Crises Report of the High-level Panel on the Global Response to Health Crises. Available at: http://www.un.org/News/dh/infocus/HLP/2016-02-05_Final_Report_Global_Response_to_Health_Crises.pdf. [Accessed: February 9, 2019].
- [55] Sazzad, H. M. S., Hossain, M. J., Gurley, E. S., Ameen, K. M. H., Parveen, S., Islam, M. S., ... Luby, S. P. (2013). Nipah virus infection outbreak with nosocomial and corpse-to-human transmission, Bangladesh. *Emerging Infectious Diseases.* <https://doi.org/10.3201/eid1902.120971>
- [56] Rahman, M., Husain, M., 2011. National guideline for management, prevention, and control of Nipah virus infection including encephalitis. Available at: http://www.iedcr.gov.bd/pdf/files/nipah/National_Nipah.pdf. [Accessed: February 9, 2019].
- [57] Chengula, A. A., Mdegela, R. H., & Kasanga, C. J. (2013). Socio-economic impact of Rift Valley fever to pastoralists and agro pastoralists in Arusha, Manyara and Morogoro regions in Tanzania. *SpringerPlus.* <https://doi.org/10.1186/2193-1801-2-549>

3rd International Students Science Congress
3-4 May 2019, İzmir - Turkey

- [58] Anyamba, A., Chretien, J.-P., Small, J., Tucker, C. J., Formenty, P. B., Richardson, J. H., ... Linthicum, K. J. (2009). Prediction of a Rift Valley fever outbreak. *Proceedings of the National Academy of Sciences*. <https://doi.org/10.1073/pnas.0806490106>
- [59] Bass, J., Tack, D. M., McCollum, A. M., Kabamba, J., Pakuta, E., Malekani, J., Reynolds, M. G. (2013). Enhancing health care worker ability to detect and care for patients with monkeypox in the Democratic Republic of the Congo. *International Health*. <https://doi.org/10.1093/inthealth/iht029>
- [60] Reynolds, M. G., McCollum, A. M., Nguete, B., Lushima, R. S., Petersen, B. W. (2017). Improving the care and treatment of monkeypox patients in low-resource settings: Applying evidence from contemporary biomedical and smallpox biodefense research. *Viruses*. <https://doi.org/10.3390/v9120380>
- [61] World Health Organization. (2019). WHO scales up Lassa fever response in affected states. Available at: <https://reliefweb.int/report/nigeria/who-scales-lassa-fever-response-affected-states>. [Accessed: February 9, 2019].
- [62] World Health Organization. (2017). Lassa fever. Available at: <https://www.who.int/en/news-room/fact-sheets/detail/lassa-fever>. [Accessed: February 9, 2019].
- [63] European Union (2018). Nigeria | Lassa Fever Outbreak – DG ECHO Daily Map | 15/03/2018. Available at: <https://reliefweb.int/map/nigeria/nigeria-lassa-fever-outbreak-dg-echo-daily-map-15032018>. [Accessed: February 9, 2019].
- [64] World Health Organization. (2018). Geographic distribution of Lassa fever in West Africa Countries, 1969-2018. Available at: <https://www.who.int/emergencies/diseases/lassa-fever/geographic-distribution.png?ua=1>. [Accessed: February 9, 2019].

Biotechnology / Biyoteknoloji

Screening for the Production of Secondary Metabolite (s) by Endophytic Fungi Isolated from *Punica granatum* in Small Scale Solid State Fermentation

Ibrahim Karidio Diori*, Şenay Hamarat Şanlier
Ege University, Faculty of Science, Dept. of Biochemistry, 35100 Bornova, İzmir
*Corresponding author: kardio_ib@outlook.fr

Keywords: endophytes, *Punica granatum*, solid-state fermentation, secondary metabolites

Discipline: Biotechnology

Abstract

Punica granatum is originated from Iran, domesticated throughout the Mediterranean regions, and is reputed for its medicinal uses; a reputation that it certainly owes to its high content of phytochemicals. However, scientific evidence supports that some of these phytochemicals are fruits of symbiosis between the plant and its hosted endophytes.

The present study aimed to investigate the secondary metabolite (s) that could eventually be produced by six of the endophytic fungi (named A through F), isolated from *P. granatum* as mentioned in details in our previous report (Karidio & Hamarat, 2018), in a set of solid-state fermentation processes on four different solid culture media namely rice, *rice supplemented with peptone*, masoor-Dal, and maize. The promising produced metabolites would be used in subsequent studies to investigate their biological activities especially anticancer activity.

The fermented media were individually extracted with ethyl acetate. Each of the extracts was loaded on TLC plates then developed with chloroform/methanol system at a ratio of 9:1. Analysis of the spots observed on TLC plates revealed the presence of fluorescent yellow and pink colored metabolites. For biotechnological production, the yellow metabolite has the highest potential; endophyte D produced the highest quantities especially on *rice supplemented with peptone* medium. However, optimization studies would be useful for improving the product's quality and yields.

Introduction

Pomegranate-derived from the Medieval Latin words *pōmum* meaning “apple” and *grānātum* meaning “having seeds”. So literally translated pomegranate means “apple with many seeds”. The botanical name for pomegranate is *P. granatum*. The genus name *Punica* derived also from Medieval Latin meaning “pertaining to Carthage” reputed for the quality of its pomegranates. However, the pomegranate is believed to be originated from Iran and domesticated throughout the Mediterranean region (Ghaderi-Ghahfarokhi *et al.*, 2018; Khadivi *et al.*, 2018; Ozguven *et al.*, 2010; Verma *et al.*, 2010).

The historical medicinal use of the extracts from different parts of *P. granatum* dates far back to ancient times as mentioned in scripts of Egyptian folk medicine. The fruit is consumed for its nutritional value, while extracts of its peels, as well as extracts from other parts of the plant, are used for their high content of phytochemicals as therapeutics for various ailments. Reported biological properties of extracts from parts of pomegranate include but are not limited to antimicrobial, antioxidant, antidiabetic, anticancer (Les *et al.*, 2015; Paguarulo *et al.*, 2016; Saeed *et al.*, 2018; Shaygannia *et al.*, 2016; Wu *et al.*, 2016).

However, not all these bioactive molecules are essentially / fully synthesized by the plant itself. In fact, to cope with adverse conditions that are increasing with global climate changes, desertification, floods and droughts, plants-endophytes' symbiosis is becoming important ecologically and globally prevalent. Endophytic fungi are extremely common and ubiquitous endosymbionts living asymptotically in plants. All plants living in the natural ecosystem are believed to host at least a few endophytic *species* within and between their tissues. Many scientific reports associate to endophytic colonization the induction of a consistent, significant and substantial metabolic change in the host plant that results in the qualitative and/or quantitative change in its phytochemical content including indole derivatives, phytosterols, peptides, polyphenols, alkaloids, lignin, flavonoids, volatile terpenoids... Among these are sometimes an array of novel, chemically and biologically valuable biomolecules which

synthesis is exclusively attributed to endophytes. These biomolecules essentially promote plant growth, germination, resistance to biotic and/or abiotic stresses as well as their accumulation in plant allows for their extraction for pharmaceutical purposes as antibiotics, anticancer, anti-viral, anti-oxidant (C Madhusudhan *et al.*, 2015; Hammerschmidt *et al.*, 2012; Tarhani & Fotouhifar, 2016; Vahedi-Darmiyan; 2017).

In the lab, scientists have been able to isolate and maintain on artificial microbiological media endophytic organisms (bacteria, fungi...), then produce from them a huge diversity of bioactive molecules. Various biotechnological fermentation techniques found applications in the lab as small scale production for research purposes. For the course of this Ph.D. thesis's ongoing research, we herein report small scale solid-state fermentations using four (4) different solid media namely rice, rice supplemented with peptone, maize, and masoor dal /*Lens culinaris* commercially available on the market using six selected fungal endophytes among those that we successfully isolated from *P. granatum* (Karidio & Hamarat, 2018). The present study aims to: (i) investigate on the qualitative and quantitative products eventually issued from the fermentation using a same organism on different culture media, (ii) determine which media best suited for the production of the eventually produced secondary metabolites and (iii) determine which organism(s) has/ have the best potential for a biotechnological production of an eventually produce secondary metabolite. The biotechnologically promising metabolite (s) would eventually serve for subsequent study to investigate for its biological activities especially anticancer activity.

Materials and Methodology

Isolation and purification of fungal endophytes

The collection of plant's tissue samples (from flowers, fruits, leaves, twigs, roots), surface sterilization, isolation and purification of the endophytic fungi from *P. granatum* tree is summarized in Figure 1, but described in detail in our previous report (Karidio & Hamarat, 2018).

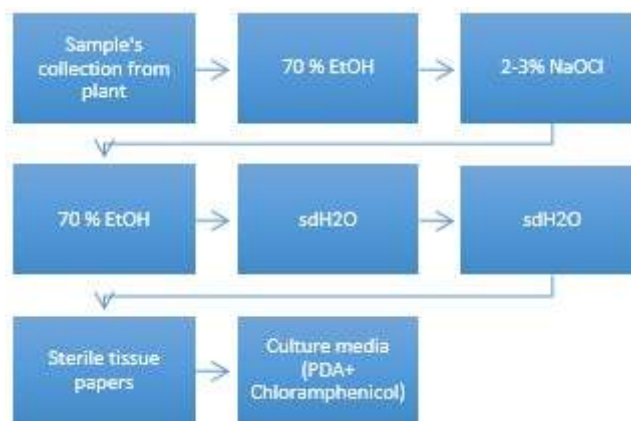


Figure 1. Collection of plant samples, surface sterilization, isolation, and purification of endophytic fungi from Punica granatum tree.

Collected plant samples were washed under running tap H₂O to eventually remove sand and dust, dried in folds of tissue paper. They were then surface sterilized as shown on the scheme by sequentially immersing them in 70% EtOH, 2-3% NaOCl, 70% EtOH and sterilized distilled water (sd H₂O) twice. The immersion time varies depending on the sample type. The surface sterilized samples were dried in folds of sterile tissue paper under aseptic conditions, then transferred onto freshly prepared microbiological artificial culture media. Many fungal species grew on the culture media. They were isolated using the hyphae-tip method

Solid-State Fermentation

The solid-state fermentation has been carried out in 100 ml Erlenmeyer flasks containing 7.5g of the solid-medium except for the “rice-supplemented with peptone flasks”, in which, to the 7.5g of rice was added 0.250g of peptone. 10ml of dH₂O was added to each of the flasks. All the flask containing culture media were autoclaved. A mycelial square of the selected fungi served as inoculum from six selected

fungi cultured on PDA. The selected endophytic fungi were named A through F. For each of the solid medium, an un-inoculated flask was kept as blank. The fermentation process lasted 10 days under static conditions at room temperature in a closed cupboard.

Extraction

The fermentation process was terminated by the addition of 50ml of EtOAc to each of the culture flasks and left to stand overnight. It was then filtered the next day to separate the EtOAc extract from the culture's mycelia and medium before it was exhaustively extracted in a separating funnel with *n*-hexane to eventually free it from fats. Each of the extracts was named after the endophytes from which culture it was derived.

Thin Layer Chromatography

Each of the extracts from the fermentative processes was loaded onto a TLC plate. The solvent system used was chloroform/methanol at the ratio 9:1.

Absorption Profile

The absorption profile of each of the extract has been determined to see at which wavelength(s) they eventually absorb light.

Results and Discussion

This study has been conducted to investigate the eventual secondary metabolite(s) that could be produced in solid-state fermentation by each of the six investigated endophytic fungi on each of the solid media. Another purpose of the present study was to compare the produced secondary metabolite (s) by a given organism in other to determine which medium suited the best for the production of each individual metabolite.

Table 1 summarizes the extracts colors from the respective fermentative processes. In general, there was no uniform color of extracts for all cultures on the same solid medium. However, the endophytes B, E, and F when grown on the four (4) different solid media gave extracts with similar color i.e. light-yellow. Endophyte A when grown on maize and endophyte C when grown on masoor-Dal and maize also gave light-yellow colored extracts. Orange colored extracts had been obtained from endophyte A grown on rice, *rice supplemented with peptone*, and masoor-Dal. Endophyte C when grown on rice and *rice supplemented with peptone*.

Table 1. Colors of the ethyl acetate extracts of the six selected endophytic fungi on each of the solid media used for the solid-state fermentation

		Colors of the ethyl acetate extracts of the endophytic culture					
		Extract A	Extract B	Extract C	Extract D	Extract E	Extract F
Solid media	Rice	Orange	Light yellow	Orange	Dark brown	Light yellow	Light yellow
	Rice + peptone	Orange	Light yellow	Orange	Dark brown	Light yellow	Light yellow
	Masoor Dal	Orange	Light yellow	Light yellow	Dark brown	Light yellow	Light yellow
	Maize	Light yellow	Light yellow	Light yellow	Dark brown	Light yellow	Light yellow

First, it has been observed that out of the six investigated endophytes, four produced detectable amounts of metabolites that appeared as spots on the TLC. Two of the extracts (A & C) developed corresponding pink spots on the TLC plates. However, only the extract from *rice supplemented with peptone* exhibited the pink spot on TLC plates. The other extracts from other solid media fermentation of the same organism showed no-detectable spot on the TLC plates. The extracts from the fermentation process of the two other organisms exhibited all yellow spot (s) on TLC. One of the organisms i.e. endophyte B, through its culture extract, developed a single yellow spot on TLC from the culture on

rice, *rice supplemented with peptone*, and masoor dal, but no-detectable spot from the extract of the culture on maize. All the observed spots from the different cultures have approximately the same R_f values. All extracts from the different culture media of the third organism (endophyte D), exhibited, each, four spots on TLC. All the spots of the different culture media correspond to each other. However, the thickness varies with respect to the culture media. The culture media *rice supplemented with peptone* seemed to exhibit the thickest spots.

Only extracts from endophyte D cultures showed more than a single spot on TLC plates. In fact, each of its extracts exhibited four (4) fluorescent spots. The spots from different extracts correspond to one another. It could be hypothesized that these spots represent the same type of molecules but with different degree of polymerization.

In general, all the absorption profiles of the extracts reflected broad peaks between 200-300nm. Moreover, some of the extracts exhibited absorption peak (s) at additional wavelengths. The extracts from the endophyte F, grown on all the four (4) solid media exhibited an additional absorption peak at 239nm. Extracts of the endophyte C, cultured on rice absorbed at 313, masoor Dal showed absorption peaks at 318 and 411nm, while its extract from the fermentative process with maize showed a broad peak between 400-433 nm. When grown on rice or maize, extracts of endophyte B's fermentation reflected additional peak at 408nm. *Rice supplemented with peptone's* extract A i.e. issued from fermentation with endophyte A, exhibited two additional peaks at 321 and 408nm. Extract D from fermented masoor-Dal exhibited additional absorption peaks at 318 and 413nm.

The absorption peaks exhibited by extracts that did not exhibit spots on TLC plates would eventually mean that their content of the absorbing molecules was not high enough to appear as a spot on the TLC plates. Besides that apparently, there was a fraction some extracts that remained stationary in some cases.

Conclusion

The essence of this study was first of all exploratory, in that, it screened for the eventual secondary metabolites that could be biotechnologically produced with the investigated endophytes on the different solid media used. By principle, in solid-state fermentation either the inoculated microorganisms produce the secondary metabolite(s) themselves, or they release it/them from the matrix.

So far, we noticed the production of two types of secondary metabolites i.e. a fluorescent pink colored one, and a fluorescent yellow colored one as exhibited as spots on TLC plates. However, for a promising production scale, the fluorescent yellowish metabolite was the best. The organisms with apparently the best biotechnological production potential on the investigated solid media was endophyte D. And *rice supplemented with peptone* was apparently the best fermentation medium.

For a more meaningful biotechnological process, it is necessary to determine the chemical structure of the yellow secondary metabolite and eventually investigate its biological activity especially anticancer potential (that interests us the most). For the endophyte D, it is also necessary to molecularly identify it. Moreover, in view of finding a better fermentation strategy with improved yield, optimization studies should be conducted especially to determine: (i) optimal rice grain size (broken / whole rice grains), (ii) optimal pH, (iii) optimal inoculum size, (iv) optimal incubation time, (v) optimal incubation temperature, (vi) optimal moisture content, (vii) optimal mineral ions content (e.g. artificial seawater), (viii) optimal N source and its amount.

In a subsequent higher scale study we shall aim to investigate the biological activities of the metabolites from endophyte D, especially their potentiality as anticancer agent.

References

- [1] C Madhusudhan, M, R Bharathi T and S Prakash, H (2015) Isolation and purification of bioactive metabolites from fungal endophytes—a review. *Current Biochemical Engineering*, 2(2): 111-117.
- [2] Ghaderi-Ghahfarokhi, M., Barzegar, M. and Nabil M (2018) Geographical Discrimination of Iranian Pomegranate Cultivars Based on Organic Acids Composition and Multivariate Analysis.
- [3] Hammerschmidt L, Wray V, Lin W, Kamilova E, Proksch P and Aly AH (2012) New styrylpyrones from the fungal endophyte *Penicillium glabrum* isolated from *Punica granatum*. *Phytochemistry Letters*, 5(3): 600-603.

3rd International Students Science Congress
3-4 May 2019, İzmir - Turkey

- [4] Karidio DI, Hamarat ŞŞ (2018) S0005: A pilote scale production of L-asparaginase, L-glutaminase, and *Taxol* from endophytic fungi isolated from *Punica granatum*. International ivekbio congress (p65-67), Istanbul, 26-28 November.
- [5] Khadivi A, Ayenehkar D, Kazemi M. and Khaleghi A (2018) Phenotypic and pomological characterization of a pomegranate (*Punica granatum* L.) germplasm collection and identification of the promising selections. *Scientia Horticulturae*, 238 : 234-245.
- [6] Les F, Prieto JM, Arbonés-Mainar JM, Valero MS and López V (2015) Bioactive properties of commercialised pomegranate (*Punica granatum*) juice: antioxidant, antiproliferative and enzyme inhibiting activities. *Food & function*, 6(6) : 2049-2057.
- [7] Özgüven AI, Yılmaz C and Keleş D (2010) August. Pomegranate biodiversity and horticultural management. In XXVIII International Horticultural Congress on Science and Horticulture for People (IHC2010): International Symposium on the 940 (pp. 21-28).
- [8] Pagliarulo C, De Vito V, Picariello G, Colicchio R, Pastore G, Salvatore P and Volpe MG, (2016) Inhibitory effect of pomegranate (*Punica granatum* L.) polyphenol extracts on the bacterial growth and survival of clinical isolates of pathogenic *Staphylococcus aureus* and *Escherichia coli*. *Food chemistry*, 190 : 824-831.
- [9] Saeed M, Naveed M, Bibi J, Kamboh AA, Arain MA, Shah QA, Alagawany M, El-Hack ME, Abdel-Latif MA, Yattoo M and Tiwari R (2018) The Promising Pharmacological Effects and Therapeutic/Medicinal Applications of *Punica Granatum* L. (Pomegranate) as a Functional Food in Humans and Animals. *Recent patents on inflammation & allergy drug discovery*, 12(1) : 24-38.
- [10] Shaygannia E, Bahmani M, Zamanzad B and Rafieian-Kopaei M (2016) A review study on *Punica granatum* L. *Journal of Evidence-Based Complementary & Alternative Medicine*, 21(3): 221-227.
- [11] Tarhani MR and Fotouhifar KB (2016) Identification of some endophytic fungi of pomegranate (*Punica granatum*) in Iran.
- [12] Vahedi-Darimiyan ME, Jahani M, Mirzaee MR. and Asgari B (2017) A noteworthy record of endophytic *Quambalaria cyanescens* from *Punica granatum* in Iran. *Czech Mycology*, 69(2) : 113-123.
- [13] Verma N, Mohanty A. and Lal A (2010) Pomegranate genetic resources and germplasm conservation: a review. *Fruit, Vegetable and Cereal Science and Biotechnology*, 4 (Special Issue 2): 120-125.
- [14] Wu J, Jahncke ML, Eifert JD, O'Keefe SF and Welbaum GE (2016) Pomegranate peel (*Punica granatum* L) extract and Chinese gall (*Galla chinensis*) extract inhibit *Vibrio parahaemolyticus* and *Listeria monocytogenes* on cooked shrimp and raw tuna. *Food Control*, 59: 695-699.

Chemistry / Kimya

Optimizing Column Chromatography Conditions for Isolation of Resveratrol Using Different Column Fillers

Zulaiha Gidado Mukhtar*, Yusuf Ibrahim Ibrahim, Abubakar Barau, Muhammad Salihu, Binta Muhammad
Kano State Polytechnic, Dept. of Science Laboratory Technology, Kano, Nigeria
Zainab Rabi, Yusuf Maitama Sule University, Dept. of Biochemistry, Kano, Nigeria
Fikret Karatas, Fırat University, Dept. of Chemistry, Elazığ, Turkey
*Corresponding author: zgmukhtar.80@gmail.com

Keywords: chromatography, resveratrol, *Vitis vinifera* seed extract, column fillers

Discipline: Chemistry, Biochemistry

Abstract

In this research we investigated a better optimum condition for column chromatography in isolating resveratrol from grape seed, using different column fillers (mobile phase), gradient elution was carried out on crude ethanolic mixture using two predetermined solvent systems (n-Hexane: Ethyl acetate and Chloroform: Methanol) against four column fillers: Silica gel, Flourosil, Activated Carbon and Clay, to confirm the purity of the isolated resveratrol we conducted standard HPLC to test against standard resveratrol chromatogram. Our findings reveal that most column fillers can isolate resveratrol. However, the most effective and efficient purification methods for extracting resveratrol are ranked in their respective decreasing order: Silica gel > Activated Carbon > Flourosil > Clay. Thus, the most effective purification method is Silica gel. Based on these findings, we conclude that: this discovery would be of enormous help in the isolation of resveratrol. We believe that this process can further enhance efficiency both for research and industrial applications.

Introduction

Resveratrol has been ranked as the most biologically important class or compounds stilbenoid. Resveratrol; (with chemical name 3, 5, 4'-trihydroxy-trans-stilbene) can be call as polyphenol phytochemical, naturally synthesized by some species of plants in response to injury or stress, this can be seen as plant's own way of inflammatory response agent, antimalarial and antioxidant properties has been attributed to resveratrol [1]. Available record indicated that; it was around the year nineteen ninety (1990s) that resveratrol was first time was discovered, red wine is the first sample in which presence of resveratrol was confirmed.

From that time (1990s) till today, a lot of investments has been made for interest in studying resveratrol and also trying to find its effect on health. Some important postulations suggested that; consumption of resveratrol from red wine might help explain the fact that French people have a comparatively low occurrence of coronary heart disease (CHD), ironically these people eat too much of high in saturated fat in their regular diets, a occurrence is what is termed as the "French Paradox" [2]. The plant biochemical pathway that lead to the anabolism of Resveratrol is known, in this pathway malonyl CoA and coumaroyl CoA are use as substrate in a reaction catalyze by an enzyme called resveratrol synthase, this process usually take place in response of an attack against resveratrol producing plant by disease causing microbes (otherwise called pathogens) [3]. Resveratrol dissolves easily in alcohols (e.g. ethanol or methanol) compound of resveratrol can exist in both trans and cis molecular configurations.

Figures 1 and 2 illustrate the perceived pathway for resveratrol production in plants.

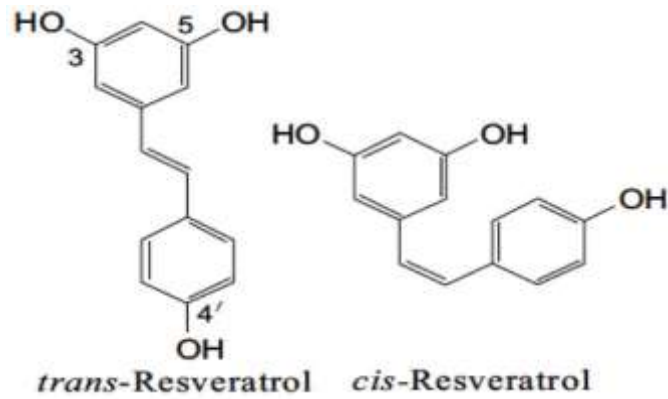


Figure 1. Isomers of resveratrol

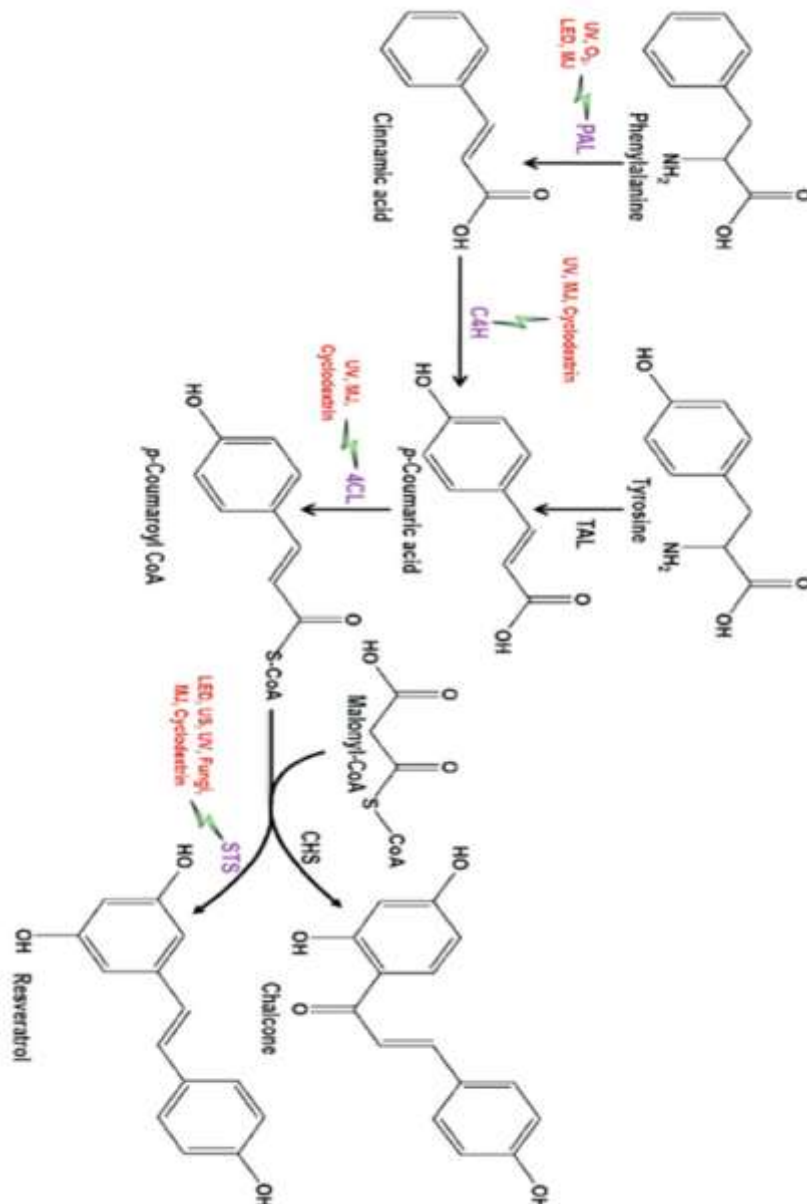


Figure 2. Synthesis of resveratrol in plant

Recently, most of efforts and increasing interests on phenolic compounds found in grapes have focus on how these compound really affect biological activities, which can be of human benefits more especially on health and general wellbeing, this include their antioxidant properties, how do they protect cardiac problems/failures, how true is their anticancer properties (as widely reported), anti-inflammation effect, their ability to reduce or retard antiaging and other general antimicrobial properties [4]. Resveratrol has been found to exert a number of protective properties on the cardiovascular system in vitro, including inhibition of both platelet activation and aggregation, but as always reported earlier, there is need for full in vivo research on all the claimed made on cardio-protective nature or resveratrol this must be now or in very near future [5-7]. Resveratrol has been suspected to be very good agent in prevention of the variety of human tumor cell lines, including those from breast, prostate, stomach, colon, pancreatic, and thyroid cancers [8]. Resveratrol has also been found improves diabetes-associated erectile dysfunction (ED) in laboratory animals. Combination medication with resveratrol and sildenafil have been found to of synergistic effect in reversing ED. The mechanisms might be attributed to its anti-oxidative properties and NO–cGMP signaling pathway upregulation [9]. Derivatives of resveratrol (2-chloro-resveratrol and 2-bromo-resveratrol), have been reported as very effective antimicrobial agent, inhibiting the growth of Gram-positive bacteria, Gram-negative bacteria and fungi [10]. The aim of this study is to carry out high performance liquid chromatography (HPLC) in determining quality, quantity and purity grade of the purified resveratrol against standard resveratrol on HPLC chromatogram.

Material and Method

Materials

Grape seeds, high performance liquid chromatograph (HPLC) auto sampler, rotary evaporator water bath, vortex mixer. Activated carbon, for adsorption chromatography, florisil for adsorption chromatography, and caly (all these are for stationary phase of column chromatography). Ethanol (analytical grade), ethyl acetate (analytical grade), acetone, n-Hexane, Chloroform, (analytical grade), methanol (analytical grade), acetonitrile (analytical grade), methanol (HPLC grade), Diethyl ether (analytical grade), Petroleum ether (analytical grade) and standard resveratrol (*cis* and *trans*) Sigma 99% will be used in the experiments. Other ancillary apparatus includes; Glass column for preparative chromatography, calibrated/standard pipettes, 10, 25, 50, 100, 150 and 250 ml conical flasks, funnels, beakers, automatic pipettes, Buchner flask/funnel, mortar and pestle.

Equipment and Chemicals

Trans-Resveratrol and *cis*-resveratrol standards were purchased from Cayman Chemical Company (Ann Arbor, MI). Emodin and quercetin standards were purchased from Santa Cruz Biotechnology, Inc. (Santa Cruz, CA). HPLC-grade methanol and formic acid were purchased from Fisher Scientific Canada. Ultrapure water (18.2 MΩ cm) was obtained using a Millipore Milli-Q 10 water system for the preparation of the buffer solution (Billerica, MA). Standard. The working solution was prepared by diluting the stock solution to obtain appropriate concentrations for calibration curves. The chemicals and reagents used in this work were of analytical grade and purchased from Sigma Chemical Co. (Darmstadt, Germany). All glassware was acid washed and rinsed with doubly distilled deionized water (ddH₂O). HPLC was performed with the Shimadzu Prominence-İ LC-2030C 3D Model with PDA detector.

Method

Extraction of resveratrol

Extraction is the most important and critical stage in isolation/purification of natural products find in plants, this is to make sure that most if not all the target compound is within the extracting medium, several very important reason for these are: in order to obtain a maximum yield, also to know exact level in w/w, w/v or v/w of the target compound from the whole sample, again this would enable comparison with other work/research possible.

Many works conducted on resveratrol has suggested several extraction methods for resveratrol some of which with are: supercritical extraction method [11], by Kinetics and modeling [12] multi-stage counter current extraction [13] but in this work we choose percolation method with ethanol/methanol 1:1

Hydrolysis and Liquid-Liquid extraction of resveratrol

The collected powder from the extraction process is dissolved in distilled water and pH is adjusted to 1 using hydrochloric acid, this is then heated under reflux at 57°C for 8 hours, this is to enable any dimer or trimer and also glycosides of resveratrol to be hydrolyzed, after the hydrolysis an extracting solvent made by mixture of ethyl acetate: ether is used to extract resveratrol from the aqueous hydrolyzing solution by liquid-liquid extraction in a separation funnel (pH adjusted to 7 using sodium carbonate before liquid-liquid extraction). The extract obtained here is used for Column chromatography analysis.

Preparation of column using different column fillers (stationary phase)

Silica Gel

40 g of Silica Gel G was measured, and it then heated at 105°C for 30 min, then it was activated by continuous heating for another 30 min at 180°C in a drying oven. The prepared Silica Gel G will be packed into chromatographic column using wet packing method [14]. The column is loaded with 0.2-0.5 g of ethanolic extract of grape seed, gradient elution using two types of mobile phase (solvent system is used) these are; n-Hexane: Ethyl-acetate: Acetonitrile (9:1:1) and Chloroform: Ethanol (7:2) at a rate of 5 mL/min, collecting the eluate 10 mL/bottle. The eluates are then vaporized, the remainder was dissolved in 10 mL methanol, then the samples were taken for HPLC analysis, in this total of 10 eluates was collected from first mobile phase system hexane: ethyl acetate: acetonitrile and total of thirty eluates was collected from chloroform: Ethanol mobile phase.

Activated Carbon

50 g of Activated Carbon was measured, this alumina is then packed into chromatographic column using wet packing method, this method is also modification of [14]. The column is loaded with 0.2-0.5 g of ethanolic extract of grape seed, gradient elution using two types of mobile phase (solvent system is used) these are; n-Hexane: Ethyl-acetate: Acetonitrile (9:1:1) and Chloroform: Ethanol (7:2) at a rate of 5 mL/min, collecting the eluate 10 mL/bottle. The eluates are then vaporized, the remainder was dissolved in 10 mL methanol, then the samples were taken for HPLC analysis, in this total of 10 eluates was collected from first mobile phase system hexane: ethyl acetate: acetonitrile and total of thirty eluates was collected from chloroform: Ethanol mobile phase.

Florisil column preparation

Florisil column is prepared by weighing exactly 30g of the adsorbent into column (it was packed according to wet method) the column is prepared using hexane: ethyl acetate (9:1) mobile phase, the column is then loaded with the crude extract obtained from grape seed, the column is washed with this mobile phase, the eluates are collected at 10mL per bottle, after collecting 15 eluates from this mobile phase, new mobile phase is then introduced this is chloroform: methanol, in this also 15 eluates were collected at 10mL per bottle, the eluates from both mobile phases are then taken for HPLC analysis of resveratrol.

Clay column preparation

The concentrated extract obtained from grape seed was loaded onto column to be chromatographed over a clay/resin column the column is prepared by measuring 30 g of Clay/resin into a beaker and packed to a column using wet packing method, the column is firstly washed with distilled water to remove any trace of sugars and other water soluble substances, and then finally eluted with 75 % (v/v) aqueous ethanol, only the ethanolic eluates are collected, as water eluate does not elute resveratrol from clay [15] total of twenty eluates were collected, and 1mL of each is transferred into HPLC vial for analysis of resveratrol.

HPLC method for the determination of resveratrol

To determine resveratrol in the samples. Resveratrol identification is to be made by comparing the relative retention times of sample peaks with standards. And the calibration curve will be used in determining amount of resveratrol in each and every sample. The following equations were used to

calculate the amounts of *cis* and *trans* resveratrol in each sample. The calculations for all concentrations of *cis* and *trans* resveratrol were conducted using standard calibration curves.

Result

Below are samples of chromatograms obtained from various stages of our investigations, as the main aim of this project suggested we need to establish an optimum condition for separation of resveratrol by column, here samples of chromatograms from two different mobile phases are presented, and thereby discussed. Table 1 shows collected eluates from Silica gel, Chloroform: Methanol mobile phase. Figure 3 illustrates chromatogram of purified resveratrol collected from silica gel column under certain analysis conditions. Table 2 shows collected eluates of activated carbon 70% ethanol mobile phase. Figure 4 illustrates activated carbon column eluate chromatogram at certain retention time and analysis conditions.

Table 1. Collected eluates from Silica gel, Chloroform: Methanol mobile phase

Eluent number	1	2	3	4	5	6	7	8	9	10	11	12	13	14	15
Presence of resveratrol	-	-	-	-	-	-	-	-	-	-	-	-	-	-	-
Eluent number	16	17	18	19	20	21	22	23	24	25	26	27	28	29	30
Presence of resveratrol	-	-	-	-	-	-	-	-	-	-	-	-	-	-	+
Eluent number	31	32	33	34	35	36	37	38	39	40	41	42	43	44	45
Presence of resveratrol	+	+	+	-	-	-	-	-	-	-	-	-	-	-	-
Eluent number	46	47	48	49	50	51	52	53	54	55	56	57	58	59	60
Presence of resveratrol	-	-	-	-	-	-	-	-	-	-	-	-	-	-	-

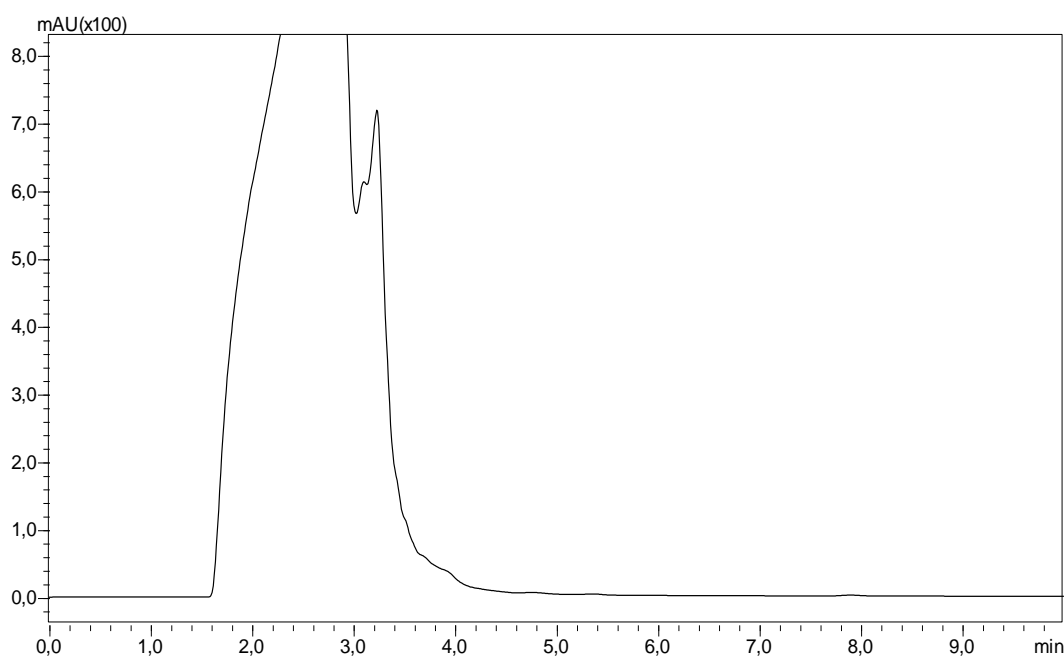


Figure 3. Chromatogram of purified resveratrol collected from silica gel column.
Analysis condition: Mobil Phase; Methanol: Acetonitrile: 0.1% Phosphoric acid (60:30:10 v/v)
Flow rate: 1.5 mL/min. Wavelength: 308 nm.

Table 2. Activated carbon 70% ethanol mobile phase

Eluent number	1	2	3	4	5	6	7	8	9	10	11	12	13	14	15	16	17	18	19	20
Presence of resveratrol	-	-	-	-	-	-	-	-	-	+	+	+	+	+	+	-	-	-	-	-

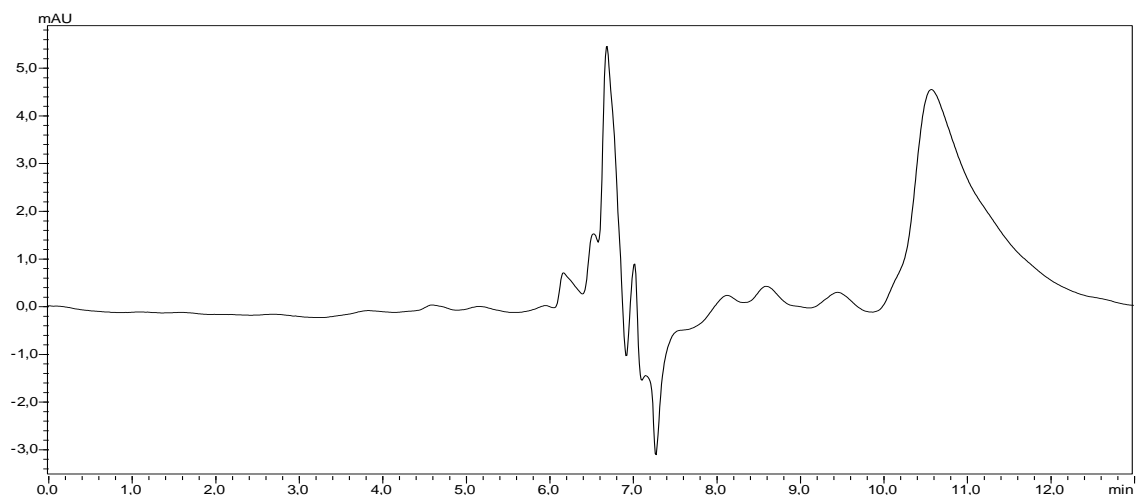


Figure 4. Activated carbon Column eluate chromatogram, Retention time 6.8-7.3 minutes
Analysis condition: Methanol: Acetonitrile: 0.1% Phosphoric acid (60:30:10 v/v)
Flow rate: 1.0 mL/min. Wavelength: 308 nm.

Table 3 shows collected eluates from Florisil column chloroform/methanol mobile phase. Figure 5 illustrates florisil column eluate chromatogram at certain retention time and analysis conditions. Table 4 shows collected eluates from clay column chloroform/methanol mobile phase. Figure 6 illustrates Resveratrol (400 MHz- DMSO-d₆) 1H-NMR spectra, purified from black grape seed by column chromatography.

Table 3. Collected eluates from Florisil column chloroform/methanol mobile phase

Eluent number	1	2	3	4	5	6	7	8	9	10	11	12	13	14	15	16	17	18	19	20
Presence of resveratrol	-	-	-	-	-	-	-	-	-	+	+	+	+	+	+	+	+	-	-	-

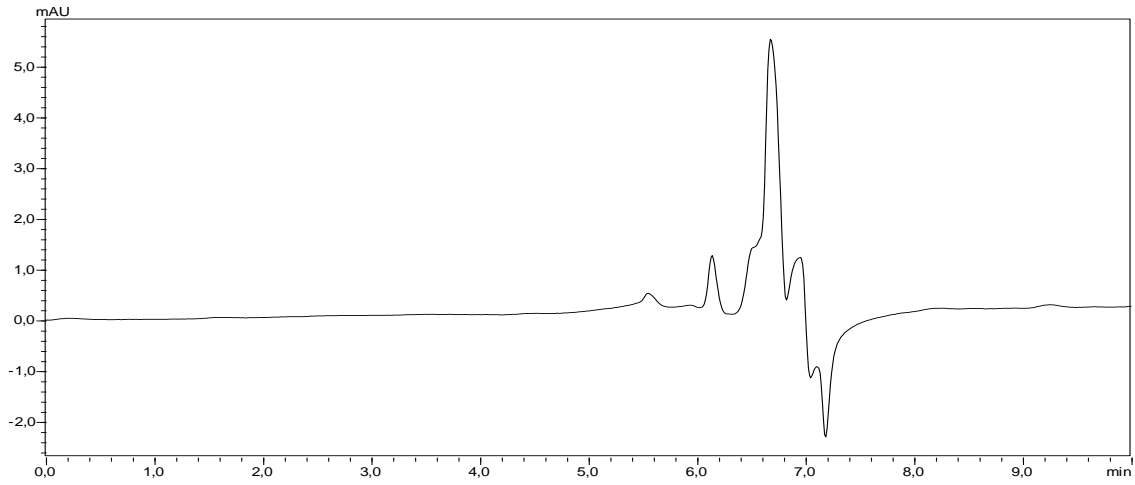


Figure 5. Florisil column eluate chromatogram. Retention time 6.8-7.3 minutes.
Analysis condition: Methanol: Acetonitrile: 0.1% Phosphoric acid (60:30:10 v/v)
Flow rate: 1.0 mL/min. Wavelength: 308 nm.

Table 4. Collected eluates from clay column chloroform/methanol mobile phase

Eluent number	1	2	3	4	5	6	7	8	9	10	11	12	13	14	15
Presence of resveratrol	-	-	-	-	-	-	-	-	-	-	-	-	-	-	-
Eluent number	16	17	18	19	20	21	22	23	24	25	26	27	28	29	30
Presence of resveratrol	-	-	-	-	-	-	-	-	-	-	-	-	-	-	-

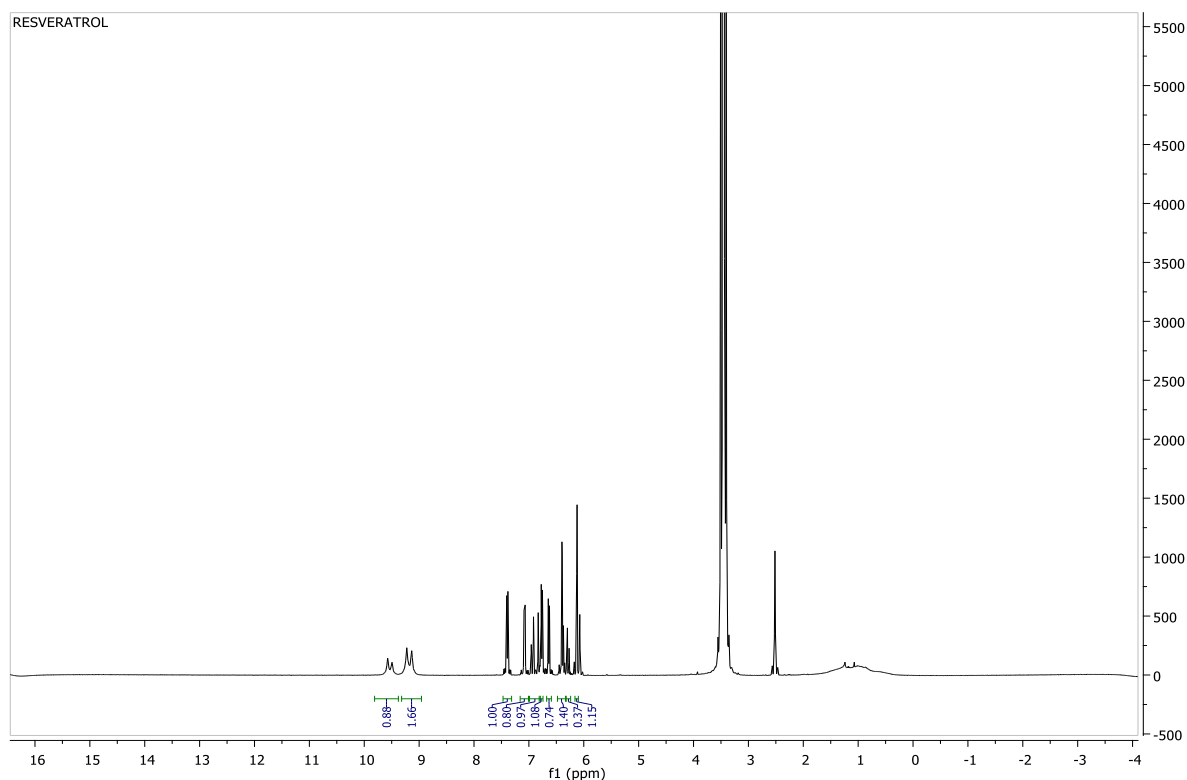


Figure 6. Resveratrol (400 MHz- DMSO- d_6) 1H -NMR spectra, purified from black grape seed by column chromatography.

The peaks at 2.56 and 3.30 ppm belong to proton residues in the solvent. Olefinic and aromatic proton peaks were observed at 6.80-7.40 ppm while the peak belonging to phenolic OH protons were observed at 9.18 and 9.51 ppm.

Discussion

Several type of column fillers/stationary phase against mobile phase are used by analytical scientist to isolate natural products and organic compounds [16]. Several researchers for decades have been trying to isolate resveratrol form different plant's sources but yet the isolation and absolute purification of this compound is still a subject of researches, some of these early attempts can be seen in [17]. From our result and finding in this research four of the combination (stationary phase/mobile phase) used in this research prove to have an average reliability in separation of resveratrol from crude extract of plants source, but from our HPLC chromatogram; silica gel has the best separation power for this compound, this is because only silica gel HPLC chromatogram, shows relatively pure resveratrol presence although two other peak appear but suspected to be resveratrol glycoside and viniferin, (see Figure 3) similar result is obtained from previous literature [18]. Another column filler with much resveratrol resolution is Activated carbon this according to [15] appear to hold resveratrol after eluting with water, it can then be recovered by using aqueous ethanolic solution as mobile phase (see Figure 4).

Florisil although not been tried before by in isolation of resveratrol, according to our literature survey, but also van be good adsorbent to isolate resveratrol and its family, but as it was notice with eluents results of florisil column from HPLC chromatogram, has a rather tailing properties in separation, but can also resolute between trans and cis isomers of resveratrol, this is a very good quality noticed with florisil that other column filler did not demonstrate even the better silica gel (see Figure 5). According to our finding here in this research, clay column is totally negative as regard to isolation of resveratrol, this is because all the resveratrol has been almost permanently (maybe covalently) adsorbed by the clay as any attempt to alter the polarity of our mobile phase in order to recover resveratrol proved abortive. The confirmation of isolated and purified resveratrol is established using both HPLC and NMR spectra as can be seen in Figure 6 after hydrolysis and silica gel column chromatogram from black grape seed shows that the purification of resveratrol has been successful.

Conclusion

In conclusion we can say that this research came up with a new insight into how resveratrol and effectively be separated from any given mixture containing resveratrol and to recommend that scientists, researchers, pharmacologist as well as nutritionists can use this method in isolating this noble compound, as we successfully isolate and purified it using this very method.

References

- [1] Lucie F (2000) Biological Effects of Resveratrol. *Life Sciences*. 66 (8):663–673
- [2] Renaud S, de Lorgeril M (1992) Alcohol, platelets, and the French paradox for coronary heart disease. *Lancet*. 339(8808):1523-1526.
- [3] Schröder G., Brown J.W., Schröder J., (1988). Molecular analysis of resveratrol synthase. cDNA, genomic clones and relationship with chalcone synthase. *Eur J Biochem*, 172 (1):161–169.
- [4] Xia E-Q, Deng G-F, Guo Y-J, Li H-B (2010) Biological activities of polyphenols from grapes. *Int. J. Mol. Sci.* 11(2), 622-646.
- [5] Pace-Asciak CR, Hahn S, Diamandis EP, Soleas G, Goldberg DM (1995) The red wine phenolics trans-resveratrol and quercetin block human platelet aggregation and eicosanoid synthesis: implications for protection against coronary heart disease. *Clin Chim Acta*. 235(2):207-219.
- [6] Wang Z, Huang Y, Zou J, Cao K, Xu Y, Wu JM (2002) Effects of red wine and wine polyphenol resveratrol on platelet aggregation in vivo and in vitro. *Int J Mol Med*. 9(1):77-79.
- [7] Kirk RI, Deitch JA, Wu JM, Lerea KM (2000) Resveratrol decreases early signaling events in washed platelets but has little effect on platelet in whole blood. *Blood Cells Mol Dis*. 26(2):144-150.
- [8] Aggarwal BB, Bhardwaj A, Aggarwal RS, Seeram NP, Shishodia S, Takada Y (2004) Role of resveratrol in prevention and therapy of cancer: preclinical and clinical studies. *Anticancer Res*. 24(5A):2783-2840.
- [9] Yufeng B, Ruihua A (2015) Resveratrol and sildenafil synergistically improve diabetes-associated erectile dysfunction in streptozotocin-induced diabetic rats. *Life Sciences* 135: 43–48.
- [10] Xiu-Zhuang L, Xia W, Chun-Jiang Z, Xiao-Ling J, Jiang-Jiang, Gui-Juan F, Bo Z (2012) Hypohalous acid-mediated halogenation of resveratrol and its role in antioxidant and antimicrobial activities. *Food Chemistry* 135(3): 1239–1244.
- [11] Benova B, Adam M, Pavli P (2010) Supercritical fluid Extraction of piceid, resveratrol and emodin from Japanese knot weed. *J. Supercrit. Fluids* 51: 325–330.
- [12] Zhang J, Zhou L, Zhang P, Liu T, Yang G, Lin R, Zhou J (2015) Extraction of polydatin and resveratrol from *Polygonum cuspidatum* root: Kinetics and modeling. *Journal of Food and Bioproducts Processing* 94:518-524
- [13] Zhang Q, Bian Y, Shi Y, Zheng S, Gua X, Zhang D, Zhu X, Wanga X, Jiang Di, Xiong Q (2015) An economical and efficient technology for the extraction of resveratrol from peanut (*Arachis hypogaea*) sprouts by multi-stage countercurrent extraction. *Journal of Food Chemistry* 179:15-25
- [14] Nakanishi K, Minakuchi H, Soga N (1998) Structure design of doublepore silica and its application to HPLC. *J. Sol-Gel Sci. Technol.* 13(1-3): 163-169.
- [15] Kamel A, Élodie R, Waffo-Téguo P, Jean-Michel M, Tristan R, Alain D (2017) Identification and quantification of stilbenes in some Tunisian red wines using UPLC-MS and HPLC-DAD. *OENO One* 51(3): 231-236.
- [16] Satyajit DS, Zahid LA, Gray I (2006) *Natural Products Isolation, Methods In Biotechnology Humana Press Inc.* 999 Riverview Drive, Suite 208 Totowa, New Jersey 07512.
- [17] Powell RG, TePaske MR, Plattner RD, White JF, Clement SL (1994) Isolation of resveratrol from *Festuca versuta* and evidence for the widespread occurrence of this stilbene in the poaceae. *Phytochemistry*, 35(2): 335-338.
- [18] Tang Z, Qin J, Xu X, Shi G, Yang H, Liang Y (2011). Applying silica gel column chromatography purify resveratrol from extracts of *Morus alba* L. Leaf. *Journal of Medicinal Plants Research* 5(14): 020-3027.

Best Solvent System for Rapid Determination of Resveratrol Using Thin Layer Chromatography

Yusuf Ibrahim Ibrahim, Zulaiha Gidado Mukhtar*, Garba Adamu, Muhammad Salihu, Binta Muhammad
Kano State Polytechnic, Dept. of Science Laboratory Technology, Kano, Nigeria
Fikret Karataş, Fırat University, Dept. of Chemistry, Elâzığ, Turkey
*Corresponding author: ywarure@gmail.com

Key words: resveratrol, thin layer chromatography, solvent system

Discipline: Chemistry, Biochemistry

Abstract

In this study Thin Layer Chromatography (TLC) was conducted using different ratio of mobile phase (pre-formulated), the main aim is to identify and establish the best solvent combination that will bring about better separation/resolution of resveratrol from any crude mixture containing resveratrol in it, forty three (43) different solvent systems was used in the study against silica gel coated TLC, after developing all the chromatogram, the result obtained shows that; n-Hexane: ethanol: acetonitrile (3:1:1.5) gave the best separation also chloroform: methanol and n-Hexane: ethyl acetate have shown a very good resolution.

Introduction

Resveratrol is one of the very important phenolic compounds found in fruits, and plants' parts in general. Presence of resveratrol has been established in more than 70 plant species distributed among 31 genera and 12 families [1] and a number of these are components of the human diet, for example, grapes, wine, grape juice, cranberries [2]. Grapes however, are considered to be among the most important human nutritional sources of resveratrol [3]. Grape seeds and skins are noble sources of phytochemicals such as garlic acid, catechin, and epicatechin and are suitable raw materials for the production of antioxidative dietary supplements. The differences in levels of the major monomeric flavanols and phenolic acids in seeds and skins from grapes of *Vitis vinifera* varieties Merlot and Chardonnay and in seeds from grapes of *Vitis rotundifolia* variety Muscadine were determined, and the antioxidant activities of these components were assessed [4].

Resveratrol has been reported to act as an antioxidant contained in red wine and prevent the development of cardiovascular diseases it has remarkable antioxidant and anti-inflammatory properties which have been considered to be responsible for the beneficial effects of red wine consumption on coronary heart disease [5]. Resveratrol has been found to exert a number of protective properties on the cardiovascular system in vitro, including inhibition of both platelet activation and aggregation [6-8].

Over the past two decades, scholars have studied the ability of resveratrol to prevent or reverse the development of abnormalities in heart structure and function in animal models of heart disease and heart failure. The results from animal studies have been promising, and very recently, this knowledge has been translated into examining the efficacy of resveratrol in humans with heart disease/failure [9].

Resveratrol (RES) possess multiple pharmacological activities in extending longevity and treatment of cardiovascular disease, diabetes and cancer [10]. Resveratrol has been found to prevent the proliferation of a variety of human tumor cell lines, including those from breast, prostate, stomach, colon, pancreatic, and thyroid cancers [11], many other in vitro and clinical studies have been conducted involving anticancer activity of resveratrol through many cellular pathways [12, 13]. Resveratrol has been confirmed to increased reactive oxygen species (ROS) production [14, 15], Resveratrol also prevents the adherence of *Salmonella typhimurium*, *E. coli*, and *Listeria monocytogenes* to human colonic cells [16]. The aim of this study, is to compare the contents of cis resveratrol and trans resveratrol forms in some fruits and plants samples.

Materials and Methods

Materials

Standard TLC plate Silica-gel coated, Iodine crystal, Ethanol (analytical grade), ethyl acetate (analytical grade), acetone, n-Hexane, Chloroform, (analytical grade), methanol (analytical grade),

acetonitrile (analytical grade), methanol (HPLC grade), Diethyl ether (analytical grade), Petroleum ether (analytical grade) and standard resveratrol (cis and trans) Sigma 99% will be used in the experiments. Other ancillary apparatus includes; calibrated/standard pipettes, 10, 25, 50, 100, 150 and 250 ml conical flasks, funnels, beakers, automatic pipettes, Buchner flask/funnel, mortar and pestle.

Equipment and Chemicals

Trans-Resveratrol and cis-resveratrol standards were purchased from Cayman Chemical Company (Ann Arbor, MI). Emodin and quercetin standards were purchased from Santa Cruz Biotechnology, Inc. (Santa Cruz, CA). HPLC-grade methanol and formic acid were purchased from Fisher Scientific Canada. Ultrapure water (18.2 MΩ cm) was obtained using a Millipore Milli-Q 10 water system for the preparation of the buffer solution (Billerica, MA). Standard. The working solution was prepared by diluting the stock solution to obtain appropriate concentrations for calibration curves. The chemicals and reagents used in this work were of analytical grade and purchased from Sigma Chemical Co. (Darmstadt, Germany). All glassware was acid washed and rinsed with doubly distilled deionized water (ddH₂O).

Methods

Sample preparation for resveratrol extraction and Isolation

The treatment of sample prior to analysis will comprise of several stages that include drying, homogenization, sieving, extraction, and then concentrating the extract [17], for the purpose of this research all edible fruit sample should be homogenize directly using a standard homogenizing machine coffee miller with mortar and pestle.

Drying seeds is carried out inside hot air ovum, the ovum is set at temperature of 65°C after thoroughly washing the sample with clean water, it is then transferred into ovum and allow to stand for 3-6 hours depending on the moisture contents of the sample to be dried, after been well dried, sample are then keep refrigerated and away from direct sun light for onward procedure. All condition for stability of resveratrol (pH, temperature and light) should be maintained as according to previous literature [18]. The first activity conducted after obtaining grape seed is washing it with water, drying it in oven at a temperature of 65 °C for 3-6 hours is to use mortar and pestle in grounding the dried seeds into fine powder, sieving is also involve to obtained a relatively more finer granules, this is to increase the available surface area for better extraction.

Extraction of resveratrol from sample

For the isolation of resveratrol from grape seed, the extraction method used is soxhlet this is in order to obtain an appreciable quantity of extract, several methods of extraction have been carried out to extract stilbene (resveratrol inclusive) in one of these researches [19], and soxhlet prove to yield good quantity of resveratrol. Polyphenols especially resveratrol has also been extracted via soxhlet extraction method on this work [20] extract resveratrol particularly from grape seed, similar to this work.

The procedure of soxhlet is as follows; 20 g dried powder of grape seed is measured into thimble (specially made from a thick filter paper), the thimble containing sample is placed in the soxhlet extractor chamber, about 150 mL of 96 % ethanol is measured into round bottom flask, the extractor is put fitted at the mouth of the flask and the flask is then mounted onto a heating mantle apparatus (as shown in Figure 1), the setup is now completed by attaching a condenser to it.

Two are three cycles of extraction are carried out per 20 g sample, this is because according to [19] after two cycle of extraction resveratrol amount that may still be present in the residue is very negligible. After collecting all the ethanolic extract, the solvent (ethanol) is then removed using rotary evaporator, the remaining what appear to be a very sticky powder is the washed/dissolved in methanol, liquid-liquid extraction is then conducted with n-Hexane, the n-hexane layer is separated from the methanol layer (resveratrol is not soluble in hexane), the hexane layer now removed any hydrophobic contaminants including oils and greases, the methanol phase is then dried at 60°C in an oven to dryness, after which the leftover powder is collected for onward process.

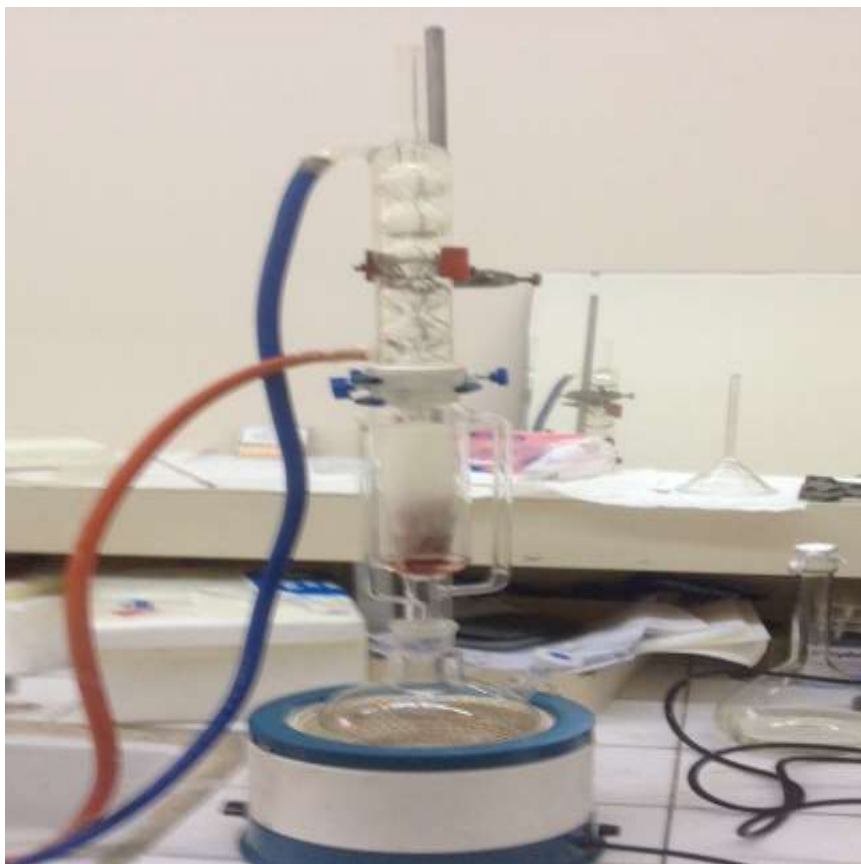


Figure 1. Soxhlet extraction setup used for solid liquid extraction of resveratrol from powdered grape seed.

TLC for the determination of best mobile phase for extract

TLC was conducted using several mixture/ratio of solvents, this is to determine the best solvent system(s) that can be used to separate resveratrol from any available food sample, according to literature some TLC system of resveratrol has been developed [21] in this an attempt is made to randomly select different solvent mixture and run TLC plate (silica gel coated, aluminum) then the best system that gives better separation and highest number of visible spots will be chosen, some of this solvent system are modification of some previous work e.g. Iodine vapour is used to develop the chromatogram for visualization [22].

The different ratio/combinations of solvent screened for this work has been tabulated in Table 1, total of 43 solvent systems was developed.

Table 1. Showing list of solvent mixer/ratio carried out against TLC for best solvent system determination

TLC plate number	Solvent system/mixture	Solvent ratio
1	Chloroform: Ethanol	4:1
2	Chloroform: Ethanol	2:1
3	Chloroform: Methanol	7:3
4	Chloroform: Methanol	4:1
5	Chloroform: Ethanol	7:2
6	Chloroform: Ethanol	7:3
7	n-Hexane: Ethyl-acetate	4:1
8	n-Hexane: Ethyl-acetate	2:1
9	Chloroform: Ethanol	7:1
10	Chloroform: Methanol	3:1
11	n-Hexane: Ethyl acetate	9:1
12	Chloroform: Methanol :	7:1.5
13	n-Hexane: Ethyl-acetate	3:1
14	n-Hexane: Ethyl-acetate	3.5:1
15	n-Hexane: Ethyl-acetate	5:1
16	n-Hexane: Ethyl-acetate	9:1
17	n-Hexane: Ethyl-acetate: Acetonitrile	9:1:1
18	n-Hexane: Ethyl-acetate: Acetonitrile	7:2:1
19	Chloroform: Methanol: Acetonitrile	9:1:1
20	n-Hexane: Ethyl-acetate: Acetonitrile	9:2:1
21	n-Hexane: Ethyl-acetate: Acetonitrile	8:2:1
22	n-Hexane: Ethyl-acetate: Acetonitrile	8:1:2
23	n-Hexane: Ethyl-acetate: Acetonitrile	10:1:1
24	n-Hexane: Ethyl-acetate: Acetonitrile	10:1:2
25	n-Hexane: Ethyl-acetate: Acetonitrile	10:2:1
26	n-Hexane: Ethyl-acetate: Methanol	10:2:1
27	n-Hexane: Ethyl-acetate	6:1
28	n-Hexane: Ethyl-acetate	4:1
29	n-Hexane: Ethyl-acetate	4:1.5
30	n-Hexane: Ethyl-acetate	4.5:1
31	n-Hexane: Ethyl-acetate	5:1
32	Chloroform: Methanol	7:2.5
33	Chloroform: Methanol	7:1.5
34	Chloroform: Methanol	1:1
35	n-Hexane: Ethyl-acetate: Ethanol	9:2:1
36	n-Hexane: Ethyl-acetate: Ethanol	9:1:2
37	n-Hexane: Ethyl-acetate: Ethanol	9:2:2
38	n-Hexane: Ethyl-acetate: Ethanol	7:2:1
39	n-Hexane: Ethyl-acetate: Ethanol	7:1:2
40	n-Hexane: Ethyl-acetate: Methanol	9:2:2
41	n-Hexane: Ethyl-acetate: Methanol	9:3:2
42	n-Hexane: Ethyl-acetate: Ethanol	4.5:1:0.5
43	n-Hexane: Ethyl-acetate: Ethanol	4.5:1:1.5

Result

After running these several tests, result was obtained, Figure 2 depicts some of TLC chromatogram, the best solvent system can easily be identified with many numbers of spots and also with better resolution.

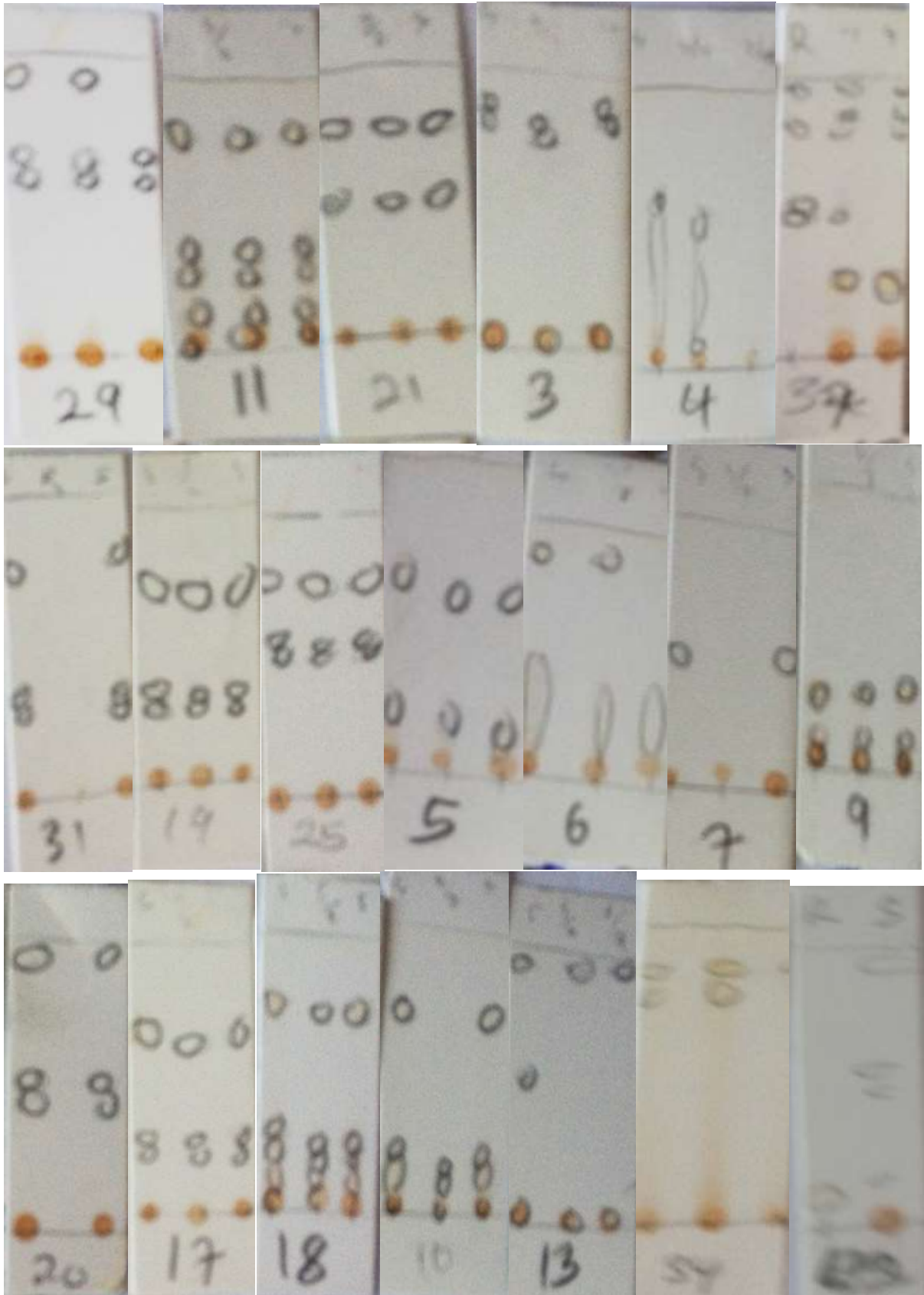


Figure 2. Pictures of silica gel coated TLC for determination of best solvent system for separation of resveratrol from crude mixer

Discussion

The aim of this section of our research is to verify and/or establish a very good solvent systems that can best separate resveratrol from any crude mixture using simple TLC, some previous work used dichloromethane on silica gel 60 coated TLC [23], others also try to find dissolution coefficient of resveratrol and other stilbenes using different mixtures of solvents [24], running more than 40 TLC plate and alternating solvent composition and ratios we found some solvent system to give a better resolution and separation of resveratrol from crude ethanolic extract containing this compound, the best developed plates here as can be seen from TLC chromatogram pictures above are: plate number 16,17,18,19 and 20 (see Figure 2 for various TLC chromatogram pictures). Although mixture of Chloroform/methanol and n-hexane/ethyl acetate are both found to separate our crude extract but only chloroform/methanol give better resolution for our target molecule (resveratrol), the former solvent system removed many fractions without moving the target molecule, this is evident when a standard resveratrol spot is run together on TLC plate with crude extract sample.

Conclusion

In conclusion, according to finding of this research we can said that; many foods/fruits/herbs that are suspected to contained some amount of resveratrol, this method can be used to establish qualitatively so far the present of this noble biomolecule, the method developed here is very simple, relatively rapid and also economically cheaper as well as very safe and can be conducted in any laboratory. We can confidently recommend this method for industries as well, in the same vain a simple modification of this method can be used to estimate quantities/amount of resveratrol from any sample of choice. The method we established here has never been reported elsewhere by any researchers according to our literature findings.

Acknowledgements

This work is financially supported by Fırat University Elazığ, Turkey (Project Number FUBAP FF.17.09).

References

- [1] Counet C, Callemien D, Collin S (2006) Chocolate and cocoa: new sources of *trans*-resveratrol and *trans*-piceid. *Food Chem.* 98: 649-657.
- [2] Wang Y, Catana F, Yang Y, Roderick R, Breemen RB (2002) An LC-MS method for analyzing total resveratrol in grape juice, cranberry juice, and wine. *J. Agric. Food Chem.* 50: 431- 435.
- [3] Careri M, Corradini C, Elviri L, Nicoletti I, Zagnoni I (2003) Direct HPLC analysis of quercetin and *trans*-resveratrol in red wine, grape, and winemaking byproducts. *J. Agric. Food Chem.* 51: 5226-5231.
- [4] Yilmaz Y, Toledo RT (2004) Major flavonoids in grape seeds and skins: antioxidant capacity of catechin, epicatechin, and gallic acid. *J. Agric. Food Chem.* 52(2): 255–260.
- [5] Surh YJ, Hurh YJ, Kang JY, Lee E, Kong G, Lee SJ (1999) Resveratrol, an antioxidant present in red wine, induces apoptosis in human promyelocytic leukemia (HL-60) cells. *Cancer Letters* 140(1–2): 1–10.
- [6] Pace-Asciak CR, Hahn S, Diamandis EP, Soleas G, Goldberg DM (1995) The red wine phenolics *trans*-resveratrol and quercetin block human platelet aggregation and eicosanoid synthesis: implications for protection against coronary heart disease. *Clin Chim Acta.* 235(2):207-219.
- [7] Wang Z, Huang Y, Zou J, Cao K, Xu Y, Wu JM (2002) Effects of red wine and wine polyphenol resveratrol on platelet aggregation in vivo and in vitro. *Int J Mol Med.* 9(1):77-79
- [8] Kirk RI, Deitch JA, Wu JM, Lerea KM (2000) Resveratrol decreases early signaling events in washed platelets but has little effect on platelet in whole blood. *Blood Cells Mol Dis.* 26(2):144-150.
- [9] Paj P, Louis XL, Thandapilly SJ, Movahed A, Zieroth S, Netticadan T (2014) Potential of resveratrol in the treatment of heart failure. *Life Sciences* 95(2): 63–71.
- [10] Brisdelli F, D'Andrea G, Bozzi A (2009) Resveratrol: a natural polyphenol with multiple chemopreventive properties. *Curr. Drug Metab.* 10(6): 530–546.

3rd International Students Science Congress
3-4 May 2019, İzmir - Turkey

- [11] Aggarwal BB, Bhardwaj A, Aggarwal RS, Seeram NP, Shishodia S, Takada Y (2004) Role of resveratrol in prevention and therapy of cancer: preclinical and clinical studies. *Anticancer Res.* 24(5A):2783-2840.
- [12] Siegel RL, Miller KD, Jemal A (2016) Cancer statistics, 2016. *CA Cancer J Clin.* 66(1): 7–30.
- [13] Tomé-Carneiro J, Larrosa M, González-Sarrías A, Tomás-Barberán FA, García-Conesa MT, Espín JC (2013) Resveratrol and clinical trials: the crossroad from in vitro studies to human evidence. *Curr. Pharm. Des.* 19: 6064–6093.
- [14] Sutton JM (2014) Neoadjuvant therapy for pancreas cancer: Past lessons and future therapies. *World J Gastroenterol* 20(42): 15564-15579. <http://dx.doi.org/10.3748/wjg.v20.i42.15564>
- [15] Miki H, Uehara N, Kimura A, Sasaki T, Yuri T, Tsubura A (2012) Resveratrol induces apoptosis via ROS-triggered autophagy in human colon cancer cells. *Int J Oncol.* 40(4):1020-1028. <http://dx.doi.org/10.3892/ijo.2012.1325>
- [16] Selma MV, Larrosa M, Beltrán D, Lucas R, Morales JC, Tomás-Barberán F, Espin JC (2012) Resveratrol and some glucosyl, glucosylacyl, and glucuronide derivatives reduce *Escherichia coli* O157:H7, *Salmonella* Typhimurium, and *Listeria monocytogenes* Scott A adhesion to colonic epithelial cell lines. *J Agric. Food Chem.* 60(30): 7367–7374.
- [17] Wang DG, Liu WY, Chen GT (2007) A simple method for the isolation and purification of resveratrol from *Polygonum cuspidatum*, *J. Pharm. Anal.* 3: 241–247.
- [18] Tang Z, Qin J, Xu X, Shi G, Yang H, Liang Y (2011) Applying silica gel column chromatography purify resveratrol from extracts of *Morus alba* L. Leaf. *Journal of Medicinal Plants Research.* 5(14): 3020-3027.
- [19] Soral I, Vrhotová N, Tříska J, Balík J, Horník Š, Cuřínová P, Sýkora J (2015) Various extraction methods for obtaining stilbenes from grape cane of *Vitis vinifera* L. *Molecules* 20: 6093-6112.
- [20] Márcia LM, Marcela B, Milena KB, Carmen MD, Marcelo SK, Lucia RC, Diógenes GC, Campo MV (2016) *Trans*-resveratrol and antioxidant activity of grape (*vitisviniferasp*) byproducts, *Brazilian Journal of Food Res.* 7(1): 66-81.
- [21] Lotz A, Spangenberg B (2016) New and sensitive TLC method to measure *trans*-resveratrol in *Physalisperuviana*, *Journal of Liquid Chromatography & Related Technologies* 39(5-6): Special Issue: Thin Layer Chromatography.
- [22] Glavnik V, Simonovska B, Albreht A, Vovk I (2012) TLC and HPLC screening of *p*-coumaric acid, *trans*-resveratrol, and pterostilbene in bacterial cultures, food supplements, and wine. *Journal of Planar Chromatography* 25:2012-2013.
- [23] Powell RG, TePaske MR, Plattner RD, White JF, Clement SL (1994) Isolation of resveratrol from *Festuca versuta* and evidence for the widespread occurrence of this stilbene in the poaceae. *Phytochemistry*, 35(2): 335-338.
- [24] Yangji W, Pi L, Liyan M, Jingming LP (2014) Separation and purification of four stilbenes from *Vitis vinifera* L. cv. Cabernet Sauvignon roots through high-speed countercurrent Chromatography. *S. Afr. J. Enol Vitic.*, 35(2): 226-231.

Urban and Regional Planning / Şehir ve Bölge Planlama

A Study on the Limitation of Motorcycle as City Transportation Case study: Bandung, Indonesia

Afina Sholihat, Necmettin Erbakan Univ., Dept. of City and Region Planning, Konya, Turkey
Corresponding author: sholihatafina@gmail.com

Keywords: motorcycle, city transportation, traffic jam, traffic accident
Discipline: Urban and Regional Planning

Abstract

The motorcycle is one of the efficient types of transportation. The size that is not too large makes it easy for people to use it. Most developing countries use motorcycles as their primary transportation. Indonesia is one of a country in Southeast Asia with the biggest motorcycle sales. Bandung, one of the cities in Indonesia, has the most motorcycle user. Motorcycle users in Bandung continue to increase from year to year. This has an impact on several factors such as traffic jams and traffic accidents. The uncontrolled number of motorcycle users in Bandung creates chaos on the road. If the number of motorcycle users continues to increase without the limits of the government, the capacity of the highway will not be enough to accommodate all vehicles in Bandung.

In this study, author investigated the impact of using motorcycles as city transportation such as the reason people choose motorcycles as primary transportation, the effect of motorcycles on traffic congestion, and the effect of motorcycles on traffic accidents. This study was carried out using a questionnaire given to random people. Aside from the data from the questionnaire, author also made direct observations to motorcycle users at Bandung.

Introduction

Motorcycles are an efficient type of transportation. The size that is not too large makes it easy for people to use it. Motorcycles are a quick and easy means of transport in modern cities. They are economical, offer better fuel efficiency and a faster commute compared to other modes of transport [1]. Motorcycle's speed is one of the reasons people use a motorcycle for city transportation. Motorcycles are compact, highly maneuverable, and have a relatively low environmental impact.

Lots of Southeast Asian countries use motorcycles as city transportation such as Indonesia, Vietnam, Thailand, Malaysia, and the Philippines. On the Southeast Asian countries scale, Indonesia is in the first position with the biggest motorcycle sales.

Bandung is one of a city in Indonesia which has the most motorcycle user. People use a motorcycle as primary transportation. The poor public transportation in Bandung encourages people to use motorcycles as a solution. Motorcycle ownership is quite easy, causing motorcycle users to increase every year. A large number of motorcycle users in Bandung has an impact on traffic congestion and high rates of traffic accidents.

Materials And Methodology

Study Area

Bandung is one of the cities in Indonesia with 167.7 km² area. Bandung was known as a touristic city. Education and economic sector in Bandung are also promising. A lot of people come to Bandung for work or education.

A lot of people use a motorcycle as their transportation rather than public transportation. The high number of motorcycle user in Bandung become a concern because of their impact on society. Therefore this study will focus on people who use a motorcycle as primary transportation in Bandung. Motorcycle users will be examined in general, regardless of the type of motorcycle.

Research Methodology

This study used numerical data as a source of research. The author also made direct observations and did not make a comparison of the object of the study, so that this research is a quantitative descriptive study.

Information for this research sourced from two types of data, primary data, and secondary data. The results of questionnaires and interviews used as primary data. While official data from government agency used as secondary data.

A questionnaire carried out between November 2018 and December 2018. There are 111 respondents randomly chosen to fill the questionnaire. The questionnaire consists of several questions such as respondent profile, the reason for using a motorcycle as city transportation, the frequency of motorcycle usage in one day, the reason for not using public transportation, the experience of having a traffic accident while using a motorcycle, and others.

Result and Discussion

Demographic Profile of the Respondent

From the questionnaire, 43.2% of respondents are male and 56.8% of the respondent is female. Most of the respondents at the age of 17-26 (93.7%) and the rest at the age of 27-36 (6.3%). 56.8% of respondent are students, 26.1% are private employees and 17.1% others occupation. Not all of the respondent lives in Bandung. 28.8% of respondent didn't live in Bandung but use their motorcycle at Bandung.

Motorcycles Rates in Bandung

Bandung is one of the cities in Indonesia where a lot of people use a motorcycle. They are using a motorcycle rather than other types of transportation because motorcycles considered as efficient transportation. Every year the number of motorcycles in Bandung continues to increase. The number of motorcycles in Bandung in 2012 was 976.933 units, in 2013 was 1.041.421 units, in 2014 was 1.113.316 units, in 2015 was 1.171.288 units, and in 2016 the number of motorcycles in Bandung reached 1.251.079 units. Base on that, the annual growth in the number of motorcycles rate is 6.37% (Figure 1).

In 2016, compared to other types of transportation, the motorcycle still the most used transportation type in Bandung (Figure 2). Motorcycle ownership which is quite easy is also the reason for people use the motorcycle in Bandung. The price is affordable and the payment that is quite easy attracts many people to buy it.

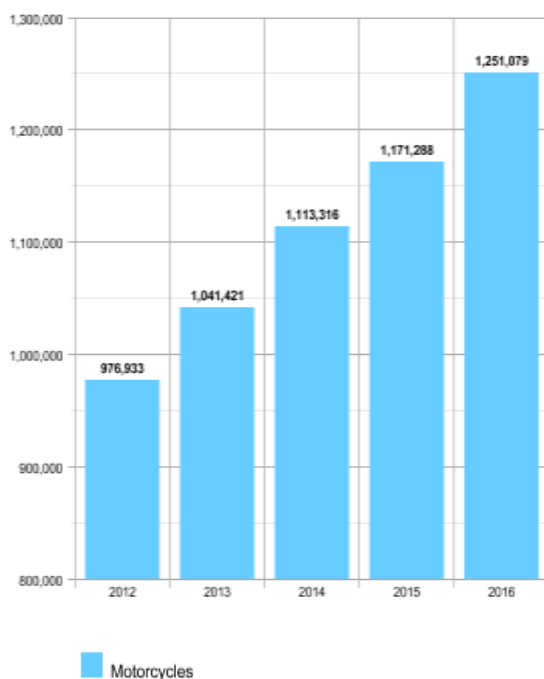


Figure 1. The number of motorcycles in Bandung from 2012 until 2016. Data from BPS-Statistics of Jawa Barat Province (2013, 2014, 2015, 2016, 2017)

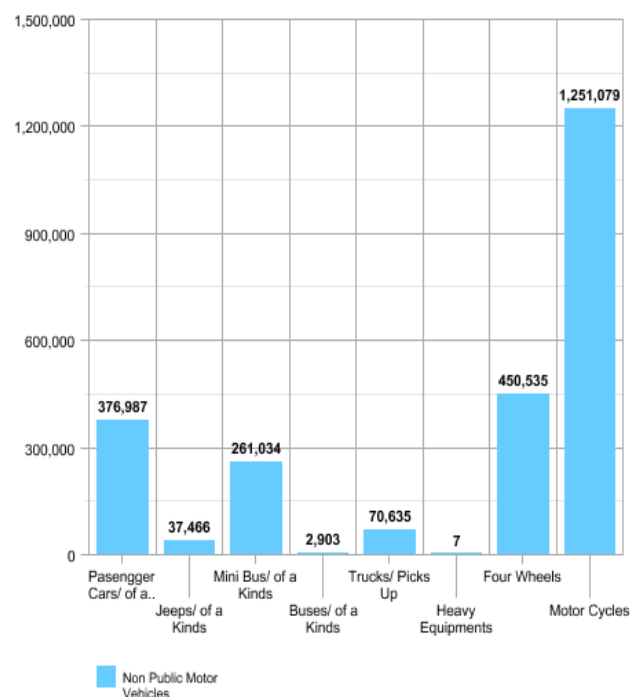


Figure 2. Number Non Public Motor Vehicle for BPKB by Branch Service in Bandung, 2016. Data from BPS-Statistics of Jawa Barat Province 2017.

The Reason Why People Use Motorcycle in Bandung

Based on the questionnaire from 111 motorcycle users in Bandung, the main reason people using a motorcycle is because of its speed. The high congestion in Bandung makes people look for fast transportation to reach their destination. 47.7% of respondents chose to use motorcycles because of their speed, while 29.7% of respondents wanted to avoid congestion (Figure 3). On the other hand, 48.6% of respondents use motorcycles for 1-2 hours a day, 41.4% for 3-4 hours, and 9.9% for 5-6 hours in one day.

66.7% of respondents did not want to use public transportation because of the long travel time. Poor facilities and services of public transportation are the most second chosen by 24.3% respondents. This is a very important consideration for the government to improve the public transportation system.

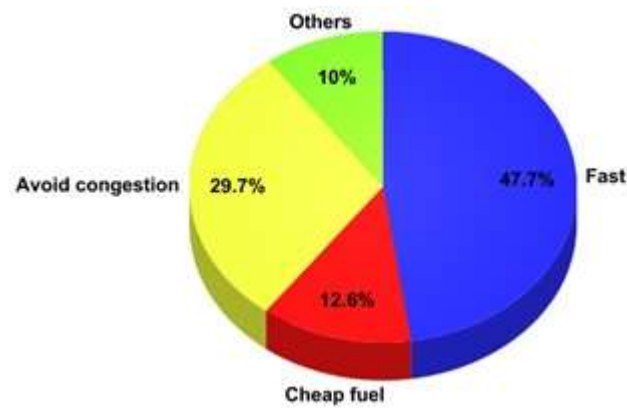


Figure 3. The Reason People Use Motorcycle in Bandung. Data from questionnaires from respondents.

Motorcycles and Traffic Congestion

Congestion is the impedance vehicles impose on each other, due to the speed-flow relationship, when the use of a transport system approaches capacity [2]. The main cause of congestion in Bandung is road capacity which is smaller than the number of vehicles. Along with population growth, the number of vehicles is also increasing. The road in Bandung is not only full of vehicles that belong to Bandung's people, but also by people outside Bandung who work or take education in Bandung.

Motorcycle, a small type of transportation, is widely used by people to avoid traffic jams, because of its movement which is not rigid as four-wheel transportation. It is known as a transition mode between pedal cycle and passenger cars in developing countries while it is serving as a solution to deal with traffic congestion in a number of developed cities [3]. The number of motorcycles that exceeded the four-wheel vehicle on the road caused congestion. Motorcycle riders will look for gaps in each road to avoid congestion. This will create irregularities on the road. Motorcycles are not the only main cause of congestion, but their existence is considered to make traffic chaotic [4].

With this case, the government tries to face this problem by providing a waiting area for motorcycles at the intersection behind the traffic lights (Figure 4), hoping that motorcycle users will become more orderly. Unfortunately, many motorcycle riders have stopped exceeding the waiting area, because the area is not sufficient enough. (Figure 5)

Traffic Accident Experienced by Motorcycle Riders

World Health Organization data shows that in 2013, more than 286,000 motorcyclists were killed in road traffic collisions. This represents almost a quarter of all road traffic deaths that year. Although the majority of motorcycle deaths occurred in low and middle-income countries, the safety of motorcyclists is a global concern [5].

69% of traffic accidents in Bandung are experienced by motorcycle riders. Although motorcycles accident in Bandung increased from 2013 to 2014, from 2014 to 2016 motorcycles accident in Bandung continued to decline (Figure 6). Even though motorcycles accident in Bandung continued to decline, in 2016 the number of these accidents was still the highest compared to the other transportation (Figure 7).

**3rd International Students Science Congress
3-4 May 2019, İzmir - Turkey**



Figure 4. Waiting area for motorcycles at the intersection. Retrieved from eproduklit-bang.pu.go.id



Figure 5. Kopo, one of intersection in Bandung. Retrieved from jabar.tribunnews.com

63% of questionnaire respondents have experienced traffic accidents. A traffic accident become a natural thing while using motorcycle.

Even though it declined, motorcycle users were the largest group contributing deaths from traffic accidents (Figure 7). In the case of accidents, motorcycle users are the riskiest parties. Factors that cause accidents according to police reports are indiscipline and excessive speed limits. The high number of motorcycle use in Bandung produce dense activity on the streets.



Figure 6. The number of motorcycles accident in Bandung from 2012 until 2016. Data from BPS-Statistics of Jawa Barat Province (2013, 2014, 2015, 2016, 2017)

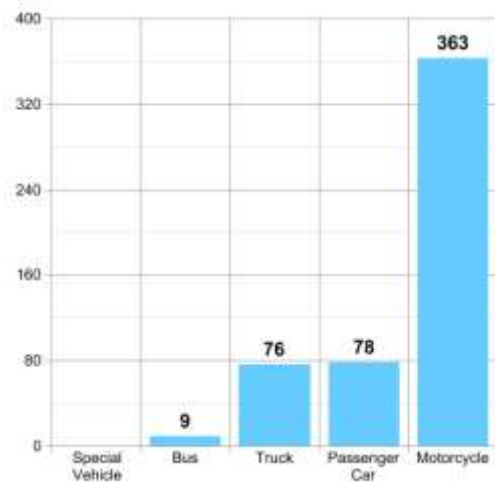


Figure 7. The number of traffic accident in Bandung, 2016. Data from BPS-Statistics of Jawa Barat Province 2017

Conclusion

Fast became the main reason for motorcycles in Bandung. In addition, the ease of motorcycle ownership also makes the number of motorcycle users in Bandung continue to increase. As the population increased in Bandung, motorcycle users also increasing. Unfortunately, road capacity is insufficient for motorcycles which always increases. Resulting in not conducive road conditions. From this irregularity, many traffic accidents are experienced by motorcycle users.

Widening the road is not a solution that can solve this problem. There needs to be government action related to motorcycles that continue to increase. Limitation of motorcycles on the road can also be one of the reduction factors in traffic jams. In addition, people need to realize how important it is to use public transportation. This needs support from the government to improve public transportation so that people want to use public transportation.

Future Outlook

The main reason people choose motorcycles rather than public transportation is that motorcycles faster than public transportation. Although public transportation is relatively cheap, and using motorcycles is more tiring, people still prefer to use motorbikes to save time. Congestion in Bandung forces people to choose motorcycles. Unfortunately, increasing motorcycle users have a negative impact on the city such as congestion increases and the number of accidents increases.

In the future, there needs to be a strategy to limit motorcycle users and increase public transportation users. There needs to be a balance between private transportation and public transportation in order to avoid chaos on roads. It will be necessary to conduct a study on people and public transportation. So it can be used as a reference to improve public transportation and can encourage people to use public transportation.

References

- [1] Velagapudi, SP, & Ray G. G. (2015). A Study on Motorcycle Usage and Comfort in Urban India. Proceedings 19th Triennial Congress of the IEA. Melbourne: International Ergonomics Association.
- [2] Zhang W (2011) Managing Traffic Congestion - Case study of Hangzhou.
- [3] Nguyen, H., Montgomery, F., & Timms, P. (2009). Should Motorcycle Be Blamed for Trafficcongestion in Vietnamese Cities? CODATU XIII – 2008 – Ho Chi Minh City (Vietnam): Challenges and Solutions for A Sustainable Development. Vietnam: CODATU conference of Urban Transport (CODATU XIII).
- [4] Darmaningtyas (2017, August 9). Executive Director of the Institute of Transportation Studies (Instran). (A. Rudi, Interviewer)
- [5] RoSPA Road Safety Research: Common Motorcycle Crash Causes. (2017, November 28). RoSPA Road Safety Research: Common Motorcycle Crash Causes. Retrieved from RoSPA Web site: <https://www.rospace.com/rospaweb/docs/advice-services/road-safety/motorcyclists/common-motorcycle-crash-causes.pdf>.

Re-assessment of Plan Decisions by Measurement of Recreation Potentials: Case Study of Manisa Keçiliköy District

Gökçe Gönüllü Sütçüoğlu*, Ahenk Karıcı, Pınar Orman

İzmir Kâtip Çelebi Üniv., Fen Bilimleri Enstitüsü, Kentsel Dönüşüm A.B.D., Çiğli Ana Kampüs, İzmir, Türkiye
Ayşe Kalaycı Önaç, İzmir Kâtip Çelebi Üniversitesi, Şehir ve Bölge Planlama Bölümü, Çiğli Ana Kampüs, İzmir, Türkiye

İletişimden sorumlu yazar: gokcegonullu@gmail.com

Anahtar Kelimeler: rekreasyon potansiyeli, Gülez yöntemi, Manisa, rekreasyon alanı

Disiplin: Kentsel Dönüşüm

Özet

İnsanoğlunun tarihsel süreç içerisinde avcı-toplayıcı hayat tarzından tarım toplumuna geçişiyle birlikte ilk kentler oluşmaya başlamıştır. Bu dönemde meydana gelen ilk kentsel hareketler içinde bulunan toplulukların ekonomik, siyasal ve sosyal işbirliklerinin oluşmasını sağlamış ve beraberinde ilk örgütsel yapıları ortaya çıkarmıştır. Zaman içinde ortaya çıkan sermaye birikimi kentleri büyük nüfus kitlelerini içerisinde barındırır hale getirmiştir. 1960'lı yıllarda ortaya çıkan, 1980'lerde sıkça kullanılmaya başlanılan, 1990'lı yıllarda ise anahtar sözcük haline gelen ve kısaca sermayenin, ticaretin ve malların dünya etrafında akışkanlığı olarak tanımlanabilen küreselleşme kavramı; kentlerin ekonomik açıdan daha da büyümesine ve kırsal nüfus için çekici hale gelmesine neden olmuştur.

Ülkemizde Cumhuriyet sonrasında başlayan kentleşme süreci 1950 sonrasında her alanda meydana gelen değişim ve gelişim hareketleri ile hız kazanmıştır. Altyapı hazırlıkları tamamlanmamış olan ve savaş sonrası yaralarını henüz sarmamış olan ülkemizde, kalkınmayı artırmak amacıyla yapılan sanayi yatırımlarının ihtiyaç duyduğu işgücünün kente ani göçü fizik mekânda ve sosyolojik anlamda büyük sorunlara yol açmıştır.

Yoğun göç baskısı altında hızlı ve kontrolsüz gelişen kentlerimizde, planlama çalışmalarının yapılamaması nedeniyle altyapı ve donatı alanları eksikliği ortaya çıkmıştır. Kontrol altına alınamayan bu süreç sorunlarıyla birlikte günümüze kadar gelmiştir. İslah İmar Planları, revizyon planları ile iyileştirilmeye çalışılan kentlerimizde bir çok sorunun yanı sıra açık ve yeşil alan eksikliği toplumun yaşam kalitesini düşüren önemli bir sorun olarak karşımıza çıkmaktadır. Açık ve yeşil alanlar; planlama aşamasında fonksiyonlar arasında doğal tamponlar olarak kullanılmalrı ve estetik katkılarının yanı sıra sosyal olarak, eğitim ve kültürel faaliyetlere imkân sağlamak, suç oranını azaltmak, rekreasyonel faaliyetlere imkân sağlamak, toplumsal gelişmeye katkıda bulunmak ve kamu sağlığını korumak gibi işlevlere de sahiptir. Geldiğimiz noktada, büyük oranda yapılaşmış olan kentlerimizde açık ve yeşil alanların nasıl artırılacağı, mevcut alanların nasıl korunacağı, insanoğlunun yaşam kaynağı olan doğaya saygılı kentlerin nasıl planlanacağı büyük önem kazanmaktadır.

Bu çalışmanın amacı, kentlerde rekreatif potansiyeli yüksek alanların belirlenmesi ve bu alanlarda plan kararlarında yapılacak değişikliklerle açık ve yeşil alan miktarının artırılabilceğini Gülez Yöntemi ile ortaya koymaktır.

Çalışmanın sonucunda, planlama çalışmaları öncesinde yapılan fiziksel analizlerle birlikte, planda rekreasyon alanı olarak tanımlanacak alanların pratik bir şekilde belirlenmesi için "Gülez Yöntemi" kullanılarak planlama çalışmalarının yürütülmesinin ekolojik dengeyi bozmayan, doğal değerleri koruyan ve kentlinin daha fazla açık ve yeşil alanlara sahip olduğu şehirler ortaya çıkaracağı; planlama çalışması daha önce yapılmış kentlerde ise, kent içinde henüz yapılaşmamış alanlarda bu yöntemle rekreasyon potansiyellerinin belirlenmesiyle açık ve yeşil alan miktarının artırılabilceği görülmüştür.

Giriş

Tarihte ilk şehirlerin günümüzden 5 bin yıl kadar önce ortaya çıkmaya başladığı düşünülmektedir. Avcı-toplayıcı hayat tarzından tarım toplumuna geçişle birlikte ilk kentler tarıma oldukça elverişli olması nedeniyle Mezopotamya, Mısır, Hindistan, Asya'nın güneydoğusunda ortaya çıkmışlardır [14].

Sümerlerce kurulduğu kabul edilen etrafi surlarla çevrili ve bir tapınak etrafında diğer yapıların yer alması ile şekillenen ilk kentler, aynı zamanda siyasal olarak birer kent devletiydi. Site adı verilen bu kent devletlerine Ur, Uruk, Eridu, Lagaş, Kiş ve Larsa gibi devletleri örnek verilebilir [1].

Kentin tanımı, içinde bulunulan dönemin özelliklerine göre farklılaşmaktadır. Milattan önce Aristo; şehirleri, insanların daha iyi bir yaşam sürmek için toplandıkları yerler olarak tanımlarken, Orta Çağın en önemli kent tanımı, Marver'in "duvarlarla çevrili insan yerleşimleri." ifadesidir. Kent tarihçisi Pirenne'de hiçbir uygarlıkta kent yaşamının ticaret ve sanayiden bağımsız olarak gelişmediğini belirtmekte, dolayısıyla kentin varlığını ekonomik gerçeklere dayandırmaktadır [3].

Mumford [13], Tarih Boyunca Kent adlı eserinde "Kent, bir topluluğun kültürünün ve erkinin yoğunlaştığı yer, zamanın bir ürünü, birikimidir" demektedir.

Başlangıçta belli bir uygarlık tarafından tarımsal ürünleri yıl boyunca korumak, güvenli bir alanda yaşamak ve dini ritüellerin birlikte yapılabilmesi adına kurulan kentler süreç içerisinde sanayi devrimi ve teknolojik gelişmelerin sonucu olarak giderek kalabalıklaşmıştır [16].

Yoğun göçlerle kalabalıklaşan ve düzensiz yapılaşan, nüfus yoğunluğu ve sağlıksız koşullar nedeniyle salgın hastalıkların ciddi bir sorun haline geldiği kentler dünya savaşları sırasında büyük yıkımlarla karşı karşıya kalmıştır. Yeniden yapılanma sürecine giren kentler; 1960'lı yıllarda ortaya çıkan, 1980'lerde sıkça kullanılmaya başlanılan, 1990'lı yıllarda ise anahtar sözcük haline gelen "Dünyanın yaşadığı, tarım ve endüstri devrimlerinden sonra ortaya çıkan, üçüncü büyük devrimin, açıkça iletişim ve bilişim devriminin görüntülerinden birisi [4]" olarak ya da kısaca sermayenin, ticaretin ve malların dünya etrafında akışkanlığı olarak tanımlanabilen küreselleşme kavramı; kentlerin ekonomik açıdan daha da büyümesine ve kırsal nüfus için çekici hale gelmesine neden olmuştur.

Ülkemizde Cumhuriyet sonrasında başlayan kentleşme süreci 1950 sonrasında her alanda meydana gelen değişim ve gelişim hareketleri ile hız kazanmıştır. Uzun savaş yıllarından sonra henüz yaralar sarılmamışken kalkınmayı hızlandırmak adına yapılan sanayi yatırımlarının ihtiyaç duyduğu işgücünün, yeterli altyapıya sahip olmayan kentlere ani göçü kentte mekânsal ve sosyolojik sorunlara yol açmıştır. Zaman içerisinde tarım politikalarındaki değişiklik, kırsal kalkınmanın yetersiz kalması nedeniyle insanların eğitim ve sağlık hizmetlerine kolay ulaşabilme ihtiyacı gibi nedenler kent nüfusunu daha da artırmıştır.

İmar planı bulunmayan, bu yoğun göç karşısında izlenecek yol haritasına sahip olmayan kentlerde altyapı ve donatı eksiklikleri ortaya çıkmıştır. Kontrol altına alınamayan bu süreç sorunlarıyla birlikte günümüze kadar gelmiştir. İslah İmar Planları ve Revizyon İmar Planları ile bu sorunlar ortadan kaldırılmaya çalışılmış olsa da kentlerdeki yüksek rant baskısı nedeniyle, yasa ve yönetmeliklerin belirlediği donatı alanları standartları bulunmasına rağmen kamulaştırma maliyetlerinin yüksekliği, uygulamada karşılaşılan sorunlar nedeniyle çözülebilmemiş değildir.

Mekânsal Planlar Yapım Yönetmeliğinin 5.i maddesinde de belirtildiği gibi kentinin kültürel, sosyal ve rekreatif ihtiyaçlarının karşılanması ve sağlıklı bir çevre ile yaşam kalitesinin artırılması kent yaşamının sürdürülebilirliği açısından oldukça önemlidir [17].

Rekreasyon genellikle serbest zamanlar içinde yapılan, bireyin kendi isteği ve iç ritmi sonucu oluşan ve bireyi fiziksel ve düşünsel yönden yeniden canlandırmayı amaçlayan, bireyin toplumsal, ekonomik ve kültürel olanakları ve yaşadığı toplumun yapısı ile bağımlı olarak yapılan fiziksel ve düşünsel etkinlikler bütünüdür. Rekreasyonda amaç dinlenmek ve enerji toplamaktır [8].

Kentsel yaşam koşulları ve çevre sorunları nedeniyle fiziksel ve ruhsal bakımdan yenilenme ihtiyacı duyan insanların çevreleri ile olan ilişkilerinin sağlıklı biçimde yürümesini sağlayabilecek, sosyal, kültürel, ekonomik ve fizyolojik faaliyetler ile boş zamanlarını değerlendirebilecek ve yitirdikleri enerjilerini yeniden kazanabilmek amacıyla rekreasyon alanlarına yönelik talepleri giderek artmaktadır [6; 7].

Bu talepler dikkate alındığında, büyük oranda yapılaşmış neredeyse bir beton yığınını anımsatan kentlerimizde açık ve yeşil alanların nasıl artırılacağı, mevcut alanların nasıl korunacağı ve işlevlendirileceği, insanoğlunun yaşam kaynağı olan doğaya saygılı kentlerin nasıl planlanacağı, sürdürülebilir kentleşmenin nasıl sağlanacağı büyük önem kazanmaktadır [18].

Plansız alanlarda rekreatif potansiyeli yüksek alanları belirleyerek yeni rekreasyon alanları oluşturmak, planlı alanlarda yeni rekreasyon alanı oluşturmaya göre nispeten daha kolaydır. Kentlerimizde rantın baskısı nedeniyle imar planı sınırları içinde, üzerinde tarımsal ürün ya da ağaç bulunan bir çok alan tüm potansiyellerine rağmen rekreasyon ya da açık alan kullanımı yerine farklı fonksiyonlar için planlanmaktadır [19].

Bu çalışmanın amacı; kentsel planlama çalışmaları sırasında rekreatif potansiyeller dikkate alınmayarak farklı fonksiyonlar için planlanmış ancak halen yapılaşmamış alanlarda, bu plan

kararlarının değiştirilmesi ile kentlerde açık ve yeşil alan miktarının ve bu alanlardan kentlilerin faydalanabileceği ekosistem hizmetlerinin artırılabilceğini ortaya koymaktır.

Bu çalışmada; “Güleç Yöntemi” ile, imar planında “Turizm Alanı” olarak planlanmış olmasına rağmen henüz yapılaşmamış örnek alanın rekreatif potansiyeli hesaplanarak plan kararlarında yapılması gereken değişiklikler ve bu değişikliklerle kent ekosistemine sağlanacak katkıların artırılması yönünde öneriler getirilmiştir.

Materyal ve Yöntem

1. Çalışma Alanı

Manisa; Ege Bölgesinde yer alan ve 1.413.000 kişi nüfuslu bir ilimizdir. Çalışma alanı olarak seçilen Manisa ili, Yunusemre İlçesi, Keçiliköy Mahallesi ise; kent merkezinin batısında, düşük yapı yoğunluğuna sahip, halen yapılaşmamış imar adalarının bulunduğu bir bölgedir [15].



Şekil 1. Çalışma alanı konumunu gösterir harita (Google Earth üzerinden hazırlanmıştır.)

Çalışma alanı; 1989 yılında yapılan ve halen yürürlükte olan imar planına göre “Turizm Tesisi” olarak planlanmıştır. İmar planı eki olan plan notlarına göre ise “Turizm Tesisi” alanlarında otel, motel, tatil köyü, pansiyon, apart otel, lokanta, yüzme havuzu, kamping vb ve villa yapılabilmektedir [15].



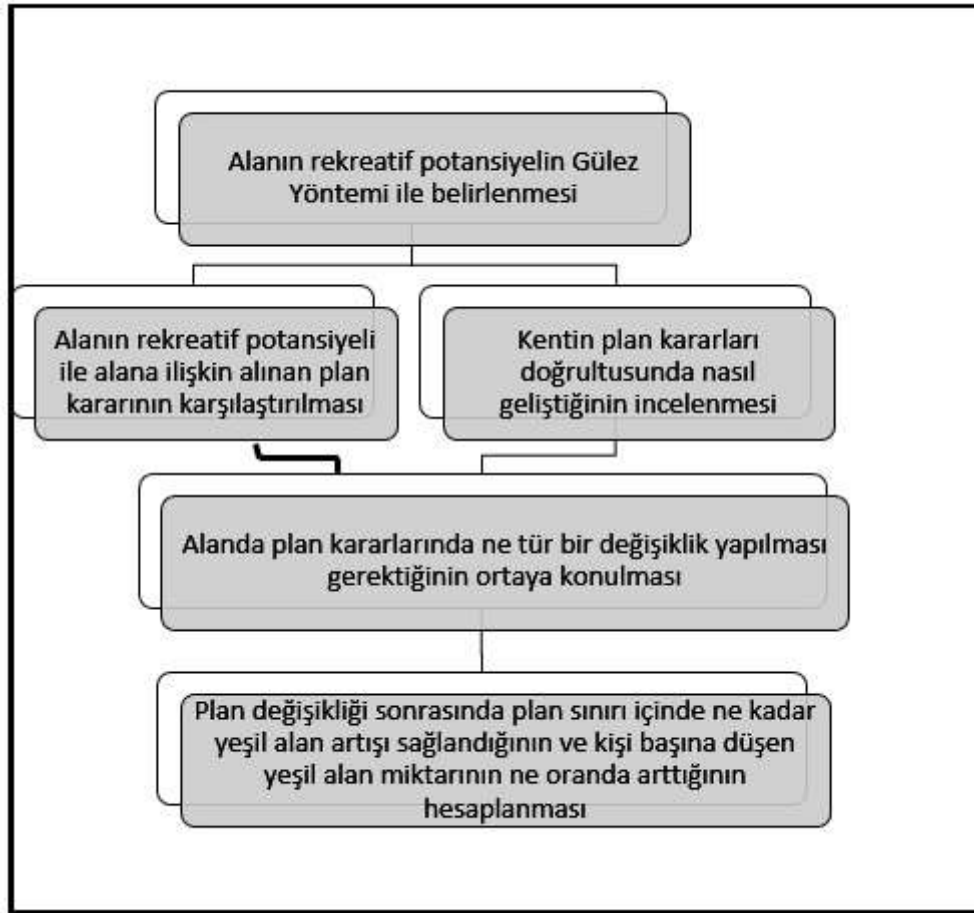
Şekil 2. Çalışma alanının yürürlükteki imar planına göre durumu (Manisa Büyükşehir Belediyesinden temin edilmiştir.)

Çalışmada kullanılan iklim verileri Meteoroloji Genel Müdürlüğünden, imar planı ve toplu ulaşım ilişkili veriler Manisa Büyükşehir Belediyesinden, kent merkezi ile alan arasındaki mesafe ve alan

konumu verileri Google Earth uydu görüntülerinden ve alanın yüzey şekli, bitki örtüsü, manzarası vb diğer veriler alana yapılan ziyarette gözlemlerle elde edilmiştir.

2. Yöntem

Çalışmanın yöntemi beş aşamadan oluşmaktadır. Öncelikle kentleşme olgusu ve kontrolsüz kentleşmenin getirisi olan donatı eksikliklerinden bahsedilmiş, daha sonra çalışma alanı tanımlanmış, Gülez yöntemi ile materyaller (çalışma alanına ilişkin veriler) değerlendirilmiş ve elde edilen bulgular hakkında tartışılmış, elde edilen sonuç değerlendirilmiş, sonraki çalışmalar için önerilerde bulunulmuştur. Çalışma alanında Gülez Yönteminin uygulanma aşamaları Şekil 3 de detaylandırılmıştır.



Şekil 3. Yöntem Akış Şeması (Yazarlar tarafından hazırlanmıştır.)

3. Gülez Yöntemi

Ülkemizde açık hava rekreasyon ihtiyaçlarının karşılanmasında önemli bir yeri olan orman içi rekreasyon alanlarının, ne düzeyde bir potansiyele sahip olduğu ya da olabileceği konusunda çeşitli çalışmalar yapılmış ve çok sayıda rekreasyon değerlendirme yöntemleri geliştirilmiştir. Çok yeni olan bu çalışmalar özellikle son 30 yılda yapılmışlardır. Bunlar arasında; CLAWSON (1959), KNETSCH 1963, KIEMSTEDT (1967), KNETSCH and DAVIS (1967), PRODAN (1968 ve 1969), PABS (1969 ve 1971), CLAVVSON and KNETSCH (1971), RUPPERT (1971), LIER (1971), BUCHWALD et al (1973), ALTAN (1976), GÜLEZ (1980) sayılabilirler. Rekreasyon potansiyelinin saptanmasına yönelik yöntemlerin çok azı bir yerin aktüel rekreasyon potansiyelini vermektedir. Bir kısmı da, bölgesel ölçekte büyük alanların rekreasyona uygunluğunu saptamaya yönelik olmaktadır. Soruna ekonomik bir yaklaşımla giren yöntemlerin çoğu, gelecek için rekreasyon potansiyelini bazı ölçütleri göz önünde tutarak tahmin etmekte fakat varolan doğal peyzaj elemanlarını değerlendirmeye almamakta ya da çok az oranda yer vermektedir [8].

1990 yılında Sümer GÜLEZ tarafından geliştirilen yöntem, ülkemiz koşullarına uygun olarak, orman içi rekreasyon alanlarının açık hava rekreasyon potansiyelinin saptanması ihtiyacından ortaya

3rd International Students Science Congress
3-4 May 2019, İzmir - Turkey

çıkıştır. Bu yöntem orman içi rekreasyon alanlarının rekreasyon potansiyellerini aşağıdaki formülle ortaya koymaktadır [8].

$$RP (\%) = P + İ + U + RK + OSE$$

Formülde değişkenler ve maksimum değerleri aşağıdaki Tablo 1’de tanımlanmıştır.

Tablo 1. Gülez Yöntemi formülü değişkenleri ve değerleri [8]

Sembol	Anlamı	Maximum Puan (Ağırlık Puanı)
P	Peyzaj Değeri	35
İ	İklim	25
U	Ulaşılabilirlik	20
RK	Rekreatif Kolaylık	20
OSE	Olumsuz Etkiler	0 (minimum – 10)
% RP	Rekreasyon Potansiyeli	100

Gülez Yönteminde hesaplamayı kolaylaştırmak amacıyla her değişkenin alt değişkenlerinin de tanımlandığı ve puanlarının belirlendiği "Orman içi Rekreasyon Potansiyeli Değerlendirme Formu" (ORPDF) düzenlenmiştir. Bu form, gözlem gibi basit bir yöntemle bile olsa potansiyellerin belirlenmesine olanak sağlamaktadır [8]. Formülde yer alan değişkenlerin alt değişkenleri ve değerleri Tablo 2’ de verilmiştir.

Tablo 2. Gülez Yöntemi formülü değişkenleri, alt değişkenleri ve değerleri [8]

Formüldeki Öğeler	Değeri Puanı	Ölçme Ölçütleri	Maximum Puan	Açıklama
Peyzaj Değeri (P)	Alanın İnyonlaşığı	10 ha.’dan büyük	4 puan	
		5 - 10 ha	3 - -	
		1 - 5 ha	2 - -	
		0,5 - 1 ha	1 - -	
	İkinci Önemli	Ağaçlık, çalı, çayır	7-8 puan	
		Yalnız ağaçlık ve çayır	6-7 - -	
		Çalı, çayır, seyrek ağaç	5-6 - -	
		Çayır, seyrek ağaçlık	4-5 - -	
	Deniz, Göl, Akarsular	Deniz kıyısı	7-8 puan	
		Göl kıyısı	6-7 - -	
Akarsu kıyısı		4-5 - -		
Deniz		1-4 - -		
Yüzyeysel Durum	Düz alan	5 puan		
	Hafif dalgalı	4 - -		
	Az meyilli, yar yarı düzük	3 - -		
	Az eğimli	2 - -		
Gözet Kalite	Panoramik görüşler	3-4 puan		
	Güzel görüş ve vivalar	2-3 - -		
	Alanın genel gözet estetik değeri	1-3 - -		
	Diğer Özellikler	Özellik doğal anıt, çağışın, mağara, tarihi ve köhnede değerler, yerün kayıpların, kayalar vb.	1-6 puan	
İklim Değeri (İ)	Sıcaklık	Yaz ayları (Haz, Tem, Ağu) ortalaması °C 16-17-18-19-20-21-22-23-24-25-24-33-32-31-30-29-28-27-26-25 P. 1, 2, 3, 4, 5, 6, 7, 8, 9, 10	10	
	Yağış	Yaz ayları (Haz, Tem, Ağu) toplamı mm -50-100-150-200-250-300-350-400 P. 8, 7, 6, 5, 4, 3, 2, 1	8	
	Güneşlenme	Yaz ayları ortalama güneşlenme saatleri saat : 0-2, 2-4, 4-6, 6-8, 8-9 Puan : 5 4 3 2 1	5	
Ulaşılabilirlik (U)	Rutubetlik	Yaz ayları ortalama rutubet oranı % m’den az 1 - 3 m’den az 1 - 3 puan	2	
	Belirli bir bölgenin Turistik Önemli	Akdeniz, Ege, Marmara kıyı bantı 5-4 puan Katadrom kıyı bantı 2-3 - - Önemli karayolu güzergahları, turizmde öncelikli yöreler 1-3 puan	4	
Olumsuz Etkiler (OSE)	Balanceda bulgulu En Az 100.000 Nüfuslu Kent Olması	20 km’ye kadar uzaklık 4-5 pu 50 - - 3-4 - - 100 - - 2-3 - - 200 - - 1-2 - -	5	
	Ulaşım Zorunlu Sorun (yolunluklu en az 5.000 m’den fazla kentsel)	4		
	Ulaşım (otaki ve otaki otaki dışı)	4		
Rekreatif Kolaylık (RK)	Ulaşım dışı diğer kolaylıklar	3		
	Piknik Tesisleri	4		
	Se Durumu	3		
	Güzellem Tesisleri	2		
	WC’ler	2		
	Otopark	2		
	Kor Alanları, Sığınak Alanları	2		
	Bakıcı ve Gözetimler	2		
	Diğer Kolaylıklar	3		
	Olumsuz Etkiler (OSE)	İlava Kirliliği	-3	
Güvenli Olmayan		-2		
Se Kirliliği		-1		
Bakımsızlık		-1		
Diğer Olumsuz Etkiler		-2		
Genel Toplam Puan ya da Ortalama Rekreasyon Potansiyeli (%)				

Formülün uygulanmasında ise iklim değeri dışındaki tüm veriler alanda değerlendirmeyi yapacak olan kişi tarafından gözlemlerle elde edilerek "Orman içi Rekreasyon Potansiyeli Değerlendirme Formu" na yazılır. İklim değeri ise, Meteoroloji Genel Müdürlüğünden elde edilerek forma eklenir ve toplam puan elde edilir. (Gülez, 1990) Toplam puana göre alanın rekreasyon değeri Tablo 3’te gösterilmiştir.

Tablo 3. Gülez Yöntemi değerlendirme sonuçları [8]

Potansiyeli	
Çok Düşük	%30'dan Aşağı
Düşük	%30 - % 45 Arası
Orta	%46 - % 60 Arası
Yüksek	%61 - % 75 Arası
Çok Yüksek	%75'den Yukarı

Bulgular ve Tartışma

Peyzaj Değeri: Çalışma alanında yerinde yapılan gözlemlerde; alanın neredeyse düz olarak tanımlanabilecek hafif dalgalı bir yüzey şekline sahip olduğu, yakınında akarsu, göl vb bulunmadığı, üzerinde seyrek zeytin ağaçları bulunduğu, çayır ve çalılıklar bulunduğu, güney doğu yönünde Spil Dağı / orman manzarasına sahip olduğu görülmüştür. Kuş türlerinin varlığı tespit edilmiş bununla birlikte Spil Dağında bulunan yabancı Yılkı Atlarının da zaman zaman bölgeye indikleri öğrenilmiştir. Buna göre alanın **Peyzaj Değeri 18** olarak hesaplanmıştır.

İklim Değeri: Meteoroloji Genel Müdürlüğünden alınan veriler ile bölgenin yaz ayları sıcaklık ortalamasının 27.5, ortalama yağış miktarının 22mm, bulutluluk oranının 1 ve ortalama rüzgar hızının 2.1 olduğu bilgisi edinilmiştir. Buna göre alanın **İklim Değeri 21** olarak hesaplanmıştır.

Ulaşılabilirlik: Manisa Büyükşehir Belediyesi Ulaşım Dairesi Başkanlığından alınan veriler doğrultusunda alana toplu ulaşım ile ulaşılabildiği, gün içinde 20 dakika aralıklarla otobüs bulunduğu öğrenilmiştir. Bununla birlikte şehir içinde bulunan çalışma alanına kentin batısında yer alan mahallelerden yürüyerek ulaşmak da mümkündür. Çalışma alanının İzmir yönünde ve İzmir-Manisa karayoluna yakın konumlu olması da önemini artırmaktadır. Buna göre alanın **Ulaşılabilirlik Değeri 16** olarak hesaplanmıştır.

Rekreatif Kolaylık: Çalışma alanında yerinde yapılan gözlemlerde rekreatif kolaylık olarak adlandırılacak bir donatının bulunmadığı tespit edilmiştir.

Olumsuz Etkenler: Çalışma alanında; organize sanayi bölgesine yakın konumlu olması nedeniyle hava kirliliği problemi bulunmaktadır. Bununda dışında olumsuz etkenlere rastlanmamıştır. Buna göre alanın **Olumsuz Etkenler Değeri -1** olarak hesaplanmıştır.

Mevcut durumda hiçbir rekreatif kolaylığa sahip olmayan alanın, yapılacak plan değişikliği ile "Rekreasyon Alanı" olarak fonksiyonlandırılmasından sonra yapılacak düzenleme ile otopark, wc, satış büfesi, piknik alanları, bekçi vb rekreatif kolaylıklar eklenmesiyle gelecekteki rekreatif değeri de artırılabilir. Güncel ve gelecekteki potansiyel rekreatif değerler aşağıdaki gibi hesaplanmıştır.

$$P + I + U + RK + OSE = \% RP$$

$$18 + 21 + 16 + 0 + -1 = \%54 \text{ Güncel değer (orta derecede rekreasyon potansiyeli)}$$

$$18 + 21 + 16 + 18 + -1 = \%72 \text{ Potansiyel değer (yüksek derecede rekreasyon potansiyeli)}$$

Yapılan hesaplamalara göre "orta derecede rekreasyon potansiyeli" ne sahip olan alan 1989 yılında yapılan imar planında "Turizm Tesisi" olarak planlanmıştır. 1989 yılı uydu görüntülerine bakıldığında örnek alan ve çevresinin benzer özelliklere sahip olduğu, hatta bölgede bir dere bulunduğu Şekil 4'de görülmektedir.



Şekil 4. Çalışma alanının 1989 uydu görüntüsündeki durumu (Google Earth uydu görüntülerinden elde edilmiştir.)

Örnek alan ve çevresi, yapılan plan çalışması sonrasında; otel, motel, tatil köyü, pansiyon, apart otel, lokanta, yüzme havuzu, kamping vb ve villa yapılabilir hale geldiğinden bölgede yapılaşma başlamış ve bugünkü halini almıştır. Rekreatif potansiyele sahip alanların bütünlüğü bozulmuş, doğal yatağında akan dere yer yer kapatılmış, ıslah edilmiş, bölgenin doğal peyzajı bozulmuştur (Şekil 5).



Şekil 5. Çalışma alanının güncel uydu görüntüsündeki durumu (Google Earth uydu görüntülerinden elde edilmiştir.)

Bu çalışma sonucunda; bölgede rekreatif potansiyele sahip bütüncül bir alan bulunmasına rağmen plan kararlarının uygulanması sonucu günümüzde büyük ölçüde yapılaşmış olduğu görülmüş, henüz yapılaşmamış olan örnek alanın güncel rekreatif potansiyel değerinin %54 olduğu, eklenebilecek rekreatif kolaylıklarla bu değer %72 ye yükseltilebileceği, imar planında "Turizm Tesis Alanı" olarak planlanmış olan çalışma alanının fonksiyonunun imar planı değişikliği ile "Rekreasyon Alanı" olarak değiştirilmesi ile Manisa kent merkezine 17.608 m² yeşil alan kazandırılmış olacağı ortaya konulmuştur.

Sonuç ve Öneriler

Manisa; güneyinde Spil Dağı, kuzeyinde Manisa Ovası, Batısında Sabuncubeli ile çevrili, kent çeperinde rekreasyon potansiyeli yüksek alanlara sahip olmasına rağmen, kent merkezinde yeterli açık ve yeşil alana sahip değildir. Yapıların hakim olduğu kentte, insanların günlük yaşam döngüsünün getirdiği baskıyı azaltmaya yardımcı açık ve yeşil alanlara daha fazla ihtiyaç duyulmaktadır. İmar planları yapılmış ancak henüz yapılaşması tamamlanmamış alanlar, bu ihtiyaçların çözümü için imar planlarının yeniden değerlendirilmesi sırasında önemli potansiyel alanlar olarak ortaya çıkmaktadır.

Çalışmada kent içinde örnek bir alan seçilerek rekreasyon potansiyeli değerlendirilmiş ve yapılacak uygulamalarla yüksek potansiyele sahip bir rekreasyon alanı olarak değerlendirilebileceği, bu durumda kişi başına düşen yeşil alan miktarının artırılmış olacağı ortaya konulmuştur. Çalışma genişletilerek, imar planı sınırları içinde bulunan ancak yapılaşması tamamlanmamış tüm alanların Gülez Yöntemi ile rekreasyon potansiyelleri belirlenmesi, belirlenen yüksek potansiyelli alanlardan en uygun olanlarının ise kamulaştırma vb maliyetler de göz önünde bulundurularak netleştirilmesi ile kişi başına düşen yeşil alan miktarının kent merkezlerinde kayda değer oranda artırılabilirliği öngörülmektedir.

Bununla birlikte henüz planlama çalışması yapılmamış ya da revizyon imar planı çalışması yapılacak olan yerleşimlerde, analiz aşamasında, uygulaması oldukça kolay olan bu yöntemle rekreasyon potansiyeli yüksek alanların belirlenmesi ve planlama çalışmaları sırasında bu alanların “Rekreasyon Alanı” olarak planlanmasının, doğaya saygılı, sürdürülebilir, kentlilerin sosyal yaşamlarına katkı sağlayan şehirlerin ortaya çıkmasında etkili olacağı düşünülmektedir.

Referanslar

- [1] Kuhrt, A., & Şendil, D. (2010) Eski çağda Yakınođu: Yaklaşık M.Ö. 3000-330. İstanbul: Türkiye İş Bankası Kültür Yayınları.
- [2] Işık, A. (2018). “İlk Şehirler ve Yazılı Medeniyete Geçiş”, Mavi Atlas Dergisi, 6(2)/2018: 46-74 .
- [3] Tonoç, M. (2017). “Kent Nedir?” Erişim Adresi: <http://sbpturkiye.com/kent-nedir.html>
- [4] Kongar, E. (2002) “Küresel Terör ve Türkiye: Küreselleşme Huntington, 11 Eylül”, Remzi Kitabevi 3.Basım
- [5] Yılmaz, M. (2015) “Türkiye’de Kırsal Nüfusun Değişimi Ve İllere Göre Dağılımı (1980-2012)”, Dođu Coğrafya Dergisi, Sayı 33:161-188.
- [6] Gülez, S. (2000) Dođa Koruma Ve Milli Parklar, Z.K.Ü. Bartın Orman Fakültesi, Ders Notları, Bartın.
- [7] Öztürk, S. (2005) “Kastamonu-Bartın Küre Dađları Milli Parkının Rekreasyonel Kaynak Deđerlerinin İrdelenmesi”, Süleyman Demirel Üniversitesi Orman Fakültesi Dergisi, Sayı:2.
- [8] Gülez, S. (1990) “Orman içi Rekreasyon Potansiyelinin Belirlenmesi İçin Bir Deđerlendirme Yöntemi”, İ.Ü. Orman Fakültesi Dergisi, Seri A, Cilt 40, Sayı 2: 132-147.
- [9] Eröz, S.S, Aslan, E. (2017) “İstranca (Yıldız) Ormanlarının Rekreasyon Potansiyelinin Gülez Metodu ile Deđerlendirilmesi”, Kesit Akademi Dergisi, Sayı 3: 83-107.
- [10] Çelik, A. Üzümcü, T. P, Çetin, İ. 2016, “Bursa İli Gölyazı Köyü’nün Açık Hava Rekreasyon Potansiyeli”, Uluslararası Sosyal ve Ekonomik Bilimler Dergisi, Sayı 6 (2): 32-40.
- [11] Surat, H. (2017) “Gülez Yöntemine Göre Deriner Baraj Gölü ve Yakın Çevresi Rekreasyonel Potansiyelinin Deđerlendirilmesi ve Alan Kullanım Önerilerinin Geliştirilmesi”, KSÜ Dođa Bilimleri Dergisi, Sayı 20(3): 247-257.
- [12] Yılmaz, H. Karaşah, B. ve Yüksel EE (2009) “Gülez Yöntemine Göre Kafkasör Kent Ormanının Rekreasyonel Potansiyelinin Deđerlendirilmesi”, Artvin Çoruh Üniv. Orman Fak. Dergisi 10 (1):53-61.
- [13] Mumford, L., Koca, G., Tosun, T. (2007) Tarih boyunca kent: Kökenleri, geçirdiđi dönüşümler ve geleceđi =The city in history: Its origins, its transformations, and its prospects. İstanbul: Ayrıntı.
- [14] Yılmaz, E. Çitçi, S. (2011) “Kentlerin Ortaya Çıkışı Ve Sosyo-Politik Açından Türkiye’de Kentleşme Dönemleri”, Elektronik Sosyal Bilimler Dergisi, Sayı 35 (1): 252-267.
- [15] Manisa Büyükşehir Belediyesi, İmar ve Şehircilik Dairesi Başkanlığı, Planlama Müdürlüğü 2019
- [16] Tekeli, I, İlkin, S. (1987) Dünyada ve Türkiye’de serbest üretim bölgelerinin dođuş ve dönüşümü. Ankara: Yurt Yayınevi.
- [17] Çevre ve Şehircilik Bakanlığı (2014) Mekansal Planlar Yapım Yönetmeliđi.
- [18] Özcan, K. (2016) “Kentlerin Kent Planlamada Sürdürülebilirlik Gündemi: Bir Kavramsallaştırma Denemesi”, Avrasya Terim Dergisi, Sayı 4 (2): 7-17.
- [19] Kahraman, T (2010) “İmar Uygulamalarında Gizli Yolsuzluk: Ayrıcalıklı Özelleştirmeler ve Kentsel Rant”, İş Ahlakı Dergisi, Sayı 6: 61-80.

Space Syntax Yöntemi ile Kentsel Açık Yeşil Alanların Erişilebilirliğinin Belirlenmesi; Bornova Büyük Park ve Âşık Veysel Rekreatyon Alanı Örneği

*Ahenk Karci Demirkol**, İzmir Kâtip Çelebi Üniv, Kentsel Dönüşüm Bölümü, Çiğli Ana Kampüs, İzmir, Türkiye

Pınar Orman, İzmir Kâtip Çelebi Üniv, Mimarlık Bölümü, Çiğli Ana Kampüs, İzmir, Türkiye
Gökçe Gönüllü Sütçüoğlu, İzmir Kâtip Çelebi Univ, Kentsel Dönüşüm Bölümü, Çiğli Ana Kampüs, İzmir, Türkiye

Ayşe Kalaycı Önaç, İzmir Katip Çelebi Üniv., Kentsel Dönüşüm Bölümü, Çiğli Ana Kampüs, İzmir, Türkiye
* İletişimden sorumlu yazar: ahnkkarci@gmail.com

Anahtar Kelimeler: Açık yeşil alanlar, Space Syntax, kullanıcı tercihleri
Disiplin: Kentsel Dönüşüm

Özet

Kentler insanlara ekonomik, sosyal ve kültürel imkânlar sağlamakta ancak insanların doğa ile bağ kuramadıkları yapay bir çevrede yaşamaya mahkum etmektedir. Kentsel açık yeşil alanlar, sundukları birçok ekosistem hizmeti yanı sıra kentlilerin doğa ile bağ kurabildikleri, rekreatif gereksinimlerini karşıladıkları alanlardır. Kente açık yeşil alan varlığının yanı sıra, kent sakinleri tarafından bu mekanların tercih edilip, kullanılır durumda olması büyük önem taşımaktadır. Bu konu ile ilgili yapılan çalışmalarda açık yeşil alanların niteliğini belirleyen başlıca kriterler; mekânların sunduğu aktivite çeşitliliği, alanların kullanım rahatlığı, sosyalleşme olanakları ve erişilebilirlikleri olarak belirtilmiştir.

Kentlerin içerisinde bulunan açık yeşil alanlar, kent ekosistemine katkılarının beraberinde, insanlar için rekreatif bir alan oluşturmaktadır. Space Syntax kentlerin analiz edilmesi için geliştirilmiştir. Mekânın, sosyal yapıyı ve hatta onu oluşturan farklı katmanları da etkileyen bir boyutu olduğundan hareketle, sosyal yapı ve mekan arasında karşılıklı bir ilişkinin varlığına inanan bir düşünce yapısı üzerine kurgulanmaktadır. Kenti okumaya yarayan bu Space Syntax sosyal yapı ve mekan dizilimi arasında bir ilişki olduğunu vurgulamaktadır.

Erişim açık yeşil alanların kullanılabilirliği açısından çok önemli bir faktördür. Yeşil alanların, çevredeki tüm akslarla bağlantılı olması büyük önem taşımaktadır. Farklı aktiviteleri bünyesinde barındıran ve yeterli büyüklükte olan açık yeşil alanlar yanlış konumlandırma nedeniyle meydana gelen erişim problemlerinden dolayı kullanıcılar tarafından tercih edilmeyebilir. Kentsel açık yeşil alanların erişilebilirlikleri yakın çevrelerinde bulunan diğer kullanımların mekânsal dizilimiyle doğrudan ilişkilidir. Münferit olarak bir alanın erişiminin belirlendiği çok sayıda çalışma bulunsun da; yeşil alanların çevrelerindeki mekan dizilimi ve kullanıcı çekme potansiyelleri arasındaki ilişkiyi irdeleyen yeterli sayıda çalışma bulunmamaktadır.

Mekanın insan faaliyetlerinin gerçekleştiği ortam, mekan diziminin ise mekandaki yapısal elemanların rastlantısal yerleşimi olarak düşünüldüğünde, sosyal yapı ve mekan karşılıklı bir etkileşim halindedir. Space Syntax kentlerin mekânsal olarak analiz edilmesi için geliştirilmiş bir yöntem olup; mekanın, sosyal yapıyı ve hatta onu oluşturan farklı katmanları da etkileyen bir boyutu olduğundan hareketle kurgulanmaktadır. Kenti okumaya yarayan Space Syntax yöntemi, sosyal yapı ve mekan dizilimi arasında bir ilişki olduğunu vurgulamaktadır. Dolayısıyla mekan dizilimi, kullanıcıların mekan tercihleri üzerinde de etkilidir. Buradan yola çıkarak; bu çalışmada kentsel açık yeşil alanların kullanım yoğunlukları ve bu alanların çevrelerindeki mekânsal dizilimi arasındaki ilişkinin tespit edilmesi amaçlanmıştır.

Çalışma alanı olarak seçilen İzmir Bornova İlçesi Büyük Park ve Âşık Veysel Rekreatyon alanlarının çevrelerinin mekânsal dizilimi Space Syntax yöntemine göre CBS yazılımından faydalanarak incelenmiş, söz konusu alanlarda belirli aralıklarda gerçekleştirilen gözlemler aracılığı ile alanların kullanım yoğunlukları tespit edilmiş ve alanların erişilebilirlikleri ile kullanım yoğunlukları kıyaslanmıştır. Alanlara hafta içi, hafta sonu ve günün farklı saatlerinde yapılan ziyaretler ve gözlem çalışmaları Bornova Büyük Parkın daha çok kullanıcı tarafından tercih edildiğini göstermiştir.

Space Syntax analizi sonucunda ise Bornova Büyük Park ve Âşık Veysel Rekreatyon Alanı çevreleri ile çevresi ile mekânsal bütünleşme durumları karşılaştırılmış, Âşık Veysel Rekreatyon Alanı'nın diğer örnek alanla kıyasla çevre kullanımları ile daha bütünleşik durumda olduğu saptanmıştır. Örnek olay

incelemelerine dayanarak, açık yeşil alanların mekansal entegrasyonu ile alanların tercihi arasında bir ilişki olmadığı bulunmuştur.

1. Giriş

Tüm dünyada kentsel alanlarda nüfus hızla artmakta, nüfus artışı ile birlikte kentleşme, insanların doğa ile bağlarının kopması, yaşam kalitesinin düşmesi gibi sorunlara neden olmaktadır [1]. Kentsel bölgelerdeki nüfus yoğunluğu ve yapılaşmış alanlar yüksek oranda enerji ve kaynak tüketimine neden olmaktadır. Bunun sonucunda ortaya çıkan çevre kirliliği, sera gazları küresel ısınmayı meydana getirmektedir [2]. Ekosistem, dünyadaki tüm organizmaların yaşadığı ve birbiriyle etkileşime girerek doğal dengenin sağlandığı alanlar olarak tanımlanabilir. Bu sistemin bileşenlerinin temel ihtiyaçları; toprak, hava ve sudur. Kentler ekosistemin bu temel ihtiyaçları karşılanamamaktadır. Yapılaşmış çevre içerisinde bulunan açık yeşil alanlar kentlerde ekosistem dengesinin korunmasına yardımcı olmaktadır [3]. Açık yeşil alanlar, Yeşil kuşaklar, parklar ve ağaçlar doğal filtre ve toz tutucu olarak kente mikroklimatik özellik kazandırır. Ayrıca ışık ve hava sağlar, gürültüyü absorbe ederler [4]. Açık yeşil alanlarda bulunan ağaçların çevre kirliliğini azaltılması ve ekosistem dengesinin sürdürülmesindeki rolü değerlendirilen bir çalışma sonucunda; kent ormanlarının ekosistem dengesini sağlaması ve şehirde yaşamakta olan insanların yaşam kalitesini uygun bitkilendirme ile az maliyetle üst yüzeye çektiği saptanmıştır [5].

Açık yeşil alanlar, rekreasyon amaçlı organize edilmiş dış mekânlar sağlarlar. İnsanların aktif ve pasif rekreatif faaliyetleri için bütün olanakları sunmaktadır. Açık yeşil alanlar kentte yaşamakta olan insanlarla, şehir arasında denge sağlarlar. Yapılaşmanın yoğun olduğu kentlerde açık alanın sağlamakta olduğu bir diğer olumlu etki ise, yapılaşmanın insan üstündeki baskısını hafifletmesidir [4]. Açık yeşil alanlar çevresinde yaşamakta olan insanların stres düzeyini düşürmede olumlu etki göstermektedir. Hollanda'da yapılan 4529 katılımcı ile gerçekleştirilen bir araştırmadan elde edilen sonuçlara göre; 3 km. yarıçapında daha fazla yeşil alan miktarına sahip alanlarda yaşamakta olan insanların stres ve genel sağlık şikâyetlerinin, bu yarıçapta düşük miktarda yeşil alan bulunan alanlarda yaşamakta olan katılımcılara göre daha az olduğu saptanmıştır [6]. Açık yeşil alanlar kentlerde farklı etnik grupta olan insanların bir araya geldikleri mekanlardır. Kentlilerin sosyal olarak kaynaşması, kültürel entegrasyonun oluşmasını sağlayarak toplumu sosyal açıdan geliştirilmesine katkıda bulunmaktadır [7].

Yürümek, kullanıcıların kentsel açık yeşil alanları keşfetmeleri için çok önemli bir araç olarak nitelendirilebilir. Yürüme yoluyla, kullanıcıların alanların farklı bölgelerine erişmeleri ve böylece tüm alanı deneyimleyerek tanımaları sağlanmaktadır. Alanın mekânsal dizilimi kullanıcıların alanı tanımasını ve memnuniyetini büyük ölçüde etkilemektedir. Ampirik bulgular, açık yeşil alanların sahip olduğu niteliklerin tanımlanması ve yürüme rotasının yakın bir ilişki içerisinde olduğunu göstermektedir [8]. Yerleşik çevre ve sosyal yaşam arasında bir etkileşim bulunmaktadır. Bu etkileşimin tutarlı bir şekilde ölçülmesini sağlayan, Space Syntax (mekan dizilimi) yöntemi Hillier ve Hanson'un çalışmaları sonucunda ortaya çıkmıştır. Space Syntax, kentsel yapılanmayı analiz etmek için bilgisayar tekniklerinin kullanımına dayanmaktadır [9]. Kentsel açık alanlarda sirkülasyon ve görüş alanlarının belirlenmesi ve potansiyellerin ortaya çıkarılması, karmaşık mimari yapılarda sirkülasyon planlama yapılması, tarihi mekanların oluşumunun okunması ve bu mekanlardaki yapı morfolojilerinin ve genotiplerinin ortaya çıkarılması, mekânsal performans ile arazi kullanımının etkileşiminin ortaya konulması, suç olgusunun ve riskli kentsel bölgelerin arasında ilişkinin irdelenmesi, mekânsal ağların kent mülkiyet ekonomisindeki etkisinin saptanması, mekana ilişkin mahremiyet, kontrol ya da sosyal yapılanmanın kavranması, kentsel planlama ve tasarımının çevresel etkilere katkısının vurgulanması Space Syntax yönteminin başlıca kullanım alanlarına örnek olarak gösterilebilmektedir [10]. İsrail'deki Bat Yam kenti örneğinde Space Syntax yöntemi kullanılarak yaya hareketi kentin şimdiki planı ve 2030 master planına göre modellenmiştir. Yapılan çalışmanın sonucunda 2030 yılında yaya hareketinin köklü bir şekilde değişmeyeceği ortaya konmuştur [11]. Amasya İli tarihi kent merkezinin açık mekanlarında yapılmış bir araştırmada ise; seçilmiş olan kentsel açık mekanlar, anket, gözlem ve Space Syntax yöntemleri kullanılarak kullanım yoğunluğu analiz edilmiştir. Anket ve gözlem çalışmalarının sonucu elde edilen veriler ile Space Syntax yöntemi ile elde edilen verilerin birbirleriyle örtüştüğü saptanmıştır [12].

Bu çalışmanın amacı; çalışma materyali olarak seçilmiş olan Bornova Âşık Veysel Rekreasyon Alanı ve Bornova Büyük Park örnek alanlarından faydalanarak; kullanım yoğunluğu ve mekânsal dizilim arasındaki ilişkiyi araştırmaktır.

2. Materyal ve Yöntem

2.1 Materyal

Bornova Büyük Park

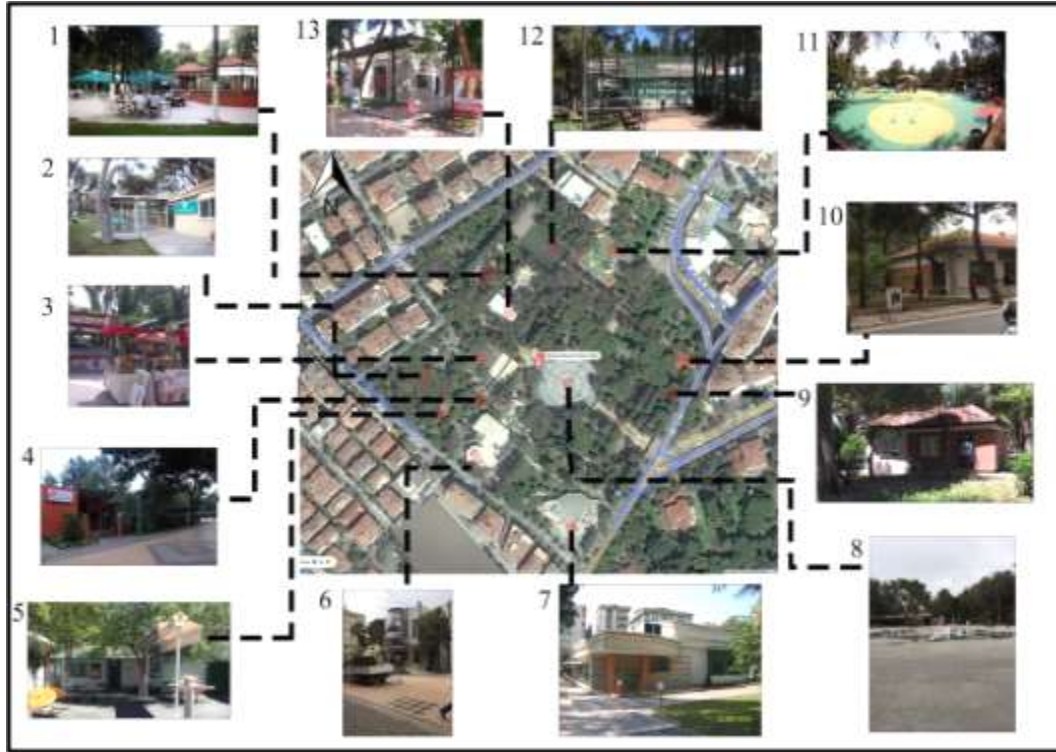
Büyük Park, Fevzi Çakmak Caddesi ve Süvari Caddesi'nin arasında konumsal açıdan Bornova Merkez'deki birçok yere yürüme mesafesinde, yaklaşık 37.842 m² büyüklüğündedir. Büyük Park'a yaya, toplu taşıma, özel araç ile ulaşım sağlanmaktadır. Alanda, çocuk etkinlik alanları, spor alanları, kafe/ restoran, konser/tiyatro alanı, Bornova kadın girişimci üretim ve işletme kooperatifi, kedi bakım evi, nikâh sarayı, gençlik merkezi içerisinde barındırmaktadır. Alanda çalı, ağaç, ağaççık ve yer örtücüler mevcuttur. Bornova Büyük Park'ta aydınlatma elemanları, oturma birimleri ve çöp kutuları bulunmaktadır (Tablo 1). Büyük Park'ın genel hatları ve alt mekanları Şekil 1'de gösterilmiştir.

Tablo 1. Bornova Büyük Park'ın olanakları

Erişim	Mevcut	Mevcut değil
Parka yaya ulaşımı	✓	
Parka toplu taşıma ulaşımı	✓	
Parka özel araç ulaşımı	✓	
Bilgilendirici tabelalar		✓
Evrensel tasarım		✓
Aktivite Alanları	Mevcut	Mevcut değil
Çocuk etkinlik alanları	✓	
Spor alanları	✓	
Bisiklet yolu		✓
Yürüyüş yolu		✓
Kafe/ Restoran varlığı	✓	
Konser/ tiyatro alanı	✓	
Diğer	Bornova kadın girişimci üretim ve işletme kooperatifi, kedi bakım evi, nikâh sarayı, gençlik merkezi	
Yeşil alan varlığı	Mevcut	Mevcut değil
Çalı		✓
Ağaç		✓
Ağaççık		✓
Yer örtücü		✓
Donatı elemanları	Mevcut	Mevcut değil
Aydınlatma	✓	
Oturma	✓	
Çöp kutusu	✓	
Tuvalet		✓

Âşık Veysel Rekreasyon Alanı

Bornova Kızılay Mahallesi'nde Bornova Pazar Yeri'nin yakınında yer alan Âşık Veysel Rekreasyon Alanı 245 dönüm arazi üzerine kurulmuştur [13]. Alana, yaya ulaşım, toplu taşıma ulaşım, özel araç ulaşım mümkündür. Âşık Veysel Rekreasyon Alanı'nda bilgilendirici tabelalar, çocuk etkinlik alanları, spor alanları, bisiklet yolu, yürüyüş yolu, kafe/ restoran, konser/tiyatro alanı ve buz sporları salonu mevcuttur. Alanda çalı, ağaç, ağaççık ve yer örtücü bitkiler mevcuttur. Âşık Veysel Rekreasyon Alanı'nda aydınlatma elemanları, oturma birimleri çöp kutuları ve halka açık tuvaletler bulunmaktadır (Tablo 2). Alanın genel hatları ve alt mekanları Şekil 1'de gösterilmiştir.



1-Kızlar Kahvesi, 2-Down kafe, 3-Portakal kafe, 4-Bornova Belediyesi Gençlik Merkezi, 5-S.S. Bornova Kadın Girişimci Üretim ve İşletme Kooperatifi, 6- Bornova Belediyesi Uğur Mumcu Sanat Merkezi, 7- Bornova Belediyesi Nikâh Sarayı, 8- Havuz, 9- Bornova Belediyesi kedi bakım evi, 10- Çınar evi, 11- Çocuk oyun alanı, 12- Halı saha, 13- Bornova Ayfer Feray Açık Hava Tiyatrosu.
Şekil 1. Büyük Park'ın genel hatları ve alt mekanları

Tablo 2. Âşık Veysel Rekreasyon Alanı'nın olanakları

Erişim	Mevcut	Mevcut değil
Parka yaya ulaşımı	✓	
Parka toplu taşıma ulaşımı	✓	
Parka özel araç ulaşımı	✓	
Bilgilendirici tabelalar	✓	
Evrensel tasarım		✓
Aktivite Alanları	Mevcut	Mevcut değil
Çocuk etkinlik alanları	✓	
Spor alanları	✓	
Bisiklet yolu	✓	
Yürüyüş yolu	✓	
Kafe/ Restoran varlığı	✓	
Konser/ tiyatro alanı	✓	
Diğer	Buz sporları alanı	
Yeşil alan varlığı	Mevcut	Mevcut değil
Çalı	✓	
Ağaç	✓	
Ağaççık	✓	
Yer örtücü	✓	

Donatı elemanları	Mevcut	Mevcut değil
Aydınlatma	✓	
Oturma	✓	
Çöp kutusu	✓	
Tuvalet	✓	



1-Amfi tiyatro, 2- Kafe, 3- göl, 4- Buz sporları salonu, 5- Spor alanları (basketbol ve voleybol sahaları, tenis kortları, mini futbol sahaları), 6- Personel barınma alanı, 7- Havuz, 8- Otopark, 9- Çocuk oyun alanı, 10- Aletli spor alanı.

Şekil 2. Âşık Veysel Rekreasyon Alanı'nın genel hatları ve alt mekanları

2.2 Yöntem

Çalışma başlıca 3 aşamadan oluşmaktadır (Şekil 3).

2.2.1. Literatür çalışması ve çalışmanın amaç, kapsamının belirlenmesi

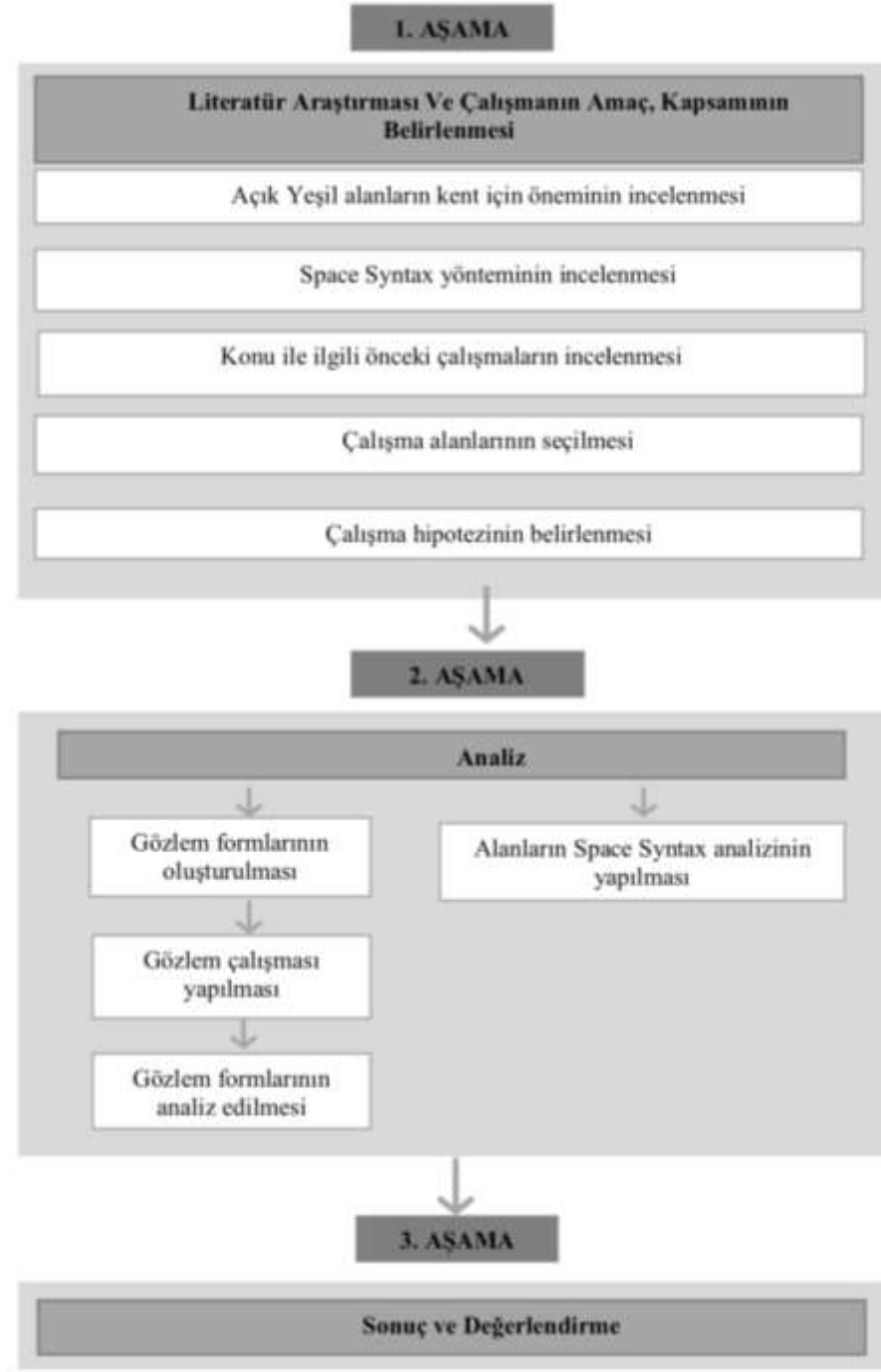
1. Aşamada kent ve kentliler için açık yeşil alanların önemi; Space Syntax yöntemi ve konu ile ilgili yapılmış çalışmalar hakkında literatür taraması yapılmıştır. Çalışma için örnek alanlar seçilmiştir. Son olarak çalışma hipotezi oluşturulmuştur.

2.2.2. Analiz

Bu aşamada gözlem çalışması ve Space Syntax yöntemi kullanılmıştır.

Gözlem

Seçilmiş olan araştırma alanlarına hafta içi ve hafta sonu olmak üzere, 10.00, 13.00, 18.00 ve 22.00 saatlerin kullanım yoğunluğunu incelemek amacıyla ziyaret edilmiştir. Gözlemler sonucu elde edilen veriler işlenmiştir.



Şekil 3. Yöntem akış şeması

Space Syntax

Bu yöntemde mekanlar arası ilişkiler düğüm ile ifade edilir. Noktalar arasında ilişkilerin açıklanması için derinlik (mean depth), bağlantısallık (connectivity), bütünleşme (integration), eş görüş (isovist) gibi kavramlar kullanılmaktadır [14].

Mekansal yapılanma, space syntax yöntemine göre, her bir biriminin erişebilirliği bütünleşme ve bağlantısallık değerleri ile hesaplanmaktadır. Bu değerler mekanın içerisindeki birimlerin komşuları arasındaki ilişkisi ve bağlantı değerini saptamak için kullanılır. Mekansal erişebilirlik ve bağlantı değerleri sayesinde mekanın kullanımını saptamaktadır [15].

Bütünleşme değeri Space Syntax yönteminde kırmızıdan mora doğru renklerle ifade edilmektedir. Kırmızı akşlar, bütünleşme değeri en yüksek; başka bir deyişle doğrudan ve kolay ulaşımı olan,

kullanımı en yüksek alanları ifade etmektedir. Mor akslar ise ayrılmış (segarated) yani kullanımı dolaylı ve zor olan alanları belirtmek için kullanılır [8].

Bağlantısallık mekanın içerisindeki program elemanlarına doğrudan bağlantı noktası sayısıdır [15]. Bağlantısallık değeri, Space Syntax yönteminde en yüksek kırmızı renkli akslar ile gösterilmektedir. Mavi akslar ise en düşük bağlantısallık değerini gösteren aksları belirtmektedir.

Çalışma alanlarına ait Google Earth görüntülerinden faydalanarak, alanların planları Autocad programına aktarılmıştır. Aktarılan planlar Space Syntax yazılımı olan DephtmapX-05 programından kullanılarak eksenel haritaları çıkarılmıştır. Çıkarılan haritaların bütünleşme ve bağlantısallık değerleri karşılaştırılmıştır

2.3 Sonuç ve Değerlendirme

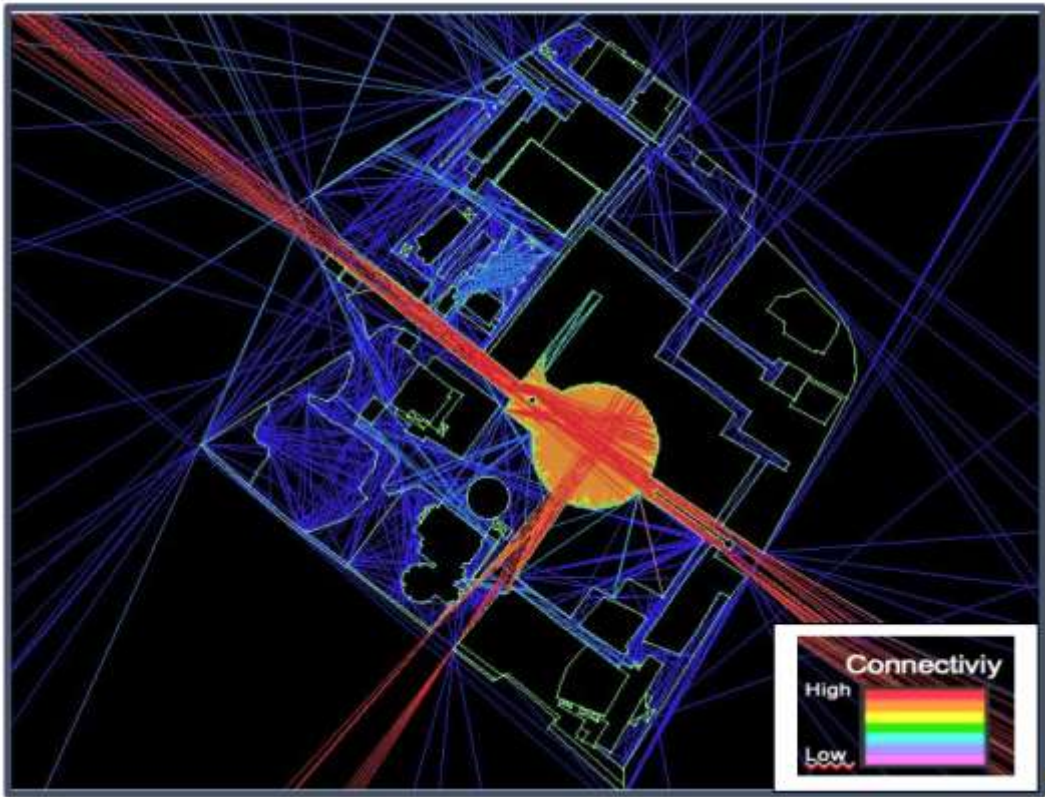
Gözlem formlarından elde edilen kullanıcı yoğunluğu ve mekanların eksenel haritaları arasında ki ilişki karşılaştırılmıştır. Açık alanların kullanım yoğunluğunda mekan diziliminin etkisi irdelenerek değerlendirilmiştir.

3. Bulgular

Büyük Park ve Âşık Veysel Rekreasyon Alan'ına ait Space Syntax yöntemine göre bağlantısallık ve bütünleşme analizleri ve yapılmış olan gözlem çalışmaların sonuçları aşağıda verilmiştir.

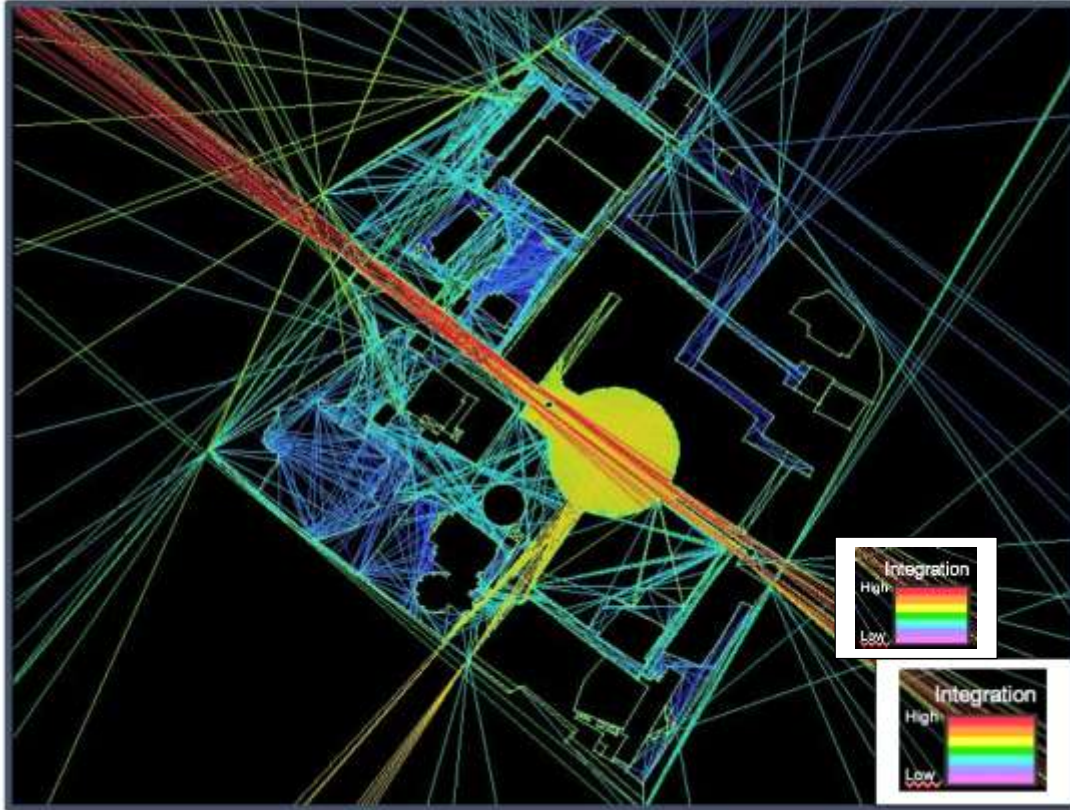
3.1 Büyük Park'a ait bulgular

Büyük Parkın ana akslarında, kuru havuzun olduğu meydana bağlantısallık değeri yüksek olarak saptanmıştır. Alanın yan akslarının bağlantısallık değeri düşük olarak görülmektedir (Şekil 4).



Şekil 4. Büyük Park'ın Bağlantısallık analizi

Büyük Park'ın bütünleşme analizine göre, ana aksın en çok bütünleşik, diğer aksların ise kısmen bütünleşik olduğu saptanmıştır (Şekil 5).



Şekil 5. Büyük Park'ın Bütünleşme analizi

Tablo 3. Büyük Park kullanım yoğunluğu

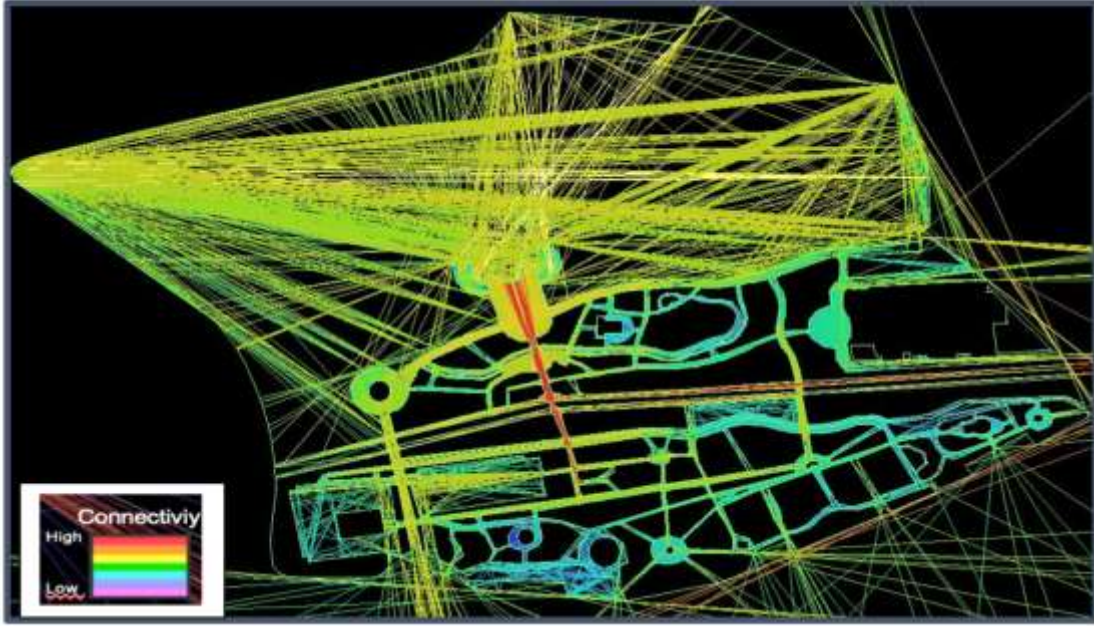
Hafta içi gözlem saatleri	Az yoğun	Orta Yoğun	Çok yoğun
10.00	✓		
13.00		✓	
18.00			✓
22.00	✓		
Hafta sonu gözlem saatleri	Az yoğun	Orta Yoğun	Çok yoğun
10.00		✓	
13.00		✓	
18.00			✓
22.00	✓		

Yapılmış olan gözlem çalışmalarına göre, çalışma alanı hafta içi 10.00 ve 22.00 saatlerinde az yoğun, 13.00 saatinde orta yoğun ve saat 18.00 da çok yoğun olarak saptanmıştır. Hafta sonu yapılmış olan gözlem çalışmasında ise alanın 10.00 ve 13.00 saatlerinde orta yoğunlukta olduğu, saat 18.00'da çok yoğun olduğu ve saat 22.00'da az yoğun olduğu sonucuna ulaşılmıştır (Tablo 3).

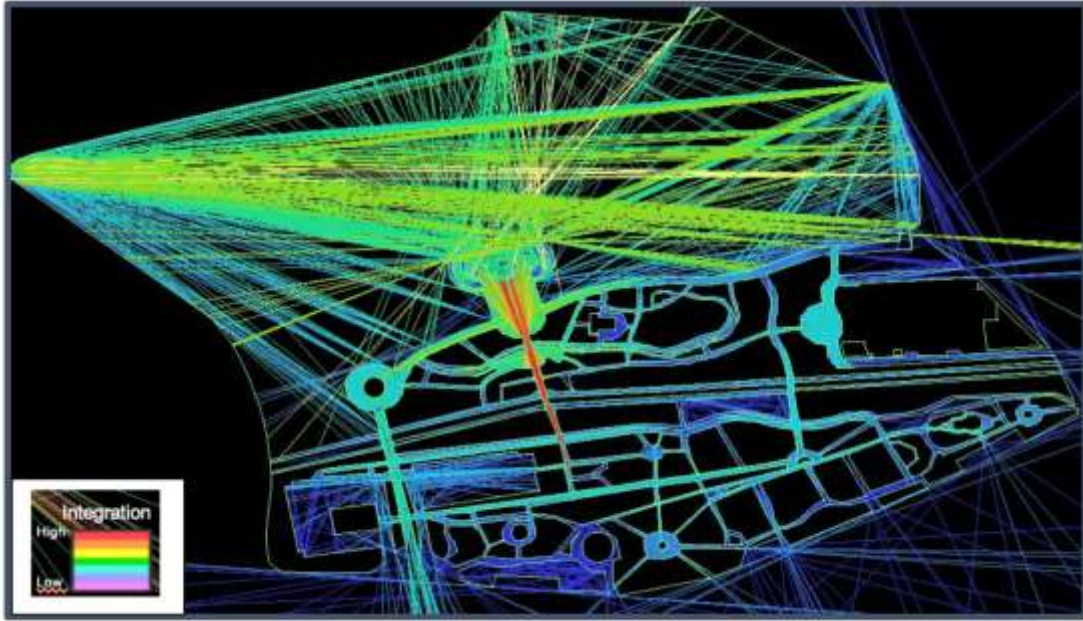
3.2 Âşık Veysel Rekreasyon Alanı'na ait bulgular

Alanın yürüme ve bisiklet yollarının etrafında ve amfi tiyatronun aksında bağlantısallık değeri yüksek olarak saptanmıştır. Ana girişin yanında konumlanmış olan meydan, havuz, spor alanların yakınındaki akslar ve gölün çevresindeki akslarda en düşük olarak hesaplanmıştır (Şekil 6).

Çalışma alanının amfi tiyatronun bulunduğu aks üzerinde bütünleşme değeri en yüksek bulunmuştur. Âşık Veysel Rekreasyon Alanı'nın ana girişi, otopark alanları, havuz, spor alanlarının bulunduğu akslarda ise bütünleşme değerinin en düşük saptandığı akslardır (Şekil 7).



Şekil 6. Aşık Veysel Rekreasyon Alanı'nın bağlantısallık analizi



Şekil 7. Aşık Veysel Rekreasyon Alanı'nın bütünleşme analizi

Tablo 4. Aşık Veysel Rekreasyon Alanı'nın kullanım yoğunluğu

Hafta içi gözlem saatleri	Az yoğun	Orta Yoğun	Çok yoğun
10.00	✓		
13.00		✓	
18.00			✓
22.00	✓		
Hafta sonu gözlem saatleri	Az yoğun	Orta Yoğun	Çok yoğun
10.00	✓		
13.00		✓	
18.00			✓
22.00	✓		

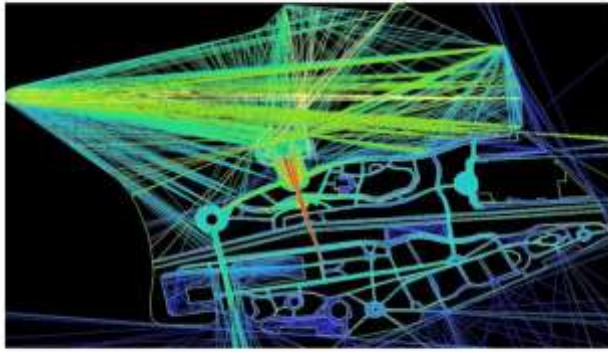
Alanın kullanım yoğunlukları Tablo 4’te belirtilmiştir. Hafta içi yapılan gözlemlere göre; 10.00 ve 18.00 saatleri arasında az yoğun, 13.00 saatinde orta yoğun ve 18.00 saatinde alanda çok yoğun kullanım olduğu saptanmıştır. Alanda yapılmış olan hafta sonu gözlemleri ise; saat 10.00 ve 22.00 az, 13.00 orta ve 18.00’da çok yoğun kullanıcı tarafında ziyaret edildiği belirlenmiştir.

4. Sonuç ve Değerlendirme

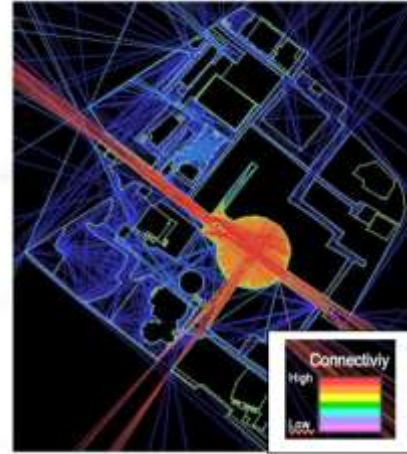
Kentsel alanlarda bulunan açık yeşil alanlar, hem kentlilere hem de kent ekosistemine olumlu katkılar sağladıkları için kentler için büyük önem taşımakta olan alanlardır. Açık yeşil alanların kullanıcılar tarafından tercih edilmesini sağlayan başlıca faktörler mekanların, aktivite ve olanakları, ulaşılabilirlik ve mekan erişimi, konforu ve imajı, sosyal olanaklarıdır [16]. Bu çalışmada çalışma materyali olarak seçilmiş olan Büyük Park ve Âşık Veysel Rekreasyon Alanı’nın Space Syntax yöntemi kullanılarak mekânsal erişim haritaları çıkarılmış ve kullanıcı yoğunluğu ile arasındaki ilişki irdelenmiştir.

Çalışma sonucunda Space Syntax analizlerine göre çalışma alanlarının mekânsal erişimleri karşılaştırılmıştır.

Bağlantısallık analizinin sonuçlarına göre Âşık Veysel Rekreasyon Alanı’nın mekânsal bağlantısallığı daha yüksek olarak saptanmıştır (Şekil 8).



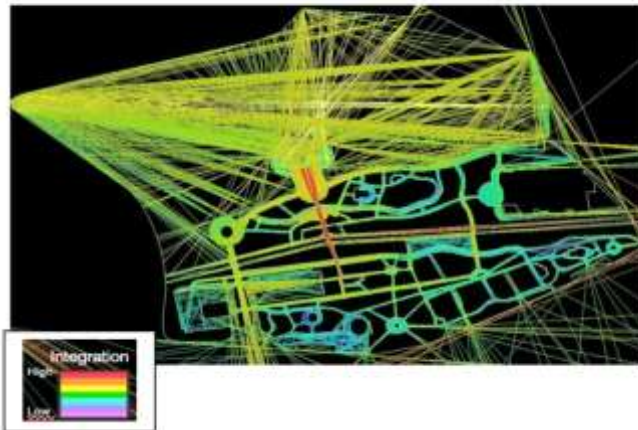
(a) Âşık Veysel Rekreasyon Alanı



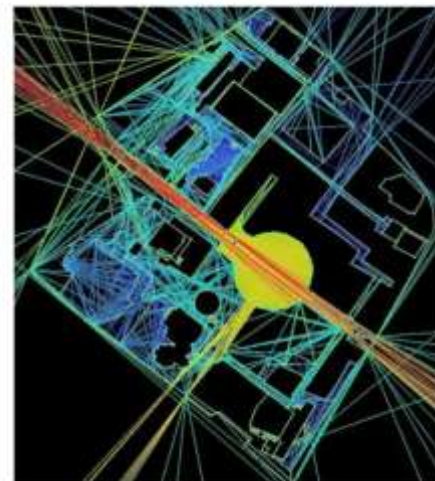
(b) Büyük Park

Şekil 8. Âşık Veysel Rekreasyon Alanı ve Bornova Büyük Park’ın bağlantısallık analizi

Alanların bütünleşme analizine göre sonuçları kıyaslandığında, Âşık Veysel Rekreasyon alanının daha bütünleşik mekânsal dizilime sahip olduğu belirlenmiştir (Şekil 9).



(a) Âşık Veysel Rekreasyon Alanı



(b) Bornova Büyük Park

Şekil 9. Âşık Veysel Rekreasyon Alanı ve Bornova Büyük Park’ın bütünleşme analizi

Tablo 5. Âşık Veysel Rekreasyon Alanı ve Büyük Park kullanım yoğunluğu

Hafta içi gözlem saatleri	Çalışma alanı	Az yoğun	Orta Yoğun	Çok yoğun
10.00	Âşık Veysel Rekreasyon A.	✓		
	Bornova Büyük Park	✓		
13.00	Âşık Veysel Rekreasyon A.		✓	
	Bornova Büyük Park		✓	
18.00	Âşık Veysel Rekreasyon A.			✓
	Bornova Büyük Park			✓
22.00	Âşık Veysel Rekreasyon A.	✓		
	Bornova Büyük Park	✓		
Hafta sonu gözlem saatleri	Çalışma alanı	Az yoğun	Orta Yoğun	Çok yoğun
10.00	Âşık Veysel Rekreasyon A.	✓		
	Bornova Büyük Park		✓	
13.00	Âşık Veysel Rekreasyon A.		✓	
	Bornova Büyük Park		✓	
18.00	Âşık Veysel Rekreasyon A.			✓
	Bornova Büyük Park			✓
22.00	Âşık Veysel Rekreasyon A.	✓		
	Bornova Büyük Park	✓		

Çalışma alanına yapılan gözlemler sonucu Tablo 5’te belirtildiği gibi Bornova Büyük Park’ın Âşık Veysel Rekreasyon Alanı’ndan daha çok kullanıcı yoğunluğuna sahip olduğu saptanmıştır.

Yapılan analizler ve çalışmaları neticesinde seçilmiş olan çalışma alanlarının kullanım yoğunluğu ve mekânsal dizilimleri arasında anlamlı bir ilişki görülmemiştir.

Âşık Veysel Rekreasyon Alanı ve Bornova Büyük Park, açık yeşil alanların kullanımını etkileyen faktörlere göre kıyaslandığında; yer seçimi, tesis çeşitliliği ve alan büyüklükleri dışında benzerlik göstermektedirler.

Âşık Veysel Rekreasyon alanı daha büyük ve Büyük Park’tan daha fazla imkânlarla sahip olmasına rağmen, Büyük Park, Âşık Veysel Rekreasyon Alanı’ndan daha fazla kullanım yoğunluğuna sahiptir. Bunun nedeni, Büyük Park’ın lokasyonunun Bornova şehir merkezi, okullar, işyerleri ve Bornova pazar yeri ile iç içe olması olarak açıklanabilir.

Referanslar

- [1] Çetin M, Kalaycı Önaç A, Şevik H, Sen Büsra (2019) Temporal and regional change of some air pollution parameters in Bursa. *Air Quality, Atmosphere & Health*. 12(3): 311-316.
- [2] Ellis EC, Ramankutty N (2008) Putting people in the map: anthropogenic biomes of the world. *Frontiers in Ecology and the Environment* 6(8): 439-447.
- [3] Forman RTT (2014) *Urban Ecology: Science of Cities*. Cambridge University Press.
- [4] Sarıkaya M (2007) Göksu Parkı’nın (Eryaman-Ankara) mevcut kullanımı ve kullanıcı beklentilerinin irdelenmesi, Yüksek Lisans Tezi, Ankara Üniversitesi, FBE, Peyzaj Mimarlığı Anabilim Dalı, Ankara.
- [5] Escobedo FJ, Kroeger T, Wagner JE (2011) Urban forests and pollution mitigation: Analyzing ecosystem services and disservices. *Environmental pollution* 159(8-9): 2078-2087.
- [6] van den Berg AE, Maas J, Verheij RA, Groenewegen PP (2010) Green space as a buffer between stressful life events and health. *Social Science & Medicine* 70(8), 1203-1210.
- [7] Peters K (2010) Being together in urban parks: Connecting public space, leisure, and diversity. *Leisure Sciences* 32(5): 418-433.
- [8] Zhai Y, Baran P (2013) Application of space syntax theory in study of urban parks and walking. *Proc. Ninth International Space Syntax Symposium* (pp. 1-13). Sejong University Seoul.

3rd International Students Science Congress
3-4 May 2019, İzmir - Turkey

- [9] Ratti C (2004) Space syntax: some inconsistencies. *Environment and Planning B: Planning and Design* 31(4): 487-499.
- [10] Yeşildal Ö (2019) Nöroloji ve mekansal biliş arasındaki ilişki bağlamında space syntax eleştirisi, Yüksek Lisans Tezi, Mimar Sinan Üniversitesi, FBE, Mimarlık Anabilim Dalı, İstanbul.
- [11] Lerman Y, Rofè Y, Omer I (2014) Using space syntax to model pedestrian movement in urban transportation planning. *Geographical Analysis*, 46(4), 392-410.
- [12] Seçkin YÇ, Dülger Türkoğlu H (2010) Amasya tarihi kent merkezi açık mekânlarının kullanım analizi. *İTÜ DERGİSİ/a*, 5(1).
- [13] <https://www.izmir.bel.tr/tr/Projeler/asik-veysel-rekreasyon-alani/1451/4>
- [14] Menderes (2014) Cumhuriyet döneminde yerel yönetim binalarının kamusal erişilebilirlik açısından mekan dizimi (space syntax) yöntemiyle irdelenmesi, Yüksek Lisans Tezi, İstanbul Teknik Üniversitesi, FBE, Mimarlık Anabilim Dalı, İstanbul.
- [15] Göksüzler (2013) Çocuğun algısında okul öncesi eğitim merkezlerinin mekansal dizim (space syntax) yöntemiyle irdelenmesi, Yüksek Lisans Tezi, İstanbul Teknik Üniversitesi, FBE, Mimarlık Anabilim Dalı, İstanbul.
- [16] Doğa Duygu, (2016) Kamusal açık mekân kullanıcılarının alan kullanımlarını etkileyen faktörlerin parklar bağlamında incelenmesi: Lüleburgaz gençlik parkı örneği, Yüksek Lisans Tezi, İstanbul Teknik Üniversitesi, FBE, Kentsel Tasarım Anabilim Dalı, İstanbul.

Civil Engineering / İnşaat Mühendisliği

Betonarme Bina Kolonları için Sünme ve Büzülme Parametrelerinin İncelenmesi

Amanullah Zamani, Mutlu Seçer*

*İzmir Kâtip Çelebi Üniv., İnşaat Mühendisliği Bölümü, Çiğli Ana Kampüs, İzmir, Türkiye
amanullahzamani28@gmail.com*

Anahtar Kelimeler: betonarme, bina, sünme, büzülme, zamana bağlı davranış

Disiplin: İnşaat Mühendisliği

Özet

Her geçen gün biraz daha gelişen teknoloji, hayatın diğer alanlarında olduğu gibi yapı endüstrisinde de etkilerini göstermektedir. En temel yapı malzemelerinden biri olan beton da bu gelişmelerden etkilenmektedir. Gelişen beton teknolojisiyle birlikte artan beton dayanımı betonarme elemanlarda daha küçük kesitlerle tasarım yapılmasına olanak sağlamıştır. Betonarme elemanların boyutlandırılmasında daha küçük kesitlerin kullanılmasıyla birlikte azalan kesit rijitliği nedeniyle yer değiştirme hesapları daha titiz bir şekilde yapılması gerekliliği ortaya çıkmıştır. Beton, birden fazla bileşenin bir araya gelmesinden oluşan bir yapı malzemesi olduğundan gösterdiği farklı davranışlar üzerinde birçok farklı çalışma yapılmıştır. Zamana bağlı etkilerden olan sünme ve büzülme davranışı da bunlar arasındadır. Betonarme elemanlarda şekil ve yer değiştirme parametrelerinin daha önemli hale gelmesiyle birlikte bu iki konu üzerinde yapılan çalışmalar daha da yoğunlaşmıştır. Zamana bağlı davranışların ortaya çıkarabileceği istenmeyen etkiler önemli seviyelere ulaşırsa yüksek katlı betonarme yapılarda için çeşitli riskli durumlar gelişebilir.

Bu çalışmada, betondaki sünme ve büzülme davranışının zaman bağlı değişimi ACI 209 ve CEB – FIB yöntemleri kullanılarak incelenmiştir. Betonarme kolon ve kiriş elemanlarda farklı yöntemler kullanılarak zamana bağlı analiz için gerekli parametreler elde edilmiştir. Çalışmada, sünme ve büzülme davranışını belirlemede kullanılan yaklaşımlar açıklanmış ve bu yöntemleri kolon kesiti dikkate alınarak sünme ve büzülme parametreleri hesap edilmiştir

Abstract

Technology which is developing each day not only affects the different areas of our lives but also shows its effects on the construction industry. Concrete, one of the basic construction materials, is being affected by this development. As a result of the advances in concrete technology, higher concrete strength values have been reached and this yielded to a decrease in the dimensions of cross sections used in the design of reinforced concrete members. With the use of smaller sections in the dimensioning of reinforced concrete elements, due to the reduced section stiffness, displacement calculations have to be made more rigorously. Since concrete is a building material consisting of a combination of multiple components, many different studies have been conducted on different behaviors. Creep and shrinkage behavior, which is one of the time-dependent effects, is among them. As the shape and displacement parameters become more important in reinforced concrete elements, the studies on these two subjects are intensified. If the undesirable effects of time-dependent behavior reach significant levels, various risky situations may develop for high-rise reinforced concrete structures.

In this study, time-dependent change of creep and shrinkage behavior in concrete was investigated by using ACI 209 and CEB - FIB methods. The parameters required for time-dependent analysis were obtained by using different methods in reinforced concrete columns and beam elements. In this study, approaches used to determine creep and shrinkage behavior are explained and creep and shrinkage parameters are calculated by taking these methods into consideration of the column section.

Giriş

Betonarme binaların sayısı gün geçtikçe artmaktadır. Özellikle gelişmekte olan ülkelerin büyük şehirlerinde, çoğunlukla betonarme olmak üzere çok sayıda yüksek bina inşa edilmektedir. Bu tür binalar için kullanım amaçlarına göre çeşitli yapı sistemleri kullanılmakta olup çerçeve sistemler oldukça yaygın kullanım alanı bulmaktadır.

Çok katlı bina çerçevelerine zati ve hareketli yükler bina ekonomik ömrü boyunca uzun süreli olarak etki edebilirler. Bu yüklerin yapılara aynı anda etkideği varsayılarak geleneksel yapı hesapları

yapılmaktadır. Ancak, özellikle çok katlı betonarme inşaatlarda inşaatın adım adım gelişiminin tasarım esnasında ihmal edilmesi gerçek davranışın modellenememesine sebep olur [1, 2]. Özellikle zati yüklerin inşaat sırasına göre binaya sıralı bir şekilde uygulanması analiz sonuçlarının doğruluğu üzerinde büyük bir etkiye sahiptir. Yüksek betonarme binalarda, betonun sünme ve büzülmesi gibi zamana bağlı etkilerinin yanı sıra inşaat sırasına bağlı meydana gelen elastik deformasyonlar nedeniyle eksenel deformasyonlar meydana gelebilir. Dikey elemanlarda meydana gelen diferansiyel eksenel kısalmalar ihmal edildiğinde aşırı yer değiştirmelere ve kabul edilemez çatlaklara yol açabilir.

Yapı inşaat adımlarının binalarda oluşturduğu zamana bağlı etkileri incelemek amacıyla, Kwak ve Kim [3], ACI 209 yöntemini kullanarak yapı inşaat adımlarını dikkate alan analitik ve deneysel çalışmalarla 10 katlı bir betonarme binada kısa ve uzun süreli yüklemeler altındaki davranış üzerinde çalışmışlardır. Kwak ve Kim [4], inşaat adımlarının betonarme çerçevelerin iç kuvvetlerini nasıl etkilediğine dair ayrıntılı bir çalışma sunmuştur. Zamana bağlı etkiler ve yapı inşaat adımları göz önüne alındığında daha fazla eğilme momentinin ve diferansiyel kolon kısalmalarının elde edildiği belirtilmektedir. Pratik bir yaklaşım geliştirmek amacıyla Kim ve Shin [5], katların gruplandırıldığı ve kolonların yığılı şekilde dikkate alınan imalat sıraları ile değerlendirildiği bir yöntem önermiştir. Her ne kadar bu yaklaşım hesaplama süresinde azalma sağladığı ifade edilse de, yığılmış katlar ile ilgili bazı sınırlar gerektiği belirtilmiştir. Pan ve diğerleri [6], esnek döşemeli 30 kattan daha düşük binalar için basit bir artımlı süperpozisyon yöntemi önermişlerdir. Ayrıca, Kim ve Abdelrazaq [7], çok katlı binalarda yüksek performanslı beton kullanımının döşeme sistemi davranışına uzun vadeli etkilerini inceleyen bir çalışma hazırlamıştır. Kompozit yapısal sistemlerdeki zamana bağlı davranışı izlemek için, Samarakody ve diğerleri [8], 60 katlı bir bina kullanarak kompozit beton dolgulu tüp kolonlu yüksek binalarda diferansiyel eksenel deformasyonu hesaplarda dikkate alabilmek için yöntem sunmuşlardır.

Bu çalışmada, zamana bağlı etkiler araştırılmış ve çok katlı betonarme bir bina kolonu dikkate alınarak sünme ve büzülme katsayıları araştırılmıştır. Sünme ve büzülme davranışları ile zamana bağlı etkilerin incelenmesi amacıyla, CEB – FIB [9] ve ACI 209 [10] yaklaşımları dikkate alınmıştır.

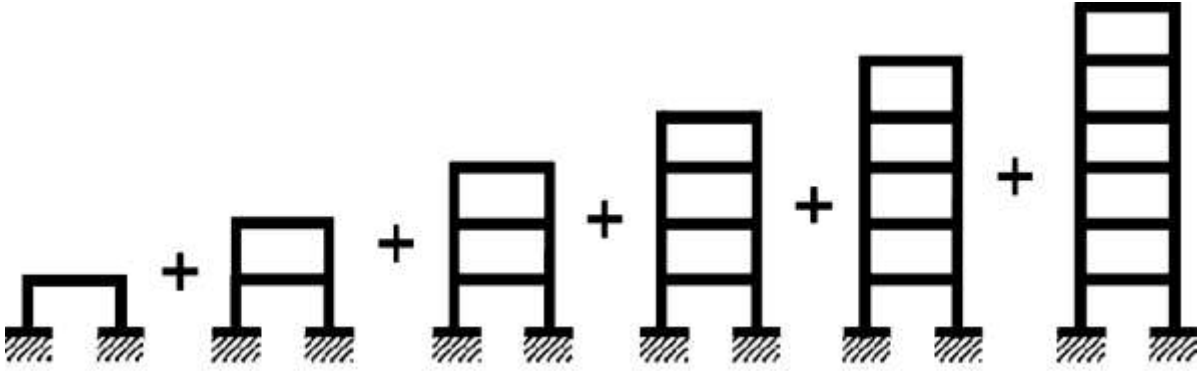
Yapım Sırasının ve Zaman Bağlı Etkilerin Yapısal Modellemesi ve Yapı Davranışına olan Etkisi

Betonarme binalar genellikle, inşaat tamamlandığında binaların tam yüke maruz kaldığı varsayımına dayalı olarak geleneksel analiz yöntemiyle tek bir adımda incelenir. Çerçeve tipi binalar, uygulamada Şekil 1'de gösterildiği gibi kat kat inşa edildiğinden, yapısal elemanların zati yükleri, ayrı aşamalarda sisteme uygulanır. Yüklerin bir adımda uygulandığı geleneksel yaklaşım ile inşaat adımlarının dikkate alındığı yaklaşım arasında bina davranışında büyük fark vardır. Bu nedenle, binanın inşaatı sırasındaki gerçek durumu hesaplara yansıtma için, inşaat sırası analizi uygulanır. Bilgisayar teknolojisindeki gelişmeler ile birlikte yapım aşamaları ve katların inşaa süreleri pratik olarak yapım sırası analizi kullanılarak yapı modellerine uygulanabilir. Bu analizlerde, her katın inşaat süresi dikkate alınır ve sonuç olarak her katın yükü ayrı ayrı uygulanır. Böylece binanın tamamlanmasına kadar olan asıl durum doğru bir şekilde modellenebilir.

Betonarme yapılarda inşaat sırasının modellenmesi, kolon kısalmalarını tam olarak belirleme imkânı verir. Bir kattaki kolon kısalmaları, kaplamaları, ara bölmeleri ve diğer yapısal olmayan bileşenlerini etkileyebilir. Bu elemanlar genellikle ilave düşey yükleri taşımak için tasarlanmadığından, herhangi bir kısalmaya maruz bırakılmamalıdır. Aksine, bölme elemanları nemden uzayabilir ve kaplamalar güneş ışığından etkilenebilir. Bu nedenle, yapısal olmayan elemanlarda oluşacak deformasyonlar, herhangi bir ilave problem yaratmaması için kontrol edilmelidir.

Ayrıca, sünme ve büzülme gibi zamana bağlı tesirlerin yapısal davranış üzerine dikkate değer etkileri vardır.

Binaların düşey elemanlarında elastik deformasyonlar ile sünme ve büzülme etkilerinden dolayı diferansiyel eksenel kısalmalar oluşabilir ve bina elemanlarında önemli mertebelerde ilave eğilme momentlerine ve kesme kuvvetlerine neden olabilir.



Şekil 1. Çerçevesel yapıların inşaat adımlarının modellenmesi

Zamana bağlı etkiler, çeşitli tasarım yönetmelik ve standartlarına göre farklı analiz yöntemleriyle hesaplanabilir. Bu çalışmada, CEB-FIB [9] ve ACI 209 [10] zamana bağlı hesaplar için dikkate alınmıştır. Sünme ve büzülme analizleri ile davranışı etkileyen parametreler verilmiştir. Sünme davranışının belirlenebilmesi için sünme katsayısının hesaplanması önemlidir. CEB-FIB [9] yaklaşımı ile sünme katsayısı denklem (1) kullanılarak hesaplanır.

$$\phi(t, t_0) = \phi_0 \cdot \beta_c(t, t_0) \quad (1)$$

Burada $\beta_c(t, t_0)$ yüklemeye sonrası sürenin sünme gelişimini tanımlamak için katsayı olup ϕ_0 bağıl nemin ve zamanla betonun karakteristik mukavemetinin etkisini dikkate alan katsayıdır [9]. CEB-FIB [9] için büzülme katsayısı denklem (2) kullanılarak hesaplanır.

$$\varepsilon_{cs}(t, t_s) = \varepsilon_{cs0} \cdot \beta_s(t - t_s) \quad (2)$$

Burada; ε_{cs0} teorik büzülme değerini, $\beta_s(t - t_s)$ eleman şekli ve boyutlarına bağlı olan fonksiyonu gösterir. Benzer şekilde, ACI 209 [10] yöntemi pratik bir yaklaşım sunar ve sünme katsayısı denklem (3) kullanılarak hesaplanır.

$$\phi^*(t) = 2,35 \cdot y_1 \cdot y_2 \cdot y_3 \cdot y_4 \cdot y_5 \cdot y_6 \quad (3)$$

Burada; $\phi^*(t)$ sünme katsayısının zaman içerisinde ulaşacağı sınır değerini, y_1 'den y_6 'ya kadar olan katsayılar ise betonun sünme davranışını etkileyen faktörlere bağlı parametrelerdir. [10]. ACI yöntemine göre [10] büzülme katsayısı ise denklem (4) – denklem (6) kullanılarak hesaplanır. Normal kür uygulanmış bir betonda denklem (4), buhar kürü uygulanmış bir betonda denklem (5) kullanılır.

$$\varepsilon_{sh}(t) = \frac{t}{t + 35} \cdot \varepsilon_{sh}^* \quad (4)$$

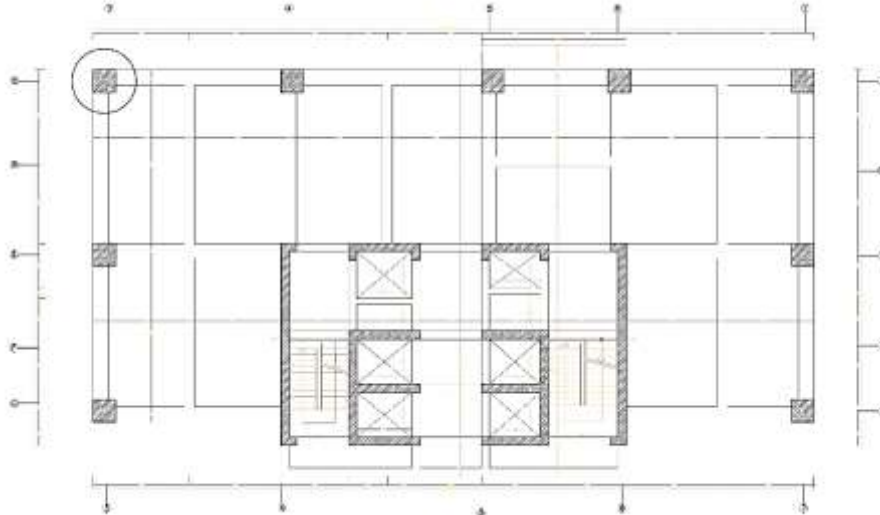
$$\varepsilon_{sh}(t) = \frac{t}{t + 55} \cdot \varepsilon_{sh}^* \quad (5)$$

$$\varepsilon_{sh}^* = 780 \cdot y_2 \cdot y_3 \cdot y_4 \cdot y_5 \cdot y_6 \cdot y_7 \cdot y_8 \quad (6)$$

Burada; ε_{sh}^* büzülmenin sınır değeri, t gün cinsinden zaman, y_2 ortamın bağıl nem oranının büzülme üzerindeki etkisini, y_3 eleman şekil ve boyutlarının büzülme üzerindeki etkisini ve diğer parametreler ise beton karışımının büzülme üzerindeki etkisini göstermektedir.

CEB –FIB ve ACI 209 Yöntemlerine göre Betonarme Elemanlarda Zamana Bağlı Sünme ve Büzülme Katsayılarının Hesabı

CEB –FIB [9] ve ACI 209 [10] yöntemlerine göre betonarme kolon elemanı için zamana bağlı davranışın modellenmesinde kullanılan sünme ve büzülme katsayıları bu bölümde hesaplanmıştır. Çalışmada kullanılan betonarme kolon 40 cm x 100 cm boyutlarındadır. Kolonda kullanılan beton sınıfı C25, donatı çeliği ise S420 ($E_s = 200000$ MPa; $f_{yk} = 420$ MPa) şeklinde dikkate alınmıştır. Zamana bağlı davranış için parametreler ilk olarak ACI 209 [10] yöntemine göre hesaplanmış daha sonra ise CEB-FIB [9] yöntemi kullanılmıştır. ACI 209 [10] kullanılarak yapılan hesapta incelenen elemanın hacim ve yüzey alanı değerleri de dikkate alınması gerektiğinden, eleman boyu 3 m olarak kabul edilmiştir. İncelenen betonarme kolon ve kolonun bulunduğu binanın kat planı Şekil 2'de verilmiştir.

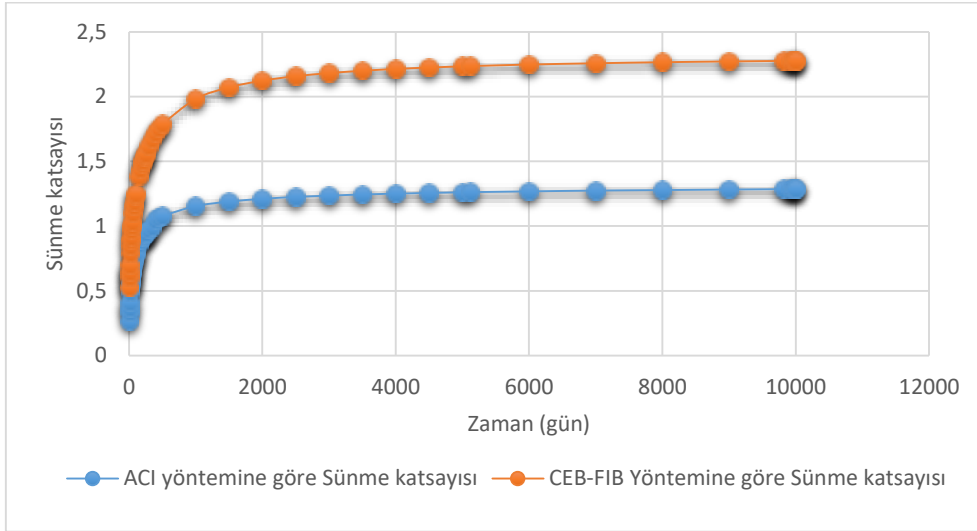


Şekil 2. Kat planı ve seçilen betonarme kolon

Betonarme kolondaki sünme davranışını inceleyebilmek amacıyla seçilen bir zaman aralığı için sünme katsayısı hesaplanmıştır. Benzer şekilde, betondaki büzülme davranışı da sünme gibi zamana bağlı bir davranış olduğundan bu davranışı inceleyebilmek amacıyla belirli günlerdeki büzülme şekil değiştirmeleri elde edilmiştir.

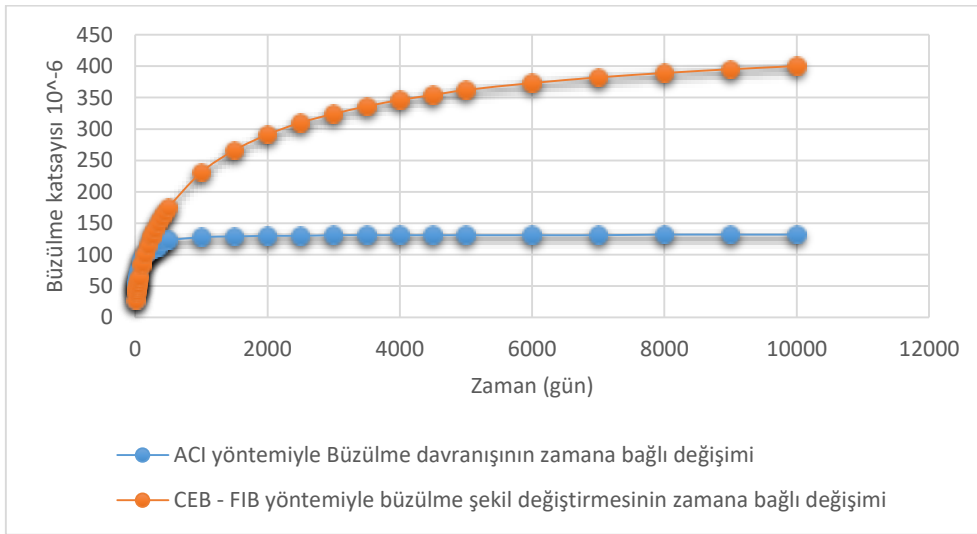
Beton, özelliğinden ötürü zaman içerisinde dayanım kazanır ve buna bağlı olan elastisite modülü de zaman içerisinde artar. Zamana bağlı davranış hesaplarında malzeme özellikleri de önemli olduğundan betona ait bu parametrelerin zaman içerisindeki değişimi de dikkate alınmıştır. Zamana bağlı hesaplarda yükün ilk uygulandığı anda beton yaşı 10 gün olarak kabul edilmiştir. Bu nedenle basınç dayanımının değişimi bu zamandan itibaren hesaplanmaya başlanmış olup hesap 10 000 gün süre için yapılmıştır. Elastisite modülü, beton basınç dayanımına bağlı bir parametre olup zamana bağlı hesaplarda zaman etkisi bir parametre olarak dikkate alınmıştır.

Çalışmada incelenen betonarme kolon için sünme katsayılarının zaman bağlı değişimleri ACI 209 [10] ve CEB-FIB [9] yöntemleri ile hesaplanmış ve Şekil 3'te verilmiştir.



Şekil 3. Sünme katsayısının zamanla değişimi

Benzer şekilde, incelenen betonarme kolon için büzülme katsayılarının zaman bağlı değişimleri ACI 209 [10] ve CEB-FIB [9] yöntemleri ile hesaplanmış ve Şekil 4’te verilmiştir.



Şekil 4. Büzülme katsayısının zamanla değişimi

Betonarme yapı elemanlarının servis yükleri altındaki davranışının incelenmesi ve servis yükleri altında zaman içerisinde ortaya çıkacak deformasyonların kabul edilebilir sınırlar içerisinde kalıp kalmadığının anlaşılması açısından zamana bağlı davranışın belirlenmesi önem taşımaktadır. Bu amaçla bu çalışmada betonun iki önemli davranışı olan sünme ve büzülmenin betonarme yapı elemanlarındaki gerilme ve şekil değiştirme değerlerindeki etkisi 10 000 günlük bir zaman süresi için incelenmiştir.

Sonuçlar

Betonarme binaların hesaplarında inşaat sırasının ve zamana bağlı etkilerin modellenmesi, betonarme yapıların inşaatlarının adım adım ve zamana bağlı şekilde yapılması nedeniyle gerçek yapı davranışın belirlenmesinde önemli bir rol oynamaktadır. Çalışmada, ACI 209 ve CEB-FIB’de verilen yöntemler kullanılarak betonun sünme ve büzülme değerleri 10 000 gün için hesaplanmıştır. Sünmenin zamana bağlı davranışa etkisi, sünme şekil değiştirmesinin ani şekil değiştirmeye oranı olarak bilinen sünme katsayısının elde edilmesiyle gösterilmiştir. Benzer şekilde, beton kürü tamamlandıktan sonra büzülme şekil değiştirmelerinin de zaman içerisindeki değişimi belirlenmiştir. Çalışmada dikkate alınan iki farklı yöntem kullanılarak hesaplanan sünme ve büzülme değerleri arasında farklar bulunduğu

3rd International Students Science Congress
3-4 May 2019, İzmir - Turkey

görülmüştür. Bu durumun nedeni, hesap yöntemlerinde kullanılan parametrelerinin sayısı ve çeşidi vb. etkenler olduğu düşünülmektedir. Yapı elemanlarının zamana bağlı davranışlarını gerçeğe yakın şekilde dikkate alabilmek için deneyler yapılmalı veya ortam şartlarını ifade edebilecek deney sonuçlarından elde edilen yaklaşımlar kullanılmalıdır. Ayrıca, bu yöntemlerden elde edilen sonuçların oldukça pratik şekilde hesaplanabilir olması nedeniyle, zamana bağlı davranış dikkate alınarak yapılacak tasarımlar için fikir verebileceği düşünülmektedir.

Teşekkür

Bu çalışma Yurtdışı Türkler ve Akraba Topluluklar Başkanlığı'nın (YTB) "Uluslararası Öğrenci Akademisi" Projesi kapsamında desteklenmiştir.

Referanslar

- [1] Kurc O, Lulec A (2013) A comparative study on different analysis approaches for estimating the axial loads on columns and structural walls at tall buildings. *The Structural Design of Tall and Special Buildings* 22: 485-493.
- [2] Au FTK, Liu CH, Lee PKK (2009) Creep and shrinkage analysis of reinforced concrete frames by history-adjusted and shrinkage-adjusted elasticity moduli. *The Structural Design of Tall and Special Buildings* 18(1): 13-35.
- [3] Kwak HG, Kim JK (2006) Time-dependent analysis of RC frame structures considering construction sequences. *Building and Environment* 41(10): 1423-1434.
- [4] Kwak HG, Kim JK (2006b) Determination of efficient shoring system in RC frame structures. *Building and Environment* 41: 1913-1923.
- [5] Kim HS, Shin SH (2011) Column shortening analysis with lumped construction sequences. *Procedia Engineering* 14: 1791-1798.
- [6] Pan LB, Liu P C, Bakoss SL (1993) Long-term shortening of concrete columns in tall buildings. *Journal of Structural Engineering* 119(7): 2258-2262.
- [7] Kim JY, Abdelrazaq AK (2009) Construction sequence analysis of the flat plate system in a high-rise building and its impact on the construction cycle. *The Structural Design of Tall and Special Buildings* 18(3): 341-349.
- [8] Samarakkody DI, Thambiratnam DP, Chan TH, Moragaspiya PH (2017) Differential axial shortening and its effects in high rise buildings with composite concrete filled tube columns. *Construction and Building Materials* 143: 659-672.
- [9] FIB-Fédération Internationale du Béton: Model Code 2010 (first complete draft). Bulletin 55, 1(5) "Materials", Lausanne.
- [10] ACI 209R-92: 1997, Prediction of Creep, Shrinkage and Temperature Effects in Concrete Structures, ACI Committee 209.

Determination of Mixing and Compaction Temperatures of Polymer Modified Bitumen through High Shear Rate Method

Ali Almusawi*, Dokuz Eylül University, The Graduate School of Natural and Applied Sciences, İzmir, Turkey
Burak Şengöz, Derya Kaya Özdemir, Ali Topal
Dokuz Eylül University, Dept. of Civil Engineering, İzmir, Turkey
*Corresponding author: ali89.engin@yahoo.com

Keywords: polymer modified bitumen, mixing temperature, compaction temperature
Discipline: Civil Engineering

Abstract

Utilization of different kinds of polymer within the bitumen has become very common in many countries since it works to improve the performance of the asphalt mixtures and rheological characteristics of the bitumen. Many organizations and agencies started to develop special specifications for the utilization of the bitumen modifiers. One of the most important factors that affects the performance of the asphalt mixtures involving polymer modified bitumen (PMB) is the temperature (i.e. mixing and compaction temperatures) where the mixing temperature determines the aggregate coating ability of the bitumen and the compaction temperature aims to achieve the design air voids. The traditional method (ASTM D 2493) of calculating the mixing and the compaction temperatures depends on viscosity measurement and it can be applied on unmodified bitumen since the base bitumen behaves like Newtonian material. On the other hand, in the case of PMB, the application of the existing method may result in high mixing and compaction temperatures because it acts as non-Newtonian material. In this study, an alternative method named High Shear Rate (both original and evolution methods) has been implemented to find suitable mixing and compaction temperatures for PMB. The PMB samples have been produced with styrene-butadiene-styrene (SBS) polymer at 5% rate within 50/70 and 160/220 penetration grade base bitumen. The results show that the high shear rate method (original method) has very similar results with the traditional method. While the results obtained by the high shear rate (evolution method) are lower than the ones obtained from the traditional method.

Introduction

Over the years base bitumen has been used in the construction of the asphalt pavement. The rapid growth rate in the traffic volumes showed a limitation in the performance of the conventional bitumen which may be clearly noticed in the earlier failures of the pavement than expected. This led to a decrease in service life and increase in the maintenance cost. To overcome such problems and to enhance the performance of the asphalt pavement, modified bitumen with polymers has been used in the last few decades[1].

Significant physical changes are clearly detected while the polymer is added to the base bitumen. The polymer, when added, it is absorbing the oily constituents and at higher concentration (more than 4%) the polymer starts to swell 10 times its volume. Thus, the bitumen becomes stiffer and more viscous.[1]

Most of the materials usually behave either as Newtonian or non-Newtonian. Newtonian behavior means that the ratio of shear rate to shear stress is constant, in other words, the viscosity of the Newtonian material is constant regardless of the shear rate. Many materials behave as Newtonian and base or unmodified bitumen is one of such materials as shown in Figure 1. [2] [3]

On the other hand, some other viscous materials are more dependent to the change in shear rate and similar materials are called non-Newtonian. The relationship between the shear rate to shear stress is not linear and the viscosity value is greatly affected by the shear rate. If the viscosity of the material is increased with the increase in shear rate, it means the material is shear thickening type. While in the condition of the viscosity decreases with any increase in shear rate, the material considered as a shear thinning type. Most of the polymer modified bitumen are behaving like non-Newtonian and shear thinning type as shown in Figure 1. [2-3].

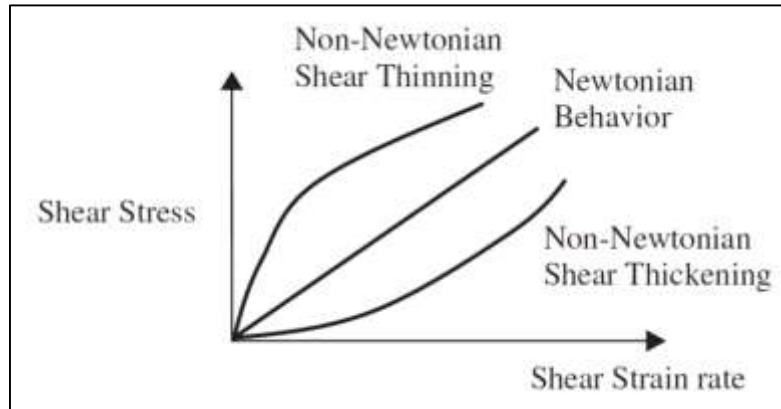


Figure 1. Newtonian and Non-Newtonian behavior [2]

With the addition of polymer into the bitumen, the viscosity increases which has a direct effect on mixing and compaction temperatures determination and the traditional method (ASTM D2493) is designed based on viscosity measurement for base or unmodified bitumen. Yildirim et al. proposed the concept of the High Shear Rate to estimate mixing and compaction temperatures of PMB in order to replace the ASTM D 2493 method. They have found that the application of the traditional method for different modified bitumen types have resulted in mixing and compaction temperatures ranging between 170 °C to 201 °C and 156 °C to 184 °C, respectively. While using the concept of HSR method (original) resulted in lower temperatures between 14-38 °C. In 2006 the same researches have noticed that the implementation of HSR (original) not always gives lower mixing and compaction temperatures for polymer modified bitumen. Thus, they have proposed some changes on the viscosity limits to find more suitable mixing and compaction temperatures for PMB. The use of the new limits has shown reduction in the temperatures between 13 °C to 52 °C [3-6].

In 2012 Rui et al. have found The application of the traditional method (ASTM D 2493) and HSR (original) resulted in high temperatures above 180 °C for the PMB. while, the application of the HSR (evolution) mostly gave mixing and compaction temperatures close the supplier's recommendation [7].

High temperatures are obtained by the application of the traditional method (ASTM D 2493), so it is necessary to investigate for an alternative method which must be more applicable and has no effect on the asphalt mixture performance [3-6].

Materials and Methodology

In this study 50/70 and 160/220 base bitumen grades supplied by DERE ASFALT were used. Some of the conventional tests have been conducted for the base bitumen such as penetration test, softening point test, and Rolling thin film oven test to measure the bitumen characteristics. Table 1 shows the test results according to the ASTM specification.

Table 1. Properties of the base bitumen

Test	Specification	Results		Specification limits	
		50/70	160/220	50/70	160/220
Penetration (25 °C; 0.1 mm)	ASTM D5 EN 1426	65	190	50-70	160-220
Softening point (°C)	ASTM D36 EN 1427	51	41	46-54	35-43
Penetration index (PI)	-	0.35	0.123	-	-
Rolling thin film oven test (RTFOT)	ASTM D2872-12				
Change of mass (%)	-	0.160	0.94	0.5 (max.)	0.5 (max.)
Penetration (25 °C; 0.1 mm)	ASTM D5 EN 1426	53	97	50 (min.)	50 (min.)
Retained penetration (%)	ASTM D36 EN 1427	82	51	50 (min.)	50 (min.)
Softening point after RTFOT (°C)	ASTM D36 EN 1427	58	50	48 (min.)	48 (min.)

The SBS polymer used was Kraton D-1101 supplied by the Shell Chemicals Company. The properties of the Kraton D-1101 polymer are presented in Table 2.

Table 2. The properties of Kraton D-1101 polymer

Composition	Specification	Kraton D 1101
Molecular structure	-	Linear
Physical properties		
Specific gravity	ASTM D792	0.94
Tensile strength at break (MPa)	ASTM D 412	31.8
Shore hardness (A)	ASTM D 2240	71
Physical form	-	Powder, pellet
Melt flow rate	ASTM D-1238	<1
Processing temperature (°C)	-	150–170
Elongation at break (%)	ASTM D 412	875

Preparation of Polymer Modified Bitumen

The SBS Kraton D 1101 concentration in the base bitumen was chosen (5%) as an optimum content [8]. High shear laboratory mixer was used to prepare the SBS polymer modified bitumen. The base bitumen first heated to (180-185 °C), and has been poured into 600 ml glass beakers. The SBS then added gradually to the base bitumen and the rotating speed was kept at 2000 rpm for 1 hour.

Determination of Mixing and Compaction Temperatures

Mixing and compaction temperatures generally are determined through the traditional method (ASTM D2493). Several alternative methods have been suggested in the literatures to implement for the polymer modified bitumen such as high shear rate, zero shear viscosity, steady shear flow and phase angle method. In this study, high shear rate method (original and evolution) has been implemented to evaluate mixing and compaction temperatures of polymer modified bitumen samples.

ASTM D 2493 Method

The machine used for this test is Brookfield viscometer. According to ASTM D 2493 this method is used to measure the viscosity of the bitumen at two temperatures 135 °C and 165 °C at a constant shear rate of 6.8 1/s. the sample size is changing according to the spindle size used (generally for spindle size 21 sample weight is 10.5-11 gr). The measured viscosity results are drawn against the temperature as shown in Figure 2. The mixing and compaction temperature limits are 0.17 ± 0.02 and 0.28 ± 0.03 , respectively [9].

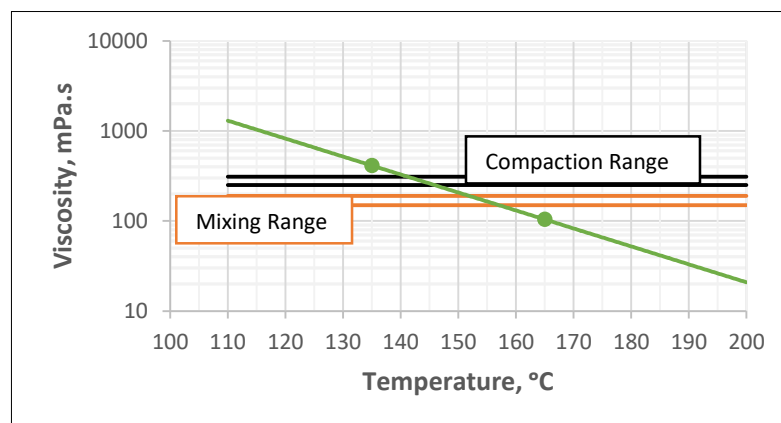


Figure 2. ASTM D 2493 Method [9]

High Shear Rate Method (HSR)

Yildirim et. al. [10] found the shear rate during the Superpave compactor is higher than the one used in ASTM D2493 method (6.8 1/s). They found the shear rate value is around 500 1/s. the viscosity at this shear rate must be calculated and used for mixing and compaction temperatures determination. In this method, Brookfield viscometer is used to find the viscosity of the bitumen at different shear rates and then drawn and extrapolated to 500 1/s shear rate as shown in Figure 3. This is done because such high shear rate cannot be measured directly using Brookfield viscometer. Similar to ASTM D2493 method, the obtained viscosity values at 135 °C and 165 °C were plotted against the temperature. Mixing and compaction temperatures are found by using the same viscosity limits used in the traditional method 0.17 ± 0.02 Pa. s and 0.28 ± 0.03 Pa. s, respectively (High Shear Rate original (HSR-O)). In attempt trying to get lower temperatures in 2006 Yildirim et. al suggested a higher viscosity range to be used which are 0.275 ± 0.03 Pa. s and 0.550 ± 0.06 Pa.s. (High Shear Rate Evolution (HSR-E)).[3]

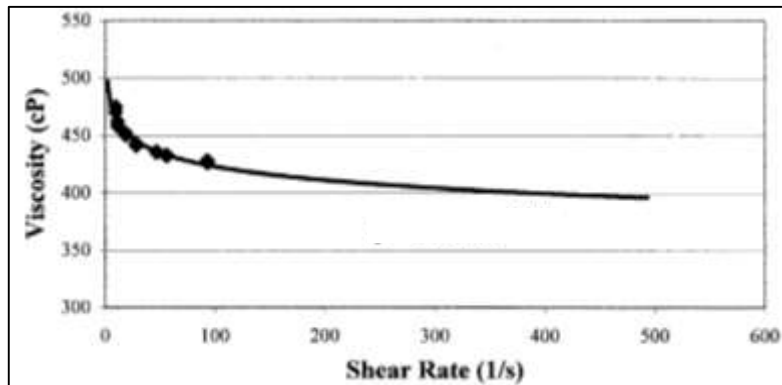


Figure 3. high shear rate method [3]

Results and Discussion

The mixing and compaction temperatures are determined based on ASTM D2493. The mixing and compaction temperatures calculation for 50/70 and 160/220 penetration grade bitumen involving 5 % SBS polymer is presented in Figure 4.

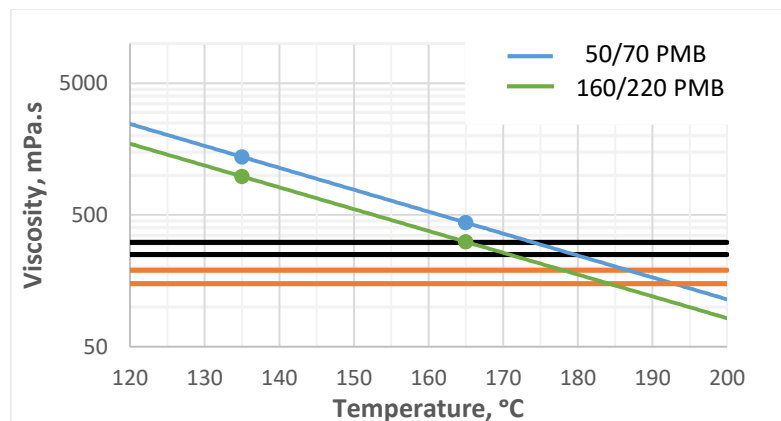


Figure 4. Mixing and compaction temperatures determination

For HSR method, at different shear rates, the viscosity values were measured and plotted. For the two PMB the data extrapolated using the power law model to find the viscosity values at shear rate around 500 1/s at two different temperatures (135 °C and 165 °C) as shown in Figure 5 and Figure 6.

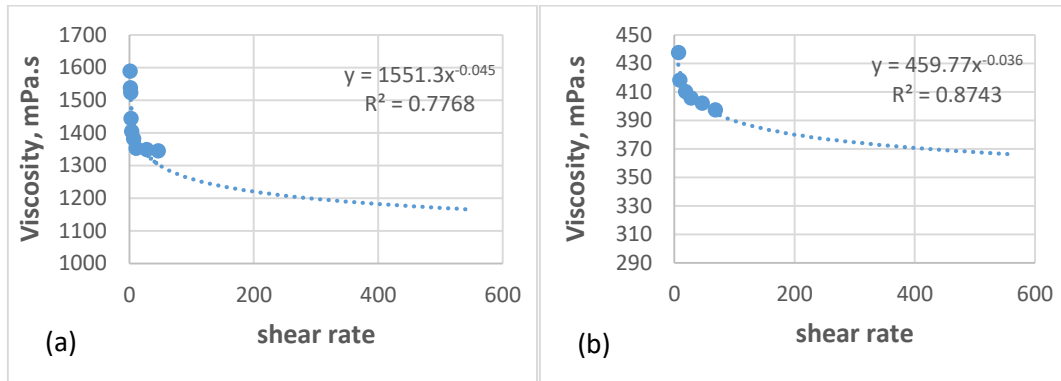


Figure 5. (a) 50/70 PMB: Viscosity versus Shear Rate at 135 °C and (b) 50/70 PMB: Viscosity versus Shear Rate at 165 °C

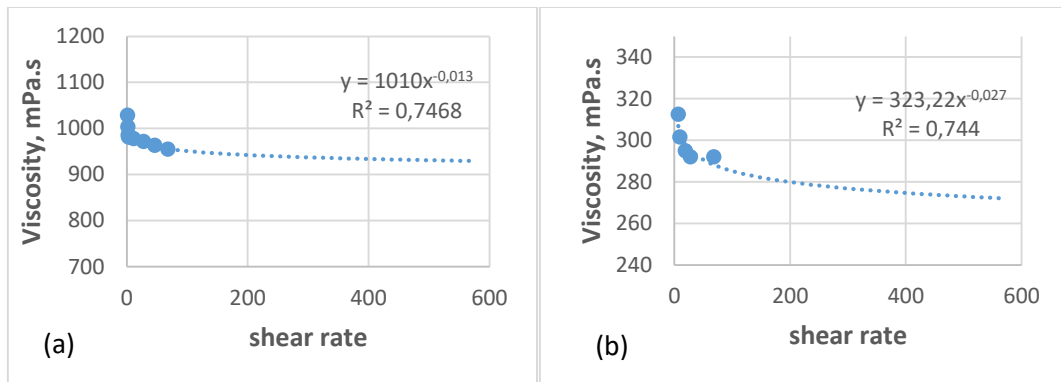


Figure 6. (a) 160/220 PMB: Viscosity versus Shear Rate at 135 °C and (b) 160/220 PMB: Viscosity versus Shear Rate at 165 °C

The viscosity values at 500 1/s at the two temperatures are then plotted in log scale versus the temperature. The mixing and compaction temperature limits were used as 0.17 ± 0.02 Pa. s and 0.28 ± 0.03 Pa. s as for (HSR O) and the new suggested limits were 0.275 ± 0.03 Pa. s and 0.550 ± 0.06 Pa. s. as for (HSR E). Table 3 summarizes the mixing and compaction temperatures results obtained for 50/70 PMB and 160/220 PMB

Table 3. Mixing and compaction temperatures results

Method	50/70 PMB		160/220 PMB	
	Mixing °C	Compaction °C	Mixing °C	Compaction °C
ASTM D2493	186-192	174-180	176-184	165-171
HSR-O	181-187	170-175	174-180	162-167
HSR-E	170-175	152-158	163-167	147-154

Clearly, the mixing and compaction temperatures determined through the implementation of the traditional method (ASTM D2493) for both polymers modified bitumen are high.

For HSR-O The mixing and compaction temperatures of 50/70 PMB and 160/220 PMB showed no much difference with the traditional method. While using the new suggested limits by HSR-E showed a clearly difference in the results. The drop in the temperature values is due to the increase in the new proposed viscosity range.

Conclusion

The ASTM D2493 procedure has been used as a reference method for determining mixing and compaction temperatures for the base bitumen. The implementation of this method gives a reasonable mixing and compaction temperatures for the base or unmodified bitumen. While the application of this method for the polymer modified bitumen resulted in high mixing and compaction temperatures. This can be attributed to the physical changes for the modified bitumen and clearly can be detected in the increase of the viscosity value which resulted in the rise of temperatures. The results of this study have shown that the obtained mixing and compaction temperatures from the application of the high shear rate method (evolution), which considers the shear dependency of the modified bitumen, are lower than the traditional method (ASTM D2493).

References

- [1] Hunter, RN, Self A, Read J, and Hobson E (2015) The shell bitumen handbook (6th edition). London: ICE Bookshop Civil Engineering Publishing.
- [2] Papagiannakis AT, Masad EA. Design and Materials. Pavement Des Mater 2008; 544.
- [3] Yildirim Y, Ideker J, Hazlett D (2006) Evaluation of Viscosity Values for Mixing and Compaction Temperatures. J Mater Civ Eng; 18: 545–553.
- [4] Micaelo R, Santos A, Duarte C (2012) Mixing and Compaction Temperatures of Asphalt Mixtures With Modified Bitumen. 5th Eurasphalt Eurobitume Congress.
- [5] West RC, Watson DE, Turner PA, and Casola JR (2010) Mixing and Compaction Temperatures of Asphalt Binders in Hot-Mix Asphalt, National Cooperative Highway Research Program, NCHRP Report 648, Transportation Research Board, Washington, D.C.
- [6] Kök BV, Yılmaz M, Akpolat M (2013) Bitüm Modifikasyonunun Karıştırma Sıkıştırma Sıcaklığı Bakımından Değerlendirilmesi. 6.Ulusal Asfalt Sempozyumu pp. 353–363.
- [7] S Micaelo R., Santos A, & Duarte C (2012). Mixing and compaction temperatures of asphalt mixtures with modified bitumen. Paper presented at the Proceedings of 5th Eurasphalt & Eurobitume Congress. Istanbul.
- [8] Sengoz B, Isikyakar G (2008) Evaluation of the properties and microstructure of SBS and EVA polymer modified bitumen. Construction and Building Materials; 22: 1897–1905.
- [9] American Society for Testing and Materials (2011) Standard Practice for Viscosity-Temperature Chart for Asphalt Binders. ASTM D2493, American Society for Testing and Materials.
- [10] Yildirim Y, Solaimanian M, and Kennedy T (2000) Mixing and compaction temperatures for hot mix asphalt concrete. The University of Texas, Austin.

Comparative Study of Marshall and Superpave Asphalt Pavement Design Methods

*Derya Kaya Özdemir**, Dokuz Eylül Univ., Dept. of Civil Engineering, Tinaztepe Campus, İzmir, Turkey
Ali Topal, Dokuz Eylül Univ., Dept. of Civil Engineering, Tinaztepe Campus, İzmir, Turkey
Ali Almusawi, Dokuz Eylül University, The Graduate School of Natural and Applied Sciences, İzmir, Turkey
Burak Şengöz, Dokuz Eylül Univ., Dept. of Civil Engineering, Tinaztepe Campus, İzmir, Turkey
*Corresponding author: d.kaya@deu.edu.tr

Keywords: asphalt mix design methods, Marshall method, superpave method

Discipline: Civil Engineering

Abstract

Highway transportation is becoming a more common requirement day by day together with the increasing of human population and evolving technology. Most of the road networks are constructed using asphalt pavement so a proper design method is necessary to carry out the rapid growth in traffic volumes. Several design methods have been developed and adopted over the years aiming to obtain optimum performance. Marshall mix design method can be considered as one of the most popular and implemented methods over the world. However, increasing demand for highways and deformations caused by the high traffic loads revealed insufficiency of Marshall mix design. Therefore, Superior Performing Asphalt Pavement (Superpave) method was developed so as to preclude the asphalt common defects such as permanent deformation, fatigue cracking and low temperature cracking by taking the region and climatic conditions into account. In this study, Marshall and Superpave mix design methods were compared with regards to specification and requirements. Also, the advantages and disadvantages of each method were discussed and the test equipment's of different methods were compared.

Introduction

Highway transportation, which is the most common type of transportation in our country and in the world, become to have wider usage network with increasing population and transportation demand. Highway construction affects the human health and the environment during the production phase moreover, comfort and safety features of the roads directly affect the environment and human life. Increasing demand for highways and permanent deformations caused by the high traffic loads revealed insufficiency of Marshall mix design which is an empirical method. Therefore, the Superpave method was developed. This method contributes to preclude permanent deformation by taking the region and climatic conditions into account.

Superpave and Marshall design methods are different specifications with including different experiments and design methods. Therefore, the physical and mechanical properties of the asphalts produced as a result of the design are changeable. The Superpave design method is becoming more and more common in the world because of its superiority. Several studies have been carried out in order to compare these two design methods [1].

In the 1950s, Valerga showed that different compaction methods might yield the same density but cause some differences in their stability and flow values. From this point of view, it has been concluded that compaction methods change the mobility and structure of the particles and so their susceptibility to deformation [2].

In another study, Maupin compared samples properties compacted with Marshall mallet and two different gyratory presses in terms of optimum bitumen ratios. The samples compacted based on the principles of the Superpave method had similar results even though different gyratory presses were used. But on the other hand, they had quite different results compared to samples produced by the Marshall method. Moreover, samples produced by gyratory presses had comparable results with the samples taken from the field. Therefore, it was concluded that the Superpave method and apparatus are more useful in terms of representing compaction in field conditions [3].

In 1998, Habib et al. investigated the examination of the Superpave method on low volume roads and compared the results with the Marshall method. At the end of the study, one of the advantages of the Marshall method was found as being suitable to local conditions and materials. However, the

**3rd International Students Science Congress
3-4 May 2019, İzmir - Turkey**

Superpave method is universally acceptable since it draws attention to parameters such as rutting, fatigue crackings, and low-temperature crackings [4].

In a different study conducted by Brown at the University of Colorado, optimum bitumen contents of asphalt samples produced by Marshall and Superpave methods were compared. As a result, the lower bitumen content was determined according to the Superpave method. In addition, the air voids were similar while the mineral voids in mineral aggregate (VMA) were significantly lower in the Superpave method. It was stated that the Superpave method is more preferable because of requiring a lower amount of bitumen [5].

In 2002, Kanneganti investigated the designs of asphalt mixtures with a maximum nominal aggregate size of 19 mm in West Virginia for high traffic volume roads with Marshall and Superpave methods. In the literature, the researcher found that the optimum bitumen amount of asphalt designed with Superpave method for all traffic levels is higher than that of the Marshall method [6].

Watson et al. (2005) reported that the number of gyration chosen for the preparation of samples equal to the density in the field is changeable according to climate and traffic conditions. In the same study, several asphalt road projects having similar traffic conditions, mixture type, aggregate type, bitumen type, gradation curve, and climate characteristics but different design methods (Marshall or Superpave) were compared in terms of bitumen content. As a result, although most of the roads produced by the Marshall method had higher optimum bitumen there were also samples with a higher optimum bitumen produced by the Superpave method [7].

In Nelson's study applied in 2005, Marshall and Superpave methods by having 9.5 mm nominal maximum grain asphalt mixes were compared according to optimum bitumen contents for heavy and medium heavy traffic conditions. According to the results, samples including limestone produced by Superpave method had higher optimum bitumen ratio in the samples containing limestone was higher than compared to Marshall design method, whereas, for samples containing fine aggregate, this situation was surprisingly reversed. That might be clarified as samples containing small diameter particles reduce the void ratio in the gyration stage of the Superpave method which caused a reduction in the optimum bitumen [8].

In a 2005 study by Namlı and Kuloğlu, comparisons were made in terms of stability, unit weight, air voids, and flow value for samples prepared with Superpave and Marshall design methods. Moreover, optimum bitumen ratios were calculated and determined a lower value for samples produced by the Superpave method. As a result, they emphasized the importance of Superpave Method specification for Turkey [9].

Mixing Design Methods

The density values of the samples compressed in the laboratory with Marshall mix design method, which had been adopted in 1943, had quite similar values in the field. However, sometimes this method did not reach the real performance levels since it was based on previous test results and the trial and error method and also it did not take the climatic characteristics into account. Moreover; impaction with the help of a hammer during compaction stage did not represent the real compaction caused by traffic. Because of all this reason, researchers tend to develop a new mix design method such as Superpave.

In Superpave design method, which was created and developed in 1987 in the light of the deficiencies of Marshall mix design method, the compression process includes gyration with a certain angle and a certain pressure in order to better represent the movement of the wheel. Gyration creates shear stress in the sample and prevents the breakage of aggregate grains during compression [10]. However; the equipment used in the Superpave design method is slightly more expensive than other methods.

Marshall Mix Design

In 1939, Bruce Marshall, an engineer of the Mississippi Department of Highways introduced the Marshall Mix Design method to the world of science. In 1943, the Union of Engineers of the US Army adopted the Marshall method to use to determine the optimum amount of bitumen based on the functions of gradation and traffic conditions [11]. The Marshall Method is used to determine the optimum bitumen content with the criteria of providing the desired density, stability and air voids [6].

The Marshall method, despite its shortcomings, is perhaps the world's most widely used mix design method. The following advantages of the method can be shown as the reason for being so widely used: [11]

- ✓ It is designed to apply stress to every part of the sample.
- ✓ It is suitable to be done quickly with minimum effort.
- ✓ it requires small, light and portable equipment.
- ✓ The properties of the samples produced in the laboratory have quite similar results with the field sample.

Marshall mix design method consists of 6 steps. These are:

1. Aggregate selection
2. Bitumen selection
3. Preparation of samples
4. Determination of density and air voids values
5. Determination of stability and flow values by Marshall Stabilometer
6. Determination of optimum bitumen content

The first step of the Marshall mix design is to determine the gradation within the specification limits [12]. Until an acceptable gradation is achieved, various control gradations are created with the aggregates of different ratios and sizes. In order to have an acceptable gradation, the percentages of fine and coarse aggregates and fillers must be within the specification limits, on the other hand, the VMA values should not be very close to the 0.45 power gradation.

In the Marshall mix design method, bitumen is classified according to penetration values which are in line with the climate characteristics of the region.

After the determination of bitumen and aggregate gradation, they mixed together at the specific temperatures in order to have asphalt blend. After that, samples are placed on the Marshall compactor and compacted with 75 impacts on both sides, as specified in the Turkish Highway Technical Specification Type-1 [13].

Determination of Density and Air void Values

Diameters, dry weight, saturated surface dry weight and the volume of the samples are measured with the help of scale and caliper after the samples are removed from the mold. By using abovementioned values, density and air void values are obtained.

Specific Gravity and Mixture Density of the Samples

The specific gravity calculation is described in ASTM D2726 / D2726M-13 in detail and the formula is given in Equation 1.

$$G_{mb} = \frac{A}{B - C} \quad (1)$$

where:

G_{mb} = Specific gravity of the sample

A = Weight of dry sample in the air (g)

B = Saturated dry surface weight of the sample (g)

C = Weight of sample in water (g)

Maximum Specific Gravity of Mixture

The specific gravity of the sample is determined based on ASTM D2041 / D2041M-11 and calculated using the following formula:

$$G_{mm} = \frac{A}{A - (B - C)} \quad (2)$$

where:

G_{mm} = Maximum specific weight

A = Weight of loose mixture in the air (g)

B = Weight of water-filled pycnometer and loose mixture (g)

C = Weight of water filled pycnometer (g)

The maximum specific gravity of the mixtures containing different amount of bitumen may be obtained by knowing the G_{mm} value for a given bitumen percentage. The effective specific gravity of the aggregate is constant and bitumen absorption potential is independent of the bitumen percentage in the blend. The effective specific gravity of aggregates, G_{se} , can be calculated as follows:

$$G_{se} = \frac{P_{mm} - P_b}{\frac{P_{mm}}{G_{mm}} - \frac{P_b}{G_b}} \quad (3)$$

where:

P_{mm} = Percentage of total loose mixture = 100

P_b = Percentage of asphalt in the mixture

G_{mm} = Maximum specific gravity of the mixture

G_b = Specific gravity of bitumen

The maximum specific gravity of the mixture with any bitumen amount can be calculated as follows:

$$G_{mm} = \frac{P_{mm}}{\frac{P_s}{G_{se}} + \frac{P_b}{G_b}} \quad (4)$$

where:

G_{mm} = Maximum specific gravity of the mixture

P_{mm} = Percentage of total loose mixture = 100

P_b = Asphalt percentage in the mixture

P_s = Percentage of aggregate in the mixture

G_{se} = Effective specific gravity of aggregates

G_b = Specific gravity of bitumen

Air Voids

Air voids are small air particles or air bubbles formed between aggregates coated by asphalt in the blend. The durability of the asphalt pavement is directly related to the air voids of the blend. The high air voids rate has some disadvantages like air and water might enter the asphalt pavement during service. On the other hand, very low air void rates cause swelling of bitumen [14].

Density is directly related to the air voids. The more the air voids, the less the density [12]. It is stated in the Technical Specifications that the density of the pavement should be chosen in such a way as to provide the required air voids.

Voids in total mixture (VTM) is calculated as follows:

$$VTM = \frac{G_{mm} - G_{mb}}{G_{mm}} \times 100 \quad (5)$$

where:

VTM = Voids in total mixture

G_{mm} = Maximum specific gravity of the mixture

G_{mb} = Specific gravity of the compressed sample

Voids in mineral aggregates (VMA)

The gap between mineral aggregates, VMA, is the volume of the void between the particles of aggregates in HMA. VMA is one of the most important design parameters affecting the durability of HMA [20]. The VMA covers all void filled with bitumen and air space and it is expressed as a percentage of the total volume of the mixture. VMA is calculated as follows:

$$VMA = 100 \left[1 - \frac{G_{mb} (1 - P_b)}{G_{sb}} \right] \quad (6)$$

where:

VMA = percentage of space between mineral aggregates

Gsb = Specific gravity of the aggregate mixture
Gmb = Specific gravity of the compressed sample
Pb = Asphalt percentage in the mixture

Voids Filled Asphalt (VFA)

Voids Filled asphalt (VFA) represents the void filled with bitumen between the aggregates. In other words, it can be said as a percentage of space filled with bitumen [14]. The purpose of the VFA ratio in the mixture is to limit the maximum gap between the mineral aggregates and accordingly the asphalt content. The percentage of VFA is calculated as follows:

$$VFA = \frac{VMA - VTM}{VMA} \times 100 \quad (7)$$

where:

VFA = voids filled asphalt (%)
VMA = voids in mineral aggregates (%)
VTM = Voids in total mixture

Determination of Stability and Flow Values by Marshall Stabilometry

Stability and flow values are determined by using Marshall stabilometry. The flow value is equal to the vertical deformation value of the sample [15]. The data recorded by the device is obtained from the display. However, the stability value obtained from the device is calibrated for only 63.5mm samples. Therefore, correction factors have been developed for samples of different sizes. Stability and flow values should be recalculated by using correction factors corresponding to the height of the sample and as a result, final values should be compared with the specification limits.

Determination of Optimum Bitumen (ASTM D2172 / D2172M-11)

Initially, volumetric parameters, stability and flow values should be determined in order to obtain the optimum bitumen content. The amount of bitumen providing abovementioned parameters within the specification limits and 4% air voids is assigned as the optimum bitumen content. Table 1 presents the Marshall design method criteria in the Highways Technical Specification for Type-1 gradation [13].

Table 1. Marshall Design Method Criteria

Design Criteria	Test Standard	Type-1 Grade
Number of Pulses per each surface	TS EN 12697-30	75
Stability (kg)	TS EN 12697-34	900
Air void (%)	TS EN 12697-8	3-5
VFA (%)	TS EN 12697-8	65-75
VMA (%)	TS EN 12697-8	14-16
Flow (mm)	TS EN 12697-34	2-4

Superpave Design Method

Superpave (Superior Performing Asphalt Pavement) mix design was developed by “Strategic Highway Research Program (SHRP)” in 1987 (USA) [16]. Gyratory Press is employed to compress the asphalt mixture within this method, and only criteria to determine optimum bitumen content is at 4% air void.

The Superpave method is developed depending on the Marshall method for high temperatures and heavy vehicle loads in the United States [8]. Furthermore, unlike the Marshall mix design method, traffic load and temperature values of the region is crucial in the selection of aggregate and bitumen [10].

Superpave Design Method consists of 7 steps. These are:

1. Aggregate selection
2. Bitumen selection
3. Preparation of the samples (including the compression process)

4. Performance tests
5. Determination of density and air voids ratio
6. Determination of optimum bitumen content
7. Evaluation of moisture sensitivity

One of the most obvious differences between the Superpave and the Marshall mix design method is the selection of aggregates. Since the aggregate properties of the asphalt pavement, which are extremely important for the performance characteristics of the asphalt pavement, are not mentioned in detail in the Superpave mixing method formed by SHRP, a group of experts came together to discuss the desired aggregate properties with the required features [17].

These are:

- Coarse aggregate angularity (ASTM D5821-13)
- Fine aggregate angularity (ASTM C1252-06)
- Elongated and flat particles (ASTM D4791-10)
- Clay content (ASTM D2419-09)

Dense gradation is used for both Superpave and Marshall Design methods. But; there are two important points in the Superpave mix design method: control points that form aggregate gradation boundaries and aggregate rates of various properties. Another remarkable point in the Superpave design method is the control points and the prohibition zone that should be considered in the selection of aggregates with a gradient graph of 0.45 power curve. Gradation should pass through the control points but not through the prohibited area [10]. The control points are the finest (0.075mm), 2.36mm, nominal maximum (12.5mm) and maximum (19mm) grain sizes. The forbidden zone has been created to balance the amount of excess sand in the blends and to remove the gradation curve from the maximum density line in order to minimize the deformation problems during the service life of the pavement [18]. Figure 1 shows the gradation limits, control points and prohibited zones of the Superpave method.

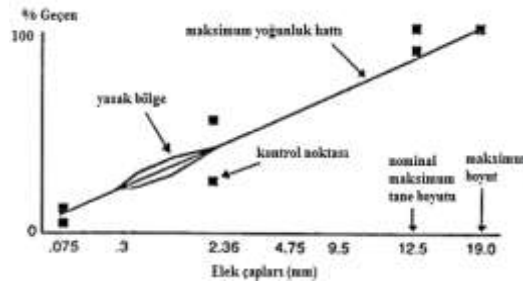


Figure 1. Superpave gradation limits

Superpave design method has a specific classification system called the performance grading (PG). In this system, bitumen is classified according to the minimum and maximum temperature degree of pavement [16]. In addition to the pavement temperature, the traffic volume and vehicle speed are also important for determining the PG [19].

Superpave gyratory press was developed to simulate the particle movements of the mixture in laboratory conditions [15].

The purpose of the gyratory press is to compress the mixture as real as it compresses under the actual pavement temperature and loading conditions. The number of gyration, the sample height at the end of the compression and the compression pressure should be determined in advance. The loading mechanism applies pressure against the reaction frame and applies a load to the loading head which will produce 600 kPa compression pressure in the sample. The asphalt samples were prepared by using molds with a diameter of 100 mm or 150 mm and compacted to a constant rotation of 30 times per minute under compression in the standard. Figure 2 shows the gyratory press and compression head.

Superpave mix design method has three different gyration number depending on the traffic volume of the road ss shown in Tables 2 and 3.



Figure 2. Gyratory press and compression head.

Table 2. Highway classifications for Superpave Mixtures

(ESAL) (million)	Application
< 0,3	Rural roads with low traffic volumes, country roads without heavy vehicle traffic
0,3 - 3	Collector roads
3 - 30	Double-lane, multi-lane, divided and partly or completely controlled transport roads, high-traffic city roads
> 30	Double lane roads with climbing lanes or roads with heavy vehicle traffic

Table 3. The gyration parameters according to traffic levels

ESAL(million)	Gyration parameters		
	Nini	Ndes	Nmax
< 0,3	6	50	75
0,3 - 3	7	75	115
3 - 30	8	100	160
> 30	9	125	205

Nini = is the number of gyration which represents the compression of the pavement during the construction phase. Compressed mixtures can be very unstable when subjected to traffic loads during construction. Samples with a traffic load equal to or greater than 3 million ESALs and having a gap of 4% in Ndes should have at least 11% air voids after gyration of Nini and it should have Gmm value of at least 89%. Higher air voids ratios cause a rapid compression of the mixture [10].

Ndes = is the number of gyration used to prepare samples equal to the density in the field under the specified traffic load. Samples prepared by Ndes gyration represents the properties of the compressed pavement by initial traffic load. A value of 4% air void is expected from the compressed sample with Ndes [27].

Nmax = is used to obtain laboratory density that can never be reached in the field. If the air void ratio compressed with Nmax is too low, the pavement may have rutting problem. The air void after Nmax is the air void of the pavement at the end of the service life and it should never be less than 2% (Gmm value must be maximum 98%).

Nmax and N_{ilk} values are a function of Ndes and they can be calculated as follows:

$$N_{ini} = (N_{des.})^{0,45} \quad (8)$$

$$N_{max} = (N_{des.})^{1,10} \quad (9)$$

where:

Nini = initial number of gyration

Ndes = Design number of gyration

**3rd International Students Science Congress
3-4 May 2019, İzmir - Turkey**

N_{max} = maximum number of gyration

The specific weight of the sample compressed with N_{ini} is calculated as follows:

$$G_{mb, N_{ini}} = \frac{h_d}{h_i} (G_{mb, N_{des}}) \quad (10)$$

where:

$G_{mb, N_{ini}}$ = specific gravity of sample compressed with N_{ini}

h_d = Height of compressed sample with N_{des}

h_i = Height of compressed sample with N_{ini}

$G_{mb, N_{des}}$ = Specific gravity of sample compressed with N_{des}

The percentage of the maximum specific gravity of the sample compressed with N_{ini} is calculated as follows:

$$\%G_{mm, N_{ini}} = 100 \frac{G_{mb, N_{ini}}}{G_{mm}} \quad (11)$$

Since P_b (binder content) is an estimated value, the VTM may not meet the 4% air void criterion. Therefore, the volumetric properties are corrected according to the 4% air void using the following equations.

$$P_{b,est} = P_{br} - (0,4 \times (4 - V_a@N_{des})) \quad (12)$$

$$VMA_{est} = VMA@N_{des} + C \times (4 - V_a@N_{des}) \quad (13)$$

$$VFA_{est} = \frac{100(VMA_{est} - V_a@N_{des})}{VMA_{est}} \quad (14)$$

$$Est\%G_{mm,ini} = \%G_{mm,ini} - (4,0 - V_a@N_{des}) \quad (15)$$

$$Est\%G_{mm,m} = \%G_{mm,m} - (4,0 - V_a@N_{des}) \quad (16)$$

where:

$P_{b,est}$ = Estimated bitumen content

P_{bt} = Percentage of bitumen content

V_a = Air void ratio in total mixture compressed with N_{des}

VMA_{est} = Estimated air void in mineral aggregate

$C = 0,1$ (when V_a less than 4%)

$C = 0,2$ (when V_a is higher or equal to 4%)

VFA_{est} = estimated voids filled asphalt

$Est\%G_{mm, ini}$ = maximum estimated specific gravity of the sample compressed with N_{ini}

$Est\%G_{mm, m}$ = maximum estimated specific gravity of the sample compressed with N_{des}

Criteria of the above-mentioned parameters used Superpave mixture design method are given in Table 4 contains with the specification limits.

Table 4. Superpave mixture design criterias

Air voids		%4				
Filler/ bitumen ratio		0,6-1,2*				
Tensile Stress Strength		Min. %80				
Voids in mineral aggregates (VMA)	Nominal maximum aggregate size					
		37,5 mm	25 mm	19 mm	12,5 mm	9,5 mm
ESAL		11	12	13	14	15
	Maximum theoretical specific gravity (%)					
	N_{ini}	N_{des}	N_{max}	Voids Filled Asphalt (VFA)		
< 0,3	≤91,5	50	≤98	70-80		
0,3 - 3	≤90,5	75	≤98	65-78		
3 - 30	≤89,0	100	≤98	65-75		
> 30	≤89,0	125	≤98	65-75		

* These criteria is given as 1.5 in Highway Technical Specification [18]

Samples prepared for each bitumen content are used to determine the optimum amount of bitumen by comparing the air voids and other Superpave criteria. The volumetric properties of the samples are developed as in the Marshall method and the graphs are drawn. The amount of bitumen corresponding to 4% air void in the number of design gyrations is considered to be as the optimum bitumen content.

Conclusion

The aim of this study was to reveal the distinctions between two asphalt mix design methods; Marshall and Superpave. According to the previous studies, there are several major differences between the two methods as follows:

- ✓ Grading of bitumen for Marshall method is penetration grade (PG) while it is performance grade for Superpave method.
- ✓ Superpave method considers the climate and traffic conditions in discordance with Marshall method.
- ✓ Selection of aggregate gradation for these two methods is different. Superpave method has some requirements such as control points and prohibited zones.
- ✓ Samples are compacted with impactation in Marshall method, however, Superpave method requires gyrations which is better simulating the field's compaction.
- ✓ The gyratory press is employed for compaction in Superpave method while Marshall Compactor is used for Marshall method.
- ✓ 4% air void ratio is the main criteria for both Marshall and Superpave methods. But, VMA, VFA, flow and stability values are other criteria which should be considered in order to determine the optimum bitumen content in the Marshall mix design method.

References

- [1] Pérez-Jiménez, F., Martínez, A. H., Miró, R., Hernández-Barrera, D., & Araya-Zamorano, L. (2014). Effect of compaction temperature and procedure on the design of asphalt mixtures using Marshall and gyratory compactors. *Construction and Building Materials*, 65, 264-269.
- [2] Vallerga, B. A. (1951). Recent laboratory compaction studies of bituminous paving mixtures. University of California, Institute of Transportation & Traffic Engineering.
- [3] Maupin, G. W. (1998). Comparison of several asphalt design methods (No. VTRC-98-R15). Virginia Transportation Research Council.
- [4] Habib, A., Hossain, M., Kaldate, R., & Fager, G. (1998). Comparison of Superpave and Marshall mixtures for low-volume roads and shoulders. *Transportation Research Record*, 1609(1), 44-50.
- [5] Brown, R. (2000). 31st Annual Rock Mountain Asphalt Conference. Colorado State University.
- [6] Kanneganti, V. (2002). Comparison of 19mm Superpave and Marshall base II mixes in west Virginia.
- [7] Watson, D. E., Brown, E. R., & Moore, J. (2005). Comparison of Superpave and Marshall mix performance in Alabama. *Transportation research record*, 1929(1), 133-140.
- [8] Nelson, J. W. (2005). Comparison of 9.5 mm Superpave and Marshall wearing I mixes in West Virginia. West Virginia University.
- [9] Namlı, R., & Kuloğlu, N. (2007). Superpave ve Marshall yöntemlerinin deneysel karşılaştırılması. *Teknik Dergi*, 18(87), 4103-4118.
- [10] Keskin, M. (2011). Superpave ve Marshall dizayn yöntemleri ile üretilmiş asfalt numunelerinin fiziksel ve mekanik özelliklerindeki farklılıkların belirlenmesi (Doctoral dissertation, Yüksek Lisans Tezi, Anadolu Üniversitesi, Fen Bilimleri Enstitüsü, Eskişehir).
- [11] White, T. D. (1985). Marshall procedures for design and quality control of asphalt mixtures. In *Association of asphalt paving technologists proc (Vol. 54)*.
- [12] Diazgranados Diaz, D. (2003). Evaluation of 4.75 mm Superpave mix criteria for West Virginia.
- [13] T.C. Bayındırlık ve İskan Bakanlığı Karayolları Genel Müdürlüğü Karayolu Teknik Şartnamesi: Ankara, Karayolları Genel Müdürlüğü., 2013.
- [14] Bayındırlık, T. C., & Karayolu, İ. B. K. G. M. (2013). *Teknik Şartnamesi: Ankara. Karayolları Genel Müdürlüğü.*
- [15] Roberts, F. L., Kandhal, P. S., Brown, E. R., Lee, D. Y., & Kennedy, T. W. (1991). Hot mix asphalt materials, mixture design and construction.

3rd International Students Science Congress
3-4 May 2019, İzmir - Turkey

- [16] Harman, T., D'Angelo, J., & Bukowski, J. (2002). Superpave asphalt mixture design workshop version 8.0. Federal Highway Administration, Washington, DC.
- [17] Superpave Mix Design, 3rd ed., Asphalt Institute: Lexington Kentucky.
- [18] Design, S. M. (1996). Superpave Series No. 2 (SP-2). Asphalt Institute, Lexington, KY.
- [19] Nallamothu, S. H. (2003). Evaluation of binder grades on rutting performance.
- [20] Shane Buchanan, M., & Ray Brown, E. (2001). Effect of superpave gyratory compactor type on compacted hot-mix asphalt density. Transportation Research Record, 1761(1), 50-60.

Review of the Implementation of the Mechanistic-Empirical Pavement Design Guide

*Mohammad Razeq Shakhan**, Dokuz Eylül University, The Graduate School of Natural and Applied Sciences, Turkey

Ali Topal, Dokuz Eylül University, Dept. of Civil Engineering, Turkey

Burak Şengöz, Dokuz Eylül University, Dept. of Civil Engineering, Turkey

Ali Almusawi, Dokuz Eylül University, The Graduate School of Natural and Applied Sciences, Turkey

*Corresponding author: raziqshakhan@yahoo.com

Keywords: empirical pavement design, mechanistic-empirical pavement design guide, advantages of MEPDG

Discipline: Civil Engineering

Abstract

After several decades of development in pavement design systems and accumulation of experience and knowledge, a new generation of pavement design method which is called the Mechanistic-Empirical Pavement Design Guide (MEPDG) was developed by the National Cooperative Highway Research Program (NCHRP) under NCHRP 1-37A research project in the United States of America in 2004. The MEPDG is an advanced and the most sophisticated pavement analysis and design method that calculates pavement structure responses and predicts different pavement performances under the combinations of traffic loading and environmental conditions into consideration of various materials properties. Many states in the United States of America and Canada and other countries have considered adopting the MEPDG to replace the empirical American Association of State Highway and Transportation Officials (AASHTO) Pavement Design Guides. In Turkey, some of the initial works have already been carried out by the General Directorate of Highways (T.C. Karayolları Genel Müdürlüğü), like obtaining the resilient modulus of various subgrade and unbound materials across the country to transition to the MEPDG. Thus, within the scope of this paper; first of all, an overview of the historical development of empirical pavement design method and Turkish Flexible Pavement Design Guide, and highlighting the limitations are given. Also, the advantages and implementation of the Mechanistic-Empirical Pavement Design Guide are reviewed. Finally, a methodology for the evaluation and the implementation of the MEPDG in Turkey are prepared.

Introduction

Pavement structural design is a complex task. Because the pavement exposes under various environmental conditions (e.g., from subzero cold to hot and from dry to saturated moisture conditions) and works under various combination of traffic loading such as axle types, axle spacing, axle wandering, and axle loads distributions that vary throughout the day, month, and season over the whole pavement design life. The response of pavement materials to loads are also quite complex and depends on temperature, moisture, loading rate, traffic volume, and other factors. That is why that American Association of State Highway (AASHTO) developed the empirical pavement design method in 1962 which was titled the AASHTO Road Test. The empirical pavement design methods were updated several times in past decades, such as AASHTO (1972, 1986, and 1993). The AASHTO pavement design guides cannot be updated easily because the empirical design equations are strictly depended to original test conditions that were carried out between 1958-1960. In the other hand, the empirical pavement design methods have no enough capability to adopt significant improvements in pavement engineering, design, improved material properties, and new technologies in the construction field [2][3][4][5][6].

The improvement of material properties and performances, growing of traffic, increasing of tire pressure and axle weight, various climatic conditions, advanced construction methods, developing of personal computers and accumulation of knowledge and experiences provided enough technical infrastructure and motivation to establish a realistic and rational method for pavement structure analysis and designing. Therefore, in 2004, The AASHTO and NCHRP developed the most advanced method in pavement analysis and designing which is currently called the MEPDG. The MEPDG has two parts. The mechanical part calculates pavement structural responses (e.g., stresses, strains, and deflections) based on engineering mechanics law. In the empirical part a series of empirical transfer regression

equations are used to predict the pavement performances (e.g., rutting, load related and non-load related cracking, as well as International Roughness Index (IRI))[6][7]. In 2008, the AASHTO published the first edition of the Mechanistic-Empirical Pavement Design Guide (MEPDG) along with Darwin-ME software and furthermore in 2013, the commercial version of the MEPDG software which is titled to AASHTOWare™ Pavement ME Design (ME Pavement Software) was released. After the development of the MEPDG, some state agencies in the United States of America (USA) have already implemented the MEPDG some others are going to conduct the local calibration of the MEPDG in next future. In 2013, a survey was conducted to identify the MEPDG implementation situation shows that three state agencies have implemented the MEPDG, 28% are trying to implement in the next two years, and half of the state agencies are going to implement in the next five years. [6][8]. Some countries such as Italy [9], Iran [10], New Mexico [11], Egypt [12], Qatar[13], China[14], and Saudi Arabia [15] have collected local design data and conducted the local calibration to facilitate the implementation of the MEPDG. In order to promote the implementation of the MEPDG in Turkey, under TÜBİTAK 105G021 (2006) project, the resilient modulus of subgrade, subbase course, and base course have been obtained from 171 experimental samples that had been collected from all 17 transportation zones. Also, an empirical equation to predict the resilient modulus of subgrade and unbound materials have been developed [16][17].

The objective of this paper is explained as follows;

1. To review the historical development of empirical pavement design methods AASHTO (1962, 1972, 1986, and 1993) and Turkish Flexible Pavement Design Guide (Karayolları Esnek Üstyapılar Projelendirme Rehberi).
2. An overview of the Mechanistic-Empirical Pavement Design Guide and the MEPDG implementation efforts in the USA and other countries.
3. To develop a methodology for verification, local calibration, and validation of the MEPDG to promote the implementation of the MEPDG in Turkey.

Empirical Pavement Design Methods

The pavement design method is empirical when to be developed based on experience or experiment. In other words, the relationship between traffic load, environmental impacts, material responses, and pavement distresses is built based on field observations. In the USA, most of the goods were carried by trains or barges before the 1950s. Therefore, the traffic volume was low on highways. Thus, high engineered pavement structures were not required, and the design of pavement layer thickness solely was based on experiences. In the mid-1950s by increasing the interstate roads better-engineered pavement structures and design standards were highly required. This requirement was met by the American Association of State Highway Officials (AASHTO) and established an empirical regression equation that represents the relationship between the number of traffic load cycling and pavement structural strength, which was measured in terms of serviceability by carrying out the most important and famous road test between 1958 to 1960 in Ottawa and Illinois States in the USA. The AASHTO Road Test formed the base of AASHTO Pavement Design Guides published from 1962 to 1993[1][5][6][4][18].

The AASHTO Road Test (1962)

The AASHTO Road Test (1958-1960) task consisted of 6 loops. The subgrade was recognized as fine grained silty clay. The soil modulus was approximately 3000 psi., maximum asphaltic layer was 6 in., maximum axle load was 48000 lb, and a total 1,114,000 axle loads were applied. The average temperate was varied from 24.5°C to -2.8°C, the annual average precipitation was 863 mm, and the average frost depth was 711 mm. The objective of the AASHTO road test was to develop a correlation between the number of load repetitions, pavement structure strength, and pavement performance. The various axle loads were represented by a single axle load (18 kips) which is called the Equivalent Single Axle Load. The pavement structural load capacity was shown by structural Number (SN). The pavement performance was represented by the Present Serviceability Index (PSI) rating from 5 to 0. The empirical regression equation to correlate abovementioned parameters is shown in equation 1 [1] [5][6].

$$\log(W_{18}) = 9.36 \times \log(SN + 1) - 0.2 + \frac{\log(4.2 - p_t) / (4.2 - 1.5)}{0.4 + 1094 / (SN + 1)^{5.19}} \quad (1)$$

where;

- W_{18} = accumulated 18 kip ESAL for the design life
 P_t = terminal serviceability
 SN = pavement structural number

The pavement performance was represented as present serviceability index (PSI) and developed an equation which is shown in equation 2.

$$PSI = 5.03 - 1.91 \times \log(1 + \overline{SV}) - 1.38 \overline{RD}^2 - 0.01 \sqrt{C + P} \quad (2)$$

where;

- SV = average of slope variance in the wheel paths
 RD = total rutting depth measured in (in.)
 C = surface cracking measured in (ft²/1000 ft²)
 P = surface patching measured in (ft²/1000 ft²)

PSI was numbered from 5 up to 0, which number 5 shows a very good condition and number 0 shows a very poor condition.

The structural number (SN) was calculated by equation 3.

$$SN = a_1 D_1 + a_2 D_2 + a_3 D_3 \quad (3)$$

where;

- a_1, a_2, a_3 = Pavement structural layer coefficients (i.e., surface (0.44), base (0.33), and subbase (0.11))
 D_1, D_2, D_3 = Layer thicknesses (surface, base, and subbase)

The AASHTO Pavement Design Guide (1972)

The AASHTO Road Test empirical equation for pavement layer thickness design was revised and added the following design factors [2] [5].

- To consider the environmental conditions effects on the pavement structural performance the Regional Factor (R) was added to the design equation. The values for R are shown in Table 1.
- The subgrade soil support (Si) was added design formula to consider the influence of local subgrade soil. The Si values varies from 1 which indicates a high plastic clay to 10 that represents crushed stone materials.

Table 2. Proposed values for regional factor (R) [2] [5]

The condition of subgrade material	R
Frozen in winter	0.2–1.0
Dry in summer	0.3–1.5
Wetted in spring	4.0–5.0

In the AASHTO pavement design guide (1972) the equation 4 is used.

$$\log(W_{18}) = 9.36 \times \log(SN + 1) - 0.2 + \frac{\log \left[\frac{\Delta PSI}{(4.2 - 1.5)} \right]}{0.4 + 1094 / (SN + 1)^{5.19}} + \log \frac{1}{R} (S_i - 3) \quad (4)$$

where;

- R = regional factor
 S_i = soil support factor

The AASHTO pavements design guide (1986 & 1993)

The AASHTO 1986 pavement design guide is a revised version of the AASHTO 1972, and the revisions can be cited as follows:

3rd International Students Science Congress
3-4 May 2019, İzmir - Turkey

- Roadbed resilient modulus which can represent better behavior of soil,
- The effect of freezing and thaw on roadbed load bearing capacity,
- Consideration of pavement drainage conditions,
- Consideration of reliability effect.

Generally, The AASHTO 1986 and 1993 pavement design guide are similar because the same design equation was used in both methods. Only some little enhancement can be counted in the AASHTO 1993 like evaluation of existing pavement, back calculation of layered moduli for prediction of structure layer coefficients, and pavement rehabilitation methods[3] [4][5]. The design equation was used in both AASHTO 1986 and 1993 is shown as follows.

$$\log(W_{18}) = Z_R S_0 + 9.36 \times \log(SN + 1) - 0.2 + \frac{\log \left[\frac{\Delta PSI}{4.2 - 1.5} \right]}{0.4 + \frac{1094}{(SN + 1)^{5.19}}} + 2.32 \log M_R - 8.07 \quad (5)$$

where;

W_{18}	=	18 kips ESAL which is predicted for the whole pavement design life
Z_R	=	reliability factor which is selected according to reliability percentage
S_0	=	combined standard error
ΔPSI	=	initial serviceability index minus Terminal index serviceability index
M_R	=	resilient modulus of subgrade (psi)
SN	=	pavement structure number

The concept of design inputs in equation (5) is explained as follows.

Reliability: The reliability effects on pavement structure is considered in term of overall uncertainty of design parameters (S_0) which varies between 0.4 and 0.5 for flexible pavements and reliability factor (Z_R) which is based on reliability percentage.

ΔPSI : The serviceability loss has three components, equation 6.

$$\Delta PSI = \Delta PSI_{TR} + \Delta PSI_{SW} + \Delta PSI_{FH} \quad (6)$$

where;

ΔPSI_{TR}	=	serviceability loss due to traffic
ΔPSI_{FH}	=	serviceability loss due to frost heave
ΔPSI_{SW}	=	serviceability loss due to swelling

W_{18} : The various axles types (single, tandem, and tridem) are converted the Equivalent Single Axle Load (ESAL) which is calculated by equation 7.

$$ESAL = AADT \times T \times T_f \times G \times D \times L \times 365 \times Y \quad (7)$$

where;

$AADT$	=	average annual daily traffic
T	=	% of vehicle
G	=	traffic growth factor
D	=	vehicle percentage in design direction
L	=	vehicle percentage in design lane
Y	=	Pavement design life

M_R : The soil resilient modulus can be obtained by triaxial resilient modulus test in laboratory and it shows the inherent capacity and ability of soil to carry the load.

SN : Indicates the structural strength that is calculated by equation (8).

$$SN = a_1 D_1 + a_2 D_2 m_2 + a_3 D_3 m_3 \quad (8)$$

Which m_2, m_3 = drainage coefficients for base and subbase that ranges from 0.4-1.4 that in original AASHTO Road Test condition were selected 1. The other parameters have been explained before. The SN concept is shown in Figure 1.

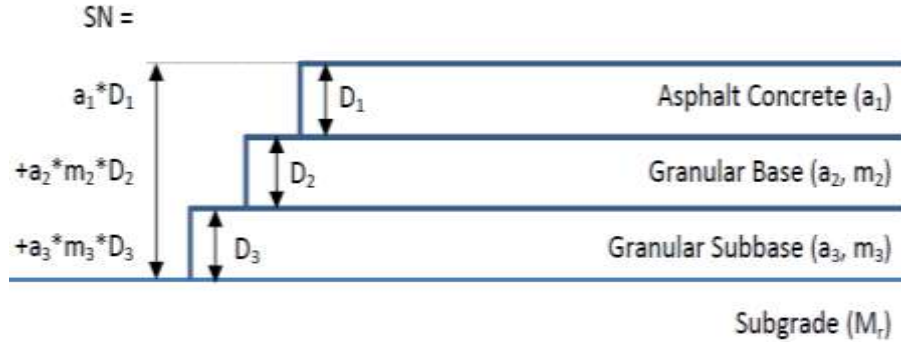


Figure 1. Structural Number Concept [6]

The purpose of equation (5) is to calculate the required SN for a proposed pavement section started from top to bottom (Figure 2). The pavement thickness layers (D_1, D_2, D_3) are calculated through SN and layer coefficients (a_1, a_2, a_3) [4] [5].

$$D_1 \geq \frac{SN_1}{a_1} \quad (9)$$

$$D_2 \geq \frac{SN_2 - a_1 D_1}{a_2 m_2} \quad (10)$$

$$D_3 \geq \frac{SN_3 - a_1 D_1 - a_2 m_2 D_2}{a_3 m_3} \quad (11)$$

Structural layer coefficient. One of the major improvements of AASHTO 1986 is the characterizing of subgrade modulus. But resilient modulus for hot mixed asphalt and base/subbase unbound materials are used in term of structural layer coefficient (a_i), because the AASHTO 1998 and 1993 were developed based on the AASHTO Road Test that structural layer coefficients was used. Structural layer coefficients are empirical values that reflect the relative load-carrying capacity of materials. The recommended values are shown in Table 2.

Table 3. Structural layer coefficient were used in AASHTO Road Test [2] [5]

Roadbed material condition	a_i
Hot Mixed Asphalt	0.44
Granular base	0.13
Subbase	0.11

Turkish Flexible Pavement Design Guide (Karayolları Esnek Üstyapılar Projelendirme Rehberi (2008))

In Turkey, the first technical specification for designing of flexible pavement (Karayolları Esnek Üstyapı Projelendirmesine Ait Fenni Şartname) was published by KGM in 1969. The General Directorate of Highways (KGM) adopted the AASHTO 1972 which was titled to the Flexible Pavement Design Guide (Karayolları Esnek Üstyapılar Projelendirme Rehberi) in 1984. The current Turkish flexible pavement design guide (Karayolları Esnek Üstyapılar Projelendirme Rehberi (2008)) that is based on the AASHTO 1986/1993 has been implemented since 2008 [17]. In this study, the current Turkish Flexible Pavement Design Guide is reviewed and compared with the AASHTO 1993. The pavement structural design equation that is used in Turkish Flexible Pavement Design Guide is shown in equation (12).

$$\log(T_{8.2}) = Z_R \times S_o + 9.36 \times \log(SN+1) - 0.20 + \frac{\log\left(\frac{\Delta PSI}{4.2-1.5}\right)}{0.40 + \frac{1094}{(SN+1)^{5.19}}} + 2.32 \times \log M_R - 8.07 \quad (12)$$

where;

T8.2	=	the number of repetitions of standard axle (8.2-ton) for whole design life
Z_R	=	standard normal deviate
S_o	=	reliability factor
ΔPSI	=	serviceability loss (p_o, p_t)
M_R	=	resilient modulus (psi)
SN	=	structure number (in)

The structural number (SN) and pavement thickness are calculated as follows.

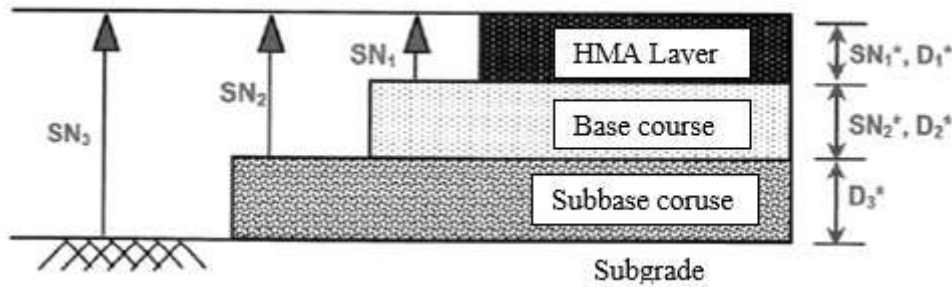


Figure 2. Structural number concept [17]

where;

SN1	=	SN is required on top of base course
SN2	=	SN is required on top of subbase course
SN3	=	SN is required on top of subgrade

$$D_1 \geq \frac{SN_1}{a_1} \quad (13)$$

$$D_2 \geq \frac{SN_2 - a_1 D_1}{a_2 m_2} \quad (14)$$

$$D_3 \geq \frac{SN_3 - a_1 D_1 - a_2 m_2 D_2}{a_3 m_3} \quad (15)$$

It is looked that there is no different between Turkish Flexible Pavement Design Guide (Karayolları Esnek Üstyapılar Projelendirme Rehberi (2008)) and AASHTO 1986/1993.

An Overview of the Mechanistic-Empirical Methods

The ME pavement design methods are known as one step ahead from empirical pavement design methods. The pavement structural responses (stresses and strains) are calculated based on engineering mechanics law, and then the pavement structural responses are transferred to pavement performances (rutting and cracking). In 1953, Kerkhoven and Dormon proposed that vertical compressive strains on the top of subgrade of a pavement can be counted as a failure criterion. In 1960, Saal and Pell indicated that it is possible to control and minimize the fatigue cracking value by decreasing the tensile strength at the bottom of the asphalt concrete layer. In 2004, the most comprehensive and recent ME Pavement Design Method which is called the MEPDG was developed by AASHTO and NCHRP [5]. The basic concept of MEPDG is depicted in Figure 3 as follows.

A pavement with layers thickness (D_1, D_2), layers modulus (E_1, E_2, E_3) and poisons' ratio (μ_1, μ_2, μ_3) is subjected under a single tire load with weight (P) and contact pressure (q), and environmental conditions as shown in Figure 4. Critical locations have been identified at the bottom of the asphalt concrete layer (A) and on the top of subgrade (B). Due to repeated traffic loading, critical point (A) is subjected to tensile strains and stresses while critical point (B) works under compression strains and stresses. The tensile strains are used as design input in the transfer function to calculate the incremental damages based on Miner's law then the incremental damage is transferred to bottom-up cracking. The compression strains and stresses on top of each layer (subgrade, base/subbase, and asphalt concrete layer) are directly transferred to rutting [6].

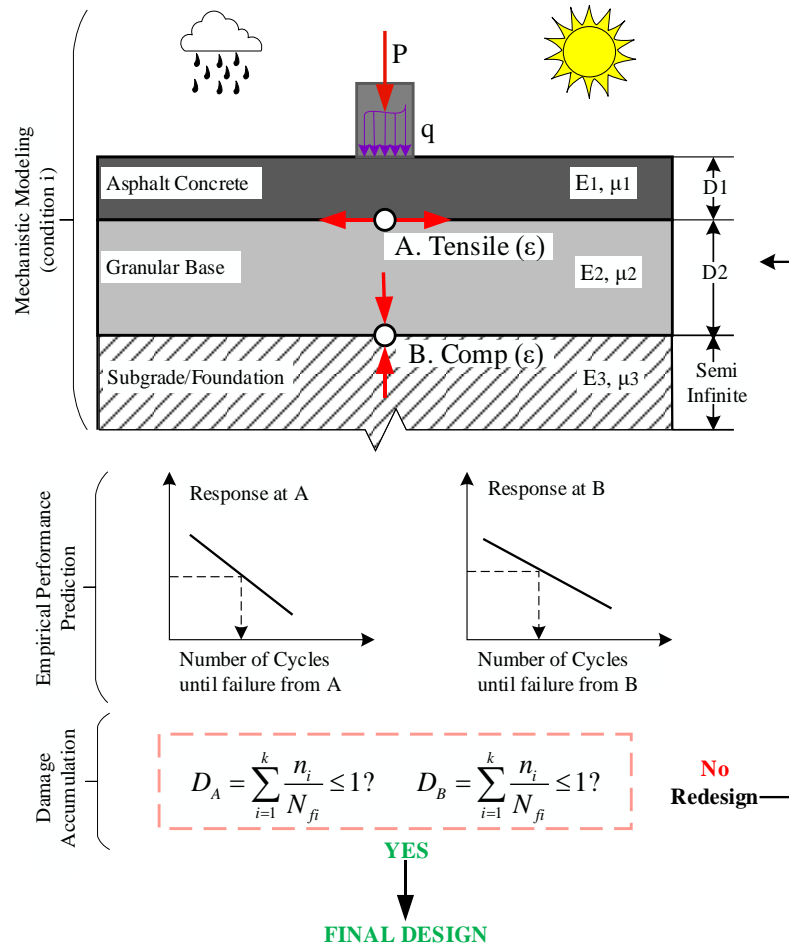


Figure 3. ME Pavement Design Concept [6]

Overview of the MEPDG and ME Pavement Software

In 2004, based on the NCHRP 1-37A project with sponsoring of the AASHTO, the most advance and sophisticated Pavement Design Method which is titled to the MEPDG was developed to alleviate various limitations of the AASHTO Conventional Pavement Design Methods to analyze and design both new and rehabilitated pavement structures according to the Mechanistic-Empirical Law. In 2008, the first edition of the AASHTO MEPDG was published, and at the same time the MEPDG was transferred to software called DARWin-ME. Subsequently, in 2013, the commercial version of the MEPDG software which is titled to the AASHTOWare Pavement ME Design (ME Pavement Software) was released. The MEPDG consists of two models: 1) Mechanistic Model, uses the Enhanced Integrated Climatic Model (EICM), structural response models, and time-dependent material property models to calculate pavement structural responses (stresses and strains) based on engineering mechanics law. Then the pavement responses are used as design inputs to compute incremental damages over time. 2) Empirical Model predicts pavement distresses (rutting, fatigue and thermal cracking as well as International Roughness Index (IRI)) incorporation of transfer equations by using the pavement structural responses/incremental damages as design inputs [6][19]. Three levels of design inputs have been established in the MEPDG based on the quality of data availability and project importance that are briefly explained as follows.

- Level 1 – Site specific and laboratory measured material properties are required (truck class, axle load distribution, dynamic modulus, nonlinear-resilient modulus as well as climate data). This level is proposed for heavily trafficked roads or when high reliability is required.
- Level 2 – Design inputs are estimated through predictive equations (dynamic modulus through Witczak predictive equation and resilient modulus is estimated from CBR values or R-values or layer coefficient ai). This level is recommended to be used for intermediate projects.

- Level 3 – Design inputs are used from software database or regional default values such as (resilient modulus is selected according to soil classification, default vehicle class distribution, axle load distribution, hourly and monthly distribution, and climate data). This level is recommended for minor project of low traffic loads.

The ME Design software is so comprehensive and complex, it operates under the general principles depicted in Figure 4. Each stage is briefly explained as follows.

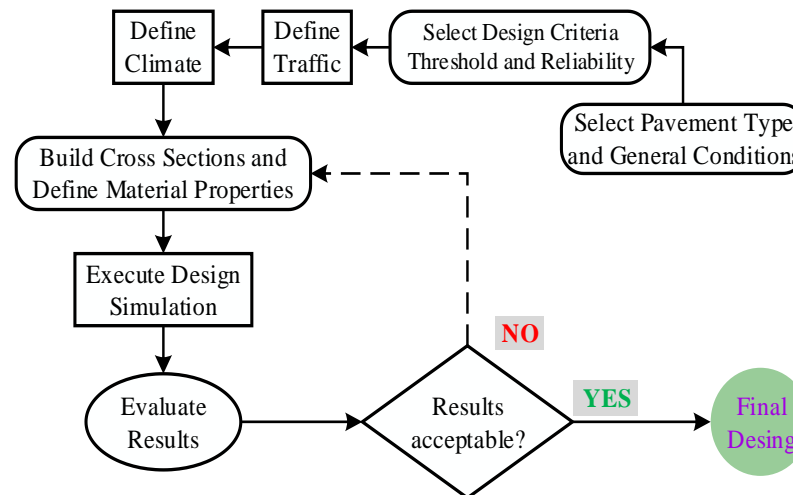


Figure 4. MEPDG & ME Design Software pavement analysis procedure

1. Select pavement type and general information: This is the first stages that designer should select the pavement type (flexible, rigid) to be designed and select the project time line.
2. Select the design criteria thresholds and reliability: In this stage designer should choose which distresses are going to be predicted and related threshold values and level of reliability. The following pavement structural distresses are predicted by ME Design Software.
 - International Roughness Index (IRI)
 - Top-down cracking
 - Bottom-up fatigue cracking
 - Thermal cracking
 - Pavement rutting (Asphalt layer, base/subbase layer, and subgrade)
 - Reflective cracking.
3. Traffic: The ME Design Software requires extensively detailed traffic design inputs which is count the advantage of MEPDG[6][19]. Traffic design inputs as listed below.
 - Traffic volume (annual, monthly and hourly), traffic growth and operational speed
 - Traffic composition
 - ✓ Vehicle class distribution
 - Axle configurations
 - ✓ Axle types, axle spacing, tire spacing and tire inflation pressure,
 - Axle weight distributions factors
 - ✓ May be adjusted on a monthly basis
 - Lateral wander of vehicles
4. Define climate: The ME Design Software uses the Enhanced Integrated Climatic Model (EICM) to calculate the variation of moisture and temperature and freezing and thawing impacts on pavement structural materials and pavement performance. The climate data for the United States of America and Canada have been embedded in software. The calculation of environmental effects on pavement materials is one of the advantages of the MEPDG. The following climatic data are required.
 - Hourly temperature,
 - Hourly precipitations,
 - Hourly cloud cover,

**3rd International Students Science Congress
3-4 May 2019, İzmir - Turkey**

- Hourly wind speed, and
 - Hourly humidity.
 - Groundwater table depth
5. **Build cross sections and material properties:** In this stage the designer adds necessary pavement layers and choose the trail layer thickness. Also, define layer material properties such as dynamic modulus and poison's ratio for hot mixed asphalt layers and resilient modulus and Poison's ratio for the unbound layers and subgrade. The material properties can be specified at three levels. The usage of Dynamic Modulus (E) of hot mixed asphalt and Resilient Modulus (MR) of unbound materials and subgrade are an innovation in pavement design method[5].
 6. **Execute Design Simulation:** After the establishment of the pavement type, design criteria, traffic, climate, cross sections, and material properties the designer may run the software. The ME Design Software runs several ME computations to predict the incremental damages over time for every pavement structural performance (stresses and strains). EICM is run to estimate the layer properties, traffic loads are simulated for each increment, and pavement structural responses are calculated at critical points. The structural responses are used as design inputs in set of transfer equations to predict different pavement distresses.
 7. **Evaluate results:** The AASHTOWare Pavement ME is an analysis software. The designer may compare the predicted distresses to allowable distresses to achieve an optimized design. This step can be time-consuming and daunting for some designers, because there are more than 100 variables to influence on pavement performances. To address this problem sensitivity analysis is done to identify and classify the variables based on their degree of sensitivity. A comprehensive sensitivity analysis may guide local designers to achieve optimized design easily. The possibility of getting an optimized design in the MEPDG is one of the advantages of this method.

Advantages of the MEPDG

The advantages of the MEPDG can be listed as follows.

- Analyze a wide range of truck class distribution, axle load distribution, and tire pressures.
- Consider material specification (dynamic modulus and resilient modulus) which are better relate to pavement performance.
- The ability of characterization of local design data
- The ability to calculate globule aging of materials and climate effects over time.
- Predicts various pavement distresses which can lead to getting the optimized design.

The MEPDG Implementation Efforts

After the development of the MEPDG and releasing the ME Pavement Software, many states inside the United States of America (USA) and some countries have attempted to implement the MEPDG. Although the guide for local calibration of the MEPDG was published by AASHTO in 2010, some agencies did not follow the guide. Instead, they followed their own local calibration methodologies. But interestingly, can highlight some similar activities [8][20][21]. Although the researchers outside of the US have followed the same methods as followed in the US but can be indicated some differences such as local data collection and analysis. Thus, the implementation practice of the MEPDG inside the US and outside the US are reviewed separately.

The MEPDG implementation efforts inside the United States of America

A survey conducted by Pierce and McGovern in 2013 indicates that 3 agencies have implemented the MEPDG and 43 agencies are going to adopt the MEPDG in next five years [8][20]. The research methodologies they followed have similar activities that are explained as follows;

- 1) Preparing local design data;
- 2) Conducting sensitivity analysis;
- 3) Establishment of design thresholds and reliability level
- 4) Evaluation (verification), local calibration and validation of the MEPDG to local materials, climate, and traffic conditions.
- 5) Preparing design manuals, software, and materials for staff training.

**3rd International Students Science Congress
3-4 May 2019, İzmir - Turkey**

- 1) Data collection: Collection and preparation of local design inputs is the first stage of MEPDG implementation. Some of the collected local design data may not be suitable for direct use in ME Pavement Software. Therefore, collected data should be developed and converted to the proper format that is required by ME Design Software.
- 2) Sensitivity analysis: The summary of reports shows that almost all states and countries have conducted sensitivity analysis. Sensitivity analysis is done to identify the degree of influence of design inputs (climate, traffic, and materials properties) on pavement performances (rutting, fatigue and thermal cracking, and IRI) and classifying them based on their sensitivity degree to facilitate the design procedure.
- 3) Pavement performance threshold values and reliability: These elements provide proposed levels of distress, the International Roughness Index (IRI), and reliability for acceptable pavement designs. Every country and state based on their own experiences established threshold values and reliability level.
- 4) Evaluation, local calibration and validation:
 - a. The MEPDG and default calibrated transfer equations are used to predict the pavement distresses for each roadway section. The predicted and measured distresses are compared to evaluate the existence of bias and standard error of the estimate for each distress prediction model for local conditions, specifications, and materials. If significant difference exists between predicted and measured distresses the local calibration is warranted [22].
 - a) Calibration is a mathematical process to eliminate any bias and reduce residual error between measured distresses and predicted distresses [22].
 - b) Validation is a process to check the accuracy of local calibrated transfer functions, if the difference between the predicted and measured distresses is not significant, the MEPDG can be adopted. Otherwise recalibration may be required [22].
- 5) Preparing design manuals, software, and materials for staff training: Design manual and software are prepared to meet the design policies and needs. Training program for pavement design engineers may be conducted through universities, consultants, or national programs.

The evaluation, local calibration, and validation efforts that have been conducted by states agencies are summarized in Table 3 and 4.

Table 4. Summary of Verification/Calibration Efforts by State [20]

State/Region	Sponsoring Agency	Year of Publication	Verification (V)/Calibration (C) Efforts												
			Bottom-up Cracking		Rutting		Thermal Cracking		IRI		Top-down Cracking				
			V	C	V	C	V	C	V	C	V	C			
Arizona	AZ DOT*/FHWA**	2014	✓	✓	✓	✓	✓	✓	✓	✓	✓	✓	✓		
Colorado	CO DOT	2013	✓	✓	✓	✓	✓	✓	✓	✓	✓	✓	✓		
Iowa	IA DOT	2013	✓		✓	✓	✓		✓		✓		✓	✓	
Missouri	MO DOT	2009	✓		✓	✓	✓	✓	✓	✓	✓	✓			
Northeastern States	NY State DOT	2011	✓	✓	✓	✓	✓			✓	✓	✓	✓	✓	✓
North Carolina	NC DOT	2011	✓	✓	✓	✓									
Ohio	OH DOT	2009			✓	✓	✓			✓	✓				
Oregon	OR DOT*/FHWA	2013	✓	✓	✓	✓	✓						✓	✓	
Tennessee	TN DOT	2013/2017	✓	✓	✓	✓				✓					
Utah	UT DOT	2009/2013	✓		✓	✓	✓			✓					
Washington	WA State	2009	✓	✓	✓	✓	✓			✓			✓	✓	
Wisconsin	WI DOT*/FHWA	2009/2014	✓		✓	✓	✓	✓	✓	✓	✓	✓			
South Carolina	SCDOT	2106/2017	✓	✓	✓	✓	✓				✓		✓	✓	✓

*DOT: Department of Transportation, **FHWA: Federal Highway Administration

Table 5. Local calibration coefficients [20][23]

Performance Model	HMA Fatigue			Bottom Up Crackign		Top Down Cracking		HMA Rutting			Base Rutting	Subgrade Rutting
	$\beta f1$	$\beta f2$	$\beta f3$	$C1$	$C2$	$C1$	$C2$	$\beta r1$	$\beta r2$	$\beta r3$	βGB	βSG
National	1	1	1	1	1	1	1	1	1	1	1	1
Arizona	0.73	0.8	0.8	0.73	0.73			3.63	1.1	0.7	0.111	1.38
Colorado	130	1	1.22	0.07	2.35			1.34	1	1	0.4	0.84
Iowa	1	1	1	1	1	0.82	1.18	1	1.15	1	0	0
Missouri	1	1	1	1	1			1.07	1	1	0.01	0.4375
NE States	NR			-0.1	1.28	-1	2	1.308	NR		2.0654	1.481
N Carolina	1.41	2.82	6.67	0.44	0.15			1.018	1	1	1.5803	1.10491
Ohio	1	1	1	1	1			0.51	1	1	0.32	0.33
Oregon	1	1	1	0.56	0.23	1.45	0.1	1.48	1	0.9	0	0
Tennessee	1	1	1	1.02	0.05			0.111	1	1	0.196	0.722
Utah	1	1	1	1	1			0.56	1	1	0.604	0.4
Washington	0.96	0.97	1.03	1.07	1	6.42	3.6	1.05	1.11	1.1	0	
Wisconsin	1	1.2	1.5	1	1			1.016	1	1	0.01	0.5731
South	5	0.8	0.8	0.47	0.47	6.44	0.27	0.24	1	1	2.997	0.397

It can be indicated that most of states out of 13 have tried to calibrate only total rutting and only some few states like Iowa calibrated Subgrade rutting, Base/Subbase layer rutting and HMA layer rutting. In order to calibrate the rutting for all layers separately the forensic investigation is warranted which some states agencies did not conduct the test[24]. Twelve states have efforted to calibrate alligator cracking and thermal cracking, eleven states have calibrated the IRI and only five states have attempted to calibrate the top-down cracking.

The MEPDG implementation efforts outside the United States of America

Recently, some countries such as Italy, Iran, New Mexico, Egypt, Qatar, China, and Saudi Arabia, have been attempting to conduct the evaluation, local calibration, and validation of MEPDG pavement performance prediction model to facilitate the implementation of the MEPDG. The research methodologies they have followed are similar to research methods that state agencies have pursued in the USA which explained in the above paragraph. Almost all countries have reported that data collection and preparation were a daunting and time-consuming task. The lack and deficiency of local design data, as well as collected in improper formats, were a common problem in those countries. Therefore, most of countries used some default design inputs or equivalent data (e.g., climate data) from the USA which might not lead to a proper local calibration and the accuracy of pavement performance prediction model would not be enhanced.

In 2012, Ciro Caliendo attempted to conduct local calibration for alligator cracking, rutting and IRI models to promote the implementation of the MEPDG in Italy. In this regard, some of the design data were collected and analyzed while some others used as defaults. Alabama's climate data was used in Italy because it was recognized to be similar to the local conditions. Italian truck traffic was different from MEPDG for the truck classification schema, vehicle distribution, and axle-load distribution. So, trucks were categorized in 5 classes (4, 5, 6, 9, and 11) and axle load distributions were calculated based on new classification. Level 3 input was used for materials such as dynamic modulus, resilient modulus of base/subbase and resilient modulus of subgrade because no forensic investigation was carried out. Because of the pavement performance data was not available in Italy, the local calibration was conducted by comparing the pavement performances prediction from MEPDG and those predicted by the Italian Method. This calibration method was significantly different from the state agencies pursued method. The study result is shown that MEPDG would overdesign compared to the Italian Method for roads with high traffic level. In contrast, the MEPDG would underestimate compared to the Italian Method for roads with low traffic level [9].

**3rd International Students Science Congress
3-4 May 2019, İzmir - Turkey**

In 2013, M Azadi et al. calibrated the fatigue cracking (alligator and longitudinal) model for the local conditions, climate, and materials in Tehran, Iran. Local design data such as pavement structure, material properties, and pavement performance were obtained from Tehran Municipality and confirmed with forensic investigations. Climate data for Tehran were obtained from Meteorological Organizations in their original formats and then converted to Enhanced Integrated Climatic Model (EICM) format for use in MEPDG software. The authors have provided no information about either local traffic data was used or default traffic data (level 3 entry input). Finally, it was found that default calibrated transfer functions extensively overestimate the fatigue cracking. The fatigue cracking was calibrated and as a result, the local calibration factors ($\beta f_1 = 1.0$, $\beta f_2 = 0.8$, $\beta f_3 = 1.5$) were suggested [10].

In 2013, Rafiqul Tarefder et al. conducted local calibration of MEPDG in New Mexico. Local design data such as traffic, climate, pavement structure, and materials were obtained from the New Mexico Department of Transportation. Pavement performances were measured with the qualitative rating rather than with quantitative measures (depth of rutting or length of cracks) in New Mexico which was not suitable to be used in MEPDG. Therefore, the pavement performances data were analyzed and converted to the proper format required by MEPDG. In this study, the pavement performance prediction models were calibrated [11].

In 2014, A. Elshaeb et al. efforted to conducted sensitivity analysis to assess the impact of Egyptian climate conditions on flexible pavement performance. Climate data (temperature, precipitation, cloud cover, humidity, and wind speed) was collated from World Weather on Line website for 16 cities in Egypt. Three hourly climate data is available on this website; therefore, climate data were converted to hourly by using linear interpolation and then transferred to EICM format. A typical flexible pavement section consists of a 5 cm AC wearing surface [air voids (V_a)=7%, effective binder content (V_{beff})=11.0%, pen 60-70 asphalt binder], 6 cm AC binder course layer (V_a =8%, V_{beff} =10.2%, pen 60-70 asphalt binder), 25 cm aggregate base course layer (resilient modulus; $M_r = 290$ MPa) resting on a subgrade soil ($M_r = 100$ MPa) was chosen, and level 3 traffic inputs were used. The sensitivity analysis result shows that AC rutting value was high in the south part compared to the north part which the weather in south part is hot while the north part is mild. Longitudinal cracking was affected by climate conditions. It was also identified that the alligator cracking was not changed for all climate conditions [12].

In 2014, H. Sadik et al. analyzed and evaluated flexible pavements for different design inputs totally 32 cases to introduce the MEPDG to State of Qatar by using MEPDG software version 1.1. The equivalent climate data from the Needles Airport in California was used. Material properties and specifications of HMA layer, base/subbase layers, and subgrade were selected from Qatar Highway Design Manual (QHDM) and default traffic data were used for all analysis. The influence of asphalt types (Pen 60/70 and PG 76-10) on conventional flexible pavement performance and composite flexible pavement were evaluated and it was found that use of modified bitumen PG 76-10 significantly improved the pavement performance [13].

In 2015, H. Ma et al. carried sensitivity analysis and conducted local calibration of thermal cracking to propose typical pavement structure and facilitate the implementation of MEPDG in China. Three flexible pavements were selected in the northeast area of China to collect design data and calibrate the thermal cracking model. Climate stations in the USA with similar altitudes and climate type were chosen to adapt for selected roadway segments. Default axle load distribution was used instead of local axle load distribution because detailed axle load distribution was not available in China. Level 3 inputs were defined and used for materials. Sensitivity analysis was carried out in MEPDG including design temperature, layer thickness, types of base and subgrade, and air voids of asphalt concrete. It was found that thermal cracking was increased in lower temperature. Local calibration was successfully done, and the longitudinal cracking model MEPDG provided a reasonable prediction on the thermal cracking in the northeast of China.[14].

In 2017, A. Alqaili et al. collected and analyzed local design data for calibration of MEPDG in Central Saudi Arabia. Local design inputs including traffic (Average Annual Daily Truck Traffic (AADTT), vehicle type, vehicle distribution factors, growth rate, daily adjustment factors, monthly adjustment factors, axle load distribution factors, axle per truck, axle configuration, and wheelbase), climate (temperature, precipitation, humidity, wind speed, and cloud cover), pavement structure, material properties, and pavement performances for three selected main roads in Riyadh were obtained

from the Saudi Ministry of Transportation and the Presidency of Meteorology and Environment in Riyadh. Saudi Arabia vehicle classification was not based on the MEPDG standard. Therefore, a new vehicle classification was carried out to be suitable to use in ME Design Software. Default axle load distribution was used for class 4 (bus) because the bus axle load was not measured by weigh in motion stations in Saudi Arabia. Pavement performances were obtained from the Saudi Ministry of Transportation. In Saudi Arabia, pavement performances are measured by using a complex vehicle (Hawkeye 2000) equipped with laser technology and digital cameras [15].

Developing a methodology for implementation of the MEPDG in Turkey

In order to implement the MEPDG for local condition, local data should be prepared and evaluation, local calibration, and validation efforts have to be carried out. Therefore, developing a methodology for data preparation and local calibration is needed. In this study, according to the *Guide for Local Calibration of the MEPDG* [22] a preliminary methodology for local data preparation and calibration of the MEPDG is developed to boost the implementation of the MEPDG in Turkey. The methodology is consisted as follows.

1. Select input level. To select the input level, a comprehensive sensitivity analysis should be done to find out the sensitivity level of local design inputs (materials, traffic, and climate). Highly sensitive inputs can be selected as level 1 and low sensitive inputs can be selected in level 3.
2. Select pavement segments. In this stage, pavement segments with three conditions survey in 10 years are selected.
3. Data Collection. Local design data are collected as following.
 - a. Pavement structure (layers thickness and date of construction).
 - b. Materials (Dynamic modulus, resilient modulus, poisson's ratio, air voids, binder content, etc.)
 - c. Traffic (Vehicle classification, vehicle distribution factors and growth rate, hourly and monthly adjustment factors, axle load distribution factors, etc.). In Turkey, vehicles are classified in five groups (cars, medium goods trucks, buses, trucks, and trailers) which are not supported by the MEPDG. Therefore, a New Trucks Classification should be done to can be used as design inputs in the MEPDG.
 - d. Climate (hourly temperature, humidity, precipitation, windspeed, cloud cover as well as groundwater table depth)
 - e. Pavement distresses (total rutting, alligator cracking, longitudinal cracking, thermal cracking, and IRI)
4. Data analysis. In this stage, the collected data should be analyzed and converted to the MEPDG required format.
5. Evaluation. In this step the prepared local design data are used as design inputs. The pavement distresses are predicted for each selected pavement segments. The predicted pavement distresses are compared to observed pavement distresses. If significant bias and standard error exist between measured and predicted distresses the local calibration should be carried out. The following Null hypothesis should be checked.

$$H^0: \sum_{i=1}^n (Y_{measured} - X_{predicted}) = 0 \quad (16)$$

where;

$Y_{measured}$ = Measured value

$X_{predicted}$ = Predicted value

6. Local calibration. In this stage, the local calibration factors in transfer functions are adjusted to remove the bias and reduce the standard error.
7. Validation. In this stage, the calibrated transfer functions are verified. If the pavement design life is as per local agency standard, the local calibration factors are inserted to ME Pavement Software for further pavement design.

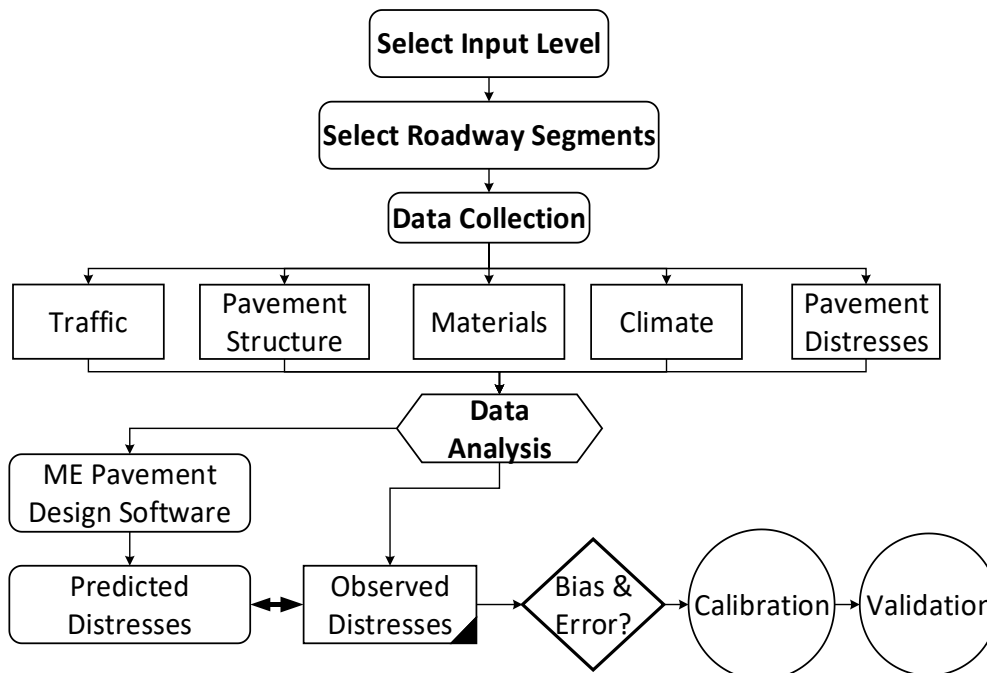


Figure 5. Methodology for local data collection and calibration of the MEPDG in Turkey

Conclusion

1. The AASHTO empirical design methods have been widely used all over the world including Turkey since the 1960s. But these methods due to the nature of empirical have many limitations and significantly limited to the original AASHTO Road Test conditions which was conducted between 1958-1960. Due to various limitations in the AASHTO empirical pavement design and high level of axle load number, most pavement designs conducted today according to the AASHTO 1993 Design Guide are extrapolations which means that pavement thickness can end to overdesign or under-design. The limitations are various and presented as follows.

1.1. One type of subgrade ($MR=3000\text{psi}$) and one climatic zone which may not be suitable to adopt in other regions.

1.2. The maximum thickness of the asphalt concrete layer was 15.24 cm (6 in).

1.3. The test duration was two years. So, the effect of material long term aging on pavement performance was not properly considered.

1.4. The number of traffic axle load was 1.114.000 which any deviation from this limit means extrapolation that may lead to under or over design.

1.5. ESAL is very simple technic than axle load spectra and tire pressure was 70 psi.

1.6. The vehicles and characteristics were used in AASHTO Road Test differ widely from modern vehicles in terms of axle configurations, tire pressures, etc.

1.7. One type of asphalt concrete mixture was used during the AASHTO Road Test. No Superpave, Stone Mastic Asphalt, etc.

1.8. The AASHTO Road Test did not count pavement rehabilitation procedures.

1.9. The AASHTO empirical method did not consider the characteristics of each layer relating to rutting, fatigue, and transverse cracking so, an optimized pavement structural design would not be possible.

1.10. The structural layer coefficients (a_i) are questionable because they are calculating by simple empirical regression constants that is not properly based on engineering rules.

2. Generally, the evaluation, local calibration, and validation efforts that have been carried out inside and outside of the USA can be distinguished with data collection and analysis. Data collection would not be a difficult task for state agencies inside the USA because the Long-Term Pavement Performance (LTPP) is a big database of design data for local calibration efforts. In contrast, lack and deficiency of local design data is a big problem for countries. Therefore, researchers used some default design inputs in local calibration effort which cannot lead to properly develop local calibration factors.

The lack and deficiency of local design data and the problem in local calibration methodology are summarized as follows.

2.1. Pavement Structure and Materials: Some researcher selected a typical pavement structure to conduct the local calibration efforts. Also, almost all researchers used pavement standard design to predict the dynamic modulus and resilient modulus.

2.2. Traffic characteristics: The collection and analysis of local traffic data was a major problem for most of researchers in countries. And most of them have not collected traffic data because the MEPDG requires extensively detailed traffic inputs which makes it a daunting task.

2.3. Climate data: The collection, analysis, and converting of climate data can be cited as a laborious task in countries. Thus, most of researchers used equivalent climate data from the USA.

2.4. Pavement performance: In some countries, the pavement distresses are measured based on qualitatively rating instead of quantitatively. Therefore, the researchers converted them into the appropriate format required for MEDPG.

2.5. Pavement performance threshold values and reliability levels: Design criteria and reliability are very important parameters in implementation of MEPDG. Most of researchers in countries used the MEPDG suggested distresses threshold values and reliability levels.

2.6. Local calibration methodology: The local calibration methods were pursued by most of the state agencies inside the USA and researchers outside of the USA had some similar activities, but the Guide for the Local Calibration of the Mechanistic-Empirical Pavement Design Guide were not followed by most of them.

References

- [1] Highway Research Board (1962) The AASHTO Road Test. National academy of sciences-national research council, Publication No. 1061, Washinton D.C.
- [2] AASHTO (1972) Interim guide for design of pavement structures. American Association of State Highway and Transportation Officials, Washington D.C.
- [3] AASHTO (1986) Guide for design of pavements structures. American Association of State Highway and Transportation Officials, Washington D.C.
- [4] AASHTO (1993) Guide for design of pavement structures. American Association of State Highway and Transportation Officials, Washinton D.C.
- [5] Schwartz CW, Carvalho RL (2007) Evaluation of mechanistic-empirical design procedure. MDSHA Project No. SP0077B41, Maryland State.
- [6] Timm DH, Roobin MM, Tran N, Rodezno C (2014) Flexible pavement design – state of the practice. NCAT Report 14-04, National Asphalt Pavement Association, Ohio.
- [7] NCHRP (2004) Guide for mechanistic-empirical design of new and rehabilitated pavement structures. National Cooperative Highway Research Program, NCHRP Project 1-37A, National Research Council, Washington D.C.
- [8] Pierce LM, Ginger M (2014) Implementation of the AASHTO mechanistic-empirical pavement design guide and software. TRB, National Research Council, Washington D.C.
- [9] Caliendo C (2012) local calibration and implementation of the mechanistic-empirical pavement design guide for flexible pavement design. J. Transp. Eng., vol. 138, no. 3, pp. 348–360. <https://ascelibrary.org/doi/pdf/10.1061/%28ASCE%29TE.1943-5436.0000328>
- [10] Azadi M, Nasimifar SM, Pouranian MR (2013) Determination of local fatigue model calibration used in mepdg for iran’s dry-no freeze region. Arab. J. Sci. Eng., vol. 38, no. 5, pp. 1031–1039. <https://link.springer.com/article/10.1007/s13369-012-0340-0>
- [11] R. Tarefder and J. I. Rodriguez-Ruiz (2013) Local calibration of mepdg for flexible pavements in new mexico. J. Transp. Eng., vol. 139, no. 10, pp. 981–991
- [12] Elshaeb MA, El-Badawy SM, Shawaly ESA (2014) Development and impact of the egyptian climatic conditions on flexible pavement performance. Am. J. Civ. Eng. Archit., vol. 2, no. 3, pp. 115–121. <http://pubs.sciepub.com/ajcea/2/3/4/>
- [13] Sadek HA, Masad EA, Sirin O, Al-Khalid H, Sadeq MA, and Little D (2014) Implementation of mechanistic-empirical pavement analysis in the State of Qatar. Int. J. Pavement Eng., vol. 15, no. 6, pp. 495–511. <https://www.tandfonline.com/doi/abs/10.1080/10298436.2013.837164>
- [14] Ma H, Wang D, Zhou C, Feng D (2015) Calibration on MEPDG low temperature cracking model

3rd International Students Science Congress
3-4 May 2019, İzmir - Turkey

- and recommendation on asphalt pavement structures in seasonal frozen region of china. Adv. Mater. Sci. Eng., vol. 2015, Article ID 830426 pp. 1–11.
- [15] Alqaili AH, Alsoliman HA (2017) Preparing data for calibration of mechanistic-empirical pavement design guide in central saudi arabia. World Acad. Sci. Eng. Technol. Int. J. Urban Civ. Eng., vol. 11, no. 2, pp. 248–255.
- [16] Güngör AG, Ahmet Sağlık A (2009) Mekanistik ampirik üstyapı tasarımında esneklik modülünün şartnamelere uyarlanması. 5th Eurasphalt & Eurobitume, pp. 455–463.
- [17] Karayolları Genel Müdürlüğü (2008) Karayolları esnek üstyapılar projelendirme rehberi. Ankara.
- [18] Huang YH (2004) Pavement Analysis and Design. Second Edition, . Pearson Educational Inc, /Prentice Hall Pearson Education Inc. and Dorling Kindersley Publishing Inc., New York.
- [19] AASHTO (2008) Mechanistic empirical pavement design guide. american association of state highway and transportation officials, Washington, D.C.
- [20] Robbins MM, Tran N, Ga L (2017) Pavement ME Design – a summary of local calibration efforts. NCAT Report 17-07, Ohio.
- [21] Li Q, Xiao DX, Wang KCP, Hall KD, Qiu Y (2011) Mechanistic-empirical pavement design guide (MEPDG): A bird's-eye view. J. Mod. Transp., vol. 19, no. June 2, pp. 114–133. <https://www.springerprofessional.de/en/mechanistic-empirical-pavement-design-guide-mepdg-a-bird-s-eye-v/10909004>
- [22] AASHTO (2010) Guide for the local calibration of the Mechanistic-Empirical Pavement Design Guide. American Association of State Highway and Transportation Officials (AASHTO), Washington D.C.
- [23] Kargah-Ostadi N, Menendez JR, Zhou Y (2018) Using Multi-Objective Optimization to Enhance Calibration of Performance Models in the Mechanistic–Empirical Pavement Design Guide. Fugro Consultants, Inc. 8613 Cross Park Drive, Austin, TX 78754, McLean State.
- [24] Kim YR, Jadoun FM, Hou T, Muthadi N (2011) Local Calibration of the MEPDG for Flexible Pavement Design, Final Report. Project No. HWY-2007-07, North Carolina State University, North Carolina.

Public Bus Network Evaluation: A Guide for Benchmarking

H S Abdulrahman, Dokuz Eylül University, Graduate School of Natural and Applied Sciences, İzmir, Turkey*

Mustafa Özüysal, Dokuz Eylül University, Dept. of Civil Engineering, İzmir, Turkey

**Corresponding author: ahas92@yahoo.com*

Keywords: benchmarking, public transport network, evaluation

Discipline: Civil engineering

Abstract

There are many systems and tools which can be used to evaluate the public transport (PT) networks be it in terms of quality and quantity. Many different performance measures exist largely due to varying field of application which are predominantly used in trend analysis, benchmarking, comparison, target setting, system improvement, and may also be used as incentives for managers and employees. Benchmarking is one of the many tools used for improvement of quality in management and can be said to be a process of identifying best management practices that an organization can emulate. In transportation organizations however, it can be used to highlight areas of low or high performance and to show where an organization is in ranking. This study focuses on PT network evaluation using basic performance indicators as a foundation for the implementation of benchmarking process. İzmir a city in Turkey is used as a case study and compared to some cities in Europe, Asia and Australia. This work can be used as a preliminary guide for evaluating PT systems by providing a basis for comparison, identification of peers, and to serve as initial step for the implementation of benchmarking.

Introduction

Modal share of public transportation(PT) is on the decline in most developing cities. The dangers of using personal mobility are well documented in literature; which includes: traffic congestion, pollution, reduction of public spaces and because of these externalities might lead to social exclusion, loss of productivity and time to mention a few.

To curb these menaces a sustainable solution by many cities encourages the use of PT (or mass transport) even though implementation of such simple policies can be a daunting one. These challenges mostly boarders around political, institutional and even a cultural one. Additionally, they require huge investments in infrastructure development and operating costs to meet the supply gap and to cope with huge demands which in most cases are scarce. Thus, there is a pressing need to ensure that whatever resources are available for transit services are put to the most effective and efficient use possible. Low cost approaches like improving service quality, accessibility and customer perceptions are however a viable solution but often neglected.

As a logical way of thought, before one can think of managing or improving a service or a system, one must be able to measure or estimate its base condition. According to a report on sustainable transportation, states that “there are no mechanism which can assess if the available transport mode is fulfilling their expectations and meeting various standards regarding environment, safety, equity, comfort etc. in most cases there are no standards”. Provision of a guide which can be used as tool for continuous monitoring and serve as basis for comparison and improvement is important especially if we are to attain a sustainable public transport [3]. Difficulties posing sufficient threat to sustainable PTs mainly stems from other modes of transportation particularly private transportation thus creating a stiff and competitive atmosphere for PTs to thrive. Therefore, necessitating the need for continuous improvement of PTs to attract more users. To improve any system one will need an objective assessment tool which can be used to gather information, make comparisons, draw valuable conclusions and consequently implement. Benchmarking is one of such tools for achieving this kind of objective [6]. Benchmarking starts from comparison of performance indicators and then leads to exchange of good practices. This management tool can be used as a guide towards sustainable PT. This study focuses on the use of basic performance indicators as a foundation for the implementation of benchmarking process. İzmir a city in Turkey and has well developed mass transportation system is used as a case study and it is compared to some cities in Europe, Asia and Australia.

Benchmarking

There are many management tools used for improvement of quality such as quality loop, self-assessment methods, benchmarking, standardization and certification, quality partnership etc. In 1970s Xerox corporation is credited to be the first company to have used benchmarking tool [8].

Benchmarking offers the opportunity to organizations to foresee areas with potentials for improvement through comparisons and search for industry's best practices that lead to better performance [2]. A benchmark is an existing, projected or reference condition that is not implemented thus, benchmarking is a process of identifying best management practices that an organization can adopt and copy. It can be used to highlight areas of low or high performance and to show where an organization is in ranking. To expatiate further, it can be said to be a structured approach to gathering, sharing of data, information, ideas and methods with the objective of comparison between partner groups which will be of mutual benefits [5].

According to TCRP,2010 “ it is a process of seeking out best practices to emulate. It involves direct contact with other organisations, delves into reason for their success, seeks to uncover transferable practices applicable to the organisation performing the analysis”[11].

A step wise methodology for benchmarking suggested by TCRP, 2010 is depicted Figure 1 below;

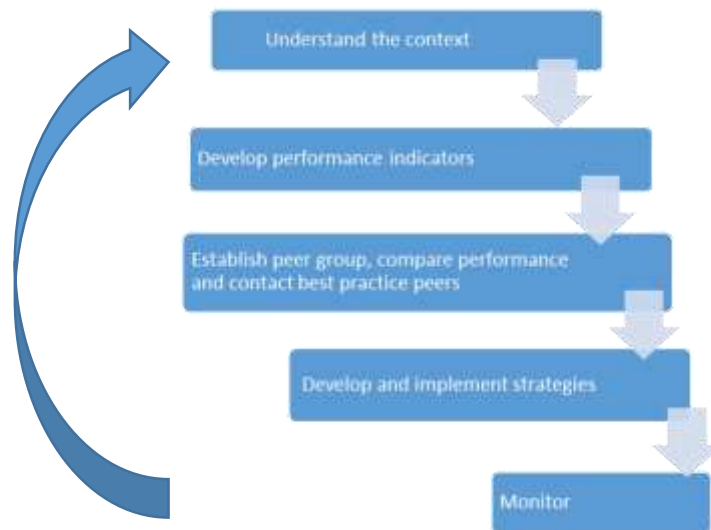


Figure 1. A stepwise methodology for benchmarking (Source; [11])

Benchmarking can be broadly categorized into two, namely;

1. Cooperative benchmarking
2. Collaborative benchmarking

In cooperative benchmarking the organizations decides the topics where performance improvement is needed and contact other organizations to obtain good practices. This is mostly used by PT organizations who can identify comparable agencies through established data collection of urban mobility indicators. While on the other hand collaborative benchmarking involves partner organizations exchange ideas, information, and good practices on issues of common interests, all expecting to achieve a higher levels of performance. Usually a third party coordinates the process and when such groups agree to meet on regular basis a benchmarking network is formed.

Benchmarking is an iterative process composed of a set of consecutive steps. It can be performed at different levels of complexity that result in different levels of depth of understanding and direction for improvement.

Broadly speaking, it is composed of four discrete and consecutive steps which is easily recognizable in the following steps below;

1. Self-analysis
2. Partnering

3. Learning
4. Implementation

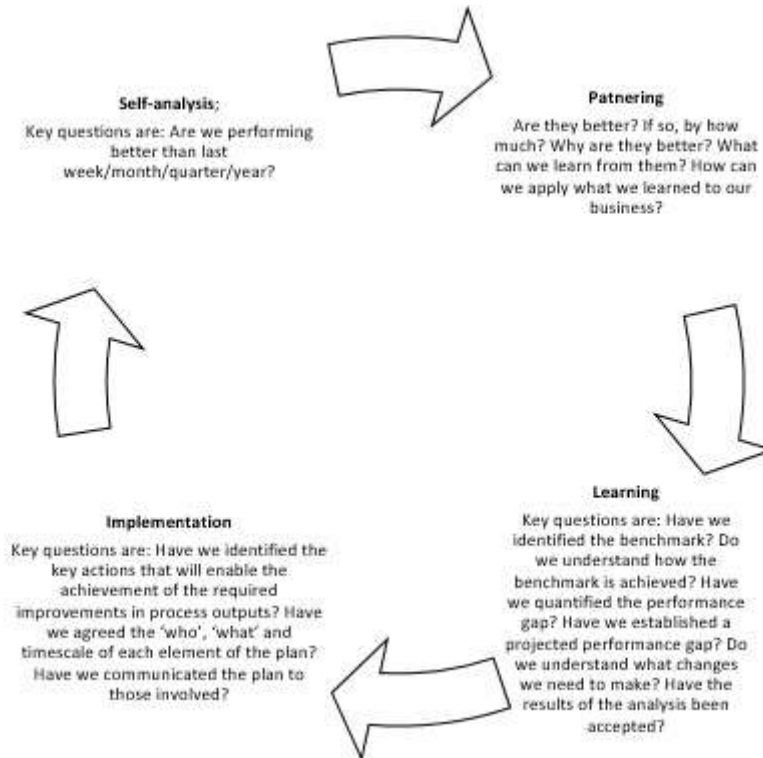


Figure 2. Benchmarking cycle

Self-analysis or trend analysis deals with performance measurement and selection of those performance topics that will further be explored. PT agencies develop indicators to measure their own performance and compare against peer performance levels or minimum performance standards to point out areas where PT agencies are underperforming. Analysis can show whether a transit agency is improving in areas of interest over time, such as carrying more rides, collecting more fare revenue, or decreasing complaints from the public even though it does not gauge how well an agency is performing relative to its potential. To move to the next level of performance evaluation, a peer comparison should be conducted.

Potential improvement can then be identified by comparison against other agencies or peer agencies. How are we performing in relation to comparable agencies? Similarity is initially determined by benchmarking topics and partners should share common characteristics. Peer selection relies on databases for many PT organizations in the US while in Europe no such database exists or is few [11]. No direct contact or sharing of knowledge occurs between agencies, other than knowledge that can be obtained passively obtained through an Internet search may or may not be anonymous. Key questions are:

The Third stage is a direct agency contact: What can we learn from our peers that will help us improve our performance? It is comparative analysis and tracking of best practices which takes place in the learning stage of the process. This stage represents the start of true benchmarking. At this level, the transit agency performing the comparison makes direct contact with one or more of its peers. More-detailed information and insights can be gained through this process than from a simple reliance on a database. Some of the reasons why this stage is important are listed below;

1. One reason for directly contacting other peers is that the measures required to answer a performance question of interest are simply not available from national databases.
2. to gain insights into what the agency's top-performing peers are doing to achieve their superior performance in an area
3. to obtain background information about a transit agency (e.g., agency policies or board composition) and to verify or ask questions about unusually high or low results

At the final stage the benchmarking agencies update their performance goals in view of comparative analysis and develop a plan to implement.

Although benchmarking was not used by PT organizations initially, it can find use and applications especially in the areas of financial performance, quality of service improvement, personal security on PT, fare policy and production costs are all examples where some researches have been conducted ([7], [12], and [10]). Other aspects are in transport policy where it can be used to show valuable policy or policies from similar organizations which have not been used previously [4]. It can also be used as a minimum standard for measuring performance either in comparison with itself during self-analysis or can be used as performance based contracts between PT authorities and operators

Benchmarking should not be confused with performance measurement as they are different concepts. Performance report is definitely not the end result of a benchmarking effort, rather it aids it by providing a set of indicators that are used to learn and improve on. The core concept of benchmarking is obviously perceived to be the notion of comparison, but to compare is not to benchmark. Comparison is static but benchmarking changes and requires further inputs in terms of learning, improvement and taking action. In most cases performance measurement or evaluation forms the very first step for any benchmarking process.

The concept is relatively new to PT organizations but there has been some international efforts and attempts to benchmark or benchmarking in transport sector. Notable efforts are listed below;

1. CoMET and NOVA: they are an international railway benchmarking clubs with main aim of comparing the urban rail systems of various cities in the world.
2. The Urban Transport Benchmarking Initiative (2003-2006) This three-year initiative benchmarked different aspects of 45 participating European cities' transport system <http://www.transpobenchmarks.eu>
3. EQUIP (1999-2000) The European Union Urban Transport Benchmarking Initiative was mainly to develop a self-assessment benchmarking handbook that will offer indicators for measuring the internal efficiency of land-based local public transport operators in EU. http://www.transport-research.info/web/projects/project_details.cfm?id=289
4. The Millennium Cities Database (2001): Mobility in Cities Database (2006)- The Millennium Cities project involved the compilation of a database of data from 100 cities in order to compare their transport systems.

<http://www UITP.org/publications/pics/pdf/MILE.pdf>

<http://www UITP.org/publications/Mobility-in-Cities-Database.cfm>.

The initiatives listed above all tend to measure aspects of operations, quality, information, user perception, transport access, energy and environmental impacts and so on as it concerns public transport.

Public Transportation System in İzmir, Turkey

İzmir Metropolitan Municipality had a population of some 3.35 million in 2010, with the areas immediately surrounding the city adding a further 0.6 million. Urban bus is the main means of public transport in the municipality, providing citywide coverage and carrying 86.5% of all passengers in 2010; metro carried 9.5% of passengers, ferries 3%, and suburban rail about 1% [13]. Even in Turkey, İzmir has one of the most developed and well integrated PT in the country and it can boast of quite a number of different modes Aysin (2011).

Public transport in İzmir consists of the following:

- Urban bus services, operated by ESHOT and Izulas, with 1,560 vehicles
- Urban ferry services, operated by Izdeniz; 24 ferries, using 8 quays
- Metro rail, operated by İzmir Metrosu; 1 line, launched in 2000
- Suburban commuter rail, operated by IzBan; 2 lines, launched in 2010
- Hinterland bus services, operated by ESHOT
- Hinterland paratransit services, operated by dolmus

No data were made available on public transport mode share, although this varies greatly across the metropolitan area. Public transport has a relatively high modal share for trips entering the central area during the peak hours (>50% on some corridors [13]. This quickly tapers off with distance from the center. Private car is the dominant mode outside the center, and paratransit dolmus (minibuses and

shared taxis) provide most of the public transport for suburban and peripheral travel. Cycling and walking have low mode shares, despite being favored in policy terms. Taxis are deregulated, plentiful, and relatively expensive (fuel is heavily taxed), and have a low share of the total travel market. Table 1 below gives PT system Characteristics of İzmir

Table 1. İzmir Public Transportation Characteristics [9]

	ESHOT	Izdeniz	İzmir Metro	Izban	Tramway
Number of stations/stops	8247	8 terminals	17	40	33
Number of cars	1,561.	24	182	73	38
Length(Km)			20.1	136	21.6
Number of routes/lines	320		1	1	2
Average daily passenger	2,832,909 approximately	50,000 approximately	350,000 approximately	300,000 approximately	110,000 approximately

What is more, Table 2 gives the break down for Bus transit

Table 2. Bus Transit [9]

Year	Number of bus stops	Number of passengers	Number of buses
2013	6915	276	1705
2014	7197	267	1604
2015	7969	253	1570
2016	8106	253	1660
2017	8247	248	1683

A general look at the trend analysis, in the Figure 3 below shows a comparison of annual ridership of different transportation between modes for the year 2013-2017. Bus transit still remains the most dominant PT system in İzmir even though a gradual decrease in ridership is noticed between the years in review. This might largely be due to improvements and development in other modes of transportation. As at 2017 the PT modal share is shown in Figure 4 which shows Eshot buses having the largest share of the annual ridership with the new tramway recording the lowest percentage.

In general terms İzmir's PT system is well developed and diverse modes which is gradually moving away from bus transit. However, not all cities have this number of modes but convey as much passengers or more. Leading this study to try and search for potential pairs by evaluating similar characteristics and comparing them to see if there is a potential benchmarking partners.

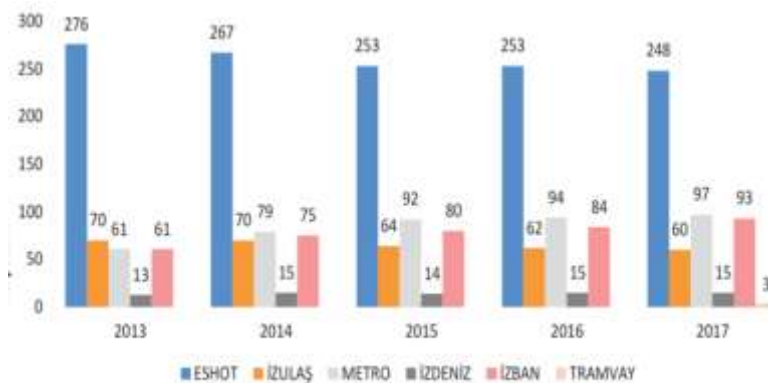


Figure 3. İzmir PT system Annual Ridership [9]

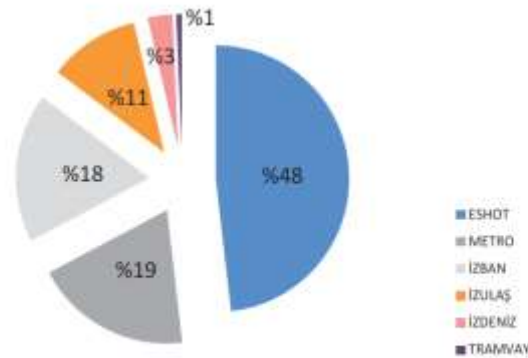


Figure 4. İzmir PT system Percentage Distribution of Ridership [9]

Some Public Transportation Evaluation Studies

A study conducted by Chhavi, 2011 on PT performance evaluation of some countries are presented in Table 3 below. These cities are well studied and well documented. These cities are compared to İzmir in a peer analysis under the following headings

1. Basic geographic and demographic
2. Existing transportation modes
3. Share of public transports

Table 3. Peer comparison [3]

	Singapore	Kuala Lumpur	Sydney	Helsinki
Area (km ²)	710	243	2500	5518
Population (million)	5.1	1.7	2.5	1.3
Modes	Rail, bus	Rail, bus	Rail, bus, ferry	Tram, metro, bus, ferry
Modal share (%)	59	14	14	32
Total number of buses	4100	978	1900	
Total number of station	130	49		
Number of bus routes	261	165	300	
Total PT ridership	5.4 million passengers/day	750,000 passengers/day	200 million passengers/year	196.1 million passengers/year (buses: 82.4, Tram:54.9, Metro:57.3 and Ferry:1.5)

Peer analysis

There are several reasons why a transit agency might want to perform a peer comparison: for example, to support an agency's commitment to continual improvement, to validate the outcome of a past agency initiative, to help support the case for additional funding, to prioritize activities or actions as part of a strategic or short-range planning process, or to respond to external questions about the agency's operation. In a peer comparison, an agency compares its performance against other similar agencies that have contributed similarly collected data to a centralized database, which may or may not

be anonymous. No direct contact or sharing of knowledge occurs between agencies, other than knowledge that can be obtained passively (e.g., from documents or data obtained through an Internet search)

The peer grouping process is perhaps the most important step in the benchmarking process. Inappropriate peers may lead to incorrect conclusions or stakeholder refusal to accept a study's results. For high-level performance comparisons, peers should have similar sizes, characteristics, and operating conditions. One should expect peers to be similar, but not identical. Different peer groups may be needed for different types of comparisons. Figure 5 below makes a comparison between a city in Turkey, İzmir with countries Singapore a city state, Kuala Lumpur, Malaysia, Sydney, Australia and Helsinki, Finland. All these cities were selected because we could source for these data easily and making the search for potential cities to form a peer. The main aim is to find information or facts which expresses basic city facts and urban transport characteristics. Basic indicators such as modal split, number of PT stops, fleet size, demographic information like population, size of area covered and some key performance indicators like ridership etc.

İzmir as a city has a larger area to be covered and has more modes of PTs it is however well below Singapore in daily ridership even though it has lesser modes of transportation with only two and more population and yet able to achieve an impressive 59% modal split. One may begin to ask questions like how possible are these results? On the other hand, Helsinki with equally large area to cover has quite an impressive modes of transportation with 32% modal split showing a trend where cities with larger areas to cover having more modes of travel and vice versa. In a similar fashion city with fewer modes have much lesser % of modal split with Singapore being an exception having the highest modal split with only 2 modes of transportation. According to the data Singapore has the highest ridership when compared to the population. Thus the ranking of these cities can be seen from the figure via different classifications.

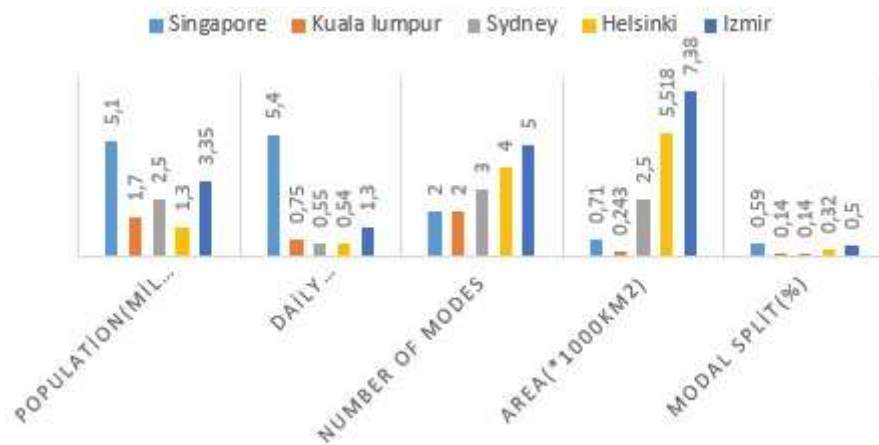


Figure 5. Peer comparison analysis

Conclusion

This study demonstrates how preliminary information about public transportation in various countries can be used to kick start a discussion on the possibility of a benchmarking process for a developing transportation system. At the initial stages of benchmarking not much can be achieved only trend analysis or self-evaluation and peer comparison analysis that can be achieved because it requires less data and at this stage it requires no formal communication with potential PT organizations

In our case no single case matches exactly with the case study but all selected peers have something in common thus generating the possibility of formulating different peer groups for different purposes.

As a recommendation individual benchmarking strides should start from searching for peer partners who are willing to provide concrete information on their services to allow for solid initial comparisons and to recognize good practices within the peers and the need to improve on collective goals and objectives.

**3rd International Students Science Congress
3-4 May 2019, İzmir - Turkey**

İzmir compares well with other cities with only Singapore having a more impressive percentage modal split and more annual ridership of PT. Helsinki for example has also diverse modes like İzmir. Thus there is need to set up different benchmarking groups for different benchmarking purposes as no single peer matches exactly with the case study. Also a more detailed comparison requires more information from these organizations. If there is to be any hope of setting benchmarking peer and subsequently learning and implementation of the improvements learned.

Some of the potential benefits are:

1. Providing an up to date, comprehensive and comparable performance data;
2. Providing opportunity for PT organizations to improve their performances quickly by learning from others with better performance;
3. Identifying good practices and implementing changes;
4. Providing organizations with continuous performance improvement;
5. Establishing a forum for organizations to share their experiences and exchange information; and Building a knowledge network mechanism to encourage development in the urban transport sector for transition and developing countries.

References

- [1] Aysin NY (2011) Integrated public transport in İzmir, Barcelona conference, CODATU
- [2] Camp RC (1986) The Search for Industry Best Practices That Lead to Superior Performance. ASQ Quality Press, Milwaukee, Wis., 1989.
- [3] Chhavi D (2011) Measuring Public Transport Performance: Lessons for developing Cities. Sustainable Urban Transport Technical Document #9. <http://www.giz.de>
- [4] Fearnley N, Gordon L, and de Vileger JTT (2002) Benchmarking transport Policy: the use of benchmarking in effectively developing and implementing transport policy. Paper presented at the European Transport Conference(AET) 2002, Cambridge, UK.
- [5] Geerlings H, Klementsitz R, Mulley C (2006) Development of a methodology for benchmarking public transportation organizations: a practical tool based on an industry sound methodology. Journal of Cleaner Production 14, 113–123.
- [6] Georgios, G. (2012). The role of benchmarking in Public transport: the case of Thessaloniki, Greece. Procedia-Social and Behavioral Sciences 48(2012)2577-2587
- [7] Henning, T.F.P., Muruvan, S., Feng, W.A., Dunn, R.C. (2011). The development of a benchmarking tool for monitoring progress towards sustainable transportation in New Zealand. Transport Policy, 18(2), 480-488.
- [8] Hillkirk, J. (1986). Xerox: American Samurai. Macmillan, New York, 1986.
- [9] İzmir Büyükşehir Belediyesi, ESHOT Genel Müdürlüğü (2011 – 2017) Faaliyet Raporu, İzmir
- [10] Taylor, N. (2006). The Urban Transport Benchmarking Initiative Year Three Final Report, European Commission.
- [11] TCRP (2010) Ryus,P., Coffel,K.,Parks,Perk,V., Cherrington, V., Arndt,J., Nakanishi,Y. and Gan A., A Methododolgy for Performance Measurement and Peer comparison in Public Trsansportation Industry. TCRP Report 141, Transportation Research Board. Washington , D.C. 2010, http://onlinepubs.trb.org/onlinepubs/tcrp/tcrp_report_88/Guidebook.pdf
- [12] Trel E, Van de Velde D (2008) Benchmarking municipal public transport operators in the Netherlands.Paper presented at the European Transport Conference(AET) 2008, The Netherlands.
- [13] World bank (2011) Tool kit on Intelligent Transportation Systems for Urban transport. <https://www.ssatp.org/sites/ssatp/files/publications/Toolkits/ITS%20Toolkit%20content/case-studies/izmir-turkey.html>

Sonlu Elemanlar Yöntemi ile Modellenen Tekerlek Paletlerinin Kıyaslanması

*Mahyar Jafarzadyeganeh**, Ege Üniv., Fen Bilimleri Enstitüsü, Ulaştırma Anabilim Dalı, İzmir, Türkiye
Mesut Tığdemir, Süleyman Demirel Üniv. İnşaat Mühendisliği Bölümü, Ulaştırma Anabilim Dalı, Isparta,
Türkiye

Brou André Venance Koffi, Ege Üniv., Fen Bilimleri Enstitüsü, Ulaştırma Anabilim Dalı, İzmir, Türkiye
*İletişimden sorumlu yazar: mahyar.yeganeh1993@gmail.com

Anahtar kelimeler: sonlu elemanlar analizi, modelleme, kar paleti

Disiplin: İnşaat Mühendisliği

Özet

Soğuk hava şartlarında meydana gelen trafik kazalarının büyük bir bölümü araba lastiklerinin yola tutunamaması sonucunda frenleme mesafesinin uzamasından meydana gelmektedir. Bu nedenle trafik kuralları gereği, özellikle ticari taşıtlarda hava sıcaklığı, 7 °C'nin altına düştüğünde kış lastiği kullanmak zorunlu hale gelmekte ve tüm taşıtlar için lastik zinciri bulundurma zorunluluğu bulunmaktadır. Mevcut kar zincirleri lastiğe ve yol yüzeyine zarar vermektedir ve ayrıca da kullanımı zordur. Günümüzde, yola tutunma özelliği bulunan farklı desen ve özelliklerdeki polimer malzemelerden üretilen paletler pratik takılması sebebiyle tercih edilmektedir.

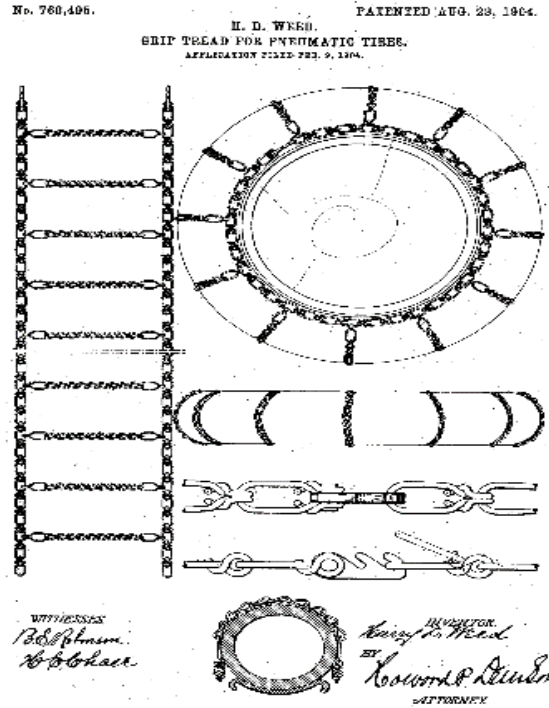
Sonlu elemanlar yöntemi, teorik olarak çözümü karmaşık olan problemlerin incelenen yapının daha basit sonlu sayıdaki alt elemanlara ayrılarak yükleme ve sınır şartları altında matrislerle ifade edilen davranışının analizine dayanan bir yöntemdir. Bu yöntem, deneysel metotlara göre daha kısa sürede ve maliyette doğru sonuçlar verebilmektedir. Bu çalışmada, sonlu elemanlar yöntemi kullanılarak desen olarak farklı iki modelde tasarlanan kar paleti taşıt lastiğine takıldığında kar kaplı bir yol üstyapısında ve tekerlekte meydana gelen deformasyon ve gerilmeler incelenmiştir. Farklı iki desende ki kar paletlerinin taşıt lastiği yol tutuşuna olan etkisi araştırılmıştır.

Giriş

Kış tekerleği ilk defa 1934 yılında Nokian Tires şirketi tarafından üretilmiştir. Başlangıçta kamyonetlerde zincir yerine kullanılması amacıyla üretilmiştir. 1936 yılında sedan araçlar için aynı şirket tarafından üretime geçilmiştir ve Hakkapeliitta tekerleği olarak adlandırılmıştır [1]. Otomotiv sanayi geliştikten sonra ilk defa Harry D. Weed tarafından 1904 yılında tekerlek zinciri New York'ta üretilmiş olup zincirin patent resmi Şekil 1'de görülmektedir [2]. Soğuk havalarda kış tekerleği takmak zorunlu olup, özellikle karlı günlerde ve buzlu zeminlerde güvenli sürüşü sadece kış tekerleği ile sağlamak mümkün değildir. Sürücülerin direksiyon hâkimiyetini sağlamakta güçlük çektiği bu aşamada güvenlik sağlayıcı unsur olarak kar zinciri ve kar paletleri kullanılmaktadır. Paletler farklı ebatlarda ve desenlerde üretilmektedir. Bunlar, hava sıcaklıkları düştüğünde tekerleğin boşa dönmesini engellemekte ve istemsiz kaymalara karşı en iyi koruma sağlamaktadır. Kar zincirinin çeşidini sürücü belirlemektedir. Fakat kar zincirinin kullanılması yasal bir zorunluluktur.

Cho, vd. [3], çalışmalarında üç boyutlu tekerlekte dönme direnci ve sıcaklık dağılımı için sayısal yöntem geliştirmeye çalışmışlardır. Devirli olarak desenlenen tekerlek modelleri, bir yapının dairesel dönmesi ile oluşturulmuştur. Histerezis kayıpları, şekil değiştirme elemanlarından ve ısı transferi analizlerden elde edilmiştir. Bu çözümlemede dönme direncinin bilgisayarda analizi ile deneysel analiz arasında %13'ten daha düşük hata olduğu tespit edilmiştir. Ayrıca tekerlek dişlerinin dönme direncine de %40 katkı sağladığı gözlemlenmiştir. Hız artması sonucunda ısı oluşum oranı ve pik sıcaklık, doğrusal orantıda artmaktadır, ancak bu durum toplam histerezis kayıp ve dönme direncinde düşüş göstermiştir. Tekerlek dişlerinin deseni dönme direncinin, pik sıcaklık ve dağılımlarında önemli rol aldığı gözlemlenmiştir.

3rd International Students Science Congress
3-4 May 2019, İzmir - Turkey



Şekil 1. Harry D. WEED tekerlek zinciri [2]

Materyal ve Yöntem

Kar palet modelleri ve tekerlek modeli SolidWorks programında tasarlanmıştır. Daha sonra ANSYS Design Modeller programında palet temas yüzeylerindeki kar malzemesi 1.8 m × 1.4 m × 0.2 m ebatlarında hazırlanmıştır. Hazırlanan modellerin analizleri ANSYS Explicit Dynamics programı ile yapılmıştır. Analizde lastik için kullanılan Mooney-Rivlin modeli parametreleri Tablo 1’de verilmiştir.

Tekerlek tasarımı Falken firması tarafından üretilen, ZIEX ZE-912 üretim koduna sahip olan, 195/50R15 özellikli tekerlek örnek alınarak hazırlanmıştır (Şekil 2). Ebat özellikleri 195/50R15 olan tekerlek desenine 8 mm diş derinliği verilmiştir. Şekil 3 ve 4’te gösterilen tekerlek bileşenleri olan ipler ve teller SolidWorks programında tekerlek içine yerleştirilmiştir ve STEP formatında ANSYS Design Modeller kısmına yüklenmiştir. Bu iplerin ve tellerin malzeme özellikleri sırasıyla Tablo 2 ve 3’te verilmiştir. Radyal tekerleklerin yapısında ipler tekerlek desenine dik ve topuklardaki demir tellere bağlı bir şekilde yerleştirilmiştir (Şekil 3). Aynı zamanda gövde ve topuk kısmında kullanılan teller, tekerlek desenine paralel olarak konulmuştur (Şekil 4).



Şekil 2. SolidWorks programı ile tasarlanan dört mevsim tekerlek



Şekil 3. Tekerlekte kullanılan ipler



Şekil 4. Tekerlekte gövde ve topukta kullanılan teller

Tablo 1. ANSYS'te lastik için Mooney-Rivlin modeli parametreleri

Özellik	Değer	Birim
C_{10}	150	kPa
C_{01}	15	kPa
Yoğunluk	1000	kg/m ³

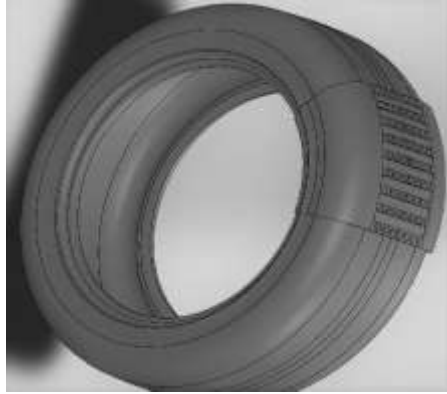
Tablo 2. İplerin malzeme özellikleri

Özellik	Değer	Birim
Elastisite modülü	9.87	GPa
Poisson oranı	0.3	-
Yoğunluk	1500	kg/m ³

Tablo 3. Tellerin malzeme özellikleri

Özellik	Değer	Birim
Elastisite modülü	172.2	GPa
Poisson oranı	0.3	-
Yoğunluk	5900	kg/m ³

Kar paletleri, SolidWorks yazılımı ile tasarlanan 195/50R15 tekerleğin dış profiline göre 15mm dış derinliğinde iki modelde tasarlanmıştır. Model 1’de dokuz düz sırada dişler yerleştirilmiştir ve her sırada 6 diş tasarlanmıştır (Şekil 5). Model 2’de ise 8 sıradan oluşan V profilinde tasarlanmıştır ve her sırada 8 diş yerleştirilmiştir (Şekil 6). Her iki palet modelinin de ana malzemesi polilaktik asittir (PLA). Bu malzemenin özellikleri ise Tablo 4’te verilmiştir.



Şekil 5. Model 1 paletli tekerlek



Şekil 6. Model 2 paletli tekerlek

Tablo 4. Polilaktik asit (PLA) özellikleri [4]

Özellik	Değer	Birim
Birim hacim ağırlığı	1251.5	kg/m ³
Elastisite modülü	1.28	GPa
Poisson oranı	0.36	-
Kayma modülü	1.287	GPa

Kar, buz kristallerinin birbirine yapıştığı hücresel form olarak kabul edilebilir. Burada kar malzemesi buz elemanlarının çok yüzlü yapıda doğrusal bağ oluşturduğu açık hücre şeklinde tanımlanmıştır. Çalışmamızda, düşük yoğunluklu kar için kabul edilen Drucker-Prager model parametreleri Tablo 5’te verilmiştir.

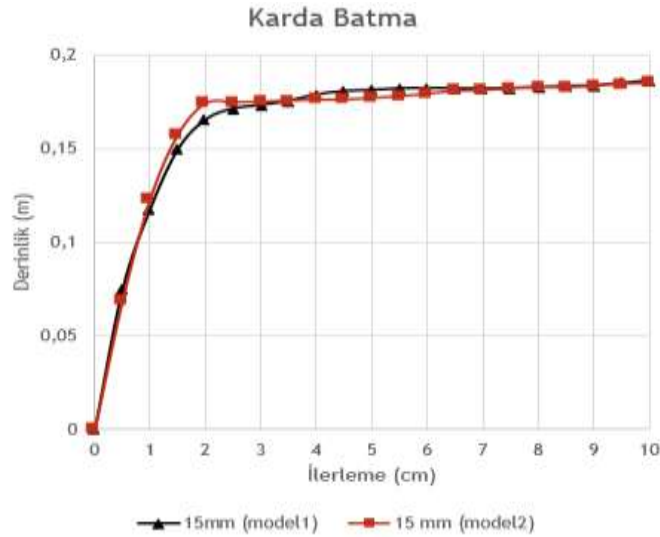
Tablo 5. Düşük yoğunluklu kar için Drucker-Prager model parametreleri [5]

Özellik	Değer	Birim
Birim hacim ağırlığı	200	kg/m ³
Elastisite modülü	13.79	MPa
Poisson oranı	0.3	-
Drucker-Prager kohezyon	5000	Pa
Drucker-Prager sürtünme açısı	22.538	Derece

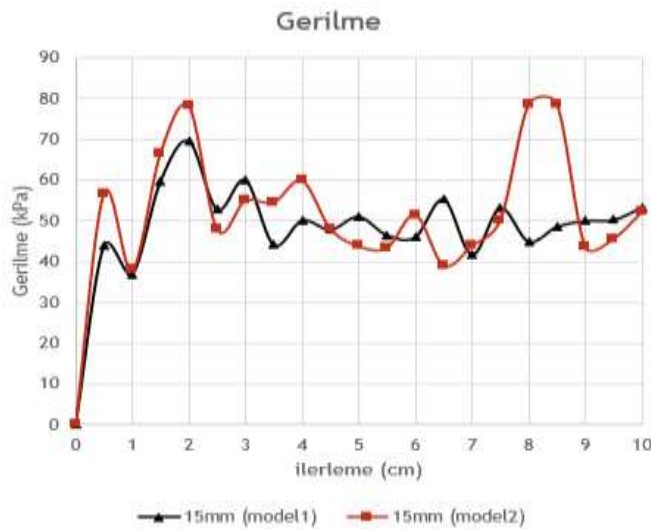
Her modelde tekerleğe 4500 N düşey yük, 200 kPa tekerlek iç basıncı, 0.5 m/s öteleme hızı, 1 rad/s açısal hız ve kar sürtünme katsayısı 0.3 olarak tanımlanmıştır.

Sonuçlar

Birinci modelde maksimum karda batma 18.63 cm olarak tespit edilmiştir. Şekil 7’de görüldüğü gibi palet 4 cm ilerledikten sonra 18-19 cm derinlikleri arasında hareket etmektedir. İkinci modelde maksimum karda batma 18.5 cm olarak tespit edilmiştir. Palet 2 cm ilerledikten sonra 18-19 cm derinlikleri arasında hareket etmiştir. İki modelde de görüldüğü gibi aynı derinlikte hareket sağlanmıştır.



Şekil 7. Karda batma

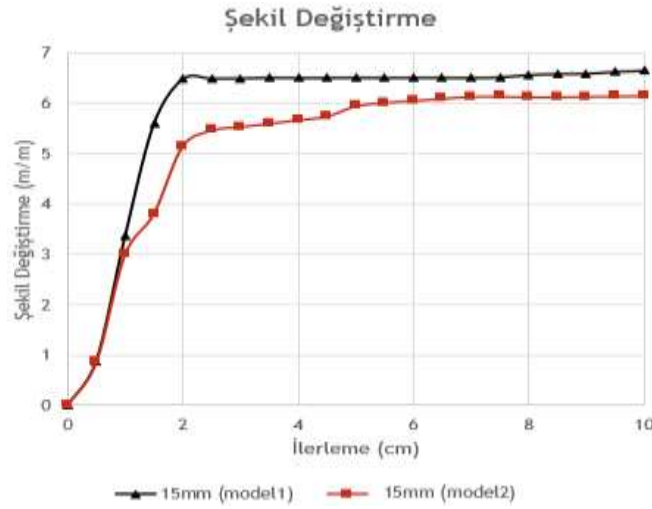


Şekil 8. Normal gerilme

3rd International Students Science Congress
3-4 May 2019, İzmir - Turkey

Birinci modelde palet ilk 2 cm ilerlemede ani yükselme normal gerilme sergilemiştir ancak 2 cm ilerlemeden sonra 40-60 kPa aralığında karda gerilme sergilemiştir. İkinci modelde palet ilk 2 cm’de ani yükselme sergilemiştir daha sonra 40-60 kPa aralığında karda normal gerilme göstermiştir. Ancak 8 cm ilerlemeden sonra ani değişim sergilemiştir (Şekil 8).

Her iki model de ilk 2 cm ilerlemede ani yükselmiştir sonrasında ise daha az ve düzgün bir değişim sergilemiştir. Ancak modelde de görüldüğü gibi paletin aynı miktarda batmasına rağmen ikinci modelin deseninden dolayı karda sıçrama (pulverizasyon) oluşmuştur. Böylece diğer modele nazaran düşük şekil değiştirme sergilemiştir (Şekil 9).



Şekil 9. Şekil değiştirme

Tartışma

- Bu analizde palet deseninin kar üzerinde batmada etkisi olmadığı gözlemlenmiştir. Her iki modelde de yaklaşık olarak aynı batma değeri meydana gelmiştir.
- Palet deseni, gerilme ve şekil değiştirmede önemli rol aldığı tespit edilmiştir. Kar üzerinde en yüksek normal gerilme model 2’de oluşurken maksimum şekil değiştirme model 1’de oluşmaktadır.

Teşekkür

Bu çalışma Yurtdışı Türkler ve Akraba Topluluklar Başkanlığı’nın (YTB) “Uluslararası Öğrenci Akademisi” Projesi kapsamında desteklenmiştir.

Kaynaklar

- [1] Omark M (2014) Brush-model Simulation of Tire-Road Friction, Luleå University of Technology Department of Engineering Sciences and Mathematics, Master’s Thesis, Sweden.
- [2] USPO, 1904. Grip-tread for pneumatic tires- Harry D. Weed, of Oanastota, New York United States Patent Office, Patented August 23, 1904, Patent no: 768,495, USA.
- [3] Cho JR (2013) Numerical estimation of rolling resistance and temperature distribution of 3-D periodic patterned tire. International Journal of Solids and Structures 50(1): 86–96
- [4] Jamshidian M, Tehrani EA, Imran M, Jacquot M, Desobry S (2010) Poly-Lactic Acid: Production, Applications, Nanocomposites, and Release Studies, Comprehensive Reviews in Food Science and Food Safety 9(5): 552–571.
- [5] Haehnel RB, Shoop SA (2004) A macroscale model for low density snow subjected to rapid loading. Cold Regions Science and Technology 40(3): 193–211.

Bitümlü Bağlayıcılarda Dinamik Kesme Reometresi ve Çoklu Gerilmeli Sünme Geri Dönme Deneylerinin Karşılaştırılması

*Brou André Venance Koffi**, Ege Üniversitesi, Fen Bilimleri Enstitüsü, İnşaat Mühendisliği Bölümü, Ulaştırma Anabilim Dalı, İzmir, Türkiye

Perviz Ahmedzade, Ege Üniversitesi, İnşaat Mühendisliği Bölümü, Ulaştırma Anabilim Dalı, İzmir, Türkiye
Mahyar Jafarzadyeganeh, Ege Üniversitesi, Fen Bilimleri Enstitüsü, İnşaat Mühendisliği Bölümü, Ulaştırma Anabilim Dalı, İzmir, Türkiye

*İletişimden sorumlu yazar: kbav19@gmail.com

Anahtar kelimeler: bitümlü bağlanıcı, DSR, MSCR, viskozite

Disiplin: İnşaat Mühendisliği

Özet

Günümüzde esnek yol kaplamaların ana malzemelerinden biri olan bitüm, sıcaklık ve yüklenme süresi ile farklı davranış gösteren kompleks, visko-elastik bir termo-plastik malzemedir. Geleneksel deney yöntemleri bitüm malzemesinin özelliklerini tam olarak sergileyememektedir. Bu nedenle geleneksel deneylere ek olarak 1988 ile 1993 yılları arasında Amerika'da ulusal ortak karayolu araştırma programı (SHRP) asfalt araştırma grubu tarafından yapılan çalışmalar sonunda Superpeve karışım dizayn yöntemi geliştirilmiştir.

Superpave karışım dizayn yönteminde geliştirilen deneylerinden biri olan dinamik kesme reometresi (DSR), bitümlü bağlayıcıların tekerlek izine dayanım amacıyla yapılan deneyinde faz açısı (δ) ve kompleks kayma modülü (G^*) kullanılarak tekerlek izi dayanımı parametresi olan « $G^*/\sin \delta$ » belirlenmektedir.

Ancak, G^* değeri, yükün uygulanması sonrası meydana gelen deformasyonun elastik veya kalıcı olma durumunu belirtmekte yetersiz kalmaktadır. Bu nedenle, farklı mertebede kayma gerilmelerinin kullanılmasıyla meydana gelen deformasyonun ayrıntılı bir biçimde incelenebildiği, çoklu gerilmeli sünme geri dönme (MSCR) deneyi NCHRP programının tarafından geliştirilmiştir. MSCR deneyinde bağlayıcıların yüksek sıcaklık performansı ve elastik deformasyonların hesaba katılarak değerlendirilmesi ve kalıcı bozulmaların tahmin edilmesi sağlanabilmektedir.

Bu çalışmada, 50/70 ve 160/220 saf bitümler DSR ve MSCR deneyleri yapılarak farklılıkları araştırılmıştır. İlk başta DSR deneyi ve bunun ardından MSCR açıklayıp bunların arasındaki farklılıklarını ortaya çıkardık.

Giriş

Son yıllarda kişi başına düşen araç sayısı, hız ve trafik yükünde ciddi bir artış görülmektedir. Bu, özellikle elastikiyet ve esneklik açısından, bitümlü bağlayıcıların gereksinimlerine neden olmuştur. Bu gereksinimler ışığında, geleneksel test yöntemleri artık bitümlü bağlayıcıları karakterize etmek için yeterli değildir. Yeni testler bile düzenli olarak geliştirilmekte ve hatta diğerleri tarafından daha da güçlenmektedir [1].

Bu çalışmada 160/220 ve 50/70 saf bitüm penetrasyonu elde edilmiştir. Geleneksel testler yapıldıktan sonra, (DSR) ve (MSCR) yapıldı. DSR ve MSCR test sonuçları benzerlik ve farklılıkları belirlemek için karşılaştırıldı.

Deneyel Program

Kullanılan malzemeler

Çalışmada bağlayıcı malzeme olarak 160/220 ve 50/70 penetrasyon sınıfına ait bitüm kullanılmıştır. Bitümlü bağlayıcıya ait fiziksel özellikler Tablo 1'de verilmiştir.

Tablo 1. Çalışmada kullanılan bitüme ait fiziksel özellikler

Bağlayıcı özelliği	Değerler	
Sınıf	50/70	160/220
Penetrasyon (mm)	68	193
Yumuşama noktası, °C	42	103

Geleneksel test yöntemleri

Bitümler üzerinde geleneksel test yöntemleri olarak da adlandırılan penetrasyon ve yumuşama noktası deneyleri yapılmıştır.

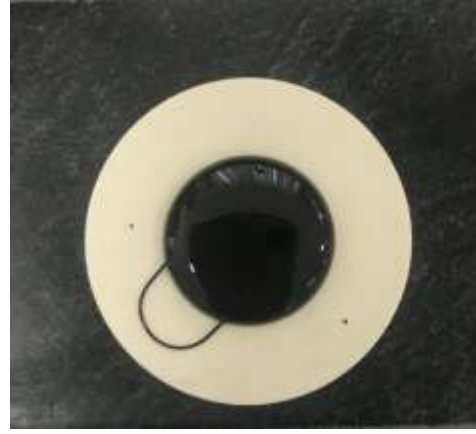
Dinamik kayma reometresi (DSR) deneyi

Şekil 1 'de gösterildiği gibi, DSR, bitümlü bağlayıcıların orta ve yüksek sıcaklıklarda viskoz ve elastik davranışlarını karakterize etmek için kullanılır. Bu karakterizasyon bağlayıcı performans sınıflandırmasının (PG) belirlenmesinde kullanılır. Diğer Superpave bağlayıcı testlerinde olduğu gibi, bitümlü bağlayıcı yerleştirileceği bölgede beklenen gerçek sıcaklıklar kullanılan test sıcaklıklarını belirler [2].

DSR deneyi yapılması için, Şekil 2'de gösterildiği gibi iki dairesel plaka arasında alınmış ince bir asfalt bağlayıcı numuneyi kullanır. Üst plaka 10 rad / s'de (1.59 Hz) dönerken alt plaka sabit. Bu deney AASHTO T 315 standardına uygundur.



Şekil 1. DSR cihazı

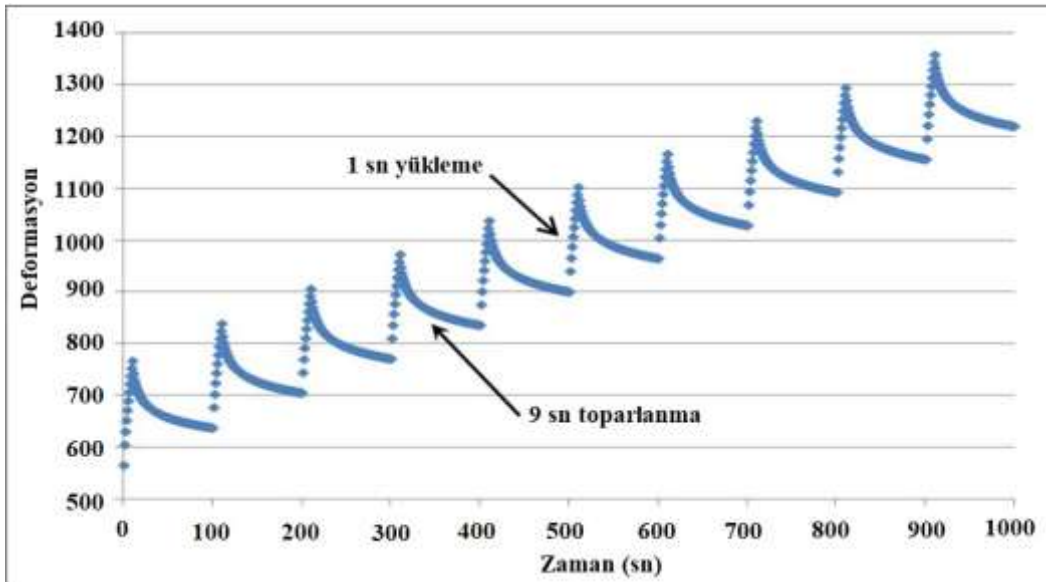


Şekil 2. DSR numunesi

Çoklu gerilmeli sünme geri dönme (MSCR) deneyi

MSCR, DSR cihazıyla yapılan bir deneydir. Bitüm numunesine bir saniye boyunca sürekli bir stres uygulanır ve bu işlem daha sonra 9 saniye dinlenmeye bırakılır. Bu kısıtlama yükleme profili 20 kez tekrarlanır: 10 kez düşük (0.1 kPa) ve 10 kez yüksek (3.2 kPa) [3].

Cihaz, tüm deney periyodu boyunca numunenin deformasyonunu ölçmek için kullanılır. Şekil 3, yükleme ve elastik geri kazanımın bir örneğini göstermektedir.



Şekil 3. MSCR deneyinde zamana bağlı deformasyon eğrisi

3rd International Students Science Congress
3-4 May 2019, İzmir - Turkey

MSCR deneyinde trafik yoğunluğu da dikkate alınmıştır. Bu trafik yoğunluğunu dikkate almak için şartname limitleri Tablo 2’de verilmiştir. Ona göre, şartnamede, standart (S), ağır (H), çok ağır (V) ve aşırı ağır (E) trafik olmak üzere dört farklı trafik sınıfı tanımlanmış [4].

Tablo 2. MSCR deneyine göre bağlayıcıların PG sınıflandırılması

Trafik Sınıfı	Trafik seviyesi / hız	Deney sıcaklığı, °C (Örnek)	Şartname Limiti	Yüksek sıcaklık performans sınıfı
Standart trafik	<10 milyon ESAL veya >72km/s	64	maks. $J_{nr,3.2} < 4,0 \text{ kPa}^{-1}$	PG 64S-Y
Ağır trafik	10-30 milyon ESAL veya 24-72 km/s	64	maks. $J_{nr,3.2} < 2,0 \text{ kPa}^{-1}$	PG 64H-Y
Çok ağır trafik	>30 milyon ESAL veya <24 km/s	64	maks. $J_{nr,3.2} < 1,0 \text{ kPa}^{-1}$	PG 64V-Y
Aşırı ağır trafik	>30 milyon ESAL veya <24 km/s	64	maks. $J_{nr,3.2} < 0,5 \text{ kPa}^{-1}$	PG 64E-Y

Deney Sonuçları

Dinamik kayma reometresi (DSR) deney sonuçları

PG sınıfların belirlenmesi için, 160/220 penetrasyonlu bitüm 46, 52 ve 58 ° C sıcaklıklarda yapıldı. 50/70 penetrasyonlu bitüm ise 52, 58, 64 ve 70 ° C sıcaklıklarda yapıldı. Superpave şartnamesine göre saf bitümler üzerinde yapılan DSR deneylerinde tekerlek izi değerinin en az 1,0 kPa, yaşlandırılmış olanlarda ise 2,20 kPa olması gerekmektedir. Bu limit değerler ve herhangi bir sıcaklık için saptanan kompleks kayma modülü (G^*), faz açısı (δ) ve tekerlek izi parametresi ($G^*/\sin\delta$) değerleri Tablo 3’te verilmiştir.

Tablo 3. Saf bitümlerin DSR deney sonuçları

Bağlayıcı	Sıcaklık (°C)	G^* (kPa)	δ (°)	$G^*/\sin \delta$ (kPa)	Limit değerler (kPa)	Sınıf	
50/70	Orijinal	52	8,70	84,80	8,71	≥ 1.00	PG 64-Y
		58	3,60	86,30	3,59		
		64	1,60	87,30	1,58		
	Yaşlandırılmış	70	0,70	88,10	0,70	≥ 2.20	
		52	18,10	81,20	18,28		
		58	7,30	83,60	7,34		
160/220	Orijinal	70	1,40	87,00	1,41	≥ 1.00	PG 58-Y
		46	5,20	85,60	5,21		
		52	2,00	86,60	2,00		
	Yaşlandırılmış	58	0,80	87,50	0,80	≥ 2.2	
		46	8,80	83,50	8,86		
		52	3,50	85,50	3,51		
		58	1,54	87,00	1,54		

Yukarıda belirtildiği gibi 50/70 penetrasyonlu bitüm yüksek sıcaklık performans sınıfı PG 64-Y, 160/220 penetrasyonlu bitüm ise PG 52-Y ‘dir.

Çoklu gerilmeli sünme geri dönme (MSCR) deney sonuçları

MSCR deneyi sonucunda bağlayıcıların önemli reolojik parametrelerinden “geri dönmeyen sünme uyumluluğu” (J_{nr}), geri kazanılan deformasyon (R), iki yükleme arasındaki geri dönmeyen sünme

3rd International Students Science Congress
3-4 May 2019, İzmir - Turkey

uyumluluğu farkı ($J_{nr, diff}$) ve iki yükleme arasındaki geri kazanılan deformasyon farkı (R_{diff}) değerleri elde edilmektedir. Bu belirlenen parametreler Superpave şartnamesindeki yüksek sıcaklık PG sınıflarını belirlemek için yapılabilmektedir.

MSCR deneyinden elde edilen sonuçlara göre, J_{nr} değerleri her iki yükleme durumunda da (0,1 kPa, 3,2 kPa) yapılmaktadır. MSCR deneyine ait parametreler Tablo 4-5'te verilmiştir

Tablo 4. Saf bitümlerin 0,1 kPa ve 3,2 kPa gerilmeye J_{nr} değerleri

Bağlayıcı türü	MSCR deneyi J_{nr} (kPa^{-1}) değerleri									
	Test sıcaklıkları									
	46 °C		52°C		58 °C		64		70	
	0,1 kPa	3,2 kPa	0,1 kPa	3,2 kPa	0,1 kPa	3,2 kPa	0,1 kPa	3,2 kPa	0,1 kPa	3,2 kPa
160/220	0,80	0,89	2,08	2,51	5,54	6,34	-	-	-	-
50/70	-	0,41	0,43	1,14	1,25	2,82	3,16	6,43	7,16	0,41

Tablo 5. Saf bitümlerin 0,1 kPa ve 3,2 kPa gerilmeye $J_{nr, diff}$ ve R_{diff} değerleri

Bağlayıcı türü	MSCR deneyi $J_{nr, diff}$ (%) ve R_{diff} (%) değerleri									
	Test sıcaklıkları									
	46 °C		52°C		58 °C		64 °C		70 °C	
	$J_{nr, diff}$	R_{diff}	$J_{nr, diff}$	R_{diff}	$J_{nr, diff}$	R_{diff}	$J_{nr, diff}$	R_{diff}	$J_{nr, diff}$	R_{diff}
160/220	10,02	71,80	20,91	107,86	14,35	703,43	-	-	-	-
50/70	-	-	7,09	48,67	9,48	87,94	12,02	143,19	11,43	- 689,19

Yukarıda belirtildiği gibi 50/70 penetrasyonlu bitüm yüksek sıcaklık performans sınıfı PG 64S-Y, 160/220 penetrasyonlu bitüm ise PG 52S-Y 'dir.

Sonuçlar

Geleneksel deneylerden sonra her iki bitüm türünde (50/70 ve 160/220) gerçekleştirilen DSR ve MSCR testleri aynı yüksek sıcaklığı verir. Bu, MSCR deneyleri sırasında uyarılacak trafiğin türünü belirtir. MSCR kurtarma, diğer PG deneylerinden daha hızlı ve daha kolay belirlenir. MSCR testi, trafik yükünden bağımsız olarak gerçek kaplama sıcaklığında yapılır. Başka bir deyişle Superpave şartname kriterlerine eklenen MSCR deneyiyle birlikte DSR deneyleriyle PG sınıfları da değiştirilmiştir.

Teşekkür

Bu çalışma Yurtdışı Türkler ve Akraba Topluluklar Başkanlığı'nın (YTB) "Uluslararası Öğrenci Akademisi" Projesi kapsamında desteklenmiştir.

Referanslar

- [1] Polacco G, Filippi S, Merusi F, Stastna G (2015) A review of the fundamentals of polymer-modified asphalts: Asphalt/polymer interactions and principles of compatibility. *Advances in Colloid and Interface Science* 224(9):72-112.
- [2] American Association of State Highway and Transportation Officials (AASHTO). *Provisional Standards*, April 2000 Edition.. Washington, D.C.
- [3] National Cooperative Highway Research Program (NCHRP) Report 648: *Mixing and Compaction Temperatures of Asphalt Binders in Hot-Mix Asphalt* (2010) Washington, D.C., 157pp.
- [4] American Association of State Highway and Transportation Officials (AASHTO) TP 70: 2013, *Method of Test for Multiple Stress Creep Recovery (MSCR) Test of Asphalt Binder Using a Dynamic Shear Rheometer (DSR)*, Washington, D.C.

An Experimental Study on the Scour around Two in Line Circular Bridge Piers with Different Diameters

Waheedullah Mohammadkhail*, Gökçen Bombar

İzmir Kâtip Çelebi Univ., Dept. of Civil Engineering, Çiğli Main Campus, İzmir, Türkiye

*Corresponding author: waheed.mohammadkhail@gmail.com

Keywords: bridge pier, two piers in line, clear water and local scour depth

Discipline: Civil Engineering

Abstract

The local scour around the bridge piers is an important subject in civil engineering and play a key role in bridge failures. Bridge scour is the engineering term for the erosion of soil surrounding the bridge foundation and it occurs when the fast moving water around a bridge removes the sediment from foundation and leave a scour hole. Most of the previous studies were based on scour around a single pier. In this study, the local scour depth around the double bridge piers with a constant discharge was analyzed.

The experimental study is conducted in 15 m long and 120 cm wide rectangular flume with a horizontal bed made of uniform sand with the median diameter of 1.07 mm. An electromagnetic flow meter is used to measure the flow rate and ultrasonic meter is used to measure the depth of the flow in downstream. The diameter of tested circular bridge piers is 12 cm and 7 cm with spacing between the two piers is 2.5 times the diameter of the greater pier and the greater piers is placed in upstream part of the channel. The experimental result were compared with empirical equations however the maximum scour depth occur at upstream pier.

Introduction

Scour is the engineering term for the erosion of soil surrounding a bridge foundation. Scour around the bridge pier is an important subject in civil engineering and many experimental studies and numerous predication equations have been developed; for example Melville [1], Melville and Sutherland [2] studied local scour around the single pier, Oliveto and Hager [3] proposed a relationship for the computation of the time dependent scour depth at the pier, Yanmaz and Altinbilek [4] and Aksoy et al [5] studied of time dependent local scour around bridge piers and Alabi [6] presented the use of collars for reducing the effects of local scour at a bridge pier together with the time aspect of the scour development.

In some studies for example by Elhimer et al. [7], Okajima et al. [8] flow characteristics around two circular piers in line have been studied, likewise Alam and Zhou [9] and Gao et al. [10], experimentally studied the flow characteristics around two tandem circular piers with different diameter. However, limited research has been done on scouring around two in line cylindrical piers, Keshavarzi et al. [11] have studied the maximum scour depth around two in line circular piers under the clear water flow condition and the result they have found that the maximum scour occur when the spacing between two piers is 2.5 D and they found that when the spacing between two piers is 1D and more than 10D the pier behave like single pier.

As a result, there exists lack of information and quantification for scouring estimation in the design of such foundations. Therefore, this study is focused on maximum scour depth around two in line circular piers with different diameter under clear-water flow conditions.

Experimental Set-up

The experiments were conducted in a rectangular flume, which is 15 m long and 120 cm wide, located at Hydraulics Laboratory of Department of Civil Engineering in İzmir Kâtip Çelebi University. Adjustable tailgate was used to control the water depth in the channel. The main water supply tank has a capacity of 24 m³ and it is located at the basement of the hydraulic laboratory. A 15 kW centrifugal pump was used in the experiment. Ultrasonic meter were used to measure the flow depth in the channel and also an ultrasonic velocity meter (Vectrino) was used to measure the distance and Vectrino is attached to a car moving over the rails launched on the two side of the concrete walls of the channel;

moreover an electromagnetic flow meter is used to obtain the discharge. A digital Go Pro camera is used to measure the scour level with time interval. The scheme of the experimental set-up with plan view and cross-section is given in Figure 1. The set-up is shown in Figure 2.

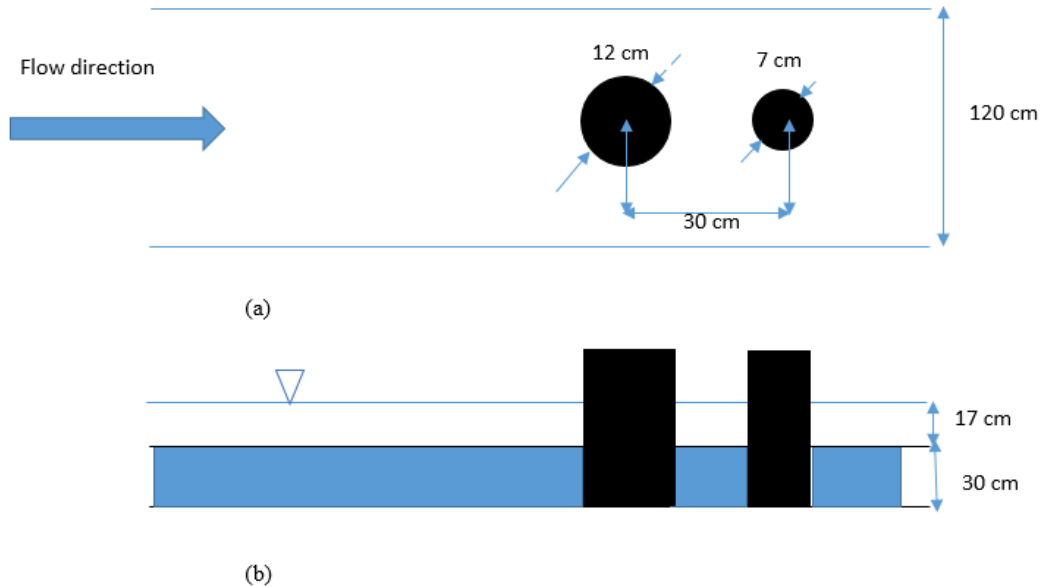


Figure 1. Scheme of experimental set-up (a) plan view (b) longitudinal section

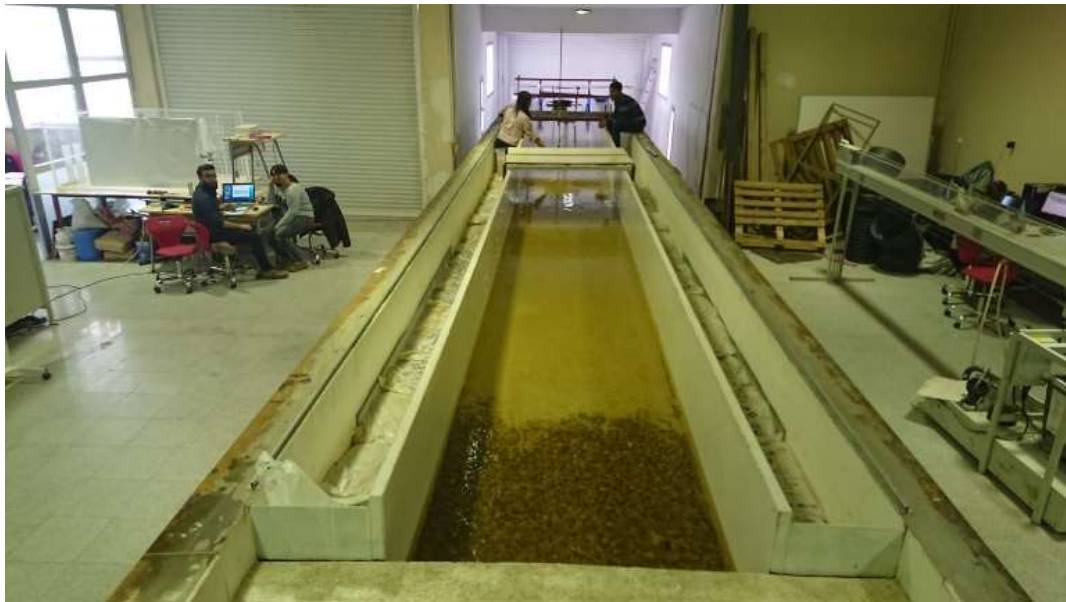


Figure 2. Experimental set-up

The upstream of the channel 2 m long floor was covered with coarse gravel to induce the development of fully turbulent flow and to prevent local scouring at the channel entrance; the rest of the channel bed material is sand layer, the median particle size was $D_{50} = 1.07$ mm and the other characteristics of the bed material are given in Table 1. The complete gradation curve is shown in Figure 3.

3rd International Students Science Congress
3-4 May 2019, İzmir - Turkey

Table 1. Sediment characteristics

Parameter	Value
Geometric mean size, D_g (mm)	1.09
Geometric standard deviation, σ_g	1.18
D_{10} (mm)	0.98
D_{16} (mm)	0.94
Median diameter, D_{50} (mm)	1.07
D_{60} (mm)	1.10
D_{65} (mm)	1.12
D_{84} (mm)	1.18
Uniformity coefficient, $C_u = D_{60} / D_{10}$	1.22

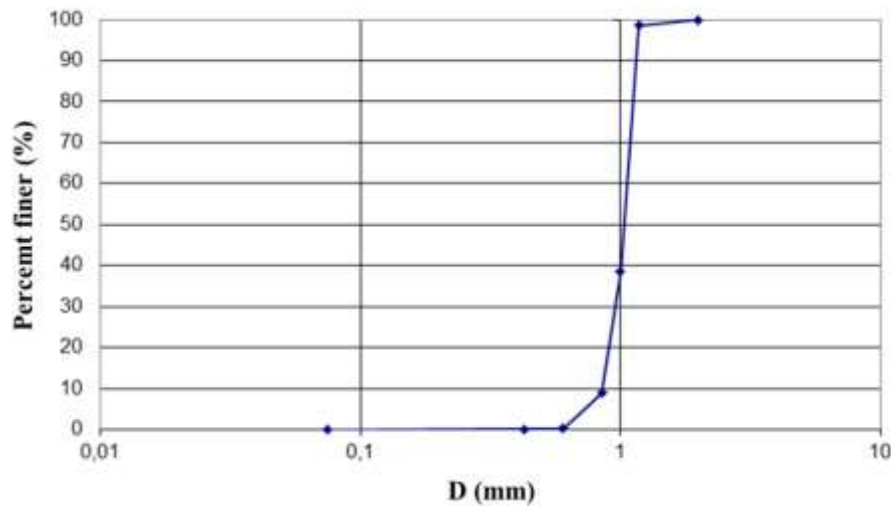


Figure 3. Grain size distribution

The experimental study was scheduled using the parameters given in Table 2 for clear water conditions, the table includes other data on the test condition, where Q is the discharge, B is the channel width, y is the flow depth, R is the hydraulic radius, V is the mean cross-sectional velocity, V_c is the critical velocity and the flow intensity V/V_c .

Table 2. Characteristics of the experiment

Parameter	Value
Q (l/s)	67
D_1 (cm)	12
D_2 (cm)	7
B (cm)	120
y (cm)	17
B/y	7.1
R (cm)	13.25
V (cm/s)	32.84
V_c (cm/s)	43.12
V/V_c	0.76
t_{duration} (hr)	144

Theoretical background

The effected parameter on the local scour around a bridge pier is flow parameters such as flow velocity, approach flow depth, fluid density and viscosity (ρ and μ), bed material characteristics (median size D_{50} , standard deviation, sediment density, critical velocity), pier geometry is also important (pier width, pier shape) and time as well.

The critical velocity V_c was determined from the logarithmic velocity profile distribution [2] as

$$\frac{V_c}{u_{*c}} = 5.75 \log\left(5.53 \frac{y}{D_{50}}\right) \quad (1)$$

where u_{*c} is the critical shear velocity

$$u_{*c} = 0.0115 + 0.0125D_{50}^{1.4} \quad 0.1 \text{ mm} < D_{50} < 1 \text{ mm} \quad (2a)$$

$$u_{*c} = 0.0305D_{50}^{0.5} - 0.0065D_{50}^{-1} \quad 1 \text{ mm} < D_{50} < 100 \text{ mm} \quad (2b)$$

In these relations u_{*c} is in m/s and sediment size is in mm.

Melville and Chiew [12] proposed a time-dependent scour depth relationship after using 84 datasets from three different researcher's laboratory experimental data.

$$\frac{d_s}{d_{se}} = \exp\left(-0.03 \left|\frac{V_c}{V} \ln\left(\frac{t}{t_e}\right)\right|^{1.6}\right) \quad (3)$$

They also proposed a formula for computing equilibrium time in the term of days of scour processes.

$$t_e = 48.26 \frac{D}{V} \left(\frac{V}{V_c} - 0.4\right) \quad \frac{y}{D} > 6 \quad (4a)$$

$$t_e = 30.89 \frac{D}{V} \left(\frac{V}{V_c} - 0.4\right) \left(\frac{y}{D}\right) \quad \frac{y}{D} < 6 \quad (4b)$$

where a new relation for time effects presented here can be used with existing equations for local scour depth estimation, as demonstrated below for the method given in [1]

$$d_s = K_{yD} K_I K_d K_t \quad (5)$$

The time factor, K_t , is given by

$$K_t = \frac{d_s}{d_{se}} \quad (6)$$

and the other factors are given below .

The effect of flow depth is calculated using the following equations:

$$\frac{D}{y} < 0.7 \quad \rightarrow \quad K_{yD} = 2.4D \quad (7a)$$

$$0.7 \leq \frac{D}{y} \leq 5 \quad \rightarrow \quad K_{yD} = 2\sqrt{yD} \quad (7b)$$

$$\frac{D}{y} > 5 \quad \rightarrow \quad K_{yD} = 4.5y \quad (7c)$$

The equations below are employed for estimating the flow intensity:

3rd International Students Science Congress
3-4 May 2019, İzmir - Turkey

$$\frac{V}{V_c} > 1 \quad \rightarrow \quad K_I = 1 \quad (8a)$$

$$\frac{V}{V_c} < 1 \quad \rightarrow \quad K_I = \frac{V}{V_v} \quad (8b)$$

By using the following simple equations, the particle size is calculated:

$$\frac{D}{D_{50}} > 25 \quad \rightarrow \quad K_d = 1 \quad (9a)$$

$$\frac{D}{D_{50}} \leq 25 \quad \rightarrow \quad K_d = 0.57 \log(2.24 \frac{D}{D_{50}}) \quad (9b)$$

Oliveto and Hager [3] proposed a relationship for the computation of the time-dependent scour depth d_s at the pier, as a function of time t .

$$\frac{d_s}{Z_R} = 0.068 N \sigma_g^{-\frac{1}{2}} F_d^{1.5} \log(T) \quad (10)$$

where $Z_R = (yD^2)^{1/3}$, N is as a shape number equal to $N=1$ for the circular pier, and $N=1.25$ for the rectangular abutment (or pier) and F_d densimetric particle Froude number considered as the dominant parameter controlling the scour process and calculated as follow.

$$F_d = \frac{V}{(g' D_{50})^{1/2}} \quad (11)$$

Dimensionless time of scour is defined by $T = \frac{t}{t_R}$

$$t_R = \frac{Z_R}{\left[\sigma_g^{1/3} (g' D_{50})^{0.5} \right]} \quad (12)$$

where reduced gravitational acceleration is g'

$$g' = \Delta g \quad (13)$$

and $\Delta = \frac{\rho_s - \rho}{\rho}$.

The reference length Z_R is calculated by the following equation,

$$Z_R = (yD^2)^{1/3} \quad (14)$$

An empirical relation was investigated by using the dimensionless time parameter proposed by Aksoy et al [5]. The proposed relation was obtained by using the least squares method which minimizes the sum of squared residuals and moreover the advantage of this empirical equation is that the only parameter requiring the calculation is the critical velocity since other parameters are the known geometric and hydraulic parameters. Therefore Eq. (9) is obtained as follows:

$$\frac{d_s}{D} = 0.8 \left(\frac{V}{V_c} \right)^{\frac{3}{2}} \left(\frac{y}{D} \right)^{0.15} (\log T_s)^{0.6} \quad (15)$$

in which T_s is the dimensionless time parameter which can be expressed as follows [5]:

$$T_s = t D_{50} (\Delta g D_{50})^{0.5} / D^2 \quad (16)$$

Result

During the experiments, the maximum scour depths were first observed at the upstream face of the pier. The greater the pier diameter and the higher the flow velocity, the greater scour depth was observed, as expected. The experimental results revealed that the dimensionless scour depths increased with the flow intensity.

Figure 4 shows the experimental results with respect to time; as can be seen, the higher the diameter, the greater scour occur is.

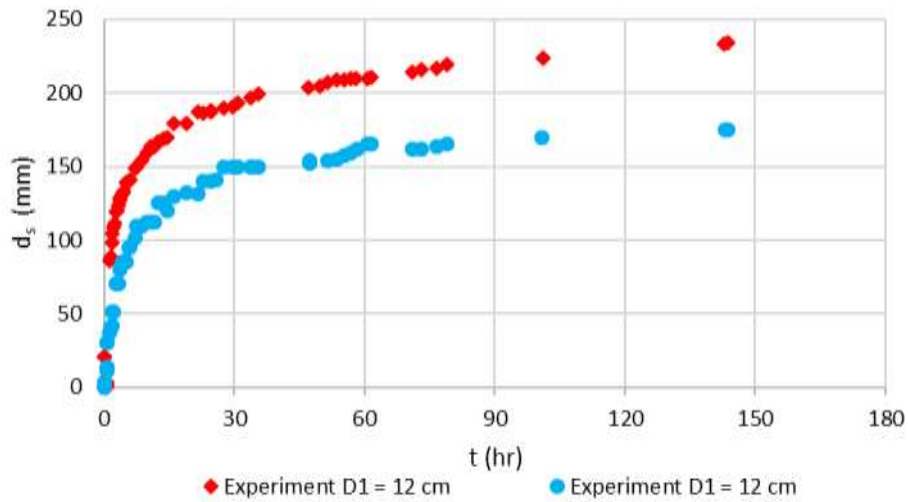


Figure 4 .Variation of scour depth with respect to time in front of the piers

The comparison between the experimental results and those computed from various empirical relations are given in Figure 5 for upstream pier (12 cm diameter). Figure 6 shows the comparison between the experimental results with empirical relations for downstream pier (7 cm diameter). The plan view of the piers and the scour hole is given in Figure 7.

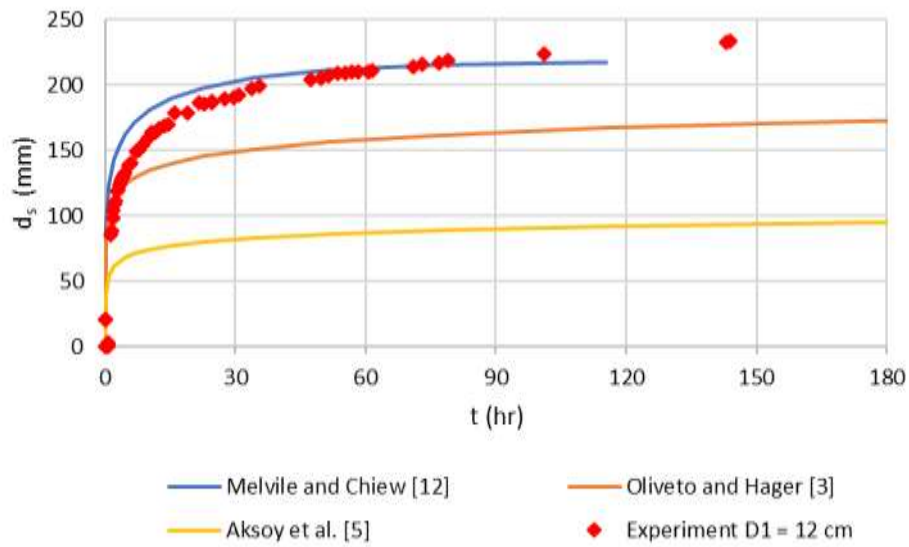


Figure 5. Comparison of the experimental result with empirical equation ($D_1 = 12$ cm)

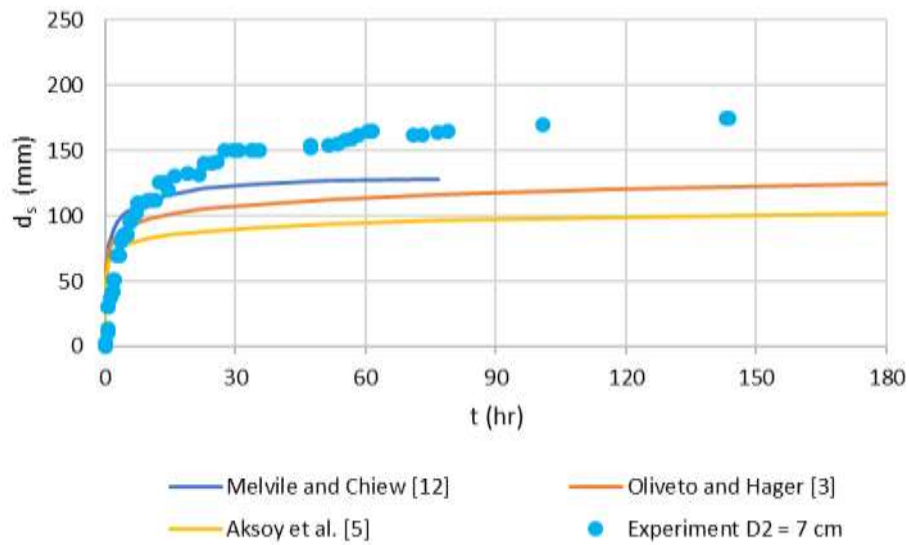


Figure 6. Comparison of the experimental result with empirical equation ($D_2 = 7$ cm)



Figure 7. Scour after 144 hours

Conclusion

Laboratory experiments were carried out to analyze the local scour around the two in line circular bridge piers with different diameter. It is concluded that the scour at the upstream pier with 12 cm diameter exceeded that at the downstream pier with 7 cm diameter.

Acknowledgment

This experimental set-up implemented within the scope of TUBITAK (Science and Technology Research Council of Turkey). And as well, the first author of this study was supported by the Presidency for Turks Abroad and Related Communities (YTB) within “International Student Academy” Project.

References

- [1] Melville BW (1997) Pier and abutment scour: integrated approach. *J Hydraul Eng* 123(2):125–136.
- [2] Melville BW, Sutherland AJ (1988) Design method for local scour at bridge piers. *J Hydraul Eng* 114(10): 1210–1226.
- [3] Oliveto G, Hager WH (2002) Temporal evolution of clear-water pier and abutment scour. *J Hydraul Eng* 128: 811–820.
- [4] Yanmaz, M, Altinbilek, HD, 1991. Study of time-dependent local scour around bridge piers. *J Hydraul Eng*, 117(10): 1247–1268.
- [5] Aksoy AÖ, Bombar G, Arkis T, Guney MS (2016) Study of the time-dependent clear water scour around circular bridge piers. *J. Hydrol. Hydromech.* 65(1): 26–34
- [6] Alabi PD (2006) Time development of local scour at a bridge pier fitted with a collar. Master Thesis, University of Saskatchewan, Canada.
- [7] Elhimer M, Harran G, Hoarau Y, Cazin S, Marchal M, Braza M (2015) Coherent and turbulent processes in the bistable regime around a tandem of cylinders including reattached flow dynamics by means of high-speed PIV. *J Fluids Struct* 60:62–79.
- [8] Okajima A, Yasui S, Kiwata T, Kimura S (2007) Flow-induced stream wise oscillation of two circular cylinders in tandem arrangement. *Int J Heat Fluid Flow* 28:552–560.
- [9] Alam MdM, Zhou Y (2008) Strouhal numbers, forces and flow structures around two tandem cylinders of different diameters. *J Fluids Struct* 24(4):505–526.
- [10] Gao Y, Etienne S, Wang X, Tan SK (2014) Experimental study on the flow around two tandem cylinders with unequal diameters. *J Ocean Univ China (Ocean Coast Sea Res)* 13(5):761–777.
- [11] Keshavarzi A, Shrestha CK, Melville B, Khabbaz H, Ranjbar-Zahedani M, Ball J (2018) Estimation of maximum scour depths at upstream of front and rear piers for two in-line circular columns. *Environmental Fluid Mechanics* 18(2): 537-550.
- [12] Melville BW., Chiew YM., (1999) Time Scale for Local Scour at Bridge Piers, *J Hydraul Eng*, 125(1), 10.1061/(ASCE)0733-9429(1999)125:1(59)

Aynı Hizadaki İki Dairesel Kesitli Köprü Ayağının Etrafında Oluşan Oyulma Üzerine Deneysel Bir Çalışma

*Aboukachi Gbangbida Nyame **, İzmir Kâtip Çelebi Üniv., İnşaat Müh. Böl., Çiğli Ana Kampüsü, İzmir, Türkiye
Gökçen Bombar, İzmir Kâtip Çelebi Üniv., İnşaat Müh. Böl., Çiğli Ana Kampüsü,, İzmir, Türkiye
**İletişimden sorumlu yazar: aboukachigbangbida@gmail.com*

Anahtar Kelimeler: Köprü ayağı, temiz su, art arda yerleştirilmiş köprü ayakları, oyulma, oyulma derinliği
Disiplin: İnşaat Mühendisliği

Özet

Oyulma, köprü ayağının etrafında hızla akan suyun tabandaki sedimentleri yerinden kaldırmasıyla gerçekleşir. Köprü ayakları gibi engellerin akışa mani olması ve akım yönünü değiştirmesi bu durumun nedenidir. Oyulma çukurları yapısal anlamda ayakların taşıma kapasitesinde zayıflamaya sebep olur ve yapının stabilitesini tehdit eder. Hidrolik açıdan oyulma derinliğinin gelişiminin sürekli olarak takip edilmesi ve yapının davranışı üzerindeki etkisinin değerlendirilmesi hayati önem taşır. Bu çalışmada, dairesel kesitli akım yönünde arka arkaya sıralanmış farklı çaplarda iki adet köprü ayağının etrafındaki temiz su oyulması incelenmiştir. Deneyler, Hidrolik Laboratuvarı'nda mevcut, 15 m uzunluğunda 120 cm genişliğindeki dikdörtgen kesitli kanalda gerçekleştirilmiştir. Membada bulunan ve çapı $D_1 = 7$ cm olan silindirik ayağın mansabında merkezler arası $2,5 D_2 = 30$ cm olacak şekilde $D_2 = 12$ cm çapında ikinci bir ayak yerleştirilmiştir. Taban malzemesi olarak medyan dane çapı 1.03 mm olan uniform dağılımlı kum kullanılmıştır. Oyulma derinliğinin zamanla değişiminin elde etmek için GoPro kamerasından yararlanılmıştır. Farklı zaman aralıklarında şeffaf köprü ayaklarının içine kamera indirilerek video kayıtları gerçekleştirilmiş ve daha sonra bu kayıtlar okunarak zaman - oyulma derinliği grafiği çizilmiştir. Deneylerin sonunda, ölçülmüş nihai oyulma derinlikleri ve literatürdeki sonuçlar karşılaştırılmıştır.

1. Giriş

Oyulma, akımın etkisiyle sedimentlerin harekete geçerek taşınması ve yığılmasıdır. Nehirlerde ve denizlerde inşa edilen yapılar (köprü, rüzgâr türbinleri vb.) hidrolik akımı ve akıntıyı engeller ve böylece oyulma oluşur (Bkz. Şekil 1). Köprü ayakları gibi bir yapı akışı engellediğinde akım engel önünde lokal olarak hızlanır ve köprü ayağı önünde çevrıntiler oluşmasına neden olur. Oluşan bu çevrıntilere atnalı çevrıntileri denir.

Oyulma derinliğinin belirlenmesi yapının stabilitesi için önemlidir. Bu derinlik limit değerine ulaştığında, yapının stabilitesi tehlike altına girer ve yıkılma riski artar. Bu riski tahmin etmek için bir çok ampirik formül geliştirilmiştir. Oyulma derinliği çeşitli faktörlere bağlıdır. Köprü ayakları etrafındaki yerel oyulmalar çok sayıda araştırmacı tarafından araştırılmıştır. Bunlardan bazıları: Laursen ve Toch [1], Melville [2], Raudkivi ve Ettema [3], Melville ve Sutherland [4], Breusers ve Raudkivi [5], Yanmaz ve Altınbilek [6], Dey ve ark. [7] ve Melville ve Coleman [8]'dir.

Oyulma derinliğinin zamanla değişimi, taban malzemesinin taşınmadığı temiz su oyulması durumunda ve taşındığı hareketli taban durumunda farklılık gösterir. Hannah [9], Ettema [10], Yanmaz ve Altınbilek [6], Kothyari ve Ark. [11], Nazariha [12], Melville ve Chiew [13], Melville ve Coleman [8], Oliveto ve Hager [14], Mia ve Nago [15] gibi birçok araştırmacı köprü ayakları etrafındaki oyulmanın zamanla değişimini incelemiştir. Breusers ve ark [16] ve Melville ve Chiew [13] çalışmalarında maksimum yerel oyulma değerine asimptotik yaklaştığını belirtmiştir. Oyulma sürecinin karmaşık yapısından dolayı verilen zamanda maksimum oyulma derinliğini tahmin etmek güçtür.

Ancak az sayıda araştırmacı, Okajima ve ark. [17], Elhimer ve ark. [18], Keshavarzi ve ark. [19], art arda dairesel kesitli köprü ayakları etrafında yerel oyulmalar üzerinde çalışmıştır.

Bu çalışmada, temiz suyun akımı yönü ile aynı yönde art arda yerleştirilmiş farklı çaplardaki iki dairesel köprü ayağı etrafındaki yerel oyulma incelemiştir. İki dairesel köprü ayağı etrafındaki oyulma derinliğinin zamansal değişimi elde edilmiştir.



Şekil 1. Köprü ayağı etrafında oluşan oyulma örneği (Wardhana ve Hadipriono [20])

2. Deney Düzeneği ve Kullanılan Cihazlar

2.1. Deney Düzeneği

Deneyler, İzmir Kâtip Çelebi Üniversitesi Hidrolik Laboratuvar'ında 15 m uzunluğunda, 120 cm genişliğinde ve 120 cm derinliğinde dikdörtgen bir kanalda gerçekleştirilmiştir (Bkz. Şekil 2).



Şekil 2. Deney düzeneği

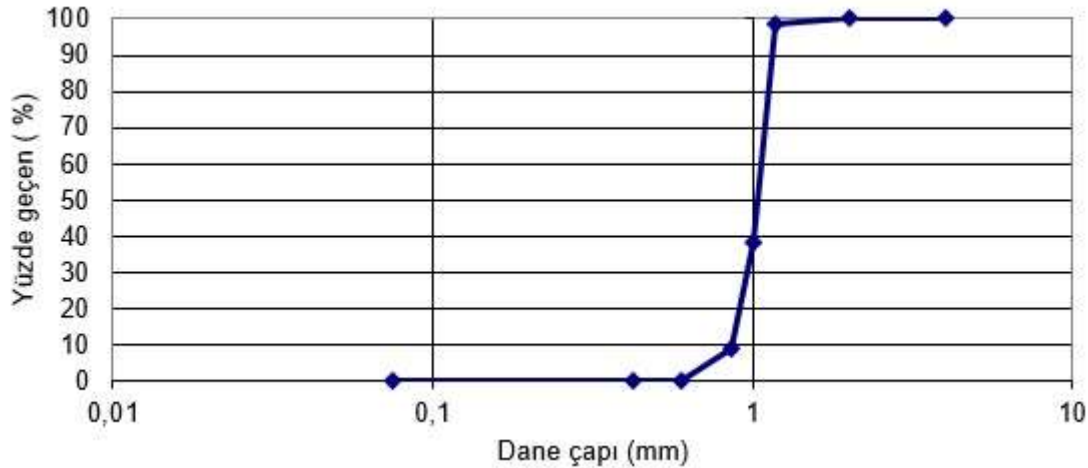
Deneylerde, $D_1 = 7$ cm ve $D_2 = 12$ cm çaplarında dairesel kesitli iki pleksi boru kullanılmıştır. Ayaklar arasında merkezden merkeze $L = 2,5D_2$ mesafe olacak şekilde membadan itibaren 10 metreye yerleştirilmiştir. Deney düzeneğinin plan görünümü Şekil 3'te verilmiştir.



Şekil 3. Aynı yönde art arda yerleştirilmiş iki dairesel köprü ayağının plan görünümü

Deney öncesi kohezyonsuz malzeme olarak kullanılan kum 30 cm kalınlığında serilmiştir. Medyan dane çapı $d_{50} = 1,03$ mm ve geometrik standart sapması $\sigma_g = 0,99$ üniformluk katsayısı $c_u = 1,12$ mm'dir. Deneylerde kullanılan sedimentin granülomerik dağılım eğrisi Şekil 4'te gösterilmiştir.

Melville ve Coleman'a [8] göre, kumun sadece σ_g 1,3'ten küçükse uniform olduğu kabul edilmektedir. Seçilen kum, düzgün şekilde derecelendirilmiştir.



Şekil 4. Granülomerik dağılım eğrisi

Temiz su oyulması durumunda gerçekleştirilen deneylerin alt parametreleri Tablo 1'de verilmiştir. Burada Q debisi, y kanaldaki suyun yüksekliği, D_1 ve D_2 sırasıyla membadan mansapta kadar köprü ayağı çapı, L merkezden merkeze iki köprü ayağı arasındaki mesafe, d_{50} medyan dane çapı, $V = Q / (By)$ akım hızı, B kanal genişliğidir.

Sedimentin harekete başlaması denklem (1) kullanılarak hesaplanmıştır. Burada V ortalama kesitsel hız olmakta, akım şiddeti $V < V_c$ ise temiz su oyulması, $V > V_c$ ise hareketli taban oyulması olmaktadır.

$$V_c = 5,75 \log\left(5,53 * \frac{y}{d_{50}}\right) * U_{*c} \quad (1)$$

Burada U_{*c} sedimentin harekete geçişini veren kritik kayma hızı olarak adlandırılmakta olup denklem (2) ile hesaplanmıştır.

$$U_{*c} = 0,0305 d_{50}^{0,5} - 0,0065 * d_{50}^{-1} \quad (2)$$

Tablo 1. Deney parametreleri

Tests	Q (m ³ /s)	y (cm)	D ₁ (cm)	D ₂ (cm)	L (cm)	d ₅₀ (mm)	V (m/s)	V _c (m/s)	V/V _c
1	0,067	17	7	12	2,5 D ₂	1,031	0,328	0,465	0,705

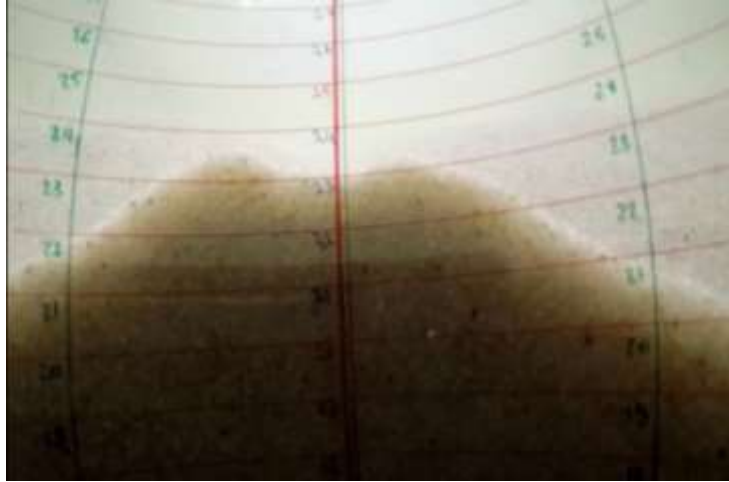
Deneylerde GoPro kamera kullanılarak ardışık sıralanmış köprü ayakları etrafında farklı zaman aralıklarında oyulmanın gelişimi kaydedilmiştir. Testin sonunda, pompa durdurulmuş ve kanaldaki tüm su tahliye edilmiştir.

2.2. Deneylerde Kullanılan Cihazlar

GoPro dijital kamerası, ardışık sıralanmış iki köprü ayağı etrafında oluşan oyulmaların farklı zaman aralıklarıyla gelişiminin izlenmesini sağlamıştır. Pompayı çalıştırmadan önce, köprü ayakları etrafındaki kum seviyesini ölçmede GoPro kamera kullanılmıştır. Pompa çalıştırıldıktan sonra yine GoPro kamera yardımıyla köprü ayakları etrafındaki farklı zaman aralıklı oyulmaları kaydedilmiştir. Tüm ölçümler GoPro kameranın silindirik köprü ayağı içine daldırılmasıyla farklı zaman aralıklarında kaydedilmiştir. Şekil 5'te deneylerde kullanılan GoPro kamerası, Şekil 6'da kameranın ayak içinde çektiği bir anlık görüntü verilmektedir.



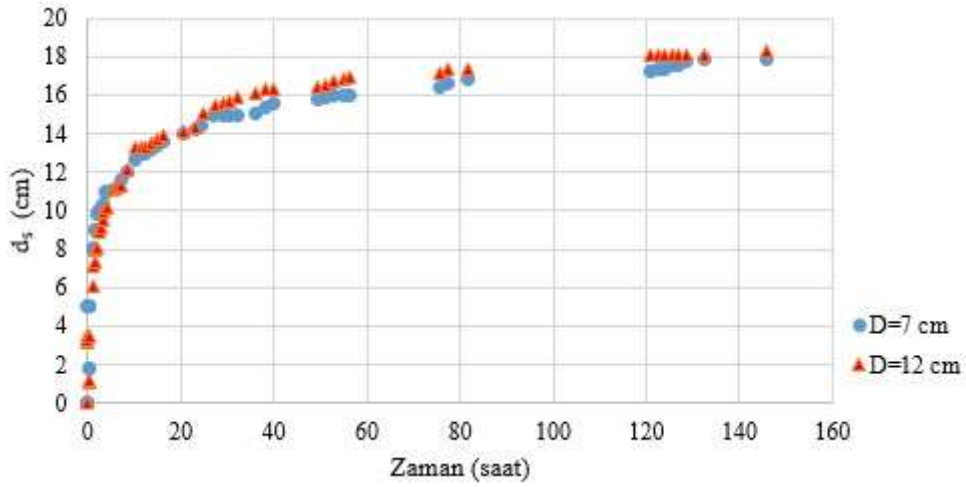
Şekil 5. GoPro kamerası



Şekil 6. GoPro kamerasının köprü ayağı içinde kaydettiği görüntü

3. Sonuçlar

Deneyler boyunca farklı zaman aralıklarında alınan ölçümlerin sonuçları Şekil 7'de sunulmuştur. Bu grafik 7 ve 12 cm çaplı köprü ayakları etrafında 180 dereceye denk gelen zamana bağlı oyulma derinliği gelişimi göstermektedir. Şekil 8'de deneylerden sonra çekilen oyulmanın fotoğrafı verilmiştir.



Şekil 7. 7 cm ve 12 cm çaplı köprü ayağı etrafında oluşan oyulma derinliğinin zamana bağlı gelişimi



Şekil 8. Köprü ayağı etrafında oluşan oyulma

4. Sonuçlar

Bu çalışmada iki dairesel kesitli köprü ayağı etrafındaki derinliklerin zamana bağlı değişimi elde edilmiştir. Farklı çaplı köprü ayaklarının ardarda sıralanması durumunda memba tarafında bulunan 7 cm çapındaki köprü ayağındaki oyulma, mansap tarafında bulunan 12 cm çaplı köprü ayağı oyulmasından kısmen daha az olduğu gözlenmiştir.

Teşekkür

İlk yazar, Yurtdışı Türkler ve Akraba Topluluklar Başkanlığı'nın (YTB) "Uluslararası Öğrenci Akademisi" Projesi kapsamında desteklenmiştir. Bu çalışma TÜBİTAK 116M519 no.lu proje kapsamında imal edilen deney düzeneği üzerinde gerçekleştirilmiştir.

Referanslar

- [1] Laursen EM, Toch A (1956) Scour around bridge piers and abutments. Bulletin No. 4. Iowa Highway Research Board, Bureau of Public Roads, Iowa.
- [2] Melville BW (1975) Local scour at bridge sites. School of Engineering, University of Auckland.
- [3] Raudkivi AJ, Ettema R (1985) Scour at cylindrical bridge piers in armored beds. J Hydraul Eng 111:713-731.
- [4] Melville BW, Sutherland AJ (1988) Design method for local scour at bridge piers. J Hydraul Eng 114:1210-1226.
- [5] Breusers HNC, Raudkivi AJ (1991) Scouring, Hydraulic Structures Design Manual Series, Vol. 2. IAHR, CRC Press, Rotterdam.
- [6] Yanmaz AM, Altınbilek HD (1991) Study of time-dependent local scour around bridge piers. J Hydraul Eng 117:1247-1268.
- [7] Dey S, Bose SK, Sastry GLN (1995) Clear water scour at circular piers: a model. J Hydraul Eng 121(12):869-876.
- [8] Melville BW, Coleman SE (2000) Bridge scour. Water Resource Publications, LLC, Denver.
- [9] Hannah CR (1978) Scour at pile groups. Department of Civil Engineering, University of Canterbury, Christchurch.
- [10] Ettema R (1980) Scour at bridge piers. Ph.D. Thesis, Dept of Civil Engineering, Univ. of Auckland.
- [11] Kothiyari UC, Garde RCJ, Raju KGR (1992) Temporal variation of scour around circular bridge piers. J Hydraul Eng 118:1091-1106.
- [12] Nazariha M (1996) Design relationship for maximum local scour depth for bridge pier groups. Ph.D. Thesis, Department of Civil Engineering, University of Ottawa.
- [13] Melville BW, Chiew Y-M (1999) Time scale for local scour at bridge piers. J Hydraul Eng 125:59-65.
- [14] Oliveto G, Hager W (2002) Temporal evolution of clear-water pier and abutment scour. J Hydraul Eng 128:811-820.
- [15] Mia M, Nago H (2003) Design method of time-dependent local scour at circular bridge pier. J Hydraul Eng 129:420-427.
- [16] Breusers NHC, Nicollet G, Shen HW (1977) Local scour around cylindrical piers. J Hydraul Res IAHR 15:211-252.
- [17] Okajima A, Yasui S, Kiwata T, Kimura S (2007) Flow-induced streamwise oscillation of two circular cylinders in tandem arrangement. Int J Heat Fluid Flow 28:552-560.
- [18] Elhimer M, Harran G, Hoarau Y, Cazin S, Marchal M, Braza M (2016) Coherent and turbulent processes in the bistable regime around a tandem of cylinders including reattached flow dynamics by means of high-speed PIV. J Fluids Struct 60:62-79.
- [19] Keshavarzi A, Shrestha CK, Melville B, Khabbaz H, Ranjbar-Zahedani M, Ball J (2018) Estimation of maximum scour depths at upstream of front and rear piers for two in-line circular columns. Environmental Fluid Mechanics, 18(2):537-550.
- [20] Wardhana, K. and Hadipriono, F.C. (2003) Analysis of Recent Bridge Failures in the United States. Journal of Performance of Constructed Facilities, 17, 144-150.
- [21] Chabert, J, Engeldinger P (1956) Etude des affouillements autour des piles des ponts. Laboratoire National d'Hydraulique, Chatou, France (in French), 118.

Review of the Relationship between Resilient Modulus and Dynamic Modulus

Mohammad Razeq Shakhan*, Dokuz Eylül University, The Graduate School of Natural and Applied Sciences, İzmir, Turkey

Ali Almusawi, Dokuz Eylül University, The Graduate School of Natural and Applied Sciences, İzmir, Turkey

Burak Şengöz, Dokuz Eylül University, Dept. of Civil Engineering, İzmir, Turkey

Ali Topal, Dokuz Eylül University, Dept. of Civil Engineering, İzmir, Turkey

*Corresponding author: raziqshakhan@yahoo.com

Keywords: resilient modulus, dynamic modulus, correlation

Discipline: Civil Engineering

Abstract

Turkey and many developing countries are attempting to move from the empirical pavement design method (AASHTO 1993) to the Mechanistic-Empirical Pavement Design Guide (MEPDG) in the near future. In the empirical pavement design method, the resilient modulus (M_r) of hot mixed asphalt (HMA) is widely used to obtain the asphalt layer coefficient (a_i) which is used for the structural analysis and design of flexible pavement. On the other hand, MEPDG uses dynamic modulus ($|E^*|$) of HMA instead of resilient modulus because it gives a better indication of the viscoelastic behavior of the asphalt mixtures. One of the major problems regarding the implementation of the MEPDG in developing countries is the collection and preparation of detailed local design inputs such as dynamic modulus for existing flexible pavements. Therefore, there is a need to find a solution to correlate the already existing M_r database to $|E^*|$ database so it can be used for evaluation and local calibration of the MEPDG. Researchers have found a strong correlation between M_r and $|E^*|$ for the same test conditions (temperature and loading frequency). Also, the correlation between the dynamic modulus and resilient modulus is mix dependent. This study is a summary and review of the literature which have been conducted in order to find a reliable and applicable relationship between the resilient modulus and dynamic modulus.

Introduction

The resilient modulus of hot mixed asphalt mixture as an important material property is widely used in the empirical pavement design. According to the ASTM D 4123[1] the resilient modulus can be calculated for the asphalt mixtures through applying a repeated load and constant frequency. From the resulting horizontal deformation, resilient modulus is calculated. The resilient modulus value generally can be used as design input to obtain the layer coefficient (a_i) for pavement structure design[2]. Figure 1 shows the repeated load and the horizontal deformation for resilient modulus.

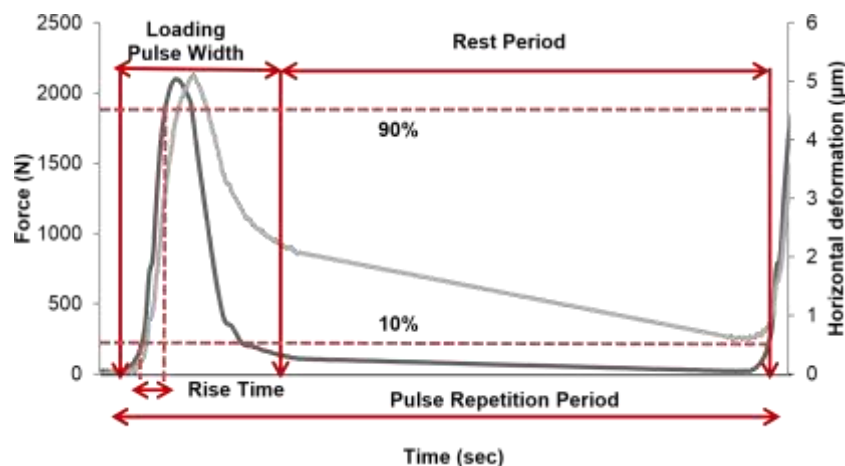


Figure 1. Force and horizontal deformation pulse shape for resilient modulus [3]

On the other hand, the dynamic modulus is also known as complex modulus can be measured, according to ASTM D3497[4], by applying axial compression strain to the asphalt mixture sample at given temperature and different frequencies to measure the recoverable axial strain which is used to calculate the dynamic modulus. The dynamic modulus value can be used in different aspects such as an indicator of the viscoelastic behavior of the asphalt mixture and for the evaluation of the rutting resistance[5]. Also, in MEPDG the dynamic modulus is used instead of the resilient modulus of the asphalt mixture to cover the full viscoelastic behavior the asphalt mixture[6]. Thus, the resilient modulus cannot be used to show such complex behavior because it is based on the elasticity theory. While the dynamic modulus test has overcome this disadvantage by the variety of the test conditions (temperature and loading frequency) which allows to have an ideal picture of the viscoelastic behavior that is observed by the drawing of the master curve of the dynamic modulus as shown in Figure 2. [3] [6].

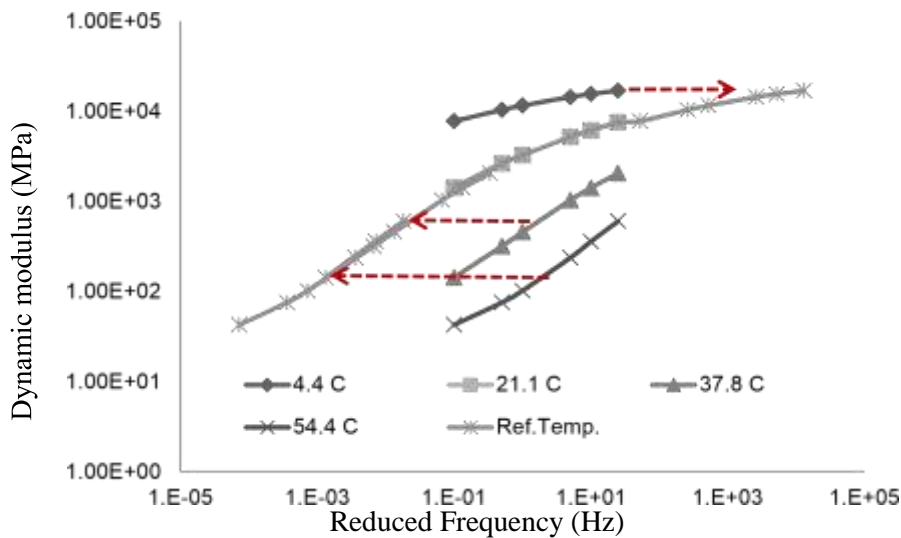


Figure 2. Dynamic modulus master curve[3]

Also, the dynamic modulus of asphalt mixture can be predicted by the empirical equation that was developed by Witczak in 1999 and it is used in the MEPDG.

$$\log E^* = 3.750063 + 0.02932\rho_{200} - 0.001767(\rho_{200})^2 + 0.05809V_a - 0.802208 \left(\frac{V_{beff}}{V_{beff} + V_a} \right) + \frac{3.871977 - 0.0021\rho_4 + 0.003958\rho_{38} - 0.000017(\rho_{38})^2 + 0.005470\rho_{34}}{1 + e^{(-0.603313 - 0.31335 \log(f) - 0.393532 \log(\lambda))}} \quad (7)$$

in which:

- E^* = dynamic modulus, 10^5 psi
- η = binder viscosity, 10^6 Poise
- f = loading frequency, Hz
- V_a = air void content, %
- V_{beff} = effective binder content, % by volume
- ρ_{34} = cumulative % retained on the 19-mm sieve
- ρ_{38} = cumulative % retained on the 9.5-mm sieve
- ρ_4 = cumulative % retained on the 4.75-mm sieve
- ρ_{200} = % passing the 0.075-mm sieve

The main disadvantage of this predictive formula is that it requires several design inputs such as binder properties, asphalt mixture volumetric characteristics, and aggregate gradation. In some cases, the collection of detailed design parameters may not be possible for the existing flexible pavements. Therefore, developing of reliable correlation between resilient and dynamic modulus is required.

Correlation between Resilient Modulus and Dynamic Modulus

After the development of the Mechanistic-Empirical Pavement Design Guide, the database for resilient modulus of hot mixed asphalt mixture may be gradually outdated and useless because the MEPDG uses dynamic modulus instead of resilient modulus for pavement analysis and design[2][6]. On the other hand, the collection and preparation of design inputs such as dynamic modulus for MEPDG is a big challenge for developing countries[7]. Therefore, developing a reliable correlation between resilient modulus and dynamic modulus to predict the dynamic modulus from the existing resilient modulus may significantly save time and decrease the research budget. The relationship between resilient modulus and dynamic modulus has been an issue of interest for researchers in the past years. Therefore, several researchers attempted to develop a correlation between resilient modulus and dynamic modulus[8].

Amare et al.[9] found a strong correlation between M_R and $|E^*|$ that is dependent on the mixture type and mixture properties. The dynamic modulus test was conducted at 5 Hz frequency load and the resilient modulus test was performed at a loading time of 0.03 second. They found that for the surface layer the dynamic modulus is equal to 1.07 times resilient modulus while, for the base layer the dynamic modulus is equal to 1.4 times resilient modulus as illustrated in Figures 3 and 4.

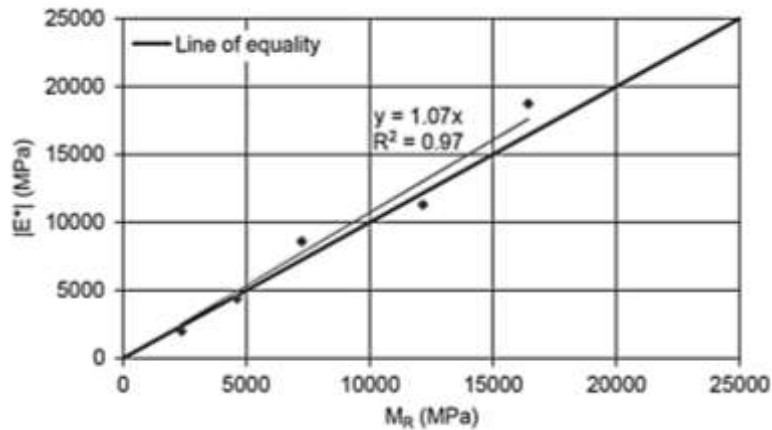


Figure 3. Comparison between dynamic modulus and resilient modulus: surface layer [9]

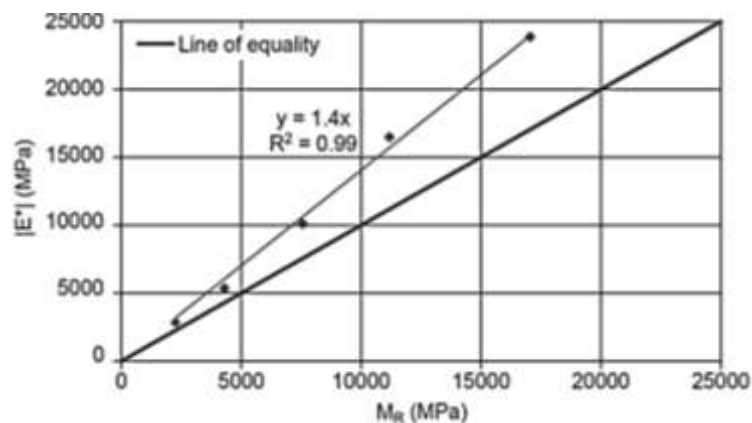


Figure 4. Comparison between dynamic modulus and resilient modulus: base layer [9]

X Shu et al.[10] proposed a practical method to convert resilient modulus to dynamic modulus through constructing a master curve. The master curve of the resilient modulus was constructed by using quadratic function and different test temperatures then the dynamic modulus was obtained by shifting upward the resilient modulus master curve. Finally, they suggested a predicted equation to convert resilient modulus value to dynamic modulus (equation 1).

$$|E^*| = \beta_0 M_{R.Predicted} \quad (8)$$

where,

β_0 = multiplication factor,

$M_{R, predicted}$ = predicted M_R value from the constructed master curve of resilient modulus.

From the comparison between measured MR and $|E^*|$ values the average ratio of $|E^*|$ to MR for the Texas mixtures is about 1.30.

W. Virgil & Yuan Xiao [11] conducted the dynamic modulus test at different loading frequencies 25 Hz, 10 Hz, 5 Hz, 1 Hz, and 0.5 Hz. He found that at 5 Hz the values of the resilient modulus and the dynamic modulus are very close as shown in Figure 4.

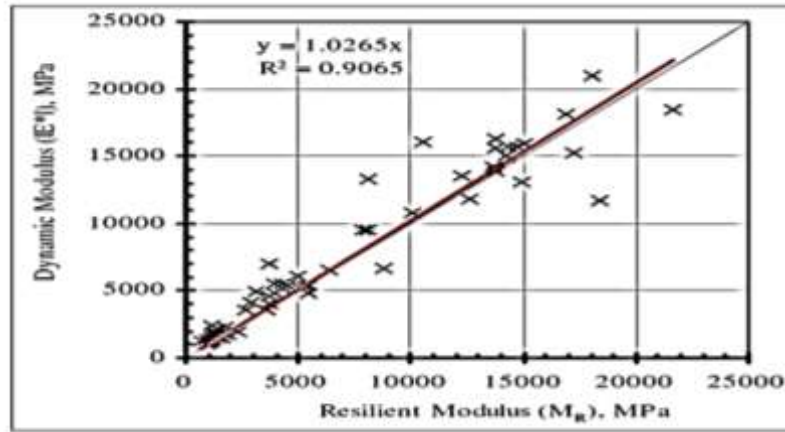


Figure 4. Resilient modulus versus dynamic complex modulus at 5 Hz [11]

Yasir Ali et al. [12] conducted resilient modulus and dynamic modulus tests at two different temperatures (25 °C and 40 °C) and various frequencies (0.1 Hz, 0.5 Hz, 1 Hz, 5 Hz, 10 Hz and 25 Hz). According to the results of the research the strong correlation can be noticed clearly at test temperature 25 °C and frequency load 5 Hz as presented in Table 1.

Table 6. Relationship of $|E^*|$ and MR

Relationship	R ²	Temperature (°C)	Frequency (Hz)
$ E^* =1.6071M_R$	0.58	25	25
$ E^* =1.3084M_R$	0.67121		10
$ E^* =1.0764M_R$	0.85		5
$ E^* =0.74941M_R$	0.58		1
$ E^* =0.5638M_R$	0.57		0.5
$ E^* =0.0823M_R$	0.08		0.1
$ E^* =0.6623M_R$	0.02	40	25
$ E^* =0.7331M_R$	0.08		10
$ E^* =0.2789M_R$	0.30		5
$ E^* =0.4456M_R$	0.44		1
$ E^* =0.5388M_R$	0.10		0.5
$ E^* =0.0073M_R$	0.003		0.1

Validation of the predicted dynamic modulus equations

Validation is a process that measure the accuracy level of the regressive equations. For this paper the test results for dynamic and resilient modulus values have been extracted from W. Virgil Ping & Yuan Xiao [11] to measure the validity of proposed dynamic modulus predictive equations [9] [11] [12]. The resilient modulus and dynamic modulus have been obtained under the same test conditions (25°C and 5 Hz). The summary of extracted resilient and dynamic modulus shown in Table 2.

Table 2. Resilient modulus (MR) and Dynamic modulus |E*|

Resilient Modulus M _R (Ksi)	Dynamic Modulus E*(Ksi)
521	1010.382
428	598.5
451	708.9
390	519.722
789	784.929
1282	966.038
629	793.326
513	520.685
566	795.165
616	747.045
532	672.212
541	588.777
931	953.667
722	882.519
790	697.684
656	787.322
766	770.487
1461	1566.964
785	779.194
578	696.163

The validation results for the predictive equations [9] [11] [12] that represented by the R² are the same (R²=0.6654) the R² values were as shown in Figures 5-7.

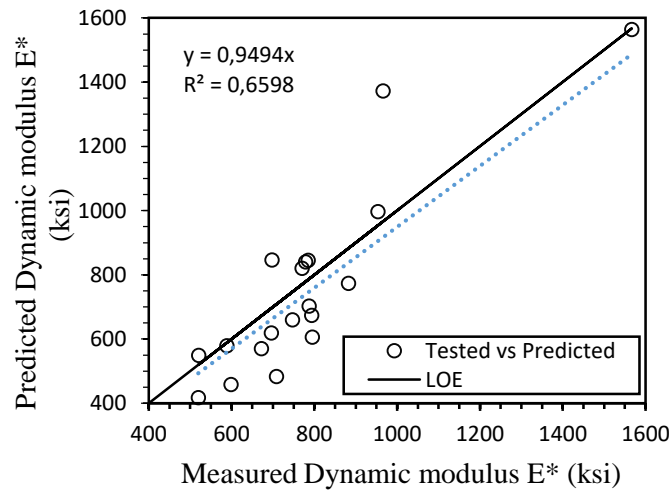


Figure 5. Measured dynamic modulus versus predicted dynamic using equation [9]

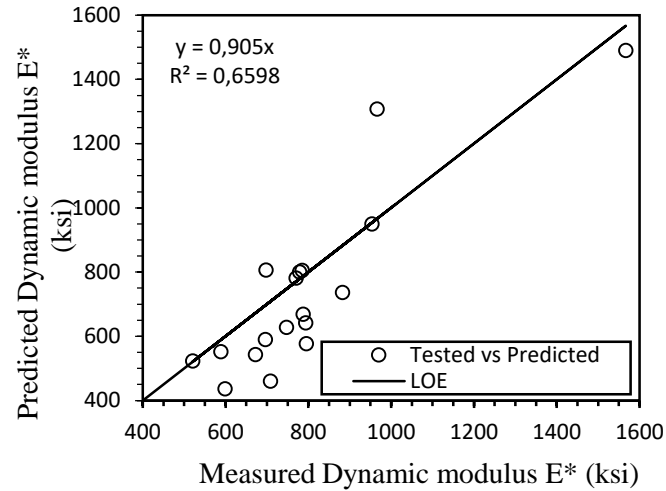


Figure 6. Measured dynamic modulus versus predicted dynamic using equation [11]

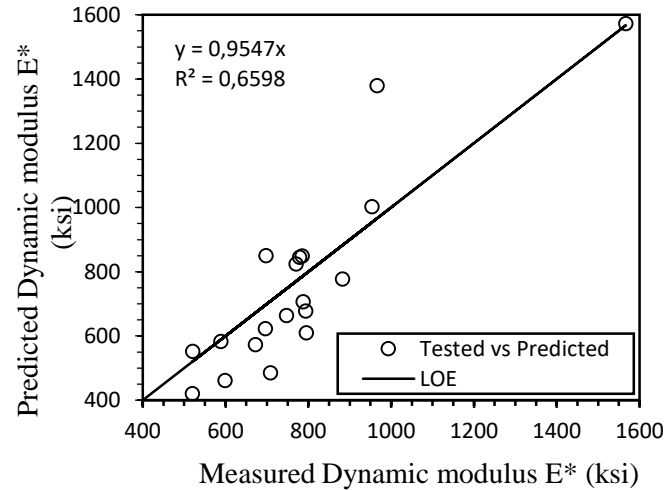


Figure 7. Measured dynamic modulus versus predicted dynamic using equation [12]

Conclusion

Most of the researches have agreed that there is a strong correlation between the resilient and dynamic modulus and it is possible to make a backcalculation from resilient aiming to obtain the dynamic modulus. On the other hand, most of the researches' results have specified different correlations. Different test conditions such as test temperature or frequency it may have a direct effect on the relationship between the dynamic modulus and resilient modulus. Also, the validation results have shown that the data are not close to the fitted regression line. Therefore, further researches are required to be conducted in order to develop a more practical correlation between resilient and dynamic modulus so it can overcome the difficulty in data collection and preparation required by the Mechanistic-Empirical Pavement Design Guide (MEPDG).

References

- [1] ASTM, (2005) Standard Test Method for Indirect Tension Test for Resilient Modulus of Bituminous Mixtures, in Annual Book of ASTM Standards, vol. i, no. Reapproved 1995: 2–5.
- [2] AASHTO, (1993) Guide for the Design of Pavement Structures. American Association of State Highway and Transportation Officials, Washington, D.C.
- [3] Jitsangiam P (2003) Comparison between resilient modulus and dynamic modulus of western Australian hot mix asphalt based on flexible pavement, in 26th ARRB Conference – Research driving efficiency, 2014, vol. 07, no. Aashto

3rd International Students Science Congress
3-4 May 2019, İzmir - Turkey

- [4] ASTM, (2016) Standard Test Method for Dynamic Modulus of Asphalt Mixtures 1, vol. 79, no. Reapproved 1995, pp. 10–12.
- [5] Asphalt Institute, (2007) *Asphalt Handbook Ms-4*, 7TH 07. Asphalt Institute
- [6] NCHRP, (2004) Guide for Mechanistic-Empirical Design of New and Rehabilitated Pavement Structures, Material Characterization
- [7] Öztürk HI, Tan EB, Şengün E, and Yaman İÖ, (2018) Farklı trafik, zemin, malzeme ve iklim koşulları için mekanistik-ampirik (M-E) yöntemle tasarlanan derzli donatısız rijit üstyapı sistemlerinin karşılaştırılması, Gazi Üniversitesi Mühendislik-Mimarlık Fakültesi Dergisi
- [8] Stempihar J, Underwood S, and G. City, (2015) Resilient Modulus to Dynamic Modulus Relationship and Pavement Analysis with the Mechanistic- Empirical Pavement Design Guide Prepared by, no. April, pp. 1–6
- [9] Loulizi A, Flintsch GW, Al-qadi IL, and Mokarem D (2006) Comparing Resilient Modulus and Dynamic Modulus of Hot-Mix Asphalt as Material Properties for Flexible Pavement Design, J. Transp. Res. Board, pp. 161–170
- [10] Shu X, Huang B and Qian G (2010) A Practical Method for Converting Resilient Modulus to Dynamic Modulus of Asphalt Mixtures, 11th Int. Conf. Asph. Pavement, Nagoya, Japan
- [11] Ping WV and Xiao Y (2008) Empirical Correlation of Indirect Tension Resilient Modulus and Complex Modulus Test Results for Asphalt Concrete Mixtures, Road Materials and Pavement Design, 9:sup1, 177-200, DOI: 10.1080/14680629.2008.9690165
- [12] Ali Y, Irfan M, Zeeshan M, Hafeez I, and Ahmed S (2018) Revisiting the relationship of dynamic and resilient modulus test for asphaltic concrete mixtures,” Constr. Build. Mater., vol. 170, pp. 698–707

Computer Science and Engineering / Bilgisayar Bilimi ve Mühendisliđi

Deep Learning Approaches in Medical Imaging

Aysegul Alaybeyoglu, İzmir Kâtip Çelebi Univ., Dept. of Computer Engineering, Çiğli Main Campus, İzmir, Türkiye

Berkay Elagoz, İzmir Kâtip Çelebi Univ., Dept. of Biomedical Engineering, Çiğli Main Campus, İzmir, Türkiye*
**Corresponding author: berkayelagoz@gmail.com*

Keywords: artificial intelligence, machine learning, deep learning, healthcare, medical imaging

Discipline: Computer Science/Engineering

Abstract

Deep learning, a subset of machine learning, utilizes a hierarchical level of artificial neural network that learns features and tasks directly from data. The artificial neural networks are built like human brain with neuron nodes connected together like a web. These artificial neurons takes input from other neuron, multiply with weight, add bias then apply activation function. Neural networks are structured in multiple hidden layers, so that artificial neurons performing simple calculations can approximate complex functions that are difficult to state explicitly. Deep learning algorithms that trained with good training sets can provide high quality results. Therefore, deep learning has a huge potential in healthcare by using medical data. In this study, some research studies in which the deep learning algorithm is used in medical imaging field have been reviewed and analyzed. In general, the results of the studies examined, deep learning is very useful when one is tasked with producing accurate decisions based on complicated data set.

Introduction

Artificial intelligence can be defined as the science and engineering of making intelligent machines [2]. Artificial intelligence can be considered as an algorithm that does not possess the cognitive, learning, or problem solving abilities that solve problem with optimal solution in intelligent manner. Machine learning is a subfield of artificial intelligence and defined as the ability to emulate human intelligence by learning from environment without being explicitly programmed [3]. Machine learning algorithm parse data, learn from feature of data make a determination or prediction about problem or statement. Deep learning is a subfield of machine learning involved in algorithms mimics structure and function of human brain using artificial neural networks. Multiple hidden layers in neural network provides scalability and performance just keep getting better as feed them more data [4]. In other words, more data, bigger models and more computation means better results.

As mentioned above, deep learning shows better performance with big data set. Deep learning algorithms that trained with good training sets can provide high quality results. Therefore, deep learning has a huge potential in healthcare by using medical data. Nowadays, deep learning is studied in various healthcare applications. Medical imaging, genomics, discovery of drug, cell scope, better and faster diagnoses of diseases, mining of medical data for better treatment, clinical analysis support for predictive decisions are major applications of deep learning in healthcare. In this study, some research studies in which the deep learning algorithm is used in medical imaging field have been reviewed and analyzed.

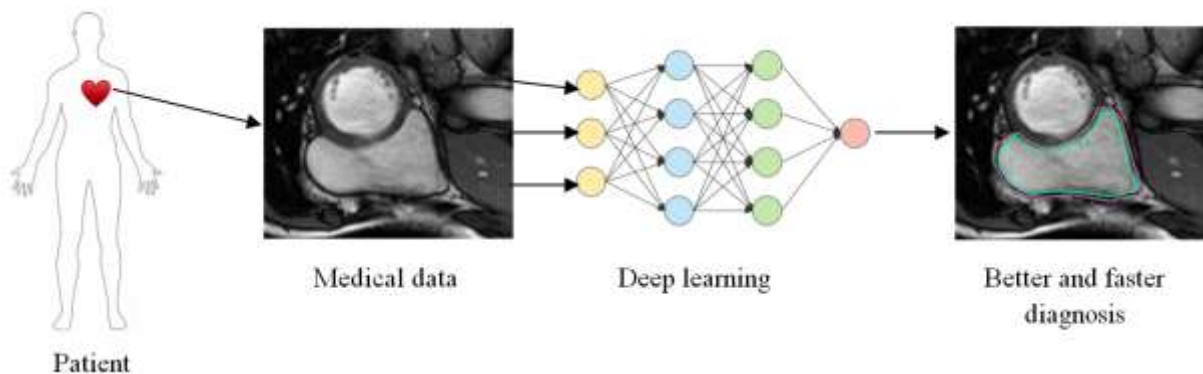


Figure 1. An overview of deep learning in medical imaging [1]

Related Works

Ultrasound Scan Plane Detection and Pancreas 3D CT Segmentation

Schlemper et al. proposed a novel attention gated (AG) model that focuses on target structures of different shapes and sizes. Attention gated models can learn to suppress irrelevant regions in input image and focus on important features. Thus, there is no need to use external tissue/organ localization modules when using convolutional neural networks (CNNs). Proposed AG models could be used in different tasks, including medical image classification and segmentation. For classification, researchers use AGs in scan plane detection for fetal ultrasound screening. For segmentation, AGs with U-net architecture are evaluated with two large 3D CT abdominal datasets. Researchers evaluated AG model in real time fetal ultrasound scan plane detection and pancreas 3D CT segmentation. Experimental results on pancreas 3D CT segmentation, Dice score of U-net model is 0.820 ± 0.043 and Dice score of attention gated U-net model is 0.831 ± 0.038 . Also pancreas recall is 0.828 ± 0.064 for U-net model and 0.840 ± 0.053 for attention gated U-net model. Researchers reached significant improvement (precision) more than 0.02 in profile, lips, kidneys, spine, 4CH, 3VV, RVOT, LVOT (body sections) for 2D fetal ultrasound image classification.

Lung CT Image Segmentation

Early detection of lung cancer is very important and reduces the mortality rate when the treatment is more likely curative. Lung CT image segmentation is an essential initial step for lung image analysis and provides accuracy to detect lung cancer. Skourt et al. worked on deep learning approach with U-net architecture for lung image segmentation. U-net architecture consists of convolutional layers in the contracting path and deconvolutional layers in the expansive path. The contracting path consists of Rectified Linear Units (RELU) and Max-pooling layers. The expansive path consists of up-convolution and convolution layers with RELU. U-net architecture takes the input images and generates corresponding masks for segmentation in training phase. U-net architecture is based on Keras and it uses Tensorflow at the backend. The results of the study show that the trained model reaches a 0.9502 dice coefficient index [5].

Brain Cancer Classification

Mohsen et al. proposed a study based on deep neural network learning architecture to classify brain tumors in brain MRIs. Methodology consists of 4 steps for classifying brain tumors. In the first step, 66 real human MRIs with 22 normal and 44 abnormal images which are glioblastoma, sarcoma and metastatic bronchogenic carcinoma tumors were collected. In the second step, Fuzzy C-means, clustering technique was used for image segmentation. In the third step, discrete wavelet transform (DWT) was used for feature extraction and principal component analysis technique (PCA) was used for feature reduction. In the fourth step, DNN with 7 hidden layers was built and trained by using 7-fold cross validation technique for classification. Also for evaluation of the DNN classifier, machine learning classification algorithms (KNN, LDA and SMO-SVM) were generated in WEKA. As a result of the study, DNN classifier reached 96.67% classification rate and showed good performance in all the performance measures over all other machine learning classifiers [6].

Breast Cancer Classification

Breast cancer is a very lethal cancer common in women. Early diagnosis of breast cancer with mammography awareness has been of great benefit in reducing mortality. Radiologists could use deep learning approach to make more accurate diagnosis. Kaur et al. used Mini-MIAS of 322 images. K-mean clustering was applied for Speed-Up Robust Features (SURF) selection. Deep learning model consists of 7 layers of convolutional neural network (CNN). Proposed deep learning system was evaluated with 10-fold cross validation. Dataset was divided into 70% training and 30% test. Region of interest is 77×100 pixel with 3 channels. According to the results, proposed deep learning system using K-mean clustering with MSVM is more accurate than using a decision tree model. When proposed deep learning system compared with base methods (MLP and J48+K-mean clustering), proposed deep learning system shows better performance overall base methods [7].

Retinal Fluid Segmentation and Detection

Lu et al. used fully convolutional neural network for segmentation and detection of retinal fluid in optical coherence tomography images. Two datasets were used for study, which are RETOUCH dataset and Kermany dataset. Retinal layer segmentation was done by graph-cut algorithm. Fully convolutional neural network was used for recognizing and labeling the fluid pixels. Random forest classification (leave one out cross validation method was used) was used for detecting and rejecting false labeled fluid regions. There are three different retinal fluids (IRF, SRF and PED) are detected by proposed deep learning system and won the first place of MICCAI RETOUCH Challenge on segmentation performance (mean dice: 0.7667) and detection performance (mean AUC: 1.00)[8].

Classification and Detection of Calcaneus Fractures

Calcaneus bone is a fragile tarsal bone and its treatment is quite difficult. Interpretation and detection of calcaneus fractures on computed tomography is a hard job. In this study, ResNet and VGG pretrained CNN models were used for classifying calcaneus fractures. Total 1931 DICOM images were used for training (80%) and testing (20%). Each DICOM image was resized 512x512 pixels to 224x224 pixels for compatibility with VGG and ResNet networks. Then, ResNet (168 layer) and VGG (23 layer) networks were trained with dataset. SURF algorithm was used for detection of bone fracture locations in CT images. The detection process consisted of the following steps: pre-processing, feature detection, feature extraction, feature matching, and contour identification. According to the result, proposed VGG and ResNet models reached 98% accuracy. ResNet classification results were used for detecting location and type of fractures using SURF algorithm. This method can detect bone fracture successfully in 10 seconds[9].

Right Ventricle Segmentation

There are cardiac diseases related with right ventricle (RV) myocardium, such as pulmonary hypertension, congenital heart disease, coronary heart disease, and dysplasia. Segmentation of right ventricle (RV) myocardium is an initial step of diagnosis of these diseases. Due to the crescent shape of right ventricle, it is hard to segment the right ventricle across MRI slices and phases. The main objective of the study is to segment the right ventricle endocardium and epicardium with a deep learning method. Firstly, localization of the region of interest (ROI) was done using an 8-layer deep convolutional network because the image contains the RV and LV. Taking the only RV region includes more meaningful features and provides more accurate results. Secondly, a deep convolutional neural network with 5 fully convolutional layers was used for segmentation of RV endocardium and epicardium. Every layer consists of a filter and kernel size is 31x31. Training is conducted for 300 iterations and batch size is 12 for each iteration. The validation set consists of 200 training slices and 132 validation slices. The code of the system is based on Python language and Keras library was used for neural network. The proposed ROI location method improves the segmentation computation efficiency to some extent.[10]

Dermoscopy Image Segmentation

Melanoma is the most lethal skin cancer type and is increasing in prevalence. Diagnosis of melanoma using a doctor's opinion by dermoscopy is subjective, not stable and could be inaccurate. Therefore, computer-aided diagnosis (CAD) systems can assist the dermatologist in making more accurate diagnoses. Skin lesion segmentation is a preprocessing step to focus on the region of interest (ROI) for these CAD systems. Manual and semi-automatic segmentation methods are subjective, time-consuming, not stable and unreliable. Bi et al. referred to their method as deep class-specific learning with probability-based step-wise integration (DCL-PSI). ResNet architecture-based fully convolutional network (FCN) was trained independently across different known classes. Researchers proposed a probability-based step-wise integration (PSI) approach to obtain better segmentation results of the skin lesion boundaries. According to the results, the proposed system achieved an average dice coefficient of 85.66% on the ISBI 2017 Skin Lesion Challenge (SLC), 91.77% on the ISBI 2016 SLC and 92.10% on the PH2 datasets[11].

Diabetic Retinopathy Detection and Classification

People with diabetes could have an eye disease called diabetic retinopathy. This is when high blood sugar levels cause damage and blockage to blood vessels in the retina that supply the retina.

Consequently, eye sometimes generates new weak blood vessels but these blood vessels can swell and leak easily. These cause vision defect for diabetes patients even blindness. Recently deep learning systems are developed for diagnosis of diabetic retinopathy. Although clinical exam methods, deep learning systems do not need to external factor and predict the diabetic retinopathy quickly in comfortable and proper way[12-14].

Yu et. al used convolutional neural network based on deep learning approach for exudate detection for diabetic retinopathy. CNN model that build with 15 hidden layers was trained with retinal images (64x64 pixels). Final deep learning model achieved 91.92% accuracy, 88.85% sensitivity and 96% specificity[15].

Mansour applied AlexNet DNN based on CNN to enable optimum diagnosis of diabetic retinopathy. Proposed model is passed several steps such as pre-processing, adaptive learning, connected component analysis, AlexNet DNN based highly dimensional feature extraction and SVM based classification to classify five different DR class. According to results AlexNet based model achieved classification accuracy of %97.93[16].

Automated Cell Counts on Tissue Sections

Current commercially available stereology systems requires well-trained humans to count hundreds of cells for each region of interest (ROI). The simplest one study may requires more than a month and money to count cells. Also, these systems prone to error due to human factors such as subjectivity, training level, recognition bias, and fatigue. Proposed deep neural network approach aims to automatically segment and estimate the total number of immunostained neurons on tissue sections. There are three main steps of this approach. First step is creating extended depth of field images that taken from z-axis images. Second step researchers utilized mask created by adaptive segmentation algorithm (ASA) and apply ASA mask to label stained cells in EDF images. Third step is training CNN model to segment and estimate the total number of cells using optical fractionator method. At the result of the study, proposed study reached %1.85 average error rate and 0.804 average dice coefficient [17].

Classification of Cervical Lymph Node Metastasis

Optimal treatment and prognosis may affected by cervical lymph node metastasis in oral cancers. There many deep learning applications in medical imaging but diagnosis of cervical lymph node metastasis in patients with oral cancers has not been studied. In this study, Arij et al. proposed deep learning image classification system and evaluated it for diagnosis of lymph node metastasis. CT images of 127 histologically proven positive lymph node metastasis and 314 histologically proven negative lymph node metastasis were used as dataset. AlexNet architecture with DIGITS library which is one of a type of convolutional neural network (CNN) architecture was used for proposed deep learning model. The AlexNet architectures contains eight layers (five convolutional layers, three fully connected layers). A five fold cross validation was used for training of deep learning model. Dataset was divided into five groups, one group was used for validation and rest of all were used for training. Training and validation processes were done with 150 epochs. Oral and maxillofacial radiologist classified dataset images with accuracy of 83.2%, sensitivity of 77.5%, specificity of 88.8%. According to results, proposed deep learning image classification system achieved accuracy of 78.2%, sensitivity of 75.4%, specificity of 81.0% [18].

Conclusion

Deep learning has high potential for medical imaging in recent years, thanks to the ease of accessing big data, high processing power and algorithmic efficiency. In this study, we examined the studies in which deep learning is used in the field of medical imaging. Deep learning mostly used for segmentation, detection and classification purposes. We tried to examine different application areas such as brain, lung, retina, dermoscopy, cardiac, pathology and breast. In general, the results of the studies examined, deep learning is very useful when one is tasked with producing accurate decisions based on complicated data set. We believe that deep learning will be more effective in medical imaging.

References

- [1] Luo G, An R, Wang K, Dong S, Zhang H (2016) A Deep Learning Network for Right Ventricle Segmentation in Short-Axis MRI. *Computing in Cardiology*. Vol 43.
- [2] McCharty J (2007) What is artificial intelligence? Stanford.
- [3] Naqa E, Issam, Li, Ruijiang, Murphy, Martin J (2015) What Is Machine Learning? *Machine Learning in Radiation Oncology*.
- [4] Ng A, What data scientists should know about deep learning? . Extract Conference 2015.
- [5] Skourt BA, Hassani AE, Majda A (2018) Lung CT Image Segmentation Using Deep Neural Networks. Elsevier.
- [6] Mohsen E, El-Dahshan ESA, El-Horbaty ESM, Salem ABM (2017) Classification using deep learning neural networks for brain tumors. *Future Computing and Informatics*. 3: p. 68-71.
- [7] Kaur P, Singh G, Kaur P (2019) Intellectual Detection and Validation of Automated Mammogram Breast Cancer Images by Multi-Class SVM using Deep Learning Classification. *Informatics in Medicine*.
- [8] Lu D, Heisler M, Lee S, Ding GW, Navajas E, Sarunic MV, Beg MF (2019) Deep-Learning based Multiclass Retinal Fluid Segmentation and Detection in Optical Coherence Tomography Images using a Fully Convolutional Neural Network. *Medical Image Analysis*.
- [9] Pranata YD, Wang KC, Wang JC, Idram I, Lai JY, Liu JW, Hsieh IE (2019) Deep learning and SURF for automated classification and detection of calcaneus fractures in CT images. *Computer Methods and Programs in Biomedicine*.
- [10] Luo G, An R, Wang K, Dong S, Zhang H (2016) A Deep Learning Network for Right Ventricle Segmentation in Short-Axis MRI. *Computing in Cardiology*.
- [11] Bi L, J.K., Ahn E, Kumar A, Feng D, Fulham M (2018) Step-wise integration of deep class-specific learning for dermoscopic image segmentation. *Pattern Recognition*.
- [12] National Eye Institute (2015) Facts About Diabetic Eye Disease. <https://nei.nih.gov/health/diabetic/retinopathy>.
- [13] American Academy of Ophthalmology (2018) What is Diabetic Retinopathy? <https://www.aaopt.org/eye-health/diseases/what-is-diabetic-retinopathy>.
- [14] Advanced Eye Care of New York (2018) Retinopathy. <http://www.advancedeyecareny.com/retinopathy/>.
- [15] Yu S, Xiao D, Kanagasingam Y (2017) Exudate detection for diabetic retinopathy with convolutional neural networks.
- [16] Mansour RF (2017) Deep-learning-based automatic computer-aided diagnosis system for diabetic retinopathy.
- [17] Alahmari SS, Goldgof D, Hall L, Phoulady HA, Patel RH, Mouton PR (2018) Automated Cell Counts on Tissue Sections by Deep Learning and Unbiased Stereology. *Journal of Chemical Neuroanatomy*.
- [18] Ariji Y, Fukuda M, Kise Y, Nozawa M, Yanashita Y, Fujita H, Katsumata A, Ariji E (2018) Contrast-enhanced CT image assessment of cervical lymph node metastasis in oral cancer patients using a deep learning system of artificial intelligence. *Oral Surgery, Oral Medicine, Oral Pathology and Oral Radiology*.

Experiments on the Fire Detection System Using a Multi-hop WSN

*Hussein M. Marah**, *Dilara Ece Öztürk*, *Orhan Dağdeviren*
Ege University, International Computer Institute, Bornova, İzmir, Turkey
Moharram Challenger, The University of Antwerp, Electronics and ICT Dept., Belgium
**Corresponding author: hussein.marah@gmail.com*

Keywords: wireless sensors network, fire detection system, TinyOS, multi-hop routing algorithm

Discipline: Computer Science and Engineering, Information Technologies

Abstract

Saving lives and valuable things has always been a very significant issue, so it is very important to warn the people and respond to the disasters such as fire, smoke and gas leak in the environment both in the opened or closed places. The time of warning is a very critical factor to respond to these incidents and to save what can be saved, especially for buildings or places that contain a significant amount of flammable material that can flame in a very short time such as papers and woods. Also, some places contain very valuable materials such as libraries, archives and records repositories. Therefore, over time, fire detection systems have gained big importance in environments containing valuable documents and information.

Wireless sensor networks (WSNs) are equipped with sensors to monitor physical or environmental conditions, such as temperature, sound, pressure, etc. Today, with the big progress in the field of technology, WSN has become increasingly widespread with the reductions in its node size and in the cost. Therefore, it has been used in many scopes and areas, such as military technology, agricultural, climate observation, and fire management. In this study, a fire detection system based on WSN has been studied. The system was developed using TinyOS for WSN application. The sensors can work cooperatively to pass their data through the network from one location to another, and this mechanism has been implemented in the proposed system by using a multi-hop algorithm for the communication between different sensor nodes in the network. Also, a software component was written in Java to display the data of the sensors with a graphical user interface. Finally, a sink node has been used which works as a bridge between the sensors and the GUI software.

Introduction

Wireless sensor networks (WSNs) are networks equipped with autonomous sensors to monitor physical or environmental conditions, such as temperature, sound, pressure, etc. Today, with the big progress in the field of technology, WSN has become increasingly widespread with the reductions in the size and in their costs. Therefore, WSN has become widespread and used in many scopes and areas, such as military technology, agricultural, climate observation, animal husbandry, and fire management. WSN has an advantage from other networks that the network can work for a long period of time with very low power consumption, also the sensors in the network can work cooperatively to pass their data through the network from one far location to another, and this mechanism can be installed by using multi-hop algorithm which is implemented in our proposed system. The sensors work on event-driven basis, in this way they can work to identify and alert from a potential situations which may occur, as a result, WSN introduce danger management system that can optimize the business processes by facilitating fast responses to unexpected situations and perform these operations with minimal communication costs [1-7].

The nodes in the WSN system have application-specific sensing features. Each node in the network transmits its data to its ancestor, the last sensor which addresses the data in the network is the output node. The output node collects the data from the other nodes in the WSN and forwards it to another network [8-12]. An overview of WSN structure is shown in Figure 1.

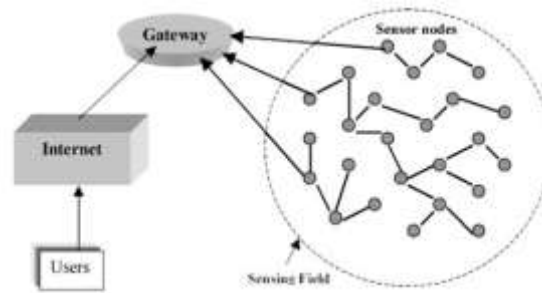


Figure 1. General structure of wireless sensor networks

System Architecture and Design

The designed system consists of two main sections. The first is the wireless sensor network itself that includes the hardware parts while the other is the software and the user side. Below the system design diagram is given, the visualization of the structure and design of the system is illustrated in Figure 2.

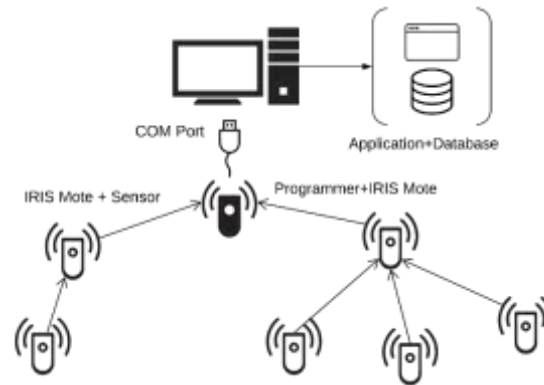


Figure 2. The architectural view of the proposed system

The designed system basically consists of the nodes that will take the measurements of the temperature, the gateway node (sink node) from which the information is collected from the other nodes, the computer application in which the information is being processed and presented, and the database in which the measured information is stored [13]. The use case diagram of the system is shown in Figure 3.

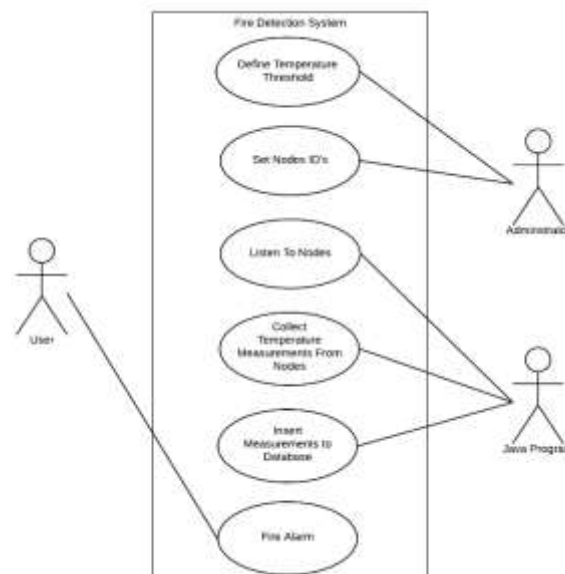


Figure 3. Use case diagram of the system

The hardware components consist of two parts, the wireless measurement system IRIS XM2110 [11], it is illustrated in Figure 4. The range for Radiofrequency (RF) of Transceiver for the IRIS XM2110 is approximately 300 m in outdoor and 50 m in indoor. This node operates at 2.4 GHz frequency and complies with the IEEE 802.15.4 standard [14]. The device has a wide range of sensor card support, but in our system a card with temperature sensors is required.



Figure 4. IRIS XM2110 system and its block diagrams

The second component is the sensor and data acquisition MDA100CB which used to obtain information (temperature), shown in Figure 5. There are mounts for light and temperature information acquisition on this card. This card is must be installed in IRIS system and work together to take the temperature measurements [13].

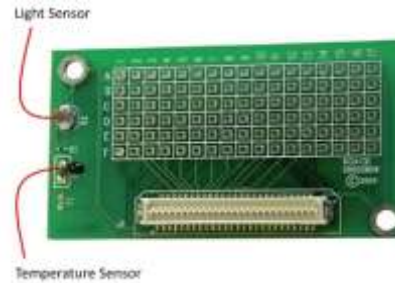


Figure 5. MDA100CB sensor card

The TinyOS operating system is used on IRIS sensor nodes. The applications are developed with a C-based programming language, which called nesC programming language. TinyOS is event-based operating system and it is a system aims to make it easier to implement applications on the low power devices [15-18]. TinyOS, which is used in processing power and memory limited devices, has a lighter structure than conventional operating systems. TinyOS consists of different components. These components are used for different purposes in applications. Each application adds the necessary components to its needs and can achieve the main goal using fewer resources. In general, TinyOS offers a variety of services to the components of a wireless sensor node.

The temperature measurement sensing component is on the MDA100CB card. There is an analog-to-digital converter (ADC) to convert the temperature measurement. There are a total of 8 ADC inputs in one node. A thermistor, YSI 44006, which is a semiconductor material as a temperature sensor, is on the card. This material has a Negative Temperature Coefficient (NTC). This means that as the temperature increases, the resistance of the material decreases. The temperature is measured by taking advantage of this property of the material. The thermistor connected to a voltage divider circuit is connected to the ADC1 input of the nodes. The temperature characteristic of the resistance of the thermistor is not linear. However, it is also possible to perform operations by accepting linearly at 0-50 degrees. The value obtained from ADC1 can be calculated as the centigrade. It is considered to be 50 C

when 1023 is taken. For example, if 544 values are read through the developed program, 544 values are 26.5 C. This measurement is also close to room temperature. [19]

Due to the needs of the system to work by using multi-hop routing, the Collection Tree Protocol (CTP) is used, this protocol collects data from different nodes and sends data by using different nodes to reach the final destination (root node), possibly by providing a versatile network layer. The collection is an essential process in the sensors network. The Collection Tree Protocol (CTP) is a reference collection protocol in TinyOS 2.x. In the next diagram Figure 6, explains how the collection protocol is working [11, 17].

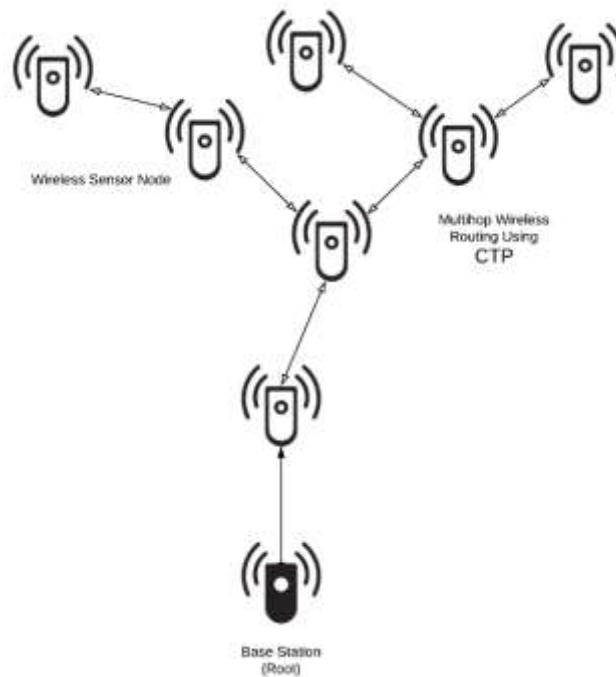


Figure 6. CTP Routing Topology

CTP is a tree-based collection protocol, in the network some nodes intend to advertise themselves as roots in the tree. The nodes in the network shape a set of routing trees to these roots. CTP is address-free which means the node does not send a packet to a specified root; it tries to choose a root by determining a next hop. Nodes generate routes to roots using a gradient-based routing. The data link layer should provide four things for CTP protocol to work properly [17]:

- 1) Provides local broadcast address.
- 2) Provides synchronous acknowledgments for unicast packets.
- 3) Supports multiple higher-level protocols.
- 4) Has single-hop 16-bit source and destination fields.

The sink node, receives the readings from the other nodes where measurements are taken with periods of 2.5 s. Accepted information is sent to the computer by the IRIS node which connected to the computer, the virtual serial communication interface becomes available when serial data are sent from the nodes, the information is transmitted through the communication interface. The application on the computer uses this interface to receive the information.

The third essential part is the software which is developed in the Java language using the NetBeans Integrated Development Environment (IDE). The computer application uses a Java Swing library to create a Graphical User Interface (GUI). In the GUI the user must enter some information such as specifying the communication port, communication speed baud rate of the nodes, node identification numbers and a temperature threshold value. After connection is established with the sink node, the nodes in the network get the temperature readings and pass them to the sink node which connected to the application, and the temperature information is shown on the screen. In this application, the hexadecimal

base (hex) temperature information is converted to degrees Celsius values. The measurements information is recorded in a database by adding the time tag according to the ID number of node. The database which was created with MySQL has a table contains the node ID number, temperature, normal or warned status and time stamp. Figure 7 shows the block definition diagram of the software.

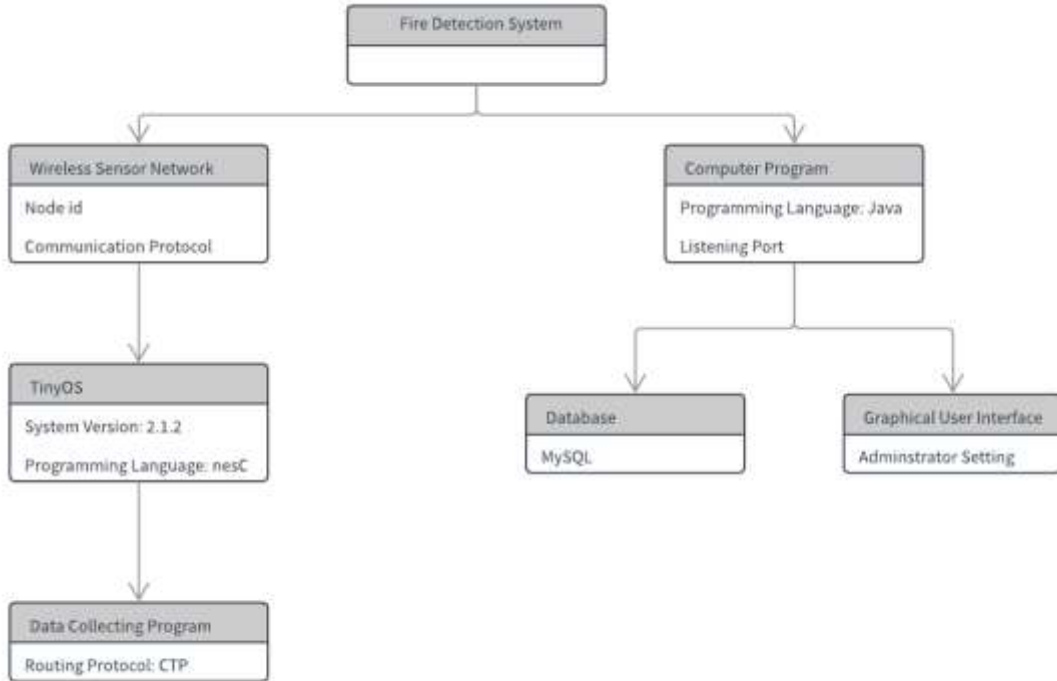


Figure 7. Block definition diagram of the system

System Programming and Implementation

In order to make the nodes in the network work according using multi-hop routing algorithm, a multi-hop routing code has been implemented in the nodes in the network. The implemented program is 'MultihopOscilloscope', it is a simple data-collection program, it periodically samples the default sensor and broadcasts a message every few readings. These readings can be displayed by developed java program. The 'MultihopOscilloscope' program works in all nodes, the root (sink) node and the other nodes, the sink node collects data (measurements) from other nodes, and the other nodes just gets temperature readings by the their sensors. Figure 8 shows how the root node works and collects data from the other nodes in the network [13].

The code part of the sink node, collects all data from other nodes and forward them to the serial for processing on the computer that connected to the network.

3rd International Students Science Congress
3-4 May 2019, İzmir - Turkey

```

event message_t*
Receive.receive(message_t* msg, void *payload, uint8_t len) {
    oscilloscope_t* in = (oscilloscope_t*)payload;
    oscilloscope_t* out;
    if (uartbusy == FALSE) {
        out = (oscilloscope_t*)call SerialSend.getPayload(&uartbuf, sizeof(oscilloscope_t));
        if (len != sizeof(oscilloscope_t) || out == NULL) {
            return msg;
        }
        else {
            memcpy(out, in, sizeof(oscilloscope_t));
        }
        uartlen = sizeof(oscilloscope_t);
        post uartSendTask();
    } else {
        // The UART is busy; queue up messages and service them when the
        // UART becomes free.
        message_t *newmsg = call UARTMessagePool.get();
        if (newmsg == NULL) {
            // drop the message on the floor if we run out of queue space.
            report_problem();
            return msg;
        }

        //Serial port busy, so enqueue.
        out = (oscilloscope_t*)call SerialSend.getPayload(newmsg, sizeof(oscilloscope_t));
        if (out == NULL) {
            return msg;
        }
        memcpy(out, in, sizeof(oscilloscope_t));

        if (call UARTQueue.enqueue(newmsg) != SUCCESS) {
            // drop the message on the floor and hang if we run out of
            // queue space without running out of queue space first (this
            // should not occur).
            call UARTMessagePool.put(newmsg);
            fatal_problem();
            return msg;
        }
    }

    return msg;
}

```

Figure 8. The code of the sink node using nesC

```

event message_t*
Snoop.receive(message_t* msg, void* payload, uint8_t len) {
    oscilloscope_t *omsg = payload;

    report_received();

    // If we receive a newer version, update our interval.
    if (omsg->version > local.version) {
        local.version = omsg->version;
        local.interval = omsg->interval;
        startTimer();
    }

    // If we hear from a future count, jump ahead but suppress our own
    // change.
    if (omsg->count > local.count) {
        local.count = omsg->count;
        suppress_count_change = TRUE;
    }

    return msg;
}

```

Figure 9. The code of the normal nodes using nesC

The code part in Figure 9 of the ‘MultihopOscilloscope’ works on the all nodes except the sink node, it makes the network hears the traffic in the network. In the user side of the system, the program will process the collect data and view it in the designed GUI on the screen [13]. Figure 10 shows excerpts of the Java code.

```

while (inputStream.available() > 0) {
    //getting input stream, wait for data to be made available
    numBytes = inputStream.read(readBuffer);
    //read serial port
    for (int v = 0; v < nodes.length; v++) {
        for (int z = 0; z < 64; z++) {
            //navigation over received packets
            if(z==0)
                System.out.println();
            System.out.printf("%s ",readBuffer[z]);
            if (readBuffer[z] == Integer.parseInt(nodes[v])) {
                //get the information according to ID
                if (readBuffer[z + 3]==0x01||readBuffer[z + 3]==0x02||readBuffer[z + 3]==0x03) {
                    String result1 = String.format
                    ("Node ID=%s, Hex=%02X%02X", nodes[v], readBuffer[z + 3], readBuffer[z + 4]);
                    //convert hex to decimal
                    hexdeg = 256 * readBuffer[z + 3] + readBuffer[z + 4];
                    //achieving centigrade degrees
                    cdeg = calculateDegree(hexdeg);
                    //System.out.printf(" Cdeg=%.02f ", cdeg);
                    String result2 = String.format(" Cdeg=%.02f \n", cdeg);
                    result = result + result1 + result2;
                    //displays the information in the screen
                    txtReadData.setText(result);
                    System.out.println();
                    if (k == 10) {
                        //After 10 readings, it records these readings in the database
                        k=0;
                    }
                    k++;
                    if (cdeg > threshold) {
                        //shows a warning allert if the heat is above the threshold
                        new ErrorMessage().setVisible(true);
                        //record the warning allert in the database
                    }
                }
            }
            System.out.println();
        }
    }
}

```

Figure 10. Java code of the program

The system has been tested within the scope of using just three nodes and sink node. Sensor nodes with numbers 22, 55 and 77 and sink node were used during the test. The layout of the nodes is given in Figure 11.

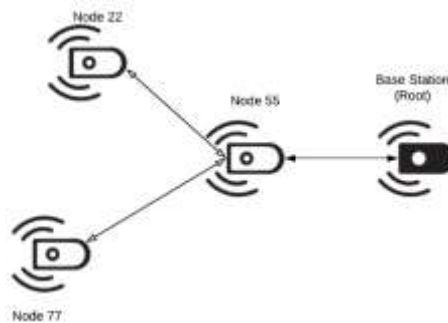


Figure 11. Layout of the tested system

A screenshot taken from the computer application during the operation of the system is also shown in Figure 12. By providing the required values, the communication speed and communication port, and the temperature threshold which was selected as 40. After the system starts working, the sink node sets itself as the root because it has the ID number 0, and the signal reaches the node 55 first. Since the message will be forwarded to the nodes 22 and 77 from the node 55, these nodes transmit the packets to the node 55. Thus, the system is working on two hops basis. A warning alert that will be triggered if the temperature exceeds the threshold can be seen in the Figure 12.



Figure 12. Screenshot of alert message

Experiments and Evaluation

Some experiments have been conducted to compare the proposed system with an industrial fire and smoke detector. With these experiments, we aim to evaluate the performance of the new system (see Figure 13). The experiments have been performed inside a box that contains the sensors of our system and the industrial fire detector. The experiments model a real fire case on a small scale. According to the results obtained from the experiments; the industrial fire detector is reacted up to 120 s to start the alarm, but the nodes in the proposed system have responded to the fire (to the rising temperature) much faster. The response was about within 30 s in average and the alerting message in the application was sent to the user. The proposed system has also some other features: easy installation and simple to operate and interact with the user. As result, the losses and damages can be drastically reduced with quick responses of the proposed system.



Figure 13. Experiment work illustration

Conclusion

In this study, a fire detection system is developed using TinyOS and Java. The main components of the system are the IRIS XM2110 node and the MDA100CB sensor card that are used to get the temperature readings from the observed environment. An experiment to evaluate and compare the system with an industrial system is conducted that is a simulation of a small real fire case on a small scale. It has been observed that the sensors in our proposed system have been responded to the arising of temperature after 30 s, also the alarm was released after the temperature exceeded the threshold value, while the industrial system has released the sound alarm after about 120 seconds of starting the fire.

Acknowledgement

The first author of this study was supported by the Presidency for Turks Abroad and Related Communities (YTB) within “International Student Academy” Project.

References

- [1] Rao S, Nithya GK, Rakesh K (2014) Development of a wireless sensor network for detecting fire and gas leaks in a collapsing building, Fifth International Conference on Computing, Communications and Networking Technologies (ICCCNT): 1-7.
- [2] Wei X, Wang Y, Dong Y (2014) Design of fire detection system in buildings based on wireless multimedia sensor networks, Proceeding of the 11th World Congress on Intelligent Control and Automation: 3008 – 3012.
- [3] Wang Z, Li Z (2012) Underground building fire emergency communication network based on mesh networks. International Conference on Computer Science and Service System: 914 – 917.
- [4] Yin K, Jiang J (2014) Application of fire monitoring and personnel evacuation in subway station based on wireless sensor network, 2014 International Conference on Audio, Language and Image Processing: 110 – 114.
- [5] Chen Y, Zhang D, Chen J, Liu K, Yang F (2016) A new fire protection system of power cable tunnel based on wireless sensor network monitoring system, 2016 IEEE 11th Conference on Industrial Electronics and Applications (ICIEA): 1103 – 1106
- [6] Zhang J, Li W, Yin Z, Liu S, Guo X (2009) Forest fire detection system based on wireless sensor network, IEEE 4th Conference on Industrial Electronics and Applications (ICIEA) 2009.
- [7] Bouabdellah K, Noureddine H, Larbi S (2013) Using wireless sensor networks for reliable forest fires detection. Procedia Computer Science 19: 794-801.
- [8] Kumar S, Rajasekaran S (2011) Detection and extinguishing forest fires using wireless sensor and actor networks. International Journal of Computer Applications 24(1): 31-35.
- [9] Liu Y, Gu Y, Chen G, Ji Y, Li J (2011) A novel accurate forest fire detection system using wireless sensor networks, Seventh Int. Conference on Mobile Ad-hoc & Sensor Networks: 52-59.
- [10] Herutomo A, Abdurrohman M, Suwastika NA, Prabowo S, Wijutomo CW (2015) Forest fire detection system reliability test using wireless sensor network and Open MTC communication platform. 3rd Int. Conference on Information and Communication Technology: 87-91.
- [11] Devadevan V, Suresh S (2016) Energy efficient routing protocol in forest fire detection system. 6th International Conference on Advanced Computing: 618-622.
- [12] Liu J, Tian Y, Qi H (2012) Wireless Sensor Networks for Fire Detection in the Library Environment. Applied Mechanics and Materials, vol. 166-169, pp. 2684-2687, 2012
- [13] Arslan S, Challenger M, Dağdeviren O (2017) Kütüphaneler için telsiz duyurğa ağı tabanlı yangın tespit sistemi, UBMK 2017.
- [14] Lu G, Xue W (2010) Adaptive weighted fusion algorithm for monitoring system of forest fire based on wireless sensor networks. 2nd Int. Conf. on Computer Modeling & Simul 4:414-417.
- [15] Liu J, Tian Y, Qi H (2012) Wireless sensor networks for fire detection in the library environment. Applied Mechanics and Materials 166: 2684-2687.
- [16] Bhattacharjee S, Roy P, Ghosh S, Misra S, Obaidat MS (2012) Wireless sensor network-based fire detection, alarming, monitoring and prevention system for Bord-and-Pillar coal mines. Journal of Systems and Software 85(3): 571-581.
- [17] Fonseca R, Gnawali O, Jamieson K, Kim S, Levis P, Woo A (2006) The Collection Tree Protocol (CTP), *TinyOS Enhancement Proposals* 123.
- [18] Soliman H, Sudan K, Mishra A (2010) A smart forest-fire early detection sensory system: Another approach of utilizing wireless sensor and neural networks, SENSORS IEEE: 1900-1904.
- [19] Demin G, Haifeng L, Anna J, Guoxin W (2014) A forest fire prediction system based on rechargeable wireless sensor networks, 4th IEEE International Conference on Network Infrastructure and Digital Content: 405 – 408.

The Average Binding Number of Trees

Ayşe Kahveci*, Manisa Celal Bayar Üniv., Dept. of Software Engineering, Manisa, Turkey

Ersin Aslan, Manisa Celal Bayar Üniv., Dept. of Software Engineering, Manisa, Turkey

*Corresponding author e-mail: a.kahveci.a@gmail.com

Keywords: Graph theory, connectivity, binding number, vulnerability

Discipline: Computer Science and Engineering

Abstract

Vulnerability in a system is a measurement of the durability in the case of a particular system reduction of functionality or completely damage of the system. It is called the hat vulnerability of the network to measure the endurance of the network until communication is interrupted by the deterioration of the connection lines between some centers or centers in a network. The centers of the network can be modeled such that the vertex of the network and the connecting lines are the distances of the graph, while investigating the strength of a communication network against disturbances that may occur in the centers or connecting lines. Various parameters can be used to measure the vulnerability, such as connectivity, integrity, binding number, average binding number. In this study, the average binding number was studied. For $v \in V(G)$, the local binding number of v is $bind_v(G) = \min_{S \in F_v(G)} \left\{ \frac{|N(S)|}{|S|} \right\}$, where $F_v(G) = \{S \subseteq V(G) | v \in S, S \neq \emptyset, N(S) \neq V(G)\}$. Furthermore, the average binding number of G is defined as $bind_{av}(G) = \frac{1}{n} \sum_{v \in V(G)} bind_v(G)$, where n is the number of vertices in graph G . In this paper, we determine the average binding number of trees. Also an algorithm for computing for the tree is given.

Introduction

Nowadays, transportation of an object or information is increasingly getting more important. Nonetheless, it is demanded that the communication is fast, safe and continuous. A network occurs from stations and communication links. It is an important question that, for any bad and negative condition how long and how a network will respond. When the network begins to lose connections or stations, it will ultimately lose its effectiveness. For this reason, networks should be constructed not only in relation to initial degradation, but also as stable as possible for possible reconstruction of the network.

The degree of v , denoted by $deg(v)$, is the cardinality of its open neighborhood. A vertex with degree one in a graph G is called pendant or a leaf or an end-vertex, and its neighbor is called its support or cut vertex. An edge incident to a leaf in a graph G is called a pendant edge. A graph with no cycle is acyclic. A tree T is a connected acyclic graph.

$G=(V,E)$ graph is consist of a non-empty cluster of vertices (V) and the edges (E) combining these non-linear vertices couples. For a G graph, open neighborhood of a vertex (u) is; $N(u) = \{v \in V(G) | (u,v) \in E(G)\}$ and closed neighborhood of a vertex (u) is; $N[u] = \{u\} \cup N(u)$. Similarly; for any subset of $S \subseteq V(G)$, open neighborhood is $N(S) = \bigcup_{u \in S} N(u)$ and closed neighborhood is $N[S] = \bigcup_{u \in S} N[u]$. A minimum vertex cover is a vertex cover having the smallest possible number of vertices for a given graph. The size of a minimum vertex cover of a graph G is known as the vertex cover number and is denoted $\alpha(G)$. The vertex independence number of a graph, often called simply "the" independence number, is the cardinality of the largest independent vertex set, i.e., the size of a maximum independent vertex set. The independence number is most commonly denoted $\beta(G)$. S defines vertex number of chosen and $N(S)$ defines the neighborhood numbers of the vertices which were chosen.

Endurance of a system for the time among any damage on centers or connection between some centers in a network until the breakdown of the network is called "vulnerability of the network". While investigating the robustness of a communication network against distortions that may occur in the centers or connecting lines, various parameters such as the number of connectivity, the number of integrity, binding number, average binding number and the toughness can be used to measure the vulnerability. n -centered a communication network can be modeled as a graph. Here, the centers of the network correspond to the tops of the graph and the links between these centers correspond to the edges of the graph.

Vulnerability in the network is a measure of the network's strength in the face of any damage to the lines representing the connection between the centers of the network or the centers. Considering that the data flow is a fundamental principle in a communication network, research should be made about what the network will be after the damage, how much of it will be damaged or the cost of reinstatement. For example, consider a country's inter-city transport network. In this case, the stations in the city centers (bus stations) form the centers of the network, and the roads between the stops create the lines between the centers. While investigating the damage on any station and / or road that was occurred for some reasons; such "What are the number of stops that have been damaged?", "What is the number of damaged roads?", "What is the number of stops that are being transported after the damaged stops and roads?", "What is the number of stops that continue without the most disconnection?" as many questions may come to mind. This is only possible by measuring the magnitude of the damage in the network or by analyzing the durability of the initial network. If these analyzes are performed while the network is being designed, the most suitable network model can be selected when the design is in progress. The first theorem of graph theory has been proved by five Swiss mathematicians by solving the question put forth on the Königsberg seven bridge by Leonhard Euler (1707-1783) in. After this solution, graph theory has been used effectively in modeling and solving many problems.

In the age of technology we live, if a network starts to lose connection lines or centers, it is ineluctable that some problems or delays will occur and even large time losses will occur. For example, if the tower in an airport is disconnected from some of the planes that want to land, an airplane trying to land without contacting the tower could cause some accidents. In this case, in order to investigate the damage to the landing field and other damages caused by this accident (such as disruption of other flights), the remaining structure must be examined after the accident. As a result of this examination, the extent of the damage is considered. For instance, the landing field at the airport may be completely damaged, or some of the landing fields is intact, and other runs can be made on the solid track. This situation can reduce the damage we suffer. Therefore, in order to investigate the damage that may occur in the communication network, the status of the remaining network should be examined following the deterioration of the communication network. Today, the reliability and vulnerability of networks that provide communication and communication are of great importance for reasons similar to those mentioned above. Communication networks; Since the centers of the chart and the connections between the centers are the diagrams of the chart, various vulnerability parameters have been defined in the charts to investigate the vulnerability of communication networks.

Graphs are considered as a model for the reliability and vulnerability of communication networks. A top of each centerline forming the communication network and the connecting lines between these centers are also referred to as graphical distances. In graph theory, the minimum value of the measurement of the neighborhood of the vertex or the vertices about the vulnerability is calculated by average binding number.

In this study, some bounds of the average binding number of some special trees are obtained. Finally, the algorithm for calculation of average binding numbers of trees is given.

Average Binding Number

For $v \in V(G)$, the local binding number of v is $bind_v(G) = \min_{S \in F_v(G)} \left\{ \frac{|N(S)|}{|S|} \right\}$, where $F_v(G) = \{S \subseteq V(G) | v \in S, S \neq \emptyset, N(S) \neq V(G)\}$. Clearly, $bind(G) = \min_{v \in V(G)} \{bind_v(G)\}$.

Furthermore, the average binding number of G is defined as $bind_{av}(G) = \frac{1}{n} \sum_{v \in V(G)} bind_v(G)$, where n is the number of vertices in graph G .

The related theorems of the average binding number and other graph parameters are provided as the followings.

Theorem 1 [1] If G is a graph of order n with the minimum degree $\delta(G)$, then

$$bind_{av}(G) \geq \frac{\delta(G)}{n - (G)}$$

Theorem 2 [1] If G is a graph of order n with covering number $\alpha(G)$ and independence number $\beta(G)$, then

$$bind_{av}(G) \leq \frac{\alpha(G)(\beta(G) + n - 1)}{n\beta(G)}.$$

Theorem 3 [1] If G is a graph of order n with the minimum degree $\delta(G)$ and maximum degree $\Delta(G)$, then

$$bind_{av}(G) \geq \frac{\delta(G)}{\Delta(G) + 1}.$$

Theorem 4 [1] If H is a spanning subgraph of G , then

$$bind_{av}(H) \leq bind_{av}(G).$$

Theorem 5 [1] If G is a graph of order n , then

$$bind(G) \leq bind_{av}(G).$$

The average parameters have been found to be more useful in some circumstances than the corresponding measures based on worst-case situations. Thus incorporating the concept of the binding number and the idea of the average lower connectivity introduces a new graph parameter called the average binding number, $bind_{av}(G)$. The average binding number gives the meaning that, if $bind_{av}(G)$ is large, then the vertices of G are well bound together in the sense that G has a lot of fairly well distributed edges.

For complete review and the following existing results on the binding number and its related concepts, we follow

Example 1: Consider the graph G in Figure 1, where $|V(G)|= 5$ and $|E(G)|= 4$.



Figure 1. Path 5

Note that $bind_{p_1} = \frac{2}{3}$, $bind_{p_2} = 1$, $bind_{p_3} = \frac{2}{3}$, $bind_{p_4} = 1$, and $bind_{p_5} = \frac{2}{3}$. It follows that

$$bind_{av}(G) = \frac{1}{5} \left(\frac{2}{3} + 1 + \frac{2}{3} + 1 + \frac{2}{3} \right) = 0.8$$

The Average Binding Number of Trees

In this section, the average binding numbers of trees, Double Star, Comet Graph and thorn Graph are calculated.

Definition 1. The double star (Figure 2) $K_{r,m}$ is a tree with diameter 3 and central vertices of degree r and m respectively, where the diameter of graph is the length of the shortest path between the most distanced vertices.

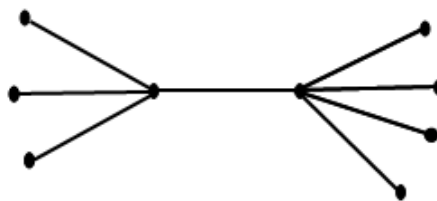


Figure 2. Double Star 4,5

Theorem 6 If $K_{r,m}$ is a double star graph with $r \geq 2$ and $m \geq 1$, then

$$bind_{av}(K_{r,m}) = \frac{3}{r+m-1}$$

Proof. Let $v \in V(K_{r,m})$, $S_v \in F_v(K_{r,m})$. There is a local binding set S_v of $V(K_{r,m})$ such that $|S_v| = r+m-2$, when S_v contains all isolated vertices in set of $K_{r,m}$, then $|N(S_v)|=2$. Thus $bind_v(K_{r,m}) = \frac{2}{r+m-2}$ for $r+m-2$ vertices of $K_{r,m}$.

If $\deg(v)=r$ then there is a local binding set S_v of $V(K_{r,m})$ such that $|S_v| = r+m-1$ and $|N(S_v)|=r+1$. Thus $bind_v(K_{r,m}) = \frac{r+1}{r+m-1}$.

If $\deg(v)=m$ then there is a local binding set S_v of $V(K_{r,m})$ such that $|S_v| = r+m-1$ and $|N(S_v)|=m+1$. Thus $bind_v(K_{r,m}) = \frac{m+1}{r+m-1}$.

By the definition

$$bind_{av}(K_{r,m}) = \frac{1}{r+m} \sum_{v \in V(K_{r,m})} bind_v(K_{r,m}) = \frac{\frac{2}{r+m-2}(r+m-2) + \frac{r+1}{r+m-1} + \frac{m+1}{r+m-1}}{r+m}$$

$$bind_{av}(K_{r,m}) = \frac{3}{r+m-1}$$

Definition 2. A comet $C_{t,r}$ is a graph obtained by identifying one end of a path $P_t \geq 2$, with the center of a star $K_{1,r}$ ($r \geq 2$). The center of $K_{1,r}$ is called the center of $C_{t,r}$.

Consider the graph G in Figure 3 where $|V(G)|= 16$ and $|E(G)|= 15$.

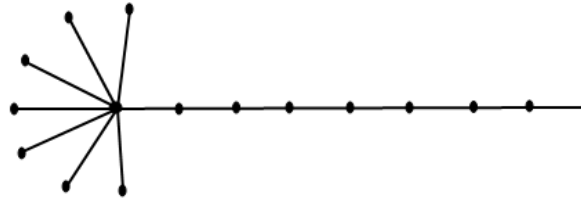


Figure 3. Comet Graph

Theorem 7 If $C_{t,r}$ is a comet graph $r \geq 2$ and $t \geq 2$, then

$$bind_{av}(C_{t,r}) = \frac{2t + 2r + 1}{(r+t)(r+1)}$$

Proof. Let the vertices of P_t be p_1, p_2, \dots, p_t in order along the path, $\deg(p_1)=1$ and $\deg(p_t)=r+1$. Let $v \in V(C_{t,r})$, $S_v \in F_v(C_{t,r})$. We distinguish two cases.

Case 1: If $v \in V(K_{1,r})$ then there is a local binding set S_v of $V(C_{t,r})$ such that $|S_v| = r$, when S_v contains all isolated vertices in set of $C_{t,r}$, then $|N(S_v)|=1$.

Case 2: Assume $v \in V(P_t)$.

- If $v=\{p_1\}$ or $v=\{p_{t-1}\}$ then we have $|S_v| = r+1$ and $|N(S_v)|=2$. Thus $bind_v(C_{t,r}) = \frac{2}{r+1}$ for two vertices.

- If $v=\{p_t\}$ then we get $|S_v| = r+1$ and $|N(S_v)|=r+2$. Thus $bind_v(C_{t,r}) = \frac{r+2}{r+1}$.

• If $v \in \{p_2, p_3, \dots, p_{t-2}\}$ then there is a local binding set S_v of $V(C_{t,r})$ such that $|S_v| = r+1$ and $|N(S_v)|=3$. Thus $bind_v(C_{t,r}) = \frac{3}{r+1}$.

By the definition

$$bind_{av}(C_{t,r}) = \frac{1}{r+t} \sum_{v \in V(C_{t,r})} bind_v(C_{t,r}) = \frac{\frac{1}{r}(r) + \frac{2}{r+1}(2) + \frac{r+2}{r+1} + \frac{2}{r+1}(t-3)}{r+t}$$

$$bind_{av}(C_{t,r}) = \frac{2t + 2r + 1}{(r+t)(r+1)}$$

There is a local binding set S_v of $V(K_{r,m})$ and such that $|S_v| = r+m-2$, when S_v contains all isolated vertices in set of $K_{r,m}$, then $|N(S_v)|=2$. Thus $bind_v(K_{r,m}) = \frac{2}{r+m-2}$ for $r+m-2$ vertices of $K_{r,m}$.

If $\deg(v)=r$ then there is a local binding set S_v of $V(K_{r,m})$ such that $|S_v| = r+m-1$ and $|N(S_v)|=r+1$. Thus $bind_v(K_{r,m}) = \frac{r+1}{r+m-1}$.

If $\deg(v)=m$ then there is a local binding set S_v of $V(K_{r,m})$ such that $|S_v| = r+m-1$ and $|N(S_v)|=m+1$. Thus $bind_v(K_{r,m}) = \frac{m+1}{r+m-1}$.

Definition 3. Let p_1, p_2, \dots, p_n be non-negative integers and G be such a graph, $V(G) = n$. The thorn graph of the graph, with parameters p_1, p_2, \dots, p_n , is obtained by attaching p_i new vertices of degree 1 to the vertex u_i of the graph G , $i = 1, 2, \dots, n$. The thorn graph of the graph G will be denoted by G^* or by $G^*(p_1, p_2, \dots, p_n)$, if the respective parameters need to be specified.

Theorem 8 Let P_n^* be a thorn graph of P_n path with every $p_i = 1$. Then

$$bind_{av}P_n^* = 1.$$

Proof. The cardinality of local binding set is $bind_v(P_n^*)$ is always the same for every vertex of any P_n^* and 1. Then, we have

$$bind_{av}P_n^* = 1.$$

Theorem 9 Let P_n^* be a thorn graph of P_n path with every $p_i = k$ and $k > 1$. Then

$$bind_{av}(P_n^*) = \frac{(k+1)n^2 + n + kn}{(nk+k)(nk+1)}.$$

Proof. Let $v \in V(P_n^*)$, $S_v \in F_v(P_n^*)$.

If $\deg(v)=1$ then there is a local binding set S_v of $V(P_n^*)$ such that $|S_v| = nk$ and $|N(S_v)|=n$. Thus $bind_v(P_n^*) = \frac{n}{nk} = \frac{1}{k}$ for nk vertices of P_n^* .

If $\deg(v)>1$ then there is a local binding set S_v of $V(P_n^*)$ such that $|S_v| = nk+1$ and $|N(S_v)|=n+k$. Thus $bind_v(P_n^*) = \frac{n+k}{nk+1}$ for n vertices of P_n^* .

By the definition

$$bind_{av}(P_n^*) = \frac{1}{(n+1)k} \sum_{v \in V(P_n^*)} bind_v(P_n^*) = \frac{\frac{1}{k}(nk) + \frac{n+k}{nk+1}(n)}{(n+1)k}$$

$$bind_{av}(P_n^*) = \frac{(k+1)n^2 + n + kn}{(nk+k)(nk+1)}.$$

Algorithm

In this section, we are giving an algorithm for determining average binding number of any tree. We will be using some variants defined below;

VG, cluster of the peaks of a G graph,

S, non-empty cluster of the peaks of VG (chosen peak quantity)

NS, neighborhood quantity of chosen peaks,

bG[v], local binding number of a tree.

Step 0. Start

Step 1. $v=0$

Step 2. $v++$

Step 3. look at the tip peaks first of the trees

Step 4. Find the bG[v] values of the v. nodes.

Step 7. If $v < VG$ then goto step 2

Step 9. $bind(av) = \frac{1}{VG} \sum_{v \in V(G)} bind_v(G)[v]$

Step 10. Stop.

The algorithm first selects the peak number and finds the neighborhood number of the selected peaks. Then each peak is the binding number is found. and is found. Finally, it returns the average binding number of the tree.

Conclusion

In this study, a new tree theoretical parameter, namely, the average binding number, as the average of the local binding number of every vertex of a tree, has been presented for the network vulnerability. Additionally, the stability of popular interconnection networks has been studied and the average binding numbers have been computed. The average binding number gives the meaning that, if $bind_{av}(G)$ is large, then the vertices of G are well bound together in the sense that G has a lot of fairly well distributed edges.

References

- [1] Aslan E (2019) The Average Binding Number of Graphs. *Scienceasia*, 45(1): 85-91
- [2] Aslan E, Bacak-Turan G (2016) Mean rupture degree of graphs. *University Politehnica of Bucharest Scientific Bulletin-Series A-Applied Mathematics and Physics* 78(1): 233–242.
- [3] Aslan E and Kırlangıç A (2011) Computing the Scattering Number and the Toughness for Gear Graphs. *Bulletin of Society of Mathematicians Banja Luka*, Vol (18): 5-15
- [4] Bacak-Turan G, Kirlangic A (2013) Neighbor integrity of transformation graphs. *International Journal of Foundations of Computer Science* 24(3): 303– 317.
- [5] Bacak-Turan G and Kirlangic A (2011) Neighbor rupture degree and the relations between other parameters. *Ars Combinatoria* (102): 333–352.
- [6] Al-Tobaili SS (2008) On the binding number of lexicographic product of wheels with some graphs. *University of Sharjah Journal of Pure & Applied Sciences* 5(15): 11–23.
- [7] Wang Z and Wang Z (2006) Relationships between rupture degree and other parameters. *International Journal of Computer Mathematics* 83(12): 839–851.
- [8] Aytaç A, Odabas ZN (2011) Residual Closeness of Wheels and Related Networks. *International Journal of Foundations of Computer Science* (22): 1229–1240.
- [9] Kurkcu OK, Aksan H (2016) Neighbor toughness of graphs. *Bulletin of the International Mathematical Virtual Institute* 255 (6): 135–141
- [10] Kirlangic A and Aytac AO (2004) The Scattering Number of Thorn Graphs. *International Journal of Computer Mathematics*, 81(3): 299-311.
- [11] Bacak G (2010) Graflarda Zedelenebilirlik Ölçümleri. *Doktora Tezi*, 33-40s.
- [12] Turaci T, Okten M (2015) Vulnerability of mycielski graphs via residual closeness. *Ars Combinatoria* (118): 419–427.
- [13] Woodall DR (1973) The binding number of a graph and its Anderson number. *The Journal of Combinatorial Theory, Series B*(15): 225–255.

Environmental Engineering / Çevre Mühendisliđi

Geospatial Distribution Analysis and Investigation of Hydrochemical Groundwater Quality for Irrigation Purposes Using GIS and Suitability Indices: Case study of Altınova-Turkey

Alex Modi Lomoro Wani*, Ayşe Muhammetoğlu, Habib Muhammetoğlu
Akdeniz University, Dept. of Environmental Engineering, Antalya, Turkey
*Corresponding author: junioralex.modi@gmail.com

Keywords: groundwater quality, hydrochemistry, GIS, Altınova
Discipline: Environmental Engineering

Abstract

Groundwater resources in Turkey are extensively used for irrigation and domestic purposes along the Mediterranean region at the south of the country. Therefore, understanding and modeling the suitability of groundwater quality for irrigation and domestic uses are crucial for the management of groundwater resources. This study was carried out over the karstic area of Altınova region in Antalya City of Turkey aiming at assessing and mapping the suitability of groundwater quality for irrigation purpose and further assess hydrochemical characteristics of the groundwater. The groundwater quality parameters and index used for assessing the suitability of water for irrigation purpose include electrical conductivity (EC) and sodium absorption ratio (SAR). Additionally, US Salinity Laboratory USSL diagram (Wilcox diagram) was plotted. The Wilcox diagram show that the computed SAR and EC values in the study area ranges within the C2-S1 and C3-S1 classes. This suggested that groundwater quality in the study area is suitable for irrigation purpose. In the overall assessment, groundwater in the study area is associated with low sodium hazard, and medium to high salinity hazard. Therefore, it was concluded that the groundwater in the study area is good for irrigation purpose in regard to SAR.

Introduction

Groundwater resources account for about one-third of freshwater on the earth, and it is a vital natural resource for energy and food security, human health and ecosystem. Groundwater is preferable water resources across the world in spite of its difficult accessibility and extraction cost for usage in irrigation, domestic and industrial purposes. This is due to being less vulnerable to anthropogenic activities and variable climatic conditions [1]. Groundwater requires less treatment than surface water and it is generally easy to purify and make it suitable for usage. Groundwater has been contaminated and depleted in many aquifers around the world either by over-pumping or other anthropogenic activities [2]. Therefore, according to [3], and [4] the quality of groundwater for domestic and irrigation uses require continuous assessment. In Turkey, the availability of water per person is less than the world average [5] and a large quantity of water approximately 70%, is allocated for agriculture. Therefore, management of agricultural water resources and protection of water quality are challenging tasks, and periodic assessment of groundwater quality for irrigation is essential.

The present study was carried out in Altınova pilot study area (PSA) which is located approximately 10 km away from Antalya City. The PSA covers an area of approximately 75 km² and is situated on a plain where the mountains recede southward forming flat areas of a travertine plateau. The area is in the northwest border of Antalya international airport between the coordinates of 36 ° 54 '0 "and 37 ° 2' 0" northern latitudes, 30 ° 43 '0 "and 30 ° 50' 0" eastern longitudes (Figure 1). The geological formation of the PSA is mainly travertine, conglomerates and alluvium of the Kursunlu formation. Approximately 63 km² of the study area is covered by the karstic travertine formation which accounts for about 85% of the total study area. The Kursunlu formation consists of conglomerates and sandstone which mostly covers the eastern part of the PSA and accounts for approximately 14%. The third geological formation is the alluvium and conglomerates which cover only 1%. From the climatological point of view, the PSA has a Mediterranean type of climate with mild, rainy winters, hot and dry summers. Based on the meteorological data collected from the nearest meteorological station to the study area (Antalya Airport) for the years between 1994 and 2017, the average yearly precipitation of Altınova area was computed as 1191.5 mm/year.

**3rd International Students Science Congress
3-4 May 2019, İzmir - Turkey**

The PSA experiences low precipitation during the summer months of June, July and August as these are the hottest months of the year in the region. The mean maximum air temperatures were reported to range between 25 to 35 °C in summer and 14 to 17 °C in winter, for the years between 1994 and 2017, respectively.

The motivation behind this research is that Antalya is one of the most important agricultural cities in the Mediterranean region of Turkey with a leading greenhouse coverage. The total area of greenhouses in Antalya province constitutes 53% of the total area of greenhouses in the country [6], yet there is still little known about the irrigation water quality in the area. Furthermore, travertine karst regions of Antalya are facing a variety of environmental problems due to lack of proper wastewater collection system and excessive use of fertilizers and pesticides in agriculture. In some parts of the PSA, septic tanks are still common and domestic wastewater is directly discharged into the travertine aquifer via septic tanks. These septic tanks are among the major sources of contamination of groundwater resources in the area. With this current threat in the area, it is undoubtedly of great importance to take safety measures to protect the quality of water in the region. For this reason, this study aims to assess groundwater quality for agricultural purpose using irrigation water quality indices.

Methodology

The data sets used in this research were collected from 25 active irrigation wells. The locations of these wells were captured by means of GPS. The physicochemical characteristics of the groundwater samples were determined by onsite measurements and laboratory analyses following the standard procedures. To ascertain the reliability of the analyses results, the ionic charge balance percentage criteria was performed for each well, based on equation 1 [7]. The ionic balance error was generally within $\pm 5\%$. The parameters used for assessing the suitability of groundwater for irrigation purpose include electrical conductivity (EC) and sodium adsorption ratio (SAR). Additionally, US Salinity Laboratory USSL diagram (Wilcox diagram) was plotted, based on the computed SAR values and measured EC, to determine the suitability of groundwater for irrigation. The SAR values were computed using the formula given in equation 2 [7]. For the calculation of SAR, all the concentration of cation and anion were represented in milliequivalents per liter (meq/L). The results of these analyses were assessed and compared with the recommended irrigation water quality [8, 9]. The concentrations of major cations and anions as percentages of meq/L, were plotted in the Stabler Diagram, using Diagram software, to describe hydrochemical composition in the aquifer system and identify major ionic dominance in the groundwater of the PSA.

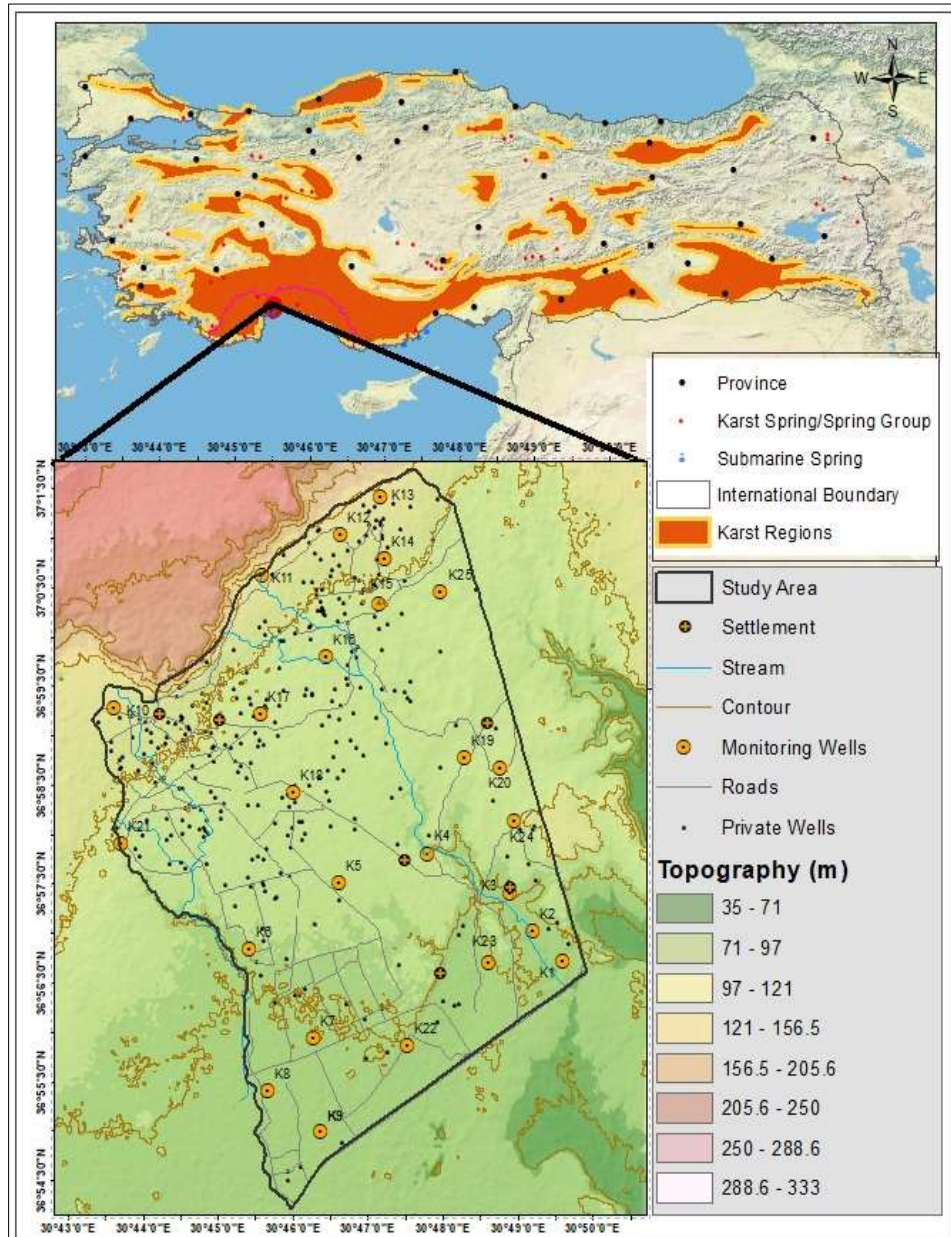


Figure 1. Karst regions in Turkey and geographical location of the study area

$$\text{Electroneutrality} = \frac{\sum \text{Cations} - \sum \text{Anions}}{\sum \text{Cations} + \sum \text{Anions}} \times 100 \quad (9)$$

$$\text{SAR} = \frac{\text{Na}^+}{\frac{\sqrt{\text{Ca}^{+2} + \text{Mg}^{+2}}}{2}} \quad (10)$$

The correlation analysis between TDS and the major anions and cations was performed to identify the hydrochemical processes and sources of salinization in the groundwater. The spatial variation of groundwater quality was assessed by geospatial analysis tool in the GIS environment. The spatial and the non-spatial database were integrated using a joint tool in ArcMap to generate spatial distribution maps of the suitability indices. Inverse Distance Weighted (IDW) spatial interpolation method was employed to delineate the distribution maps in ArcGIS 10.3.0.

Results

Hydrochemical characteristics

The overall summary of groundwater quality monitoring results from 25 active irrigation wells in the PSA is presented at Table 7 with the guideline values of agricultural water quality [8]. The pH values of groundwater samples varied from 6.88 to 7.30 with an average value of 7.10 which indicates neutral to weak alkaline water. The dominance of major ions in the groundwater samples of the PSA were in the order of $\text{Ca}^{++} > \text{Na}^+ > \text{Mg}^{++} > \text{K}^+$ (Figure 2). Among these ions, Ca^{++} concentration was the highest in the groundwater samples. The concentrations of Ca^{++} ion ranged from 75.6 to 162 mg/L (3.78 - 8.10 meq/L) with an average of 111.98 mg/L (5.6 meq/L). The concentrations of Na^+ ion was within the acceptable range of irrigation water quality. The concentrations of K^+ in the groundwater samples were relatively low in the entire PSA and all the samples were within the acceptable limits for safe agricultural water, except K6, which was relatively higher than the usual range of irrigation water quality. The dominance of the key anions in the study area were in the order of $\text{HCO}_3^- > \text{Cl}^- > \text{SO}_4^{-2}$ (Figure 2). HCO_3^- was relatively the dominant anion group observed in the groundwater samples. The concentrations of HCO_3^- varied from 132.8 to 439.2 mg/L (2.18 to 2.63 meq/L), with a mean value of 278 mg/L (4.59 meq/L). The high values of HCO_3^- might be associated with the geological formation of the PSA which is predominantly limestone and sandstones. The Cl^- concentrations ranged from 2.94 to 93.20 mg/L (0.08 to 2.63 meq/L) with an average of 23.36 mg/L (0.66 meq/L). The concentrations of SO_4^{-2} showed high variation within the range of 2.08 to 153.4 mg/L (0.04 to 3.19 meq/L) with a mean value of 31.53 mg/L (0.65 meq/L). The relationship between major ions (Ca^{++} , Na^+ , Mg^{++} , K^+ , HCO_3^- , Cl^- , SO_4^{-2} , HCO_3^-) and TDS were significant (Figure 3).

Table 7. Results of water quality monitoring study and the guideline values for irrigation water

Parameter	Symbol	Mean	Min	Max	Guideline value	NSAR*	
Electrical Conductivity (dS/m)	EC	0.7	0.42	0.96	0 – 3	dS/m	0
Total Dissolved Solids (mg/L)	TDS	429.3	267.98	611.99	0 – 2000	mg/L	0
Calcium (meq/L)	Ca^{++}	5.60	3.78	8.10	0 – 20	meq/L	0
Magnesium (meq/L)	Mg^{++}	0.53	0.12	1.99	0 – 5	meq/L	0
Sodium (meq/L)	Na^+	0.54	0.21	1.05	0 – 40	meq/L	0
Bicarbonate (meq/L)	HCO_3^-	4.59	2.18	7.20	0 – 10	meq/L	0
Chloride (meq/L)	Cl^-	0.66	0.08	2.63	0 – 30	meq/L	0
Sulphate (meq/L)	SO_4^{-2}	0.66	0.04	3.19	0 – 20	meq/L	0
Nitrate (mg/L)	NO_3^-	45.75	0.34	>100			
Potassium (mg/L)	K^+	0.05	1.04	8.3	0 – 2	mg/L	0
pH	pH	7.10	6.88	7.30	6.0 – 8.5	-	0
Sodium Adsorption Ratio (meq/L)	SAR	0.30	0.14	0.56	0 – 15	meq/L	0

NSAR* = Number of samples above range, where the range value limit is based on guidelines for irrigation water quality [8]. Min and Max denote minimum and maximum values, respectively.

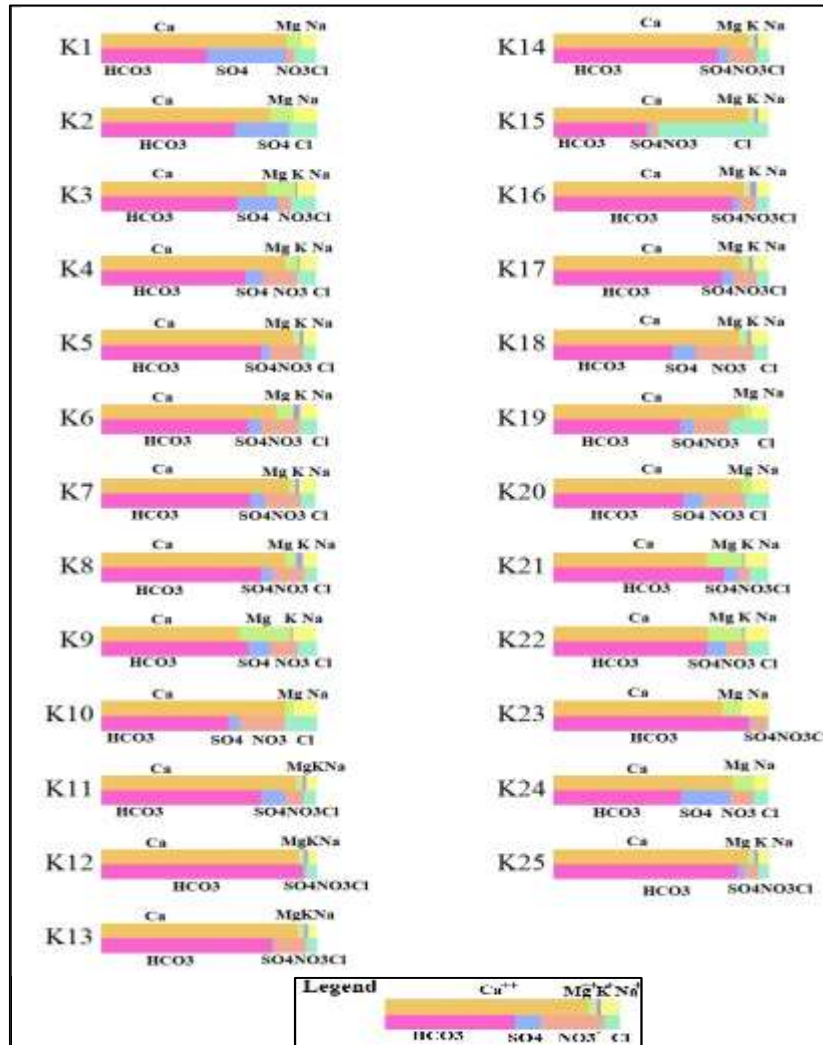


Figure 2. Stabler diagram illustrating major ionic dominance in the PSA

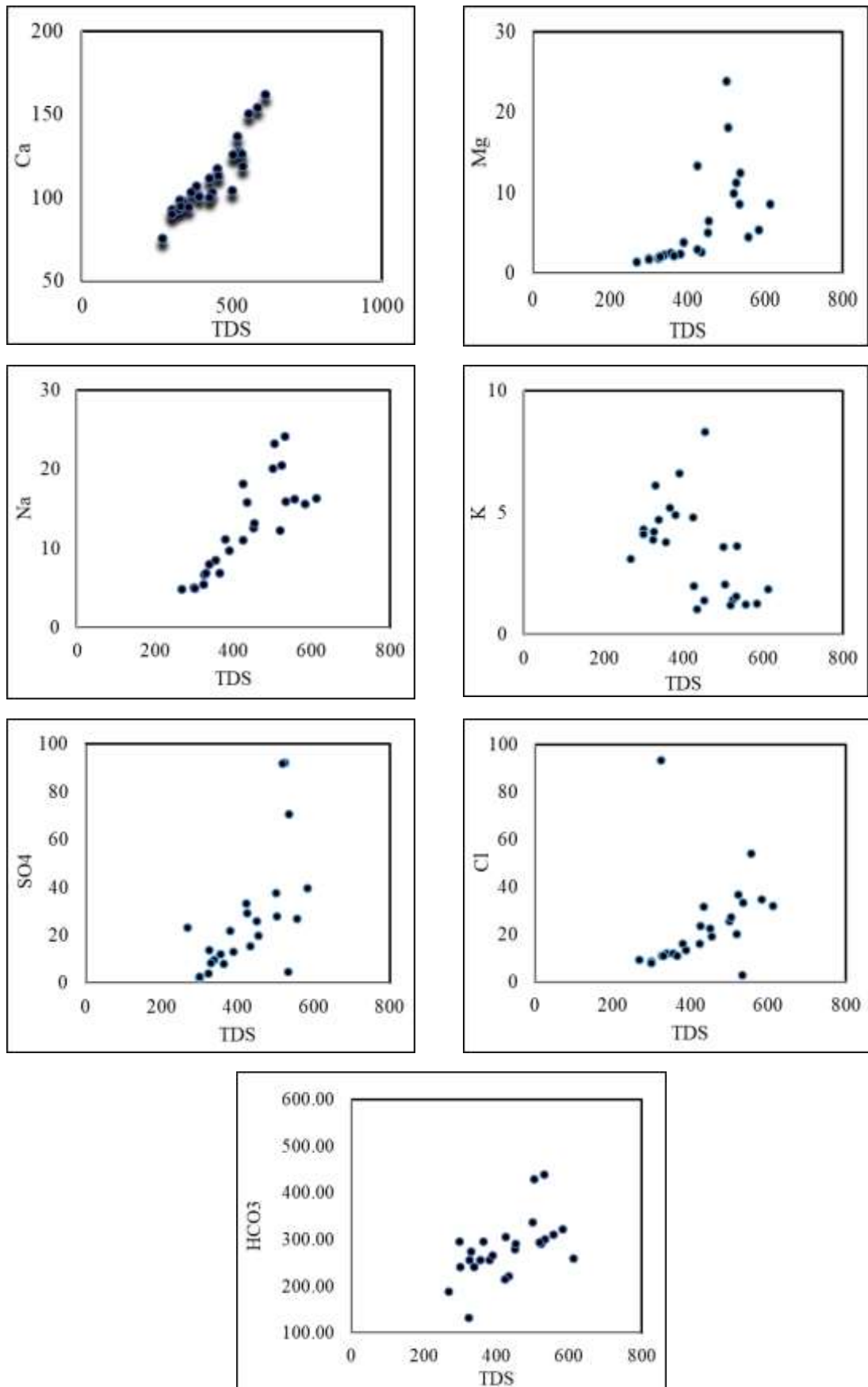


Figure 3. Correlation matrix of the major ions and TDS values (units are in mg/L)

Some parameters showed a strong correlation with TDS, with a high regression coefficient ($r \geq 0.5$). TDS values were strongly correlated with major ions such as Ca^{++} ($r = 0.9$), Mg^{++} ($r = 0.6$), Na^+ ($r = 0.8$), HCO_3^- ($r = 0.6$), SO_4^{2-} ($r = 0.7$). The high correlations between the major ions and TDS clearly showed that the major ions contribute to the salinization of groundwater in the PSA. Consequently, the salinization of groundwater could be resulting from the increase of ionic concentration due to interactions between groundwater and geological formation [10]. Another interesting point to mention is that sample K2 in the non-karstic area had the lowest NO_3^- concentration. Similarly, the lowest NO_3^- and the highest Cl^- concentrations were observed in sample K12 in the karstic region of the PSA.

Suitability for irrigation

The salinity level and other irrigation water quality indices such as Sodium Adsorption Ratio (SAR) were used in assessing the suitability of the water in the PSA for irrigation purposes. The suitability of groundwater quality for irrigation purpose is provisional on the effect of mineral constituents of water on both soil and plant [11]. An elevated level of dissolved ions in irrigation water alter the plant yield and soil. Salts in soil or water lessen water availability to the crops as well as hindering the absorption of water to soil which in turn affects the productivity of plants [11]. The results of the analyses showed that the computed SAR values in the PSA ranged from 0.14 to 0.56 meq/L with an average value of 0.30 meq/L. All sampling points in the PSA were within C2-S1 and C3-S1 class (Figure 4a). This suggested that groundwater quality in the study area is suitable for irrigation purpose. The Wilcox diagram (Figure 4a) shows that groundwater samples were within (C2-S1) class, indicating excellent sodium hazard and good salinity level. On the other hand, samples fell within the C3-S1 group, indicating high salinity and excellent sodium hazard types. From irrigation point of view, considering the combination of EC and SAR values, it is safe to say that groundwater of the PSA is suitable for irrigation purpose. However, in regard to EC, 68% of the samples were in medium class and 32% of the samples in the non-karstic area showed elevated EC values. Therefore, to reduce the salinity effect, mixing of groundwater in the samples with high salinity was recommended before any irrigation activity. Figure 4b illustrates the spatial distribution of SAR in the PSA. Although all samples were within the suitable range, some high values occurred in the samples located in the west and northeast of the PSA.

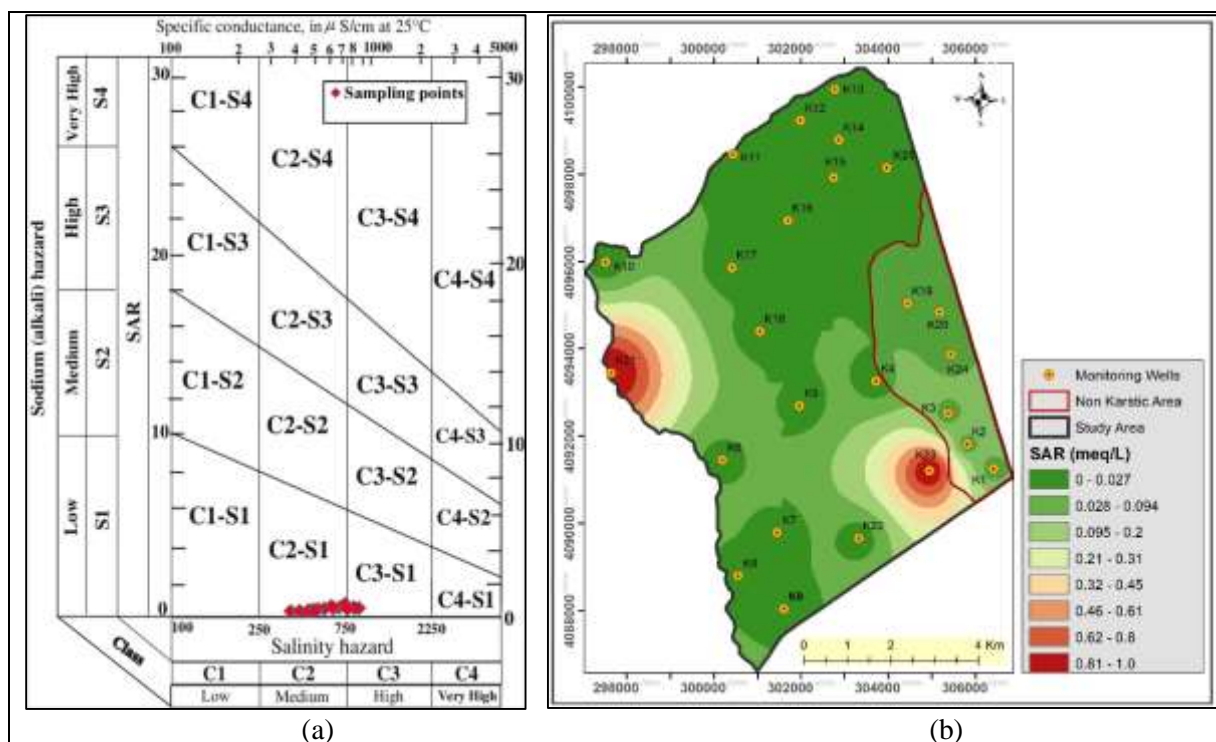


Figure 4. a) Wilcox diagram for assessing irrigation water quality, b) spatial distribution of SAR in the PSA

Conclusion

The results of groundwater hydrochemistry for Altınova region was assessed for their suitability for irrigation purpose. The dominance of the major cations and anions in the groundwater were as follows: $Ca^{++} > Na^{+} > Mg^{++} > K^{+}$ and $HCO_3^{-} > Cl^{-} > SO_4^{-2}$. Generally, the dominant water type in the study area was Ca- HCO_3 facies. TDS had significant relations with major ions which played a role in the salinization of groundwater in the study area. According to Wilcox Diagram, most of the groundwater samples fell within the C2-S1 and C3-S1 classes, highlighting medium to high salinity hazard and low sodium content class. This indicated that the groundwater of the PSA is suitable for irrigation purpose in regard to sodium hazards. These results also showed that groundwater samples were mostly at a good salinity level, where some of the samples had high salinity. In overall assessment, groundwater in the PSA was associated with low sodium hazard and it can be concluded that the groundwater is good for irrigation purpose.

Acknowledgments

This research study was supported by The Scientific and Technological Research Council of Turkey (Project No.114Y696) and Akdeniz University in Antalya, Turkey. The first author expresses his sincere thanks to Prof. Dr. Ayşe Muhammetoğlu and Prof. Dr. Habib Muhammetoğlu for their continuous support. The author also acknowledges the Turkish scholarship (YTB) for their support.

References

- [1] Daanoba E, Musah S, Zango S, and Mateko H. (2018) Comparative Analysis of Fluoride Concentrations in Groundwaters in Northern and Southern Ghana: Implications for the Contaminant Sources. *Earth Syst. Environ.*
- [2] Maliva RG (2016) *Aquifer Characterization Techniques*, No. 4. Switzerland. Springer Hydrogeology,
- [3] Peiyue Li (2015) Hydrochemical appraisal of groundwater quality for drinking and irrigation purposes and the major influencing factors : a case study in and around Hua County , China. *Arab. J. Geosci.* 2 (126).
- [4] Berhe BA (2017) Assessment of hydrogeochemistry and environmental isotopes of surface and groundwaters in the Kütahya Plain Turkey. *Journal of African Earth Sciences* 134, 230–240.
- [5] Fayrap A and Sargın AH (2015) Agricultural Groundwater Management in Turkey, in International Commission on Irrigation and Drainage 26th Euro-mediterranean Regional Conference and Workshops Innovate to improve Irrigation performances. No. October, 2–5.
- [6] Yilmaz I, Sayin C, and Ozkan B (2005) Turkish greenhouse industry: Past, present, and future. *New Zeal. J. Crop Hortic. Sci.*, 33 (3), 233–240.
- [7] Richards L (1954) Diagnosis and improvement of saline and alkali soil, 60 Hand bo. Washington DC: US Dept. of Agriculture.
- [8] Ayers R and Westcot DW (1994) Food, agriculture organization of the United Nations (FAO), Water quality for agriculture. Rome.
- [9] USSL United States Salinity Laboratory (1954) Diagnosis and improvement of saline and alkali soils, Handbook 6. New York: US Department of Agriculture.
- [10] Ketata FHM, Bouhlil R, and Gueddari M. (2011) Hydrogeochemical characteristics and assessment of drinking water quality in Zeuss – Koutine aquifer, southeastern Tunisia, 283–298.
- [11] Ben A. and Kamel MÆ (2009) Geochemical study of groundwater mineralization in the Grombalia shallow aquifer , north-eastern Tunisia : implication of irrigation and industrial waste water accounting, 555–566.

Management of Non-Revenue Water (NRW) in Municipal Water Distribution Networks: Antalya-Turkey Case Study

*Simge Enderoğlu**, *Ayşe Muhammetoğlu*, *Habib Muhammetoğlu*
Akdeniz University, Dept. of Environmental Engineering, Antalya, Turkey
Corresponding authors: smgenderoglu@gmail.com, aysemuh@akdeniz.edu.tr

Keywords: Non-revenue water (NRW), water losses, water budget, NRW management

Discipline: Civil & Environmental Engineering

Abstract

Non-Revenue Water (NRW) is a serious problem in municipal water distribution networks all over the world. The level of NRW exceeds 50% of System Input Volume (SIV) in many undeveloped and developing countries while it is less than 10% in well-developed countries such as Germany and the Netherlands. NRW includes physical water losses, apparent water losses and unbilled authorized consumption (UAC). Total water losses includes physical water losses and apparent water losses. The objective of this study is to compare NRW levels and its components for different municipalities in Turkey and to present NRW management practices applied in Antalya, as a case study.

Introduction

Water resources are under an increasing stress due to impacts of climate change, population increase and economic development. Water scarcity is recognized as a main threat particularly in the Mediterranean area. Thus, water utilities must become highly efficient throughout the entire water supply process, to guarantee sufficient quantities of good quality water. Since water is one of the most valuable natural resources, water losses in the Water Distribution System (WDS) represent an urgent problem that needs to be managed [1]. Total water losses include Physical/Real losses and Apparent/Commercial losses (Figure 1). Water losses may occur at several points of a Water Supply System (WSS) including treatment works, trunk mains, service reservoirs, WDS, water meters and billing system. Water losses usually represent the biggest part of the so-called non revenue Water (NRW), which is the water that does not bring in revenues to the water utility. The percentage of NRW is reported to be less than 10% for some developed countries, but it could even exceed 70% for undeveloped countries as well [2].

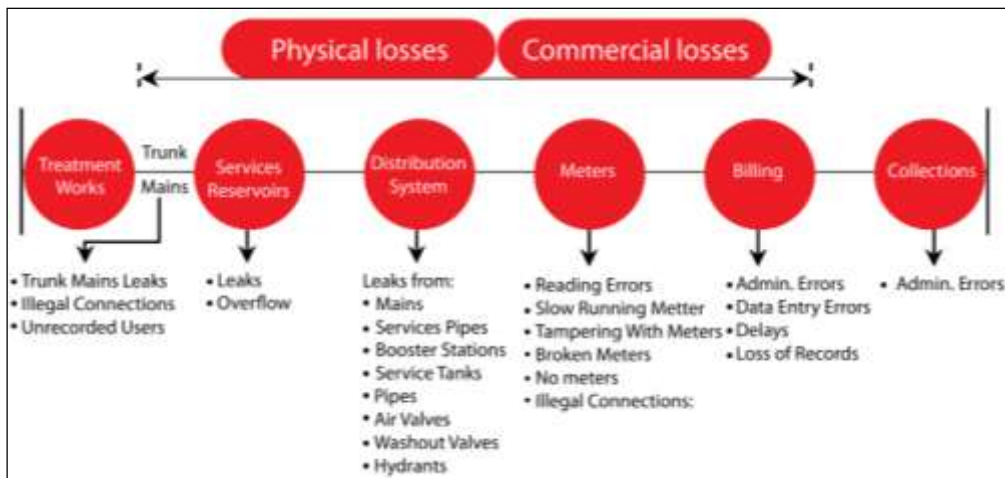


Figure 1. Typical losses from a water supply system [3]

The objective of this study is to compare NRW levels and its components for different municipalities in Turkey and to present NRW management practices applied in Antalya, as a case study.

Methods

A new regulation on water losses management “*Control of Water Losses from Drinking Water Supply and Distribution Systems*” was issued in May 2014 taking into consideration the methods used to detect and reduce water losses [4]. In July 2015, practical and technical procedure for detecting and reducing water losses was issued [5]. The new regulation obligates the metropolitan and provincial municipalities to reduce water losses to 30% in 2019 and to 25% in 2023. All the water authorities in Turkey need to report the yearly standard Water Balance (WB) given in Table 1.

Table 1. Water balance showing water losses and NRW components [4]

System Input Volume	Authorised Consumption	Billed Authorised Consumption	Billed Metered Consumption	Revenue Water	
			Billed Unmetered Consumption		
		Unbilled Authorised Consumption	Unbilled Metered Consumption		Non-Revenue Water
			Unbilled Unmetered Consumption		
	Water Losses	Apparent Losses	Unauthorised Consumption		
			Customer Meter Inaccuracies and Data Handling Errors		
		Physical Losses	Leakage on Transmission and Distribution Mains, and Service Connections		
			Leakage and Overflows from Storage Tanks		

Common methods to reduce physical water losses include hydraulic modelling, pressure management and acoustic systems. On the other hand, common methods to reduce apparent water losses include reducing water theft, water meters inaccuracy and data handling errors. The following actions are listed in the regulation to detect and reduce water losses [6]:

- All water supplied to users should be measured by water meters. Water meters should be installed to all users including the unbilled users such as religious facilities, parks and public toilets.
- The water meters should be read and recorded regularly.
- The age of water meters should not exceed 10 years.
- Yearly WB should be carried out and reported to the related Ministry.
- Critical pressure and flow rates should be monitored regularly where maximum water pressure should not exceed 60 m if possible.
- The elements and data sets of the WDN should be digitized into Geographical Information System (GIS).
- Acoustic equipment should be used to reduce physical water losses.
- Hydraulic modelling should be carried out.

Results

Water Losses in Turkey

According to yearly WB reports of 19 municipalities in Turkey, the average NRW level is 44% and water losses are around 40% (Figure 2). Antalya Water and Wastewater Administration (ASAT) applies hydraulic modelling, pressure management, acoustic systems, increases the accuracy of water meters and controls Unbilled Authorized Consumption (UAC) which lead to a considerable reduction of NRW

in the city. All water users, including unbilled ones, are metered in Antalya and provides a good case study for NRW management. The recent WB of Antalya City for the year 2018 is presented in Table 2.

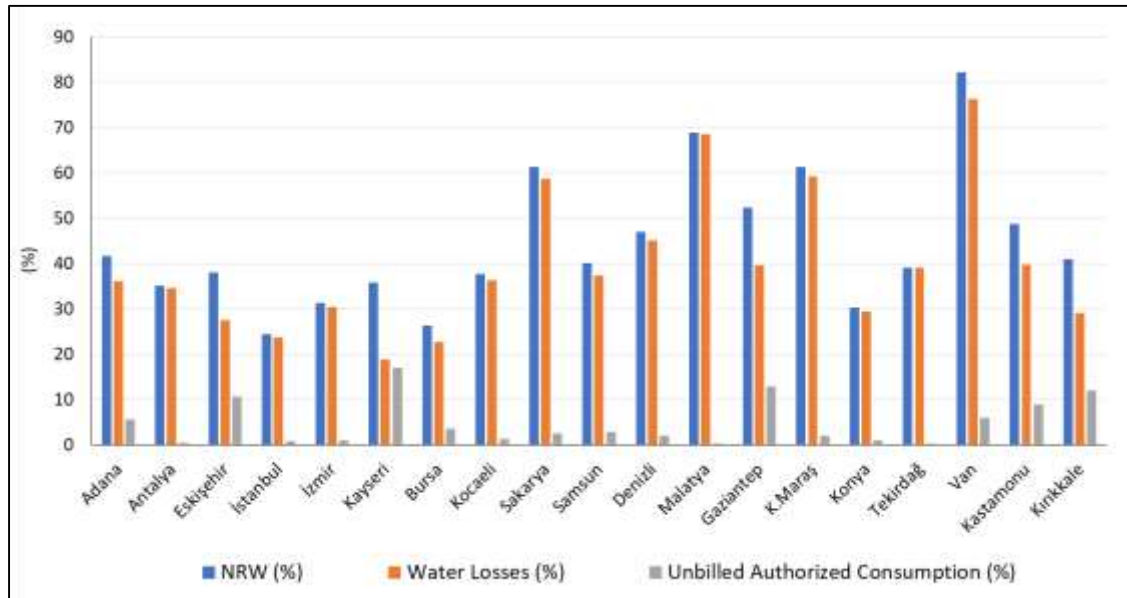


Figure 2. The percentage values of NRW, water losses and unbilled authorized consumption for some municipalities in Turkey (using data for the years between 2014 and 2017)

Table 2. WB of Antalya City for the year 2018 [7]

System Input Volume 140.412.955 m ³ /year (100%)	Authorised Consumption 76.991.188 m ³ /year (54.83%)	Billed Authorised Consumption 76.730.837 m ³ /year (54.65%)	Billed Metered Consumption 76.730.837 m ³ /year (54.65%)	Revenue Water 76.730.837 m ³ /year (54.65%)	
			Billed Unmetered Consumption 0 m ³ /year (0%)		
	Water Losses 63.421.767 m ³ /year (45.17%)	Unbilled Authorised Consumption 260.351 m ³ /year (0.19%)		Unbilled Metered Consumption 260.351 m ³ /year (0.19%)	Non-Revenue Water 63.682.118 m ³ /year (45.35%)
				Unbilled Unmetered Consumption 0 m ³ /year (0%)	
		Apparent Losses 10.844.091 m ³ /year (7.72%)		Unauthorised Consumption 65.324 m ³ /year (0.05%)	
			Physical Losses 52.577.676 m ³ /year (37.45%)	Customer Meter Inaccuracies and Data Handling Errors 10.778.766 m ³ /year (7.68%)	
	Leakage on Transmission and Distribution Mains, and Service Connections 51.573.202 m ³ /year (36.73%)				
	Leakage and Overflows from Storage Tanks 1.004.474 m ³ /year (0.72%)				

According to WB of Antalya City for the year 2018, NRW and water losses account for approximately 45% of SIV. The reported values of apparent and physical water losses are 7.72% and 37.45%, respectively. More strict water losses reduction strategies are needed for further reduction of NRW.

Reducing Physical Water Losses

The physical water losses management strategy includes (i) pressure management, (ii) speed and quality of repairs, (iii) active leakage control, and (iv) pipeline and asset management. Physical water losses were reduced at some District Metered Areas (DMAs) in Antalya City by pressure management (Figure 3). In these applications Pressure Reducing Valves (PRVs) were installed within the WDN. Active leakage control is also practiced in Antalya using both simple and advanced acoustic equipment and techniques.

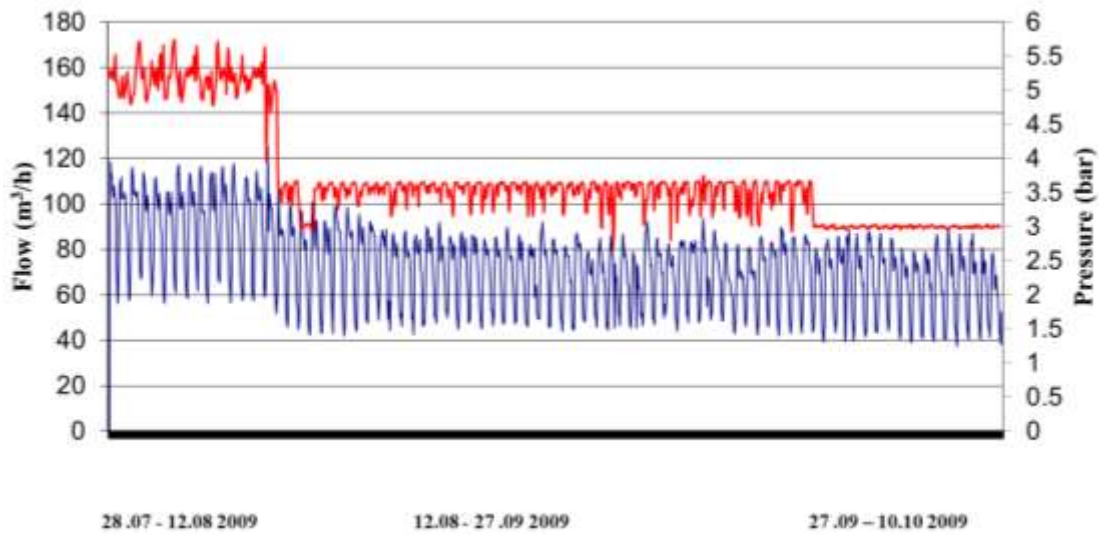


Figure 3. Physical water losses reduction by pressure management in Antalya City

Reducing Apparent Water Losses

Apparent water losses is not visible, which leads many water utilities to neglect apparent losses and focus on physical losses. However, reducing apparent losses increases revenue. Apparent losses can be divided into four basic divisions, namely: i. meter accuracy, ii. illegal use (unauthorised consumption), iii. meter reading errors and iv. data handling and billing errors. In many cases, water passes through the meters but is not recorded accurately. Installation of more accurate water meters (C Class) reduced apparent water losses in Antalya (Figure 4).

Post Meter Leakage Reduction

Post meter leakage reduction is very important for water saving and reducing NRW. With the new advances in water meters, smart meters gained an importance and they started to appear in modern WDNs. In a recent research project study, supported by TÜBİTAK (Project No: 118Y104), smart meters were installed at several pilot locations in Antalya City for post meter leakage detection and reduction (Figure 5). Smart meters can measure water consumption for the prescribed time intervals (eg. every hour) and send the recorded data at specified periods to the main servers for further analysis. A typical water consumption profile of a smart meter installed within the mentioned research project is presented at Figure 6, where post meter leakage can be observed clearly due to continuous consumption of water for seven days a week and 24 hours a day.

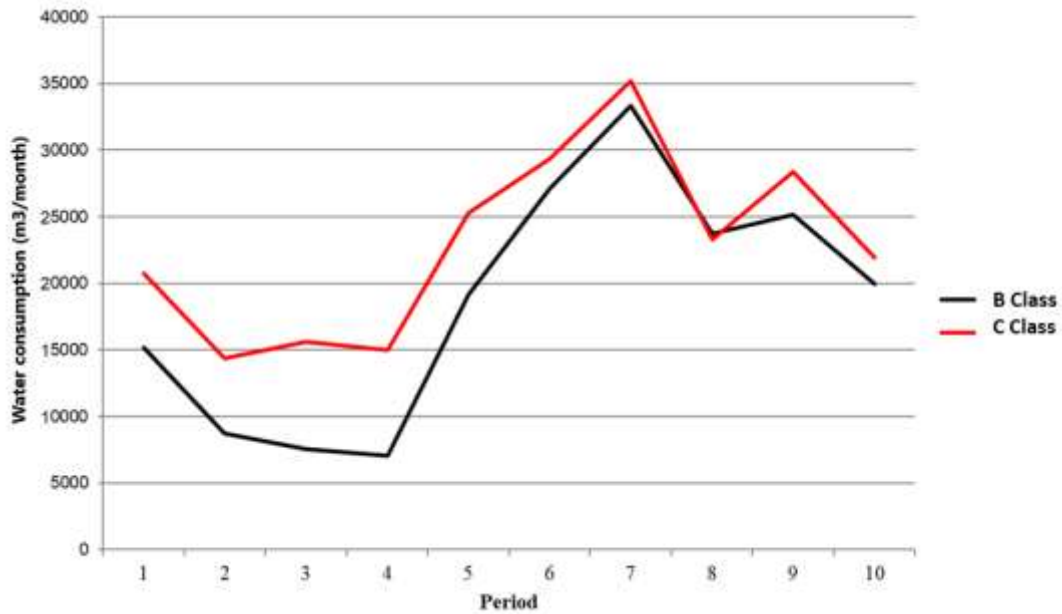


Figure 4. Apparent water losses reduction by installing more accurate water meters



Figure 5. Installation of a smart meter for post meter leakage detection

Conclusion

Total water losses include apparent and real water losses. By reducing water losses, water resources are protected and many economic gains can be achieved. NRW and water losses are different. And generally NRW is higher than water losses. NRW should be reduced to save the energy used in treating and pumping the water and protect the drinking water resources. In Antalya, physical and apparent water losses are reduced by applying different methods such as pressure management, acoustic methods, and improving water meter accuracy. Recently, smart meters are used for reducing NRW and post meter leakage.

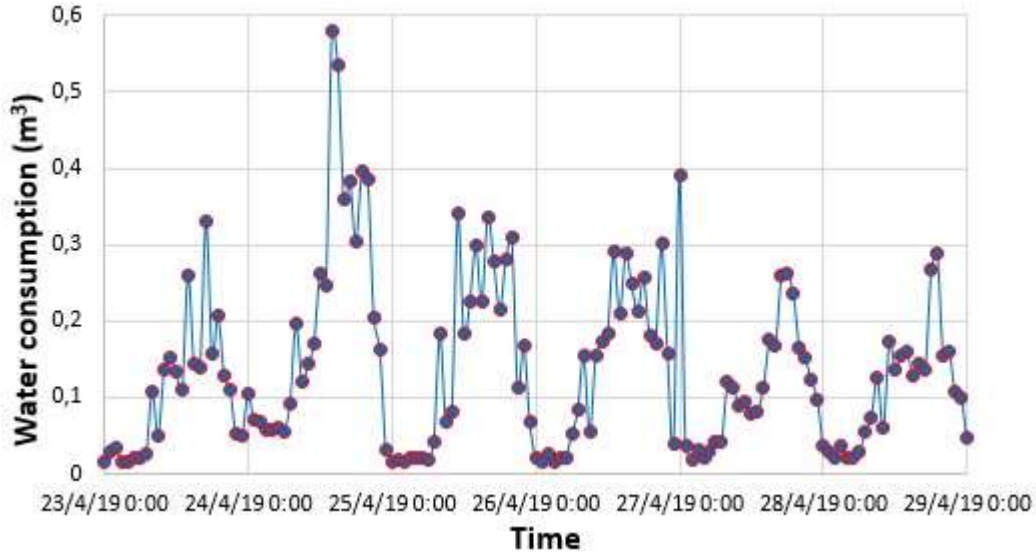


Figure 6. Hourly water consumption values measured by a newly installed smart meter

Acknowledgement

Thanks to the Scientific and Technological Research Council of Turkey, TÜBİTAK (Project No. 118Y104), Antalya Water and Wastewater Administration (ASAT) of Antalya Metropolitan City.

References

- [1] Kanakoudis, V and Muhammetoglu, H (2014). Urban Water Pipe Networks Management Towards Non-Revenue Water Reduction: Two Case Studies from Greece and Turkey, CLEAN-Soil, Air, Water, 42(7), 880-892.
- [2] IBNET (2017) The International Benchmarking Network for Water and Sanitation Utilities, Knoema. Retrieved May 2019, from <https://knoema.com/IBNNETWSU2011/the-international-benchmarking-network-for-water-and-sanitation-utilities?tsId=1007880>.
- [3] MNRW (2008) The Manager's Non-Revenue Water Handbook, A Guide to Understanding Water Losses, 2008 Ranail & USAID. Retrieved May 2019, from https://warrington.ufl.edu/centers/purc/docs/resources_NRWManagersHandbook.pdf
- [4] İçme Suyu Temin ve Dağıtım Sistemlerindeki Su Kayıplarının Kontrolü Yönetmeliği, 8 Mayıs 2014 (Resmi Gazete, Sayı: 28994).
- [5] İçme Suyu Temin ve Dağıtım Sistemlerindeki Su Kayıplarının Kontrolü Yönetmeliği Teknik Usuller Tebliği, 16 Temmuz 2015 (Resmi Gazete, Sayı: 29418).
- [6] Muhammetoglu A, Muhammetoglu H, Adıgüzel A, İritaş Ö, Karaaslan Y (2018) Management of Water Losses in Water Supply and Distribution Networks in Turkey, Turkish Journal of Water Science & Management, 2(1): 58-75.
- [7] İçmesuyu Temin ve Dağıtım Sistemlerindeki Su Kayıpları Yıllık Raporu, Antalya Büyükşehir Belediyesi, Mart 2019.

Smart Water Management for Smart Cities

Mustafa Bolbol, Habib Muhammetoğlu, Ayşe Muhammetoğlu*
Akdeniz University, Dept. of Environmental Engineering, Antalya, Turkey
Corresponding authors: mustafa.bolbol.1992@gmail.com

Keywords: Smart water management, smart cities, automated meter reading, SCADA

Discipline: Environmental Engineering

Abstract

Due to high increase rate of population in cities all over the world, modern infrastructures gained an importance. In this respect, the concept of smart cities appeared aiming at maintaining a high level of life for the urban dwellers and enabling sustainable water management of the cities. Smart water management (SWM) is a crucial part of smart cities as it integrates the information and communication technology (ICT) into the management of water supply systems. The SWM improves the water quality and lessens the water losses and over abstraction of water resources.

Introduction

In recent years, the number of cities and urban dwellers have increased all over the world. The United Nations (UN) declared on May 2018 that 55% of global population settles in urban areas, and this projection is expected to rise up to 68% by 2050. Megacities are defined by the UN as a city with a population of more than 10 million. It is declared by the UN that the world is projected to have 43 megacities by 2030 [1]. Generally, the cities worldwide face a challenge of increasing population growth rate with time, and water suppliers are stressed by population growth and water scarcity. Therefore, management of water losses in water supply systems became ever more important than before to enable the cities to be expanded sustainably, operated efficiently, and preserve a high level of life for the inhabitants. Accordingly, the term of Smart Cities forms the future suggestion for overcoming the challenges of water in megacities. Six sectors are working together to create smart cities and make it more livable, sustainable and efficient for its inhabitants. These sectors are smart energy, smart mobility, smart public services, smart water, smart buildings and smart integration [2]. The Smart Water Management (SWM) is an innovative term which describes the use of Information and Communication Technology (ICT) to provide a real-time data automatically to be used in resolving water challenges through integrated water resource management. It is designed to gather meaningful and actionable data about the flow, pressure and water distribution of the city [3]. The rapid development of smart technologies provides innovative and integrated solutions. The needed technologies to be integrated with SWM are water quality sensors, smart monitoring systems and leak detection instruments. By these technologies, SWM enables water suppliers to reduce the non-revenue water (NRW) by detecting leaks quickly and control the provided water quality and quantity. There are many achievable benefits of applying SWM: environmentally; it contributes to reducing the depletion of groundwater and surface-water resources, reduction in CO₂ emissions, reducing water consumption and improving water quality. Socially, SWM raises opportunities of community-led decision-making, achieves greater collaboration with community and greater security of water quality to consumers. Economically, SWM reduces the future infrastructure costs by reducing water losses through leakage, improving the capacity of water supply systems and creating jobs in SWM project research, design, development and implementation [3]. In this paper, the components of SWM and the application of SWM in many cities worldwide are presented. The results show the achievable benefits of implementing SWM for water utilities.

Methodology

The body of SWM consists of key elements of ICTs to transfer hydraulic real-time data of the provided water such as pressure and flow rate besides water quality data to improve decision-making processes. The elements of ICTs are real-time monitoring (RTM) units, satellite imagery, Geographic Information Systems (GIS) and Supervisory Control and Data Acquisition (SCADA) system (Figure 1a). The telecommunication part involves units for data transmission and smart field instruments like smart meters, smart pumps, pressure loggers, water quality sensors, flood sensors and smart valves

(Figure1b). These elements work in harmony to reduce the non-revenue water (NRW) besides achieving sustainability and safety of water supply systems.

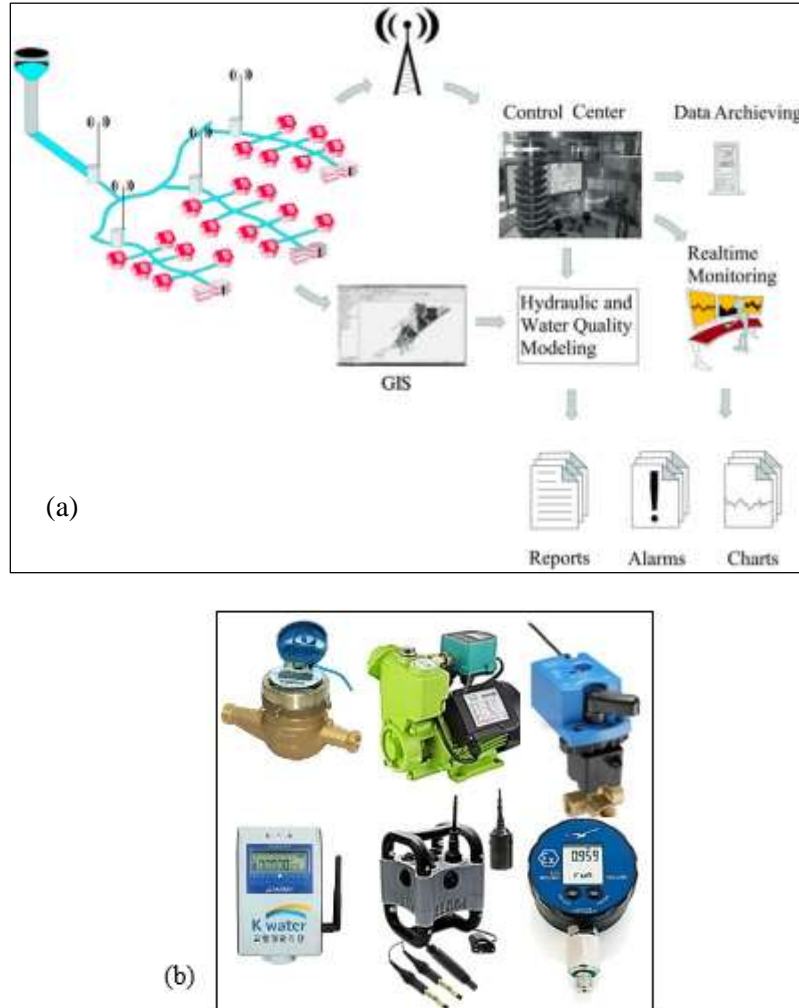


Figure 1. (a) A scheme of the SCADA system [4] (b) Smart meter, smart pump, smart valve, data transmitter, water quality sensor and pressure logger

Kara et al. [4] have studied the integrated RTM-SCADA system in Antalya City. As shown in Figure 22, the integrated system includes nine pumping stations, 24 service reservoirs, 74 deep well pumps, and RTM units installed on the water mains which involve 110 electromagnetic flow meters, smart valves (open, closed, and partially open), water quality analyzers (pH, temperature, free residual chlorine, turbidity) and pressure meters. Additionally, 1200 automatic meter reading (AMR) systems was installed in one of the discrete metered areas (DMAs) in Antalya City and used later for physical losses determination.

Schultz et al. [5] reported the benefits of a research project of installing smart metering system in 85000 residential subscribers in Sacramento City, California in United States of America. A graphical user interface (GUI) application was developed within the scope of the project to provide the customers an augmented information of their household consumption and post-meter leakage alarms as shown in Figure 3.

SWM was applied in Seosan City of Korea, as a solution of drought concerns in the city. As shown in Figure 4, The SWM in Seosan City consists of smart metering system aiming at achieving remote metering of customer consumption, dividing the water distribution network to DMAs, leakage analysis and applying pressure management using the date transmitted from the field to be involved in the hydraulic modelling study [3].

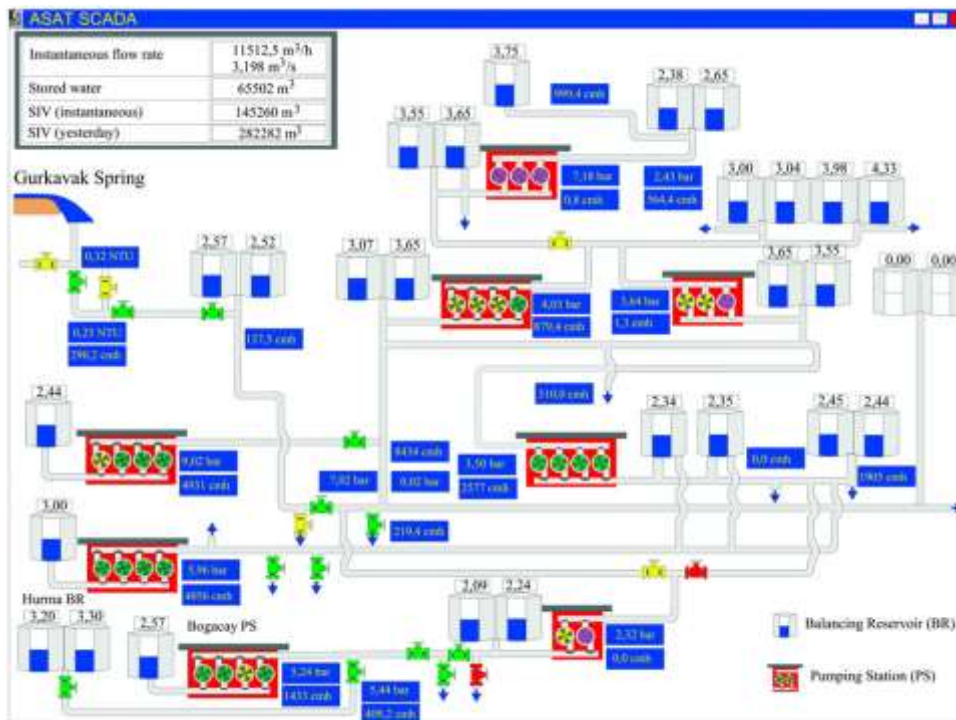


Figure 2. A screenshot of the integrated RTM-SCADA system in Antalya [4]



Figure 3. A screenshot of the developed customer application connected with smart meters [5]

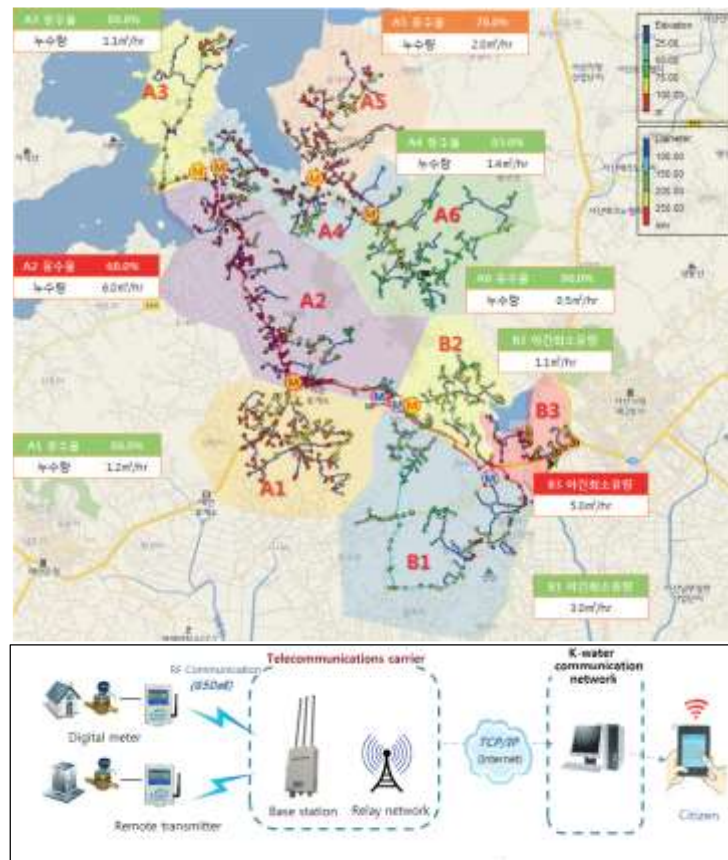


Figure 4. A scheme of the SWM applied in Seosan City

Results

Within four years, the integrated RTM-SCADA system of Antalya water supply system helped in reducing the total water losses in one of the districts (Konyaaltı) by 28.55% and reducing daily energy consumption by 33.65%. Besides that, the payback period of the integrated system was estimated to be less than one year. Additionally, the integrated RTM-SCADA system provided very good data sets for pressure management, hydraulic and water quality modeling.

The smart metering systems applied in Sacramento City showed that 10% of end-user water consumption was estimated as leakage. However, use of the integrated (GUI)-smart metering system led to reduce post-meter leakage by 7%. Additionally, the leak duration was reduced by 17%, compared with the subscribers who did not install smart meters.

With the application of smart metering system in Seosan City of South Korea for one year, the revenue of water increased by 20% as compared with the first half of the year. Additionally, it enabled two subscribers to detect post-meter leakages and reduce 55% of their water use and 70% of their water bills [3].

Smart meters using AMR technology provides individual water consumption patterns to water utilities and customers which helps to analyze and control water usage and improve post meter leakage detection. In a recent research project study, supported by TÜBİTAK (Project No: 118Y104), smart meters were installed at several pilot locations in Antalya City for post meter leakage detection and reduction. The smart meter using AMR technology could measure water consumption for the prescribed time intervals (eg. every hour) and send the recorded data at specified periods to the main servers for further analysis (Figure 5). This application presents a good case study for rapid detection of water leakage and leakage amount in the installed area (Figure 6).

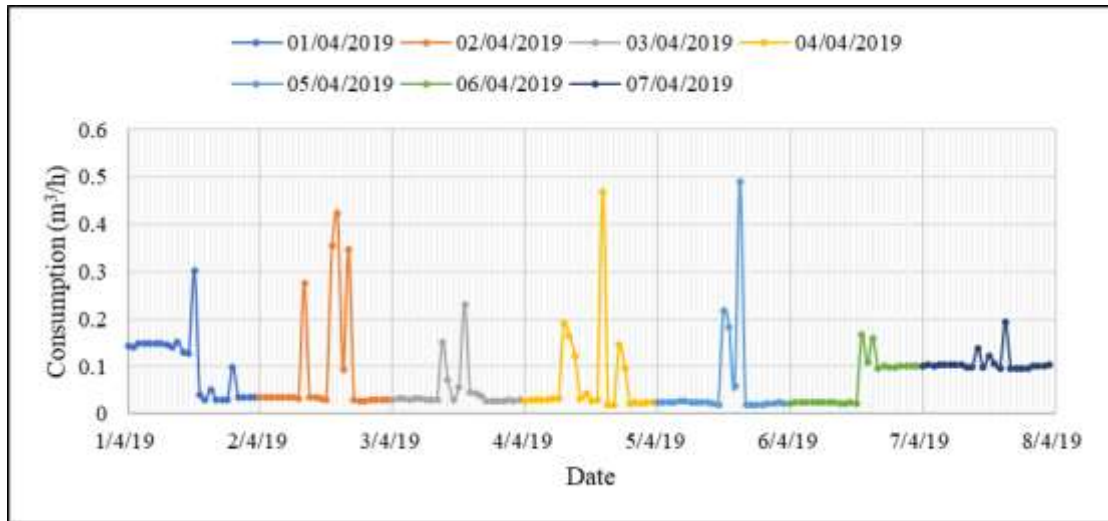


Figure 5. Hourly water consumption values measured by a newly installed smart meter at the pilot location

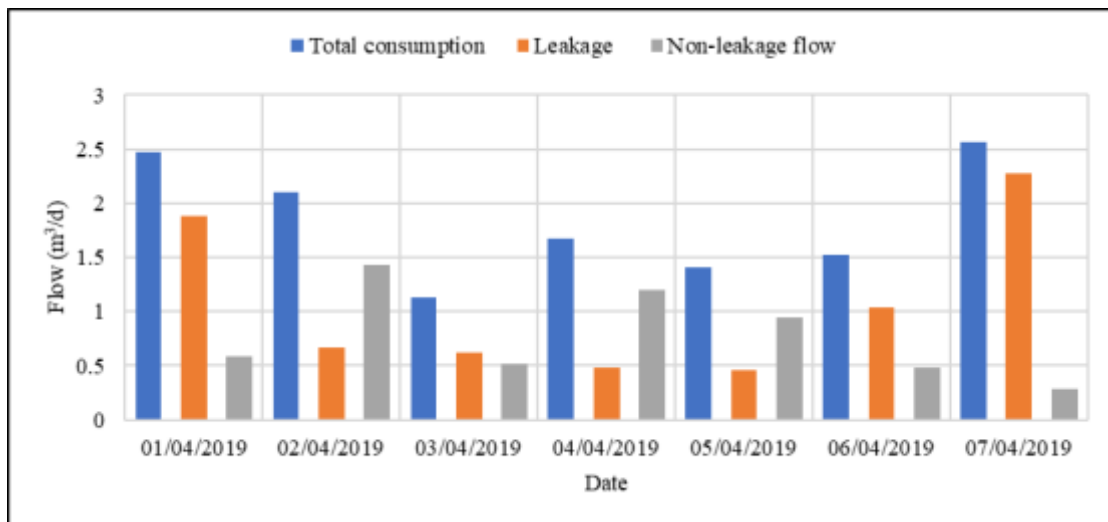


Figure 6. Total consumption of water measured by installed smart meter and computed values of leakage and non-leakage flow at the pilot location

Conclusion

The SWM is an essential tool to maintain sustainable management and operation of water supply services in the cities and smart meters or automated meter readings enable accurate water demand forecast and hydraulic modelling applications. Post-meter leakage reduction is very important for water saving and reducing NRW. With the new advances in water meters, smart meters gained an importance and they started to appear in advanced water distribution networks.

Acknowledgment

Thanks to the Scientific and Technology Research Council of Turkey (TÜBİTAK) (Project No. 118Y104) and Antalya Water and Wastewater Administration (ASAT) for their support.

References

- [1] UN (2018) United Nation: Department of Economic and Social Affairs. <https://www.un.org/development/desa/en/news/population/2018-revision-of-world-urbanization-prospects.html> (Accessed 20 May 2019).

3rd International Students Science Congress
3-4 May 2019, İzmir - Turkey

- [2] Water World (2013) Smart Water: A Key Building Block of the Smart City of the Future <https://www.waterworld.com/international/wastewater/article/16190746/smart-water-a-key-building-block-of-the-smart-city-of-the-future> (Accessed 20 May 2019).
- [3] K-water (2018) Smart Water Management: Case Study Report, K-water, 200 Sintanjinor, Daedeokgu, Deajeon, Korea, 34350, 2018.
- [4] Kara S, Karadirek IE, Muhammetoglu A and Muhammetoglu H (2016) Real time monitoring and control in water distribution systems for improving operational efficiency, *Desalination and Water Treatment*, 57 (25), 11506-11519.
- [5] Schultz W, Javey S and Sorokina A (2018) Smart Water Meters and Data Analytics Decrease Wasted Water Due to Leaks, American Water Works Association (AWWA), California.

Food Engineering / Gıda Mühendisliđi

Effects of Storage Time and Different Storage Conditions on Some Quality Characteristics of Chicken Eggs

Nusiba Alsiddig Badawi, Cemalettin Sarıçoban*

Selcuk Univ., Dept. Food Engineering, Campus-Konya -Turkey

Tag Eldeen Ali Abd alrahman, Dept. Food Science and Technology AL-Zaeim AL-Azhari University. P.O. Box 1432. Khartoum North 13311, Sudan.

**Corresponding author nussiba14@gmail.com*

Keywords: food engineering, chicken egg

Discipline: Food Engineering

Abstract

This study aimed to evaluate the effect of treatments and different storage conditions on some quality characteristics of chicken eggs. Samples were collected in medium scale from Khartoum North randomly, and analysed for quality parameters at the same day of production, then samples were divided in to (A) stored at temperature (4-6 °C), (B) stored at room temperature, (C) treated by wax and stored at room temperature, (D) stored at ventilated area and (E) stored under directly the sun from 8Am – 2 Pm. The analysis is done every 0, 10 and 20 days.

Physical and microbiological analysis of samples were conducted on (zero, 10 and 20 days) during storage and the analysis of the samples showed significant different among the treatments and grades ($p \leq 0.01$).

The samples in (E) storage condition recorded highest air cell mean value (19.43ml) in 20 days and the lowest value was recorded by samples (A) storage condition in 10 days from the storage period, the yolk index value was record the highest value in (A) storage condition (0.48 ml) by the samples in zero day while the lowest value recorded by samples in (C) storage condition in 20 days storage period, all samples recorded the highest Haugh unit value in 0 day while in 20 days the lowest value recorded by the samples in (E) storage condition, all the samples treated with wax recorded the highest shell thickness value while the lowest value recorded by the samples in (E) storage condition, the samples in (E) storage condition scored the lowest pH value in 20 days from the storage period while the samples in zero day from stored period recorded the highest value. Microbial analysis scored the presence of microbial-load in all samples, all samples recorded low load and the same time all samples are free of salmonella spp. The study concluded that the storage condition affected on the egg quality and safety when compared the requirement of SDS 751/2007 Table egg, moreover the cold storage were ideal on the eggs. Finally the study recommended that the Public awareness important and understand the role of egg buying and selling to availability good handling, as well as the further in effects of fungus and moulds in egg, Also further study needed to evaluate the potential of chemical hazards in chicken eggs.

Introduction

The laying cycle of a chicken flock usually covers a span of about 12 months. Egg production begins when the birds reach about 18-22 weeks of age, depending on the breed and season. Flock production rises sharply and reaches a peak of about 90%, 6-8 weeks later. Production then gradually declines to about 65% after 12 months of lay [1].

There are many factors that can adversely affect egg production unravelling the cause of a sudden drop in egg production requires a thorough investigation into the history of the flock. Egg production can be affected by many factors such as feed consumption (quality and quantity), water intake, intensity and duration of light received parasite infestation, disease, and numerous management and environmental factors.

The chicken egg is one of the finest foods, offering men an almost complete balance of essential nutrients with proteins, vitamins, minerals and fatty acids of great biological value. In addition to being one of the foods of lowest cost, it increases the consumption of food of high nutritional value for the low-income population [1]. About 95% of poultry feed constituents are produced locally such as sorghum (energy), oilseed cakes (protein). Also there is increase in the local demands to satisfy the needs of restaurants, hotels and the large companies. The FAO estimates needs per capita poultry meat around 9 kg and 169 egg annually, respectively.

Kramer (1951) [2] defined quality as “the sum of characteristics of a given food item which influence the acceptability or preference for that food by the consumer”. Based on this definition, it is clear that egg quality will mean different things to different people and the consumer’s perception of quality is likely to vary depending on their intended use of the egg and their own preferences. This is clearly illustrated by a brief review of the regulatory requirements for eggs sold around the world.

Consumers are increasingly concerned about the safety of their food, such as meat, and egg products. Most commodity groups have adopted Good Practices, Total Quality Management (TQM) or Quality Assurance Programs (QAPs) for their companies [3].

After processing, eggs should be stored at 45 degrees to prevent microbial growth. Humidity should be kept at 70 to 85%. Clean eggs stored at these conditions will keep for three months. In a standard refrigerator, where the humidity is lower, washed eggs only keep for five weeks. In large-scale commercial production, eggs usually reach the packing plant only a few days after hens lay those [4]. In USA eggs packed under federal regulations require the pack date to be displayed on the carton. It is a three-digit Julian date that represents the consecutive day of the year. The carton is also dated with the sell-by or expiration date (Exp.), depending on the state. Eggs with a federal grade must be sold within 30 days from day of pack [4]. The USDA recommends that consumers buy eggs before the expiration date and use them within 3 to 5 weeks. Agricultural Marketing Service rule prohibited the repackaging of eggs previously shipped for retail sale that were packed under its grading program. Small specialty producers should sell their eggs within seven days of lay so that the eggs are as fresh as or fresher than conventional eggs [5].

The egg, as laid at 40.56 °C (105 °F), normally has no air cell. As the egg cools, an air cell forms usually in the large end of the egg and develops between the two shell membranes. The air cell is formed as a result of the different rates of contraction between the shell and its contents [5].

Over time, the white and yolk of an egg lose quality. The yolk absorbs water from the white. Moisture and carbon dioxide in the white evaporate through the pores, allowing more air to penetrate the shell, and the air cell becomes larger. If broken open, the egg’s contents would cover a wider area. The white would be thinner, losing some of its thickening and leavening powers. The yolk would be flatter, larger and more easily broken. The chalazae, the twisted cord-like strands of egg white that anchor the yolk in the center of the white, would be less prominent and weaker, allowing the yolk to move off center. Refrigeration slows the loss of quality over time [5].

The storage of consumption eggs at a temperature of +40 °C and an air relative humidity of 84% assure a good stability in time for physical indexes which define the egg quality. In the same context we must pay attention on the effects exercised by the storing regimes used by some sellers on eggs quality, with rigorous impact on consumer’s health [1].

The Sudanese Standards and Metrology Organization (SSMO) is authority responsible for quality control to all foodstuff manufactured in the Sudan for local use as well as export or import. The SSMO developed the national standard, rules and procedures to foodstuff including testing and certification procedure based on the standards, guidelines and recommendation established by Codex Alimentarius (CAC) and the International Office of Epizootics (OIE). The SSMO Technical Administration is the competent authority in the field of quality control and laboratories analysis of many foodstuff [6]. Regarding poultry and poultry products the SSMO developed 30 national standard concerning poultry and poultry products through the activities of the poultry Technical committee [3]. This study aimed to evaluate the effect of treatments and different storage conditions on some quality characteristics of chicken eggs.

Materials and Methods

Sources of egg samples: The samples were collected randomly from farm in Khartoum North, Sudan.

Methods: The physical characters of eggs like the egg weights, specific gravity were measured. After measuring the external characters, the eggs were broken open on the egg breaking stand to measure their qualities.

Physical and Physicochemical analysis

Air cell: The distance between egg shell and membrane was measured by virnier caliper (Triclebrand, Shanghi, China).

Yolk index: Yolk index was calculated by the measure of the yolk height and yolk diameter according to [7].

Haugh unit: Haugh unit was calculated by Haugh unit formula according to [8].

Thickness of shell: Shell thickness measured using micrometer (Mitutoyo-Japan).

Egg pH: pH value measured by pH meter (TPYE and CO., LTD., Cambridge, U.K).

Microbiological analysis

Total viable count: Total viable count was carried out using the pour plate count method as described by Harrigan, 1998 [9] and Hassan, 2011 [10], Harrigan and Mac Conce, 1976 [11].

Detection of *Salmonella* spp: was triple sugar slopes. Production of a black colour at the bottom, confirmed the measured using black metallic sheen discrete colonies indicated the presence of *Salmonella* spp. A confirmatory test was carried out by taking a discrete black sheen colony and sub-culturing it in presence of *Salmonella* as described by Harrigan (1998) [10] and Hassan, 2011 [10]; Harrigan and MacCance, 1976 [11].

Statistical analysis: Data generated was subjected to statistical analysis (SAS) Version09, using one-way ANOVA (RCD) design; and then mean were tested and separated using Duncan's Multiple Range Test (DMRT) referred to Hassan, 2011 [10]; Steel *et al.*, 1997 [12].

Results and discussion

Air cell size: The data showed significantly different effect ($P \leq 0.01$) among the treatments chicken eggs samples. The result was obtained the highest value in sample (E) storage condition, (19.43 ml) in 20 days, while the lowest value was recorded by samples (A) storage condition in 10 days from the storage period (Table 1). Also the data showed significantly different effect ($P \leq 0.01$) among the treatments egg samples during storage. The result was obtained the highest value were increased gradually during storage period, then the lowest value were at the beginning of storage. These variations may be due to the treatments effect and grade also may be due to the storage period temperature. The results were fully agreed with Hassan (2011) [10] who found that, the air cell size forms usually in the large end of the egg and between the two shell membranes, moreover big samples increase in the air cell than other samples because decrease in exposure area. The air cell is formed as a result different rates of contraction between the shell and its contents. The egg, at temperature 40.56 °C (105°F), normally has no air cell and when the egg cooled [4]. The results were agreement with Jin *et al* (2011) [13] who found that as the storage temperature and time increased, egg weight significantly ($p < 0.001$) decreased. Interactions between storage time and temperature were significant ($p < 0.001$) with respect to egg weight loss. These results are in agreement with those of Samli *et al.* (2005) [14], who reported significant ($p < 0.001$) egg weight reductions of 2.08 and 3.11%, respectively, within 5 and 10 d of storage at 29 °C. Similar weight losses were also reported by Akyurek and Okur (2009) [7].

Yolk index: The data showed significantly different effect ($P \leq 0.01$) among the treatments chicken eggs samples. The result of the yolk index value was record the highest value in (A) storage condition (0.48 ml) by the samples in zero day, while the lowest value recorded by samples in (C) storage condition in 20 days storage period (Table 1). Also the data showed significantly different effect ($P \leq 0.01$) among the treatments chicken eggs samples during storage. The result was obtained the highest value were increased gradually during storage period, then the lowest value were at the beginning of storage. These variations may be due to the effect of treatments and grade also may be due to temperature of storage period. The big samples are decrease in yolk index than other samples because decrease in exposure area and increase loss of water. The results are in fully agreed with Hassan (2011) [10] who found that, the yolk height decreased approximately 10% with temperature increasing from 5 to 23 °C with only a slight decrease with storage time. For yolk width, minimum change was observed with either temperature or storage time. Both yolk highest and yolk width had the lowest value [15]. These results are in agreement with those of Scott and Silversides (2000) [16] and Samli *et al.* (2005) [14]. Samli *et al.* (2005) [14] also reported significant ($P < 0.001$) decrease in egg weight, albumen height, Haugh unit, albumen and yolk indices with increase in storage time. In their study, albumen height decreased from 9.16 to 4.75 mm, Haugh unit from 91.4 to 40.6 and yolk index from 44.1 to 32.7 within 10 days of storage. In addition, the increase in albumen and yolk width observed in this study has also been reported by Keener *et al.* (2006) [15]. The general decline in albumen and yolk quality as eggs aged is in

agreement with the findings of Fasenko et al. (1995) [17]; Monira et al. (2003) [18] and Miles and Henry (2004) [19] who observed a decline in albumen and yolk indices with increase in storage time.

Haugh unit: The data showed significantly different effect ($P \leq 0.01$) among the treatments egg samples. The result was obtained the highest Haugh unit value in 0 day while the lowest value recorded in 20 days by the samples in (E) storage (Table 1). Also, the data showed significantly different effect ($P \leq 0.01$) among the treatments egg samples during storage. The result was obtained the highest value were increased gradually during storage period, then the lowest value were at the beginning of storage. These variations may be due to the effect of treatments and grade also may be due to storage period. The big samples are decrease in Haugh unit than other samples because decrease exposure area and increase loss of water. The results are in full agreement with Hassan (2011) [10] who found that, the Haugh units (HU) are the standard method for determination of interior egg quality. These results are in typical to those of Scott and Silversides (2000) [16] and Samli et al. (2005) [14]. Samli et al. (2005) [14] also reported significant ($P < 0.001$) decrease in egg weight, albumen height, Haugh unit, albumen and yolk indices with increase in storage time. In their study, albumen height decreased from 9.16 to 4.75 mm, Haugh unit from 91.4 to 40.6 and yolk index from 44.1 to 32.7 within 10 days of storage. In addition, the increase in albumen and yolk width observed in this study has also been reported by Keener et al. (2006) [15]. The general decline in albumen and yolk quality as eggs aged is in agreement with the findings of Fasenko et al. (1995) [17]; Monira et al. (2003) [18] and Miles and Henry (2004) [19] who observed a decline in albumen and yolk indices with increase in storage time. The rate of quality loss as measured by HU is a nonlinear function [8]. Several researchers have questioned the validity of the method and its correction for egg weight. For example, Eisen et al. (1962) [20] compared direct albumen height measurement and calculated HU and found a bias in the HU regression. They reported that the correction for egg weight results in an overestimation of albumen height in smaller eggs and an underestimation of albumen height in larger eggs. Although its validity has been questioned, Williams (1992) [21] reviewed factors that affect albumen height. A few nutritional factors have been implicated, but, overall, nutrition is relatively unimportant. The major influences on albumen height are the strain and age of the hen laying the egg and storage time and conditions.

Shell thickness: The data showed significantly different effect ($P \leq 0.01$) among the treatments chicken eggs samples. The result was obtained the highest value in sample C (1.13 ml, 1.76 ml and 1.95 ml) were showed in (big, medium and small) respectively, while the lowest value recorded in sample E (0.28 ml, 0.46 and 0.73 ml) were showed in (big, medium and small) respectively (Table 1). Also the data showed significantly different effect ($P \leq 0.01$) among the treatments chicken eggs samples during storage. The result recorded the highest shell thickness value in all the samples treated with wax while the lowest value recorded by the samples in (E) storage condition. These variations may be due to the effect of treatments and grade also may be due to storage period. The C samples are increase in shell thickness than other samples because treatment with wax. The results are fully agreed with Hassan (2011) [10] who found that, the structural quality of the shell egg is important to the processor because eggs that are structurally sound will arrive to the consumer in the best condition [16]. There was no difference in shell weight from 0 to 10 d of storage at 21°C, whereas at the storage temperatures of 5 and 29 °C there were significant ($p < 0.001$) decreases in shell weight with increasing storage time. These results are in agreement with those of Samli et al. (2005) [14] who found that shell weight changed significantly ($p < 0.05$) with storage time and temperature. In contrast, Silversides and Scott (2001) [22] reported that changes in shell weight were unclear within 10 d of storage.

The egg pH: The data showed significantly different effect ($P \leq 0.01$) among the treatments chicken eggs samples. The samples in (E) storage condition scored the lowest pH value in 20 days from the storage period while the samples in zero day from stored period recorded the highest pH value (Table 1). Also the data showed significantly different effect ($P \leq 0.01$) among the treatments chicken eggs samples during storage. The result was obtained the highest value were increased gradually during storage period, then the lowest value were at the beginning of storage. These variations may be due to the effect of treatments and grade also may be due to storage period. The all samples are decrease in pH values because increase loss of water and carbon dioxide. The results are fully agreed with Hassan (2011) [10] who found that, the egg pH when compared to the recommended level by Sudanese Standard (SDS 751/2007). Storage can modify some characteristics of the egg including loss of water, carbon dioxide and a subsequent increase in the pH of the albumen [7]. These findings are in agreement with

results reported by other researchers [16, 14, 7]. In contrast, Walsh et al. (1995) [23] reported that neither storage time nor temperature influenced albumen pH. The increase in yolk pH was not as large as the increase in albumen pH, and yolk pH did not differ during 10 d of storage at 29 °C. In contrast, Samli et al. (2005) [14] showed that yolk pH differed from 5.75 to 6.08 during 10 d of storage at 29 °C. The present results are in agreement with those of other researchers [14, 7] who also found that increases in yolk pH were significantly affected by storage time, but not by temperature. In addition, a highly significant interaction between storage time and temperature was observed for yolk pH ($p < 0.001$).

Table 1. Effects of storage time and different storage conditions on some quality characteristics of chicken eggs

Storage time (days)	Treatments				
	A	B	C	D	E
Air cell					
0	5.10±1.00 ^{bA}	5.10±1.00 ^{bA}	5.10±1.00 ^{aA}	5.10±1.00 ^{bA}	5.10±1.00 ^{cA}
10	4.43±1.53 ^{bC}	20.77±3.06 ^{aA}	5.77±3.21 ^{aC}	19.37±2.05 ^{aAB}	13.77±1.53 ^{bB}
20	10.70±0.69 ^{aB}	17.70±1.22 ^{aA}	8.37±1.42 ^{aB}	17.77±1.53 ^{aA}	19.43±3.21 ^{aA}
Yolk Index					
0	0.50±0.04 ^{aA}	0.50±0.04 ^{aA}	0.50±0.04 ^{aA}	0.50±0.04 ^{aA}	0.50±0.04 ^{aA}
10	0.40±0.03 ^{bA}	0.22±0.02 ^{bC}	0.27±0.01 ^{bBC}	0.31±0.03 ^{bB}	0.32±0.01 ^{bB}
20	0.40±0.01 ^{bA}	0.20±0.03 ^{bB}	0.14±0.02 ^{cC}	0.16±0.02 ^{cBC}	0.17±0.02 ^{cBC}
Haugh Unit					
0	87.77±5.75 ^{aA}	87.77±5.75 ^{aA}	87.77±5.75 ^{aA}	87.77±5.75 ^{abA}	90.13±2.87 ^{aA}
10	91.27±2.65 ^{aA}	65.90±10.61 ^{bB}	91.20±3.12 ^{aA}	91.93±2.93 ^{aA}	84.53±9.59 ^{aA}
20	85.07±3.52 ^{aA}	80.30±3.81 ^{abA}	82.27±2.58 ^{aA}	77.00±4.85 ^{bA}	67.63±15.08 ^{aA}
Shell Thickness (mm)					
0	0.71±0.40 ^{aB}	0.59±0.07 ^{aBC}	1.76±0.08 ^{aA}	0.56±0.10 ^{aBC}	0.47±0.67 ^{aC}
10	0.65±0.11 ^{aB}	0.58±0.08 ^{aB}	1.76±0.08 ^{aA}	0.56±0.10 ^{aB}	0.47±0.07 ^{aB}
20	0.64±0.10 ^{aB}	0.62±0.08 ^{aB}	1.73±0.08 ^{aA}	0.56±0.10 ^{aB}	0.47±0.07 ^{aB}
pH					
0	8.85±1.00 ^{aA}	8.82±1.00 ^{aA}	8.82±1.00 ^{aA}	8.82±1.00 ^{aA}	8.82±1.00 ^{aA}
10	8.20±0.02 ^{bA}	7.87±0.04 ^{bB}	7.52±0.03 ^{bC}	7.90±0.03 ^{bB}	6.81±0.03 ^{bD}
20	8.05±0.04 ^{cA}	7.04±0.04 ^{cC}	7.18±0.03 ^{cB}	7.17±0.04 ^{cB}	6.78±0.03 ^{bD}

^{a-c} Means within columns with different superscript letters are significantly different ($p < 0.05$).

^{A-F} Means within rows with different superscript letters are significantly different ($p < 0.05$).

Values are means of triplicate samples (\pm SD).

A: Cold storage; B: Room temperature; C: Room temperature (treated with wax); D: Ventilation; E: Heat of the sun for 2-8 h + room temperature

Conclusion

The data of air cell size on different grades of egg and storage conditions was obtained the highest value in sample E, while the lowest value recorded in all samples. The data of yolk index on different grades of egg and storage conditions was obtained were increased gradually during storage period, then the lowest value were reported at the beginning of storage. The data of egg haugh unit on different grades of egg and storage conditions was obtained the haugh unit showed highest value in all samples, while the lowest value recorded by sample E. The data of shell thickness on different grades of egg and

storage conditions was obtained were increased gradually during storage period, then the lowest value were reported at the beginning of storage. The data of egg pH on different grades of egg and storage conditions was obtained the highest value in all samples, while sample E recorded the lowest value. The data showed significantly of total viable count of bacteria on different grades of egg and storage conditions was obtained the highest value were increased gradually during storage period, then the lowest value were at the beginning of storage. Lastly the data of Salmonella spp on different grades of egg and storage conditions was obtained free Salmonella spp in all samples.

Acknowledgement

This research was produced from the Master Thesis of Nusiba Alsiddig Badawi. The authors would like to thank the AL-Zaeim AL-Azhari University for their technological support.

References

- [1] Matt D, Veromann E, Luik A (2009) Effect of Housing System on Biological Composition of Chicken Eggs. *Agronomy Research* 662-667.
- [2] Kramer A (1951) What is quality and how can it be measured: From a food technology point of view. In: Market Demand and Product Quality. Mktg. Res. Workshop Rept., Michigan State College.
- [3] Osman OA, Mohammed KE (2008) The SSMO Annual Report 2007, Accomplishment and challenges the Five-Year plan. *Sudanese Journal of Standards and Metrology* 2 (1,2): 1-17.
- [4] USDA (2008) Risk Analysis. United State Department of Agriculture 22(2): 203
- [5] Philip J (2009) Proper Handling of Eggs: From Hen to Consumption. *Poultry extension specialist. Animal and Poultry Science* 2902-1091.
- [6] Osman OA, Elhussien AM, Harbi MS (2008) SSMO Role in Food Safety, Overview. *Sudanese Journal of Standards and Metrology* 2(1, 2): 18-25.
- [7] Akyurek H, Okur AA (2009) Effect of Storage Time, Temperature and Hen Age on Egg Quality in Free-range Layer Hens. *Journal of Animal and Veterinary Advances* 8: 1953-1958.
- [8] Haugh RR (1937) The Haugh unit for measuring egg quality U.S. *Egg Poultry Mag.* 43: 552-573
- [9] Harrigan FW (1998) *Laboratory Methods in Food Microbiology*. 3rd edition. Academic Press of London. London. U.K.
- [10] Hassan MAA (2011) Evaluation of table egg quality according to Sudanese Standard. M. Sc in Al-Zeim Al-Zhari University .Faculty of Post Graduate Studies and Scientific Research, Khartoum. Sudan.
- [11] Harrigan FW, MacCance ME (1976) *Laboratory Methods in Food Microbiology*. Academic Press of London. U.K. New York and San Francisco.
- [12] Steel RDG, Torrie TH, Dickey DA (1997) *Principle and Procedures of Statistics: A biometrical approach*. 3rd. McGraw-hill, New York, U.S.A.
- [13] Jin JH, Lee KT, Lee WI, Han YK (2011) Effect of Storage Temperature and Time on the Quality of Eggs from Laying Hens at Peak Production. *Asian-Aust. j. Amin. Sci.* 24(2): 2279-284.
- [14] Samli HE, Agna A, Senkoğlu N (2005) Effects of storage time and temperature on egg quality in old laying hens. *J. Appl. Poult. Res.* 14: 548-533.
- [15] Keene KM, Lacrosse JD, Curtis PA, Adderson KE, Farkas BE (2000) The influence of rapid air cooling and carbon dioxide cooling and subsequent storage in air and carbon dioxide on shell egg quality. *Poultry Sci.* 79: 1067-1071.
- [16] Scott TA, Silversides FG (2000) The effect of storage and strain of hen on egg quality. *Poult. Sci.* 79: 1725-1729.
- [17] Fasnko GN, Christensen VL, Bakst MR, Petite JN (1995) Evaluating yolk membranes from short and long stored turkey eggs using transmission electron microscopy. *Poultry Sci.* 74(Suppl. 1): 44. (Abstr).
- [18] Monira KN, Salhuddin M, Miah G (2004) Effect of breed and holding period on egg quality characteristics of chicken. *International Journal of Poultry Science* 2: 261-263.
- [19] Miles, R.D and P.R. Henry. (2004). Effect of time and storage condition on albumen quality of eggs from hens fed Vanadium. *Journal of Applied Poultry Research.* 13(4): 619-627.

3rd International Students Science Congress
3-4 May 2019, İzmir - Turkey

- [20] Eisen EJ, Bohren BB, Mckean HE (1962) The Haugh unit as a measure of egg albumen quality. Poul. Sci. 41: 1461–1468.
- [21] Williams KC (1992) Some factors affecting albumen quality with particular reference to Haugh unit score. World's Poultry Science 48: 5-16.
- [22] Silversides FG, Scott TA (2001) Effect of storage and layer age on quality of eggs from two lines of hens. Poul. Sci. 80: 1240-1245.
- [23] Walsh TJ, Rizk RE, Brake J (1995) Effect of temperature and carbon dioxide on albumin characteristics, loss, and early embryonic mortality of long stored hatching eggs. Poultry Sci. 74: 1403-1410.

Chemical Interesterification of Palm Olein, Palm Stearin, Palm Mid Fraction, Sunflower oil and Soybean Oil Blends and its Effects on Melting Point, Solid Fat Content and Triglycerides

Vassiriki Cissé, Fahri Yemişçioğlu, Merve Yazılıkaya*
Ege University, Dept. of Food Engineering, Bornova, İzmir, Turkey
**Corresponding author: aboubakcisse@hotmail.com*

Keywords: chemical interesterification, solid fat content, melting point, triglycerides, fractionated palm oil
Discipline: Food Engineering

Abstract

Fractionated palm oil as such as palm stearin, palm olein, palm mid fraction were mixed in various ratios with different polyunsaturated oils like Sunflower Oil and Soybean Oil. They were submitted to chemical (randomization) interesterification (CIE) reaction that is a rearrangement of fatty acids of triglycerides resulting to new triglycerides formation. However, this reaction influenced the physicochemical characteristics (melting point, solid fat content, and triglycerides) that were assessed before and after CIE. Melting point and solid fat content values were varied due to the appearance of new triglycerides and chemical interesterification. Some triglyceride amounts were both increased and decreased and miscibility of others blends was effective. Solid Fat Content values of Palm Mid fraction were zero to 30 and 35°C with Sunflower oil blend and those of Palm Olein were zero to 20 , 30 , 35°C with Sunflower Oil and Soybean Oil blends. The obtained values after chemical interesterification of fractionated fats and polyunsaturated oils are shown that physicochemical modification was realized and effective.

Introduction

Intesterification (IE) is one the modification techniques of edible oils and fats used to facilitate the rearrangement of Fatty Acid (FA) localized or esterified to glycerol of triglyceride (triacylglycerol, TAG). IE causes the randomization of the distribution of fatty acids in the triglyceride called intraesterification and between triglycerides called interesterification, in oils and fats until a thermodynamic equilibrium is reached [1]. Thus, this leads to changes in the composition of the TAG and thus its physical characteristics. The FA exchanges resulting from the IE lead to changes in the physical characteristics of the oils and fats because in nature, they are not randomly distributed between the TAGs present. In most oils and fats, the 2-position of the TAG molecules is preferentially occupied by unsaturated fatty acids [2]. Interesterified oils/fats are recognized free of Trans Fatty Acid (TFA) during all its production contrarily to hydrogenation that has been abandoned by many manufacturers due to the appearance of TFA in hydrogenated oils and fats [3]. IE is divided into 2 types which are really different according to used catalyst: Chemical Interesterification (CIE) in which is used catalyst like sodium methylate and enzymatic interesterification (EIE) using lipase as enzyme to produce interesterified oils or fats [4]. CIE is used, in this study, to produce fat and to discuss the effect of this technique on different vegetable oil/fat. It also called random interesterification due to the fatty acid distribution on 1, 2, 3 position of TGA by sodium methylate [5].

Palm stearin (PS), palm olein (PO) and palm mid fraction (PMF) are edible oils and fats that are obtained from crystallization-fractionation modification technique of palm oil [6]. PS and PO are issued from the first phase of palm oil fractionation. PS is harder than PO and PMF because of its high saturated acids like palmitic and stearic acids and its high melting point (44-55°C) [7]. Then PS is solid at body temperature, due to that, it is used in shortening, Margarine and spread fats formulation. However It is sometimes blamed because it melts hardly at body temperature and its plasticity is also low. For this reason, PS is more often blended and/or interesterified with some polyunsaturated vegetable oils like Sunflower Oil (SFO), Soybean Oil (SO) what contain more linoleic and oleic acids [8]. PO is less hard than PS and appear liquid phase at body temperature. PMF is obtained from the second phase of palm oil fractionation which is harder than PO but more less than PS. It can use to produce butter or Cacao Butter Equivalent [9].

The purposes of this work were to investigate the effect of CIE on the TAG composition, MP, FAC and SFC of PS, PMF, PO, SFO, SO and blends thereof in various ratios. The interaction of these oils and fats and their compatibility (miscibility) are also discussed. Obtained fats will be used into margarine, shortening and spread formulation.

Materials and Methods

Samples

Main vegetable oils used in this work were refined, bleached and deodorized SFO and SO which were obtained from one of Turkey's Oil Manufacturer called Orkide in İzmir. Others fats that used were palm stearin, palm olein and palm mid fraction obtained also from IFFCO Industries, İzmir, Turkey.

Oil/fat blend preparation

To realize chemical interesterification, different oil/fat in various ratios was blended to eliminate the crystal phase and to obtain a homogenous blend. The blend has been realized according to following ratios:

For Sunflower Oil:

SFO/PS – A(80:20) , D(70:30) , G(60:40) , J(50:50) ; SFO/PO – B(80:20) , E(70:30) , H(60:40) , K(50:50) ; SFO/PMF - C(80:20) , F(70:30) , I(60:40) , L(50:50).

For Soybean Oil:

SO/PS – A(80:20) , D(70:30) , G(60:40) , J(50:50) ; SO/PO – B(80:20) , E(70:30) , H(60:40) , K(50:50); SO/PMF – C(80:20) , F(70:30) , I(60:40) , L(50:50).

Random (chemical) interesterification reaction

The oils were subjected to a drying at 80°C to eliminate water or high moisture because it can deactivate or slow down the catalyst activity (sodium metal). Sodium metal (1%) was added to facilitate the reaction and during 30 minutes, the sample was stirred up at 120 rpm under vacuum (25 mbar) in a rotary evaporator. Brown colour appeared when the reaction was realized. The reaction was deactivated by hot water addition, the mixture was washed eliminating soap phase and transferred into separate funnel to continue washing. After soap phase elimination, reactant (phenolphthalein) was used to test washing efficiency. The mixture was dried under vacuum at 80°C and filtered by filter paper. Obtained mixture is Interesterified oils were transferred into the bottle and stored until different analysis.

Melting Point (SMP)

Interesterified oils/fats were subjected to melting point to determine exactly the temperature at what the first droplet appears in the capillary tube. This is also temperature at what the fat becomes soft. According to AOCS Cc 3-25 method [10], melting points were measured. Analysis was replicated in two and values were reported.

Solid Fat Content (SFC)

SFC is a ratio of solid that oil has after drying at different temperature. In this experiment, SFC was determined according to IUPAC 2.150 (b) [11]. Bruker Minispec PC 100 NMR was used and all samples were melted in water heater at 90°C during 1 hour and cooled in a box containing cold water (0°C– 30 mm). According to temperatures 20, 30, 35°C, samples were reheated and SFC measured. The results were mentioned and treated.

Fatty Acid Composition (FAC)

FAC are amount of different fatty acids contained in the oils/fats or blended oil interesterified oils. To determine FAC, fatty acids were methylized by the addition of 0,4 ml KOH (2N methanol KOH) and 4 ml hexane into 200 mg sample (interesterified oil) [12]. FAC were realized with Agilent technologies 7820A, GC system, Supelco SP2380, capillary column (60 m length *0.25 mm id *0.2 µm film thickness). The detector and injector temperature were set at 240°C. The flow rate was 1.0 ml/min and column temperature was 150°C for all oils/fats. 1µl sample was injected into an Agilent technology.

Triglycerides profiles

Non interesterified and interesterified fats were subjected to reversed-phase HPLC method (Gilson Villiers-el-bel, France) to determine TAG. Acetone and acetonitrile (75:25, V/V) was used and RP-18 column (250 mm * 4 mm) of 5- μ m size (Merck). The flow rate was 1.0 ml/ min as eluent. 20 μ l of the sample was injected and TAG values were reported.

Statistical analysis

Analyses of general linear models and response surfaces were performed using the SAS® (Cary, NC) statistical package as described by Ali and Dimick [13]. R^2 values, which indicate model fits for each of the constructed ternary diagrams, were determined and were found.

Results and Discussions

Fatty acid composition

In this step, fatty acid composition values of fractionated oils (PS, PO, and PMF) and SFO, SO were given in Table 1 in which two parts showing fatty acid composition before chemical interesterification. Before interesterification, the oils/fats were used such as SFO and SO were composed in majority of oleic acid 38.6%, linoleic acid 55.37% and oleic acid 26.23%, linoleic acid 47.85% respectively. Jun Jin et al. [14] reported in their study that FAC of SFO were oleic acid 24.3% and linoleic acid 65.1%; and main FAC of SO was oleic acid 24% and linoleic acid 55.4% [15]. The fractionated fats/oils contained high amount of saturated FA (palmitic acid 32-44 %, stearic acid 6-15%) and unsaturated FA (oleic acid 28-48%). According to SFO, SO and fractionated oils/fats FAC, the FA profile of CIE blends are not changed because It was not appeared trans fatty acid. It shows that CIE has not affected the degree of saturation of polyunsaturated acids. But the FA of certain fats are distributed over position in TAG [16].

Table 1. Fatty acid composition of SFO, SO, fractionated fats and CIE blends

	C14:0	C16:0	C16:1	C18:0	C18:1	C18:2	C18:3	C20:0	C22:0	C24:0
SFO	–	–	–	4.09	38.6	55.37	0.19	0.34	2.06	0.36
SO	–	12.99	–	6.04	26.23	47.85	5.71	0.74	0.44	–
PO	–	35.64	–	14.26	38.08	12.01	–	–	–	–
PS	–	43.45	–	11.79	28.10	16.66	–	–	–	–
PMF	0.46	32.37	0.11	6.01	48.05	9.82	0.13	0.78	0.18	0.22
SFO:PMF	0.082	9.06	0.06	4.55	39.89	42.69	0.07	0.68	1.69	0.74
SFO:PO	0.16	13.06	0.095	3.99	39.34	42.07	0.08	0.32	0.50	0.19
SFO:PS	0.14	13.79	0.07	4.48	36.29	42.67	0.06	0.49	1.17	0.45
SO:PO	0.10	11.96	0.07	5.23	29.90	45.11	5.79	0.88	0.48	0.16
SO:PS	0.17	16.74	0.07	5.21	26.96	43.98	5.25	0.81	0.32	0.12
SO:PMF	–	18.51	–	13.83	28.83	36.04	2.78	–	–	–

PS: palm stearin, PO: palm olein, PMF: palm mid fraction and CIE: chemical interesterification

Slip Melting Point

In Figure 1, the SMP of PS, PO, PMF and SO, SFO were introduced and compared between themselves. Initial Melting Points (IMP) of PS were high (57.6°C) than that of PMF (31°C) and PO (20°C), those of SO and SFO were 6°C and 5°C respectively. High melting point of PS was due to high presence of length chain of saturated fatty acid as palmitic acid (43.45 %) and oleic acid (28.10 %) [17]. SMP of PMF also resulted to high saturated carbon chains of fatty acid (palmitic and oleic acids) [18]. SO and SFO had low melting point due to high amount of double liaison and presence of mono- and polyunsaturated FA (linoleic , oleic acids) [18]. IMP (PS, PMF) were high that those of NCIE blends when they were blended with SO and SFO. It was due to high amount of mono- and polyunsaturated FA.

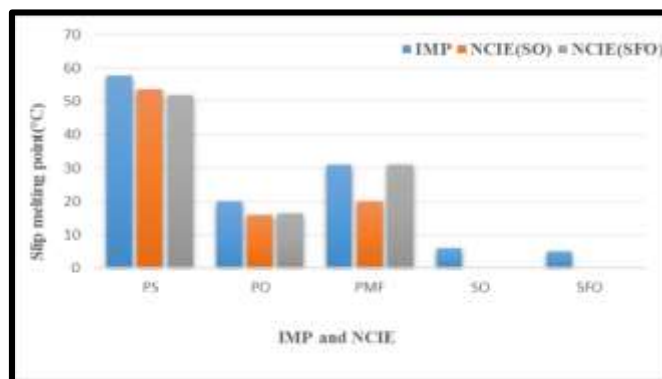


Figure 1. Slip Melting Points of origin material and NCIE blends

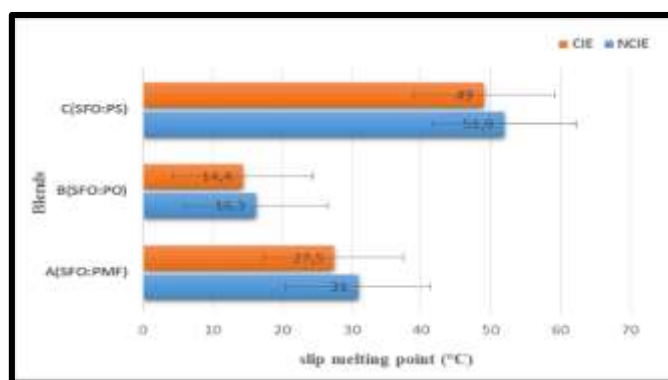


Figure 2. Slip Melting Points of NCIE and CIE blends with SFO

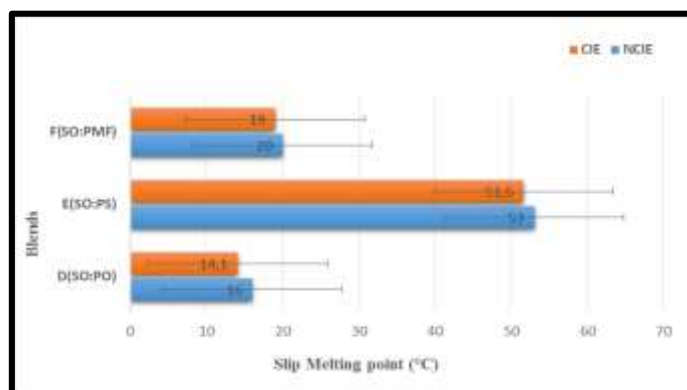


Figure 3. Slip Melting Points of NCIE and CIE blends with SO

The SMP of CIE and NCIE blends are given in Figures 2 and 3. SMP of CIE had decreased in all ratios of blend (A, B, C, D, E, F) according to the melting point of NCIE blends. That change of SMP was due to effect of chemical interesterification that rearranges the FA of TAG and due to PS, PO, PMF are diluted in polyunsaturated oils (SO and SFO). CIE melting point of SO and CIE melting point of SFO were different because of high linolenic acid amount, then double liaison [19].

Solid Fat Content (SFC)

SFC is the amount of fat crystal contained in a fat or a mixture of fat that gives the physical appearance of solid products. It is also the determination of compatibility of materials contained in the mixture of saturated and unsaturated oils (mono- and polyunsaturated) [20]. The SFC values of the original oils /fats and interesterified mixtures are presented in Table 2. SFC of PS had a high at all temperatures to which it was subjected. This PS value was due to triglycerides containing acids that have high melting points (S_2U or S_3). That collaborate with the results of the studies by Hazirah (2012) and Noor (2007) [18, 21]. SFC of PMF decreased significantly from 20°C to 30°C and was zero at 35°C.

It contained fat crystals at 30°C due to high amount of mono-unsaturated fatty acid and saturated fatty acid chains.

PO, SO, SFO were liquid from 30 to 35°C because of the high number of mono- and polyunsaturated fatty acids and also their low melting point. This tendency is justified by Soekopitojo (2009) [22].

The different SFC of fractionated palm oil blends with canola and SFO tended to decrease regard to before and after interesterification (Figure 4). With SFO, SFC value was little crystal (solid) at 35°C in all blending ratios, due to the presence of the high melting point of glyceride elements (PPP, POP). However SFC of SFO/PS decreased when temperature increased due to SU₂ of SFO TAGs (more monounsaturated-polyunsaturated fatty acids in TAG). Except in the case of SFO / PS (80:20), (70:30) which increased to before and after interesterification at all temperatures (20°C, 30°C, 35°C) (Figure 1). This increase is explained by the eutectic interaction between the oils (SFO/PS) demonstrating a better miscibility (compatibility). This is demonstrated by Dieffenbacher, 1988 [23] and Timms, 1984 [24]. SFC of SFO/PMF decreased at all temperatures and was liquid above 30°C in all proportions of the mixture except in case 50:50 (Figure 5).

With the mixture of SO and PS, PMF; SFC of SO/PS and SO/PMF decreased considerably at all temperatures, this is due to the high amount of U₃ TAG (low melting point, polyunsaturated) in SO and solid crystal dilution in PS and PMF (Figure 6 and 7). In case of SO/PS, all the proportions of mixture tended to a linear combination except that of 50:50 which presented a sinusoidal combination under any temperatures. Noor et al. (2007) [21] indicated in his study that the physical characteristic of the oil mixture components represented no linear combination, thus showing the interaction between the materials of the mixture. This interaction is eutectic interaction between SO and PS indicating better miscibility what is generally used in margarines, shortening, spread manufacturing. PO blend in SO and SFO was liquid at all temperatures and blend ratios. That was due to the presence of U₃ TAGs of SO and SFO (mono- and polyunsaturated FA) and the dilution of low semi-crystals of PO [25].

CIE Binary blends (SFO/PS, SFO/PMF or SO/PS, SO/PMF) were significantly affected depending on the interesterification reaction. SFC of these different interesterified mixtures decreased with respect to SFCs of Non-interesterified mixtures, because of the components of TAGs according to oils or fats. The CIE binary mixtures with SO and SFO had no influence on the one and the other in the production of interesterified fat according to Table 2.

Triglyceride Composition

TAG composition of SFO, SO, PS, PMF, PO and their blends before and after chemical interesterification is shown in Table 3. Dominating TAG of SFO and SO were LLL, OLL, OLO, PLO, PLL and SO were LLL, OLL, PLL, OLO, PLO where L: linoleic acid, O: oleic acid, P: palmitic acid [26]. The main TAG of PO and PMF were PLO, PLP, POP, PPP, POO and those of PS were PLP, POP, PPP, POO. PMF and Po contained appreciable amount of SOS and SOO. Noor et al.,(2002) [26] revealed in his study that S₂U and S₃ TAG were high amount in PS, PMF, PO and main U₂S and U₃ in SFO. Chemical interesterification realized on SFO, SO, PS, PMF and PO generated little changes in their TAG compositions, the main TAG of SFO as PLL, LLL, were reduced rather from 9.1, 10.6, 23.5 before CIE to 8.9, 10.1, 23.4 after CIE. Those TAG were not hardly altered. For the same fat, an increase of certain main TAG like OLL, PLO from 27.3, 8.9 to 28.7 and 9.1 respectively obtained. Change obtained was not so significant.

In the case of SO, there is not significant change between the TAG, except LLL decreased from 30.1 before CIE to 26.4 following CIE, it was hardly altered. CIE of fractionated oils/fats generated an important change in the proportion of TAG of PS in which PPP was hardly affected increasing from 19 before CIE to 24.7 after CIE. In the others (PMF, PO) the few change was observed in the proportions of main TAG.

For the binary blends of several fat (Table 4), the TAG of this binary blends could not be identified because of randomization or chemical interesterification which led to appear many new TAG and the complex interaction (varying permutation). They try to have the similar carbon numbers. The TAG profiles of the interesterified blends showed more amounts than the starting blends, as the relative concentration of several TAG increased, others decreased and new TAG have been synthesized. Zainal and Yussoff (1999) [27] found and reported this result.

Table 2. Solid Fat Contents (area %) of CIE and NCIE blends of SFO and SO

		20°C		30°C		35°C	
		BI	AI	BI	AI	BI	AI
A(SFO:PMF)	80:20	1.2	0.5	–	–	–	–
	70:30	1.8	0.8	–	–	–	–
	60:40	2.2	3.1	0.1	0.4	–	–
	50:50	4	4.5	0.3	0.8	–	–
B(SFO:PO)	80:20	–	–	–	–	–	–
	70:30	–	–	–	–	–	–
	60:40	–	–	–	–	–	–
	50:50	–	–	–	–	–	–
C(SFO:PS)	80:20	8.6	14.9	5.6	9.9	4.2	7.5
	70:30	15.4	9.1	10.5	6	8.2	4.4
	60:40	20.8	20	13.6	13	10.9	9.7
	50:50	27.3	24.1	18.3	14.8	14.4	11.2
D(SO:PO)	80:20	–	–	–	–	–	–
	70:30	–	–	–	–	–	–
	60:40	–	–	–	–	–	–
	50:50	–	–	–	–	–	–
E(SO:PS)	80:20	8.2	7.8	5.1	4.8	4	3.6
	70:30	13.4	13.2	8.3	7.8	6.3	6.1
	60:40	18.6	18.3	11.2	11.4	8.6	8.4
	50:50	25	12	15.5	5.3	11.9	3.9
F(SO:PMF)	80:20	0.9	0.6	0	0.1	–	–
	70:30	2.2	2.4	0.3	0.3	–	–
	60:40	3.2	3.3	0.6	0.5	–	–
	50:50	5	4.6	0.9	1.1	–	–
PS		67.5		46.8		37.7	
PMF		23.7		3.4		–	
SO		–		–		–	
SFO		–		–		–	

AI: after interesterification, BI: before interesterification, NCIE: Non chemical interesterification, CIE: chemical interesterification

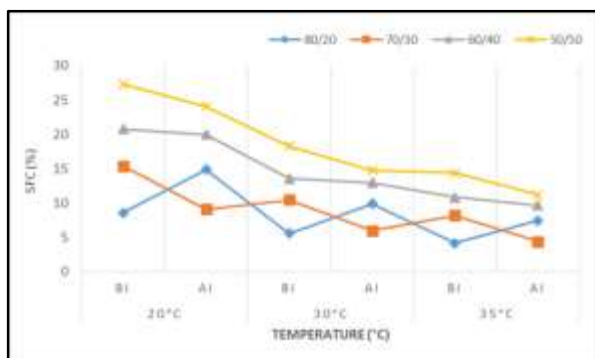


Figure 4. Solid Fat content of SFO/PS blends and CIE according to blending ratio

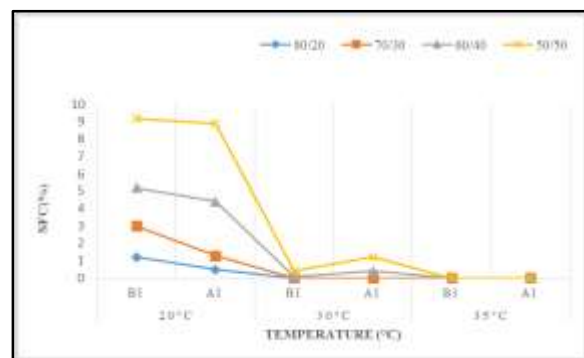


Figure 5. Solid Fat content of SFO/PMF blends and CIE according to blending ratio

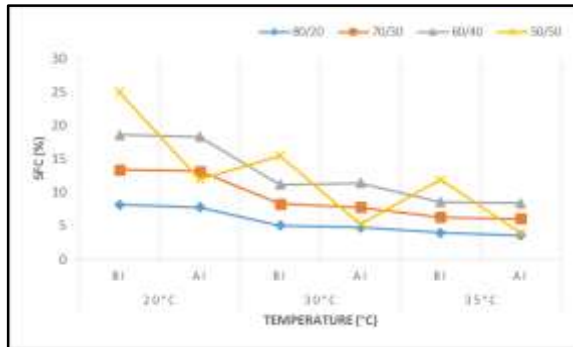


Figure 6. Solid Fat content of SO/PS blends and CIE according to blending ratio

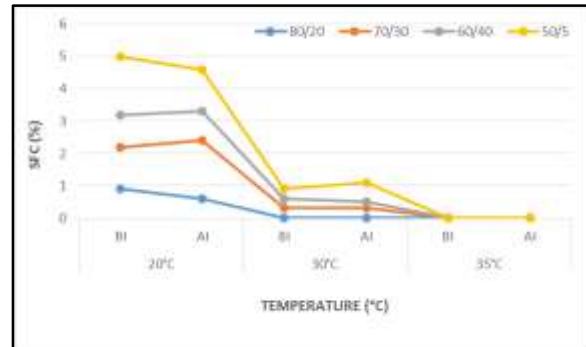


Figure 7. Solid Fat content of SO/PMF blends and CIE according to blending ratio

Table 3. Triglyceride composition (area %) of SFO, SO, Palm Stearin, Palm olein (PO) and Palm Mid Fraction (PMF) before (NCIE) and after (CIE) chemical interesterification

	SFO		SO		PS		PMF		PO	
	NCIE	CIE	NCIE	CIE	NCIE	CIE	NCIE	CIE	NCIE	CIE
LLL	23.5	23.4	30.1	26.8	–	–	–	–	–	–
LLM	–	–	–	–	–	–	–	–	–	–
LMM	–	–	–	–	–	–	–	–	–	–
MMM	–	–	–	–	–	–	–	–	–	–
OLL	27.3	28.7	29.3	29.1	–	–	0.7	0.8	0.9	1.0
PLL	9.1	8.9	7.9	7.6	0.5	0.2	1.4	1.4	2.8	2.4
OLO	10.6	10.1	9.5	10.6	0.6	0.4	3.7	4	5.2	5.8
PLO	8.9	9.1	9.2	9.3	0.4	0.3	7.9	8.9	10.9	11.3
MOO	–	–	–	–	–	–	–	–	–	–
PLP	0.3	0.2	0.15	0.1	6.8	6.5	7.1	7.1	7.1	7.2
MOP	–	–	–	–	–	–	–	–	–	–
POP	0.4	0.6	0.4	0.6	37.6	37.8	26.9	26.8	23	23.2
POS	0.2	0.2	0.3	0.4	0.8	0.7	6.0	5.9	3.7	3.5
SOS	–	–	–	–	–	–	0.7	0.6	0.5	0.4
PPP	0.6	1.0	1.0	1.5	19	24.7	12.1	12.0	7.9	7.6
OOO	–	–	2.8	2.7	–	–	4.9	4.8	6.5	7.1
POO	3.7	3.8	4	4.2	17	17.7	22.1	21.9	24.6	24.3
SOO	0.9	0.4	0.6	0.6	2	1.7	1.7	1.6	1.9	2
PPS	0.2	0.5	0.3	0.4	4.2	5	3.6	3.5	2.2	2.1

Table 4. Triglyceride composition (area %) of SFO, SO, Palm Stearin (PS), Palm olein (PO) and Palm Mid Fraction (PMF) blends before (NCIE) and after (CIE) chemical interesterification

	SO/PS		SO/PMF		SO/PO		SFO/PS		SFO/PMF		SFO/PO	
	NCIE	CIE	NCIE	CIE	NCIE	CIE	NCIE	CIE	NCIE	CIE	NCIE	CIE
LLL	17.0	4.0	23.0	7.6	15.8	13.4	20.1	16.1	19.9	9.8	18.9	5.1
LLM	–	–	–	–	–	–	–	–	–	–	–	–
LMM	–	–	–	–	–	–	–	–	–	–	–	–
MMM	–	–	–	–	–	–	–	–	–	–	–	–
OLL	17.9	11.8	25.1	16.8	15.3	5.1	19.8	16.3	18.1	17.3	18.1	3.9
PLL	6.0	10.9	1.4	0.8	5.6	7.0	9.1	12.8	8.9	11.9	5.0	3.5
OLO	5.3	19.1	0.9	0.1	6.3	15.1	9.3	10.2	9.0	12.0	8.0	12.3
PLO	6.8	3.0	4.1	2.2	6.1	14.3	8.7	14.1	7.8	15.4	7.6	13.2
MOO	–	–	–	–	–	–	–	–	–	–	–	–
PLP	5.0	9.7	4.0	1.8	–	–	1.9	4.5	2.0	5.4	2.1	5.2
MOP	–	–	–	–	–	–	–	–	–	–	–	–
POP	23.0	20.5	13.3	4.8	15.9	14.9	12.3	4.3	13.0	4.1	16.1	6.3
POS	3.9	1.8	2.9	14.4	2.9	3.0	1.3	1.2	1.2	1.2	2.3	2.0
SOS	–	–	0.1	7.2	0.3	0.1	–	–	0.2	–	0.5	0.1
PPP	8.3	4.8	1.5	3.0	8.3	5.2	4.0	1.9	3.9	1.2	3.9	3.7
OOO	2.1	0.1	1.2	0.2	2.4	0.5	1.8	0.6	1.5	0.3	2.6	0.7
POO	6.9	10.1	8.0	1.3	5.8	12.5	7.1	7.2	6.9	7.0	9.9	10.1
SOO	1.2	1.2	1.0	3.1	1.3	1.0	0.8	0.8	0.6	0.5	0.5	0.4
PPS	0.4	0.3	10.0	12.1	0.2	0.3	2.5	1.5	2.2	2.3	2.0	1.7

Conclusion

This study has demonstrated that the binary blends of several oils (SFO, SO and/or fractionated palm oil) and with random interesterification (CIE) could provide new fat products that are free trans fatty acid and having desired SFC, SMP, FA and triglycerides.

CIE is the method that permitted to modify the characteristics of origin oils/fats, blends and to improve the compatibility (miscibility) of oils and blend materials. Those binary blends could be used in margarine, shortening and spread formulation.

Acknowledgement

The first author of this study was supported by the Presidency for Turks Abroad and Related Communities (YTB) within “International Student Academy” Project.

References

- [1] Idris NA, Dian NLHM (2005) Interesterified palm products as alternatives to hydrogenation. *Asia Pacific Journal of Clinic Nutrition* 14(4):396-401.
- [2] Rousseau D, Forestiere K, Hill AR, Marangoni AG (1996) Restructuring butter fat through blending and chemical interesterification. I. Melting behavior and triacylglycerol modification. *J. Am. Oil Chem. Sc.* 73: 963-972.
- [3] Marangoni, A.G, Rousseau D. (1998). Chemical and enzymatic modification of butterfat and butterfat canola oil blends. *Food Research International*, 31(8), 595-599.
- [4] Sreenivasan, B. (1976). Interesterification of fats. *J. Am. Oil Chem. Sc.* 55:796-805.
- [5] Rai Muhammad Amir, Muhammad Asim Ahabbir, Moazzam Rafiq khan, Shahzad Hussain (2012). Interesterification of fats and oils. A review. *Pak. J. Food. Sci.* 22(3)143-153

3rd International Students Science Congress
3-4 May 2019, İzmir - Turkey

- [6] Gümüskesen A. S., Yemişçioğlu. (2010). Bitkisel sıvı ve katı yağ üretim teknolojisi. Meta Basım. 975-94208
- [7] Aini, I. N. & Miskandar, M.S. (2007). Utilization of palm oil and palm products in shortening and margarines. *Eur. J. Lipid Sci Technol.* 109(4) 422-432
- [8] H.M.D Noor Lida, A.R. Md. Ali. (1998). Physicochemical characteristics of palm based oil blends for the production of reduced fat spreads. *J. Am. Oil Chem. Sc.* 75, 1625-1631.
- [9] Geoff talbot, Kevin W. Smith, Fred W. Cain (2006). Solvent fractionation of palm oil. *Inform.* 17(5) 324-326
- [10] American Oil Chemists' Society (2005). Official methods and recommended practices of the American Oil Chemists' Society. Champaign Illinois.
- [11] IUPAC Norm version. (1987). 2.150 (ex 2.323). Solid content determination in fat by NMR (low Resolution NMR)
- [12] Garcia-Gonzalez, D.L., Aparicio-Ruiz, R. And Morales, M.t. (2014). Chemical characterization of organic and non-organic virgin olive oils. *OCL* 21(5), D506.
- [13] Md. Ali, A.R., and P.S. Dimick, (1994). Thermal Analysis of palm mid-fraction, cocoa butter, and milk fat blends by differential scanning calorimetry. *J. Am. Oil Chem. Soc.* 71:299–302.
- [14] Juan Jui, Liang tie, Ligen Zheng, Min Cheng, Dan Xie, Quigzhe Jui & Xingguo wang. (2018). Characteristic of palm mid fraction produced from different fractionation paths and their potential usages. *Int. Journal of Food Properties* (21) 58-69
- [15] Luke Aaron Farno (2005). Oil and fatty acid profiles of soybeans (Maturity group IV, V, and VI). *Fac. of the graduation college of the Oklahoma State University*, P1-2
- [16] D. A. Allen (1996). Interesterification- A vital tool for the future? *Lipid Technol.* (8) 11-15
- [17] Pawitchaya Podchong, Chui Ping tan, SopRK Sonwai, Derick Rousseau. (2018). Composition and crystallization behavior of solvent-fractionated palm stearin. *Int. Journal of Food Properties* (21):496-509.
- [18] Siti Hazirah, M.F., Norizzah, A.R. And Zaliha, O. (2012). Effect of chemical interesterification on the physical properties of palm stearin , PKO, SFO blends. *The Malaysia J. of Analytical Sc.* 16(3) 297-308
- [19] W. P. Charteris , M. K. Kekeogh.(1991). Fats and oils in table spreads. *Lipid Technol.* (3) 16-22
- [20] G. S. Krawczyk, G. S. Buliga, D. T. Bertrand, W. M. Humpreys. (1996). Reviewing the technology of low fat spreads. *Inform.* (7) 635-639.
- [21] Noor L. H. M., K. S, Nor A.I. (2007). Effect of chemical interesterification on TAG and SFC of PS, SFO and PKO blends. *Eur. J. Lipid Sci, Technol.* (109)147-156
- [22] S. Soekopitojo, P. Hariyadi, t. R. Muchtadi and N. Andarwlan. (2009). Enzymatic interesterification of palm mid fraction blends for the production of cocoa butter equivalents. *AS. J. Food Ag-Ind* 2(04):807-816.
- [23] Dieffenbacher. (1988). The optimal use of oils and fats in foods. Nestec Ltd. Technical Assistance, Vevey (Switzerland). P21-31.
- [24] Timms, R. E. (1984). Phase behavior of fats and the mixture. *Progress in Lipid Research*, (23) 1-38.
- [25] Nathalie De Clercq, Sabine D., Mai t. N., V. Gibson, Koen D. (2012). Enzymatic interesterification of Po and fraction: Monitoring the degree of interesterification using different methods. *JAOCS.* (89) 219-229
- [26] Noor L. H. M. D. , K. Sundram, W. L. Siew , A. Aminah, S. Mamot (2002) TAG composition and SFC of PO, SFO, PKO blends before and after CIE. *JAOCS.* Vol79 No.11.
- [27] Zainal, Z., and M.S.A. Yusoff. (1999). Enzymatic interesterification of palm stearin and palm kernel olein. *Ibid.* 76:1003–1008.

Geological Engineering / Jeoloji Mühendisliđi

Land Use/Land Cover Classification of a Sentinel 2 Image: Forecariah, Guinea Case Study

Yousseuf Camara, İzmir Kâtip Çelebi University, Graduate School of Applied and Natural Sciences, Dept. of Geomatics Engineering, İzmir, Turkey*

M. Güven Koçak, İzmir Kâtip Çelebi University, Dept. of Geomatics Engineering, İzmir, Turkey

**Corresponding author: youbenibra@gmail.com*

Keywords: land use/land cover classification, Sentinel-2, random forest classifier, support vector classifier, deep learning, Eclipse DL4J, Guinea, EnMAP-Box, Weka

Discipline: Geomatics Engineering

Abstract

Cities attract people from rural areas within a land because they provide employment opportunities and infrastructure for better living. More land areas are demanded within and around the cities as a result of population increases. Urban areas expand to the cities' periphery and thus land degradation is observed in forms of deforestation, converting agricultural land to non-agricultural, etc. Remote sensors with high time resolution can provide a valuable tool to monitor the changes occurring due to anthropogenic pressure on land usage. Sentinel 2 MSI is one such system delivering high resolution images with 10 m ground sampling distance and 5-day revisit frequency. In this study we classified a Sentinel 2 image of Forecariah region covering 585 sqkm. The region was selected as a case study because it lies in close proximity to Conakry, capital city of Guinea, having more than 1/5 of the country's population. Land cover classes are adopted from Globeland30 types (<http://www.globallandcover.com>) as water, wetland, agriculture, vegetation, bare-land and built-up areas. Train and test data were collected by using very high-resolution images under Google Earth close to Sentinel 2 image acquisition date. The thematic map of the study area was obtained by using random forest (RF), support vector (SV) classifiers and deep learning (DL). We run RF and SV classifiers in EnMAP-Box Python plugin for QGIS and DL in Weka. The classification results were assessed by using 10-fold cross validation for each method. RF, SV and DL delivered overall accuracies of 83%, 86%, and 91%, respectively. DL gave the best result which can be used for generating future land use/land cover change maps in the area by using Sentinel 2 images.

Introduction

Classification is one of the frequently used tools in generating thematic maps from satellite images. Accurate land use/land cover (LULC) mapping requires supervised classification where user provides ground truth at selected locations for each class to be predicted. LULC mapping has been gaining importance because the features on the earth's surface change with time. Temporal change at a location and its proximity gives clues about the conversion of the land use types. Monitoring the change asks for high accurate satellite data of the location at a given time period. Processing and analysing remote sensing data will furnish imperative information for future critical decision-making processes such as efficient land administration, climate change issues, etc. The US Landsat system has readily been available since 70s and has been providing users with 30 m resolution. A newer system initiated by the Copernicus Program of the EU, Sentinel 2, delivers images with 10 m resolution in visible and NIR region since 2015. The users can download images of 5-day-temporal resolution acquired by the twin satellites (Sentinel 2A/2B). This high temporal and spatial resolution can be used for monitoring developing areas. Such a developing region, Forecariah-Guinea, has been selected for LULC mapping and its Sentinel 2 image was analyzed within this study. Our analysis consisted of applying three supervised classification methods: random forest, support vector machine, and deep learning.

Study Area

Forecariah area was selected in Guinea, West Africa with an area of 585 sqkm within the latitudes 9° 40' 42.2" N and 9° 24' 60" N, longitudes 13° 26' 19" W and 13° 50' 51" W. The area has an approximate population around 240000 residents. The region was selected as a case study because it lies close to Conakry, the capital city of Guinea, having more than one fifth of the country's population. The area has a tropical climate with only two seasons: the sunny season and the raining season with 3784

mm/year precipitation [1]. In 2018, Guinea has an estimated population of 13.05 million, which ranks 74th in the world. The population grew from 8.7 million in 2000 to its current state, which corresponds to 3.3% annual increase. Although the country has rich mineral reserves of bauxite, iron, gold, diamond, uranium, petrol, silver etc., it is not recognized by its mineral resources. Its mild climate enables the production of banana, cacao, cafe, pineapple, mango, orange, cotton, papaya, cashew, rice, fonyo, potatoes, and so forth. This zone was chosen for its proximity to the capital city, Conakry. It was indicated by previous urbanization study that Conakry's rapid urban growth can be explained by being one of the most mass migration centres from the rural areas due to socioeconomic and physical factors. The urban population was estimated at nearly 3.7 million, or 34.7% of the population [2,3].

Data and Methods

We downloaded the image used in this study from the Copernicus Open Access Hub (<https://scihub.copernicus.eu/>). Acquisition date of the atmospherically corrected level 2A image is February 19, 2019. A Sentinel-2 image provides 10m spatial resolution in four of its 13 bands. We extracted these four bands including visible and near-infrared ones (b2, b3, b4, b8) and created a subset of the image focusing to the study area. This pre-processing was performed under Sentinel Application Platform (SNAP 6.0). Train and test polygons were collected in the image by using Google Earth, which hosts very high-resolution images. Land cover class names were adopted from globeland30 [4] as: water, wetland, agricultural area, vegetation area, bare-land and built-up. We carried out three classification algorithms within the study: random forest (RF), support vector (SV) and deep learning (DL). RF and SV were applied under EnMAP-Box which is a python extension in QGIS, where Weka provided the third classification method with the library Eclipse Deeplearning4j. Region of interest used in this study is presented in Figure 1.

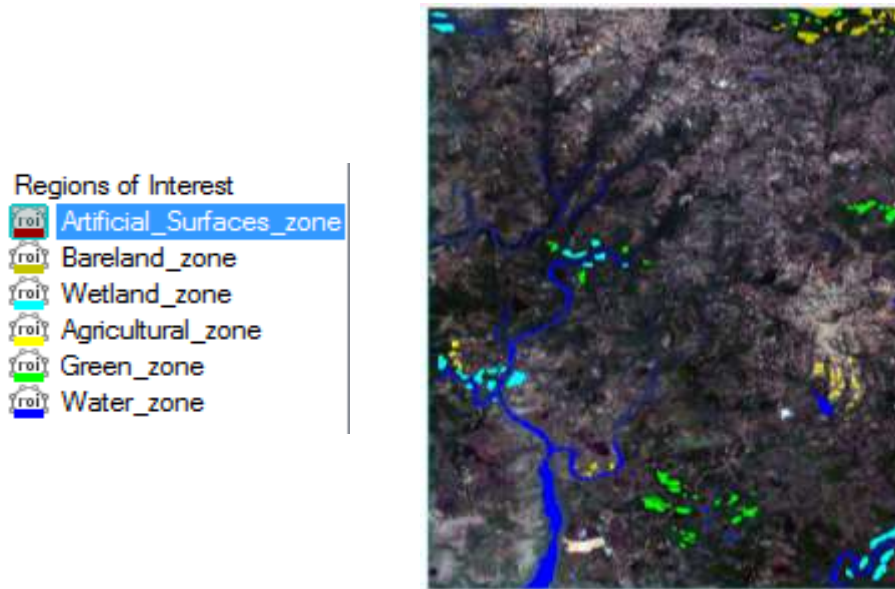


Figure 1. Region of interest used in the study

We classified our test site by using RF based on decision tree (DT) method. RF generates many DTs by using randomly selected training vectors and produces the best vote for the decision. EnMAP-Box uses RF library available under scikit-learn which is a machine learning platform working under Python environment (<https://scikit-learn.org>). We fed the number of decision trees as 100 and the program determined the number of randomly selected features as the square root of the number of features (Figure 2.)

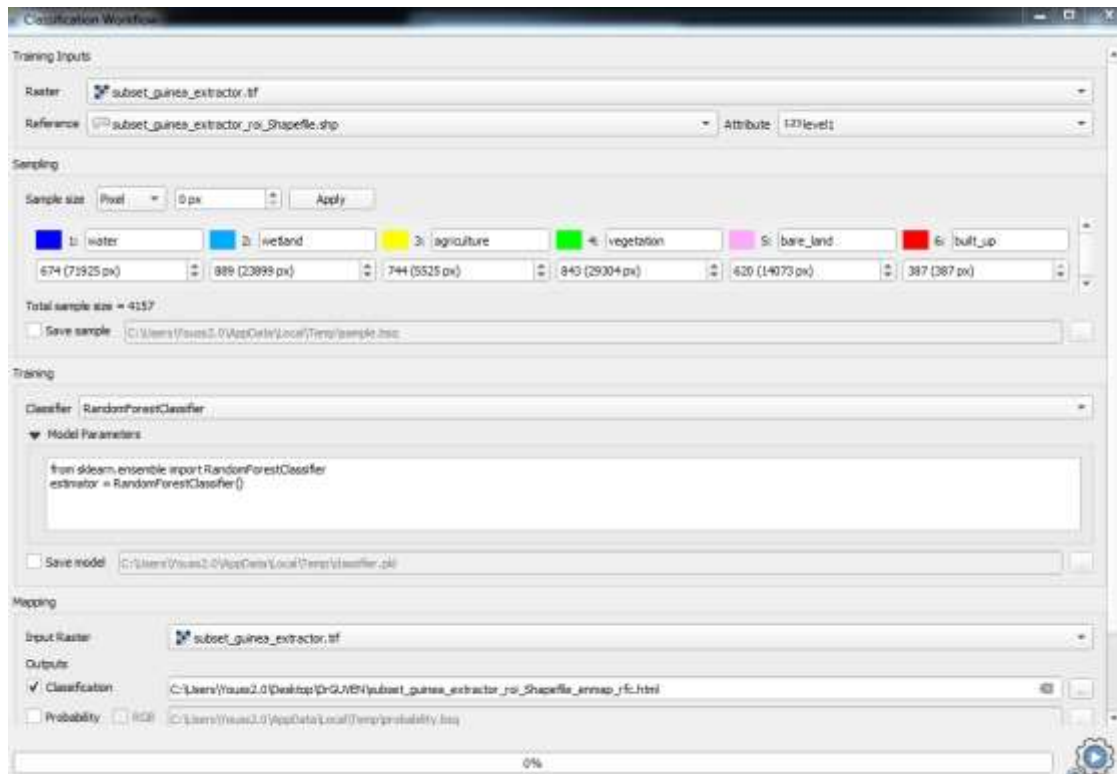


Figure 2. RF classification method settings

Our second method SV classifier uses the non-linear algorithm which finds the best hyperplane maximizing the margin between the classes. SV classifier under EnMAP-Box was utilized in this study. It uses the library under scikit-learn working with Python platform. We used as the kernel the Gaussian radial basis function whose parameters are adopted as default values given by the program (Figure 3).

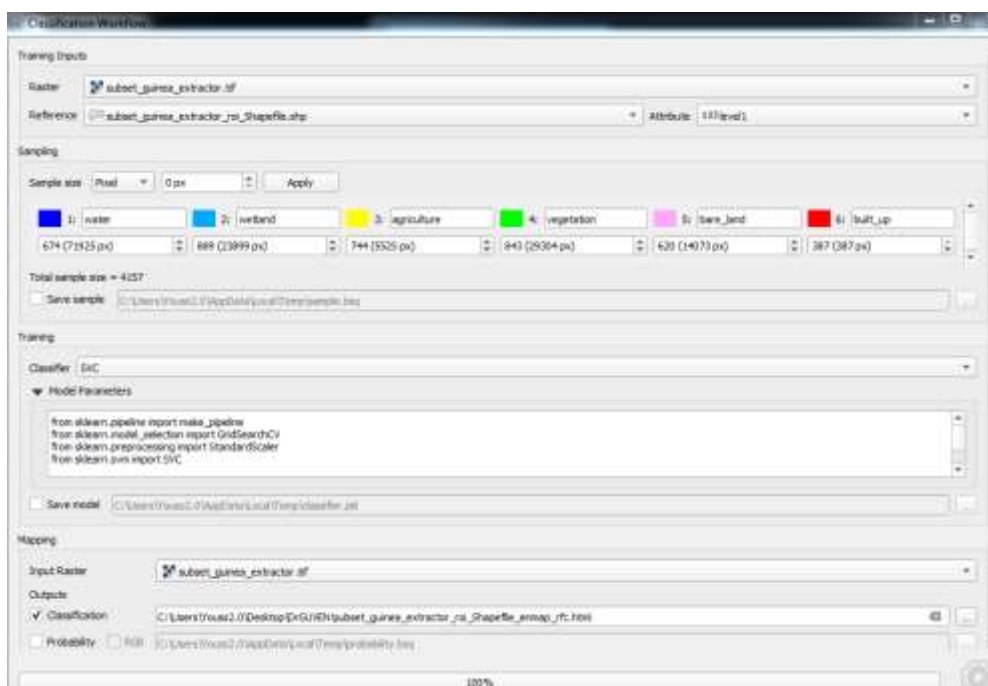


Figure 3. SV classification method settings

The last method was the DL method based on a neural network (NN) classifier. The classification was carried out with Eclipse DeepLearning4j algorithm under Weka. While EnMAP-Box accepts training and test pixels as shape file, Weka accepts only in text format. The software does not take the image as tif file therefore the image was converted to csv file which consisted of around six million rows. Within the parameters we set the number of epochs to 10 and the batch size to 100 (Figure 4)

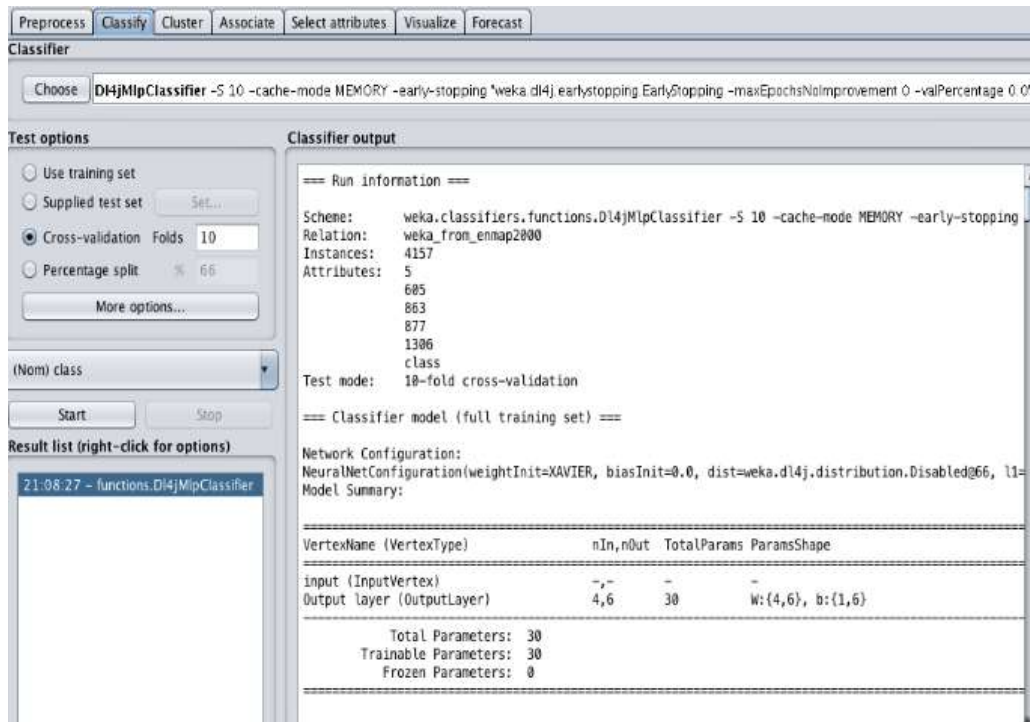


Figure 4. Weka DL environment

Results and Discussion

We assessed the accuracy of each classification by using 10-fold cross validation. Here the ground truth data were divided into ten equal size subgroups and each 10% subset was selected iteratively as validation data set. Ten classifications were carried out with the remaining %90 of the entire ground truth data. We computed thus accuracies ten times. The overall accuracies were obtained as 83.34%, 86.22%, and 91.32% for RF, SV, DL, respectively (Figures 5,6,7). SV gave slightly better results than the RF. RF took less computational demand than the other two systems where DL computation time was the highest. On a Pentium 5 machine with 16GB RAM capacity, RF performed the computation in half a day. Computation times for SV and DL were both approximately one full day and three full days, respectively.

The best accurately classified class was observed as water class, whose brightness values differ from other classes. We obtained the bare-land class as the least accurate class in RF and DL but not in SV. Bare-land and wetland classes mixed up into each other because the location of the pixels belonging to these classes lie within their transition zone.

DL yielded the best result among the studied classifiers. The disadvantage of the method is its high computational cost leading to longer processing time. We will test in the future another DL algorithm on the free platform Orfeo Toolbox which uses Tensorflow.

We plan to monitor the changes in the study area by using Sentinel 2 images with the open source tools at no cost. Thus, a change map will be created and updated at certain intervals which will be utilized by policy makers in order to keep tracking LULC changes. These maps can be used within a decision based system which then will improve the land administration capability of the authorities.

Accuracies

Measure	Estimate [%]	95 % Confidence Interval [%]	
Overall Accuracy	83.35	82.0	84.46
Kappa Accuracy	79.78	78.4	81.15
Mean F1 Accuracy	82.99	-	-

Class-wise Accuracies

Map class	User's Accuracy [%]			Producer's Accuracy [%]			F1 Accuracy		
	Estimate	95 % Interval		Estimate	95% Interval		Estimate	95% Interval	
(1) water	98.96	98.59	99.32	98.52	97.75	99.28	98.74	98.27	99.2
(2) wetland	80.67	79.48	81.87	80.76	78.54	82.99	80.72	79.23	82.21
(3) agriculture	83.14	82.11	84.17	86.83	84.56	89.09	84.94	83.62	86.27
(4) vegetation	81.45	80.3	82.59	82.8	80.49	85.11	82.12	80.66	83.57
(5) bare_land	74.66	73.29	76.04	71.29	68.22	74.36	72.94	71.16	74.71
(6) built_up	80.27	78.99	81.55	76.74	73.12	80.36	78.47	76.76	80.18

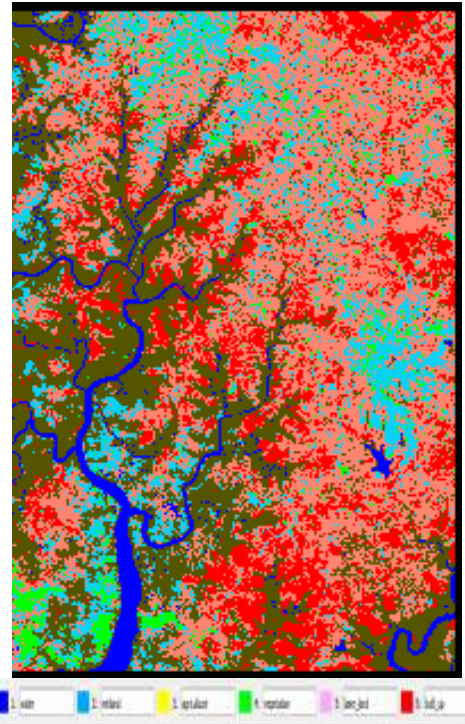


Figure 5. RF cross validation results and classification map

Accuracies

Measure	Estimate [%]	95 % Confidence Interval [%]	
Overall Accuracy	86.22	85.0	87.22
Kappa Accuracy	83.22	81.95	84.49
Mean F1 Accuracy	85.53	-	-

Class-wise Accuracies

Map class	User's Accuracy [%]			Producer's Accuracy [%]			F1 Accuracy		
	Estimate	95 % Interval		Estimate	95% Interval		Estimate	95% Interval	
(1) class1	99.41	99.14	99.67	99.26	98.68	99.84	99.33	99.0	99.67
(2) class 2	79.81	78.77	80.86	86.28	84.2	88.36	82.92	81.6	84.24
(3) class 3	85.0	84.15	85.85	91.4	89.27	93.53	88.08	86.96	89.2
(4) class 4	86.51	85.59	87.43	89.8	87.74	91.86	88.13	86.94	89.31
(5) class 5	82.54	81.11	83.97	67.1	64.04	70.15	74.02	72.19	75.85
(6) class 6	85.76	84.46	87.05	76.23	72.81	79.64	80.71	79.0	82.42

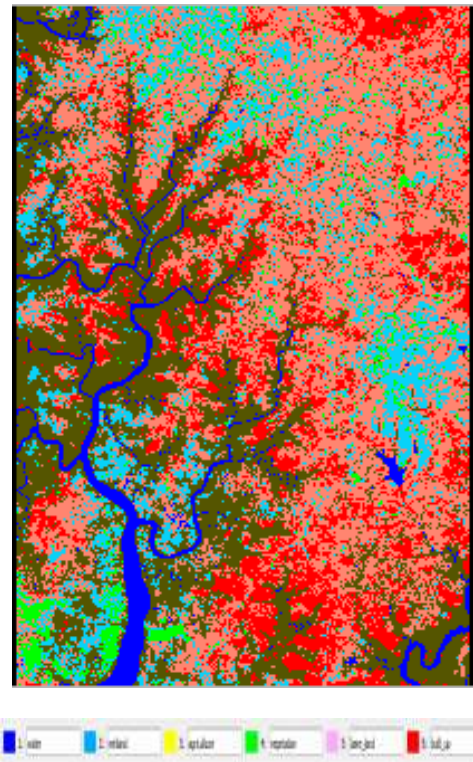


Figure 6. SV cross validation results and classification map

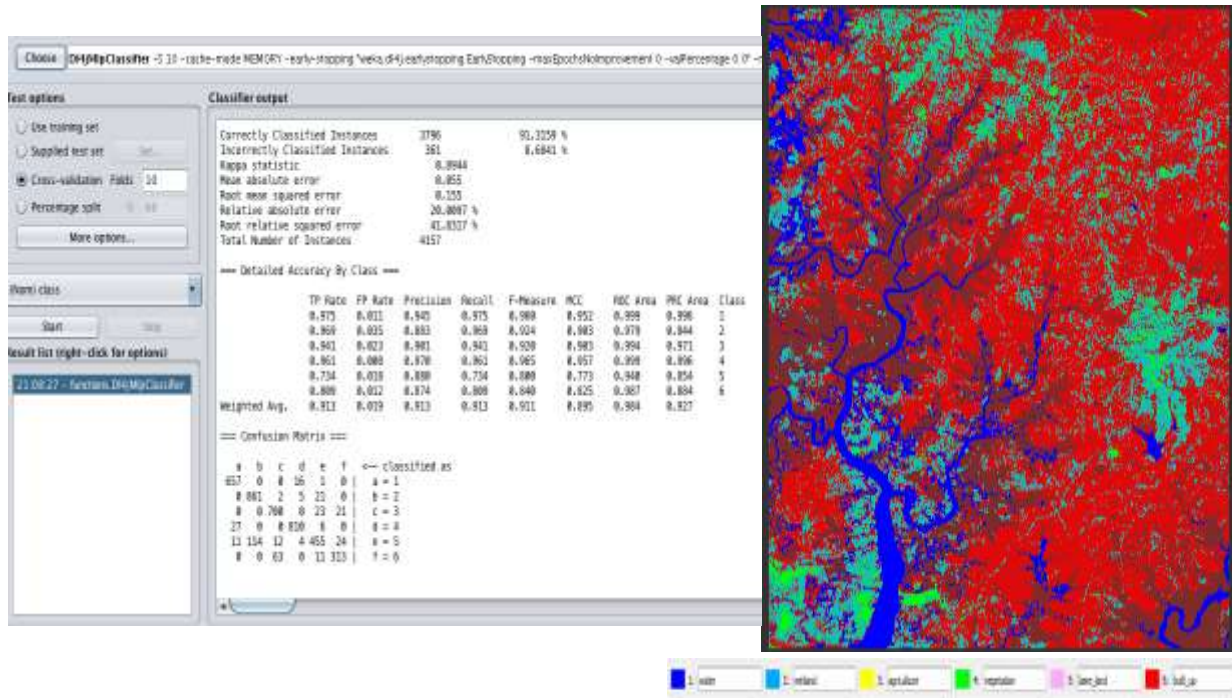


Figure 7. DL cross validation results and classification map

Acknowledgement

The first author of this study was supported by the Presidency for Turks Abroad and Related Communities (YTB) within “International Student Academy” Project.

References

- [1] Climate Conakry, <https://en.climate data.org/africa/guinea/conakry/conakry-527/>
- [2] African Economic Outlook 2017 Entrepreneurship and Industrialisation 16th ed., 2017 Ogdensburg, NY, USA. ISBN 9789264274259.
- [3] Traore A, Watanabe T (2017) Modeling determinants of urban growth in Conakry, Guinea: A Spatial logistic approach. MDPI Urban Science 1(2): 15pp.
- [4] Chen J, Chen J, Liao A., et al. (2016) Remote sensing mapping of global land cover [M]. Science Press, Beijing.

Industrial Engineering / Endüstri Mühendisliđi

Markov Decision Processes in Inventory Management: Finding Optimal Production Scheduling of Limestones in Trakya

Abubakari Sumaila, Umay Uzunoğlu Koçer*
Dokuz Eylül University., Dept. of Statistics, Tinaztepe Main Campus, İzmir, Turkey
**Corresponding author: abubakarismaila3@gmail.com*

Keywords: Markov decision process, inventory management, dynamic programming
Discipline: Statistics, Industrial Engineering

Abstract

The application of stochastic sequential decision theory in inventory management has gained tremendous recognition in recent years. In this paper, we study an inventory management problem related to the processing of limestones, a case study in the region of Trakya, Turkey. The goal is to minimize expected production costs over the production period. We thus, seek an optimal inventory control policy/schedule of the problem herein studied. It is the optimal policy that guards the decision maker from incurring avoidable losses during production. This paper solely looks at the derivation of a recursive relation that minimizes production and holding costs. An inventory control policy for this study is approached from the Markov decision process (MDP) perspective. We model and solve the problem through dynamic programming approach. This is done by identifying five key components of the problem, namely; the decision epochs, the state space, the action space, the transition probabilities and the discounted costs. The insights obtained from the analysis of the optimal policy are translated into effective mechanisms for controlling inventory. The optimal policy obtained is assessed for performance by means of numerical study. We seek optimality or near-optimality of our policy to the problem.

Introduction

In recent years, MDPs, a special branch of stochastic sequential decision theory has gained tremendous recognition in diverse fields of research, viz; communication engineering, ecology, economics/finance, and many more. Computer scientists, management scientists, economists, statisticians etc. have found new applications of MDPs through theoretical advances in this field of study. The single most important issue of concern to any decision maker is making the right decisions. Here, right decision is defined as a decision which minimizes costs incurred or maximizes expected total rewards. We all make decisions. These decisions we make have both immediate and long-term consequences. Invariably, this would imply that today's decisions have direct impact on tomorrow's decisions, and tomorrow's decisions on the next day's decisions. Of course, decisions are made with some degree of uncertainty, which in itself makes it a huge issue of concern in the production industry.

The uses of limestones in modern times are immeasurable. As a result of the calcium carbonate content present in limestones, there is a history of varying uses of limestones; from the earliest civilizations in history to usage today. It is a highly valuable resource in many industries such as in building and construction industry, in agriculture and of course, heavy industries like steel production industry. Citing available statistics for usage of limestones in New Zealand alone, it is estimated that in the year 2010, New Zealand used 2 million tonnes of limestones for marl and cement, 1.9 million tonnes for agriculture, and 874 460 tonnes for industry and roading. The calcium carbonate in limestones has long been recognized as an agent for regulating acidity in soil, which facilitates the growth of crops, thereby increasing crop yield. In the construction of roads, parks and driveways, bitumen is used with solid aggregate, as fillers. In mining, powdered limestone is used as a dust suppressant in coal mines. In this way, it helps provide passive fire protection and prevent explosions underground. In the beautification of smart cities, decorative limestone aggregates, chippings and grits are used in landscaping projects such as cycling ways and footpaths, driveways and car parks as well as for ground cover in gardens and rockeries. The uses of limestones are non-exhaustively numerous for discussion.

In this paper, we deal with inventory management of limestones processing. The prime goal is to derive a recursive formulation that minimizes monthly production of limestones, a case study in Trakya. Limestones are processed continuously throughout the year, in a manner that is designed to meet foreseen demands (demands are stochastic). Processing limestones is done monthly after assessing the

quantity currently in inventory and storage (end of period inventory). A pictorial representation of this process is illustrated in Figure 1.



Figure 1. A pictorial representation of inventory management process

Problem Description and Assumptions

The application part of this study focuses on an international limestone production firm. The firm has processing plants that process limestones in large scale, and has many factories in different locations. In each location, limestones are produced, stored and sold in tonnes. Since demand requirements are stochastic from period to period, it is often economical to produce more limestones than needed, and store the excess quantity to meet future demands. In production, limes are processed in a number of furnaces. In our application, we take a case study of one limestone production factory in Trakya, a region in the northwestern part of Turkey. Due to the factory's strict policy of confidentiality of demand data, the factory has chosen to share neither demand nor cost information. As a result of that, demand data has been simulated by using the mean and variance values they declared. Also, cost data has been generated by using the information the firm shared. Random monthly distribution of demands is shown in Figure 2.

In determining the production schedule for the next 12 months, we restrict our model to a single processing site, which is a factory located in Trakya. We assume the 4 furnaces process limestones continuously throughout the year, and operate independently of one another during operations. Each furnace processes on the average 250 tonnes per day. Instead of separately considering the average processing rate for each furnace, we aggregate all the 4 averages into a single measure. This enable us formulate the problem as a single item inventory system, periodically reviewed. Each furnace works 330 days in a year. The remaining 1 month is allocated for maintenance and repairs. Excess production is stored in a storage area which has a capacity of 1000 tonnes. Further assumptions of the model are summarized as follows:

- i. Demands for limestones are stochastic during the planned period,
- ii. The factory processes more limestones than necessary, such that excess amount is stored for future time,
- iii. Demands for any period are met before the beginning of the next period,
- iv. Fluctuations in the cost of fuel, electricity and labour are negligible throughout the 12-month period.

Throughout the system, the sequence of events are as follows:

- i. The state of the system which is the inventory level for period t is reviewed,

- ii. Based on the state of the system, the production amount for that period is determined,
- iii. The demand for that period is realized,
- iv. The cost incurred is assessed.

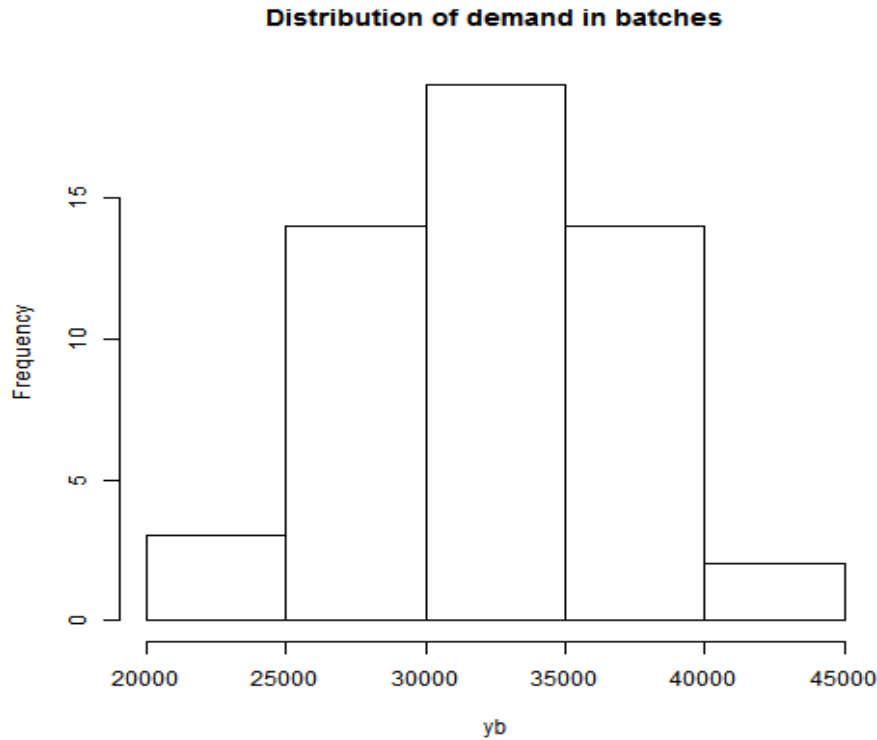


Figure 2. Random monthly distribution of limestones

Model Formulation

In order to find an optimal policy, the problem is formulated as a discrete-time MDP. The planning horizon is considered infinite. The formulation of the problem as a Markov decision process is explained below. We consider time in discrete periods, which is examined in monthly.

Decision epoch

Production decisions are made on weekly basis before the beginning of the production next week. This production decisions continue throughout the 12-month period. The model here is an infinite time horizon model with the set of time periods as:

$$T = \{1, 2, 3 \dots\}$$

State of the inventory system

Since the state variable expresses the system description in a given time period, it is defined as the *entering inventory*. Let state variable I_t represent the inventory level (in batches) at the beginning of time period t . The inventory level in period t depends only on the previous period; it does not depend on the previous history of the system states. Hence I_t describes a Markov chain with discrete state space and the state variable may take values in discrete state space $S = \{0, 1, \dots, 20\}$.

Actions

Actions describe the decisions to be made in the corresponding time periods. Decisions are made by considering the system state I_t . For our problem, inventory level on hand is reviewed and a decision is made relative to the production amount in the corresponding period. Let the decision variable X_t represent the production amount in period t . Production is made large enough so that stock-outs never

occur. To enforce this constraint, it is ensured that the summation of the entering inventory and the production amount should be at least maximum demand occurrence in batches. Mathematically;

$$i + x \geq 37$$

As an upper bound, there is a production capacity given by the company. The production amount may be at maximum of 28 batches in a week. On the other hand, as another restriction; the transferred amount ($i + x - d$) may be 20 batches at most. Otherwise there may be more inventory than the maximum capacity on the storage which is impossible. Hence,

$$i + x \leq \text{maximum storage} + \text{minimum demand}$$

$$i + x \leq 46$$

The restriction for the production amount can then be expressed as:

$$37 - i \leq x \leq \min\{28, (46 - i)\}$$

State transitions and transition probabilities

Transition probabilities are determined by using the demand distribution, as shown in Table 1. After specifying the state space of the system, the actions (discrete too) can be taken, which causes the state of the system to evolve into a new state or in an unchanged state. The events that cause a transition from one state to the next are:

- i. The inventory level of the system I_t at the discrete decision epochs. Thus, how many batches of limestones are available at the warehouse?
- ii. Production amount X_t from the 4 furnaces at the end of decision epoch.

Table 1. Stochasticity of demand of limestones

Demand (x10 ³ tonnes)	Demand (in batches)	$P(D = d)$
585 < D < 625	24	0.0377
625 < D < 665	26	0.0609
665 < D < 705	27	0.0874
705 < D < 745	29	0.1124
745 < D < 785	31	0.1293
785 < D < 825	32	0.1786
825 < D < 865	34	0.1223
865 < D < 905	35	0.1005
905 < D < 945	37	0.0741
945 < D < 985	39	0.0485
985 < D < 1025	40	0.0285
1025 < D < 1065	42	0.0198

Cost function

Expected total cost is calculated weekly and has two main components, namely; production and holding cost. Let $c(x)$ be the expected cost in the current period as a result of making decision I_t . In other words, $c(x)$ is the cost of processing $x \in X_t$ units of limestones. Given that the unit production cost as 15 units per week, and h units is the unit weekly holding cost. It is calculated based on annual interest rate, and found to be 2 units. To find the expected holding cost, the unit holding cost is multiplied by average inventory level for period t . The expected demand in batches is computed and found to be 32.10 batches.

For an inventory level i and production amount x , the total cost for the current period is:

$$c_{ix} = c(x) + h(i + x - \mu_D)$$

Summarizing these components of MDPs, we may pictorially represent it as in Figure 3.

Markov Decision Process (MDP)

S - Set of States

A - Set of Actions

$\Pr(s'|a, s)$ - Transitions

$R(s,a)$ - Reward/Cost

D - Demand distribution

β - discount factor

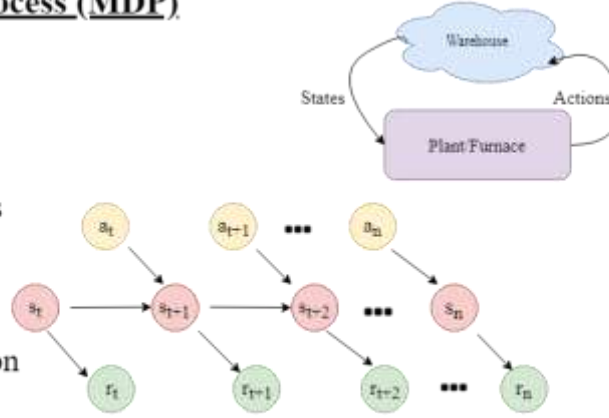


Figure 3. Components of a Markov decision process

Deriving the Recursive Relation (Results)

We define $f_t(i)$ to be the minimum expected net cost incurred during the periods $t, t + 1, \dots, 12$, given that the inventory at the beginning of period t is i units, a unit holding cost of 1.70TL. Any inventory at the end of period 12 can be sold at 2.50 TL per batch. Hence, we may write;

$$f_t(i) = \min\{c(x) + h(i + x - \mu_D)P(D = d_i) + f_{t+1}(i + x - \mu_D)$$

For $f_{12}(i)$, this formulation expands to:

$$f_{12}(i) = \min_x \left\{ c(x) + 0.0377(i + x - 26) * 1.7 + 0.0609(i + x - 27) * 1.7 \right. \\ + 0.0874(i + x - 28) * 1.7 + 0.1124(i + x - 29) * 1.7 \\ + 0.1293(i + x - 30) * 1.7 + 0.1486(i + x - 31) * 1.7 \\ + 0.1323(i + x - 32) * 1.7 + 0.1105(i + x - 33) * 1.7 \\ + 0.0741(i + x - 34) * 1.7 + 0.0585(i + x - 35) * 1.7 \\ + 0.0285(i + x - 36) * 1.7 + 0.0198(i + x - 37) * 1.7 \\ - 0.0377(i + x - 26) * 2.5 - 0.0609(i + x - 27) * 2.5 \\ - 0.0874(i + x - 28) * 2.5 - 0.1124(i + x - 29) * 2.5 \\ - 0.1293(i + x - 30) * 2.5 - 0.1486(i + x - 31) * 2.5 \\ - 0.1323(i + x - 32) * 2.5 - 0.1105(i + x - 33) * 2.5 \\ - 0.0741(i + x - 34) * 2.5 - 0.0585(i + x - 35) * 2.5 \\ \left. - 0.0285(i + x - 36) * 2.5 - 0.0198(i + x - 37) * 2.5 \right\}$$

where the minimization is over only nonnegative integer values, in the range:

$$37 - i \leq x \leq \min\{28, (46 - i)\}$$

Since stockouts are not allowed, demand is met only when entering inventory and production amount is at least 37 batches. Thus, $i + x \geq 37$ or $x \geq 37 - i$. We know the firm's production capacity to be 28 batches. But from the distribution of random demands (maximum demand = 37), it is necessary that at the beginning of period 1, the firm holds 9 batches. Also, to ensure that ending inventory for period 12 does not exceed holding capacity, we must have $i + x - d \leq 20$ batches or $x \leq 20 - i$. Hence x is a member of $\{0, 1, \dots, 28\}$. That is to say: $37 - i \leq x \leq \min\{28, (46 - i)\}$. Note that we define $x_t(i)$ to be the production level in period t that attains minimum in equation above. Our goal is to work backwards until $f_1(1)$ is determined. Notice that each period's ending inventory must be nonnegative and cannot exceed 20 batches, the state during each period must be one of $\{0, 1, 2, \dots, 20\}$. We begin the computation with $x_t(9) = 20$ batches during period 1. For periods $t = \{1, 2, 3, \dots, 11\}$, we derive a recursive relation for $f_t(i)$ by observing that, for any month t production level x , the expected costs incurred during periods $t, t + 1, t + 2, \dots, 12$ are the sum of the expected costs incurred during period t and the expected costs during periods $t + 1, t + 2, \dots, 12$. We observe that, during periods $t + 1, t + 2, \dots, 11$, no salvage value is received. If we act optimally in the periods $\{t + 1, t + 2, \dots, 12\}$, $f_{11}(i)$ can be computed as follows:

$$f_{11}(i) = \min_x \left\{ c(x) + 0.0377f_{12}(i + x - 26) * 1.7 + 0.0609f_{12}(i + x - 27) * 1.7 \right. \\ + 0.0874f_{12}(i + x - 28) * 1.7 + 0.1124f_{12}(i + x - 29) * 1.7 \\ + 0.1293f_{12}(i + x - 30) * 1.7 + 0.1486f_{12}(i + x - 31) * 1.7 \\ + 0.1323f_{12}(i + x - 32) * 1.7 + 0.1105f_{12}(i + x - 33) * 1.7 \\ + 0.0741f_{12}(i + x - 34) * 1.7 + 0.0585f_{12}(i + x - 35) * 1.7 \\ \left. + 0.0285f_{12}(i + x - 36) * 1.7 + 0.0198f_{12}(i + x - 37) * 1.7 \right\}$$

Therefore, we can write a generalized recursive form for $f_t(i)$ for the periods $t = 1, 2, \dots, 10$ as:

$$f_t(i) = \min_x \left\{ c(x) + 0.0377f_{t+1}(i + x - 26) * 1.7 + 0.0609f_{t+1}(i + x - 27) * 1.7 \right. \\ + 0.0874f_{t+1}(i + x - 28) * 1.7 + 0.1124f_{t+1}(i + x - 29) * 1.7 \\ + 0.1293f_{t+1}(i + x - 30) * 1.7 + 0.1486f_{t+1}(i + x - 31) * 1.7 \\ + 0.1323f_{t+1}(i + x - 32) * 1.7 + 0.1105f_{t+1}(i + x - 33) * 1.7 \\ + 0.0741f_{t+1}(i + x - 34) * 1.7 + 0.0585f_{t+1}(i + x - 35) * 1.7 \\ \left. + 0.0285f_{t+1}(i + x - 36) * 1.7 + 0.0198f_{t+1}(i + x - 37) * 1.7 \right\}$$

Concluding Remarks

In this study, a production scheduling problem is attempted using Markov decision process (MDP) as mathematical modeling framework. A recursive formulation has been derived for the limestones processing problem, a case study in the region of Trakya, Turkey. As an extension to this approach, a numerical study of the problem is hoped to reveal further insights into the solution structure.

Acknowledgements

This study was supported by the Presidency for Turks Abroad and Related Communities (YTB) within “International Student Academy” Project.

References

- [1] Ahiska SS, Appaji SR, King RE, Warsing Jr. DP (2013) A Markov decision process-based policy characterization approach for a stochastic inventory control problem with unreliable sourcing. *International Journal of Production Economics*, 144 (2): 485–496.
- [2] Puterman ML (2005) *Markov Decision Processes. Discrete Stochastic Dynamic Programming*. Wiley-Interscience ISBN: 978-0-471-72782-8.
- [3] Winston WL (2003) *Operations Research: Applications and Algorithms*, Duxbury Press.
- [4] Zipkin PH (2000) *Foundations of Inventory Management*, McGraw-Hill, New York.
- [5] Zheng Y-S (1991) A simple proof for the optimality of (s, S) policies in infinite-horizon inventory systems. *Journal of Applied Probability* 28(4): 802–810.
- [6] Ozguven EE, Ozbay K (2013) A secure and efficient inventory management system for disasters. *Transportation Research Part C: Emerging Technologies* 29: 171–196.
- [7] Anderson TW, Goodman LA (1957) Statistical inference about Markov chains. *The Annals of Mathematical Statistics* 28(1): 89–110.

Mathematics / Matematik

A Rational Parametrization of Cubic Bezier-Like Spiral Curve and its Applications

Aslı Ayar*, Bayram Şahin

Ege University, Dept. of Mathematics, Bornova, 35100, İzmir, Turkey

*Corresponding author: asliayar1@gmail.com

Keywords: Bezier like polynomials, Bezier like curve, Bezier spiral, planar curves, transition curves

Discipline: Mathematics, Computer Science and Engineering

Introduction

Investigating curves and surfaces is very important for computer aided design (CAD) and manufacturing (CAM). Bezier curves have been great importance for CAD and CAM because of their polynomial structure [1]. Also, these curves are related to their control points and have a control polygon. Designers modify of the curve by using this control polygon. Due to polynomial structure of these curves, some problems occur. For instance, construction of conics with these curves is very difficult. This is the reason, researchers try to find new curves which have common properties with Bezier curves. If the designer wants to change curve in a small area, this affects all curve. The studies in this area have become the focus of researchers and many presentations of curves and surfaces have derived.

Recently, many authors seek new curves with shape parameters. It is targeted that users can interactively change curve with shape parameters. Considering curves with shape parameters, researchers have started to modify representation of curves. Thus, extension of the Bezier is obtained; see Han [3] and [7].

Planar cubic Bezier Curves have been commonly used in computer aided design. Also, transition curves are the most important object of highway design. Because these curves are defined by using curvature function. Spiral curves are most popular of these curves. A spiral is a curve at which radius of the curve is inversely proportional to its length, i.e curvature of these curvature varies monotonically with their arc length. Therefore, spiral curves have no internal curvature extreme, cusps, loops and inflection points. Also Cornu Spiral which contains Fresnel function is the most known and used spiral curve in engineering. Because of Fresnel function, some difficulties occur for using in computer aided design. For these reasons, a cubic Bezier spiral has been developed as an alternative to Cornu spiral in [6].

In this talk, we consider a rational parametrization of Bezier like curve with a shape parameter, introduced by Allaoui and Goudjo in [1]. Basis functions of these curves were obtained by adding a shape parameter to Bernstein basis functions using a class of rational parametrization. Basis functions are rational with including polynomial numerator and denominator. Then by incorporating control points with these basis functions, the curve is defined and is called a rational parametrization of Bezier like curve with a shape parameter.

We research condition for a rational parametrization of Bezier like curve with a shape parameter to be a spiral. We also check this curve in terms of Bloss curve.

Preliminaries

\mathbf{a} is any vector and its parametric form is $\mathbf{a} = (u_x, u_y)$.

$$\|\mathbf{a}\| = \sqrt{a_x^2 + a_y^2}$$

is the norm of vector \mathbf{a} . The dot product of two vectors, \mathbf{a} and \mathbf{b} is

$$\mathbf{a} \cdot \mathbf{b} = a_x b_x + a_y b_y$$

and the cross product of these two vectors is

$$\mathbf{a} \times \mathbf{b} = \|\mathbf{a}\| \|\mathbf{b}\| \sin \theta$$

where the angle θ is positive angle. The derivative of function \mathbf{f} is denoted by \mathbf{f}' , [5].

The signed curvature of a Bezier like curve $\mathbf{f}(t)$ is defined by [2]

$$\kappa(t) = \frac{\mathbf{f}'(t) \times \mathbf{f}''(t)}{\|\mathbf{f}'(t)\|^3}. \quad (1)$$

The radius of curvature r is given by $r = \frac{1}{\kappa}$. If $\kappa(t) = 0$ for all $t \in [0,1]$ then the curve $\mathbf{f}(t)$ reduces to straight line. If $\kappa(t) = 0$ for any $t \in [0,1]$ then the curve has a point of inflection. \mathbf{t} is the unit tangent vector and \mathbf{n} is the unit normal vector to $\mathbf{f}(t)$ at t . The angle is anti-clockwise from \mathbf{t} to \mathbf{n} is $\pi/2$.

We now recall the notions of Bezier Curves and Bloss Curves.

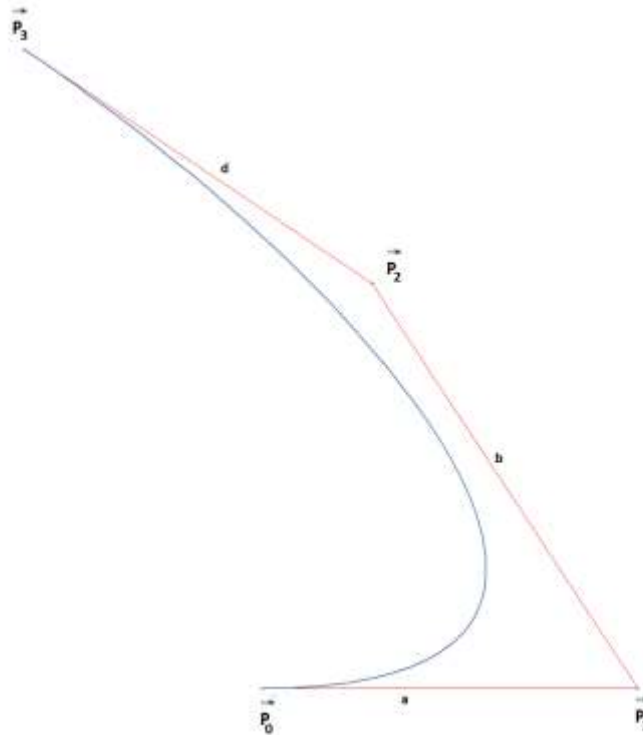


Figure 1. A cubic rational parametrization of Bezier like curve

Definition 1: [1] For a cubic rational parametrization of Bezier like curve, its basis functions $B_{0,3}(t)$, $B_{1,3}(t)$, $B_{2,3}(t)$ and $B_{3,3}(t)$ are described by Bernstein polynomials as follows:

$$\begin{aligned} B_{0,3}(t) &= \frac{(1-t)^3(-1+\lambda)}{(-1+t+\lambda)^3}, \\ B_{1,3}(t) &= \frac{3(1-t)^2t(-1+\lambda)\lambda}{(-1+t+\lambda)^3}, \\ B_{2,3}(t) &= \frac{3(1-t)t^2(-1+\lambda)\lambda^2}{(-1+t+\lambda)^3}, \\ B_{3,3}(t) &= \frac{t^3\lambda^3}{(-1+t+\lambda)^3} \end{aligned}$$

where $t \in [0,1]$ and $\lambda \in (\infty, 0] \cup [1, \infty)$. A cubic rational parametrization of Bezier like curve is defined as

$$\mathbf{f}(t) = \sum_{i=0}^3 B_{i,3}(t)\mathbf{P}_i = B_{0,3}(t)\mathbf{P}_0 + B_{1,3}(t)\mathbf{P}_1 + B_{2,3}(t)\mathbf{P}_2 + B_{3,3}(t)\mathbf{P}_3, \quad t \in [0,1] \quad (2)$$

where $\mathbf{P}_i (i = 0,1,2,3)$ in E^2 are control points. Additionally, we suppose that the beginning point of the curve is origin i.e. $\mathbf{P}_0 = (0,0)$ and the other control points are

$$\begin{aligned} \mathbf{P}_1 &= \mathbf{P}_0 + a \mathbf{t} \\ \mathbf{P}_2 &= \mathbf{P}_1 + b \cos \theta \mathbf{t} + b \sin \theta \mathbf{n} \\ \mathbf{P}_3 &= \mathbf{P}_2 + d \cos(\theta + \varphi) \mathbf{t} + d \sin(\theta + \varphi) \mathbf{n} \end{aligned} \quad (3)$$

where $\|\mathbf{P}_1 - \mathbf{P}_0\| = a$, $\|\mathbf{P}_2 - \mathbf{P}_1\| = b$ and $\|\mathbf{P}_3 - \mathbf{P}_2\| = d$. Here θ and φ are positive angles respectively from $\|\mathbf{P}_1 - \mathbf{P}_0\|$ to $\|\mathbf{P}_2 - \mathbf{P}_1\|$ and $\|\mathbf{P}_3 - \mathbf{P}_2\|$ to $\|\mathbf{P}_2 - \mathbf{P}_1\|$. \mathbf{t} and \mathbf{n} are respectively the unit tangent vector and the unit normal vector at the beginning point of Bezier curve, see also Figure 1.

Definition 2: If a curve is a spiral then it yields the basic design conditions of transition curve, i.e. the curvature at the starting point should be zero and should rise to maximum value at the end point. Also for $t \in (0,1)$, its curvature varies monotonically with their arc length.

The curve, which addition to these conditions also satisfies the conditions

$$\kappa'(0) = 0$$

and

$$\kappa'(1) = 0$$

is called a Bloss Curve, where $\kappa(t)$ is the curvature of curve and $\kappa'(t)$ is the derivative of $\kappa(t)$, i.e. derivative of the curvature at the beginning and ending points are zero [4].

Fundamentals of Method

Theorem 1: If the control points of a planar cubic rational parametrization of Bezier like curve e given in (3) are

$$\begin{aligned} \mathbf{P}_1 &= \mathbf{P}_0 + a \mathbf{t} \\ \mathbf{P}_2 &= \mathbf{P}_1 + b \cos \theta \mathbf{t} + b \sin \theta \mathbf{n} \\ \mathbf{P}_3 &= \mathbf{P}_2 + d \cos(\theta + \varphi) \mathbf{t} + d \sin(\theta + \varphi) \mathbf{n} \end{aligned}$$

where $\theta = 0$,

$$a = b = \frac{3cd^2(-1 + \lambda) \csc \varphi}{2(-3 + 2\lambda)},$$

$$d = \frac{(-11 + 8\lambda) \tan \varphi}{9c(-3 + 2\lambda)}$$

and $\lambda \in (1.5, 2.3]$, then Bezier like curve is a spiral.

Proof: Let $f(t)$ be a planar Bezier like curve given in (2). From (1), the curvature of a Bezier like curve $f(t)$ is obtained as

$$\begin{aligned} \kappa(t) &= \frac{(2(-1 + \lambda)^2 \lambda^3 (ab(-1 + t)^2 (-1 + \lambda)^2 \sin \theta + dt\lambda(bt(-1 + \lambda)\lambda \sin \varphi \\ &\quad + a(-1 + \lambda + t(1 - 3\lambda + \lambda^2)) \sin(\theta + \varphi))) \\ &\quad / (3(-1 + t \\ &\quad + \lambda)^8 (\frac{1}{(-1 + t + \lambda)^8} (-1 \\ &\quad + \lambda)^2 \lambda^2 ((a(-1 + t)(-1 + t + \lambda - 5t\lambda + 2t\lambda^2) \\ &\quad + 2b(-1 + t)t(-1 + \lambda)\lambda \cos \theta - dt^2 \lambda^2 \cos(\theta + \varphi))^2 \\ &\quad + t^2 \lambda^2 (-2b(-1 + t)(-1 + \lambda) \sin \theta + dt\lambda \sin(\theta + \varphi))^2))^{3/2}} \end{aligned} \quad (4)$$

where θ and φ are positive angles respectively from $\|\mathbf{P}_1 - \mathbf{P}_0\|$ to $\|\mathbf{P}_2 - \mathbf{P}_1\|$ and $\|\mathbf{P}_3 - \mathbf{P}_2\|$ to $\|\mathbf{P}_2 - \mathbf{P}_1\|$.

At the beginning point, the curvature is

$$\kappa(0) = \frac{2b(-1 + \lambda)^2 \sin \theta}{3a^2} = 0.$$

$\kappa(0) = 0$, then $\theta = 0$. At the ending point, the curvature is

$$\kappa(1) = \frac{2b(-3 + 2\lambda) \sin \varphi}{3d^2(-1 + \lambda)} = c.$$

Using this equation, we obtain

$$b = \frac{3cd^2(-1 + \lambda) \csc \varphi}{2(-3 + 2\lambda)}$$

and the derivative of $\kappa(t)$ at $t = 1$ is

$$\kappa'(1) = \frac{c(-1 + \lambda)(11 - 8\lambda + 9cd(-3 + 2\lambda)\cot\varphi)}{\lambda(-3 + 2\lambda)} = 0.$$

From this equation, we have

$$d = \frac{(-11 + 8\lambda) \tan \varphi}{9c(-3 + 2\lambda)}.$$

The derivative of $\kappa(t)$ is

$$\begin{aligned} \kappa'(t) = & (216c(-1 + t)(11 - 8\lambda)^2(3 - 2\lambda)^5(-1 + \lambda)^4\lambda(-1 + t + \lambda)^3(11 - \\ & 19\lambda + 8\lambda^2)^3(-11 - 8\lambda)^2(-1 + \lambda)^4 - t(11 - 8\lambda)^2(-1 + \lambda)^3(4 + \lambda) + t^2(-1 + \\ & \lambda)^2(-726 + 693\lambda + 13839\lambda^2 - 32944\lambda^3 + 28808\lambda^4 - 11008\lambda^5 + 1536\lambda^6) + \\ & t^4(-121 + 55\lambda + 13807\lambda^2 - 85297\lambda^3 + 227496\lambda^4 - 330912\lambda^5 + 281824\lambda^6 - \\ & 140608\lambda^7 + 38144\lambda^8 - 4352\lambda^9) + t^3(484 - 825\lambda - 27321\lambda^2 + 145839\lambda^3 - \\ & 322817\lambda^4 + 387224\lambda^5 - 270552\lambda^6 + 109472\lambda^7 - 23552\lambda^8 + 2048\lambda^9) + 12t^2(3 - \\ & 2\lambda)^2\lambda^2((-1 + \lambda)^2(-11 + 8\lambda) + t(22 - 203\lambda + 389\lambda^2 - 272\lambda^3 + 64\lambda^4) + \\ & t^2(-11 + 173\lambda - 608\lambda^2 + 776\lambda^3 - 416\lambda^4 + 80\lambda^5))\text{Cos}[2\varphi]\text{Sec}[\varphi]^2)/((11 - \\ & 19\lambda + 8\lambda^2)^2(-1 + \lambda)^2(-11 + 8\lambda) + t^2(-11 + 96\lambda - 158\lambda^2 + 96\lambda^3 - 20\lambda^4) + \\ & 2t(11 - 63\lambda + 106\lambda^2 - 70\lambda^3 + 16\lambda^4) + 3t^2(3 - 2\lambda)^2\lambda^2\text{Cos}[2\varphi])^2\text{Sec}[\varphi]^2 + \\ & 36t^4(11 - 8\lambda)^2(3 - 2\lambda)^4(-1 + \lambda)^2\lambda^4\text{Sin}[\varphi]^2)^{5/2}. \end{aligned}$$

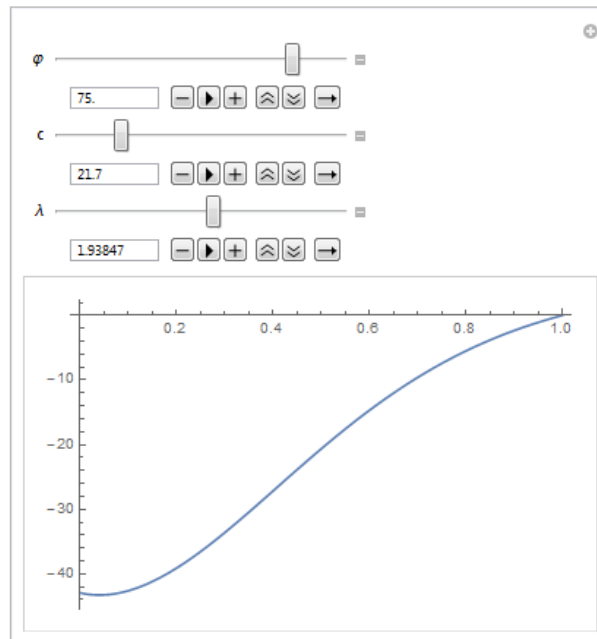


Figure 2. Graph of $\kappa'(t)$ for $\lambda \in (1.5, 2.3]$

If $\lambda \in (1.5, 2.3]$, then $\kappa'(t)$ does not change sign in $t \in [0, 1]$, see also Figure 2. Thus this curve is a spiral curve, see Figure 3.

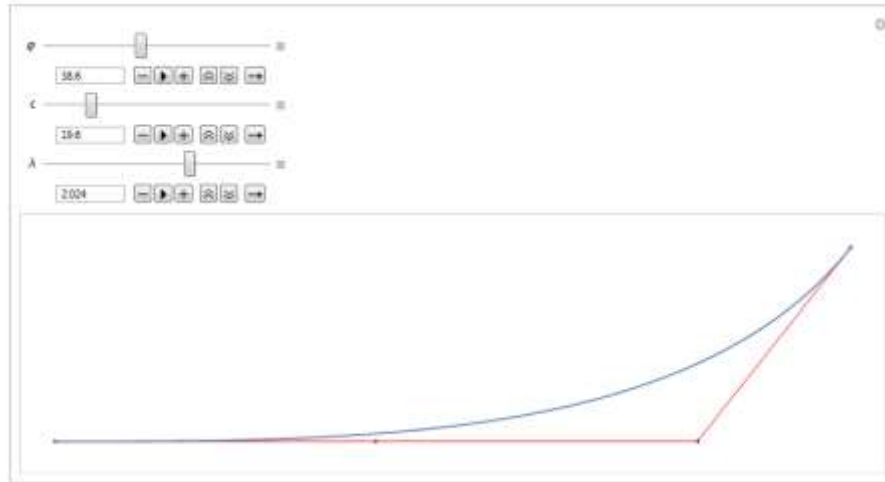


Figure 3. A cubic rational parametrization of Bezier like Spiral

Theorem 2: A planar cubic rational parametrization of Bezier like curve given in (2) is not a Bloss curve.

Proof: Let $f(t)$ be a planar Bezier like curve given in (2). From theorem (1), $f(t)$ Bezier like curve is a spiral, $\lambda \in (1.5, 2.3]$. Also its control points are

$$\begin{aligned} P_1 &= P_0 + a t \\ P_2 &= P_1 + b \cos \theta t + b \sin \theta n \\ P_3 &= P_2 + d \cos(\theta + \varphi) t + d \sin(\theta + \varphi) n \end{aligned}$$

where $\theta = 0$,

$$\begin{aligned} a = b &= \frac{3cd^2(-1 + \lambda) \csc \varphi}{2(-3 + 2\lambda)}, \\ d &= \frac{(-11 + 8\lambda) \tan \varphi}{9c(-3 + 2\lambda)}. \end{aligned}$$

From these conditions, the curvature of Bezier like curve at $t = 1$, $\kappa(1) = c$ and derivative of its at the ending point $\kappa'(1) = 0$. The derivative of curvature at the beginning point is

$$\kappa'(0) = \frac{216c\lambda(-3 + 2\lambda)^5 \cos[\varphi]^3}{(-1 + \lambda)(-11 + 8\lambda)^3}.$$

From the condition $\kappa'(0) = 0$ of Bloss curve, φ must be zero or $\lambda = 0$ or $\lambda = 1.5$. If φ is equal to zero, $f(t)$ is not a curve. If $f(t)$ Bezier like curve is a spiral, $\lambda \in (1.5, 2.3]$. Therefore, $f(t)$ Bezier like curve is not a Bloss curve conditions other than lines.

References

- [1] Allaoui M, Goudjo A (2018) A Rational Parametrization of Bezier Like Curves, arXiv:1804.10406.
- [2] Farin, G (2002) Curves And Surfaces For CAGD: A Practical Guide, Academic Press.
- [3] Han X, Ma Y, Huang X (2009) A cubic trigonometric Bezier curve with two shape parameters, Applied Mathematics Letters 22, 226-231.
- [4] Kobryn A (2017) Transition Curves For Highway Geometric Design. Springer Tracts on Transportation and Traffic, Springer Book 14.
- [5] Millman RS, Parker GD (1977) Elements of Differential Geometry, Englewood Cliffs, N.J.:Prentice-Hall
- [6] Walton DJ, Meek DS (1996) A planar cubic Bezier spiral, Journal of Computational and Applied Mathematics 72, 85-100.
- [7] Zhu Y, Han X (2014) Curves and surfaces construction based on new basis with exponential functions, Acta Appl. Math., 129, 129-183.

A Reliable Numerical Approximation to Physical Pendulum Equation using Dickson Polynomials

Ömür Kivanç Kürkçü*, İzmir University of Economics, Dept. of Mathematics, İzmir, Turkey

Ersin Aslan, Manisa Celal Bayar Univ., Dept. of Software Engineering, Manisa, Turkey

Mehmet Sezer, Manisa Celal Bayar Univ., Dept. of Mathematics, Manisa, Turkey

*Corresponding author e-mail: omur.kivanc@ieu.edu.tr

Keywords: Dickson polynomials, physical pendulum, matrix-collocation method

Discipline: Mathematics

Abstract

In this study, the physical damped-undamped pendulum equation of nonlinear type is considered using a matrix-collocation method based on Dickson polynomials. This equation governs the oscillatory behavior of the damped-undamped pendulum, which occurs in mechanical problems. It is worth specifying that the pendulum equation possesses a sinusoidal nonlinearity in its structure, which makes it a very difficult problem. The method contains a simple algebraic matrix-collocation system and Dickson polynomials with the parameter- α . Thus, the method provides a clear and efficient approximation to the pendulum equation. A computer routine of the method is established and run on Mathematica to handle sensitively the mentioned equation. The outcomes obtained from the routine are presented in figures and tables. In figures, the oscillatory behaviors and their limits cycles are determined with a combination between the proposed method and Laplace-Padé method. Numerical results are also interpreted in tables. According to all these investigations, one can state that the proposed method is highly effective, clear and reliable.

Introduction

It is well known that differential equations and their some classes appear in many applied sciences, such as mathematics, mechanics, fluid mechanics, physics, ecology, biology, engineering etc. It is also evident that as these equations are evolved for different aims, their analytical treatments become much harder. Thus, numerical methods are proposed to treat them numerically, some of which are Taylor [1], Dickson matrix-collocation [2-7], He's homotopy perturbation [8], variational iteration [9] and Adomian decomposition methods [10]. In this study, the Dickson matrix-collocation method involving a parameter- α is proposed to solve the physical damped-undamped pendulum equation of nonlinear type [11-14]

$$y''(t) + \mu y'(t) + \sin(\lambda y(t)) = 0, \quad a \leq t \leq b, \quad (1)$$

subject to the initial conditions $y(0) = 0$ and $y'(0) = 1$. Here,

- $\mu \geq 0$ and $\lambda > 0$ represent the damping and periodic forces, respectively;
- This equation is reduced to the undamped form for $\mu = 0$;
- For $\mu = 0$ and $\lambda = 1$, the exact solution of Eq. (1) is (see [11])

$$y(t) = 2 \arcsin\left(\frac{1}{2} \operatorname{sn}\left(t, \frac{1}{4}\right)\right),$$

where $\operatorname{sn}(t, \bullet)$ is the Jacobian elliptic function.

Method

Previously, the Dickson matrix-collocation method was applied to some specific nonlinear problems, such as quadratic and cubic nonlinear differential equations [4]. It was observed that this method

presented highly effective results. For this aim, in this section, we develop this method to treat the physical pendulum equation involving sinusoidal nonlinearity in the form (1).

We seek the Dickson polynomial solution of Eq. (1) in the form [2-7]

$$y(t) \cong y_N(t) = \sum_{n=0}^N y_n D_n(t, \alpha), \quad (2)$$

where y_n 's are unknown Dickson coefficients.

The collocation points we use in the matrices are defined to be

$$t_i = a + \left(\frac{b-a}{N}\right)i, \quad i = 0, 1, \dots, N, \quad a = t_0 < t_1 < \dots < t_N = b. \quad (3)$$

The matrix relation of the Dickson polynomial solution (2) is (see [2-7])

$$y(t) \cong y_N(t) = \mathbf{D}(t, \alpha) \mathbf{Y}, \quad \mathbf{D}(t, \alpha) = \mathbf{X}(t) \mathbf{S}(\alpha) \Rightarrow y(t) = \mathbf{X}(t) \mathbf{S}(\alpha) \mathbf{Y}, \quad (4)$$

where

$$\mathbf{X}(t) = [1 \quad t \quad t^2 \quad \dots \quad t^N] \quad \text{and} \quad \mathbf{Y} = [y_0 \quad y_1 \quad \dots \quad y_N]^T.$$

Taking the first and second order derivative of Eq. (4), it holds that (see [2-7])

$$y'(t) = \mathbf{X}(t) \mathbf{B} \mathbf{S}(\alpha) \mathbf{Y} \quad \text{and} \quad y''(t) = \mathbf{X}(t) \mathbf{B}^2 \mathbf{S}(\alpha) \mathbf{Y}, \quad (5)$$

where

$$\mathbf{B} = \begin{bmatrix} 0 & 1 & 0 & 0 & \dots & 0 \\ 0 & 0 & 2 & 0 & \dots & 0 \\ 0 & 0 & 0 & 3 & \dots & 0 \\ \vdots & \vdots & \vdots & \vdots & \ddots & \vdots \\ 0 & 0 & 0 & 0 & 0 & N \\ 0 & 0 & 0 & 0 & 0 & 0 \end{bmatrix}.$$

On the other hand, the sinusoidal nonlinearity in Eq. (1) can be written as

$$\sin(\lambda y(t)) = \lambda y(t) - \frac{\lambda^3 y^3(t)}{6} + \frac{\lambda^5 y^5(t)}{120}.$$

Thus, a new form of Eq. (1) is transformed to the pendulum equation of quintic nonlinear type

$$y''(t) + \mu y'(t) + \lambda y(t) - \frac{\lambda^3 y^3(t)}{6} + \frac{\lambda^5 y^5(t)}{120} = 0, \quad (6)$$

Using Eq. (3) and Eq. (4), the matrix relation of the cubic nonlinear part of Eq. (6) is constructed as (see [4])

$$\left[\frac{\lambda^3}{6} y^3(t_i) \right]_{(N+1) \times 1} = \frac{\lambda^3}{6} \mathbf{XS}(\alpha) \overset{1-}{\mathbf{X}} \overset{1-}{\mathbf{S}}(\alpha) \overset{2-}{\mathbf{X}} \overset{2-}{\mathbf{S}}(\alpha) \overset{2-}{\mathbf{Y}}, \quad (7)$$

where

$$\overset{2-}{\mathbf{X}} = \text{diag} \left[\overset{1-}{\mathbf{X}} \right]_{(N+1)^2 \times (N+1)^3}, \quad \overset{2-}{\mathbf{S}}(\alpha) = \text{diag} \left[\overset{1-}{\mathbf{S}}(\alpha) \right]_{(N+1)^3 \times (N+1)^3}, \quad \overset{2-}{\mathbf{Y}} = \left[y_0 \overset{1-}{\mathbf{Y}} \quad y_1 \overset{1-}{\mathbf{Y}} \quad \cdots \quad y_N \overset{1-}{\mathbf{Y}} \right]^T_{1 \times (N+1)^3},$$

such that for brevity, the signs (1-) and (2-) represent the lines over the matrices in accordance with their dimensions. For example,

$$\overset{1-}{\mathbf{X}} = \bar{\mathbf{X}} \quad \text{and} \quad \overset{2-}{\mathbf{X}} = \bar{\bar{\mathbf{X}}}.$$

Similarly using Eq. (3) and Eq. (4), we now introduce the matrix relation of the quintic nonlinear part of Eq. (6) as

$$\left[\frac{\lambda^5}{120} y^5(t_i) \right]_{(N+1) \times 1} = \frac{\lambda^5}{120} \mathbf{XS}(\alpha) \overset{1-}{\mathbf{X}} \overset{1-}{\mathbf{S}}(\alpha) \overset{2-}{\mathbf{X}} \overset{2-}{\mathbf{S}}(\alpha) \overset{3-}{\mathbf{X}} \overset{3-}{\mathbf{S}}(\alpha) \overset{4-}{\mathbf{X}} \overset{4-}{\mathbf{S}}(\alpha) \overset{4-}{\mathbf{Y}}, \quad (8)$$

where

$$\begin{aligned} \overset{3-}{\mathbf{X}} &= \text{diag} \left[\overset{2-}{\mathbf{X}} \right]_{(N+1)^3 \times (N+1)^4}, \quad \overset{3-}{\mathbf{S}}(\alpha) = \text{diag} \left[\overset{2-}{\mathbf{S}}(\alpha) \right]_{(N+1)^4 \times (N+1)^4}, \quad \overset{4-}{\mathbf{X}} = \text{diag} \left[\overset{3-}{\mathbf{X}} \right]_{(N+1)^4 \times (N+1)^5}, \\ \overset{4-}{\mathbf{S}}(\alpha) &= \text{diag} \left[\overset{3-}{\mathbf{S}}(\alpha) \right]_{(N+1)^5 \times (N+1)^5}, \quad \overset{3-}{\mathbf{Y}} = \left[y_0 \overset{2-}{\mathbf{Y}} \quad y_1 \overset{2-}{\mathbf{Y}} \quad \cdots \quad y_N \overset{2-}{\mathbf{Y}} \right]^T_{1 \times (N+1)^4}, \\ \overset{4-}{\mathbf{Y}} &= \left[y_0 \overset{3-}{\mathbf{Y}} \quad y_1 \overset{3-}{\mathbf{Y}} \quad \cdots \quad y_N \overset{3-}{\mathbf{Y}} \right]^T_{1 \times (N+1)^5}. \end{aligned}$$

Substituting Eqs. (4), (5), (7) and (8) into Eq. (6), we can eventually state the fundamental matrix equation of Eq. (6) as

$$\begin{aligned} (\mathbf{XB}^2 + \mu \mathbf{XB} + \lambda \mathbf{X}) \mathbf{S}(\alpha) \mathbf{Y} + \frac{\lambda^3}{6} \mathbf{XS}(\alpha) \overset{1-}{\mathbf{X}} \overset{1-}{\mathbf{S}}(\alpha) \overset{2-}{\mathbf{X}} \overset{2-}{\mathbf{S}}(\alpha) \overset{2-}{\mathbf{Y}} \\ + \frac{\lambda^5}{120} \mathbf{XS}(\alpha) \overset{1-}{\mathbf{X}} \overset{1-}{\mathbf{S}}(\alpha) \overset{2-}{\mathbf{X}} \overset{2-}{\mathbf{S}}(\alpha) \overset{3-}{\mathbf{X}} \overset{3-}{\mathbf{S}}(\alpha) \overset{4-}{\mathbf{X}} \overset{4-}{\mathbf{S}}(\alpha) \overset{4-}{\mathbf{Y}} = 0, \end{aligned}$$

or briefly

$$\mathbf{WY} + \mathbf{ZY} + \mathbf{TY} = 0. \quad (9)$$

After removing any two rows of \mathbf{W} , \mathbf{Z} and \mathbf{T} in Eq. (9), we then insert the initial conditions into the matrix \mathbf{Y} and two zero matrices are also inserted into the matrices $\overset{2-}{\mathbf{Y}}$ and $\overset{4-}{\mathbf{Y}}$. Solving this system of nonlinear algebraic equations, we can reach the unknown Dickson coefficients and then these are inserted into Eq. (4), which constructs the Dickson polynomial solution.

We can estimate long time behavior of the Dickson polynomial solutions by employing a combination between the proposed method and Laplace-Padé method [15,16]. Using the Dickson polynomial solution, this combination can be described as follows [15,16]:

Step 1: $G(s) \leftarrow L\{y_N(t)\} = \int_0^{\infty} y_N(t)e^{-st} dt$, where $L\{\cdot\}$ is the Laplace transform,

Step 2: Insert $s \rightarrow 1/t$ into $G(s)$,

Step 3: $H(s) \leftarrow H\left(\frac{1}{t}\right) \leftarrow P\left[G\left(\frac{1}{t}\right)\right]$, where K and L are the numerator and denominator degrees of Padé approximant $P[\cdot]$,

Step 4: $y_{P,N}(t) \leftarrow L^{-1}\{H(s)\}$.

Numerical Examples

We handle two physical pendulum equations to show the effectiveness and reliability of the method. We encode a computer program routine of the method on Mathematica 11, which is run by a PC equipped with 3.30 Ghz CPU and 8 GB Ram.

Example 1: [11-14] Consider the undamped physical pendulum equation

$$y''(t) + \sin(\lambda y(t)) = 0, \quad 0 \leq t \leq 1, \quad (10)$$

subject to the initial conditions $y(0) = 0$ and $y'(0) = 1$. Let us solve this equation using the proposed method and a routine built in Mathematica, in order to compare the efficiency of the proposed method. The routine can be constructed as

$$\text{NDSolve}\{\{y''[t] + \text{Sin}[\lambda * y[t]] == 0, y[0] == 0, y'[0] == 1\}, y[t], \{t, 0, 1\}\}[[1, 1, 2]],$$

which returns the numerical solution of Eq. (10) on the time interval $[0,1]$ for different λ .

The Dickson polynomial solutions and the solution obtained by Mathematica (MS) are illustrated for different the values of λ and α in Figure 1. The oscillatory behavior of these solutions is simulated in Figure 2, after applying Laplace-Padé technique to the Dickson polynomial solution $y_5(t)$ with $\alpha = 1$. Table 1 presents the absolute errors with respect to N .

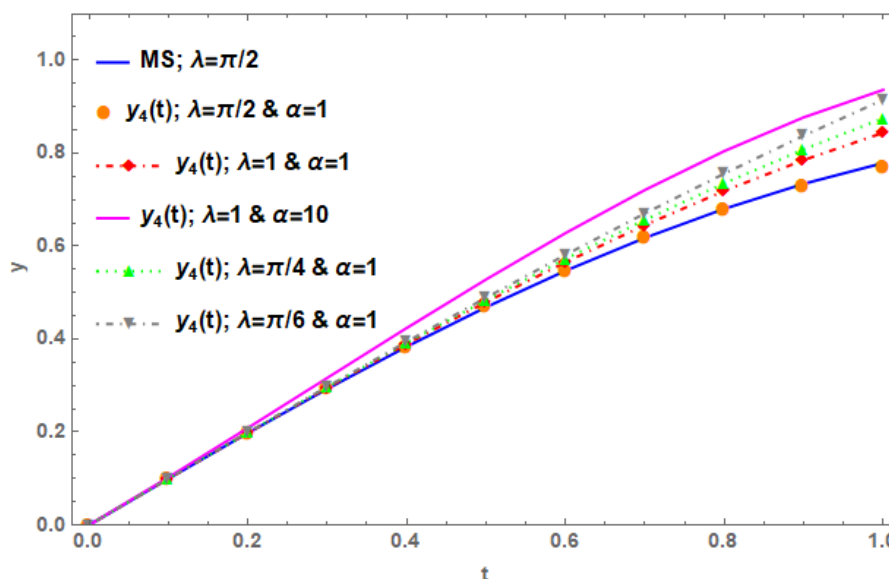


Figure 1. Displacement of the Dickson polynomial solution with respect to λ and α for Example 1.

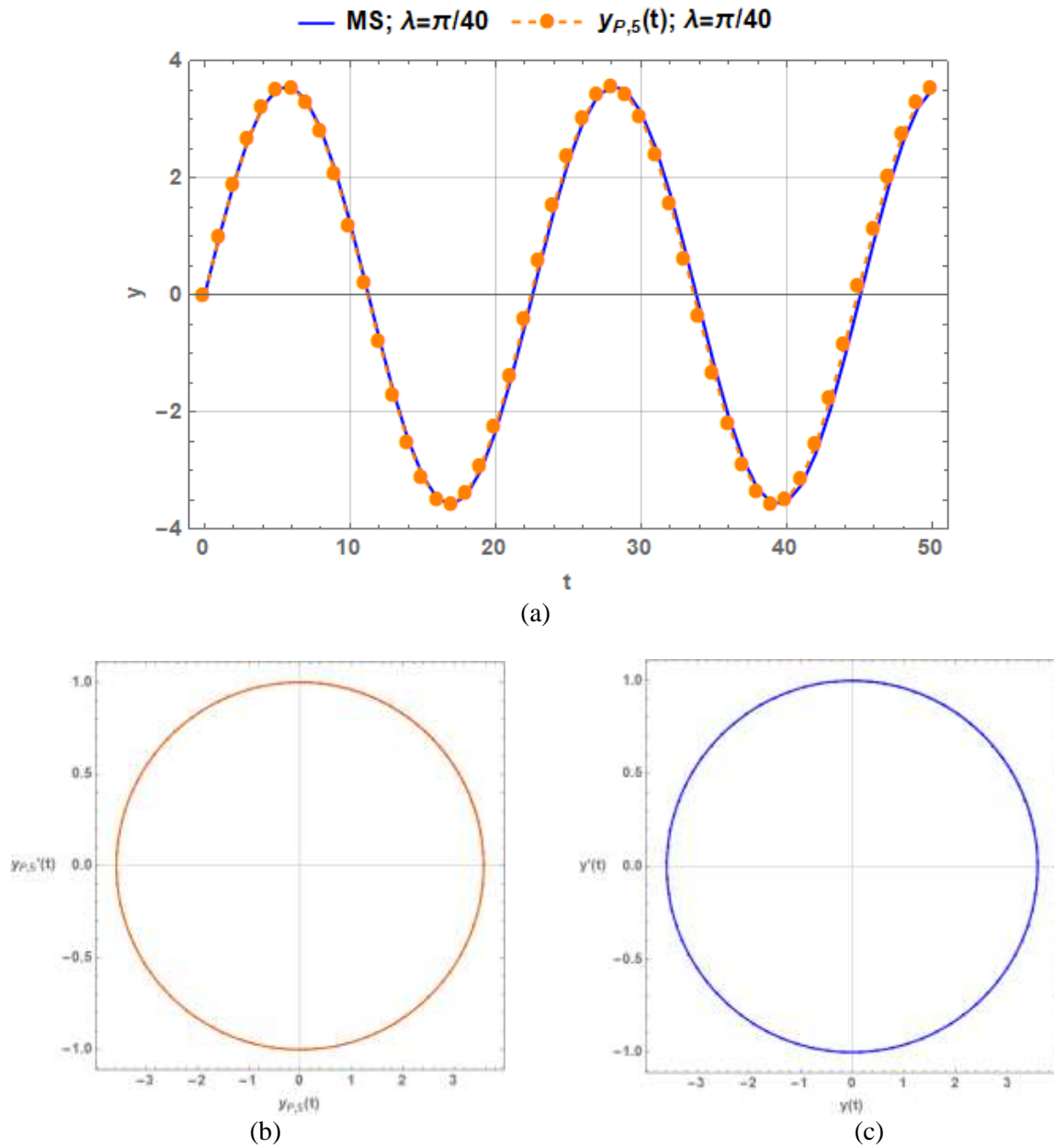


Figure 2. (a) The oscillatory behavior of the solutions on $[0,50]$ and their the phase plane diagrams (b) and (c) for Example 1.

Table 1. Comparison of the absolute errors with $\alpha = 1.5$ for Example 1.

t_i	$ e_3(t_i) $	$ e_4(t_i) $	$ e_3(t_i) $	$ e_4(t_i) $
	$\lambda = 1$	$\lambda = 1$	$\lambda = \pi/6$	$\lambda = \pi/6$
0.2	$1.13e-04$	$3.67e-05$	$1.48e-05$	$1.41e-06$
0.4	$7.79e-04$	$2.12e-05$	$9.15e-05$	$8.58e-06$
0.6	$1.96e-03$	$1.68e-04$	$1.63e-04$	$1.50e-05$
0.8	$2.59e-03$	$2.86e-04$	$8.63e-05$	$1.38e-04$
1.0	$3.12e-04$	$2.95e-03$	$1.31e-03$	$8.42e-04$

Example 2: [11-14] Consider the damped physical pendulum equation

$$y''(t) + \mu y'(t) + \sin(\lambda y(t)) = 0, \quad 0 \leq t \leq 1,$$

subject to the initial conditions $y(0) = 0$ and $y'(0) = 1$. This equation is immediately solved with the proposed method for $N = \{4, 5\}$. Then, the Laplace-Padé technique is applied to the Dickson polynomial solutions. The obtained solutions are compared with the solution of Mathematica (MS), where NDSolve routine can be constructed as

$$\text{NDSolve}[\{y''[t] + \mu * y'[t] + \text{Sin}[\lambda * y[t]] == 0, y[0] == 0, y'[0] == 1\}, y[t], \{t, 0, 1\}][[1, 1, 2]].$$

Table 2 clearly indicates the inconsistent displacement of the Dickson polynomial solution as α is increased. On the time interval $[0, 40]$, the damped oscillatory behavior of the Dickson polynomial solutions with $\alpha = 1$ and their phase plane diagrams are simulated with respect to the damping force μ in Figure 3 and Figure 4, respectively.

Table 2. Numerical displacement of the Dickson polynomial solution with respect to α for Example 2 with $\mu = 0.4$ and $\lambda = 1$.

t_i	Exact solution	$y_5(t_i);$ $\alpha = 1$	$y_5(t_i);$ $\alpha = 5$	$y_5(t_i);$ $\alpha = 6$
0.2	0.19093285	0.19104889	0.18939844	0.18657833
0.4	0.35993401	0.36046466	0.35384568	0.34243275
0.6	0.50247137	0.50360372	0.48879555	0.46310675
0.8	0.61561572	0.61715312	0.59119495	0.54601379
1.0	0.69794041	0.69920603	0.65955678	0.59050074

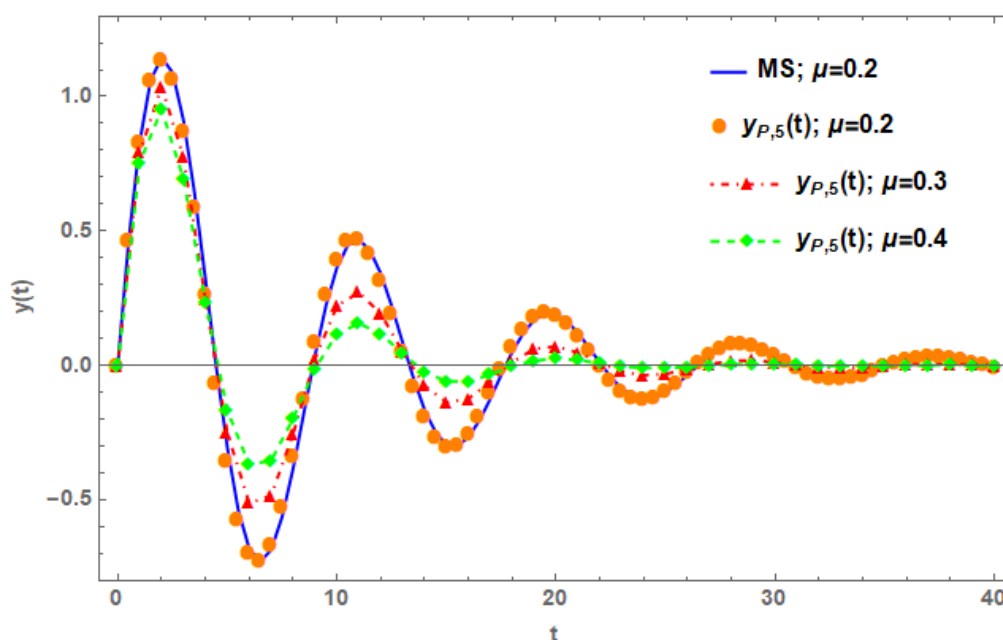


Figure 3. Damped oscillatory behavior of the solutions with respect to μ for Example 2 with $\lambda = \pi / 6$.

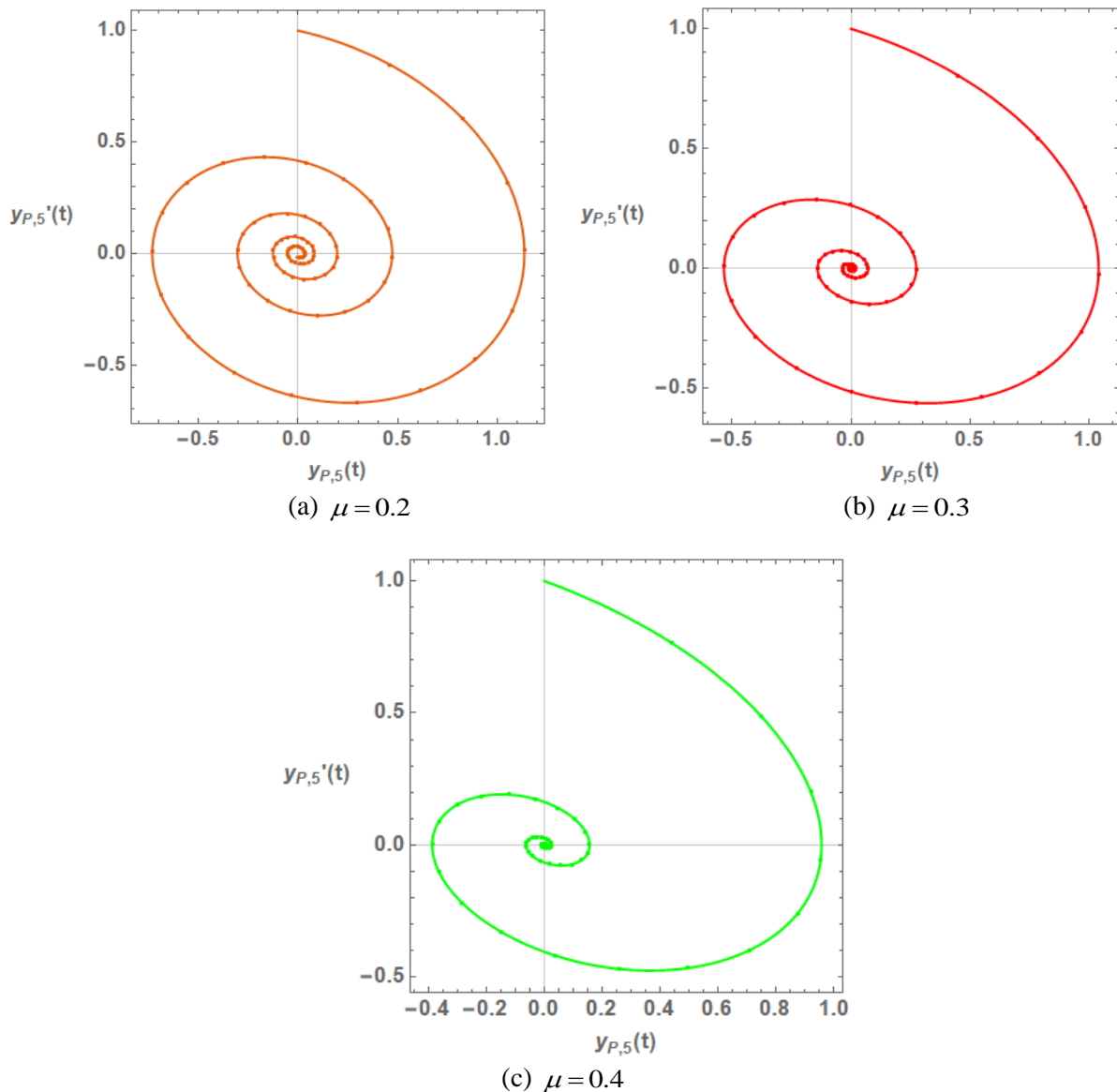


Figure 4. The phase planes of the damped oscillatory solutions with respect to μ for Example 2 with $\lambda = \pi / 6$.

Conclusions

We have reached the numerical solutions of the physical pendulum equation using and developing the Dickson matrix collocation method. The numerical and graphical results have been illustrated in figures and tables. It can be easily observed that the obtained solutions have overlapped with the exact or Mathematica solutions. Phase plane behaviors of them have also simulated. On the other hand, the displacement of the solutions has been monitored with respect to the parameter- α . Eventually, one can state that the proposed method is very proper for investigating the numerical solution of the physical pendulum equation.

References

- [1] Gülsu M, Sezer, M (2011) A Taylor collocation method for solving high-order linear pantograph equations with linear functional argument. Numer. Methods Partial Differ. Equ. 27: 1628–1638.
- [2] Kürkçü ÖK, Aslan E, Sezer, M (2016) A numerical approach with error estimation to solve general integro-differential-difference equations using Dickson polynomials. Appl. Math. Comput. 276: 324–339.

3rd International Students Science Congress
3-4 May 2019, İzmir - Turkey

- [3] Kürkçü ÖK, Aslan E, Sezer, M (2017) A novel collocation method based on residual error analysis for solving integro-differential equations using hybrid Dickson and Taylor polynomials. *Sains Malays.* 46:335–347.
- [4] Kürkçü ÖK, Aslan E, Sezer, M (2017) A numerical method for solving some model problems arising in science and convergence analysis based on residual function. *Appl. Numer. Math.* 121: 134–148.
- [5] Kürkçü ÖK, Aslan E, Sezer, M, İlhan Ö (2018) A numerical approach technique for solving generalized delay integro-differential equations with functional bounds by means of Dickson polynomials. *Int. J. Comput. Methods* 15(5):1850039.
- [6] Kürkçü ÖK, Aslan E, Sezer, M (2018) A Numerical Method for Solving Functional Differential Equations with Delays. *2nd International Students Science Congress*, pp. 72-77, İzmir, Turkey.
- [7] Kürkçü ÖK, Aslan E, Sezer M (2019) An inventive numerical method for solving the most general form of integro-differential equations with functional delays and characteristic behavior of orthoexponential residual function. *Comput. Appl. Math.* 38: 34.
- [8] He JH (1999) Homotopy perturbation technique. *Comput. Methods Appl. Mech. Eng.* 178:257-262.
- [9] He JH (1999) Variational iteration method-a kind of non-linear analytical technique: Some examples. *Int. J. Nonlinear Mech.* 34: 699–708.
- [10] Adomian G (1988) A review of the decomposition method in applied mathematics. *J. Math. Anal. Appl.* 135: 501–544.
- [11] Duan J-S (2011) New recurrence algorithms for the nonclassic Adomian polynomials. *Comput. Math. Appl.* 62: 2961–2977.
- [12] Nagle RK, Saff EB, Snider AD (2011) *Fundamentals of Differential Equations and Boundary Value Problems.* (6th ed.), Pearson, 2011
- [13] Enns RH, McGuire GC (2001) *Nonlinear Physics with Mathematica for Scientists and Engineers.* Birkhäuser, Boston.
- [14] Jordan D, Smith P (2007) *Nonlinear Ordinary Differential Equations: Problems and Solutions.* Oxford Texts in Applied & Engineering Mathematics 11, Oxford University Press Inc., New York
- [15] Momani S, Ertürk VS (2008) Solutions of non-linear oscillators by the modified differential transform method. *Comput. Math. Appl.* 55: 833–842.
- [16] Sweilam NH, Khader MM (2009) Exact solutions of some coupled nonlinear partial differential equations using the homotopy perturbation method. *Comput. Math. Appl.* 58: 2134–2141.

Pell Matrix Collocation Method for Solving Damped Wave Equation

*Seda Çayan**, Manisa Celal Bayar University, Dept. of Mathematics, Manisa, Turkey
Mehmet Sezer, Manisa Celal Bayar University, Dept. of Mathematics, Manisa, Turkey
Mehmet Çevik, İzmir Kâtip Çelebi University, Dept. of Mechanical Engineering, İzmir, Turkey
 *Corresponding author: seda_cayan@hotmail.com

Keywords: Pell polynomials and series, matrix and collocation methods, damped wave equation
Discipline: Mathematics

Abstract

In this study, we investigate the approximate solutions of one-dimensional linear damped wave equation subject to initial and boundary conditions. For this purpose, we look for a solution in the truncated Pell series form. The technique we have used is a matrix method based on to the matrix forms of Pell polynomials and their derivatives together with the collocation points. Also, some numerical examples together with error analysis are performed to illustrate the efficiency of the method and the obtained results are scrutinized and interpreted.

Introduction

The wave equations play a important role in several physical problems. They are used by physicists and engineers in explaining the propagation of water waves, sound waves, electromagnetic waves, the transmission of electric signals in a cable, the vibrations of a string or a membrane, seismic waves, gravity waves and oscillatory waves. In this study, we consider the wave equation with viscous damping

$$u_{tt}(x,t) + ku_t(x,t) = c^2 u_{xx}(x,t) \quad (1)$$

under the initial conditions

$$u(x,0) = \varphi_1(x) \quad \text{and} \quad u_t(x,0) = \varphi_2(x), \quad a \leq x \leq b \quad (2)$$

and Neumann boundary conditions

$$u_x(a,t) = \varphi_3(t) \quad \text{and} \quad u_x(b,t) = \varphi_4(t), \quad 0 \leq t \leq T \quad (3)$$

Here $\varphi_1(x)$, $\varphi_2(x)$, $\varphi_3(t)$ and $\varphi_4(t)$ are continuous functions, the parameter k is the viscous damping coefficient and the constant c is the propagation speed of the wave. We use Pell Matrix Collocation Method (PMCM) for obtaining the approximate solutions of the damped wave Eq. (1) under the given conditions. For our purpose, we first assume the approximate solution of the problem (1)-(3) in the truncated Pell series form

$$u(x,t) \cong u_N(x,t) = \sum_{m=0}^N \sum_{n=0}^N a_{m,n} P_{m+1,n+1}(x,t); \quad P_{m+1,n+1}(x,t) = P_{m+1}(x)P_{n+1}(t) \quad (4)$$

where $u_N(x,t)$ is the approximate solution of Eq. (1); $a_{m,n}$, ($m, n = 0, 1, \dots, N$) are the unknown Pell polynomials coefficients; N is chosen as any positive integer such that $N \geq 2$. Pell polynomials $P_n(x)$ are defined by the generating function:

$$(1 - 2xt - t^2)^{-1} = \sum_{n=0}^{\infty} P_{n+1}(x)t^n$$

and from standard methods, the explicit representations of Pell polynomials are obtained as

$$P_n(x) = \sum_{k=0}^{\lfloor \frac{n-1}{2} \rfloor} \binom{n-k-1}{k} 2^{n-2k-1} x^{n-2k-1}. \quad (5)$$

Also, Pell Polynomials are defined by the recurrence relations

$$P_n(x) = 2xP_{n-1}(x) + P_{n-2}(x), \quad n \geq 2, \quad P_0(x) = 0, \quad P_1(x) = 1.$$

Fundamental Matrix Relation and Method of Solution

By using the relation (5), we can write the matrix form of Pell polynomials as follows:

$$\underbrace{\begin{bmatrix} P_1(x) \\ P_2(x) \\ P_3(x) \\ P_4(x) \\ P_5(x) \\ \vdots \\ P_N(x); \\ (N \text{ odd}) \\ P_N(x); \\ (N \text{ even}) \end{bmatrix}}_{\mathbf{P}(x)^T} = \underbrace{\begin{bmatrix} 1 & 0 & 0 & 0 & 0 & \cdots & 0 \\ 0 & 2^1 \binom{1}{0} & 0 & 0 & 0 & \cdots & 0 \\ 2^0 \binom{1}{1} & 0 & 2^2 \binom{2}{0} & 0 & 0 & \cdots & 0 \\ 0 & 2^1 \binom{2}{1} & 0 & 2^3 \binom{3}{0} & 0 & \cdots & 0 \\ 2^0 \binom{2}{2} & 0 & 2^2 \binom{3}{1} & 0 & 2^4 \binom{4}{0} & \cdots & 0 \\ \vdots & \vdots & \vdots & \vdots & \vdots & \ddots & \vdots \\ 2^0 \binom{N-1}{2} & 0 & 2^2 \binom{N+1}{2} & 0 & 2^4 \binom{N+3}{2} & \cdots & 2^{N-1} \binom{N-1}{0} \\ 0 & 2^1 \binom{N}{2} & 0 & 2^3 \binom{N+2}{2} & 0 & \cdots & 2^{N-1} \binom{N-1}{0} \end{bmatrix}}_{\mathbf{S}^T} \underbrace{\begin{bmatrix} x^0 \\ x^1 \\ x^2 \\ x^3 \\ x^4 \\ \vdots \\ x^{N-1} \\ x^{N-1} \end{bmatrix}}_{\mathbf{X}(x)^T}$$

or in the compact form

$$\mathbf{P}(x)^T = \mathbf{S}^T \mathbf{X}(x)^T \Rightarrow \mathbf{P}(x) = \mathbf{X}(x) \mathbf{S}. \quad (6)$$

Then, by substituting the expression (6) into (3), we obtain the following matrix relations:

$$u_N(x, t) = \mathbf{P}(x) \bar{\mathbf{P}}(t) \mathbf{A} \quad \text{or} \quad u_N(x, t) = \mathbf{X}(x) \mathbf{S} \bar{\mathbf{X}}(t) \bar{\mathbf{S}} \mathbf{A} \quad (7)$$

where

$$\begin{aligned} \mathbf{P}(x) &= [P_1(x) \ P_2(x) \ \cdots \ P_{N+1}(x)], & \bar{\mathbf{P}}(t) &= \text{diag}[\mathbf{P}(t), \mathbf{P}(t), \dots, \mathbf{P}(t)], \\ \mathbf{A} &= [a_{0,0} \ a_{0,1} \ \cdots \ a_{0,N} \ a_{1,0} \ a_{1,1} \ \cdots \ a_{1,N} \ \cdots \ a_{N,0} \ a_{N,1} \ \cdots \ a_{N,N}]^T, \\ \mathbf{A} &= [\mathbf{A}_0 \ \mathbf{A}_1 \ \cdots \ \mathbf{A}_N]^T; \quad \mathbf{A}_i = [a_{i,0} \ a_{i,1} \ \cdots \ a_{i,N}]^T, \quad (i=0,1,2,\dots,N) \\ \mathbf{X}(x) &= [1 \ x \ \cdots \ x^N], & \bar{\mathbf{X}}(t) &= \text{diag}[\mathbf{X}(t), \mathbf{X}(t), \dots, \mathbf{X}(t)] \\ \mathbf{S}^0 &= \mathbf{I} = \text{diag}[1,1,\dots,1], & \bar{\mathbf{S}} &= \text{diag}[\mathbf{S}, \mathbf{S}, \dots, \mathbf{S}]. \end{aligned}$$

On the other hand, the relation between the matrix $\mathbf{X}(x)$ and its derivatives $\mathbf{X}'(x)$ and $\mathbf{X}''(x)$ are

$$\mathbf{X}'(x) = \mathbf{X}(x)\mathbf{B}, \quad \mathbf{X}''(x) = \mathbf{X}'(x)\mathbf{B} = \mathbf{X}(x)\mathbf{B}^2 \quad (8)$$

and the relation between the matrix $\bar{\mathbf{X}}(t)$ and its derivatives $\bar{\mathbf{X}}'(t)$ and $\bar{\mathbf{X}}''(t)$ are [6-7]

$$\bar{\mathbf{X}}'(t) = \bar{\mathbf{X}}(t)\bar{\mathbf{B}}, \quad \bar{\mathbf{X}}''(t) = \bar{\mathbf{X}}'(t)\bar{\mathbf{B}} = \bar{\mathbf{X}}(t)\bar{\mathbf{B}}^2; \quad (9)$$

$$\mathbf{B} = \begin{bmatrix} 0 & 1 & 0 & \cdots & 0 \\ 0 & 0 & 2 & \cdots & 0 \\ \vdots & \vdots & \vdots & \ddots & \vdots \\ 0 & 0 & 0 & \cdots & N \\ 0 & 0 & 0 & \cdots & 0 \end{bmatrix}, \quad \mathbf{B}^0 = \mathbf{I} = \text{diag}[1,1,1,\dots,1], \quad \bar{\mathbf{B}} = \text{diag}[\mathbf{B}, \mathbf{B}, \mathbf{B}, \dots, \mathbf{B}].$$

Then, we organize the following matrix relations of the derivatives u_t , u_{xx} and u_{tt} , by using the relations (6) – (9):

$$\begin{aligned} u_t(x,t) &= \mathbf{P}(x)\bar{\mathbf{P}}'(t)\mathbf{A} = \mathbf{X}(x)\mathbf{S}\bar{\mathbf{X}}'(t)\bar{\mathbf{S}}\mathbf{A} = \mathbf{X}(x)\mathbf{S}\bar{\mathbf{X}}(t)\bar{\mathbf{B}}\bar{\mathbf{S}}\mathbf{A} \\ u_{xx}(x,t) &= \mathbf{P}''(x)\bar{\mathbf{P}}(t)\mathbf{A} = \mathbf{X}''(x)\mathbf{S}\bar{\mathbf{X}}(t)\bar{\mathbf{S}}\mathbf{A} = \mathbf{X}(x)\mathbf{B}^2\mathbf{S}\bar{\mathbf{X}}(t)\bar{\mathbf{S}}\mathbf{A} \\ u_{tt}(x,t) &= \mathbf{P}(x)\bar{\mathbf{P}}''(t)\mathbf{A} = \mathbf{X}(x)\mathbf{S}\bar{\mathbf{X}}''(t)\bar{\mathbf{S}}\mathbf{A} = \mathbf{X}(x)\mathbf{S}\bar{\mathbf{X}}(t)\bar{\mathbf{B}}^2\bar{\mathbf{S}}\mathbf{A}. \end{aligned} \quad (10)$$

By substituting the relations (10) into Eq. (1) we have the fundamental matrix form for Eq. (1):

$$\mathbf{X}(x)\mathbf{S}\bar{\mathbf{X}}(t)\bar{\mathbf{B}}^2\bar{\mathbf{S}}\mathbf{A} + k\mathbf{S}\bar{\mathbf{X}}(t)\bar{\mathbf{B}}\bar{\mathbf{S}}\mathbf{A} = c^2 \mathbf{X}(x)\mathbf{B}^2\mathbf{S}\bar{\mathbf{X}}(t)\bar{\mathbf{S}}\mathbf{A}$$

or

$$\underbrace{\left\{ \mathbf{X}(x)\mathbf{S}\bar{\mathbf{X}}(t)\bar{\mathbf{B}}^2\bar{\mathbf{S}} + k\mathbf{S}\bar{\mathbf{X}}(t)\bar{\mathbf{B}}\bar{\mathbf{S}} - c^2 \mathbf{X}(x)\mathbf{B}^2\mathbf{S}\bar{\mathbf{X}}(t)\bar{\mathbf{S}} \right\}}_{\mathbf{W}(x,t)} \mathbf{A} = 0;$$

or shortly

$$\mathbf{W}(x,t)\mathbf{A} = 0. \quad (11)$$

By putting the collocation points, for $x \in [a, b]$ and $t \in [0, T]$,

$$x_i = a + \frac{b-a}{N}i, \quad t_j = \frac{T}{N}j, \quad i, j = 0, 1, 2, \dots, N \quad (12)$$

into Eq. (11), then we have the system of the matrix equations for $i = 0, 1, 2, \dots, N$:

$$\left. \begin{array}{l} \mathbf{W}(x_0, t_0)\mathbf{A} = 0 \\ \mathbf{W}(x_0, t_1)\mathbf{A} = 0 \\ \vdots \\ \mathbf{W}(x_0, t_N)\mathbf{A} = 0 \end{array} \right\} \mathbf{W}_0\mathbf{A} = \mathbf{0} \\
 \left. \begin{array}{l} \mathbf{W}(x_1, t_0)\mathbf{A} = 0 \\ \mathbf{W}(x_1, t_1)\mathbf{A} = 0 \\ \vdots \\ \mathbf{W}(x_1, t_N)\mathbf{A} = 0 \end{array} \right\} \mathbf{W}_1\mathbf{A} = \mathbf{0} \\
 \vdots \\
 \left. \begin{array}{l} \mathbf{W}(x_N, t_0)\mathbf{A} = 0 \\ \mathbf{W}(x_N, t_1)\mathbf{A} = 0 \\ \vdots \\ \mathbf{W}(x_N, t_N)\mathbf{A} = 0 \end{array} \right\} \mathbf{W}_N\mathbf{A} = \mathbf{0}
 \end{array} \Rightarrow \mathbf{W}_i\mathbf{A} = \mathbf{0}, \quad \mathbf{W} = \begin{bmatrix} \mathbf{W}_0 \\ \mathbf{W}_1 \\ \vdots \\ \mathbf{W}_N \end{bmatrix}; \quad \mathbf{W}_i = \begin{bmatrix} \mathbf{W}(x_i, t_0) \\ \mathbf{W}(x_i, t_1) \\ \vdots \\ \mathbf{W}(x_i, t_N) \end{bmatrix} \quad (13)$$

Hence, we can write Eq. (13) as

$$\mathbf{W}\mathbf{A} = \mathbf{0} \quad \text{or} \quad [\mathbf{W}; \mathbf{0}]. \quad (14)$$

Thus, the fundamental matrix equation of (1) is defined in the form (14). Similarly, we are able to obtain the corresponding matrix form for the conditions (2) – (3) as follows

$$\begin{aligned} u(x, 0) &= \mathbf{X}(x)\mathbf{S}\bar{\mathbf{X}}(0)\bar{\mathbf{S}}\mathbf{A}, & u_t(x, 0) &= \mathbf{X}(x)\mathbf{S}\bar{\mathbf{X}}(0)\bar{\mathbf{B}}\bar{\mathbf{S}}\mathbf{A}, \\ u_x(a, t) &= \mathbf{X}(a)\mathbf{B}\mathbf{S}\bar{\mathbf{X}}(t)\bar{\mathbf{S}}\mathbf{A} & \text{and} & \quad u_x(b, t) = \mathbf{X}(b)\mathbf{B}\mathbf{S}\bar{\mathbf{X}}(t)\bar{\mathbf{S}}\mathbf{A}. \end{aligned}$$

We can organize these expressions as follows:

$$\begin{aligned} \mathbf{U}_1(x, 0)\mathbf{A} &= \varphi_1(x), \quad \mathbf{U}_2(x, 0)\mathbf{A} = \varphi_2(x), \quad \mathbf{U}_3(a, t)\mathbf{A} = \varphi_3(t) \quad \text{and} \quad \mathbf{U}_4(b, t)\mathbf{A} = \varphi_4(t); \\ \mathbf{U}_1(x, 0) &= \mathbf{X}(x)\mathbf{S}\bar{\mathbf{X}}(0)\bar{\mathbf{S}}, & \mathbf{U}_2(x, 0) &= \mathbf{X}(x)\mathbf{S}\bar{\mathbf{X}}(0)\bar{\mathbf{B}}\bar{\mathbf{S}} \\ \mathbf{U}_3(a, t) &= \mathbf{X}(a)\mathbf{B}\mathbf{S}\bar{\mathbf{X}}(t)\bar{\mathbf{S}} & \text{and} & \quad \mathbf{U}_4(b, t) = \mathbf{X}(b)\mathbf{B}\mathbf{S}\bar{\mathbf{X}}(t)\bar{\mathbf{S}}. \end{aligned}$$

and by putting the collocation points, for $x \in [a, b]$ and $t \in [0, T]$,

$$x_i = a + \frac{b-a}{N}i, \quad t_j = \frac{T}{N}j, \quad i, j = 1, 2, \dots, N-1$$

$$\mathbf{U}_1(x_i, 0)\mathbf{A} = \varphi_1(x_i), \quad \mathbf{U}_2(x_i, T)\mathbf{A} = \varphi_2(x_i), \quad \mathbf{U}_3(a, t_j)\mathbf{A} = \varphi_3(t_j) \quad \text{and} \quad \mathbf{U}_4(b, t_j)\mathbf{A} = \varphi_4(t_j).$$

Hence

$$\mathbf{U}_1 = \begin{bmatrix} \mathbf{U}_1(x_1, 0) \\ \mathbf{U}_1(x_2, 0) \\ \vdots \\ \mathbf{U}_1(x_N, 0) \end{bmatrix}, \quad \mathbf{U}_2 = \begin{bmatrix} \mathbf{U}_2(x_1, T) \\ \mathbf{U}_2(x_2, T) \\ \vdots \\ \mathbf{U}_2(x_N, T) \end{bmatrix}, \quad \mathbf{U}_3 = \begin{bmatrix} \mathbf{U}_3(a, t_1) \\ \mathbf{U}_3(a, t_2) \\ \vdots \\ \mathbf{U}_3(a, t_N) \end{bmatrix}, \quad \mathbf{U}_4 = \begin{bmatrix} \mathbf{U}_4(b, t_1) \\ \mathbf{U}_4(b, t_2) \\ \vdots \\ \mathbf{U}_4(b, t_N) \end{bmatrix}$$

$$\Phi_1 = [\varphi_1(x_1) \quad \varphi_1(x_2) \quad \cdots \quad \varphi_1(x_N)]^T, \quad \Phi_2 = [\varphi_2(x_1) \quad \varphi_2(x_2) \quad \cdots \quad \varphi_2(x_N)]^T$$

$$\Phi_3 = [\varphi_3(t_1) \quad \varphi_3(t_2) \quad \cdots \quad \varphi_3(t_N)]^T \quad \text{and} \quad \Phi_4 = [\varphi_4(t_1) \quad \varphi_4(t_2) \quad \cdots \quad \varphi_4(t_N)]^T$$

or shortly

$$U_i \mathbf{A} = \Phi_i \quad \text{or} \quad [U_i; \Phi_i], \quad (i=1,2,3,4) \quad (15)$$

To obtain the solution of Eq.(1) under the initial conditions (2) and the Neumann conditions (3), the following augmented matrix is constructed by replacing any rows of matrix (14) with rows of matrices (15), so we have new augmented matrix

$$\tilde{\mathbf{W}}\mathbf{A} = \tilde{\mathbf{G}} \quad \text{or} \quad [\tilde{\mathbf{W}}; \tilde{\mathbf{G}}]$$

If $\text{rank}(\tilde{\mathbf{W}}) = \text{rank}(\tilde{\mathbf{W}}; \tilde{\mathbf{G}}) = (N+1)^2$, the solution of the augmented matrix $[\tilde{\mathbf{w}}; \tilde{\mathbf{G}}]$ is $\mathbf{A} = (\tilde{\mathbf{W}})^{-1} \tilde{\mathbf{G}}$ and \mathbf{A} is uniquely determined. Thus, the unknown Pell polynomial coefficients are obtained and the approximate solution $u_N(x, t)$ is found in the form (4).

Residual Error Estimation

In this section, the error estimation based on residual function $R_N(x, t)$ for Eq.(4) is given and also the accuracy of Pell polynomial solution is performed. Here, residual function $R_N(x, t)$ can be defined by

$$R_N(x, t) = L[u_N(x, t)] - g(x, t); \quad L[u(x, t)] = g(x, t)$$

where $u_N(x, t)$ is approximate solution defined by (4) and L is the linear operator. For the selected points $x = x_i$, $a \leq x_i \leq b$ and $t = t_j$, $0 \leq t_j \leq T$:

$$R_N(x_i, t_j) = \left| \frac{\partial^2 u_N(x_i, t_j)}{\partial t^2} + k \frac{\partial u_N(x_i, t_j)}{\partial t} - c^2 \frac{\partial^2 u_N(x_i, t_j)}{\partial x^2} \right| \cong 0$$

where $R_N(x_i, t_j) \leq 10^{-k_{ij}} = 10^{-k}$ (k is positive integer). If $\max 10^{-k_{ij}} = 10^{-k}$ is prescribed, then the truncation limit N is increased until the difference $R_N(x_i, t_j)$ at each of the points becomes smaller than the prescribed 10^{-k} . On the other hand, by means of the mean value of the function $|R_N(x, t)|$, the accuracy of the solution can be controlled and the error can be estimated. For this purpose, by using mean value theorem for double integrals, the upper bound of the mean error $\overline{R_N}$ can be estimated as follows:

$$\left| \int_0^T \int_a^b R_N(x, t) dx dt \right| \leq \int_0^T \int_a^b |R_N(x, t)| dx dt, \quad a \leq x \leq b, 0 \leq t \leq T.$$

$$R_N(x_0, t_0) = \frac{\int_0^T \int_a^b R_N(x, t) dx dt}{(b-a)(T-0)}; \quad x_0 \in [a, b], t_0 \in [0, T]$$

from this relations

$$\left| \int_0^T \int_a^b R_N(x,t) dx dt \right| = |R_N(x_0, t_0)| |(b-a)(T-0)| \Rightarrow |R_N(x_0, t_0)| |(b-a)(T-0)| \leq \int_0^T \int_a^b |R_N(x,t)| dx dt$$

$$\Rightarrow |R_N(x_0, t_0)| \leq \frac{\int_0^T \int_a^b |R_N(x,t)| dx dt}{(b-a)(T-0)} = \overline{R}_N.$$

Numerical Example

Let us consider a damped wave equation [8] given by

$$\frac{\partial^2 u}{\partial t^2} + \frac{\sigma}{\varepsilon} \frac{\partial u}{\partial t} = \frac{1}{\mu \varepsilon} \frac{\partial^2 u}{\partial x^2} \quad (0 \leq x \leq 1, t \geq 0) \quad (16)$$

under the initial conditions

$$u(x, 0) = \cos(\pi x), \quad u_t(x, 0) = \operatorname{Re} \lambda \cos(\pi x),$$

and the homogeneous Neumann conditions

$$u_x(0, t) = 0, \quad u_x(1, t) = 0.$$

Here ε is capacitivity or permittivity ($F m^{-1}$), μ is inductivity or permeability ($H m^{-1}$) and σ is conductivity ($mhos m^{-1}$). If $\sigma = 0$ is taken, then the given PDE transforms to classical wave equation.

The analytical solution to Eq. (16) is

$$u(x, t) = e^{\operatorname{Re} \lambda t} \cos(\operatorname{Im} \lambda t) \cos(\pi x);$$

$$\operatorname{Re} \lambda = -\frac{1}{2} \frac{\sigma}{\varepsilon} \quad \text{and} \quad \operatorname{Im} \lambda = \frac{1}{2} \left(\sqrt{4\pi^2 \frac{1}{\mu \varepsilon} - \left(\frac{\sigma}{\varepsilon} \right)^2} \right).$$

For solving this problem, we suppose $u_N(x, t)$ is approximated by the truncated Pell series form

$$u_N(x, t) = \sum_{m=0}^N \sum_{n=0}^N a_{m,n} P_{m+1,n+1}(x, t), \quad (0 \leq x \leq 1, t \geq 0).$$

By using the procedure in Section 2, the fundamental matrix relations for the equation and conditions are computed and then the Pell coefficients are found. Approximate solutions of the problem were calculated by using Pell Matrix Collocation Method (PMCM) for $N = 25$, $N = 28$ and $N = 32$. Numerical results can be seen in Table 1 and Figures 1-4.

Table 1. Comparison of the absolute error for $t = 1$ and upper bound of the error for $0 \leq t \leq 4$

x	$\varepsilon = 1, \mu = 1, \sigma = 0$				$\varepsilon = 1, \mu = 1, \sigma = 1$			
	Pell Matrix Collocation Method			Spline Collocation Method [8]	Pell Matrix Collocation Method			Spline Collocation Method [8]
	$N = 25$	$N = 28$	$N = 32$		$N = 25$	$N = 28$	$N = 32$	
0.0	1.4E-07	8.8E-09	5.4E-09	2.5E-05	5.7E-08	1.2E-08	3.4E-08	1.3E-05
0.2	2.1E-07	1.1E-08	5.9E-09	2.0E-05	1.0E-07	8.6E-08	2.5E-08	1.1E-05
0.4	1.8E-06	2.3E-08	1.4E-08	2.0E-06	4.9E-07	5.9E-07	2.2E-08	1.0E-06
0.6	5.6E-06	7.4E-08	7.8E-08	2.0E-06	2.2E-06	2.3E-06	2.1E-07	1.0E-06
0.8	1.1E-05	2.1E-07	4.4E-07	2.0E-05	7.1E-06	6.4E-06	7.5E-07	1.1E-05
1.0	1.7E-05	4.0E-07	1.7E-06	2.5E-05	1.6E-05	1.4E-05	1.7E-06	1.3E-05
\overline{R}_N	2.1E-03	9.7E-04	2.3E-04	—	3.0E-03	5.3E-03	2.5E-04	—

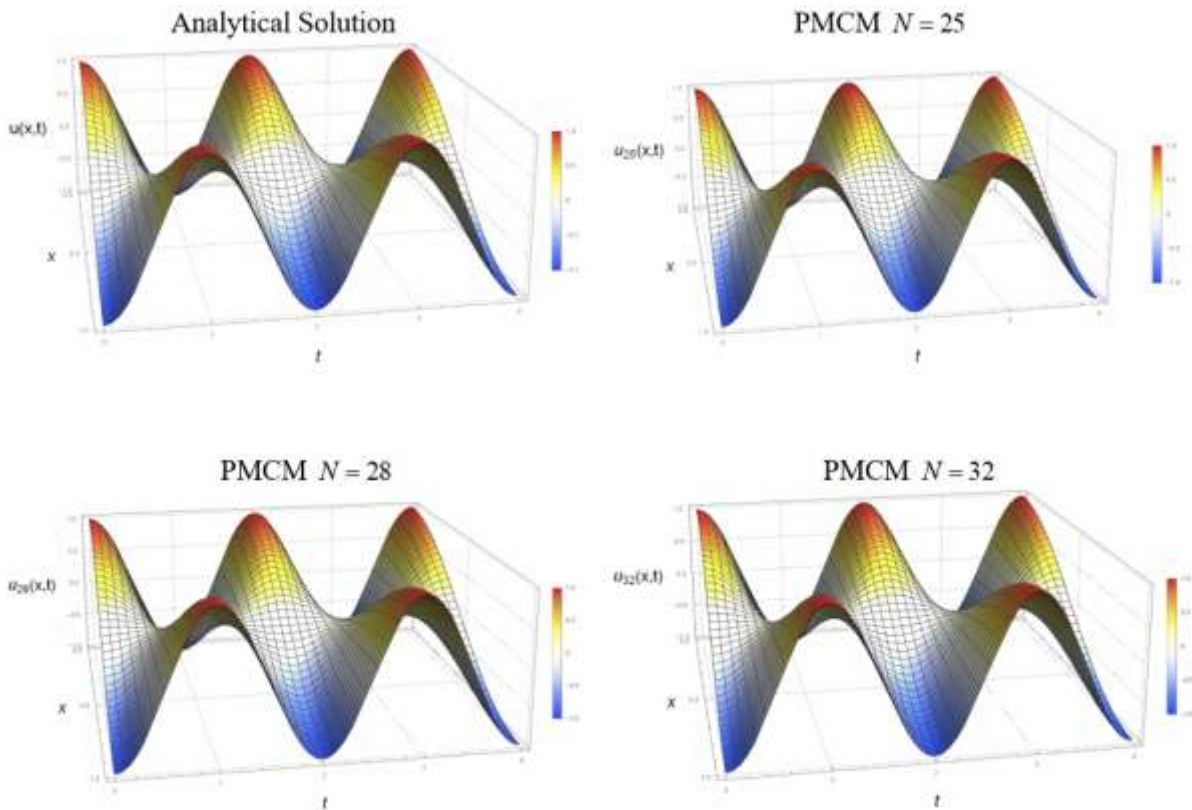


Figure 1. Analytical and approximate solutions for $\varepsilon=1$, $\mu=1$ and $\sigma=0$ (with no damping)

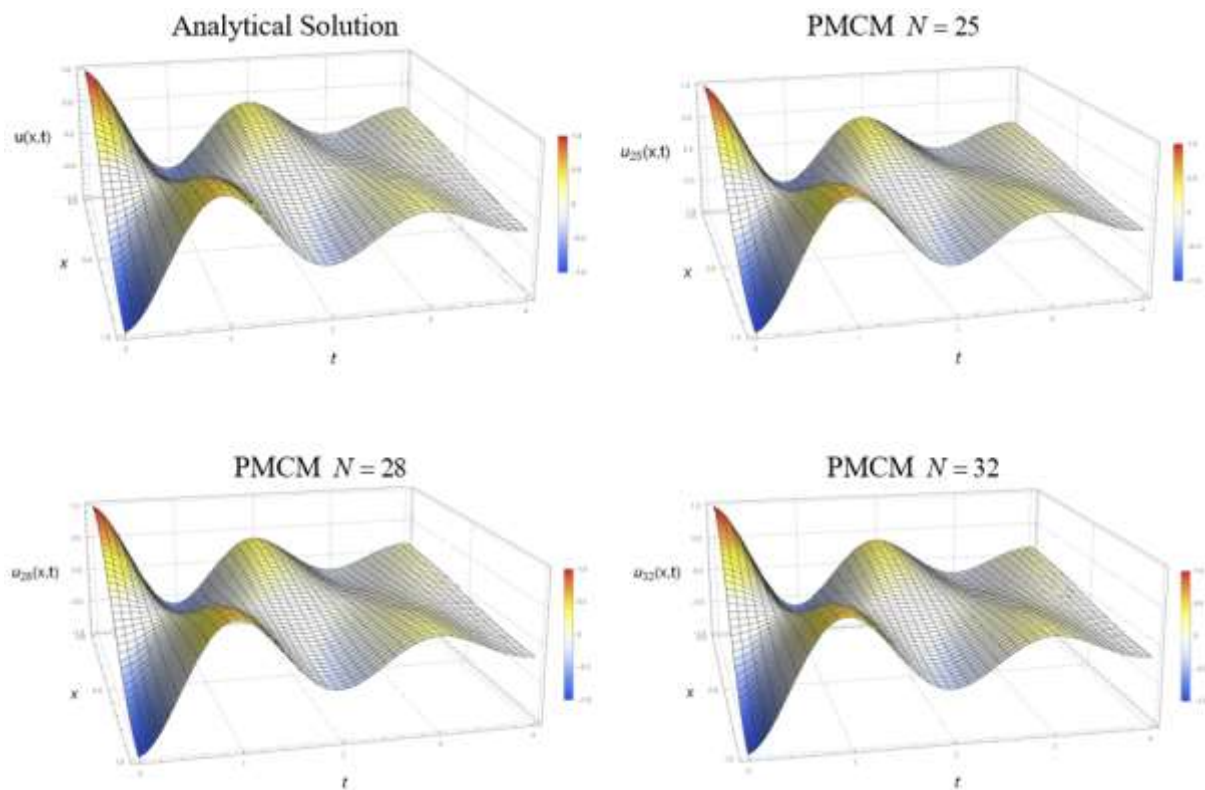


Figure 2. Analytical and approximate solutions for $\varepsilon=1$, $\mu=1$ and $\sigma=1$ (with damping)

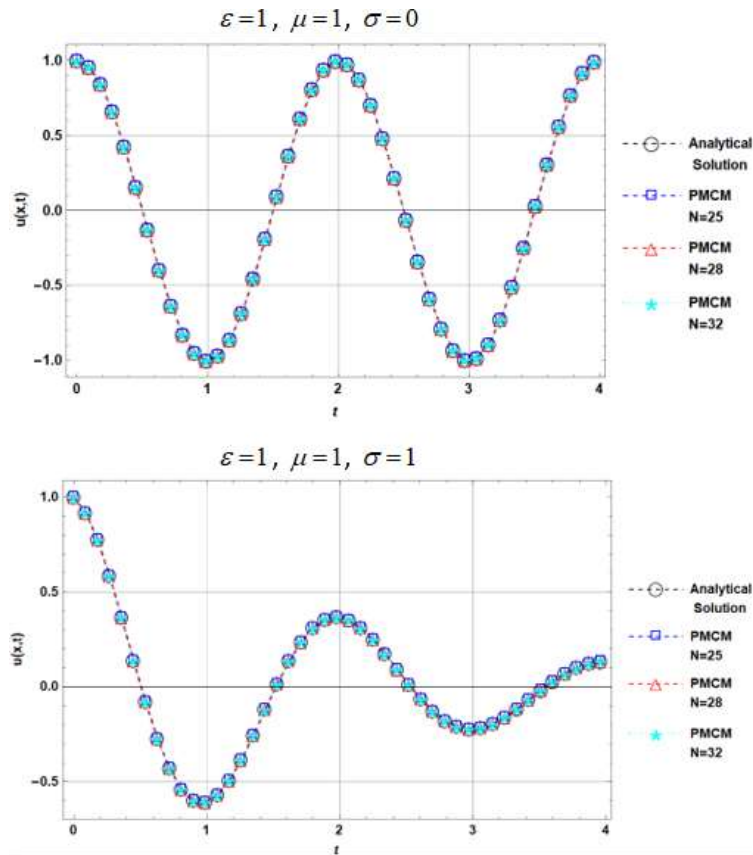


Figure 3. Comparison of the exact and approximate solutions for $x=0$

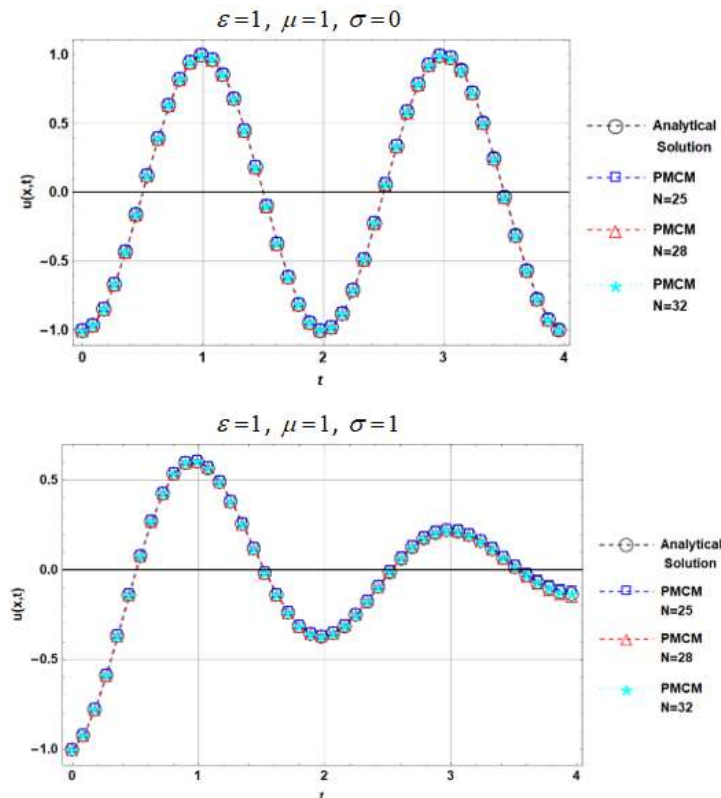


Figure 4. Comparison of the exact and approximate solutions for $x=1$

Conclusion

In the present study, we considered the one-dimensional linear damped wave equation under the initial and boundary conditions. The approximate solutions of this equation was obtained by using Pell matrix collocation method. Also, an error analysis technique based on residual function was developed for our problem.

We applied the method to a numerical example to show its usefulness and obtained numerical results for this examples. It is seen from Table 1 that the approximate solutions are close to the analytical solution when the values of N are selected high enough. In other words, the numerical results show that the accuracy improves when the values of N are increased.

References

- [1] Wazwaz A-M (2009) Partial Differential Equations and Solitary Waves Theory. Springer-Verlag Berlin Heidelberg.
- [2] Yener N (2011) A simple solution for the damped wave equation with a special class of boundary conditions using the Laplace transform. Progress in Electromagnetics Research B, 33: 69–82.
- [3] Mounim AS (2008) A space-time mixed-hybrid finite element method for the damped wave equation. Numerical Methods for Partial Differential Equations, 24(2): 368-382.
- [4] Koshy T (2014) Pell and Pell-Lucas Numbers with Applications. Springer, New York.
- [5] Djordjevic GB, Milovanovic GV (2014) Special cases of polynomials. University of Nis, Faculty of Technology, Leskovac.
- [6] Çayan S, Sezer M, Çevik M (2018) A numerical solution of Cauchy problem for partial differential equations by means of Pell polynomials. International Students Science Congress, İzmir, Proceedings, 102-108.
- [7] Bülbül B, Sezer M (2011) A Taylor matrix method for the solution of a two-dimensional linear hyperbolic equation. Applied Mathematics Letters, 24(10): 1716-1720.
- [8] Schiesser WE (2017) Spline collocation methods for partial differential equations- with applications in R. Wiley, USA.

Bernoulli Series Approach for a Class of Fredholm-type Integro-Differential Equations with Proportional Delays

Duygu Dönmez Demir*, Manisa Celal Bayar Univ., Dept. of Mathematics, Manisa, Türkiye
Alpha Peter Lukonde, Manisa Celal Bayar Univ., Institute of Natural and Applied Sciences, Manisa, Türkiye
Mehmet Sezer, Manisa Celal Bayar Univ., Dept. of Mathematics, Manisa, Türkiye
*Corresponding author: duygu.donmez@cbu.edu.tr

Keywords: Bernoulli polynomials and series, Fredholm integro-differential equations, matrix -collocation method, proportional delay

Discipline: Mathematics

Abstract

In recent years, there exists an increasing interest in models related to delay integro-differential equations in many scientific areas such as biology, physics and engineering. Furthermore, the approximation methods for this type of problems have been developed by many authors. In this study, we consider a class of high order Fredholm type integro-differential equations with proportional delays and we develop a matrix-collocation method based on finite Taylor and Bernoulli series to find the approximate solutions of this type equations subject to appropriate initial conditions. The method reduces the solution of the mentioned equations to the solution of a matrix equation corresponding to system of algebraic equations with unknown Bernoulli coefficients. Besides, the error analysis together with numerical results are introduced to illustrate the efficiency of proposed method.

1. Introduction

In this study, our main aim is to find the approximate solutions of a higher-order Fredholm-integro differential equation with proportional delays using Bernoulli polynomials. The general form of such an equation is given as

$$\sum_{k=0}^m p_k(x) y^{(k)}(\alpha_k x) = g(x) + \int_a^b \sum_{j=0}^{m_1} K_j(x,t) y^{(j)}(\beta_j t) dt; \quad m_1 \leq m, a \leq x, t \leq b \quad (1)$$

$$y^{(k)}(a) = \lambda_k; \quad k = 0, 1, 2, \dots, m-1 \quad (2)$$

where $p_k(x)$, $K_j(x,t)$ and $g(x)$ are continuous functions on the interval $a \leq x, t \leq b$; α_k and β_j are real constants defined on the open interval $(0,1)$. The approximate solution of this problem is assumed in the truncated Bernoulli series form

$$y(x) \cong y_N(x) = \sum_{n=0}^N a_n B_n(x) \quad (3)$$

where a_n ($n = 0, 1, 2, \dots, N$) are the unknown coefficients of Bernoulli polynomials $B_n(x)$. Bernoulli polynomials are defined [5] as $B_n(x) = \sum_{k=0}^n \binom{n}{k} B_k x^{n-k}$ or $\frac{ue^{ux}}{e^u - 1} = \sum_{n \geq 0} B_n(x) \frac{u^n}{n!}$ and their

derivatives are defined as $B_n'(x) = n B_{n-1}(x)$. We note that $B_n(0) = B_n$, where B_n denotes a Bernoulli number.

2. Important Matrix Relations

Using the assumed solution $y(x)$ of (1) which is given by a truncated Bernoulli series (3) for $n = 0, 1, 2, \dots, N$ we can convert the finite series (3) to the matrix form as

$$y(x) \cong y_N(x) = \mathbf{B}(x) \mathbf{A} \quad (4)$$

where

3rd International Students Science Congress
3-4 May 2019, İzmir - Turkey

$\mathbf{B}(x) = [B_0(x) B_1(x) B_2(x) \cdots B_N(x)]$; $\mathbf{A} = [a_0 a_1 a_2 \cdots a_N]^T$. Using Bernoulli Polynomials, one obtains the matrix $\mathbf{B}(x)$ as

$$\mathbf{B}(x) = \mathbf{X}(x)\mathbf{L}; \quad \mathbf{X}(x) = [1 \ x \ x^2 \ x^3 \ \cdots \ x^N] \quad (5)$$

Substituting (5) into (4), we obtain the solution $y(x)$ as follows

$$y(x) \cong y_N(x) = \mathbf{X}(x)\mathbf{L}\mathbf{A} \quad (6)$$

From (6), we obtain the derivative of $y(x)$ with respect to x as

$$y^{(k)}(x) \cong y_N^{(k)}(x) = \mathbf{X}^{(k)}(x)\mathbf{L}\mathbf{A} \quad (7)$$

where, the matrix \mathbf{L} is defined by

$$\mathbf{L} = \begin{bmatrix} \binom{0}{0}B_0 & \binom{1}{1}B_1 & \binom{2}{2}B_2 & \binom{3}{3}B_3 \cdots & \binom{N}{N}B_N \\ 0 & \binom{1}{0}B_0 & \binom{2}{1}B_1 & \binom{3}{2}B_2 \cdots & \binom{N}{N-1}B_{N-1} \\ 0 & 0 & \binom{2}{0}B_0 & \binom{3}{1}B_1 \cdots & \binom{N}{N-2}B_{N-2} \\ 0 & 0 & 0 & \binom{3}{0}B_0 \cdots & \binom{N}{N-3}B_{N-3} \\ \vdots & \vdots & \vdots & \vdots & \vdots \\ 0 & 0 & 0 & 0 \cdots & \binom{N}{0}B_0 \end{bmatrix}$$

Now, we obtain the matrix relation between the $\mathbf{X}(x)$ matrix and its derivative $\mathbf{X}^{(k)}(x)$ as follows

$$\mathbf{X}^{(k)}(x) = \mathbf{X}(x)\mathbf{C}^k; \quad k = 0, 1, 2, \dots, m \quad (8)$$

where

$$\mathbf{C} = \begin{bmatrix} 0 & 1 & 0 & \cdots & 0 \\ 0 & 0 & 2 & \cdots & 0 \\ \vdots & \vdots & \vdots & \ddots & \vdots \\ 0 & 0 & 0 & \cdots & N \\ 0 & 0 & 0 & 0 & 0 \end{bmatrix} \text{ and } \mathbf{C}^0 = \begin{bmatrix} 1 & 0 & 0 & \cdots & 0 \\ 0 & 1 & 0 & \cdots & 0 \\ 0 & 0 & 1 & \cdots & 0 \\ \vdots & \vdots & \vdots & \ddots & \vdots \\ 0 & 0 & 0 & \cdots & 1 \end{bmatrix}.$$

Substituting (8) into (7) yields

$$y^{(k)}(x) \cong y_N^{(k)}(x) = \mathbf{X}(x)\mathbf{C}^k\mathbf{L}\mathbf{A}. \quad (9)$$

Let

$$x \rightarrow \alpha_k x$$

$$y^{(k)}(\alpha_k x) = \mathbf{X}(\alpha_k x)\mathbf{C}^k\mathbf{L}\mathbf{A}; \quad (10)$$

$$\mathbf{X}(\alpha_k x) = [(\alpha_k x)^0 \ (\alpha_k x)^1 \ \cdots \ (\alpha_k x)^N].$$

Then, we obtain

$$\mathbf{X}(\alpha_k x) = \mathbf{X}(x)\mathbf{D}(\alpha_k) \quad (11)$$

where

$$D(\alpha_k) = \begin{bmatrix} \alpha_k^0 & 0 & 0 & \cdots & 0 \\ 0 & \alpha_k^1 & 0 & \cdots & 0 \\ 0 & 0 & \alpha_k^2 & \cdots & 0 \\ \vdots & \vdots & \vdots & \cdots & \vdots \\ 0 & 0 & 0 & \cdots & \alpha_k^N \end{bmatrix}.$$

Substituting (11) into (10) we get the following

$$y^{(k)}(\alpha_k x) = X(x)D(\alpha_k)C^k LA; \quad k = 0, 1, 2, \dots, m \quad (12)$$

Similarly, the matrix form of the term $y^{(j)}(\beta_j t)$ becomes

$$y^{(j)}(\beta_j t) = X(t)D(\beta_j)C^j LA; \quad j = 0, 1, 2, \dots, m_1 \quad (13)$$

Now let us write the kernel function $K_j(x, t)$, by the means of a truncated Maclaurin series, as

$$K_j(x, t) = \sum_{p=0}^N \sum_{q=0}^N k_{pq}^j x^p t^q; \quad k_{pq}^j = \frac{1}{p!q!} \frac{\partial^{p+q} K_j(0,0)}{\partial x^p \partial t^q}; \quad p, q = 0, 1, 2, \dots, N \quad (14)$$

Performing the necessary operations on (14) gives the matrix form of the kernel function as follows,

$$K_j(x, t) = X(x)K_j X^T(t); \quad K_j = [k_{pq}^j]; \quad p, q = 0, 1, \dots, N. \quad (15)$$

Substituting (12), (13) and (15) into (1) yields

$$\sum_{k=0}^m p_k(x)X(x)D(\alpha_k)C^k LA = g(x) + \sum_{j=0}^{m_1} \int_a^b X(x)K_j X^T(t)X(t)D(\beta_j)C^j LA dt \quad (16.a)$$

Since the integral is with respect to t , we get other terms out of the integral sign and integrate it as

$$Q = \int_a^b X^T(t)X(t)dt \Rightarrow Q = \int_a^b [t^{i+j}]dt \Rightarrow Q = \left[\frac{b^{i+j+1} - a^{i+j+1}}{i+j+1} \right]; \quad Q = [q_{ij}]; \quad i, j = 0, 1, \dots, N \quad (16.b)$$

Substituting (16.b) into (16.a) yields

$$\sum_{k=0}^m p_k(x)X(x)D(\alpha_k)C^k LA = g(x) + \sum_{j=0}^{m_1} X(x)K_j Q D(\beta_j)C^j LA. \quad (17)$$

Relation (17) is completely an algebraic expression which can be easily solved.

3. Collocation Method

In this section we are going to establish the fundamental matrix equation which corresponds to (1) by applying to (17) the collocation points defined by

$$x_i = a + \frac{b-a}{N}i, \quad i = 0, 1, \dots, N \quad (18)$$

Substituting (18) into (17) gives the system of matrix equations

$$\sum_{k=0}^m p_k(x_i)X(x_i)D(\alpha_k)C^k LA = g(x_i) + X(x_i) \sum_{j=0}^{m_1} K_j Q D(\beta_j)C^j LA \quad (19)$$

Applying the collocation points to (19) yields

$$\left(\underbrace{\sum_{k=0}^m P_k X D(\alpha_k) C^k L - X \sum_{j=0}^{m_1} K_j Q D(\beta_j) C^j L}_W \right) A = G; \quad P_k = \begin{bmatrix} p_k(x_0) & 0 & \cdots & 0 \\ 0 & p_k(x_1) & \cdots & 0 \\ \vdots & \vdots & \ddots & \vdots \\ 0 & 0 & \cdots & p_k(x_N) \end{bmatrix}$$

The above matrix relation can be written in the compact form as

$$WA = G \quad (20)$$

or in the augmented matrix form as

$$[W;G] = \begin{bmatrix} w_{00} & w_{01} & w_{02} & \cdots & w_{0N} & ; & g(x_0) \\ w_{10} & w_{11} & w_{12} & \cdots & w_{1N} & ; & g(x_1) \\ \vdots & \vdots & \vdots & \ddots & \vdots & ; & \vdots \\ w_{N0} & w_{N1} & w_{N2} & \cdots & w_{NN} & ; & g(x_N) \end{bmatrix}.$$

Applying the initial conditions (2) to the relation (7), we get

$$V_i = \sum_{k=0}^{m-1} (a_{ik} X(a) D(\alpha_k) C^k L) = [v_{i0} \ v_{i1} \ \cdots \ v_{iN}] \quad ; \quad V_i A = [\lambda_i] \quad \text{or} \quad [V_i; \lambda_i]; \quad i = 0, 1, 2, \dots, m-1 \quad (21)$$

Now, we going to replace m rows into the matrix equation (20) by m rows from (21) and get the new augmented matrix in the following form

$$[\tilde{W};\tilde{G}] = \begin{bmatrix} w_{00} & w_{01} & w_{02} & \cdots & w_{0N} & ; & g(x_0) \\ w_{10} & w_{11} & w_{12} & \cdots & w_{1N} & ; & g(x_1) \\ \vdots & \vdots & \vdots & \ddots & \vdots & ; & \vdots \\ w_{(N-m)0} & w_{(N-m)1} & w_{(N-m)2} & \cdots & w_{(N-m)N} & ; & g(x_{N-m}) \\ v_{00} & v_{01} & v_{02} & \cdots & v_{0N} & ; & \lambda_0 \\ v_{10} & v_{11} & v_{12} & \cdots & v_{1N} & ; & \lambda_1 \\ \vdots & \vdots & \vdots & \ddots & \vdots & ; & \vdots \\ v_{(m-1)0} & v_{(m-1)1} & v_{(m-1)2} & \cdots & v_{(m-1)N} & ; & \lambda_{m-1} \end{bmatrix}$$

When $rank \tilde{W} = rank [\tilde{W};\tilde{G}] = N+1$, then we conclude that $A = (\tilde{W})^{-1} \tilde{G}$. Here, A is the coefficient matrix of the Bernoulli series (3). Therefore, the solution of Eq. (1) is found by the Bernoulli polynomials as $y(x) \cong y_N(x) = \sum_{n=0}^N a_n B_n(x)$.

4. Residual Error and Absolute Error Analysis

Since we are obtaining approximate solutions, they are some errors or Residuals which are encountered during the process. In this section, we introduce the Residual error method and the classical absolute error method. According to [6], when the solution $y_N(x)$ and its derivatives are substituted in (1), the resulting equation must be approximately as follows;

$$R_N(x_i) = \sum_{k=0}^m p_k(x_i) y^{(k)}(\alpha_k x_i) + \int_a^b \sum_{j=0}^{m_1} K_j(x_i, t) y^{(j)}(\beta_j t) dt - g(x_i) \cong 0 \quad (22)$$

$x_i \in [a, b] (i = 0, 1, 2, \dots)$ or $R_N(x_i) \leq 10^{-k_i}$ where k_i is any positive number. Predetermining $\max 10^{-k_i} = 10^{-k}$, then the truncation limit N is increased until the difference $R_N(x_i)$ at each points smaller than predetermined 10^{-k} . Therefore, if $R_N(x_i) \rightarrow 0$ when N is sufficiently large enough, then the error decreases. The accuracy of the solution can be checked and the error can be estimated by the residual function $R_N(x)$ as expressed in [6]. Here, we use the inequality $\left| \int_a^b R_N(x) dx \right| \leq \int_a^b |R_N(x)| dx$ and the integral

mean value theorem, the upper bound of the mean error \bar{R}_N is obtained as $R_N(c) \leq \frac{a}{b-a} \int_a^b |R_N(x)| dx = \bar{R}_N$.

Absolute error is given by $R = |\text{Exact solution} - \text{Approximate solution}| = |y(x) - y_N(x)|$.

5. Numerical Examples

Example 1: Let us consider the Fredholm integro-differential equation with proportional delays

$$y''(x) + 2xy\left(\frac{1}{2}x\right) = \frac{1}{2}x^3 - \frac{129}{64}x + \frac{7}{3} + \int_0^1 xt y\left(\frac{1}{4}t\right) dt + \int_0^1 (x-t)y'\left(\frac{1}{2}t\right) dt; \quad 0 \leq x, t \leq 1 \quad (23)$$

with the initial conditions $y(0) = -1$, $y'(0) = 0$. The exact solution to this question is $y(x) = x^2 - 1$.

Now, let us find a Bernoulli polynomial solution. From (23),

$$p_0(x) = 2x, p_1(x) = 0, p_2(x) = 1, K_0(x, t) = xt, K_1(x-t), \alpha_0 = \frac{1}{2}, \alpha_1 = 0, \alpha_2 = 1, \beta_0 = \frac{1}{4}, \beta_1 = \frac{1}{2}. \text{ For } N = 2 \text{ in}$$

$[0, 1]$, the collocation points becomes $x_0 = 0$, $x_1 = \frac{1}{2}$, $x_2 = 1$. The fundamental matrix equation of the problem is

$$\left\{ \left[P_0 X D(\alpha_0) C^0 L + P_1 X D(\alpha_1) C^1 L + P_2 X D(\alpha_2) C^2 L \right] - \left[X \left(K_0 Q D(\beta_0) C^0 L + K_1 Q D(\beta_1) C^1 L \right) \right] \right\} A = G;$$

$$P_0 = \begin{bmatrix} 0 & 0 & 0 \\ 0 & 1 & 0 \\ 0 & 0 & 2 \end{bmatrix}, P_1 = \begin{bmatrix} 0 & 0 & 0 \\ 0 & 0 & 0 \\ 0 & 0 & 0 \end{bmatrix}, P_2 = \begin{bmatrix} 1 & 0 & 0 \\ 0 & 1 & 0 \\ 0 & 0 & 1 \end{bmatrix}, L = \begin{bmatrix} 1 & -\frac{1}{2} & \frac{1}{6} \\ 0 & 1 & -1 \\ 0 & 0 & 1 \end{bmatrix}, G = \begin{bmatrix} \frac{7}{3} \\ \frac{533}{384} \\ \frac{157}{192} \end{bmatrix}, K_0 = \begin{bmatrix} 0 & 0 & 0 \\ 0 & 1 & 0 \\ 0 & 0 & 0 \end{bmatrix}$$

$$C^1 = \begin{bmatrix} 0 & 1 & 0 \\ 0 & 0 & 2 \\ 0 & 0 & 0 \end{bmatrix}, C^2 = \begin{bmatrix} 0 & 0 & 2 \\ 0 & 0 & 0 \\ 0 & 0 & 0 \end{bmatrix}, C^0 = \begin{bmatrix} 1 & 0 & 0 \\ 0 & 1 & 0 \\ 0 & 0 & 1 \end{bmatrix}, Q = \begin{bmatrix} 1 & \frac{1}{2} & \frac{1}{3} \\ \frac{1}{2} & \frac{1}{3} & \frac{1}{4} \\ \frac{1}{3} & \frac{1}{4} & \frac{1}{5} \end{bmatrix}, X = \begin{bmatrix} 1 & 0 & 0 \\ 1 & \frac{1}{2} & \frac{1}{4} \\ 1 & 1 & 1 \end{bmatrix}, K_1 = \begin{bmatrix} 0 & -1 & 0 \\ 1 & 0 & 0 \\ 0 & 0 & 0 \end{bmatrix}$$

$$D(\alpha_0) = \begin{bmatrix} 1 & 0 & 0 \\ 0 & \frac{1}{2} & 0 \\ 0 & 0 & \frac{1}{4} \end{bmatrix}, D(\alpha_2) = \begin{bmatrix} 1 & 0 & 0 \\ 0 & 1 & 0 \\ 0 & 0 & 1 \end{bmatrix}, D(\beta_0) = \begin{bmatrix} 1 & 0 & 0 \\ 0 & \frac{1}{4} & 0 \\ 0 & 0 & \frac{1}{16} \end{bmatrix}, D(\beta_1) = \begin{bmatrix} 1 & 0 & 0 \\ 0 & \frac{1}{2} & 0 \\ 0 & 0 & \frac{1}{4} \end{bmatrix}$$

Performing the necessary operations on the fundamental matrix equation, the augmented matrix is obtained as

$$[W; G] = \begin{bmatrix} 0 & \frac{1}{2} & \frac{11}{6} & ; & \frac{7}{3} \\ \frac{3}{4} & -\frac{1}{6} & 263 & ; & \frac{533}{384} \\ \frac{3}{2} & -\frac{1}{3} & \frac{413}{192} & ; & \frac{157}{192} \end{bmatrix}.$$

Using (21), we apply initial conditions to $y(x)$ and get the matrices for initial conditions as

$$[v_0; \lambda_0] = \begin{bmatrix} 1 & -\frac{1}{2} & \frac{1}{6} & ; & -1 \end{bmatrix}, [v_1; \lambda_1] = \begin{bmatrix} 0 & 1 & -1 & ; & 0 \end{bmatrix}. \text{ The new augmented matrix is}$$

found by replacing two rows in the original augmented matrix with the initial condition row matrices. Therefore, the new augmented matrix is

$$[\tilde{W}; \tilde{G}] = \begin{bmatrix} 0 & \frac{1}{2} & \frac{11}{6} & ; & \frac{7}{3} \\ 1 & -\frac{1}{2} & \frac{1}{6} & ; & -1 \\ 0 & 1 & -1 & ; & 0 \end{bmatrix}.$$

After solving the system of three unknowns, Bernoulli coefficient matrix is obtained as $A = \left[-\frac{2}{3} \quad 1 \quad 1\right]^T$, $a_0 = -\frac{2}{3}$, $a_1 = 1$, $a_2 = 1$. Substituting the values of a_n into (3) for $n = 0, 1, 2$ gives the approximate solution to the problem as $y_2(x) = x^2 - 1$, which is the exact solution.

Example 2: Consider the Fredholm integro-differential equation with proportional delays

$$y''(x) + y'\left(\frac{1}{2}x\right) + xy\left(\frac{1}{3}x\right) = g(x) + \int_0^1 xt y\left(\frac{1}{4}t\right) dt + \int_0^1 (x+t)y'\left(\frac{1}{2}t\right) dt; \quad 0 \leq x, t \leq 1 \quad (24)$$

where $g(x) = e^x + e^{\frac{1}{2}x} + xe^{\frac{1}{3}x} - 1.889137542x - 0.702557458$ and $y(0) = 1, y'(0) = 1$. The exact solution to this problem is $y(x) = e^x$. Let us find the Bernoulli Polynomial solution in the form $y_N(x) = \sum_{n=0}^N a_n B_n(x)$. For $N = 2$ in $[0, 1]$, the collocation points becomes $x_0 = 0, x_1 = \frac{1}{2}, x_2 = 1$. The fundamental matrix equation of the problem is

$$\left\{ \left[P_0 X D(\alpha_0) C^0 L + P_1 X D(\alpha_1) C^1 L + P_2 X D(\alpha_2) C^2 L \right] - \left[X \left(K_0 Q D(\beta_0) C^0 L + K_1 Q D(\beta_1) C^1 L \right) \right] \right\} A = G$$

Performing the necessary operations on the fundamental matrix equation, the augmented matrix is obtained as

$$[W; G] = \begin{bmatrix} 0 & \frac{1}{2} & \frac{7}{6} & ; & 1.297442542 \\ -\frac{1}{2} & -\frac{2}{3} & \frac{253}{192} & ; & 1.876300665 \\ 0 & 0 & 9 & ; & 3.170920524 \end{bmatrix}.$$

Using (21), we apply initial conditions to $y(x)$ and get the matrices for initial conditions $[v_0; \lambda_0] = \left[1 \quad -\frac{1}{2} \quad \frac{1}{6} \quad ; \quad 1 \right]$, $[v_1; \lambda_1] = [0 \quad 1 \quad -1 \quad ; \quad 1]$. Replacing two rows in the above augmented matrix with the initial condition row matrices yields the new augmented matrix as

$$[\tilde{W}; \tilde{G}] = \begin{bmatrix} 0 & \frac{1}{2} & \frac{7}{6} & ; & 1.297442542 \\ 1 & -\frac{1}{2} & \frac{1}{6} & ; & 1 \\ 0 & 1 & -1 & ; & 1 \end{bmatrix}.$$

Solving this system of the unknowns, Bernoulli coefficient matrix is obtained as $A = [1.6594885084 \quad 1.4784655252 \quad 0.4784655252]^T$. Therefore, we obtain the approximate solution

as $y_2(x) \cong 0.9999999997 + 0.9999999998x + 0.4784655252x^2$. The numerical results are shown in Table 1, Table 3 and Figure 1 (a,b,c). Figure 2 indicate the Residual functions. For $N=4,6$, the obtained approximate solutions are

$$y_4(x) \cong 1 + x + 0.4994668468x^2 + 0.1525443523x^3 + 0.0640013638200139x^4$$

$$y_6(x) \cong 0.9999999998 + 0.9999999998x + 0.5007086331x^2 + 0.1924559694x^3 - 0.01698894335x^4 + 0.05848558444x^5 - 0.0134727664379862x^6$$

Example 3: Consider

$$y'(x) + \sin(x)y\left(\frac{1}{2}x\right) = g(x) + \int_0^1 x^2 t y\left(\frac{1}{2}t\right) dt; \quad 0 \leq x, t \leq 1 \quad (25)$$

where $g(x) = \cos(x) + \sin(x)\sin\left(\frac{1}{2}x\right) - \left[4\sin\left(\frac{1}{2}\right) - 2\cos\left(\frac{1}{2}\right)\right]x^2$ and $y(0) = 0$. The exact solution of the problem is $y(x) = \sin(x)$. The results are given in Table 2 and Figure 1 (d), Table 4 shows the absolute errors. The Bernoulli Polynomial approximate solution is obtained for $N=3$. Therefore, the approximate solution is

$$y_3(x) \cong 5 \cdot 10^{-11} + 0.9999999994x - 0.0219236103x^2 - 0.1382358560x^3.$$

Table 1. The comparison of the exact solution $y(x)$ and the approximate solution $y_N(x)$

x	Exact	Approximate $y_2(x)$	Approximate $y_4(x)$	Approximate $y_6(x)$
0	1	0.9999999997	1	0.9999999998
0.2	1.221402758	1.219138621	1.221301431	1.221558664
0.4	1.491824698	1.476554484	1.491315969	1.492539354
0.6	1.822118800	1.772247589	1.821052222	1.823543084
0.8	2.225540928	2.106217936	2.223976449	2.227665061
1	2.718281828	2.478465525	2.716012563	2.721188477

Table 2. The comparison of the exact solution $y(x)$ and the approximate solution $y_N(x)$

x	Exact	Approximate $y_3(x)$
0	0	$5 \cdot 10^{-11}$
0.2	0.1986693308	0.1980171688
0.4	0.3894183423	0.3876451274
0.6	0.5646424734	0.5622485550
0.8	0.7173560909	0.7151921307
1	0.8414709848	0.8398405331

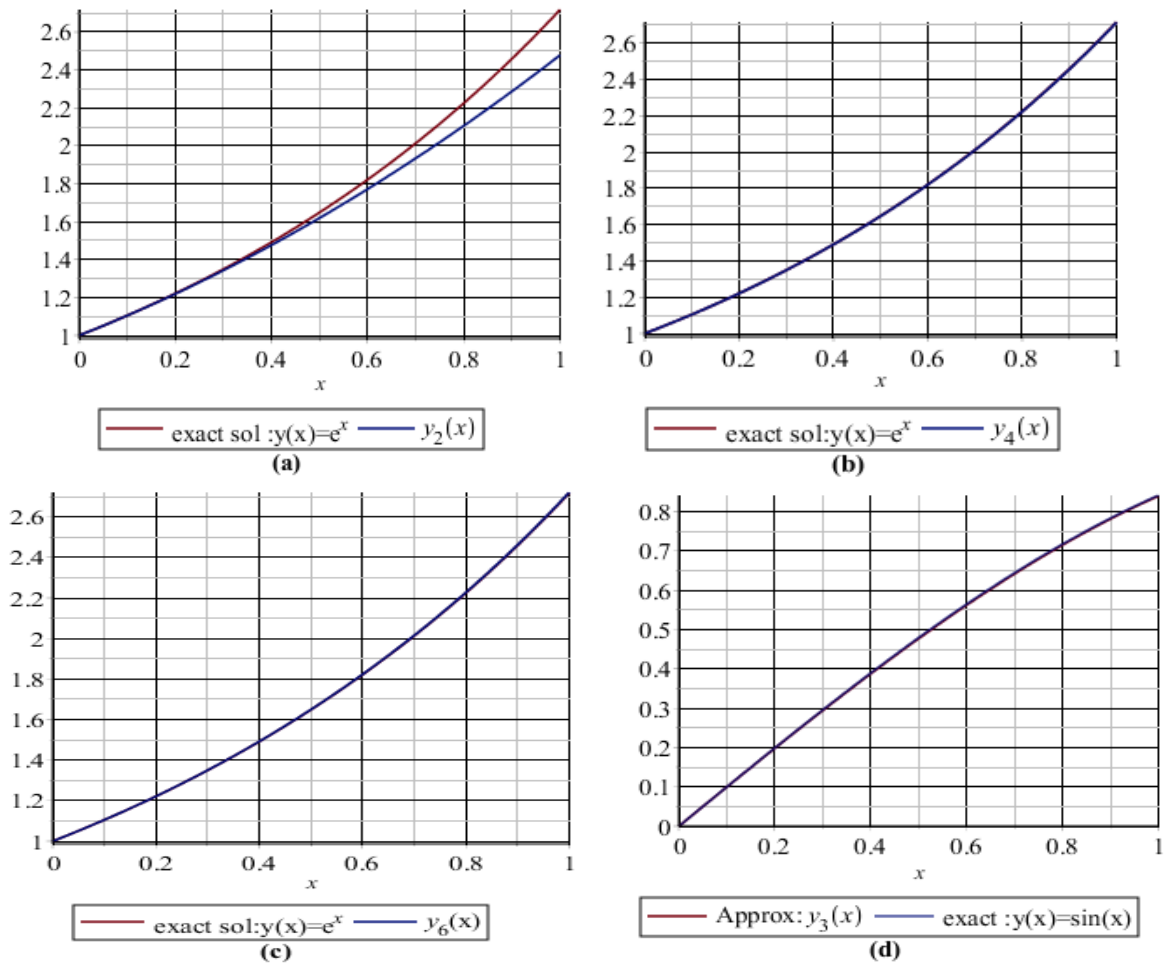


Figure 1. The comparisons of the exact and the approximate solutions of Example 2 (a,b,c) and Example 3 (d)

Table 3. Absolute errors for Example 2

x	$N=2$	$N=4$	$N=6$
0	$3 \cdot 10^{-10}$	0	0
0.2	0.002264137	0.000101371299	0.000155906
0.4	0.015270214	0.000508729049	0.000714656
0.6	0.049871211	0.001066578349	0.001424284
0.8	0.119322992	0.001564476900	0.002124133
1	0.239816303	0.002269265	0.002906649

Table 4. Absolute error for Example 3

x	$N=3$
0	$5 \cdot 10^{-11}$
0.2	0.000652162160
0.4	0.001773214832
0.6	0.00239391841
0.8	0.00216396016
1	0.0016304517

The residual errors for Example 2 are calculated as $\bar{R}_2 = 0.7488675254$, $\bar{R}_4 = 0.006345928358$ and $\bar{R}_6 = 0.004032751582$. For Example 3, the residual error is $\bar{R}_3 = 0.001564528482$.

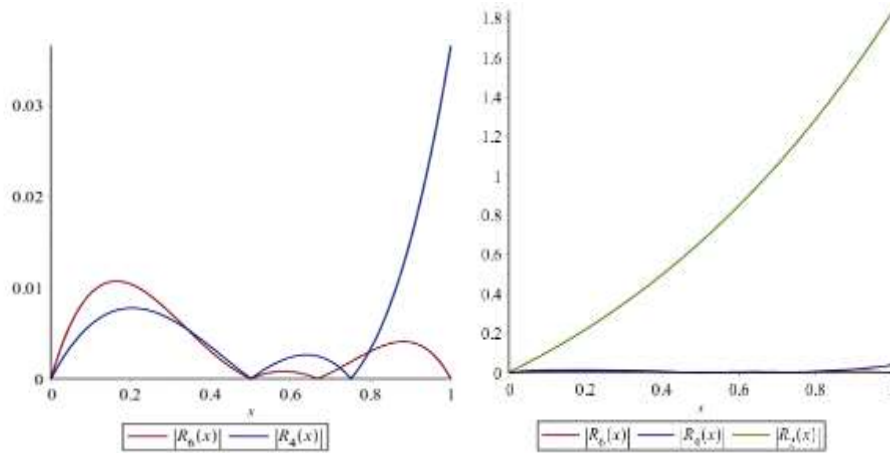


Figure 2. Residual functions in Example 2

6. Conclusion

In this study, we introduce a Bernoulli matrix-collocation method for solving a Fredholm type integro-differential equation with proportional delays. To check the accuracy of the solution, we present the method of error analysis. The proposed method and its error analysis is applied to some numerical examples. Comparisons of the numerical results with the exact solution shows that as N becomes larger the approximate solution becomes closer to the exact solution. The graphical representations also shows how close the approximate solution is to the exact solution. The advantage of the method is that this type of problems can be easily solved using computer programs such as MAPLE, MATLAB and MATHEMATICA. In this study, numerical examples are calculated by using MAPLE. Consequently this method can also be extended to different types of equations.

References

- [1] Erdem K, Yalçınbaş S, Sezer M (2013) A Bernoulli polynomial approach with residual correction for solving mixed linear Fredholm integro-differential-difference equations. *J. Differ. Equ. Appl.* 19(10): 1619-1631.
- [2] Chen X, Wang L (2010) The variational iteration method for solving a neutral functional-differential equation with proportional delays. *Computers & Mathematics with Applications* 59(8): 2696-2702.
- [3] Chu W, Shou RR (2010) Convolutions of Bernoulli and Euler polynomials. *Sarajevo Journal of Mathematics* 6(18): 147-163.
- [4] Biazar J, Ghanbari B (2012) The homotopy perturbation method for solving neutral functional-differential equations with proportional delays. *Journal of King Saud Univ.-Science* 24: 33-37.
- [5] Baykuş Savaşaneril N, Sezer M (2017) Hybrid Taylor-Lucas collocation method for numerical solution of high-order Pantograph type delay differential equations with variables delays. *Appl. Math. Inf. Sci.* 11(6) 1795-1801.
- [6] Dönmez Demir D, Çınardalı T, Kürkçü Ö K, Sezer M (2019) The Legendre matrix-collocation approach for some nonlinear differential equations arising in physics and mechanics. *European Journal of Science and Technology* 15:289-296.

A Numerical Technique Based on Boole Polynomials for Solving Fredholm Integro-Differential Equations

Hale Gül Dağ*, Kübra Erdem Biçer

Manisa Celal Bayar Univ., Dept. of Mathematics, Manisa, Türkiye

*Corresponding author: halegul.dag@hotmail.com

Keywords: numerical methods, approximate solutions; integro-differential equations, Boole polynomials

Discipline: Mathematics

Abstract

The main purpose of this study is to improve a method based on Boole polynomials and collocation points for solving Fredholm integro-differential equations approximately. For this purpose, primarily the approximate solution is written in terms of Boole polynomials. Using Boole polynomials, their derivatives and collocation points, a matrix equation is obtained. Then the main problem reduces to a matrix equation which corresponds to a system of linear algebraic equations. After solving this system, the unknown Boole coefficients of the approximate solution of given problem are obtained. The solutions are obtained as the truncated Boole series which are defined in the interval $[a, b]$. To demonstrate validity and applicability of this technique, it is applied to boundary-value problems and also an error analysis is developed. All numerical computations have been performed on the computer programs. The numerical results obtained by using this method are compared in tables and figures.

Introduction

The integro differential equations, which are an important part of applied mathematics is intertwined with of problems arising from the real world. For this reason, integro differential equation systems are frequently encountered in science, such as physics, biology, engineering, chemistry and electrostatic. Since the analytical solution of these systems of equations is difficult; methods such as the differential transform method [17], the Bernoulli polynomial approach method [4], the exponential method [19], the Bernstein operational matrix approach method [18], the Tau numerical solution method [1], the Bernoulli matrix-collocation method [6], the Bessel matrix method [11], the Taylor collocation method [5], the Modified decomposition method [16], the Adomian's decomposition method [12], the Laguerre polynomial solution method [13], the Spectral Homotopy Analysis Method [14] and the Taylor matrix method [20] are preferred as a numerical solution [2],[3],[7],[8],[9],[10].

In this study, a numerical method based on Boole polynomial is developed in order to solve the m th order linear Fredholm integro-differential equations. In this method, Fredholm integro differential equation is associated with Boole derivatives and is reduced from the system of linear algebraic equation to the system of matrix equations. Boole collocation method is also be used to reach the solution. The examples which have exact and approximate solutions are given in order to demonstrate the applicability of this method. In addition, the available results are compared. An approximate solution will be sought of the m th order linear Fredholm integro-differential equation

$$\sum_{k=0}^m P_k(x)y^{(k)}(x) = g(x) + \lambda \int_a^b K(x,t)y(t)dt, \quad a \leq x, t \leq b \quad (1)$$

with mixed conditions

$$\sum_{k=0}^{m-1} (a_{jk}y^k(a) + b_{jk}y^k(b)) = \lambda_j; \quad j = 0,1,2,3, \dots, m-1 \quad (2)$$

where $y^{(k)}(x)$ is an unknown function, the known function $P_k(x)$, $g(x)$ and kernel function $K(x, t)$ are defined in the interval $a \leq x, t \leq b$. a_{jk} , b_{jk} and λ_j are fixed numbers. The aim is to obtain the approximate solution of Eq. (1) in the form of the Boole polynomial given below

$$y(x) \cong y_N(x) = \sum_{n=0}^N a_n R_n(x) \quad (3)$$

where $R_n(x)$ is the Boole polynomial and $a_n, n=0,1,2,\dots,N$ is the unknown coefficients of the Boole polynomial. Charles Jordan has stated the general equation of the Boole polynomial as follows [21].

$$R_n(x) = \sum_{m=0}^{n+1} \frac{(-1)^m}{2^m} \binom{x}{n-m} \quad (4)$$

The defined form of the Boole polynomial is

$$\sum_{n=0}^{\infty} \frac{R_n(x)}{n!} t^n = \frac{2(1+t)^x}{2+t}. \quad (5)$$

Fundamental Matrix Relations

The matrix relation of Boole polynomial is written as

$$\mathbf{R}(x) = \mathbf{X}(x)\mathbf{H}^T \quad (6)$$

where \mathbf{H}^T is coefficient matrix and also

$$\mathbf{R}(x) = [R_0(x) \ R_1(x) \ R_2(x) \ R_3(x) \ \dots \ R_N(x)],$$

$$\mathbf{R}(x) = \left[1 \quad x - \frac{1}{2} \quad x^2 - 2x + \frac{1}{2} \quad x^3 - \frac{9}{2}x^2 + 5x - \frac{3}{4} \quad \dots \quad R_N(x) \right],$$

$$\mathbf{X}(x) = [1 \quad x \quad x^2 \quad x^3 \quad \dots \quad x^N],$$

$$\mathbf{H} = \begin{bmatrix} 1 & 0 & 0 & 0 & 0 & \dots \\ -\frac{1}{2} & 1 & 0 & 0 & 0 & \dots \\ \frac{1}{2} & -2 & 1 & 0 & 0 & \dots \\ -\frac{3}{4} & 5 & -\frac{9}{2} & 1 & 0 & \dots \\ \frac{3}{2} & -16 & 20 & -8 & 1 & \dots \\ \vdots & \vdots & \vdots & \vdots & \vdots & \dots \\ \vdots & \vdots & \vdots & \vdots & \vdots & \dots \end{bmatrix} \text{ and } \mathbf{H}^T = \begin{bmatrix} 1 & -\frac{1}{2} & \frac{1}{2} & -\frac{3}{4} & \frac{3}{2} & \dots \\ 0 & 1 & -2 & 5 & -16 & \dots \\ 0 & 0 & 1 & -\frac{9}{2} & 20 & \dots \\ 0 & 0 & 0 & 1 & -8 & \dots \\ 0 & 0 & 0 & 0 & 1 & \dots \\ \vdots & \vdots & \vdots & \vdots & \vdots & \dots \\ \vdots & \vdots & \vdots & \vdots & \vdots & \dots \end{bmatrix}.$$

The Eq. (1) is written in the form below

$$L(x) = g(x) + \lambda I(x) \quad (7)$$

where

$$L(x) = \sum_{k=0}^m P_k(x) y^{(k)}(x) \text{ and } I(x) = \int_a^b K(x,t)y(t)dt.$$

Matrix Relation for the Differential Part $L(x)$

The matrix relation is shown for the solution $y(x)$ as

$$y(x) = \mathbf{R}(x)\mathbf{A} \quad (8)$$

and the k th derivative of the solution $y(x)$ is

$$y^{(k)}(x) = \mathbf{R}^{(k)}(x)\mathbf{A}. \quad (9)$$

If the Eq. (6) is written in this matrix relation, the following form is obtained.

$$y^{(k)}(x) = \mathbf{X}^{(k)}(x)\mathbf{H}^T\mathbf{A} \quad (10)$$

Since it is

$$\mathbf{X}^{(k)}(x) = \mathbf{X}(x)\mathbf{E}^k \quad (11)$$

in this form, the new equation is obtained as

$$y^{(k)}(x) = \mathbf{X}(x)\mathbf{E}^k\mathbf{H}^T\mathbf{A} \quad (12)$$

where

$$\mathbf{E} = \begin{bmatrix} 0 & 1 & 0 & 0 & \dots & 0 \\ 0 & 0 & 2 & 0 & \dots & 0 \\ \cdot & \cdot & \cdot & \cdot & \dots & \cdot \\ \cdot & \cdot & \cdot & \cdot & \dots & \cdot \\ \cdot & \cdot & \cdot & \cdot & \dots & \cdot \\ 0 & 0 & 0 & 0 & \dots & k \\ 0 & 0 & 0 & 0 & \dots & 0 \end{bmatrix} \text{ and } \mathbf{A} = \begin{bmatrix} a_0 \\ a_1 \\ a_2 \\ \cdot \\ \cdot \\ a_N \end{bmatrix}. a_0, a_1, \dots, a_N \text{ is unknown Boole coefficients.}$$

According to the Eq. (6) the Eq. (12) is written as

$$y^{(k)}(x) = \mathbf{R}(x)(\mathbf{H}^T)^{-1}\mathbf{E}^k\mathbf{H}^T\mathbf{A} \quad (13)$$

or

$$y^{(k)}(x) = \mathbf{R}(x)\mathbf{D}^k\mathbf{A} \quad (14)$$

where

$$\mathbf{D}^k = (\mathbf{H}^T)^{-1}\mathbf{E}^k\mathbf{H}^T.$$

So, matrix \mathbf{D} is derivative transition matrix of Boole polynomial. In that time, the general matrix form of the differential part is obtained as

$$L(x) = \sum_{k=0}^m P_k(x) \mathbf{R}(x)\mathbf{D}^k\mathbf{A}. \quad (15)$$

Matrix Relation for the Integral Part $I(x)$

Integral part of m th order linear Fredholm integro-differential equation is defined by

$$I(x) = \int_a^b K(x, t)y(t)dt. \quad (16)$$

If the Eq. (8) is placed in this form, the following matrix relation as

$$I(x) = \int_a^b K(x, t)\mathbf{R}(t)\mathbf{A}dt \quad (17)$$

is obtained. The form of the kernel function $K(x, t)$ for Taylor polynomial is expressed by

$$K(x, t) = \mathbf{X}(x)^T \mathbf{K}_{rs} \mathbf{X}^T(t) \quad (18)$$

where

$$K(x, t) = \sum_{r=0}^N \sum_{s=0}^N {}^T k_{mn}^{rs} x^m t^n \rightarrow {}^T k_{mn}^{rs} = \frac{1}{m!n!} \frac{\partial^{m+n} k_{rs}(0,0)}{\partial x^m \partial t^n}, \quad m, n = 0, 1, 2, \dots, N$$

and

$${}^T \mathbf{K}_{rs} = \begin{bmatrix} k_{00} & k_{01} & k_{02} & \dots & k_{0n} \\ k_{10} & k_{11} & k_{12} & \dots & k_{1n} \\ \cdot & \cdot & \cdot & \dots & \cdot \\ \cdot & \cdot & \cdot & \dots & \cdot \\ \cdot & \cdot & \cdot & \dots & \cdot \\ k_{m0} & k_{m1} & k_{m2} & \dots & k_{mn} \end{bmatrix}.$$

Same way, the form of the kernel function $K(x, t)$ of the m th order linear Fredholm integro-differential equation for Boole polynomial is expressed by

$$K(x, t) = \mathbf{R}(x) {}^R \mathbf{K}_{rs} \mathbf{R}^T(t) \quad (19)$$

where

$$K(x, t) = \sum_{r=0}^N \sum_{s=0}^N {}^R k_{mn}^{rs} R_m(x) R_n(t), \quad m, n = 0, 1, 2, \dots, N.$$

From (18) and (19), the following matrix relation is obtained.

$${}^R\mathbf{K}_{rs} = (\mathbf{H}^T)^{-1T} \mathbf{K}_{rs} \mathbf{H}^{-1} \quad (20)$$

If the Eq. (19) is placed in the Eq. (17), the following matrix relation is obtained for the integral part of the m th order linear Fredholm integro-differential equation.

$$\mathbf{I}(x) = \int_a^b \mathbf{R}(x) {}^R\mathbf{K}_{rs} \mathbf{R}^T(t) \mathbf{R}(t) \mathbf{A} dt \quad (21)$$

Then, integral part becomes the

$$\mathbf{I}(x) = \mathbf{R}(x) {}^R\mathbf{K}_{rs} \mathbf{Q} \mathbf{A} \quad (22)$$

where

$$\mathbf{Q} = \int_a^b \mathbf{R}^T(t) \mathbf{R}(t) dt.$$

Matrix Relation for Conditions

The corresponding matrix form of conditions (2) can be obtained by Eq. (14) as

$$\sum_{k=0}^{m-1} (a_{jk} \mathbf{R}(a) + b_{jk} \mathbf{R}(b)) \mathbf{D}^k \mathbf{A} = \lambda_k; \quad j = 0, 1, 2, \dots, m-1. \quad (23)$$

Collocation Method

Matrix relations (15) and (22) are substituted in the Eq. (7) to form the main matrix equation to the Eq. (1). Thus

$$\sum_{k=0}^m P_k(x) \mathbf{R}(x) \mathbf{D}^k \mathbf{A} = g(x) + \lambda \mathbf{R}(x) {}^R\mathbf{K}_{rs} \mathbf{Q} \mathbf{A} \quad (24)$$

is the main matrix equation. The collocation points x_i are defined as

$$x_i = a + \frac{b-a}{N} i, \quad i = 0, 1, \dots, N. \quad (25)$$

By using this points the following matrix equation is obtained.

$$\sum_{k=0}^m P_k(x_i) \mathbf{R}(x_i) \mathbf{D}^k \mathbf{A} = g(x_i) + \lambda \mathbf{R}(x_i) {}^R\mathbf{K}_{rs} \mathbf{Q} \mathbf{A} \quad (26)$$

It is briefly shown as

$$\left\{ \sum_{k=0}^m \mathbf{P}_k(x_i) \mathbf{R}(x_i) \mathbf{D}^k - \lambda \mathbf{R}(x_i) {}^R\mathbf{K}_{rs} \mathbf{Q} \right\} \mathbf{A} = \mathbf{G} \quad (27)$$

where

$$\mathbf{P}_k(x_i) = \begin{bmatrix} \mathbf{P}_k(x_0) & 0 & \dots & 0 \\ 0 & \mathbf{P}_k(x_1) & \dots & 0 \\ \vdots & \vdots & \ddots & \vdots \\ \vdots & \vdots & \ddots & \vdots \\ \vdots & \vdots & \ddots & \vdots \\ 0 & 0 & \dots & \mathbf{P}_k(x_N) \end{bmatrix}, \quad \mathbf{G} = \begin{bmatrix} g(x_0) \\ g(x_1) \\ \vdots \\ g(x_N) \end{bmatrix} \text{ and}$$

$$\mathbf{R}(x_i) = \begin{bmatrix} R_0(x_0) & R_1(x_0) & R_2(x_0) & R_3(x_0) & \dots & R_N(x_0) \\ R_0(x_1) & R_1(x_1) & R_2(x_1) & R_3(x_1) & \dots & R_N(x_1) \\ \vdots & \vdots & \vdots & \vdots & \ddots & \vdots \\ \vdots & \vdots & \vdots & \vdots & \ddots & \vdots \\ R_0(x_N) & R_1(x_N) & R_2(x_N) & R_3(x_N) & \dots & R_N(x_N) \end{bmatrix}.$$

The matrix Eq. (27) of Eq. (1) is written as

$$\mathbf{WA} = \mathbf{G} \text{ or } [\mathbf{W}; \mathbf{G}] \quad (28)$$

where

$$\mathbf{W} = \sum_{k=0}^m \mathbf{P}_k(x_i) \mathbf{R}(x_i) \mathbf{D}^k - \lambda \mathbf{R}(x_i)^R \mathbf{K}_{rs} \mathbf{Q}.$$

As a result of all these operations, a system of $(N + 1)$ linear algebraic equation is gained with unknown Boole coefficients a_0, a_1, \dots, a_N . Also the matrix form of the conditions (23) is written as

$$\mathbf{U}_j \mathbf{A} = [\lambda_i] \text{ ya da } [U_i; \lambda_i]; \quad j = 0, 1, 2, \dots, m - 1 \quad (29)$$

where

$$\mathbf{U}_j = \sum_{k=0}^{m-1} (a_{jk} \mathbf{R}(a) + b_{jk} \mathbf{R}(b)) \mathbf{D}^k = [u_{j0} \quad u_{j1} \quad u_{j2} \quad \dots \quad u_{jN}], \quad j = 0, 1, 2, \dots, m - 1.$$

To arrive the solution of Eq. (1) under conditions (2), the following augmented matrix is regulated by replacing the row matrices (29) by the last m rows of the matrix. Thus, new augmented matrix is obtained as

$$\tilde{\mathbf{W}} \mathbf{A} = \tilde{\mathbf{G}}.$$

In that case, augmented matrix system is written as

$$[\tilde{\mathbf{W}}; \tilde{\mathbf{G}}] = \begin{bmatrix} w_{00} & w_{01} & w_{02} & \dots & w_{0N} & ; & g(x_0) \\ w_{10} & w_{11} & w_{12} & \dots & w_{1N} & ; & g(x_1) \\ \cdot & \cdot & \cdot & \dots & \cdot & \cdot & \cdot \\ \cdot & \cdot & \cdot & \dots & \cdot & \cdot & \cdot \\ \cdot & \cdot & \cdot & \dots & \cdot & \cdot & \cdot \\ w_{(N-m)0} & w_{(N-m)1} & w_{(N-m)2} & \dots & w_{(N-m)N} & ; & g(x_{N-m}) \\ u_{00} & u_{01} & u_{02} & \dots & u_{0N} & ; & \lambda_0 \\ u_{10} & u_{11} & u_{12} & \dots & u_{1N} & ; & \lambda_1 \\ \cdot & \cdot & \cdot & \dots & \cdot & \cdot & \cdot \\ \cdot & \cdot & \cdot & \dots & \cdot & \cdot & \cdot \\ \cdot & \cdot & \cdot & \dots & \cdot & \cdot & \cdot \\ u_{(m-1)0} & u_{(m-1)1} & u_{(m-1)2} & \dots & u_{(m-1)N} & ; & \lambda_{m-1} \end{bmatrix}. \quad (30)$$

If $\text{rank} \tilde{\mathbf{W}} = \text{rank} [\tilde{\mathbf{W}}; \tilde{\mathbf{G}}] = N + 1$ is, the augmented matrix is written as

$$\mathbf{A} = (\tilde{\mathbf{W}})^{-1} \tilde{\mathbf{G}}. \quad (31)$$

When the Boole coefficients a_0, a_1, \dots, a_N are substituted in Eq. (3), $y_N(x)$ is obtained. Since $y_N(x)$ is a solution of the Eq. (1), $y_N(x)$ should provide this equation approximately when $y_N(x)$ and its derivatives are written in Eq. (1). So the absolute error function can be obtained as follows

$$e(x_q) = |y_N(x_q) - y(x_q)| \cong 0 \quad (32)$$

for $\forall x = x_q \in [a, b]$.

Numerical Examples

Example 1: Firstly, linear Fredholm integro-differential equation given as

$$y''(x) - 2xy'(x) = -\frac{39}{10}x^2 + 4x + 2 - 3 \int_0^1 x^2 t^2 y(t) dt, \quad 0 \leq x, t \leq 1 \quad (33)$$

with the boundary conditions $y(0) = 1, y(1) = 0$ and the approximate solution by the truncated Boole series

$$y(x) = \sum_{n=0}^N a_n R_n(x)$$

3rd International Students Science Congress
3-4 May 2019, İzmir - Turkey

is discussed where $N = 3$, $P_0(x) = 1$, $P_1(x) = -2x$, $\lambda = -3$, $g(x) = -\frac{39}{10}x^2 + 4x + 2$, $a = 0$, $b = 1$ and $K(x, t) = x^2t^2$. The collocation points (25) for $N = 3$ are calculated as

$$\left\{x_0 = 0, x_1 = \frac{1}{3}, x_2 = \frac{2}{3}, x_3 = 1\right\}$$

and from Eq. (27), the fundamental matrix equation of the problem is

$$[\mathbf{P}_0\mathbf{R}\mathbf{D}^2 + \mathbf{P}_1\mathbf{R}\mathbf{D} - \lambda \mathbf{R}^R\mathbf{K}_{rs}\mathbf{Q}]\mathbf{A} = \mathbf{G}.$$

After some operations, the following matrices are obtained.

$$\mathbf{P}_0 = \begin{bmatrix} 1 & 0 & 0 & 0 \\ 0 & 1 & 0 & 0 \\ 0 & 0 & 1 & 0 \\ 0 & 0 & 0 & 1 \end{bmatrix}, \mathbf{P}_1 = \begin{bmatrix} 0 & 0 & 0 & 0 \\ 0 & -\frac{2}{3} & 0 & 0 \\ 0 & 0 & -\frac{4}{3} & 0 \\ 0 & 0 & 0 & -2 \end{bmatrix}, \mathbf{D} = \begin{bmatrix} 0 & 1 & 0 & 0 \\ 0 & 0 & 2 & 0 \\ 0 & 0 & 0 & 3 \\ 0 & 0 & 0 & 0 \end{bmatrix}, \mathbf{G} = \begin{bmatrix} 2 \\ 29 \\ 10 \\ 44 \\ 15 \\ 21 \\ 10 \end{bmatrix},$$

$$\mathbf{R} = \begin{bmatrix} 1 & -\frac{1}{2} & \frac{1}{2} & -\frac{3}{4} \\ 1 & -\frac{1}{6} & -\frac{1}{18} & \frac{49}{108} \\ 1 & \frac{1}{6} & -\frac{7}{18} & \frac{108}{95} \\ 1 & \frac{1}{2} & -\frac{1}{2} & \frac{3}{4} \end{bmatrix}, {}^R\mathbf{K}_{rs} = \begin{bmatrix} \frac{1}{4} & 1 & \frac{1}{2} & 0 \\ 1 & 4 & 2 & 0 \\ \frac{1}{2} & 2 & 1 & 0 \\ 0 & 0 & 0 & 0 \end{bmatrix}, \mathbf{Q} = \begin{bmatrix} 1 & 0 & -\frac{1}{6} & \frac{1}{2} \\ 0 & \frac{1}{12} & -\frac{1}{12} & \frac{7}{60} \\ -\frac{1}{6} & -\frac{1}{12} & \frac{7}{60} & -\frac{13}{60} \\ \frac{1}{2} & \frac{7}{60} & -\frac{13}{60} & \frac{779}{1680} \end{bmatrix} \text{ and } \mathbf{A} = \begin{bmatrix} a_0 \\ a_1 \\ a_2 \\ a_3 \end{bmatrix}.$$

The augmented matrix for this fundamental matrix equation is calculated as

$$[\mathbf{W}; \mathbf{G}] = \begin{bmatrix} 0 & 0 & 2 & -9 & ; & 2 \\ 1 & 23 & 128 & 127 & ; & 29 \\ 9 & -36 & 45 & -15 & ; & 10 \\ 4 & 11 & 122 & 229 & ; & 44 \\ 9 & -9 & 45 & -45 & ; & 15 \\ 1 & 7 & 8 & 1 & ; & 21 \\ 1 & -\frac{7}{4} & \frac{8}{5} & -\frac{1}{5} & ; & \frac{10}{10} \end{bmatrix}.$$

From Eq. (29), the matrix form for the boundary conditions become

$$[\mathbf{U}_0; \lambda_0] = \left[1 \quad -\frac{1}{2} \quad \frac{1}{2} \quad -\frac{3}{4} \quad ; \quad 1\right] \text{ and } [\mathbf{U}_1; \lambda_1] = [0 \quad 1 \quad -2 \quad 5 \quad ; \quad -2].$$

From Eq. (30), the new augmented matrix based on the conditions is calculated as

$$[\mathbf{W}; \mathbf{G}] = \begin{bmatrix} 0 & 0 & 2 & -9 & ; & 2 \\ 1 & 23 & 128 & 127 & ; & 29 \\ 9 & -36 & 45 & -15 & ; & 10 \\ 1 & -\frac{1}{2} & \frac{1}{2} & -\frac{3}{4} & ; & 1 \\ 0 & 1 & -2 & 5 & ; & -2 \end{bmatrix}.$$

The unknown Boole coefficients are found from the solution of this matrix as

$$\mathbf{A} = \begin{bmatrix} \frac{1}{2} & 0 & 1 & 0 \end{bmatrix}.$$

As a result, if the Boole coefficients are placed in the Eq. (3), $y(x) = x^2 - 2x + 1$ is the approximate solution. This is the exact solution.

Example 2: In this example, linear Fredholm integro-differential equation is given as

3rd International Students Science Congress
3-4 May 2019, İzmir - Turkey

$$y^l(x) = (x + 1)e^x - x + \int_0^1 xy(t)dt, 0 \leq x, t \leq 1. \quad (34)$$

Exact solution is $y(x) = xe^x$ and boundary condition $y(0) = 0$ [15]. The fundamental matrix equation of the problem is

$$[P_0RD - \lambda R^R K_{rs} Q]A = G.$$

At that time, if necessary operations are taken, the following approximate solutions are calculated for $N = 5, N = 7$ and $N = 10$.

$$\begin{aligned} y_5(x) &= 0.0677477594013x^5 + 0.142004818753x^4 + 0.50973034525x^3 \\ &\quad + 0.998563502239x^2 + x \\ y_7(x) &= 0.00227725849959x^7 + 0.00699684012281x^6 + 0.0426662701383x^5 \\ &\quad + 0.166263705833x^4 + 0.500084460191x^3 + 0.999992530084x^2 + x \\ y_{10}(x) &= 0.00000453690126896x^{10} + 0.000020652981329x^9 + 0.000203685920715x^8 \\ &\quad + 0.00138475967554x^7 + 0.00833541450457x^6 + 0.0416659888668x^5 \\ &\quad + 0.166666804906x^4 + 0.49999998379x^3 + 1.00000000086x^2 + x \end{aligned}$$

The exact and approximate solutions of the equation are given in Table 1 and their graphics are drawn in Figure 1. Also, error functions of the numerical results are given in Table 2 and plotted in Figure 2.

Table 1. The comparison of exact solution and Boole solutions

	Exact Solution	Approximate Solutions		
x_i	$y(x_i) = x_i e^{x_i}$	$y_5(x_i) = x_i e^{x_i}$	$y_7(x_i) = x_i e^{x_i}$	$y_{10}(x_i) = x_i e^{x_i}$
0	0.0	0.0	0.0	0.0
0.2	0.244280551632	0.2442692698446	0.2442805289673	0.244280551633
0.4	0.5967298790565	0.5967219628705	0.5967298538586	0.5967298790575
0.6	1.093271280234	1.093256505661	1.09327125291	1.093271280235
0.8	1.780432742794	1.780427337762	1.780432715558	1.780432742795
1	2.718281828459	2.718046425642	2.718281064868	2.718281828408

Table 2. The comparison of error functions $N = 5, N = 7$ and $N = 10$

	Absolute Error Functions		
x_i	$ e_5(x_i) $	$ e_7(x_i) $	$ e_{10}(x_i) $
0	0.0	0.0	0.0
0.2	1.1282e-05	2.2665e-08	9.7586e-13
0.4	7.9162e-06	2.5198e-08	9.9687e-13
0.6	1.4775e-05	2.7325e-08	9.7788e-13
0.8	5.4050e-06	2.7236e-08	8.2467e-13
1	2.3540e-04	7.6359e-07	5.1028e-11

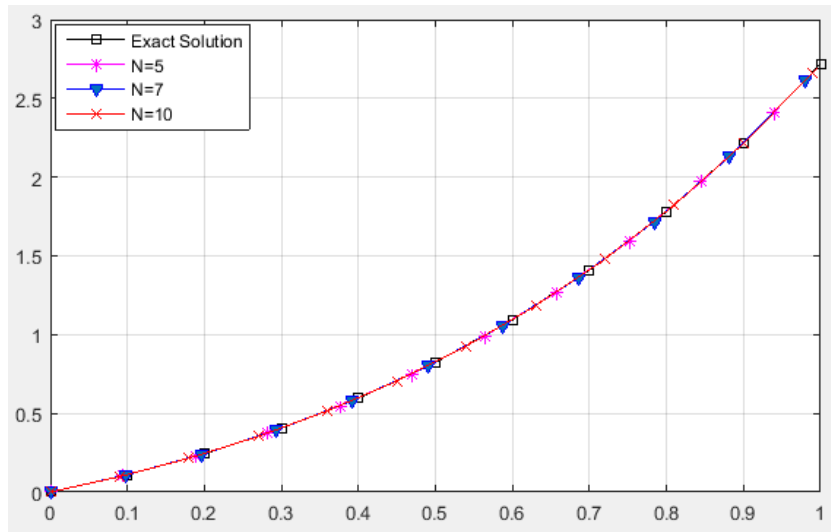


Figure 1. The comparison of exact solution and approximate solutions

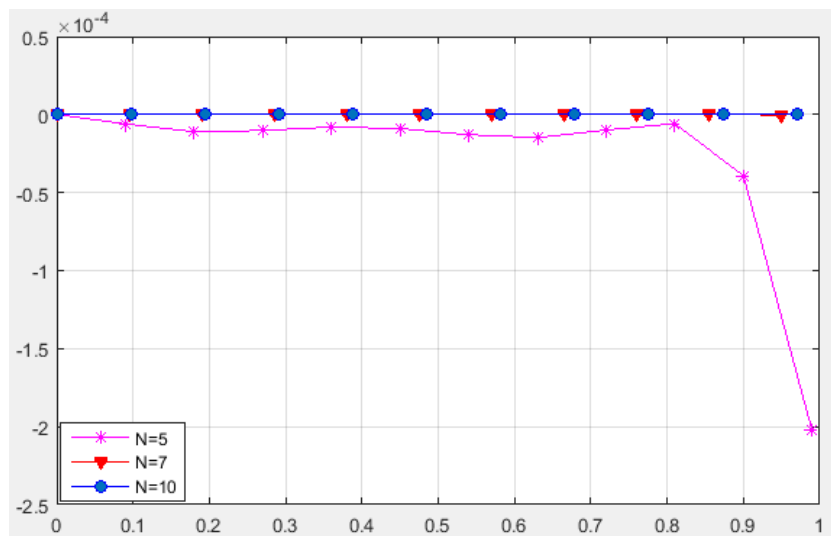


Figure 2. The comparison of error functions $N = 5, N = 7$ and $N = 10$

Example 3: In this example, linear Fredholm integro-differential equation given as

$$y''(x) = -\sin x + \cos x + \left(2 - \frac{\pi}{2}\right)x - \int_0^{\frac{\pi}{2}} xty(t)dt, \quad 0 \leq x, t \leq \frac{\pi}{2} \quad (35)$$

exact solution of Eq. (35) is $y(x) = \sin x - \cos x$ and conditions are $y(0) = -1, y'(0) = 1$ [22]. For $N = 8, N = 11$ and $N = 13$, the comparison of the exact and the approximate solutions is plotted in Figure 3. Also, the absolute error functions are compared in Figure 4.

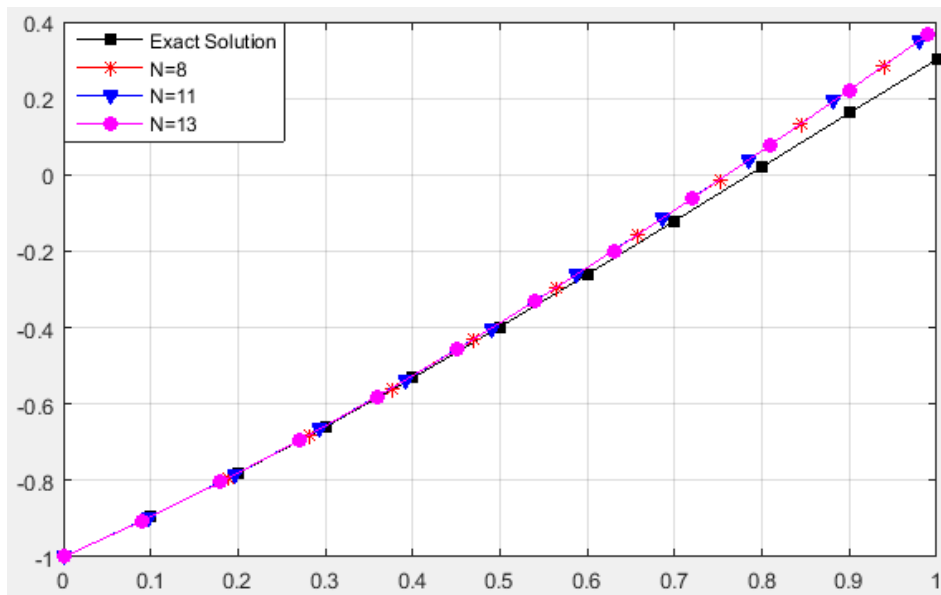


Figure 3. Exact solution and approximate solutions

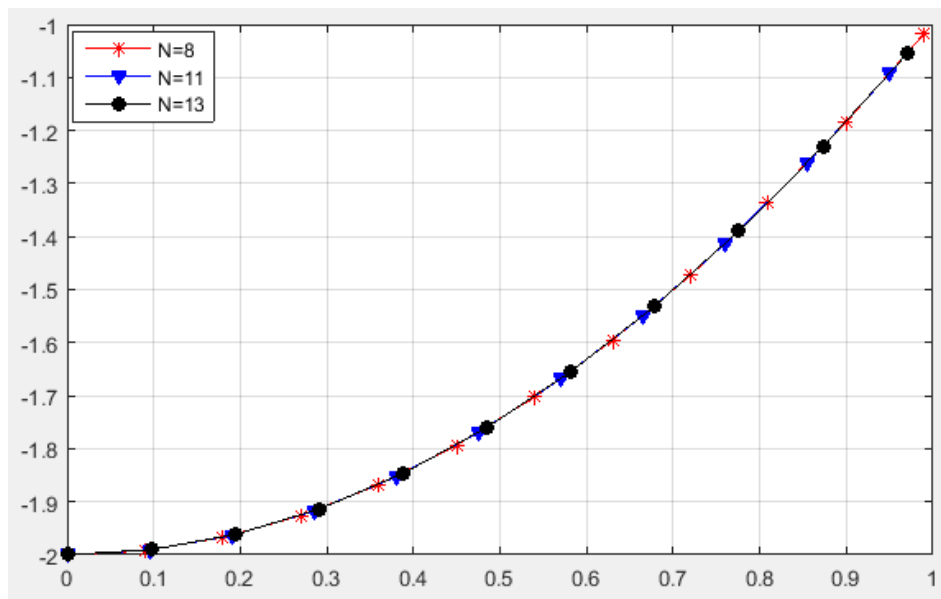


Figure 4. The comparison of error functions $N = 8$, $N = 11$ and $N = 13$

Conclusion

In this study, a method has been developed using Boole polynomial to solve the linear Fredholm integro-differential equation. This method is tested by calculating the exact solution, approximate solution and error function of some numerical examples. The graphics and tables of the error function and approximate solution have been given. As a result, the validity and applicability of the method has been observed. The computer code written in MATLAB has been used for calculations.

References

- [1] Hosseini S M (2003) Tau numerical solution of Fredholm integro-differential equations with arbitrary polynomials bases. *Appl. Math. Model.* 27:145–154.
- [2] Sezer M, Gülsu M (2005) A new polynomial approach for solving difference and Fredholm integro-difference equations with mixed argument. *Appl. Math. Comput.* 171: 332–344.
- [3] Kurt N, Sezer M (2008) Polynomial solution of high-order linear Fredholm integro-differential equations with constant coefficients. *J. Franklin Inst.* 345: 839–850.

- [4] Erdem K, Yalçınbaş, Sezer M (2013) A Bernoulli polynomial approach with residual correction for solving mixed linear Fredholm integro-differential-difference equations. *Journal of Difference Equations and Applications* 19:1619–1631.
- [5] Bellour A, Bousselsal M (2014) Numerical solution of delay integro-differential equations by using Taylor collocation method. *Math. Meth. Appl. Sci.* 37:1491–1506.
- [6] Erdem Biçer K, Sezer M (2017) Bernoulli matrix-collocation method for solving general functional integro-differential equations with hybrid delays. *Journal of Inequalities and Special Functions* 8(3):85-99.
- [7] Berenguer MI, Gámez D, López Linares AJ (2017) Solution of systems of integro-differential equations using numerical treatment of fixed point. *J. Comp. and Appl. Math.* 315: 343–353.
- [8] Turkyilmazoglu M (2014) An effective approach for numerical solutions of high-order Fredholm integro-differential equations. *Appl. Math. Comput.* 227: 384–398.
- [9] Behiry SH (2014) Solution of nonlinear Fredholm integro-differential equations using a hybrid of block pulse functions and normalized Bernstein polynomials. *J. Comp. and Appl. Math.* 260: 258–265.
- [10] Maleknejad K, Rostami Y (2014) Numerical solution for integro-differential equations by using quartic B-spline wavelet and operational matrices. *International Scholarly and Scientific Research & Innovation* 8(7): 1032-1039.
- [11] Yuzbası S, Sahin N, Sezer M (2011) Bessel matrix method for solving high-order linear Fredholm integro-differential equations. *J. Adv. Res. Appl. Math.* 3: 23-47.
- [12] Vahidi AR, Babolian E, Asadi Cordshooli GH, Azimzadeh Z (2009) Numerical solution of Fredholm integro-differential equation by Adomian's decomposition method. *Int. Journal of Math. Analysis* 3(36): 1769 – 1773.
- [13] Baykus Savaseneril N, Sezer M (2016) Laguerre polynomial solution of high- order linear Fredholm integro-differential equations. *NTMSCI* 4(2): 273-284.
- [14] Pashazadeh Atabakan Z, Kazemi Nasab A, Kılıçman A, and Eshkuvatov ZK (2013) Numerical solution of nonlinear Fredholm integro differential equations using spectral homotopy analysis method. *Mathematical Problems in Engineering* 2013: Article ID 674364. <http://dx.doi.org/10.1155/2013/674364>
- [15] Bichi SL, Lawal LH, Lawan SM, Bello MY (2018) Direct-homotopy analysis for solving Fredholm integro-differential equations. *J. Phys.: Conf. Ser.* 1123: Article ID012036.[doi:10.1088/1742-6596/1123/1/012036](https://doi.org/10.1088/1742-6596/1123/1/012036).
- [16] Rabbani M, Zarali B (2012) Solution of Fredholm Integro-Differential Equations System by Modified Decomposition Method. *TJMCS* 5(4): 258-264.
- [17] Behiry SH, Mohamed SI (2012) Solving high-order nonlinear Volterra-Fredholm integro-differential equations by differential transform method. *Natural Science* 4(8): 581-587.
- [18] Maleknejad K, Basirat B, Hashemizadeh E (2012) A Bernstein operational matrix approach for solving a system of high order linear Volterra–Fredholm integro-differential equations. *Mathematical and Computer Modelling* 55: 1363–1372.
- [19] Yuzbası S (2018) An exponential method to solve linear Fredholm–Volterra integro-differential equations and residual improvement. *Turk J Math* 42: 2546 – 2562.
- [20] Kurt N, Cevik M (2008) Polynomial solution of the single degree of freedom system by Taylor matrix method. *Mechanics Research Communications* 35: 530–536.
- [21] Jordan C., (1950). *Calculus of Finite Differences*. Chelsea Publishing Company, New York.
- [22] Karim MF, Mohamad M, Rusiman MS, Che-Him N, Roslan R, Khalid K (2018) ADM for solving linear second-order Fredholm integro-differential equations. *J. Phys.: Conf. Ser.* 995: Article ID 012009. [doi :10.1088/1742-6596/995/1/012009](https://doi.org/10.1088/1742-6596/995/1/012009)

Stirling Matrix-Collocation Method to Solve Systems of Functional Differential Equations with Deviating Argument

Ülker Başar*, Manisa Celal Bayar University, Dept. of Mathematics, 45140, Manisa, Turkey
Mehmet Sezer, Manisa Celal Bayar University, Dept. of Mathematics, 45140, Manisa, Turkey
Nurcan Baykuş Savaşaneril, Dokuz Eylül University, İzmir Vocational School, İzmir, Turkey
*Corresponding author e-mail: ulkerbasar@hotmail.com

Keywords: system of functional differential equations; Stirling polynomials and series; matrix-collocation method; residual error analysis

Discipline: Mathematics

Abstract

In this paper, a numerical collocation method based on Stirling polynomials is presented to solve the system of linear functional differential equations with variable coefficients under the mixed conditions. This method transforms the functional system along with conditions into a matrix equation by means of collocation points and the truncated Stirling series. Some illustrative examples, which arise in physics, biology, chemistry and mechanics and so on, are given to indicate the reliability and efficiency of the method. Also, a technique based on residual functions is performed to check the accuracy of the problem.

Introduction

The systems of differential, difference, differential-difference and delay differential equations have been confronted in many scientific and technological problems such as engineering, physics and mechanics. Most of the systems have no analytic solutions, so numerical techniques have been required such as Adomian decomposition method [4], Differential transformation method [1], Runge-Kutta method [6], variational iteration method [9], homotopy perturbation method [10], homotopy analysis method [11], Taylor collocation method [7-8].

In this study, we introduce a novel collocation method based on Stirling polynomials for solving the system of linear functional differential equations in the form

$$\sum_{k=0}^m \sum_{j=1}^J P_{ij}^k(x) y_j^{(k)}(\alpha_{jk}x + \beta_{jk}) = g_i(x), \quad i=1,2,\dots,J, \quad 0 \leq a \leq x \leq b \quad (1)$$

under the mixed conditions

$$y_j^{(k)}(a) = \lambda_{jk}; \quad j=1,2,\dots,J, \quad k=0,1,\dots,m-1. \quad (2)$$

where $y_j^{(0)}(x) = y_j(x)$, $j=1,2,\dots,J$ are unknown functions; $P_{ij}^{(k)}(x)$ and $g_i(x)$ are continuous functions on $[a, b]$ and λ_{jk} , α_{jk} and β_{jk} is real constant coefficients. Here, we assume that the system (1) under the mixed conditions (2) has approximate solutions in the truncated Stirling series form

$$y_j(x) = \sum_{n=0}^N a_{jn} S_n(x), \quad j=1,2,\dots,J \quad (3)$$

where a_{jn} , ($n=0,1,2,\dots,N$) are the unknown Stirling coefficients and $S_n(x)$, ($n=0,1,\dots,N$) are the Stirling polynomials defined by

$$S_n(x) = (-1)^n n! \sum_{k=0}^n \left[\sum_{j=k}^n \frac{S_1(j+1, k+1)}{(n+j)!} \sum_{i=0}^j (-1)^i \binom{n+j}{j-i} S_2(n+i, i) \right] x^k$$

or

$$S_n(x) = (-1)^n n! T_{nk} x^k, \quad (n=0,1,\dots,N, \quad n \geq 0)$$

where

$$T_{nk} = \sum_{j=k}^n \frac{S_1(j+1, k+1)}{(n+j)!} \sum_{i=0}^j (-1)^i \binom{n+j}{j-i} S_2(n+i, i) \quad [9]$$

In addition, in order to find the approximate solutions of the problem (1) – (2), we can use the collocation points defined by

$$x_r = a + \frac{b-a}{N} r; r=0,1,\dots,N. \quad (4)$$

Fundamental Matrix Relations

In this section, we convert the expressions (1) – (3) to the matrix forms. In order to achieve our aim, firstly, we can write the Stirling polynomials $S_n(x)$ in the matrix form

$$S(x) = X(x)T \quad (5)$$

where

$$S(x) = [S_0(x) \quad S_1(x) \quad S_2(x) \quad \dots \quad S_N(x)], \quad X(x) = [1 \quad x \quad x^2 \quad \dots \quad x^N]$$

and

$$T^T = \begin{bmatrix} (-1)^0 0! T_{00} & 0 & 0 & 0 & \dots & 0 \\ (-1)^1 1! T_{10} & (-1)^1 1! T_{11} & 0 & 0 & \dots & 0 \\ (-1)^2 2! T_{20} & (-1)^2 2! T_{21} & (-1)^2 2! T_{22} & 0 & \dots & 0 \\ (-1)^3 3! T_{30} & (-1)^3 3! T_{31} & (-1)^3 3! T_{32} & (-1)^3 3! T_{33} & \dots & 0 \\ \vdots & \vdots & \vdots & \vdots & \vdots & \vdots \\ (-1)^N N! T_{N0} & (-1)^N N! T_{N1} & (-1)^N N! T_{N2} & (-1)^N N! T_{N3} & \dots & (-1)^N N! T_{NN} \end{bmatrix}.$$

Also, the approximate solutions $y_j(x)$ in (3) can be expressed as

$$y_j(x) = S(x)A_j, \quad j=1,2,\dots,J \quad (6)$$

where

$$A_j = [a_{j0} \quad a_{j1} \quad a_{j2} \quad \dots \quad a_{jN}]^T.$$

By using (5) and (6), we obtain the relation

$$y_j(x) = X(x)TA_j. \quad (7)$$

Besides, it is obvious that the relation between $X(x)$ and its derivatives $X^{(k)}(x)$ can be written as

$$X^{(k)}(x) = X(x)B^k \quad (8)$$

where

$$B = \begin{bmatrix} 0 & 1 & 0 & \dots & 0 \\ 0 & 0 & 2 & \dots & 0 \\ \vdots & \vdots & \vdots & \vdots & \vdots \\ 0 & 0 & 0 & \dots & N \\ 0 & 0 & 0 & \dots & 0 \end{bmatrix}.$$

Thus, from the relations (7) and (8), we obtain the matrix relations

$$y_j^{(k)}(x) = X(x)B^k TA_j, \quad j=1,2,\dots,J. \quad (9)$$

By putting $x \rightarrow \alpha_{jk}x + \beta_{jk}$ into the relation (9), we have

$$y_j^{(k)}(\alpha_{jk}x + \beta_{jk}) = X(\alpha_{jk}x + \beta_{jk})B^k TA_j, \quad j=1,2,\dots,J. \quad (10)$$

On the other hand, it is well-known that the relation between $X(\alpha_{jk}x + \beta_{jk})$ and $X(x)$ is

$$X(\alpha_{jk}x + \beta_{jk}) = X(x).B(\alpha_{jk}, \beta_{jk}) \quad (11)$$

where, for $\alpha_{jk} \neq 0$ and $\beta_{jk} = 0$, [7]

$$\mathbf{B}(\alpha_{jk}, 0) = \begin{bmatrix} \alpha_{jk}^0 & 0 & 0 & \dots & 0 \\ 0 & \alpha_{jk}^1 & 0 & \dots & 0 \\ 0 & 0 & \alpha_{jk}^2 & \dots & 0 \\ \vdots & \vdots & \vdots & \ddots & \vdots \\ 0 & 0 & 0 & \dots & \alpha_{jk}^N \end{bmatrix} \text{ and } \alpha_{jk} \neq 0 \text{ and } \beta_{jk} \neq 0 \text{ [7]}$$

$$\mathbf{B}(\alpha_{jk}, \beta_{jk}) = \begin{bmatrix} \binom{0}{0} \alpha_{jk}^0 \beta_{jk}^0 & \binom{1}{0} \alpha_{jk}^0 \beta_{jk}^1 & \binom{2}{0} \alpha_{jk}^0 \beta_{jk}^2 & \dots & \binom{N}{0} \alpha_{jk}^0 \beta_{jk}^N \\ 0 & \binom{1}{1} \alpha_{jk}^1 \beta_{jk}^0 & \binom{2}{1} \alpha_{jk}^1 \beta_{jk}^1 & \dots & \binom{N}{1} \alpha_{jk}^1 \beta_{jk}^{N-1} \\ 0 & 0 & \binom{2}{2} \alpha_{jk}^2 \beta_{jk}^0 & \dots & \binom{N}{2} \alpha_{jk}^2 \beta_{jk}^{N-2} \\ \vdots & \vdots & \vdots & \ddots & \vdots \\ 0 & 0 & 0 & \dots & \binom{N}{N} \alpha_{jk}^N \beta_{jk}^0 \end{bmatrix}$$

Substituting (11) into (10) fields

$$y_j^{(k)}(\alpha_{jk}x + \beta_{jk}) = \mathbf{X}(x)\mathbf{B}(\alpha_{jk}, \beta_{jk})\mathbf{B}^k\mathbf{TA}_j, \quad j=1,2,\dots,J \quad (12)$$

Stirling Matrix Collocation Method

Firstly, the system (1) by using (9) and (12) for $i,j=1,2,\dots,J$ can be written in the following matrix form:

$$\sum_{k=0}^m \mathbf{P}_k(x)\mathbf{Y}^{(k)}(\alpha_kx + \beta_k) = \mathbf{G}(x) \Rightarrow \sum_{k=0}^m \mathbf{P}_k(x)\bar{\mathbf{X}}(x)\bar{\mathbf{B}}(\alpha_k, \beta_k)(\bar{\mathbf{B}})^k \bar{\mathbf{TA}} = \mathbf{G}(x) \quad (13)$$

so that

$$\mathbf{P}_k(x) = \begin{bmatrix} P_{11}^k(x) & P_{12}^k(x) & \dots & P_{1J}^k(x) \\ P_{21}^k(x) & P_{22}^k(x) & \dots & P_{2J}^k(x) \\ \vdots & \vdots & \ddots & \vdots \\ P_{J1}^k(x) & P_{J2}^k(x) & \dots & P_{JJ}^k(x) \end{bmatrix}, \quad \mathbf{G}(x) = \begin{bmatrix} g_1(x) \\ g_2(x) \\ \vdots \\ g_J(x) \end{bmatrix},$$

$$\mathbf{Y}^{(k)}(\alpha_kx + \beta_k) = \begin{bmatrix} y_1^{(k)}(\alpha_{1k}x + \beta_{1k}) \\ y_2^{(k)}(\alpha_{2k}x + \beta_{2k}) \\ \vdots \\ y_J^{(k)}(\alpha_{Jk}x + \beta_{Jk}) \end{bmatrix} = \begin{bmatrix} \mathbf{X}(x)\mathbf{B}(\alpha_{1k}, \beta_{1k})\mathbf{B}^k\mathbf{TA}_1 \\ \mathbf{X}(x)\mathbf{B}(\alpha_{2k}, \beta_{2k})\mathbf{B}^k\mathbf{TA}_2 \\ \vdots \\ \mathbf{X}(x)\mathbf{B}(\alpha_{Jk}, \beta_{Jk})\mathbf{B}^k\mathbf{TA}_J \end{bmatrix} = \bar{\mathbf{X}}(x)\bar{\mathbf{B}}(\alpha_k, \beta_k)(\bar{\mathbf{B}})^k \bar{\mathbf{TA}}$$

where

$$\bar{\mathbf{B}}(\alpha_k, \beta_k) = \begin{bmatrix} \mathbf{B}(\alpha_{1k}, \beta_{1k}) & 0 & \dots & 0 \\ 0 & \mathbf{B}(\alpha_{2k}, \beta_{2k}) & \dots & 0 \\ \vdots & \vdots & \ddots & \vdots \\ 0 & 0 & \dots & \mathbf{B}(\alpha_{Jk}, \beta_{Jk}) \end{bmatrix}, \quad \bar{\mathbf{B}}^k = \begin{bmatrix} \mathbf{B}^k & 0 & \dots & 0 \\ 0 & \mathbf{B}^k & \dots & 0 \\ \vdots & \vdots & \ddots & \vdots \\ 0 & 0 & \dots & \mathbf{B}^k \end{bmatrix},$$

$$\bar{X}(x) = \begin{bmatrix} X(x) & 0 & \dots & 0 \\ 0 & X(x) & \dots & 0 \\ \vdots & \vdots & \ddots & \vdots \\ 0 & 0 & \dots & X(x) \end{bmatrix}, \quad \bar{T} = \begin{bmatrix} T & 0 & \dots & 0 \\ 0 & T & \dots & 0 \\ \vdots & \vdots & \ddots & \vdots \\ 0 & 0 & \dots & T \end{bmatrix}, \quad A = \begin{bmatrix} A_1 \\ A_2 \\ \vdots \\ A_J \end{bmatrix}.$$

By using the collocation points (4) into Eq. (13) we obtain the system of the matrix equations

$$\sum_{k=0}^m P_k(x_r) \bar{X}(x_r) \bar{B}(\alpha_k, \beta_k) (\bar{B})^k \bar{T} A = G(x_r), \quad r=0,1,\dots,N$$

or briefly, the fundamental matrix equation

$$\sum_{k=0}^m P_k \bar{X} \bar{B}(\alpha_k, \beta_k) (\bar{B})^k \bar{T} A = G \quad (14)$$

where

$$P_k = \begin{bmatrix} P_k(x_0) & 0 & \dots & 0 \\ 0 & P_k(x_1) & \dots & 0 \\ \vdots & \vdots & \ddots & \vdots \\ 0 & 0 & \dots & P_k(x_N) \end{bmatrix}, \quad \bar{X} = \begin{bmatrix} \bar{X}(x_0) & 0 & \dots & 0 \\ 0 & \bar{X}(x_1) & \dots & 0 \\ \vdots & \vdots & \ddots & \vdots \\ 0 & 0 & \dots & \bar{X}(x_N) \end{bmatrix},$$

$$G = \begin{bmatrix} G(x_0) \\ G(x_1) \\ \vdots \\ G(x_N) \end{bmatrix}, \quad \bar{B}(\alpha_k, \beta_k) = \begin{bmatrix} \bar{B}(\alpha_k, \beta_k) \\ \bar{B}(\alpha_k, \beta_k) \\ \vdots \\ \bar{B}(\alpha_k, \beta_k) \end{bmatrix}.$$

Eq.(14) corresponding to Eq.(1) can be shown by

$$WA = G \text{ or } [W; G]; \quad W = \sum_{k=0}^m P_k \bar{X} \bar{B}(\alpha_k, \beta_k) (\bar{B})^k \bar{T} = [w_{p,q}], \quad p,q=1,2,\dots,J(N+1). \quad (15)$$

where we have a system of $J(N+1)$ linear algebraic equations with $J(N+1)$ unknown Stirling

coefficients; $W = \sum_{k=0}^m P_k \bar{X} \bar{B}(\alpha_k, \beta_k) (\bar{B})^k \bar{T} = [w_{p,q}], \quad p,q=1,2,\dots,J(N+1).$

By using the relation (9), we get the matrix form of the conditions (2) for $j=1,2,\dots,J, \quad k=0,1,\dots,m-1$ as follows:

$$\begin{bmatrix} y_1^{(k)}(a) \\ y_2^{(k)}(a) \\ \vdots \\ y_J^{(k)}(a) \end{bmatrix} = \begin{bmatrix} X(a)B^k T & 0 & \dots & 0 \\ 0 & X(a)B^k T & \dots & 0 \\ \vdots & \vdots & \ddots & \vdots \\ 0 & 0 & \dots & X(a)B^k T \end{bmatrix} \begin{bmatrix} A_1 \\ A_2 \\ \vdots \\ A_J \end{bmatrix} = \begin{bmatrix} \lambda_{1k} \\ \lambda_{2k} \\ \vdots \\ \lambda_{Jk} \end{bmatrix}$$

or briefly

$$U_k A = \lambda_k \text{ or } [U_k; \lambda_k]. \quad (16)$$

Therefore, the rows of the matrix (16) are replaced by last rows of the matrix (15), we obtain the new augmented matrix

$$[\tilde{W}; \tilde{G}] \quad (17)$$

If we have a singular matrix \tilde{W} , rows of the matrix (22) can be replaced by any rows of the matrix (20)

If $\text{rank } \tilde{W} = \text{rank } [\tilde{W}; \tilde{G}] = r(N+1)$, then we have

$$A = (\tilde{W})^{-1} \tilde{G}. \quad (18)$$

Accordingly, the unknown Stirling coefficients matrix A is determined. So we can find the Stirling polynomial solutions, $y_N(x) = \sum_{n=0}^N a_n S_n(x)$, $n=0,1,2,\dots,N$.

Residual Error Analysis

In this section, we develop an error estimation technique for the Stirling polynomial approximations of the problem (1) – (2) by means of the residual correction method [3] and then, by using this technique we improve the approximate solution.

Firstly, the residual function of the method can be defined as

$$R_{iN}(x) = L[y_{iN}(x)] - g_i(x), \quad i=1,2,\dots,k \quad (19)$$

where $L[y_{iN}(x)] \cong g_i(x)$ and $y_{iN}(x)$, $i=0,1,2,\dots,k$ are the Stirling polynomial solutions (3) of the problem (1) – (2). Then $y_{jN}(x)$ correspond the problem

$$\left\{ \begin{array}{l} \sum_{k=0}^m \sum_{j=1}^J P_{ij}^{(k)}(x) y_j^{(k)}(\alpha_{jk}x + \beta_{jk}) = g_i(x) + R_{iN}(x), \quad i=1,2,\dots,k \\ y_j^{(k)}(a) = \lambda_{jk}, \quad j=1,2,\dots,J, \quad k=0,1,\dots,m-1 \end{array} \right\}$$

Further, the error function $e_{jN}(x)$ can be determined as

$$e_{jN}(x) = y_j(x) - y_{jN}(x) \quad (20)$$

where $y_j(x)$, $j=1,2,\dots,k$ are the exact solutions of the problem (1) – (2). From Eqs. (1), (2), (19) and (20), we obtain the system of the error differential equations

$$L[e_{iN}(x)] = L[y_i(x)] - L[y_{iN}(x)] = -R_{iN}(x)$$

and the error problem

$$\left\{ \begin{array}{l} \sum_{k=0}^m \sum_{j=1}^J P_{ij}^{(k)}(x) e_{jN}^{(k)}(\alpha_{jk}x + \beta_{jk}) = -R_{iN}(x), \quad i=1,2,\dots,k \\ e_{jN}^{(k)}(a) = 0, \quad j=1,2,\dots,J, \quad k=0,1,\dots,m-1 \end{array} \right\} \quad (21)$$

The error problem (21) can be settled by using the presented method in Section 2. So, we obtain the approximation $e_{jN,M}(x)$ to $e_{jN}(x)$ as follows;

$$e_{jN,M}(x) = \sum_{n=0}^M a_{jN}^* S_n(x), \quad M > N, \quad j=1,2,\dots,J.$$

Consequently, the corrected Stirling polynomial solution $y_{jN,M}(x) = y_{jN}(x) + e_{jN,M}(x)$ is obtained by means of the polynomials $y_{jN}(x)$ and $e_{jN,M}(x)$. In addition, we construct the error function $e_{jN}(x) = y_j(x) - y_{jN}(x)$, the estimated error function $e_{jN,M}(x)$ and the corrected error function $E_{jN,M}(x) = e_{jN}(x) - e_{jN,M}(x) = y_j(x) - y_{jN,M}(x)$ [7].

Illustration

In this section, a numerical example of the problem (1) is given to illustrate the accuracy and effectiveness properties of the method.

Example: First, we consider the system of linear differential difference equations

$$\left\{ \begin{array}{l} y_1'(x) - xy_1(x-1) + xy_2(x) = -x^2 + 3x + 2 \\ y_2'(x) + 2xy_1(x) + 2xy_2(\frac{1}{2}x-1) = 5x^2 - 4x + 1 \end{array} \right\} \quad (28)$$

with the initial conditions $y_1(0) = -1$, $y_2(0) = 0$. The general structure is as follows;

$$\sum_{k=0}^1 \sum_{j=1}^2 P_{ij}^k(x) Y_j^{(k)}(\alpha_{kj}x + \beta_{kj}) = g_i(x), \quad i=1,2$$

or clearly,

- $P_{11}^0(x)Y_1^0(\alpha_{10}x + \beta_{10}) + P_{12}^0(x)Y_2^0(\alpha_{20}x + \beta_{20}) + P_{11}^1(x)Y_1^1(\alpha_{11}x + \beta_{11}) + P_{12}^1(x)Y_2^1(\alpha_{21}x + \beta_{21}) = g_1(x)$
- $P_{21}^0(x)Y_1^0(\alpha_{10}x + \beta_{10}) + P_{22}^0(x)Y_2^0(\alpha_{20}x + \beta_{20}) + P_{21}^1(x)Y_1^1(\alpha_{11}x + \beta_{11}) + P_{22}^1(x)Y_2^1(\alpha_{21}x + \beta_{21}) = g_2(x)$

Also, we get

$$\begin{aligned} P_{11}^0(x) &= -x, \quad \alpha_{10} = 1, \quad \beta_{10} = -1, \quad P_{12}^0(x) = x, \quad \alpha_{20} = 1, \quad \beta_{20} = 0, \quad P_{11}^1(x) = 1, \quad \alpha_{11} = 1, \quad \beta_{11} = 0, \\ P_{21}^0(x) &= 2x, \quad \alpha_{10} = 1, \quad \beta_{10} = 0, \quad P_{22}^0(x) = 2x, \quad \alpha_{20} = \frac{1}{2}, \quad \beta_{20} = -1, \quad P_{22}^1(x) = 1, \quad \alpha_{21} = 1, \quad \beta_{21} = 0, \\ g_1(x) &= -x^2 + 3x + 2, \quad g_2(x) = 5x^2 - 4x + 1. \end{aligned}$$

The approximate solutions $y_2(x)$ for $N = 2$ is given by

$$y_2(x) = \sum_{n=0}^2 a_n S_n(x),$$

For $a = 0$, $b=1$ and $N = 2$, we have $\left\{ x_0 = 0, x_1 = \frac{1}{2}, x_2 = 1 \right\}$.

From Eq. (19), the fundamental matrix equation of the problem (28) becomes

$$\sum_{k=0}^1 P_k \bar{X} \bar{B}(\alpha_k, \beta_k) (\bar{B})^k \bar{T} A = G,$$

$$W = P_0 \bar{X} \bar{B}(\alpha_0, \beta_0) (\bar{B})^0 \bar{T} + P_1 \bar{X} \bar{B}(\alpha_1, \beta_1) (\bar{B})^1 \bar{T}$$

where

$$P_k = \begin{bmatrix} P_k(x_0) & 0 & 0 \\ 0 & P_k(x_1) & 0 \\ 0 & 0 & P_k(x_2) \end{bmatrix}, \quad P_k(x) = \begin{bmatrix} P_{11}^k(x) & P_{12}^k(x) \\ P_{21}^k(x) & P_{22}^k(x) \end{bmatrix}, \quad P_0(x) = \begin{bmatrix} -x & x \\ 2x & 2x \end{bmatrix}, \quad P_1(x) = \begin{bmatrix} 1 & 0 \\ 0 & 1 \end{bmatrix}$$

$$\bar{X} = \begin{bmatrix} \bar{X}(x_0) & 0 & 0 \\ 0 & \bar{X}(x_1) & 0 \\ 0 & 0 & \bar{X}(x_2) \end{bmatrix}, \quad \bar{X}(x) = \begin{bmatrix} X(x) & 0 \\ 0 & X(x) \end{bmatrix},$$

$$B(\alpha_k, \beta_k) = \begin{bmatrix} B(\alpha_{1k}, \beta_{1k}) & 0 \\ 0 & B(\alpha_{2k}, \beta_{2k}) \end{bmatrix},$$

$$\bar{B}(\alpha_k, \beta_k) = \text{diag} [B(\alpha_k, \beta_k) \quad B(\alpha_k, \beta_k) \quad \dots \quad B(\alpha_k, \beta_k)],$$

$$(\bar{B})^k = \text{diag} [B^k \quad B^k \quad \dots \quad B^k], \quad G = \begin{bmatrix} G(x_0) \\ G(x_1) \\ G(x_2) \end{bmatrix}, \quad G(x) = \begin{bmatrix} g_1(x) \\ g_2(x) \end{bmatrix}, \quad \bar{T} = \begin{bmatrix} T & 0 \\ 0 & T \end{bmatrix},$$

$$y_1(0) = X(0)TA_1 = \lambda_{10}, \quad y_2(0) = X(0)TA_2 = \lambda_{20},$$

$$\begin{bmatrix} 1 & \frac{1}{2} & \frac{1}{6} \end{bmatrix} A_1 = -1, \quad \begin{bmatrix} 1 & \frac{1}{2} & \frac{1}{6} \end{bmatrix} A_2 = 0.$$

The augmented matrix for this fundamental matrix equation is calculated as

$$[W; G] = \begin{bmatrix} 0 & \frac{1}{2} & \frac{5}{12} & 0 & 0 & 0; & 2 \\ 0 & 0 & 0 & 0 & \frac{1}{2} & \frac{5}{12}; & \frac{13}{4} \\ -\frac{1}{2} & \frac{3}{8} & \frac{21}{32} & \frac{1}{2} & \frac{3}{8} & \frac{7}{32}; & 4 \\ 1 & \frac{1}{4} & \frac{1}{48} & 1 & \frac{5}{4} & \frac{53}{48}; & 1 \\ -1 & 0 & \frac{3}{4} & 1 & 1 & \frac{5}{6}; & \frac{1}{4} \\ 2 & 1 & \frac{1}{3} & 2 & \frac{5}{2} & \frac{31}{12}; & 2 \end{bmatrix}$$

From Eq. (22), the matrix form for initial conditions is computed as

$$[U_k; \lambda_k] = \begin{bmatrix} 1 & \frac{1}{2} & \frac{1}{6} & 0 & 0 & 0; & -1 \\ 0 & 0 & 0 & 1 & \frac{1}{2} & \frac{1}{6}; & 0 \end{bmatrix}$$

Hence, the new augmented matrix based on conditions from systems (22) can be obtained as follows

$$[\tilde{W}; \tilde{G}] = \begin{bmatrix} 0 & \frac{1}{2} & \frac{5}{12} & 0 & 0 & 0; & 2 \\ 0 & 0 & 0 & 0 & \frac{1}{2} & \frac{5}{12}; & \frac{13}{4} \\ 1 & \frac{1}{2} & \frac{1}{6} & 0 & 0 & 0; & -1 \\ 0 & 0 & 0 & 1 & \frac{1}{2} & \frac{1}{6}; & 0 \\ -1 & 0 & \frac{3}{4} & 1 & 1 & \frac{5}{6}; & \frac{1}{4} \\ 2 & 1 & \frac{1}{3} & 2 & \frac{5}{2} & \frac{31}{12}; & 2 \end{bmatrix}$$

By solving this system, substituting the resulting unknown Stirling coefficients matrix into Eq. (3) we obtain the exact solutions for $N=2$ as $y_1(x) = 2x - 1$ and $y_2(x) = x - x^2$.

Conclusions

Generally, it is analytically difficult to solve the functional systems such as the high-order linear differential-difference equations system. Hereby, approximate solutions are required. In this study, a new collocation method based on the Stirling polynomials have been introduced with the aid of the

residual error technique for solving system of linear functional differential equations. As it has been seen from the results, the developed method is very useful and prevalent.

References

- [1] Abdel-Halim Hassan IH (2008) Application to differential transformation method for solving systems of differential equations. *Appl. Math. Model.* 32(12): 2552—2559.
- [2] Çetin M, Sezer M, Güler C (2015) Lucas polynomial approach for system of high-order linear differential equations and residual error estimation. *Math. Probl. Eng.* 2015 Article ID 625984.
- [3] Çelik-İ, (2006) Collocation method and residual correction using Chebyshev series, *Appl. Math. Comput.*, 174(2): 910.
- [4] Dehghan M, Shakeri -F (2008) Accurate approximate solution to nonlinear oscillators in which the restoring force is inversely proportional to the dependent variable, *Phys. Scr.*, 78(6): 11.
- [5] Feng Q, Bai NG (2017) A closed form for the Stirling polynomials in terms of the Stirling numbers, *Tbilisi Mathematical Journal* 10(4): 153-158.
- [6] Ismail F, Suleiman M (2001) Solving delay differential equations using intervalwise partitioning by Runge-Kutta method, *Appl. Math. Comput.*, 121(1): 37.
- [7] Sezer M, Akyüz-Daşcıoğlu A (2007) A Taylor method for numerical solution of generalized pantograph equations with linear functional argument. *J. Comput. Appl. Math.*, 200: 217–225.
- [8] Baykuş Savaşaneril N, Sezer M (2016) Laguerre polynomial solution of highorder linear fredholm integro-differential equations. *New Trends in Math. Sci.*, 4(2): 273–284.
- [9] Saadatmandi A, Dehghan M (2009) Variational iteration method for solving a generalized pantograph equation. *Comput. Math. Appl.*, 58(11): 2190.
- [10] Shakeri F, Dehghan M (2008) Solution of delay differential equations via a homotopy perturbation method. *Math. Comput. Model.*, 48(3-4): 486.
- [11] Zurigat M, Momani S, Odibat Z, Alawneh A (2010) The homotopy analysis method for handling systems of fractional differential equations. *Appl. Math. Model.*, 34(1): 24.

Numerical Solutions of Fredholm Type Integro-Differential Equations Mixed Delays by Means of Bell Matrix-Collocation Method

Gökçe Yıldız*, Mehmet Sezer

Manisa Celal Bayar Univ., Dept. of Mathematics, Manisa, Türkiye

*Corresponding author: gokceyldz3@gmail.com

Keywords: Bell polynomials, matrix and collocation methods, Fredholm integro differential equations, mixed delay, residual error estimation

Discipline: Mathematics

Abstract

The main aim of this study is to apply the Bell polynomials for the solution of high order linear Fredholm integro differential equations with variable coefficient and mixed delays under the initial-boundary conditions. The technique we have used is essentially based on the truncated Bell series and its matrix representations along with collocation points. For our aim, we consider the high order linear Fredholm type delay integro differential equations with variable coefficients having mixed delays. Also, in an attempt to show the efficiency and applicability of the proposed method, some numerical examples together with residual error analysis are presented; the results are discussed.

Introduction

The delay integro-differential equations (DIDEs), which are a combination of delay differential and integral equations, have been of great interest to researchers for many years. There are many application areas to illustrate engineering, mechanics, physics, chemistry, astronomy, biology, economics, oscillation theory [1-6]. Due to the fore mentioned DIDEs usually difficult to solve analytically, a numerical method is needed. In this work, we develop a framework to obtain the numerical solution of the high-order linear Fredholm type delay integro-differential equation with variable coefficients

$$\sum_{k=0}^m \sum_{j=0}^J P_{kj}(x) y^{(k)} (\alpha_{kj}x + \beta_{kj}) = g(x) + \int_a^b \sum_{l=0}^{m_1} K_l(x, t) y^{(l)} (\lambda_l t + \mu_l) dt, \quad a \leq x, t \leq b \quad (1)$$

with the initial conditions

$$y^{(k)}(a) = \gamma_k, k = 0, 1, \dots, m - 1 \quad (2)$$

Our aim is to obtain an approximate solution of (1) in the following Bell polynomial form

$$y(x) \cong y_N(x) = \sum_{n=0}^N a_n B_n(x) \quad (3)$$

Here $P_{kj}(x)$, $K_l(x, t)$ and $g(x)$ are known functions defined on the interval $a \leq x, t \leq b$;

α_{kj} , β_{kj} , λ_l , μ_l , γ_k are suitable constants; a_n , $n = 0, 1, \dots, N$, are unknown Bell coefficients and $B_n(x)$, $n = 0, 1, \dots, N$ are the Bell polynomials defined by

$$B_n(x) = \sum_{k=0}^n S(n, k) x^k \quad (4)$$

where

$$S(n, k) = \sum_{j=0}^k \frac{(-1)^{k-j}}{k!} \binom{k}{j} \cdot j^n$$

are Stirling numbers of the second kind [3,8-9].

Fundamental Matrix Relations

First of all, we can write the Bell polynomials $B_n(x)$ in the matrix form as follows:

$$\mathbf{B}(x) = \mathbf{X}(x)\mathbf{S} \quad (5)$$

where

$$\mathbf{B}(x) = [B_0(x) \ B_1(x) \ \dots \ B_N(x)] \quad , \quad \mathbf{X}(x) = [1 \ x \ x^2 \ \dots \ x^N]$$

and

$$\mathbf{S} = \begin{bmatrix} S(0,0) & S(1,0) & S(2,0) & \dots & S(N,0) \\ 0 & S(1,1) & S(2,1) & \dots & S(N,1) \\ 0 & 0 & S(2,2) & \dots & S(N,2) \\ \vdots & \vdots & \vdots & \ddots & \vdots \\ 0 & 0 & 0 & \dots & S(N,N) \end{bmatrix}$$

Let us show Eq. (1) in the form

$$D(x) = g(x) + I(x) \quad (6)$$

where the functional differential part is

$$D(x) = \sum_{k=0}^m \sum_{j=0}^J P_{kj}(x) y^{(k)} (\alpha_{kj}x + \beta_{kj})$$

and Fredholm integral part is

$$I(x) = \int_a^b \sum_{l=0}^{m_1} K_l(x, t) y^{(l)} (\lambda_l t + \mu_l) dt.$$

Now we transform the parts $D(x), I(x)$ and the conditions (2) to matrix forms.

Matrix relation for the differential part $D(x)$

Let us consider the solution $y(x)$ of (1) and its k -th derivative $y^{(k)}(x)$ of defined by the truncated Bell series (3). Then, we can put the finite series (3) in the matrix form

$$y(x) = \mathbf{B}(x)\mathbf{A} ; \mathbf{A} = [a_0 \ a_1 \ \dots \ a_N]^T \quad (7)$$

and its k -th derivative becomes

$$y^{(k)}(x) = \mathbf{B}^{(k)}(x)\mathbf{A} \quad (8)$$

By substituting (5) into (7) we obtain that

$$y(x) = \mathbf{X}(x)\mathbf{S}\mathbf{A}. \quad (9)$$

On the other hand, it is clearly seen [12] that the relation between the matrix $\mathbf{X}(x)$ and its k th derivative $\mathbf{X}^{(k)}(x)$ is

$$\mathbf{X}^{(k)}(x) = \mathbf{X}(x)\mathbf{M}^k \quad (10)$$

where

$$\mathbf{M} = \begin{bmatrix} 0 & 1 & 0 & \dots & 0 \\ 0 & 0 & 2 & \dots & 0 \\ \vdots & \vdots & \vdots & \dots & \vdots \\ 0 & 0 & 0 & \dots & N \\ 0 & 0 & 0 & \dots & 0 \end{bmatrix}, \quad \mathbf{M}^0 = \begin{bmatrix} 1 & 0 & 0 & \dots & 0 \\ 0 & 1 & 0 & \dots & 0 \\ 0 & 0 & 1 & \dots & 0 \\ \vdots & \vdots & \vdots & \ddots & \vdots \\ 0 & 0 & 0 & \dots & 1 \end{bmatrix}.$$

From the matrix relations (8), (9) and (10), we can write the following matrix form

$$y^{(k)}(x) = \mathbf{B}^{(k)}(x)\mathbf{A} = \mathbf{X}^{(k)}(x)\mathbf{S}\mathbf{A} = \mathbf{X}(x)\mathbf{M}^k\mathbf{S}\mathbf{A}. \quad (11)$$

Similarly, if we put $x \rightarrow \alpha_{kj}x + \beta_{kj}$ into (11), [10,11] we obtain the matrix relation

$$y^{(k)}(\alpha_{kj}x + \beta_{kj}) = \mathbf{X}^{(k)}(\alpha_{kj}x + \beta_{kj})\mathbf{S}\mathbf{A} = \mathbf{X}(x)\mathbf{M}(\alpha_{kj}, \beta_{kj})\mathbf{M}^k\mathbf{S}\mathbf{A} \quad (12)$$

where

$$\mathbf{M}(\alpha_{kj}, \beta_{kj}) = \begin{bmatrix} \binom{0}{0}(\alpha_{kj})^0(\beta_{kj})^0 & \binom{1}{0}(\alpha_{kj})^0(\beta_{kj})^1 & \binom{2}{0}(\alpha_{kj})^0(\beta_{kj})^2 & \cdots & \binom{N}{0}(\alpha_{kj})^0(\beta_{kj})^N \\ 0 & \binom{1}{1}(\alpha_{kj})^1(\beta_{kj})^0 & \binom{2}{1}(\alpha_{kj})^1(\beta_{kj})^1 & \cdots & \binom{N}{1}(\alpha_{kj})^1(\beta_{kj})^{N-1} \\ 0 & 0 & \binom{2}{2}(\alpha_{kj})^2(\beta_{kj})^0 & \cdots & \binom{N}{2}(\alpha_{kj})^2(\beta_{kj})^{N-2} \\ \vdots & \vdots & \vdots & \ddots & \vdots \\ 0 & 0 & 0 & \cdots & \binom{N}{N}(\alpha_{kj})^N(\beta_{kj})^0 \end{bmatrix}$$

By substituting the expression (12) into Eq. (6), we get the matrix relation

$$D(x) = \sum_{k=0}^m \sum_{j=0}^J P_{kj}(x) y^{(k)} (\alpha_{kj}x + \beta_{kj}).$$

Matrix Representation for Fredholm Integral Part

Let us find the matrix form for the Fredholm integral part $I(x)$. The kernel function can be $K_l(x, t)$ approximated by the truncated Maclaurin series

$$K_l(x, t) = \sum_{p=0}^N \sum_{q=0}^N k_{pq} x^p t^q \quad (13)$$

where

$$k_{pq} = \frac{1}{p!q!} \frac{\partial^{p+q} K(0,0)}{\partial x^p \partial t^q}, \quad p, q = 0, 1, \dots, N$$

The expression (13) convert to the matrix form

$$K_l(x, t) = \mathbf{X}(x) \mathbf{K}_l \mathbf{X}^T(t) \quad \text{where } \mathbf{K}_l = [k_{pq}]. \quad (14)$$

Similarly expression (12) we get matrix relation for $y^{(l)}(\lambda_l t + \mu_l)$ as follows

$$y^{(l)}(\lambda_l t + \mu_l) = \mathbf{X}(t) \mathbf{M}(\lambda_l, \mu_l) \mathbf{M}^l \mathbf{S} \mathbf{A} \quad (15)$$

Substituting relations (14) and (15) in the Fredholm part, we obtain

$$\begin{aligned} I(x) &= \int_a^b \sum_{l=0}^{m_1} \mathbf{X}(x) \mathbf{K}_l \mathbf{X}^T(t) \mathbf{X}(t) \mathbf{M}(\lambda_l, \mu_l) \mathbf{M}^l \mathbf{S} \mathbf{A} \, dt \\ &= \sum_{l=0}^{m_1} \mathbf{X}(x) \mathbf{K}_l \mathbf{Q} \mathbf{M}(\lambda_l, \mu_l) \mathbf{M}^l \mathbf{S} \mathbf{A} \end{aligned} \quad (16)$$

so that

$$\mathbf{Q} = [q_{ij}] = \int_a^b \mathbf{X}^T(t) \mathbf{X}(t) dt \quad \text{and} \quad q_{ij} = \frac{b^{i+j+1} - a^{i+j+1}}{i+j+1} \quad \text{where } i, j = 0, 1, 2, \dots, N.$$

Matrix relation for the conditions

Let us define the matrix form of the conditions given by (2) using expression (11) that can be written as

$$y^{(k)}(a) = \mathbf{X}(a) \mathbf{M}^k \mathbf{S} \mathbf{A} = \gamma_k, \quad k = 0, 1, \dots, m-1 \quad (17)$$

Method of Solution

In an attempt to construct a fundamental matrix equation, substituting the matrix relations (12) and (16) into (1) we obtain that

$$\sum_{k=0}^m \sum_{j=0}^J P_{kj} \mathbf{X}(x) \mathbf{M}(\alpha_{kj}, \beta_{kj}) \mathbf{M}^k \mathbf{S} \mathbf{A} - \sum_{l=0}^{m_1} \mathbf{X}(x) \mathbf{K}_l \mathbf{Q} \mathbf{M}(\lambda_l, \mu_l) \mathbf{M}^l \mathbf{S} \mathbf{A} = g(x) \quad (18)$$

The collocation points x_i are defined by

$$x_i = a + \frac{b-a}{N} i, \quad i = 0, 1, \dots, N. \quad (19)$$

and by using the points (19), it is obtained the system of the matrix equations

$$\sum_{k=0}^m \sum_{j=0}^J P_{kj}(x_i) \mathbf{X}(x_i) \mathbf{M}(\alpha_{kj}, \beta_{kj}) \mathbf{M}^k \mathbf{S} \mathbf{A} - \sum_{l=0}^{m_1} \mathbf{X}(x_i) \mathbf{K}_l \mathbf{Q} \mathbf{M}(\lambda_l, \mu_l) \mathbf{M}^l \mathbf{S} \mathbf{A} = g(x_i) \quad (20)$$

or briefly the fundamental matrix equation

$$\left\{ \sum_{k=0}^m \sum_{j=0}^J \mathbf{P}_{kj} \mathbf{X} \mathbf{M}(\alpha_{kj}, \beta_{kj}) \mathbf{M}^k \mathbf{S} - \sum_{l=0}^{m_1} \mathbf{X} \mathbf{K}_l \mathbf{Q} \mathbf{M}(\lambda_l, \mu_l) \mathbf{M}^l \mathbf{S} \right\} \mathbf{A} = \mathbf{G}$$

where

$$\mathbf{P}_{kj} = \begin{bmatrix} P_{kj}(x_0) & 0 & \dots & 0 \\ 0 & P_{kj}(x_1) & \dots & 0 \\ \vdots & \vdots & \ddots & \vdots \\ 0 & 0 & \dots & P_{kj}(x_N) \end{bmatrix}, \mathbf{G} = \begin{bmatrix} g(x_1) \\ g(x_2) \\ \vdots \\ g(x_N) \end{bmatrix}$$

The fundamental matrix Eq. (20) for (1) corresponds to a system of $(N + 1)$ algebraic equation for the $(N + 1)$ unknown coefficients $a_0, a_1, a_2, \dots, a_N$. Concisely we can write as

$$\mathbf{W} \mathbf{A} = \mathbf{G} \quad \text{or} \quad [\mathbf{W}; \mathbf{G}] \quad (21)$$

where

$$\mathbf{W} = \sum_{k=0}^m \sum_{j=0}^J \mathbf{P}_{kj} \mathbf{X} \mathbf{M}(\alpha_{kj}, \beta_{kj}) \mathbf{M}^k \mathbf{S} - \sum_{l=0}^{m_1} \mathbf{X} \mathbf{K}_l \mathbf{Q} \mathbf{M}(\lambda_l, \mu_l) \mathbf{M}^l \mathbf{S}$$

On the other hand, the matrix form (17) for the conditions can be written as

$$\mathbf{U}_k \mathbf{A} = \gamma_k \quad \text{ya da} \quad [\mathbf{U}; \gamma_k], \quad k = 0, 1, \dots, m-1 \quad (22)$$

where

$$\mathbf{U} = \mathbf{X}(a) \mathbf{M}^k \mathbf{S} \mathbf{A} = [u_{k0} \quad u_{k1} \quad \dots \quad u_{kN}].$$

To obtain the solution of (1) under conditions (2), by replacing the rows in matrix equation (21) by the last m rows of matrix equation (22), we have the required new augmented matrix system

$$[\tilde{\mathbf{W}}; \tilde{\mathbf{G}}] = \begin{bmatrix} w_{00} & w_{01} & w_{02} & \dots & w_{0N} & ; & g(x_0) \\ w_{10} & w_{11} & w_{12} & \dots & w_{1N} & ; & g(x_1) \\ \cdot & \cdot & \cdot & \dots & \cdot & \cdot & \cdot \\ \cdot & \cdot & \cdot & \dots & \cdot & \cdot & \cdot \\ w_{(N-m)0} & w_{(N-m)1} & w_{(N-m)2} & \dots & w_{(N-m)N} & ; & g(x_{N-m}) \\ u_{00} & u_{01} & u_{02} & \dots & u_{0N} & ; & \gamma_0 \\ u_{10} & u_{11} & u_{12} & \dots & u_{1N} & ; & \gamma_1 \\ \cdot & \cdot & \cdot & \dots & \cdot & \cdot & \cdot \\ \cdot & \cdot & \cdot & \dots & \cdot & \cdot & \cdot \\ u_{(m-1)0} & u_{(m-1)1} & u_{(m-1)2} & \dots & u_{(m-1)N} & ; & \gamma_{m-1} \end{bmatrix}$$

If $\text{rank}(\tilde{\mathbf{W}}) = \text{rank}[\tilde{\mathbf{W}}; \tilde{\mathbf{G}}] = N + 1$, then we can write

$$\mathbf{A} = (\tilde{\mathbf{W}})^{-1} \tilde{\mathbf{G}}.$$

Thus the matrix \mathbf{A} (there by the coefficients $a_0, a_1, a_2, \dots, a_N$) is uniquely determined and the Eq. (1) under the coefficient equation (2) has unique solution. This solution is given by truncated Bell series

$$y(x) \cong y_N(x) = \sum_{n=0}^N a_n B_n(x).$$

Residual Correction and Error Estimation

We can easily check the accuracy of the obtained solutions as follows. Since the truncated Bell series (3) is the approximate solution of (1), when the function $y_N(x)$ and its derivatives are substituted in (1), the resulting equation must be satisfied approximately; that is, for $x = x_q \in [a, b]$, $q = 0, 1, \dots$

$$R_N(x_q) = \sum_{k=0}^m \sum_{j=0}^J P_{kj}(x_q) y_N^{(k)} (\alpha_{kj} x_q + \beta_{kj}) - \int_a^b \sum_{l=0}^{m_1} K_l(x_q, t) y_N^{(l)} (\lambda_l t + \mu_l) dt - g(x_q) \cong 0$$

or

$$R_N(x_q) \leq 10^{-k_q}, (k_q \text{ is any positive integer}).$$

If $\max 10^{-k_q} = 10^{-k}$ (k is a positive integer) is prescribed, then the truncation limit N is increased until the difference $R_N(x_q)$ at each of the points becomes smaller than the prescribed 10^{-k} . Therefore, if $R_N(x_q) \rightarrow 0$ when N is sufficiently large enough, then the error decreases.

On the other hand, by means of the residual function defined by $R_N(x)$ and the mean value of the function $|R_N(x)|$ on the interval $[a, b]$, the accuracy of the solution can be controlled and the error can be estimated [7]. Thus, we can estimate the upper bound of the mean error $\overline{R_N}$ as follows:

$$\left| \int_a^b R_N(x) dx \right| \leq \int_a^b |R_N(x)| dx$$

and

$$\begin{aligned} \int_a^b |R_N(x)| dx &= (b-a) |R_N(c)|, a \leq c \leq b \\ \Rightarrow \left| \int_a^b R_N(x) dx \right| &= (b-a) |R_N(c)| \Rightarrow (b-a) |R_N(c)| \leq \int_a^b |R_N(x)| dx \\ &\Downarrow \\ |R_N(c)| &\leq \frac{\int_a^b |R_N(x)| dx}{b-a} = \overline{R_N} \end{aligned}$$

Numerical Examples

Example 1: Let us first consider the second order linear Fredholm type delay integro-differential equation given by

$$y''(x) - (x^2 + 1)y' \left(\frac{1}{2}x + 1 \right) + xy(x) = -2x^2 - \frac{4x}{3} - 2 + \int_{-1}^1 xty(t-1)dt$$

with initial conditions $y(0) = 1, y'(0) = 2$ and the approximate solution $y(x)$ by the truncated Bell series

$$y(x) \cong y_N(x) = \sum_{n=0}^N a_n B_n(x).$$

Here $P_{00}(x) = x, P_{10}(x) = -(x^2 + 1), \alpha_{10} = 1/2, \beta_{10} = 1, P_{20}(x) = 1, K_0(x, t) = xt$ and $g(x) = -2x^2 - \frac{x}{4} - 2$. Then for $N = 2$, the collocation points are

$$x_0 = -1, x_1 = 0, x_2 = 1$$

and from Eq. (24), the fundamental matrix equation of the problem is

$$\left\{ P_{20} \mathbf{X} \mathbf{M}^2 \mathbf{S} + P_{10} \mathbf{X} \mathbf{M} \left(\frac{1}{2}, 1 \right) \mathbf{M} \mathbf{S} + P_{00} \mathbf{X} \mathbf{M}^0 \mathbf{S} - \mathbf{X} \mathbf{K} \mathbf{Q} \mathbf{M} (1, -1) \mathbf{M}^0 \mathbf{S} \right\} \mathbf{A} = \mathbf{G}$$

where

$$P_{00} = \begin{bmatrix} -1 & 0 & 0 \\ 0 & 0 & 0 \\ 0 & 0 & 1 \end{bmatrix}, P_{10} = \begin{bmatrix} -2 & 0 & 0 \\ 0 & -1 & 0 \\ 0 & 0 & -2 \end{bmatrix}, P_{20} = \begin{bmatrix} 1 & 0 & 0 \\ 0 & 1 & 0 \\ 0 & 0 & 1 \end{bmatrix}$$

$$\mathbf{S} = \begin{bmatrix} 1 & 0 & 0 \\ 0 & 1 & 1 \\ 0 & 0 & 1 \end{bmatrix}, \mathbf{K} = \begin{bmatrix} 0 & 0 & 0 \\ 0 & 1 & 0 \\ 0 & 0 & 0 \end{bmatrix}, \mathbf{Q} = \begin{bmatrix} 2 & 0 & 2/3 \\ 0 & 2/3 & 0 \\ 2/3 & 0 & 2/5 \end{bmatrix}, \mathbf{X} = \begin{bmatrix} 1 & -1 & 1 \\ 1 & 0 & 0 \\ 1 & 1 & 1 \end{bmatrix}$$

$$\mathbf{M} = \begin{bmatrix} 0 & 1 & 0 \\ 0 & 0 & 2 \\ 0 & 0 & 0 \end{bmatrix}, \mathbf{M} \left(\frac{1}{2}, 1 \right) = \begin{bmatrix} 1 & 1 & 1 \\ 0 & \frac{1}{2} & 1 \\ 0 & 0 & \frac{1}{4} \end{bmatrix}, \mathbf{M} (1, -1) = \begin{bmatrix} 1 & -1 & 1 \\ 0 & 1 & -2 \\ 0 & 0 & 1 \end{bmatrix}, \mathbf{G} = \begin{bmatrix} -8/3 \\ -2 \\ -16/3 \end{bmatrix}$$

The augmented matrix for this fundamental matrix equation is calculated as

$$[\mathbf{W}; \mathbf{G}] = \begin{bmatrix} -1 & -1 & -2/3 & ; & -8/3 \\ 0 & -1 & -1 & ; & -2 \\ 1 & -1 & -16/3 & ; & -16/3 \end{bmatrix}$$

From Eg.(26), the matrix forms for the initial conditions are

$$[\mathbf{U}_0; \gamma_0] = [1 \ 0 \ 0 \ ; \ 1] \text{ and } [\mathbf{U}_1; \gamma_1] = [0 \ 1 \ 1 \ ; \ 2]$$

From system (27), the new augmented matrix based on conditions can be obtained as follows:

$$[\tilde{\mathbf{W}}; \tilde{\mathbf{G}}] = \begin{bmatrix} -1 & -1 & -2/3 & ; & -8/3 \\ 1 & 0 & 0 & ; & 1 \\ 0 & 1 & 1 & ; & 2 \end{bmatrix}$$

Solving this system, the unknown Bell coefficient matrix is obtained as

$$\mathbf{A} = [1 \ 1 \ 1]^T$$

By substituting the above Bell coefficient matrix into equation (7), we obtain the approximate solution $y(x) = x^2 + 2x + 1$ which is the exact solution.

Example 2: Let us first consider the Bell series solution second order linear Fredholm type delay integro-differential equation given by

$$y''(x) + (x-1)y'(x-1) - y(x) = (x-1)e^{(x-1)} - x(1-e^{-2}) + \int_{-1}^1 xy'(x-1)dt$$

with initial condition $y(0) = 1$ and $y'(0) = 1$ The exact solution of problem is $y(x) = e^x$ and we seek the approximate solution $y_N(x)$ as a truncated Bell series:

$$y(x) \cong y_N(x) = \sum_{n=0}^N a_n B_n(x).$$

Here,

$$P_{00}(x) = -1, P_{10}(x) = x-1, P_{20}(x) = 1, K_0(x, t) = x \text{ and } g(x) = (x-1)e^{(x-1)} - x(1-e^{-2}).$$

Then for $N = 3$; the collocation points are $\{x_0 = -1, x_1 = -1/3, x_2 = 1/3, x_3 = 1\}$ and from equation (24), the fundamental matrix equation of the problem is defined by

$$\{P_{20} \mathbf{X} \mathbf{M}^2 \mathbf{S} + P_{10} \mathbf{X} \mathbf{M} (1, -1) \mathbf{M} \mathbf{S} + P_{00} \mathbf{X} \mathbf{M}^0 \mathbf{S} - \mathbf{X} \mathbf{K} \mathbf{Q} \mathbf{M} (1, -1) \mathbf{M}^0 \mathbf{S}\} \mathbf{A} = \mathbf{G}$$

From Equation (26), the matrix forms for the initial conditions are

$$[\mathbf{U}_0; \gamma_0] = [1 \ 0 \ 0 \ 0 \ ; \ 1] \text{ and } [\mathbf{U}_1; \gamma_1] = [0 \ 1 \ 1 \ 1 \ ; \ 1]$$

and the matrices are computed as

$$[\mathbf{W}; \mathbf{G}] = \begin{bmatrix} -1 & 1 & 6 & -5 & ; & 1444/2431 \\ -1 & -1/3 & 34/9 & 151/27 & ; & -1461/23102 \\ -1 & -5/3 & 22/9 & 245/27 & ; & -1691/2682 \\ -1 & -3 & 2 & 9 & ; & -2102/2431 \end{bmatrix}$$

Then, we have the new augmented matrix

$$[\tilde{\mathbf{W}}; \tilde{\mathbf{G}}] = \begin{bmatrix} -1 & 1 & 6 & -5 & ; & 1444/2431 \\ 1 & 0 & 0 & 0 & ; & 1 \\ -1 & -5/3 & 22/9 & 245/27 & ; & -1691/2682 \\ 0 & 1 & 1 & 1 & ; & 1 \end{bmatrix}$$

Solving this system, the unknown Bell coefficient matrix is obtained as

$$\mathbf{A} = [1 \ 1 \ 0.5335 \ 0.0987]^T.$$

Therefore, we obtain the approximate solution $y_3(x) = 1 + x + 0.5335x^2 + 0.0987x^3$. For $N=4, 5$ and 6 by using the same procedure, the following solutions are obtained:

$$y_4(x) = 1 + x + 0.4986x^2 + 0.1482x^3 + 0.0206x^4$$

$$y_5(x) = 1 + x + 0.4806x^2 + 0.1678x^3 + 0.0387x^4 + 0.0040x^5$$

$$y_6(x) = 1 + x + 0.5151x^2 + 0.1660x^3 + 0.0431x^4 + 0.0099x^5 + 0.0013x^6.$$

Table 1. Comparison of the absolute errors of Example 2 for $N= 3, 4, 5, 6$.

x_i	$y(x) = e^{x_i}$	$ e_3(x_i) $	$ e_4(x_i) $	$ e_5(x_i) $	$ e_6(x_i) $
-1	0.3679	0.0669	0.031	0.0204	0.0157
-0.5	0.6065	0.0145	8.8184e-04	0.0051	0.0039
0	1	0	0	0	0
0.5	1.6487	0.0030	0.0043	0.0051	0.0038
1	2.7183	0.0861	0.0509	0.0272	0.0171

The comparison is shown in Figures 1 and 2.

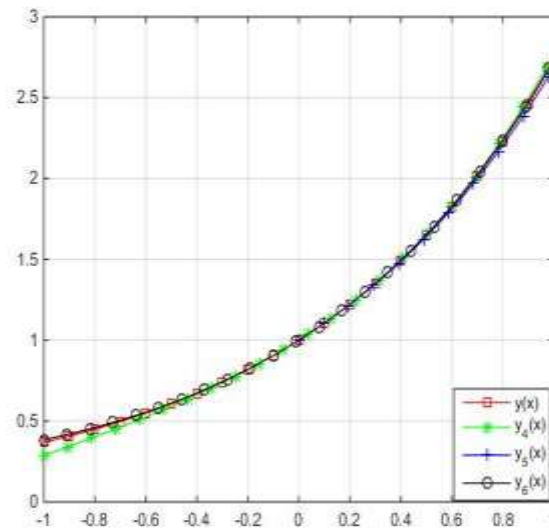


Figure 1. Numerical and exact solutions of Example 2 for $N = 4, 5, 6$

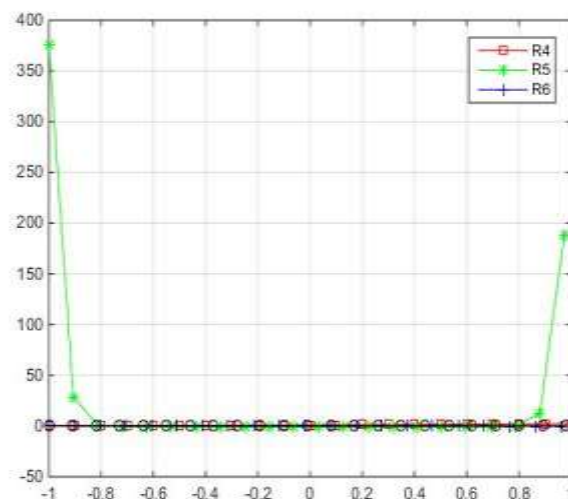


Figure 2. Residual error functions of Example 2 for $N = 4, 5, 6$

Conclusion

In this study, a new method was developed by using Bell polynomials for the solution of high order linear Fredholm type delay integro-differential equations. To illustrate the validity and applicability of this method, explanatory examples were solved, and an error analysis based on the residual function was performed to show the accuracy of the results. These comparisons and error estimates show that the proposed method is highly effective. We have calculated the solutions with the help of Matlab.

References

- [1] Erdem K, Yalçınbaş S, and Sezer M (2013) A Bernoulli polynomial approach with residual correction for solving mixed linear Fredholm integro differential-difference equations. *J. Difference Equ. Appl.* 19(10):1619–1631.
- [2] Bell E.T (1934), Exponential polynomials, *Ann. Math.* 35(2):258-277.
- [3] Van Gorder R.A (2010) Recursive Relations for Bell Polynomials of Arbitrary Positive Non-Integer Order. *International Mathematical Forum* 5(37):1819-1821.

3rd International Students Science Congress
3-4 May 2019, İzmir - Turkey

- [4] Kurt N, Sezer M (2008) Polynomial solution of high-order linear Fredholm integrodifferential equations with constant coefficients. J. Franklin Inst. 345:839–850.
- [5] Balcı M, Sezer M (2015) Hybrid Euler-Taylor matrix method for solving of generalized linear redholm integro-differential difference equations. Applied Mathmematics and Computation
- [6] Lakestani M, Razzaghi M, Dehghan M (2006) Semorthogonal spline wavelets approximation for Fredholm integro-differential equation. Hindawi Publishing Corporation Mathematical Problems in Engineering.
- [7] Mollaoğlu T, Sezer M (2017) A numerical approach with residual error estimation for solution of high-order linear differential-difference equations by using Gegenbauer polynomials. CBU J.of Sci.13(1):39-49.
- [8] Başar U, Sezer M (2018) Numerical solution based on Stirling polynomials for solving generalized linear integro-differential equations with mixed functional arguments. Proceeding of 2. International University Industry Cooperation, R&D and Innovation Congress. 141-148.
- [9] Çam Ş (2005) Stirling Sayıları. Matematik Dünyası 30-34.
- [10] Şahin N, Yüzbaşı Ş, Sezer M (2011) A Bessel polynomial approach for solving general linear Fredholm integro-differential–difference equations. International Journal of Computer Mathematics 88(14): 3093-3111.
- [11] Gürbüz B, Sezer M, Güler C (2014) Laguerre collocation method for solving Fredholm integro-differential equations with functional arguments. Journal of Applied Mathematics Article ID 682398, 12 pp.
- [12] Yalçınbaş S, Akkaya T (2012) A numerical approach for solving linear integro-differential-difference equations with Boubaker polynomial bases. Ain Shams Engineering Journal 3(2): 153-161.

Gegenbauer-Taylor Matrix Technique for Neutral Type Second Order Functional Integro-Differential Equations with Variable Bounds

Tuğçe Özalp*, Mehmet Sezer

Manisa Celal Bayar Üniv., Dept. of Mathematics, Manisa, Turkey

*Corresponding author: tugce.mollaoglu@hotmail.com

Keywords: Gegenbauer-Taylor matrix, integro-differential equations

Discipline: Mathematics

Abstract

In this study, a practical matrix method, which is related to collocation points, is presented to find approximate solutions of second-order linear neutral type functional integro-differential equations with variable bounds under the mixed conditions in terms of orthogonal Gegenbauer polynomials defined on the interval $[-1,1]$. The proposed method is based on the matrix forms of the truncated Gegenbauer and Taylor series and their derivatives using the collocation points. Then the solution of the problem is transformed to the solution of a matrix equation with unknown coefficients and the approximate solution is obtained in terms of Gegenbauer or Taylor polynomials. Besides, an efficient residual error estimation for the mentioned matrix method is introduced. In order to demonstrate the validity and applicability of the method, some examples are presented and the comparisons are performed with existing results by means of figures and tables.

Introduction

In this study, we consider the second-order linear neutral type functional integro-differential equation

$$(y(t) + P(t)y(\alpha t + \beta))^{(2)} = R(t)y(t) + \underbrace{\int_{\tau_1(t)}^{\tau_2(t)} K(t,s)y(s)ds}_{I(t)} + f(x) \quad (1)$$

under the conditions

$$\sum_{k=0}^{m-1} (a_{kl}y^{(k)}(a) + b_{kl}y^{(k)}(b)) = \lambda_l, l = 0, 1 \quad (2)$$

where

$$(P(t)y(\alpha t + \beta))^{(2)} = \sum_{k=0}^2 \binom{2}{k} P(t)^{(2-k)} X(h(t)) B^k T(\lambda) A \quad (3)$$

and the known functions $P(t), R(t), K(t, s)$ are defined on interval $[-1,1]$, the function $K(t, s)$ can be expanded Maclaurin series and the constants $\lambda_l, a_{kl}, b_{kl}$ are appropriate constants. Most of these equations have not analytical solution and so, numerical methods may be required to obtain their approximate solutions. In recent years, some matrix and collocation methods to solve linear and nonlinear differential, integral, integro-differential, integro-differential-difference and neutral type functional have been presented in many articles by Sezer and coworkers [4-8].

Our aim is to develop a new collocation method based on Gegenbauer polynomials and to find the approximate solutions of the problem (1) - (2) as the truncated Gegenbauer series defined by

$$y(t) \cong y_N(t) = \sum_{n=0}^N a_n G_n(t, \lambda), N \geq m, -1 \leq t \leq 1 \quad (4)$$

where $a_n, n = 0, 1, \dots, N$ are unknown coefficients; $G_n(t, \lambda)$, classical polynomials orthogonal on the interval $(-1,1)$ with respect to the weight function $w \rightarrow (1 - t^2)^{\lambda-1/2}$ ($\lambda > -1/2$), denote the Gegenbauer polynomials defined by [1-3]

$$G_n(t, \lambda) = \sum_{k=0}^{\lfloor \frac{n}{2} \rfloor} (-1)^k \frac{(\lambda)_{n-k}}{k! (n-2k)!} (2t)^{n-2k} \quad (5)$$

with $G_0(t, \lambda) = 1$ and $G_1(t, \lambda) = 2\lambda t$. On the other hand, by using (5), the first five Gegenbauer polynomials (see Figure 1) are given by

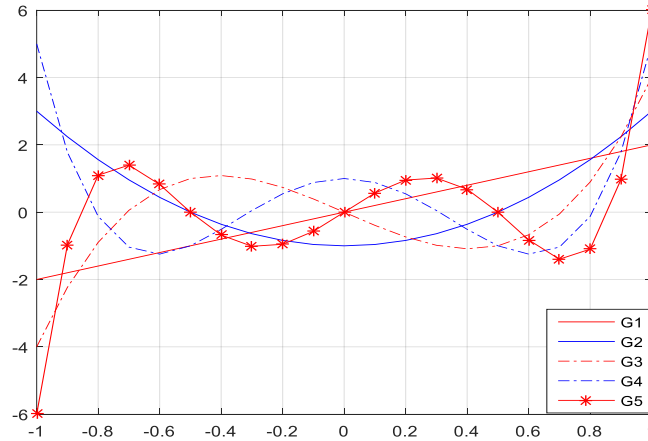


Figure 1. The first five Gegenbauer polynomials for $\lambda = 1$

Fundamental Matrix Relations

Let us consider the solution $y(t)$ of Eq. (1) defined by the truncated Gegenbauer series (4) :

$$y(t) \cong y_N(t) = \sum_{n=0}^N a_n \mathbf{G}_n(t, \lambda), N \geq m, -1 \leq t \leq 1.$$

Then we can convert the finite series (4) to the matrix form as, for $n = 0, 1, \dots, N$,

$$y(t) \cong y_N(t) = \mathbf{G}(t, \lambda) \mathbf{A} \quad (6)$$

where $\mathbf{G}(t, \lambda) = [G_0(t) \ G_1(t) \ \dots \ G_N(t)]$ and $\mathbf{A} = [a_0 \ a_1 \ \dots \ a_N]^T$. On the other hand, by using the relation (5), the matrix $\mathbf{G}(t, \lambda)$ is obtained as

$$\mathbf{G}(t, \lambda) = \mathbf{X}(t) \mathbf{T}(\lambda); \quad \mathbf{X}(t) = [1 \ t \ t^2 \ \dots \ t^N] \quad (7)$$

If N is odd,

$$\mathbf{T} = \begin{bmatrix} 1 & 0 & (-1)^1 \frac{2^0(\lambda)_1}{1!0!} & 0 & \dots & 0 \\ 0 & (-1)^0 \frac{2^1(\lambda)_2}{0!1!} & 0 & (-1)^1 \frac{2^1(\lambda)_2}{1!1!} & \dots & (-1)^{\frac{(N-1)}{2}} \frac{2^1(\lambda)_{\frac{(N+1)}{2}}}{\left(\frac{N-1}{2}\right)!1!} \\ 0 & 0 & (-1)^0 \frac{2^2(\lambda)_2}{0!2!} & 0 & \dots & 0 \\ 0 & 0 & 0 & (-1)^0 \frac{2^3(\lambda)_3}{0!3!} & \dots & (-1)^{\frac{(N-3)}{2}} \frac{2^3(\lambda)_{\frac{(N+3)}{2}}}{\left(\frac{N-3}{2}\right)!3!} \\ \vdots & \vdots & \vdots & \vdots & \ddots & \vdots \\ 0 & 0 & 0 & 0 & \dots & (-1)^0 \frac{2^N(\lambda)_N}{0!N!} \end{bmatrix}$$

If N is even,

$$\mathbf{T} = \begin{bmatrix} 1 & 0 & (-1)^1 \frac{2^0(\lambda)_1}{1!0!} & 0 & \dots & (-1)^{\frac{N}{2}} \frac{2^0(\lambda)_{\frac{N}{2}}}{\left(\frac{N}{2}\right)!1!} \\ 0 & (-1)^0 \frac{2^1(\lambda)_2}{0!1!} & 0 & (-1)^1 \frac{2^1(\lambda)_2}{1!1!} & \dots & 0 \\ 0 & 0 & (-1)^0 \frac{2^2(\lambda)_2}{0!2!} & 0 & \dots & (-1)^{\frac{(N-2)}{2}} \frac{2^2(\lambda)_{\frac{(N+2)}{2}}}{\left(\frac{N-2}{2}\right)!2!} \\ 0 & 0 & 0 & (-1)^0 \frac{2^3(\lambda)_3}{0!3!} & \dots & 0 \\ \vdots & \vdots & \vdots & \vdots & \ddots & \vdots \\ 0 & 0 & 0 & 0 & \dots & (-1)^0 \frac{2^N(\lambda)_N}{0!N!} \end{bmatrix}$$

Also, it is clearly seen from (7) that the derivative $\mathbf{G}^{(k)}(t, \lambda)$ is

$$\mathbf{G}^{(k)}(t, \lambda) = \mathbf{X}(t)\mathbf{B}^k\mathbf{T}(\lambda), k = 0, 1 \quad (8)$$

where

$$\mathbf{B} = \begin{bmatrix} 0 & 1 & 0 & \cdots & 0 \\ 0 & 0 & 2 & \cdots & 0 \\ \vdots & \vdots & \vdots & \cdots & \vdots \\ 0 & 0 & 0 & \cdots & N \\ 0 & 0 & 0 & \cdots & 0 \end{bmatrix}, \mathbf{B}^0 = \begin{bmatrix} 1 & 0 & 0 & \cdots & 0 \\ 0 & 1 & 0 & \cdots & 0 \\ 0 & 0 & 1 & \cdots & 0 \\ \vdots & \vdots & \vdots & \ddots & \vdots \\ 0 & 0 & 0 & \cdots & 1 \end{bmatrix}$$

By using the relations (6), (7) and (8), we have the matrix relations

$$y^{(k)}(t) \cong y_N^{(k)}(t) = \mathbf{G}^{(k)}(t, \lambda)\mathbf{A} = \mathbf{X}^{(k)}(t)\mathbf{T}(\lambda)\mathbf{A} = \mathbf{X}(t)\mathbf{B}^k\mathbf{T}(\lambda)\mathbf{A}, \quad k = 0, 1, 2 \quad (9)$$

By substituting $t \rightarrow \alpha t + \beta$, $k \rightarrow r$ into the relation (9), we get $r = 0, 1, 2$,

$$y^{(r)}(\alpha t + \beta) = \mathbf{X}(\alpha t + \beta)\mathbf{B}^r\mathbf{T}(\lambda) = \mathbf{X}(t)\mathbf{B}(\alpha, \beta)\mathbf{B}^r\mathbf{T}(\lambda)\mathbf{A} \quad (10)$$

where for $\alpha \neq 0, \beta \neq 0$,

$$\mathbf{B}(\alpha, \beta) = \begin{bmatrix} \binom{0}{0} \alpha^0 \beta^0 & \binom{1}{0} \alpha^0 \beta^1 & \binom{2}{0} \alpha^0 \beta^2 & \cdots & \binom{N}{0} \alpha^0 \beta^N \\ 0 & \binom{1}{1} \alpha^1 \beta^0 & \binom{2}{1} \alpha^1 \beta^1 & \cdots & \binom{N}{1} \alpha^1 \beta^{N-1} \\ 0 & 0 & \binom{2}{2} \alpha^2 \beta^0 & \cdots & \binom{N}{2} \alpha^2 \beta^{N-2} \\ \vdots & \vdots & \vdots & \ddots & \vdots \\ 0 & 0 & 0 & \cdots & \binom{N}{N} \alpha^N \beta^0 \end{bmatrix}$$

for $\alpha \neq 0, \beta = 0, \mathbf{B}(\alpha, 0) = \text{diag}[\alpha^0 \quad \alpha^1 \quad \cdots \quad \alpha^N]$.

The kernel function $\mathbf{K}(t, s)$ can be approximated by the truncated Maclaurin series

$$\mathbf{K}(t, s) = \sum_{p=0}^N \sum_{q=0}^N k_{pq} t^p s^q \quad (11)$$

where

$$k_{pq} = \frac{1}{p! q!} \frac{\partial^{p+q} K(0,0)}{\partial t^p \partial s^q}, \quad p, q = 0, 1, 2, \dots, N.$$

The expression (11) can be put in the matrix form

$$\mathbf{K}(t, s) = \mathbf{X}(t)\mathbf{K}\mathbf{X}^T(s), \quad \mathbf{K} = [k_{pq}], p, q = 0, 1, 2, \dots, N \quad (12)$$

By substituting the matrix forms (9) and (12) into integral part $\mathbf{I}(t)$ in Eq. (1), we have the matrix relation

$$\mathbf{I}(t) = \int_{\tau_1(t)}^{\tau_2(t)} \mathbf{X}(t)\mathbf{K}\mathbf{X}^T(s)\mathbf{X}(s)\mathbf{T}(\lambda)\mathbf{A} ds = \mathbf{X}(t)\mathbf{K} \int_{\tau_1(t)}^{\tau_2(t)} \mathbf{X}^T(s)\mathbf{X}(s)\mathbf{T}(\lambda)\mathbf{A} ds, \quad (13)$$

where

$$\mathbf{Q}_f = \int_{\tau_1(t)}^{\tau_2(t)} \mathbf{X}^T(s)\mathbf{X}(s) ds = [r_{pq}],$$

$$r_{pq} = \frac{\tau_2(t)^{p+q+1} - \tau_1(t)^{p+q+1}}{p+q+1}, p, q = 0, 1, 2, \dots, N \quad (14)$$

From Eq. (12), (13) and (14), the following relation is obtained;

$$\mathbf{I}(t) = \mathbf{X}\mathbf{K}\mathbf{Q}_f\mathbf{T}(\lambda)\mathbf{A} \quad (15)$$

Hence, by substituting the matrix relations (9), (10) and (15) into (1) and (3), the matrix equation corresponding to Eq.(1) for $k = 0, 1, 2$ becomes

$$\begin{aligned} \mathbf{X}(t)\mathbf{B}^2\mathbf{T}(\lambda)\mathbf{A} + \sum_{k=0}^2 \binom{2}{k} \mathbf{P}^{(2-k)}(t)\mathbf{X}(t)\mathbf{B}(\alpha, \beta)\mathbf{B}^k\mathbf{T}(\lambda)\mathbf{A} \\ = \mathbf{R}(t)\mathbf{X}(t)\mathbf{T}(\lambda)\mathbf{A} + \mathbf{X}(t)\mathbf{K}\mathbf{Q}_f(t)\mathbf{T}(\lambda)\mathbf{A} + \mathbf{F}(t) \end{aligned} \quad (16)$$

Gegenbauer Collocation Method

For constructing the fundamental matrix equation, we first consider the collocation points defined by,

$$t_i = a + \frac{b-a}{N}i, (Standard) i = 0, 1, 2$$

Then, by using these collocation points into (16) and simplifying, we have the fundamental matrix equation

$$\left(\mathbf{X}\mathbf{B}^2\mathbf{T}(\lambda) + \sum_{k=0}^2 \binom{2}{k} \mathbf{P}^{(2-k)}\mathbf{X}\mathbf{B}(\alpha, \beta)\mathbf{B}^k\mathbf{T}(\lambda) - \mathbf{R}\mathbf{X}\mathbf{T}(\lambda) - \bar{\mathbf{X}}\bar{\mathbf{K}}\bar{\mathbf{Q}}_f\mathbf{T}(\lambda) \right) \mathbf{A} = \mathbf{F} \quad (17)$$

where

$$\begin{aligned} \bar{\mathbf{K}} &= \text{diag}[\mathbf{K} \quad \mathbf{K} \quad \dots \quad \mathbf{K}] \\ \mathbf{R} &= \text{diag}[R(t_0) \quad R(t_1) \quad \dots \quad R(t_N)] \\ \bar{\mathbf{X}} &= \text{diag}[\mathbf{X}(t_0) \quad \mathbf{X}(t_1) \quad \dots \quad \mathbf{X}(t_N)] \\ \mathbf{P}^{(2-k)} &= \text{diag}[p^{(2-k)}(t_0) \quad p^{(2-k)}(t_1) \quad \dots \quad p^{(2-k)}(t_N)], k = 0, 1, 2 \end{aligned}$$

so that

$$\mathbf{X} = \begin{bmatrix} \mathbf{X}(t_0) \\ \mathbf{X}(t_1) \\ \vdots \\ \mathbf{X}(t_N) \end{bmatrix} = \begin{bmatrix} 1 & t_0 & \dots & t_0^N \\ 1 & t_1 & \dots & t_1^N \\ \vdots & \vdots & \ddots & \vdots \\ 1 & t_N & \dots & t_N^N \end{bmatrix}, \bar{\mathbf{Q}}_f = \begin{bmatrix} \mathbf{Q}_f(t_0) \\ \mathbf{Q}_f(t_1) \\ \vdots \\ \mathbf{Q}_f(t_N) \end{bmatrix}, \mathbf{F} = \begin{bmatrix} f(t_0) \\ f(t_1) \\ \vdots \\ f(t_N) \end{bmatrix}.$$

Now we can find the fundamental matrix form for the conditions (2), by using the relation (9), as follows:

$$\sum_{k=0}^{m-1} (a_{kl}\mathbf{X}(a) + b_{kl}\mathbf{X}(b)) \mathbf{B}^k\mathbf{T}(\lambda)\mathbf{A} = \lambda_l, l = 0, 1, \quad (18)$$

Hence, we can write the fundamental matrix equations (17) and (18) corresponding to Eq.(1) and the conditions (2), as respectively,

$$\mathbf{W}\mathbf{A} = \mathbf{F} \text{ or } [\mathbf{W}; \mathbf{F}] \quad (19)$$

and

$$\mathbf{U}_l\mathbf{A} = \lambda_l \text{ or } [\mathbf{U}_l; \lambda_l], l = 0, 1 \quad (20)$$

where

$$\begin{aligned} \mathbf{W} = [w_{pq}] &= \left(\mathbf{X}\mathbf{B}^2\mathbf{T}(\lambda) + \sum_{k=0}^2 \binom{2}{k} \mathbf{P}^{(2-k)}\mathbf{X}\mathbf{B}(\alpha, \beta)\mathbf{B}^k\mathbf{T}(\lambda) - \mathbf{R}\mathbf{X}\mathbf{T}(\lambda) - \bar{\mathbf{X}}\bar{\mathbf{K}}\bar{\mathbf{Q}}_f\mathbf{T}(\lambda) \right) \\ \mathbf{U}_l = [u_{l0} \quad u_{l1} \quad \dots \quad u_{lN}] &= \sum_{k=0}^{m-1} (a_{kl}\mathbf{X}(a) + b_{kl}\mathbf{X}(b)) \mathbf{B}^k\mathbf{T}(\lambda), l = 0, 1, \end{aligned}$$

Consequently, to obtain the solution of Eq.(1) under the conditions (2), by replacing the row matrices (19) by the last (or any) m rows of the augmented matrix (20), we have the required matrix

$$[\tilde{\mathbf{W}}; \tilde{\mathbf{F}}] \text{ or } \tilde{\mathbf{W}}\mathbf{A} = \tilde{\mathbf{F}}. \quad (21)$$

If $\text{rank}\tilde{\mathbf{W}} = \text{rank}[\tilde{\mathbf{W}}; \tilde{\mathbf{F}}] = N + 1$, then we can write $\mathbf{A} = (\tilde{\mathbf{W}})^{-1}\tilde{\mathbf{F}}$. Thus the matrix A (thereby the coefficients a_0, a_1, \dots, a_N) is uniquely determined. Eq.(1) under the conditions (2) has a unique solution. Hence, the problem (1) – (2) has a unique solution in terms of Gegenbauer polynomials in the form (3).

Accuracy of Solutions and Residual Error Estimation

We can easily check the accuracy of the obtained solutions as follows. Since the truncated Gegenbauer series (3) is approximate solution of (1), when the function $y_N(t)$ and its derivatives are substituted in Eq.(1), the resulting equation must be satisfied approximately; that is, for $t = t_q \in [a, b], q = 0, 1, \dots$

$$R_N(t_q) = y_N^{(k)}(t_q) + \sum_{k=0}^2 \binom{2}{k} P(t_q)^{(2-k)} y_N^{(k)}(\alpha t_q + \beta) - R(t_q) y_N(t_q) - I(t_q) - f(t_q) \cong 0$$

or

$$R_N(t_q) \leq 10^{-k_q}, (k_q \text{ is any positive integer}).$$

If $\max 10^{-k_q} = 10^{-k}$ (k is a positive integer) is prescribed, then the truncation limit N is increased until the difference $R_N(t_q)$ at each of the points becomes smaller than the prescribed 10^{-k} . Therefore, if $R_N(t_q) \rightarrow 0$, when N is sufficiently large enough, then the error decreases.

On the other hand, by means of the residual function defined by $R_N(t)$ and the mean value of the function $|R_N(t)|$ on the interval $[a, b]$, the accuracy of the solution can be controlled and the error can be estimated [6-9]. Also, we can estimate the upper bound of the mean error $\overline{R_N}$ as follows:

$$\left| \int_a^b R_N(t) dx \right| = (b-a) |R_N(c)| \leq \int_a^b |R_N(t)| dt, a \leq c \leq b$$

$$(b-a) |R_N(c)| \leq \int_a^b |R_N(t)| dt \Rightarrow |R_N(c)| \leq \frac{\int_a^b |R_N(t)| dt}{b-a} = \overline{R_N}$$

Numerical Examples

In this section, several numerical examples are given to illustrate the accuracy and effectiveness of the method, and all of them are performed on the computer using a program written in Matlab. The absolute errors in the tables are the values of

$$|e_N(t)| = |y(t) - y_N(t)|$$

at selected points.

Example 1: Let us consider linear neutral type functional integro-differential equation

$$[y(t) + t^2 y(2t-1)]'' = y(t) + \int_t^{2t-1} (t+s)y(s)ds + f(t), -1 \leq t \leq 1$$

with the initial conditions $y(0) = 1, y'(0) = 0$.

The exact solution of problem is $y(x) = \cos(t), \lambda = 1$

$f(t) = (1 - 4t^2) \cos(2t - 1) + (1 - 11t) \sin(2t - 1) + (2t - 1) \cos(t)$. Firstly, let us compute the approximate solution defined by

$$y_2(t) = \sum_{n=0}^2 a_n G_n(t, \lambda)$$

The set of the collocation points for $N = 2$ is calculated as $\{t_0 = -1, t_1 = 0, t_2 = 1\}$ and from Eq.(17), the fundamental matrix equation of the problem is written as

$$\{\mathbf{XB}^2 \mathbf{T}(\lambda) + \mathbf{P}^{(2)} \mathbf{XB}(-1,1) \mathbf{T}(\lambda) + 2\mathbf{P}^{(1)} \mathbf{XB}(-1,1) \mathbf{BT}(\lambda) + \mathbf{P}^{(0)} \mathbf{XB}(-1,1) \mathbf{B}^2 \mathbf{T}(\lambda) - \mathbf{RXT}(\lambda) - \overline{\mathbf{XKQ}}_f \mathbf{T}(\lambda)\} \mathbf{A} = \mathbf{F}$$

From Eq. (20), we obtain the matrix form for the initial condition:

$$[\mathbf{U}_0; \lambda_0] = [1 \quad 0 \quad -1 \quad ; \quad 1] \text{ and } [\mathbf{U}_1; \lambda_1] = [0 \quad 2 \quad 0 \quad ; \quad 0].$$

Therefore, from Eq. (21), the new augmented matrix is calculated as

$$[\tilde{\mathbf{W}}; \tilde{\mathbf{F}}] = \begin{bmatrix} 1 & 0 & -1 & ; & 1 \\ 1/2 & -10/3 & 29/2 & ; & -445/342 \\ 0 & 2 & 0 & ; & 0 \end{bmatrix}$$

Solving this system, the unknown coefficients matrix is obtained as

$$\mathbf{A} = [447/508 \quad 0 \quad -308/2565]^T.$$

Therefore, we obtain the approximate solution $y_2(x) = 1 - 0.4803x^2$. For $N = 3, 4, 5$ the obtained approximate solutions and the upper bounds of the estimated errors are

$$y_3(x) = 1 - 0.2897x^2 + 0.1331x^3, y_4(x) = 1 - 0.4342x^2 + 0.1510x^3 + 0.0540x^4,$$

$$y_5(x) = 1 - 0.0246x^2 + 0.0467x^3 - 0.4857x^4 - 0.1665x^5$$

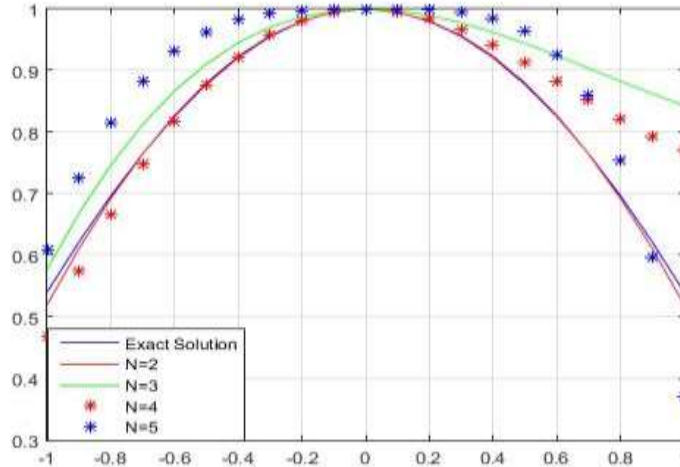


Figure 2. Numerical and exact solutions of Example 1 for $N = 2, 3, 4, 5$

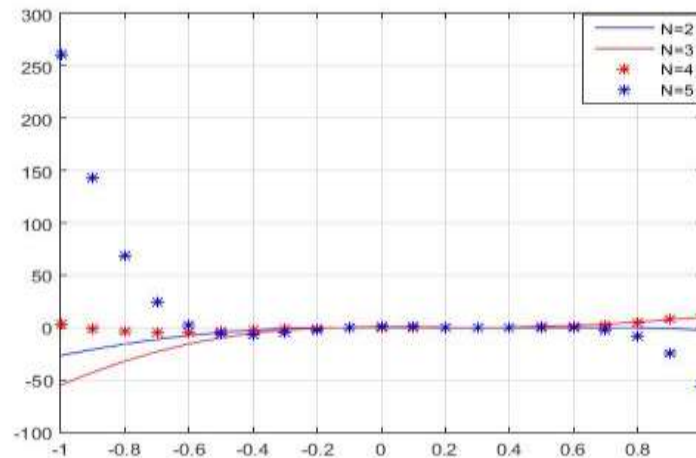


Figure 3. Residual error functions of Example 1 for $N = 2, 3, 4, 5$

Table 1. Comparison of the absolute errors of Example 1 for $N = 2, 3, 4, 5$

t	$y(x) = \cos(t)$	$ e_2(t) $	$ e_3(t) $	$ e_4(t) $	$ e_5(t) $
-1	0.5403	0.0206	0.0369	0.1795	0.0692
-0.5	0.8776	0.0023	0.0334	0.0084	0.0853
0	1	0	0	0	0
0.5	0.8776	0.0023	0.0666	0.0294	0.0865
1	0.5403	0.0206	0.3031	0.1225	0.1704

Example 2: Firstly, consider the integro-differential equation

$$[y(t) + ty(t-1)]'' = 2ty(t) + \int_t^{t-1} (t-s)y(s)ds + f(t), -1 \leq t \leq 1$$

with the initial condition $y(0) = 1, y'(0) = -1$. The exact solution of problem is $y(t) = e^{-t}$, $\lambda = 1$ and $f(t) = (t - 2)e^{1-t} + (2 - 2t)e^{-t}$. Let us compute the approximate solution defined by

$$y_2(t) = \sum_{n=0}^2 a_n G_n(t, \lambda)$$

The set of the collocation points for $N = 2$ is calculated as $\{t_0 = -1, t_1 = 0, t_2 = 1\}$ and from Eq.(18), the fundamental matrix equation of the problem is written as

$$\{\mathbf{XB}^2\mathbf{T}(\lambda) + \mathbf{P}^{(2)}\mathbf{XB}(1, -1)\mathbf{T}(\lambda) + 2\mathbf{P}^{(1)}\mathbf{XB}(1, -1)\mathbf{BT}(\lambda) + \mathbf{P}^{(0)}\mathbf{XB}(1, -1)\mathbf{B}^0\mathbf{T}(\lambda) - \mathbf{RXT}(\lambda) - \overline{\mathbf{XKQ}}_f\mathbf{T}(\lambda)\}\mathbf{A} = \mathbf{F}$$

From Eq. (20), we obtain the matrix form for the initial condition :

$$[\mathbf{U}_0; \lambda_0] = [1 \quad 0 \quad -1 \quad ; \quad 1] \text{ and } [\mathbf{U}_1; \lambda_1] = [0 \quad 2 \quad 0 \quad ; \quad -1].$$

Therefore, from Eq. (21), the new augmented matrix is calculated as

$$[\tilde{\mathbf{W}}; \tilde{\mathbf{F}}] = \begin{bmatrix} 1 & 0 & -1 & ; & 1 \\ 0 & 2 & 0 & ; & -1 \\ -3/2 & 1/3 & 59/6 & ; & -1 \end{bmatrix}$$

Solving this system, the unknown coefficients matrix is obtained as $\mathbf{A} = [27/25 \quad -1/2 \quad 2/25]^T$. Therefore, we obtain the approximate solution $y_2(x) = 1 - x + 0.32x^2$. For $N = 3, 5$ the obtained approximate solutions and the upper bounds of the estimated errors are

$$y_3(x) = 1 - x + 0.6289x^2 - 0.1589x^3,$$

$$y_5(x) = 1 - x + 0.4656x^2 - 0.1681x^3 + 0.0519x^4 - 0.0079x^5$$

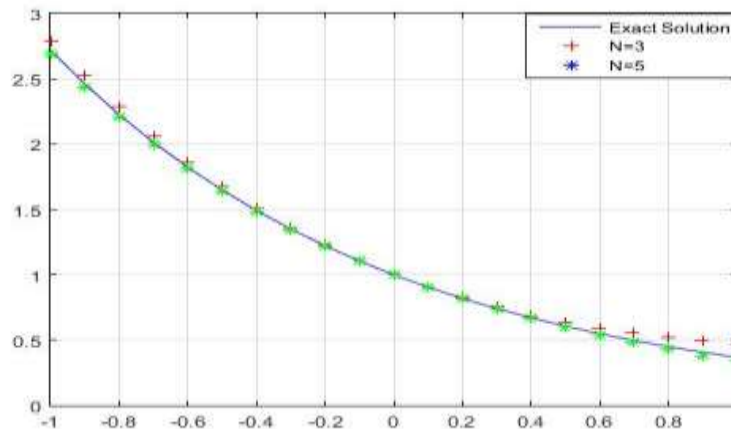


Figure 4. Numerical and exact solutions of Example 2 for $N = 2, 3, 5$

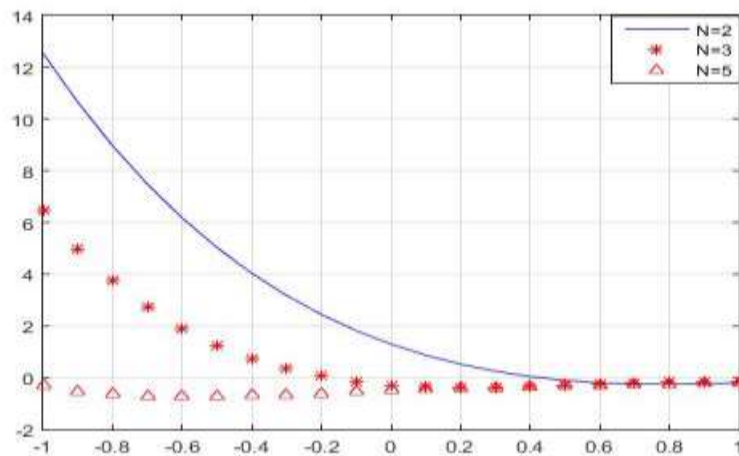


Figure 5. Residual error functions of Example 2 for $N = 2, 3, 5$

Table 2. Comparison of the absolute errors of Example 2 for $N = 2, 3, 5$

t	$y(x) = e^{-t}$	$ e_2(t) $	$ e_3(t) $	$ e_5(t) $
-1	2.7183	0.3983	0.0695	0.0248
-0.5	1.6487	0.0687	0.0284	0.0078
0	1	0	0	0
0.5	0.6065	0.0265	0.0308	0.0081
1	0.3679	0.0479	0.1021	0.0264

Conclusion

In this study, using Gegenbauer polynomials, to numerically solve the second-order linear neutral type functional integro-differential equations is presented. An error analysis technique has introduced for the method by using the residual function. To get the best approximation, the truncation limit N must be chosen large enough. It is observed from the tables and figures that the proposed error estimation is very effective. In addition, it is observed from the numerical values of the approximate solutions and the error estimations that the developed method is quite effective and applicative.

References

- [1] Kim DS, Kim T, Rim S-H (2012) Some identities involving Gegenbauer polynomials, *Advances in Difference Equations* 2012:219.
- [2] Rashed MT (2004) Numerical solution of functional differential, integral and integro-differential equations, *Appl. Numer. Math.* 156:485–492.
- [3] Khan S, Al-Gonah AA, Yasmin G (2012) Generalized and mixed type Gegenbauer polynomials, *J. Math. Anal. Appl.* 390:197-207.
- [4] Gümgüm S, Baykuş Savaşaneril N, Kürkçü ÖK, Sezer M (2018) A numerical technique based on Lucas polynomials together with standard and Chebyshev-Lobatto collocation points for solving functional integro-differential equations involving variable delays, *Sakarya University Journal of Science*, 22 (6), 1659-1668.
- [5] Baykuş N, Sezer M (2017) Hybrid Taylor-Lucas collocation method for numerical solution of high-order pantograph type delay differential equations with variables delays, *Appl. Math. Inf. Sci.* 11(6): 1795-1801.
- [6] B. Gürbüz, M. Sezer, C. Güler, (2014) Laguerre collocation method for solving Fredholm integro-differential equations with functional arguments, *J.Appl.Math.*2014, Article ID 682398, 12 pp.
- [7] Yüzbaşı Ş, Gök E, Sezer M (2014) Laguerre matrix method with the residual error estimation for solutions of a class of delay differential equations, *Math. Meth. Appl. Sci.*, 453-463.

3rd International Students Science Congress
3-4 May 2019, İzmir - Turkey

- [8] Şahin N, Yüzbaşı Ş, Sezer M (2011) A Bessel polynomial approach for solving general linear Fredholm integro- differential –difference equations. *Int.J.Comput.Math.*88 (14), 3093-3111.
- [9] Mollaoğlu T, Sezer M (2017) A numerical approach with residual error estimation for solution of high-order linear differential-difference equations by using Gegenbauer polynomials. *CBU J. of Sci.* 13(1): 39-49.

Boubaker Collocation Method for Neutral Functional-Differential Equations with Proportional Delays

Elif Zinnur Aykotalp*, Mehmet Sezer
Manisa Celal Bayar Univ., Dept. of Mathematics, Manisa, Türkiye
*Corresponding author: aykotalp.elif@gmail.com

Keywords: Boubaker polynomials, collocation methods, neutral differential equations, residual error estimation
Discipline: Mathematics

Abstract

In this study, the Boubaker collocation method has been presented to solve high order neutral functional–differential equations with proportional delays. The proposed method is based on the matrix forms of Boubaker polynomials and their derivatives along with the collocation points. The used technique reduces the problem to a matrix equation corresponding to a set of algebraic equations with the unknown Boubaker coefficients. Also, an error analysis based on residual function is performed and some numerical examples are given to illustrate the efficiency and accuracy of the method.

Introduction

The main aim of this study is to apply the Boubaker polynomials to find the approximate solutions of high order neutral functional–differential equations with proportional delays under the initial conditions. The method is based on the matrix forms of Boubaker polynomials and their derivatives by means of the collocation points. For this aim, we consider the neutral functional-differential equation in the form [1,3,5]

$$(y(t) - cy(\tau_m t))^{(m)} = \beta y(t) + \sum_{k=0}^{m-1} P_k(t) y^{(k)}(\alpha_k t) + g(t) \quad (1)$$

with the initial conditions

$$\sum_{k=0}^{m-1} a_{jk} y^{(k)}(0) = \lambda_j, \quad j = 0, 1, \dots, m-1 \quad (2)$$

and look for the approximate solution in the truncated Boubaker series

$$y(t) \cong y_N(t) = \sum_{n=0}^N a_n B_n(t) \quad N \geq m, \quad a \leq t \leq b \quad (3)$$

where $a_n, n = 0, 1, \dots, N$ are unknown coefficients; $B_n(t), n = 0, 1, \dots, N$, denote the Boubaker polynomials defined by [2,4]

$$B_n(t) = \sum_{p=0}^{\lfloor n/2 \rfloor} (-1)^p \frac{(n-4p)}{(n-p)} \binom{n-p}{p} t^{n-2p}. \quad (4)$$

or recursively

$$B_n(t) = tB_{n-1}(t) - B_{n-2}(t); \quad n \geq 2$$

with $B_0(t) = 1$ and $B_1(t) = t$.

On the other hand, by using (4), the first four Boubaker polynomials are given by

$$B_0(t) = 1, \quad B_1(t) = t, \quad B_2(t) = t^2 + 2, \quad B_3(t) = t^3 + t, \dots$$

and the Boubaker polynomials $B_n(t)$ can be defined through the differential equation:

$$(t^2 - 1)(3nt^2 + n - 2)B_n''(t) + 3t(nt^2 + 3n - 2)B_n'(t) - n(3n^2t^2 + n^2 - 6n + 8)B_n(t) = 0.$$

Fundamental Matrix Relations

Let us consider the solution $y(t)$ of Eq. (1) defined by the truncated Boubaker series (3). Then we can convert the finite series (3) to the matrix form as, for $n = 0, 1, \dots, N$,

$$y(t) \cong y_N(t) = \mathbf{B}(t) \mathbf{A} \quad (5)$$

where

$$\mathbf{B}(t) = [B_0(t) \ B_1(t) \ \dots \ B_N(t)], \quad \mathbf{A} = [a_0 \ a_1 \ \dots \ a_N]^T.$$

On the other hand, by using the relation (4), the matrix $\mathbf{B}(t)$ is obtained as

$$\mathbf{B}(t) = \mathbf{X}(t) \mathbf{H} \quad (6)$$

where

$$\mathbf{X}(t) = [1 \ t \ \dots \ t^N]$$

if N is odd,

$$\mathbf{H}^T = \begin{bmatrix} \phi_{0,0} & 0 & 0 & \dots & 0 & 0 \\ 0 & \phi_{1,0} & 0 & \dots & 0 & 0 \\ \phi_{2,1} & 0 & \phi_{2,0} & \dots & 0 & 0 \\ \vdots & \vdots & \vdots & \ddots & \vdots & \vdots \\ \phi_{N-1, \frac{N-1}{2}} & 0 & \phi_{N-1, \frac{N-3}{2}} & \dots & \phi_{N-1,0} & 0 \\ 0 & \phi_{N, \frac{N-1}{2}} & 0 & \dots & 0 & \phi_{N,0} \end{bmatrix}$$

if N is even,

$$\mathbf{H}^T = \begin{bmatrix} \phi_{0,0} & 0 & 0 & \dots & 0 & 0 \\ 0 & \phi_{1,0} & 0 & \dots & 0 & 0 \\ \phi_{2,1} & 0 & \phi_{2,0} & \dots & 0 & 0 \\ \vdots & \vdots & \vdots & \ddots & \vdots & \vdots \\ 0 & \phi_{N-1, \frac{N-2}{2}} & 0 & \dots & \phi_{N-1,0} & 0 \\ \phi_{N, \frac{N}{2}} & 0 & \phi_{N, \frac{N-2}{2}} & \dots & 0 & \phi_{N,0} \end{bmatrix}$$

where

$$B_n(t) = \sum_{p=0}^{\lfloor n/2 \rfloor} \phi_{n,p} t^{n-2p}, \quad n = 0, 1, \dots, N, \quad p = 0, 1, \dots, \left\lfloor \frac{n}{2} \right\rfloor,$$

$$\phi_{n,p} = \left[\frac{(n-4p)(n-p)}{(n-p)} \binom{n-p}{p} \right] (-1)^p.$$

Also, it is clearly seen from (6) that the relation between the matrix $X(t)$ and derivative $B^{(k)}(t)$ is

$$\mathbf{B}^{(k)}(t) = \mathbf{X}(t) \mathbf{M}^k \mathbf{H}, \quad k = 0, 1, 2, \dots, m \quad (7)$$

3rd International Students Science Congress
3-4 May 2019, İzmir - Turkey

$$\mathbf{M} = \begin{bmatrix} 0 & 1 & 0 & \cdots & 0 & 0 \\ 0 & 0 & 2 & \cdots & 0 & 0 \\ 0 & 0 & 0 & \cdots & 0 & 0 \\ \vdots & \vdots & \vdots & \ddots & \vdots & \vdots \\ 0 & 0 & 0 & \cdots & 0 & N \\ 0 & 0 & 0 & \cdots & 0 & 0 \end{bmatrix}.$$

By using the relations (5), (6) and (7), we have the matrix relations

$$\begin{aligned} y^{(k)} &\cong y_N^{(k)} = \mathbf{B}^{(k)}(t) \mathbf{A} \\ &= \mathbf{X}^{(k)}(t) \mathbf{H} \mathbf{A} = \mathbf{X}(t) \mathbf{M}^k \mathbf{H} \mathbf{A}, \quad k = 0, 1, \dots \end{aligned} \quad (8)$$

By substituting $t \rightarrow \alpha_k t$ into the relation (8), we get, $k = 0, 1, 2, \dots$

$$\begin{aligned} y^{(k)}(\alpha_k t) &= \mathbf{X}(\alpha_k t) \mathbf{M}^k \mathbf{H} \mathbf{A} \\ &= \mathbf{X}(t) \mathbf{D}(\alpha_k) \mathbf{M}^k \mathbf{H} \mathbf{A} \end{aligned} \quad (9)$$

so that, for $\alpha_k \neq 0$,

$$\mathbf{D}(\alpha_k) = \begin{bmatrix} \begin{pmatrix} 0 \\ 0 \end{pmatrix} \alpha_k^0 & 0 & 0 & \cdots & 0 \\ 0 & \begin{pmatrix} 1 \\ 1 \end{pmatrix} \alpha_k^1 & 0 & \cdots & 0 \\ 0 & 0 & \begin{pmatrix} 2 \\ 2 \end{pmatrix} \alpha_k^2 & \cdots & 0 \\ \vdots & \vdots & \vdots & \ddots & \vdots \\ 0 & 0 & 0 & \cdots & \begin{pmatrix} N \\ N \end{pmatrix} \alpha_k^N \end{bmatrix}.$$

By substituting $t \rightarrow \tau_m t$ into the relation (8), we get, $k = m$

$$\begin{aligned} y^{(m)}(\tau_m t) &= \mathbf{X}(\tau_m t) \mathbf{M}^m \mathbf{H} \mathbf{A} \\ &= \mathbf{X}(t) \mathbf{D}(\tau_m) \mathbf{M}^m \mathbf{H} \mathbf{A} \end{aligned} \quad (10)$$

so that, for $\tau_m \neq 0$,

$$\mathbf{D}(\tau_m) = \begin{bmatrix} \begin{pmatrix} 0 \\ 0 \end{pmatrix} \tau_m^0 & 0 & 0 & \cdots & 0 \\ 0 & \begin{pmatrix} 1 \\ 1 \end{pmatrix} \tau_m^1 & 0 & \cdots & 0 \\ 0 & 0 & \begin{pmatrix} 2 \\ 2 \end{pmatrix} \tau_m^2 & \cdots & 0 \\ \vdots & \vdots & \vdots & \ddots & \vdots \\ 0 & 0 & 0 & \cdots & \begin{pmatrix} N \\ N \end{pmatrix} \tau_m^N \end{bmatrix}.$$

Boubaker Collocation Method

For constructing the fundamental matrix equation, we first consider the collocation points defined by

$$t_i = a + \frac{b-a}{N} i, \quad i = 0, 1, \dots, N. \quad (11)$$

Then, by using the collocation points (11) into Eq (1) and then into (8), (9) and (10), we have the system of the equations

$$y^{(m)}(t_i) - cy^{(m)}(\tau_m t_i) = \beta y(t_i) + \sum_{k=0}^{m-1} P_k(t_i) y^{(k)}(\alpha_k t_i) + g(t_i)$$

or briefly the matrix equation

$$\mathbf{Y}^{(m)} - c\mathbf{Y}^{(m)}(\tau_m) = \beta\mathbf{Y}^{(0)} + \sum_{k=0}^{m-1} P_k \mathbf{Y}^{(k)}(\alpha_k) + \mathbf{G}$$

or clearly fundamental matrix equation

$$\left\{ \mathbf{X}\mathbf{M}^m - c\mathbf{X}\mathbf{D}(\tau_m)\mathbf{M}^m - \beta\mathbf{X}\mathbf{M}^0 - \sum_{k=0}^{m-1} P_k \mathbf{X}\mathbf{D}(\alpha_k)\mathbf{M}^k \right\} \mathbf{H}\mathbf{A} = \mathbf{G} \quad (12)$$

so that

$$\begin{aligned} \mathbf{P}_k &= \text{diag} [P_k(t_0) \quad P_k(t_1) \quad \dots \quad P_k(t_N)], \\ \mathbf{Y}^{(m)} &= \begin{bmatrix} y^{(m)}(t_0) \\ y^{(m)}(t_1) \\ \vdots \\ y^{(m)}(t_N) \end{bmatrix} = \begin{bmatrix} \mathbf{X}(t_0)\mathbf{M}^m\mathbf{H}\mathbf{A} \\ \mathbf{X}(t_1)\mathbf{M}^m\mathbf{H}\mathbf{A} \\ \vdots \\ \mathbf{X}(t_N)\mathbf{M}^m\mathbf{H}\mathbf{A} \end{bmatrix} = \mathbf{X}\mathbf{M}^m\mathbf{H}\mathbf{A}, \\ \mathbf{Y}^{(k)}(\alpha_k) &= \begin{bmatrix} y^{(k)}(\alpha_k t_0) \\ y^{(k)}(\alpha_k t_1) \\ \vdots \\ y^{(k)}(\alpha_k t_N) \end{bmatrix} = \begin{bmatrix} \mathbf{X}(t_0)\mathbf{D}(\alpha_k)\mathbf{M}^k\mathbf{H}\mathbf{A} \\ \mathbf{X}(t_1)\mathbf{D}(\alpha_k)\mathbf{M}^k\mathbf{H}\mathbf{A} \\ \vdots \\ \mathbf{X}(t_N)\mathbf{D}(\alpha_k)\mathbf{M}^k\mathbf{H}\mathbf{A} \end{bmatrix} = \mathbf{X}\mathbf{D}(\alpha_k)\mathbf{M}^k\mathbf{H}\mathbf{A}, \\ \mathbf{Y}^{(m)}(\tau_m) &= \begin{bmatrix} y^{(m)}(\tau_m t_0) \\ y^{(m)}(\tau_m t_1) \\ \vdots \\ y^{(m)}(\tau_m t_N) \end{bmatrix} = \begin{bmatrix} \mathbf{X}(t_0)\mathbf{D}(\tau_m)\mathbf{M}^m\mathbf{H}\mathbf{A} \\ \mathbf{X}(t_1)\mathbf{D}(\tau_m)\mathbf{M}^m\mathbf{H}\mathbf{A} \\ \vdots \\ \mathbf{X}(t_N)\mathbf{D}(\tau_m)\mathbf{M}^m\mathbf{H}\mathbf{A} \end{bmatrix} = \mathbf{X}\mathbf{D}(\tau_m)\mathbf{M}^m\mathbf{H}\mathbf{A}, \end{aligned}$$

$$\mathbf{X} = \begin{bmatrix} \mathbf{X}(t_0) \\ \mathbf{X}(t_1) \\ \vdots \\ \mathbf{X}(t_N) \end{bmatrix} = \begin{bmatrix} 1 & t_0 & \cdots & t_0^N \\ 1 & t_1 & \cdots & t_1^N \\ \vdots & \vdots & \ddots & \vdots \\ 1 & t_N & \cdots & t_N^N \end{bmatrix}, \mathbf{G} = \begin{bmatrix} g(t_0) \\ g(t_1) \\ \vdots \\ g(t_N) \end{bmatrix}.$$

Then we can write the fundamental matrix equations (12) and similarly, the matrix equations of the initial conditions (2), respectively, as follows:

$$\mathbf{WA} = \mathbf{G} \text{ or } [\mathbf{W}; \mathbf{G}] \quad (13)$$

and

$$\mathbf{U}_l \mathbf{A} = \lambda_l \text{ or } [\mathbf{U}_l; \lambda_l], l = 0, 1, \dots, m-1 \quad (14)$$

where

$$\mathbf{W} = \left\{ \mathbf{X} \mathbf{M}^m - c \mathbf{X} \mathbf{D}(\tau_m) \mathbf{M}^m - \beta \mathbf{X} \mathbf{M}^0 - \sum_{k=0}^{m-1} \mathbf{P}_k \mathbf{X} \mathbf{D}(\alpha_k) \mathbf{M}^k \right\} \mathbf{H}$$

$$\mathbf{U}_l = [u_{l0} \quad u_{l1} \quad \cdots \quad u_{lN}].$$

Consequently, to obtain the solution of Eq. (1) under the conditions (2), by replacing the row matrices (14) by the last (or any) m rows of the augmented matrix (13), we have the required matrix

$$[\mathbf{W}; \mathbf{G}] \text{ or } \mathbf{WA} = \mathbf{G}. \quad (15)$$

If $\text{rank} \tilde{\mathbf{W}} = \text{rank} [\tilde{\mathbf{W}}; \tilde{\mathbf{G}}] = N + 1$, then we can write $\mathbf{A} = (\tilde{\mathbf{W}})^{-1} \tilde{\mathbf{G}}$. Thus the matrix \mathbf{A} (thereby the coefficients a_0, a_1, \dots, a_N) is uniquely determined. Eq. (1) under the conditions (2) has a unique solution. Hence, the problem (1)-(2) has a unique solution in terms of Boubaker polynomials in the form (3).

Accuracy of Solutions and Residual Error Estimation

We can easily check the accuracy of the obtained solutions as follows. Since the truncated Boubaker series (3) is the approximate solution of (1), when the function $y_N(t)$ and its derivatives are substituted in Eq. (1), the resulting equation must be satisfied approximately;

that is, for $t = t_q \in [a, b], q = 0, 1, \dots$

$$R_N(t_q) = y_N^{(m)}(t_q) - c y_N^{(m)}(\tau_m t_q) - \beta y_N(t_q) + \sum_{k=0}^{m-1} P_k(t_q) y_N^{(k)}(\alpha_k t_q) - g(t_q) \cong 0$$

or

$$R_N(t_q) \leq 10^{-k_q}, (k_q \text{ is any positive integer}).$$

If $\max 10^{-k_q} = 10^{-k}$ (k is a positive integer) is prescribed, then the truncation limit N is increased until the difference $R_N(t_q)$ at each of the selected points becomes smaller than the prescribed 10^{-k} [6-8].

Numerical Examples

In this section, several numerical examples are given to illustrate the accuracy and effectiveness of the method, and all of them are performed on the computer using a program written in Matlab. The absolute errors in the tables are the values of

$$|e_N(t)| = |y(t) - y_N(t)|$$

at selected points.

Example 1: Consider the following third-order neutral functional differential equation with proportional delay:

$$y'''(t) - 2y'\left(\frac{t}{2}\right) = \frac{1}{2}y(t) + \frac{3t}{2}y''\left(\frac{t}{3}\right) - 2t^3 - 18t^2, \quad 0 \leq t \leq 1,$$

with the initial conditions $y(0) = 48$, $y'(0) = 0$, $y''(0) = 0$. The exact solution is $y(t) = 4t^3 + 48$.

$$c = 2, \tau = 1/2, \beta = 1/2, P(t) = (3/2)t, \alpha = 1/3, g(t) = -2t^3 - 18t^2.$$

Firstly, let us seek the approximate solution defined by

$$y_3(t) = \sum_{n=0}^3 a_n B_n(t).$$

For this purpose, the set of the collocation points (10) for $N = 3$ is calculated as

$$\{t_0 = 0, t_1 = 1/3, t_2 = 2/3, t_3 = 1\}$$

and from Eq. (12), the fundamental matrix equation of the problem is written as

$$\left\{ \mathbf{X}\mathbf{M}^3\mathbf{H} - 2\mathbf{X}\mathbf{D}\left(\frac{1}{2}\right)\mathbf{M}^1\mathbf{H} - \frac{1}{2}\mathbf{X}\mathbf{H} - \sum_{k=0}^3 \mathbf{P}_k\mathbf{X}\mathbf{D}\left(\frac{1}{3}\right)\mathbf{M}^k\mathbf{H} \right\} \mathbf{A} = \mathbf{G}$$

Hence, the augmented matrix for the fundamental matrix equation can be written as

$$[\mathbf{W}; \mathbf{G}] = \begin{bmatrix} -1/2 & -2 & -5/2 & 4 & ; & 0 \\ -1/2 & -13/16 & -29/9 & 58/27 & ; & -52/27 \\ -1/2 & -7/3 & -73/18 & -4/27 & ; & -50/27 \\ -1/2 & -5/2 & -5 & -3 & ; & -36 \end{bmatrix}.$$

From Eq. (13), we obtain the matrix form for the initial conditions:

$$[u_0; \lambda_0] = [1 \ 0 \ 2 \ 0 ; 48]$$

$$[u_1; \lambda_1] = [0 \ 1 \ 0 \ 1 ; 0]$$

$$[u_2; \lambda_2] = [0 \ 0 \ 2 \ 0 ; 0]$$

Therefore, from Eq. (14), the new augmented matrix is calculated as

$$[\tilde{\mathbf{W}}; \tilde{\mathbf{G}}] = \begin{bmatrix} -1/2 & -2 & -5/2 & 4 & ; & 0 \\ 1 & 0 & 2 & 0 & ; & 48 \\ 0 & 1 & 0 & 1 & ; & 0 \\ 0 & 0 & 2 & 0 & ; & 0 \end{bmatrix}.$$

Solving this system, the unknown coefficients matrix is obtained as

$$\mathbf{A} = [48 \ -4 \ 0 \ 4]^T.$$

Therefore, we obtain the approximate solution as

$$y_3(t) = \sum_{n=0}^3 a_n B_n(t) = a_0 B_0(t) + a_1 B_1(t) + a_2 B_2(t) + a_3 B_3(t) \rightarrow y_3(t) = 4t^3 + 48$$

which is the exact solution.

Example 2: Consider the following first-order neutral functional differential equation with proportional delay:

$$y'(t) - \frac{1}{2}y'\left(\frac{t}{2}\right) = \frac{1}{2}y(t) + \frac{1}{2}y''\left(\frac{t}{2}\right) - \frac{3}{2}e^{-t}, \quad 0 \leq t \leq 1,$$

with the initial conditions $y(0) = 1$, $y'(0) = -1$, $y''(0) = 1$. The exact solution is $y(t) = e^{-t}$.

Let us compute the approximate solution defined by

$$y_4(t) = \sum_{n=0}^4 a_n B_n(t).$$

The set of the collocation points for $N = 4$ is calculated as

$$\left\{ x_0 = 0, x_1 = \frac{1}{4}, x_2 = \frac{1}{2}, x_3 = \frac{3}{4}, x_4 = 1 \right\}$$

and from Eq. (12), the fundamental matrix equation of the problem is written as

$$\left\{ \mathbf{X} \mathbf{M}^1 \mathbf{H} - \frac{1}{2} \mathbf{X} \mathbf{D} \left(\frac{1}{2} \right) \mathbf{M}^1 \mathbf{H} - \frac{1}{2} \mathbf{X} \mathbf{H} - \sum_{k=0}^2 \mathbf{P}_k \mathbf{X} \mathbf{D} \left(\frac{1}{2} \right) \mathbf{M}^k \mathbf{H} \right\} \mathbf{A} = \mathbf{G}$$

The augmented matrix for the fundamental matrix equation can be written as

$$[\mathbf{W}; \mathbf{G}] = \begin{bmatrix} -1/2 & 1/2 & -2 & 1/2 & 1 & ; & -3/2 \\ -1/2 & 3/8 & -53/32 & 5/32 & 493/512 & ; & -3/2 e^{-1/4} \\ -1/2 & 1/4 & -11/8 & 3/32 & 17/16 & ; & -3/2 e^{-1/2} \\ -1/2 & 1/8 & -37/32 & 17/64 & 809/512 & ; & -3/2 e^{-3/4} \\ -1/2 & 0 & -1 & 5/8 & 11/4 & ; & -3/2 e^{-1} \end{bmatrix}.$$

From Eq. (13), we obtain the matrix form for the initial conditions:

$$[u_0; \lambda_0] = [1 \ 0 \ 2 \ 0 \ -2 \ ; \ 1]$$

$$[u_1; \lambda_1] = [0 \ 1 \ 0 \ 1 \ 0 \ ; \ -1]$$

$$[u_2; \lambda_2] = [0 \ 0 \ 2 \ 0 \ 0 \ ; \ 1].$$

Solving this system, we have shown the approximate solutions for $N = 4, N = 7$, and $N = 8$ are compared with the exact solutions in Table 1, Figure 1 and Figure 2.

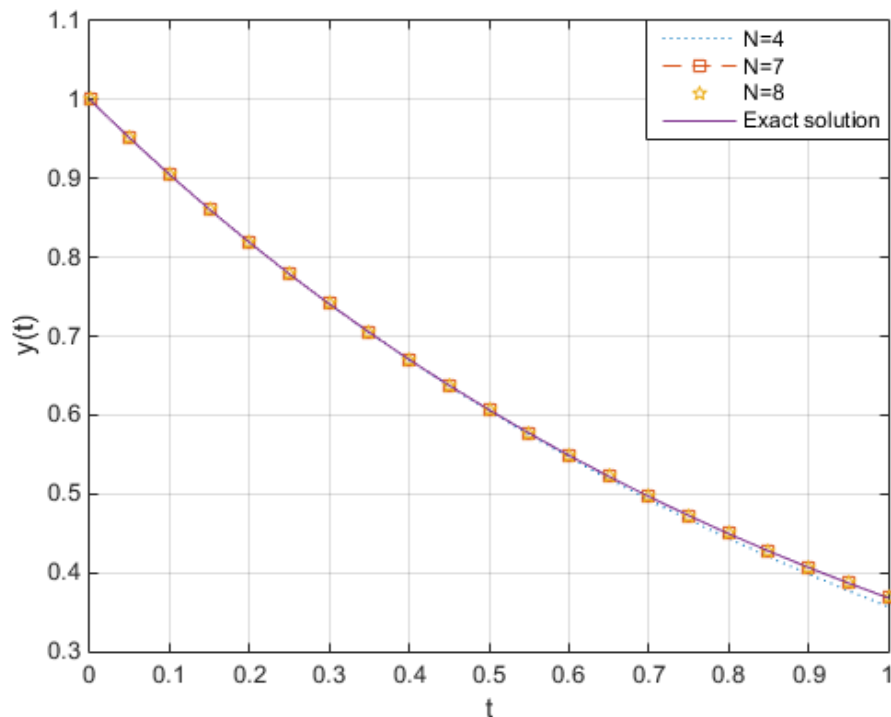


Figure 1. Graphics of the exact solution and numerical solutions of Example 2 for $N = 4, 7, 8$

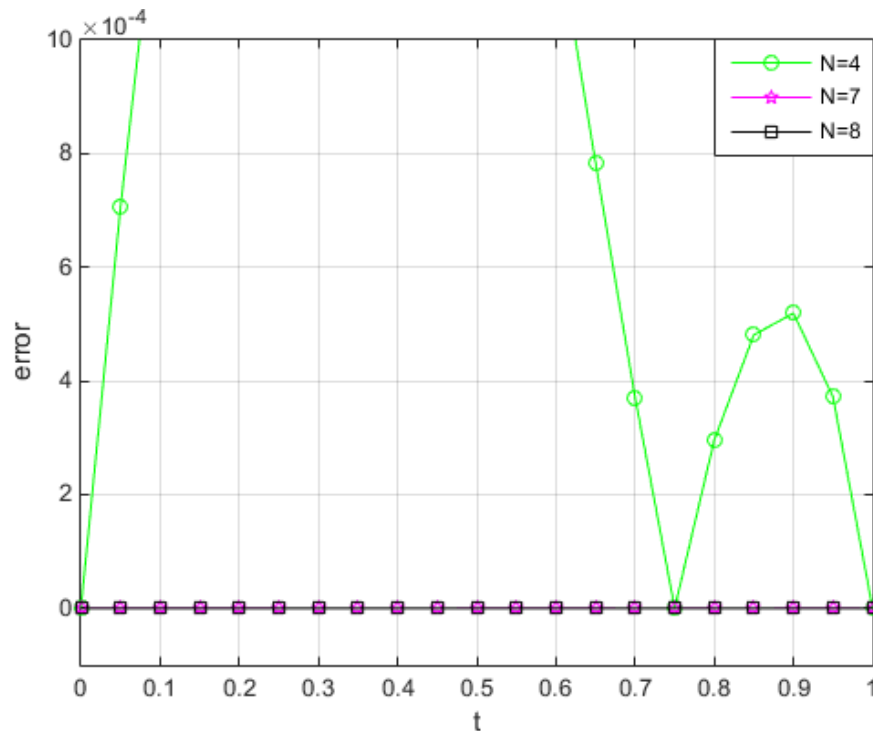


Figure 2. Graphics of residual error functions of Example 2 for $N = 4, 7, 8$

Table 1. Numerical results of Example 2

x_i	Exact Solution	N=4		N=7		N=8	
		$y(x_i)$	$ e(x_i) $	$y(x_i)$	$ e(x_i) $	$y(x_i)$	$ e(x_i) $
0	1.000000000	1.000000000	0,0	1.000000000	8.3484e-18	1.000000000	3.5562e-17
0.2	0.8187307531	0.8186407531	0.00009	0.8187307549	1.7899e-09	0.8187307532	1.3799e-10
0.4	0.670320046	0.6695543086	7.6574e-04	0.6703201795	1.3342e-07	0.6703200568	1.0778e-08
0.6	0.5488116361	0.5461912505	2.6204e-03	0.5488123192	6.8312e-07	0.5488116912	5.5129e-08
0.8	0.4493289641	0.4432870147	6.0419e-03	0.4493307669	1.8028e-06	0.4493291098	1.4568e-07
1.0	0.3678794412	0.3568618897	1.1018e-02	0.3678829499	3.5087e-06	0.3678797237	2.8250e-07

Conclusion

A new matrix method based on Boubaker polynomials and collocation points is proposed to solve the neutral functional–differential equations with proportional delays. The convenience of using Boubaker polynomial expansion is that they have shown to be effective in approximating the given function, at the same time, fast and efficiently. An error analysis technique based on residual function is also developed and applied to three sample problems to demonstrate the validity and applicability of the method. By using this technique it is possible to estimate the error function even when the exact solution is not known. In three of the examples, it is confirmed that the Boubaker polynomial solution method yields quite acceptable results and the accuracy of the solution can significantly be increased by error correction and residual function. The results of the present method have been compared with the different values of N .

References

- [1] Akgönüllü N, Şahin N, Sezer M (2011) A Hermite collocation method for the approximate solutions of high-order linear Fredholm integro-differential equations, Numerical Methods Partial Differential Eq. 27, 1707–1721.

3rd International Students Science Congress
3-4 May 2019, İzmir - Turkey

- [2] Akkaya T, Yalçınbaş S, Sezer M (2013) Numeric solutions for the pantograph type delay differential equation using first Boubaker polynomials, *Applied Mathematics & Computation* 219, 9484-9492.
- [3] Iserles A (1997) On neutral functional-differential equations with proportional delays, *J.Math. Anal. Appl.*, 207, 73-95.
- [4] Boubaker K (2007) On modified Boubaker polynomials: some differential and analytical properties of the new polynomials issued from an attempt for solving bi-varied heat equation, *Trends Appl. Sci. Res.* 2(6), 540–544.
- [5] Chenga X, Chen Z, Zhang Q (2015) An approximate solution for a neutral functional–differential equation with proportional delays, *Applied Mathematics and Computation* 260, 27–34.
- [6] Gülsu M, Sezer M (2005) A method for the approximate solution of the high-order linear difference equations in terms of Taylor polynomials, *Intern. J. Comput. Math.* 82(5), 629-641.
- [7] Arıkoğlu AI (2006) Solution of difference equations by using differential transform method, *Appl. Matth. Comput.* 174, 1216- 1228.
- [8] Sezer M, Gülsu M, 2005. Polynomial solution of the most general linear Fredholm integro-differential-difference equation by means of Taylor matrix method, *Complex variables*, 50(5), 367-382.

On Kannan Type Mappings in Near Soft Metric Spaces

Simge Öztunç*, Manisa Celal Bayar University, Dept. of Mathematics, Manisa, Turkey,
Ali Mutlu, Manisa Celal Bayar University, Dept. of Mathematics, Manisa, Turkey
Kaan Özdemir, Manisa Celal Bayar University, The Institute of Natural and Applied Sciences, Manisa, Turkey
*Corresponding Author: simge.oztunc@cbu.edu.tr

Keywords: soft metric, soft near metric, soft fixed point theorems

Discipline: Mathematics, Topology

A. M. S. Classification: 03E72,47H10,54H25.

Abstract

This paper considers near soft metric space and Kannan type mappings. Some soft fixed point theorems are proved for soft near metric space.

Introduction

The concept of soft sets was propounded by Molodtsov [12] in 1999 as a new mathematical tool. Since the inception of this subject many mathematicians developed the topological and algebraic properties of soft set theory, for details see [2,16,19].

On the other hand, the concept soft metric was defined in 2013 by Das and Samanta [4] and improved by Hosseinzadeh [8]. Hosseinzadeh restated the definition soft metric and investigated some theoretical properties of soft metrics spaces in 2017. Also, fundamentals of soft fixed point theorems are obtained in Hosseinzadeh's paper. However some important properties and results for fixed point theory and soft fixed point theory can be found at [1,3,5,6,7,13,17,18].

In current study we consider the near soft metric space and Kannan type mappings [9,10]. We obtain and prove some soft fixed point theorems for Kannan Type mappings in near soft metric space.

1. Preliminaries

Definition 1.1 [12] A pair (\mathbb{F}, A) is said to be a soft set over the universe X , where \mathbb{F} is a mapping given by $\mathbb{F} : A \rightarrow P(X)$.

In other words, a soft set over X , is a parameterized family of subsets of the universe X . For any parameter $x \in A$, $\mathbb{F}(x)$ may be considered as the set of x -approximate elements of the soft set (\mathbb{F}, A) .

Definition 1.2 [8] Let $A \subseteq E$ be a set of parameters. We say the ordered pair (a, r) is a soft parametric scalar if $r \in \mathbb{R}$ and $a \in A$. The parametric scalar (a, r) called nonnegative if $r \geq 0$. Let (a, r) and (b, r') be two soft parametric scalars. We say (a, r) is no less than (b, r') and we write $(a, r) \succeq (b, r')$, if $r \geq r'$.

Definition 1.3 [8] Let (\mathbb{F}, A) be a soft set over X . We call a function f on (\mathbb{F}, A) is parametric scalar valued, if there are functions $f_1 : A \rightarrow A$ and $f_2 : \mathbb{F}(A) \rightarrow \mathbb{R}$ such that $f(\mathbb{F}, A) = (f_1, f_2)(A, \mathbb{F}(A))$.

Similarly, we can extent above defined parametric scalar valued function as $f : (\mathbb{F}, A) \times (\mathbb{F}, A) \rightarrow (A, \mathbb{R})$ by $f(A \times A, \mathbb{F}(A) \times \mathbb{F}(A)) = (f_1, f_2)(A \times A, \mathbb{F}(A) \times \mathbb{F}(A))$, where $f_1 : A \times A \rightarrow A$ and $f_2 : \mathbb{F}(A) \times \mathbb{F}(A) \rightarrow \mathbb{R}$.

Definition 1.4 [15] Let $\tilde{\pi} : A \times A \rightarrow A$ be a scalar valued parametric function. The parametric scalar valued function $\mathfrak{D}_N : (\mathbb{F}, A) \times (\mathbb{F}, A) \rightarrow (A, \mathbb{R}^+ \cup \{0\})$ is called to be a near soft metric on (\mathbb{F}, A) if \mathfrak{D}_N satisfies the following conditions:

NSM1) $\mathfrak{D}_N((a, \mathbb{F}(a)), (b, \mathbb{F}(b))) \geq (\tilde{\pi}(a, b), 0)$, and equality holds whenever $a = b$.

NSM2 $\mathfrak{D}_N((a, \mathbb{F}(a)), (b, \mathbb{F}(b))) = (\tilde{\pi}(a, b), 0) \Leftrightarrow$ for all $((a, \mathbb{F}(a)), (b, \mathbb{F}(b))) \in (\mathbb{F}, A)$,
 $(a, \mathbb{F}(a)) = (b, \mathbb{F}(b))$ for all $a, b \in A, a = b$

NSM3 $\mathfrak{D}_N((a, \mathbb{F}(a)), (b, \mathbb{F}(b))) = \mathfrak{D}_N((b, \mathbb{F}(b)), (a, \mathbb{F}(a)))$, for all $a, b \in A$,

NSM4 $\mathfrak{D}_N((a, \mathbb{F}(a)), (c, \mathbb{F}(c))) \leq (c, r)\mathfrak{D}_N((a, \mathbb{F}(a)), (b, \mathbb{F}(b))) + \mathfrak{D}_N((b, \mathbb{F}(b)), (c, \mathbb{F}(c)))$
for all $a, b, c \in A$ and $(c, r) \geq (1, r)$

Then we say the pair $((\mathbb{F}, A), \mathfrak{D}_N)$ is a near soft metric space over X .

Definition 1.5 [15] Let (\mathbb{F}, A) be a soft set over X . A soft sequence in (\mathbb{F}, A) is a function $f : N \rightarrow (\mathbb{F}, A)$ by setting $f(n) = (\mathbb{F}_n, A)$ such that (\mathbb{F}_n, A) is a soft subset of (\mathbb{F}, A) for $n \in N$, and we denote it by $\{(\mathbb{F}_n, A)\}_{n=1}^{\infty}$.

Definition 1.6 [15] Let (\mathbb{F}, A) be a soft set over X . Let \mathfrak{D}_N be a near soft metric on (\mathbb{F}, A) , $\{(\mathbb{F}_n, A)\}_{n=1}^{\infty}$ be a soft sequence in (\mathbb{F}, A) and $(x, \mathbb{F}(x)) \in (\mathbb{F}, A)$. Then we say $\{(\mathbb{F}_n, A)\}_{n=1}^{\infty}$ converges to $(x, \mathbb{F}(x))$, if for every positive number ϵ , there exists a naturel number N such that for every natural number n which $n \geq N$, we have $\mathfrak{D}_N(a, \mathbb{F}_n(a),) \leq (\tilde{\pi}(a, x), \epsilon)$.

Definition 1.7 [8] Let (\mathbb{F}, A) be a soft set over X , let \mathfrak{D}_N be a meter on (\mathbb{F}, A) , $\{(\mathbb{F}_n, A)\}_{n=1}^{\infty}$ be a soft sequence in (\mathbb{F}, A) . If $(\mathbb{F}_n, A)_{n=1}^{\infty}$ is convergent in (\mathbb{F}, A) , then it converges to unique element of (F, A) .

Definition 1.8 [15] Let (\mathbb{F}, A) be a soft set over X . Let \mathfrak{D}_N be a near soft metric on (\mathbb{F}, A) and $\{(\mathbb{F}_n, A)\}_{n=1}^{\infty}$ be a soft sequence in (\mathbb{F}, A) . Then we say $(\mathbb{F}_n, A)_{n=1}^{\infty}$ is a Cauchy soft sequence, if for every positive number ϵ , there exists a natural number N such that for every natural number n, m which $n, m \geq N$, we have $\mathfrak{D}_N((a, \mathbb{F}_n(a)), (a, \mathbb{F}_m(a))) \leq (\tilde{\pi}(a, a), \epsilon)$.

Proposition 1.9 [15] Let $((\mathbb{F}, A), \mathfrak{D}_N)$ be a near soft metric space over X , and let $\{(\mathbb{F}_n, A)\}_{n=1}^{\infty}$ be a convergent soft sequence in (\mathbb{F}, A) . Then $\{(\mathbb{F}_n, A)\}_{n=1}^{\infty}$ is a Cauchy soft sequence.

Definition 1.10 [15] Let (\mathbb{F}, A) be a soft set over X , let \mathfrak{D}_N be a near soft metric on (\mathbb{F}, A) . We say that (\mathbb{F}, A) is a complete near soft metric space if every Cauchy soft sequence converges in (\mathbb{F}, A) .

Theorem 1.11 [15] Let $((\mathbb{F}, A), \mathfrak{D}_N)$, and $((\mathbb{F}', A'), \mathfrak{D}'_N)$ be two near soft metric spaces over X and Y respectively. Let $f = (f_1, f_2) : ((\mathbb{F}, A), \mathfrak{D}_N) \rightarrow ((\mathbb{F}', A'), \mathfrak{D}'_N)$ be a soft mapping. Then f is soft continuous if and only if for every $(x, \mathbb{F}(x)) \in (\mathbb{F}, A)$ and every positive number ϵ , there exists a positive number δ such that for every $(y, \mathbb{F}(y)) \in (\mathbb{F}, A)$
 $\mathfrak{D}'_N((f(x, \mathbb{F}(x))), f((y, \mathbb{F}(y)))) \leq (\tilde{\pi}'(\tilde{\pi}(x, y)), \epsilon)$ whenever
 $\mathfrak{D}_N(f(x, \mathbb{F}(x)), f((y, \mathbb{F}(y)))) \leq (\tilde{\pi}(x, y), \delta)$.

Definition 1.12 [15] Let $((\mathbb{F}, A), \mathfrak{D}_N)$ be a near soft metric space over X and $f : ((\mathbb{F}, A), \mathfrak{D}_N) \rightarrow ((\mathbb{F}, A), \mathfrak{D}_N)$ be a soft mapping. We say that f is soft contractive if there is a positive number c with $0 < c < 1$ such that
 $\mathfrak{D}_N((f(x, \mathbb{F}(x))), f((y, \mathbb{F}(y)))) \leq c\mathfrak{D}_N((x, \mathbb{F}(x)), (y, \mathbb{F}(y)))$, for all $x, y \in A$.

Theorem 1.13 [15] Soft contractive mapping is soft continuous in near soft metric space $((\mathbb{F}, A), \mathfrak{D}_N)$.

Definition 1.14 [15] Let $((\mathbb{F}, A), \mathcal{D}_N)$ be a complete near soft metric space over X and let $f : ((\mathbb{F}, A), \mathcal{D}_N) \rightarrow ((\mathbb{F}, A), \mathcal{D}_N)$ be a soft mapping. A fixed soft set for f is a soft subset of (\mathbb{F}, A) such as $(x, \mathbb{F}(x))$ such that $f((x, \mathbb{F}(x))) = (x, \mathbb{F}(x))$.

Definition 1.15 [9] Let (X, d) be a complete metric space. The self-map $T : X \rightarrow X$ be a mapping such that there exist $K < 1/2$ satisfying

$$d(Tx, Ty) \leq K[d(x, Tx) + d(y, Ty)].$$

Then T is named a Kannan contraction type map .

2. Soft Fixed Point Theorems for Near Soft Metric Spaces

Theorem 2.1 Let (\mathbb{F}, E) be a nonempty soft closed subset of a soft complete near metric space $((\mathbb{F}, E), \mathcal{D}_n)$ and let $T : (\mathbb{F}, E) \rightarrow (\mathbb{F}, E)$ be a mapping such that there exists $K < 1$ satisfying

$$((x, \mathbb{F}(x)), T(y, \mathbb{F}(y))) \leq K[D((x, \mathbb{F}(x)), T(x, \mathbb{F}(x))) + D((y, \mathbb{F}(y)), T(y, \mathbb{F}(y)))]$$

Assume that there exist parametric scalars $(a, r), (b, r')$ such that $0 \leq r < 1$ and $r' > 0$ with $a, b \in E$. If for arbitrary $(x, \mathbb{F}(x)) \in (\mathbb{F}, E)$ there exists $(u, \mathbb{F}(u)) \in (\mathbb{F}, E)$ such that

$$\mathcal{D}_N((u, \mathbb{F}(u)), T(u, \mathbb{F}(u))) \leq r \cdot \mathcal{D}_N((x, \mathbb{F}(x)), T(x, \mathbb{F}(x)))$$

and

$$\mathcal{D}_N((u, \mathbb{F}(u)), (x, \mathbb{F}(x))) \leq r' \mathcal{D}_N((x, \mathbb{F}(x)), T(x, \mathbb{F}(x)))$$

than T has at least one fixed point set.

Proof:

Let $(x_0, \mathbb{F}(x_0)) \in (\mathbb{F}, E)$ be an arbitrary soft point. Consider a sequence $\{(\mathbb{F}_n, E)\}_{n=1}^{\infty}$ satisfies

$$\mathcal{D}_N(T(\mathbb{F}_{n+1}, E), (\mathbb{F}_{n+1}, E)) \leq r \mathcal{D}_N(T(\mathbb{F}_n, E), (\mathbb{F}_n, E))$$

$$\mathcal{D}_N((\mathbb{F}_{n+1}, E), (\mathbb{F}_n, E)) \leq r' \mathcal{D}_N(T(\mathbb{F}_n, E), (\mathbb{F}_n, E))$$

$n = 0, 1, 2, \dots$

Since

$$\begin{aligned} \mathcal{D}_N((\mathbb{F}_{n+1}, E), (\mathbb{F}_n, E)) &\leq r' \mathcal{D}_N(T(\mathbb{F}_n, E), (\mathbb{F}_n, E)) \\ &\leq r \cdot r^n \mathcal{D}_N(T(\mathbb{F}_0, E), (\mathbb{F}_0, E)) \end{aligned}$$

It is without trouble to see that $\{(\mathbb{F}_n, E)\}_{n=1}^{\infty}$ is a Cauchy soft sequence in (\mathbb{F}, E) . By using completeness of (\mathbb{F}, E) there exist $(v, \mathbb{F}(v)) \in (\mathbb{F}, E)$ such that $\lim_{n \rightarrow \infty} (\mathbb{F}_n, E) = (v, \mathbb{F}(v))$

$$\begin{aligned} \mathcal{D}_N(T(v, \mathbb{F}(v)), (v, \mathbb{F}(v))) &\leq c \mathcal{D}_N(T(v, \mathbb{F}(v)), T(x_n, \mathbb{F}(x_n))) + \mathcal{D}_N(T(x_n, \mathbb{F}(x_n)), T(v, \mathbb{F}(v))) \\ &\leq c \mathcal{D}_N(T(v, \mathbb{F}(v)), T(x_n, \mathbb{F}(x_n))) + c \cdot c' [\mathcal{D}_N(T(x_n, \mathbb{F}(x_n)), (x_n, \mathbb{F}(x_n))) \\ &\quad + \mathcal{D}_N((x_n, \mathbb{F}(x_n)), (v, \mathbb{F}(v)))] \end{aligned}$$

$$\begin{aligned} \mathcal{D}_N(T(v, \mathbb{F}(v)), (v, \mathbb{F}(v))) &\leq c \cdot K [\mathcal{D}_N((v, \mathbb{F}(v)), T(v, \mathbb{F}(v))) + \mathcal{D}_N((x_n, \mathbb{F}(x_n)), T(x_n, \mathbb{F}(x_n)))] \\ &\quad + c \cdot c' \mathcal{D}_N(T(x_n, \mathbb{F}(x_n)), (x_n, \mathbb{F}(x_n))) + c \cdot c' \mathcal{D}_N((x_n, \mathbb{F}(x_n)), (v, \mathbb{F}(v))) \end{aligned}$$

as $n \rightarrow \infty$ left hand side goes zero. Hence $T(v, \mathbb{F}(v)) = (v, \mathbb{F}(v))$. \square

Theorem 2.2 Let $((\mathbb{F}, E), D)$ be a soft complete metric space let $T : (\mathbb{F}, E) \rightarrow (\mathbb{F}, E)$ be a mapping such that there exists $K < 1/2$ satisfying

$$\mathcal{D}_N(T(x, \mathbb{F}_x), T(y, \mathbb{F}_y)) \leq K[\mathcal{D}_N((x, \mathbb{F}_x), T(x, \mathbb{F}_x)) + \mathcal{D}_N((y, \mathbb{F}_y), T(y, \mathbb{F}_y))]$$

for all $x, y \in X$.

Then, T has one and only fixed soft point $(v, \mathbb{F}_v) \in (\mathbb{F}, E)$, and for any $(x, \mathbb{F}_x) \in (\mathbb{F}, E)$ the soft sequence of iterates $\{T^n(x, \mathbb{F}_x)\}$ converges to (v, \mathbb{F}_v) and

$$\mathfrak{D}_N(T^{n+1}(x, \mathbb{F}_x), (v, \mathbb{F}_v)) \leq K \cdot \left(\frac{K}{1-K}\right)^n \cdot \mathfrak{D}_N((x, \mathbb{F}_x), T(x, \mathbb{F}_x))$$

$n = 0, 1, 2, \dots$

Proof:

For any $(x, \mathbb{F}) \in (\mathbb{F}, E)$ let $(u, \mathbb{F}_u) = T(x, \mathbb{F}_x)$ Then

$$\begin{aligned} \mathfrak{D}_N((u, \mathbb{F}_u), T(u, \mathbb{F}_u)) &= \mathfrak{D}_N(T(x, \mathbb{F}_x), T(u, \mathbb{F}_u)) \\ &\leq K[\mathfrak{D}_N((x, \mathbb{F}_x), T(x, \mathbb{F}_x)) + \mathfrak{D}_N((u, \mathbb{F}_u), T(u, \mathbb{F}_u))] \end{aligned}$$

Then we have

$$\mathfrak{D}_N((u, \mathbb{F}_u), T(u, \mathbb{F}_u)) \leq \frac{K}{1-K} \mathfrak{D}_N((x, \mathbb{F}_x), T(x, \mathbb{F}_x))$$

where by assumption $\frac{K}{1-K} \leq 1$ and $\mathfrak{D}_N((u, \mathbb{F}_u), (x, \mathbb{F}_x)) = \mathfrak{D}_N(T(x, \mathbb{F}_x), (x, \mathbb{F}_x))$. Now arbitrary

$(x_0, \mathbb{F}_{x_0}) \in (\mathbb{F}, E)$ we can inductively define a sequence $\{(x_{n+1}, \mathbb{F}_{x_{n+1}}) = T(x_n, \mathbb{F}_{x_n})\}$. This sequence convergent $\lim_{n \rightarrow \infty} (x_n, \mathbb{F}_{x_n}) = (v, \mathbb{F}_v)$ and $T(v, \mathbb{F}_v) = (v, \mathbb{F}_v)$. Suppose (z, \mathbb{F}_z) is other fixed point of T . Then

$$\begin{aligned} 0 < \mathfrak{D}_N((v, \mathbb{F}_v), (z, \mathbb{F}_z)) &= \mathfrak{D}_N(T(v, \mathbb{F}_v), T(z, \mathbb{F}_z)) \\ &\leq K[\mathfrak{D}_N((v, \mathbb{F}_v), T(v, \mathbb{F}_v)) + \mathfrak{D}_N((z, \mathbb{F}_z), T(z, \mathbb{F}_z))] = 0 \end{aligned}$$

This is a contradiction. Hence T has one and only fixed point $(v, \mathbb{F}_v) \in (\mathbb{F}, E)$. Since for each $(x, \mathbb{F}_x) \in (\mathbb{F}, E)$

$$\begin{aligned} \mathfrak{D}_N(T^{n+1}(x, \mathbb{F}_x), T^n(x, \mathbb{F}_x)) &\leq K[\mathfrak{D}_N(T^n(x, \mathbb{F}_x), T^{n+1}(x, \mathbb{F}_x))] + \mathfrak{D}_N(T^{n-1}(x, \mathbb{F}_x), T^n(x, \mathbb{F}_x)) \\ &\leq \frac{K}{1-K} \cdot \mathfrak{D}_N(T^n(x, \mathbb{F}_x), T^{n-1}(x, \mathbb{F}_x)) \end{aligned}$$

Then we have

$$\begin{aligned} \mathfrak{D}_N(T^{n+1}(x, \mathbb{F}_x), (v, \mathbb{F}_v)) &\leq K[\mathfrak{D}_N(T^n(x, \mathbb{F}_x), T^{n+1}(x, \mathbb{F}_x)) + \mathfrak{D}_N((v, \mathbb{F}_v), T(v, \mathbb{F}_v))] \\ &= K[\mathfrak{D}_N(T^{n+1}(x, \mathbb{F}_x), T^n(x, \mathbb{F}_x))] \\ &= K \cdot \left(\frac{K}{K-1}\right)^n \cdot \mathfrak{D}_N(T(x, \mathbb{F}_x), (x, \mathbb{F}_x)) \end{aligned}$$

for $n = 0, 1, 2, \dots$ □

References

- [1] Altıntaş İ, Şimşek D, Taşköprü K (2017) Topology of soft cone metric spaces. AIP Conference Proceedings. 1880, 030006, <https://doi.org/10.1063/1.50006056>
- [2] Aras ÇGG, Posul H (2016) On some new operations in probabilistic soft set theory. European Journal of Pure and Applied Mathematics 9(3): 333-339.
- [3] Banach S (1922) Sur les operations dans les ensembles abstrait set leur application aux equations integrales. Fund Math. 3: 133-181.
- [4] Das S, Samanta SK (2013) Soft Metric. Annals of Fuzzy Mathematics and Informatics 6(1): 77-94.

3rd International Students Science Congress
3-4 May 2019, İzmir - Turkey

- [5] Fagin R, Kumar R, Sivakumar D (2003) Comparing top k lists, *SIAM Journal on Discrete Mathematics* 17(1): 134-160.
- [6] Gornicki J (2017) Fixed point theorems Kannan type mappings. *Journal of Fixed Point Theory and Applications Monthly* 19: 2145-2152.
- [7] Guler AC, Yıldırım ED, Ozbakır OB (2016) A fixed point theorem on Soft G – metric spaces. *J. Nonlinear Sci. Appl.*, 9: 885-894.
- [8] Hosseinzadeh H (2017) Fixed point theorems on soft metric spaces. *Journal of Fixed Point Theory and Applications* 19(2): 1625-1647.
- [9] Kannan R (1968) Some results on fixed point. *Bull. Cal. Math. Soc.*, 60, 71-76.
- [10] Kannan R (1969) Some results on fixed point II. *Amer. Math. Monthly*, 76, 405-408.
- [11] Maji PK, Biswas R, Roy AR (2003) Soft Set Theory. *Comput. Math. Appl.*, 45: 555-562.
- [12] Molodtsov D (1999) Soft set theory-first result. *Comput. Math. Appl.*, 37: 19- 31.
- [13] Mutlu A, Yolcu N, Mutlu B (2016) Fixed point theorems in partially ordered rectangular metric spaces. *British Journal of Mathematics and Computer Science* 15(2):1-9.
- [14] Öztunç S, Mutlu A, Aslan S (2019) Some Kannan type fixed point results in rectangular soft metric space and an application of fixed point for thermal science problem. *Thermal Science*, 23(1) S215-S225 2019, doi: <https://doi.org/10.2298/TSCI181102035O>.
- [15] Öztunç S, Mutlu A, Özdemir K (2018) Some soft fixed point results for soft near metric spaces. 2nd International Students Science Congress, İzmir, Turkey. *Proceedings Book*: 65-71.
- [16] Shabir M, Naz M (2011) On soft topological spaces. *Computers & Mathematics with Applications* 61(7): 1786-1799.
- [17] Şimşek D, Altıntaş İ, Ersoy S, Abdullayev F, İmaş Kızı M, Taşköprü K, Kesik D, Abılayeva E, Oğul B, Çemşitov N (2018) An introduction to soft cone metric spaces and some fixed point theorems. *MANAS Journal of Engineering (MJEN)*. 6(1): 59-89.
- [18] Yazar MI, Aras ÇG, Bayramov S (2016) Fixed point theorems of soft contractive mappings. *Filomat*, 30(2): 269-27.
- [19] Zorlutuna İ, Çakır H (2015) On continuity of soft mappings. *Appl. Math. Inf. Sci.* 9(1): 403-409.

New Results in Near Soft Metric Spaces

*Simge Öztunç**, Manisa Celal Bayar University, Dept. of Mathematics, Manisa, Turkey,
Ali Mutlu, Manisa Celal Bayar University, Dept. of Mathematics, Manisa, Turkey,
Kaan Özdemir, Manisa Celal Bayar University, The Institute of Naturel and Applied Sciences, Manisa, Turkey
 *Corresponding Author: simge.oztunc@cbu.edu.tr

Keywords: soft metric, soft near metric, soft fixed point theorems

Discipline: Mathematics, Topology

Abstract

In current study we investigate the new properties of soft near metric spaces and prove some results concerning about contractive mappings by using the soft near metric.

Introduction

Soft set theory which is revealed by Molodtsov [10] in 1999 and investigated by Maji et al [9] contains disjunctive equipment for express mathematical with different view point. Other details of soft set theory can be found at [2,14,17]. In other respects, the theory of fixed point has a substantial role in different speciality of mathematics. Fundamental of Fixed Point theory was investigated by Banach [3]. As a new metric, Fagin et all [5] defined the near metric in 2003. Soft metric spaces were defined by Das and Samanta [4] in 2013 and Hosseinzadeh [8] improved theoretical properties of soft metric spaces by initiating new definition of soft metric. For some details for fixed point theory and soft fixed point theory, readers can refer to [1,6,7,11,12,15,16].

1. Preliminaries

Definition 1.1. [10] A pair (\mathbb{F}, A) is said to be a soft set over the universe X , where \mathbb{F} is a mapping given by $\mathbb{F} : A \rightarrow P(X)$.

In other words, a soft set over X is a parameterized family of subsets of the universe U . For any parameter $x \in A$, $F(x)$ may be considered as the set of x - approximate elements of the soft set (\mathbb{F}, A) .

Definition 1.2. [8] Let $A \subseteq E$ be a set of parameters. We say the ordered pair (a, r) is a soft parametric scalar if $r \in R$ and $a \in A$. The parametric scalar (r, a) called nonnegative if $r \geq 0$. Let (a, r) and (b, r') be two soft parametric scalars. We say (a, r) is no less than (b, r') and we write $(a, r) \succeq (b, r')$, if $r \geq r'$.

Definition 1.3. [8] Let $A \subseteq E$ be a set of parameters. Let (a, r) and (b, r') be two soft parametric scalars. Then we define addition between soft parametric scalars and scalar multiplication on soft parametric scalars as follows

$$(a, r) \dot{+} (b, r') = (a, b, r + r'), \text{ and}$$

$$\lambda(a, r) = (a, \lambda r), \text{ for every } \lambda \in R.$$

Definition 1.4. [8] Let (\mathbb{F}, A) be a soft set over X . We call a function f on (\mathbb{F}, A) is parametric scalar valued, if there are functions $f_1 : A \rightarrow A$ and $f_2 : F(A) \rightarrow R$ such that $f(\mathbb{F}, A) = (f_1, f_2)(A, \mathbb{F}(A))$.

Similarly, we can extent above defined parametric scalar valued function as $f : (\mathbb{F}, A) \times (\mathbb{F}, A) \rightarrow (A, R)$ by $f(A \times A, \mathbb{F}(A) \times \mathbb{F}(A)) = (f_1, f_2)(A \times A, \mathbb{F}(A) \times \mathbb{F}(A))$, where $f_1 : A \times A \rightarrow A$ and $f_2 : \mathbb{F}(A) \times \mathbb{F}(A) \rightarrow R$.

Definition 1.5.[13] Let $\tilde{\pi} : A \times A \rightarrow A$ be a scalar valued parametric function. The parametric scalar valued function $\mathcal{D}_N : (\mathbb{F}, A) \times (\mathbb{F}, A) \rightarrow (A, \mathbb{R}^+ \cup \{0\})$ is called to be a near soft metric on (\mathbb{F}, A) if \mathcal{D}_N satisfies the following conditions:

NSM1) $\mathcal{D}_N((a, \mathbb{F}(a)), (b, \mathbb{F}(b))) \geq (\tilde{\pi}(a, b), 0)$, and equality holds whenever $a = b$.

NSM2 $\mathfrak{D}_N((a, \mathbb{F}(a)), (b, \mathbb{F}(b))) = (\tilde{\pi}(a, b), 0) \Leftrightarrow$ for all $((a, \mathbb{F}(a)), (b, \mathbb{F}(b))) \in (\mathbb{F}, A)$,
 $(a, \mathbb{F}(a)) = (b, \mathbb{F}(b))$ [for all $a, b \in A, a = b$]

NSM3 $\mathfrak{D}_N((a, \mathbb{F}(a)), (b, \mathbb{F}(b))) = \mathfrak{D}_R((b, \mathbb{F}(b)), (a, \mathbb{F}(a)))$, for all $a, b \in A$

NSM4 $\mathfrak{D}_N((a, \mathbb{F}(a)), (c, \mathbb{F}(c))) \leq (c, r)\mathfrak{D}_N((a, \mathbb{F}(a)), (b, \mathbb{F}(b))) + \mathfrak{D}_N(b, \mathbb{F}(b)), (c, \mathbb{F}(c)))$ for all
 $a, b, c \in A$ and $(c, r) \geq (1, r)$

Then we say the pair $((\mathbb{F}, A), \mathfrak{D}_N)$ is a near soft metric space over X .

Definition 1.6. [8] Let (\mathbb{F}, A) be a soft set over X . A soft sequence in (\mathbb{F}, A) is a function
 $f : N \rightarrow (\mathbb{F}, A)$ by setting $f(n) = (\mathbb{F}_n, A)$ such that (\mathbb{F}_n, A) is a soft subset of (\mathbb{F}, A) for $n \in N$, and
we denote it by $\{(\mathbb{F}_n, A)\}_{n=1}^{\infty}$.

Definition 1.7. [13] Let (\mathbb{F}, A) be a soft set over X . Let \mathfrak{D}_R be a near soft metric on (\mathbb{F}, A) ,
 $\{(\mathbb{F}_n, A)\}_{n=1}^{\infty}$ be a soft sequence in (\mathbb{F}, A) and $(x, \mathbb{F}(x)) \in (\mathbb{F}, A)$. Then we say $\{(\mathbb{F}_n, A)\}_{n=1}^{\infty}$ converges
to $(x, \mathbb{F}(x))$, if for every positive number ϵ , there exists a natural number N such that for every
natural number n which $n \geq N$, we have

$$\mathfrak{D}_N(a, \mathbb{F}_n(a),) \leq (\tilde{\pi}(a, x), \epsilon).$$

Definition 1.8. [13] Let (\mathbb{F}, A) be a soft set over X . Let \mathfrak{D}_N be a near soft metric on (\mathbb{F}, A) and
 $\{(\mathbb{F}_n, A)\}_{n=1}^{\infty}$ be a soft sequence in (\mathbb{F}, A) . Then we say $\{(\mathbb{F}_n, A)\}_{n=1}^{\infty}$ is a Cauchy soft sequence, if for
every positive number ϵ , there exists a natural number N such that for every natural number n, m
which $n, m \geq N$, we have

$$\mathfrak{D}_N((a, \mathbb{F}_n(a)), (a, \mathbb{F}_m(a))) \leq (\tilde{\pi}(a, a), \epsilon).$$

Proposition 1.9. [13] Let $((\mathbb{F}, A), \mathfrak{D}_N)$ be a near soft metric space over X , and let $\{(\mathbb{F}_n, A)\}_{n=1}^{\infty}$ be a
convergent soft sequence in (\mathbb{F}, A) . Then $\{(\mathbb{F}_n, A)\}_{n=1}^{\infty}$ is a Cauchy soft sequence.

Definition 1.10. [13] Let (\mathbb{F}, A) be a soft set over X , let \mathfrak{D}_N be a near soft metric on (\mathbb{F}, A) . We say
that (\mathbb{F}, A) is a complete soft near metric space if every Cauchy soft sequence converges in (\mathbb{F}, A) .

Theorem 1.11. [13] Let $((\mathbb{F}, A), \mathfrak{D}_p)$ and $((\mathbb{F}', A'), \mathfrak{D}'_p)$ be two near soft metric spaces over X and
 Y respectively. Let $f = (f_1, f_2) : ((\mathbb{F}, A), \mathfrak{D}_N) \rightarrow ((\mathbb{F}', A'), \mathfrak{D}'_N)$ be a soft mapping. Then f is soft
continuous if and only if for every $(x, \mathbb{F}(x)) \in (\mathbb{F}, A)$ and every positive number ϵ , there exists a
positive number δ such that for every $(y, \mathbb{F}(y)) \in (\mathbb{F}, A)$

$$\mathfrak{D}'_N((f(x, \mathbb{F}(x))), f((y, \mathbb{F}(y)))) \leq (\tilde{\pi}'(\tilde{\pi}(x, y)), \epsilon)$$

whenever $\mathfrak{D}'_N(f(x, \mathbb{F}(x))), f((y, \mathbb{F}(y))) \leq (\tilde{\pi}(x, y), \delta)$.

Definition 1.12. [13] Let $((\mathbb{F}, A), \mathfrak{D}_N)$ be a near soft metric space over X and
 $f : ((\mathbb{F}, A), \mathfrak{D}_N) \rightarrow ((\mathbb{F}, A), \mathfrak{D}_N)$ be a soft mapping. We say that f is soft contractive if there is a
positive number c with $0 < c < 1$ such that

$$\mathfrak{D}_N((f(x, \mathbb{F}(x))), f((y, \mathbb{F}(y)))) \leq c\mathfrak{D}_N((x, \mathbb{F}(x)), (y, \mathbb{F}(y))), \text{ for all } x, y \in A.$$

Theorem 1.13. [13] Soft contractive mapping is soft continuous in near soft metric space $((\mathbb{F}, A), \mathfrak{D}_N)$.

Definition 1.14. [13] Let $((\mathbb{F}, A), \mathcal{D}_N)$ be a complete near soft metric space over X and let $f : ((\mathbb{F}, A), \mathcal{D}_N) \rightarrow ((\mathbb{F}, A), \mathcal{D}_N)$ be a soft mapping. A fixed soft set for f is a soft subset of (\mathbb{F}, A) such as $(x, \mathbb{F}(x))$ such that $f((x, \mathbb{F}(x))) = (x, \mathbb{F}(x))$.

2. Soft Fixed Point Theorems for Near Soft Metric Spaces

Theorem 2.1. Let $((\mathbb{F}, A), \mathcal{D}_N)$ be a complete near soft metric space over X , and let

$T : \mathcal{D}_N((a, \mathbb{F}(a)), (a', r)) \rightarrow ((\mathbb{F}, A), \mathcal{D}_N)$ be a soft continuous mapping such that

$$\mathcal{D}_N(T(a, \mathbb{F}(a)), (a, \mathbb{F}(a))) < (\lambda, k)(a', r),$$

where $(\lambda, k) > (1, k)$. Then T has a unique fixed soft set in $\mathcal{D}_N((a, \mathbb{F}(a)), (a', r))$.

Proof:

$$\begin{aligned} \mathcal{D}_N(T(b, \mathbb{F}(b)), (a, \mathbb{F}(a))) &\leq (\lambda, k)[\mathcal{D}_N(T(b, \mathbb{F}(b)), T(a, \mathbb{F}(a))) + \mathcal{D}_N(T(a, \mathbb{F}(a)), (a, \mathbb{F}(a)))] \\ &\leq (\lambda, k)\mathcal{D}_N(T(b, \mathbb{F}(b)), T(a, \mathbb{F}(a))) + (\lambda, r)\mathcal{D}_N(T(a, \mathbb{F}(a)), (a, \mathbb{F}(a))) \\ &\leq (\lambda, k).c.\mathcal{D}_N((b, \mathbb{F}(b)), (a, \mathbb{F}(a))) + (\lambda, r)(1-r)(a', r_0) \\ &\leq (\lambda, k) \cdot c \cdot (a', r_0) + (\lambda, r)(1-c)(a', r_0) = (\lambda, k)(a', r_0) \end{aligned}$$

where $(\lambda, k) > (1, k)$. □

Theorem 2.2. Let $((\mathbb{F}, A), \mathcal{D}_N)$ be a complete near soft metric space over X , and suppose there exists a such that for each $(a, \mathbb{F}(a)), (b, \mathbb{F}(b)) \in (\mathbb{F}, A)$ soft mapping $T : (\mathbb{F}, A) \rightarrow (\mathbb{F}, A)$ such that $T(a, \mathbb{F}(a)) = (T_1(a), T_2(\mathbb{F}(a))) = (T_1(a), \mathbb{F}(T_1(a)))$ for every $(a, \mathbb{F}(a)) \in (\mathbb{F}, A)$ and it satisfies

$$\mathcal{D}_N((T(a, \mathbb{F}(a)), T(b, \mathbb{F}(b)))) \leq \alpha(\lambda, k)(\lambda', k')\mathcal{D}_N((a, \mathbb{F}(a)), (b, \mathbb{F}(b)))$$

for every $(a, \mathbb{F}(a)), (b, \mathbb{F}(b)) \in (\mathbb{F}, A)$. Then T has a unique fixed soft set.

Proof: Put the fixed soft set $(a, \mathbb{F}(a)) \in (\mathbb{F}, A)$. Let $(a_n, \mathbb{F}(a_n)) = T^n(a, \mathbb{F}(a))$ for $n \in \mathbb{N}$. We will bring about the proof in two steps

Step 1: We claim that $\lim_{n \rightarrow \infty} \mathcal{D}_N((a_n, \mathbb{F}(a_n)), (a_{n+1}, \mathbb{F}(a_{n+1}))) = 0$. Since T is contraction

$$\begin{aligned} \mathcal{D}_N((a_n, \mathbb{F}(a_n)), (a_{n+1}, \mathbb{F}(a_{n+1}))) &= \mathcal{D}_N(T^n(a, \mathbb{F}(a)), T^{n+1}(a, \mathbb{F}(a))) \\ &\leq \alpha \mathcal{D}_N(T^{n-1}(a, \mathbb{F}(a)), (a, \mathbb{F}(a))) \mathcal{D}_N(T^{n-1}(a, \mathbb{F}(a)), T^n(a, \mathbb{F}(a))) \\ &= \alpha \mathcal{D}_N((a_{n-1}, \mathbb{F}(a_{n-1})), T(a_n, \mathbb{F}(a_{n+1}))) \mathcal{D}_N(T(a_{n-1}, \mathbb{F}(a_{n-1})), T^n(a_{n+1}, \mathbb{F}(a_n))) \\ &\leq \mathcal{D}_N((a_{n-1}, \mathbb{F}(a_{n-1})), (a_n, \mathbb{F}(a_n))) \\ &\leq \alpha \mathcal{D}_N(T^{n-1}(a, \mathbb{F}(a)), (a, \mathbb{F}(a))) \overline{\mathcal{D}_N(T^{n-1}(a, \mathbb{F}(a)), T^n(a, \mathbb{F}(a)))} \\ &= \alpha \overline{\mathcal{D}_N((a_{n-1}, \mathbb{F}(a_{n-1})), T(a_n, \mathbb{F}(a_{n+1})))} \overline{\mathcal{D}_N(T(a_{n-1}, \mathbb{F}(a_{n-1})), T^n(a_{n+1}, \mathbb{F}(a_n)))} \\ &\leq \overline{\mathcal{D}_N((a_{n-1}, \mathbb{F}(a_{n-1})), (a_n, \mathbb{F}(a_n)))} \end{aligned}$$

Thus

$\mathcal{D}_N((a_n, \mathbb{F}(a_n)), (a_{n+1}, \mathbb{F}(a_{n+1}))) \leq \mathcal{D}_N((a_{n-1}, \mathbb{F}(a_{n-1})), (a_n, \mathbb{F}(a_n)))$ so the sequence $\mathcal{D}_N((a_n, \mathbb{F}(a_n)), (a_{n+1}, \mathbb{F}(a_{n+1})))$ is decreasing. Then $\lim_{n \rightarrow \infty} \mathcal{D}_N((a_n, \mathbb{F}(a_n)), (a_{n+1}, \mathbb{F}(a_{n+1}))) = (b, r)$. Due to contradiction method, suppose $(b, r) \neq 0$ or $r \neq 0$. By the inequality we have

$$\mathcal{D}_N((a_{n+1}, \mathbb{F}(a_{n+1})), (a_{n+2}, \mathbb{F}(a_{n+2}))) \leq 2\alpha(\mathcal{D}_N((a_n, \mathbb{F}(a_n)), (a_{n+1}, \mathbb{F}(a_{n+1})))) \mathcal{D}_N((a_n, \mathbb{F}(a_n)), (a_{n+1}, \mathbb{F}(a_{n+1})))$$

Then letting $n \rightarrow \infty$. we have $(b, r) \leq \lim_{n \rightarrow \infty} \mathcal{D}_N((a_n, \mathbb{F}(a_n)), (a_{n+1}, \mathbb{F}(a_{n+1}))) (b, r)$

3rd International Students Science Congress
3-4 May 2019, İzmir - Turkey

$$\frac{1}{r}(b, 1) \leq \frac{1}{r} \mathcal{D}_N((a_n, \mathbb{F}_{a_n}), (a_{n+1}, \mathbb{F}_{a_{n+1}}))$$

This follows

$$(b, 1) \leq (b, \lim_{n \rightarrow \infty} \alpha(\mathcal{D}_N((a_n, \mathbb{F}_{a_n}), (a_{n+1}, \mathbb{F}_{a_{n+1}}))))$$

Thus $\lim_{n \rightarrow \infty} \alpha(\mathcal{D}_N((a_n, \mathbb{F}_{a_n}), (a_{n+1}, \mathbb{F}_{a_{n+1}}))) \geq 1$. This is contradiction and shows that our assertion is true.

Step 2:

$\{(a_n, \mathbb{F}(a_n))\}$ is a Cauchy soft sequence. By contradiction method

$\lim_{m, n \rightarrow \infty} \sup \mathcal{D}_N((a_n, \mathbb{F}_{a_n}), (a_m, \mathbb{F}(a_m))) \geq (a, 0)$ for every $a \in A$. By the 4. property of soft near metric

$$\begin{aligned} \mathcal{D}_N((a_n, \mathbb{F}(a_n)), (a_m, \mathbb{F}(a_m))) &\leq (\lambda, k) [\mathcal{D}_N((a_n, \mathbb{F}_{a_n}), (a_{n+1}, \mathbb{F}(a_{n+1}))) \\ &\quad + \mathcal{D}_N((a_{n+1}, \mathbb{F}(a_{n+1})), (a_m, \mathbb{F}(a_m)))] \\ &\leq \mathcal{D}_N((a_n, \mathbb{F}(a_n)), (a_{n+1}, \mathbb{F}(a_{n+1}))) \\ &\quad + (\lambda, k) \mathcal{D}_N((a_{n+1}, \mathbb{F}(a_{n+1})), (a_m, \mathbb{F}(a_m))) \\ &\leq (\lambda, k) \mathcal{D}_N((a_n, \mathbb{F}(a_n)), (a_{n+1}, \mathbb{F}(a_{n+1}))) \\ &\quad + (\lambda, k)(\lambda', k') [\overline{\mathcal{D}_N((a_{n+1}, \mathbb{F}(a_{n+1})), (a_{m+1}, \mathbb{F}(a_{m+1})))} \\ &\quad + \overline{\mathcal{D}_N((a_{m+1}, \mathbb{F}(a_{m+1})), (a_m, \mathbb{F}(a_m)))] \\ &\leq (\lambda, k) \overline{\mathcal{D}_N((a_n, \mathbb{F}_{a_n}), (a_{n+1}, \mathbb{F}(a_{n+1})))} \\ &\quad + (\lambda, k)(\lambda', k') \alpha \overline{\mathcal{D}_N((a_n, \mathbb{F}(a_n)), (a_m, \mathbb{F}(a_m)))} \\ &\quad \overline{\mathcal{D}_N((a_n, \mathbb{F}(a_n)), (a_m, \mathbb{F}(a_m)))} \end{aligned}$$

$$\begin{aligned} &[1 - \alpha(\lambda, k)(\lambda', k')(\mathcal{D}_N((a_n, \mathbb{F}(a_n)), (a_m, \mathbb{F}(a_m))))] \mathcal{D}_N((a_n, \mathbb{F}(a_n)), (a_m, \mathbb{F}(a_m))) \\ &\leq (\lambda, k) \mathcal{D}_N((a_n, \mathbb{F}(a_n)), (a_{n+1}, \mathbb{F}(a_{n+1}))) + (\lambda, k)(\lambda', k') \mathcal{D}_N((a_{n+1}, \mathbb{F}(a_{n+1})), (a_m, \mathbb{F}(a_m))) \end{aligned}$$

Step 1 implies

$$[1 - \alpha(\lambda, k)(\lambda', k') \lim_{n \rightarrow \infty} \mathcal{D}_N((a_n, \mathbb{F}(a_n)), (a_m, \mathbb{F}(a_m)))] \mathcal{D}_N((a_n, \mathbb{F}(a_n)), (a_m, \mathbb{F}(a_m))) \leq (a, 0)$$

For $a \in A$. In this situation one of the below situations can be occur

i) $[1 - \alpha(\lambda, k)(\lambda', k') \lim_{n \rightarrow \infty} \mathcal{D}_N((a_n, \mathbb{F}(a_n)), (a_m, \mathbb{F}(a_m)))] = 0$

ii) $\lim_{n \rightarrow \infty} \mathcal{D}_N((a_n, \mathbb{F}(a_n)), (a_m, \mathbb{F}(a_m))) = (a, 0)$ for all $a \in A$.

According to our presumption ii) is not possible. So

$$\alpha(\lambda, k)(\lambda', k') \lim_{n \rightarrow \infty} \mathcal{D}_N((a_n, \mathbb{F}(a_n)), (a_m, \mathbb{F}(a_m))) = 1$$

Definition of α implies $(\lambda, k)(\lambda', k') \lim_{n \rightarrow \infty} \mathcal{D}_N((a_n, \mathbb{F}(a_n)), (a_m, \mathbb{F}(a_m))) \rightarrow (a, 0)$ for all $a \in A$

For uniqueness, assume that $(b, \mathbb{F}(b))$ is distinct soft fixed point of T , namely, $T(b, \mathbb{F}(b)) = (b, \mathbb{F}(b))$ from the contractive condition on T we have

$$\begin{aligned} \mathcal{D}_N(T(a, \mathbb{F}(a)), T(b, \mathbb{F}(b))) &= \mathcal{D}_N((a, \mathbb{F}(a)), (b, \mathbb{F}(b))) \\ &\leq \alpha(\mathcal{D}_N((a, \mathbb{F}(a)), (b, \mathbb{F}(b)))) \mathcal{D}_N((a, \mathbb{F}(a)), (b, \mathbb{F}(b))) \\ &\mathcal{D}_N((a, \mathbb{F}(a)), (b, \mathbb{F}(b))) (1 - \alpha) \mathcal{D}_N((a, \mathbb{F}(a)), (b, \mathbb{F}(b))) \leq 0 \end{aligned}$$

Therefore $\mathcal{D}_N(a, \mathbb{F}(a)), (b, \mathbb{F}(b))) = 0$ or $(1-\alpha)(\mathcal{D}_N((a, \mathbb{F}(a)), (b, \mathbb{F}(b)))) = 0$ from definition of soft near metric and property of α we have $T((b, \mathbb{F}(b)), (b, \mathbb{F}(b))) = (a, \mathbb{F}(a))$ as desired. \square

References

- [1] Altıntaş İ, Şimşek D, Taşköprü K (2017) Topology of soft cone metric spaces. AIP Conference Proceedings. 1880, 030006, <https://doi.org/10.1063/1.50006056>
- [2] Aras ÇGG, Posul H (2016) On some new operations in probabilistic soft set theory. European Journal of Pure and Applied Mathematics 9(3): 333-339.
- [3] Banach S (1922) Sur les opérations dans les ensembles abstraits et leur application aux équations intégrales. Fund Math. 3: 133-181.
- [4] Das S, Samanta SK (2013) Soft Metric. Annals of Fuzzy Mathematics and Informatics 6(1): 77-94.
- [5] Fagin R, Kumar R, Sivakumar D (2003) Comparing top k lists, SIAM Journal on Discrete Mathematics 17(1): 134-160.
- [6] Gornicki J (2017) Fixed point theorems Kannan type mappings. Journal of Fixed Point Theory and Applications Monthly 19: 2145-2152.
- [7] Guler AC, Yıldırım ED, Ozbakır OB (2016) A fixed point theorem on Soft G -metric spaces. J. Nonlinear Sci. Appl., 9: 885-894.
- [8] Hosseinzadeh H (2017) Fixed point theorems on soft metric spaces. Journal of Fixed Point Theory and Applications 19(2): 1625-1647.
- [9] Maji PK, Biswas R, Roy AR (2003) Soft Set Theory. Comput. Math. Appl., 45: 555-562.
- [10] Molodtsov D (1999) Soft set theory-first result. Comput. Math. Appl., 37: 19- 31.
- [11] Mutlu A, Yolcu N, Mutlu B (2016) Fixed point theorems in partially ordered rectangular metric spaces. British Journal of Mathematics and Computer Science 15(2):1-9.
- [12] Öztunç S, Mutlu A, Aslan S (2019) Some Kannan type fixed point results in rectangular soft metric space and an application of fixed point for thermal science problem. Thermal Science, 23(1) S215-S225 2019, <https://doi.org/10.2298/TSCI181102035O>.
- [13] Öztunç S, Mutlu A, Özdemir K (2018) Some soft fixed point results for soft near metric spaces. 2nd International Students Science Congress, İzmir, Turkey. Proceedings Book: 65-71.
- [14] Shabir M, Naz M (2011) On soft topological spaces. Computers & Mathematics with Applications 61(7): 1786-1799.
- [15] Şimşek D, Altıntaş İ, Ersoy S, Abdullayev F, İmaş Kızı M, Taşköprü K, Kesik D, Abılayeva E, Ogul B, Çemşitov N (2018) An introduction to soft cone metric spaces and some fixed point theorems. MANAS Journal of Engineering (MJEN). 6(1): 59-89.
- [16] Yazar MI, Aras ÇG, Bayramov S (2016) Fixed point theorems of soft contractive mappings. Filomat, 30(2): 269-27.
- [17] Zorlutuna İ, Çakır H (2015) On continuity of soft mappings. Appl. Math. Inf. Sci. 9(1): 403-409.

On Kannan Type Mappings in Steinhaus Transform Soft Metric Spaces

Simge Öztunç*, Manisa Celal Bayar University, Dept. of Mathematics, Manisa, Turkey

Ali Mutlu, Manisa Celal Bayar University, Dept. of Mathematics, Manisa, Turkey

Nurettin Yılmaz, Manisa Celal Bayar University, The Institute of Naturel and Applied Sciences, Manisa, Turkey

*Corresponding Author: simge.oztunc@cbu.edu.tr

Keywords: soft metric, Steinhaus transform soft metric, soft fixed point theorems

Discipline: Mathematics, Topology

Abstract

In this paper we focus on the biotope transform soft metric or Steinhaus transform soft metric, and Kannan type mappings. We obtain some properties for this mapping and prove some fixed point theorems for Kannan type mappings in Steinhaus-Transform soft metric space.

Introduction

Soft set theory which is introduced by Molodsov [12] in 1999 become a popular subject of mathematics. Many mathematicians such as [2,10,16,19] studied on topological and algebraic properties of soft sets and used it as a new tool for state many problems.

However, fixed point theory has a big role in many branches of mathematics, engineering naturel and applied science. Fundamentals of fixed point theory was given by Banach [3] in 1922.

On the other hand, Das and Samanta [4] gave the definition of soft metric in 2013 and in 2017 Hosseinzadeh [7] improved the theory and stated the now definition of soft metric. Different kind of metric and soft metric spaces and different type of fixed and soft fixed point theorems are studied in [1,5,6,11,14,15,17,18].

In this paper we focus on Kannan type mappings [8,9] and we prove some fixed point theorems for Kannan type mapping for Steinhaus-Transform soft metric space.

3. Prelimineries

Definition 1.1. [12] A pair (\mathbb{S}, A) is said to be a soft set over the universe X , where \mathbb{S} is a transformation given by $\mathbb{S} : A \rightarrow P(X)$.

In other words, a soft set over X is a parameterized family of subsets of the universe X . For any parameter $x \in A$, $\mathbb{S}(x)$ may be regarded as the set of X - approximate elements of the soft set (\mathbb{S}, A) .

Definition 1.2. [7] Let $A \subseteq E$ be a set of parameters. It is said that the ordered pair (a, r) is a soft parametric scalar if $r \in \mathbb{R}$ and $a \in A$. The parametric scalar (r, a) named nonnegative if $r \geq 0$. Let (a, r) and (b, r') be two soft parametric scalars. It is said that (a, r) is no less than (b, r') and it is written as $(a, r) \succeq (b, r')$, if $r \geq r'$.

Definition 1.3. [7] Let $A \subseteq E$ be a set of parameters. Let (a, r) and (b, r') be two soft parametric scalars. Then we define addition between soft parametric scalars and scalar multiplication on soft parametric scalars as follows

$$(a, r) \dot{+} (b, r') = (a, b, r + r'), \text{ and}$$

$$\lambda (a, r) = (a, \lambda r), \text{ for every } \lambda \in \mathbb{R}.$$

Definition 1.4. [15] Let (\mathbb{S}, A) be a soft set over X and let $\tilde{\pi} : A \times A \rightarrow A$ be parametric function.

We say the parametric scalar valued function $\mathcal{D} : (\mathbb{S}, A) \times (\mathbb{S}, A) \rightarrow (A, \mathbb{R}^+ \setminus \{0\})$ a soft meter on (\mathbb{S}, A) if \mathcal{D} satisfies in the following conditions:

$$(1) \mathcal{D}_p((a, \mathbb{S}(a)), (b, \mathbb{S}(b))) \succeq (\tilde{\pi}(a, b), 0), \text{ and equality is satisfied, whenever } a = b.$$

$$(2) \mathcal{D}_p((a, \mathbb{S}(a)), (b, \mathbb{S}(b))) = \mathcal{D}((b, \mathbb{S}(b)), (a, \mathbb{S}(a))), \text{ for all } a, b \in A.$$

(3) $\mathfrak{D}_p((a, \mathbb{S}(a)), (c, \mathbb{S}(c))) \leq \mathfrak{D}((a, \mathbb{S}(a)), (b, \mathbb{S}(b))) + \mathfrak{D}((b, \mathbb{S}(b)), (c, \mathbb{S}(c)))$, for all $a, b, c \in A$.

(4)

$$\mathfrak{D}_p((a, \mathbb{S}(a)), (b, \mathbb{S}(b))) = \frac{2\mathfrak{D}((a, \mathbb{S}(a)), (b, \mathbb{S}(b)))}{\mathfrak{D}((a, \mathbb{S}(a)), (c, \mathbb{S}(c))) + \mathfrak{D}_p((b, \mathbb{S}(b)), (c, \mathbb{S}(c))) + \mathfrak{D}((a, \mathbb{S}(a)), (b, \mathbb{S}(b)))}$$

We call the pair $((\mathbb{S}, A), \mathfrak{D}_p)$ is a soft Steinhaus transform metric space over X .

Definition 1.5. [7] Let (\mathbb{S}, A) be a soft set over X . A soft sequence in (\mathbb{S}, A) is a function $f : \mathbb{N} \rightarrow (\mathbb{S}, A)$ by setting $f(n) = (\mathbb{S}_n, A)$ such that (\mathbb{S}_n, A) is a soft subset of (\mathbb{S}, A) for $n \in \mathbb{N}$, and we denote it by $\{(\mathbb{S}_n, A)\}_{n=1}^{\infty}$.

Definition 1.6. [15] Let (\mathbb{S}, A) be a soft set over X . Let \mathfrak{D}_p be a Steinhaus transform soft metric on (\mathbb{S}, A) , $\{(\mathbb{S}_n, A)\}_{n=1}^{\infty}$ be a soft sequence in (\mathbb{S}, A) and $(x, \mathbb{S}(x)) \in (\mathbb{S}, A)$. Then we say $\{(\mathbb{S}_n, A)\}_{n=1}^{\infty}$ converges to $(x, \mathbb{S}(x))$, if for every positive number ϵ , there subsist a naturel number N such that for every $n \in \mathbb{N}$ which $n \geq N$, we have

$$\mathfrak{D}_p(a, \mathbb{S}_n(a), (x, \mathbb{S}(x))) \leq (\tilde{\pi}(a, x), \epsilon).$$

Theorem 1.7. [7] Let (\mathbb{S}, A) be a soft set over X , let \mathfrak{D} be a meter on (\mathbb{S}, A) , $\{(\mathbb{S}_n, A)\}_{n=1}^{\infty}$ be a soft sequence in (\mathbb{S}, A) . If $(\mathbb{S}, A), \{(\mathbb{S}_n, A)\}_{n=1}^{\infty}$ is convergent in (\mathbb{S}, A) , then it converges to unique element of (\mathbb{S}, A) .

Definition 1.8. [15] Let (\mathbb{S}, A) be a soft set over X . Let \mathfrak{D}_p be a Steinhaus transform soft metric on (\mathbb{S}, A) and $\{(\mathbb{S}_n, A)\}_{n=1}^{\infty}$ be a soft sequence in (\mathbb{S}, A) . Then we say $\{(\mathbb{S}_n, A)\}_{n=1}^{\infty}$ is a Cauchy soft sequence, if for every positive number ϵ , there subsist a natural number N such that for every natural number n, m which $n, m \geq N$, we have

$$\mathfrak{D}_p((a, \mathbb{S}_n(a)), (a, \mathbb{S}_m(a))) \leq (\tilde{\pi}(a, a), \epsilon).$$

Proposition 1.9. [15] Let $((\mathbb{S}, A), \mathfrak{D}_p)$ be a Steinhaus transform soft metric space over X , and let $\{(\mathbb{S}_n, A)\}_{n=1}^{\infty}$ be a convergent soft sequence in (\mathbb{S}, A) . Then $\{(\mathbb{S}_n, A)\}_{n=1}^{\infty}$ is a Cauchy soft sequence.

Definition 1.10. [15] Let (\mathbb{S}, A) be a soft set over X , let \mathfrak{D}_p be a Steinhaus transform soft metric on (\mathbb{S}, A) . We say that (\mathbb{S}, A) is a complete Steinhaus transform soft metric space if every Cauchy soft sequence converges in (\mathbb{S}, A) .

Theorem 1.11. [15] Let $((\mathbb{S}, A), \mathfrak{D}_p)$ and $((\mathbb{S}', A'), \mathfrak{D}'_p)$ be two Steinhaus transform soft metric spaces over X and Y respectively. Let $f = (f_1, f_2) : ((\mathbb{S}, A), \mathfrak{D}_p) \rightarrow ((\mathbb{S}', A'), \mathfrak{D}'_p)$ be a soft mapping. Then f is soft continuous if and only if for every $(x, \mathbb{S}(x)) \in (\mathbb{S}, A)$ and every positive number ϵ , there subsist a positive number δ such that for every $(y, \mathbb{S}(y)) \in (\mathbb{S}, A)$

$$\mathfrak{D}'_p((f(x, \mathbb{S}(x))), f((y, \mathbb{S}(y)))) \leq (\tilde{\pi}'(\tilde{\pi}(x, y)), \epsilon)$$

whenever $\mathfrak{D}'_p(f(x, F(x)), f((y, F(y)))) \leq (\tilde{\pi}(x, y), \delta)$.

Definition 1.12. [15] Let $((F, A), \mathcal{D}_p)$ be a Steinhaus transform soft metric space over X and $f : ((\mathbb{S}, A), \mathcal{D}_p) \rightarrow ((\mathbb{S}, A), \mathcal{D}_p)$ be a soft mapping. We say that f is soft contractive if there is a positive number c with $0 < c < 1$ such that

$$\mathcal{D}_p((f(x, \mathbb{S}(x))), f((y, \mathbb{S}(y)))) \leq c \mathcal{D}_p((x, \mathbb{S}(x)), (y, \mathbb{S}(y))), \text{ for all } x, y \in A.$$

Theorem 1.13. [15] Soft contractive mapping is soft continuous in Steinhaus transform soft metric space $((\mathbb{S}, A), \mathcal{D}_p)$.

Definition 1.14. [15] Let $((\mathbb{S}, A), \mathcal{D}_p)$ be a complete Steinhaus transform soft metric space over X and let $f : ((\mathbb{S}, A), \mathcal{D}_p) \rightarrow ((\mathbb{S}, A), \mathcal{D}_p)$ be a soft mapping. A fixed soft set for f is a soft subset of (\mathbb{S}, A) such as $(x, \mathbb{S}(x))$ such that $f((x, \mathbb{S}(x))) = (x, \mathbb{S}(x))$.

Definition 1.15. [8] Let (X, d) be a complete metric space. The self-map $T : X \rightarrow X$ be a mapping such that there exist $K < 1/2$ satisfying

$$d(Tx, Ty) \leq K[d(x, Tx) + d(y, Ty)].$$

Then T is named a Kannan contraction type map.

4. Some Soft Fixed Point Theorems for Steinhaus Transform Soft Metric Spaces

Theorem 2.1. Let (\mathbb{S}, E) be a nonempty soft closed subset of a soft complete space $((\mathbb{S}, E), \mathcal{D}_p)$ and let $T : (\mathbb{S}, E) \rightarrow (\mathbb{S}, E)$ be a mapping such that there exists satisfying $K < 1$

$$\mathcal{D}_p(T((x, \mathbb{S}(x))), T((y, \mathbb{S}(y)))) \leq K[D((x, \mathbb{S}(x))), T((x, \mathbb{S}(x))) + D((y, \mathbb{S}(y))), T((y, \mathbb{S}(y)))]$$

for all $(x, \mathbb{S}(x)), (y, \mathbb{S}(y)) \in (\mathbb{S}, E)$.

Assume that there exist parametric scalars $(a, r), (b, r')$ such that $0 \leq r < 1$ and $r' > 0$ with $a, b \in E$. If for arbitrary $(x, \mathbb{S}(x)) \in (\mathbb{S}, E)$ there exists $(u, \mathbb{S}(u)) \in (\mathbb{S}, E)$ such that

$$\mathcal{D}_p((u, \mathbb{S}(u)), T((u, \mathbb{S}(u)))) \leq r \cdot \mathcal{D}_p((x, \mathbb{S}(x)), T((x, \mathbb{S}(x)))) \text{ and}$$

$$\mathcal{D}_p((u, \mathbb{S}(u)), (x, \mathbb{S}(x))) \leq r' \cdot \mathcal{D}_p((x, \mathbb{S}(x)), T((x, \mathbb{S}(x)))) \text{ then } T \text{ has at least one fixed point set.}$$

Proof: Let $(x_0, \mathbb{S}(x_0)) \in (\mathbb{S}, E)$ be an arbitrary soft point. Consider a sequence $\{(\mathbb{S}_n, E)\}_{n=1}^{\infty}$ satisfies

$$\mathcal{D}_p(T(\mathbb{S}_{n+1}, E), (\mathbb{S}_{n+1}, E)) \leq r \cdot \mathcal{D}_p(T(\mathbb{S}_n, E), (\mathbb{S}_n, E))$$

$$\mathcal{D}_p((\mathbb{S}_{n+1}, E), (\mathbb{S}_n, E)) \leq r' \cdot \mathcal{D}_p(T(\mathbb{S}_n, E), (\mathbb{S}_n, E)), n = 0, 1, 2, \dots$$

Since

$$\mathcal{D}_p((\mathbb{S}_{n+1}, E), (\mathbb{S}_n, E)) \leq r' \cdot \mathcal{D}_p(T(\mathbb{S}_n, E), (\mathbb{S}_n, E)) \leq r' \cdot r^n \cdot \mathcal{D}_p(T(\mathbb{S}_0, E), (\mathbb{S}_0, E)) \}$$

$$\begin{aligned} \mathcal{D}_p(T(v, \mathbb{S}_v), (v, \mathbb{S}_v)) &= \frac{2\mathcal{D}_p(T(v, \mathbb{S}_v), (v, \mathbb{S}_v))}{\mathcal{D}_p(T(v, \mathbb{S}_v), (\mathbb{S}_n, E)) + \mathcal{D}_p((v, \mathbb{S}_v), (\mathbb{S}_n, E)) + \mathcal{D}_p(T(v, \mathbb{S}_v), (v, \mathbb{S}_v))} \\ &\leq 2\mathcal{D}_p(T(v, \mathbb{S}_v), (v, \mathbb{S}_v)) \\ &\leq 2[\mathcal{D}_p((v, \mathbb{S}_v), T(v, \mathbb{S}_v)) + \mathcal{D}_p(T(\mathbb{S}_n, E), (\mathbb{S}_n, E)) \\ &\quad + \mathcal{D}_p((\mathbb{S}_n, E), (v, \mathbb{S}_v))] + \mathcal{D}_p((\mathbb{S}_n, E), (v, \mathbb{S}_v)) \\ &\leq 2[K[\mathcal{D}_p((v, \mathbb{S}_v), T(v, \mathbb{S}_v)) + \overline{\mathcal{D}_p((\mathbb{S}_n, E), T(\mathbb{S}_n, E))}] \\ &\quad + \overline{\mathcal{D}_p(T(\mathbb{S}_n, E), (\mathbb{S}_n, E))} + \overline{\mathcal{D}_p((\mathbb{S}_n, E), (v, \mathbb{S}_v))}] \end{aligned}$$

$$\begin{aligned} \mathcal{D}_p(T(v, \mathbb{S}_v), (v, \mathbb{S}_v)) &\leq 2K\mathcal{D}_p((v, \mathbb{S}_v), T(v, \mathbb{S}_v)) + 2K\mathcal{D}_p((\mathbb{S}_n, E), T(\mathbb{S}_n, E)) \\ &\quad + 2\mathcal{D}_p(T(\mathbb{S}_n, E), (\mathbb{S}_n, E)) + 2\mathcal{D}_p((\mathbb{S}_n, E), (v, \mathbb{S}_v)) \\ \mathcal{D}_p(T(v, \mathbb{S}_v), (v, \mathbb{S}_v)) - 2K\mathcal{D}_p((v, \mathbb{S}_v), T(v, \mathbb{S}_v)) &\leq 2K\mathcal{D}_p((\mathbb{S}_n, E), T(\mathbb{S}_n, E)) \\ &\quad + 2\mathcal{D}_p(T(\mathbb{S}_n, E), (\mathbb{S}_n, E)) + 2\mathcal{D}_p((\mathbb{S}_n, E), (v, \mathbb{S}_v)) \\ (1-2K)\mathcal{D}_p(T(v, \mathbb{S}_v), (v, \mathbb{S}_v)) &\leq (2K+2)\mathcal{D}_p((\mathbb{S}_n, E), T(\mathbb{S}_n, E)) + 2\mathcal{D}_p((\mathbb{S}_n, E), (v, \mathbb{S}_v)) \\ \mathcal{D}_p(T(v, \mathbb{S}_v), (v, \mathbb{S}_v)) &\leq \frac{2K+2}{1-2K}\mathcal{D}_p((\mathbb{S}_n, E), T(\mathbb{S}_n, E)) + \frac{2}{1-2K}\mathcal{D}_p((\mathbb{S}_n, E), (v, \mathbb{S}_v)) \\ &\leq \frac{2K+2}{1-2K}r^n\mathcal{D}_p(T(x_0, \mathbb{S}_{x_0}), (x_0, \mathbb{S}_{x_0})) + \frac{2}{1-2K}\mathcal{D}_p((\mathbb{S}_n, E), (v, \mathbb{S}_v)) \rightarrow 0 \end{aligned}$$

as $n \rightarrow \infty$. Hence $T(v) = v$. ■

Theorem 2.2. Let $((\mathbb{S}, E), \mathcal{D}_p)$ be a soft complete metric space let $T : (\mathbb{S}, E) \rightarrow (\mathbb{S}, E)$ be a mapping such that there exists $K < \frac{1}{2}$ satisfying

$$D(T(x, \mathbb{S}_x), T(y, \mathbb{S}_y)) \leq K[\mathcal{D}_p((x, \mathbb{S}_x), T(x, \mathbb{S}_x)) + \mathcal{D}_p((y, \mathbb{S}_y), T(y, \mathbb{S}_y))] \quad \text{for all } x, y \in X \dots (1)$$

Then, T has a unique fixed soft point $(v, \mathbb{S}_v) \in (\mathbb{S}, E)$, and for any $(x, \mathbb{S}_x) \in (\mathbb{S}, E)$ the soft sequence of iterates $\{T^n(x, \mathbb{S}_x)\}$ converges to (v, \mathbb{S}_v) and

$$\mathcal{D}_p(T^{n+1}(x, \mathbb{S}_x), (v, \mathbb{S}_v)) \leq 2K \cdot \left(\frac{2K}{1-2K}\right)^n \cdot \mathcal{D}_p((x, \mathbb{S}_x), T(x, \mathbb{S}_x)), n = 0, 1, 2, \dots$$

Proof: For any $(x, \mathbb{S}_x) \in (\mathbb{S}, E)$ let $(u, \mathbb{S}_u) = T(x, \mathbb{S}_x)$ Then

$$\mathcal{D}_p((u, \mathbb{S}_u), T(u, \mathbb{S}_u)) = \frac{2\mathcal{D}_p((u, \mathbb{S}_u), T(u, \mathbb{S}_u))}{\mathcal{D}_p(T(u, \mathbb{S}_u), T(x_n, \mathbb{S}_{x_n})) + \mathcal{D}_p((u, \mathbb{S}_u), (x_n, \mathbb{S}_{x_n})) + \mathcal{D}_p(T(u, \mathbb{S}_u), (u, \mathbb{S}_u))}$$

$$\mathcal{D}_p(T(x, \mathbb{S}_x), T(u, \mathbb{S}_u)) = \frac{2\mathcal{D}_p(T(x, \mathbb{S}_x), T(u, \mathbb{S}_u))}{\mathcal{D}_p(T(u, \mathbb{S}_u), (x_n, \mathbb{S}_{x_n})) + \mathcal{D}_p(T(x, \mathbb{S}_x), (x_n, \mathbb{S}_{x_n})) + \mathcal{D}_p(T(u, \mathbb{S}_u), T(x, \mathbb{S}_x))}$$

$$\begin{aligned}
 &\leq 2 \mathcal{D}_p((u, \mathbb{S}u), T(u, \mathbb{S}u)) = 2 \mathcal{D}_p(T(x, \mathbb{S}x), T(u, \mathbb{S}u)) \\
 &\leq 2K [\mathcal{D}_p((x, \mathbb{S}x), T(x, \mathbb{S}x)) + \mathcal{D}_p((u, \mathbb{S}u), T(u, \mathbb{S}u))] \\
 \mathcal{D}_p((u, \mathbb{S}u), T(u, \mathbb{S}u)) &= \mathcal{D}_p(T(x, \mathbb{S}x), T(u, \mathbb{S}u)) \leq 2K \mathcal{D}_p((x, \mathbb{S}x), T(x, \mathbb{S}x)) + 2K \mathcal{D}_p((u, \mathbb{S}u), T(u, \mathbb{S}u)) \\
 \mathcal{D}_p((u, \mathbb{S}u), T(u, \mathbb{S}u)) - 2K \mathcal{D}_p((u, \mathbb{S}u), T(u, \mathbb{S}u)) &\leq 2K \overline{\mathcal{D}_p((x, \mathbb{S}x), T(x, \mathbb{S}x))} \\
 (1 - 2K) \overline{\mathcal{D}_p((u, \mathbb{S}u), T(u, \mathbb{S}u))} &\leq 2K \overline{\mathcal{D}_p((x, \mathbb{S}x), T(x, \mathbb{S}x))} \\
 \overline{\mathcal{D}_p((u, \mathbb{S}u), T(u, \mathbb{S}u))} &\leq \frac{2K}{1 - 2K} \overline{\mathcal{D}_p((x, \mathbb{S}x), T(x, \mathbb{S}x))} \\
 0 < \mathcal{D}_p((v, \mathbb{S}v), (z, \mathbb{S}z)) &= \mathcal{D}_p(T(v, \mathbb{S}v), T(z, \mathbb{S}z)) \leq 2K [\mathcal{D}_p((v, \mathbb{S}v), T(v, \mathbb{S}v)) + \mathcal{D}_p((z, \mathbb{S}z), T(z, \mathbb{S}z))] \\
 &= 0 \\
 \mathcal{D}_p(T^{n+1}(x, \mathbb{S}x), T^n(x, \mathbb{S}x)) &\leq 2K [\mathcal{D}_p(T^n(x, \mathbb{S}x), T^{n+1}(x, \mathbb{S}x)) + \mathcal{D}_p(T^{n-1}(x, \mathbb{S}x), T^n(x, \mathbb{S}x))] \\
 \mathcal{D}_p(T^{n+1}(x, \mathbb{S}x), T^n(x, \mathbb{S}x)) &\leq \frac{2K}{1 - 2K} \cdot \mathcal{D}_p(T^n(x, \mathbb{S}x), T^{n-1}(x, \mathbb{S}x)) \\
 \overline{\mathcal{D}_p(T^{n+1}(x, \mathbb{S}x), (v, \mathbb{S}v))} &\leq 2K [\overline{\mathcal{D}_p(T^n(x, \mathbb{S}x), T^{n+1}(x, \mathbb{S}x))} + \overline{\mathcal{D}_p((v, \mathbb{S}v), T(v, \mathbb{S}v))}] \\
 &= 2K \cdot \overline{\mathcal{D}_p(T^{n+1}(x, \mathbb{S}x), T^n(x, \mathbb{S}x))} \\
 &\leq 2K \cdot \left(\frac{2K}{1 - 2K}\right)^n \mathcal{D}_p(T(x, \mathbb{S}x), (x, \mathbb{S}x)), \quad n = 0, 1, 2, \dots \quad \blacksquare
 \end{aligned}$$

References

- [1] Altıntaş İ, Şimşek D, Taşköprü K (2017) Topology of soft cone metric spaces. AIP Conference Proceedings. 1880, 030006, <https://doi.org/10.1063/1.50006056>
- [2] Aras ÇGG, Posul H (2016) On some new operations in probabilistic soft set theory. European Journal of Pure and Applied Mathematics 9(3): 333-339.
- [3] Banach S (1922) Sur les opérations dans les ensembles abstraits et leur application aux équations intégrales. Fund Math. 3: 133-181.
- [4] Das S, Samanta SK (2013) Soft Metric. Annals of Fuzzy Mathematics and Informatics 6(1): 77-94.
- [5] Gornicki J (2017) Fixed point theorems Kannan type mappings. Journal of Fixed Point Theory and Applications Monthly 19: 2145-2152.
- [6] Guler AC, Yıldırım ED, Ozbakır OB (2016) A fixed point theorem on Soft G -metric spaces. J. Nonlinear Sci. Appl., 9: 885-894.
- [7] Hosseinzadeh H (2017) Fixed point theorems on soft metric spaces. Journal of Fixed Point Theory and Applications 19(2): 1625-1647.
- [8] Kannan R., (1968) Some results on fixed point. Bull. Cal. Math. Soc., 60, 71-76.
- [9] Kannan R., (1969) Some results on fixed point II. Amer. Math. Monthly, 76, 405-408.
- [10] Maji PK, Biswas R, Roy AR (2003) Soft Set Theory. Comput. Math. Appl., 45: 555-562.
- [11] Marczewski E, Steinhaus H (1957) On a certain distance of sets and the corresponding distance of functions. Collect. Math. 6(1): 319-327.
- [12] Molodtsov D (1999) Soft set theory-first result. Comput. Math. Appl., 37: 19- 31.
- [13] Mutlu A, Yolcu N, Mutlu B (2016) Fixed point theorems in partially ordered rectangular metric spaces. British Journal of Mathematics and Computer Science 15(2):1-9.
- [14] Öztunç S, Mutlu A, Aslan S (2019) Some Kannan type fixed point results in rectangular soft metric space and an application of fixed point for thermal science problem. Thermal Science, 23(1) S215-S225 2019, <https://doi.org/10.2298/TSCI181102035O>.
- [15] Öztunç S, Mutlu A, Yılmaz N (2018) Some soft fixed point theorems by using Steinhaus transform soft metric. 2nd International Students Science Congress, İzmir, Turkey. Proceeding Book: 83-89.

3rd International Students Science Congress
3-4 May 2019, İzmir - Turkey

- [16] Shabir M., Naz M (2011) On soft topological spaces. *Computers & Mathematics with Applications* 61(7): 1786-1799.
- [17] Şimşek D, Altıntaş İ, Ersoy S, Abdullayev F, İmaş Kızı M, Taşkoprü K, Kesik D, Abılayeva E, Ogul B, Çemşitov N (2018) An introduction to soft cone metric spaces and some fixed point theorems. *MANAS Journal of Engineering (MJEN)*. 6(1): 59-89.
- [18] Yazar Mİ., Aras ÇG, Bayramov S. (2016) Fixed Point Theorems of Soft Contractive Mappings. *Filomat*, 30(2): 269-27.
- [19] Zorlutuna İ, Çakır H (2015) On continuity of soft mappings. *Appl. Math. Inf. Sci.* 9(1): 403-409.

Some Remarks on Steinhaus Transform Soft Metric Spaces

*Simge Öztunç**, Manisa Celal Bayar University, Dept of Mathematics, Manisa, Turkey

Ali Mutlu, Manisa Celal Bayar University, Dept of Mathematics, Manisa, Turkey

Nurettin Yılmaz, Manisa Celal Bayar University, The Institute of Naturel and Applied Sciences, Manisa, Turkey

*Corresponding Author: simge.oztunc@cbu.edu.tr

Keywords: soft metric, Steinhaus transform soft metric, soft fixed point theorems

Discipline: Mathematics, Topology

Abstract

In this paper we focus on the biotope transform metric or Steinhaus transform soft metric. We obtain and prove some fixed point theorems for Stainhaus-Transform soft metric space.

Introduction

In 1999 Molodsov [10] introduced the notion of soft sets and the theory of soft sets is studied by many branches of mathematics. Details of soft set theory can be found at [2,8,14,17].

Otherwise fixed point theory has a crucial role in mathematics and has great areas of usages in engineering, natural and applied science. Banach Contraction Theorem [2] is one of the fundamentals of fixed point theory. Several fixed point theorems are proved in [5,9,11].

As a combination of soft set and fixed point theory Das and Samanta [4] introduced a new metric called "soft metric" in 2013. After then Hosseinzadeh [7] redefined the soft metric spaces and brought a new view point.

Different types of soft metrics are studied many mathematics [1,6,12,13,15,16]. One of them is Steinhaus transform soft metric which is introduced last year. This paper considers some fixed point theorems for Steinhaus transform soft metric space.

5. Preliminaries

Definition 1.1. [10] A pair (F, A) is said to be a soft set over the universe U , where F is a mapping given by $F : A \rightarrow P(U)$.

In other words, a soft set over U is a parameterized family of subsets of the universe U . For any parameter $x \in A$, $F(x)$ may be considered as the set of x - approximate elements of the soft set (F, A) .

Definition 1.2. [7] Let $A \subseteq E$ be a set of parameters. We say the ordered pair (a, r) is a soft parametric scalar if $r \in R$ and $a \in A$. The parametric scalar (r, a) called nonnegative if $r \geq 0$. Let (a, r) and (b, r') be two soft parametric scalars. We say (a, r) is no less than (b, r') and we write $(a, r) \succeq (b, r')$, if $r \geq r'$.

Definition 1.3. [7] Let $A \subseteq E$ be a set of parameters. Let (a, r) and (b, r') be two soft parametric scalars. Then we define addition between soft parametric scalars and scalar multiplication on soft parametric scalars as follows

$$(a, r) \dot{+} (b, r') = (a, b, r + r'), \text{ and}$$

$$\lambda(a, r) = (a, \lambda r), \text{ for every } \lambda \in R.$$

Definition 1.4.[13] Let (F, A) be a soft set over X and let $\tilde{\pi} : A \times A \rightarrow A$ be parametric function.

We say the parametric scalar valued function $\mathcal{D} : (F, A) \times (F, A) \rightarrow (A, R^+ \setminus \{0\})$ a soft meter on (F, A) if \mathcal{D} satisfies in the following conditions:

$$(1) \mathcal{D}_p((a, F(a)), (b, F(b))) \succeq (\tilde{\pi}(a, b), 0), \text{ and equality holds, whenever } a = b.$$

$$(2) \mathcal{D}_p((a, F(a)), (b, F(b))) = \mathcal{D}((b, F(b)), (a, F(a))), \text{ for all } a, b \in A.$$

$$(3) \mathcal{D}_p((a, F(a)), (c, F(c))) \preceq \mathcal{D}((a, F(a)), (b, F(b))) \dot{+} \mathcal{D}((b, F(b)), (c, F(c))), \text{ for all } a, b, c \in A.$$

$$(4) \mathfrak{D}_p((a, F(a)), (b, F(b))) = \frac{2\mathfrak{D}((a, F(a)), (b, F(b)))}{\mathfrak{D}((a, F(a)), (c, F(c))) + \mathfrak{D}_p((b, F(b)), (c, F(c))) + \mathfrak{D}((a, F(a)), (b, F(b)))}$$

We say the pair $((F, A), \mathfrak{D}_p)$ is a soft Steinhaus transform metric space over X .

Definition 1.5. [7] Let (F, A) be a soft set over X . A soft sequence in (F, A) is a function $f : N \rightarrow (F, A)$ by setting $f(n) = (F_n, A)$ such that (F_n, A) is a soft subset of (F, A) for $n \in N$, and we denote it by $\{(F_n, A)\}_{n=1}^{\infty}$.

Definition 1.6. [13] Let (F, A) be a soft set over X . Let \mathfrak{D}_p be a Steinhaus transform soft metric on (F, A) , $\{(F_n, A)\}_{n=1}^{\infty}$ be a soft sequence in (F, A) and $(x, F(x)) \in (F, A)$. Then we say $\{(F_n, A)\}_{n=1}^{\infty}$ converges to $(x, F(x))$, if for every positive number ϵ , there exists a natural number N such that for every natural number n which $n \geq N$, we have

$$\mathfrak{D}_p(a, F_n(a), (x, F(x))) \leq (\tilde{\pi}(a, x), \epsilon).$$

Theorem 1.7. [13] Let (F, A) be a soft set over X , let \mathfrak{D} be a meter on (F, A) , $\{(F_n, A)\}_{n=1}^{\infty}$ be a soft sequence in (F, A) . If $(F, A), \{(F_n, A)\}_{n=1}^{\infty}$ is convergent in (F, A) , then it converges to unique element of (F, A) .

Definition 1.8. [13] Let (F, A) be a soft set over X . Let \mathfrak{D}_p be a Steinhaus transform soft metric on (F, A) and $\{(F_n, A)\}_{n=1}^{\infty}$ be a soft sequence in (F, A) . Then we say $\{(F_n, A)\}_{n=1}^{\infty}$ is a Cauchy soft sequence, if for every positive number ϵ , there exists a natural number N such that for every natural number n, m which $n, m \geq N$, we have

$$\mathfrak{D}_p((a, F_n(a)), (a, F_m(a))) \leq (\tilde{\pi}(a, a), \epsilon).$$

Proposition 1.9. [13] Let $((F, A), \mathfrak{D}_p)$ be a Steinhaus transform soft metric space over X , and let $\{(F_n, A)\}_{n=1}^{\infty}$ be a convergent soft sequence in (F, A) . Then $\{(F_n, A)\}_{n=1}^{\infty}$ is a Cauchy soft sequence.

Definition 1.10. [13] Let (F, A) be a soft set over X , let \mathfrak{D}_p be a Steinhaus transform soft metric on (F, A) . We say that (F, A) is a complete Steinhaus transform soft metric space if every Cauchy soft sequence converges in (F, A) .

Theorem 1.11. [13] Let $((F, A), \mathfrak{D}_p)$ and $((F', A'), \mathfrak{D}'_p)$ be two Steinhaus transform soft metric spaces over X and Y respectively. Let $f = (f_1, f_2) : ((F, A), \mathfrak{D}_p) \rightarrow ((F', A'), \mathfrak{D}'_p)$ be a soft mapping. Then f is soft continuous if and only if for every $(x, F(x)) \in (F, A)$ and every positive number ϵ , there exists a positive number δ such that for every $(y, F(y)) \in (F, A)$

$$\mathfrak{D}'_p((f(x, F(x))), f((y, F(y)))) \leq (\tilde{\pi}'(\tilde{\pi}(x, y)), \epsilon)$$

whenever $\mathfrak{D}'_p(f(x, F(x)), f((y, F(y)))) \leq (\tilde{\pi}(x, y), \delta)$.

Definition 1.12. [13] Let $((F, A), \mathfrak{D}_p)$ be a Steinhaus transform soft metric space over X and f be a soft mapping. We say that f is soft contractive if there is a positive number c with $0 < c < 1$ such that

$$\mathfrak{D}_p((f(x, F(x))), f((y, F(y)))) \leq c\mathfrak{D}_p((x, F(x)), (y, F(y))), \text{ for all } x, y \in A.$$

Theorem 1.13. [13] Soft contractive mapping is soft continuous in Steinhaus transform soft metric space $((F, A), \mathfrak{D}_p)$.

Definition 1.14. [13] Let $((F, A), \mathcal{D}_p)$ be a complete Steinhaus transform soft metric space over X and let $f : ((F, A), \mathcal{D}_p) \rightarrow ((F, A), \mathcal{D}_p)$ be a soft mapping. A fixed soft set for f is a soft subset of (F, A) such as $(x, F(x))$ such that $f((x, F(x))) = (x, F(x))$.

6. Main Result

Theorem 2.1. Let $((F, A), \mathcal{D}_p)$ be a complete Steinhaus transform soft metric space over X , and let $T : B_{\mathcal{D}_p}((a, F(a)), (a', r)) \rightarrow ((F, A), \mathcal{D}_p)$ be a soft contraction mapping with

$$\mathcal{D}_p(T(a, F(a)), (a, F(a))) < (1-c)(a', r),$$

where $0 < c < 1$. Then T has a unique fixed soft set in $B_{\mathcal{D}_p}((a, F(a)), (a', r))$.

Proof: Clearly there is an $r_0 \geq 0$ such that $0 \leq (a', r_0) \leq (a', r)$ with $\mathcal{D}_p(T(a, F(a)), (a, F(a))) < (1-c)(a', r_0)$

Take

$$T : \overline{B_{\mathcal{D}_p}((a, F(a)), (a', r_0))} \rightarrow \overline{B_{\mathcal{D}_p}((a, F(a)), (a', r_0))}$$

If $(b, F(b)) \in \overline{B_{\mathcal{D}_p}((a, F(a)), (a', r_0))}$ then by the 4. property of Steinhaus Transform Soft Metric

$$\begin{aligned} \mathcal{D}_p(T(b, F(b)), (a, F(a))) &= \frac{2\mathcal{D}_p(T(b, F(b)), (a, F(a)))}{\mathcal{D}_p((a, F(a)), (c, F(c))) \dot{+} \mathcal{D}_p(T(b, F(b)), (c, F(c))) \dot{+} \mathcal{D}_p((a, F(a)), T(b, F(b)))} \\ &\leq 2\mathcal{D}_p(T(b, F(b)), (a, F(a))) \\ &\leq 2[\mathcal{D}_p(T(b, F(b)), T(a, F(a))) \dot{+} \mathcal{D}_p(T(a, F(a)), (a, F(a)))] \\ &\leq 2\mathcal{D}_p(T(b, F(b)), T(a, F(a))) \dot{+} 2\overline{\mathcal{D}_p(T(a, F(a)), (a, F(a)))} \\ &\leq 2c\overline{\mathcal{D}_p((b, F(b)), (a, F(a)))} \dot{+} 2(1-c)(a', r_0) \\ &= 2(a', r_0) \end{aligned}$$

Since $\overline{B_{\mathcal{D}_p}((a, F(a)), (a', r_0))} \subseteq \overline{B_{\mathcal{D}_p}((a, F(a)), (a', r))}$. Because of the Banach contraction of the theorem for Steinhaus transform soft metric space we conclude that T has a unique fixed soft set in $\overline{B_{\mathcal{D}_p}((a, F(a)), (a', r_0))} \subseteq \overline{B_{\mathcal{D}_p}((a, F(a)), (a', r))}$. ■

Theorem 2.2. Let $((F, A), \mathcal{D}_p)$ be a complete Steinhaus transform soft metric space over X , and suppose there exists α such that for each $(a, F(a)), (b, F(b)) \in (F, A)$ soft mapping $T : (F, A) \rightarrow (F, A)$ such that $T(a, F(a)) = (T_1(a), T_2(F(a))) = (T_1(a), F(T_1(a)))$ for every $(a, F(a)) \in (F, A)$ and it satisfies:

$$\mathcal{D}_p(T(a, F(a)), (b, F(b))) \leq 2\alpha(\mathcal{D}_p((a, F(a)), (b, F(b))))\mathcal{D}_p((a, F(a)), (b, F(b))), \dots (1)$$

for every $(a, F(a)), (b, F(b)) \in (F, A)$. Then T has a unique fixed soft set.

Proof: Put the fixed soft set $(a, F(a)) \in (F, A)$ and let

$$(a_n, F(a_n)) = T^n(a, F(a)), \text{ for } n \in \mathbb{N}. \text{ We will proof the theorem in two steps.}$$

Step1: We claim that

$$\lim_{n \rightarrow \infty} \mathcal{D}_p((a_n, F(a_n)), (a_{n+1}, F(a_{n+1}))) = 0.$$

Since T is contraction mapping

$$\begin{aligned} \mathfrak{D}_p((a_n, F(a_n)), (a_{n+1}, F(a_{n+1}))) &= \mathfrak{D}_p(T^n(a, F(a)), T^{n+1}(a, F(a))) \\ &= \frac{2\mathfrak{D}_p(T^n(a, F(a)), T^{n+1}(a, F(a)))}{\mathfrak{D}_p(T^n(a, F(a)), T^{n-1}(a, F(a))) \dot{+} \mathfrak{D}_p(T^{n+1}(a, F(a)), T^{n-1}(a, F(a))) \dot{+} \mathfrak{D}_p(T^n(a, F(a)), T^{n-1}(a, F(a)))} \\ &\leq \mathfrak{D}_p(T^n(a, F(a)), T^{n+1}(a, F(a))) \\ &\leq 2\alpha(\mathfrak{D}_p(T^{n-1}(a, F(a)), T^n(a, F(a)))) \cdot \mathfrak{D}_p(T^{n-1}(a, F(a)), T^n(a, F(a))) \\ &= 2\alpha(\mathfrak{D}_p((a_{n-1}, F(a_{n-1})), T(a_n, F(a_n)))) \cdot \mathfrak{D}_p(T(a_{n-1}, F(a_{n-1})), T(a_n, F(a_n))) \\ &\leq 2\mathfrak{D}_p((a_{n-1}, F(a_{n-1})), (a_n, F(a_n))) \end{aligned}$$

Thus

$$\mathfrak{D}_p((a_n, F(a_n)), (a_{n+1}, F(a_{n+1}))) \leq 2\mathfrak{D}_p((a_{n-1}, F(a_{n-1})), (a_n, F(a_n))) \quad \text{hence the sequence}$$

$\mathfrak{D}_p((a_n, F(a_n)), (a_{n+1}, F(a_{n+1})))$ is decreasing. Then

$$\lim_{n \rightarrow \infty} \mathfrak{D}_p((a_n, F(a_n)), (a_{n+1}, F(a_{n+1}))) = (b, r).$$

Assume toward a contradiction that $(b, r) \neq 0$ or $r \neq 0$. By the inequality (1) we have

$$\mathfrak{D}_p((a_{n+1}, F(a_{n+1})), (a_{n+2}, F(a_{n+2}))) \leq 2\alpha(\mathfrak{D}_p((a_n, F(a_n)), (a_{n+1}, F(a_{n+1})))) \mathfrak{D}_p((a_n, F(a_n)), (a_{n+1}, F(a_{n+1}))).$$

Then letting $n \rightarrow \infty$, we have

$$(b, r) \leq \lim_{n \rightarrow \infty} 2\alpha(\mathfrak{D}_p((a_n, F(a_n)), (a_{n+1}, F(a_{n+1}))))(b, 1).$$

This follows

$$(b, 1) \leq (b, \lim_{n \rightarrow \infty} 2\alpha(\mathfrak{D}_p((a_n, F(a_n)), (a_{n+1}, F(a_{n+1})))))) \geq 1.$$

This is a contradiction and shows that claim is true.

Step2: We claim that $(a_n, F(a_n))$ is a Cauchy soft sequence. Assume toward a contradiction that

$$\lim_{n, m \rightarrow \infty} \mathfrak{D}_p((a_n, F(a_n)), (a_m, F(a_m))) > (a, 0), \text{ for every } a \in A.$$

By the triangle property and the 4. property of Steinhaus Transform Soft Metric

$$\begin{aligned} \mathfrak{D}_p((a_n, F(a_n)), (a_m, F(a_m))) &= \\ &= \frac{2\mathfrak{D}_p((a_n, F(a_n)), (a_m, F(a_m)))}{\mathfrak{D}_p((a_n, F(a_n)), (a_{m+1}, F(a_{m+1}))) \dot{+} \mathfrak{D}_p((a_m, F(a_m)), (a_{m+1}, F(a_{m+1}))) \dot{+} \mathfrak{D}_p((a_n, F(a_n)), (a_m, F(a_m)))} \\ &\leq 2\mathfrak{D}_p((a_n, F(a_n)), (a_m, F(a_m))) \\ &\leq 2[\mathfrak{D}_p((a_n, F(a_n)), (a_{n+1}, F(a_{n+1}))) \dot{+} \mathfrak{D}_p((a_{n+1}, F(a_{n+1})), (a_{m+1}, F(a_{m+1}))) \\ &\quad \dot{+} \mathfrak{D}_p((a_{m+1}, F(a_{m+1})), (a_m, F(a_m)))] \\ &\leq 2\mathfrak{D}_p((a_n, F(a_n)), (a_{n+1}, F(a_{n+1}))) \dot{+} 2\mathfrak{D}_p((a_{n+1}, F(a_{n+1})), (a_{m+1}, F(a_{m+1}))) \\ &\quad \dot{+} 2\alpha\mathfrak{D}_p((a_n, F(a_n)), (a_m, F(a_m))) \cdot \overline{\mathfrak{D}_p((a_n, F(a_n)), (a_m, F(a_m)))} \end{aligned}$$

Then

$$\begin{aligned} [1 - 2\alpha\mathfrak{D}_p((a_n, F(a_n)), (a_m, F(a_m)))] \mathfrak{D}_p((a_n, F(a_n)), (a_m, F(a_m))) \\ \leq 2\mathfrak{D}_p((a_n, F(a_n)), (a_{n+1}, F(a_{n+1}))) \dot{+} 2\mathfrak{D}_p((a_{m+1}, F(a_{m+1})), (a_m, F(a_m))) \end{aligned}$$

Step 1 implies

$$(1 - 2\alpha)\mathfrak{D}_p((a_n, F(a_n)), (a_m, F(a_m))) \cdot \mathfrak{D}_p((a_n, F(a_n)), (a_m, F(a_m))) \leq (a, 0)$$

for every $a \in A$. Therefore, one of the following situations can be occur.

$$i) 1 - \lim_{n \rightarrow \infty} 2\alpha(\mathcal{D}_p((a_n, F(a_n)), (a_m, F(a_m)))) = 0$$

$$ii) \mathcal{D}_p((a_n, F(a_n)), (a_m, F(a_m))) = (a, 0) \text{ for all } a \in A.$$

According to our assumption case (ii) cannot be happen. So $\lim_{n \rightarrow \infty} 2\alpha(\mathcal{D}_p((a_n, F(a_n)), (a_m, F(a_m)))) = 1$. Definition of α implies that

$2\mathcal{D}_p((a_n, F(a_n)), (a_m, F(a_m))) \rightarrow (a, 0)$, for all $a \in A$. Hence $(a_n, F(a_n))$ is a Cauchy soft sequence. Let $(a, F(a)) \in (F, A)$. Since (F, A) is complete Steinhaus transform soft metric space and $T^n(a, F(a))$ is a Cauchy soft sequence, so there is a $(z, F(z)) \in (F, A)$ such that $\lim_{n \rightarrow \infty} T^n(a, F(a)) = (z, F(z))$. Because of the soft continuity of T , we obtain that $T(z, F(z)) = (z, F(z))$.

For uniqueness, suppose that $(b, F(b))$ another soft fixed point of T , that is $T(b, F(b)) = (b, F(b))$. From the Steinhaus transform property and contractive condition on T we have:

$$\begin{aligned} & \mathcal{D}_p(T(a, F(a)), T(b, F(b))) \\ &= \frac{2\mathcal{D}_p(T(a, F(a)), T(b, F(b)))}{\mathcal{D}_p(T(a, F(a)), T(c, F(c))) + \mathcal{D}_p(T(b, F(b)), T(c, F(c))) + \mathcal{D}_p(T(a, F(a)), T(b, F(b)))} \\ &\leq 2\mathcal{D}_p(T(a, F(a)), T(b, F(b))) \leq 2\alpha\mathcal{D}_p(T(a, F(a)), T(b, F(b))) \cdot \mathcal{D}_p(T(a, F(a)), T(b, F(b))) \end{aligned}$$

Thus

$$2\mathcal{D}_p(T(a, F(a)), T(b, F(b)))(1 - \alpha(\mathcal{D}_p(T(a, F(a)), T(b, F(b)))) \leq 0$$

Therefore

$$\mathcal{D}_p(T(a, F(a)), T(b, F(b))) = 0 \text{ or } 1 - \alpha\mathcal{D}_p(T(a, F(a)), T(b, F(b))) = 0$$

From the definition Steinhaus transform soft metric and property of α we conclude that $T(b, F(b)) = (b, F(b)) = (a, F(a))$. ■

References

- [1] Altıntaş İ, Şimşek D, Taşköprü K (2017) Topology of soft cone metric spaces. AIP Conference Proceedings. 1880, 030006, <https://doi.org/10.1063/1.50006056>
- [2] Aras ÇGG, Posul H (2016) On some new operations in probabilistic soft set theory. European Journal of Pure and Applied Mathematics 9(3): 333-339.
- [3] Banach S (1922) Sur les operations dans les ensembles abstrait set leur application aux equations integrales. Fund Math. 3: 133-181.
- [4] Das S, Samanta SK (2013) Soft Metric. Annals of Fuzzy Mathematics and Informatics 6(1): 77-94.
- [5] Gornicki J (2017) Fixed point theorems Kannan type mappings. Journal of Fixed Point Theory and Applications Monthly 19: 2145-2152.
- [6] Guler AC, Yıldırım ED, Ozbakır OB (2016) A fixed point theorem on Soft G -metric spaces. J. Nonlinear Sci. Appl., 9: 885-894.
- [7] Hosseinzadeh H (2017) Fixed point theorems on soft metric spaces. Journal of Fixed Point Theory and Applications 19(2): 1625-1647.
- [8] Maji PK, Biswas R, Roy AR (2003) Soft Set Theory. Comput. Math. Appl., 45: 555-562.
- [9] Marczewski E, Steinhaus H (1957) On a certain distance of sets and the corresponding distance of functions. Collect. Math. 6(1): 319-327.
- [10] Molodtsov D (1999) Soft set theory-first result. Comput. Math. Appl., 37: 19- 31.
- [11] Mutlu A, Yolcu N, Mutlu B (2016) Fixed point theorems in partially ordered rectangular metric spaces. British Journal of Mathematics and Computer Science 15(2):1-9.

3rd International Students Science Congress
3-4 May 2019, İzmir - Turkey

- [12] Öztunç S, Mutlu A, Aslan S (2019) Some Kannan type fixed point results in rectangular soft metric space and an application of fixed point for thermal science problem. *Thermal Science*, 23(1) S215-S225 2019, <https://doi.org/10.2298/TSCI181102035O>.
- [13] Öztunç S, Mutlu A, Yılmaz N (2018) Some soft fixed point theorems by using Steinhaus transform soft metric. 2nd International Students Science Congress, İzmir, Turkey. *Proceeding Book*: 83-89.
- [14] Shabir M., Naz M., (2011) On soft topological spaces. *Computers & Mathematics with Applications* 61(7): 1786-1799.
- [15] Şimşek, D., Altıntaş, İ., Ersoy, S., Abdullayev, F., İmaş Kızı, M., Taşköprü, K., Kesik, D., Abılayeva, E., Ogul, B., Çemşitov, N., (2018) An Introduction to Soft Cone Metric Spaces and Some Fixed Point Theorems. *MANAS Journal of Engineering (MJEN)*. 6(1): 59-89.
- [16] Yazar MI, Aras ÇG, Bayramov S. (2016) Fixed Point Theorems of Soft Contractive Mappings. *Filomat*, 30(2): 269-27.
- [17] Zorlutuna İ, Çakır H (2015) On continuity of soft mappings. *Appl. Math. Inf. Sci.* 9(1): 403-409.

Remarks on Rectangular Soft Metric Spaces

Simge Öztunç*, Manisa Celal Bayar University, Dept of Mathematics, Manisa, Turkey

Ali Mutlu, Manisa Celal Bayar University, Dept of Mathematics, Manisa, Turkey

Sedat Aslan, Manisa Celal Bayar University, The Institute of Naturel and Applied Sciences, Manisa, Turkey

*Corresponding Author: simge.oztunc@cbu.edu.tr

Keywords: soft metric, soft near metric, soft fixed point theorems

Discipline: Mathematics, Topology

Abstract

In this paper we introduce the partial rectangular soft metric space. Then we give the definitions of \tilde{O} – Cauchy soft sequence and \tilde{O} – complete partial rectangular soft metric space. Also we prove some properties deal with \tilde{O} – Cauchy soft sequence and \tilde{O} – completeness.

1. Introduction

In recent years soft set theory become a popular subject of mathematics which has studied by many mathematicians [8,10,16,19]. On the other hand, metric spaces have great deal of usage area in many branches of mathematics, engineering, naturel and applied science. In 1922, Banach [2] gave the fundamentals of fixed point theory. Many mathematicians studied on different types of metric spaces and properties of them.

Rectangular metric which is also called generalized metric is defined by Branciari [3] in 2000. Dung and Hang [5] gave the definition of partial rectangular metric by merging partial metric [9] and rectangular metric. Some details for rectangular and partial rectangular spaces can be seen in [11,12]. Also soft metric spaces are defined by Das and Samanta [4] in 2013 and improved by Hosseinzadeh [7] in 2017. So, many mathematicians studied on various soft metric space [1,6,13,14,15,17,18].

In this paper we investigate some Cauchy property and soft completeness for partial rectangular soft metric spaces.

2. Preliminaries

Definition 1.1. [10] Let E be a parameter set. A pair (F, E) is said to be a soft set over the universe X where F is a mapping given by $F : E \rightarrow P(X)$.

That is to say, a soft set over X is a parameterized family of subsets of the universal set X . For any parameter $x \in E$, $F(x)$ may be regarded as the set of X – approximate elements of the soft set (F, E) .

Definition 1.2. [7] Let $A \subseteq E$ be a set of parameters. The ordered pairwise (α, t) is called to be a soft parametric scalar if $t \in \mathbb{R}$ and $\alpha \in A$. The parametric scalar (α, t) called nonnegative if $t \geq 0$. Let (α, t) and (β, t') be two soft parametric scalars. (α, t) is said to be no less than (β, t') and it is written as $(\alpha, t) \succeq (\beta, t')$, if $t \geq t'$.

Definition 1.3. [7] Let $A \subseteq E$ be a set of parameters. Let (a, r) and (b, r') be two soft parametric scalars. Then we define addition between soft parametric scalars and scalar multiplication on soft parametric scalars as follows

$$(a, r) \dot{+} (b, r') = (a, b, r + r'), \text{ and}$$
$$\lambda(a, r) = (a, \lambda r), \text{ for every } \lambda \in \mathbb{R}.$$

Definition 1.4. [7] Let (F, A) be a soft set over X . We call a function f on (F, A) is parametric scalar valued, if there are functions $f_1 : A \rightarrow A$ and $f_2 : F(A) \rightarrow \mathbb{R}$ such that $f(F, A) = (f_1, f_2)(A, F(A))$.

Similarly, we can extend above defined parametric scalar valued function as $f : (F, A) \times (F, A) \rightarrow (A, R)$ by $f(A \times A, F(A) \times F(A)) = (f_1, f_2)(A \times A, F(A) \times F(A))$, where $f_1 : A \times A \rightarrow A$ and $f_2 : F(A) \times F(A) \rightarrow R$.

Definition 1.5.[13] Suppose that $\tilde{\varphi} : E \times E \rightarrow E$ be a scalar valued parametric function. The parametric scalar valued function $\mathfrak{D}_R : (F, E) \times (F, E) \rightarrow (E, R^+ \cup \{0\})$ is called to be a rectangular soft metric on (F, E) if \mathfrak{D}_R satisfies the following properties:

(RSM1) $\mathfrak{D}_R((x, F(x)), (y, F(y))) \geq (\tilde{\varphi}(x, y), 0)$, if $x = y$, then the equality holds.

(RSM2) $\mathfrak{D}_R((x, F(x)), (y, F(y))) = (\tilde{\varphi}(x, y), 0) \Leftrightarrow$ for all $((x, F(x)), (y, F(y))) \in (F, E)$, $(x, F(x)) = (y, F(y))$ [for all $x, y \in E, x = y$]

(RSM3) $\mathfrak{D}_R((x, F(x)), (y, F(y))) = \mathfrak{D}_R((y, F(y)), (x, F(x)))$, for all $x, y \in E$

(RSM4) $\mathfrak{D}_R((x, F(x)), (y, F(y))) \leq \mathfrak{D}_R((x, F(x)), (z, F(z))) + \mathfrak{D}_R((z, F(z)), (t, F(t))) + \mathfrak{D}_R((t, F(t)), (y, F(y)))$ for all $x, y, z, t \in E$.

Then we say the pair $((F, E), \mathfrak{D}_R)$ is a rectangular soft metric space over X .

Definition 1.6. [7] Assume that (F, E) be a soft set over X . A soft sequence in (F, E) is a function $f : N \rightarrow (F, E)$ equipped with $f(n) = (F_n, E)$ such that (F_n, E) is a soft subset of (F, E) for $n \in N$, and it is symbolized by $\{(F_n, E)\}_{n=1}^{\infty}$.

Definition 1.7. [13] Presume that (F, E) be a soft set over X . Let \mathfrak{D}_R be a rectangular soft metric on (F, E) , $\{(F_n, E)\}_{n=1}^{\infty}$ be a soft sequence in (F, E) and $(x, F(x)) \in (F, E)$. Then we state that the $\{(F_n, E)\}_{n=1}^{\infty}$ converges to $(x, F(x))$, if for every positive number ϵ , there subsist a naturel number N such that for all $n \in \mathbb{N}$ which $n \geq N$, we have

$$\mathfrak{D}_R((a, F_n(a)), (x, F(x))) \leq (\tilde{\varphi}(a, x), \epsilon).$$

Definition 1.8. [13] Suspect that (F, E) be a soft set over X . Let \mathfrak{D}_R be a rectangular soft metric on (F, E) and $\{(F_n, E)\}_{n=1}^{\infty}$ be a soft sequence in (F, E) . Then we express that $\{(F_n, E)\}_{n=1}^{\infty}$ is a Cauchy soft sequence, if for every positive number ϵ , there subsist a natural number N such that for every natural number n, m which $n, m \geq N$, we have

$$\mathfrak{D}_R((a, F_n(a)), (a, F_m(a))) \leq (\tilde{\varphi}(a, a), \epsilon).$$

Theorem 1.9. [13] Assume that (F, E) be a soft set over X , let \mathfrak{D}_R be a meter on (F, E) and $(F_n, E)_{n=1}^{\infty}$ be a soft Cauchy sequence in (F, E) . If $(F_n, E)_{n=1}^{\infty}$ is convergent in (F, E) , then it converges to unique element of (F, E) .

Definition 1.10. [13] Let (F, E) be a soft set over X , let \mathfrak{D}_R be a rectangular soft metric on (F, E) . (F, E) is said to be a complete rectangular soft metric space if every Cauchy soft sequence converges in (F, E) .

Theorem 1.11. [13] Let $((F, E), \mathfrak{D}_R)$ and $((F', E'), \mathfrak{D}'_R)$ be two rectangular soft metric spaces over X and Y respectively. Let $f = (f_1, f_2) : ((F, E), \mathfrak{D}_R) \rightarrow ((F', E'), \mathfrak{D}'_R)$ be a soft mapping. Then f

is soft continuous iff for all $(a, F(a)) \in (F, E)$ and every positive number ϵ , there exists a positive number δ such that for every $(b, F(b)) \in (F, E)$.

$$\mathcal{D}_R'((f(a, F(a))), f((b, F(b)))) \leq (\tilde{\varphi}'(\tilde{\varphi}(a, b)), \epsilon) \text{ whenever}$$

$$\mathcal{D}_R((a, F(a)), (b, F(b))) \leq (\tilde{\varphi}(a, b), \delta).$$

Definition 1.12. [13] Let $((F, E), \mathcal{D}_R)$ be a rectangular soft metric space over X and

$f : ((F, E), \mathcal{D}_R) \rightarrow ((F, E), \mathcal{D}_R)$ be a soft mapping. Then f is called to be soft contractive if there is a positive number λ with $0 < \lambda < 1$ such that

$$\mathcal{D}_R((f(a, F(a))), f((b, F(b)))) \leq \lambda \mathcal{D}_R((a, F(a)), (b, F(b))),$$

for all $a, b \in E$.

Theorem 1.13. [13] Soft contractive mapping is soft continuous in rectangular soft metric space $((F, E), \mathcal{D}_R)$.

Definition 1.14. [13] Let $((F, E), \mathcal{D}_R)$ be a complete rectangular soft metric space over X and let

$f : ((F, E), \mathcal{D}_R) \rightarrow ((F, E), \mathcal{D}_R)$ be a soft mapping. A fixed soft set for f is a soft subset of (F, E) such as $(a, F(a))$ such that $f((a, F(a))) = (a, F(a))$.

3. Main Results

Definition 2.1. Suppose $\varphi : E \times E \rightarrow E$ be a scalar valued parametric function. The parametric scalar valued function $\mathcal{D}_{R_p} : (F, E) \times (F, E) \rightarrow (E, R^+ \cup \{0\})$ is called to be partial rectangular soft metric on (F, E) if \mathcal{D}_{R_p} satisfies the following properties:

for all $(x, F(x)), (y, F(y)) \in (F, E)$

(1) $\mathcal{D}_{R_p}((x, F(x)), (y, F(y))) \geq 0$

(2) $(x, F(x)) = (y, F(y)) \Leftrightarrow \mathcal{D}_{R_p}((x, F(x)), (y, F(y))) = \mathcal{D}_{R_p}((x, F(x)), (x, F(x)))$
 $= \mathcal{D}_{R_p}((y, F(y)), (y, F(y))).$

(3) $\mathcal{D}_{R_p}((x, F(x)), (x, F(x))) \leq \mathcal{D}_{R_p}((x, F(x)), (y, F(y)))$

(4) $\mathcal{D}_{R_p}((x, F(x)), (y, F(y))) = \mathcal{D}_{R_p}((y, F(y)), (x, F(x)))$

(5)

$$\mathcal{D}_{R_p}((x, F(x)), (y, F(y))) \leq \mathcal{D}_{R_p}((x, F(x)), (w, F(w))) + \mathcal{D}_{R_p}((w, F(w)), (z, F(z))) + \mathcal{D}_{R_p}((z, F(z)), (y, F(y)))$$

$$- \mathcal{D}_{R_p}((w, F(w)), (w, F(w))) - \mathcal{D}_{R_p}((z, F(z)), (z, F(z)))$$

for all distinct soft points $(w, F(w)), (z, F(z)) \in (F, E)$ $((x, F(x)) \neq (y, F(y)))$.

The pair $((F, E), \mathcal{D}_{R_p})$ is called a partial rectangular soft metric space.

Definition 2.2. Let $((F, E), \mathcal{D}_{R_p})$ be a partial rectangular soft metric space.

(1) A sequence $\{(x_n, F(x_n))\}$ is called to converge to a soft point $(x, F(x)) \in (F, E)$, written $\lim_{n \rightarrow \infty} (x_n, F(x_n)) = (x, F(x))$, if $\lim_{n \rightarrow \infty} \mathcal{D}_{R_p}((x_n, F(x_n)), (x, F(x))) = \mathcal{D}_{R_p}((x, F(x)), (x, F(x)))$.

(2) A sequence $\{(x_n, F(x_n))\}$ is called soft Cauchy if $\lim_{n, m \rightarrow \infty} \mathcal{D}_{R_p}((x_n, F(x_n)), (x_m, F(x_m)))$ exists and is finite.

(3) $((F, E), \mathcal{D}_{R_p})$ is called complete if for each soft Cauchy sequence $\{(x_n, F(x_n))\}$ there exists $(x, F(x)) \in (F, E)$ such that

$$\lim_{n,m \rightarrow \infty} \mathcal{D}_{R_p}((x_n, F(x_n)), (x_m, F(x_m))) = \lim_{n \rightarrow \infty} \mathcal{D}_{R_p}((x_n, F(x_n)), (x, F(x))) = \mathcal{D}_{R_p}((x, F(x)), (x, F(x))).$$

Note that every rectangular soft metric space is a partial rectangular soft metric space.

Definition 2.3. Let $((F, E), \mathcal{D}_{R_p})$ be a partial rectangular metric space.

(1) A soft sequence $\{(x_n, F(x_n))\} \subset (F, E)$ is called \tilde{O} -Cauchy if $\lim_{n,m \rightarrow \infty} \mathcal{D}_{R_p}((x_n, F(x_n)), (x_m, F(x_m))) = (0, F(0))$.

(2) $((F, E), \mathcal{D}_{R_p})$ is called \tilde{O} -complete if for each \tilde{O} -Cauchy soft sequence $\{(x_n, F(x_n))\}$ in (F, E) , there exists some $(x, F(x)) \in (F, E)$ such that

$$\begin{aligned} \lim_{n \rightarrow \infty} \mathcal{D}_{R_p}((x_n, F(x_n)), (x, F(x))) &= \mathcal{D}_{R_p}((x, F(x)), (x, F(x))) \\ &= \lim_{n,m \rightarrow \infty} \mathcal{D}_{R_p}((x_m, F(x_m)), (x_n, F(x_n))) \\ &= (0, F(0)). \end{aligned}$$

Theorem 2.4. Let $((F, E), \mathcal{D}_{R_p})$ be a partial rectangular metric space.

(1) If $((F, E), \mathcal{D}_{R_p})$ is complete, then it is \tilde{O} -complete.

(2) If $(x_n, F(x_n)) \neq (x, F(x))$, $(y_n, F(y_n)) \neq (y, F(y))$, $(x_n, F(x_n)) \neq (y_n, F(y_n))$ for all $n \in \mathbb{N}$ and $\lim_{n \rightarrow \infty} (x_n, F(x_n)) = (x, F(x))$, $\lim_{n \rightarrow \infty} (y_n, F(y_n)) = (y, F(y))$,

$\mathcal{D}_{R_p}((x, F(x)), (x, F(x))) = \mathcal{D}_{R_p}((y, F(y)), (y, F(y))) = (0, F(0))$, then

$$\lim_{n \rightarrow \infty} \mathcal{D}_{R_p}((x_n, F(x_n)), (y_n, F(y_n))) = \mathcal{D}_{R_p}((x, F(x)), (y, F(y))).$$

Proof:

(1) Let $((F, E), \mathcal{D}_{R_p})$ is complete then for each Cauchy soft sequence; there exists $(x, F(x)) \in (F, E)$ such that

$$\lim_{n,m \rightarrow \infty} \mathcal{D}_{R_p}((x_n, F(x_n)), (x_m, F(x_m))) = \lim_{n \rightarrow \infty} \mathcal{D}_{R_p}((x_n, F(x_n)), (x, F(x))) = \mathcal{D}_{R_p}((x, F(x)), (x, F(x))). \quad (1)$$

Assume $\{(x_n, F(x_n))\}$ is any \tilde{O} -Cauchy soft sequence. Then

$$\lim_{n,m \rightarrow \infty} \mathcal{D}_{R_p}((x_n, F(x_n)), (x_m, F(x_m))) = (0, F(0)).$$

By using the (1) equality we can write

$$\begin{aligned} \lim_{n \rightarrow \infty} \mathcal{D}_{R_p}((x_n, F(x_n)), (x, F(x))) &= \mathcal{D}_{R_p}((x, F(x)), (x, F(x))) \\ &= \lim_{n,m \rightarrow \infty} \mathcal{D}_{R_p}((x_m, F(x_m)), (x_n, F(x_n))) \\ &= (0, F(0)). \end{aligned}$$

Hence $((F, E), \mathcal{D}_{R_p})$ is \tilde{O} -complete.

(2) For each $n \in \mathbb{N}$, we have

$$\begin{aligned} & \mathfrak{D}_{R_p}((x, F(x)), (y, F(y))) - \mathfrak{D}_{R_p}((x_n, F(x_n)), (y_n, F(y_n))) \\ & \leq \mathfrak{D}_{R_p}((x, F(x)), (x_n, F(x_n))) + \mathfrak{D}_{R_p}((x_n, F(x_n)), (y_n, F(y_n))) \\ & \quad + \mathfrak{D}_{R_p}((y_n, F(y_n)), (y, F(y))) - \mathfrak{D}_{R_p}((x_n, F(x_n)), (x_n, F(x_n))) \\ & \quad - \mathfrak{D}_{R_p}((y_n, F(y_n)), (y_n, F(y_n))) - \mathfrak{D}_{R_p}((x_n, F(x_n)), (y_n, F(y_n))) \quad (*) \\ & \leq \overline{\mathfrak{D}_{R_p}((x, F(x)), (x_n, F(x_n)))} + \overline{\mathfrak{D}_{R_p}((y, F(y)), (y_n, F(y_n)))} \end{aligned}$$

$$\begin{aligned} & \mathfrak{D}_{R_p}((x_n, F(x_n)), (y_n, F(y_n))) - \mathfrak{D}_{R_p}((x, F(x)), (y, F(y))) \\ & \leq \mathfrak{D}_{R_p}((x_n, F(x_n)), (x, F(x))) + \mathfrak{D}_{R_p}((x, F(x)), (y, F(y))) \\ & \quad + \mathfrak{D}_{R_p}((y, F(y)), (y_n, F(y_n))) - \mathfrak{D}_{R_p}((x, F(x)), (x, F(x))) \\ & \quad - \mathfrak{D}_{R_p}((y, F(y)), (y, F(y))) - \mathfrak{D}_{R_p}((x, F(x)), (y, F(y))) \quad (**) \\ & \leq \overline{\mathfrak{D}_{R_p}((x_n, F(x_n)), (x, F(x)))} + \overline{\mathfrak{D}_{R_p}((y, F(y)), (y_n, F(y_n)))} \end{aligned}$$

From (*) and (**) we have

$$\begin{aligned} & |\mathfrak{D}_{R_p}((x, F(x)), (y, F(y))) - \mathfrak{D}_{R_p}((x_n, F(x_n)), (y_n, F(y_n)))| \\ & \leq \overline{\mathfrak{D}_{R_p}((x_n, F(x_n)), (x, F(x)))} + \overline{\mathfrak{D}_{R_p}((y, F(y)), (y_n, F(y_n)))} \quad (***) \quad \square \end{aligned}$$

References

- [1] Altıntaş İ, Şimşek D, Taşköprü K (2017) Topology of soft cone metric spaces. AIP Conference Proceedings. 1880, 030006, <https://doi.org/10.1063/1.50006056>
- [2] Banach S (1922) Sur les opérations dans les ensembles abstraits et leur application aux équations intégrales. Fund Math. 3: 133-181.
- [3] Branciari A (2000) A fixed point theorem of Banach-Caccioppoli type on a class of generalized metric spaces, Publ. Math. Debrecen, 57 : 31-37.
- [4] Das S, Samanta SK (2013) Soft Metric. Annals of Fuzzy Mathematics and Informatics 6(1): 77-94.
- [5] Dung NV, Hang VTL (2014) A note on partial rectangular metric spaces. Mathematica Moravica. 18(1): 1-8.
- [6] Guler AC, Yıldırım ED, Ozbakır O B (2016) A fixed point theorem on soft G - metric Spaces. J. Nonlinear Sci. Appl., 9: 885-894.
- [7] Hosseinzadeh H (2017) Fixed point theorems on soft metric spaces. Journal of Fixed Point Theory and Applications 19(2): 1625-1647.
- [8] Maji PK, Biswas R, Roy AR (2003) Soft Set Theory. Comput. Math. Appl., 45: 555-562.
- [9] Matthews S. G., (1994), Partial metric topology, Ann. New York Acad. Sci. 728: 183-197.
- [10] Molodtsov D (1999) Soft set theory-first result. Comput. Math. Appl., 37: 19- 31.
- [11] Mutlu A, Yolcu N, Mutlu B (2016) Fixed point theorems in partially ordered rectangular metric spaces. British Journal of Mathematics and Computer Science 15(2):1-9.
- [12] Mutlu A, Yolcu N, Mutlu B (2016) A survey on Kannan mappings in universalized metric spaces. British Journal of Mathematics and Computer Science, 15(6): 1-6.
- [13] Öztunç S, Mutlu A, Aslan S (2018) Some soft fixed point results for soft near metric spaces. 2nd International Students Science Congress, İzmir, Turkey. Abstract Book: 102.
- [14] Öztunç S, Mutlu A, Aslan S (2019) Some Kannan type fixed point results in rectangular soft metric space and an application of fixed point for thermal science problem. Thermal Science, 23(1) S215-S225.
- [15] Öztunç S, Aslan S (2019) Jungck type fixed point results for weakly compatible mappings in a rectangular soft metric space. Journal of Inequalities and Applications, 2019(145): 1-14.

3rd International Students Science Congress
3-4 May 2019, İzmir - Turkey

- [16] Shabir M, Naz M (2011) On soft topological spaces. *Computers & Mathematics with Applications* 61(7): 1786-1799.
- [17] Şimşek, D, Altıntaş İ, Ersoy S, Abdullayev F, İmaş Kızı M, Taşköprü K, Kesik D, Abılayeva E, Oğul B, Çemşitov N (2018) An introduction to soft cone metric spaces and some fixed point theorems. *MANAS Journal of Engineering (MJEN)*. 6(1): 59-89.
- [18] Yazar Mİ, Aras ÇG, Bayramov S (2016) Fixed point theorems of soft contractive mappings. *Filomat*, 30(2): 269-27.
- [19] Zorlutuna İ, Çakır H (2015) On continuity of soft mappings. *Appl. Math. Inf. Sci.* 9(1): 403-409.

Aspects on Fixed Point Theorems in Rectangular Soft Metric Spaces

Simge Öztunç*, Manisa Celal Bayar University, Dept of Mathematics, Manisa, Turkey

Ali Mutlu, Manisa Celal Bayar University, Dept of Mathematics, Manisa, Turkey

Sedat Aslan, Manisa Celal Bayar University, The Institute of Naturel and Applied Sciences, Manisa, Turkey

*Corresponding Author: simge.oztunc@cbu.edu.tr

Keywords: soft metric, soft near metric, soft fixed point theorems

Discipline: Mathematics, Topology

Abstract

In current study we recall some basic notions from rectangular soft metric spaces. We obtain a prove a coupled soft fixed point theorem by using soft rectangular and soft Hausdorff property.

Introduction

Fixed point theorems are very important devices in many branches of mathematics, engineering, naturel and applied sciences.

In 2013, Das and Samanta [4] introduced the soft metric space by using the fundamentals of soft set theory which is propounded by Molodtsov [8] in 1999 and studied by many mathematicians such [7,13,15,16] In 2017, Hosseinzadeh [6] brought a new perspective by redefining the soft metric.

In recent years many mathematicians have studied on different types of soft metric spaces by combining the other known metrics such as soft rectangular metric [10,11,12], soft G-metric [5] and soft cone metric [1,14] So this causes to obtain a plenty of fixed point theorems in different kinds soft metric spaces. Other details for rectangular metric spaces can be founded at [3, 9].

In this paper we obtain and prove a fixed point theorem by using rectangular soft metric under some special conditions for soft continuous mapping.

1. Preliminaries

Definition 1.1. [8] Let E be a parameter set. A pair (F, E) is said to be a soft set over the universe X where F is a mapping given by $F : E \rightarrow P(X)$.

That is to say, a soft set over X is a parameterized family of subsets of the universal set X . For any parameter $x \in E$, $F(x)$ may be regarded as the set of X - approximate elements of the soft set (F, E) .

Definition 1.2. [7] Assume that (F, E) and (F', E') be two soft sets over X . It is said that (F, E) is a soft subset of (F', E') and it is denoted by $(F, E) \subseteq (F', E')$ if

(1) $E \subseteq E'$, and

(2) $F(a) \subseteq F'(a)$, for all $a \in E$.

(F, E) is said to be a soft super set of (F', E') , if (F', E') is a soft subset of (F, E) . It is symbolized by $(F, E) \supseteq (F', E')$.

Definition 1.3. [7] Let (F, E) be soft set over X . Then (F, E) is called to be null soft set denoted by Φ if for every $e \in E$, $F(e) = \emptyset$.

(2) (F, E) is called to be absolute soft set denoted by \tilde{E} if for every $e \in E$, $F(e) = X$.

Definition 1.4. [6] Let $A \subseteq E$ be a set of parameters. The ordered pairwise (α, t) is called to be a soft parametric scalar if $t \in \mathbb{R}$ and $\alpha \in A$. The parametric scalar (α, t) called nonnegative if $t \geq 0$. Let (α, t) and (β, t') be two soft parametric scalars. (α, t) is said to be no less than (β, t') and it is written as $(\alpha, t) \succeq (\beta, t')$, if $t \geq t'$.

Definition 1.5. [6] Let $A \subseteq E$ be a set of parameters. Let (a, r) and (b, r') be two soft parametric scalars. Then we define addition between soft parametric scalars and scalar multiplication on soft parametric scalars as follows

$$(a, r) \dot{+} (b, r') = (a, b, r + r'), \text{ and}$$

$$\lambda(a, r) = (a, \lambda r), \text{ for every } \lambda \in R.$$

Definition 1.6. [6] Let (F, A) be a soft set over X . We call a function f on (F, A) is parametric scalar valued, if there are functions $f_1: A \rightarrow A$ and $f_2: F(A) \rightarrow R$ such that $f(F, A) = (f_1, f_2)(A, F(A))$.

Similarly, we can extent above defined parametric scalar valued function as $f: (F, A) \times (F, A) \rightarrow (A, R)$ by $f(A \times A, F(A) \times F(A)) = (f_1, f_2)(A \times A, F(A) \times F(A))$, where $f_1: A \times A \rightarrow A$ and $f_2: F(A) \times F(A) \rightarrow R$.

Definition 1.7. [10] Suppose that $\tilde{\varphi}: E \times E \rightarrow E$ be a scalar valued parametric function. The parametric scalar valued function $\mathfrak{D}_R: (F, E) \times (F, E) \rightarrow (E, R^+ \cup \{0\})$ is called to be a rectangular soft metric on (F, E) if \mathfrak{D}_R satisfies the following properties:

(RSM1) $\mathfrak{D}_R((x, F(x)), (y, F(y))) \geq (\tilde{\varphi}(x, y), 0)$, if $x = y$, then the equality holds.

(RSM2) $\mathfrak{D}_R((x, F(x)), (y, F(y))) = (\tilde{\varphi}(x, y), 0) \Leftrightarrow$ for all $((x, F(x)), (y, F(y))) \in (F, E)$,

$(x, F(x)) = (y, F(y))$ [for all $x, y \in E, x = y$]

(RSM3) $\mathfrak{D}_R((x, F(x)), (y, F(y))) = \mathfrak{D}_R((y, F(y)), (x, F(x)))$, for all $x, y \in E$

(RSM4) $\mathfrak{D}_R((x, F(x)), (y, F(y))) \leq \mathfrak{D}_R((x, F(x)), (z, F(z))) + \mathfrak{D}_R((z, F(z)), (t, F(t))) + \mathfrak{D}_R((t, F(t)), (y, F(y)))$ for all $x, y, z, t \in E$.

Then we say the pair $((F, E), \mathfrak{D}_R)$ is a rectangular soft metric space over X .

Definition 1.8. [6] Assume that (F, E) be a soft set over X . A soft sequence in (F, E) is a function $f: N \rightarrow (F, E)$ equipped with $f(n) = (F_n, E)$ such that (F_n, E) is a soft subset of (F, E) for $n \in N$, and it is symbolized by $\{(F_n, E)\}_{n=1}^{\infty}$.

Definition 1.9. [10] Presume that (F, E) be a soft set over X . Let \mathfrak{D}_R be a rectangular soft metric on (F, E) , $\{(F_n, E)\}_{n=1}^{\infty}$ be a soft sequence in (F, E) and $(x, F(x)) \in (F, E)$. Then we state that the $\{(F_n, E)\}_{n=1}^{\infty}$ converges to $(x, F(x))$, if for every positive number ϵ , there subsist a naturel number N such that for all $n \in \mathbb{N}$ which $n \geq N$, we have

$$\mathfrak{D}_R((a, F_n(a)), (x, F(x))) \leq (\tilde{\varphi}(a, x), \epsilon).$$

Definition 1.10. [10] Suspect that (F, E) be a soft set over X . Let \mathfrak{D}_R be a rectangular soft metric on (F, E) and $\{(F_n, E)\}_{n=1}^{\infty}$ be a soft sequence in (F, E) . Then we express that $\{(F_n, E)\}_{n=1}^{\infty}$ is a Cauchy soft sequence, if for every positive number ϵ , there subsist a natural number N such that for every natural number n, m which $n, m \geq N$, we have

$$\mathfrak{D}_R((a, F_n(a)), (a, F_m(a))) \leq (\tilde{\varphi}(a, a), \epsilon).$$

Theorem 1.9. [10] Assume that (F, E) be a soft set over X , let \mathfrak{D}_R be a meter on (F, E) and $(F_n, E)_{n=1}^{\infty}$ be a soft Cauchy sequence in (F, E) . If $(F_n, E)_{n=1}^{\infty}$ is convergent in (F, E) , then it converges to unique element of (F, E) .

Definition 1.11. [10] Let (F, E) be a soft set over X , let \mathfrak{D}_R be a rectangular soft metric on (F, E) . (F, E) is said to be a complete rectangular soft metric space if every Cauchy soft sequence converges in (F, E) .

Theorem 1.12. [10] Let $((F, E), \mathfrak{D}_R)$ and $((F', E'), \mathfrak{D}'_R)$ be two rectangular soft metric spaces over X and Y respectively. Let $f = (f_1, f_2) : ((F, E), \mathfrak{D}_R) \rightarrow ((F', E'), \mathfrak{D}'_R)$ be a soft mapping. Then f is soft continuous iff for all $(a, F(a)) \in (F, E)$ and every positive number ϵ , there exists a positive number δ such that for every $(b, F(b)) \in (F, E)$.

$$\mathfrak{D}'_R((f(a, F(a))), f((b, F(b)))) \leq (\tilde{\varphi}'(\tilde{\varphi}(a, b)), \epsilon) \text{ whenever}$$

$$\mathfrak{D}_R((a, F(a)), (b, F(b))) \leq (\tilde{\varphi}(a, b), \delta).$$

Definition 1.13. [10] Let $((F, E), \mathfrak{D}_R)$ be a rectangular soft metric space over X and

$f : ((F, E), \mathfrak{D}_R) \rightarrow ((F, E), \mathfrak{D}_R)$ be a soft mapping. Then f is called to be soft contractive if there is a positive number λ with $0 < \lambda < 1$ such that

$$\mathfrak{D}_R((f(a, F(a))), f((b, F(b)))) \leq \lambda \mathfrak{D}_R((a, F(a)), (b, F(b))),$$

for all $a, b \in E$.

Theorem 1.14. [10] Soft contractive mapping is soft continuous in rectangular soft metric space $((F, E), \mathfrak{D}_R)$.

Definition 1.15. [10] Let $((F, E), \mathfrak{D}_R)$ be a complete rectangular soft metric space over X and let

$f : ((F, E), \mathfrak{D}_R) \rightarrow ((F, E), \mathfrak{D}_R)$ be a soft mapping. A fixed soft set for f is a soft subset of (F, E) such as $(a, F(a))$ such that $f((a, F(a))) = (a, F(a))$.

The following theorems is soft rectangular version one of the fundamental fixed point theorem given by Banach.

Theorem 1.16. [2] (Banach Contraction Theorem for Rectangular Soft Metric Space)

Let $((F, E), \mathfrak{D}_R)$ be a complete rectangular soft metric space over X , and

$f : ((F, E), \mathfrak{D}_R) \rightarrow ((F, E), \mathfrak{D}_R)$ be rectangular soft contractive mapping. Then f has unique fixed soft set.

Theorem 1.17. [13] Every soft metric space is soft Hausdorff space.

2. Soft Fixed Point Theorems for Rectangular Soft Metric Spaces

Theorem 2.1. Suppose $((F, E), \mathfrak{D}_R)$ is rectangular soft metric space. Assume

$\varphi, \theta : (F, [0, \infty)) \rightarrow (F, [0, \infty))$ soft parametric scalar valued mappings such that $\varphi = (\varphi_1, \varphi_2)$ and $\theta = (\theta_1, \theta_2)$ and $\varphi(t) < t, \theta(t) < t$ and for each $t > 0, \lim_{r \rightarrow t^+} \varphi(r) < t, \lim_{r \rightarrow t^+} \theta(r) < t$. Also, suppose that

the following condition satisfied for soft continuous mapping
 $T : (F, E) \times (F, E) \rightarrow (F, E)$

$$\begin{aligned} & \mathfrak{D}_R((T((x, F(x)), (y, F(y))), (T((u, F(u)), (v, F(v)))))) \\ & \leq (\varphi_1, \varphi_2)(\rho_s(((x, F(x)), (y, F(y))), ((u, F(u)), (v, F(v))))) \\ & \quad - (\theta_1, \theta_2)(\rho_s(((x, F(x)), (y, F(y))), ((u, F(u)), (v, F(v))))) \end{aligned} \quad (1)$$

for all $(x, F(x)), (y, F(y)), (u, F(u)), (v, F(v)) \in (F, E)$ for which

$$(x, F(x)) \leq_s (u, F(u)), (y, F(y)) \geq_s (v, F(v)). \quad \text{There} \quad \text{subsisit}$$

$$((x_0, F(x_0)), (y_0, F(y_0))) \in (F, E) \times (F, E) \quad \text{with} \quad (x_0, F(x_0)) <_s T((x_0, F(x_0)), (y_0, F(y_0))),$$

$$(y_0, F(y_0)) \geq_s T((y_0, F(y_0)), (x_0, F(x_0))). \quad \text{Then } T \text{ has a unique coupled fixed point.}$$

Proof:

$(x_0, F(x_0)), (y_0, F(y_0)) \in (F, E)$ are two soft points with $(x_0, F(x_0)) <_s T((x_0, F(x_0)), (y_0, F(y_0))),$
 $(y_0, F(y_0)) \geq_s T((y_0, F(y_0)), (x_0, F(x_0))).$ Let $(x_1, F(x_1)) = T((x_0, F(x_0)), (y_0, F(y_0)))$ and
 $(y_1, F(y_1)) \geq_s T((y_0, F(y_0)), (x_0, F(x_0))).$ Then $x_0 <_s x_1, y_0 \geq_s y_1; F(x_0) \subset F(x_1)$ and
 $F(y_0) \supseteq F(y_1).$

$(x_2, F(x_2)) = T((x_1, F(x_1)), (y_1, F(y_1))), \quad (y_2, F(y_2)) = T((y_1, F(y_1)), (x_1, F(x_1))).$ The mixed
 monotone property is satisfied by T , obtaining $x_1 < x_2, y_1 \geq y_2; F(x_1) \subset F(x_2)$ and $F(y_1) \supseteq F(y_2).$

By continuing this method we obtain two soft sequence $\{(x_n, F(x_n)), (y_n, F(y_n))\}$ in (F, E) with
 $(x_{n+1}, F(x_{n+1})) = T((x_n, F(x_n)), (y_n, F(y_n))), \quad (y_{n+1}, F(y_{n+1})) \geq_s T((y_n, F(y_n)), (x_n, F(x_n))),$

$$(x_0, F(x_0)) <_s (x_1, F(x_1)) <_s \cdots <_s (x_n, F(x_n)) <_s (x_{n+1}, F(x_{n+1})) <_s \cdots \quad (2)$$

and

$$(y_0, F(y_0)) \geq_s (y_1, F(y_1)) \geq_s \cdots \geq_s (y_n, F(y_n)) \geq_s (y_{n+1}, F(y_{n+1})) \geq_s \cdots \quad (3)$$

This means

$$x_0 <_s x_1 <_s x_2 <_s \cdots <_s x_n <_s x_{n+1} <_s \cdots,$$

$$F(x_0) \subset F(x_1) \subset \cdots \subset F(x_n) \subset F(x_{n+1}) \subset \cdots, \text{ and}$$

$$y_0 \geq_s y_1 \geq_s y_2 \geq_s \cdots \geq_s y_n \geq_s y_{n+1} \geq_s \cdots,$$

$$F(y_0) \supseteq F(y_1) \supseteq F(y_2) \supseteq \cdots \supseteq F(y_n) \supseteq F(y_{n+1}) \supseteq \cdots$$

$$\begin{aligned} \delta_n &= \rho_s((((x_n, F(x_n)), (y_n, F(y_n))), ((x_{n+1}, F(x_{n+1})), (y_{n+1}, F(y_{n+1})))))) \\ &= \frac{\mathfrak{D}_R(((x_n, F(x_n)), (x_{n+1}, F(x_{n+1})))) + \mathfrak{D}_R(((y_n, F(y_n)), (y_{n+1}, F(y_{n+1}))))}{2} \end{aligned} \quad (4)$$

We show that $\delta_n < \delta_{n+1}$. Now, enforcing if the inequality (1) is implemented with

$$(((x, F(x)), (y, F(y)))) = (((x_n, F(x_n)), (y_n, F(y_n)))),$$

$$(((u, F(u)), (v, F(v)))) = (((x_{n-1}, F(x_{n-1})), (y_{n-1}, F(y_{n-1}))))), \text{ for all } n \geq 0.$$

Utilizing properties of $\varphi = (\varphi_1, \varphi_2)$, we get

$$\mathfrak{D}_R((T((x_n, F(x_n)), (y_n, F(y_n))), (T((x_{n-1}, F(x_{n-1})), (y_{n-1}, F(y_{n-1})))))) = \mathfrak{D}_{RR}(((x_{n+1}, F(x_{n+1})), (x_n, F(x_n))))$$

$$\begin{aligned}
 &\leq (\varphi_1, \varphi_2)(\rho_s(((x_n, F(x_n)), (y_n, F(y_n))))), ((x_{n-1}, F(x_{n-1})), (y_{n-1}, F(y_{n-1})))) \\
 &\quad - (\theta_1, \theta_2)(\rho_s(((x_n, F(x_n)), (y_n, F(y_n))))), ((x_{n+1}, F(x_{n+1})), (y_{n+1}, F(y_{n+1})))) \\
 &\leq \varphi(((x_n, F(x_n)), (y_n, F(y_n))))), ((x_{n-1}, F(x_{n-1})), (y_{n-1}, F(y_{n-1})))) \\
 &< (\rho_s(((x_n, F(x_n)), (y_n, F(y_n))))), ((x_{n-1}, F(x_{n-1})), (y_{n-1}, F(y_{n-1})))) \tag{5}
 \end{aligned}$$

Similarly, we can obtain

$$\mathfrak{D}_R(((y_{n+1}, F(y_{n+1})), (y_n, F(y_n)))) < (\rho_s(((x_n, F(x_n)), (y_n, F(y_n))))), ((x_{n-1}, F(x_{n-1})), (y_{n-1}, F(y_{n-1})))) \tag{6}$$

Then we acquire

$$\begin{aligned}
 &\frac{\mathfrak{D}_R(((x_{n+1}, F(x_{n+1})), (x_n, F(x_n)))) + \mathfrak{D}_R(((y_{n+1}, F(y_{n+1})), (y_n, F(y_n))))}{2} \\
 &< (\rho_s(((x_n, F(x_n)), (y_n, F(y_n))))), ((x_{n-1}, F(x_{n-1})), (y_{n-1}, F(y_{n-1}))))).
 \end{aligned}$$

That is $\delta_n < \delta_{n+1}$. Thus $\{\delta_n\}$ is monotone decreasing bounded to the bottom. Hereby there subsist a $\delta_n \geq 0$ with $\lim_{n \rightarrow \infty} \delta_n = \delta$.

Demonstrating $\delta = 0$. Supposing the contrary $\delta > 0$. At that time from (1) obtaining

$$\begin{aligned}
 &\mathfrak{D}_R((T((x_n, F(x_n)), (y_n, F(y_n))))), (T((x_{n-1}, F(x_{n-1})), (y_{n-1}, F(y_{n-1})))))) = \mathfrak{D}_R(((x_{n+1}, F(x_{n+1})), (x_n, F(x_n)))) \\
 &\leq (\varphi_1, \varphi_2)(\rho_s(((x_n, F(x_n)), (y_n, F(y_n))))), ((x_{n-1}, F(x_{n-1})), (y_{n-1}, F(y_{n-1})))) \\
 &\quad - (\theta_1, \theta_2)(\rho_s(((x_n, F(x_n)), (y_n, F(y_n))))), ((x_{n+1}, F(x_{n+1})), (y_{n+1}, F(y_{n+1})))) \\
 &\leq (\varphi_1, \varphi_2)(\rho_s(((x_n, F(x_n)), (y_n, F(y_n))))), ((x_{n-1}, F(x_{n-1})), (y_{n-1}, F(y_{n-1})))) \tag{7}
 \end{aligned}$$

Similarly, we can obtain

$$\mathfrak{D}_R(((y_{n+1}, F(y_{n+1})), (y_n, F(y_n)))) \leq (\varphi_1, \varphi_2)(\rho_s(((x_n, F(x_n)), (y_n, F(y_n))))), ((x_{n-1}, F(x_{n-1})), (y_{n-1}, F(y_{n-1})))) \tag{8}$$

Thus we get

$$\begin{aligned}
 &\frac{\mathfrak{D}_R(((x_{n+1}, F(x_{n+1})), (x_n, F(x_n)))) + \mathfrak{D}_R(((y_{n+1}, F(y_{n+1})), (y_n, F(y_n))))}{2} \\
 &< \rho_s(((x_n, F(x_n)), (y_n, F(y_n))))), ((x_{n-1}, F(x_{n-1})), (y_{n-1}, F(y_{n-1})))) \tag{9}
 \end{aligned}$$

While $n \rightarrow \infty$ in (9), getting $\delta = \lim_{n \rightarrow \infty} \delta_n < \lim_{n \rightarrow \infty} \delta_{n-1} = \delta$.

So the incompatibility is obtained. Hence $\delta = 0$. Namely

$$\begin{aligned}
 &\lim_{n \rightarrow \infty} \rho_s(((x_n, F(x_n)), (y_n, F(y_n))))), ((x_{n+1}, F(x_{n+1})), (y_{n+1}, F(y_{n+1})))) \\
 &= \lim_{n \rightarrow \infty} \frac{\mathfrak{D}_R(((x_{n+1}, F(x_{n+1})), (x_n, F(x_n)))) + \mathfrak{D}_R(((y_{n+1}, F(y_{n+1})), (y_n, F(y_n))))}{2} = 0
 \end{aligned}$$

Thus

$$\begin{aligned}
 &\lim_{n \rightarrow \infty} \mathfrak{D}_R(((x_n, F(x_n)), (x_{n+1}, F(x_{n+1})))) = 0 \text{ and} \\
 &\lim_{n \rightarrow \infty} \mathfrak{D}_R(((y_n, F(y_n)), (y_{n+1}, F(y_{n+1})))) = 0. \tag{10}
 \end{aligned}$$

Evidencing $\{(x_n, F(x_n))\}$, $\{(y_n, F(y_n))\}$ are soft Cauchy sequences in rectangular soft metric space.

To accept the opposite that at least one of $\{(x_n, F(x_n))\}$ or $\{(y_n, F(y_n))\}$ is not soft Cauchy sequence

in soft rectangular metric space. At that time there exist on $\epsilon > 0$ when obtaining two subsequences $\{(x_{n(i)}, F(x_{n(i)}))\}$ and $\{(x_{m(i)}, F(x_{m(i)}))\}$ of $\{(x_n, F(x_n))\}$ with $n(i)$ is the smallest index where $n(i) > m(i) > i$,

$$\mathfrak{D}_R(((x_{m(i)}, F(x_{m(i)})), (x_{n(i)}, F(x_{n(i)})))) + \mathfrak{D}_R(((y_{m(i)}, F(y_{m(i)})), (y_{n(i)}, F(y_{n(i)})))) \geq \epsilon. \quad (11)$$

This means that

$$\mathfrak{D}_R(((x_{m(i)}, F(x_{m(i)})), (x_{n(i)-1}, F(x_{n(i)-1})))) + \mathfrak{D}_R(((y_{m(i)}, F(y_{m(i)})), (y_{n(i)-1}, F(y_{n(i)-1})))) < \epsilon. \quad (12)$$

By third properties of rectangular soft metric, we obtain

$$\begin{aligned} \mathfrak{D}_R(((x_{m(i)}, F(x_{m(i)})), (x_{n(i)}, F(x_{n(i)})))) &\leq \mathfrak{D}_R(((x_{m(i)}, F(x_{m(i)})), (x_{m(i)-1}, F(x_{m(i)-1})))) \\ &\quad + \mathfrak{D}_R(((x_{m(i)-1}, F(x_{m(i)-1})), (x_{n(i)-1}, F(x_{n(i)-1})))) \\ &\quad + \mathfrak{D}_R(((x_{n(i)-1}, F(x_{n(i)-1})), (x_{n(i)}, F(x_{n(i)})))) \end{aligned} \quad (13)$$

Similarly, from third properties of rectangular soft metric, we can obtain

$$\begin{aligned} \mathfrak{D}_R(((y_{m(i)}, F(y_{m(i)})), (y_{n(i)}, F(y_{n(i)})))) &\leq \mathfrak{D}_R(((y_{m(i)}, F(y_{m(i)})), (y_{m(i)-1}, F(y_{m(i)-1})))) \\ &\quad + \mathfrak{D}_R(((y_{m(i)-1}, F(y_{m(i)-1})), (y_{n(i)-1}, F(y_{n(i)-1})))) \\ &\quad + \mathfrak{D}_R(((y_{n(i)-1}, F(y_{n(i)-1})), (y_{n(i)}, F(y_{n(i)})))) \end{aligned} \quad (14)$$

By adding (13) and (14), from (10), (11) and (12)

$$\begin{aligned} &\mathfrak{D}_R(((x_{m(i)}, F(x_{m(i)})), (x_{n(i)}, F(x_{n(i)})))) + \mathfrak{D}_R(((y_{m(i)}, F(y_{m(i)})), (y_{n(i)}, F(y_{n(i)})))) \\ &\leq [\mathfrak{D}_R(((x_{m(i)}, F(x_{m(i)})), (x_{m(i)-1}, F(x_{m(i)-1})))) + \mathfrak{D}_R(((y_{m(i)}, F(y_{m(i)})), (y_{m(i)-1}, F(y_{m(i)-1}))))] \\ &\quad + [\mathfrak{D}_R(((x_{m(i)-1}, F(x_{m(i)-1})), (x_{n(i)-1}, F(x_{n(i)-1})))) + \mathfrak{D}_R(((y_{m(i)-1}, F(y_{m(i)-1})), (y_{n(i)-1}, F(y_{n(i)-1}))))] \\ &\quad + [\mathfrak{D}_R(((x_{n(i)-1}, F(x_{n(i)-1})), (x_{n(i)}, F(x_{n(i)})))) + \mathfrak{D}_R(((y_{n(i)-1}, F(y_{n(i)-1})), (y_{n(i)}, F(y_{n(i)}))))] \end{aligned} \quad (15)$$

Getting the limit as $i \rightarrow \infty$ in (15), obtaining by (10), (11)

$$\begin{aligned} \epsilon &\leq \lim_{n \rightarrow \infty} [\mathfrak{D}_R(((x_{m(i)}, F(x_{m(i)})), (x_{n(i)}, F(x_{n(i)})))) + \mathfrak{D}_R(((y_{m(i)}, F(y_{m(i)})), (y_{n(i)}, F(y_{n(i)}))))] \\ &\leq \lim_{n \rightarrow \infty} [\mathfrak{D}_R(((x_{m(i)-1}, F(x_{m(i)-1})), (x_{n(i)-1}, F(x_{n(i)-1})))) + \mathfrak{D}_R(((y_{m(i)-1}, F(y_{m(i)-1})), (y_{n(i)-1}, F(y_{n(i)-1}))))]. \end{aligned} \quad (16)$$

Similarly, from third properties of rectangular soft metric, we can obtain

$$\begin{aligned} &\mathfrak{D}_R(((x_{m(i)-1}, F(x_{m(i)-1})), (x_{n(i)-1}, F(x_{n(i)-1})))) + \mathfrak{D}_R(((y_{m(i)-1}, F(y_{m(i)-1})), (y_{n(i)-1}, F(y_{n(i)-1})))) \\ &\leq [\mathfrak{D}_R(((x_{m(i)-1}, F(x_{m(i)-1})), (x_{m(i)}, F(x_{m(i)})))) + \mathfrak{D}_R(((y_{m(i)-1}, F(y_{m(i)-1})), (y_{m(i)}, F(y_{m(i)}))))] \\ &\quad + [\mathfrak{D}_R(((x_{m(i)}, F(x_{m(i)})), (x_{n(i)}, F(x_{n(i)})))) + \mathfrak{D}_R(((y_{m(i)}, F(y_{m(i)})), (y_{n(i)}, F(y_{n(i)}))))] \\ &\quad + [\mathfrak{D}_R(((x_{n(i)}, F(x_{n(i)})), (x_{n(i)-1}, F(x_{n(i)-1})))) + \mathfrak{D}_R(((y_{n(i)}, F(y_{n(i)})), (y_{n(i)-1}, F(y_{n(i)-1}))))]. \end{aligned} \quad (17)$$

Having the limit as $i \rightarrow \infty$ in (17), we get by (10), (11), (16)

$$\begin{aligned} &\lim_{i \rightarrow \infty} [\mathfrak{D}_R(((x_{m(i)}, F(x_{m(i)})), (x_{n(i)}, F(x_{n(i)})))) + \mathfrak{D}_R(((y_{m(i)}, F(y_{m(i)})), (y_{n(i)}, F(y_{n(i)}))))] \\ &\lim_{i \rightarrow \infty} [\mathfrak{D}_R(((x_{m(i)-1}, F(x_{m(i)-1})), (x_{n(i)-1}, F(x_{n(i)-1})))) + \mathfrak{D}_R(((y_{m(i)-1}, F(y_{m(i)-1})), (y_{n(i)-1}, F(y_{n(i)-1}))))]. \end{aligned} \quad (18)$$

Applying inequality (1) with

$$\begin{aligned} ((x, F(x)), (y, F(y))) &= ((x_{m(i)-1}, F(x_{m(i)-1})), (y_{m(i)-1}, F(y_{m(i)-1}))), \\ (((u, F(u)), (v, F(v)))) &= ((x_{n(i)-1}, F(x_{n(i)-1})), (y_{n(i)-1}, F(y_{n(i)-1}))) \\ \mathfrak{D}_R(((x_{m(i)}, F(x_{m(i)})), (x_{n(i)}, F(x_{n(i)})))) &= \mathfrak{D}_R(T((x_{m(i)-1}, F(x_{m(i)-1})), (x_{m(i)-1}, F(x_{m(i)-1}))), \\ T((x_{n(i)-1}, F(x_{n(i)-1})), (x_{n(i)-1}, F(x_{n(i)-1})))) &\leq (\varphi_1, \varphi_2)(\rho_s(((x_{m(i)-1}, F(x_{m(i)-1})), (y_{m(i)-1}, F(y_{m(i)-1}))), \\ (((x_{n(i)-1}, F(x_{n(i)-1})), (y_{n(i)-1}, F(y_{n(i)-1})))))) & \\ (((x_{n(i)-1}, F(x_{n(i)-1})), (y_{n(i)-1}, F(y_{n(i)-1})))) & \\ \leq \rho_s(((x_{m(i)-1}, F(x_{m(i)-1})), (y_{m(i)-1}, F(y_{m(i)-1})))) &, (((x_{n(i)-1}, F(x_{n(i)-1})), (y_{n(i)-1}, F(y_{n(i)-1})))))) \end{aligned} \quad (19)$$

Similarly, we get

$$\begin{aligned} \mathfrak{D}_R(((y_{m(i)}, F(y_{m(i)})), (y_{n(i)}, F(y_{n(i)})))) & \\ \leq \rho_s(((x_{m(i)-1}, F(x_{m(i)-1})), (y_{m(i)-1}, F(y_{m(i)-1})))) &, (((x_{n(i)-1}, F(x_{n(i)-1})), (y_{n(i)-1}, F(y_{n(i)-1})))))) \end{aligned} \quad (20)$$

Before by adding (19) and (20) and after taking the limit $i \rightarrow \infty$, we get

$$\begin{aligned} \lim_{i \rightarrow \infty} [\mathfrak{D}_R(((x_{m(i)}, F(x_{m(i)})), (x_{n(i)}, F(x_{n(i)})))) &+ \mathfrak{D}_R(((y_{m(i)}, F(y_{m(i)})), (y_{n(i)}, F(y_{n(i)}))))] \\ < \lim_{i \rightarrow \infty} [\mathfrak{D}_R(((x_{m(i)-1}, F(x_{m(i)-1})), (x_{n(i)-1}, F(x_{n(i)-1})))) &+ \mathfrak{D}_R(((y_{m(i)-1}, F(y_{m(i)-1})), (y_{n(i)-1}, F(y_{n(i)-1}))))]. \end{aligned}$$

From (18), this is a contradiction. Then $\{(x_n, F(x_n))\}$, $\{(y_n, F(y_n))\}$ are rectangular soft metric space Cauchy sequences. Because $((F, E), \mathfrak{D}_R)$ is exact there subsist $(x, F(x)), (y, F(y)) \in (F, E)$ with $\lim_{n \rightarrow \infty} (x_n, F(x_n)) = (x, F(x))$ and

$$\lim_{n \rightarrow \infty} (y_n, F(y_n)) = (y, F(y)). \quad (21)$$

From soft continuity of T and since (F, E) is soft Hausdorff, obtaining

$$(x, F(x)) = \lim_{n \rightarrow \infty} (x_{n+1}, F(x_{n+1})) = \lim_{n \rightarrow \infty} T((x_n, F(x_n)), (y_n, F(y_n))) = T((x, F(x)), (y, F(y))),$$

and

$$(y, F(y)) = \lim_{n \rightarrow \infty} (y_{n+1}, F(y_{n+1})) = \lim_{n \rightarrow \infty} T((y_n, F(y_n)), (x_n, F(x_n))) = T((y, F(y)), (x, F(x))). \quad \square$$

References

- [1] Altıntaş İ, Şimşek D, Taşköprü K (2017) Topology of soft cone metric spaces. AIP Conference Proceedings. 1880, 030006, <https://doi.org/10.1063/1.50006056>
- [2] Banach S (1922) Sur les operations dans les ensembles abstrait set leur application aux equations integrales. Fund Math. 3: 133-181.
- [3] Branciari A (2000) A fixed point theorem of Banach-Caccioppoli type on a class of generalized metric spaces, Publ. Math. Debrecen, 57 : 31-37.
- [4] Das S, Samanta SK (2013) Soft Metric. Annals of Fuzzy Mathematics and Informatics 6(1): 77-94.
- [5] Guler AC, Yıldırım ED, Ozbakır O B (2016) A fixed point theorem on soft G – metric Spaces. J. Nonlinear Sci. Appl., 9: 885-894.
- [6] Hosseinzadeh H (2017) Fixed point theorems on soft metric spaces. Journal of Fixed Point Theory and Applications 19(2): 1625-1647.
- [7] Maji PK, Biswas R, Roy AR (2003) Soft Set Theory. Comput. Math. Appl., 45: 555-562.

3rd International Students Science Congress
3-4 May 2019, İzmir - Turkey

- [8] Molodtsov D., (1999) Soft Set Theory-First Result. *Comput. Math. Appl.*, 37: 19- 31.
- [9] Mutlu A, Yolcu N, Mutlu B (2016) Fixed point theorems in partially ordered rectangular metric spaces. *British Journal of Mathematics and Computer Science* 15(2):1-9.
- [10] Öztunç S, Mutlu A, Aslan S (2018) Some soft fixed point results for soft near metric spaces. 2nd International Students Science Congress, İzmir, Turkey. *Abstract Book*: 102.
- [11] Öztunç S, Mutlu A, Aslan S (2019) Some Kannan type fixed point results in rectangular soft metric space and an application of fixed point for thermal science problem. *Thermal Science*, 23(1) S215-S225.
- [12] Öztunç S, Aslan S (2019) Jungck type fixed point results for weakly compatible mappings in a rectangular soft metric space. *Journal of Inequalities and Applications*, 2019(145): 1-14.
- [13] Shabir M, Naz M (2011) On soft topological spaces. *Computers & Mathematics with Applications* 61(7): 1786-1799.
- [14] Şimşek, D, Altıntaş İ, Ersoy S, Abdullayev F, İmaş Kızı M, Taşköprü K, Kesik D, Abılayeva E, Ogul B, Çemşitov N (2018) An introduction to soft cone metric spaces and some fixed point theorems. *MANAS Journal of Engineering (MJEN)*. 6(1): 59-89.
- [15] Yazar MI, Aras ÇG, Bayramov S (2016) Fixed point theorems of soft contractive mappings. *Filomat*, 30(2): 269-27.
- [16] Zorlutuna İ, Çakır H (2015) On continuity of soft mappings. *Appl. Math. Inf. Sci.* 9(1): 403-409.

Domination Parameters in Graph Theory

Derya Doğan Durgun*, Manisa Celal Bayar University, Dept. of Mathematics, Manisa, Turkey
Niyazi Emre Toprakkaya, Manisa Celal Bayar University, The Institute of Natural and Applied Sciences,
Manisa, Turkey

*Corresponding author: derya.dogan@cbu.edu.tr

Keywords: graph theory, vulnerability, domination

Discipline: Mathematics

Abstract

A graph is a pair of sets $G = (V, E)$, where V is the set of vertices and E is the set of edges, formed by pairs of vertices. A graph $G = (V, E)$ is finite, undirected and simple with the vertex set V and edge set E . There are many models of dominating and relative types of sets in graphs, which have appeared in the research literature for the past 40 years. A Roman dominating function on a graph $G = (V, E)$ is a function $f: V \rightarrow \{0, 1, 2\}$ satisfying the condition that every vertex u for which $f(u) = 0$ is adjacent to at least one vertex v for which $f(v) = 2$. The weight of a Roman dominating function is the value $f(V) = \sum_{u \in V} f(u)$. The minimum weight of a Roman dominating function on a graph G is called the Roman domination number of G . In this paper, we consider roman domination number of some graphs.

1. Introduction

A graph is a pair of sets $G = (V, E)$, where V is the set of vertices and E is the set of edges, formed by pairs of vertices. A graph $G = (V, E)$ is finite, undirected and simple with the vertex set V and edge set E .

An area of graph theory that has received attention during recent decades is that of domination in graphs. A vertex v in a graph G is said to dominate itself and each of its neighbors, that is, v dominates the vertices in its closed neighborhood $N[v]$. A set S of vertices of G is a dominating set of G if every vertex of G is dominated by at least one vertex of S . Equivalently, a set S of vertices of G is a dominating set if every vertex in $V(G) - S$ is adjacent to at least one vertex in S . The minimum cardinality among the dominating sets of G is called the domination number of G and is denoted by $\gamma(G)$. A dominating set of cardinality $\gamma(G)$ is then referred to as a minimum dominating set.

Dominating sets appear to have their origins in the game of chess, where the goal is to cover or dominate the squares of a chessboard by certain chess pieces. In 1862 Carl Friedrich de Jaenisch considered the problem of determining the minimum number of queens that can be placed on a chessboard such that every square is either occupied by a queen or can be occupied by one of the queens in a single move.

We study a variant of the domination number which is suggested by the recent article in Scientific American by Ian Stewart, entitled "Defend the Roman Empire!" [8]. A Roman dominating function (RDF) on a graph $G = (V, E)$ is a function $f: V \rightarrow \{0, 1, 2\}$ satisfying the condition that every vertex u for which $f(u) = 0$ is adjacent to at least one vertex v for which $f(v) = 2$. For a RDF f , let $V_i(f) = \{v \in V(G) : f(v) = i\}$ in the context of a fixed RDF, we suppress the argument and simply write V_0, V_1, V_2 . Since this partition determines f , we can equivalently write $f = \{V_0, V_1, V_2\}$. The weight of a Roman dominating function is the value $f(V) = \sum_{u \in V} f(u)$, which equals $|V_1| + 2|V_2|$.

In this paper, roman domination number of comet, double comet and comb graphs are generalized and given with their proofs.

2. Preliminary

For $t \geq 2$ and $r \geq 1$, comet graph $C_{t,r}$ with $t+r$ vertices is the graph obtained by identifying one end of the path P_t with the center of the star $K_{1,r}$.

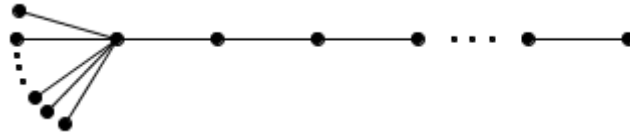


Figure 1. Figure of a comet graph

For $a, b \geq 1$, $n \geq a+b+2$ by $DC(n, a, b)$ we denote a double comet, which is a tree composed of a path containing $n-a-b$ vertices with a pendent vertices attached to one of the ends of the path and b pendent vertices attached to the other end of the path.

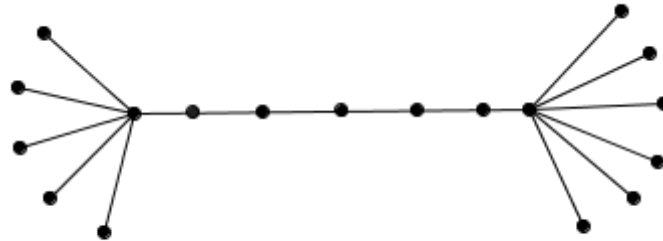


Figure 2. Figure of a double comet graph

A vertex of a graph is said to be pendent if its neighborhood contains exactly one vertex. An edge of a graph is said to be pendent if one of its vertices is a pendent vertex.

The Comb Graph $P_n \theta K_1$, is the graph obtained from a path P_n by attaching pendent edge at each vertex of the path and is denoted by P_n^+ .

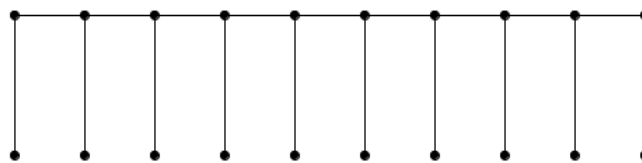


Figure 3. Figure of a Comb Graph

3. Main Results

In this section, we shall give roman domination numbers of two different graphs. The proof of roman domination number for the comb graph, we use w_i^+ for the pendent vertices of w_i .

Theorem 3.1. Let $G = C_{t,r}$ be a comet graph where $t \geq 2$ and $r \geq 1$. Then the roman domination number of G is equal to

3rd International Students Science Congress
3-4 May 2019, İzmir - Turkey

$$\gamma_R(C_{t,r}) = \begin{cases} 2\frac{t}{3} + 1 & t \equiv 0(\text{mod } 3) \\ 2\left\lceil \frac{t}{3} \right\rceil & \text{otherwise} \end{cases}$$

Proof: Roman domination number of the comet graph is considered in three cases. Let $D = V_1 \cup V_2$ be the roman dominating set.

Case 1: $t \equiv 0(\text{mod } 3)$.

In order to dominate $u_1, u_2, u_3, \dots, u_r$, w_1 and w_0 vertices, w_0 vertex should be taken into V_2 set. To dominate w_{t-3} , w_{t-2} and w_{t-4} vertices, w_{t-3} vertex should be taken into V_2 set. To dominate w_{t-1} vertex, w_{t-1} itself should be taken into V_1 set. For the rest vertices of the graph which are not dominated, w_t vertices should be taken into V_2 set which satisfy $t \equiv 0(\text{mod } 3)$. Then $V_2 = \{w_0, w_3, w_6, \dots, w_{t-3}\}$ and $V_1 = \{w_{t-1}\}$. The roman dominating set consists of $D = V_1 \cup V_2 = \{w_0, w_3, w_6, \dots, w_{t-3}, w_{t-1}\}$.

So that $\gamma_R(C_{t,r}) = 1 + 2\left(\frac{t-6-3}{3} + 1 + 2\right)$ then we get $\gamma_R(C_{t,r}) = 2\frac{t}{3} + 1$.

Case 2: $t \equiv 1(\text{mod } 3)$.

i) In order to dominate $u_1, u_2, u_3, \dots, u_r$, w_1 and w_0 vertices, w_0 vertex should be taken into V_2 set. To dominate w_{t-2} , w_{t-3} and w_{t-1} vertices, w_{t-2} vertex should be taken into V_2 set. For the rest vertices of the graph which are not dominated, w_t vertices should be taken into V_2 set which satisfy $t \equiv 0(\text{mod } 3)$. Because of the w_{t-2} vertex is dominated by w_{t-4} vertex at the same time, taking w_{t-1} vertex into V_2 set instead of w_{t-2} vertex does not change the result. Then $V_2 = \{w_0, w_3, w_6, \dots, w_{t-2}\}$ or $V_2 = \{w_0, w_3, w_6, \dots, w_{t-1}\}$ and $V_1 = \emptyset$. The roman dominating set consists of $D = V_1 \cup V_2 = \{w_0, w_3, w_6, \dots, w_{t-4}, w_{t-2}\}$ or $D = V_1 \cup V_2 = \{w_0, w_3, w_6, \dots, w_{t-4}, w_{t-1}\}$.

So that $\gamma_R(C_{t,r}) = 2\left(\frac{t-4-3}{3} + 1 + 2\right)$, then we get $\gamma_R(C_{t,r}) = 2\left(\frac{t+2}{3}\right) = 2\left\lceil \frac{t}{3} \right\rceil$.

ii) In order to dominate $u_1, u_2, u_3, \dots, u_r$, w_1 and w_0 vertices, w_0 vertex should be taken into V_2 set. To dominate w_{t-4} , w_{t-5} and w_{t-3} vertices, w_{t-4} vertex should be taken into V_2 set. To dominate w_{t-1} and w_{t-2} vertices, w_{t-1} and w_{t-2} themselves should be taken into V_1 set. For the rest vertices of the graph which are not dominated, w_t vertices should be taken into V_2 set which satisfy $t \equiv 0(\text{mod } 3)$. Then $V_2 = \{w_0, w_3, w_6, \dots, w_{t-2}\}$ and $V_1 = \{w_{t-2}, w_{t-1}\}$. The roman dominating set consists of $D = V_1 \cup V_2 = \{w_0, w_3, w_6, \dots, w_{t-4}, w_{t-2}, w_{t-1}\}$.

So $\gamma_R(C_{t,r}) = 2 + 2\left(\frac{t-7-3}{3} + 1 + 2\right)$ then we get $\gamma_R(C_{t,r}) = 2\left(\frac{t+2}{3}\right) = 2\left\lceil \frac{t}{3} \right\rceil$.

Case 3: $t \equiv 2(\text{mod } 3)$.

In order to dominate $u_1, u_2, u_3, \dots, u_r$, w_1 and w_0 vertices, w_0 vertex should be taken into V_2 set. To dominate w_{t-2} , w_{t-3} and w_{t-1} vertices, w_{t-2} vertex should be taken into V_2 set. For the rest vertices of the graph which are not dominated, w_t vertices should be taken into V_2 set which satisfy $t \equiv 0(\text{mod } 3)$. Then $V_2 = \{w_0, w_3, w_6, \dots, w_{t-2}\}$ and $V_1 = \emptyset$. The roman dominating set consists of $D = V_1 \cup V_2 = \{w_0, w_3, w_6, \dots, w_{t-5}, w_{t-2}\}$.

Therefore $\gamma_R(C_{t,r}) = 2\left(\frac{t-5-3}{3} + 1 + 2\right)$ then we get $\gamma_R(C_{t,r}) = 2\left(\frac{t+1}{3}\right) = 2\left\lceil \frac{t}{3} \right\rceil$.

Theorem 3.2. Let $G = P_n^+$ be a comb graph. The roman domination number of G is

$$\gamma_R(P_n^+) = \begin{cases} 4\left\lceil \frac{n}{3} \right\rceil + 2 & n \equiv 1(\text{mod } 3) \\ 4\frac{n}{3} & n \equiv 0(\text{mod } 3) \\ 4\left\lceil \frac{n}{3} \right\rceil - 1 & n \equiv 2(\text{mod } 3) \end{cases}$$

Proof: Proof of the roman domination number of the comb graph is considered in three cases. Let $D = V_1 \cup V_2$ be the roman dominating set.

Case 1: $n \equiv 0(\text{mod } 3)$.

In order to dominate w_{t-1} , w_t , w_{t+1} and w_t^+ vertices, w_t vertices should be taken into V_2 set which satisfy $t \equiv 1(\text{mod } 3)$. For the rest vertices of the graph which are not dominated, w_{t-1}^+ and w_{t+1}^+ vertices should be taken into V_1 set which satisfy $t \equiv 1(\text{mod } 3)$. Then $V_2 = \{w_1, w_4, w_7, \dots, w_{n-5}, w_{n-2}\}$ and $V_1 = \{w_0^+, w_2^+, w_3^+, w_5^+, \dots, w_{n-3}^+, w_{n-1}^+\}$. The roman dominating set consists of $D = V_1 \cup V_2 = \{w_0^+, w_1, w_2^+, w_3^+, w_4, w_5^+, w_7, \dots, w_{n-5}, w_{n-3}^+, w_{n-2}, w_{n-1}^+\}$.

So that $\gamma_R(P_n^+) = 2\frac{n}{3} + 2\left(\frac{n-2-1}{3} + 1\right)$ then we get $\gamma_R(P_n^+) = 4\frac{n}{3}$.

Case 2: $n \equiv 1(\text{mod } 3)$

i) In order to dominate w_{t-1} , w_t , w_{t+1} and w_t^+ vertices, w_t vertices should be taken into V_2 set which satisfy $t \equiv 1(\text{mod } 3)$. To dominate w_{n-1} and w_{n-1}^+ vertices, w_{n-1} or w_{n-1}^+ vertex should be taken into V_2 set. For the rest vertices of the graph which are not dominated, w_{t-1}^+ and w_{t+1}^+ vertices should be taken into V_1 set which satisfy $t \equiv 1(\text{mod } 3)$. Then $V_2 = \{w_1, w_4, w_7, \dots, w_{n-6}, w_{n-3}, w_{n-1}\}$ or $V_2 = \{w_1, w_4, w_7, \dots, w_{n-6}, w_{n-3}, w_{n-1}^+\}$ and $V_1 = \{w_0^+, w_2^+, w_3^+, w_5^+, \dots, w_{n-4}^+, w_{n-2}^+\}$. The roman dominating set consists of

$$D = V_1 \cup V_2 = \{w_0^+, w_1, w_2^+, w_3^+, w_4, w_5^+, w_7, \dots, w_{n-6}, w_{n-5}^+, w_{n-4}, w_{n-3}, w_{n-2}, w_{n-1}\}$$

or

$$D = V_1 \cup V_2 = \{w_0^+, w_1, w_2^+, w_3^+, w_4, w_5^+, w_7, \dots, w_{n-6}, w_{n-5}^+, w_{n-4}, w_{n-3}, w_{n-2}, w_{n-1}^+\}.$$

Thus, $\gamma_R(P_n^+) = 2 \frac{n-1}{3} + 2(\frac{n-3-1}{3} + 1 + 1)$ then we get $\gamma_R(P_n^+) = 4 \left\lfloor \frac{n}{3} \right\rfloor + 2$.

ii) In order to dominate w_{t-1}, w_t, w_{t+1} and w_t^+ vertices, w_t vertices should be taken into V_2 set which satisfy $t \equiv 1(\text{mod } 3)$. To dominate w_{n-1} and w_{n-1}^+ vertices, w_{n-1} and w_{n-1}^+ vertex should be taken into V_1 set. For the rest vertices of the graph which are not dominated, w_{t-1}^+ and w_{t+1}^+ vertices should be taken into V_1 set which satisfy $t \equiv 1(\text{mod } 3)$. Then $V_2 = \{w_1, w_4, w_7, \dots, w_{n-6}, w_{n-3}\}$ and $V_1 = \{w_0^+, w_2^+, w_3^+, w_5^+, \dots, w_{n-4}^+, w_{n-2}^+, w_{n-1}^+, w_{n-1}\}$. The roman dominating set consists of

$$D = V_1 \cup V_2 = \{w_0^+, w_1, w_2^+, w_3^+, w_4, w_5^+, w_7, \dots, w_{n-6}, w_{n-5}^+, w_{n-4}^+, w_{n-3}, w_{n-2}^+, w_{n-1}, w_{n-1}^+\}.$$

So that $\gamma_R(P_n^+) = 2 \frac{n-1}{3} + 2 + 2(\frac{n-3-1}{3} + 1)$ then we get $\gamma_R(P_n^+) = 4 \left\lfloor \frac{n}{3} \right\rfloor + 2$.

Case 3: $n \equiv 2(\text{mod } 3)$.

i) In order to dominate w_{t-1}, w_t, w_{t+1} and w_t^+ vertices, w_t vertices should be taken into V_2 set which satisfy $t \equiv 1(\text{mod } 3)$. For the rest vertices of the graph which are not dominated, w_{t-1}^+ and w_{t+1}^+ vertices should be taken into V_1 set which satisfy $t \equiv 1(\text{mod } 3)$. Then $V_2 = \{w_1, w_4, w_7, \dots, w_{n-4}, w_{n-1}\}$ and $V_1 = \{w_0^+, w_2^+, w_3^+, w_5^+, \dots, w_{n-3}^+, w_{n-2}^+\}$. The roman dominating set consists of $D = V_1 \cup V_2 = \{w_0^+, w_1, w_2^+, w_3^+, w_4, w_5^+, w_6^+, w_7, \dots, w_{n-4}, w_{n-3}^+, w_{n-2}^+, w_{n-1}\}$.

So that $\gamma_R(P_n^+) = 2 \frac{n-2}{3} + 1 + 2(\frac{n-1-1}{3} + 1)$ then we get $\gamma_R(P_n^+) = 4 \left\lfloor \frac{n}{3} \right\rfloor - 1$.

ii) In order to dominate w_{t-1}, w_t, w_{t+1} and w_t^+ vertices, w_t vertices should be taken into V_2 set which satisfy $t \equiv 1(\text{mod } 3)$. To dominate w_{n-2}, w_{n-1} and w_{n-2}^+ w_{n-2} vertex should be taken into V_2 set. To dominate w_{n-1}^+ vertex, w_{n-1}^+ vertex itself should be taken into V_1 set. For the rest vertices of the graph which are not dominated, w_{t-1}^+ and w_{t+1}^+ vertices should be taken into V_1 set which satisfy $t \equiv 1(\text{mod } 3)$. Then $V_2 = \{w_1, w_4, w_7, \dots, w_{n-4}, w_{n-2}\}$ and $V_1 = \{w_0^+, w_2^+, w_3^+, w_5^+, \dots, w_{n-3}^+, w_{n-1}^+\}$. The roman dominating set consists of

$$D = V_1 \cup V_2 = \{w_0^+, w_1, w_2^+, w_3^+, w_4, w_5^+, w_6^+, w_7, \dots, w_{n-4}, w_{n-3}^+, w_{n-2}, w_{n-1}^+\}.$$

Therefore, $\gamma_R(P_n^+) = 2 \frac{n-2}{3} + 1 + 2(\frac{n-4-1}{3} + 1 + 1)$ then we get $\gamma_R(P_n^+) = 4 \left\lfloor \frac{n}{3} \right\rfloor - 1$.

References

- [1] Chartrand G, Lesniak L, Zhang P (2016) Graphs and Digraphs, Taylor&Francis Group, New York.
- [2] Doğan Durgun D, Lökçü B (2015) Strong domination number of some graphs. Celal Bayar Üniversitesi Journal of Science 11(2): 89-91.
- [3] Dogan Durgun D, Altundag FN (2017) Liar's Domination in Graphs Bulletin of IMVI 7: 407-415.
- [4] Haynes TW, Hedetniemi ST, Slater PJ (1998) Domination in graphs. Advanced Topic Marcel Dekker Inc New York.
- [5] Haynes TW, Hedetniemi ST, Slater PJ (1998) Fundamentals of Domination in Graphs Marcel Dekker, Inc, New York.

3rd International Students Science Congress
3-4 May 2019, İzmir - Turkey

- [6] Cockayne EJ, Dreyer PA, M. Hedetniemi SM, Hedetniemi ST (2004) Roman Domination in graphs, *Discrete Math.*, 278: 11-22.
- [7] ReVelle CS (1997) Can you protect the Roman Empire? *Johns Hopkins Magazine*, 49 p.40.
- [8] Stewart I (1999) Defend the Roman Empire! *Sci. Amer.*, 281: 136-139.
- [9] Gayathri B, Duraisamy M, Selvi MT (2007) Proceedings of the international conference on mathematics and computer science, Chennai, India, 1, *ICMCS*: 119-124.
- [10] Cygan M, Pilipczuk M, Skrekovski R (2011) Relation between Randic index and avarege distance of trees, *Match Communications in Mathematical and Computer Chemistry*, 66: 605-612.
- [11] Bagga KS, Beineke LW, Goddard W, Lipman MJ, Pippert RE (1992) A survey of integrity. *Discrete Applied Mathematics* 37: 13-28

An Euler Matrix Technique for Solving Nonlinear Duffing Differential Equation by Using Euler Polynomials

Deniz Elmacı*, Dokuz Eylül University, Bergama Vocational School, İzmir, Turkey
Nurcan Baykuş Savaşaneril, Dokuz Eylül University, İzmir Vocational School, İzmir, Turkey
Mehmet Sezer, Manisa Celal Bayar University, Dept. of Mathematics, Manisa, Turkey
*Corresponding author: deniz.elmaci@deu.edu.tr

Keywords: Euler polynomials, matrix and collocation methods, Duffing equations, nonlinear differential equations, residual error estimation

Discipline: Mathematics

Abstract

Nonlinear Duffing differential equations arise in the study of the nonlinear problems and the related initial and boundary value problems play an important role in various scientific fields such as physics, astrophysics, engineering, biology and communication theory. In recent years, to solve these problems both analytically and numerically, several numerical and analytical methods have been given. But it may not be possible to find the analytical solutions. So, in this study, we develop an efficient operational matrix method for the approximate solution of nonlinear Duffing differential equations under the mixed conditions. This technique is a matrix method based on collocation points along with the truncated Euler series, and reduces the solution of nonlinear Duffing differential equation to the solution of a matrix equation which corresponds to a system of nonlinear algebraic equations with unknown Euler coefficients. The acquired approximate solutions subject to initial or boundary conditions are obtained in terms of Euler polynomials. Also, some examples together with error analysis techniques are given to demonstrate the validity and applicability of the present method, and the comparisons are made with existing results.

Introduction

In recent years, the attention has been focused on nonlinear problems [1-2,8-9]; one of the most fundamental equations in the study of the nonlinear is also the Duffing differential equation [3-4] defined by

$$\sum_{k=0}^2 P_k(x)y^{(k)}(x) + Q(x)y^3(x) = f(x), \quad a \leq x \leq b \quad (1)$$

with the initial conditions

$$\sum_{k=0}^1 a_{kj}y^{(k)}(a) = \lambda_j, \quad j = 0, 1 \quad (2)$$

where $P_k(x)$, $Q(x)$ and $f(x)$ are functions defined on the interval $a \leq x \leq b$; a_{kj} and λ_j are appropriate real constants; $y(x)$ is an unknown function to be determined. For our purpose, we assume the approximate solution of the problem (1), (2) in the truncated Euler series form [6]

$$y(x) \cong y_N(x) = \sum_{n=0}^N a_n E_n(x), \quad a \leq x \leq b \quad (3)$$

where $E_n(t)$ denotes the Euler-Taylor polynomials [5,7] defined by

$$\frac{2e^{xt}}{e^t + 1} = \sum_{n=0}^{\infty} E_n(x) \frac{t^n}{n!}, \quad |t| < \pi \quad (4)$$

Euler numbers ε_n can be obtained by the generating function

$$\frac{2}{e^t + e^{-t}} = \sum_{n=0}^{\infty} \frac{\varepsilon_n}{n!} t^n \quad (5)$$

And the connection between Euler numbers (5) and Euler polynomials (4) is given by

$$E_n(1/2) = 2^{-n} \varepsilon_n, \quad n=0,1,2,\dots \quad (6)$$

Euler polynomials are strictly connected with Bernoulli ones, and are used in Taylor in the Taylor expansion in a neighborhood of the origin of trigonometric and hyperbolic secant functions, Recursive computation of Euler polynomials can be obtained by using the following formula;

$$E_n(x) + \sum_{k=0}^n \binom{n}{k} E_k(x) = 2x^n, \quad n=1,2,\dots \quad (7)$$

Also, Euler polynomials $E_n(x)$ can be defined as polynomials of degree $n \geq 0$ satisfying the conditions

$$E'_m(x) = mE_{m-1}(x), \quad m \geq 1. \quad (8)$$

$$E_m(x+1) + E_m(x) = 2x^m, \quad m \geq 1. \quad (9)$$

By using (6), (7) or (9) the first Euler and Euler polynomials respectively are given by

$$\varepsilon_0 = 1, \quad \varepsilon_1 = 0, \quad \varepsilon_2 = -1, \quad \varepsilon_3 = 0, \quad \varepsilon_4 = 5, \quad \varepsilon_5 = 0, \quad \varepsilon_6 = -61, \quad \varepsilon_7 = 0$$

$$E_0(x) = 1, \quad E_1(x) = x - \frac{1}{2}, \quad E_2(x) = x^2 - x$$

$$E_3(x) = x^3 - \frac{3}{2}x^2 + \frac{1}{4}, \quad E_4(x) = x^4 - 2x^3 + 2, \dots$$

Fundamental Matrix Relations and Method

In this section we convert the expressions defined in (1) and (2) to the matrix forms by the following procedure: Firstly, the function $y(x)$ defined by (3) and its derivatives can be written in the matrix form

$$y_N(x) = \mathbf{E}(x)\mathbf{A} \quad \mathbf{X}(x) = \mathbf{E}(x)\mathbf{M}^T \Rightarrow \mathbf{E}(x) = \mathbf{X}(x)(\mathbf{M}^T)^{-1} \quad (10)$$

where

$$\mathbf{E}(x) = [E_0(x) \quad E_1(x) \quad \dots \quad E_N(x)], \quad \mathbf{X}(x) = [1 \quad x \quad \dots \quad x^N]$$

$$\mathbf{A} = [a_0 \quad a_1 \quad \dots \quad a_N]^T \quad \text{and} \quad \mathbf{M} = \begin{bmatrix} 1 & 0 & 0 & \dots & 0 \\ \frac{1}{2} \binom{1}{0} & 1 & 0 & \dots & 0 \\ \frac{1}{2} \binom{2}{0} & \frac{1}{2} \binom{2}{1} & 1 & \dots & 0 \\ \vdots & \vdots & \vdots & \ddots & \vdots \\ \frac{1}{2} \binom{N}{0} & \frac{1}{2} \binom{N}{1} & \frac{1}{2} \binom{N}{2} & \dots & 1 \end{bmatrix}$$

As follows:

$$\begin{bmatrix} 1 \\ x \\ x^2 \\ \vdots \\ x^N \end{bmatrix} = \underbrace{\begin{bmatrix} 1 & 0 & 0 & \dots & 0 \\ \frac{1}{2} \binom{1}{0} & 1 & 0 & \dots & 0 \\ \frac{1}{2} \binom{2}{0} & \frac{1}{2} \binom{2}{1} & 1 & \dots & 0 \\ \vdots & \vdots & \vdots & \ddots & \vdots \\ \frac{1}{2} \binom{N}{0} & \frac{1}{2} \binom{N}{1} & \frac{1}{2} \binom{N}{2} & \dots & 1 \end{bmatrix}}_{\mathbf{M}} \begin{bmatrix} E_0(x) \\ E_0(x) \\ E_0(x) \\ \vdots \\ E_0(t) \end{bmatrix} = \mathbf{E}^T(x)$$

Also, it is clearly seen that from (8) and (10), the relation between the matrix $\mathbf{E}(x)$ and its derivative $\mathbf{E}'(x)$ is

$$\mathbf{E}'(x) = \mathbf{X}'(x) \left(\mathbf{M}^T \right)^{-1} = \mathbf{X}(x) \mathbf{B} \left(\mathbf{M}^T \right)^{-1} \quad (11)$$

And that repeating the process

$$\begin{aligned} \mathbf{E}''(x) &= \mathbf{X}''(x) \left(\mathbf{M}^T \right)^{-1} = \left(\mathbf{X}(x) \mathbf{B} \right)' \left(\mathbf{M}^T \right)^{-1} = \mathbf{X}(x) \mathbf{B}^2 \left(\mathbf{M}^T \right)^{-1} \\ \mathbf{E}'''(x) &= \mathbf{X}(x) \mathbf{B}^3 \left(\mathbf{M}^T \right)^{-1} \\ &\vdots \\ \mathbf{E}^{(k)}(x) &= \mathbf{X}(x) \mathbf{B}^k \left(\mathbf{M}^T \right)^{-1}, \quad k=0,1,2,\dots \end{aligned} \quad (12)$$

where

$$\mathbf{B} = \begin{bmatrix} 0 & 1 & 0 & \dots & 0 \\ 0 & 0 & 2 & \dots & 0 \\ \vdots & \vdots & \vdots & \ddots & \vdots \\ 0 & 0 & 0 & 0 & N \\ 0 & 0 & 0 & 0 & 0 \end{bmatrix}, \quad \mathbf{B}^0 = \begin{bmatrix} 1 & 0 & 0 & \dots & 0 \\ 0 & 1 & 0 & \dots & 0 \\ \vdots & \vdots & \vdots & \ddots & \vdots \\ 0 & 0 & 0 & \dots & 0 \\ 0 & 0 & 0 & \dots & 1 \end{bmatrix}$$

$$y^{(k)}(x) = y_N^k(x) = \mathbf{E}^{(k)}(x) \mathbf{A} = \mathbf{X}(x) \mathbf{B}^k \left(\mathbf{M}^T \right)^{-1} \mathbf{A}, \quad k=0,1,2,\dots \quad (13)$$

In similar way to the matrix equation (13), it follows that the matrix representation of $y^3(x)$ becomes

$$y^3(x) = \mathbf{E}(x) \bar{\mathbf{E}}(x) \bar{\bar{\mathbf{E}}}(x) \bar{\bar{\bar{\mathbf{A}}}} = \mathbf{X}(x) \mathbf{B}^k \left(\mathbf{M}^T \right)^{-1} \bar{\mathbf{X}}(x) \mathbf{B}^k \left(\mathbf{M}^T \right)^{-1} \bar{\bar{\mathbf{X}}}(x) \mathbf{B}^k \left(\mathbf{M}^T \right)^{-1} \bar{\bar{\bar{\mathbf{A}}}} \quad (14)$$

where

$$\begin{aligned} \bar{\mathbf{X}}(x) &= \text{diag} \left[\mathbf{X}(x) \quad \mathbf{X}(x) \quad \dots \quad \mathbf{X}(x) \right]_{(N+1) \times (n+1)^2} \\ \left(\mathbf{M}^T \right)^{-1} &= \text{diag} \left[\left(\mathbf{M}^T \right)^{-1} \quad \left(\mathbf{M}^T \right)^{-1} \quad \dots \quad \left(\mathbf{M}^T \right)^{-1} \right]_{(N+1)^2 \times (N+1)^2} \\ \bar{\bar{\mathbf{X}}}(x) &= \text{diag} \left[\bar{\mathbf{X}}(x) \quad \bar{\mathbf{X}}(x) \quad \dots \quad \bar{\mathbf{X}}(x) \right]_{(N+1)^2 \times (N+1)^3} \\ \bar{\bar{\bar{\mathbf{A}}}} &= \text{diag} \left[\left(\mathbf{M}^T \right)^{-1} \quad \left(\mathbf{M}^T \right)^{-1} \quad \dots \quad \left(\mathbf{M}^T \right)^{-1} \right]_{(N+1)^3 \times (N+1)^3} \\ \mathbf{A} &= \begin{bmatrix} a_0 \\ a_1 \\ \vdots \\ a_N \end{bmatrix}_{(N+1) \times 1} & \bar{\mathbf{A}} &= \begin{bmatrix} a_0 \mathbf{A} \\ a_1 \mathbf{A} \\ \vdots \\ a_N \mathbf{A} \end{bmatrix}_{(N+1)^2 \times 1} & \bar{\bar{\mathbf{A}}} &= \begin{bmatrix} a_0 \bar{\mathbf{A}} \\ a_1 \bar{\mathbf{A}} \\ \vdots \\ a_N \bar{\mathbf{A}} \end{bmatrix}_{(N+1)^3 \times 1} \end{aligned}$$

To obtain the Euler polynomial solution of Eq. (1) in the form (3) we firstly compute the Euler coefficients by means of the collocation points defined by

$$x_i = a + \frac{b-a}{N} i, \quad i = 0, 1, 2, \dots, N$$

For this purpose, by substituting the collocation points into matrix equation (1) we obtain the system of matrix equation

$$\sum_{k=0}^2 P_k(x_i) y^{(k)}(x_i) + Q(x_i) y^3(x_i) = f(x_i) \quad \text{or briefly}$$

$$\sum_{k=0}^2 P_k y^{(k)} + Qy^3 = F \quad (15)$$

where

$$\mathbf{P}_k = \begin{bmatrix} P_k(x_0) & 0 & 0 & \cdots & 0 \\ 0 & P_k(x_1) & 0 & \cdots & 0 \\ 0 & 0 & P_k(x_2) & \cdots & 0 \\ \vdots & \vdots & \vdots & \ddots & \vdots \\ 0 & 0 & 0 & 0 & P_k(x_N) \end{bmatrix} \quad \mathbf{Q} = \begin{bmatrix} Q(x_0) & 0 & 0 & \cdots & 0 \\ 0 & Q(x_1) & 0 & \cdots & 0 \\ 0 & 0 & Q(x_2) & \cdots & 0 \\ \vdots & \vdots & \vdots & \ddots & \vdots \\ 0 & 0 & 0 & 0 & Q(x_N) \end{bmatrix}$$

$$\mathbf{Y}^{(k)} = \begin{bmatrix} y^{(k)}(x_0) \\ y^{(k)}(x_1) \\ \vdots \\ y^{(k)}(x_N) \end{bmatrix} = \mathbf{X}(x) \mathbf{B}^k (\mathbf{M}^T)^{-1} \mathbf{A} \quad \mathbf{X} = \begin{bmatrix} X(x_0) \\ X(x_1) \\ \vdots \\ X(x_N) \end{bmatrix} = \begin{bmatrix} 1 & x_0 & \cdots & x_0^N \\ 1 & x_1 & \cdots & x_1^N \\ \vdots & \vdots & \ddots & \vdots \\ 1 & x_N & \cdots & x_N^N \end{bmatrix} \quad \mathbf{F} = \begin{bmatrix} f(x_0) \\ f(x_1) \\ \vdots \\ f(x_N) \end{bmatrix}$$

On the other hand,

$$\mathbf{Y}^{(3)} = \begin{bmatrix} y^3(x_0) \\ y^3(x_1) \\ \vdots \\ y^3(x_N) \end{bmatrix} = \begin{bmatrix} \mathbf{X}(x_0) (\mathbf{M}^T)^{-1} \mathbf{B}^k \overline{\mathbf{X}}(x_0) (\mathbf{M}^T)^{-1} \mathbf{B}^k \overline{\overline{\mathbf{X}}}(x_0) (\mathbf{M}^T)^{-1} \mathbf{B}^k \\ \mathbf{X}(x_1) (\mathbf{M}^T)^{-1} \mathbf{B}^k \overline{\mathbf{X}}(x_1) (\mathbf{M}^T)^{-1} \mathbf{B}^k \overline{\overline{\mathbf{X}}}(x_1) (\mathbf{M}^T)^{-1} \mathbf{B}^k \\ \vdots \\ \mathbf{X}(x_N) (\mathbf{M}^T)^{-1} \mathbf{B}^k \overline{\mathbf{X}}(x_N) (\mathbf{M}^T)^{-1} \mathbf{B}^k \overline{\overline{\mathbf{X}}}(x_N) (\mathbf{M}^T)^{-1} \mathbf{B}^k \end{bmatrix} \overline{\overline{\mathbf{A}}} = \mathbf{C}^* \overline{\overline{\mathbf{A}}}$$

There for, by means of the matrix relation (15) and its matrices in the fundamental matrix equation corresponding to eq. (1) becomes as follows.

$$\sum_{k=0}^2 \mathbf{P}_k \mathbf{X}(x) \mathbf{B}^k (\mathbf{M}^T)^{-1} \mathbf{A} + \mathbf{Q} \mathbf{C}^* \overline{\overline{\mathbf{A}}} = \mathbf{F} \Rightarrow \mathbf{W} \mathbf{A} + \mathbf{V} \overline{\overline{\mathbf{A}}} = \mathbf{F} \Leftrightarrow [\mathbf{W}; \mathbf{V}; \mathbf{F}] \quad (16)$$

And clearly

$$[\mathbf{W}; \mathbf{V}; \mathbf{F}] = \begin{bmatrix} w_{0,0} & w_{0,1} & \cdots & w_{0,N} & ; & v_{0,0} & v_{0,1} & \cdots & v_{0,(n+1)^3-1} & : & f(x_0) \\ w_{1,0} & w_{1,1} & \cdots & w_{1,N} & ; & v_{1,0} & v_{1,1} & \cdots & v_{1,(N+1)^3-1} & : & f(x_1) \\ \vdots & \vdots & \ddots & \vdots & ; & \vdots & \vdots & \ddots & \vdots & : & \vdots \\ w_{N,0} & w_{N,1} & \cdots & w_{N,N} & ; & v_{N,0} & v_{N,1} & \cdots & v_{N,(N+1)^3-1} & : & F(x_N) \end{bmatrix} \quad (17)$$

Next, by means of relations (10), we can obtain the corresponding matrix forms for the initial conditions (2) as

$$\sum_{k=0}^1 a_{ij} \mathbf{X}(a) \mathbf{B}^k (\mathbf{M}^T)^{-1} = \lambda_j \Rightarrow \mathbf{U} \mathbf{A} + \mathbf{O}^* \overline{\overline{\mathbf{A}}} = \lambda \Leftrightarrow [\mathbf{U}; \mathbf{O}^*; \lambda]$$

$$[\mathbf{U}; \mathbf{O}^*; \lambda] = \begin{bmatrix} u_{00} & u_{01} & \cdots & u_{0N} & ; & 0 & 0 & \cdots & 0 & ; & \lambda_0 \\ u_{10} & u_{11} & \cdots & u_{1N} & ; & 0 & 0 & \cdots & 0 & ; & \lambda_1 \end{bmatrix}$$

Consequently, to obtain the solution of Eq.(1) under the conditions (2), by replacing the row matrices (18) by the last two rows of the augmented matrix (17), we have the required augmented matrix as follows;

$$[\tilde{\mathbf{W}}; \tilde{\mathbf{V}}; \tilde{\mathbf{F}}] = \begin{bmatrix} w_{00} & w_{01} & \cdots & w_{0N} & ; & v_{00} & v_{01} & \cdots & v_{0(N+1)^3} & ; & f(x_0) \\ w_{10} & w_{11} & \cdots & w_{1N} & ; & v_{10} & v_{11} & \cdots & v_{1(N+1)^3} & ; & f(x_1) \\ \vdots & \vdots & \vdots & \vdots & ; & \vdots & \vdots & \vdots & \vdots & ; & \vdots \\ w_{N-2,0} & w_{N-2,1} & \cdots & w_{N-2,N} & ; & v_{00} & v_{00} & \cdots & v_{N-2,(N+1)^3} & ; & f(x_{N-2}) \\ u_{00} & u_{01} & \cdots & u_{0N} & ; & 0 & 0 & \cdots & 0 & ; & \lambda_0 \\ u_{10} & u_{11} & \cdots & u_{1N} & ; & 0 & 0 & \cdots & 0 & ; & \lambda_1 \end{bmatrix} \quad (19)$$

From the nonlinear algebraic system (14), that is, from the matrix equation $\tilde{\mathbf{W}}\mathbf{A} + \tilde{\mathbf{V}}\mathbf{A} = \tilde{\mathbf{F}}$ the unknown Euler polynomial coefficients a_n ($n=0,1,\dots,N$) are determined. Thus, the truncated Euler series solution (3) is obtained. By solving the matrix Eq. (19), the unknown Euler coefficients a_n are determined. Thus, we get Euler polynomial solution

$$y_N(x) = \sum_{n=0}^N a_n E(x) = a_0 E_0(x) + a_1 E_1(x) + a_2 E_2(x)$$

Accuracy of Solutions and Residual Error Estimation

We can easily check the accuracy of the obtained solutions as follows. Since the truncated Boubaker series (3) is the approximate solution of (1), when the function $y_N(x)$ and its derivatives are substituted in Eq.(1), the resulting equation must be satisfied approximately; that is, for $x = x_q \in [a, b]$, $q = 0, 1, \dots$

$$\mathbf{R}_N(x_q) = \sum_{k=0}^2 \mathbf{P}_k(x_q) y_N^{(k)}(x_q) + \mathbf{Q}(x_q) y_N^3(x_q) - f(x_q) \cong 0 \quad (20)$$

or

$$\mathbf{R}_N(x_q) \leq 10^{-kq}$$

If $\max 10^{-kq} = 10^{-k}$ (k is a positive integer) is prescribed, then the truncation limit N is increased until the difference $\mathbf{R}_N(x_q)$ at each of the selected points becomes smaller than the prescribed 10^{-k} .

On the other hand, by means of the residual function defined by $\mathbf{R}_N(x)$ and the mean value of the function $|\mathbf{R}_N(x)|$ on the interval $[a, b]$, the accuracy of the solution can be controlled and the error can be estimated. If $\mathbf{R}_N(x) \rightarrow 0$ when N is sufficiently large enough, then the error decreases. Also, by using the Mean-Value Theorem, we can estimate the upper bound of the mean error, $\bar{\mathbf{R}}_N(x)$ as follows:

$$\left| \int_a^b \mathbf{R}_N(x) dx \right| \leq \int_a^b |\mathbf{R}_N(x)| dx \quad (21)$$

and

$$\left| \int_a^b \mathbf{R}_N(x) dx \right| = (b-a) |\mathbf{R}_N(c)|, a \leq c \leq b \quad (12)$$

$$\Rightarrow (b-a) |\mathbf{R}_N(c)| \leq \int_a^b |\mathbf{R}_N(x)| dx$$

$$\Rightarrow |\mathbf{R}_N(c)| \leq \frac{\int_a^b |\mathbf{R}_N(x)| dx}{(b-a)} = \bar{\mathbf{R}}_N$$

Numerical Example

The method of this study is useful in finding the solutions of Duffing equations in terms of Euler polynomials. We illustrate it by the following example. Numerical computations have been done using Mathematica 9.

Example: We consider the Duffing equation in the following type,

$$2y''(x) - y'(x) - y(x) + y^3(x) = e^{3x}, \quad 0 \leq x \leq 1$$

under the initial conditions

$$y(0) = 1 \quad y'(0) = 1$$

exact solution is $y(x) = e^x$.

$$P_0(x) = -1 \quad P_1(x) = -1 \quad P_2(x) = 2 \quad Q(x) = 1 \quad f(x) = e^{3x}$$

this relations are defined. $N=2$ for, truncated approximate solution in the form of Euler series

$$y(x) = \sum_{n=0}^2 a_n E_n(x).$$

thereafter,

$$x_0 = 0 \quad x_1 = \frac{1}{2} \quad x_2 = 1$$

using the collocation points and the developed method, the fundamental matrix equation of the problem is obtained as follows

$$\sum_{k=0}^2 \mathbf{P}_k \mathbf{X}(x) \mathbf{B}^k (\mathbf{M}^T)^{-1} \mathbf{A} + \mathbf{Q} \mathbf{C}^* \bar{\mathbf{A}} = \mathbf{F} \Rightarrow \mathbf{W} \mathbf{A} + \mathbf{V} \bar{\mathbf{A}} = \mathbf{F} \Leftrightarrow [\mathbf{W}; \mathbf{V}; \mathbf{F}]$$

$$\mathbf{P}_0 \mathbf{X}(x) \mathbf{B}^0 + \mathbf{P}_1 \mathbf{X}(x) \mathbf{B}^1 + \mathbf{P}_2 \mathbf{X}(x) \mathbf{B}^2 \quad \mathbf{M}^T \quad \bar{\mathbf{A}} + \mathbf{Q} \mathbf{A}^* \bar{\mathbf{A}} = \mathbf{F}$$

and

$$\mathbf{P}_0 = \begin{bmatrix} -1 & 0 & 0 \\ 0 & -1 & 0 \\ 0 & 0 & -1 \end{bmatrix} \quad \mathbf{P}_1 = \begin{bmatrix} -1 & 0 & 0 \\ 0 & -1 & 0 \\ 0 & 0 & -1 \end{bmatrix} \quad \mathbf{P}_2 = \begin{bmatrix} 2 & 0 & 0 \\ 0 & 2 & 0 \\ 0 & 0 & 2 \end{bmatrix} \quad \mathbf{B}^0 = \begin{bmatrix} 1 & 0 & 0 \\ 0 & 1 & 0 \\ 0 & 0 & 1 \end{bmatrix} \quad \mathbf{B}^1 = \begin{bmatrix} 0 & 1 & 0 \\ 0 & 0 & 2 \\ 0 & 0 & 0 \end{bmatrix}$$

$$\mathbf{B}^2 = \begin{bmatrix} 0 & 0 & 2 \\ 0 & 0 & 0 \\ 0 & 0 & 0 \end{bmatrix} \quad \mathbf{Q} = \begin{bmatrix} 1 & 0 & 0 \\ 0 & 1 & 0 \\ 0 & 0 & 1 \end{bmatrix} \quad \mathbf{F} = \begin{bmatrix} 1 \\ e^{\frac{1}{2}} \\ e \end{bmatrix}$$

$$\mathbf{X} = \begin{bmatrix} \mathbf{X}(0) \\ \mathbf{X}(\frac{1}{2}) \\ \mathbf{X}(1) \end{bmatrix} = \begin{bmatrix} 1 & 0 & 0 \\ 1 & \frac{1}{2} & \frac{1}{4} \\ 1 & 1 & 1 \end{bmatrix} \quad \bar{\mathbf{X}} = \begin{bmatrix} 1 & 0 & 0 & 0 & 0 & 0 & 0 & 0 & 0 \\ 0 & 0 & 0 & 1 & \frac{1}{2} & \frac{1}{4} & 0 & 0 & 0 \\ 0 & 0 & 0 & 0 & 0 & 0 & 1 & 1 & 1 \end{bmatrix}$$

$$\mathbf{M} = \begin{bmatrix} 1 & 0 & 0 \\ \frac{1}{2} & 1 & 0 \\ \frac{1}{2} & 1 & 1 \end{bmatrix} \quad \mathbf{M}^T = \begin{bmatrix} 1 & \frac{1}{2} & \frac{1}{2} \\ 0 & 1 & 1 \\ 0 & 0 & 1 \end{bmatrix} \quad (\mathbf{M}^T)^{-1} = \begin{bmatrix} 1 & \frac{-1}{2} & 0 \\ 0 & 1 & -1 \\ 0 & 0 & 1 \end{bmatrix}$$

$$\mathbf{W} = (\mathbf{P}_0 \mathbf{X}(x) \mathbf{B}^0 + \mathbf{P}_1 \mathbf{X}(x) \mathbf{B}^1 + \mathbf{P}_2 \mathbf{X}(x) \mathbf{B}^2) (\mathbf{M}^T)^{-1} = \begin{bmatrix} -1 & \frac{-1}{2} & 5 \\ -1 & -1 & \frac{17}{4} \\ -1 & \frac{-3}{2} & 3 \end{bmatrix} \quad \mathbf{V} = \mathbf{Q} \mathbf{C}^*$$

3rd International Students Science Congress
3-4 May 2019, İzmir - Turkey

- [4] Feng Z (2006) Monotonous property of non-oscillations of the damped Duffing's equation, *Chaos, Solitons and Fractals* 28: 463–471.
- [5] Balcı MA, Sezer M (2016), Hybrid Euler-Taylor matrix method for solving of generalized linear Fredholm integro-differential difference equations, *Applied Mathematics and Computation*, 273: 33–41,
- [6] Cheon GS (2003) A note on the Bernoulli and Euler polynomials, *Applied Mathematics Letters* 16, 365-368.
- [7] Baykuş Savaşaneril N, Sezer M (2017) Hybrid Taylor Lucas collocation method for numerical solution of high-order pantograph type delay differential equations with variables delays, *Appl.Math. Inf. Sci.* 11: 1795-1801.
- [8] Gümgüm S, Baykuş Savaşaneril N, Kürkçü, ÖK, Sezer M., (2019) Lucas polynomial solution of nonlinear differential equations with variable delay, *Hacettepe J. Math. Stat.* doi: 10.15672/hujms.460975
- [9] Gümgüm S, Ersoy Özdek D, Özaltun G (2019) Legendre wavelet solution of high order nonlinear ordinary delay differential equations. *Turkish Journal of Mathematics*, doi: 10.3906/mat-1901-109.

Euler-Taylor Matrix Technique for Solving a Class of High Order Delay Differential Equations with Nonlinear Terms

Deniz Elmacı*, Dokuz Eylül University, Bergama Vocational School, İzmir, Turkey
Nurcan Baykuş Savaşaneril, Dokuz Eylül University, İzmir Vocational School, İzmir, Turkey
Mehmet Sezer, Manisa Celal Bayar University, Dept. of Mathematics, Manisa, Turkey
*Corresponding author: deniz.elmaci@deu.edu.tr

Keywords: Euler and Taylor polynomials, delay differential equations, matrix and collocation methods, nonlinear differential equation

Discipline: Mathematics

Abstract

Nonlinear delay differential equations and the related initial and boundary value problems play an important role in astrophysics, physics and engineering. In recent years, in order to solve these type problems arising in various branches of applied sciences, several numerical and analytical methods have been given. But it may not be possible to find the analytical solutions of such problems. Furthermore, the approximation methods for these problems have been developed by many authors. In this study, we consider a class of high order delay functional differential equations with variable coefficients containing first order nonlinear terms; then we develop an operational matrix-collocation method based on Euler and Taylor polynomials to find the approximate solutions of these type equations subject to appropriate initial or boundary conditions. The used method reduces the solution of the given equations to the solution of a matrix equation which corresponds to system of algebraic equations with unknown Euler coefficients. Besides some numerical examples along with residual error analysis are performed to illustrate the efficiency of the present method.

Introduction

Nonlinear delay differential equations and the related problems with mixed conditions have a wide range of application in science and engineering. These type problems are usually used in modeling of physical phenomena and play an important role in the applied sciences [1].

In this study, we consider the following high-order delay differential equation having the first order nonlinear terms:

$$\sum_{k=0}^m \sum_{j=1}^J P_{kj}(t) y^{(k)}(\alpha_{kj}t + \beta_{kj}) = g(t) + \sum_{p=0}^1 \sum_{q=0}^p Q_{pq}(t) y^{(p)}(t) y^{(q)}(t), \quad (1)$$

under the mixed conditions

$$\sum_{k=0}^{m-1} (a_{kj} y^{(k)}(a) + b_{kj} y^{(k)}(b)) = \mu_j, \quad j = 0, 1, \dots, m-1 \quad (2)$$

where the coefficients $P_{kj}(t)$, $Q_{pq}(t)$ and $g(t)$ are functions defined on the interval $a \leq t \leq b$; a_{kj} , b_{kj} , α_{kj} , β_{kj} and μ_j are appropriate constants; $y(t)$ is the unknown solution function. The solution of Eq.(1) is generally difficult; thereby numerical methods are required to obtain their the approximate solutions. For this purpose, the many methods have been used in literature [2-6]. In this study, we seek the Euler polynomials solution of the problem (1)-(2) in the finite series form

$$y(t) \cong y_N(t) = \sum_{n=0}^N a_n E_n(t), \quad a \leq t \leq b \quad (3)$$

where $E_n(t)$ denotes the Euler polynomials defined by

$$\frac{2e^{xt}}{e^t + 1} = \sum_{n=0}^{\infty} E_n(x) \frac{t^n}{n!}, \quad |t| < \pi. \quad (4)$$

Euler polynomials are strictly connected with Bernoulli ones, and are used in the Taylor expansion in a neighborhood of the origin of trigonometric and hyperbolic secant functions, Recursive computation of Euler polynomials can be obtained by using the following formula

$$E_n(x) + \sum_{k=0}^n \binom{n}{k} E_k(x) = 2x^n, \quad n=1,2,\dots \quad (5)$$

Also, Euler polynomials $E_n(x)$ can be defined as polynomials of degree $n \geq 0$ satisfying the conditions

$$E'_m(x) = mE_{m-1}(x), \quad m \geq 1 \quad \text{and} \quad E_m(x+1) + E_m(x) = 2x^m, \quad m \geq 1. \quad (6)$$

By using (4), (5) or (6) the first Euler polynomials are given by

$$E_0(x) = 1, \quad E_1(x) = x - \frac{1}{2}, \quad E_2(x) = x^2 - x$$

$$E_3(x) = x^3 - \frac{3}{2}x^2 + \frac{1}{4}, \quad E_4(x) = x^4 - 2x^3 + 2, \dots$$

Matrix relations for Euler and Taylor polynomials

Let us consider the high order delay differential equations Eq.(1) and find the matrix forms of each term in the equation. Firstly, we can convert the desired solution $y(t)$ defined by the truncated Euler series (3) of Eq.(1) to the matrix form, for $n=0,1,2,\dots,N$, as

$$y(t) \cong y_N(t) = \mathbf{E}(t)\mathbf{A}, \quad (7)$$

where

$$\mathbf{E}(t) = [E_0(t) \quad E_1(t) \quad \dots \quad E_N(t)], \quad \mathbf{A} = [a_0 \quad a_1 \quad \dots \quad a_N]^T.$$

On the other hand, using Euler polynomials and Taylor expansion, and by means of (5), the matrix relation between standard base matrix and Euler base matrix is constructed as

$$\begin{bmatrix} 1 \\ t \\ t^2 \\ \vdots \\ t^N \end{bmatrix} = \begin{bmatrix} 1 & 0 & 0 & \dots & 0 \\ \frac{1}{2} \binom{1}{0} & 1 & 0 & \dots & 0 \\ \frac{1}{2} \binom{2}{0} & \frac{1}{2} \binom{2}{1} & 1 & \dots & 0 \\ \vdots & \vdots & \vdots & \ddots & \vdots \\ \frac{1}{2} \binom{N}{0} & \frac{1}{2} \binom{N}{1} & \frac{1}{2} \binom{N}{2} & \dots & 1 \end{bmatrix} \begin{bmatrix} E_0(t) \\ E_0(t) \\ E_0(t) \\ \vdots \\ E_0(t) \end{bmatrix};$$

$$\mathbf{T}^T(t) = \underbrace{\begin{bmatrix} 1 & 0 & 0 & \dots & 0 \\ \frac{1}{2} \binom{1}{0} & 1 & 0 & \dots & 0 \\ \frac{1}{2} \binom{2}{0} & \frac{1}{2} \binom{2}{1} & 1 & \dots & 0 \\ \vdots & \vdots & \vdots & \ddots & \vdots \\ \frac{1}{2} \binom{N}{0} & \frac{1}{2} \binom{N}{1} & \frac{1}{2} \binom{N}{2} & \dots & 1 \end{bmatrix}}_{\mathbf{M}^T} \mathbf{E}^T(t)$$

$$\mathbf{T}^T(t) = \mathbf{M}^T \mathbf{E}^T(t) \Leftrightarrow \mathbf{T}(t) = \mathbf{E}(t)\mathbf{M} \Rightarrow \mathbf{E}(t) = \mathbf{T}(t)\mathbf{M}^{-1} \quad (8)$$

where

$$\mathbf{E}(t) = [E_0(t) \quad E_1(t) \quad \dots \quad E_N(t)], \quad \mathbf{T}(t) = [1 \quad t \quad \dots \quad t^N]$$

$$\mathbf{M}^T = \begin{bmatrix} 1 & 0 & 0 & \cdots & 0 \\ \frac{1}{2} \begin{pmatrix} 1 \\ 0 \end{pmatrix} & 1 & 0 & \cdots & 0 \\ \frac{1}{2} \begin{pmatrix} 2 \\ 0 \end{pmatrix} & \frac{1}{2} \begin{pmatrix} 2 \\ 1 \end{pmatrix} & 1 & \cdots & 0 \\ \vdots & \vdots & \vdots & \ddots & \vdots \\ \frac{1}{2} \begin{pmatrix} N \\ 0 \end{pmatrix} & \frac{1}{2} \begin{pmatrix} N \\ 1 \end{pmatrix} & \frac{1}{2} \begin{pmatrix} N \\ 2 \end{pmatrix} & \cdots & 1 \end{bmatrix}.$$

From (6) and (8) it is clearly seen that the relation between the matrix $\mathbf{E}(t)$ and its derivative $\mathbf{E}'(t)$ is

$$\mathbf{E}(t) = \mathbf{T}(t)\mathbf{M}^{-1} \Rightarrow \mathbf{E}'(t) = \mathbf{T}'(t)\mathbf{M}^{-1} = \mathbf{T}(t)\mathbf{B}\mathbf{M}^{-1} \text{ or } \mathbf{E}'(t) = \mathbf{E}(t)\mathbf{B}$$

and that repeating the process

$$\mathbf{E}''(t) = \mathbf{T}''(t)\mathbf{M}^{-1} = \mathbf{T}'(t)\mathbf{B}\mathbf{M}^{-1} = \mathbf{T}(t)\mathbf{B}^2\mathbf{M}^{-1}$$

$$\mathbf{E}'''(t) = \mathbf{T}(t)\mathbf{B}^3\mathbf{M}^{-1}$$

\vdots

$$\mathbf{E}^{(k)}(t) = \mathbf{T}(t)\mathbf{B}^k\mathbf{M}^{-1} \text{ or } \mathbf{E}^{(k)}(t) = \mathbf{E}(t)\mathbf{B}^k, \quad k=0,1,2,\dots$$

(9)

where

$$\mathbf{B} = \begin{bmatrix} 0 & 1 & 0 & \cdots & 0 \\ 0 & 0 & 2 & \cdots & 0 \\ \vdots & \vdots & \vdots & \ddots & \vdots \\ 0 & 0 & 0 & 0 & N \\ 0 & 0 & 0 & 0 & 0 \end{bmatrix}, \quad \mathbf{B}^0 = \begin{bmatrix} 1 & 0 & 0 & \cdots & 0 \\ 0 & 1 & 0 & \cdots & 0 \\ \vdots & \vdots & \vdots & \ddots & \vdots \\ 0 & 0 & 0 & \cdots & 0 \\ 0 & 0 & 0 & \cdots & 1 \end{bmatrix}.$$

From the matrix relations (7) -(9), it follows that

$$\mathbf{y}^{(k)}(t) = \mathbf{E}^{(k)}(t)\mathbf{A} = \mathbf{T}(t)\mathbf{B}^k\mathbf{M}^{-1}\mathbf{A} \quad k=0,1,2,\dots$$

(10)

or

$$\mathbf{y}^{(k)}(t) = \mathbf{E}^{(k)}(t)\mathbf{A} = \mathbf{E}(t)\mathbf{B}^k\mathbf{A}, \quad k=0,1,2,\dots$$

(11)

By putting $t \rightarrow \alpha_{kj}t + \beta_{kj}$ into the relation (10), we have

$$\mathbf{y}^{(k)}(\alpha_{kj}t + \beta_{kj}) = \mathbf{T}(t)\mathbf{S}(\alpha_{kj}, \beta_{kj})\mathbf{B}^k\mathbf{M}^{-1}\mathbf{A}$$

(12)

where

$$\mathbf{S}(\alpha_{kj}, \beta_{kj}) = \begin{bmatrix} \begin{pmatrix} 0 \\ 0 \end{pmatrix} \alpha_{kj}^0 \beta_{kj}^0 & \begin{pmatrix} 1 \\ 0 \end{pmatrix} \alpha_{kj}^0 \beta_{kj}^1 & \begin{pmatrix} 2 \\ 0 \end{pmatrix} \alpha_{kj}^0 \beta_{kj}^2 & \cdots & \begin{pmatrix} N \\ 0 \end{pmatrix} \alpha_{kj}^0 \beta_{kj}^N \\ 0 & \begin{pmatrix} 1 \\ 1 \end{pmatrix} \alpha_{kj}^1 \beta_{kj}^0 & \begin{pmatrix} 2 \\ 1 \end{pmatrix} \alpha_{kj}^1 \beta_{kj}^1 & \cdots & \begin{pmatrix} N \\ 1 \end{pmatrix} \alpha_{kj}^1 \beta_{kj}^{N-1} \\ 0 & 0 & \begin{pmatrix} 2 \\ 2 \end{pmatrix} \alpha_{kj}^2 \beta_{kj}^0 & \cdots & \begin{pmatrix} N \\ 2 \end{pmatrix} \alpha_{kj}^2 \beta_{kj}^{N-2} \\ \vdots & \vdots & \vdots & \ddots & \vdots \\ 0 & 0 & 0 & \cdots & \begin{pmatrix} N \\ N \end{pmatrix} \alpha_{kj}^N \beta_{kj}^0 \end{bmatrix}$$

In similar manner, from (11), the matrix form of the nonlinear part $y^{(p)}(t)y^{(q)}(t)$ in Eq.(1) can be written as, for $p, q=0,1$,

$$y^{(p)}(t)y^{(q)}(t) = \mathbf{E}(t)\mathbf{B}^p \overline{\mathbf{E}(t)\mathbf{B}^q \mathbf{A}}, \quad (13)$$

where

$$\overline{\mathbf{E}(t)} = \text{diag}[\mathbf{E}(t) \quad \mathbf{E}(t) \quad \cdots \quad \mathbf{E}(t)]$$

$$\overline{\mathbf{B}^q} = \text{diag}[\mathbf{B}^q \quad \mathbf{B}^q \quad \cdots \quad \mathbf{B}^q], \quad \overline{\mathbf{A}} = [a_0\mathbf{A} \quad a_1\mathbf{A} \quad \cdots \quad a_N\mathbf{A}]^T$$

By substituting the matrix relations (12) and (13) into Eq.(1) and then by using the collocation points

$$t_i = a + \frac{b-a}{N}i, \quad i = 0, 1, \dots, N$$

we obtain the system of matrix equations

$$\sum_{k=0}^m \sum_{j=1}^J P_{kj}(t_i) \mathbf{T}(t_i) \mathbf{S}(\alpha_{kj}, \beta_{kj}) \mathbf{B}^k \mathbf{M}^{-1} \mathbf{A} = g(t_i) + \sum_{p=0}^1 \sum_{q=0}^p Q_{pq}(t_i) \mathbf{E}(t_i) \mathbf{B}^p \overline{\mathbf{E}(t_i)\mathbf{B}^q \mathbf{A}}$$

or briefly the fundamental matrix relation

$$\sum_{k=0}^m \sum_{j=1}^J \mathbf{P}_{kj} \mathbf{T} \mathbf{S}_{kj} \mathbf{B}^k \mathbf{M}^{-1} \mathbf{A} - \sum_{p=0}^1 \sum_{q=0}^p \mathbf{Q}_{pq} \mathbf{R}_{pq} \overline{\mathbf{A}} = \mathbf{G}$$

or the compact form

$$\mathbf{W}\mathbf{A} + \mathbf{V}\overline{\mathbf{A}} = \mathbf{G} \Rightarrow [\mathbf{W}; \mathbf{V}; \mathbf{G}] \quad (14)$$

where

$$\mathbf{W} = \sum_{k=0}^m \sum_{j=1}^J \mathbf{P}_{kj} \mathbf{T} \mathbf{S}_{kj} \mathbf{B}^k \mathbf{M}^{-1}, \quad \mathbf{V} = - \sum_{p=0}^1 \sum_{q=0}^p \mathbf{Q}_{pq} \mathbf{R}_{pq}$$

$$\mathbf{P}_{kj} = \text{diag}[P_{kj}(t_0) \quad P_{kj}(t_1) \quad \cdots \quad P_{kj}(t_N)]$$

$$\mathbf{Q}_{pq} = \text{diag}[Q_{pq}(t_0) \quad Q_{pq}(t_1) \quad \cdots \quad Q_{pq}(t_N)]$$

$$\mathbf{S}_{kj} = \mathbf{S}(\alpha_{kj}, \beta_{kj})$$

$$\mathbf{T} = \begin{bmatrix} \mathbf{T}(t_0) \\ \mathbf{T}(t_1) \\ \vdots \\ \mathbf{T}(t_N) \end{bmatrix}, \quad \mathbf{G} = \begin{bmatrix} g(t_0) \\ g(t_1) \\ \vdots \\ g(t_N) \end{bmatrix}, \quad \mathbf{R}_{pq} = \begin{bmatrix} \overline{\mathbf{E}(t_0)\mathbf{B}^p \mathbf{E}(t_0)\mathbf{B}^q} \\ \overline{\mathbf{E}(t_1)\mathbf{B}^p \mathbf{E}(t_1)\mathbf{B}^q} \\ \vdots \\ \overline{\mathbf{E}(t_N)\mathbf{B}^p \mathbf{E}(t_N)\mathbf{B}^q} \end{bmatrix}$$

By using the matrix relation (11), the matrix form for the conditions (2) is obtained as

$$\sum_{k=0}^{m-1} (a_{kj}\mathbf{E}(a) + b_{kj}\mathbf{E}(b)) \mathbf{B}^k \mathbf{A} = \mu_j, \quad j = 0, 1, \dots, m-1$$

or briefly

$$\mathbf{U}_j \mathbf{A} + \mathbf{O}_j \overline{\mathbf{A}} = \mu_j \Leftrightarrow [\mathbf{U}_j \quad ; \quad \mathbf{O}_j \quad ; \quad \mu_j] \quad (15)$$

$$\mathbf{U}_j = \sum_{k=0}^{m-1} (a_{kj}\mathbf{E}(a) + b_{kj}\mathbf{E}(b)) \mathbf{B}^k, \quad \mathbf{O}_j = [0 \quad 0 \quad \cdots \quad 0]_{1 \times (N+1)^2}, \quad j = 0, 1, \dots, m-1$$

Consequently, we replace the any m rows of (14) by the row matrices (15) and thus the desired augmented matrix is obtained as

$$[\mathbf{W}; \mathbf{V}; \tilde{\mathbf{G}}] \text{ or } \mathbf{W}\mathbf{A} + \mathbf{V}\overline{\mathbf{A}} = \tilde{\mathbf{G}};$$

which correspond to the system of nonlinear algebraic equations with the Euler coefficients $\alpha_n, n = 0, 1, \dots, N$. From the solution of this system, the matrix \mathbf{A} is obtained and the solution of (1)-(2) becomes

$$y(t) \cong y_N(t) = \mathbf{E}(t) \mathbf{A} = \mathbf{T}(t) \mathbf{M}^{-1} \mathbf{A}.$$

Numerical Example

The method of this study is useful in finding the solutions of delay differential equations in terms of Euler polynomials. We illustrate it by the following example. Numerical computations have been done using Mathematica 9.

Example: We consider the Duffing equation in the following type,

$$y'(t) + 3y(t-1) - e^{-t}y^2 = 3e^{t-1}$$

under the initial conditions

$$y(0) = 1$$

exact solution is $y(t) = e^t$.

$$\sum_{k=0}^1 \sum_{j=1}^2 P_{kj}(t) y^{(k)}(\alpha_{kj}t + \beta_{kj}) = g(t) + \sum_{p=0}^1 \sum_{q=0}^p Q_{pq}(t) y^{(p)}(t) y^{(q)}(t)$$

$$\begin{aligned} & \sum_{k=0}^1 P_{k1}(t) y^{(k)}(\alpha_{k1}t + \beta_{k1}) + P_{k2}(t) y^{(k)}(\alpha_{k2}t + \beta_{k2}) \\ & = g(t) + \sum_{q=0}^0 Q_{0q}(t) y^{(0)}(t) y^{(q)}(t) + \sum_{q=0}^1 Q_{1q}(t) y^{(1)}(t) y^{(q)}(t) \end{aligned}$$

$$P_{11}(t) = 1, \alpha_{11} = 1, \beta_{11} = 0, P_{02}(t) = 3, \alpha_{02} = 1, \beta_{02} = -1, Q_{00}(t) = e^{-t}, g(t) = 3e^{t-1}$$

$$N = 2, 0 \leq t \leq 1, t_0 = 0, t_1 = \frac{1}{2}, t_2 = 1$$

$$\sum_{k=0}^1 \sum_{j=1}^2 P_{kj} \mathbf{T} S_{kj} \mathbf{B}^k \mathbf{M}^{-1} \mathbf{A} - \sum_{p=0}^1 \sum_{q=0}^p Q_{pq} \mathbf{R}_{pq} \bar{\mathbf{A}} = \mathbf{G}$$

$$P_{02} = \text{diag} \left[P_{02}(0) \quad P_{02}\left(\frac{1}{2}\right) \quad P_{02}(1) \right] = \begin{bmatrix} 3 & 0 & 0 \\ 0 & 3 & 0 \\ 0 & 0 & 3 \end{bmatrix}$$

$$P_{11} = \text{diag} \left[P_{11}(0) \quad P_{11}\left(\frac{1}{2}\right) \quad P_{11}(1) \right] = \begin{bmatrix} 1 & 0 & 0 \\ 0 & 1 & 0 \\ 0 & 0 & 1 \end{bmatrix}$$

$$B^0 = \begin{bmatrix} 1 & 0 & 0 \\ 0 & 1 & 0 \\ 0 & 0 & 1 \end{bmatrix} \quad B^1 = \begin{bmatrix} 0 & 1 & 0 \\ 0 & 0 & 2 \\ 0 & 0 & 0 \end{bmatrix}$$

$$\mathbf{T} = \begin{bmatrix} \mathbf{T}(0) \\ \mathbf{T}\left(\frac{1}{2}\right) \\ \mathbf{T}(1) \end{bmatrix} = \begin{bmatrix} 1 & 0 & 0 \\ 1 & \frac{1}{2} & \frac{1}{4} \\ 1 & 1 & 1 \end{bmatrix}$$

$$M^{-1} = \begin{bmatrix} 1 & -\frac{1}{2} & 0 \\ 0 & 1 & -1 \\ 0 & 0 & 1 \end{bmatrix}$$

$$S_{02} = S(\alpha_{02}, \beta_{02}) = S(1, -1) = \begin{bmatrix} 1 & -1 & 1 \\ 0 & 1 & -2 \\ 0 & 0 & 1 \end{bmatrix}$$

$$S_{11} = S(\alpha_{11}, \beta_{11}) = S(1, 0) = \begin{bmatrix} 1 & 0 & 0 \\ 0 & 1 & 0 \\ 0 & 0 & 1 \end{bmatrix}$$

$$W = P_{02} T S_{02} B^0 M^{-1} + P_{11} T S_{11} B^1 M^{-1} = \begin{bmatrix} 3 & -\frac{7}{2} & 5 \\ 3 & -2 & \frac{9}{4} \\ 3 & -\frac{1}{2} & 1 \end{bmatrix}$$

$$V = -(Q_{00} R_{00}), \quad Q_{00}(t) = e^{-t} \quad Q_{00} = \begin{bmatrix} Q_{00}(0) & 0 & 0 \\ 0 & Q_{00}(\frac{1}{2}) & 0 \\ 0 & 0 & Q_{00}(1) \end{bmatrix} = \begin{bmatrix} e^0 & 0 & 0 \\ 0 & e^{-\frac{1}{2}} & 0 \\ 0 & 0 & e^{-1} \end{bmatrix}$$

$$R_{00} = \begin{bmatrix} E(0) B^0 \overline{E(0) B^0} \\ E(\frac{1}{2}) B^0 \overline{E(\frac{1}{2}) B^0} \\ E(1) B^0 \overline{E(1) B^0} \end{bmatrix} = \begin{bmatrix} E(0) \overline{E(0)} \\ E(\frac{1}{2}) \overline{E(\frac{1}{2})} \\ E(1) \overline{E(1)} \end{bmatrix}$$

$$E(t) = T(t) M^{-1} = \begin{bmatrix} 1 & t & t^2 \end{bmatrix} \begin{bmatrix} 1 & -\frac{1}{2} & 0 \\ 0 & 1 & -1 \\ 0 & 0 & 1 \end{bmatrix} = \begin{bmatrix} 1 & t - \frac{1}{2} & t^2 - t \end{bmatrix} \quad E(0) = \begin{bmatrix} 1 & -\frac{1}{2} & 0 \end{bmatrix}$$

$$E(\frac{1}{2}) = \begin{bmatrix} 1 & 0 & -\frac{1}{4} \end{bmatrix} \quad E = \begin{bmatrix} \frac{1}{2} & 1 \end{bmatrix} \quad G = \begin{bmatrix} g(0) \\ g(\frac{1}{2}) \\ g(1) \end{bmatrix} = \begin{bmatrix} 3e^{-1} \\ 3e^{-\frac{1}{2}} \\ 3 \end{bmatrix}$$

$$E(0) \overline{E(0)} = \begin{bmatrix} 1 & -\frac{1}{2} & 0 \end{bmatrix} \begin{bmatrix} E(0) & 0 & 0 \\ 0 & E(0) & 0 \\ 0 & 0 & E(0) \end{bmatrix}$$

$$\begin{aligned}
 &= \begin{bmatrix} E(0) & -\frac{1}{2}E(0) & 0 \end{bmatrix} = \begin{bmatrix} 1 & -\frac{1}{2} & 0 & -\frac{1}{2} & 0 & \frac{1}{8} & 0 & 0 & 0 \end{bmatrix} \\
 E\left(\frac{1}{2}\right)\overline{E\left(\frac{1}{2}\right)} &= \begin{bmatrix} 1 & 0 & -\frac{1}{4} \end{bmatrix} \begin{bmatrix} E\left(\frac{1}{2}\right) & 0 & 0 \\ 0 & E\left(\frac{1}{2}\right) & 0 \\ 0 & 0 & E\left(\frac{1}{2}\right) \end{bmatrix} \\
 &= \begin{bmatrix} E\left(\frac{1}{2}\right) & 0 & -\frac{1}{4}E\left(\frac{1}{2}\right) \end{bmatrix} = \begin{bmatrix} 1 & 0 & -\frac{1}{4} & 0 & 0 & 0 & -\frac{1}{4} & 0 & \frac{1}{16} \end{bmatrix} \\
 E(1)\overline{E(1)} &= \begin{bmatrix} 1 & \frac{1}{2} & 0 \end{bmatrix} \begin{bmatrix} E(1) & 0 & 0 \\ 0 & E(1) & 0 \\ 0 & 0 & E(1) \end{bmatrix} \\
 &= \begin{bmatrix} E(1) & \frac{1}{2}E(1) & 0 \end{bmatrix} = \begin{bmatrix} 1 & \frac{1}{2} & 0 & \frac{1}{2} & \frac{1}{4} & 0 & 0 & 0 & 0 \end{bmatrix} \\
 R_{00} &= \begin{bmatrix} E(0)\overline{E(0)} \\ E\left(\frac{1}{2}\right)\overline{E\left(\frac{1}{2}\right)} \\ E(1)\overline{E(1)} \end{bmatrix} = \begin{bmatrix} 1 & -\frac{1}{2} & 0 & -\frac{1}{2} & 0 & \frac{1}{8} & 0 & 0 & 0 \\ 1 & 0 & -\frac{1}{4} & 0 & 0 & 0 & -\frac{1}{4} & 0 & \frac{1}{16} \\ 1 & \frac{1}{2} & 0 & \frac{1}{2} & \frac{1}{4} & 0 & 0 & 0 & 0 \end{bmatrix} \\
 V = -Q_{00}R_{00} &= \begin{bmatrix} -1 & 0 & 0 \\ 0 & -e^{-\frac{1}{2}} & 0 \\ 0 & 0 & -e^{-1} \end{bmatrix} \begin{bmatrix} 1 & -\frac{1}{2} & 0 & -\frac{1}{2} & 0 & \frac{1}{8} & 0 & 0 & 0 \\ 1 & 0 & -\frac{1}{4} & 0 & 0 & 0 & -\frac{1}{4} & 0 & \frac{1}{16} \\ 1 & \frac{1}{2} & 0 & \frac{1}{2} & \frac{1}{4} & 0 & 0 & 0 & 0 \end{bmatrix} \\
 &= \begin{bmatrix} -1 & \frac{1}{2} & 0 & \frac{1}{2} & 0 & -\frac{1}{8} & 0 & 0 & 0 \\ -e^{-\frac{1}{2}} & 0 & -\frac{1}{4}e^{-\frac{1}{2}} & 0 & 0 & 0 & \frac{1}{4}e^{-\frac{1}{2}} & 0 & -\frac{1}{16}e^{-\frac{1}{2}} \\ -e^{-1} & -\frac{1}{2}e^{-1} & 0 & -\frac{1}{2}e^{-1} & -\frac{1}{4}e^{-1} & 0 & 0 & 0 & 0 \end{bmatrix} \\
 U_0 &= \begin{bmatrix} 1 & -\frac{1}{2} & 0 \end{bmatrix} \quad O_0 \quad [\quad = \quad] \\
 WA + V\overline{A} = G &\Rightarrow [W; V; G] \quad U_0A + O_0\overline{A} = 1 \Rightarrow [U_0; O_0; 1]
 \end{aligned}$$

$$\begin{aligned}
 [W; V; G] &= \\
 \left[\begin{array}{ccc|ccc|ccc|ccc}
 3 & -\frac{7}{2} & 5 & -1 & \frac{1}{2} & 0 & \frac{1}{2} & 0 & -\frac{1}{8} & 0 & 0 & 0 & 0 \\
 3 & -2 & \frac{9}{4} & -e^{-\frac{1}{2}} & 0 & -\frac{1}{4}e^{-\frac{1}{2}} & 0 & 0 & 0 & \frac{1}{4}e^{-\frac{1}{2}} & 0 & -\frac{1}{16}e^{-\frac{1}{2}} & 3e^{-\frac{1}{2}} \\
 3 & -\frac{1}{2} & 1 & -e^{-1} & -\frac{1}{2}e^{-1} & 0 & -\frac{1}{2}e^{-1} & -\frac{1}{4}e^{-1} & 0 & 0 & 0 & 0 & 3
 \end{array} \right] \\
 [\tilde{W}; \tilde{V}; \tilde{G}] &= \\
 \left[\begin{array}{ccc|ccc|ccc|ccc}
 3 & -\frac{7}{2} & 5 & -1 & \frac{1}{2} & 0 & \frac{1}{2} & 0 & -\frac{1}{8} & 0 & 0 & 0 & 3e^{-1} \\
 3 & -2 & \frac{9}{4} & -e^{-\frac{1}{2}} & 0 & -\frac{1}{4}e^{-\frac{1}{2}} & 0 & 0 & 0 & \frac{1}{4}e^{-\frac{1}{2}} & 0 & -\frac{1}{16}e^{-\frac{1}{2}} & 3e^{-\frac{1}{2}} \\
 1 & -\frac{1}{2} & 1 & 0 & 0 & 0 & 0 & 0 & 0 & 0 & 0 & 0 & 1
 \end{array} \right]
 \end{aligned}$$

Matrix of unknown coefficients by solving this system $A = \begin{bmatrix} \frac{7}{4} & \frac{3}{2} & \frac{1}{2} \end{bmatrix}^T$ and so

$$y_2(t) = E(t)A = E_0(t)a_0 + E_1(t)a_1 + E_2(t)a_2 = 1 \cdot \frac{7}{4} + (t - \frac{1}{2}) \cdot \frac{3}{2} + (t^2 - t) \cdot \frac{1}{2} = 1 + t + \frac{t^2}{2}$$

which is exact solution expanded.

Conclusion

We have presented a collocation method based on Euler polynomial for the solutions of the High Order Delay Differential Equations with nonlinear terms. Also, by using the techniques given, the control of the solutions are performed. If the exact solution of the problem is exist as polynomial solution as example, then the exact solution can be found by this technique. It is observed that the presented technique gives good results which is too close to exact solution. Also, the proposed technique can be used to test reliability of the solutions of the other problems. Euler matrix method provides two main advantages: it is very simple to construct the main matrix equations and to do computer programming. Another considerable advantage is that computational time of the method is so short.

References

- [1] Fried I (1979) Numerical Solution of Differential Equations, Academic Press, NewYork,
- [2] Jordan DW, Smith P (2007) Nonlinear Ordinary Differential Equations: An introduction for Scientists and Engineers, 4th Edition. Oxford University Press, NewYork, 2007.
- [3] Gülsu M, Sezer M, (1996) On the Solutions of the Riccati equation by the Taylor matrix method, J. Appl. Math. 27 (6) 821-834.
- [4] Baykuş-Savaşaneril N, Sezer M (2017) Hybrid Taylor-Lucas Collocation Method for Numerical Solution of High- Order Pantograph Type Delay Differential Equations with Variables Delays Appl. Math. Inf. Sci. 11, No. 6, 1795-1801.
- [5] Baykuş-Savaşaneril N, Sezer M (2019) Lucas Matrix Method for a Class of Nonlinear Delay Fredholm Integro Differential Equations, International Conference on Mathematics
- [6] Gümgüm S, Ersoy Özdek D, Özaltun G (2019) Legendre wavelet solution of high order nonlinear ordinary delay differential equations. Turkish Journal of Mathematics, doi: 10.3906/mat-1901-109.

q-Homotopy Analysis Transform Method for Differential Equations having Quadratic Nonlinearity

Ali Konuralp*, Manisa Celal Bayar University, Dept. of Mathematics, Manisa, Türkiye
Zeyyan Öztaş, Manisa Celal Bayar University, Institute of Natural and Applied Sciences, Manisa Türkiye
*Corresponding author: ali.konuralp@cbu.edu.tr

Keywords: q-Homotopy analysis transform method, quadratic nonlinearity, numerical solutions
Discipline: Mathematics

Abstract

The paper deals with the solutions of differential equations having quadratic nonlinearity obtained by the q-homotopy analysis transform method (q-HATM). The q-HATM, combined by the q-homotopy analysis method and Laplace transform method, can be applied to a wide class of the partial and ordinary differential equations. In this study, especially Ricatti differential equation and Fisher equation which have quadratic nonlinear terms, are considered to obtain solutions from the convergent series type.

1. Introduction

The methods used to solve nonlinear differential equations are being developed, updated and edited in order to have a more effective use in terms of transaction volume. In this study, a solution algorithm based on the q-HATM to solve some differential equations having quadratic nonlinearity such as Ricatti differential equation and Fisher equation that models linear diffusion and nonlinear growth, is presented. The mentioned method is obtained by taking the Laplace transform method and applying q-homotopy analysis method [1-3] which is developed to increase the interval of the convergence of homotopy analysis method (HAM). HAM [4-6] was proposed firstly by Liao. It is independent of any small/large physical parameters. Furthermore, to control the convergence of the truncated solution series and to adjust convergence regions, the auxiliary parameter is provided. By using HAM, a nonlinear differential equation is transformed to linear differential equations so one can overcome the difficulty in the case of the strong nonlinearity by choosing auxiliary parameter appropriately. The fundamental difference of q-homotopy analysis method (q-HAM) is considering two parameters n and h as against the HAM which contains on the parameter h . The advantage of the HATM [7-8] is the ability to combine HAM and Laplace transform method for obtaining a convergent series that converges rapidly. Also, the q-HATM [9-11] is an improvement of the embedding parameter $q \in \left[0, \frac{1}{n}\right]$ in HATM. Thus, an upper convergence criterion has been introduced. For these reasons, in this study the important problems including quadratic nonlinear terms are considered to show the applicability of the q-HATM method to those equations.

2. q-Homotopy Analysis Transform Method (q-HATM)

The main theory of q-HATM has already given in many papers [9-11]. In this part we present solution methodology of q-HATM for Ricatti differential equations [12] and Fisher differential equations [13].

2.1 Applications to Ricatti Differential Equations

The Ricatti differential equation is considered of the form

$$D_x u = A(x)u^2(x) + B(x)u(x) + C(x), u(0) = u_0 \quad x_0 \leq x \leq x_1 \quad (1)$$

where $D_x u$ denotes the derivative of the function $u(x)$, $B(x)u(x) = R(u)$, $A(x)u^2(x) = N(u)$ and $C(x)$ is given function. Here, R is the linear differential operator while the nonlinear differential operator is denoted by N . Therefore Eq. (1) becomes

$$D_x u - Nu^2(x) - Ru(x) = C(x).$$

By applying Laplace transform to Eq. (1) yields

$$\begin{aligned} \mathcal{L}\{D_x u\} - \mathcal{L}\{A(x)u^2(x)\} - \mathcal{L}\{B(x)u(x)\} &= \mathcal{L}\{C(x)\} \\ s\mathcal{L}\{u\} - u(0) - \mathcal{L}\{A(x)u^2(x)\} - \mathcal{L}\{B(x)u(x)\} &= \mathcal{L}\{C(x)\} \end{aligned} \quad (2)$$

on simplification

$$\mathcal{L}\{u\} - \frac{1}{s}u_0 - \frac{1}{s}\mathcal{L}\{A(x)u^2(x) + B(x)u(x) + C(x)\} = 0. \quad (3)$$

Let $u = \phi(x, q)$ be the real function x and q , then the nonlinear operator is taken as follows

$$N[\phi(x, q)] = \mathcal{L}\{\phi(x, q)\} - \frac{1}{s}u_0 - \frac{1}{s}\mathcal{L}\{A(x)\phi^2(x, q) + B(x)\phi(x, q)\} - \frac{1}{s}\mathcal{L}\{C(x)\} \quad (4)$$

where $q \in \left[0, \frac{1}{n}\right]$ for $n \geq 1$ is embedding parameter.

Then a homotopy

$$(1 - nq)\mathcal{L}\{\phi(x, q) - u_0\} = hqH(x)N(\phi(x, q)) \quad (5)$$

is constructed where \mathcal{L} denotes Laplacian operator, $H(x)$ and h are nonzero auxiliary function and nonzero parameter respectively, $u_0(x) = u(0)$ is initial value. Putting $q = 0$ and $q = \frac{1}{n}$ to Eq. (5) gives

$$u_0 = \phi(x, 0) \text{ and } u(x) = \phi\left(x, \frac{1}{n}\right). \quad (6)$$

With the increase of q from 0 to $\frac{1}{n}$, the solution of $\phi(x, q)$ varies from initial guess u_0 to the solution $u(x)$. To have an effect of embedding parameter q on the solution function, one takes the Taylor series expansion of $\phi(x, q)$ about q , we get

$$\phi(x, q) = u_0 + \sum_{m=1}^{\infty} u_m(x)q^m \quad (7)$$

where

$$u_m(x) = \frac{1}{m!}\phi^{(m)}(x, q)\Big|_{q=0} = 0. \quad (8)$$

The convergence of series (7) can be extended by an appropriate choice of h , n and $H(x)$ in (5). If we take $q = \frac{1}{n}$ and denote the vectors u_m in (7) as

$$\vec{u}_m = \{u_0, u_1(x), u_2(x), \dots, u_m(x)\} \quad (9)$$

then

$$u(x) = u_0 + \sum_{m=1}^{\infty} u_m(x)\left(\frac{1}{n}\right)^m. \quad (10)$$

So, the Eq. (5) becomes

$$\begin{aligned} (1 - nq)\mathcal{L}\left\{u_0 + \sum_{m=1}^{\infty} u_m(x)q^m - u_0\right\} &= hqH(x)N\left(u_0 + \sum_{m=1}^{\infty} u_m(x)q^m\right) \\ (1 - nq)\mathcal{L}\left\{\sum_{m=1}^{\infty} u_m(x)q^m\right\} &= hqH(x)\mathcal{L}\left\{u_0 + \sum_{m=1}^{\infty} u_m(x)q^m\right\} - \frac{1}{s}u_0 - \frac{1}{s}\mathcal{L}\{A(x)\phi^2(x, q) + B(x)\phi(x, q)\} \\ &\quad - \frac{1}{s}\mathcal{L}\{C(x)\} \end{aligned}$$

Taking the m^{th} derivative of (5) with respect to q and dividing those by $m!$ while $q = 0$, we obtain m^{th} order deformation which is given by

$$\mathcal{L}[u_m(x) - k_m u_{m-1}(x)] = hH(x)\mathfrak{R}_m(\vec{u}_{m-1}). \quad (11)$$

and by taking inverse Laplace transform method we get

$$u_m(x) = k_m u_{m-1}(x) + h\mathcal{L}^{-1}[H(x)\mathfrak{R}_m(\vec{u}_{m-1})] \quad (12)$$

where

$$\mathfrak{R}_m(\vec{u}_{m-1}) = \frac{1}{(m-1)!} \frac{\partial^{m-1} N[\phi(x, q)]}{\partial q^{m-1}} \Big|_{q=0} \quad (13)$$

and

$$k_m = n \text{ for } m > 1 \text{ and } k_m = 0 \text{ otherwise.} \quad (14)$$

2.2 Applications to Fisher Equations

The following dimensionless equation involves the linear diffusion and nonlinear growth the model is

$$u_t(x, t) = u_{xx} + \alpha(1 - u^\beta(x, t))u(x, t) - a \quad (15)$$

where α , β and a are constants.

If $a = 0$, $\alpha = 1$ and $\beta = 1$ then we have the logistic growth-diffusion process in the form.

$$u_t = u_{xx} + u(1 - u), \quad x \in \mathbb{R}, \quad t > 0 \quad (16)$$

with given condition $u(x, 0) = u_0(x)$

Starting to take the Laplace transform of Eq. (16) leads to the following algebraic equation

$$\begin{aligned} \mathcal{L}\{u_t\} &= \mathcal{L}\{u_{xx} + u(1 - u)\} \\ s\mathcal{L}\{u\} - u_0(x, 0) &= \mathcal{L}\{u_{xx}\} + \mathcal{L}\{u(1 - u)\} \\ \mathcal{L}\{u\} - \frac{1}{s}u_0(x, 0) &= \frac{1}{s}\mathcal{L}\{u_{xx}\} + \frac{1}{s}\mathcal{L}\{u(1 - u)\}. \end{aligned} \quad (17)$$

Therefore, we choose the nonlinear operator as

$$N[\phi(x, t; q)] = \mathcal{L}\{\phi(x, t; q)\} - \left(1 - \frac{k_m}{n}\right)\frac{u_0}{s} - \frac{1}{s}\mathcal{L}\{\phi_{xx}(x, t; q) + \phi(x, t; q)(1 - \phi(x, t; q))\} \quad (18)$$

where $q \in \left[0, \frac{1}{n}\right]$ for $n \geq 1$ is embedding parameter and $\phi(x, t; q)$ is real function of x, t and q and construct a homotopy as

$$(1 - qn)\mathcal{L}\{\phi(x, t; q) - u_0(x, t)\} = hqH(x, t)N[\phi(x, t; q)] \quad (19)$$

where \mathcal{L} denotes Laplacian operator, $H(x)$ and h are nonzero auxiliary function and nonzero parameter respectively. m^{th} order deformation equation is

$$\mathcal{L}\{u_m(x, t) - k_m u_{m-1}(x, t)\} = h\mathfrak{R}_m(\vec{u}_{m-1}) \quad (20)$$

where

$$u_m(x, t) = \frac{1}{m!} + \left. \frac{\partial^m \phi(x, t; q)}{\partial q^m} \right|_{q=0} \quad (21)$$

and

$$\mathfrak{R}_m(\vec{u}_{m-1}) = \left. \frac{1}{(m-1)!} \frac{\partial^{m-1} N[\phi(x, t; q)]}{\partial q^{m-1}} \right|_{q=0}. \quad (22)$$

The truncated series

$$\sum_{m=1}^{\infty} u_m(x, t) \left(\frac{1}{n}\right)^m \quad (23)$$

is the appropriate solution of $u(x, t)$.

Thus

$$\begin{aligned} \mathfrak{R}_m(\vec{u}_{m-1}) &= \mathcal{L}\{u_{m-1}\} - \left(1 - \frac{k_m}{n}\right)\frac{u_0}{s} - \frac{1}{s}\mathcal{L}\left\{u_{m-1} - \sum_{i=0}^{m-1} u_{m-1-i} u_i\right\} \end{aligned} \quad (24)$$

and taking inverse Laplace transformation of Eq. (24) yields the components of vectors

$$u_m(x, t) = k_m u_{m-1}(x, t) + h\mathcal{L}^{-1}\mathfrak{R}_m(\vec{u}_{m-1}). \quad (25)$$

3. Numerical Examples

Example 1:

Consider the following Riccati differential equation

$$D_x u = 2u(x) - u^2(x) + 1 \quad (26)$$

subject to $u(0) = 0$ where the exact solution of Eq. (26) is

$$u = 1 + \sqrt{2} \tan h + \left(\sqrt{2x} + \left(\frac{1}{2}\right) \log\left(\frac{\sqrt{2}-1}{\sqrt{2}+1}\right)\right) \quad (27)$$

By taking Laplace transform on both sides of Eq. (26), we obtain

$$\mathcal{L}\{u\} + \frac{1}{s}\mathcal{L}\{2u(x)\} - \frac{1}{s}\mathcal{L}\{u^2(x)\} + \frac{1}{s}\mathcal{L}\{1\} = 0. \quad (28)$$

Choosing $u = \phi(x, q)$, N can be written as

$$N[\phi(x, q)] = \mathcal{L}\{\phi(x, q)\} + \frac{1}{s}\mathcal{L}\{2\phi(x, q)\} - \frac{1}{s}\mathcal{L}\{\phi(x, q)^2\} + \frac{1}{s}\mathcal{L}\{1\} \quad (29)$$

where $q \in \left[0, \frac{1}{n}\right]$. For this example, the homotopy can be constructed as

$$\begin{aligned} (1 - nq)\mathcal{L}\{\phi(x, q) - u_0\} &= hqH(x)N(\phi(x, q)) \\ (1 - nq)\mathcal{L}\{\phi(x, q) - u_0\} &= hqH(x)\mathcal{L}\{\phi(x, q)\} + \frac{1}{s}\mathcal{L}\{2\phi(x, q)\} - \frac{1}{s}\mathcal{L}\{\phi(x, q)^2\} + \frac{1}{s}\mathcal{L}\{1\} \end{aligned} \quad (30)$$

where \mathcal{L} denotes Laplacian operator, $n \geq 1$, $q \in \left[0, \frac{1}{n}\right]$ is embedding parameter, $H(x) = 1$ auxiliary function, $h \neq 0$ is an auxiliary parameter, $u_0(x) = u(0)$ is initial value and $\phi(x, q)$ is an unknown function.

The series solution of Eq. (26) is given by Eq. (9). For this problem the truncation order is chosen as to be 7 which gives the seventh order polynomial solution. Then the deformation equation of order m is

$$\mathcal{L}[u_m(x) - k_m u_{m-1}(x)] = hH(x)\mathfrak{R}_m(\vec{u}_{m-1}), \quad 0 \leq m \leq 7. \quad (31)$$

The inverse Laplace transform is applied to Eq. (31) and we have

$$u_m(x) = k_m u_{m-1}(x) + h\mathcal{L}^{-1}[\mathfrak{R}_m(\vec{u}_{m-1})], \quad 0 \leq m \leq 7. \quad (32)$$

Consequently, the first seven term of q-HATM series approximate solutions

$$\begin{aligned} u_0(x) &= 0 \\ u_1(x) &= -hx \\ u_2(x) &= -hx(1 + h + n - hx) \\ u_3(x) &= -\frac{1}{3}hx(3(1 + n + n^2) - 3h(1 + 2n)(-1 + x) + h^2(3 - 6x + x^2)) \\ u_4(x) &= -\frac{1}{3}hx \left(3(1 + n + n^2 + n^3) - 3h(1 + 2n + 3n^2)(-1 + x) + h^3(3 - 9x + 3x^2 + x^3) \right. \\ &\quad \left. + 3h^2(1 - 2x + n(3 - 6x + x^2)) \right) \\ u_5(x) &= \frac{1}{15}hx(-15(1 + n + n^2 + n^3 + n^4) + 15h(1 + 2n + 3n^2 + 4n^3)(-1 + x) + h^4(-15 \\ &\quad + 60x - 30x^2 - 20x^3 + 7x^4) - 5h^2(3 + n(9 - 18x) - 6x - x^2 + 6n^2(3 - 6x \\ &\quad + x^2)) - 5h^3(3(1 - 3x + x^3) + 4n(3 - 9x + 3x^2 + x^3))) \\ u_6(x) &= -\frac{1}{45}hx(45(1 + n + n^2 + n^3 + n^4 + n^5) - 45h(1 + 2n + 3n^2 + 4n^3 + 5n^4)(-1 + x) \\ &\quad + h^5(45 - 225x + 150x^2 + 150x^3 - 105x^4 + 7x^5) + 15h^2(3 + n^2(18 - 36x) \\ &\quad - 6x - 2x^2 + 10n^3(3 - 6x + x^2) - 3n(-3 + 6x + x^2)) + 15h^3(3 - 9x - 3x^2 \\ &\quad + 5x^3 + 12n(1 - 3x + x^3) + 10n^2(3 - 9x + 3x^2 + x^3)) - 3h^4(-15 + 60x \\ &\quad - 60x^3 + 14x^4 + 5n(-15 + 60x - 30x^2 - 20x^3 + 7x^4))) \\ u_7(x) &= -h(1 + n + n^2 + n^3 + n^4 + n^5 + n^6)x + h^2(1 + 2n + 3n^2 + 4n^3 + 5n^4 + 6n^5)(-1 \\ &\quad + x)x + h^7(-x + 6x^2 - 5x^3 - \frac{20x^4}{3} + 7x^5 - \frac{14x^6}{15} - \frac{53x^7}{315}) + h^3x(-1 + 2x + x^2 \\ &\quad + 10n^3(-1 + 2x) - 5n^4(3 - 6x + x^2) + 2n^2(-3 + 6x + x^2) + n(-3 + 6x \\ &\quad + 2x^2)) - \frac{1}{3}h^4x(3 - 9x - 6x^2 + 7x^3 + 30n^2(1 - 3x + x^3) + 20n^3(3 - 9x + 3x^2 \\ &\quad + x^3) + 4n(3 - 9x - 3x^2 + 5x^3)) + \frac{1}{15}h^5x(-15 + 60x + 30x^2 - 100x^3 + 19x^4 \\ &\quad + 15n^2(-15 + 60x - 30x^2 - 20x^3 + 7x^4) + 5n(-15 + 60x - 60x^3 + 14x^4)) \\ &\quad - \frac{1}{45}h^6x(45 - 225x + 450x^3 - 210x^4 - x^5 + 6n(45 - 225x + 150x^2 + 150x^3 \\ &\quad - 105x^4 + 7x^5))) \end{aligned}$$

Therefore, we obtain the series solution (9) as

$$\begin{aligned} u(x) &= u_0(x) + \sum_{i=1}^7 u_i(x) \left(\frac{1}{n}\right)^m \\ &= -\frac{1}{315n^7}hx(315(1 + 2n + 3n^2 + 4n^3 + 5n^4 + 6n^5 + 7n^6) - 315h(1 + 3n \\ &\quad + 6n^2 + 10n^3 + 15n^4 + 21n^5)(-1 + x) + h^6(315 - 1890x + 1575x^2 + 2100x^3 \\ &\quad - 2205x^4 + 294x^5 + 53x^6) + 105h^2(-60n^3(-1 + 2x) + 35n^4(3 - 6x + x^2) \\ &\quad - 3(-1 + 2x + x^2) - 10n^2(-3 + 6x + x^2) - 4n(-3 + 6x + 2x^2)) + 105h^3(3 \\ &\quad - 9x - 6x^2 + 7x^3 + 45n^2(1 - 3x + x^3) + 35n^3(3 - 9x + 3x^2 + x^3) + 5n(3 - 9x \\ &\quad - 3x^2 + 5x^3)) - 21h^4(-15 + 60x + 30x^2 - 100x^3 + 19x^4 + 21n^2(-15 + 60x \\ &\quad - 30x^2 - 20x^3 + 7x^4) + 6n(-15 + 60x - 60x^3 + 14x^4)) + 7h^5(45 - 225x \\ &\quad + 450x^3 - 210x^4 - x^5 + 7n(45 - 225x + 150x^2 + 150x^3 - 105x^4 + 7x^5))) \end{aligned}$$

This truncated series has two parameters h and n that can be chosen as to adjust and control the convergence region of it. From Figure 1 it can be seen that the approximate solution agrees with the exact solution for the neighborhood of the value $h = -4.219882$, $n = 12$. Figure 2 shows the graph of the absolute error $e_7(x)$ that is the absolute value of the difference between the exact solution and the approximate solution $u_7(x)$ as $e_7(x) = |\text{Exact solution} - u_7(x)|$. The errors are getting bigger on the right side of the interval of x .

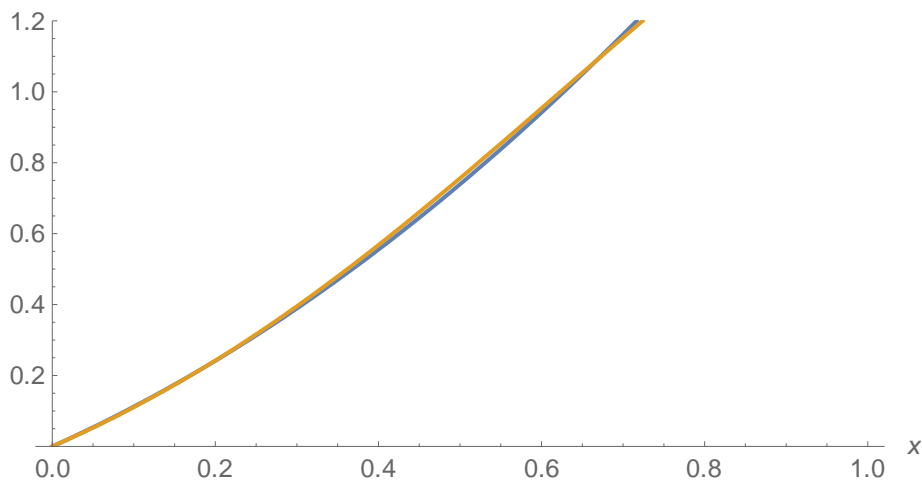


Figure 1. Comparison of the exact solution (yellow curve) and the approximate solution (blue curve) for $h = -4.219882751999999$, $n = 12$.

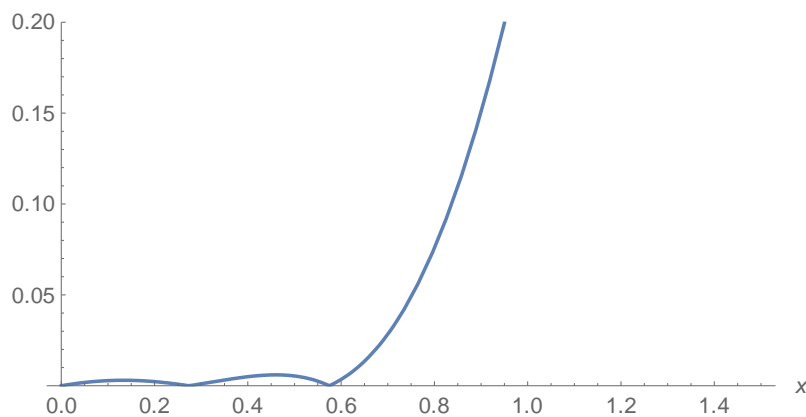


Figure 2. The error function $e_7(x)$ for $h = -4.429912637439997$, $n = 12$

Example 2:

Consider again the Fisher equation that is given by Eq. (15). According to the solution procedure given in Section 3.2, by using the formula (25) we have

$$u_m(x) = k_m u_{m-1}(x) + h\mathcal{L}^{-1}[\mathfrak{R}_m(\bar{u}_{m-1})], \quad 0 \leq m \leq 5 \quad (33)$$

as the first five terms of q-HATM series that are the terms of the approximate solution of Eq (16) are

$$u_0(x) = \lambda$$

$$u_1(x) = h(2 + t(-1 + \lambda))\lambda$$

$$u_2(x) = \frac{1}{2}h\lambda(2n(2 + t(-1 + \lambda)) + h(4 + 2t(-3 + 5\lambda) + t^2(1 - 3\lambda + 2\lambda^2)))$$

$$u_3(x) = \frac{1}{6}h\lambda(6n^2(2 + t(-1 + \lambda)) + 6hn(4 + 2t(-3 + 5\lambda) + t^2(1 - 3\lambda + 2\lambda^2)) + h^2(12 + 6t(-5 + 13\lambda) + 6t^2(2 - 9\lambda + 8\lambda^2) + t^3(-1 + 7\lambda - 12\lambda^2 + 6\lambda^3)))$$

$$\begin{aligned}
 u_4(x) &= \frac{1}{24}h\lambda(24n^3(2 + t(-1 + \lambda)) + 36hn^2(4 + 2t(-3 + 5\lambda) + t^2(1 - 3\lambda + 2\lambda^2)) \\
 &\quad + 12h^2n(12 + 6t(-5 + 13\lambda) + 6t^2(2 - 9\lambda + 8\lambda^2) + t^3(-1 + 7\lambda - 12\lambda^2 + 6\lambda^3)) \\
 &\quad + h^3(48 + 24t(-7 + 25\lambda) + 36t^2(3 - 19\lambda + 22\lambda^2) + 4t^3(-5 + 49\lambda - 108\lambda^2 \\
 &\quad + 66\lambda^3) + t^4(1 - 15\lambda + 50\lambda^2 - 60\lambda^3 + 24\lambda^4))) \\
 u_5(x) &= hn^4(2 + t(-1 + \lambda))\lambda + 2h^2n^3\lambda(4 + 2t(-3 + 5\lambda) + t^2(1 - 3\lambda + 2\lambda^2)) \\
 &\quad + h^3n^2\lambda(12 + 6t(-5 + 13\lambda) + 6t^2(2 - 9\lambda + 8\lambda^2) + t^3(-1 + 7\lambda - 12\lambda^2 + 6\lambda^3)) \\
 &\quad + \frac{1}{6}h^4n\lambda(48 + 24t(-7 + 25\lambda) + 36t^2(3 - 19\lambda + 22\lambda^2) \\
 &\quad + 4t^3(-5 + 49\lambda - 108\lambda^2 + 66\lambda^3) + t^4(1 - 15\lambda + 50\lambda^2 - 60\lambda^3 + 24\lambda^4)) \\
 &\quad + \frac{1}{120}h^5\lambda(240 + 120t(-9 + 41\lambda) + 240t^2(4 - 33\lambda + 48\lambda^2) \\
 &\quad + 40t^3(-7 + 91\lambda - 252\lambda^2 + 186\lambda^3) + 10t^4(3 - 60\lambda + 250\lambda^2 - 360\lambda^3 + 168\lambda^4) \\
 &\quad + t^5(-1 + 31\lambda - 180\lambda^2 + 390\lambda^3 - 360\lambda^4 + 120\lambda^5)).
 \end{aligned}$$

Therefore, we obtain the series solution (23) as

$$\begin{aligned}
 u(x) &= u_0(x) + \sum_{i=1}^5 u_i(x) \left(\frac{1}{n}\right)^m \\
 &= \frac{1}{120n^5}\lambda(120n^5 + 600hn^4(2 + t(-1 + \lambda)) + 600h^2n^3(4 + 2t(-3 + 5\lambda) + t^2(1 \\
 &\quad - 3\lambda + 2\lambda^2)) + 200h^3n^2(12 + 6t(-5 + 13\lambda) + 6t^2(2 - 9\lambda + 8\lambda^2) + t^3(-1 + 7\lambda \\
 &\quad - 12\lambda^2 + 6\lambda^3)) + 25h^4n(48 + 24t(-7 + 25\lambda) + 36t^2(3 - 19\lambda + 22\lambda^2) \\
 &\quad + 4t^3(-5 + 49\lambda - 108\lambda^2 + 66\lambda^3) + t^4(1 - 15\lambda + 50\lambda^2 - 60\lambda^3 + 24\lambda^4)) \\
 &\quad + h^5(240 + 120t(-9 + 41\lambda) + 240t^2(4 - 33\lambda + 48\lambda^2) + 40t^3(-7 + 91\lambda \\
 &\quad - 252\lambda^2 + 186\lambda^3) + 10t^4(3 - 60\lambda + 250\lambda^2 - 360\lambda^3 + 168\lambda^4) + t^5(-1 + 31\lambda \\
 &\quad - 180\lambda^2 + 390\lambda^3 - 360\lambda^4 + 120\lambda^5)))
 \end{aligned}$$

This truncated series has two parameters h and n that can be chosen as to adjust and control the convergence region of it. If we choose $h = -1$ and $n = 1$, then we have the exact solution of the problem as

$$\begin{aligned}
 &\lambda - t(-1 + \lambda)\lambda + \frac{1}{2}t^2\lambda(1 - 3\lambda + 2\lambda^2) - \frac{1}{6}t^3\lambda(-1 + 7\lambda - 12\lambda^2 + 6\lambda^3) + \frac{1}{24}t^4\lambda(1 - 15\lambda + \\
 &\quad 50\lambda^2 - 60\lambda^3 + 24\lambda^4) - \frac{1}{120}t^5\lambda(-1 + 31\lambda - 180\lambda^2 + 390\lambda^3 - 360\lambda^4 + 120\lambda^5).
 \end{aligned}$$

Our solution is also agree with the solution that is obtained by using Fourier transform Homotopy Perturbation method in [13].

4. Conclusions

We achieved to get numerical solutions of the Ricatti and Fisher equations successfully by using the q-homotopy analysis transform method. The Ricatti differential equation and The Fisher equation that models the logistic growth-diffusion process subject to some initial conditions are considered because of having the quadratic nonlinear terms. The obtained solutions showed that the equations having quadratic nonlinearities can be solved exactly and approximately. The approximate solutions can be obtained in the form of semi-analytical function. These solutions are the functions of h and n ($n \geq 1$) that allows us to adjust and control the convergence of the series solutions.

References

- [1] El-Tawil MA, Huseen SN (2012) The q-homotopy analysis method (q-HAM). Int. J. Appl. Math. Mech 8(15), 51-75.
- [2] El-Tawil MA, Huseen SN (2013) On the convergence of the q-homotopy analysis method. Int. J. Appl. Contempt. Math. Sci 8:481-497.

3rd International Students Science Congress
3-4 May 2019, İzmir - Turkey

- [3] Iyiola O, Soh MA, Enyi CD (2013) Generalised homotopy analysis method (q-HAM) for solving foam drainage equation of time fractional type, *Journal Mesa* 4(4)Ç 429-440.
- [4] Liao SJ (2003) *Beyond Perturbation: Introduction to Homotopy Analysis Method*. Chapman & Hall/CRC Press, Boca Raton, FL.
- [5] Chen YM, Liu JK (2010) Homotopy analysis method for limit cycle oscillations of an airfoil with cubic nonlinearities. *Journal of Vibration and Control*, 16(2): 163-179.
- [6] Liao SJ (2010) On the relationship between the homotopy analysis method and Euler transform. *Commun Nonlinear Sci Numer Simulat*, 15:1421-1431.
- [7] Khana M, Gondal MA, Hussain I, Vanani SK (2012) A new comparative study between homotopy analysis transform method and homotopy perturbation transform method on a semi-infinite domain. *Mathematical and Computer Modelling*, 55(3-4): 1143-1150.
- [8] Gondal MA, Arife AS, Khan M, Hussain I (2011) An Efficient Numerical Method for Solving Linear and Nonlinear Partial Differential Equations by Combining Homotopy Analysis and Transform Method. *World Applied Sciences Journal* 14(12): 1786-1791.
- [9] Singh J, Kumar D, Swroop R (2016) Numerical solution of time-and space-fractional coupled Burger's equations via homotopy algorithm. *Alexandria Engineering Journal*, 55:1753-1763.
- [10] Prakash A, Kaur H (2018) q-homotopy analysis transform method for space and time-fractional KdV-Burgers equation. *Nonlinear Sci. Lett. A*, 9(1):44-61.
- [11] Kumar D, Singh J, Baleanu D (2017) A new analysis for fractional model of regularized long-wave equation arising in ion acoustic plasma. *Mathematical Methods in the Applied Sciences*, 40(15), 5642-5653.
- [12] Saad KM, Al-Shomrani AA (2016) An application of homotopy analysis transform method for Riccati differential equation of fractional order. *Journal of Fractional Calculus and Applications*. 7(1): 61-72.
- [13] Abbaszadeh M, Nourazar S (2017) An Application of the Fourier Transform Homotopy Perturbation Method for the Solution of Nonlinear Fisher Equation. *Mechanics Letters*. 1:14-22.

Recent Results on Topologic and Geometric Properties of Fractional Difference Sequence Spaces

Faruk Özger*

İzmir Kâtip Çelebi Univ., Dept. of Engineering Sciences, Çiğli Main Campus, İzmir, Türkiye

*Corresponding author: farukozger@gmail.com

Keywords: fractional spaces, difference sequence spaces, matrix transformations

Discipline: Mathematics

1. Introduction

The gamma function of a real number x is defined by an improper integral:

$$\Gamma(x) = \int_0^{\infty} e^{-t} t^{x-1} dt.$$

The fractional difference operator for a fraction $\tilde{\alpha}$ was defined in [1] as

$$\Delta^{(\tilde{\alpha})}(x_k) = \sum_{i=0}^{\infty} (-1)^i \frac{\Gamma(\tilde{\alpha}+1)}{i! \Gamma(\tilde{\alpha}-i+1)} x_{k-i}.$$

Let m be a positive integer, then recall the difference operators $\Delta^{(1)}$ and $\Delta^{(m)}$ are defined by:

$$(\Delta^{(1)}x)_k = \Delta^{(1)}x_k = x_k - x_{k-1}$$

and

$$(\Delta^{(m)}x)_k = \sum_{i=0}^m (-1)^i \binom{m}{i} x_{k-i}.$$

We write Δ and $\Delta^{(m)}$ for the matrices with $\Delta_{nk} = (\Delta^{(1)}e^{(k)})_n$ and $\Delta_{nk}^{(m)} = (\Delta^{(m)}e^{(k)})_n$ for all n and k . The topological properties of some spaces that are constructed by the matrix operator $\Delta^{(m)}$ were studied in the paper [2]. Some identities and estimates for the Hausdorff measure of noncompactness of matrix operators from $\Delta^{(m)}$ -type spaces into the sets of bounded ℓ_{∞} , convergent c , null sequences c_0 and also absolutely convergent series were established in [2].

In this survey work, we consider some recent studies [4-6] about fractional sets of sequences and focus on the topologic and geometric properties of them.

We give the needed definitions and notations.

The β dual of a set X is defined by

$$X^{\beta} = \{a \in \omega : a \cdot x \in cs \text{ for all } x \in X\}.$$

Note that $c_0^{\beta} = c^{\beta} = \ell_{\infty}^{\beta} = \ell_1$ and $\ell_p^{\beta} = \ell_q$. Here q is the conjugate of p , it means $q = p/(p-1)$ for $1 < p < \infty$, $q = \infty$ for $p = 1$ and $q = 1$ for $p = \infty$.

Given any infinite matrix $A = (a_{nk})_{n,k=0}^{\infty}$ of complex numbers and any sequence x , we write $A_n = (a_{nk})_{k=0}^{\infty}$ for the sequence in the n^{th} row of A , $A_n x = \sum_{k=0}^{\infty} a_{nk} x_k$ ($n = 0, 1, \dots$) and $Ax = (A_n x)_{n=0}^{\infty}$, provided $A_n \in X^{\beta}$ for all n .

If X and Y are subsets of ω , then

$$X_A = \{x \in \omega : Ax \in X\}$$

denotes the matrix domain of A in X and (X, Y) is the class of all infinite matrices that map X into Y ; so $A \in (X, Y)$ if and only if $X \subset Y_A$.

An infinite matrix $T = (t_{nk})$ is called a triangle if $t_{nn} \neq 0$ and $t_{nk} = 0$ for all $k > n$. We denote its inverse by S . A BK space is a Banach space with continuous coordinates. A BK space X is said to have AK if every sequence $x \in X$ has the unique representation $x = \sum_k x_k e^{(k)}$.

We consider the following fractional difference sets of sequences for $1 \leq p < \infty$ in [4,5]:

$$\begin{aligned} c_0(\Delta^{(\alpha)}) &= \{\rho \in \omega : \lim_k \Delta^{(\alpha)}(\rho_k) = 0\}, \\ c(\Delta^{(\alpha)}) &= \{\rho \in \omega : \lim_k \Delta^{(\alpha)}(\rho_k) \text{ exists}\}, \\ \ell_{\infty}(\Delta^{(\alpha)}) &= \{\rho \in \omega : \sup_k |\Delta^{(\alpha)}(\rho_k)| < \infty\}, \end{aligned}$$

$$\ell_p(\Delta(\tilde{\alpha})) := \left\{ x = (x_k) \in \omega : \sum_{n=0}^{\infty} \left| \sum_{i=0}^{\infty} (-1)^i \frac{\Gamma(\tilde{\alpha} + 1)}{i! \Gamma(\tilde{\alpha} - i + 1)} x_{n-i} \right|^p < \infty \right\}.$$

2. Main Results

Theorem 2.1 [5] We have

• $a \in (c_0(\Delta(\alpha)))^\beta$ if and only if

$$\sum_k \left| \sum_{j=k}^{\infty} (-1)^{j-k} \frac{\Gamma(-\alpha+1)}{(j-k)! \Gamma(-\alpha-j+k+1)} a_j \right| < \infty \quad (2.1)$$

and

$$\sup_l \left(\sum_{k=0}^n \left| \sum_{j=l}^{\infty} (-1)^{j-k} \frac{\Gamma(-\alpha+1)}{(j-k)! \Gamma(-\alpha-j+k+1)} a_j \right| \right) < \infty; \quad (2.2)$$

furthermore, if $a \in (c_0(\Delta(\alpha)))^\beta$ then $\forall \rho \in c_0(\Delta(\alpha))$ we have

$$\sum_k a_k \rho_k = \sum_k \left(\sum_{j=k}^{\infty} (-1)^{j-k} \frac{\Gamma(-\alpha+1)}{(j-k)! \Gamma(-\alpha-j+k+1)} a_j \right) \sigma_k.$$

• $a \in (c(\Delta(\tilde{\alpha})))^\beta$ if and only if (2.1), (2.2) and

$$\lim_l \sum_{k=0}^l \left(\sum_{j=l}^{\infty} (-1)^{j-k} \frac{\Gamma(-\alpha+1)}{(j-k)! \Gamma(-\alpha-j+k+1)} a_j \right) = \rho; \quad (2.4)$$

furthermore, if $a \in (c(\Delta(\alpha)))^\beta$ then $\forall \rho \in c(\Delta(\alpha))$ we have

$$\sum_k a_k \rho_k = \sum_k \left(\sum_{j=k}^{\infty} (-1)^{j-k} \frac{\Gamma(-\alpha+1)}{(j-k)! \Gamma(-\alpha-j+k+1)} a_j \right) \sigma_k - \rho \lim_k \sigma_k.$$

• $a \in (\ell_\infty(\Delta(\tilde{\alpha})))^\beta$ if and only if (2.1) and

$$\lim_l \sum_{k=0}^l \left| \sum_{j=l}^{\infty} (-1)^{j-k} \frac{\Gamma(-\alpha+1)}{(j-k)! \Gamma(-\alpha-j+k+1)} a_j \right| = 0;$$

furthermore, if $a \in (\ell_\infty(\Delta(\alpha)))^\beta$ then (2.4) holds $\forall \rho \in \ell_\infty(\Delta(\alpha))$.

Theorem 2.2 [5] The operator norm of the set $c(\Delta(\tilde{\alpha}))$ is given.

• Let $A \in (c(\Delta(\alpha)), \mu)$, where μ is any of the spaces c_0 , c or ℓ_∞ . Then we have

$$\|L_A\| =$$

$$\sup_n \left(\sum_k \left| \sum_{j=k}^{\infty} (-1)^{j-k} \frac{\Gamma(-\alpha+1)}{(j-k)! \Gamma(-\alpha-j+k+1)} a_{nj} \right| + |\gamma_n| \right),$$

where $\gamma_n = \lim_m \sum_{k=0}^m \psi_{mk}^{(A_n)} c$ for $n = 0, 1, \dots$

• Let $A \in (c(\Delta(\alpha)), \ell_1)$ and $\Omega_2 = \|A\|_{(c(\Delta(\alpha)), 1)}$. Then we have $\Omega_2 \leq \|L_A\| \leq 4\Omega_2$, where

$$\Omega_2 = \sup_{\substack{N \subset \mathbb{N} \\ N \text{ finite}}} \left(\sum_k \left| \sum_{n \in N} \sum_{j=k}^{\infty} (-1)^{j-k} \frac{\Gamma(-\alpha+1)}{(j-k)! \Gamma(-\alpha-j+k+1)} a_{nj} \right| + \left| \sum_{n \in N} \gamma_n \right| \right).$$

Theorem 2.3 [4] If $a = (a_k) \in (\ell_p(\Delta(\tilde{\alpha})))^\beta$, then $\bar{a} = (\bar{a}_k) \in \ell_q$ and the equality

$$\sum_{k=0}^{\infty} a_k x_k = \sum_{k=0}^{\infty} \bar{a}_k y_k$$

is satisfied for every $x = (x_k) \in \ell_p(\Delta(\tilde{\alpha}))$, where $1 \leq p \leq \infty$ and

$$\bar{a}_k = \sum_{i=k}^{\infty} (-1)^{i-k} \frac{\Gamma(-\tilde{\alpha}+1)}{(i-k)! \Gamma(-\tilde{\alpha}-i+k+1)} a_i.$$

Let us now denote $S = S_{\ell_p}$ and $\hat{S} = S_{\ell_p(\Delta(\tilde{\alpha}))}$ for the sake of brevity.

Theorem 2.4 [4] Let $1 \leq p < \infty$ and $\bar{a} = (\bar{a}_k)$ be defined as in Eq. (2.3), then we have

$$\|a\|_{\ell_p^*(\Delta(\tilde{\alpha}))} = \|\bar{a}\|_{\ell_q} = \begin{cases} \left(\sum_{k=0}^{\infty} |\bar{a}_k|^q \right)^{\frac{1}{q}} & (1 < p < \infty), \\ \sup_k |\bar{a}_k| & (p = 1), \end{cases}$$

for all $a = (a_k) \in (\ell_p(\Delta(\tilde{\alpha})))^\beta$.

Theorem 2.5 [5] Let $\lambda = c_0(\Delta^{(\alpha)})$ or $\lambda = \ell_\infty(\Delta^{(\alpha)})$.

• Let $\mu = c_0, c, \ell_\infty$. If $A \in (\lambda_T, \mu)$ then, putting

$$\|A\|_{(\lambda_T, \infty)} = \sup_n \sum_k \left| \sum_{j=k}^{\infty} (-1)^{j-k} \frac{\Gamma(-\alpha + 1)}{(j-k)! \Gamma(-\alpha - j + k + 1)} a_{nj} \right|,$$

we have $\|L_A\| = \|A\|_{(\lambda_T, \infty)}$.

• If $A \in (\lambda_T, \ell_1)$ and $\Omega_1 = \|A\|_{(\lambda_T, 1)}$. Then we have $\Omega_1 \leq \|L_A\| \leq 4\Omega_1$, where

$$\Omega_1 = \sup_{\substack{N \subset \mathbb{N} \\ N\text{-finite}}} \sum_k \left| \sum_{n \in N} \sum_{j=k}^{\infty} (-1)^{j-k} \frac{\Gamma(-\alpha + 1)}{(j-k)! \Gamma(-\alpha - j + k + 1)} a_{nj} \right|.$$

Theorem 2.6 [4] Let A be in any of the classes $(\ell_p(\Delta^{(\tilde{\alpha})}), c_0)$, $(\ell_p(\Delta^{(\tilde{\alpha})}), c)$ or $(\ell_p(\Delta^{(\tilde{\alpha})}), \ell_\infty)$, then

$$\|L_A\| = \|A\|_{(\ell_p(\Delta^{(\tilde{\alpha})}), \ell_\infty)},$$

where $1 \leq p < \infty$ and

$$\|A\|_{(\ell_p(\Delta^{(\tilde{\alpha})}), \ell_\infty)} = \sup_n (\sum_{k=0}^{\infty} |\hat{a}_{nk}|^q)^{\frac{1}{q}} < \infty.$$

Theorem 2.7 [4] Let $1 \leq p < \infty$ and $A \in (\ell_p(\Delta^{(\tilde{\alpha})}), \ell_1)$, then

$$\|A\|_{(\ell_p(\Delta^{(\tilde{\alpha})}), \ell_1)} \leq \|L_A\| \leq 4 \cdot \|A\|_{(\ell_p(\Delta^{(\tilde{\alpha})}), \ell_1)},$$

where

$$\|A\|_{(\ell_p(\Delta^{(\tilde{\alpha})}), \ell_1)} = \sup_{N \in \mathcal{F}} (\sum_{k=0}^{\infty} |\sum_{n \in N} \hat{a}_{nk}|) < \infty.$$

The geometric properties of an ℓ_p type fractional difference sequence space is considered in [3]. We only give the main theorems without proof:

Theorem 2.6 [3] Defined ℓ_p type fractional difference sequence space is rotunt if and only if $p \leq 1$.

Theorem 2.7 [3] Defined ℓ_p type fractional difference sequence space has H property

Theorem 2.8 [3] Defined ℓ_p type fractional difference sequence space is k uniformly convex.

Theorem 2.9 [3] Defined ℓ_p type fractional difference sequence space has beta property.

Theorem 2.10 [3] Defined ℓ_p type fractional difference sequence space has Opial property.

References

- [1] Baliarsingh P (2015) Some new difference sequence spaces of fractional order and their dual spaces, Appl. Math. Comput., 219(18), 9737–9742.
- [2] Çolak R, Et M (1997) On some generalized difference sequence spaces and related matrix transformations, Hokkaido Math. J. 26(3), 483–492.
- [3] Özger F. (2019) Some geometric characterizations of a fractional Banach set, Commun. Fac. Sci. Univ. Ank. Ser. A1 Math. Stat. 68(1) : 546-558.
- [4] Özger F (2019) Characterizations of compact operators on ℓ_p -type fractional sets of sequences, Demonstr. Math. 52(1) : 105-115.
- [5] Özger F (2019) Compact Operators on the Sets of Fractional Difference Sequences. Sakarya University Journal of Science 23(3), 425-434, DOI: 10.16984/saufenbilder.463368.

Some Recent Results on Compactness Conditions of Fractional Difference Sequence Spaces

Faruk Özger*

İzmir Kâtip Çelebi Univ., Dept. of Engineering Sciences, Çiğli Main Campus, İzmir, Türkiye

*Corresponding author: farukozger@gmail.com

Keywords: Hausdorff measure of noncompactness, compact operators, fractional spaces

Discipline: Mathematics

Introduction

The fractional difference operator for a fraction $\tilde{\alpha}$ was defined in [1] as

$$\Delta^{(\tilde{\alpha})}(x_k) = \sum_{i=0}^{\infty} (-1)^i \frac{\Gamma(\tilde{\alpha} + 1)}{i! \Gamma(\tilde{\alpha} - i + 1)} x_{k-i}.$$

It is assumed that this series defined is convergent for $x \in \omega$. This infinite sum becomes a finite sum if $\tilde{\alpha}$ is a nonnegative integer.

The inverse of fractional difference matrix is given by

$$\Delta_{nk}^{(-\tilde{\alpha})} = \begin{cases} (-1)^{n-k} \frac{\Gamma(-\tilde{\alpha}+1)}{(n-k)! \Gamma(-\tilde{\alpha}-n+k+1)} & (0 \leq k \leq n), \\ 0 & (k > n). \end{cases}$$

In this survey work, we consider some recent studied fractional sets of sequences and focus on the characterizations of some matrix classes. We obtain some identities and estimates for the Hausdorff measure of noncompactness of matrix operators from fractional type spaces into the sets of bounded ℓ_{∞} , convergent c , null sequences c_0 and also absolutely convergent series. We finally obtain compact conditions of these spaces. The results of this work are based on the papers [2-4].

2. Main Results

Theorem 2.1 The identities or estimates for L_A when $A \in (\lambda(\Delta^{(\alpha)}), \mu)$, where $\mu \in \{\ell_{\infty}, c_0, c, \ell_1\}$ and $\lambda \in \{\ell_{\infty}, c_0, c\}$ can be read from the following table:

Table 1. Identities or estimates for L_A when $A \in (\lambda(\Delta^{(\alpha)}), \mu)$

From/To	$\ell_{\infty}(\Delta^{(\alpha)})$	$c_0(\Delta^{(\alpha)})$	$c(\Delta^{(\alpha)})$
ℓ_{∞}	1	1	2
c_0	3	3	4
c	5	5	6
ℓ_1	7	7	8

Here

- (1) $0 \leq \|L_A\|_{\chi} \leq \lim_{r \rightarrow \infty} \left(\sup_{n \geq r} \sum_{k=0}^{\infty} |\hat{a}_{nk}| \right);$
- (2) $0 \leq \|L_A\|_{\chi} \leq \lim_{r \rightarrow \infty} \left(\sup_{n \geq r} \sum_{k=0}^{\infty} |\hat{a}_{nk}| + |\gamma_n| \right);$
- (3) $\|L_A\|_{\chi} = \lim_{r \rightarrow \infty} \|\hat{A}^{[p]}\|_{(\ell_{\infty}, \ell_{\infty})};$
- (4) $\|L_A\|_{\chi} = \lim_{r \rightarrow \infty} \left(\sup_{n \geq r} \sum_{k=0}^{\infty} |\hat{a}_{nk}| + |\gamma_n| \right);$
- (5) $\frac{1}{2} \cdot \lim_{r \rightarrow \infty} \|\hat{B}^{[p]}\|_{((\ell_{\infty}, \ell_{\infty}))} \leq \|L_A\|_{\chi} \leq \lim_{r \rightarrow \infty} \|\hat{B}^{[p]}\|_{((\ell_{\infty}, \ell_{\infty}))};$
- (6) $\frac{1}{2} \cdot \lim_{r \rightarrow \infty} \left(\sup_{n \geq r} \sum_{k=0}^{\infty} |\hat{b}_{nk}| + |\delta_n| \right) \leq \|L_A\|_{\chi} \leq \lim_{r \rightarrow \infty} \left(\sup_{n \geq r} \sum_{k=0}^{\infty} |\hat{b}_{nk}| + |\delta_n| \right);$
- (7) $\lim_{r \rightarrow \infty} \sup_{N \subset \mathbb{N}_0} \left\| \sum_{n \in N} \hat{A}_n^{[p]} \right\|_1 \leq \|L_A\|_{\chi} \leq 4 \lim_{r \rightarrow \infty} \sup_{N \subset \mathbb{N}_0} \left\| \sum_{n \in N} \hat{A}_n^{[p]} \right\|_1;$
finite finite

(8) $\limsup_{\substack{r \rightarrow \infty \\ N \subset \mathbb{N}_0 \\ \text{finite}}} \left(\left\| \sum_{n \in N} \hat{A}_n^{[p]} \right\|_1 + |\sum_{n \in N} \gamma_n| \right) \leq \|L_A\|_{\mathcal{X}} \leq 4 \limsup_{\substack{r \rightarrow \infty \\ N \subset \mathbb{N}_0 \\ \text{finite}}} \left(\left\| \sum_{n \in N} \hat{A}_n^{[p]} \right\|_1 + |\sum_{n \in N} \gamma_n| \right),$
where the notations used in the theorem are defined in [4].

Theorem 2.2 [3]

Table 2. Necessary and sufficient conditions for an operator to be compact for $1 < p < \infty$.

	$\ell_p(\Delta^{(\tilde{\alpha})})$	$\ell_1(\Delta^{(\tilde{\alpha})})$
c_0	1.	5.
c	2.	6.
ℓ_∞	3.	7.
ℓ_1	4.	8.

1. $\limsup_{r \rightarrow \infty} \sup_{n \geq r} \left(\sum_{k=0}^{\infty} \left| \sum_{j=k}^{\infty} (-1)^{j-k} \frac{\Gamma(-\tilde{\alpha}+1)}{(j-k)! \Gamma(-\tilde{\alpha}+j-k+1)} a_{nj} \right|^q \right)^{\frac{1}{q}} = 0.$
2. $\limsup_{r \rightarrow \infty} \sup_{n \geq r} \left(\sum_{k=0}^{\infty} \left| \sum_{j=k}^{\infty} (-1)^{j-k} \frac{\Gamma(-\tilde{\alpha}+1)}{(j-k)! \Gamma(-\tilde{\alpha}+j-k+1)} a_{nj} - \lim_{n \rightarrow \infty} \hat{a}_{nk} \right|^q \right)^{\frac{1}{q}} = 0.$
3. $\limsup_{r \rightarrow \infty} \sup_n \left(\sum_{k=r+1}^{\infty} \left| \sum_{j=k}^{\infty} (-1)^{j-k} \frac{\Gamma(-\tilde{\alpha}+1)}{(j-k)! \Gamma(-\tilde{\alpha}+j-k+1)} a_{nj} \right|^q \right)^{\frac{1}{q}} = 0.$
4. $\limsup_{r \rightarrow \infty} \sup_{N \in \mathcal{F}_r} \left(\sum_{k=0}^{\infty} \left| \sum_{n \in N} \sum_{j=k}^{\infty} (-1)^{j-k} \frac{\Gamma(-\tilde{\alpha}+1)}{(j-k)! \Gamma(-\tilde{\alpha}+j-k+1)} a_{nj} \right|^q \right)^{\frac{1}{q}} = 0.$
5. $\limsup_{r \rightarrow \infty} \sup_{n \geq r} \left(\sup_k \left| \sum_{j=k}^{\infty} (-1)^{j-k} \frac{\Gamma(-\tilde{\alpha}+1)}{(j-k)! \Gamma(-\tilde{\alpha}+j-k+1)} a_{nj} \right| \right) = 0.$
6. $\limsup_{r \rightarrow \infty} \sup_{n \geq r} \left(\sup_k \left| \sum_{j=k}^{\infty} (-1)^{j-k} \frac{\Gamma(-\tilde{\alpha}+1)}{(j-k)! \Gamma(-\tilde{\alpha}+j-k+1)} a_{nj} - \lim_{n \rightarrow \infty} \hat{a}_{nk} \right| \right) = 0.$
7. $\limsup_{m \rightarrow \infty} \sup_{1 \leq n \leq m} |\hat{a}_{n,k_1} - \hat{a}_{n,k_2}| = \sup_n |\hat{a}_{n,k_1} - \hat{a}_{n,k_2}|$, uniformly in k_1 and k_2 , ($1 \leq k_1, k_2 < \infty$).
8. $\limsup_{r \rightarrow \infty} \sup_k \sum_{n=r}^{\infty} \left| \sum_{j=k}^{\infty} (-1)^{j-k} \frac{\Gamma(-\tilde{\alpha}+1)}{(j-k)! \Gamma(-\tilde{\alpha}+j-k+1)} a_{nj} \right| = 0.$

Theorem 2.3 Let $A \in (\ell_\infty(\Delta^{(\tilde{\alpha})}), \ell_\infty)$. Then L_A is compact if and only if $\limsup_{r \rightarrow \infty} \sum_{k=r+1}^{\infty} |\hat{a}_{nk}| = 0$.

Theorem 2.4 Let $1 < p < \infty$ and $q = \frac{p}{p-1}$.

- If $A \in (\ell_p(\Delta^{(\tilde{\alpha})}), \ell_\infty)$, then L_A is compact if and only if $\limsup_{r \rightarrow \infty} \sup_n \left(\sum_{k=r+1}^{\infty} |\hat{a}_{nk}|^q \right)^{\frac{1}{q}} = 0$.
- If $A \in (\ell_1(\Delta^{(\tilde{\alpha})}), \ell_\infty)$, then L_A is compact if and only if

$$\limsup_{m \rightarrow \infty} \sup_{1 \leq n \leq m} |\hat{a}_{n,k_1} - \hat{a}_{n,k_2}| = \sup_n |\hat{a}_{n,k_1} - \hat{a}_{n,k_2}|$$

uniformly in k_1 and k_2 ($1 \leq k_1, k_2 < \infty$).

Theorem 2.5 [2] Let $1 \leq p < \infty$ and Ψ be a triangle. Then we have $A \in (\ell_1(\Delta^{(\tilde{\alpha})}), \ell_p(\Psi))$ if and only if

$$\sup_k \sum_{n=0}^{\infty} \left| \sum_{i=0}^n \sum_{j=k}^{\infty} (-1)^{j-k} \frac{\Gamma(-\tilde{\alpha}+1)}{(j-k)! \Gamma(-\tilde{\alpha}-j+k+1)} \psi_{ni} a_{ij} \right|^p < \infty$$

and for all $n = 0, 1, \dots$

$$\sup_{m,k} \left| \sum_{j=m}^{\infty} (-1)^{j-k} \frac{\Gamma(-\tilde{\alpha}+1)}{(j-k)! \Gamma(-\tilde{\alpha}-j+k+1)} a_{nj} \right| < \infty.$$

Theorem 2.6 [2] Let Ψ be a triangle. Then we have $A \in (c(\Delta^{(\tilde{\alpha})}), c(\Psi))$ if and only if

$$\begin{aligned} & \sup_n \sum_{k=0}^{\infty} \left| \sum_{i=0}^n \sum_{j=k}^{\infty} (-1)^{j-k} \frac{\Gamma(-\tilde{\alpha}+1)}{(j-k)! \Gamma(-\tilde{\alpha}+j-k+1)} \psi_{ni} a_{ij} \right| < \infty, \\ & \lim_{n \rightarrow \infty} \sum_{i=0}^n \sum_{j=k}^{\infty} (-1)^{j-k} \frac{\Gamma(-\tilde{\alpha}+1)}{(j-k)! \Gamma(-\tilde{\alpha}+j-k+1)} \psi_{ni} a_{ij} = \hat{\xi}_k \text{ exists for all } k, \\ & \sup_m \sum_{k=0}^m \left| \sum_{j=m}^{\infty} (-1)^{j-k} \frac{\Gamma(-\tilde{\alpha}+1)}{(j-k)! \Gamma(-\tilde{\alpha}+j-k+1)} \psi_{ni} a_{ij} \right| < \infty \text{ for each } n, \\ & \lim_{m \rightarrow \infty} \sum_{k=0}^m \sum_{i=0}^n \sum_{j=k}^{\infty} (-1)^{j-k} \frac{\Gamma(-\tilde{\alpha}+1)}{(j-k)! \Gamma(-\tilde{\alpha}+j-k+1)} \psi_{ni} a_{ij} = \xi_n \text{ exists for each } n, \\ & \lim_{n \rightarrow \infty} \left(\sum_{k=0}^{\infty} \sum_{i=0}^n \sum_{j=k}^{\infty} (-1)^{j-k} \frac{\Gamma(-\tilde{\alpha}+1)}{(j-k)! \Gamma(-\tilde{\alpha}+j-k+1)} \psi_{ni} a_{ij} - \xi_n \right) = \zeta \text{ exists.} \end{aligned}$$

Theorem 2.7 [2] Let Ψ be a triangle. Then we have $A \in (c_0(\Delta^{(\tilde{\alpha})}), c_0(\Psi))$ if and only if

$$\begin{aligned} & \sup_n \sum_{k=0}^{\infty} \left| \sum_{i=0}^n \sum_{j=k}^{\infty} (-1)^{j-k} \frac{\Gamma(-\tilde{\alpha}+1)}{(j-k)! \Gamma(-\tilde{\alpha}+j-k+1)} \psi_{ni} a_{ij} \right| < \infty, \\ & \sup_m \sum_{k=0}^m \left| \sum_{j=m}^{\infty} (-1)^{j-k} \frac{\Gamma(-\tilde{\alpha}+1)}{(j-k)! \Gamma(-\tilde{\alpha}+j-k+1)} \psi_{ni} a_{ij} \right| < \infty \end{aligned}$$

and

$$\lim_{n \rightarrow \infty} \sum_{i=0}^n \sum_{j=k}^{\infty} (-1)^{j-k} \frac{\Gamma(-\tilde{\alpha}+1)}{(j-k)! \Gamma(-\tilde{\alpha}+j-k+1)} \psi_{ni} a_{ij} = 0.$$

The compactness conditions for the classes $(c_0(\Delta^{(\tilde{\alpha})}), c_0(\Psi))$, $(c(\Delta^{(\tilde{\alpha})}), c(\Psi))$ and $(\ell_1(\Delta^{(\tilde{\alpha})}), \ell_1(\Psi))$, where Ψ is an arbitrary triangle, is given in [2].

Theorem 2.8 [2] Let Ψ be a triangle. Then, the following statements hold:

- If $A \in (c_0(\Delta^{(\tilde{\alpha})}), c_0(\Psi))$ then $L_A \in \mathcal{C}(c_0(\Delta^{(\tilde{\alpha})}), c_0(\Psi))$ if and only if $Y = 0$, where Y is defined as in [2, Theorem 4.4].
- If $A \in (c(\Delta^{(\tilde{\alpha})}), c(\Psi))$ then $L_A \in \mathcal{C}(c(\Delta^{(\tilde{\alpha})}), c(\Psi))$ if and only if $\Omega = 0$, where Ω is defined as in [2, Theorem 4.5].
- If $A \in (\ell_1(\Delta^{(\tilde{\alpha})}), \ell_1(\Psi))$ then $L_A \in \mathcal{C}(\ell_1(\Delta^{(\tilde{\alpha})}), \ell_1(\Psi))$ if and only if $\Lambda = 0$, where Λ is defined as in [2, Theorem 4.6].

References

- [1] Baliarsingh P (2015) Some new difference sequence spaces of fractional order and their dual spaces, Appl. Math. Comput., 219(18), 9737–9742.
- [2] Özger, F (2019) Some general results on fractional Banach sets, Turk. J. Math. 43(2), doi: 10.3906/mat-1802-82.
- [3] Özger F (2019) Characterizations of compact operators on ℓ_p -type fractional sets of sequences, Demonstr. Math. 52(1) : 105-115.
- [4] Özger F (2019) Compact operators on the sets of fractional difference sequences, Sakarya University Journal of Science 23(3).

Freud Polynomial Solutions of Linear First Order Generalized Pantograph Differential Equations

Ali Konuralp*, Manisa Celal Bayar University, Dept. of Mathematics, Manisa, Türkiye
Gizem Hayta, Manisa Celal Bayar Univ., Institute of Natural and Applied Science, Manisa, Türkiye
*Corresponding author: ali.konuralp@cbu.edu.tr

Keywords: Freud polynomials, delay differential equations, collocation method

Discipline: Mathematics

Abstract

In this study, it is aimed to propose a numerical method based on Freud Polynomials [11,12] with matrix formulations for the first order generalized pantograph differential equations to obtain their numerical solutions under the given condition. Linear generalized pantograph differential equations are solved by various methods [5-9]. The form of the equations considered here is

$$\sum_{j=0}^m \sum_{i=0}^1 P_{ij}(t) y^{(i)}(a_{ij}t + b_{ij}) = g(t), \quad a \leq t \leq b, \quad (1)$$

subject to the condition $\alpha y(a) + \beta y(b) = \gamma$ where $P_{ij}(t)$ are the variable coefficients, a_{ij} and b_{ij} are real constants for $i = 0, 1, j = 0, \dots, m, m \in \mathbb{N}, \alpha, \beta$ and γ are real numbers. Let introduce an infinite series that can be a solution of (1) in terms of Freud Polynomials as

$$y(t) = \sum_{n=0}^{\infty} a_n Fr_n(t), \quad (2)$$

where $Fr_n(t)$ is the n^{th} Freud polynomial and a_n is the n^{th} coefficient related with that polynomial. For the approximate solution, it is taken the first $N+1$ terms of (2),

$$y(t) \cong y_N(t) = \sum_{n=0}^N a_n Fr_n(t). \quad (3)$$

The method used here is inspired by the study of Sezer [5]. By using the matrix relations, the given equation (1) is written in the matrix form. Then obtained matrix equation is transformed to an algebraic system of the equations by implementing one by one the collocation points chosen in the domain of (1). After changing one row of the last matrix with the row consisting of the given condition, the matrix equation is checked to have a solution, if it has, the solution yields the coefficients a_n of the Freud polynomials. Therefore, the approximate solution is obtained in the form of (3). The proposed method is applied to a test problem in order to show the efficiency and applicable of it.

1. Introduction

The interest in finding the numerical solutions of differential-difference equations has been increased considerably in many areas for analyzing the real world applications in the last decades[1-3]. Linear first order generalized pantograph equations are solved by using different kinds of solution techniques such as Adomian decomposition method[4], Taylor matrix method[5], Bernoulli operational matrix method[6], Genocchi operational matrix method[7], and much more. In this study we propose a collocation method based on Freud polynomials and their matrix representations. We focus on the first order linear generalized pantograph differential equations in order to find their numerical solutions.

Let us consider the first-order linear differential-difference equation with variable coefficients (1) subject to (2) where $P_{ij}(t)$ and $g(t)$ are functions defined on $a \leq t \leq b; a_{ij}, b_{ij}$ and γ_i are given constants. The approximate series solution of (1) is denoted by

$$y_N(t) = \sum_{n=0}^N a_n Fr_n(t); \quad a \leq t \leq b \quad (4)$$

which is in the truncated series form. The approximate solution is then the linear combination of n^{th} Freud polynomials for $n = 1, 2, \dots, N$ whose coefficients needs to be determined.

2. Freud Polynomials

The set of Freud polynomials $\{Fr_n(t)\}_{n=0}^{\infty}$ is the orthogonal set defined on whole real line with respect to exponential-type weight $\exp(-t^4)$. The polynomials satisfy the three-term recurrence relation

$$Fr_{n+1}(t) = tFr_n(t) - \beta_n Fr_{n-1}(t) \quad (5)$$

subject to Freud equations

$$4\beta_n(\beta_{n-1} + \beta_n + \beta_{n+1}) = n \quad (6)$$

with initial conditions

$$\beta_0 = 0$$

$$\beta_1 = \frac{\int_{-\infty}^{\infty} t^2 \exp(-t^4) dt}{\int_{-\infty}^{\infty} \exp(-t^4) dt} = \frac{\Gamma\left(\frac{3}{4}\right)}{\Gamma\left(\frac{1}{4}\right)}$$

The first few terms are given by

$$Fr_0(t) = 1, Fr_1(t) = t, Fr_2(t) = t^2 + \frac{\Gamma\left(\frac{3}{4}\right)}{\Gamma\left(\frac{1}{4}\right)} - \frac{\Gamma\left(\frac{5}{4}\right)}{\Gamma\left(\frac{3}{4}\right)}, Fr_3(t) = t^3 - \frac{4t\Gamma\left(\frac{3}{4}\right)^3}{\Gamma\left(\frac{1}{4}\right)^3 - 4\Gamma\left(\frac{1}{4}\right)\Gamma\left(\frac{3}{4}\right)^2}, \dots$$

3. Matrix Forms

In the matrix form, the Freud polynomials $Fr_n(t)$ can be taken as

$$F^T(t) = S^T X^T(t) \Rightarrow F(t) = X(t)S \quad (7)$$

where $F(t) = [Fr_0(t) Fr_1(t) Fr_2(t) \dots Fr_N(t)]$, $X(t) = [1 \ t \ t^2 \dots t^N]$ and S is the transformation matrix that transforms the matrix of Freud polynomials to the base matrix $X(t)$. The general form of S is constructed by using our user-defined code in Mathematica package.

According to above matrix notations, the solution $y(t)$ and its first derivate $y'(t)$ are denoted by

$$y_N(t) = F(t)A \quad (8)$$

and

$$y'_N(t) = F'(t)A \quad (9)$$

respectively where

$$A = [a_0 \ a_1 \ a_2 \dots \ a_N]^T \quad (10)$$

is the coefficient matrix. Now by substituting (7) into (8) and (9), the solution matrix and its first derivative are obtained as

$$y_N(t) = X(t)SA \quad (11)$$

and

$$y'_N(t) = X'(t)SA \quad (12)$$

Getting a relation between $X'(t)$ and $X(t)$ leads an iterative formula to find the higher order derivatives in terms of $X(t)$, so it can be easily found that

$$X'(t) = X(t)B \quad (13)$$

where

$$B = \begin{bmatrix} 0 & 1 & 0 & \dots & 0 & 0 & 0 \\ 0 & 0 & 2 & \dots & 0 & 0 & 0 \\ 0 & 0 & 0 & \dots & 0 & 0 & 0 \\ \vdots & \vdots & \vdots & & \vdots & \vdots & \vdots \\ 0 & 0 & 0 & & 0 & 0 & N \\ 0 & 0 & 0 & & 0 & 0 & 0 \end{bmatrix}$$

Then, it can also be obtained that the matrix relations

$$y'_N(t) = X(t) B S A \quad (14)$$

by using (13) in Eq.(12). If we put $a_{ij}t + b_{ij}$ instead of t in (8), we have the matrix form

$$y_N(a_{ij}t + b_{ij}) = F(a_{ij}t + b_{ij}) A \quad (15)$$

Again we assume the following relation to get matrix form of $X(a_{ij}t + b_{ij})$ in terms of $X(t)$

$$X(a_{ij}t + b_{ij}) = X(t) \beta(a_{ij}, b_{ij}) \quad (16)$$

where

$$\beta(a_{ij}, b_{ij}) = \begin{bmatrix} \binom{0}{0} a_{ij}^0 b_{ij}^0 & \binom{1}{0} a_{ij}^0 b_{ij}^1 & \dots & \binom{N}{0} a_{ij}^0 b_{ij}^N \\ 0 & \binom{1}{1} a_{ij}^1 b_{ij}^0 & \dots & \binom{N}{1} a_{ij}^1 b_{ij}^{N-1} \\ \vdots & \vdots & \ddots & \vdots \\ 0 & 0 & \dots & \binom{N}{N} a_{ij}^N b_{ij}^0 \end{bmatrix}.$$

By using The first derivative of (16) is

$$X'(a_{ij}t + b_{ij}) = X(t) \beta(a_{ij}, b_{ij}) B \quad (17)$$

and therefore

$$y'_N(a_{ij}t + b_{ij}) = X(t) \beta(a_{ij}, b_{ij}) B S A. \quad (18)$$

For the condition (2), the corresponding matrix relation is given as

$$(\alpha X(a) + \beta X(b)) S A = \gamma \quad (19)$$

by means of (11).

4. Method of Solution

In this section, to obtain the fundamental matrix equation corresponding to Eq. (1), the matrix relations (18) and (16) are substituted into Eq. (1), then the matrix equation

$$\sum_{j=0}^m \sum_{i=0}^1 P_{ij}(t) X(t) \beta(a_{ij}, b_{ij}) B^i S A = g(t), \quad (20)$$

is constructed. Now let the collocation points t_i be defined by

$$t_i = a + \left(\frac{b-a}{N}\right)i, \quad i = 0, 1, \dots, N \quad \text{or} \quad t_i = \frac{b-a}{2} + \frac{a-b}{2} \cos(\pi i / N) \quad (21)$$

Putting the collocation points in (20) respectively yields the system of the matrix equations

$$\sum_{j=0}^m \sum_{i=0}^1 P_{ij}(t_i) X(t_i) \beta(a_{ij}, b_{ij}) B^i S A = g(t_i), \quad 0 \leq i \leq N \quad (22)$$

or shortly the fundamental matrix equation becomes

$$\left[\sum_{j=0}^m \sum_{i=0}^1 P_{ij}(t_i) X(t_i) \beta(a_{ij}, b_{ij}) B^i S \right] A = G \quad (23)$$

where

$$P_{ij} = \begin{bmatrix} P_{ij}(t_0) & 0 & \dots & 0 \\ 0 & P_{ij}(t_1) & \dots & 0 \\ 0 & 0 & \ddots & 0 \\ 0 & 0 & \dots & P_{ij}(t_N) \end{bmatrix}, \quad X(t) = \begin{bmatrix} X(t_0) \\ X(t_1) \\ \vdots \\ X(t_N) \end{bmatrix} = \begin{bmatrix} 1 & t_0 & \dots & t_0^N \\ 1 & t_1 & \dots & t_1^N \\ \vdots & \vdots & \ddots & \vdots \\ 1 & t_N & \dots & t_N^N \end{bmatrix},$$

$$G = \begin{bmatrix} g(t_0) \\ g(t_1) \\ \vdots \\ g(t_N) \end{bmatrix}.$$

Then, the augmented form of (23) is

$$WA = G \text{ or } [W; G] \quad (24)$$

where W is the matrix in the parenthesis in Eq. (23). On the other hand, we can express the matrix form (19) for the conditions as

$$UA = \gamma \text{ or } [U; \gamma] \quad (25)$$

where

$$U = (\alpha X(a) + \beta X(b)) S = [u_1 \quad u_2 \quad u_3 \quad \dots \quad u_N]$$

For adding the effect of the condition (2) into (24), we replace the row matrix (25) by the m^{th} row of the matrix (24), so the new augmented matrix can be given as

$$\tilde{W}A = \tilde{G} \quad (26)$$

where

$$[\tilde{W}; \tilde{G}] = \begin{bmatrix} w_{11} & w_{12} & \dots & w_{1N} & ; & g(t_0) \\ w_{21} & w_{22} & \dots & w_{2N} & ; & g(t_1) \\ \vdots & \vdots & \vdots & \vdots & ; & \vdots \\ w_{(m-1)1} & w_{(m-1)2} & \dots & w_{(m-1)N} & ; & g(t_m) \\ u_1 & u_2 & \dots & u_N & ; & \gamma \\ \vdots & \vdots & \vdots & \vdots & ; & \vdots \\ w_{(N+1)1} & w_{(N+1)2} & \dots & w_{(N+1)N} & ; & g(t_N) \end{bmatrix}_{(N+1) \times (N+1)} \quad (27)$$

To have a unique solution to the system (26), we check the ranks of \tilde{W} and $[\tilde{W}; \tilde{G}]$ as usual, if they both have same and $N + 1$ then the coefficients matrix A which corresponds to the coefficients of Freud polynomials can be determined uniquely by

$$A = (\tilde{W})^{-1} \tilde{G}. \quad (28)$$

Consequently, the truncated Freud series (3) is the approximate solution to the initial value problem (1) subject to (2) which is constituted both (28) and Freud polynomials.

5. The Error of the Approximate Solution

The absolute error of the approximate solution (3) is

$$e(t_i) = |y_N(t_i) - y(t_i)| \cong 0 \quad (29)$$

for $t_i \in [a, b]$, $i = 1, 2, 3, \dots$. We can control the error by changing the truncation number N and using the residual function

$$E(t) = \left| \sum_{j=0}^m \sum_{i=0}^1 P_{ij}(t) X(t) \beta(a_{ij}, b_{ij}) B^i S A - g(t) \right|. \quad (30)$$

The error limits then can be obtained by substituting the nodal points into the residual function. To have the smaller error limits, the truncation limit N is increased until one gets the desired balance.

6. Numerical Examples

Example 6.1: Let us first consider the pantograph equation;

$$y'(t/2) + y(t) = 1 + t, \quad 0 \leq t \leq 1$$

with the initial conditions $y(0) = 0$. The exact solution of the problem is $y(t) = t$. In this problem, $g(t) = 1 + t$, $P_{00}(t) = 1$, $P_{10}(t) = 1$, $a_{00} = 1$, $a_{10} = 1/2$, $b_{00} = 0$, $b_{10} = 0$

Let us seek the approximate solution $y_3(t)$ defined by the truncated exponential series

$$y_3(t) = \sum_{n=0}^3 a_n Fr_n(t)$$

The set of the collocation points (21) for $N = 3$ is computed as $\{t_0 = 0, t_1 = 1/3, t_2 = 2/3, t_3 = 1\}$.

The fundamental matrix equation can be given by (23) as

$$\{P_{00}(t_0)X(t_0)\beta(a_{00}, b_{00})B^0S + P_{10}(t_1)X(t_0)\beta(a_{10}, b_{10})B^1S\} = G$$

where

$$X = \begin{bmatrix} 1 & 0 & 0 & 0 \\ 1 & 0.25 & 0.0625 & 0.015625 \\ 1 & 0.75 & 0.5625 & 0.421875 \\ 1 & 1 & 1 & 1 \end{bmatrix}, P_{00} = \begin{bmatrix} 1 & 0 & 0 & 0 \\ 0 & 1 & 0 & 0 \\ 0 & 0 & 1 & 0 \\ 0 & 0 & 0 & 1 \end{bmatrix}, P_{10} = \begin{bmatrix} 1 & 0 & 0 & 0 \\ 0 & 1 & 0 & 0 \\ 0 & 0 & 1 & 0 \\ 0 & 0 & 0 & 1 \end{bmatrix}, G = \begin{bmatrix} 1 \\ 4/3 \\ 5/3 \\ 2 \end{bmatrix}$$

$$\beta(1, 0) = \begin{bmatrix} 1 & 0 & 0 & 0 \\ 0 & 1 & 0 & 0 \\ 0 & 0 & 1 & 0 \\ 0 & 0 & 0 & 1 \end{bmatrix}, \beta(1/2, 0) = \begin{bmatrix} 1 & 0 & 0 & 0 \\ 0 & 1/2 & 0 & 0 \\ 0 & 0 & 1/4 & 0 \\ 0 & 0 & 0 & 1/8 \end{bmatrix}, B^1 = \begin{bmatrix} 0 & 1 & 0 & 0 \\ 0 & 0 & 2 & 0 \\ 0 & 0 & 0 & 3 \\ 0 & 0 & 0 & 0 \end{bmatrix},$$

$$S = \begin{bmatrix} 1 & 0 & -0.40168 & 0 \\ 0 & 1 & 0 & -0.284397 \\ 0 & 0 & 1 & 0 \\ 0 & 0 & 0 & 1 \end{bmatrix}$$

The augmented matrix (24) is obtained as

$$[W;G]=\begin{bmatrix} 1. & 1. & -0.4016796597635174 & -0.28439738603734865 & 1 \\ 1. & 1.3333333333333333 & 0.04276478468092704 & -0.2588261443460945 & \frac{4}{3} \\ 1. & 1.6666666666666665 & 0.7094314513475937 & 0.1556339862340485 & \frac{5}{3} \\ 1. & 2. & 1.5983203402364827 & 1.1812052279253027 & 2 \end{bmatrix}$$

The augmented matrix forms of the condition is

$$[U;\gamma]=\begin{bmatrix} 1 & 0 & -0.40168 & 0 & ; & 0 \end{bmatrix}$$

From (26), according to the condition the new augmented matrix is written by inserting the condition row matrix to $[W;G]$ then we have $[\tilde{W};\tilde{G}]$. The coefficients (a_0, a_1, a_2, a_3) are solved from the that system of algebraic equations and by substituting it into Eq. (4), one yields the exact solution $y(t) = t$.

Table 1. Numerical results for Example 6.1

t	Exact Solution	Approximate Solution	Absolute error	Residual Error $R_n(t_i)$
0.	0.	0.	0.	0.
0.2	0.2	0.20000000000000007	$5.551115123125783 \times 10^{-17}$	$6.661338147750939 \times 10^{-16}$
0.4	0.4	0.40000000000000002	$1.665334536937734 \times 10^{-16}$	$6.661338147750939 \times 10^{-16}$
0.6	0.6	0.60000000000000004	$3.330669073875469 \times 10^{-16}$	$8.881784197001252 \times 10^{-16}$
0.8	0.8	0.80000000000000004	$3.330669073875469 \times 10^{-16}$	$1.110223024625156 \times 10^{-15}$
1.	1.	1.00000000000000002	$2.220446049250313 \times 10^{-16}$	$8.881784197001252 \times 10^{-16}$

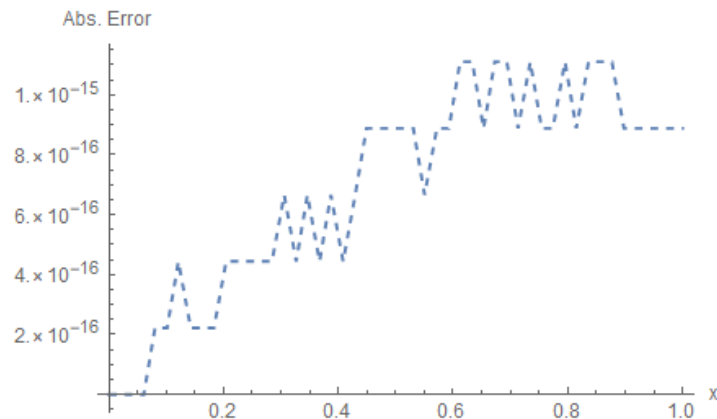


Figure 1. Absolute error of the approximate solution for N=3

Example 6.2: Let us first consider the pantograph equation;

$$y'(t) - 3y(t-3) = 10 - 3t, \quad 0 \leq t \leq 1$$

with the initial conditions $y(0) = 0$. The exact solution of the problem is $y(t) = t$. In this problem, $g(t) = 10 - 3t, P_{00}(t) = -3, P_{10}(t) = 1, a_{00} = 1, a_{10} = 1, b_{00} = -3, b_{10} = 0, b_{01} = 1$

Let us seek the approximate solution $y_3(t)$ defined by the truncated series

$$y_3(t) = \sum_{n=0}^3 a_n Fr_n(t)$$

The set of the collocation points (21) for $N = 3$ is computed as $t_0 = 0, t_1 = 0.25, t_2 = 0.75$ and $t_3 = 1$

From Eq. (23), the fundamental matrix equation can be written as

$$\{P_{00}(t_0)X(t_0)\beta(a_{00}, b_{00})B^0S + P_{10}(t_1)X(t_0)\beta(a_{10}, b_{10})B^1S\} = G$$

where

$$X = \begin{bmatrix} 1 & 0 & 0 & 0 \\ 1 & 0.25 & 0.0625 & 0.015625 \\ 1 & 0.75 & 0.5625 & 0.421875 \\ 1 & 1 & 1 & 1 \end{bmatrix}, P_{00} = \begin{bmatrix} -3 & 0 & 0 & 0 \\ 0 & -3 & 0 & 0 \\ 0 & 0 & -3 & 0 \\ 0 & 0 & 0 & -3 \end{bmatrix}, P_{10} = \begin{bmatrix} 1 & 0 & 0 & 0 \\ 0 & 1 & 0 & 0 \\ 0 & 0 & 1 & 0 \\ 0 & 0 & 0 & 1 \end{bmatrix},$$

$$G = \begin{bmatrix} 10 \\ 9.25 \\ 7.75 \\ 7 \end{bmatrix}, \beta(1, -3) = \begin{bmatrix} 1 & -3 & 9 & -27 \\ 0 & 1 & -6 & 27 \\ 0 & 0 & 1 & -9 \\ 0 & 0 & 0 & 1 \end{bmatrix}, B^1 = \begin{bmatrix} 0 & 1 & 0 & 0 \\ 0 & 0 & 2 & 0 \\ 0 & 0 & 0 & 0 \\ 0 & 0 & 0 & 0 \end{bmatrix}, S = \begin{bmatrix} 1 & 0 & -\frac{1}{2} & 6 \\ 0 & 1 & 0 & -\frac{3}{2} \\ 0 & 0 & 1 & 0 \\ 0 & 0 & 0 & 1 \end{bmatrix}$$

The augmented matrix (24) is obtained as

$$[W; G] = \begin{bmatrix} -3 & 10 & -25.794961020709447 & 78.1560261396265 & ; & 10 \\ -3 & 9.25 & -20.982461020709447 & 59.947449179154525 & ; & 9.25 \\ -3 & 7.75 & -12.482461020709447 & 33.65529525821055 & ; & 7.75 \\ -3 & 7 & -8.794961020709447 & 25.00921829773856 & ; & 7. \end{bmatrix}$$

The augmented matrix form of the condition is $[U; \gamma] = [1 \ 0 \ -0.40168 \ 0 \ ; \ 0]$.

From (26), according to the condition the new augmented matrix is written by inserting the condition row matrix to $[W; G]$ then we have $[\tilde{W}; \tilde{G}]$. The coefficients (a_0, a_1, a_2, a_3) are solved from the that system of algebraic equations and by substituting it into Eq. (4), one yields the exact solution $y(t) = t$.

Example 6.3: Let us take the equation $y'(1+t) - 3y(1+t) + 2e^{1+t} = 0$ which have exact solution e^t . The solution series in the form of Eq. (4) for N=6 is

$$y_6(t) = 1 + 0.998301656238x + 0.507038751965t^2 + 0.152993612175t^3$$

$$+ 0.0551800371964t^4 + 0.00071812248t^5 + 0.003487375122t^6$$

Table 2. Numerical results for Example 6.3 for N=6

t_i	Exact Solution	Approximate Solution	Absolute error	Residual Error $R_n(t_i)$
0.	1.	1.0000000000000044	$4.4408920985 \times 10^{-15}$	$1.59872115546 \times 10^{-14}$
0.2	1.2214027581601	1.221254571274436	0.00014818688573381	$3.271896336087 \times 10^{-7}$
0.4	1.4918246976412	1.4916727008040598	0.00015199683721056	$8.184420625667 \times 10^{-7}$
0.6	1.8221188003905	1.8219314456791091	0.00018735471139996	$9.727415619664 \times 10^{-7}$
0.8	2.2255409284924	2.2252301077568863	0.00031082073558152	$5.529547184579 \times 10^{-7}$
1.	2.7182818284590	2.7177195551791	0.00056227327994529	$1.669775429036 \times 10^{-13}$

The solution series in the form of Eq. (4) for N=10 is

$$y_{10}(t) = 0.9999999 + 0.99999593t + 0.50001263t^2 + 0.16662901t^3 + 0.041726767t^4 \\ + 0.008261885t^5 + 0.001446309322155453t^6 + 0.000165116t^7 + 0.00003789t^8 \\ - 6.543 \times 10^{-7}t^9 + 7.6639 \times 10^{-7}t^{10}$$

Table 3. Numerical results for Example 6.3 for N=10

t_i	Exact Solution	Approximate Solution	Absolute error	Residual Error $R_n(t_i)$
0.	1.	0.9999999999999956	$4.4408920985 \times 10^{-15}$	$6.12843109593 \times 10^{-14}$
0.2	1.2214027581601699	1.2214022247471938	$5.33412976011 \times 10^{-7}$	$7.54951656745 \times 10^{-14}$
0.4	1.4918246976412703	1.4918236759681867	0.00000102167308368	$1.06581410364 \times 10^{-14}$
0.6	1.822118800390509	1.8221169404790984	0.00000185991141066	$2.55795384873 \times 10^{-13}$
0.8	2.225540928492468	2.2255375404856643	0.00000338800680355	$9.2903462700 \times 10^{-13}$
1.	2.718281828459045	2.7182756551661753	0.00000617329286978	$2.2719603975 \times 10^{-12}$

Example 6.4: Finally, consider the linear delay differential equation

$$y'(t) + y(t) + y(0.8t) = 0, \quad y(0) = 1$$

which is solved numerically by Bernoulli collocation method and Bernoulli operational matrix method[5,6]. Applying the methodology expressed in method of solution we have the following figures and table.

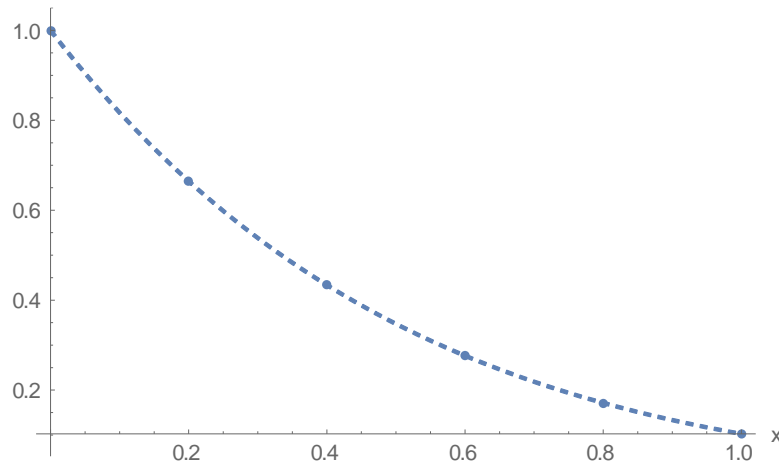


Figure 2. Approximate solution and the obtained solutions from [5,6] error of the approximate solution for N=7

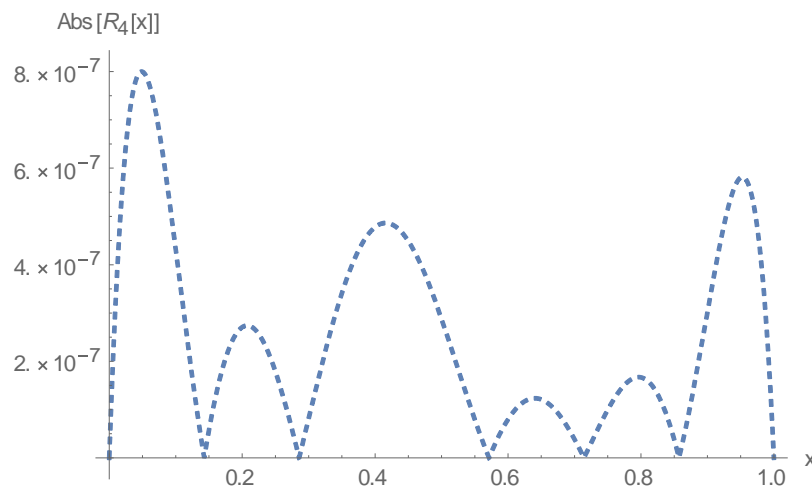


Figure 3. The residual errors of approximate solution for N=7

Table 4. Numerical results for Example 6.4

t_i	Solution[5,6]	Approximate Solution $y_7(t_i)$	Residual Error $R_7(t_i)$
0.	1	0.9999999999890079	$2.98152613709135 \times 10^{-11}$
0.2	0.66491	0.6646909568529564	$2.706151267517498 \times 10^{-7}$
0.4	0.43356	0.4335607306990325	$4.779743165705952 \times 10^{-7}$
0.6	0.276482	0.27648225522236897	$7.961016479374195 \times 10^{-8}$
0.8	0.1714841	0.1714840647298615	$1.666067193095699 \times 10^{-7}$
1.	0.10267	0.10267013920571122	$6.209643910182194 \times 10^{-11}$

Conclusion

In this study, the numerical solutions of linear delay differential equations are obtained by using a novel matrix method based on Freud polynomials. The Freud matrix method gives the exact or the approximate solutions of the problems that are in the form of the equations having pantograph, proportional or linear delays. User defined program we have written in Mathematica according to the algorithm proposed here both reduces the CPU time and saves the memory of computer. As a result of the smooth application of the proposed method to the test problems and the consistency of the solutions of the test problems with the solutions in the literature, different solution methods that can be obtained with this polynomial will be found over time.

References

- [1] Andre A, Keller (2010) Generalized delay differential equations to economic dynamics and control. In Proceedings of the 2010 American conference on Applied mathematics (AMERICAN-MATH'10), Stephen Lagakos, Leonid Perlovsky, Manoj Jha, Brindusa Covaci, Azami Zaharim, and Nikos Mastorakis (Eds.). World Scientific and Engineering Academy and Society (WSEAS), Stevens Point, Wisconsin, USA, 278-286.
- [2] Dehghan M, Shakeri F (2008). The use of the decomposition procedure of Adomian for solving a delay differential equation arising in electrodynamics. *Physica Scripta (Online)*, 78(6), 11. doi:101088/0031-8949/78/06/065004
- [3] Ockendon JR, Tayler AB, Temple GF James (1971) The dynamics of a current collection system for an electric locomotive, 322, *Proc. R. Soc. Lond.*
- [4] Evans DJ, Raslan KR (2005) The Adomian decomposition method for solving delay differential equation. *Int. J. Comput. Math.* 82(1):49-54.
- [5] Sezer M, Daşcıoğlu AA (2007) A Taylor method for numerical solution of generalized pantograph equations with linear functional argument. *Journal of Computational and Applied Mathematics* 200(1):217-225.
- [6] Tohidi E, Bhrawy AH, Erfani K (2013) A collocation method based on Bernoulli operational matrix for numerical solution of generalized pantograph equation, *Appl. Math. Model.*, 37:4283-4294
- [7] Isah A, Phang C (2017) Operational matrix based on Genocchi polynomials for solution of delay differential equations. *Ain Shams Eng J.* 2017.
- [8] Derfel G, Iserles A (1997) The pantograph equation in the complex plane. *J. Math. Anal. Appl.* 213:117-132.
- [9] Liu MZ, Li D (2004) Properties of analytic solution and numerical solution of multi-pantograph equation. *Appl. Math. Comput.* 155:853-871.
- [10] Pinelas S (2014) Asymptotic Behavior of Solutions to Mixed Type Differential Equations. *Electronic Journal of Differential Equations* 2014(210):1-9.
- [11] Bonan SS, Clark DS (1990) Estimates of the Hermite and the Freud Polynomials. *Journal of Approximation Theory* 63:210-224.
- [12] Clarkson PA, Jordaan K (2018) Properties of generalized Freud polynomials. *Journal of Approximation Theory* 225:148-175.

Sea Surface Temperature Prediction Model for Indonesian Waters

*Azalya Rahmatika**, University of Malaya, Dept. of Bioinformatics, Kuala Lumpur, Malaysia

Hizir Sofyan, University of Syiah Kuala, Dept. of Statistics, Banda Aceh, Indonesia

Salmawaty Ariff, University of Syiah Kuala, Dept. of Mathematics, Banda Aceh, Indonesia

*Corresponding author: azalayahmatika@gmail.com

Keywords: prediction model, forecasting, sea surface temperature

Discipline: Mathematics

Abstract

This study aimed to build a prediction model to forecast monthly average of sea surface temperature (SST) by using Box-Jenkins model. Data used in this study was extracted from USA National Centers for Environmental Prediction (NCEP) files from January 2001 until December 2012 for a point whose latitude was 5° 53' and longitude was 95° 11'. That point is located on Sabang waters, Aceh Province, Indonesia. The majority of inhabitants living in Sabang island works as a fisher or any activities related to recreational sectors. For those reasons, any changes occurred in Sabang waters may affect the income of people living in this island. One of the most important alterations needed to be considered was the change of sea surface temperature. This aspect became crucial because the life of some living things occupying the waters depends on it. For instance, the life of coral reef as a food producer for fish is closely related to water temperature. Moreover, it has its own temperature threshold for surviving. To make the SST prediction model, software R was used. Before building the model, the stationarity of SST data, which was the most important assumption for time series model, was tested by using Augmented Dickey Fuller (ADF) test and Box-Cox test. For model identification step, autocorrelation function (ACF) and partial autocorrelation (PACF) were investigated to find out some candidate models. The last step was model estimation and validation. For this step, AIC and BIC values were calculated in order to obtain models that satisfy parsimony aspect. In addition of AIC and BIC values, model evaluation by using MSE, RMSE, and MAPE value was also performed. To confirm that error values made by the selected model had satisfied white noise assumption, Ljung-Box test was performed. After undergoing all steps for building Box-Jenkins model, the best prediction model to forecast SST for Indonesian waters was SARIMA (1, 0, 4)(1, 1, 1)₁₂.

Introduction

The results of the 2004 post-tsunami study showed that the number of reef fish species in the waters of Sabang and its surrounding areas was 425 species from 44 families [1]. Ironically, the preservation of reef fish in Indonesian waters was at serious threat. This happened along with the high threat to the coral reef population which was a vital habitat for reef fish, namely as a place for spawning, nurturing, the place where to get food, and even as the food source itself [1].

A local daily newspaper in Aceh Province, Serambi Indonesia, 10 June 2014 edition, reported that since 24 May 2014 there had been thousands death of fish in Sabang waters. The Aceh Marine and Fisheries department, which examined dead fish samples, stated that the suspicion of the death of reef fish began with an increase in Sabang sea surface temperature. High temperatures cause algae that lived on the reef to burn. Some types of algae that had been charred can produce poisons so that when it was consumed by fish, it can cause death.

Based on the explanation above, it was assumed that there was a close relationship between the condition of coral reefs, abundance of reef fish, and sea surface temperature. In addition, coral bleaching of around 60-80% had occurred in Sabang waters from March to May 2010 due to increased water temperatures during that period [2]. This reduced coral cover had resulted in a decrease in the number of fish species in Sabang waters by up to 50%.

The objective of this study was to develop a prediction model that can forecast sea surface temperature (SST). The result of this study can be used for further research or even to be considered in some decision that aims to preserve the environment.

Research Methodology

The first step to construct a mathematical model to predict sea surface temperature by using the Box-Jenkins model was collecting the data series. Data of sea surface temperature (in °C) used for this study were monthly average data and they were extracted from the USA National Centers for Environmental Prediction (NCEP) file by using software GrADS. This data was recorded at the geographical point around Sabang waters, namely at 5° 53' North Latitude and 95° 11' East Longitude because around the point, there were four places where coral reefs grew close together, namely Ujung Seurawan, Rubiah Channel, Rubiah Sea Tourism Park, and Batee Meuronon. Whereas at other points, the coral reef growth was far apart. Thus, it was assumed that this point can represent the temperature of Sabang waters in general.

The variable used to represent temperature was y indexed t , where y_t for $t = 1, 2, 3, \dots, T$. Box-Jenkins model were developed by two main models, namely AR (autoregressive) and MA (moving average) model [3]. Yet, if the data series had seasonal factor, then some adjustments were applied to both model. Main assumptions of Box-Jenkins model were stationarity for its mean and variance [3]. Some tests were performed to check the assumptions. To check the stationarity of its mean, Augmented Dickey Fuller (ADF) test was performed, while Box-Cox Transformation was applied to check the stationarity of its variance.

After the data series met all assumptions, the next step was model identification stage. On this stage, Autocorrelation Function (ACF) and Partial Autocorrelation Function (PACF) plot were investigated to determine the order of MA and AR model, respectively. This stage produced some candidate models that had to be tested on the next step, namely model estimation and evaluation. To estimate the model, software R was used. Furthermore, some tests were conducted to evaluate the estimated models. To check if the models fulfilled parsimony aspect, Akaike's Information Criteria (AIC) and Bayesian Information Criterion (BIC) were performed. While to check the residual assumption (*white noise* assumption), Ljung-Box test was conducted. In model application step, the error values generated by the selected model were calculated by using error criteria MSE, RMSE, and MAPE. After undergone all stages, the best model was obtained. Then, the model was used to forecast the sea surface temperature of Sabang island in the future.

Result and Discussion

Data on sea surface temperature (in °C) from January 2001 to December 2012 were divided into two parts, 3/4 parts were for parameter estimation and 1/4 part were for forecasting activities. Thus, the data used for parameter estimation was data from January 2001 to December 2009, while data for forecasting purposes were from January 2010 to December 2012.

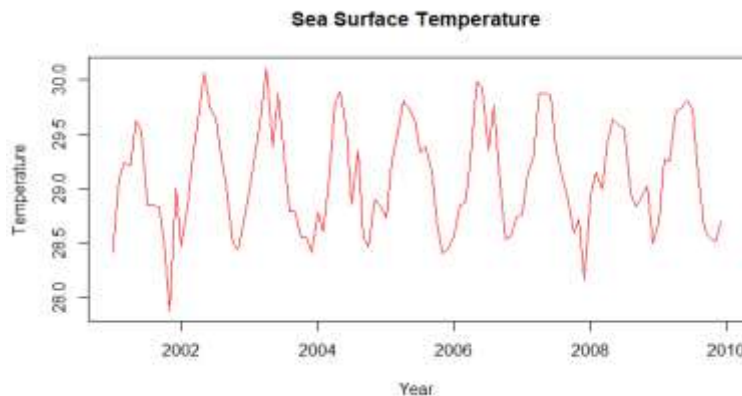


Figure 1. Plot of temperature data from January 2001 - December 2009

To test data stationarity on its mean, the Augmented Dickey Fuller Test (ADF) was used, the calculation of which was done by using software R. The calculated p -value was 0.01. If the value of the significance level (α) used in this study was 0.05 (confident interval 95%), then the p -value = $0.01 < \alpha = 0.05$. This led to the decision to reject H_0 with the conclusion that the data series was stationary.

To find out if the data was stationary for its variance or not, Box-Cox Transformation was used. Based on the calculation by using software R, the value of the transformation parameter λ obtained in the first test was -1. The value of $\lambda = -1$ means that the data series variance was not stationary. Thus, data had to undergo transformation. The transformation that needed to be done for data series having transformation parameter value $\lambda = -1$ was $1/y_t$.

The value of the transformation parameter λ obtained from the second test using the transformed data was $\lambda = 1$ which means that the data series had been stationary. Therefore, this transformation data will be used in all stages of model construction. However, for forecasting activities, the transformed data series must be transformed back so that the temperature value that will be obtained was in its initial range.

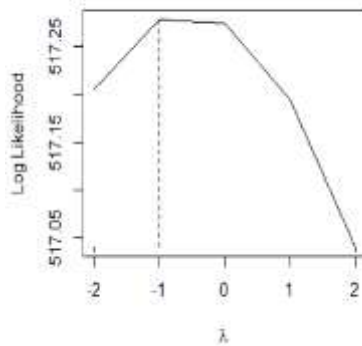


Figure 2. Box-Cox result before transformation

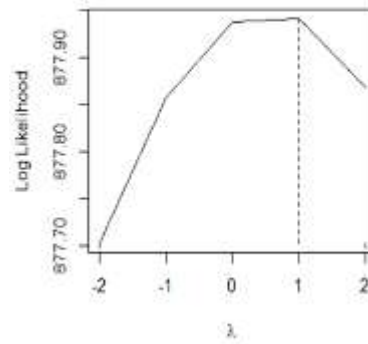


Figure 3. Box-Cox result after transformation

Model Identification

At this stage, an analysis of the ACF and PACF plots was carried out to determine in which bar the time lag was statistically significant. The significance border of the autocorrelation bar was represented by the blue dashed line in Figures 4 and 5.

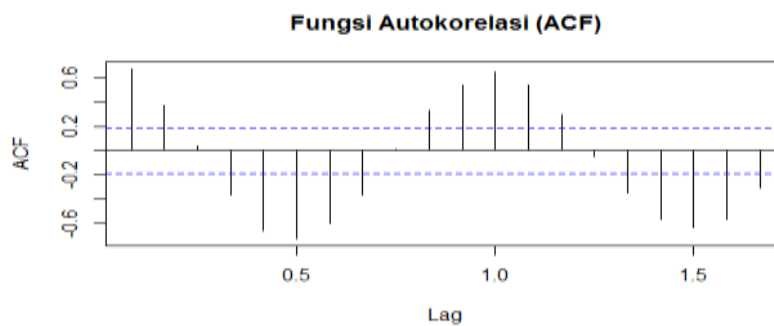


Figure 4. Autocorrelation function plot

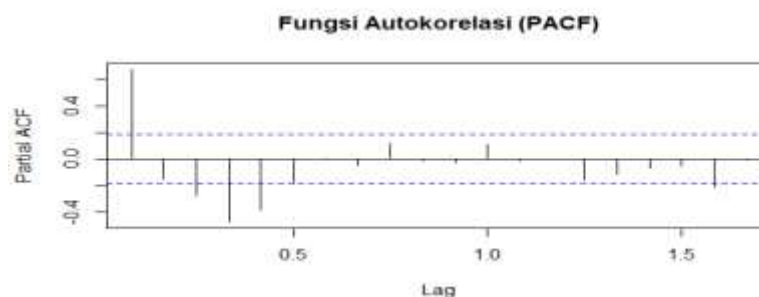


Figure 5. Partial autocorrelation function plot

Autocorrelation bar in ACF and PACF plots (Figure 4 and 5) formed a regular pattern that indicates that the data series had seasonal factor. Therefore, seasonal differentiation must be performed on the data series to eliminate seasonal factor.

Seasonal Differencing

Seasonal difference order 1 was defined as $z_t = y_t - y_{t-s}$. Because the data was monthly data, the value of index s was 12. The ACF and PACF plot of the differentiated data was:

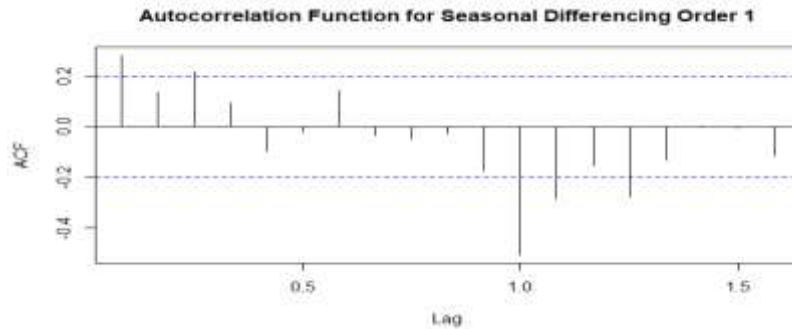


Figure 6. Autocorrelation function plot for seasonal differencing order 1

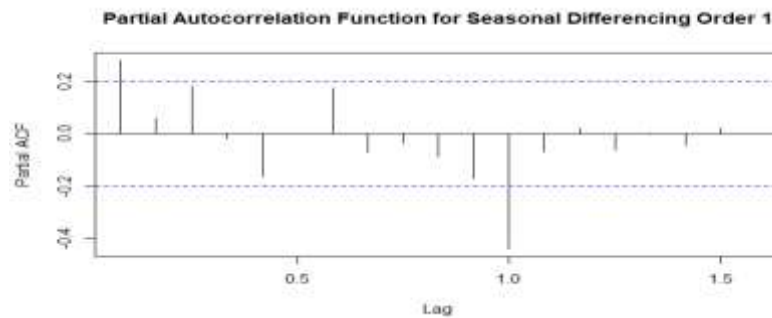


Figure 7. Partial autocorrelation function plot for seasonal differencing order 1

Seasonal differencing order 1 order was sufficient to eliminate seasonal factor from the data series so that there was no need to perform a second order seasonal differentiation process. Thus, a correlogram of the first order seasonal difference can be analyzed to determine some tentative models that were suitable to represent data.

Based on the correlogram above, there are four tentative models that were suitable to represent data series, they were:

- SARIMA (1, 0, 1) (1, 1, 1)₁₂
- SARIMA (1, 0, 2) (1, 1, 1)₁₂
- SARIMA (1, 0, 3) (1, 1, 1)₁₂
- SARIMA (1, 0, 4) (1, 1, 1)₁₂

Those four models will be tested on the next stage to determine the best model that fulfilled all statistical assumptions.

Model Estimation and Validation

After calculating with R software, the parameter values of the tentative models were as follows:

- SARIMA (1, 0, 1)(1, 1, 1)₁₂

$$y_t = 0.6820y_{t-1} + 0.9606y_{t-12} - 0.6551y_{t-13} - 0.0394y_{t-24} - 0.0269y_{t-25} + \varepsilon_t + 0.5580\varepsilon_{t-1} + 0.8243\varepsilon_{t-12} + 0.4599\varepsilon_{t-13}$$
- SARIMA (1, 0, 2)(1, 1, 1)₁₂

$$y_t = 0.6803y_{t-1} + 0.9608y_{t-12} - 0.6536y_{t-13} + 0.0392y_{t-24} - 0.0267y_{t-25} + \varepsilon_t + 0.5561\varepsilon_{t-1} + 0.0001\varepsilon_{t-3} + 0.8247\varepsilon_{t-12} + 0.4586\varepsilon_{t-13} + 0.00008\varepsilon_{t-15}$$

- SARIMA (1, 0, 3)(1, 1, 1)₁₂

$$y_t = 0.1119y_{t-1} + 0.9824y_{t-12} - 0.1099y_{t-13} + 0.0176y_{t-24} - 0.0020y_{t-25} + \varepsilon_t - 0.0062\varepsilon_{t-1} - 0.0349\varepsilon_{t-3} + 0.9955\varepsilon_{t-12} - 0.3345\varepsilon_{t-13} - 0.0347\varepsilon_{t-15} - 0.3268\varepsilon_{t-25}$$

- SARIMA (1, 0, 4)(1, 1, 1)₁₂

$$y_t = -0.1443y_{t-1} + 0.9852y_{t-12} + 0.1422y_{t-13} + 0.0148y_{t-24} + 0.0021y_{t-25} + \varepsilon_t - 0.2686\varepsilon_{t-1} - 0.0749\varepsilon_{t-3} + 0.9995\varepsilon_{t-12} - 0.6116\varepsilon_{t-13} - 0.1922\varepsilon_{t-15} - 0.3429\varepsilon_{t-25} - 0.1172\varepsilon_{t-27}$$

Then the AIC and BIC values were calculated to select a model that meets the parsimony aspect. The following was a recapitulation table of the AIC and BIC values calculated using software R.

Table 1. Recapitulation of AIC and BIC value

Model	AIC	BIC
(1, 0, 1)(1, 1, 1) ₁₂	-14.97795	-15.85378
(1, 0, 2)(1, 1, 1) ₁₂	-14.95962	-15.81061
(1, 0, 3)(1, 1, 1) ₁₂	-15.13329	-15.95945
(1, 0, 4)(1, 1, 1) ₁₂	-15.12025	-15.92158

From Table 1, it can be seen that the smallest AIC and BIC values among the tentative models were obtained by SARIMA model (1, 0, 3) (1, 1, 1)₁₂. However, SARIMA (1, 0, 4) (1, 1, 1)₁₂ models that have the second smallest AIC and BIC values will also be chosen to be tested at the next stage so that it can be used as a comparison model.

Ljung-Box test was conducted to determine whether the residuals generated by the selected model have met the assumption of *white noise* ($\varepsilon_t \sim N(0, \sigma_\varepsilon^2)$) or not. The hypothesis and decision-making criteria in the test were:

H₀: the residual was white noise

H₁: the residual was not white noise

After being tested, it can be concluded that both SARIMA (1, 0, 3) (1, 1, 1)₁₂ and SARIMA (1, 0, 4) (1, 1, 1)₁₂ models met the white noise assumption, so that they can be applied for forecasting activity.

Model Application

SARIMA model (1, 0, 3) (1, 1, 1)₁₂ and SARIMA (1, 0, 4) (1, 1, 1)₁₂ were tested for forecasting activities. The data used was data on sea surface temperature from January 2010 to December 2012.

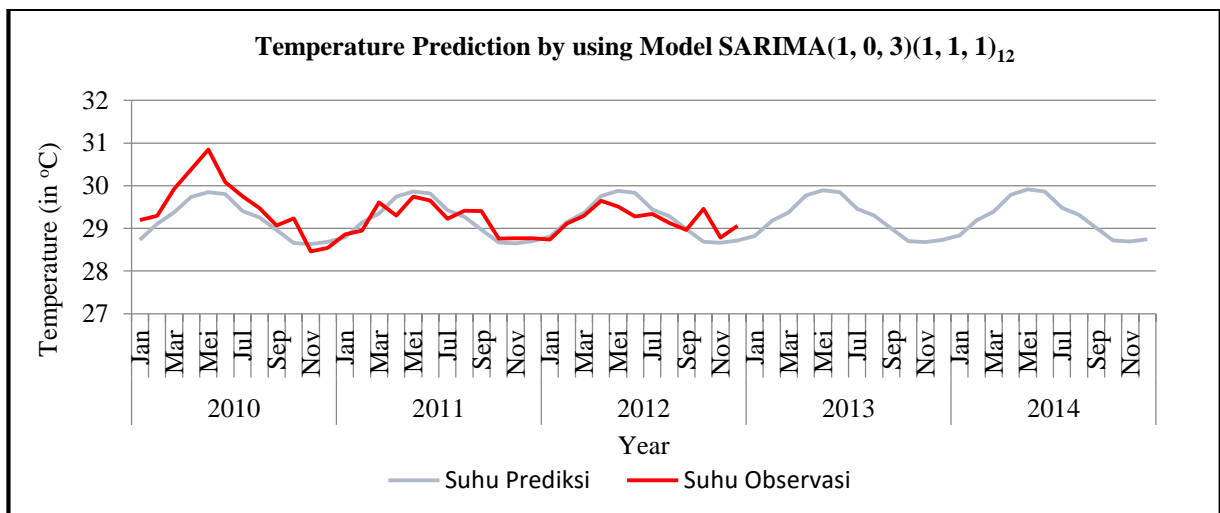


Figure 8. Temperature prediction by using model SARIMA (1,0,3)(1,1,1)₁₂

For Figure 8, blue line indicated prediction temperature while red line indicated real temperature.

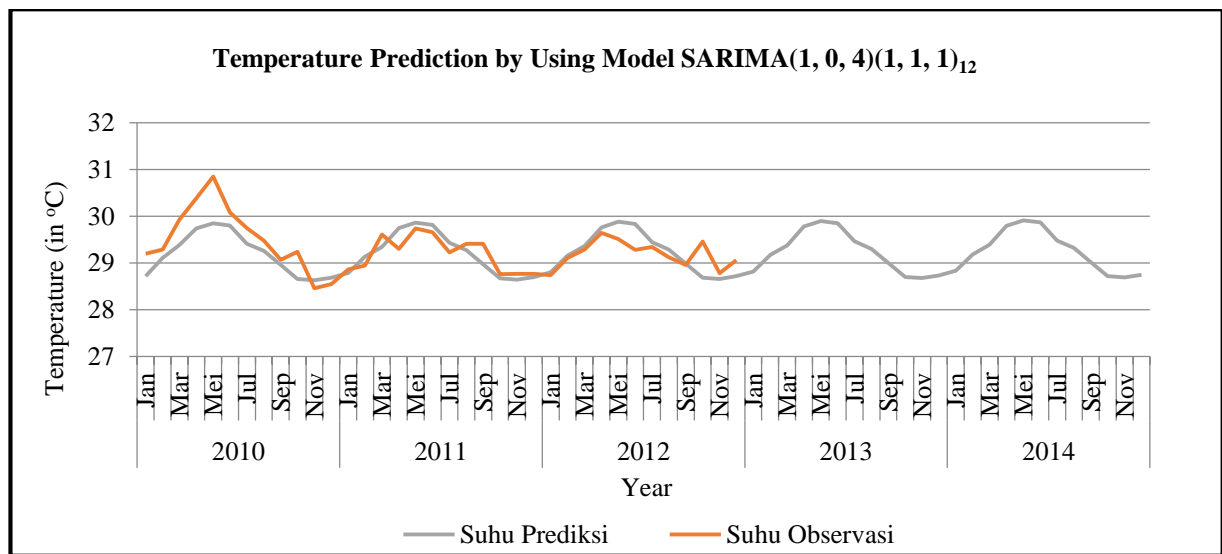


Figure 9. Temperature prediction by using model SARIMA (1,0,4)(1,1,1)₁₂

For Figure 9, grey line indicated prediction temperature while orange line indicated real temperature.

The following were the values of MSE, RMSE, and MAPE of the two models:

Table 2. MSE, RMSE, and MAPE values

Model	MSE	RMSE	MAPE
SARIMA (1, 0, 3)(1, 1, 1) ₁₂	0.123715088	0.351731557	0.913663941
SARIMA (1, 0, 4)(1, 1, 1) ₁₂	0.123661346	0.351655152	0.913610251
The difference of residual value for both model	5.3742×10^{-5}	7.64047×10^{-5}	5.36893×10^{-5}

According to Table 2, it can be seen that the model that had the smallest MSE, RMSE, and MAPE values was SARIMA model (1, 0, 4) (1, 1, 1)₁₂. Thus, the best model among all tentative models was the SARIMA model (1, 0, 4) (1, 1, 1)₁₂.

To predict one step forward, the model became:

$$y_{t+1} = -0.1443y_t + 0.9852y_{t-11} + 0.1422y_{t-12} + 0.0148y_{t-23} + 0.0021y_{t-24} + \varepsilon_{t+1} - 0.2686\varepsilon_t - 0.0749\varepsilon_{t-2} + 0.9995\varepsilon_{t-11} - 0.6116\varepsilon_{t-12} - 0.1922\varepsilon_{t-14} - 0.3429\varepsilon_{t-24} - 0.1172\varepsilon_{t-26}$$

The R^2 value for the model was 0.83. Thus, the model can represent observational data from January 2010 to December 2012 up to 83%. After undergoing chi-square test, the value of $\chi^2_{\text{count}} = 0.152$ was obtained. The value χ^2_{table} for $\alpha = 0.05$ and the degree of freedom $T-1 = 36 - 1 = 35$ was 49,802. The conclusion of the chi-square test was that there was insufficient proof to reject H_0 which meant that SARIMA (1, 0, 4) (1, 1, 1)₁₂ model was suitable to represent the data. Following was the forecasting value made by using SARIMA (1, 0, 4) (1, 1, 1)₁₂ until December 2018.

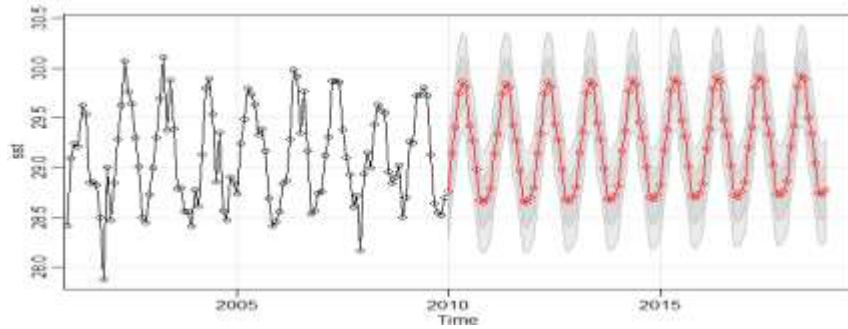


Figure 10. Forecasting data by using model SARIMA (1, 0, 4) (1, 1, 1)₁₂

Conclusion

The conclusion of this study were:

1. The best Box-Jenkins model to predict sea surface temperature was SARIMA (1,0,4)(1,1,1)₁₂
2. The reliability of the model was 95%
3. The selected model can cover the data up to 83%

References

- [1] Rudi E, dan Muchsin I (2011) Ikan Karang Perairan Aceh dan Sekitarnya. Penerbit Lubuk Agung, Bandung.
- [2] Rudi E, Iskandar T, Fadli N, Hidayati (2012) Effect of Coral Bleaching on Reef Fish Fisheries at Sabang. Proceeding of the 12th International Coral Reef Symposium, Cairns, Australia, 9-13 July 2012.
- [3] Lazim MA (2011) Introductory Business Forecasting a Practical Approach. 3rd Edition. UiTM Press. Kuala Lumpur.

Mechanical Engineering / Makina Mühendisliđi

Kompozit ve Çelik Güçlendirme Halkalarının Depolama Tankının Burkulma Yüküne Etkisi

Emre Çabuk, Dokuz Eylül Üniv., Fen Bilimleri Enst., Tınaztepe Kampüsü, İzmir, Türkiye*

Yusuf Arman, Dokuz Eylül Üniv., Makina Müh. Böl. Tınaztepe Kampüsü, İzmir, Türkiye

**İletişimden sorumlu yazar: mrcabuk@hotmail.com*

Anahtar Kelimeler: kompozit, burkulma yükü, depolama tankı, güçlendirme halkası

Disiplin: Makina Mühendisliği

Özet

Bu çalışma kapsamında her alanda yaygınlaşan kompozit malzeme teknolojilerinden yararlanılarak, özellikle büyük kapasiteli tanklarda hedeflenen dış basınç (vakumlama basıncı) değerlerini emniyetle karşılayacak daha hafif tank üretimi için analizler yapılmıştır. Bu amaçla, proses işleminde kullanılan bir tank modeli alınarak güçlendirme halkası olmadan dış basınç analizi yapılmıştır. Daha sonra tank çevresi çelik halka ile güçlendirilerek kuşak kalınlığı ve genişliği değiştirilerek kritik burkulma yükündeki farklar ortaya konulmuştur. En son olarak, çelik kuşak yerine kompozit malzemeden (karbon/epoksi) sarımlarla oluşturulan kuşakla hibrit bir model elde edilmiştir. Kompozit kuşak ve çelik kuşak arasındaki farklar ve burkulma yüküne etkileri araştırılmıştır.

Giriş

Hammadde-ürün arasındaki ilişkiler, petrokimya, azot sanayi tesisleri, kimya ve gıda madde üretimi yapan tesisler geliştikçe, sıvı ve sıvılaştırılmış hammadde veya ürünlerin depolanması, taşınması veya proses işlemler için kapalı kaplara olan ihtiyaç artmaktadır. Bu ihtiyaca dayanarak günümüzde çeşitli fonksiyon, kapasite ve yapı formunda kapalı kaplar yapılmaktadır. Yüksek kapasiteli depolama tanklarının iç basınç veya dış basınç nedeniyle deformasyonu, gerek depolanan madde gerekse tankın kendi yapısından dolayı insana, çevreye, ekonomiye ve canlı yaşamına karşı büyük tehdit oluşturmaktadır. Dış basınç iç basınca göre aniden gelişen ve düşük kapasitelerde deformasyona neden olduğundan dikkat edilmesi gereken bir olgudur.

Günümüz yapılarında depolama tankları ince kabuk yapıda oluşturulmaktadır. Kabın kalınlığı diğer büyüklüklerle karşılaştırıldığında çok küçük ($R_m/t > 10$ Burada; R_m = ortalama tank yarıçapı, t =tank cidar kalınlığı) olduğunda, ince kabuk olarak kabul edilir [1]. En yaygın ince kabuk teorileri doğrusal elastik kavramlarına dayalı olanlardır. Doğrusal kabuk teorileri, küçük elastik deformasyonlar sergileyen kabuklar için yeterli gerilmeleri ve deformasyonları öngörür [2]. Kabuk burkulma olgusu üzerinde birçok çalışma yapılmıştır. Timoshenko, düzgün aksenal bası yüküne maruz kalan dairesel bir silindirik kabuk için, diferansiyel denklemleri formüle ederek, çözümlerini ortaya koymuştur [3]. Donnel ve Wan, düzgün aksenal basınç kuvvetleri altında ince silindirik kabukların bükülme üzerindeki etkisini analiz etmişler ve genel denklemleri türetmişlerdir [4]. Flügge, silindirik kabuklar için aksenal ve iç basıncın kombine etkisi üzerine çalışmıştır [5]. Von Mises, uçlarından basit mesnetli takviyesiz silindirik kabuk için dış basınç ve aksenal olarak uygulanan sıkıştırma kuvvetlerinin birleşik yüklenmesine maruz kalan silindirik kabuklar için doğrusal bükülme formülünü ortaya koymuştur [6]. Widenburg ve Trilling ise çalışmalarında kritik burkulma basınç formülünü Von Mises'den farklı olarak silindirin çevresi boyunca oluşacak burkulma dalgası sayısı (n) değerine bağlı olmaksızın geliştirmişlerdir [7].

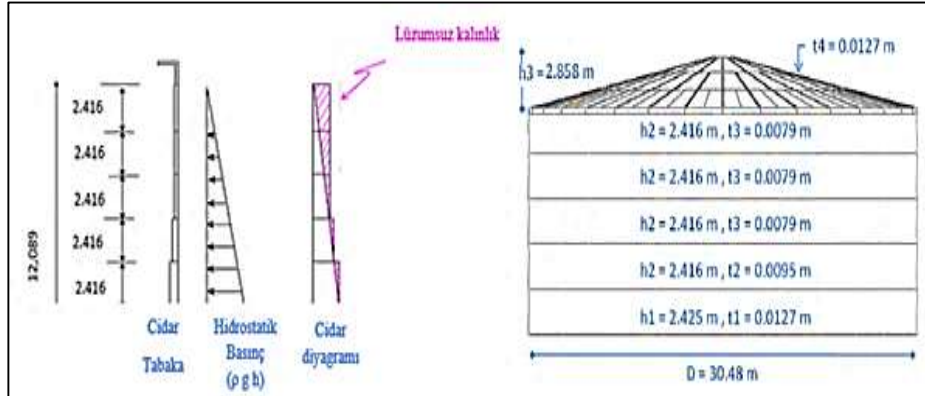
Hidrostatik basınç yani durağan sıvının basıncı, derinliğe bağlı olarak artar. Bu nedenle dikey tanklar ve silolar kademeli duvar kalınlığına sahip silindirik kabuklar olarak inşa edilir. Dikey tankların tabakaları, iç basınca bağlı olarak minimum duvar kalınlığında tasarlanırken; tankın üst bölgesi, alt kısma göre ince tasarlanır. Dış basınca maruz ince duvar kalınlığına sahip kabuk üst bölgesi alt bölgesine göre daha önceden burkulmaya ve deformasyona uğrayacaktır. Tankın üst tabakalarının kritik burkulma yükü alt tabakaya göre düşük olmasından dolayı tankın ilk burkulması üst tabakada meydana gelirken, alt kısımlar hem radyal hem de aksenal yönlerde üst tabakanın burkulmasına sınırlama sağlar [8]. Dış basınca maruz kademeli tank duvarı hakkındaki çalışmalar ise Resinger ve Greiner tarafından, yarı membran teorisine dayanarak üç kademeli silindir için diyagramları ortaya koyarak, kritik burkulma yükü için ortalama duvar kalınlığının kullanılmasının yanlış olabileceğini belirtmişlerdir [9].

Üst cidar kalınlığına sahip birçok depolama tankı için, hem çevresel hem de aksenel baskıları taşımak için bu bölgenin burkulma direncini arttırmak için bir halka ile güçlendirilmesi gerekir. Dış basınca karşı kademeli depolama tanklarının tasarlanmasında halka ile güçlendirme göz önünde bulundurulması gerekir. Greiner, 56 m çapında ve 26 m uzunluğunda bir silindirin tavanından 8 m altında çok küçük boyutlu bir halka ile güçlendirilmesi sonucu (halka şeklindeki plaka: 100 x 12 mm), güçlendirilmemiş durumdaki silindirin burkulma direncini yaklaşık % 50 artırmıştır [8].

Sabit duvar kalınlığındaki kabuklar için farklı durumlarda çok sayıda çözüm mevcuttur. Değişken, yani kademeli duvar kalınlığı ve güçlendirici halkalarla sınırlandırılmış silindirler için, çözümler doğrusal burkulma denklemleri temelinde sayısal olarak türetilmiştir [2]. Çalışma kapsamında sayısal analiz yöntemi olan sonlu elemanlar yöntemi ile kademeli depolama tankında güçlendirme halkasının kuşak kalınlığı ve genişliği değiştirilerek kritik burkulma yükündeki farkları ortaya konulmuştur. En son olarak halka kompozit malzemeden tasarlanarak çelik halka ile karşılaştırılmıştır.

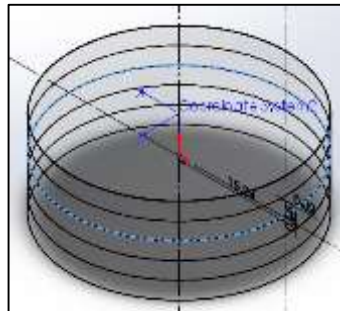
Materyal ve Yöntem

Yapılan üç boyutlu burkulma analizde, modelleme ve analiz için solidwork ve simulation sonlu elemanlar paketi kullanılmıştır. Modellenen tankın dış boyutları bir su deposunun benzeri olacaktır. Şekil 1’ de modellenen tankın cidar kalınlık diyagramı gösterilmektedir. Depolama tankı kademeli olarak modellenmiştir. Tank taban tabakaları hidrostatik basınçtan dolayı daha kalın oluşturulurken üst tabakalar daha ince tasarlanmıştır.



Şekil 1 Modellenen tankın cidar kalınlık dizayn diyagramı [10]

Dış basınç durumunda tank bütünlüğünü korumak ve dayanımı artırmak için tank çevresi çelik kuşak ile sarılmıştır. Tankın şekli dikkate alındığında, tankın en ince kısmı olan üst tabaka burkulma sonucu dengesizliğin ve yer değiştirmenin en fazla olduğu konumdur. Takviye plakası tabandan 7,250 m yükseklikte tankın kabuk kalınlığı 0,0079 m olan kısmında kaynak yerine yerleştirilmiştir (Şekil 2).



Şekil 2 Güçlendirme halkası konumu

Model ve güçlendirme halkası malzemesi çelik malzeme özelliklerinde aşağıdaki gibi seçilmiştir;

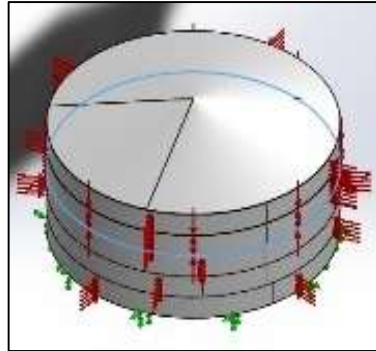
- Elastisite Modülü: E=206 GPa Akma Gerilmesi =350 MPa
- Poisson Oranı (ν)=0,3 Öz kütle (ρ)= 7850 kg/m³

Kompozit malzemedan modellenen güçlendirme halkası özellikleri tablo 1'deki gibidir. Kompozit malzeme olarak Karbon – Epoksi kullanılmıştır. Aşağıdaki tablo matris elemanı olarak epoksi ve fiber elemanı olarak karbonun mekanik ve fiziksel özelliklerinden yararlanılarak mikro analiz ile ortotropik kompozit malzeme özellikleri belirlenerek oluşturulmuştur.

Tablo 1. Karbon- Epoksi Malzeme

Karbon -Epoksi	
Fiber Hacimsel Oranı (V_f)	0,55
Yoğunluk (kg/m^3)	1530
Lif yönündeki Elastisite Modülü; E_1 (GPa)	128
Liflere dik yöndeki Elastisite Modülü: E_2 (GPa)	7,4
Poisson Oranının (ν_{12})	0,3
Kayma Modülünün G_{12} (GPa)	2,71

Tank cidar kalınlığı tank çapı ile karşılaştırıldığında çok küçük olduğu için ince kabuk (shell) elemanlar oluşturulmuştur. Serbestlik tipleri, tüm serbestlik dereceleri (u_x , u_y , u_z , rot_x , rot_y ve rot_z) sınırlandırılmış şekilde model üzerindeki taban yüzeyine uygulanmıştır. Yük olarak tankın dış kısmına yan yüzeylere $1 N/m^2$ hidrostatik basınç uygulanmıştır (Şekil 3).

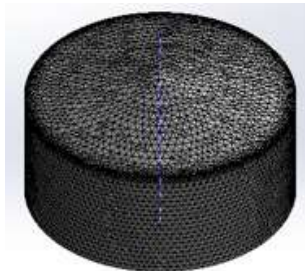


Şekil 3. Sınır şartları

Minimum eleman boyutu 0,21 m ve maksimum eleman boyutu 0,83 m olan 15315 küçük elemanlar ağı oluşturuldu. Mesh tipi olarak kabuk mesh olup eğri tabanlıdır. Yüksek kalite mesh yapılarak jakobien denetim yapılmıştır (Tablo 2).

Tablo 2. Mesh bilgisi

Mesh type:	Shell Mesh Using Surfaces
Mesher Used:	Curvature based mesh
Jacobian check for Shell:	On
Maximum element size:	0.831971 m
Minimum element size:	0.219118 m
Mesh Quality:	High
Total Nodes:	30635
Total Elements:	15315

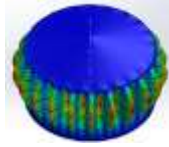
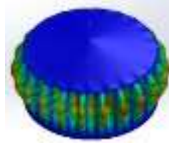
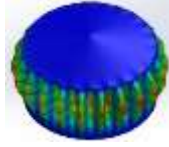
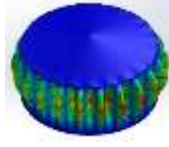
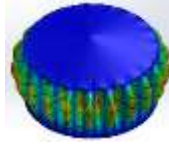


Bulgular ve Tartışma

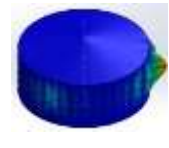
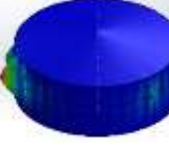
Tablo 3'de güçlendirme halkası genişliği 50 mm sabit iken halka kalınlığı 1 mm artırımlarla, tablo 4'de ise güçlendirme halkası kalınlığı 50 mm sabit iken halka genişliği 1 mm artırımlarla yükseltilecek,

güçlendirme halkasının kalınlığa ve genişliğe bağlı burkulma kritik yükleri, mod şekilleri ve yer değiştirmeleri görülmektedir. Oluşturulan tabloda kalınlıkla kastedilen güçlendirme halkasının tankın radyal yönündeki boyutu kastedilirken, genişlikle tankın eksenî yönündeki boyutu kastedilmektedir. Tablo 5’de güçlendirme halkasız ve kompozit yapıdaki güçlendirme halkalı tankın analizi görülmektedir.

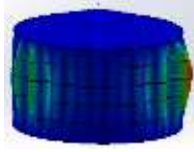
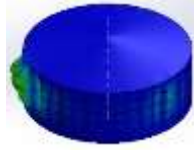
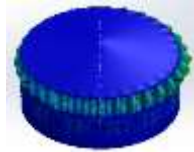
Tablo 3. Halka genişliği 50 mm sabitliğindeki güçlendirme halkalı tank

Halka genişliği (mm)	Halka kalınlığı (mm)	Çelik halka ağırlığı (N)	Tank burkulma kritik yük (N/m ²)	Maximum yer değiştirme (mm)	Mod şekli
50	12	4422.16	2563.3	11.8631	
50	13	4790.67	2618.9	11.91	
50	14	5159.18	2680.0	12.15	
50	15	5527.70	2745.1	14.92	
50	16	5896.2	2815.1	11.98	

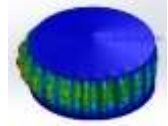
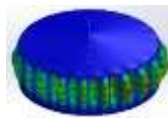
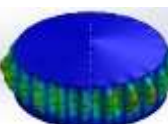
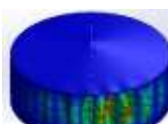

Tablo 4. Halka kalınlığı 50 mm sabitliğindeki güçlendirme halkalı tank

Halka genişliği (mm)	Halka kalınlığı (mm)	Çelik halka ağırlığı (N)	Tank burkulma kritik yük (N/m ²)	Maximum yer değiştirme (mm)	Mod şekli
12	50	4422.16	3252.17	43.5	
13	50	4790.67	3537.2	45.66	

3rd International Students Science Congress
3-4 May 2019, İzmir - Turkey

14	50	5159.18	4101.7	40.04	
15	50	5527.70	4166.6	40.28	
16	50	5896.2	4779.4	20.17	

Tablo 5. Güçlendirme halkasız ve kompozit güçlendirme halkalı tank

Halka genişliği (mm)	Halka kalınlığı (mm)	Tabaka açıları	Kompozit halka ağırlığı (N)	Tank burkulma kritik yük (N/m ²)	Maximum yer değiştirme (mm)	Mod şekli
-	-	-	-	2210.4	16.4569	
50	16	0°	1149,2	2745.68	18.9487	
50	16	90°	1149,2	2466.7	16.4382	
16	50	0°	1149,2	4371	36.5267	
16	50	90°	1149,2	2797.35	36.9038	

Güçlendirme halkası olmayan tank modelinde kritik yük 2210,4 N/m² elde edilmiştir. Çelik güçlendirme halkası ile oluşturulan modelde kuşak genişliği 50 mm’de sabit tutulup, kuşak kalınlığı 12 mm’den 16 mm’ye kadar 1 milimetrelık artırımlarda burkulma yükü, halkasız modele göre küçük miktarlarda artmıştır. Burada mod şekli incelendiğinde; tanktaki yer değiştirmeye, tankın bütününün katılmakla beraber en yüksek yer değiştirmenin cidar kalınlığının en düşük olduğu bölgede meydana geldiği görülmektedir (Tablo 3). Tablo 4 incelendiğinde; kuşak kalınlığı 50 mm’de sabit tutulup, kuşak genişliği 12 mm’den 16 mm’ye kadar 1 milimetrelık artırımlarında burkulma yükü, halkasız modele

göre büyük oranda artışlar gözlenmektedir. Burkulma yükündeki büyük artışlar ile birlikte büyük yer değiştirmeler oluşmuştur. Mod şekilleri incelendiğinde; yer değiştirmenin lokal meydana geldiği, tank cidar kalınlığının minimum olan bölgesinde daha fazla iken alt bölgesinde sınırlı katılım olmuştur. Halka kalınlığı 16 mm’de ise halka yer değiştirmede tam bir sınırlayıcı olduğu görülmektedir. Tablo 5’de kompozit malzemeden oluşturulmuş güçlendirme halkasının faklı tabaka açılarında ve çelik halkanın optimum burkulma yükü sağlayan boyutlarındaki kompozit halkanın kritik yükleri görülmektedir.

Sonuç

Tablo 3,4 ve 5 bütün olarak incelendiğinde; en yüksek burkulma kritik yük, halka genişliği 16 mm halka kalınlığının 50 mm olduğu boyutlarda meydana geldiği görülmüştür. Bu boyutlarda halkanın tam bir sınırlayıcı eleman gibi davrandığı görüldü. Aynı boyutlarda ancak halka genişliğinin 50 mm, kalınlığının 16 mm olduğu durumda kritik yükün halkasız modele göre fazla artmadığı ve yer değiştirmeye tankın bütününe katılarak, tank için sınırlayıcı etkisinin az olduğu görüldü. Bu durum güçlendirme halkasının tankın radyal yönündeki boyutlarının, eksenine göre burkulma yüküne etkisinin daha fazla olduğu görülür. Kompozit malzeme ile modellenen güçlendirme halkasında maksimum kritik yükü, tabaka açısı 0° yani fiber yönünün tank çevresi boyunca uzanan modelde, halkanın tankın radyal yönündeki boyutunun 50 mm olduğu modelde meydana gelmiştir. Aynı boyutlu çelik halka ile yakın kritik yük elde edilmiştir. Kompozit malzeme ile oluşturulan halka modeli ile çelik model ağırlık olarak karşılaştırıldığında kompozit malzemenin güçlendirme halkası olarak en uygun çözüm olduğu düşünülmektedir.

Referanslar

- [1] Moss DR (2004) Pressure vessel pressure vessel: Illustrated procedures for solving major pressure major pressure problems. Oxford, UK: Elsevier.
- [2] Ventsel E, Krauthammer T (2001) Thin plates and shells theory, analysis, and applications. New York, Basel: Marcel Dekker Inc.
- [3] Timoshenko SP and Gere J (1961) Theory of elastic stability. New York: McGraw-Hill.
- [4] Donnel LH and Wan, CC (1950) Effect of imperfection on the buckling of thin cylinders and columns under axial compression. J Appl Mech, vol. 17, No. 1, pp. 73–83
- [5] Flügge W, (1932) Die Stabilität der Kreiszyllinderschale, Ing-Arch, vol. 3, pp. 463–506
- [6] Von Mises R (1929) The critical external pressure for cylindrical tubes, Festschrift zum 70 Geburtstag von Prof. Dr. A. Stodola, Zurich, pp. 418-430.
- [7] Windenburg DE, Trilling G (1934) Collapse by instability of thin cylindrical shells under external pressure, Transactions of the A.S.M.E., Vol. 56, No. 11.
- [8] Greiner R (2004). Cylindrical shells under uniform external pressure. J. Teng, & J. Rotter içinde, Buckling of thin metal shells (s. 154-175). London: Spon Press.
- [9] Resinger F and Greiner R (1976). Praktische beulberechnung oberirdischer zylindrischer tankbauwerke für unterdruck. Stahlbau 45, 10–15.
- [10] Abreu JC, Calabro HD, Jaca R, Godoy LA, Burgos CA (2015) Buckling estimates for oil storage tanks: Effect of simplified modeling of the roof and wind girder. Thin-Walled Structures. doi:10.1016/j.tws.2015.02.006

Punch Shear and Low Velocity Impact Behaviours of Laminated Composites

*Akim Djele**, Dokuz Eylül University, The Graduate School of Natural and Applied Sciences, İzmir, Turkey
Ramazan Karakuzu, Dokuz Eylül University, Department of Mechanical Engineering, İzmir, Turkey
Akar Doğan

Dokuz Eylül University, Department of Mechanical Engineering, İzmir, Turkey
Munzur University, Department of Mechanical Engineering, Tunceli, Turkey

*Corresponding author: djakvrai@gmail.com

Keywords: punch shear test, low velocity impact test, S2 glass/epoxy, hybrid carbon-kevlar/epoxy

Discipline: Mechanical Engineering

Abstract

Composites are widely used in many applications thanks to their high strength-weight ratio. Transverse loading can cause serious damage to composite materials such as delamination, fiber breakage and matrix cracking. In this study, the punch shear and low velocity impact behaviors of composite materials were investigated. The punch shear apparatus is fabricated in accordance with the previous researches and the quasi-static tests (QST) is performed by using Universal Shimadzu Tensile Testing Machine with the designed apparatus. Various speeds of crosshead were chosen for quasi-static tests. Low velocity impact (LVI) tests is also carried out by using CEAST Fractovis Plus impact test machine at four different impact energies. S2 glass/epoxy and hybrid carbon-kevlar/epoxy composite specimens with dimensions of 100x100 mm were used for both QST and LVI test. Flat-nose penetrators with a cylindrical punch diameter of 12.70 mm were mounted to the test machines. After the experiments, the load-displacement graphs is plotted and the absorbed energy computed and determined. The both results were compared and a relationship founded.

Introduction

Impact on composites is a well-studied subject. Composites are widely used in military and commercial applications where light weight damage tolerant structures are required. The composite plays the crucial role of absorbing energy due to various interlaminar and intralaminar damage mechanisms such as delamination, fiber breakage and matrix cracking. [1] In recent years, the demand of materials having superior properties with low cost has led to the development of fiber-reinforced composites to replace metals in structural applications. The property of high strength to weight ratio of carbon and glass fiber reinforced composite structures has made them attractive for production of next generation materials. So many researchers have paid attention about damage and impact properties on composites in order to understand those mechanisms. Quasi-static tests are the proper choice to characterize impact events providing much simpler and cheaper way. The low velocity impact events are considered as quasi static in which dynamic effects can be neglected [2]. These composite materials and/or structures during their service life undergo various loading conditions. The most critical condition among them is the impact loading due to the laminated nature of these structures. When subjected to low- or high velocity impact, the composites behavior becomes very complicated due to phenomena such as fibers breakage, delamination, dishing deformation, plugging failure. [3]. Low and high temperature impact behaviors of laminated composites were investigated [4-5]. In this study, it is aimed to investigate the different factors of the two main test specially the low velocity impact and quasi-static punch shear test.

Experimental Procedure

The experiments were performed on the laminated material composites. So the composite materials were manufactured by using Kevlar/epoxy, S2 Glass/epoxy and by the vacuum infusion method (Figure 1). Quasi-static punch shear apparatus has been conceived and equipped on the Universal Shimadzu tensile test machine (Figure 2) with 100 kN capacity in order to perform the quasi static shear test on the composite. Various speeds 1mm/min, 10mm/min, 20mm/min, 40mm/min and 60mm/min of crosshead were chosen for quasi-static tests. Low velocity impact (LVI) tests were also carried out by using CEAST Fractovis Plus impact test machine (Figure 2) at four different impact energies, 20J, 30J,

50J, and 80J. S2 glass/epoxy and hybrid carbon-kevlar/epoxy composite specimens with dimensions of 100x100 mm were used for both QST and LVI tests. Experiments were performed at the room temperature by right circular cylinder punch diameter of 12.70 mm mounted to the test machines. After the experiments, the load-displacement graphs were plotted and the absorbed energy computed and determined.

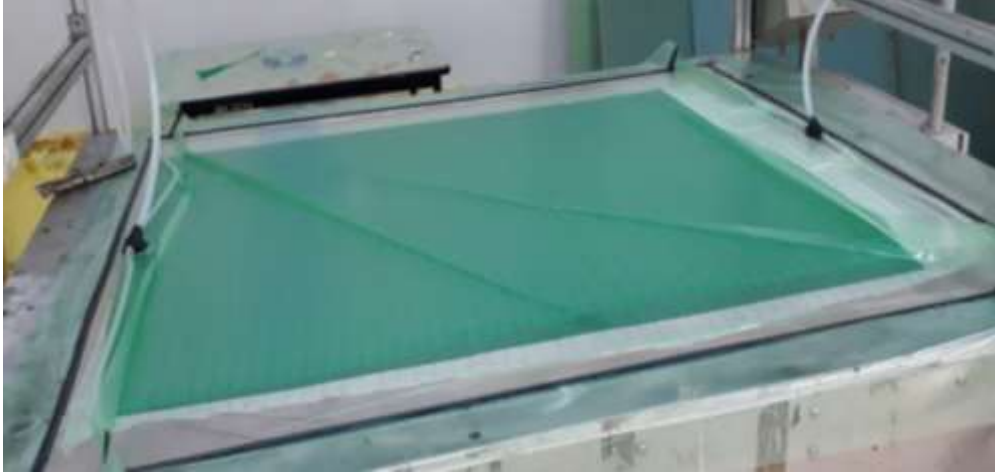


Figure 1. Vacuum assisted resin infusion method



(a)



(b)

Figure 2. (a) Ceast Fractovis-Plus impact test machine, (b) Tensile Testing Machine with punch-shear test apparatus

Results

To obtain the results for interpretation we needed to plot the load-deflection graphs of each specimen, and determined the absorbed energies in different aspects in order to have more details about the experimentation. Below are different plotted diagram.

It has been observed from Figure 3 that rebounding occurs in composite specimens with 20J and 30J impact energy. Contact force increases by increase of impact energy. After penetration, contact force does not change significantly. Penetration and perforation exist at 50J and 80 J, respectively.

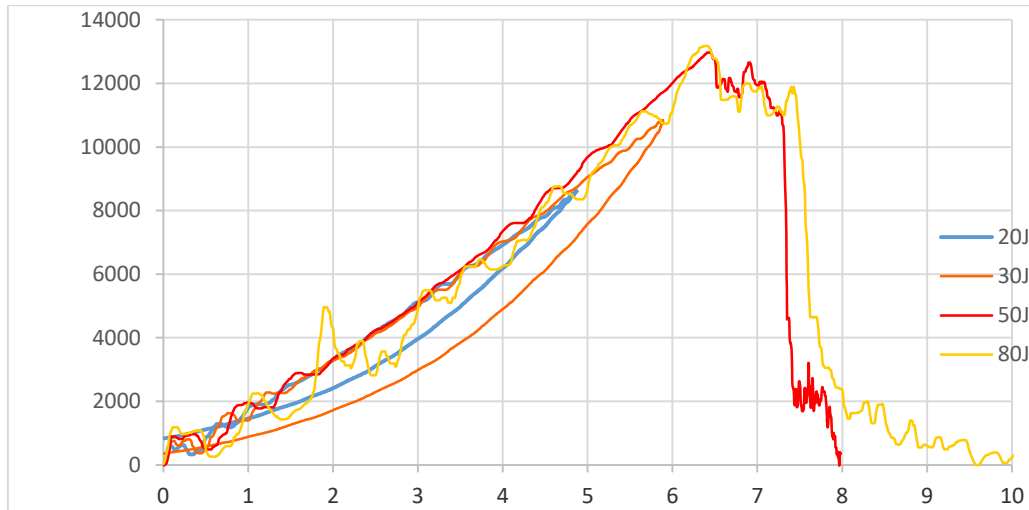


Figure 3. Force-deflection diagrams for S2 glass/epoxy composite in impact test

It has been shown in Figure 4 that rebounding exists in the composite specimen with 20J impact energy. In the other impact energies, contact force diagrams show similar behaviors.

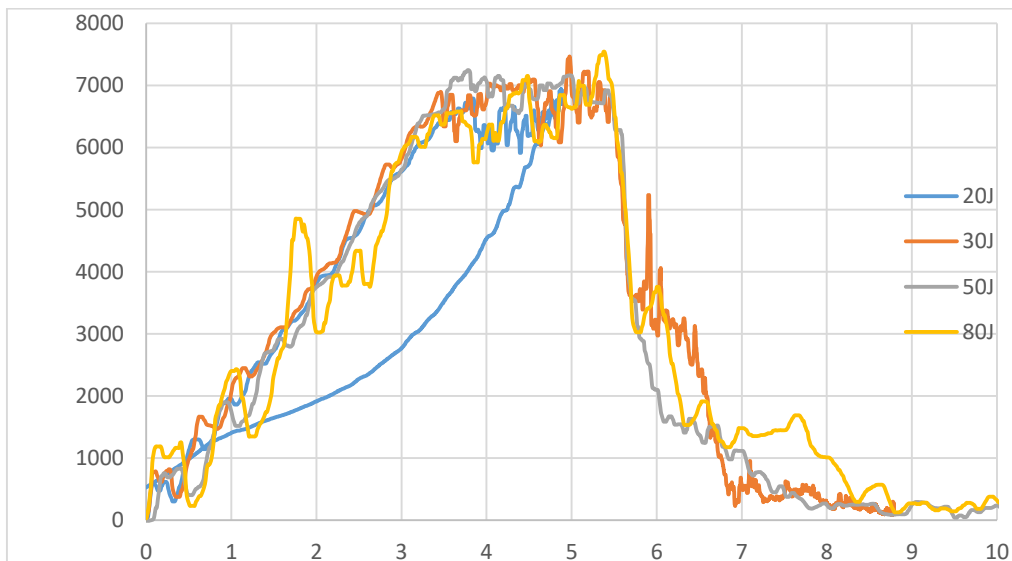


Figure 4. Force-deflection diagram for Hybrid carbon-kevlar/epoxy composite in impact test

It has been observed from Figure 5 with all the various speeds that the composite specimen undergo perforation.

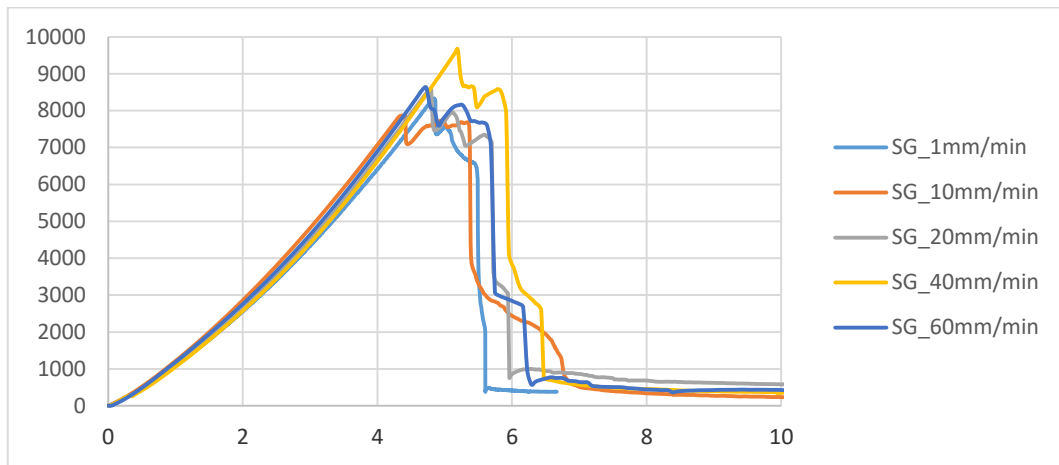


Figure 5. Force-deflection diagram for S2 glass /epoxy composite in quasi-static test

It has been shown in Figure 6 that with all the various speeds the composite specimens undergo perforation.

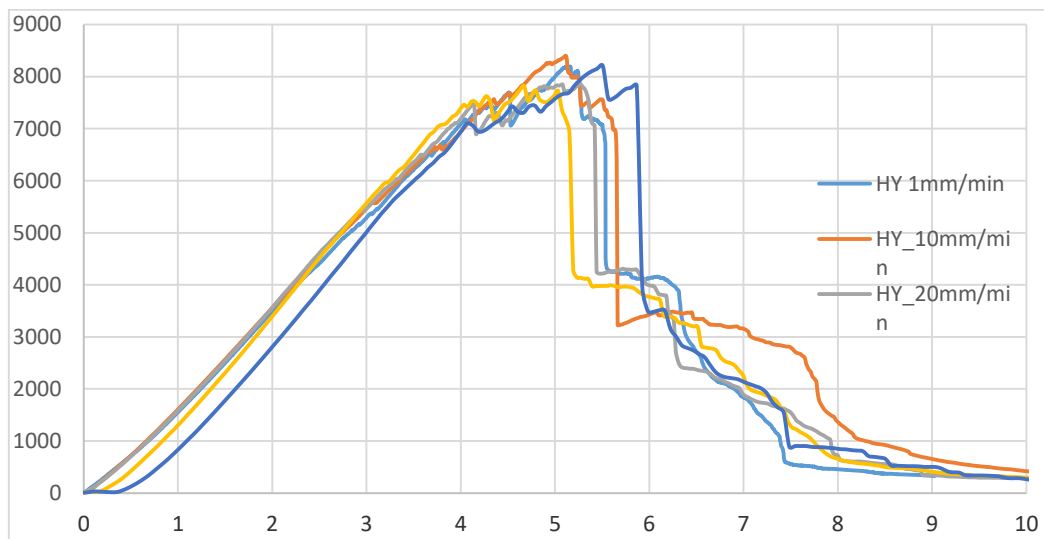


Figure 6. Force-deflection diagram for Hybrid carbon-kevlar/epoxy composite in quasi-static test

From Figure 7, it is noticed that all the specimens undergo perforation at all the cases. Impact test and quasi-static test diagrams are similar for hybrid carbon-kevlar/epoxy while they are different from each other for S2 glass/epoxy.

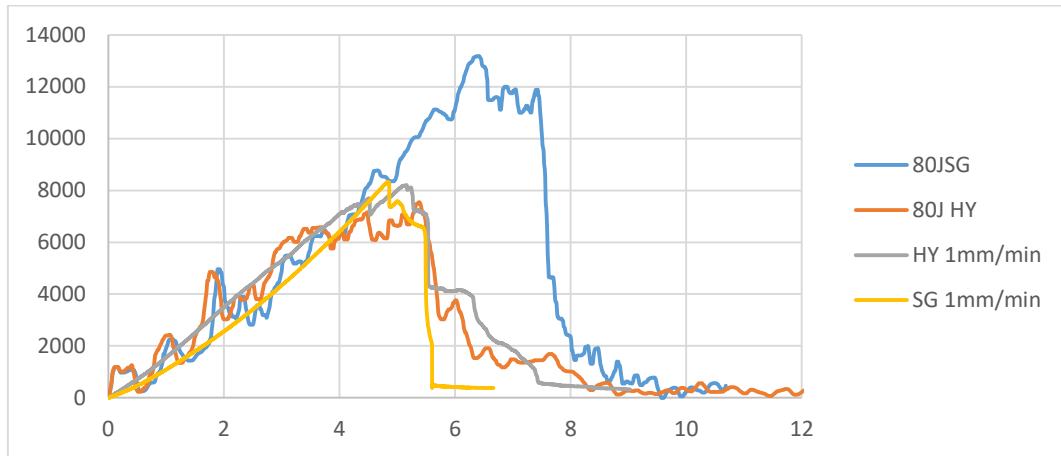


Figure 7. Comparison of force-deflection diagrams for the S2 glass/epoxy and Hybrid carbon-kevlar/epoxy composites at QST 1mm/min and LVI 80 J

From Figure 8, the observed graphs it can be inferred that the value of the absorbed energy of Hybrid carbon-kevlar/epoxy with the two tests showed an almost constancy over results while the S2 glass/epoxy present two different results with the two methods.

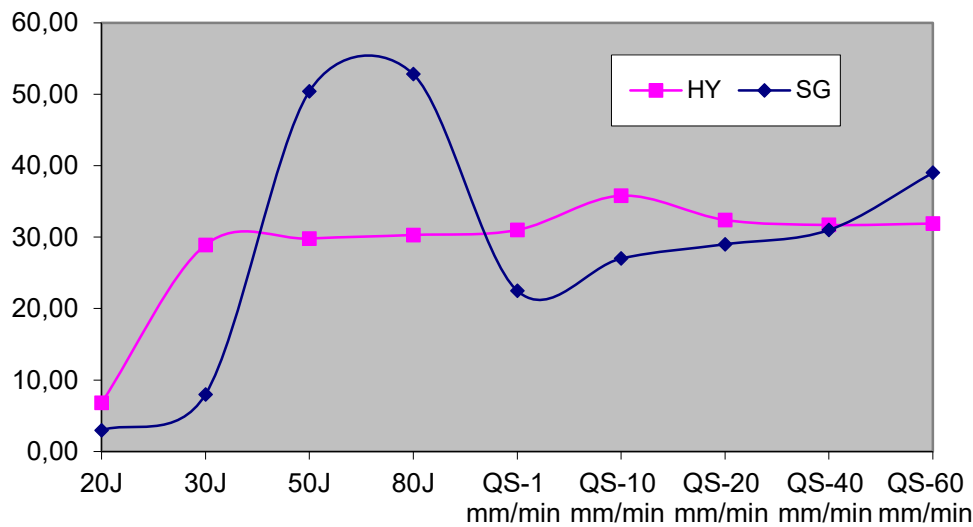


Figure 8. Absorbed energy of LVI and QST diagram for S2 glass/epoxy and Hybrid carbon-kevlar/epoxy composite

From Figure 9, the observed graphs, a rebounding is noticed which start from the 20J value and at 50J a perforation of the S2 glass/epoxy specimen and a rebounding which start from the 20J value and at 30J a perforation of the hybrid carbon-kevlar specimen.

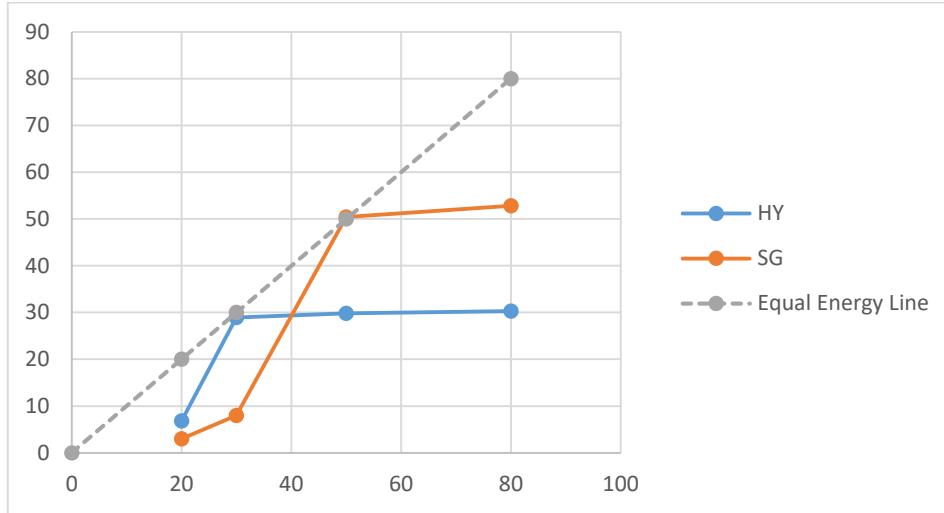


Figure 9. Absorbed energy and Impact energy diagram

Conclusion

In this study two different test, the quasi static punch shear and low velocity impact behaviors have been performed on two different types of laminated composite material. The results after the experimentation showed that the S2 Glass /epoxy composite specimen present more resistance than Hybrid carbon-kevlar/epoxy composite specimen. However, hybrid carbon kevlar/epoxy composites shows better stable behavior than S2 glass/epoxy in considering force-deflection diagrams both impact and quasi-static tests.

Acknowledgement

This study was supported by the Presidency for Turks Abroad and Related Communities (YTB) within “International Student Academy” Project.

References

- [1] Xiao JR, Gama BA, Gillespie Jr. JW (2007) Progressive damage and delamination in plain weave S-2 glass/SC-15 composites under quasi-static punch-shear loading. *Composite Structures* 78(2): 182-196.
- [2] Bulut M, Erkliğ A, Yeter E (2016) Hybridization effects on quasi-static penetration resistance in fiber reinforced hybrid composite laminates. *Composites Part B: Engineering* 98(1): 9-22.
- [3] Sadeghi M, Pol MH (2017) Investigation of behaviors of glass/epoxy laminate composites reinforced with carbon nanotubes under quasi-static punch shear loading. *Journal of Sandwich Structures and Materials*. 21(4):1535-1556.
- [4] Aktaş M, Karakuzu R, Icten BM (2011) Thermal impact behavior of glass-epoxy laminated composite plates, *Journal of Thermoplastic Composite Materials*. 24(4): 535-553.
- [5] Icten BM, Atas C, Aktas M, Karakuzu R (2009) Low temperature effect on impact response of quasi-isotropic glass/epoxy laminated plates. *Composite Structures* 91(3): 318–323.

Drop Weight Impact Response of Laminated Composites

Hüseyin Erdem Yalkın*, Dokuz Eylül University, The Graduate School of Natural and Applied Science,
Tınaztepe Campus, Buca, İzmir, Turkey

Ramazan Karakuzu, Dokuz Eylül University, Dept. of Mechanical Engineering, Tınaztepe Campus, Buca, İzmir,
Turkey

*Corresponding author: erdemyalkin@gmail.com

Keywords: glass fiber, laminated composites, drop weight impact, LS-DYNA

Discipline: Mechanical Engineering

Abstract

This paper is concerned with behaviour of laminated composites under drop weight impact. Two different energy values of 10J and 20J used for experimental and numerical studies. Constant mass and different impactor velocities were used to determine energy values. The laminate had $[\pm 45/(0/90)_2]_s$ oriented unidirectional E-glass reinforcing materials and epoxy resin for matrix material. Numerical simulations were performed using LS-DYNA finite element analysis software. It was observed that contact force-time curves, contact force-deflection curves, velocity-time curves, deflection-time curves and absorbed energy values of the experimental and numerical analysis were compatible with each other.

Introduction

With increasing use of composites in transportation, military, ground and air vehicles, ship structures, infrastructure, sporting goods and the power industry, the understanding of impact behavior is critical for composite designers and end-users. A wealth of knowledge has been published on impact response of composite materials and structures. Yet, with continually emerging materials and processes there is a lack of systematic structure property-performance relationships that provide guidelines on impact behavior of composites [1].

Aslan et al. [2] studied low-velocity impact of response of (0/90/0/90)_s oriented E-glass/epoxy composites with experimentally and numerically. Impact tests were completed with impactor masses of 135 g and 2600 g, an impact velocity of 3 m/s and three different specimen dimensions. Experiments were done with vertical drop weight testing machine and numerical simulation was completed with 3DIMPACT finite element analysis code. It was concluded the smaller width of rectangular composite laminates has higher contact duration. Karakuzu et al. [3] studied the effects of impact energy, impactor mass and impact velocity on the maximum contact force, maximum deflection, contact time, absorbed energy, and overall damage area of [0/30/60/90]_s stacked glass/epoxy laminated composites, experimentally with drop weight testing machine and numerically with 3DIMPACT finite element code. As it was seen that the numerical results were good agreement with experimental results. Heimbs et al. [4] investigated the effect of a compressive preload on the low velocity impact behavior of carbon fiber-reinforced composite plate. MAT054 Enhanced_Composite_Damage material card and Contact_Automatic_Surface_to_Surface_Tiebreak contact card including delamination were preferred. Simulation results were showed a good correlation to the experimental data in terms of force and energy plots. Menna et al. [5] studied glass/epoxy laminates of different thickness were subjected to transverse impact at different energy levels and modelled by Finite element method. LS-DYNA software was preferred with Automatic_Surface_to_Surface_Tiebreak delamination contact model card and MAT020 Rijid and MAT059 Composite_Failure_Model material cards used. Sufficient agreement was obtained numerical predictions and experimental results. Maio et al. [6] also studied on low velocity impact on composite plates with LS-DYNA software. Progressive damage material card MAT 162 Composite_Msc_Dmg and contact definition between impactor and laminate, Automatic_Surface_to_Surface_Contact card were used. Good agreement with the experimental result shape and orientation of the delaminations were observed. Sevkati et al. [7] investigated drop weight impact behaviour of woven S2glass - IM7graphite fibers/toughened epoxy hybrid composites with two lay-up sequences both experimentally and numerically. MAT020 rigid for steel impactor and MAT022 Composite_Damage material model were created in order to model composite part. Contact_Automatic_Surface_To_Surface_Tiebreak and Eroding_Surface_To_Surface contact model were used between the steel impactor and composite. Good agreement between experimental and FE

results were achieved when comparing dynamic force, strain histories and damage patterns between experimental measurements and finite element simulations. Berk et al. [8] presented an experimental and numerical investigation on low velocity impact of woven S2 glass/epoxy and woven aramid/epoxy composite plates with two different energy level. LS-DYNA was used in order to perform numerical simulations. MAT020 Rigid material card for impactor and MAT055 Mat_Enhanced_Composite_Damage material cards were used. In order to model interaction between layers and impactor, Contact_Automatic_Nodes_to_Surface contact card preferred. In order to model interaction between composite layers, contact card with stress based delamination that Contact_Automatic_One_Way_Surface_to_Surface_Tiebreak were used. It was observed that experimental and numerical results in good agreement.

In this study, laminated $[\pm 45/(0/90)_2]_s$ oriented glass fiber epoxy composite laminates were tested at different energy values with drop weight testing machine. Specimens were analysed numerically with LS-DYNA. Then numerical and experimental results were compared with each other considering contact force-time curves, contact force-deflection curves, velocity-time curves, deflection-time curves and absorbed energy values.

Methodology

Laminated composite contained $[\pm 45/(0/90)_2]_s$ oriented unidirectional E-glass, total 12 layers each layer had 300 g/m² areal density. The thickness of the structure was about 3 mm. Laminated composites were manufactured by vacuum-assisted resin infusion process with using epoxy resin were post cured in an oven at 80°C and 15 hours [9]. Specimens were cut with diamond saw at a size of 100 mm x 150 mm. Ceast Fractovis Plus drop weight impact test machine were used. The impactor had 12.7 mm (0.5 in.) diameter hemispherical steel nose. The nose was connected to a force transducer. Data was taken from force transducer during the impact tests by a data acquisition system. Drop weight impact test machine software based on Newton's second law and kinematics relations. The software converts the time and contact force history data to the velocity, deflection and absorbed energy history data. The impactor had an additional mass. Total impactor weight was 4.96 kg.

Springs use for obtain extra impact velocity. Velocity sensor detects impactor velocity just before impactor reach the specimen. The specimen was clamped between the pneumatic circular fixture and lower circular support before the test. The inner diameter of the pneumatic clamping fixture was 76.2 mm. Anti-rebounding system prevents specimen to the second impact during test. Constant mass and 2.01 m/s, 2.84 m/s, impactor velocities used for determine 10J, 20J energy values, respectively.

The same boundary conditions of the experimental analysis were defined for the numerical analysis. In order to model interaction between composite structure and impactor, Contact_Automatic_Surface_to_Surface contact card with soft constraint formulation was used. MAT020 Rigid material model was used for an impactor and circular supports. Impactor and composite layers friction was neglected. Modelled impactor density increased for get same weight with experimental test impactor. All numerical data was taken from modelled impactor. Underintegrated shell elements of the type Belytschko-Tsay, element formulation option 2 was used. For hourglass control Flanagan-Belytschko stiffness form option 4 was used. The optimum parameters of element size, contact penalty stiffness were used. The influence of these parameters were investigated by Heimbs et al [4]. MAT058 Laminated_Composite_Fabric, depending on the type of failure surface, this model may be used to model composite materials with unidirectional layers, complete laminates, and woven fabrics. This model is implemented for shell and thick shell elements a continuum damage mechanics based material model were used [10].

The delamination definition Contact_Automatic_One_Way_Surface_To_Surface_Tiebreak with failure law option 8 was adopted between shell layers [10]. Tiebreak contact algorithm based on the knowledge of the interlaminar properties of the material in terms of normal and shear strengths. Among the different formulations available in LS-DYNA, the penalty contact formulation. Using this approach, each ply is modelled as a shell layer of elements, but the nodes between plies initially in contact are tied together, inhibiting sliding motions, until a failure criterion is reached, corresponding to delamination onset. In particular, the nodal stress is monitored throughout the analysis and implemented in the interface strength-based failure criterion:

$$\left(\frac{|\sigma_n|}{NFLS}\right)^2 + \left(\frac{|\sigma_s|}{SFLS}\right)^2 \geq 1 \quad (1)$$

Where σ_n and σ_s are the current normal and shear stresses, respectively, and NFLS, SFLS the normal and shear interlaminar strengths to be set in the contact definition. When Eq. (1) is fulfilled, contact stress is linearly reduced to zero as a function of the distance between two points initially in contact. As soon as a defined critical crack opening (CCRIT) is reached, the tie contact definition for those nodes is released. Once the tie component of the contact definition is deleted, the contact for those nodes converts into a standard surface-to-surface definition preventing interpenetration [5].

Laminated composite had 12 layers of unidirectional E-glass. Modelling all layers were caused numerical instabilities and time consuming. Because of that laminated composite modelled as 6 layers of shell elements with 5 delaminations. Each shell element had 2 internal integration points according to ply orientation. Laminated composite was modelled as shown in Figure 1. The modelled impactor had 12.7 mm (0.5 in.) diameter spherical and had 4.92 kg weight. Circular support modelled with shell elements. Laminated composite modelled as 6 layers and 2 mm mesh density.

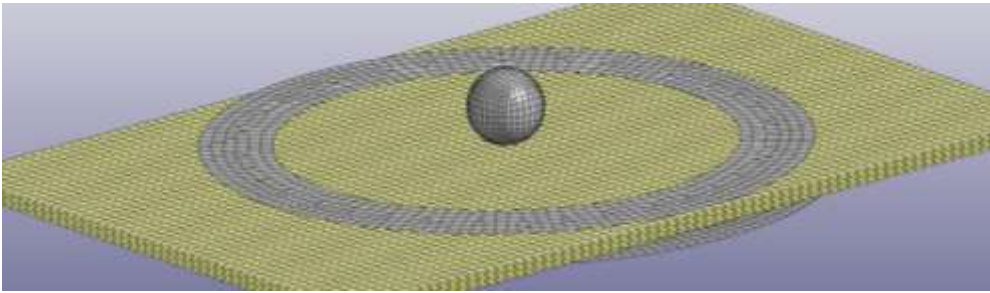


Figure 1. Numerical analysis model

Results

Drop weight impact test of laminated composites were investigated for 2 different energy values numerically with LS-DYNA software and were compared with the experimental results. Different energy values were obtained by changing impactor velocity to 2.01 m/s, 2.84 m/s values.

Contact force-time curves and contact force-deflection curves are given for 10 J Figure 2. “-exp” means experimental result and “-num” means numerical result. As seen in the given curves both maximum contact force values are nearly 4000 N. There is a little difference of deflection value between 5.6 mm for experimental and 6.8 mm for numerical analysis. Difference between experimental and numerical results for velocity-time was 0.6 ms and deflection-time curves for 10J are given in Figure 3.

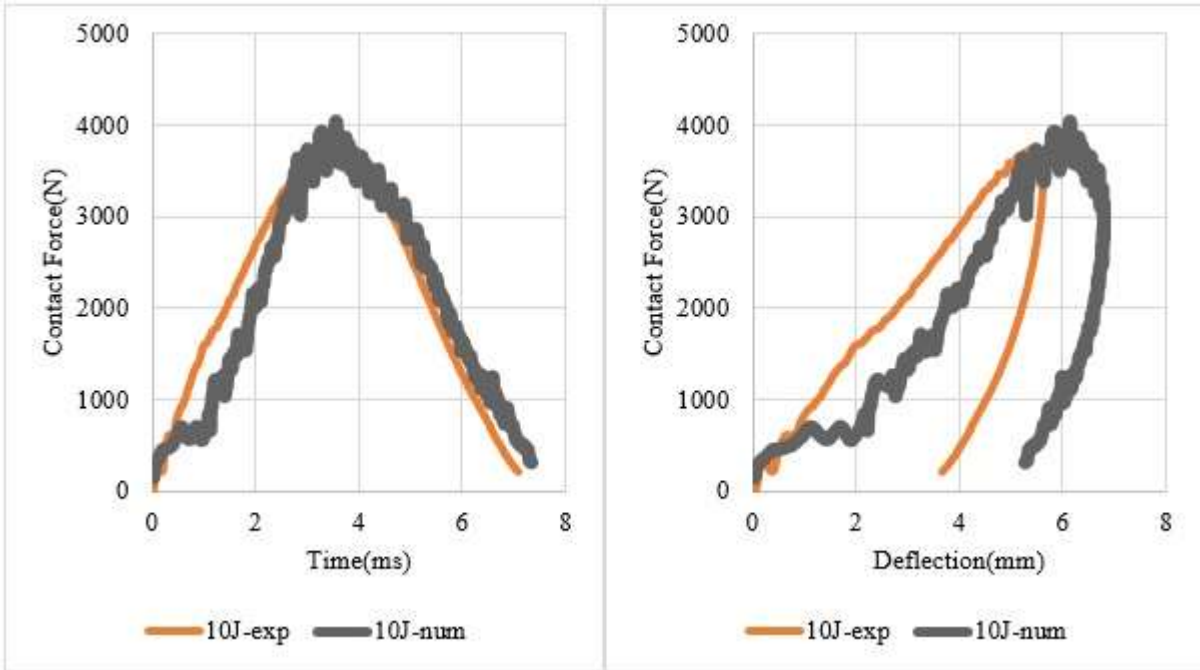


Figure 2. Contact force-time curves (left) and contact force-deflection curves (right) for 10J

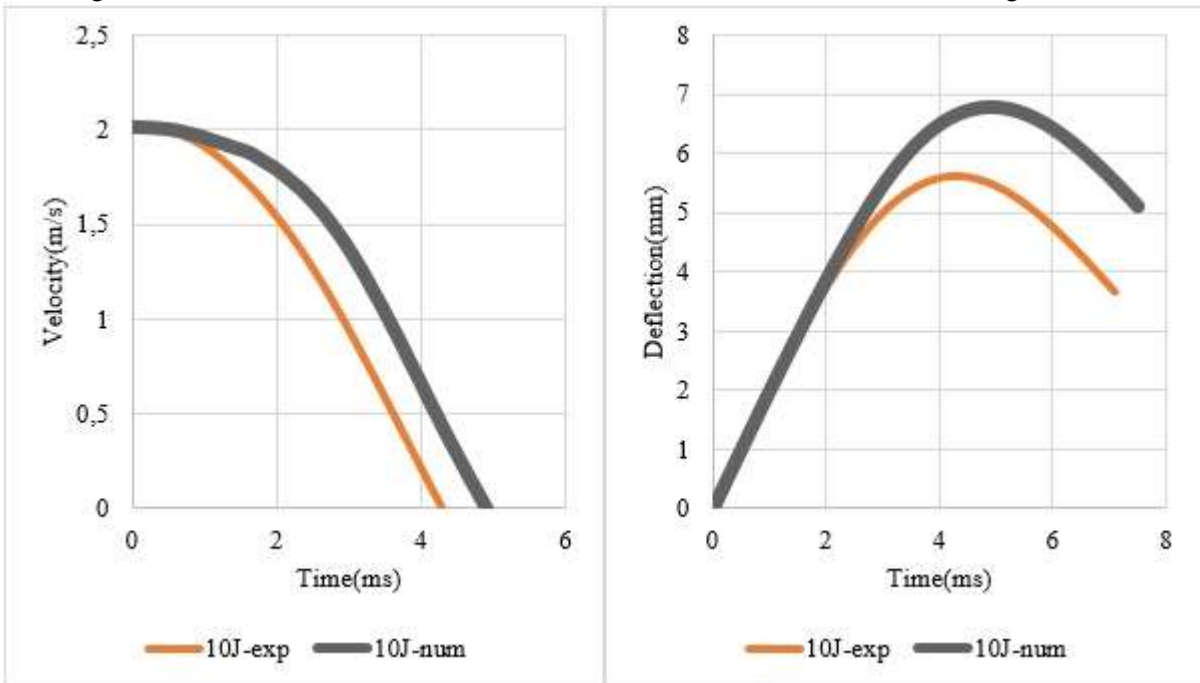


Figure 3. Velocity-time curves (left) and deflection-time curves (right) for 10J

Contact force-time curves and contact force-deflection curves are given for 20 J Figure 4. As seen in the given curves maximum force value difference is about 550 N. Maximum deflection value difference is only 1 mm. Other obtained results velocity-time curves and deflection-time curves are given in Figure 5.

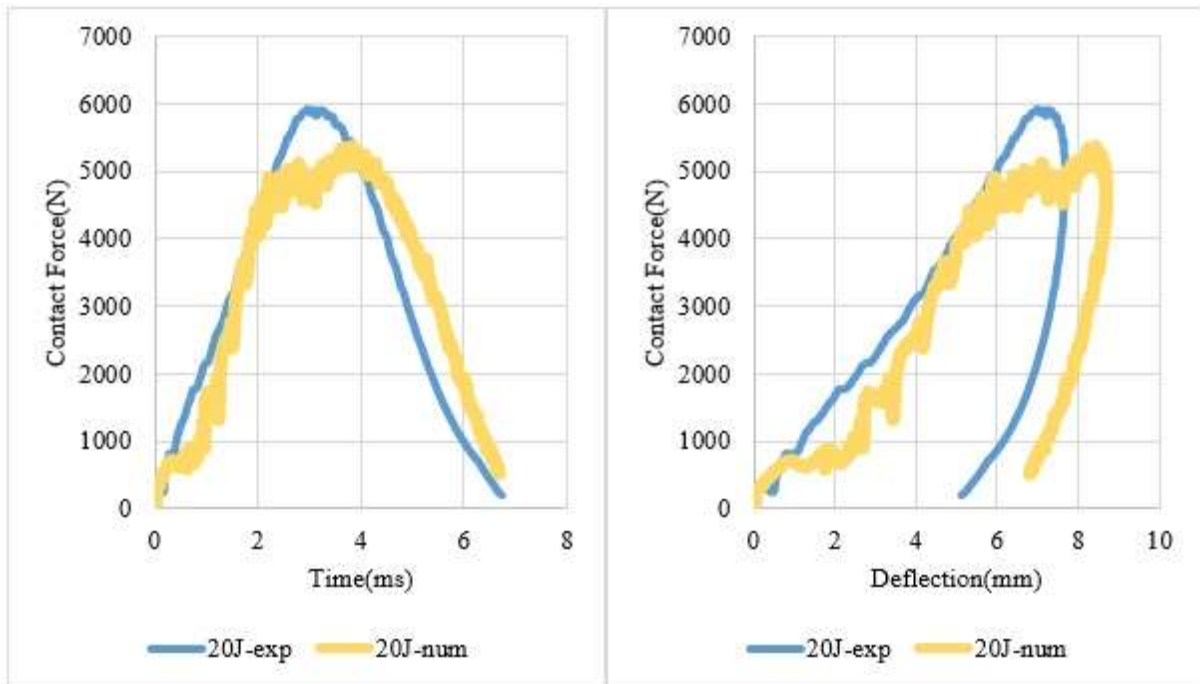


Figure 4. Contact force-time curves (left) and contact force-deflection curves (right) for 20J

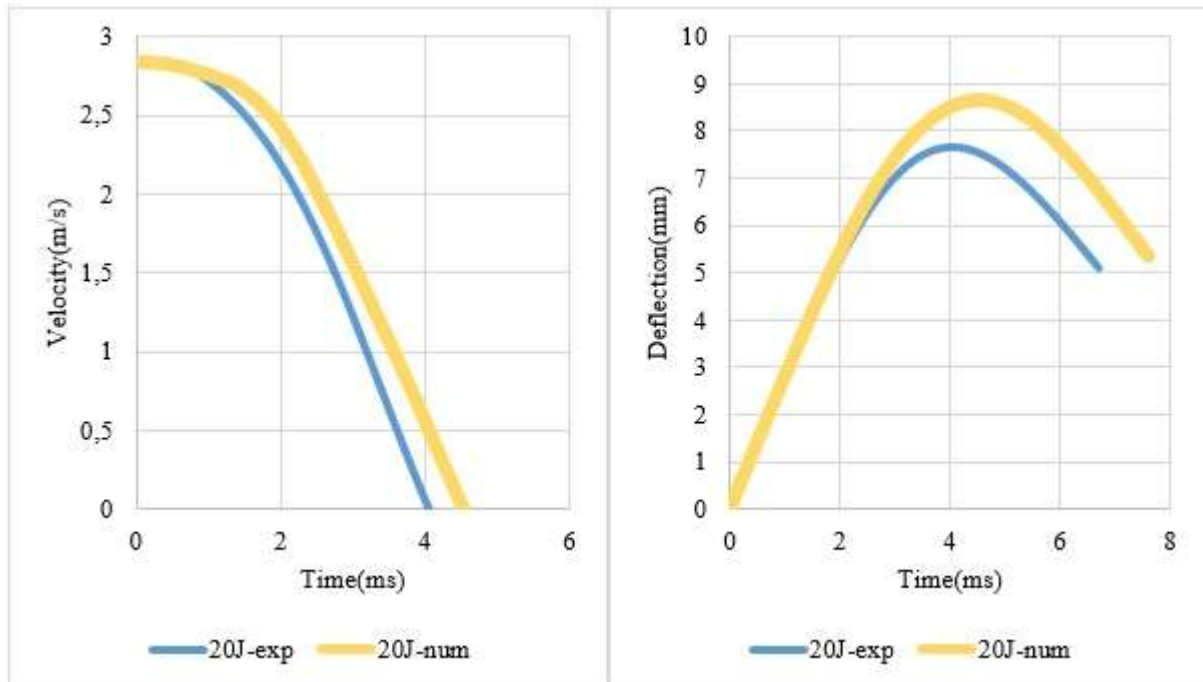


Figure 5. Velocity-time curves (left) and deflection-time curves (right) for 20J

Energy time curves both experimental and numerical analysis for all energy values are given in Figure 6. Absorbed energy values given in Table 1. As shown in the given energy values of experimental and numerical results so close each other. There are 0.1J and 0.6J absorbed energy difference between experimental and numerical analysis for 10J and 20J impact energy.

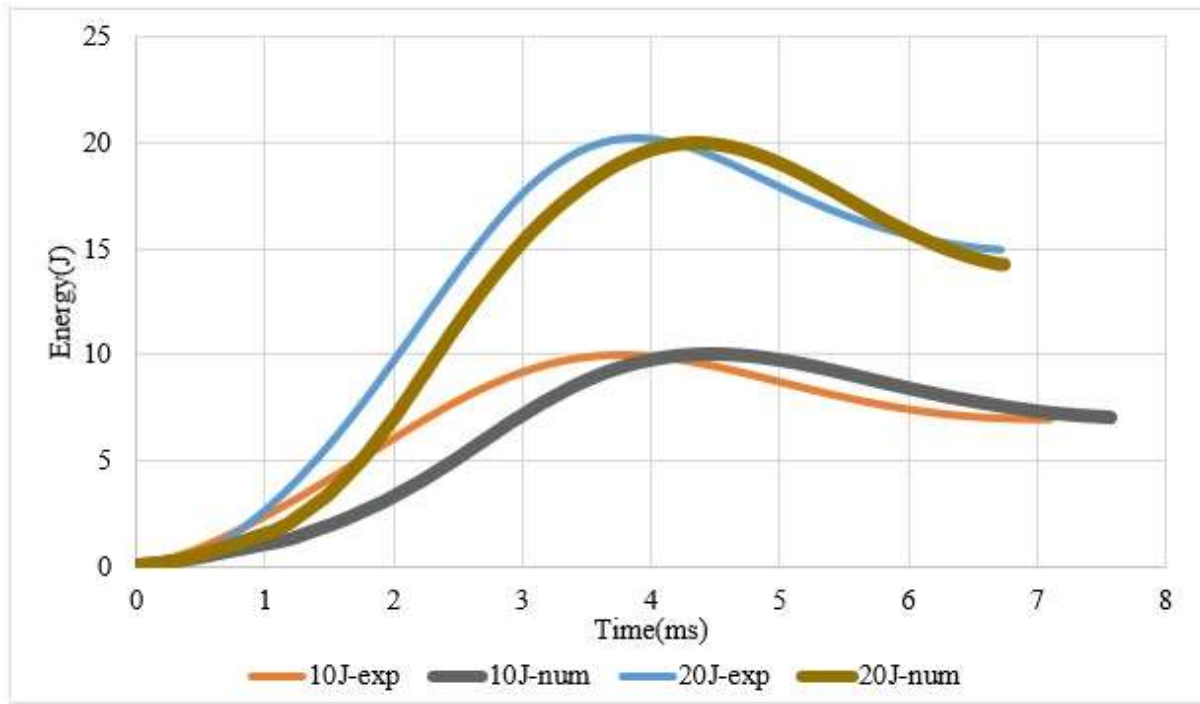


Figure 6. Absorbed energy curves

Table 1. Absorbed energy values

Impact Energy	Absorbed Energy (J) Experimental	Absorbed Energy (J) Numerical
10J	7,1	7,0
20J	14,9	14,3

Conclusion

In this study, drop weight impact test of laminated glass fiber/epoxy composites was analysed numerically with LS-DYNA software. Numerical results were compared with experimental results. It was observed that contact force-time curves, contact force-deflection curves, velocity-time curves, deflection-time curves and absorbed energy values of the experimental and numerical analysis were compatible with each other. As seen from given curves contact force and deflection values depend on impact velocity. All experimental and numerical analysis results of contact force deflection curves showed that low velocity impact mode was rebounding. Applied energy values were not enough for penetration and perforation modes. As a result constant mass and increasing impactor velocity, maximum contact force, maximum deflection and absorbed energy values increase.

References

- [1] Abrate S (2011) Impact Engineering of Composite Structures. Springer Wien New York, Udine.
- [2] Aslan Z, Karakuzu R, Okutan B (2003) The response of laminated composite plates under low-velocity impact loading. Composite Structures 59:119–127. [https://doi.org/10.1016/S0263-8223\(02\)00185-X](https://doi.org/10.1016/S0263-8223(02)00185-X)
- [3] Karakuzu R, Erbil E, Aktas M (2010) Impact characterization of glass/epoxy composite plates: An experimental and numerical study. Composites Part B 41:388-395. <https://doi.org/10.1016/j.compositesb.2010.02.003>
- [4] Heimbs S, Heller S, Middendorf P (2008) Simulation of Low Velocity Impact on Composite Plates with Compressive Preload. 7th LS DYNA Anwender forum, Bamberg.

**3rd International Students Science Congress
3-4 May 2019, İzmir - Turkey**

- [5] Menna C, Asprone D, Caprino G, Lapressto V, Prota A (2011) Numerical simulation of impact tests on GFRP composite laminates. *International Journal of Impact Engineering* 38:677-685 <https://doi.org/10.1016/j.ijimpeng.2011.03.003>
- [6] Maio L, Monaco E, Ricci F, Lecce L (2013) Simulation of low velocity impact on composite laminates with progressive failure analysis. *Composite Structures* 103:75-85 <https://doi.org/10.1016/j.compstruct.2013.02.027>
- [7] Sevkat E, Liaw B, Delale F (2013) Drop-weight impact response of hybrid composites impacted by impactor of various geometries. *Materials and Design* 52:67-77. <https://doi.org/10.1016/j.matdes.2013.05.016>
- [8] Berk B, Karakuzu R, Icten BM, Arikan V, Arman Y, Atas C, Goren A (2016) An experimental and numerical investigation on low velocity impact behavior of composite plates. *Journal of Composite Materials* 50(25):3551–3559.
- [9] Goren A, Atas C (2008) Manufacturing of polymer matrix composites using vacuum assisted resin infusion molding. *Archives of Materials Science and Engineering* 34:117-120.
- [10] Hallquist JO (2006) LS-DYNA theory manual. Corporation, Livermore, California: Livermore Software Technology.

Omuz Eklemine Farklı Kas Gruplarının Sonlu Elemanlar Metodu ile Analizi ve Değerlendirilmesi

*Devrim Tümer**, Dokuz Eylül Üniv., Makine Mühendisliği Bölümü, İzmir, Türkiye
Yusuf Arman, Dokuz Eylül Üniv., Makine Mühendisliği Bölümü, İzmir, Türkiye
Musa Güngörürler, Dokuz Eylül Üniv., Biyomekanik Bölümü, İzmir, Türkiye
Hasan Havıçoğlu, Dokuz Eylül Üniv., Tıp Fakültesi, Ortopedi Bölümü, İzmir, Türkiye
*İletişimden sorumlu yazar: devrim.tumer35@gmail.com

Anahtar Kelimeler: rotator cuff, deltoid, omuz biyomekaniği, sonlu elemanlar kas modeli, kas-iskelet modeli
Disiplin: Makine Mühendisliği

Özet

Bu çalışmada, bir insan omuz kas – iskelet sistemi oluşturularak, herhangi bir kasta meydana gelebilecek bir güç kaybının diğer kas gruplarını nasıl etkilediği araştırılmıştır. Bu kapsamda, histolojik, patolojik rahatsızlığı bulunmayan ve omuz eklemine implant olmayan sağlıklı bir insanın izni ile, magnetic resonance imaging (MRI) değerleri elde edilmiştir. Çalışmada kullanılan jenerik model çekilen MR görüntülerine uyarlanarak istenilen model elde edilmiştir. Elde edilen model üzerine 30° dış rotasyon verilerek sırasıyla %100, %50 ve %0 infraspinatus kası etkinliğinde analizler yapılmış ve değerlendirilmiştir.

Keywords: rotator cuff, deltoid, shoulder biomechanics, finite element muscle model, musculoskeletal model
Discipline: Mechanical Engineering

Abstract

In this study, by forming an human shoulder musculoskeletal system, it has been researched that how a loss of strength which may occur in any muscle influence other muscles groups. In this context, by permission of a healthy human who has no histological, pathologic disorder and has no an implant on his glenohumeral joint, magnetic resonance imaging (MRI) values have been attained. By applying 30° external rotation on the obtained model, analyses have been implemented and assessed for %100, %50 and %0 infraspinatus muscle efficiency, respectively.

Giriş

Biyoloji ve fizyoloji gibi alanları mühendislik mekaniği açısından ele alan bir bilim olarak tanımlanan biyomekanik, mekanik prensipleri göz önünde bulundurarak, insan vücudu üzerine uygulanan herhangi bir mekanik girdinin kemik, eklem ve kas sağlığı üzerine olan etkisi ile ilgilenir [1]. Makine mühendisliği prensiplerinin canlı organizmaya uyarlanması ile mühendislik açısından organizmayı hücre düzeyinde, hücrelerin uygulanan bir dış yüke verdikleri cevaplar, doku seviyesinde, normal yürüme esnasında anterior çapraz ligamanlardaki strain değerleri, tüm yapısal vücut düzeyinde ise, günlük yaşam aktiviteleri esnasında eklem temas kuvvetleri kapsamında inceler [2]. Bu özellikler çalışma kapsamında, üst ekstremité için external-internal rotasyon, flexion-extension, abduction-adduction gibi hareketler göz önünde bulundurularak değerlendirilmelidir.

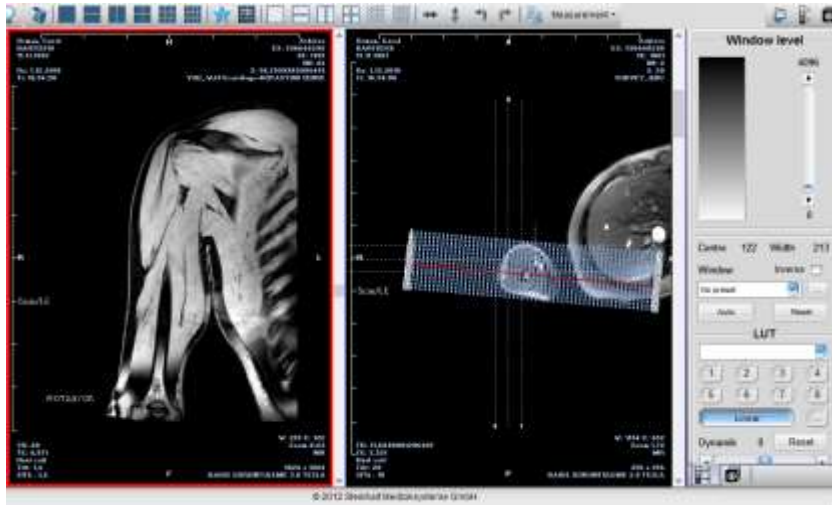
Literatürde de bu hareketler göz önünde bulundurularak yapılmış, omuz biyomekaniği üzerine bir çok çalışma görmek mümkündür. Kas, tendon modelleme gibi etmenler ön planda tutularak, farklı sonlu elemanlar modellerinin sonuçlara olan etkisini araştırmak üzere, moment kolunun, her kas grubundaki fiberler boyunca nasıl değiştiğini deltoid, rotator cuff kas ve tendon gruplarının 3D sonlu elemanlar modelini oluşturularak, line-segment modeli ile kıyaslayan, kas tendon gruplarında meydana gelebilecek herhangi bir tam veya kısmi yırtılmalarının sonlu elemanlar analizlerini değerlendiren, abduksiyon açısına bağlı rotator cuff yırtıklarının gelişimini, ilerlemesini ve mekanizmasının nasıl işlediğini ve ayrıca supraspinatus kasındaki abduksiyona bağlı gerilmedeki değişimleri araştıran, sonlu elemanlar modeli kullanılarak kas – tendon yapılarında meydana gelen hasarlara ilişkin dikiş konfigürasyonları, pozisyonları ve dikişlere uygulanan öngerilme değerlerinin rotator cuff tedavilerini ne denli etkilediğini araştıran çalışmalar görmek mümkündür [3-6].

Bu çalışmanın amacı ise, jenerik bir model kullanılarak, bir insan omuz kas-iskelet sistemi modeli oluşturmak ve modellenen yapı üzerine 30° bir dış rotasyon verilerek rotasyona bağlı omuz eklemine

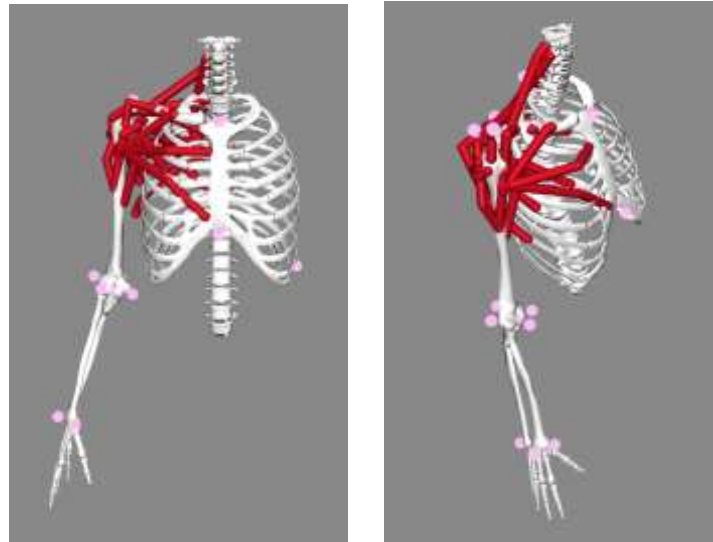
kas gruplarının gerilme değerleri, infraspinatus kasının %100, %50 ve %0 etkinlik değerleri için elde etmektir. Bunu amaçlayarak, external rotasyon sırasında maksimal çalışan infraspinatus kasındaki bir güç kaybına ilişkin ya da infraspinatus kasının tamamen işlevsiz durumu için diğer kas gruplarının güç kaybını hangi düzeyde kompanse ettiği belirlenmiştir [7].

Metot

Çalışmada, öncelikle herhangi bir rahatsızlığı bulunmayan üzerinde implant bir malzeme olmayan sağlıklı bir insanın izni ile MR görüntüleri çekilmiştir. Sonrasında, jenerik bir model OpenSim 4.0 programında açılıp MR görüntüleri üzerinde belirlenen marker noktaları baz alınarak jenerik model istenilen forma uyarlanmıştır [8]. Sınır şartları olarak, yapı üzerinde throax fixe edilmiş, clavícula, scapula, humerus, ulna, radius ve sağ el serbestliğine ise izin verilmiştir.



Şekil 1. MR görüntüleri



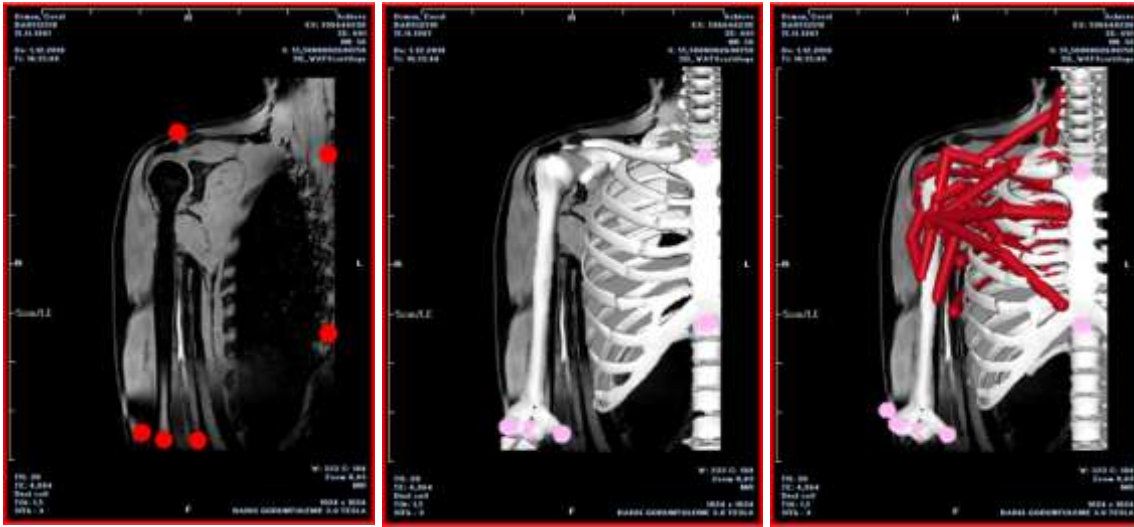
Şekil 2. Jenerik model

Gerilme hesapları açısından 30° external rotasyon esnasında, kas kuvvetlerindeki değişimleri belirleyebilmek adına, başlangıçta her bir kasa ait maksimum izometrik kuvvet değerleri, optimal fiber uzunlukları, tendon gevşeklik uzunluğu, maksimum kasılma hızı, maksimum tendon strain ve maksimum kas strain değerleri jenerik model ile belirlenmiştir. Bu veriler belirlendikten sonra, jenerik model üzerinden rotasyon verme işlemi için seçilen 6 adet marker noktası MR görüntüleri üzerindeki marker noktaları ile kıyaslanmış ve farklı koordinat değerlerinde oldukları tespit edilmiştir. 6 adet

marker seçim nedeni, jenerik model ile kıyaslandığında çekilen MR görüntülerinin vücudun belirli bir bölümünü kapsamasındandır.



Şekil 3. Kas – kemik doku için coronal görüntü ve marker atanması

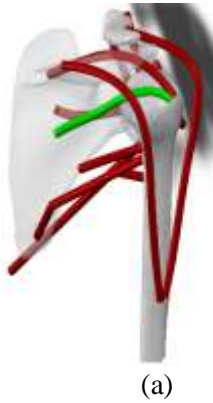


Şekil 4. MR görüntülerinin üzerinde belirlenen markerların jenerik model üzerine aktarımı ve uygunluk durumu

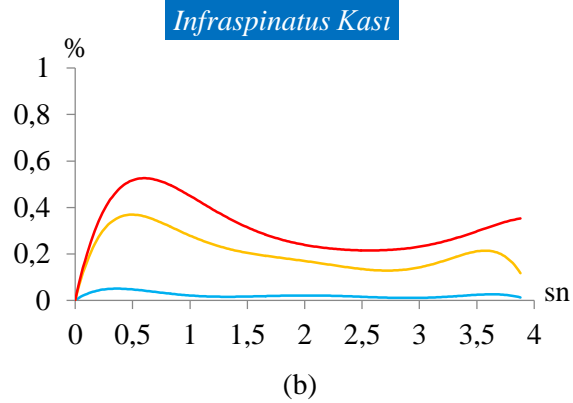
Şekil 4 üzerinde ifade edildiği gibi MR görüntüleri üzerinde belirlenen kırmızı noktalar ile gösterilen markerların koordinatları OpenSim 4.0 üzerinde jenerik modele aktarılarak kas – iskelet modelinin çekilen MR görüntülerine dayalı analiz öncesi son hali elde edilmiştir. Bu aşamadan sonra external rotasyon işlemi en etkin kas grupları olan infraspinatus, teres minor, supraspinatus, subscapularis, deltoid posterior kasları için rotasyon işlemi gerçekleştirilmiş ve analiz sonuçları değerlendirilmiştir.

Sonuçlar

Analizler OpenSim 4.0 programında MR görüntülerine uyarlanan jenerik model üzerine uygulanan 30° external rotasyon boyunca, external rotasyonda etkin kas grupları göz önünde bulundurularak gerçekleştirilmiş ve rotasyonda en etkin kas olan infraspinatus kasındaki yarı güç kaybı ve tam işlevsiz hali baz alınarak rotasyon boyunca diğer kaslardaki kuvvet değişimleri zamana bağlı yüzdelik değerleri grafiksel olarak izah edilmiştir.



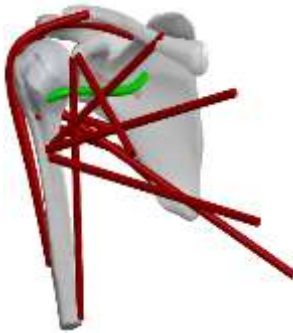
(a)



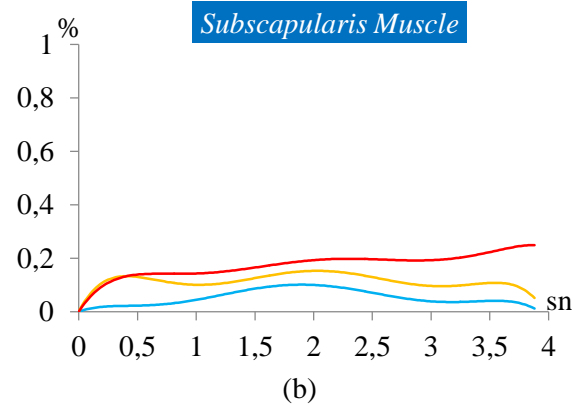
(b)

Şekil 5. (a) Omuz biyomekaniği üzerinde infraspinatus kası gösterimi, (b) infraspinatus kasına ilişkin tam, yarı güç ve tamamen işlevsiz kas kuvveti etkinlik değerleri

External rotasyon için en etkin kas kuvveti Şekil 5. (a)' da gösterilmiş olup, infraspinatus kasının tam, yarı güç için kas kuvveti değerlerindeki değişim ve tamamen işlevsiz durumu OpenSim 4.0 analiz programı üzerinden 4 saniyelik bir rotasyon işlemi boyunca belirlenmiştir. Şekil 5. (b)' de zamana bağlı kas kuvveti değerlerindeki değişimler kırmızı hat ile %100 güç konumu, turuncu hat ile %50 güç konumu, mavi hat ile %0 güç konumu ifade edilmiş ve infraspinatustaki bu değişimlere bağlı diğer kas gruplarındaki kuvvet değerleri elde edilmiştir.



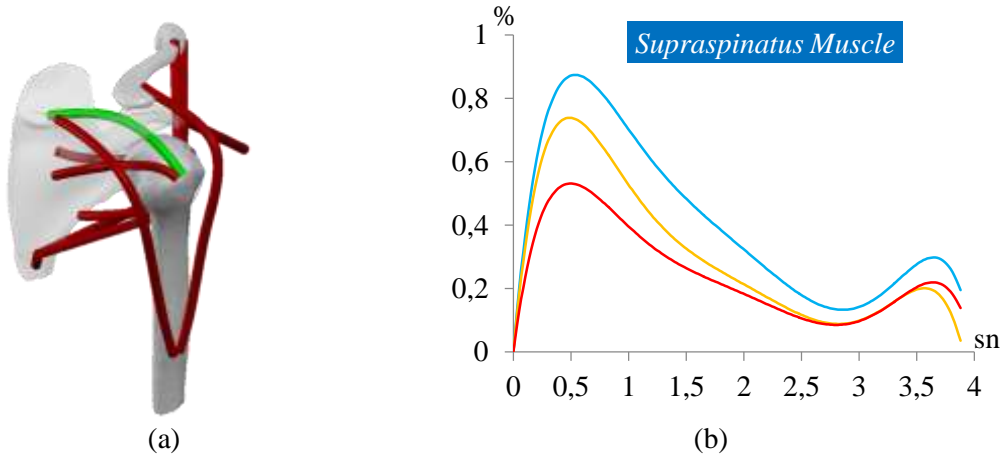
(a)



(b)

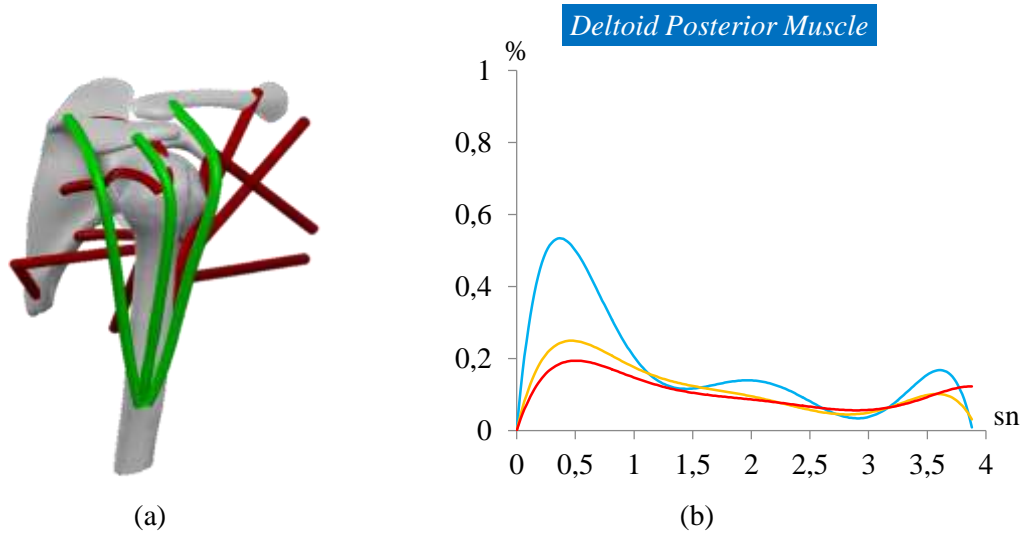
Şekil 6. (a) Subscapularis kası gösterimi, (b) subscapularis kasının tam, yarı güç ve tamamen işlevsiz infraspinatus kas kuvveti değerlerine bağlı external rotasyondaki etkinlik değerleri

Rotator cuff kaslarını oluşturan 4 adet kastan en güçlü olanlarından bir tanesi subscapularis kası olmasının yanı sıra bu kas omuz eklemi hareketinde internal rotasyonda oldukça etkindir ve bununla birlikte external rotasyonda en etkin kas olan infraspinatus kasındaki kademeli düşüş, birbirleriyle olan ilişki düşünüldüğünde, subscapularis kasında da belirli düzeylerde güç kaybı oluşumuna ve dolayısı ile infraspinatus kası güç kaybını telafi edememe gibi bir durum söz konusu olmuştur [9,10]. Şekil 6. (b)' deki grafikte de görüleceği üzere kırmızı hatta infraspinatus gücü maksimal değerde iken subscapularis kasından alınan verim maksimal düzeydedir ve yine benzer şekilde infraspinatus kasında meydana gelen kısmi güç kayıpları ve işlevsizlik durumunda, subscapularis kasında da ciddi anlamda güç kaybı meydana gelmiştir.



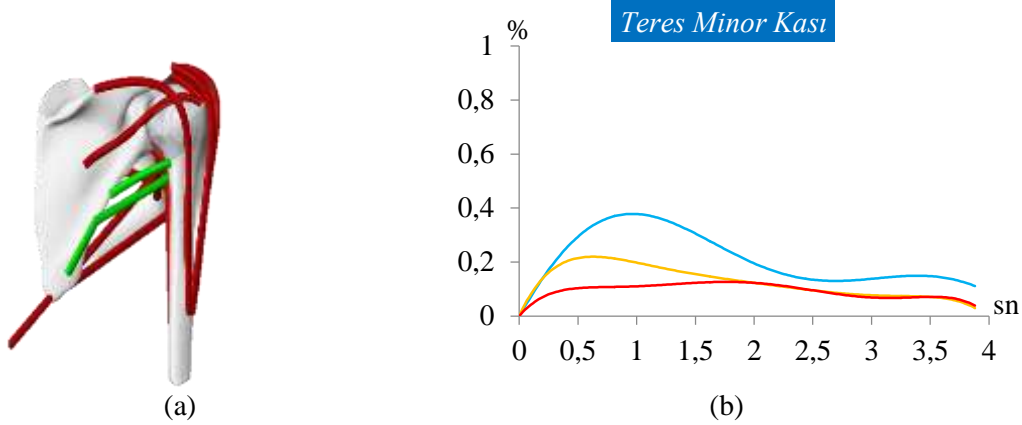
Şekil 7. (a) Supraspinatus kası gösterimi, (b) Supraspinatus kasının tam, yarı güç ve tamamen işlevsiz infraspinatus kas kuvveti değişimine bağlı external rotasyondaki etkinlik değerleri

Şekil 7. (b)' de supraspinatus kası kendi maksimum kas kuvvetinin % 90'ına yakın bir değerde kuvvet değişimi göstererek infraspinatustan dolayı meydana gelen güç kaybını oldukça iyi bir şekilde kompanse etmeye çalıştığı anlaşılabilir.



Şekil 8. (a) Deltoid anterior, middle, posterior kası gösterimleri, (b) Deltoid posterior kasının tam, yarı güç ve tamamen işlevsiz infraspinatus kas kuvveti değişimine bağlı external rotasyondaki etkinlik değerleri

Deltoid posterior kası, supraspinatusdan daha düşük ancak teres minorden daha yüksek seviyede olacak şekilde güç kaybını kompanse etmeye çalışmıştır. Analizler yapılırken deltoid anterior, middle ve posterior göz önünde bulundurulmuş ancak anterior ve middleda posteriordaki kadar güç kaybı telafi edilememiştir. Bu nedenle deltoid posterior kası baz alınarak, external rotasyon işlemi için analiz sonuçları grafiksel olarak verilmiştir.



Şekil 9. (a) Teres minor kası gösterimi, (b) teres minor kasının tam, yarı güç ve tamamen işlevsiz infraspinatus kas kuvveti değişimine bağlı external rotasyondaki etkinlik değerleri

Teres minor kasında, infraspinatusta meydana gelen kademeli güç kaybına bağlı, teres minor kas kuvveti değerlerinde artış olduğu gözlenmiştir. Rotasyonel hareket boyunca teres minor kası infraspinatustaki güç kaybını, maksimal teres minor kasının % 40'ına yakın bir seviyede kompanse ettiği görülmektedir.

Elde edilen bu değerler ışığında, infraspinatus kasının güç kaybına bağlı ya da tamamen yırtılması durumunda, external rotasyonda etkin diğer kas gruplarının bu olası güç kaybını ne derece karşılayabildiği yüzdelik değerler ile ifade edilmiştir. Sonuç olarak, external rotasyonda olası bir infraspinatus yırtığında, subscapularis kas kuvvetinde de orantılı bir düşüş olduğu belirlenmiştir. Infraspinatus güç kaybını, supraspinatus, deltoid posterior ve teres minor kaslarının telafi etmeye çalıştığı ve yüzdelik değerlere bakıldığında güç kaybını kompanse etmede en önemli kasın % 90' a yakın bir etkinlikte supraspinatus kası olduğu ve akabinde deltoid posterior kasının %60' a yakın bir etkinlikte, teres minor kasının ise % 40' a yakın bir etkinlikte olduğu belirlenmiştir.

Sonuç

External rotasyon işlemi sırasında infraspinatus kasındaki güç kayıplarına bağlı diğer kaslardaki kuvvet değişim değerlerinin ortalamasının, her bir kasa ait literatürde tanımlı cross-sectional area değerlerine oranlanması ile istenilen kas grubu için gerilme değerleri elde edilebilmektedir ve bu sayede omuz ekleminin kapsül ve kaslarının, yırtık ve farklı tedavi yöntemlerinin değerlendirilmesinde temel oluşturulmuştur.

Teşekkür

Bu çalışmanın yürütülmesine olan katkısından dolayı Prof.Dr. Ramazan Karakuzu hocamıza teşekkür ederiz.

Referanslar

- [1] Kaufman K, An K (2017) Biomechanics, Kelley and Firestein's Textbook of Rheumatology (Tenth Edition) 1 78-79. <http://dx.doi.org/10.1016/B978-0-323-31696-5.00006-1>
- [2] Koff MK (2015) Biomechanics of peripheral joints, Rheumatology (Six Edition) 1, 65-71. <https://doi.org/10.1016/B978-0-323-09138-1.00009-7>
- [3] Webb JD, Blemker SS, Delp SL (2014) 3D finite element models of shoulder muscles for computing lines of actions and moment arms, Journal of Computer Methods in Biomechanics and Biomedical Engineering 17 (8) 829-837. <https://doi.org/10.1080/10255842.2012.719605>
- [4] Quental C, Folgado J, Monteiro J, Sarmento M (2016) Full-thickness tears of the supraspinatus tendon: A three-dimensional finite element analysis, Journal of Biomechanics 49 3962-3970. <http://dx.doi.org/10.1016/j.jbiomech.2016.11.049>
- [5] Inoue A, Chosa E, Goto K, Tajima N (2013) Nonlinear stress analysis of the supraspinatus tendon using three-dimensional finite element analysis, Journal of Knee Surgery, Sports Traumatology, Arthroscopy, 21 1151-1157. <http://doi.org/10.1007/s00167-012-2008-4>

3rd International Students Science Congress
3-4 May 2019, İzmir - Turkey

- [6] Mantovani M, Pellegrini A, Garofalo P, Baudi P (2016) A 3D finite element model for geometrical and mechanical comparison of different supraspinatus repair techniques, *Journal of shoulder and elbow surgery*, 25 557-563. <http://dx.doi.org/10.1016/j.jse.2015.09.002>
- [7] Kurokawa D, Sano H, Nagamoto H, Omi R, Shinozaki N, Watanuki S, Kishimoto KN, Yamamoto N, Hiraoka K, Tashiro M, Itoi E (2014) Muscle activity pattern of the shoulder external rotators differs in adduction and abduction: an analysis using positron emission tomography, *Journal of Shoulder Elbow Surgery* 23 658-664. <http://dx.doi.org/10.1016/j.jse.2013.12.021>
- [8] Wu W, Lee PVS, Bryant AL, Galea M, Ackland DC (2016) Subject-specific musculoskeletal modeling in the evaluation of shoulder muscle and joint function, *Journal of Biomechanics*, 49 (15) 3626-3634. <https://doi.org/10.1016/j.jbiomech.2016.09.025>
- [9] Waldman SD (2009) The infraspinatus muscle, *Pain review*, Section 1 87. <https://doi.org/10.1016/B978-1-4160-5893-9.00043-5>
- [10] Waldman SD (2009) The subscapularis muscle, *Pain review*, Section 1 88. <https://doi.org/10.1016/B978-1-4160-5893-9.00044-7>

Low Velocity Impact Response of Thermoplastic Composites Reinforced with Metal Turnings

Ata Pourfarivarnezhad*, Dokuz Eylül Univ., The Graduate School of Natural and Applied Sciences, Dept. of Mechanical Engineering, Tinaztepe Campus, İzmir, Turkey
Okan Özdemir, Dokuz Eylül Univ., Dept. of Mechanical Engineering, Tinaztepe Campus, İzmir, Turkey
*Corresponding author: atafarivar@gmail.com

Keywords: thermoplastic composites, low velocity impact test, aluminum metal wastes
Discipline: Mechanical Engineering

Abstract

Today, the usage of sandwich composites made of thermoplastic materials is often encountered in places where high strength and lightness are required. In this study, thermoplastic sandwich composites, which are thought to be used in different application areas, have been produced with aluminum metal wastes in 4 mm thicknesses and 100x100 mm dimensions. Different impact energies (10, 20, 30, 40 and 50J) and different temperatures (23°C - room temperature and 75°C) have been tested in the low velocity impact tests.

Introduction

Composite materials are called materials created by combining two or more same or different groups of materials with the best properties at a macro level in order to collect new and single materials. A composite material generally consists of a low modulus and strength resin or metallic matrix. Composite materials can take different properties of their components. The following features can be provided by the production of composite materials:

- High strength and high rigidity,
- High fatigue strength,
- Excellent wear resistance,
- High temperature capacity,
- Good corrosion resistance,
- Good thermal and heat conductivity,
- Low weight,
- Charm and aesthetic appearance [1].

Today, light weight composite structures are in high demand and they are using in many important industries such as aerospace, automotive, construction and marine [1].

Thermoplastics, which are widely used in both automotive and aircraft industry, are also called thermal softening resins. Thermoplastics are softening when they are heated. Also, they are hardening again when they are cooled. They have coefficient of thermal expansion of about 5 times that of metals. Its specific heat is higher 4 times of metals and 2 times of ceramics and its thermal conductivity is lower 3 times than metals. [2]. One of the most important advantages of thermoplastic is recyclability. Because of this feature, in recent years, researchers have interested to produce composites with a thermoplastic matrix [3]. The response of composite structures against low velocity impact (LVI) has received great attention in recent studies [3-5]. The best example of a low-velocity impact is the damages can occur during the manufacturing and maintenance of composites. The low-velocity impact affects mechanical properties and causes some damages in composites such as matrix cracking, delamination, fiber fracture and fiber–matrix debonding. These damages lead to structural fracture and penetration [6-7].

In this experimental investigation, in order to investigate the impact behavior of thermoplastic structures low velocity impact tests of the composites were performed at different temperatures (room temperature and 75°C). Metal wastes may seem unused and worthless at first glance, and the best way to get rid of them is to destroy. The recycling industry is a very important part of the industry of every country, and products that are recycled from these metal wastes can be used in many places [8]. The use of waste materials as raw material is very important for preventing environmental pollution. In this study, aluminum metal wastes have put to thermoplastic composite as a reinforcement material at weight

fraction of 10%. Low velocity impact tests (LVI) were carried out at different impact energies and different temperatures and compared with neat composites.

Methodology

Materials

The materials used in this study are uniaxial E-glass reinforced polypropylene as a face sheet. Long glass fiber reinforced polypropylene (LGFRPP) granules with a fiber ratio of 60% and aluminum metal wastes were used as a core material.



Figure 1. The materials used in manufacturing of composite

In the current study, long glass fiber reinforced polypropylene granules at 60% fiber ratio and metal wastes are put into the molds homogeneously according to the desired plate thickness. The weight fraction of the metal wastes is 10%. After that, uniaxial polypropylene laminates were placed in the lower and upper layers of the composites in the form of [0/90/core/90/0].

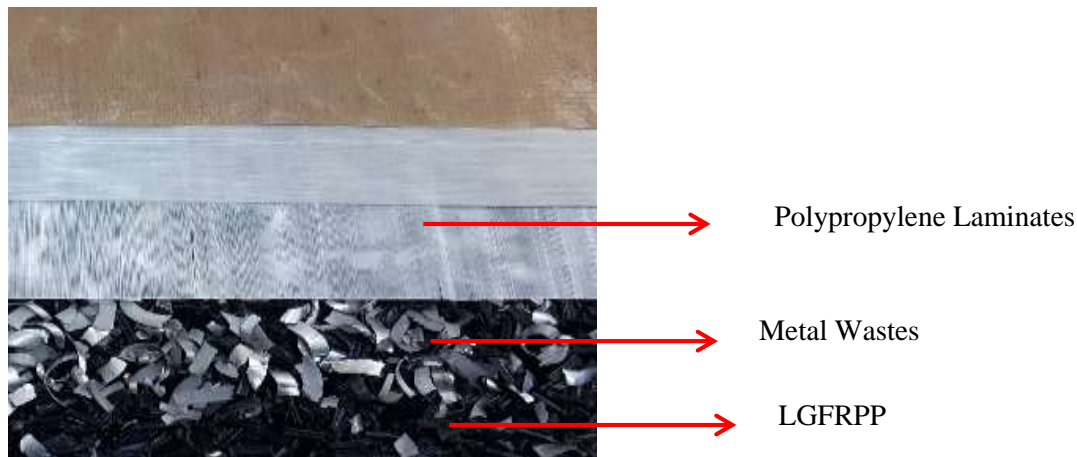


Figure 2. The manufacturing steps of composite

Mechanical Properties

The mechanical properties of the Long Glass Fiber Reinforced Polypropylene (LGFRPP) granules with a fiber ratio of 60% are given in Table 1.

Table 1. Mechanical Properties of LGFRPP Granules [9]

Mechanical Properties	Value	Unit	Test Method
Density	1.43	g/cm ³	ISO 1183
Tensile Strength	125	MPa	ISO 527
Tensile Module	13800	MPa	ISO 527
Bending Strength	215	MPa	ISO 178
Bending Module	11250	MPa	ISO 178

Longitudinal modulus (E_1), transverse modulus (E_2), longitudinal tensile strength (X_t), transverse tensile strength (Y_t) and the Poisson's ratio of the polypropylene laminates (ν_{12}) are given in Table2 [10].

Table 2. Mechanical Properties of Polypropylene Laminates [10]

X_t (MPa)	Y_t (MPa)	E_1 (GPa)	E_2 (GPa)	ν_{12}
265 ±12	22 ±1.9	13.5	1.4	0.231

Manufacturing

In order to produce the impact test specimens, 12mm granules are placed to mold with the dimension of 350x350 mm. LGFRPP composites were obtained by pressing the granules between the hot plates of a compression press under 0.8 MPa at 175°C for 80 min.

After 80 min, the composites were left to cooling for 6 h at 0.8 MPa pressure in order to prevent warping. As the end of this process, 4 mm thick 350x350 mm composite plates were produced. The composite plates that have been produced in 2 types (reinforced and neat) were cut by using water saw in the dimension of 100x100mm (Figure 3).

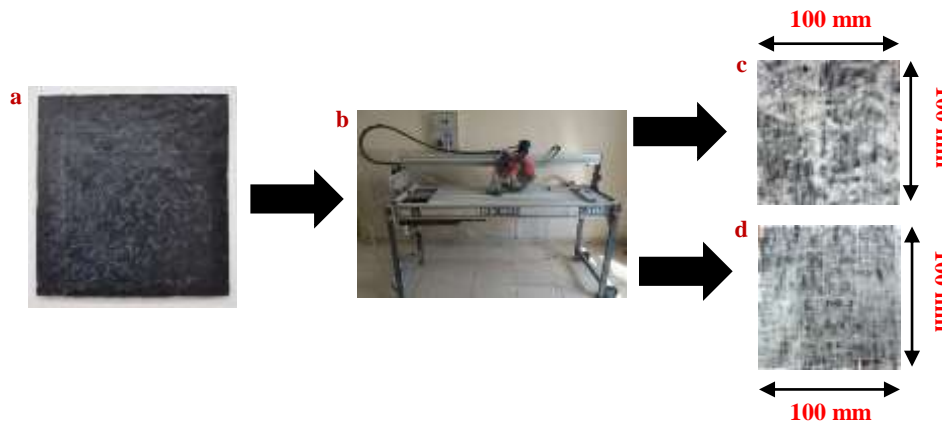


Figure 3. a) Composite Plate, b) Water Saw, c) 10% Metal Wastes Reinforced Specimen d) Neat Specimen

Low Velocity Impact Test

After the specimens have been manufactured in different types, they are tested in two different temperatures (23°C - room temperature and 75°C). Different impact energy levels of 10J, 20J, 30J, 40J and 50J were implemented in accordance with ASTM D 3763. Impact tests were performed in CEAST-Fractovis Plus testing machine. The impactor used in the tests is the semi-spherical with a load capacity of 22kN (Figure 4).



Figure 4. Low velocity impact testing machine and impactor

Results

In the current study, force-deformation and energy-time graphs are drawn for each sample with the data obtained from the impact tests. Contact force-deformation diagrams of the composites reinforced with 10% aluminum metal waste are given in Figure 5. In the impact energy levels of 10J and 20J, rebounding case was observed in both temperatures. In the 30J, penetration was occurred at 23°C but rebounding case was obtained at 75°C. In the higher impact energies, the impactor passes from the upper and lower surfaces of the composites implying the perforation case.

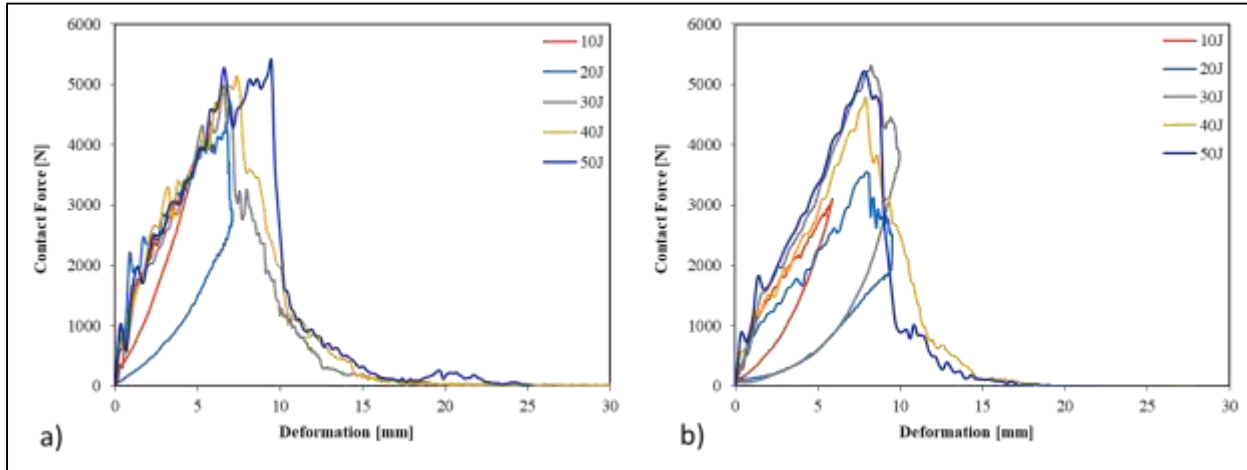


Figure 5. Contact force-deformation diagrams of 10% aluminum reinforced composite a) 23°C and b) 75°C

Energy-time diagrams of the 10% aluminum reinforced composites impacted at 23°C and 75°C are given in Figure 6. Rebounding situation was observed at 23°C temperature at an impact energy level of 10J and 20J. On the other hand, at 75°C, rebounding case were obtained at 10J, 20J and 30J impact energies. After the penetration energy, the absorbed energy values continue to increase at 23°C but at 75°C the absorbed energy values begin to concentrate in certain energy.

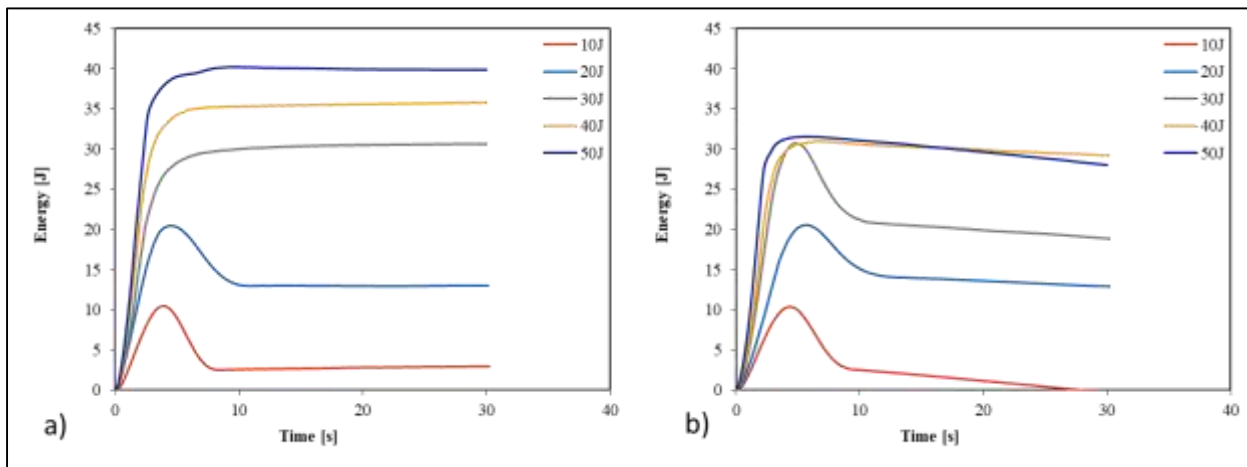


Figure 6. Energy-time diagrams of 10% aluminum reinforced composite a) 23°C and b) 75°C

Contact force-deformation diagrams of the neat composite impacted at 23°C and 75°C are given in Figure 7. Rebounding situation observed at 23°C temperature condition in 10J and 20J and 30J. Impact energy level of 30J, penetration case was observed at 75°C. After the impact energy level of 30J, perforation case was observed in both conditions.

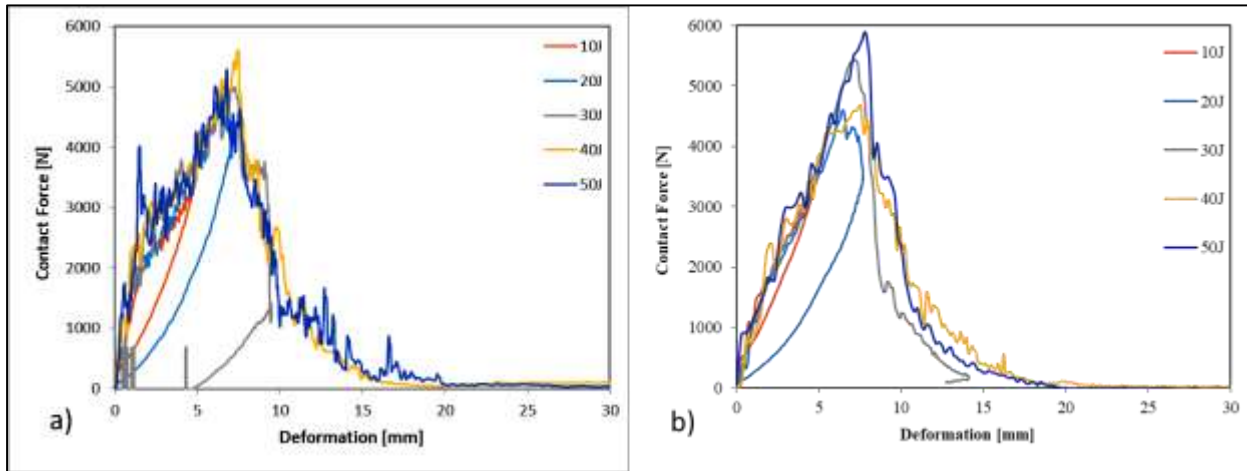


Figure 7. Contact Force-Deformation Diagrams of the Neat Composite a) 23°C and b) 75°C

Energy-time diagrams of the neat composite at 23°C and 75°C are given in Figure 8. Rebounding situation was observed at 75°C temperature condition in 10J and 20J. On the other hand, rebounding case was obtained at 23°C temperature condition in 10J, 20J and 30J. After the penetration energy, the absorbed energy values continue to increase at 75°C, but at 23°C the absorbed energy values begin to concentrate in certain energy.

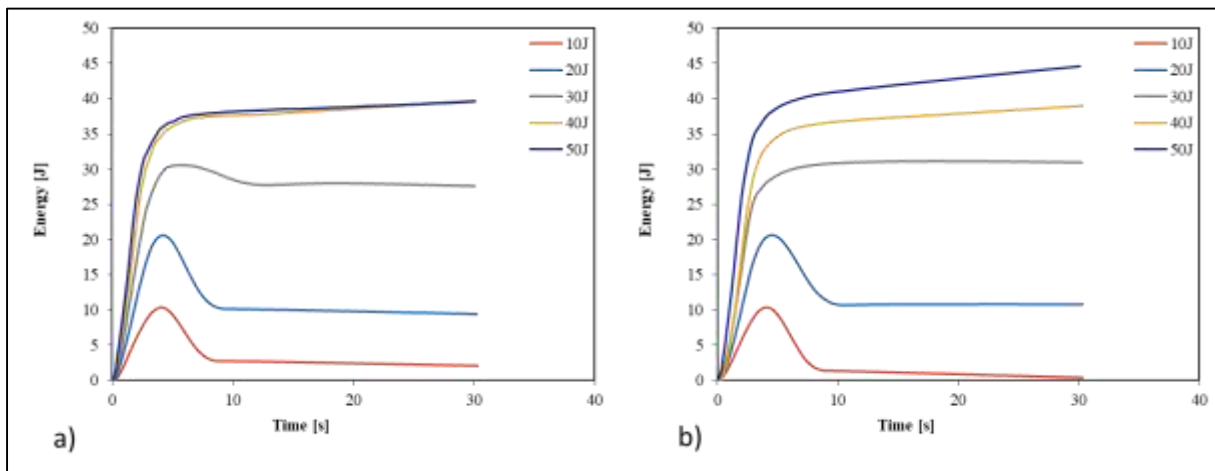


Figure 8. Energy-time diagrams of the neat composite a) 23°C and b) 75°C

Conclusion

In this study two kind of thermoplastic composite have produced. Aluminum reinforced composite and neat composite were tested in several impact energies at two different temperature conditions in order to investigate the low velocity impact behavior of these composites. From the obtain results and graphs, main conclusions are listed:

- Maximum contact force of the composites does not change seriously after the impact energy level of 30J.
- Perforation energy increases at high temperatures in the reinforced specimen compared to neat composites.
- Maximum contact force after the perforation case has become more stable in the reinforced specimens.
- In the aluminum reinforced specimen, the absorbed energy until the perforation case at 75°C is better compared to neat composites.
- When the aluminum metal wastes 10% was used in thermoplastic composites, absorbed energy increased by about 8% compared to neat composites.

References

- [1] Şahin Ş (2015) Kompozit Malzemelere Giriş (3rd. edition) Seçkin Yayıncılık, Ankara.
- [2] Campbell FC (2010) Structural Composite Materials. ASM International, Ohio.
- [3] Sjöblom PO, Hartness JT, Cordell TM (1988) On low-velocity impact testing of composite materials J Compos Mater, 22(1): 30-52.
- [4] Cantwell WC, Morton J (1991) The impact resistance of composite materials – a review Composites 22(5): 347-362.
- [5] Abrate S (1991) Impact on laminated composite materials Appl Mech Rev 44: 155-190.
- [6] S. Boria, A.Scattina, G.Belingardi (2017) Impact behavior of a fully thermoplastic composite, Composite Structures Volume 167: 63-75. <https://doi.org/10.1016/j.compstruct.2017.01.083>.
- [7] M. Aktaş, R. Karakuzu, Y.Arman (2009) Compression-after impact behavior of laminated composite plates subjected to low velocity impact in high temperatures, Composite Structures 89: 77-82.
- [8] https://www.wikipedia.com/wiki/recycling_by_material.
- [9] <http://www.nuhkompozit.com.tr/duramax-LFT60-PP.html>.
- [10] Okan O, Nahit O, Halis K (2018) Single and repeated impact behaviors of bio-sandwich structures consisting of thermoplastic face sheets and different balsa core thicknesses, Composites Part B: Engineering 149: 49-57. <https://doi.org/10.1016/j.compositesb.2018.05.016> .

Silindirik Buzdolabı Tasarımı

Başak Mülayim, Ahmet Şanlıtürk, Ali Yurddaş
Manisa Celal Bayar Üniv., Makine Müh. Bölümü, İhan Varank Yerleşkesi, Manisa, Türkiye
İletişimden sorumlu yazar: basakmulayim@yahoo.com

Anahtar Kelimeler: Silindirik buzdolabı, Isı transferi, Yıllık enerji tüketimi
Disiplin: Makine mühendisliği

Özet

Piyasada üretilmekte olan ticari, dikdörtgenler prizması şeklindeki buzdolaplarının görüş alanı, sabit rafları, konumu için duvara ihtiyaç duyması vb. özellikleri ile modern ihtiyaçlar için yeterli olmamaktadır. Bu sorunu çözmek için silindirik bir buzdolabı tasarlanmıştır. Bu tasarım için gerekli olan ısı hesapları yapılmıştır.

Key Words: Cylindrical commercial refrigerator, Heat transfer, Annual energy consumption
Discipline: Mechanical Engineering

Abstract

Commercial, rectangular prism-shaped refrigerators are produced in the market, the field of view, fixed shelves, the need for a wall for the position, etc. With its features it is not enough for modern needs. A cylindrical refrigerator was designed to solve this problem and the necessary thermal calculations are made for this design.

1. Giriş

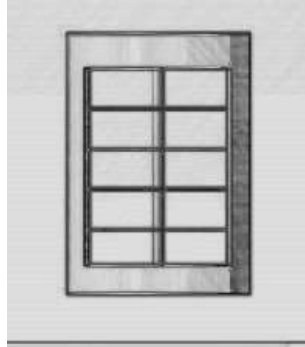
Piyasada üretilmekte olan dikdörtgenler prizması şeklindeki buzdolaplarının ticari anlamda, modern çağın ihtiyaçlarına yeterli gelmemesi sebebiyle silindirik ve saydam yüzeyli tasarım gerekli görülmüş ve bu doğrultuda ısı ve görsel tasarımı yapılmıştır.

Willard L Morrison'ın 1945'ten itibaren 4 yıl boyunca patentini yenilediği silindirik buzdolabı tasarımı bulunmaktadır. W.L.Morrison'ın bu tasarımı tamamen metalik ve kapalı yüzeylerden ve yanda kompresör için ayrı bir bölümden oluşmaktadır [1]. Matthew C. Montgomery'nin patentini ilk alış tarihi 1995 olan ve 2019'da güncellediği silindirik buzdolabının, günümüzde kullanılmakta olan dikdörtgenler prizması şeklindeki buzdolabıyla benzer prensipte çalıştığı ancak silindirik yüzey ile olduğu görülmektedir. Saydam olmayan yüzeyli buzdolabının patentinden, dondurucu kısmının da bulunduğu görülmektedir [2]. Albert Einstein'ın toksik dumanları sızdıran ve Almanya'daki bazı insanların ölümüne neden olan buzdolabını duyduktan sonra, yeni, daha güvenli bir buzdolabı icat etmeye karar vermesi üzerine, öğrencisi Leo Szilard ile birlikte, sabit bir basınçta çalışan, hareketli herhangi bir parçası olmayan, toksik duman riskini ortadan kaldıran buzdolabı yaratmak için bir araya gelmiş, tasarım için 45 farklı patent almışlardır. Güneş ısıtılmalı buzdolabı yapılabilir mi sorusunu akla getiren tasarım, içini soğuk tutmak için dışarıdan ısınması gereken bir yapıdadır [3].

Silindirik, içeriklerin kolaylıkla görülmesini sağlayan cam kapak yapılı tasarım sayesinde Silindirik Ticari Buzdolabı Tasarımında kullanıcı kolaylığı amaçlanmış, yapılan hesaplar doğrultusunda da %33 verim elde edilmiştir.

2. Silindirik Buzdolabı Isıl Tasarımı

Piyasada üretilmekte olan ticari segmentteki dikdörtgenler prizması şeklindeki buzdolaplarının tek görüş alanı, sabit rafları, stabilizasyonu için duvara ihtiyaç duyması vb. özellikleri ile modern ihtiyaçları karşılamakta yetersizliğini gidermek için silindirik tasarım gerekli görülmüş; bu doğrultuda ısı hesapları ve tasarımı gerçekleştirilmiştir.



Şekil 1. Silindirik Ticari Buzdolabı

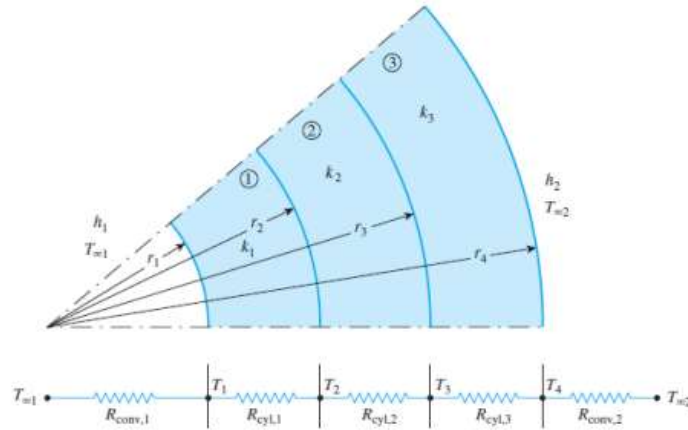
3. Temel Yönetici Denklemler

Bu tasarım silindirik olarak yapılmış olduğu için silindirin alan formülü kullanılmıştır. Silindirin alan formülüne Denklem (1) 'den ulaşılabilmektedir. [4]

$$A_{\text{silindir}} = (2\pi rh) + (2\pi r^2) \quad (1)$$

Silindir ve alüminyum yüzey için ölçülandırıldığı takdirde, alüminyum yüzeyin alanının, silindirin yüzey alanının 5'te 2'si olması sebebi ile alüminyum yüzeyin ısıl direnci bulunurken genel denklemin 2/5 ile çarpıldığı işlemlerde görülmektedir. Aynı şekilde, cam yüzeyin alanının, silindirik yüzey alanının 5'te 3'ünü kaplaması sebebiyle, cam yüzeyin ısıl direnci hesaplanırken, genel denklemin 3/5 ile çarpıldığı görülmektedir.

Çok katmanlı silindir için ısı transfer hesaplarında aşağıdaki görselden (Şekil 2)'den yararlanılmaktadır [4]



Şekil 2. Çok katmanlı silindirde ısı transferi [4]

Yukarıdaki görselde görülen her iki yönden taşınım olan üç katmanlı silindirdeki ısı transferi dirençler şeklinde gösterilmektedir. [4]

$$R_{\text{total,AI}} = 2k\pi r_5^2 \frac{1}{t} + \frac{2}{5} \left[\frac{1}{h_1 A_1} + \frac{\ln\left(\frac{r_2}{r_1}\right)}{2\pi L k_1} + \frac{\ln\left(\frac{r_3}{r_2}\right)}{2\pi L k_2} + \frac{\ln\left(\frac{r_4}{r_3}\right)}{2\pi L k_3} + \frac{1}{h_2 A_4} \right] \quad (3)$$

burada $A_1 = 2\pi r_1 L$ ve $A_4 = 2\pi r_2 L$ 'dir. Denklem 3'te ayrıca silindirik tabakaların termal dirençlerini karşılık gelen küresel olanlarla değiştirerek, üç katmanlı bir küresel kabuk için de kullanılabilir. ısıl direnç açısından, dirençlerin seri halinde olduğunu ve bu nedenle toplam ısıl dirençlerin, ısı akışı yolundaki tek tek ısıl dirençlerin aritmetik toplamı olduğuna dikkat edilmesi gerekmektedir.[4]

$$R_{\text{total,cam}} = \frac{3}{5} \left[\frac{1}{h_1 A_1} + \frac{\ln\left(\frac{r_2}{r_1}\right)}{2\pi L k_1} + \frac{\ln\left(\frac{r_3}{r_2}\right)}{2\pi L k_2} + \frac{\ln\left(\frac{r_4}{r_3}\right)}{2\pi L k_3} + \frac{1}{h_2 A_4} \right] \quad (4)$$

buradaki formülde Denklem 3'te olduğu gibi aynı denklem ele alınarak cam yüzeydeki ısıl direnç hesaplaması yapılmıştır.[4]

$$\dot{Q}_{\text{toplam}} = \frac{T_{\infty 1} - T_{\infty 2}}{R_{\text{total}}} \quad (5)$$

buradaki formülde çoğu zaman farklı malzemelerden oluşan birkaç katmandan oluşan düzlemlerle karşılaşıldığında kullanılmaktadır. Yani, bilinen sıcaklıktaki iki yüzey arasındaki sıcaklık farkını, aralarındaki toplam termal dirençle bölerek Q_{toplam} hesaplanmaktadır. Buradaki $T_{\infty 1}$ iç sıcaklık, $T_{\infty 2}$ ise dış sıcaklık olarak alınır [4].

$$W_{\text{net}} = \frac{\dot{Q}_{\text{toplam}}}{\text{COP}} \quad (6)$$

buradaki formülde yapılan net iş hesaplanmaktadır. Denklem 5'te bulunan Q_{toplam} hesaplanan COP(coefficient of performance) bölünerek istenilen net iş elde edilmektedir. Buradaki COP aşağıdaki gibi hesaplanabilir:

$$\text{COP} = \frac{\text{atılan ısı}}{\text{gerekli güç}} \quad (7)$$

COP yani soğutma sisteminin performans katsayısı, ısı çekme işlemi sırasında elde edilen soğutma yükünün, sistemin çalışması için gerekli güç toplamına bölümüdür.

$$\eta = \frac{W_{\text{net}}}{Q_H} \quad (8)$$

buradaki verim hesabında W_{net} değerinin eldesi denklem 6'da bahsedilmiştir. Bulunan W_{net} değeri ile toplam ısı transferi toplanarak Q_H elde edilmektedir. W_{net} değerinin Q_H değerine bölünmesi ile de ısı verim elde edilmektedir.

4. Silindirik Yüzeydeki Isı Transfer Hesaplamaları

Kabuller: Sürekli, Kararlı, Tek Boyutlu Sistem, Zorlanmış Taşınım, Laminer Akış; $T_{iç}=4^{\circ}\text{C}$, $T_{dış}=25^{\circ}\text{C}$; Mil ve raflardaki ısı transferi ihmal; gıda, mil ve raflardaki iç direnç ve hava direnci ihmal. Gıdalardaki sıcaklık homojen; $k_{\text{gıda}}=1.2\text{W/mK}$; COP=2; Gıdadan çekilen ısı=70kJ/dk; Menteşe ve Cıvata bağlantıları, boya ihmal. Yalıtım malzemesi poliüretan. Metal yüzeyler alüminyum.

Silindirik yüzeyden ısı transferi formülleri ve taban ile tavan için düz yüzeyden ısı transferi formüllerinin bir araya getirilerek kullanılması ile hesaplar gerçekleştirilmiştir.

Ölçülendirmeler:

Buzdolabının;

- Yüksekliği: 2250 mm
- Kapı yüksekliği: 1700 mm
- Kompresör alanı yüksekliği: 250 mm
- Kondenser alanı yüksekliği: 300 mm
- Raf aralığı: 300mm
- Raf alanı: 5.20 m²
- İç yarıçapı: 650mm
- Dış Yarıçapı: 690 mm ± 1 mm

Alüminyum yüzeyin alanının, silindirin yüzey alanının 5'te 3'ü olması sebebi ile alüminyum yüzeyin ısı direnci bulunurken 2/5 ile çarpıldığı Denklem 9'da görülmektedir. Aynı şekilde, cam yüzeyin alanının, silindirik yüzey alanının 5'te 3'ünü kaplaması sebebiyle, cam yüzeyin ısı direnci hesaplanırken 3/5 ile çarpım gerçekleştirildiği Denklem 10'da görülmektedir.

$$A_{\text{silindir,Al}} = \left(2\pi r h * \frac{2}{5}\right) + (2\pi r^2) \quad (9)$$

Yukarıdaki denklem, denklem 1'e taban ve tavan alanının eklenmesi ile elde edilmiştir. Silindirik dolabın alüminyum kısmının yanal yüzey alanı için $\left(2\pi r h * \frac{2}{5}\right)$ ifadesinin; buzdolabının, alüminyum olan tavan ve taban alanı için de $2\pi r^2$ ifadesinin kullanıldığı görülmektedir.

$$A_{\text{silindir,cam}} = \left(2\pi r h * \frac{3}{5}\right) \quad (10)$$

Şekil 2'de, çok katmanlı silindir için ısı transferi gösterilmektedir. Tasarlanan buzdolabı için $T_{\infty 1}$ sıcaklıkta olan ortam, buzdolabının gıda konulan iç kısmıdır. 1 olarak numaralandırılan bölüm ise

alüminyum levhadır. 2 ile numaralandırılan bölüm poliüretan köpüğü; 3 ile numaralandırılan bölüm ise yine 1 numaralı kısım gibi alüminyum levhayı (et kalınlığı şeklinde) göstermektedir. $T_{\infty 2}$ ile belirtilen bölge ise buzdolabının bulunduğu ortamdır.

$T_{\infty 1} = 4^{\circ}\text{C} = 277^{\circ}\text{K}$ ve $T_{\infty 2} = 25^{\circ}\text{C} = 298^{\circ}\text{K}$ olarak kabul edildiğinden “Kabuller” başlığında bahsedilmiştir. $T_{\infty 1} = 4^{\circ}\text{C} = 277^{\circ}\text{K}$ için $h=25 \text{ W/m}^2 \text{ K}$

$$R_{\text{total,Al}} = 2k\pi r_5^2 \frac{1}{t} + \frac{2}{5} \left[\frac{1}{h_1 A_1} + \frac{\text{Ln}\left(\frac{r_2}{r_1}\right)}{2\pi L k_1} + \frac{\text{Ln}\left(\frac{r_3}{r_2}\right)}{2\pi L k_2} + \frac{\text{Ln}\left(\frac{r_4}{r_3}\right)}{2\pi L k_3} + \frac{1}{h_2 A_4} \right] \quad (11)$$

Yukarıdaki denklemden(Denklem 11) görüleceği gibi benzer işlemler cam yüzey için de Denklem 12’deki gibi yapılır.

$$R_{\text{total,cam}} = \frac{3}{5} \left[\frac{1}{h_1 A_1} + \frac{\text{Ln}\left(\frac{r_2}{r_1}\right)}{2\pi L k_1} + \frac{\text{Ln}\left(\frac{r_3}{r_2}\right)}{2\pi L k_2} + \frac{\text{Ln}\left(\frac{r_4}{r_3}\right)}{2\pi L k_3} + \frac{1}{h_2 A_4} \right] \quad (12)$$

$k_{\text{hava}}=0.026(\text{W/mC})$; $k_{\text{Al}}=205(\text{W/mC})$; $k_p=0.02$ [4] ;

Konvektif ısı transfer katsayısı, zorlamalı taşınımında gaz akışı gözetilerek $h_1 = h_2 = 25 \text{ W/m}^2 \text{ K}$ olarak alınmıştır. [4]

$$\dot{Q}_{\text{toplama}} = \frac{T_{\infty 1} - T_{\infty 2}}{R_{\text{total}}} \quad (5)$$

Denklem 5’te $R_{\text{total,Al}} = 6.277$ değeri yerine yazılarak $|\dot{Q}_{\text{toplama, Al}}| = 3.345 \text{ J/sn}$ değeri bulunmuştur. Yine denklem 5’te $R_{\text{total,cam}}$ değeri yerine yazılarak $|\dot{Q}_{\text{toplama, cam}}|$ değeri -2.941 J/sn olarak bulunmuştur.

$\dot{Q}_{\text{toplama, Al}} + \dot{Q}_{\text{toplama, cam}} + \dot{Q}_{\text{toplama, gıda}} = \dot{Q}_{\text{toplama}} = 1173.286 \text{ J/sn}$ olarak bulunmuştur.

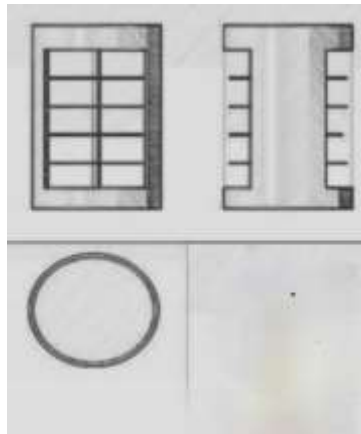
$W_{\text{net}} = \frac{\dot{Q}_{\text{toplama}}}{\text{COP}}$ denkleminde(Denklem6) bulunan $W_{\text{net}} = 586.64 \text{ Watt}$ değeri ile \dot{Q}_{toplama} toplanarak Q_H değeri 1759.930 J/sn olarak hesaplanmıştır.

$$\eta = \frac{W_{\text{net}}}{Q_H} \quad (8)$$

Denklem 5’den ve Denklem 6’dan elde edilen değerler Denklem 8’de yerine yazılarak verim %33 olarak hesaplanmıştır.

5. Tasarım

Şekil 3’teki Silindirik buzdolabı görselinde, yapılan hesaplar sonrasında çizilen buzdolabının tasarımı görülmektedir.



Şekil 3. Silindirik buzdolabı görseli

6. Sonuç

- Piyasada bulunan dikdörtgenler prizması biçimindeki ticari buzdolaplarına kıyasla 4 kat iç hacim kazancı sağlanması tasarlanmıştır.
- Yapılan hesaplamalar sonucunda, tasarladığımız silindirik ticari buzdolabında %33 ısı verim elde edilmiştir.
- Piyasadaki buzdolaplarına oranla, kapağın dışarıya açılarak içeride hacim kaplamaması ve kapaklarda raf bulunmaması vb. özellikler sayesinde iç hacimden kazanç elde edilirken, cam raf tasarımları ile, alt raflardaki ürün çeşitlerinin kullanıcıya sunulmasında kolaylık sağlanmıştır.
- Hareketli raflar sayesinde, kullanıcının ürüne gittiği değil, ürünün kullanıcıya geldiği pratik bir sistem amaçlanarak görsel tasarım gerçekleştirilmiştir.
- En alt raftan ürün erişiminin ergonomik olması amaçlanarak, en altın bir üstündeki rafta, en alt rafa ulaşan açıklık tasarlanmıştır.
- Dikdörtgenler prizması şeklindeki buzdolaplarında olduğu gibi, konumlandırılması için duvara olan ihtiyaç ortadan kalkmıştır.
- Cam ve silindirik çift taraflı kapak tasarımı gerçekleştirilmiş olması sebebi ile konumlandırıldığı noktada aynı anda tek kullanıcıya değil birden çok kullanıcıya kullanım alanı sağlanmıştır.

Kaynakça

- [1] Morrison L (1945) Cylindrical Domestic Refrigerator, US2487259A
- [2] Matthew C. Montgomery (1995) Cylindrical Combined Refrigerator and Freezer, US Patent D368271S,
- [3] Einstein A, Szilard L (1927) Refrigeration, US Patent 1781541A.
- [4] Çengel Y. Isı Transferi Pratik Yaklaşım -3.Basım. İzmir: Güven Bilimsel.

Low Velocity Impact Response of Aluminum Honeycomb/Glass Fiber Reinforced Sandwich Structures

Halis Kandaş, Dokuz Eylül Univ., The Graduate School of Natural and Applied Sciences, Dept. of Mechanical Engineering, Tinaztepe Campus, İzmir, Turkey*

Okan Özdemir, Dokuz Eylül Univ., Dept. of Mechanical Engineering, Tinaztepe Campus, İzmir, Turkey

**Corresponding Author: haliskandas1@gmail.com*

Keywords: sandwich composite, low velocity impact, aluminum honeycomb, epoxy adhesive

Discipline: Mechanical Engineering

Abstract

In this study, glass fiber reinforced polypropylene prepregs and woven fabrics were used as a facing material and aluminum honeycomb were used as a core material. Epoxy resin was also used for bonding core and facing materials. After manufacturing composite specimens, low velocity impact tests were executed according to ASTM 3763 standard. The low velocity impact behavior of sandwich composites were investigated at different impact energies (20, 40 and 60 J) by using different impactor shapes. According to the obtained results, maximum contact force of the flat impactor is higher than the hemispherical impactor at all impact energy levels.

Introduction

A sandwich composite is a material made out of two thin facesheets and a core material. Facesheet is preferred to be stiff, strong and relatively dense material and mostly made from metal or fiber composite materials. On the other hand, core is expected to be a lightweight material and core materials use in the composite material for improving bending stiffness [1].

Material properties of the structural sandwich composites are changed, as the materials change at different sections of composites [2]. Because of this change, each section of composite absorbs different level of energy in the impact phenomenon. Paulius et al. [3] used composite facesheets and polypropylene hexagonal honeycomb core sandwich composites to investigate the impact behavior of different parts of sandwich composite. They showed that honeycomb core in the sandwich composite absorbed around 50-95% of impact energy. Top facesheet about absorbed between 7–35% of the impact energy. Some researchers show and focus the importance of core material in the sandwich composites [4]. Among these, Park et al. [5] have shown that the impact response of composite was greatly influenced by core thickness.

A small number of researchers have investigated the effect of impactor shapes on the low velocity impact responses [6]. Mitrevski et al. [7] investigated the effect of impactor shape on the impact behavior of carbon/epoxy laminates, experimentally. Wang et al. [8] studied the effect of impactor shape on the impact response of sandwich composites with different core and facesheet thicknesses at different impact energy levels, experimentally and numerically. They found that different impactor shapes have great effects on damage mechanisms in the low velocity impact case.

In this research, effect of different shaped impactors on the impact response of thermoplastic-metal based sandwich composites was investigated experimentally.

Methodology

In this study, an unprecedented model of sandwich composite was manufactured. In facesheet parts of this composite, combination of long glass fiber reinforced polypropylene granules and glass fibers woven were used. Aluminum honeycomb was used as a core material and epoxy resin was used as adhesive agent between facesheet and core. The picture of materials used in manufacturing of composite panels is given in Figure 1.

Long glass fiber reinforced polypropylene granules manufactured with pultrusion method was used in the facesheet materials. Fiber ratio of granules was 30%. Mechanical properties of granules are given in Table 1 [9].

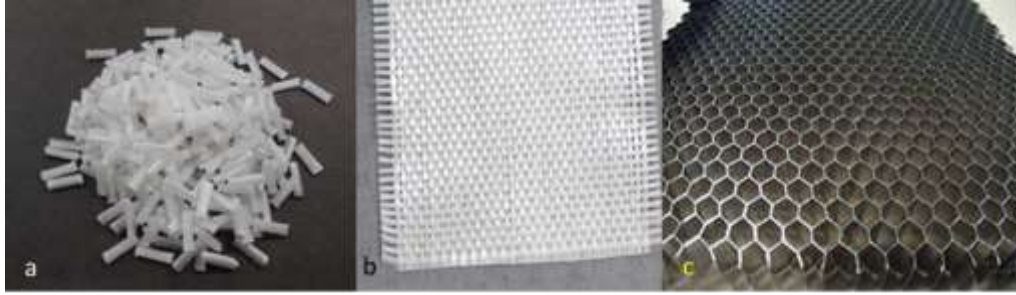


Figure 1. a) Long glass fiber/polypropylene granule, b) Woven glass fiber and c) Aluminum honeycomb

Table 1. Mechanical properties of granules [9]

Mechanical Properties	Value	Unit	Test Method
Density	1,12	g/cm ³	ISO 1183
Tensile Strength	105	MPa	ISO 527
Tensile Module	6500	MPa	ISO 527
Bending Strength	148	MPa	ISO 178
Bending Module	5700	MPa	ISO 178
IZOD Impact Resistance, Unnotched (11J)	34	kJ/m ²	ISO 180
IZOD Impact Resistance, Notched (11J)	12,5	kJ/m ²	ISO 180
HDT (0,45 MPa)	157	°C	ISO 75B

The facesheet plates of the sandwich composite plates were manufactured in Fontijne Presses - LabEcon60 Laboratory Platen Press machine. The hot press has 400 x 400 mm platens. Platens can be reach to 300 °C temperature and 600 kN force.

In the manufacturing process of facesheet plates, firstly, 110 gr granules were placed to mold homogeneously. Thereafter, two glass fiber woven laminates put to the mid-section of the mold. Finally, 110 gr granules were placed to top laminate homogeneously. Facesheet panels was covered with teflon films from its upper and bottom surfaces in order to prevent the sticking of the panel to the press platens. Then, this structure was placed to hot press and processed at 180 °C temperature under 100 kN for 60 minutes. After 60 minutes, composite left to cooling to the room temperature for 7 hours. At the end of the cooling process, 2 mm thick plates were taken out from press.

After 350 x 350 mm plates were manufactured, they cut to 100 x 100 mm. Sizing process was performed by using water refrigerated diamond blade to prevent composites have any unnecessary damage. All manufacturing and sizing processes are given in Figure 2.

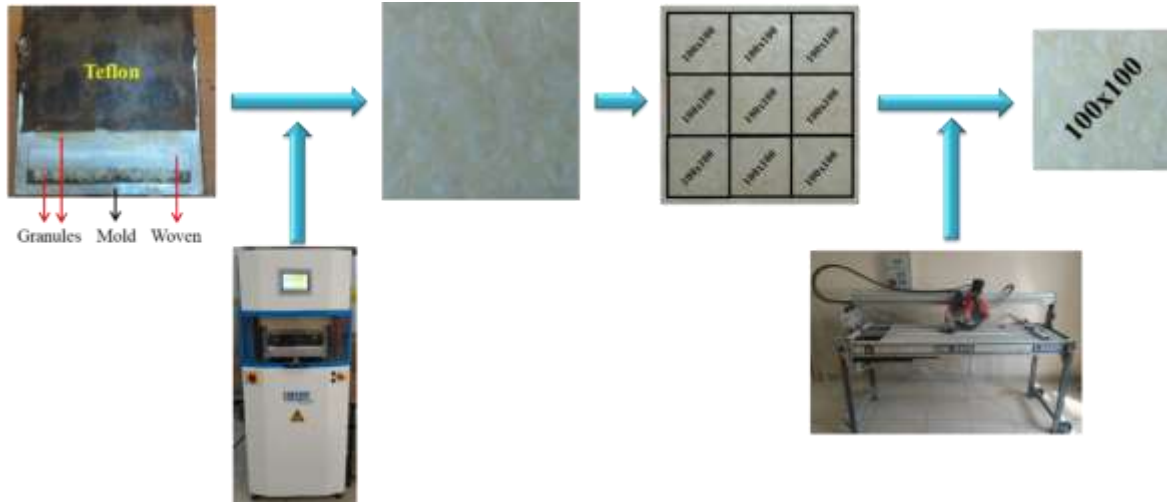


Figure 2. Facesheet plate manufacturing and sizing processes

Besides, 10 mm thick AL002720 coded aluminum honeycomb cut to the 100x100 mm size. After that, facesheet plates bonded to each side of honeycomb with 10 gr adhesive. MGS LR160 epoxy resin and MGS LH160 hardener mixture was used. Mixing ratio of adhesive is 3:1. In the bonding process, firstly, prepared adhesive applied to the facesheet plate. After that, facesheet plates connected to the core structure. They placed to an oven at 80 °C for two hours for curing adhesive. At the end of this process, sandwich composite specimen was manufactured. Bonding process of facesheet plates and core are shown in Figure 3.

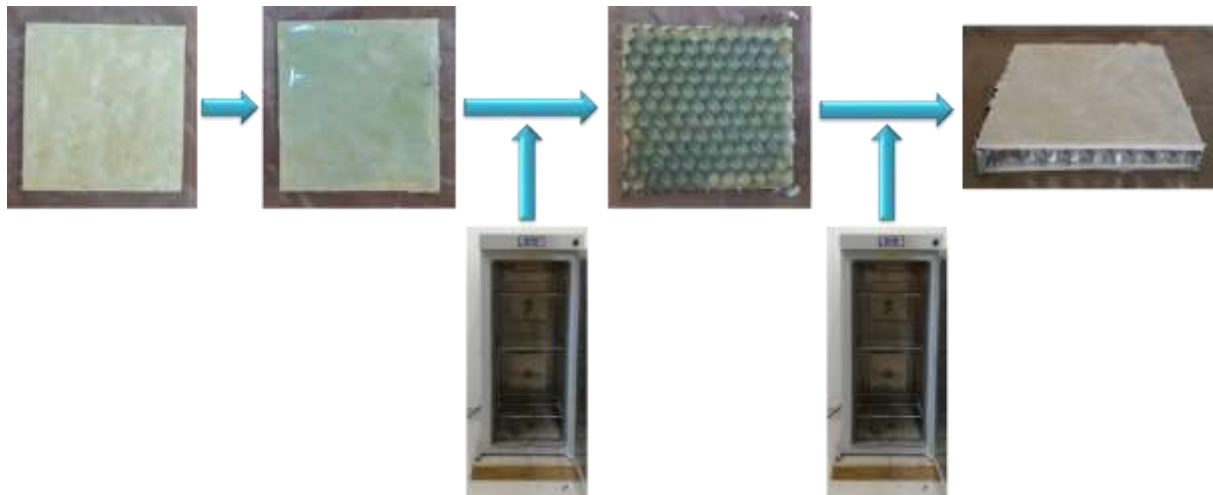


Figure 3. Bonding process of composite

Since composites have been used in many applications areas, it is very likely that these composites can be exposed to impact damages. In this study, low velocity impact tests were performed with flat shaped and hemispherical shaped impactor noses at 12.7 mm diameter. These impact tests were carried out at 20J, 40J and 60J energies in Fractovis Plus low velocity impact testing machine. The equipment was used in the experimental study of this research are given in Figure 4.

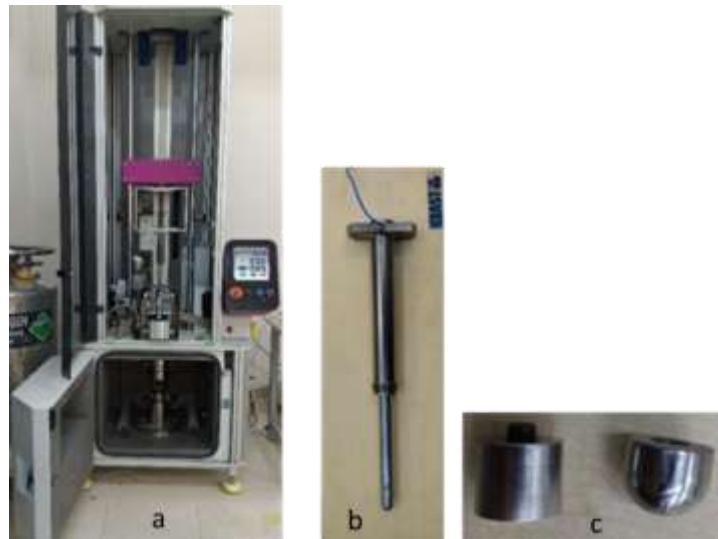


Figure 4. a) Low Velocity impact device, b) Impactor and c) Impactor noses

Results

In order to compare impact behavior of this composite, contact force – deformation diagrams of the specimens was investigated in detail in Figure 5. In 20J energy, rebounding case was observed in flat shaped impactor, but in the hemispherical shaped impactor upper, facesheet plate of the composite was perforated. At the 40J and 60J impact energy levels, all specimens were perforated and maximum deformation values in 60J energies are higher than 40J energies for both hemispherical and flat shaped impactors.

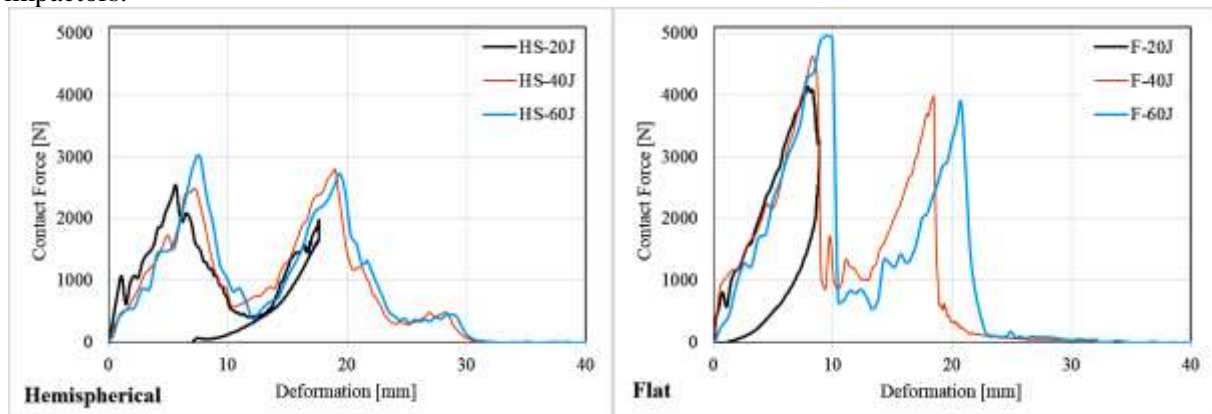


Figure 5. Contact force – deformation diagrams of hemispherical and flat shaped impactors

To understand composites impact behavior better, the change of maximum contact force of hemispherical and flat shaped impactors along with impact energy are given in Figure 6. In the flat shaped impactors, maximum contact force of composites is higher than the hemispherical shaped impactors in all energy values.

3rd International Students Science Congress
3-4 May 2019, İzmir - Turkey

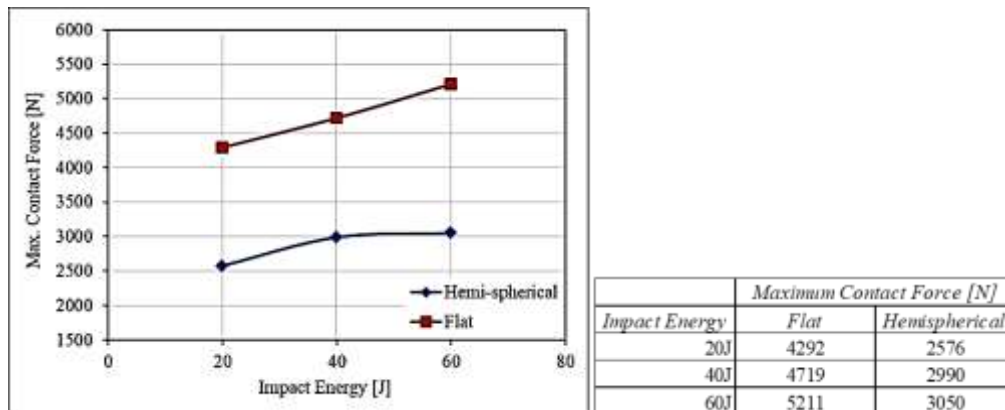


Figure 6. Maximum contact force – impact energy

Energy – time diagrams of the specimens are given in Figure 7. In energy – time diagrams, the rebounding case was observed at an impact energy level of 20J. After the 20 J, the absorbed energy does not change significantly.

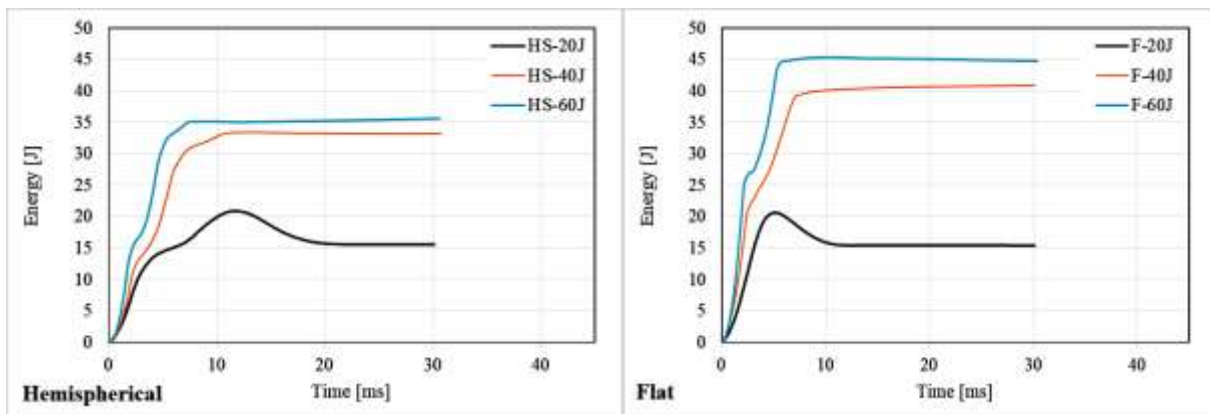


Figure 7. Energy – time diagrams of hemispherical and flat shaped impactors

To investigate energy reactions better, absorbed energy – impact energy diagrams of composites was given in Figure 8. In this diagram, the perforation thresholds of flat shaped impactor are higher than the hemispherical shaped impactor. Moreover, flat shaped impactor is higher absorbs energy for all energy levels.

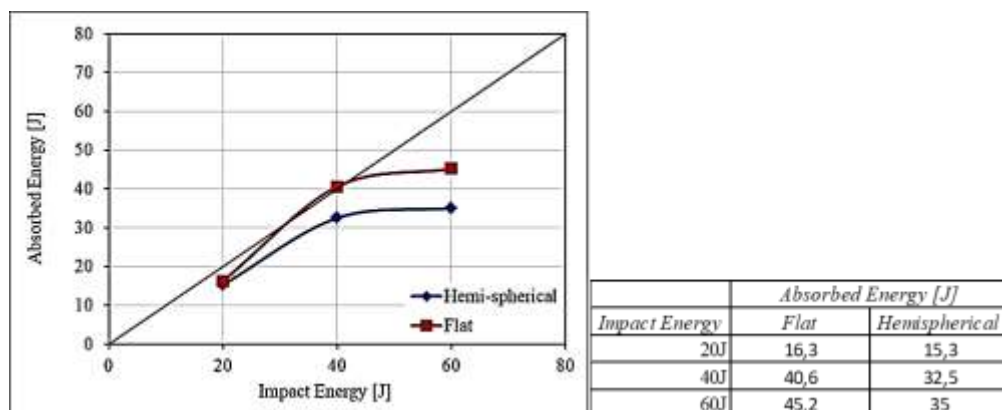


Figure 8. Absorbed energy – impact energy

Conclusions

In this study, impact response of sandwich composite with glass fiber reinforced thermoplastic face sheet and aluminum honey comb core investigated experimentally. Impact tests were carried out at 20J, 40J and 60J energy values with hemispherical and flat shaped impactors. The obtained conclusion can be summarized as:

- Maximum contact force of flat impactor is around 1.7 times higher than hemi-spherical.
- Maximum deformations of flat shaped impactor are smaller than hemi-spherical.
- Penetration energy of flat impactor is higher than hemi-spherical.
- Absorbed energy values are higher at flat shaped impactor.

References

- [1] Carlsson LA Kardomateas GA (2006) Structural and failure mechanics of sandwich composites Springer
- [2] Arbaoui J, Schmitt Y, Pierrot JL, Royer FX (2014) Effect of core thickness and intermediate layers on mechanical properties of polypropylene honeycomb multi-layer sandwich structures. Archives of Metallurgy and Materials, 59(1): 11-16.
- [3] Paulius G, Daiva Z, Vitalis L, Marian O (2010) Experimental and numerical study of impact energy absorption of safety important honeycomb core sandwich structures. Material Science 16(2):119–123.
- [4] Tan CY, Akil H Md. (2012) Impact response of fiber metal laminate sandwich composite structure with polypropylene honeycomb core. Composites Part B 43:1433-1438.
- [5] Park JH, Ha SK, kang KW, Kim CW, Kim HS (2008) Impact damage resistance of sandwich structure subjected to low velocity impact. Journal of Materials Processing Technology 201:425–430.
- [6] Kurşun A, Şenel M, Enginsoy H. M, Bayraktar E. (2016) Effect of impactor shapes on the low velocity impact damage of sandwich composite plate: Experimental study and modelling. Composites Part B 86:143-151.
- [7] Mitrevski T, Marshall IH, Thomson RS, Jones R. (2006) Low-velocity impacts on preloaded GFRP specimens with various impactor shapes. Composite Structures 76(3):209-217.
- [8] Wang J, Waas AM, Wang H. (2013) Experimental and numerical study on the low velocity impact behavior of foam-core sandwich panels. Composite Structures 96: 298-311.
- [9] <http://www.nuhkompozit.com.tr/duramax-LFT30-PP.html>

PID Algoritması ile Çizgi İzleyen Robot Kontrolü

Emrah Kuzu, Süleyman Murat Bağdatlı,
Manisa Celal Bayar Üniv., Makine Mühendisliği Bölümü, Yunussemre, Manisa, Türkiye
İletişimden sorumlu yazar: emrah.kuzu@cbu.edu.tr

Anahtar Kelimeler: pid, line follower, robot

Disiplin: mechanical engineering, mechatronics engineering

Giriş

Robotik ve otomasyon sistemlerinde sistemlerin artık kararlı ve hızlı bir şekilde sonuca ulaşmak için birçok algoritma geliştirilmektedir [2]. PID bir kontrol geri bildirim mekanizması olarak oldukça başarılı ve yaygın bir biçimde kullanılmaktadır. Hesaplanan hata ile giriş-çıkış arasında kontrol sağlanır. Hesaplanan hata P (Proportional) Oransal I (Integral) İntegral D (Derivative) Türevsel işlemlerin ardından tekrardan sisteme uygular. Sistem sürekli olarak bu işlemi tekrarlar. Bu şekilde amaçlanan referans değeri için, hata minimize edilir [3].

Bu çalışmada çizgi izleyen robotların yüksek hızlarda karşılaştıkları rotadan çıkma durumları için PID algoritması uygulanmıştır. 8 adet analog sensör ile çizgi tespit edilmiş olup, 4. ve 5. sensörler istenilen rota (referans) olarak kabul edilmiştir. Diğer sensörler ise hata olarak belirlenmiştir. En yüksek hata katsayısı birinci ve sekizinci sensörlere tanımlanmıştır. Mikroişlemci olarak Atmega328p kullanılmıştır. Sistem üzerinde PID algoritması uygulanmış ve uygulanmamış tur zamanları tablo halinde sunulmuştur [1].

PID Algoritması

K_p , K_i ve K_d katsayıların matematiksel hesaplanması ile oluşan bir algoritmadır. Burada en uygun katsayıları bulmak, algoritmanın en önemli noktalarından bir tanesidir. Bu katsayıları bulmak için farklı yöntemler mevcuttur. Genel olarak deneme yanılma yapılarak katsayılar belirlenmeye çalışılır.[7]

$$Hata = Ref - Okunan \quad (1)$$

$$Hatad = Hata - E_{Hata} \quad (2)$$

$$P = K_p \cdot Hata \quad (3)$$

$$I = I + (K_i \cdot Hata \cdot dt) \quad (4)$$

$$D = (K_d * Hatad)/dt \quad (5)$$

$$PID = P + I + D \quad (6)$$

$$E_{Hata} = Hata \quad (7)$$

PID, otomatik kontrolün olduğu hemen hemen her sistemde uygulanabilir. Buradaki kazanç katsayıları her sistem için farklı değerler ifade etmektedir. Tasarlanan sistem başka bir noktada tekrar uygulamasında dahi katsayılar tekrar hesaplanması gerekebilir. [1,5]

P katsayısı otomatik kontrol sisteminin, ölçülen hataya karşı tepkiyi belirler. Büyük bir değer olursa denge noktasını geçer, küçük olursa hatayı kapatma süresi uzar. Bu etkiyi daha yumuşak geçişlerle kapatmak için hatadaki değişim hesaplanır. Bir önceki hata ile bir ölçülen hata ise D katsayısı ile belirlenir. Toplam hata, sistemin geçmişte yaptığı hatayı minimize etmek için hesaplanır ve I katsayısıyla belirlenir [6]. PID algoritması denklem 7' deki gibi

$$u(t) = MV(t) = K_p e(t) + K_i \int_0^1 e(\tau) d\tau + K_d \frac{d}{dt} e(t) \quad (8)$$

$$u(t) \quad PID \text{ denetleyici çıkışı} \quad (9)$$

$$e(t) \quad Hata \quad (10)$$

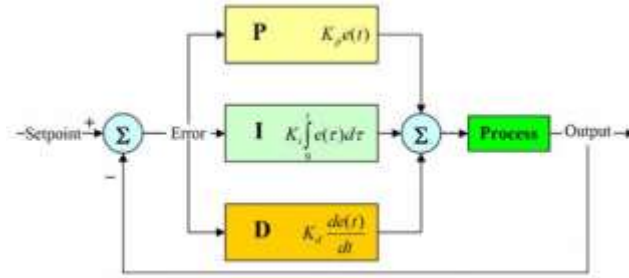
$$K_p \quad Oransal etki kazancı \quad (11)$$

$$K_d \quad Oransal etki kazancı \quad (12)$$

$$K_i \quad İntegral etki kazancı \quad (13)$$

$$\tau \quad Zaman \quad (14)$$

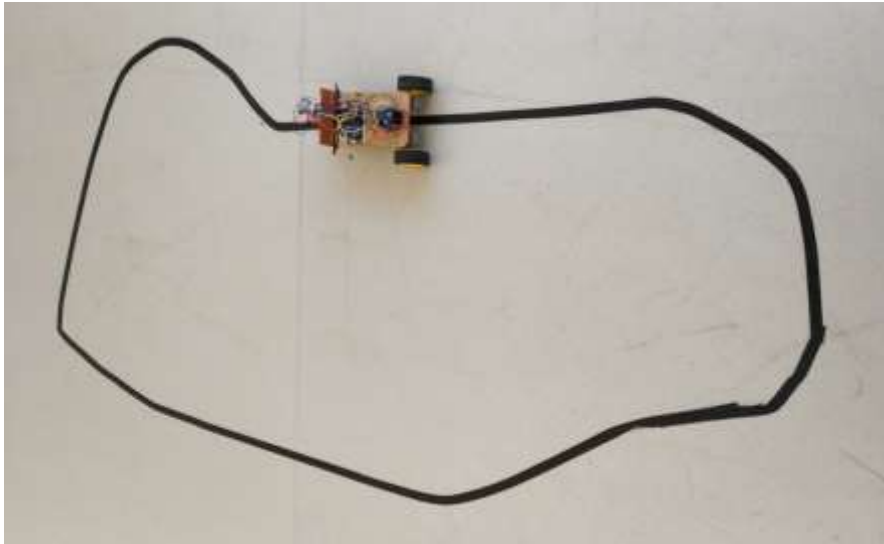
verilmiştir.



Şekil 4. PID döngüsü

Uygulama

Oluşturulan model yazılım algoritmasına ait akış diyagramına uygun olarak 8 adet mesafe sensöründen gelen veriler ile robot gövdesinin siyah zeminde açtığı farklılıklarını algılar. Elde edilen veriler mikroşlemcide PID algoritması ile yorumlanarak motorlara gerekli tahrik için mikroşlemci tarafından komut gönderilir. Takip edilecek yol orta derece zorlukta bir yol belirlenmiştir. Kullanılan motorlar 200 rpm hız ile çalışabilmektedirler.



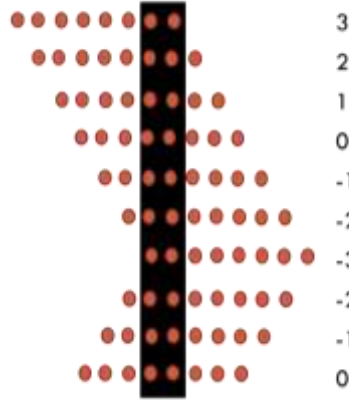
Şekil 5. Rota

Deney yolu tam tur olacak şekilde seçilmiş ve tam tur sonuçları süre olarak kaydedilmiştir. PID kontrol karşılık on-off kontrol süreleri tutulmuştur. Yolun toplam uzunluğu 2.57 m'dir. Çizgi tespiti için kullanılan 8 adet sensör mevcut olup bunları seviye eşitleme ile dijital çıkış alınmaktadır. Siyah ve beyaz farkı 0 ve 1 olarak ifade etmektedir. Beyaz alanda 1 siyah alanda 0 çıkışı vermektedir. 8 adet sensörden merkezdeki 2 adet sensör referans kabul edilmiştir. Diğer sensörler ise konumlarına göre hata katsayısı belirlenmiş ve buna göre hata oranı hesaplanmıştır.



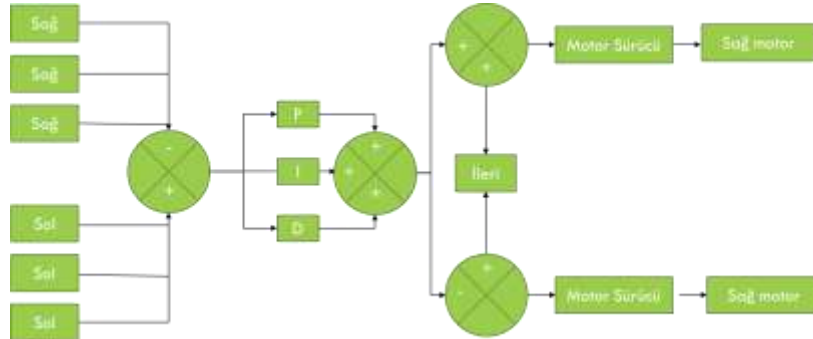
Şekil 6. Sensörler

Sensörlerden alınan veriler ile hata katsayıları Şekil 7’ de belirtilmiştir. Bu katsayılar yolun şekline göre tekrar belirlenebilir. “3” ve “-3” olarak belirlenen katsayılar daha yüksek değerlerdeki katsayılar için tekrar hesaplama yapılması gerekmektedir.



Şekil 7. Sensör hata katsayıları

Sensörlerden okunan değerler yorumlandıktan sonra sonuç negatif ise sola, pozitif ise sağa yönlendirme yapılmaktadır. Burada her döngü PWM değerini artırmakta ve sınır değeri olan 255’ e yaklaştığında 255 değerinde sabit tutulmaktadır.



Şekil 8 . PID döngüsü

$$PID_p = K_p \cdot hata; \quad (15)$$

$$PID_i = PID_i + (K_i \cdot hata); \quad (16)$$

$$PID_d = K_d \cdot ((hata - E_{hata}) / cycletime); \quad (17)$$

$$motorhiz = PID_p + PID_i + PID_d \quad (18)$$

$$E_{hata} = Hata; \quad (19)$$

$$sagmtr = sgmtrsbt - motorhiz \quad (20)$$

$$solmtr = slmtrsbt + motorhiz \quad (21)$$

Algoritma için hesaplama zamanı “cycletime” değişkeni ile tutulmaktadır. PID sonucunda elde edilen sonuç aracın sağa ya da sola dönüşüne karar vermektedir. Negatif sonuç gelir ise sağ motor PWM değerini artırıp sola dönüşü, pozitif ise sağ motor PWM değerini azaltıp sağa dönüşü yapmaktadır. Hata olarak ifade edilen değişken çizgiden ne kadar saptığı ile ifade edilmektedir.[7]



Şekil 9. Hata ölçüm örnekleri

K_p , K_i , K_d katsayıları deneysel olarak elde edilmiştir. En uygun değerler olarak
 K_p için 12
 K_d için 2.5
 K_i için 0.7 olarak elde edilmiştir.

Yöntem

Toplam hata hesaplanırken katsayılar kullanılır. Burada önemli olan K_p , K_i ve K_d katsayılarının belirlenmesidir.[4] Bu katsayılar sistemin kararlı gelmesinde önemli rol oynar. Bu katsayıları belirlemek çeşitli algoritmalar mevcut olup en çok kullanılan Ziegler Nichols yöntemidir. Bu deneyde, deneme yanılma ile karar verilmiştir.

Tablo 1. Sensör okuma durumları

Okunan sensör	Hata	Okunan sensör	Hata	Okunan sensör	Hata
00011000	0	10000000	-3	00000100	1
00010000	0	01000000	-2	00000010	2
00001000	0	00100000	-1	00000001	3

Tablo 1' de çizgiyi algıladığı alan '1' çizgiyi algılayamadığı alan ise '0' olarak belirlenmiştir. Analog sensör kullanılmış olup eşik değeri bu uygulama için 120 olarak belirlenmiştir. 120 ve üstü değerler 1 kabul edilmiştir. Türev hesabı için mikro denetleyicinin timer (zamanlayıcı) kullanılmıştır. [6]

Sonuçlar

Bu çalışmada hızlı çizgi izleyen robotlar için PID algoritması uygulanmış olup deneysel olarak algoritmanın üstünlüğü kabul görmüştür. PID algoritması PI, PD gibi farklı yapılarda tur zamanı kaydedilmiştir. Tur olarak başlama ve bitiş süresi olarak veriler toplanmıştır. En başarılı sonuç PID ile elde edilmiştir. PID algoritmasına en yakın olarak PI sonuç vermiştir.

Referanslar

- [1] Balaji V, Balaji M, Chandrasekaran M, Ahamedkhan MKA, Elamvazuthi I (2015). Optimization of PID Control for High Speed Line Tracking Robots IEEE International Symposium on Robotics and Intelligent Sensors (IEEE IRIS2015).151-152: <https://doi.org/10.1016/j.procs.2015.12.329>
- [2] Bağdatlı SM, Okwudire CE, Ulsoy AG (2014) Linear quadratic design of passive vibration isolators. Dynamic Systems and Control Conference V003T50A003-V003T50A003:1-1.
- [3] Kuzu E, Çengelci B (2016) PID Control Algorithm with Arduino. International Conference on 1st Engeneering Technology and Applied Sciences, ICT-130:3-5
- [4] Arıkan Y, Çaşka S, Gayretli A, Oğuz Y (2015) Otomatik Kontrol Ulusal Toplantısı, TOK'2015: 3.
- [5] Beschi M, Adamini R, Marini A, Visioli A (2015) Using of the Robotic Operating System for PID control education (2015) IFAC-PapersOnLine 1-1
- [6] Pakdaman M, Mehdi Sanaatiyan M (2009) Design and implementation of line follower robot. Second International Conference on Computer and Electrical Engineering
- [7] Mahmud K, Abdullah-Al-Nahid H, Al Mamun A (2012) Implementation of autonomous line follower robot. 2012 International Conference on Informatics, Electronics & Vision (ICIEV)
- [8] Jen F, Trung Mai B (2012) Building an autonomous line tracing car with PID algorithm. Proceedings of the 10th World Congress on Intelligent Control and Automation.

Analysis of Complex Thermodynamic Steam and Gas Turbine Cycles Using Cycle Pad

Alif Diambu Ngimbi, Kinshasa University, Dept. of Mechanical Engineering, Lemba Campus, Kinshasa, Democratic Republic of Congo

Corresponding author: anasrouline1@gmail.com

Keywords: thermal power plants, working fluid, turbo-alternator, gas turbine, steam turbine, CyclePad

Discipline: Mechanical Engineering

Abstract

With modernization, the need for electricity is gradually increasing. The electricity consumption of a nation is an indicator of its economic power. The use of thermal power plants for the production of electricity goes back long periods. The state change energy of a working fluid is collected to rotate a turbo-alternator group following a thermodynamic cycle. The energy of the working fluid that can be air or water vapor is used depending on whether it is a gas turbine (combustion) or a steam turbine.

In this paper, we present the thermodynamic analysis of two gas turbine plants (simple and complex) and two steam turbine plants (simple and complex) that can supply 275 MW of power to the shaft. That is to say that it can supply cities whose annual demand does not exceed 2.4 GWh, the case of Turkish cities like Kastamonu, Kütahya, Malatya, Erzurum, Diyarbakir, etc. (according to data collected in 2016) or Democratic Republic of Congo's cities like Nord-Kivu, Kasai Oriental, etc. (data collected in 2014) using the thermodynamic software CyclePad. This analysis allows us to make the sensitivity analysis of some parameters according to the variation of others in order to improve the outcome with optimal efficiency.

Introduction

The universe in all that constitutes it is a great fountain of energy. This energy that moves, nourishes, illuminates, is also the same energy that places nations that know how to produce and manage it in the rank of great power. The amount of energy a nation produces and more precisely the amount it consumes is an indicator that shows that its economy is alive and has enough to do with that energy. Based on energy in its electrical form, the habitat with its daily needs is as much needed as the industry. The recent sketch of world energy consumption in Figure 1 shows that China alone accounts for 20% of world energy consumption, followed by the United States at 19%, Europe at 15%, Russia at 6% and the remaining 40% is spread across all other countries. And statistical data from 2014 and 2016 respectively in Figures 2 and 3 show that gas and steam turbines represent a large portion of global electricity production. Although current research is focused on reducing electricity production as much as possible by polluting means, there is still far from being any hope of eliminating the use of these types of equipment, so there is a strong reason to conduct studies to achieve optimal efficiency, which means producing much more electricity with low pollution.

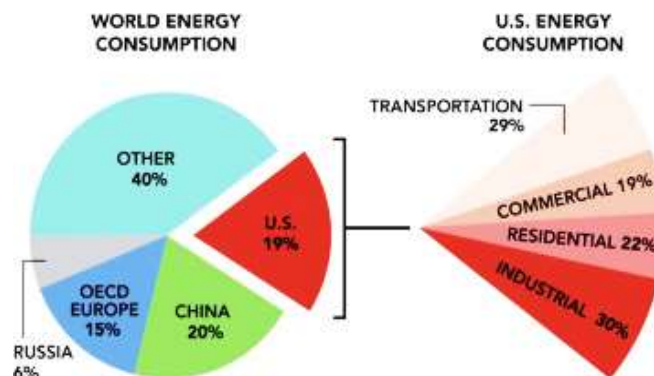


Figure 1. World Energy Consumption [12]

World Power Generation Capacities
from All Energy Sources
in 2014 (GW)

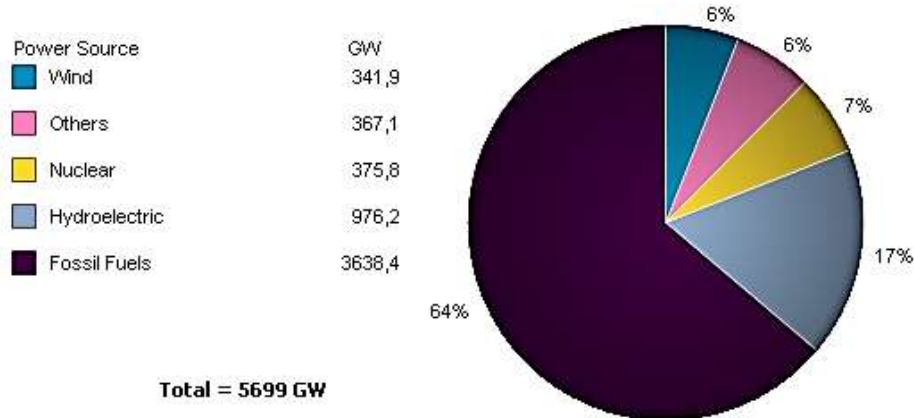
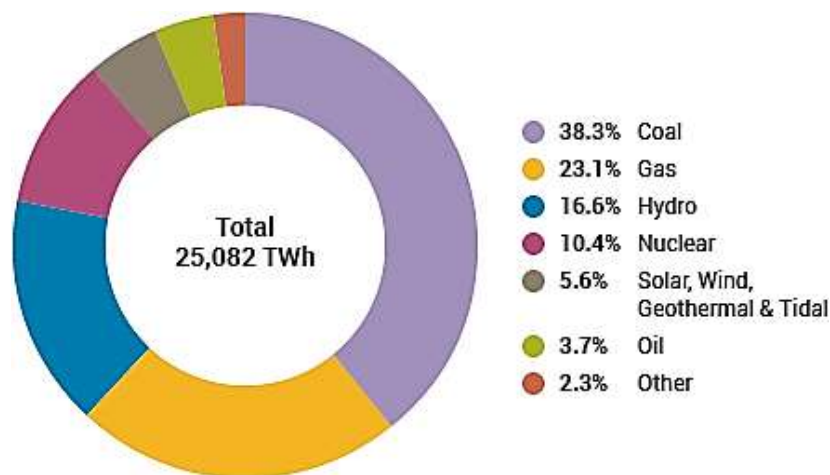


Figure 2. Breakdown of Electricity Generation by Energy Source [13]



Source: IEA Electricity Information 2018

Figure 3. World Electricity Production by Source 2016 [14]

A recent study by Payam N. et al. (March 2015) showed that globally, the residential energy market is dominated by traditional biomass (40% of the total) followed by electricity (21%) and natural gas (20%), but the total proportion of fossil fuels has decreased over the past decade [3]. Based on Figure 3 above, we observe that electrical production involving gas and steam turbines represents more than 70% of world production.

This work makes a theoretical study from the thermodynamic point of view of gas and steam turbines in two different configurations for each, to present the important thermodynamic points of these machines that influence performance, using an Intelligent Computer Aided Instruction (ICAI) software called CyclePad. When the thermodynamic analysis of a power or energy production system is done by traditional means known by using, for example, equations of state, tables (Mollier, Steam, Gas...), a lot of time is required to reach the solution. CyclePad saves time and avoids some calculation mistakes.

CyclePad has been codeveloped by Oxford University and Northwestern University since 1995 and evaluated by Professor C. Wu in the Mechanical Engineering Department at the U.S. Naval Academy. It follows the same basic steps used in the traditional or physical design process. The user builds his cycle design, runs it through analysis, validates results, refines the design, and iterates this process until the cycle's performance is optimized. The difference is that the user manages this process virtually through a computer, much more quickly, easily, and cost-efficiently [4].

Methodology

In the process of producing electricity using the energy of fluids are classified the machines using the energy of the air (gas turbine) and that of the water vapor (Steam Turbine), from the chemical energy, through the mechanical to end up with the electrical.

Chemical energy \longrightarrow Mechanical energy \longrightarrow Electrical energy

Figure 4. Electricity production process

In this paper, we present two models of steam turbines and two models of gas turbines, which will provide 275 MW of net power according to certain initial values that we have set. One of each of two models is a basic machine and the other is complex.

First of all, we start by showing the reliability of the results obtained by CyclePad by comparing them with some calculations made in a traditional way. The error being very small, CyclePad's results were reliable and good. Then, we constructed and analyzed each of the cycles of our models by changing some parameters and observing how they varied from others using the sensitivity analysis tools presented in CyclePad.

Results

In the case of the basic gas turbine, the air being the working fluid, working at a pressure of 10 bar (At the compressor inlet), the minimum temperature being 50°C and the maximum temperature 850°C, the pressure at the compressor outlet has been determined for optimal performance. The compression ratio for optimal power is given by:

$$x = \sqrt{\theta} \quad [9] \quad (1)$$

where θ is the ratio between the maximum and minimum temperature of the cycle.

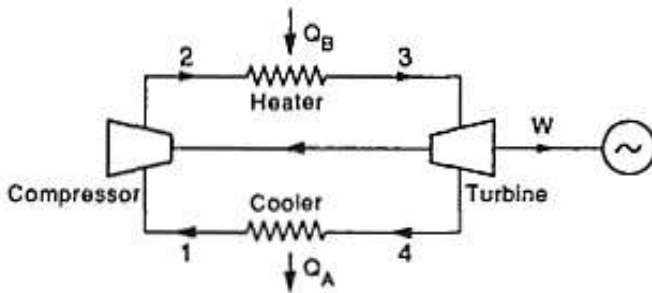


Figure 5. Joule-Brayton basic Gas Turbine cycle [9]

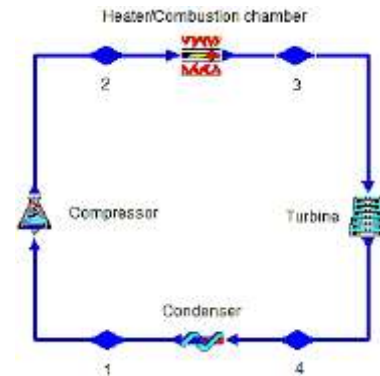


Figure 6. CyclePad representation of the basic Gas Turbine cycle

$$x = \sqrt{\frac{T_3}{T_1}} \Rightarrow \frac{p_2}{p_1} \Big|_{\text{opt}} = \sqrt{\frac{T_3^{(\frac{\gamma}{\gamma-1})}}{T_1}} \Rightarrow \frac{p_2}{p_1} \Big|_{\text{opt}} = \sqrt{\frac{(850+273)^{(1,4)}}{(50+273)}} = 8,85 \Rightarrow p_2 = 88,5 \text{ bars}$$

By hand computation we found:

Compression work W_c

$$w_c = h_2 - h_1 = C_p(T_2 - T_1) = C_p T_1 \left(\frac{T_2}{T_1} - 1 \right) = C_p T_1 \left(\left(\frac{p_2}{p_1} \right)^{\frac{\gamma-1}{\gamma}} - 1 \right) \text{ where } C_{p,air} = 1,005 \frac{\text{kJ}}{\text{kg K}} = 1,005 * (50 + 273) * \left((8,85)^{\frac{0,4}{1,4}} - 1 \right) = 280,61 \frac{\text{kJ}}{\text{kg}} \quad (2)$$

Relaxation work W_d

$$w_d = h_3 - h_4 = C_p(T_3 - T_4) = C_p T_3 \left(1 - \frac{T_4}{T_3}\right) = C_p T_3 \left(1 - \left(\frac{p_4}{p_3}\right)^{\frac{\gamma-1}{\gamma}}\right)$$

$$= C_p T_3 \left(1 - \left(\frac{p_2}{p_1}\right)^{\frac{1-\gamma}{\gamma}}\right) \text{ Car } p_1 = p_4 \text{ et } p_2 = p_3 \quad (3)$$

$$\Rightarrow w_d = 1,005 * (850 + 273) * \left(1 - (8,85)^{\left(\frac{-0,4}{1,4}\right)}\right) = 523,28 \frac{\text{kJ}}{\text{kg}}$$

Useful work W_u .

$$w_u = w_d - w_c = 523,28 - 280,61 = 242,67 \frac{\text{kJ}}{\text{kg}} \quad (4)$$

The efficiency

$$\eta_{th} = \frac{w_u}{q} = \frac{w_d - w_c}{C_p(T_3 - T_2)} = \frac{w_d - w_c}{C_p T_1 \left(\frac{T_3}{T_1} - \frac{T_2}{T_1}\right)} = \frac{w_d - w_c}{C_p T_1 \left(\theta - \left(\frac{p_2}{p_1}\right)^{\frac{\gamma-1}{\gamma}}\right)}$$

$$\Rightarrow \eta_{th} = \frac{242,67}{1,005 * 323 \left(\frac{1123}{323} - (8,85)^{\left(\frac{0,4}{1,4}\right)}\right)} = \frac{242,67}{523,38} = 0.4636 \text{ soit, } 46,36 \% \quad (5)$$

The mass flow rate.

$$\dot{m} = \frac{P_u}{w_u} = \frac{275000}{242,67} = 1133,22 \frac{\text{kg}}{\text{s}} \quad (6)$$

The results from CyclePad with the same initial values are given in the Table 1 compared with values of hand calculation values presented above.

Table 1. Comparison of manual calculation results with CyclePad results

	$w_c \left[\frac{\text{kJ}}{\text{kg}}\right]$	$w_d \left[\frac{\text{kJ}}{\text{kg}}\right]$	$w_u \left[\frac{\text{kJ}}{\text{kg}}\right]$	η_{th}	Mass flow rate $\dot{m} \left[\frac{\text{kg}}{\text{s}}\right]$
Hand calculation	280,61	523,28	242,67	46,36	1133,22
CyclePad values	280,3	522,5	242,2	46,37	1135,31
Relative error to hand calculation	0,0011 or 0,1 %	0,0015 or 0,15 %	0,19 %	0,02 %	0,18 %

The results in this table show that CyclePad is reliable.

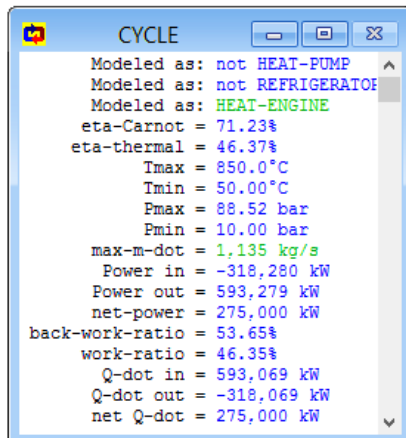


Figure 7. Result of the cycle

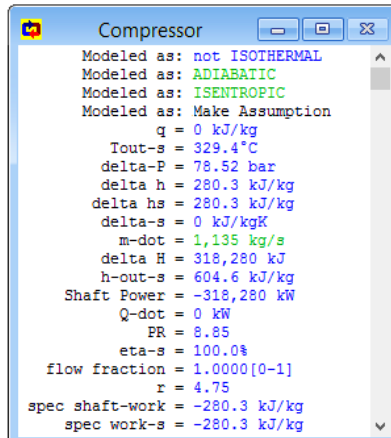


Figure 8. Compressor result

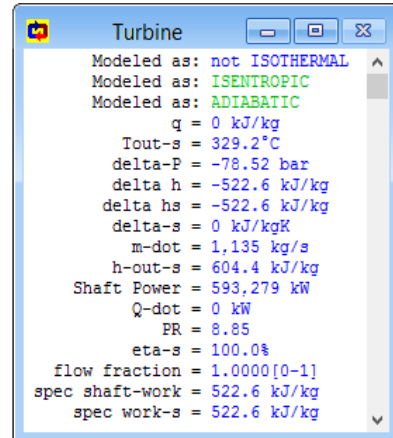


Figure 9. Gas Turbine result

Sensitivity analyses and the cycle diagram are presented in the following curves:

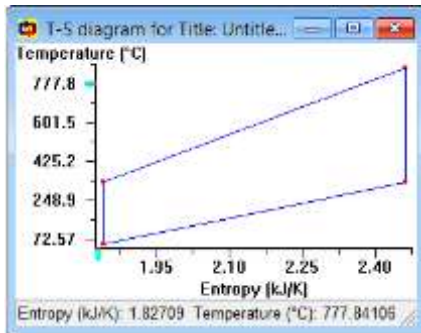


Figure 10. T-S diagram of the cycle

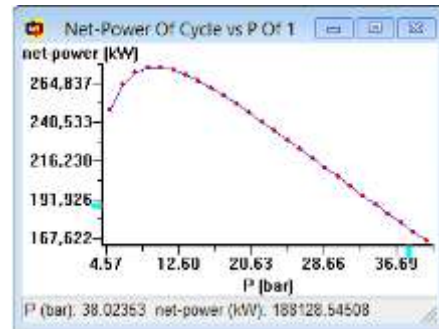


Figure 11. Influence of P1 on the Net-Power

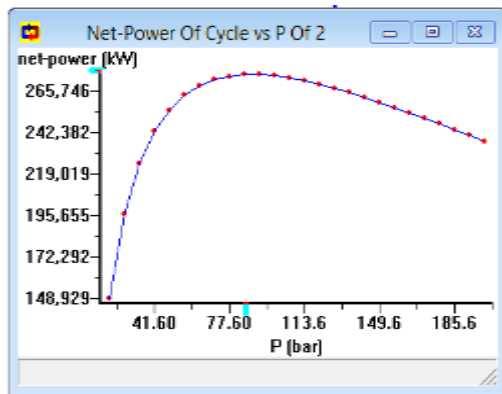


Figure 12. Influence of P2 on the Net-Power

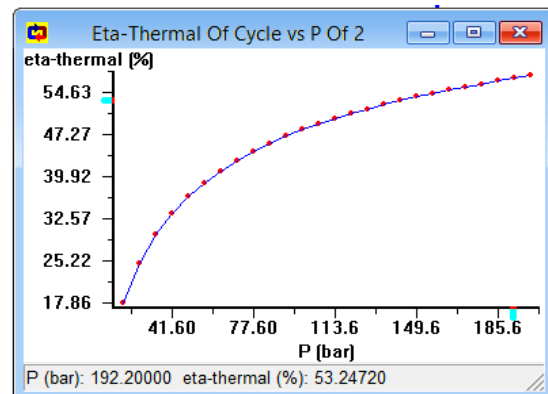


Figure 13. Influence of P2 on the cycle thermal efficiency

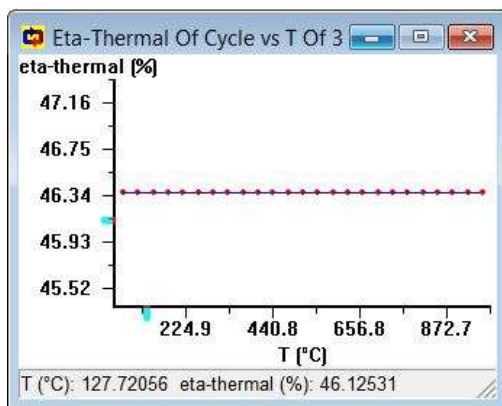


Figure 14. Influence of T3 on the efficiency for the reversible cycle

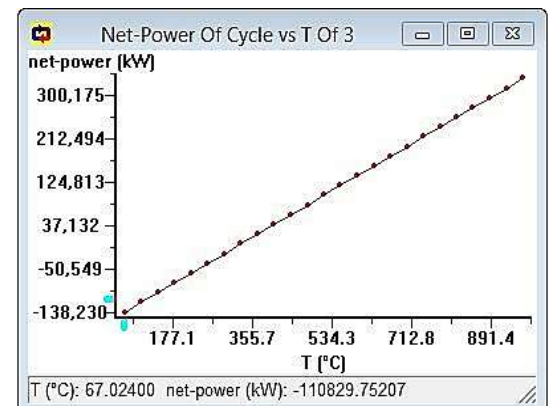


Figure 15. Influence of T3 on the Net-power for the reversible cycle

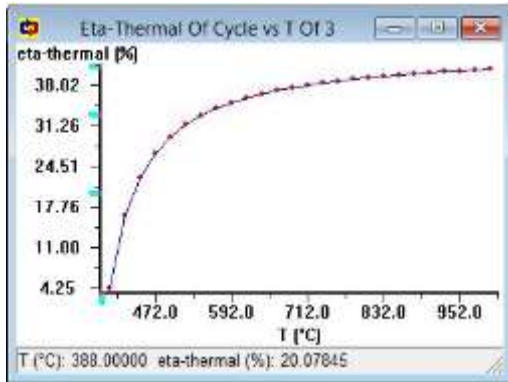


Figure 16. Influence of T3 on the efficiency for the irreversible cycle (5% of irreversibility)

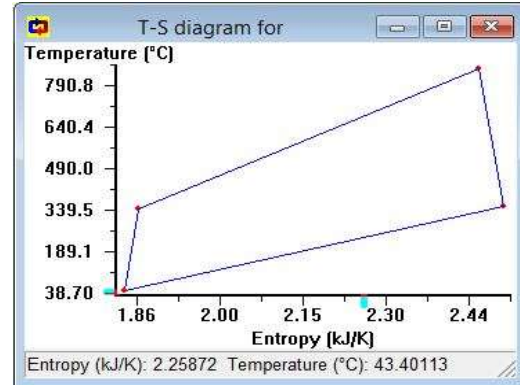


Figure 17. Irreversible cycle diagram

Some improvements are made to the basic cycle by adding one regeneration and two inter-coolings to get the complex cycle. The compression ratio for optimal performance is given by:

$$\pi_{opt} = \sqrt{\frac{p_2}{p_1}} = \sqrt{\frac{88,5}{10}} = 2,975. \quad (7)$$

The improvement in the basic cycle allows the use of smaller compressors with a reduced flow rate of 963.1 kg/s for the same net power with an efficiency of 51.74%.

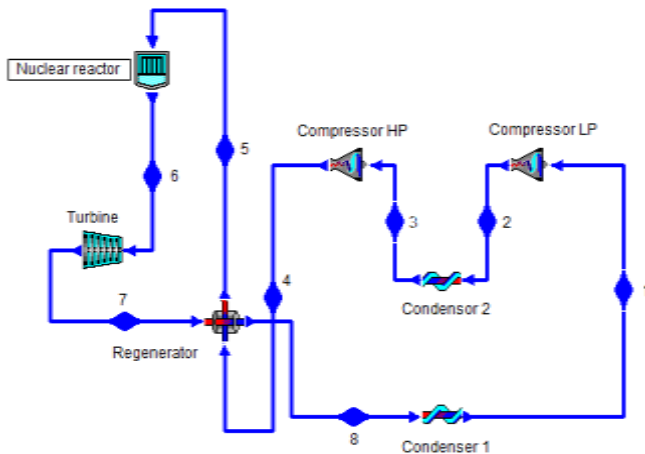


Figure 18. CyclePad representation of the complex Gas Turbine cycle

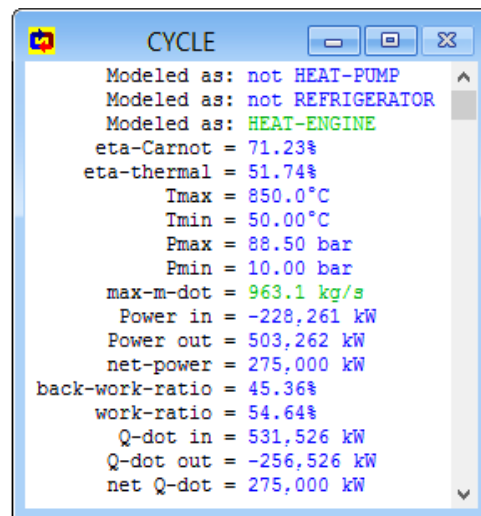


Figure 19. Result of the cycle

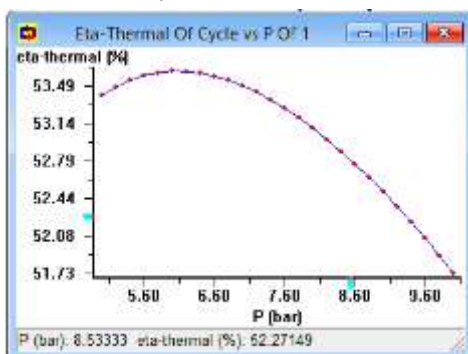


Figure 20. Influence of P1 on the cycle efficiency

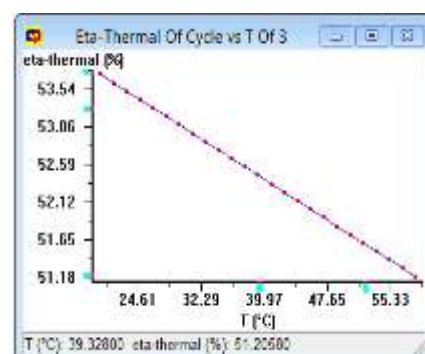


Figure 21. Influence of T3 on the efficiency

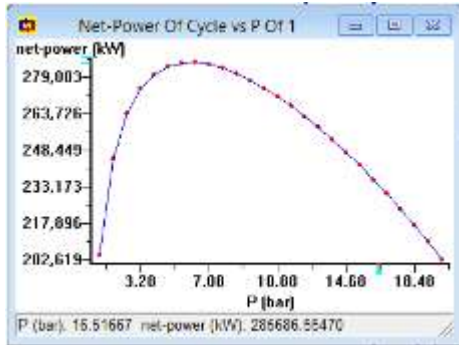


Figure 22. Influence of P1 on the net power

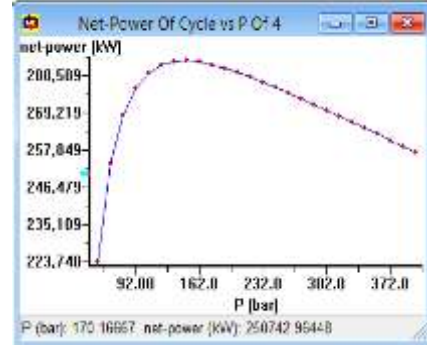


Figure 23. Influence of P4 on the net Power

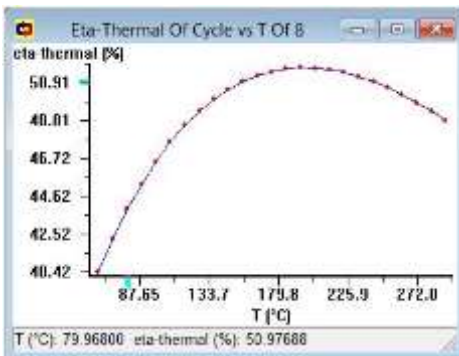


Figure 24. Influence of T8 on the efficiency

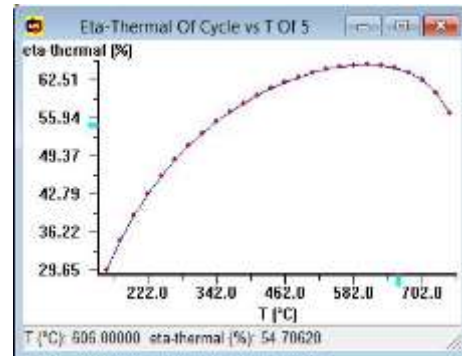


Figure 25. Influence of T5 on the efficiency

Now we will do the same study like the one we have just presented above, for the case of steam turbines. The aim is to produce 275 MW of net power, the complex and basic cycle is based on the model of the Indian Point nuclear power plant in the United States of America.

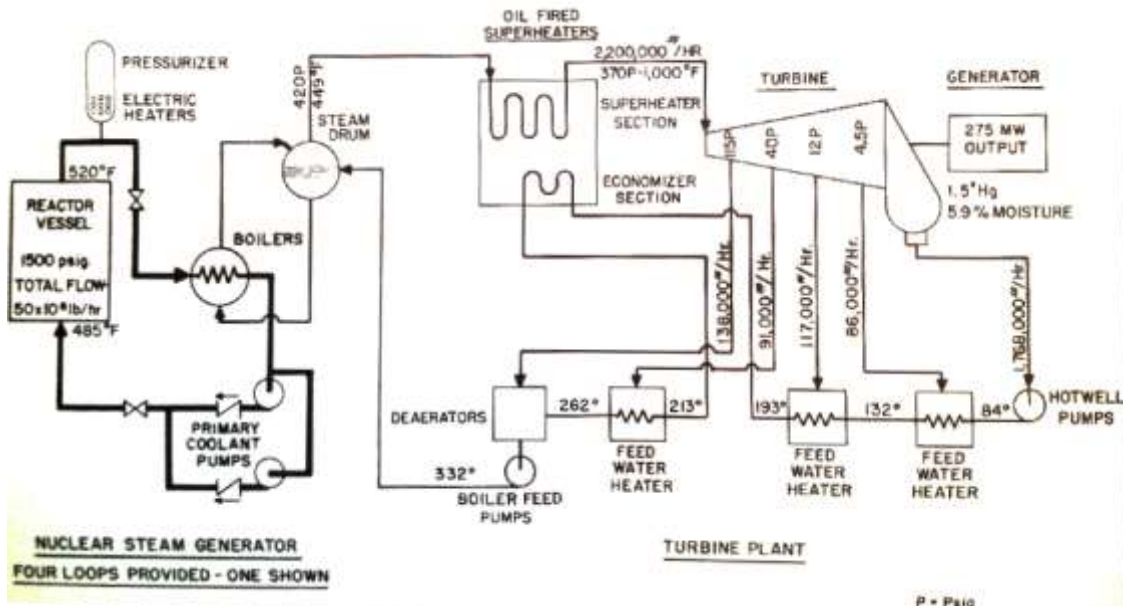


Figure 26. Indian Point System Flow Diagram [15]

According to the image above, the plant operates at a maximum temperature of 537.8°C with a maximum pressure of 103.4 bar. At the outlet of the last turbine, the vapor quality must be 94.1%. The basic steam turbine we present operates according to the Rankine cycle. The boiler will replace the

nuclear steam generator of the complex machine. For this purpose, the maximum pressure to be considered for the basic turbine will be 28.96 bar.

The result of the simple cycle is as follows:

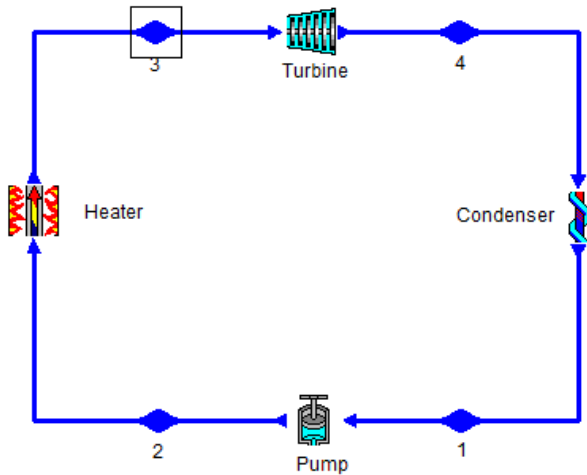


Figure 27. Basic Rankine Cycle

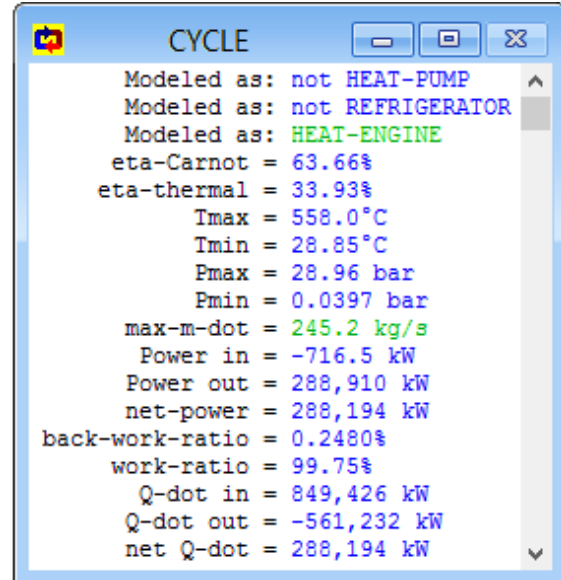


Figure 28. Cycle results

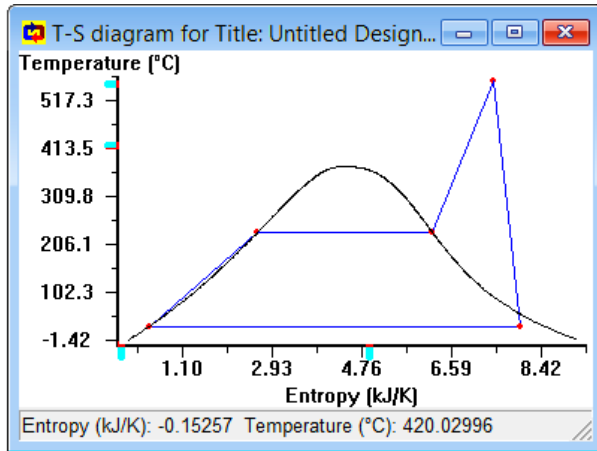


Figure 29. Basic Rankine Cycle diagram

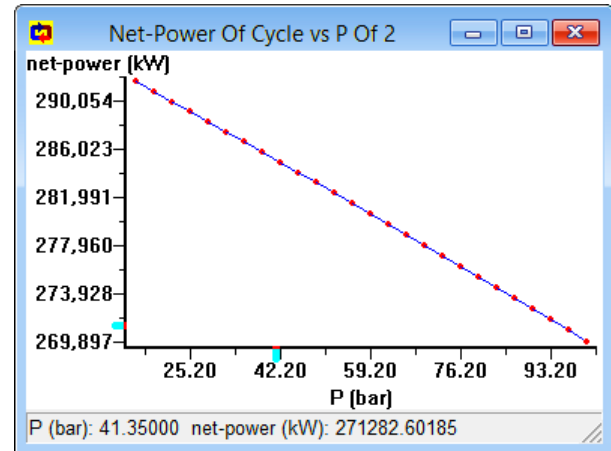


Figure 30. Influence of P2 on the net Power

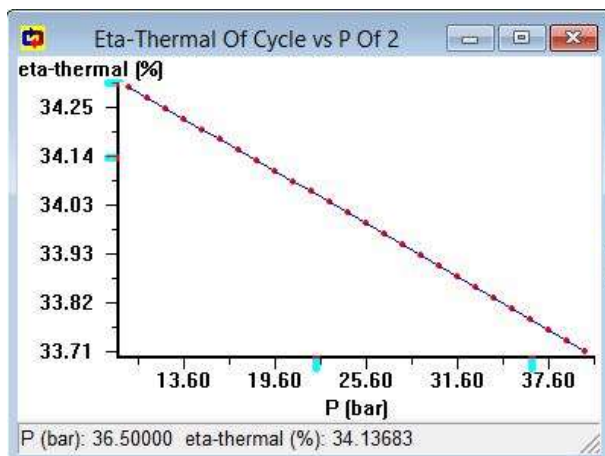


Figure 31. Influence of P2 on the efficiency

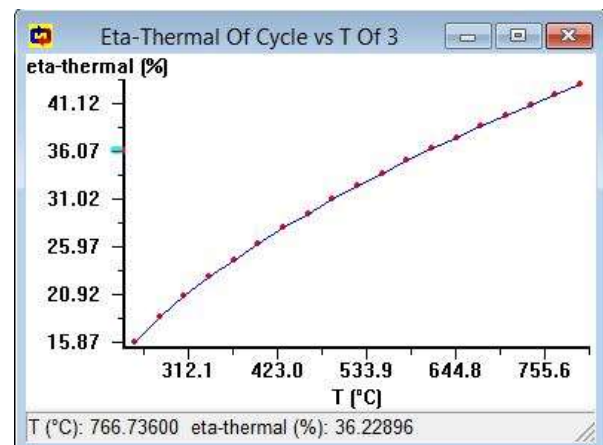


Figure 32. Influence of T3 on the efficiency

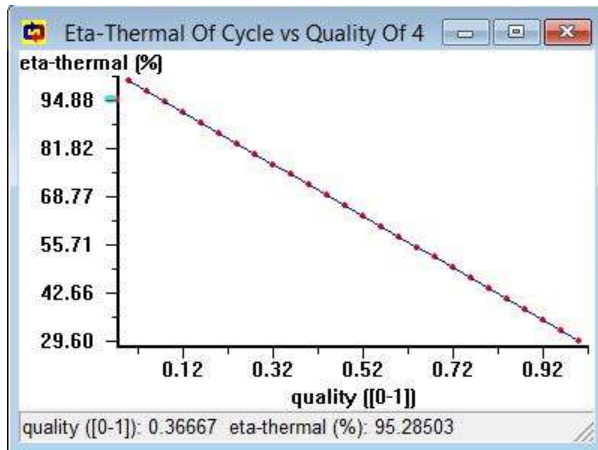


Figure 33. Influence of vapor quality on the efficiency

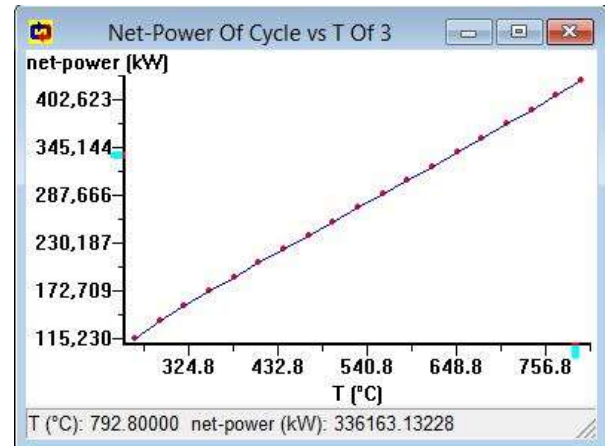


Figure 34. Influence of T3 on the Net Power

The result for the complex cycle is presented below:

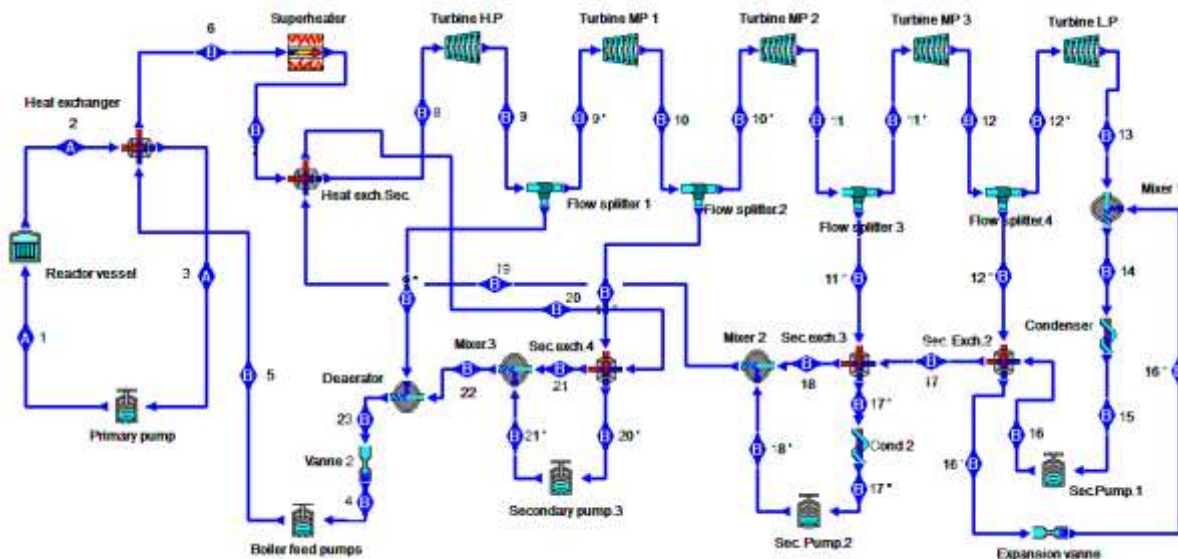


Figure 35. Indian Point System Flow Diagram by CyclePad.

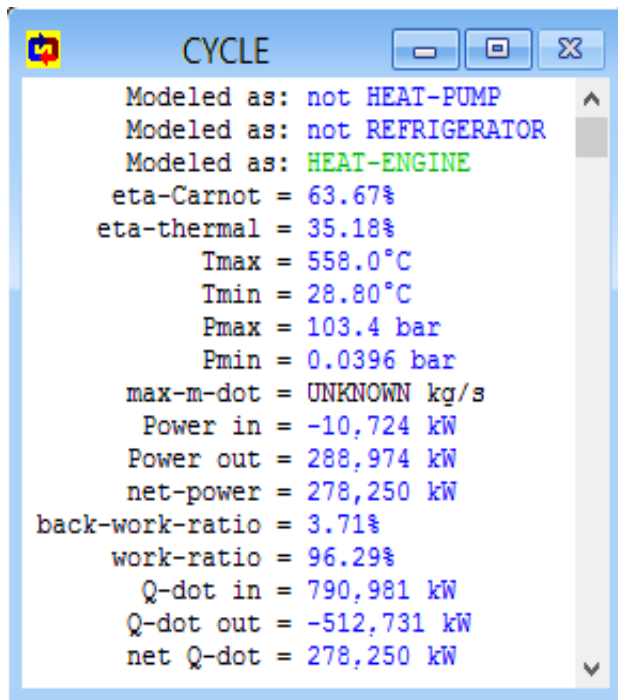


Figure 36. Indian Point Cycle Result

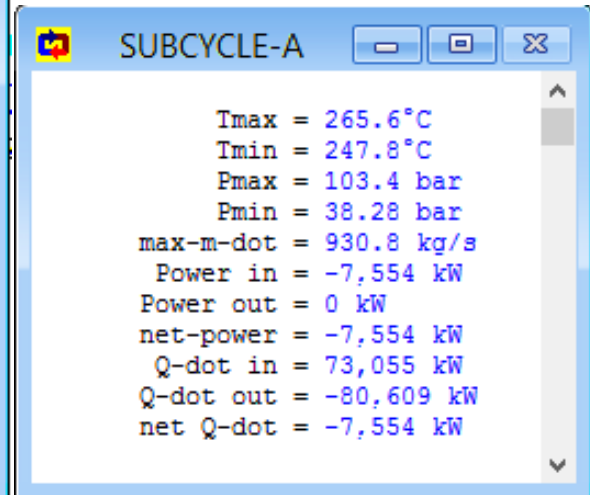


Figure 37. Nuclear side Cycle Result

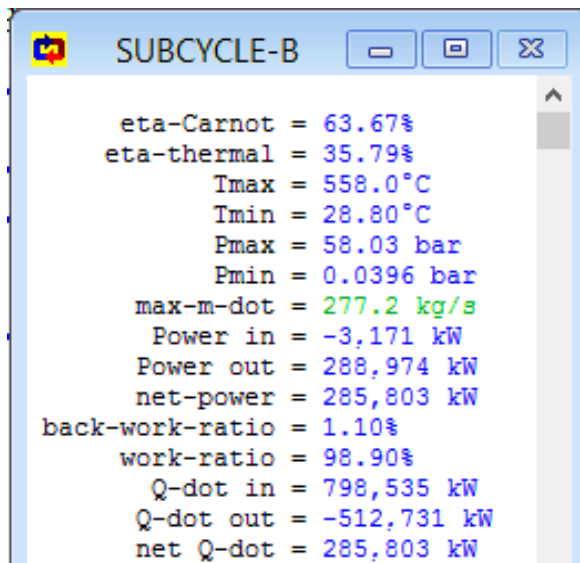


Figure 38. Power side Cycle Result

Discussion

CyclePad is a very important tool in the study of thermodynamic cycles, it will save a lot of time. An analysis that could take a long time can be done in a few minutes.

Based on the results of this study, we draw the following conclusions:

- For the same net shaft power, with the same minimum and maximum conditions, our complex gas turbine has an efficiency of 5.37% higher than the basic gas turbine.
- The basic steam turbine has a lower efficiency of about 1.86% than the complex steam turbine.
- The sensitivity analysis showed that the net power curve as a function of the compressor inlet pressure of the basic gas turbine has a maximum at around 10 bars. The thermal efficiency and the net power of the cycle will be maximum if the pressure at the compressor outlet increases

**3rd International Students Science Congress
3-4 May 2019, İzmir - Turkey**

without exceeding the maximum point of the net power sensitivity curve as a function of this pressure. This pressure is around 88 bar.

- The increase in the maximum temperature improves the net power of the cycle without affecting the efficiency in the case of reversible theoretical transformations, whereas in the case of real transformations, this temperature only influences the increase in efficiency beyond values above 400°C.
- Improvements in the basic gas turbine cycle show that the pressure curve at the inlet of the first compressor as a function of efficiency has a maximum at around 6.1 bar. At this same point, the net power is maximum. The temperature curves at both outputs of the regenerator as a function of efficiency also present a maximum, which would imply that in the construction of these machines, the regenerator must be the subject of a judicious choice.
- For the steam turbine (Rankine) cycle, increasing the pressure at the pump outlet and the quality of the liquid at the turbine outlet has a negative effect on the efficiency and the net power of the cycle, increasing the maximum cycle temperature improves the efficiency and net power of the machine.

Conclusion

This study analyzed some of the elements influencing the performance of thermodynamic cycles of steam and gas turbines using CyclePad, a virtual laboratory for building and analyzing thermodynamic cycles. In addition to the fact that the use of CyclePad saves time, it also increases the analytical capacity of its users by the fact that thanks to sensitivity analysis, we can observe how the machine would behave when certain parameters change according to others. In the case of this study, for example, the results would provide a general idea of the order of magnitude of the machines and their capacity. But it should be noted that theoretical prerequisites and traditional calculation (Manual) of thermodynamic cycles are necessary to become familiar with CyclePad and understand the origin of the errors that the software displays to be able to avoid them later. For the same power at the alternator shaft, this study once showed that the improved cycles perform better than the basic ones. Compression and temperature ratios influence the performance of the machines. The use of two small compressors, for example with a regenerator with intermediate cooling in the improved gas turbine, has improved the efficiency and the net power at a lower air flow rate.

Acknowledgment

We thank Professor Sumuna Temo of the Polytechnic Faculty of the University of Kinshasa, for having supervised this work, without forgetting all those who work day and night to ensure that young researchers evolve and find the opportunity to publish the product of their research. Right due to İzmir International Guest Student Association and the Presidency for Turks Abroad and Related Communities.

References

- [1] Koçak İ, Boran K (2019) Türkiye'deki illerin elektrik tüketim etkinliklerinin veri zarflama analizi ile değerlendirilmesi, *Journal of Polytechnic*, 22(2): 351-365.
- [2] Ministère des Ressources Hydrauliques (2014) Atlas du Ministère des Ressources Hydrauliques, ANAPI, Kinshasa/D.R.Congo.
- [3] Nejat P, Jomehzadeh F, Taheri MM, Gohari M, Majid MZ (2015) A global review of energy consumption, CO₂ emissions and policy in the residential sector (with an overview of the top ten CO₂ emitting countries). *Renewable and Sustainable Energy Reviews* 43:843-862. <https://doi.org/10.1016/j.rser.2014.11.066>
- [4] Wu C (2004) *Thermodynamic Cycles: Computer Aided Design and Optimization*, Marcel Dekker, New York.
- [5] Forbus KD, et al (1999) CyclePad: An articulate virtual laboratory for engineering thermodynamics. *Artificial Intelligence*, 144 (1-2) 297-347.

3rd International Students Science Congress
3-4 May 2019, İzmir - Turkey

- [6] Baher J (1997) Using CyclePad-an “articulate” software laboratory-in thermodynamics education, IEEE Proc. Frontiers in Education 27th Annual Conference. Teaching and Learning in an Era of Change.
- [7] Wu C (1999) Teaching Rankine Cycle by using an intelligent computer-aided instruction software, International Journal of Mechanical Engineering Education 27(4) : 337-346.
- [8] Makhanlall D, Zhang F, Xu R, Jiang P (2015) Exergy-topological analysis and optimization of a binary power plant utilizing medium-grade geothermal energy, Applied Thermal Engineering 88: 459-463, <http://dx.doi.org/10.1016/j.applthermaleng.2014.09.017>.
- [9] Horlock JH (2003) Advanced Gas Turbine Cycles, Elsevier Science.
- [10] William JC (1998) Thermodynamic Cycles, CRC PRESS LLC, Florida, USA.
- [11] Wu C (2007) Thermodynamics and heat powered cycles: A cognitive engineering approach, Nova Science Publishers, USA.
- [12] Nejat P, Jomehzadeh F, Taheri MM, Gohari M, Majid MZ (2015) A global review of energy consumption, CO₂ emissions and policy in the residential sector (with an overview of the top ten CO₂ emitting countries). Renewable and Sustainable Energy Reviews 43:843-862.
- [13] The Shift Project Data Portal (May 15, 2019) Breakdown of Electricity Capacity by Energy Source, Retrieved from: <http://www.tsp-data-portal.org/Breakdown-of-Electricity-Capacity-by-Energy-Source#tspQvChart>
- [14] World Nuclear Association (May 15, 2019) Nuclear Power in the World Today, Retrieved from: <http://www.world-nuclear.org/information-library/current-and-future-generation/nuclear-power-in-the-world-today.aspx>
- [15] Davis W. (May 15, 2019) Nuclear energy news: Atomic Power Review, Retrieved from: <https://atomicpowerreview.blogspot.com/search?q=indian+point>

Free Vibration Analysis of Axially Exponentially Functionally Graded Beams by Differential Quadrature Method

Sümeyye Sınır*, Manisa Celal Bayar Univ., Dept. of Mechanical Engineering, Manisa, Türkiye
Mehmet Çevik, İzmir Kâtip Çelebi Univ., Dept. of Mechanical Engineering, İzmir, Türkiye
B. Gültekin Sınır, Manisa Celal Bayar Univ., Dept. of Civil Engineering, Manisa, Türkiye
*Corresponding author: sumeyyesinir@gmail.com

Keywords: functionally graded material (FGM), differential quadrature method (DQM), free vibration, beam
Discipline: Mechanical Engineering

Abstract

The axially exponentially functionally graded linear Euler-Bernoulli beam model is considered. The dimensionless form of the equation is obtained. Free vibration analysis is carried out by differential quadrature method (DQM), natural frequencies and mod shapes are obtained. The effects of exponential material gradient exponent k are illustrated.

Introduction

Functionally Graded Materials (FGMs) are inhomogeneous composites made up of two different materials, generally a metal and a ceramic, with a smooth and predefined continuous variation of properties in axial (longitudinal) direction, transverse direction or occasionally in both directions. FGMs are attracting growing attention and are getting increasingly widely used every day in many engineering disciplines.

FGM beams which are graded in the thickness (transverse) direction are frequently considered in the literature [1-3], still there are also numerous studies investigating FGM beams with axially varying material properties [4-8]. Free vibration analysis of FGM beams is one of the topics often investigated by researchers [1-9].

Power law is one of the most frequently used material gradients [4], another is exponential material gradient [9] and another one is trigonometric material gradient [3].

In this study, the axially exponentially functionally graded linear Euler-Bernoulli beam model is considered. The equation of motion is given with dimensional variables and parameters for obtaining global solutions. Free vibration analysis is carried out by differential quadrature method (DQM), natural frequencies and mod shapes are obtained.

Equation of Motion

The equation of motion of axially functionally graded Euler-Bernoulli beam is as [1-2, 4-7]

$$E(x)Iw^{iv} + 2E'(x)Iw''' + E''(x)Iw'' + \rho(x)A\ddot{w} = 0 \quad (1)$$

Here $w = w(x, t)$ denotes transverse deflection of a point on the x -axis, x -axis coincides with the centroidal axis of the undeformed beam, t is time, $E(x)$ is the Young's modulus, $\rho(x)$ is the density of the material, I is the area moment of inertia, A is the cross-sectional area.

The material properties vary axially according to exponential material gradient. The elasticity modulus and exponential material gradient is as [9]

$$E(x) = E_0 e^{\frac{kx}{L}} \quad (2)$$

$$\rho(x) = \rho_0 e^{\frac{kx}{L}} \quad (3)$$

where E_0 is the Young's modulus of the beam at the starting configuration of the beam, ρ_0 is the density of the beam at the starting configuration of the beam, and k denotes non-negative exponential material gradient exponent.

Non-dimensionalization

For obtaining global solutions, the non-dimensional form of the governing equation is obtained. The non-dimensional terms used for this purpose are

$$\zeta = \frac{x}{L}, \quad v = \frac{w}{L}, \quad \tau = \frac{t}{L^2} \sqrt{\frac{E_0 I}{\rho_0 A}} \quad (4)$$

The non-dimensional form of the equation of motion is

$$\tilde{E}(\zeta)v^{iv} + 2\tilde{E}'(\zeta)v^{iii} + \tilde{E}''(\zeta)v^{ii} + \tilde{\rho}(\zeta)\dot{v} = F(\zeta, \tau) \quad (5)$$

$$\tilde{E} = \tilde{E}(\zeta) = \frac{E(x)}{E_0} \quad (6)$$

$$\tilde{\rho} = \tilde{\rho}(\zeta) = \frac{\rho(x)}{\rho_0} \quad (7)$$

$$F(\zeta, \tau) = \frac{q(x, t)L^3}{E_0 I} \quad (8)$$

Solution

Free vibration analysis is carried out by differential quadrature method (DQM). For the free vibration analysis, the following equation is considered,

$$\tilde{E}(\zeta)v^{iv} + 2\tilde{E}'(\zeta)v^{iii} + \tilde{E}''(\zeta)v^{ii} + \tilde{\rho}(\zeta)\dot{v} = 0 \quad (9)$$

The boundary conditions are given in Eq. (10) for pinned-pinned supports,

$$v''(1, \tau) = v(0, \tau) = 0 \text{ and } v(1, \tau) = v(0, \tau) = 0 \quad (10)$$

In DQM, the derivative of a function may be represented as the weighted linear sum of the function values at all discrete points

$$\frac{dX_n(\zeta_i)}{d\zeta} = \sum_{j=1}^S c_{ij}^{(1)} X_n(\zeta_j), \quad i = 1, 2, \dots, S \quad (11)$$

The higher order derivative of a function can be given as follows

$$\frac{d^\xi X_n(\zeta_i)}{d\zeta^\xi} = \sum_{j=1}^S c_{ij}^{(\xi)} X_n(\zeta_j), \quad i = 1, 2, \dots, S \quad (12)$$

The grid points are defined as

$$\zeta_i = \frac{i-1}{S-1}, \quad i = 1, 2, \dots, S \quad (13)$$

The following relations for calculating the weighting coefficients are given

$$M(\zeta) = \prod_{i=1}^S (\zeta - \zeta_i) \quad (14)$$

$$M^{(1)}(\zeta_i) = \prod_{j=1, j \neq i}^S (\zeta_i - \zeta_j), \quad i = 1, 2, \dots, S \quad (15)$$

$$c_{ij}^{(1)} = \frac{M^{(1)}(\zeta_i)}{(\zeta_i - \zeta_j)M^{(1)}(\zeta_j)}, \quad i \neq j; i, j = 1, 2, \dots, S \quad (16)$$

$$c_{ii}^{(1)} = - \sum_{j=1, j \neq i}^S \zeta_{ij}^{(1)}, \quad i = 1, 2, \dots, S \quad (17)$$

$$c_{ii}^{(\xi)} = - \sum_{j=1, j \neq i}^S \zeta_{ij}^{(\xi)}, \quad i = 1, 2, \dots, S, \quad (18)$$

The solution of the linear equation is as

$$v = X(\zeta)e^{i\omega\tau} \quad (19)$$

Substituting the solution to the equation of motion (9) and (10), one can obtain

$$\tilde{E}X_n^{iv} + 2\tilde{E}'X_n''' + \tilde{E}''X_n'' - \tilde{\rho}\omega_n^2X_n = 0 \quad (20)$$

$$X_n''(1) = X_n''(0) = 0 \text{ and } X_n(1) = X_n(0) = 0 \quad (21)$$

The discretized equation of motion is as

$$\begin{aligned} & \tilde{E}(\zeta_i) \sum_{j=1}^S c_{ij}^{(4)} X_n(\zeta_j) \\ & + 2\tilde{E}'(\zeta_j) \sum_{j=1}^S c_{ij}^{(3)} X_n(\zeta_j) + \tilde{E}''(\zeta_j) \sum_{j=1}^S c_{ij}^{(2)} X_n(\zeta_j) \\ & - \omega_n^2 \tilde{\rho}(\zeta_j) X_n(\zeta_j) = 0, \quad i = 1, 2, 3, \dots, S \end{aligned} \quad (22)$$

The discretized boundary conditions for pinned-pinned supports

$$\begin{aligned} X_n(\zeta_1) = 0, & \quad \sum_{j=2}^{S-1} c_{1j}^{(2)} X_n(\zeta_j) = 0 \\ X_n(\zeta_S) = 0, & \quad \sum_{j=2}^{S-1} c_{Sj}^{(2)} X_n(\zeta_j) = 0 \end{aligned} \quad (23)$$

From discretized boundary conditions

$$\begin{aligned}
 X_n(\zeta_2) &= -\frac{1}{K} \sum_{j=3}^{S-2} K_1 X_n(\zeta_j) \\
 X_n(\zeta_{S-1}) &= -\frac{1}{K} \sum_{j=3}^{S-2} K_2 X_n(\zeta_j)
 \end{aligned} \tag{24}$$

Here,

$$\begin{aligned}
 K_1 &= c_{Sj}^{(2)} c_{1,S-1}^{(2)} - c_{1j}^{(2)} c_{S,S-1}^{(2)} \\
 K_2 &= c_{S2}^{(2)} c_{1,j}^{(2)} - c_{12}^{(2)} c_{Sj}^{(2)}
 \end{aligned} \tag{25}$$

Substituting the discretized boundary conditions into the discretized equation of motion, we obtain

$$\begin{aligned}
 \tilde{E}(\zeta_i) \sum_{j=3}^{S-2} \left(c_{ij}^{(4)} - \frac{c_{i2}^{(4)} K_1 + c_{iS}^{(4)} K_2}{K} \right) X_n(\zeta_j) \\
 + 2\tilde{E}'(\zeta_i) \sum_{j=3}^{S-2} \left(c_{ij}^{(3)} - \frac{c_{i2}^{(3)} K_1 + c_{iS}^{(3)} K_2}{K} \right) X_n(\zeta_j) \\
 + \tilde{E}''(\zeta_i) \sum_{j=3}^{S-2} \left(c_{ij}^{(2)} - \frac{c_{i2}^{(2)} K_1 + c_{iS}^{(2)} K_2}{K} \right) X_n(\zeta_j) \\
 - \omega_n^2 \tilde{\rho}(\zeta_i) X_n(\zeta_i) = 0, \quad i = 3, \dots, S-2
 \end{aligned} \tag{26}$$

The natural frequencies and the mode shapes are obtained from this algebraic equations system.

Numerical Results

The first three modes natural frequencies for different k values are obtained and given Table 1. The natural frequencies are lower when the value of exponent k increases.

Table 1. The natural frequencies of the beam

n	Pinned-Pinned						
	$k = 0$	$k = 0.1$	$k = 0.3$	$k = 0.5$	$k = 1$	$k = 1.5$	$k = 2$
1	9.8696	9.8656	9.8336	9.7694	9.4636	8.9365	8.1574
2	39.4784	39.4749	39.4467	39.3903	39.1255	38.6834	38.0664
3	88.8264	88.8231	88.7959	88.7417	88.4872	88.0640	87.4766

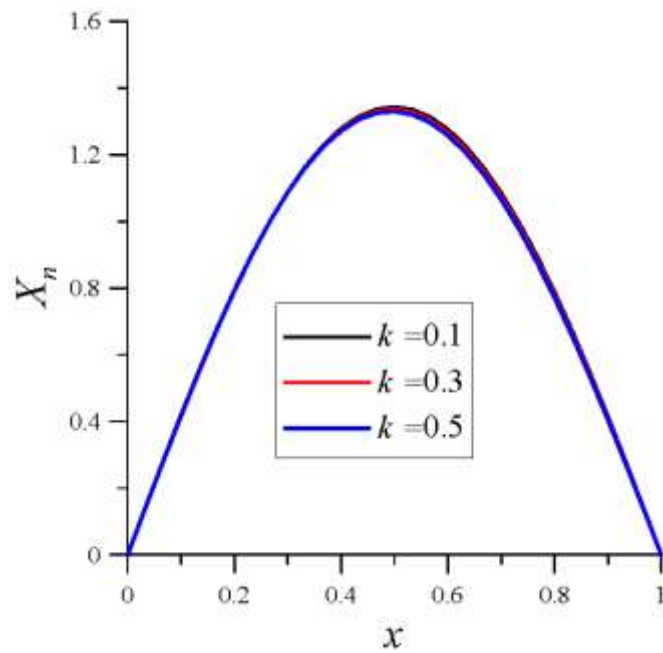


Figure 1. The first mode graphics of the beam for different k values

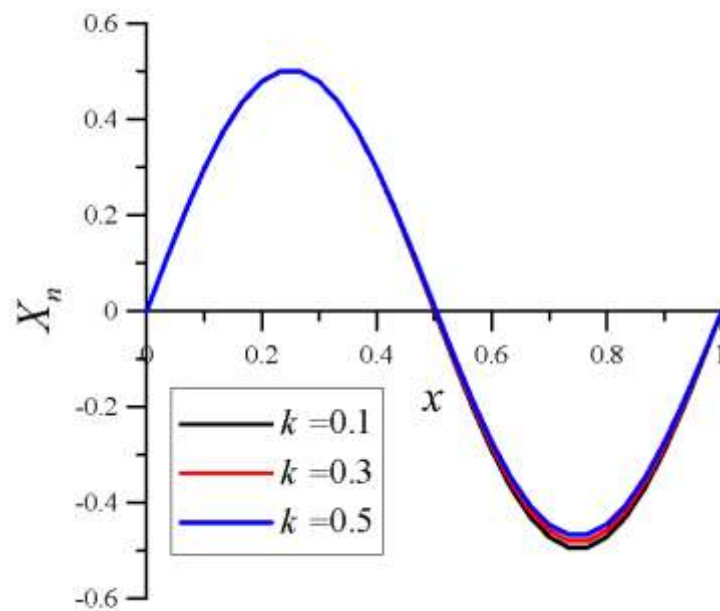


Figure 2. The second mode graphics of the beam for different k values

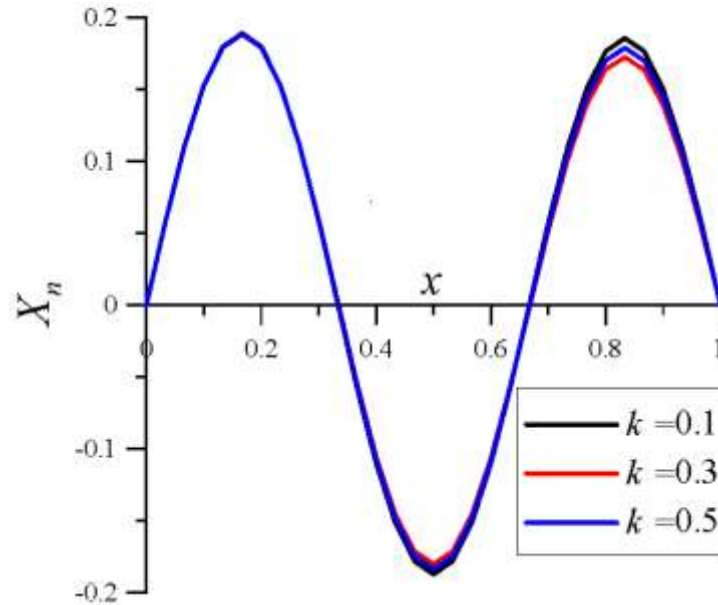


Figure 3. The third mode graphics of the beam for different k values

Conclusion

The mode shapes of the first three modes for different k values are obtained. The first, second and third mode shapes are given with Figures 1, 2 and 3, respectively. The vibration amplitudes decrease as k increases.

References

- [1] Jin C, Wang X. (2015) Accurate free vibration analysis of Euler functionally graded beams by the weak form quadrature element method. *Composite Structures* 125: 41-50.
- [2] Pradhan KK, Chakraverty S (2013) Free vibration of Euler and Timoshenko functionally graded beams by Rayleigh-Ritz method. *Composites: Part B* 51: 175–184
- [3] Şimşek M (2010) Non-linear vibration analysis of a functionally graded Timoshenko beam under action of a moving harmonic load. *Composite Structures* 92: 2532–2546.
- [4] Sınır S, Çevik M, Sınır BG (2018) Nonlinear free and forced vibration analyses of axially functionally graded Euler-Bernoulli beams with non-uniform cross-section. *Composites Part B* 148: 123-131.
- [5] Huang Y, Li XF (2010) A new approach for free vibration of axially functionally graded beams with non-uniform cross-section. *Journal of Sound and Vibration* 329: 2291–303.
- [6] Lee JW, Lee JY (2017) Free vibration analysis of functionally graded Bernoulli-Euler beams using an exact transfer matrix expression. *International Journal of Mechanical Sciences* 122: 1–17.
- [7] Kumar S, Mitra A, Roy H (2015) Geometrically nonlinear free vibration analysis of axially functionally graded taper beams. *Engineering Science and Technology, An International Journal* 18:579-593
- [8] Huang Y, Yang LE, Luo QZ (2013) Free vibration of axially functionally graded Timoshenko beams with non-uniform cross-section. *Composites: Part B* 45: 1493-1498.
- [9] Li XF, Kang YA, Wu JX (2013) Exact frequency equations of free vibration of exponentially functionally graded beams. *Applied Acoustics* 74(3): 413-420.

Deniz Suyu Desalinasyon Teknikleri Konusundaki Son Gelişmeler

Harris J. N. Welepe, Hüseyin Günerhan*

Ege Üniversitesi, Makine Mühendisliği Bölümü, Bornova Ana Kampüsü, İzmir, Türkiye

**İletişimden sorumlu yazar: harrisharrismail@gmail.com*

Anahtar Kelimeler: deniz suyu desalinasyonu, distilasyon teknolojileri, membran teknolojileri, enerjetik ve ekserjetik verimler, verimlilik

Disiplin: Makine Mühendisliği

Özet

Deniz suyu desalinasyon teknolojileri dalındaki güncel araştırmalar, desalinasyon sistemlerinin enerjetik ve ekserjetik verimlerini ve verimliliğini arttırmayı ve tatlı suyun maliyetini düşürmeyi amaçlamaktadır. Bu bağlamda bu çalışma kaydedilmekte ve önemini bulmaktadır. Distilasyon teknolojileri ve membran teknolojileri olmak üzere mevcut deniz suyu desalinasyon teknolojilerini gözden geçirmekte ve bu teknolojilere dair sistemlerin performanslarını iyileştirmedeki en son gelişmeleri, bu iyileştirme çalışmalarında karşılaşılan problemleri ve bu teknolojilerin ürettiği problemleri sunmaktadır. Distilasyon teknolojilerinde, havza bazlı güneş damıtıcı ve nemlendirme-nem alma güneş damıtıcı ile daha fazla ilgilenmekte. Membran teknolojilerinde ters osmoz ve membran distilasyonu ile ilgilenmektedir. Çünkü o teknolojiler güncel konulardır. Bu çalışmadan, havza bazlı güneş damıtıcının performansını iyileştirme çalışmalarının yutucu yüzeyden havzada bulunan suya ısı transferini arttırmaya odaklandığı görülmektedir. Nanopartiküllü deniz suyu kullanımı, oluklu yutucu yüzeyler kullanımı, kanatlı yutucu yüzeyler kullanımı, vb., olmak üzere bu ısı transferini artırma tekniklerindedir. Nemlendirme - nem alma güneş damıtıcı için bu çalışmalar, su buharı yoğunlaşma gizli ısısının ve reddedilen salamuranın (çok tuzlu suyun) ısısının geri kazanımından oluşmaktadır. Ve desalinasyon teknolojilerinden önemli ölçüde daha yüksek verimliliği ve verimi, ve ondan elde edilen tatlı suyun bir metre küp başına düşük maliyeti nedeniyle dünyada çok yaygın ve çok kullanılan bir desalinasyon tekniği olan ters osmoz ile ilgili olarak, endüstriyel tesisler düzeyinde, salamuranın denize deşarjı problemleri kaydedilmekte. O problemler denizdeki susal yaşam için ciddi bir tehdit oluşturmaktadır. Membran distilasyonu ise, derinlemesine henüz incelenmemiş, ancak umut verici olmaya devam eden yeni bir tekniktir. Sonunda, çevre dostu ve ucuz desalinasyon teknikleri elde etmek amacıyla ve böylece dünya nüfusu artmasının neden olduğu öngörülen tatlı su kıtlığı sorununu çözmek için araştırmalar sürekli yapılmaktadır.

1. Giriş

Gezeganimizde mevcut olan su miktarının 1380 milyon Km³ olduğu tahmin edilmektedir [1]. Bu miktarın yaklaşık % 97'si, insan, hayvan, bitki ve endüstriyel tüketimine uygun olmayan tuzlu su olan deniz ve okyanus sularını temsil etmektedir. Kalan yüzde, gezegende mevcut olan ve tüketime uygun olan tatlı su miktarıdır ve bunun % 75'i, sömürülmesine izin vermeyen kutup buzulları seviyesindedir. Geri kalanı, akarsular, göllerin ve yeraltı sularını oluşturmaktadır [2].

Tatlı su talebi büyüyüp sürekli büyüyen dünya nüfusunu izlemektedir. Bu nedenle önümüzdeki yıllarda tatlı su kıtlığı riskinin dışlanmadığı açıktır. Bu gerçek, insanlara yeni tatlı su kaynaklarını düşündürmüştür. Deniz ve okyanus sularının büyük miktarda mevcut olduğundan tatlı suyu elde etmek için onları tuzdan arındırılması gündeme gelmiştir. Suları tuzdan arındıran proseslere desalinasyon prosesleri denir.

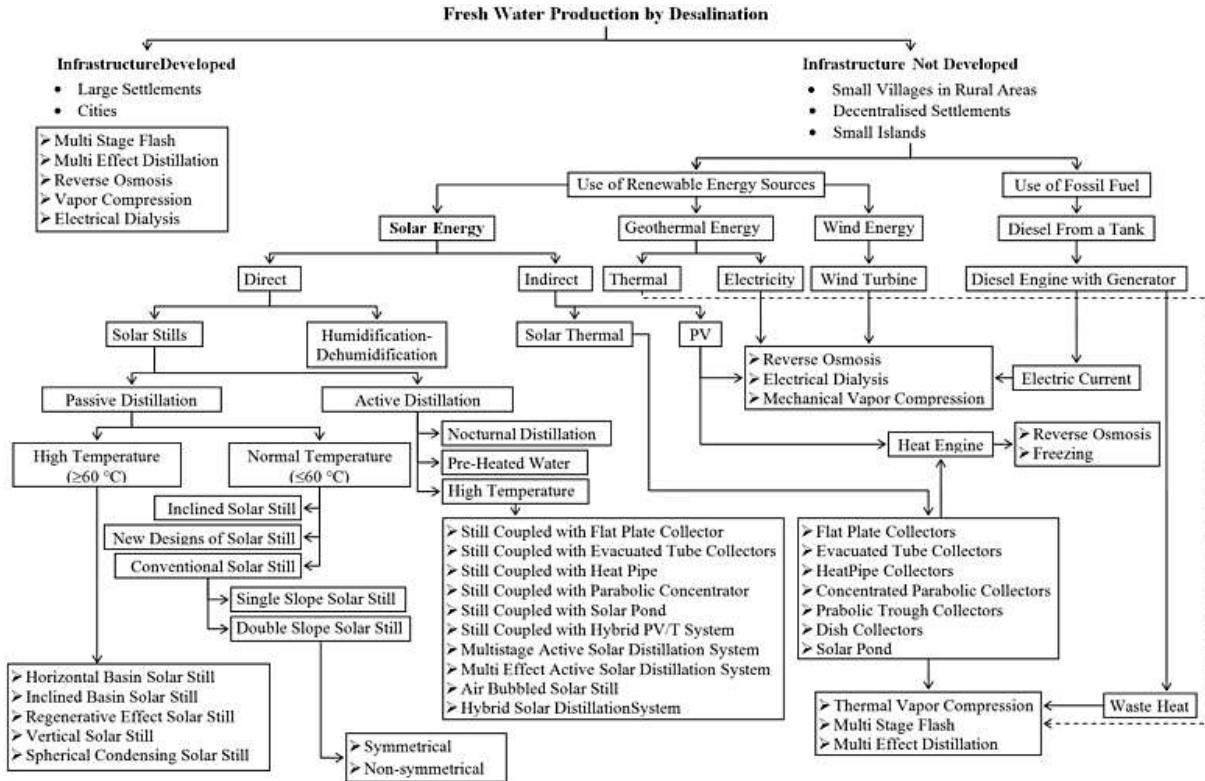
Deniz suyu desalinasyon teknolojileri dört gruba ayrılır: membran teknolojileri, distilasyon teknolojileri, iyon değişimi teknolojileri ve donma teknolojileri [2].

Bu çalışma distilasyon teknolojileri ve membran teknolojileri ile ilgilenmekte, özellikle distilasyon teknolojileri konusunda havza bazlı güneş damıtıcı ve nemlendirme-nem alma güneş damıtıcı ile daha fazla ilgilenip membran teknolojileri konusunda ters osmoz ve membran distilasyonu ile ilgilenmektedir. Çünkü o teknolojiler daha güncel ve çekici konulardır.

2. Metodoloji

Şekil 1 tatlı su üretimi için kullanılan desalinasyon teknolojilerini ayrıntılarıyla sunmaktadır.

Tablo 1 endüstriyel desalinasyon teknolojilerini, distilasyon teknolojileri ve membran teknolojileri olarak sınıflandırıp karşılaştırma analizi yapmaktadır.



Şekil 1. Tatlı su üretimi için kullanılan desalinasyon teknolojileri [3]

Tablo 1. Desalinasyon teknolojilerini karşılaştırma analizi (2013 yılının verileri) [4]

Desalinasyon Grubu	Teknoloji	Kurulmuş fabrika yüzdesi	Ortalama tatlı su üretimi (m ³ /gün)	Üretilen tatlı suyun maliyeti (\$US/m ³)
Distilasyon teknolojileri	MSF		50 000 - 70 000	23 000 - 528 000 m ³ /gün : 0,56 - 1,75 91 000 - 320 000 m ³ /gün : 0,52 - 1,01
	MED	~25%	5 000 - 15 000	12 000 - 55 000 m ³ /gün : 0,95 - 1,5 < 100 m ³ /gün : 2,0 - 8,0
	MVC		100 - 3 000	30 000 m ³ /gün : 0,87 - 0,95
	TVC		10 000 - 30 000	1 000 m ³ /gün : 2,0 - 2,6
Membran teknolojileri	RO	~75%	~ 130 000	100 000 - 320 000 m ³ /gün : 0,45 - 0,66 15 000 - 60 000 m ³ /gün : 0,48 - 1,62 1 000 - 4 800 m ³ /gün : 0,7 - 1,72
	ED	Deniz suyu için deneysel aşamada	2 - 145 000	Büyük kapasite : 0,6 Küçük kapasite : 1,05

Tablo 1'de görüldüğü gibi endüstriyel distilasyon teknolojileri konusunda çok etkili distilasyon (MED: Multi-Effects Distillation), çok kademeli ani distilasyon (MSF: Multi-Stages Flash), buhar mekanik sıkıştırma (MVC: Mechanical Vapor Compression), buhar termal sıkıştırma (TVC: Thermo Vapor Compression) teknolojileri bahsedilmektedir. Havza bazlı güneş damıtıcı (Solar Still) ve nemlendirme - nem alma (humidification - dehumidification) güneş damıtıcı teknolojileri ise güneş enerjisini çok yönlü kullanma arzusunun çekici ve güncel teknolojilerdir. Ama buna rağmen çok düşük verimlilik/maliyet oranına sahip olduklarından dolayı endüstriyel desalinasyon teknolojileri konusunda yer almamaktadır. Bu yüzden bu çalışma, performanslarını iyileştirme çalışmalarını sunmaktadır.

Endüstriyel membran teknolojileri konusu ise ters osmoz (RO: Reverse Osmosis) tarafından hâkim olunmaktadır. Bir de ters osmoz bütün endüstriyel desalinasyon teknolojilerine hâkim olmaktadır. Bandelier [5], ters osmoz, elektrodializ (ED) ve nanofiltrasyon (NF) teknolojilerini endüstriyel membran teknolojileri olarak ve membran distilasyonunu çekici ve derinlemesine henüz incelenmemiş bir teknoloji olarak bahsetmekte. Bu yüzden sonraki bölümde ters osmozun çalışma prensibi, çevrede ürettiği problemler ve membran distilasyon teknikleri ve çalışma prensipleri sunulmaktadır.

3. Bulgular

3.1 Distilasyon teknolojileri

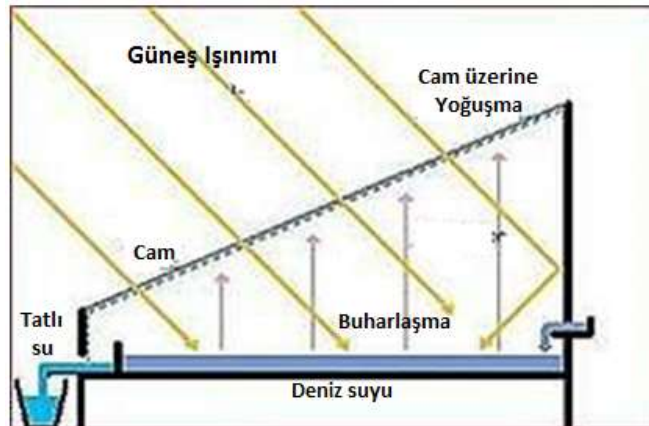
Metodoloji bölümünde anlatıldığı gibi bu kısımda Havza bazlı güneş damıtıcı ve nemlendirme – nem alma güneş damıtıcı teknolojileri ele alınmaktadır.

3.1.1. Havza bazlı güneş damıtıcı

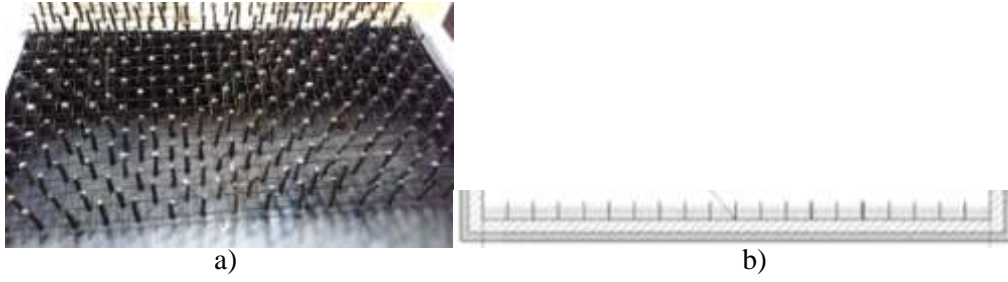
Deniz suyu desalinasyon temel sistemidir. Sera etkisiyle çalışmaktadır. Şekil 2’de bu sistemin şematik diyagramı sunulmuştur. Güneş ışınımı camı geçip havzadaki yutucu yüzey tarafından soğurulur. Yutucu yüzey güneş ışınımını soğurunca ısınır taşınım ısı transferiyle deniz suyuna ısı enerjisi transfer eder. Deniz suyu ısınır buharlaşır camın üzerine yoğunlaşır ve tatlı su elde edilir.

Bu temel sistemin enerjetik ve ekserjetik verimleri ve verimliliği çok düşük olduğundan onları iyileştirmek amacıyla araştırmacılar başarılı teknikler tasarlayıp denemiştir. Bu tekniklerden üç tanesi aşağıda gösterilmektedir. Amacı, yutucu yüzeyden deniz suyuna ısı transferinin artmasıdır.

- Kanatlı yutucu yüzey kullanımı: Şekil 3’te görüldüğü gibi kanatlar yutucu yüzeyin üzerine yerleştirildiği için yutucu yüzey ve deniz suyu arasında temas alanının çoğalmasını sağlayıp ısı transferi artırır. Kanatlar, demir, bakır, alüminyum, paslanmaz çelik, cam gibi iyi ısı iletkenliği olan farklı malzemelerden yapılabilir. Bu kanatların optimal boyutlar, konfigürasyon ve sayısı deneysel olarak tespit edilir. Bir de şu var ki, mikro-kanatlar kullanımı kanatların yutucu yüzeyin üzerindeki gölgesinin boyutlarını azaltacaktır ve böylece yutucu yüzeye gelen güneş ışınımı önlemeyecektir. Bu, yeni bir kavramdır ve havza bazlı güneş damıtıcı uygulamalarında henüz kullanmamıştır. Mikro-kanatlar ve pürüzlü yutucu yüzey kullanımı daha iyi sonuçlar verebilir [6].
- Oluklu yutucu yüzey kullanımı: Şekil 4’te gösterilmektedir. Oluklu yutucu yüzey de yutucu yüzey ve deniz suyu arasında temas alanının çoğalmasını sağlayarak ısı transferi artırır.
- Nanopartiküllü deniz suyu kullanımı: Şekil 5’te gösterilmektedir. Nanopartiküller deniz suyunun içine konmaktadır. Konsantrasyonları 0,04 ila 0,2% değişebilir ve optimal değerleri deneysel olarak tespit edilir. Nanopartiküller, genellikle Al_2O_3 , CuO , Cu_2O gibi metaloksitlerdir. Ancak yeni umut verici ve henüz incelenmemiş malzemeler de var. Onlardan grafen, karbon nanotüpleri, organik, inorganik ve hibrit nanomalzemeler vardır [6].



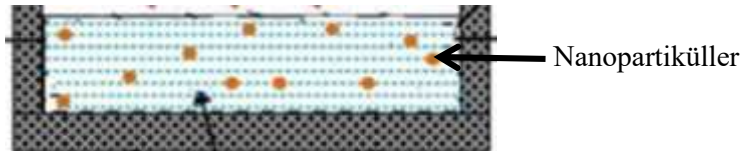
Şekil 2. Havza bazlı güneş damıtıcı. [7]



Şekil 3. Kanatlı yutucu yüzey. a) fotoğraf b) şema. [6]



Şekil 4. Oluklu yutucu yüzey. a) fotoğraf b) şema. [6]

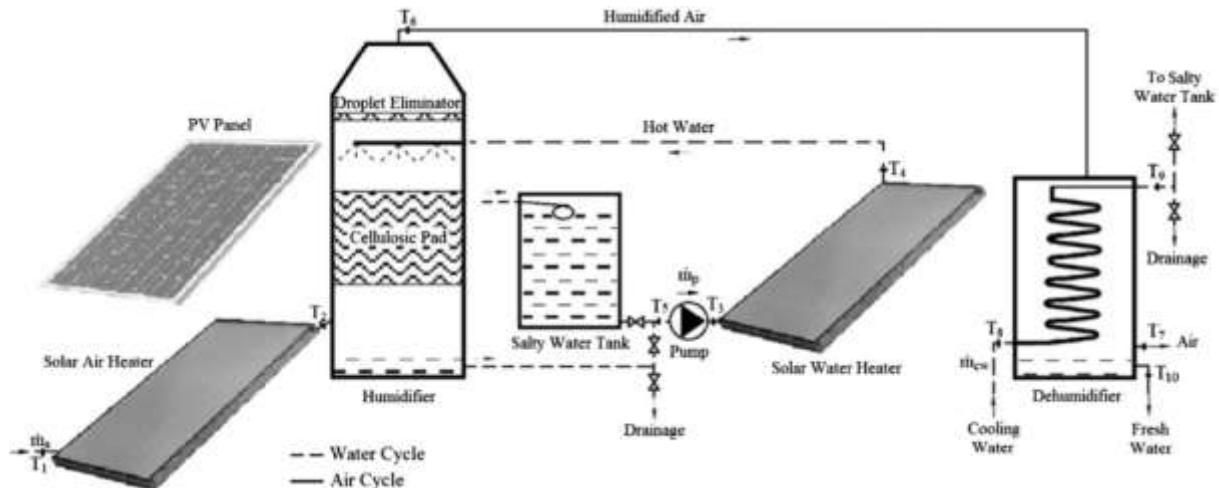


Şekil 5. Nanopartiküllü deniz suyu. [6]

3.1.2. Nemlendirme – nem alma güneş damıtıcı

Bu teknolojinin çok sistemleri vardır. Ama temel çalışma prensibi aynıdır. Şekil 6 bir sistem örneği sunmakta. Bu sistemde hava güneş hava ısıtıcısı (güneş enerjisi kolektörü) ve su güneş su ısıtıcısı (güneş enerjisi kolektörü) tarafından ısıtılır. PV paneliyle çalışan bir sirkülasyon pompası ile her ikisi de nemlendiriciye gönderilip selülozik pedde birbirine temas eder. Bu temas sırasında, hava su buharı ile yüklenip nem alma bölümüne gönderilir. Oradayken su buharı yoğunlaşarak tatlı su oluşturur ve kuru hava nem alma bölümünden çıkar.

Bu sistemin enerjetik ve ekserjetik verimlerinin artması için nemlendiriciden çıkan tuzlu suyun bir miktarı güneş su ısıtıcısına tekrar gönderilip kullanılır. Isıl veriminin artırılması tatlı su üretimini artırır. Şimdilik bu teknik, böyle bir sistemin verimliliğinin artması için araştırmacılar tarafından kullanılıp genel bir teknik olmuştur.



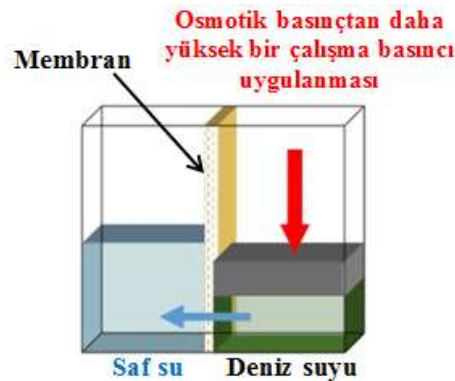
Şekil 6. Nemlendirme – nem alma güneş damıtıcı. [8]

3.2 Membran teknolojileri

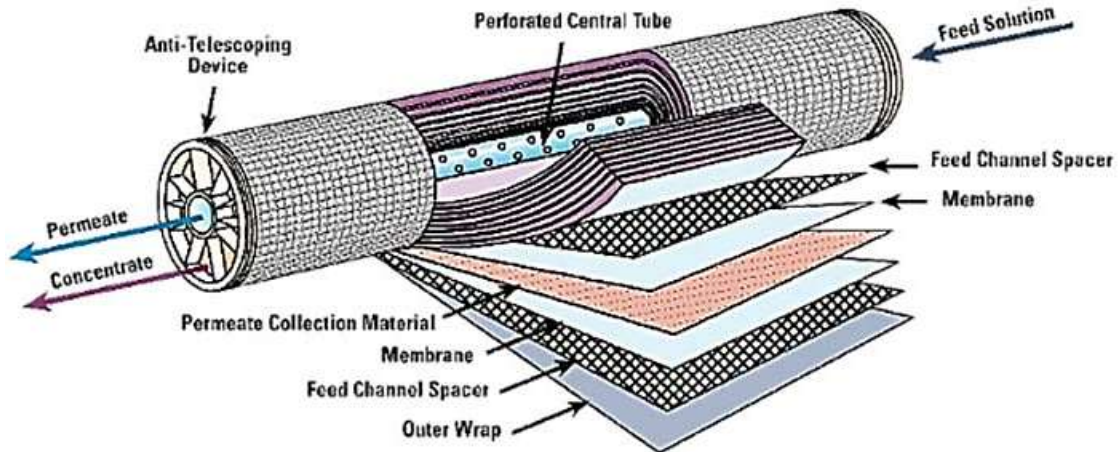
3.2.1. Ters osmoz

Şekil 7’de açıklandığı gibi deniz suyu desalinasyonu konusunda ters osmozun çalışma prensibi, osmotik basınçtan daha yüksek bir çalışma basıncı uygulayarak saf suyun deniz suyundan ayrılıp bir membrandan geçmesidir. Ters osmoz teknolojinde kullanılan membranlar genellikle selüloz asetat, selüloz triasetat, akrilik poliamidepoliasit + zirkonyum oksit, poliamid malzemelerindedir. Gözeneklerinin çapı $0,0005 \mu\text{m}$ ’den küçüktür [9]. Bir membran, $50 \mu\text{m}$ kalınlığında bir destek katmanından ve yaklaşık $0.2 \mu\text{m}$ kalınlığında bir bariyer katmanından oluşur [10]. Şekil 8 ters osmozun bir elemanının bileşenlerini göstermekte.

Ters osmoz deniz suyundan tatlı su elde etmek için en yaygın, en çok kullanılan ve verimli bir teknolojidir. Ancak çalışması sırasında endüstriyel distilasyon teknolojileri gibi çevrede önemli bir probleme neden olmaktadır. Bu problem denize büyük miktarda salamuranın (çok tuzlu su) atılmasıdır. Örneğin, Örneğin, Akdeniz’de suyun doğal tuzluluğu 37 ila 38 g/L arasındadır ve salamuranın tuzluluğu 70 g/L’ye ulaşabilir [11]. Gerçekten desalinasyon prosesinin sonunda atık olarak salamura kalmaktadır. [12]’ye göre dünyada endüstriyel desalinasyon tesislerinden her gün toplam 95 milyon m³ tatlı su üretilmiş ve 141,5 milyon m³ salamura atık olarak çıkarmış. Birleşik Milletler bu duruma karşı alarm vermiştir. Gerçekte endüstriyel desalinasyon proseslerinde bazı kimyasal malzemeler kullanılmakta ve salamurada bulunmaktadır. Salamura denize atılınca desalinasyon tesislerine yakın susal yaşamı rahatsız edip ona ciddi bir tehdit temsil eder [4].



Şekil 7. Deniz suyu desalinasyonu konusunda ters osmozun çalışma prensibi [5]



Şekil 8. Ters osmozun bir elemanının bileşenleri [5]

3.2.2. Membran distilasyonu

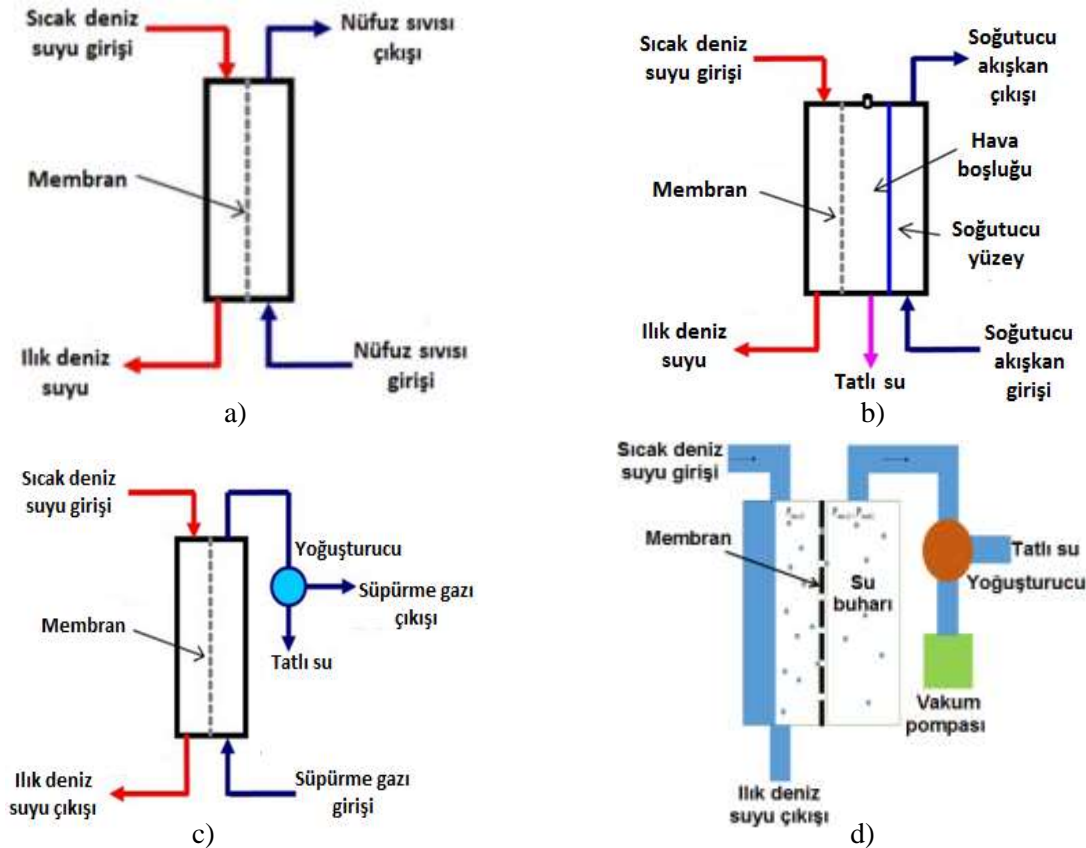
Membran distilasyonunu çekici kılan özelliği endüstriyel distilasyon teknolojilerinin tersine daha düşük sıcaklıkta ve ters osmozun tersine yüksek basınçlar gerekmeden çalışabilmedir.

Membran distilasyonu bir sistemi iki ana bölümden oluşmaktadır: sıcak bölüm ve soğuk bölüm. Sıcak deniz suyu 70 °C civarında olan bir sıcaklıkla sıcak bölüme girip geçmektedir. Bu iki bölüm hidrofobik bir membran tarafından ayrıldığı için sıvı su değil sadece su buharı membrandan geçebilir. Bu bölümlerin arasında sıcaklık farkı 10 ila 20 °C değişir. Bu sıcaklık farkı membranın iki tarafında buhar bağıl basınç farkına neden olmakta ve sıcak bölümdeki buhar bağıl basıncı daha yüksek olduğundan su buharı sıcak bölümden soğuk bölüme geçmektedir [5]. Su buharı soğuk bölüme varınca yoğunlaştırulup tatlı suyu oluşturmaktadır.

Dört tane yoğunlaşma tekniği mevcut olup membran distilasyon tekniklerini belirtmektedir [13, 14] :

- Direkt Temaslı Membran Distilasyonu (DCMD: Direct Contact Membrane Distillation): Soğuk nüfuz sıvısı membrana temas edip membrandan geçen su buharını çekip yoğunlaştırır. Nüfuz sıvısı saf sudur [15].
- Hava Boşluğu Membran Distilasyonu (AGMD: Air Gap Membrane Distillation): Hava boşluğu buhar bağıl basınç farkını yüksek ve neredeyse sabit değerde tutar. Soğutucu bir akışkan soğuk bölümden geçip soğutucu yüzeyi soğütür. Su buharı soğutucu yüzeye temas ederken yoğunlaşır ve tatlı suyu elde edilir.
- Süpürme Gazlı Membran Distilasyonu (SGMD: Sweeping Gas Membrane Distillation): Süpürme gazı azot, argon gibi soygazdır [16]. O gaz membran geçen su buharını süpürüp dış yoğunlaştırucuya gönderir. Yoğuşarak tatlı su elde edilir, süpürme gazı yenilenip tekrar sirküle eder.
- Vakumlu Membran Distilasyonu (VMD: Vacuum Membrane Distillation): Bir vakum pompası membrandan geçen su buharını pompalayarak buhar bağıl basınç farkını yüksek ve neredeyse sabit değerde tutar. Pompalanmış su buharı vakum pompasına varmadan yoğunlaştırucu tarafından yoğunlaştırulur ve tatlı su elde edilir.

Şekil 9’da bu dört membran distilasyon tekniği sunulmuştur.



Şekil 9. Membran distilasyon teknikleri. a) DCMD b) AGMD c) SGMD d) VMD [13]

Kullanılan membranların kalınlığı 40 ila 250 μm değişir ve gözenekleri 0,2 μm 'den büyük değildir. Poliviniliden florür (PVDF: polyvinylidene fluoride), polipropilen (PP: polypropylene) veya politetrafloroetilen (PTFE: polytetrafluoroethylene, Teflon olarak iyi bilinir) maddelerinden yapırlar [5, 14].

4. Sonuç

Bu çalışmada deniz suyu endüstriyel desalinasyon teknolojilerinin iki gruba ayrıldığı görülmüştür: distilasyon teknolojileri ve membran teknolojileri. Isıl enerji kaynağının maliyeti uygun olduğunda, MED (çok etkili distilasyon) ve MSF (çok kademeli ani distilasyon) teknolojileri endüstriyel ölçekte kullanılmaktadır. Sera etkisi ve nemlendirme-nem alma esaslı distilasyon teknolojileri, en az verimli teknolojiler ve sistemin ömrü boyunca çok düşük verimlilik/maliyet oranına sahipler. Bundan dolayı onlar sadece çok küçük birimler için kullanılır ve iyileştirme araştırmaları devam etmektedir. Membran teknolojileri, özellikle ters ozmoz, dünyada en yaygındır ve daha çok kullanılır, çünkü desalinasyon tesisinin ömrü boyunca daha iyi bir verimlilik/maliyet oranına sahipler. Ancak çalışması sırasında atık olarak ortaya çıkan salamuranın denize atıldığı için desalinasyon tesislerine yakın susal yaşama ciddi bir tehdit temsil etmektedir. Membran distilasyonu ise distilasyon teknolojilerinin tersine daha düşük sıcaklıkta ve ters osmozun tersine yüksek basınçlar gerekmeden çalıştığı için çekici ve çok umut verici, ancak henüz derinlemesine incelenmemiş bir teknolojidir.

Teşekkür

Bu çalışma Yurtdışı Türkler ve Akraba Topluluklar Başkanlığı'nın (YTB) "Uluslararası Öğrenci Akademisi" Projesi kapsamında desteklenmiştir.

Referanslar

- [1] Retiel N, Abdessemed F, Bettahar M (2007) Etude expérimentale d'un distillateur solaire plan amélioré. *Revue des Energies Renouvelables*. 11(4): 635–642.
- [2] Sellami MH (2014) Etude et amélioration des techniques de distillation solaire dans la région Sud-Est Algérien (Ouargla). Thèse de Doctorat: Sciences Physiques, Physiques Energétique. Université Kasdi Merbah Ouargla: Algérie.
- [3] Emrah D (2015). Solar-Powered Desalination. Chapter 5, Department of Mechanical Engineering, Karabuk University, Karabuk, Turkey.
- [4] SIA Partners (2017) Dessalement de l'eau de mer : des évolutions nécessaires pour accompagner l'essor du secteur. <http://www.energie.sia-partners.com/20170112/dessalement-de-leau-de-mer-des-evolutions-necessaires-pour-accompagner-lessor-du-secteur>
- [5] Bandelier P (2016) Le dessalement d'eau de mer et des eaux saumâtres. *Encyclopédie de l'énergie*. <https://www.encyclopedie-energie.org/le-dessalement-deau-de-mer-et-des-eaux-saumatres/>
- [6] Hardik KJ, Kalpesh VM (2018) A review on numerous means of enhancing heat transfer rate in solar thermal based desalination devices. *Renewable & Sustainable Energy Reviews* 93:302-317.
- [7] Outils Solaires (2012) Distillation solaire. <http://www.outilssolaires.com/developpement-durable/energie-solaire>
- [8] Emrah D, Serkan Ç (2016) Energy, exergy, economic and environmental (4E) analysis of a solar desalination system with humidification-dehumidification. *Energy Conversion and Management* 126: 12–19.
- [9] Chay L. (2005) Etude comparative des membranes utilisées en production d'eau potable : microfiltration, ultrafiltration, nanofiltration et osmose inverse. ENGREF Centre de Montpellier, Office International de l'Eau – SNIDE, Limoges.
- [10] Toray Advanced Materials Korea (2009) Introduction to Reverse Osmosis Membrane. <http://www.csmfilter.com/csm/upload/TechManual/Types.pdf>
- [11] Magnan P (2013) Le boom de la désalinisation. https://www.francetvinfo.fr/monde/le-boom-de-la-desalinisation_3072023.html
- [12] Valo M. (2019) Dessalement de l'eau: l'ONU alerte sur les quantités de saumure déversées. https://www.lemonde.fr/planete/article/2019/01/14/dessalement-de-l-eau-l-onu-alerte-sur-les-quantites-de-saumure-deversees_5409002_3244.html

3rd International Students Science Congress
3-4 May 2019, İzmir - Turkey

- [13] Energies Renouvelables et Environnement - Bureau d'Etudes Industrielles (2013) Distillation Membranaire. <http://hmf.enseeiht.fr/travaux/bei/beiere/content/distillation-membranaire>
- [14] Jantaporn W. (2016) Technologies membranaires innovantes pour la réutilisation des eaux. Thèse de Doctorat: Génie des procédés et de l'Environnement. Université de Toulouse, France.
- [15] Tomaszewska M (2012) Direct Contact Membrane Distillation (DCMD) Applications. Springer, Berlin.
- [16] Kaushik N (2017) Membrane Separation Processes. Vallabh Vidyanagar.

Tavuk Tüyü Fiber/PLA Biyokompozitin Mekanik Özelliklerine Uzun Süreli Yaşlandırmanın Etkisinin İncelenmesi

Tarkan Akderya*, Uğur Özmen

Manisa Celal Bayar Üniversitesi, Makine Mühendisliği Bölümü, Muradiye, Manisa, Türkiye
Buket Okutan Baba, İzmir Kâtip Çelebi Üniversitesi, Makine Mühendisliği Bölümü, Çiğli, İzmir, Türkiye

*İletişimden sorumlu yazar: takderya@gmail.com

Anahtar kelimeler: Tavuk tüyü fiber/PLA, biyokompozit, mekanik özellikler, uzun süreli yaşlandırma
Disiplin: Makine Mühendisliği

Giriş

Dünya çapında araştırmacılar, endüstrinin üretim süreçlerini hızlandırabilecek ve sürdürülebilirliğe yönelik ihtiyaçlara da hizmet edebilecek niş ürünler bulma yarışına girmişlerdir. Küresel ısınmanın etkilerini hafifletmek için çevre dostu malzemeler arayışı, çoğu sanayileşmiş ülkenin gündeminde olup geri dönüştürülebilir, biyolojik olarak parçalanabilen ürünlerin veya sıfır emisyonlu malzemelerin üretimi için önerilerde bulunulmuştur [1]. Bugün kullanılan en umut verici biyopolimerlerden biri olan polilaktasit (PLA), biyoyumumluluk ile biyobozunurluk dahil elverişli özelliklere sahip olmasından ve yenilenebilir kaynaklardan üretilmesinden ötürü tercih edilmektedir [2]. PLA, çoğu ekipmanda nispeten yüksek mukavemet ve işleme kabiliyeti avantajları sunar, ancak kırılabilirliği nedeniyle pratik uygulamalar için genellikle takviye gerekir [3,4]. Uzun Tavuk Tüyü Fiberi / PLA (TTF / PLA) kompozit malzemesi, takviye fiber olarak tavuk tüyü fiberlerinin kullanıldığı bir biyokompozittir. Tavuk tüyleri kümes hayvanı endüstrisindeki atık ürünlerdir; geleneksel takviye malzemelerine kıyasla düşük yoğunluklu, düşük maliyetli, biyolojik bozunabilirlik, yenilenebilirlik ve geri dönüştürülebilirlik özellikleri gibi benzersiz avantajlara sahiptirler [5]. Bu çalışma kapsamında; uzun süreli (43800 saat) atmosferik yaşlandırma prosesinin, uzun TTF / PLA biyokompozit malzemelerin mekanik özelliklerine olan etkileri gözlemlenmiştir.

Materyal Üretimi ve Yaşlandırma Prosesi

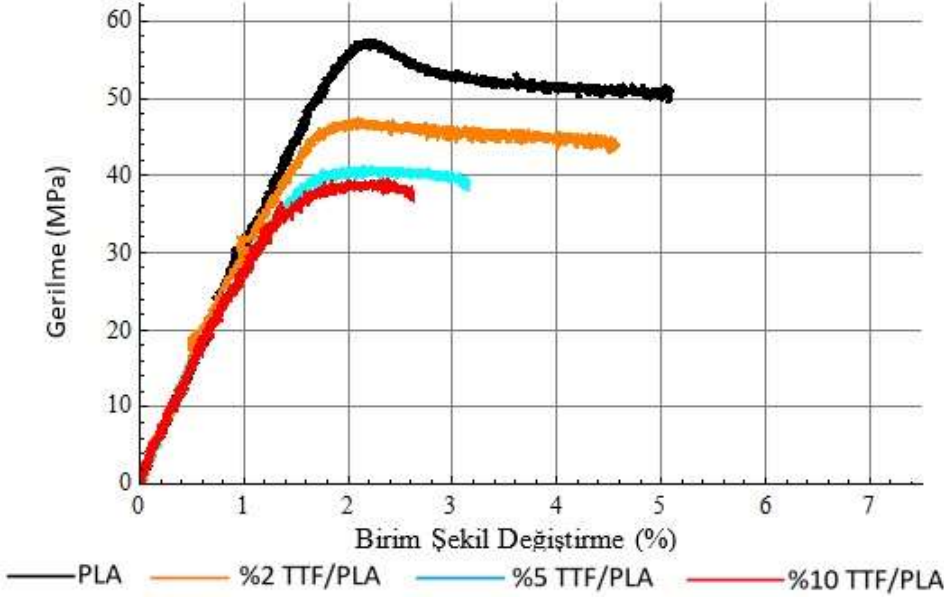
Kompozit üretiminin ilk aşamasını tavuk tüylerinin üretime hazırlanması oluşturmaktadır. Ana tüy omurgasından ayrılan 20-40 µm çapa ve yaklaşık 20 mm uzunluğa sahip tavuk tüyü fiberleri sterilizasyon amacıyla 24 saat suda bekletildikten sonra 60°C sıcaklıkta 6 saat fırında bırakılarak nemi alınmıştır. Üretime hazırlanan tavuk tüyü fiberleri ve PLA malzemeleri, tavuk tüyü kütle oranı %2, %5 ve %10 olacak şekilde hassas tartıda tartılıp WiseStir HT-50AX marka mekanik karıştırıcı yardımı ile bir araya getirilmiştir. ThermoFisher EuroLab 16 XL çift vidalı ekstruder ile biyokompozit üretimi tamamlanmış ve enjeksiyon kalıplama ile yapılması planlanan çekme testleri için standart numuneler elde edilmiştir [6]. Atmosferik uzun süreli yaşlandırmanın mekanik özelliklere etkilerini gözlemleyebilmek amacıyla, PLA ve Tavuk tüyü fiber / PLA biyokompozit numuneler özel bir kap içerisinde, %45±5 nem oranında ve 23±2 °C'de 43800 saat laboratuvar ortamında bekletilmiştir. Biyokompozit numuneler ideal yaşam ortamında ve direkt olarak güneş ışığı ve hava akımından etkilenmeyecek şekilde konuşlandırılmışlardır.

Bulgular

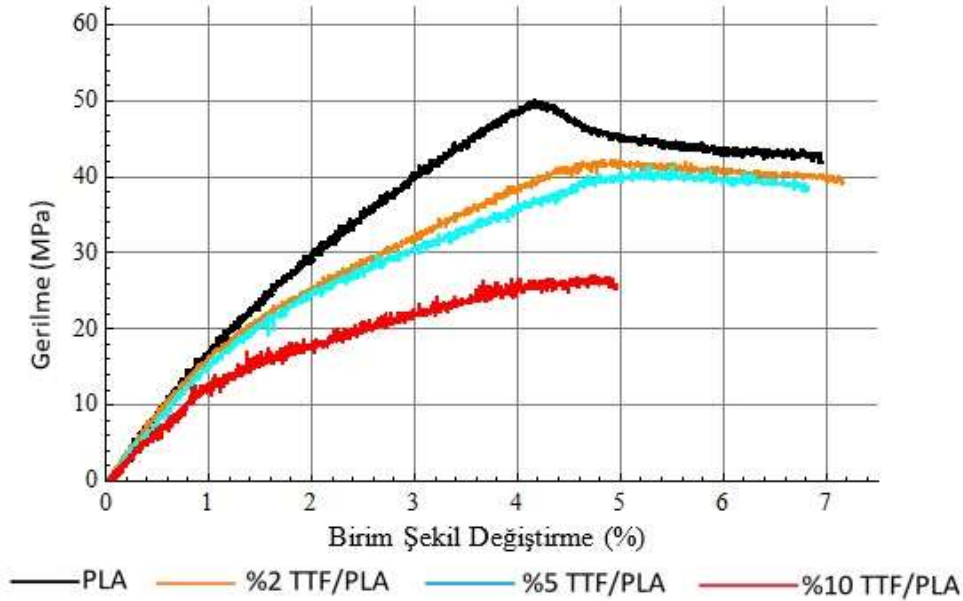
Biyokompozit numunelerin mekanik özelliklerinin belirlenebilmesi amacıyla 100 kN kapasiteli ve video ekstansometreli Shimadzu çekme testi cihazı kullanılmıştır. ISO 527 standardına göre ölçülendirilen biyokompozit numuneler, her parametreden en az 3 adet olacak şekilde, çekme test cihazında 1 mm / 1 dk hızında ve oda sıcaklığında çekilmiştir. Çekme testi sonuçlarına göre, Gerilme – Birim şekil değiştirme grafikleri hazırlanmış ve bu grafikteki her numuneye ait eğrinin eğiminden de elastisite modülleri belirlenmiştir.

Şekil 1 ve Şekil 2'de sırasıyla yaşlandırılmamış ve yaşlandırılmış numunelere ait gerilme – birim şekil değiştirme grafikleri verilmiştir. Şekil 1'e göre, yaşlandırılmamış numuneler içerisinde en yüksek çekme dayanımı değerine saf PLA numunesi sahipken, bu değer fiberin kütle oranının çeşitlendirildiği biyokompozitlerde fiber içeriği ile ters orantılı olacak şekilde, fiber içeriği arttıkça

düşmekte ve en düşük değerini %10 TTF / PLA biyokompozit numunesinde almaktadır. Bu durum, üretim sürecinde fiberlerin gelişi güzel doğrultuda ve homojen dağılmamasından kaynaklı olabilir.



Şekil 1 Yaşlandırılmamış [7] uzun tavuk tüyü fiber / PLA biyokompozit gerilme – birim şekil değişime grafiği

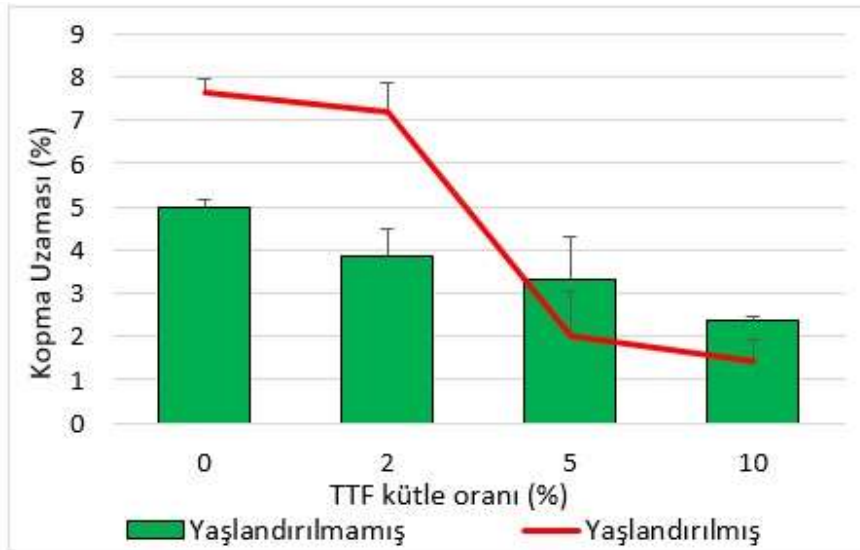


Şekil 2 Yaşlandırılmış uzun tavuk tüyü fiber/ PLA biyokompozit gerilme – birim şekil değişime grafiği

Yaşlandırılmamış numuneler içerisinde en yüksek birim şekil değişime değerine %2 TTF / PLA numuneleri sahiptir. Şekil 2'ye göre, yaşlandırılmış numuneler içerisinde en yüksek çekme dayanımı değerine yine saf PLA numuneleri sahiptir. Yaşlandırılmış numuneler içerisinde fiber içeriğinin kütleli olarak artması ile çekme dayanımı değeri düşmekte ve en düşük değerini %10 TTF / PLA biyokompozit numuneleri göstermektedir. Yaşlandırılmış numuneler içerisinde en yüksek birim şekil değişime değeri saf PLA, %2 ve %5 TTF / PLA numunelerine aittir. Yaşlandırılmış ve yaşlandırılmamış numuneler arasında en düşük birim şekil değişime değerine %10 TTF / PLA numuneleri sahiptir. Aynı kütleli fiber oranına sahip biyokompozit numuneler kendi içlerinde karşılaştırıldığında; saf PLA'nın

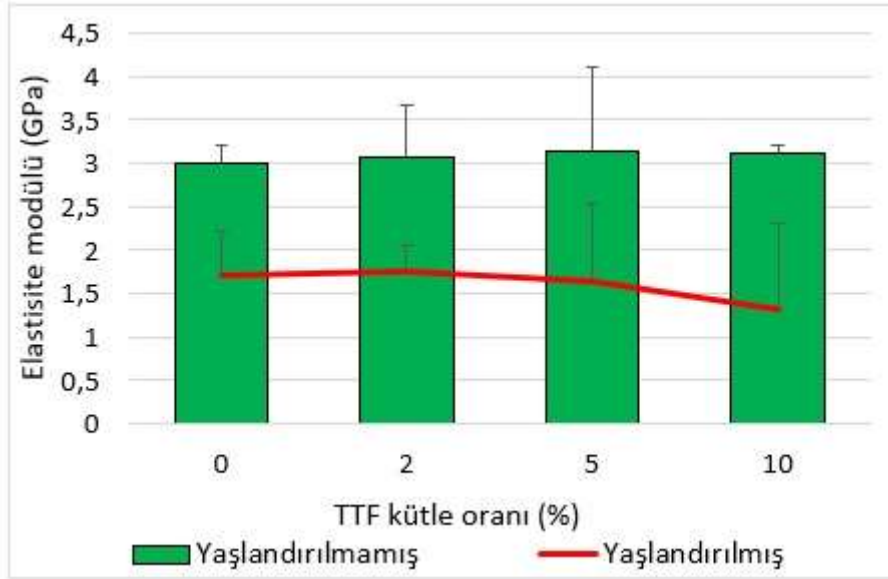
çekme dayanımı yaşlandırmanın etkisi ile %11,71 değer kaybederek 50,06 MPa değerine düşmüş, %2 TTF / PLA'nın çekme dayanımı %10,86 değer kaybı ile 42,25 MPa değerine düşmüş, %5 TTF / PLA biyokompozit numunenin çekme dayanımında herhangi bir değişiklik gözlemlenmezken bu değer %10 TTF / PLA numune de ise %26,34 değer kaybı ile sonuçlanmıştır.

Şekil 1 ve Şekil 2'de sırasıyla yaşlandırılmamış ve yaşlandırılmış numunelere ait gerilme – birim şekil değiştirme grafikleri verilmiştir. Şekil 1'e göre, yaşlandırılmamış numuneler içerisinde en yüksek çekme dayanımı değerine saf PLA numunesi sahipken, bu değer fiberin kütsel oranının çeşitlendirildiği biyokompozitlerde fiber içeriği ile ters orantılı olacak şekilde, fiber içeriği arttıkça düşmekte ve en düşük değerini %10 TTF / PLA biyokompozit numunesinde almaktadır. Bu durum, üretim sürecinde fiberlerin gelişi güzel doğrultuda ve homojen dağılmamasından kaynaklı olabilir. Yaşlandırılmamış numuneler içerisinde en yüksek birim şekil değiştirme değerine %2 TTF / PLA numuneleri sahiptir. Şekil 2'ye göre, yaşlandırılmış numuneler içerisinde en yüksek çekme dayanımı değerine yine saf PLA numuneleri sahiptir. Yaşlandırılmış numuneler içerisinde fiber içeriğinin kütsel olarak artması ile çekme dayanımı değeri düşmekte ve en düşük değerini %10 TTF / PLA biyokompozit numuneleri göstermektedir. Yaşlandırılmış numuneler içerisinde en yüksek birim şekil değiştirme değeri saf PLA, %2 ve %5 TTF / PLA numunelerine aittir. Yaşlandırılmış ve yaşlandırılmamış numuneler arasında en düşük birim şekil değiştirme değerine %10 TTF / PLA numuneleri sahiptir. Aynı kütsel fiber oranına sahip biyokompozit numuneler kendi içlerinde karşılaştırıldığında; saf PLA'nın çekme dayanımı yaşlandırmanın etkisi ile %11,71 değer kaybederek 50,06 MPa değerine düşmüş, %2 TTF / PLA'nın çekme dayanımı %10,86 değer kaybı ile 42,25 MPa değerine düşmüş, %5 TTF / PLA biyokompozit numunenin çekme dayanımında herhangi bir değişiklik gözlemlenmezken bu değer %10 TTF / PLA numune de ise %26,34 değer kaybı ile sonuçlanmıştır.



Şekil 3 Yaşlandırılmamış [7] ve yaşlandırılmış TTF / PLA biyokompozit malzemelere ait kopma uzaması - TTF kütle oranı grafiği

Yaşlandırılmamış ve yaşlandırılmış biyokompozit numunelere ait kopma uzaması – TTF kütle oranı ve elastisite modülü – TTF kütle oranı grafikleri sırasıyla Şekil 3 ve Şekil 4'te verilmiştir. Şekil 3'e göre, yaşlandırılmamış ve yaşlandırılmış numunelerin kütsel TTF oranı arttıkça kopma uzaması değeri azalmıştır. Yalnız, yaşlandırılmış saf PLA ve %2 TTF / PLA numunelerinin kopma uzaması değerleri aynı oranda TTF içeren biyokompozit numunelere göre daha yüksektir. Elastisite modüllerinin karşılaştırmalı olarak verildiği Şekil 4'e göre, yaşlandırılmamış numunelerin elastisite modülleri tüm numuneler için birbirine oldukça yakın değerlerde seyrederken, yaşlandırılmış numunelerde saf PLA, %2 TTF / PLA ve %5 TTF / PLA numunelerinde birbirine yakın değerlerde olduğu görülmektedir. Yaşlandırılmış numuneler içerisinde en düşük elastisite modülü ve kopma uzaması değerlerine %10 TTF / PLA numuneleri sahiptir.



Şekil 4 Yaşlandırılmamış [7] ve yaşlandırılmış TTF / PLA biyokompozit malzemelere ait elastisite modülü - TTF kütle oranı grafiği

Elyaf ile güçlendirilmiş kompozit malzemelerdeki elyaf ile matris arasındaki arayüz bağının kalitesi kompozit malzemenin özelliklerini önemli ölçüde etkileyebilir. Bu bağın kalitesi yaşlandırma, termal süreçler, nem, yorulma gibi farklı servis koşullarından etkilenmektedir. Bu etkilenme dolayısı ile de kompozit malzemenin fiberleri ile matris arasındaki bağın kalitesi önemli ölçüde azalabilir. Bu sebeple karakteristik servis koşullarının, kompozit malzemeyi oluşturan fiberler ile matris arasındaki arayüz bağlantısına etkisinin bilinmesi erken uyarı sistemi gibi kullanılabilir [8, 9]. Sunulan çalışmada incelenen TTF / PLA biyokompozit malzemeler için yaşlandırma prosesi, tavuk tüyü fiberler ile matris malzeme olan PLA arasındaki arayüz bağının olumsuz etkilenmesine sebep olmuştur. Ayrıca, fiberlerin ve matrisinin degradasyonuna sebep olabilen bu süreç sonunda, herhangi bir yükleme esnasında yükleme doğrultusundaki yükün taşınmasına yardımcı olması beklenen fiberlerin görevlerini başarı ile yerine getirememesinden kaynaklanan mekanik özelliklerde gerilemeler görülmektedir [10]. Bu çalışmada incelenen biyokompozit numunelerin mekanik özelliklerindeki düşüşler bu sebeplerden kaynaklanabilir.

Sonuç

Uzun tavuk tüyü fiber ile güçlendirilmiş PLA matrisinden oluşan TTF / PLA biyokompozit malzemenin uzun süreli atmosferik ortamda bulundurulması ilkesine dayanan uzun süreli yaşlandırma prosesinin, biyokompozit malzemenin mekanik özelliklerine olan etkilerinin araştırıldığı bu çalışmanın sonuçları şu şekildedir;

- ❖ Yaşlandırma prosesinin etkisi ile saf PLA da dahil olmak üzere tüm TTF / PLA biyokompozit malzemelerin çekme dayanımları düşmüştür. En ciddi düşüş %26,04 değer kaybı ile %10 TTF/PLA biyokompozit numunelerinde görülmektedir.
- ❖ Yaşlandırılmış saf PLA ve %2 TTF / PLA numuneleri aynı oranda TTF içeren yaşlandırılmamış biyokompozitlerle kıyaslandığında, kopma uzaması değerleri artmış buna karşı elastisite modülü değerleri azalmıştır. Bu numunelerin sünekliklerinin yaşlandırma prosesinin etkisi ile arttığı ve daha sünek hale geldikleri görülmüştür.
- ❖ Tüm yaşlandırılmış numunelerin elastisite modülleri yaşlandırılmamışlara kıyasla daha düşüktür. En düşük elastisite modülü değerine 1,31 GPa değeri ile yaşlandırılmış %10 TTF / PLA numunesi sahiptir.

Kaynaklar

- [1] Rwawiire J, Wandera S (2012) Biocomposites, proceedings of XVth international scientific and practical workshop: physics of fibrous materials: 67-73.
- [2] Garlotta D (2001) A literature review of Poly(Lactic Acid). Journal of Polymers and the Environment 9:63-84. <https://doi.org/10.1023/A:1020200822435>
- [3] Oksman K, Selin JF (2004) Plastics and composites from polylactic acid. Natural fibers, plastics and composites. Kluwer Academic Publishers, Boston: 149–65.
- [4] Huda MS, Drzal LT, Mohanty AK, Misra M (2006) Chopped glass and recycled newspaper as reinforcement fibers in injection molded poly(lactic acid) (PLA) composites: a comparative study. Composite Science and Technology 6:1813–1824.
- [5] Reddy N, Yang Y (2007) Structure and Properties of Chicken Feather Barbs as Natural Protein Fibers. Journal of Polymers and the Environment 15:81-87.
- [6] Özmen U (2015) Doğal fiber takviyeli kompozitlerin üretimi, mekanik ve termal özelliklerinin tespiti. Y. Lisans Tezi
- [7] Okutan Baba B, Özmen U (2015) Preparation and mechanical characterization of chicken feather/PLA composites. Polymer Composites 38(5):837-845. <https://doi.org/10.1002/pc.23644>
- [8] Kim J O, Bau H H (1992) A study of the fiber-matrix interface in composite materials. Journal of Applied Mechanics 59:163-165. <https://doi.org/10.1115/1.2899482>
- [9] Hashin Z (1990) Thermoelastic properties of fiber composites with imperfect interface. Mechanics of Materials 8(4):333-348. [https://doi.org/10.1016/0167-6636\(90\)90051-G](https://doi.org/10.1016/0167-6636(90)90051-G)
- [10] Akderya T, Çevik M (2018) Investigation of thermal-oil environmental ageing effect on mechanical and thermal behaviours of E-glass fibre/epoxy composites. Journal of Polymer Research 25:214-235. <https://doi.org/10.1007/s10965-018-1615-2>

Simfizis Pubis Ayrılmasının Plak ile Tespitinin Sonlu Elemanlar Yöntemi İle Analizi

*Mustafa Batuhan Emiroğlu**, Dokuz Eylül Üniv., Fen Bilimleri Enstitüsü, Makina Mühendisliği Bölümü,
Tınaztepe Kampüsü, İzmir, Türkiye

Yusuf Arman, Dokuz Eylül Üniv., Makina Mühendisliği Bölümü, Tınaztepe Kampüsü, İzmir, Türkiye
Ahmet Karakaşlı, Dokuz Eylül Üniv., Tıp Fakültesi, Ortopedi ve Travmatoloji Bölümü, İnciraltı Kampüsü, İzmir,
Türkiye

*İletişimden sorumlu yazar: mbatuhanemiroglu@gmail.com

Anahtar Kelimeler: biyomekanik, sonlu elemanlar analizi, pelvis, simfizis pubis

Disiplin: Makina Mühendisliği

Özet

Simfizis pubis ayrışması genellikle yüksek enerji sebebiyle meydana gelen cerrahi müdahale ile fiksasyon gerektiren hayati yaralanma türüdür. Bu yaralanmaların tedavisinde yoğun olarak plak ile tespit yöntemi kullanılmaktadır. Bu çalışmada; 32 yaşındaki kadın hastadan alınan bilgisayarlı tomografi verisi ile oluşturulan üç boyutlu pelvis katı modeline, ansys programında simfizis pubis ayrışması uygulanmıştır. Ardından 3,5 mm kalınlığında 6 delikli ve 4,5 mm kalınlığında 4 delikli iki farklı plak ile tespit yapılmıştır. İki ayak üzerindeki yüklenme durumunda, iki sabitleme yöntemi mekanik açıdan birbiriyle karşılaştırılmıştır. 4 delikli plakta, 6 delikli plaktan % 53 daha fazla von mises gerilmesi meydana geldiği görülmüştür. Bununla beraber cerrahi müdahale gerçekleşmeden önce tedavinin hasta üzerine uygunluğu ve yeterliliğinin izlenebilmesi ve değerlendirilebilmesi sağlanmıştır.

Giriş

Biyomekanik temel olarak sağlık ve mühendislik bilimlerini, problemlere çözüm üretmek ve yenilikçi yaklaşımlar sağlamak amacıyla ortak paydada birleştiren multidisipliner bir çalışma alanıdır. Biyomekanik çalışmaların odak noktasında mekanik ilke ve yaklaşımlar çerçevesinde canlıların hareket mekanizmaları, oluşan kuvvetlerin etkileri, canlı ve cansız dokular üzerinde zorlanma durumları yer almaktadır. Yapılan çalışmalar tedavi yöntemlerinin test edilmesine ve geliştirilmesine olanak sağlamaktadır. İlk modern biyomekanik çalışmalarına bakıldığında, Stephen Hales'in 18. yüzyılda ilk kez kan basıncını ölçmeyi başararak göze çarpmaktadır[1]. Biyomekanik çalışmalar organlara ait tanıların konulması, tedavilerin oluşturulması ve mevcut tedavilerin geliştirilmesine olanak sağlamasının yanı sıra tedavi cihazlarının tasarım aşamasına da katkıda bulunmaktadır.

Biyomekanik çalışmalarda karmaşık problemlerin matematiksel modele indirgenerek hassas olarak çözülebilmesi için sonlu elemanlar stres analizi yönteminden faydalanılmaktadır. Bu yöntem sistemin sürekli daha küçük parçalara ayrılarak bir matematiksel model haline getirilmesi olarak tanımlanabilir. [2]. Teknolojideki gelişmeler sayesinde, sonlu elemanlar analiz yöntemini kullanan özel yazılımlar kullanılmaya başlanmıştır. Bu yazılımlar karmaşık biyomekanik problemlerin istenen malzeme özelliklerini ve yüklenme koşullarını içerecek şekilde simüle edilmesine olanak sağlamaktadır. Sonlu elemanlar stres analizi yöntemi; sonlu elemanlar katı modelinin oluşturulması, analiz için gerekli verilerin girilmesi ve analizin gerçekleştirilmesi olmak üzere üç basamaktan oluşur.

Genel olarak biyomekanik çalışmalara konu olan yapılar düzgün ve basit geometrilere sahip olmadıkları için modelleme yapmak oldukça zordur. Bu nedenle sonlu elemanlar stres analizinin ilk basamağı olan katı modelin oluşturulması esnasında bilgisayarlı tomografi verisinden yararlanılmaktadır. Bilgisayarlı tomografi, insan ya da kadavralardan bilgisayar ve x ışınları yardımıyla kesit şeklinde görüntü alma işlemidir [3]. Alınan kesit görüntüleri uygun yazılımlar kullanılarak analiz için gerekli olan üç boyutlu katı model haline getirilmektedir.

Biyomekanik çalışmaların odak noktaları incelendiğinde kemik ve eklem yapılarına sıkça rastlanmaktadır. Pelvis kırıkları iskelet sisteminin önemli yaralanmaları arasında yer almaktadır. Pelvis kırıkları tüm kırıkların yaklaşık olarak %1-3'ünü oluşturmaktadır [4].

Pelvis üst vücut yüklerini alt uzuvlara aktarma işlevini gören ve insan hareketinde kritik öneme sahip olan düşük ağırlıklı, yüksek mukavemetli geometrik yapıdır [5]. Yürüme sırasında kalça eklemi boyunca vücut ağırlığından üç kat fazla kuvvet meydana gelmektedir. Bu kuvvet koşma ve merdiven çıkma gibi aktiviteler esnasında vücut ağırlığının altı katına kadar çıkabilmektedir [6].

Simfizis pubis, pelvis yapısı üzerinde iki pubis kemiği arasında bulunan eklemdir. Simfizis pubis ayrışması yüksek enerjiden kaynaklanan bir yaralanma türüdür. Epidemiyolojik çalışmalar, simfizis pubis ayrışmasının; pelvik halka yaralanmalarının % 2 ile % 16'sını ve tüm yaralanmaların % 4,6'sını oluşturduğunu göstermektedir [5]. Yüksek enerji sebebiyle oluşan pelvik halka yaralanmalarına müdahale edilmesi hastanın hayati parametrelerini stabilize etmek açısından büyük önem taşımaktadır. Tedavi için literatürde bulunan plak ile tespit, vida ile tespit gibi çeşitli fiksasyon yöntemlerinden biri seçilmelidir. İdeal fiksasyon yönteminin seçilmesi için zamanla elde edilen doğrulanmış sonuçlara ve pelvis numuneleri üzerinde yapılan karşılaştırılmalı çalışmalara başvurulması faydalı olacaktır [7].

Literatüre bakıldığında ilk olarak sonlu elemanlar analizi yönteminin pelvis yaralanmalarına uygulanabilirliğinin sorgulandığı görülmektedir. Bu bağlamda yapılan çalışmada, oluşturulan simfizis pubis sonlu elemanlar modelinden elde edilen sonuçların deneysel olarak elde edilen sonuçlarla örtüştüğü tespit edilmiştir. İlgili çalışmada kadın ve erkek simfizis pubis modellerine çeki ve bası kuvvetleri uygulanmış ayrıca eğilme direnci araştırılmıştır. [8] Sonlu elemanlar analizi yöntemi numuneye özgü pelvik modellerinin oluşturulmasını hızlandırarak, pelvis ve diğer kas iskelet yapılarında bu yöntemin başarıyla uygulanmasına temel oluşturmuştur

Simfizis pubis fiksasyonunu konu alan bir başka çalışmada ise beş farklı fiksasyon yöntemi farklı yüklenme koşulları altında sonlu elemanlar analizi yöntemi kullanılarak biyomekanik karakteristik açısından karşılaştırılmıştır. Plak kullanılan yöntemler; tek plak ile tespit ve çift plak ile tespittir. Bu çalışmada, çift ayak üzerindeki yüklenme durumunda en iyi sonuç iki vidanın çapraz kullanılması yöntemi ile alınmıştır [9].

Bu çalışmada simfizis pubis ayrışmasının fiksasyonunda en çok kullanılan yöntemlerden biri olan plak ile tespit konu alınmıştır. Bilgisayarlı tomografi verisinden elde edilen simfizis pubis modelinde ayrışma oluşturulmuştur. Ardından 3,5 mm kalınlığında 6 delikli ve 4,5 mm kalınlığında 4 delikli iki farklı plak ile tespit yapılmıştır. İki ayak üzerindeki yüklenme durumunda iki sabitleme yöntemi mekanik açıdan birbiriyle karşılaştırılmıştır. Bununla beraber cerrahi müdahale gerçekleşmeden önce tedavinin hasta üzerine uygunluğu ve yeterliliğinin izlenebilmesi ve değerlendirilebilmesi sağlanmıştır.

Metodoloji

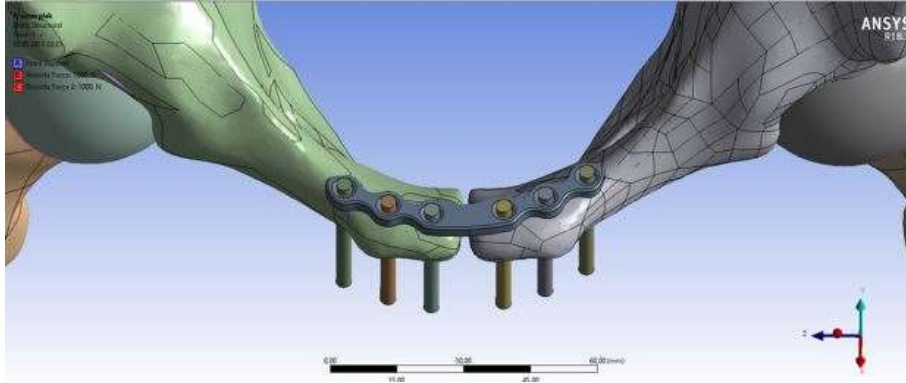
Çalışmada kullanılan kırkırdak ve kemiğe ait malzeme özellikleri, lineer elastik izotropik olarak düşünülmüş ve literatürde kabul gören değerler alınmıştır. Tespit elemanlarının geometrisi ve malzeme özellikleri için katalog verileri esas alınmıştır. Kullanılan malzeme özellikleri Tablo 1'de verilmiştir.

Tablo 1. Malzeme Özellikleri [10]

	Elastisite Modülü (MPa)	Poisson Oranı
Kemik	17000	0,30
Kırkırdak	10	0,49
Plak ve Vida	200000	0,30

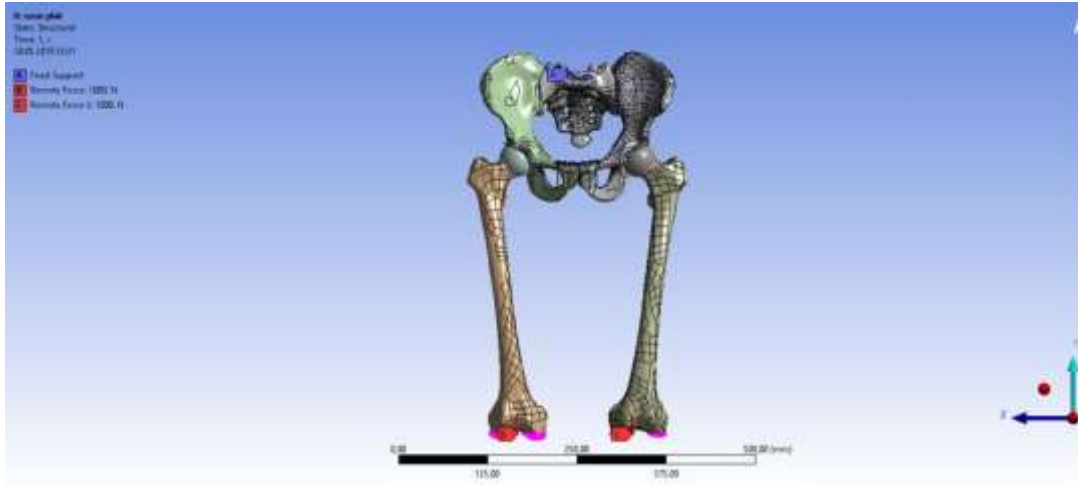
Üç boyutlu insan simfizis pubis modeli 32 yaşında sağlıklı, kadın bir hastaya ait olan bilgisayarlı tomografi verisinden oluşturulmuştur. DICOM formatında alınan tomografi verisi Meshmixer ve Mimics Medical programlarından yararlanılarak STL formatında meshlenmiş katı modele dönüştürülmüştür. Katı modele dönüştürülen STL formatındaki tomografi verisi Solidworks programı yardımıyla parasolid formatına dönüştürülmüş ve model üzerinde simfizis pubis ayrışması oluşturulmuştur. Parasolid; oluşturulan katı modelin sonlu elemanlar analizi yöntemini kullanan Ansys programında incelenebilmesi için gerekli olan dosya türüdür.

Çalışmada gerçekleştirilen statik analizlerde, iki farklı fiksasyon yöntemi için de iki ayak üzerindeki yüklenme durumu incelenmiştir. Öncelikle 3,5 mm kalınlığındaki 6 delikli plak ile tespit gerçekleştirilmiştir. Tespitin meshlenmiş hali Şekil 1'de verilmiştir.



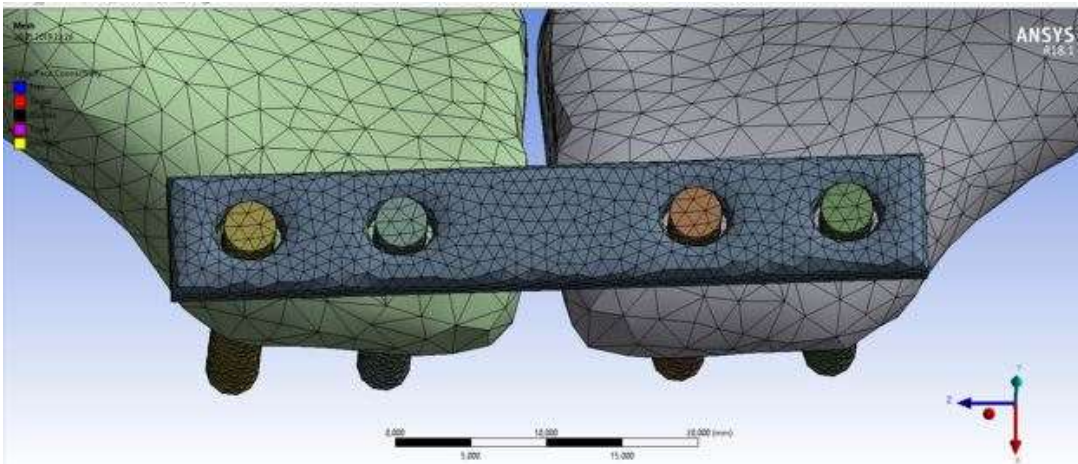
Şekil 1. 6 delikli plak ile tespit

Literatüre uygun olarak sabitleme yapılarak iki bacak üzerinden 1000'er Newtonluk kuvvet uygulanmıştır. Uygulanan kuvvetler Şekil 2'de gösterilmiştir.



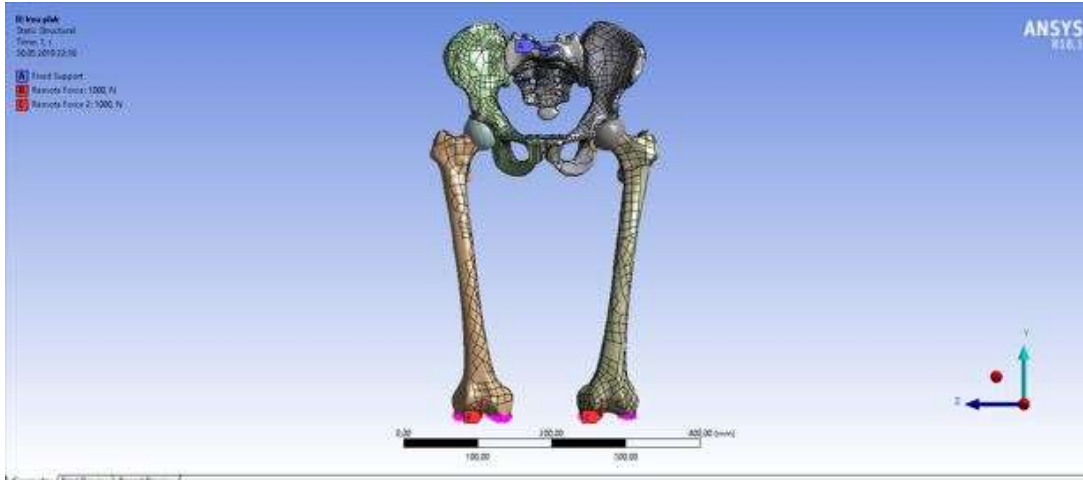
Şekil 2. 6 delikli plak ile tespitte uygulanan kuvvetler

İkinci olarak 4,5 mm kalınlığındaki 4 delikli plak ile tespit gerçekleştirilmiştir. Tespitin meshlenmiş hali Şekil 3'de verilmiştir.



Şekil 3. 4 delikli plak ile tespit

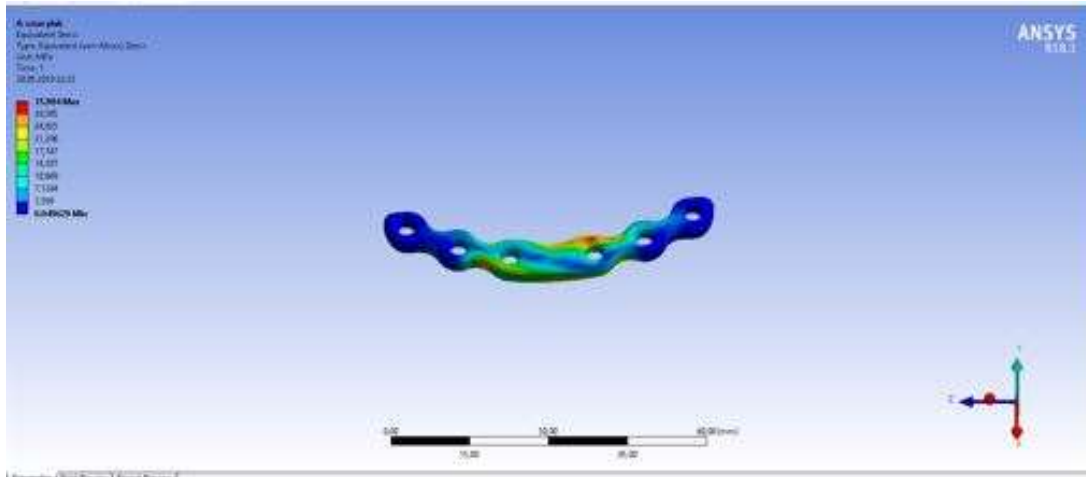
Literatüre uygun olarak sabitleme yapılarak iki bacak üzerinden 1000'er Newtonluk kuvvet uygulanmıştır. Uygulanan kuvvetler Şekil 4'de gösterilmiştir.



Şekil 4. 4 delikli plak ile tespitte uygulanan kuvvetler

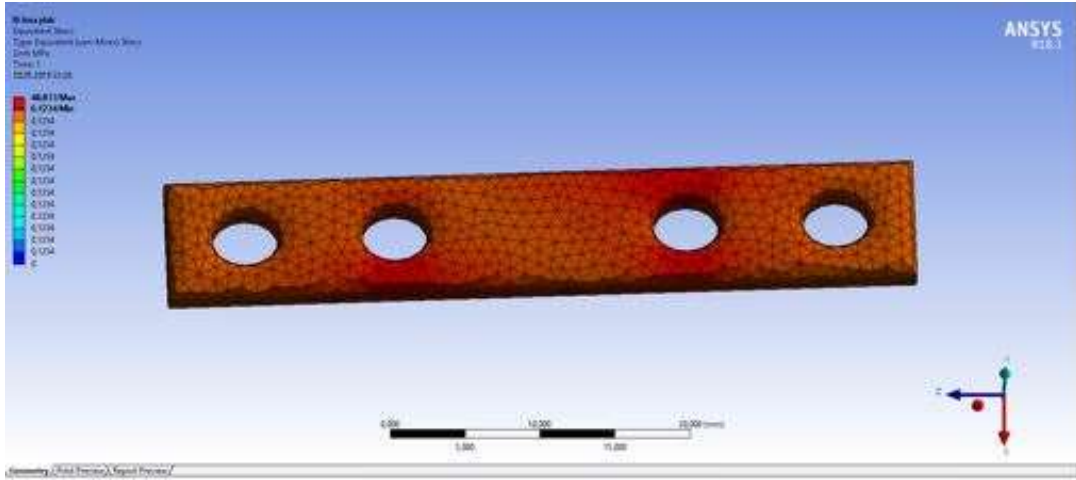
Sonuçlar

Plak ile tespit yönteminin biyomekaniği söz konusu olduğunda, tespit gerçekleştirilen bölgedeki yük aktarımının hem plak hem de kemik üzerinden olduğu bilinmektedir. Biyomekanik özelliklere etki eden parametrelerden biri de plak geometrisidir. Bu çalışmada aynı yükleme şartları altında; biri 3,5 mm kalınlığında 6 delikli, diğeri 4,5 mm kalınlığında 4 delikli iki plak ile tespit yapılmıştır. Uygulanan tedavinin ömrü plakların ömrüne birinci dereceden bağlıdır. Bu sebeple iki plakta oluşan Von-Mises gerilmeleri ve asal şekil değiştirmeler karşılaştırılmıştır. 6 delikli plakta oluşan maksimum von mises gerilmesi 31,90 MPA olup gerilme dağılımı Şekil 5’de verilmiştir.



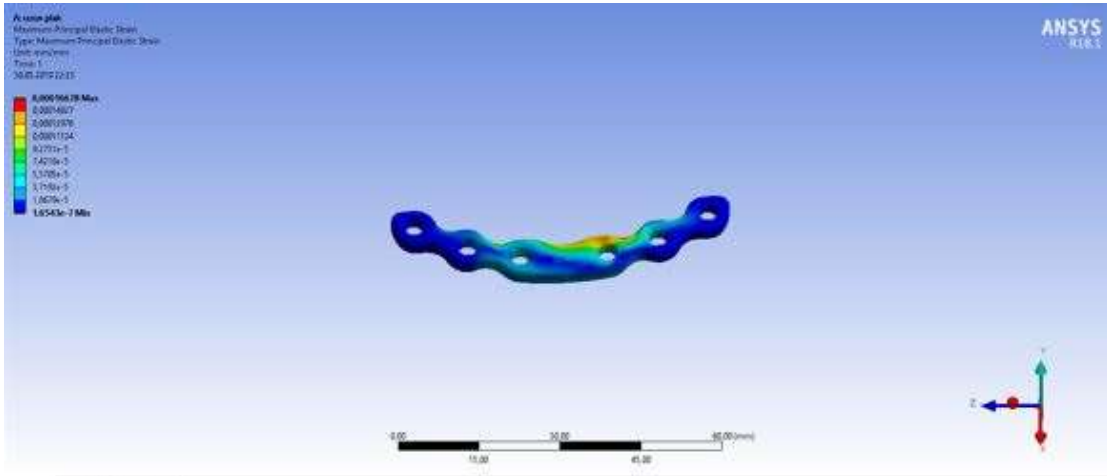
Şekil 5. 6 delikli plak gerilme dağılımı

4 delikli plakta oluşan maksimum von mises gerilmesi 48,87 MPA olup gerilme dağılımı Şekil 6’da verilmiştir.



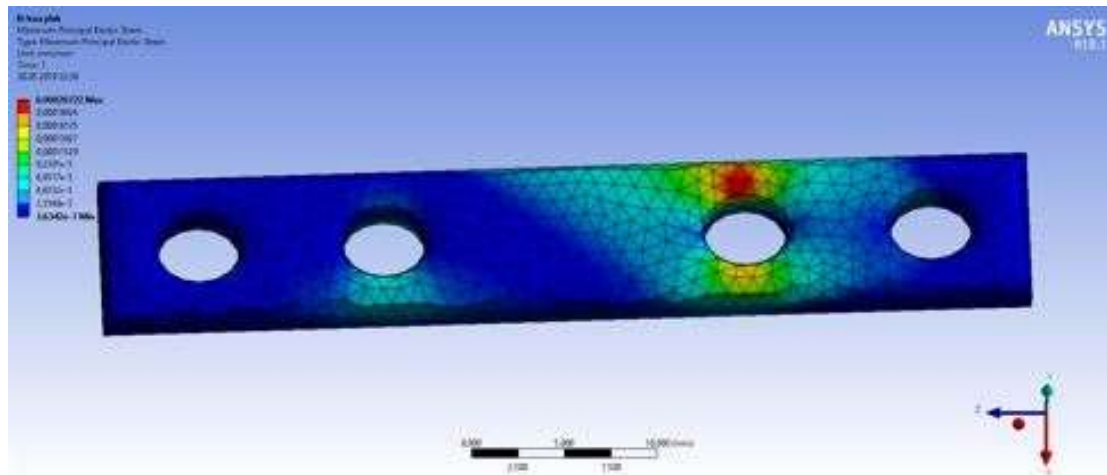
Şekil 6. 4 delikli plak gerilme dağılımı

6 delikli plakta oluşan maksimum asal şekil değiştirme 0,00016678 olup dağılımı Şekil 7'de verilmiştir.



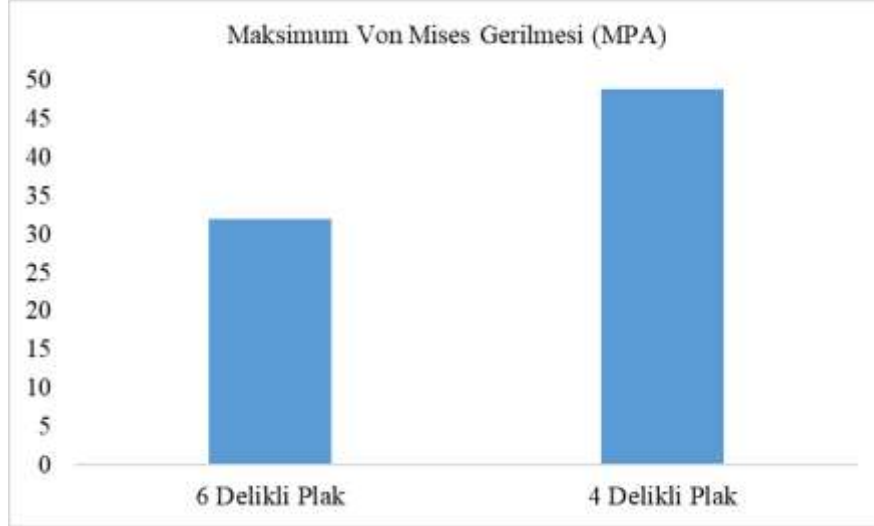
Şekil 7. 6 delikli plak asal şekil değiştirme dağılımı

4 delikli plakta oluşan maksimum asal şekil değiştirme 0,00020722 olup dağılımı Şekil 8'de verilmiştir.



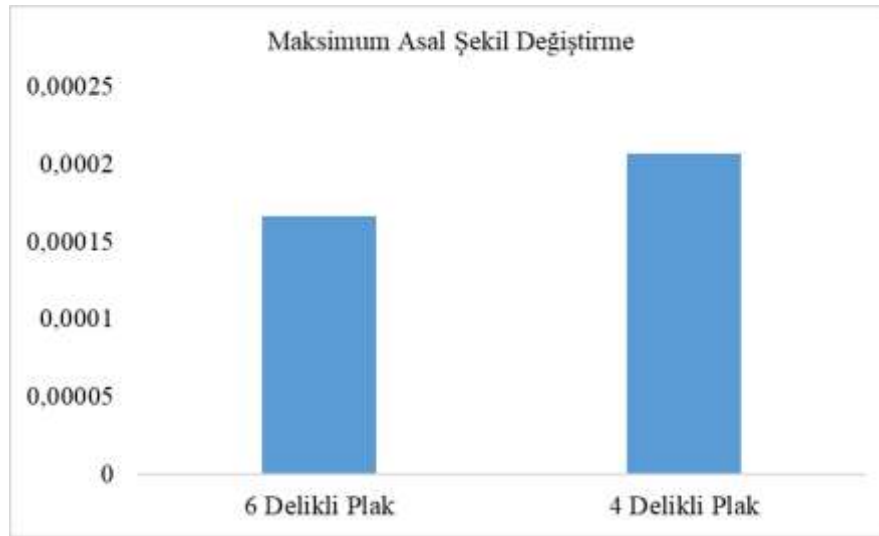
Şekil 8. 4 delikli plak asal şekil değiştirme dağılımı

Şekil 9’da iki plak için maksimum Von Mises gerilme değerleri grafikte gösterilmiştir. 4 delikli plakta, 6 delikli plaktan % 53 daha fazla gerilme meydana geldiği görülmüştür.



Şekil 9. Maksimum Von Mises gerilmesi karşılaştırması

Şekil 10’da iki plak için maksimum asal şekil değiştirme değerleri grafikte gösterilmiştir. 4 delikli plakta, 6 delikli plaktan % 24 daha fazla asal şekil değiştirme meydana geldiği görülmüştür.



Şekil 10. Maksimum asal şekil değiştirme karşılaştırması

Çalışmada her iki plak için de maksimum von mises gerilmeleri beklendiği üzere delik yakınlarında meydana gelmiştir. Plak ile kemik arasındaki bağlantı yüzey miktarı arttıkça gerilme miktarının azaldığı görülmüştür. Bu hastada daha uzun ömürlü bir tedavi için 6 delikli plağın seçilmesi gerektiği belirlenmiştir. Böylece cerrahi müdahale gerçekleşmeden önce tedavinin hasta üzerine uygunluğu ve yeterliliğinin izlenebilmesi ve değerlendirilebilmesi sağlanmıştır.

Referanslar

- [1] Nigg MB, Herzog W (2008) Biomechanics Principles and Applications, CRC Pres, Boca Raton.
- [2] Zienkiewic Z, Olgierd Cecil vd. (1977) The Finite Element Method. London: McGraw-Hill.
- [3] Özkan R (2005) Bilgisayarlı Tomografinin Temel Prensipleri.
- [4] Arazi M, Kutlu A, Tarakçıoğlu N, vd. (1995) Stabil olmayan pelvis kırıklarının tedavisinde Selçuk tipi pelvis eksternal fiksator uygulamaları. Acta Orthop Traumatol Turc, 29: 299-305.

**3rd International Students Science Congress
3-4 May 2019, İzmir - Turkey**

- [5] Yao F, He Y, QianH, Zhou D, Li Q (2015) Comparison of biomechanical characteristics and pelvic ring stability using different fixation methods to treat pubic symphysis diastasis : A finite element study, *Medicine*, 94(49): e2207.
- [6] Hu P, Wu T, Wang HZ, Qi XZ, Yao J, Cheng XD, Chen W, Zhang YZ (2017) Influence of different boundary conditions in finite element analysis on pelvic biomechanical load transmission. *Orthopaedic surgery*, 9(1): 115-122.
- [7] Sztrinkai G, Bodzay T, Pajor S, Erdös P, Vendegh Z, Jonas Z, Varadi K (2014) Further development of our finite element pelvic model to compare fixation methods for pelvic fractures. *Eklemler Hastalıkları Cerrahisi*, 25(1): 8-14.
- [8] Li Z, Alonso JE, Kim JE, Davidson JS, Etheridge BS, Eberhardt AW (2006) Three-dimensional finite element models of the human pubic symphysis with viscohyperelastic soft tissues. *Annals of Biomedical Engineering*, 34(9): 1452-1462.
- [9] Yao F, He Y, Qian H, Zhou D, Li Q (2015) Comparison of biomechanical characteristics and pelvic ring stability using different fixation methods to treat pubic symphysis diastasis: a finite element study. *Medicine*, 94:49.
- [10] Yu KH, Hong JJ, Guo XS, Zhou DS (2015) Comparison of reconstruction plate screw fixation and percutaneous cannulated screw fixation in treatment of Tile B1 type pubic symphysis diastasis: a finite element analysis and 10-year clinical experience. *Journal of Orthopaedic Surgery and Research* 10(1): 151.

Finite Element Stress Analysis of a Functionally Graded Plate

*Alif Diambu Ngimbi**, Dokuz Eylül University, Dept. of Mechanical Engineering, Tınaztepe Campus, 35390
Buca, İzmir, Türkiye

Mehmet Çevik, İzmir Katip Çelebi Univ., Dept. of Mechanical Engineering, Çiğli Main Campus, İzmir, Türkiye
*Corresponding author: anasrouidine1@gmail.com

Keywords: Functionally graded material (FGM), finite element analysis, ANSYS APDL

Discipline: Mechanical Engineering

Abstract

Many components used in engineering require properties that vary with position. On the only component, one may want at the same time a great resistance or heat refractor capacity and high hardness. By sandwiching two materials having different properties, in the case of constraint, a large concentration of stress appears on the bonding surface. To avoid this adverse effect, Functionally Graded Materials (FGMs) are used. In these materials, the passage from one material to another is done gradually. In one direction, as the percentage of material 1 increases, that of material 2 decreases.

In this paper, we analyze a functionally graded plate (FGP) that is stressed in pressure using ANSYS Parametric Design Language (APDL). This model is the common case of the blades of gas and combustion turbines subjected to the pressure of the working fluid at high temperature. The model used in the present study ideal combination is ceramic for its thermal resistance and steel for its mechanical resistance properties.

Introduction

For many years, laminated composite materials have remained at the center of research for their applications in several fields. However, numerous defects are presumable in these composite materials including the residual stresses due to the difference of layer properties, shearing on the adhesion surface, etc. To overcome the aforesaid drawbacks, in the past few decades, together with the development of additive manufacturing technology, FGMs emerged with great success in many domains.

A group of Japanese material researchers was the first team who invented FGM in 1984 with the sole purpose to complete the Aerospace Niino of the NAL project [1] that has aimed to maintain a thermal barrier in a 10 mm thickness material of spacecraft moving at over 28,000 km/h, the orbiter hits air molecules and builds up heat from friction (2000K at the outer surface and 1000K at the inner surface).

FGMs are used in different fields including aerospace, chemical plants, optics, energy conversion, biomaterials, electronics, nuclear energy, etc. where thermal barrier and mechanical resistance is needed, such as in manufacturing of rocket nozzle, thermal barrier coatings for turbine blades, wings and engine casting, brake rotors, solar domes, composite piping system, combustion chambers, racing car breaks, flywheels, dielectric motors, helicopter components, heat exchanger panels and engine parts, machine and forming tools, artificial bones, diesel engine pistons, racing bicycle and vehicle frames.

FGM is characterized by two or more basic stages where material attributes like physical, chemical, mechanical, etc. change evenly, uninterruptedly and smoothly with spatial position to efficiently respond to the surrounding mechanical loads and attenuate defects due to sudden variation in thermomechanical properties of laminated composites [2]. Thus, the main advantage of FGM is that no internal boundaries exist and the interfacial stress concentrations can be avoided [3]. In FGM, the material can be graded in various ways by employing various grading laws, three of which are: Power law function, Exponential law function and Sigmoid law function [2].

▪ Power law function

The Power function model is the most commonly used function in FGP studies. FGMs that obey the power function rule are called (P-FGM). The power function expresses direct property variation or volume fraction change according to a power function [4].

Consider the plate model below in Figure 1.



Figure 1. Illustration of FGM structure

$$V_i(z) = \left(\frac{z}{H}\right)^n \quad (i=1,2 \text{ for 2 materials}) \quad (1)$$

with

$$\sum_i V_i(z) = 1 \quad (2)$$

$$P(z) = (P_2 - P_1)V_1(yz) + P_1 \quad (3)$$

where $V_i(z)$ is the volume of material i at any point y throughout the thickness H ; P_i is the property of material i , n is power law index.

- Exponential law function

The exponential law is basically used to deal with problems related to fracture mechanism of FGM [2].

$$V_i(z) = e^{\frac{nz}{H}} \quad (i=1, 2) \quad (4)$$

$$P(z) = V_1(z)P_1 = P_1 e^{\frac{nz}{H}} \quad \text{and} \quad n = \ln\left(\frac{P_2}{P_1}\right) \quad (5)$$

- Sigmoid law function

FGMs that obey the Sigmoid power function rule are called (S-FGM). The sigmoid power function is the combination of two different power functions, one for the positive range of y and the other for the negative range of y [4]. This is illustrated in Figure 2.

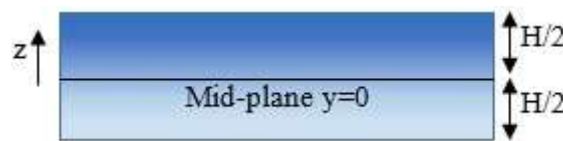


Figure 2. FGM plate section and coordinates

$$V_i(y) = \begin{cases} \left(\frac{1}{2} + \frac{z}{H}\right)^n, & -\frac{H}{2} \leq z \leq 0 \\ \left(\frac{1}{2} - \frac{z}{H}\right)^n, & 0 \leq z \leq \frac{H}{2} \end{cases} \quad (6)$$

In this study, a square FGP is investigated. The upper part of the plate is made of stainless steel and the composition gradually changes from stainless steel to ceramic (the lower part). Ceramics can withstand high-temperature environments due to their better thermal resistance characteristics, whereas steel constituents provide stronger mechanical performance and reduce the possibility of catastrophic fracture of the plate [5,6].

By definition, a plate is a structural element with planform dimensions that are large compared to its thickness and is subjected to loads that cause bending deformation in addition to stretching. A rectangular plate is shown in Figure 3 with typical coordinate system [4].

Some assumptions for the FGP studied are:

- The thickness of the plate is small when compared with other dimensions
- The effect of rotatory inertia is negligible.

- The normal to the undeformed middle surface remains straight and normal to the deformed middle surface, and unstretched in length.
- Material properties for each same ordinate x are homogenous and isotropic.
- Creeps are neglected and perfect bonding is assumed.
- Temperature independent material constants.
- The plate is initially in a stress-free state.

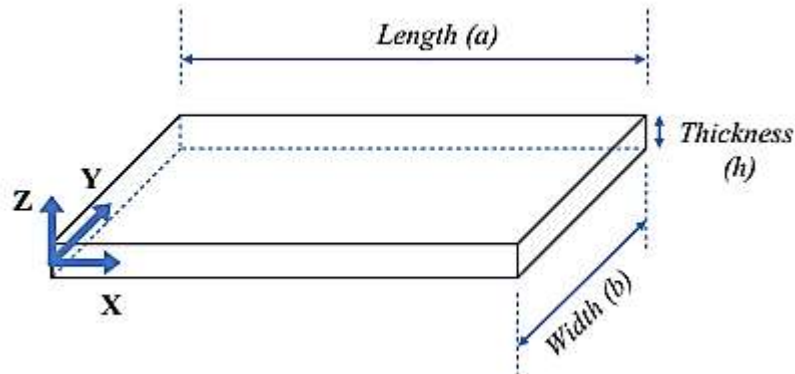


Figure 3. Rectangular plate structure [4]

The FGP model of the current study is a similar case with Gas turbine blades; this plate is expected to withstand a highly elevated temperature without failure. Normally, in addition to the thermal loads, there are mechanical loads acting in the form of pressure. In that case, the FGP has to withstand both the thermal and mechanical loads at the same time.

Shiota and Miyamoto [7] presented different researches dealing with FGMs in their book. Yet, studies where thermal and mechanical loads are applied on gas turbine blade type FGPs are to be performed.

Problem Formulation and Methodology

The model considered in this study is a model similar to a Gas turbine blade. The hot gas is at high temperature and high pressure strike the blade. The face of the blade in direct contact with the hot gas is made of ceramic (Alumina Al_2O_3) and the opposite face is made of stainless steel (Grade304/UNS S30400). The plate has a porosity functionally graded from two materials. The subscripts 1 and 2 denote respectively Alumina (1) and stainless steel (2) constituents. V_1 and V_2 are the volume fractions of material 1 and material 2. The volume fractions are distributed over the z -direction according to Eqn (1). Figure 4 illustrates the effect of the grading parameter on the unit thickness volume fraction.

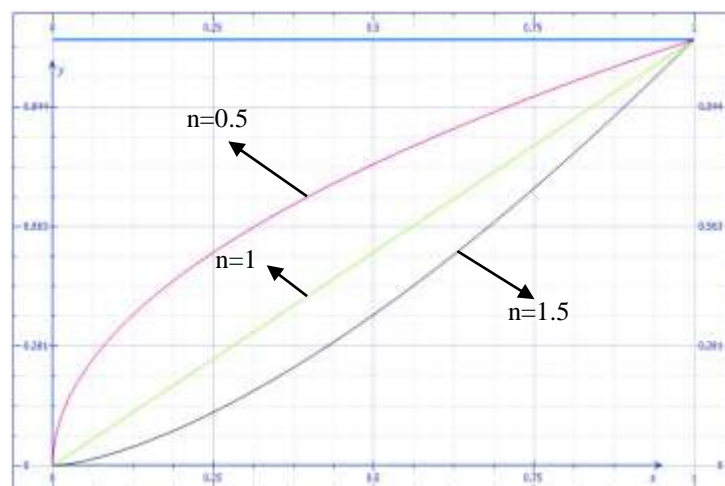


Figure 4. Effect of the grading parameter on the unit thickness volume fraction ($n = 0.5, 1$ and 1.5)

For material 1 rich composition $n > 1$, while for material 2 rich composition $n < 1$. The variation of material 1 and material 2 compositions is linear if $n = 1$.

The material properties of FGMs P_f along the thickness of the plate, such as Young's modulus E_f , Poisson's ratio $\nu(y)$ and the coefficient of thermal expansion $\alpha(y)$, can be determined according to the Modified Mixing Law (Voigt model) [8,9] by:

$$P_f = \sum_{i=1} P_i V_i \quad (9)$$

For our current study case (2 materials),

$$P_f = P_1 V_1 + P_2 V_2 \quad (10)$$

where P_i and V_i are the material properties and volume fraction of the constituent material i , and the sum of the volume fractions of all the constituent materials makes 1.

Besides the effectiveness of the Voigt model to analyze FGM, the so-called Mori-Tanaka model is also used. This scheme is mainly fruitful for materials with regular matrix phase and irregular particulate phase. The conclusion of previous studies revealed that the consequences of both models are not much different from each other; i.e. only 0.65% difference of frequencies were found [2].

There is actually no specified material module for the direct analysis of FGP in ANSYS. Therefore, in the present work, a simple method involving the assignment of properties to each element individually was used. The unidirectional FGP is divided into a number of layers. Each layer has a different material definition depending on the distribution direction.

The Finite Element Method (FEM) is widely used for numerical simulation structural geometry. ANSYS was used to build the FE models and to run the analysis.

In our analysis the plate is analyzed utilizing the four-noded finite strain layered shell element (Shell-181). This element is well-suited for linear, large rotation, and large strain nonlinear applications. In the element domain, both full and reduced integration schemes are supported. It also accounts for load stiffness effects of distributed pressures. Shell-181 can be used for layered applications for modeling composite shells. The accuracy in modeling composite shells is governed by the first-order shear-deformation theory. Figure 5 illustrates the finite element type –Shell 181- used in the analysis [10].

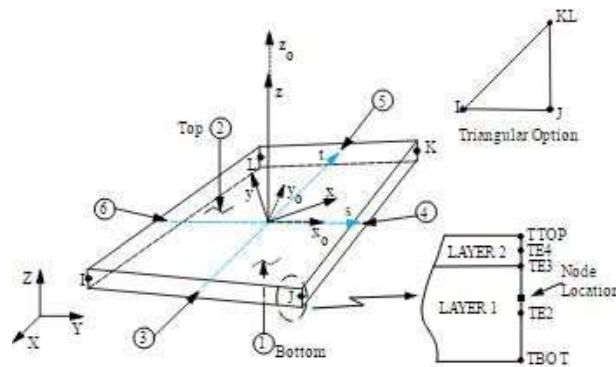


Figure 5. Shell 181 geometry [10]

Verification of the Model

For the present study, a 10 mm thick, 50 cm by 50 cm square plate model is considered. Displacement and stress analysis on a steel, a ceramic plate and a composite homogeneous isotropic elastic ceramic-stainless steel plate having the same size as the FGP are investigated. For the power-law variation-based FGP, two grading parameters are used; $n = 1$ and $n = 1.5$. For the steel, ceramic (Alumina) and composite ceramic-steel based plates, data from Table 1 was used. A uniformly distributed load of 40 kPa (pressure to match the model of a gas turbine blade) is applied to the ceramic face. For the validation of results, analytical results of a simple study case of a cantilever plate uniformly loaded by the same distributed load are compared to the same study case done by ANSYS.

**3rd International Students Science Congress
3-4 May 2019, İzmir - Turkey**

Table 1. Material properties for UNS-S30400/Al₂O₃ [8]

FGM number	Material designation	E (GPa)	Poisson's ratio ν	ρ (kg/m ³)
Material 1	Alumina (Al ₂ O ₃)	320.2	0.3	3970
Material 2	Stainless steel (UNS S30400)	207.78	0.3	8166

The FGM is considered to be a plate of uniform thickness sliced into 10 smaller layers of 1 mm each. There are some models to account for the property variation in the thickness direction, in the literature [11]. For the power function law defined in Eqns. (1-3) is considered in this study.

Using data from Table 1 and the power law in Eqns (1-3), different values of layerwise material properties of 10 layers have been computed and assigned individually to each layer of 1 mm thickness. These values are shown in Table 2 for power law indexes $n = 1$ and $n = 1.5$. The values are computed for the midplane of each layer. Poisson's ratio (ν) is assumed to be constant as 0.3 throughout the plate.

Table 2. Layerwise material properties of the FGM

No	Z (mm)	n = 1			n = 1.5		
		V_1	E (GPa)	ρ (kg/m ³)	V_1	E (GPa)	ρ (kg/m ³)
1	0.5	0.05	314.579	4179.8	0.01118034	318.9431062	4016.912706
2	1.5	0.15	303.337	4599.4	0.05809475	313.6689882	4213.765572
3	2.5	0.25	292.095	5019	0.125	306.1475	4494.5
4	3.5	0.35	280.853	5438.6	0.207062792	296.9220009	4838.835477
5	4.5	0.45	269.611	5858.2	0.301869177	286.2638671	5236.643067
6	5.5	0.55	258.369	6277.8	0.407890917	274.3449031	5681.510287
7	6.5	0.65	247.127	6697.4	0.524046754	261.286664	6168.900178
8	7.5	0.75	235.885	7117	0.649519053	247.1810681	6695.381946
9	8.5	0.85	224.643	7536.6	0.783661279	232.100799	7258.242726
10	9.5	0.95	213.401	7956.2	0.925945463	216.1052111	7855.267162

We considered a square cantilever plate having one clamped edge and three free edges. A study by Chang Fo-van [12] of a uniformly loaded square cantilever plate gives the deflections at the midside of the free edge by three methods: exact solution, Kantorovich method and FEM. These deflection values are compared with those of our model for two different meshes in Table 3. We tested two FE models; first having 98000 (70*70*20) elements and second having 500000 (100*100*50) elements. The agreement between the our results and others is well within the engineering accuracy, as can be seen. The results also revealed that 98000 elements are sufficient for the analysis.

Table 3. Comparison of deflection values for steel and ceramic plates

	Max. deflection in steel plate (m)	Max. deflection in ceramic plate (m)
Exact solution [12]	0.017214189	0.011835751
Kantorovich method [12]	0.015661565	0.010768233
FEM [12]	0.016955746	0.011658058
Present method (98000 elements)	0.016982	0.01102
Present method (500000 elements)	0.016944	0.010996

Results and Discussion

The results obtained using the Shell 181 element type in ANSYS with 98000 mesh elements for the two different power law indexes are given in Table 4. Another case -a composite plate composed of one steel layer and one ceramic layer, each 5 mm thick- is also presented. It is observed from the values that maximum deflection values of composite and FGPs are between those of homogeneous material plates. The deflection value depends upon the power law index.

Table 4. Max. deflection values obtained for composite plate and FGP

	Max. deflection
Steel-ceramic composite plate	0.013836
FGP (n = 1)	0.013567
FGP (n = 1.5)	0.013201

The maximum normal stress due to bending at the clamped edge is calculated analytically as 303.468 MPa for a uniformly distributed load $q = 40$ kPa; while the the same stress value is determined as 303 MPa for our model. Figure 6 illustrates the deflected shape of steel plate subjected to the given uniformly distributed load, for 500000 elements.

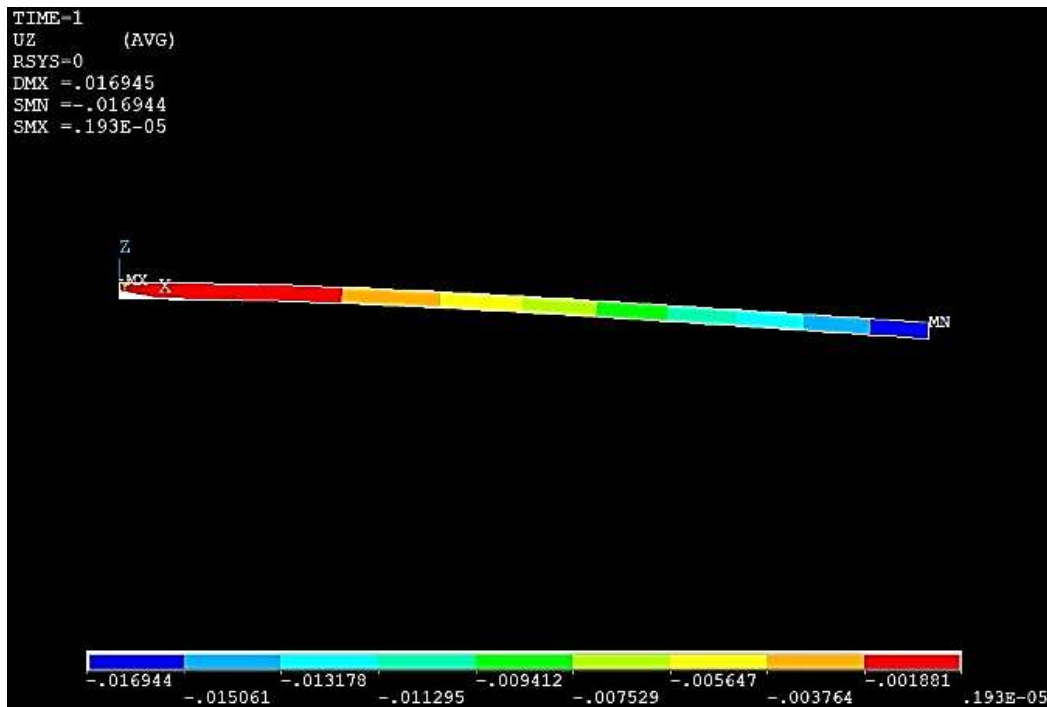


Figure 6. Deflected shape of the steel plate having 500000 elements

Conclusion

FGMs have opened the new horizon of research in the field of advanced materials sciences with a wide range of applications in numerous engineering disciplines. This is because of their design flexibility and remarkable performance. In this paper a square cantilever FGP has been modeled and analyzed using ANSYS APDL. The model is verified by comparing its results with those others in the literature. It has been found that Shell 181 element provides close results to the exact results. It is seen that the FGP presents a behavior that is a hybrid of both materials used and that the way the material distribution is set in the FGP influences its behaviour.

Acknowledgement

This study was supported by the Presidency for Turks Abroad and Related Communities (YTB) within “International Student Academy” Project.

References

- [1] Bhandari M, Purohit K (2014) Analysis of functionally graded material plate under transverse load for various boundary conditions, IOSR Journal of Mechanical and Civil Engineering 10(5): 46-55.
- [2] Naebe M, Shirvanimoghaddam (2016) Functionally Graded Materials: A review of fabrication and properties. Materials Today 5: 223-245.
- [3] Tawakol AE (2014) Stress concentration analysis in functionally graded plates with elliptic holes under biaxial loadings. Ain Shams Engineering Journal 5(3):839-850.
- [4] Ahmed Hassan AH, Kurgan N (2019) A review on buckling analysis of functionally graded plates under thermo-mechanical loads. Int Journal of Engineering & Applied Sciences 11(1):345-368.
- [5] Demirhan P, Taşkın V (2019) Static analysis of simply supported functionally graded sandwich plates by using four variable plate theory. Teknik Dergi 30(2): 8987-9007.
- [6] Ichikawa K (2001) Functionally graded materials in the 21st century: A Workshop on Trends and Forecasts. Springer, Boston, MA.
- [7] Shiota I, Miyamoto Y (1996) Functionally Graded Materials 1996, Elsevier Science B.V. Amsterdam, The Netherlands.
- [8] Singh MS, Thangaratnam K (2014) Analysis of functionally graded plates and shells: stress, buckling and free vibration. Journal of Aerospace Sciences & Technologies V66 N2/803.
- [9] Liu W, Cheng X (2018) A systematic approach based on voxel modelling and APDL analysis for functional-graded-material objects. Procedia CIRP 78:138-143.
- [10] Sharma AK, Sharma P, Chauhan PS, Bhadoria SS (2018) Study on harmonic analysis of functionally graded plates using FEM. Int J Applied Mechanics and Engineering 23(4):941-961.
- [11] Sınır S, Çevik M, Sınır BG (2018) Nonlinear free and forced vibration analyses of axially functionally graded Euler-Bernoulli beams with non-uniform cross-section. Composites Part B: Engineering 148: 123-131.
- [12] Fo-van C (1980) Bending of uniformly cantilever rectangular plates. Applied Mathematics and Mechanics 1(3): 371-383.

Studying the Condition Based Maintenance Dataset of Naval Propulsion Plants Using Regression ANN

Mohamad Mehyo*, Hakan Özcan, Ahmed Hassan Ahmed Hassan
Ondokuz Mayıs Univ., Dept. of Mechanical Engineering, Samsun, Turkey
*Corresponding author: 15210438@stu.omu.edu.tr

Keywords: Artificial Neural Network, MATLAB Neural Networks Toolbox, naval propulsion plants, modeling
Discipline: Mechanical Engineering

Abstract

In this work, applying and experimenting various options effects of a feed-forward artificial neural network (ANN) is used to obtain regression model that predicts GT Compressor decay state coefficient and GT Turbine decay state coefficient of naval propulsion plants. Based on 16 inputs, dataset is obtained from an open online source, consists of huge amount of data point, 11935 data points have been carried out by means of a numerical simulator of a naval vessel (Frigate) characterized by a Gas Turbine (GT) propulsion plant. The different blocks forming the complete simulator (Propeller, Hull, GT, Gear Box, and Controller) have been developed and fine-tuned over the year on several similar real propulsion plants. In view of these observations, the available data are in agreement with a possible real vessel. Many neural networks are created and trained with various settings and sub-datasets and then compared to observe the effect of each variation. After the factors which affects the learning operation was studied. It is taken some of the data in order to test the best ANN that had been learned by taking 20 random values from all data and compare their results with the actual outputs.

1. Introduction

The behavior of a ship under towing operation does not only depend on ship characteristics but it is heavily influenced by a series of boundary conditions which should be carefully considered from time to time. This is not so simple when critical conditions occur and the safety and integrity of the ship are entrusted mainly to the captain experience and sensitivity. Sometimes this is not enough and underestimation of the real situation can compromise seriously the safety of the ship. As a matter of fact, the evaluation of all playing variables and of their consequences on the ship could be very complex and it requires specific calculation tools and large computational time [8]. For this reason, machine learning approaches can be used [9, 10]. One of these methods is artificial neural networks (ANNs).

ANN is a set of processing units called neurons. The ANN can be used to approximate the relationship between input and output signals of the system [1]. The field of ANN has crossed different stages of development. One of the most important steps was achieved when Cybenko (1989) proved that they could be used as universal approximators [2]. A negative stage was brought by the book of Minsky and Papert called Perceptrons. This negative phase was overcome when algorithms for training of multilayer ANN were proposed in the decade of the 80 s. Since then much work has been done regarding ANN and their application to many different fields [3]. The major advantage of using ANN is a non-parametric model while most of the statistical methods are a parametric model that needs a higher background of a statistic. In addition, ANNs are highly non-linear modeling (main advantage). However, ANN is black box learning approach, cannot interpret the relationship between input and output and cannot deal with uncertainty. Neural networks are good at fitting functions. In fact, there is proof that a fairly simple neural network can fit any practical function [7]. Neural Network Toolbox™ provides algorithms, functions, and apps to create, train, visualize and simulate neural networks [4]. It includes algorithms and tools for regression, pattern recognition, classification, clustering, deep learning, time series, and dynamic systems, and many others which cover the usage of ANN models. The workflow for the neural network design process has seven primary steps:

1. Collecting data.
2. Creating the network.
3. Configuring the network.
4. Initializing the weights and biases.
5. Training the network.

6. Validating the network.
7. Using the network.

Some of these steps could be done automatically using default values and settings in the toolbox; however, the user can set every detail by himself. Neural Network Toolbox offers four levels of design i.e. four different levels at which the Neural Network Toolbox™ software can be used [7,11]. The first level is represented by the GUIs. These provide a quick way to access the power of the toolbox for many problems of function fitting, pattern recognition, clustering and time series analysis. In addition, a .m Matlab code script can be generated with the desired level of details copying settings used in the network study. The second level of toolbox use is through basic command-line operations. The command-line functions use simple argument lists with intelligent default settings for function parameters. (user can override all of the default settings, for increased functionality.) The third level of toolbox use is customization of the toolbox. This advanced capability allows the user to create custom neural networks, while still having access to the full functionality of the toolbox. The fourth level of toolbox usage is the ability to modify any of the code files contained in the toolbox. Every computational component is written in MATLAB® code and is fully accessible.

2. Regression ANN in MATLAB

Regression (Fit Data) in Neural Network Toolbox in Matlab can be accessed using GUI or command-line functions. There are two GUIs can be used to design and train the network:

1. Neural Network Tool (nntool), which is the general neural network tool, offers full control of settings. Using this GUI, the user can design any type of neural network, not only the regression ANN.
2. Neural Fitting tool (nftool), which leads the user through solving a data fitting problem, solving it with a two-layer feedforward network trained with Levenberg-Marquardt or scale conjugate gradient back-propagation. It has limited set of options. The user can select data from the MATLAB® workspace or use one of the example datasets. After training the network, evaluate its performance using mean squared error and regression analysis. Further, analyze the results using visualization tools such as a regression fit or histogram of the errors. The user can then evaluate the performance of the network on a test set [4,7].

3. Preparing data and settings

3.1. Data Collection

Dataset is obtained from an open online source, consists of huge amount of data point, 11935 data points have been carried out by means of a numerical simulator of a naval vessel (Frigate) characterized by a Gas Turbine (GT) propulsion plant. The different blocks forming the complete simulator (Propeller, Hull, GT, Gear Box, and Controller) have been developed and fine-tuned over the year on several similar real propulsion plants. In view of these observations, the available data are in agreement with a possible real vessel. In this release of the simulator it is also possible to take into account the performance decay over time of the GT components such as GT compressor and turbines [6,8]. Dataset features can be summarized as:

3.2. Sub dataset selection

Since the main goal of this work is to apply and test regression with neural network, so no need for all the dataset (Table 1). Only a smaller subset is systematically picked from the dataset to train, validate and initial test of the network. Matlab Neural Network toolbox divides the dataset to subsets of train, validate and test, by default percentages as 75, 15 and 15%. Since we have huge dataset, we can run the test on it, so we will reduce the test subset to 0%, training subset will be 75% and validation subset will be 25%. Finally, test is performed with all the data points from the original dataset and compared with different subset sizes [11].

Table 1. Features (dataset) summary [6]

Feature	Symbol	Type	minimum	maximum	unit
Lever position	lp	Input	1.138	9.3	----
Ship speed	v	Input	3	27	knots
Gas turbine (GT) shaft torque	GTT	Input	253.547	72784.87	kN m
GT rate of revolutions	GTn	Input	1307.67	3560.741	rpm
Gas generator rate of revolutions	GGn	Input	6589.002	9797.103	rpm
Starboard propeller torque	Ts	Input	5.304	645.249	kN
Port propeller torque	Tp	Input	5.304	645.249	kN
High pressure (HP) turbine exit temperature	T48	Input	442.364	1115.797	K
GT compressor inlet air temperature	T1	Input	288	288	K
GT compressor outlet air temperature	T2	Input	540.442	789.094	K
HP turbine exit pressure	P48	Input	1.093	4.56	bar
GT compressor inlet air pressure	P1	Input	0.998	0.998	bar
GT compressor outlet air pressure	P2	Input	5.828	23.14	bar
GT exhaust gas pressure	Pexh	Input	1.019	1.052	bar
Turbine injection control	TIC	Input	0	92.556	%
Fuel flow	mf	Input	0.068	1.832	kg/s
GT compressor decay state coefficient	CGTC	Output	0.95	1	----
GT turbine decay state coefficient	GTC	Output	0.975	1	----

3.3. Normalization

One way to improve training networks is to linearly normalize inputs and outputs to a certain range. The standard normalization maps the feature to the range of $(-1, 1)$; which is default in the Matlab Neural Network toolbox; both inputs and outputs are normalized by default. Other range may be used, e.g. $(0.1, 0.9)$. Another normalization practice is to map feature to a range with specified mean and variance. Typically the mean would be 0 and standard deviation would be 1. Since Matlab Neural Network toolbox makes this step for us, we do not have to worry about it. However, mapping to range $(0.1, 0.9)$ is also applied and results are compared to the use of not normalized data [11].

3.4. Setting of networks

* **Two-layer feed-forward network (default):** We are using the tan-sigmoid transfer function in the hidden layer, and a linear output layer. This is the standard network for function approximation. This network has been shown to be a universal approximating network.

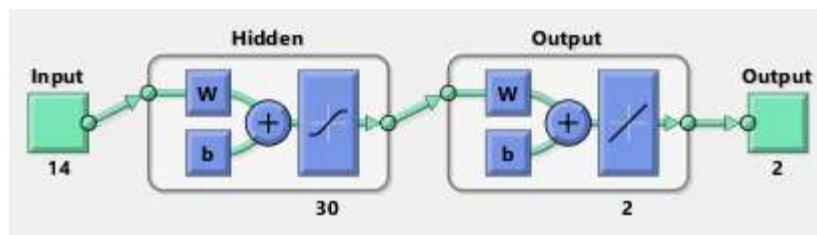


Figure 1. Regression neural network structure

* **Training algorithms:** here we will examine two algorithms: (trainlm) Levenberg Marquardt algorithm (default) and (trainbr) Bayesian regularization algorithm.

* **Hidden layer size:** The number of neurons in the hidden layer will depend on the function to be approximated, Figure 1 shows an example of regression neural network structure. This is something that cannot generally be known before training. Levenberg-Marquardt algorithm needs the number of neurons (hidden layer size) to be given to the algorithm.
In addition, the effect of the hidden layer size will be examined in this study [11].

4. Application and Results

In this study:

* **Test:** is always refers to test of all the dataset (11934 observations) which gives results that are more realistic.

* **Performance:** is always the mean of squared errors (MSE).

Here we study many aspects of the neural networks:

4.1. Variation of results using the same settings and sub-datasets data:

Training the same network with the same settings and the same dataset gives different output each run; because of [11]:

- The randomness of the initial weights and bias at every training run of the neural network.
- The randomness of dividing the dataset into the train, validate and test sets.

For this experiment, settings which are used for each run are shown in Table 2.

Table 2. The settings used to train the same network with the same settings

Dataset size	50
Variables used:	lp,v,GTT,GTn,GGn,Ts,Tp,T48,T2,P48,P2,Pexh,TIC,mf
Hidden layer size (#neurons)	30
Training Function	Levenberg-Marquardt algorithm (trainlm)

Results are shown in Table 3; we can observe this behavior of variation in resulted network each run. By looking at the resulted performance (MSE) values for the same test data, we can see that it varies between 0.73313 up to 0.9474. And the resulted performance (MSE) values varies between 0.00012541 and 1.8885e-05.

Table 3. Variation of results

Run	Training Performance	Validation Performance	Training Regression coefficient	Validation Regression coefficient	Test Performance	Test Regression coefficient	Stopping Criteria	#Epochs	Best Epoch
1	1.7933e-06	6.0999e-06	0.99669	0.98533	2.1195e-05	0.94339	Validation	35	29
2	2.4759e-05	9.4221e-05	0.94962	0.81841	6.8137e-05	0.79039	Validation	21	15
3	8.106e-06	2.1541e-05	0.98407	0.96289	2.4932e-05	0.93202	Validation	40	34
4	1.9351e-06	1.2967e-05	0.99626	0.9755	1.8885e-05	0.9474	Validation	44	38
5	7.5073e-06	1.8625e-05	0.98602	0.9702	3.133e-05	0.9219	Validation	40	34
6	8.4965e-09	6.1897e-06	0.99998	0.99046	2.9636e-05	0.92382	Minimum gradient	78	78
7	3.8544e-06	1.8469e-05	0.99288	0.94557	2.3733e-05	0.93681	Validation	56	50
8	3.5363e-05	0.00010208	0.93415	0.80189	0.00012541	0.73313	Validation	25	19
9	1.4276e-08	1.935e-06	0.99998	0.99702	2.9024e-05	0.91884	Validation	65	59
10	5.1905e-06	1.7963e-05	0.99042	0.97303	3.1927e-05	0.923	Validation	36	30

4.2. Effect of different values of hidden layer size (number of neurons)

To examine the effect of the hidden layer size, the network is trained with the settings in Table 4.

**3rd International Students Science Congress
3-4 May 2019, İzmir - Turkey**

Table 4. The settings used to examine the effect of the hidden layer size

Dataset size	50
Variables used:	lp,v,GTT,GTn,GGn,Ts,Tp,T48,T2,P48,P2,Pexh,TIC,mf
Hidden layer size (#neurons)	[1,2,3,4,5,6,7,8,9,10,15,20,25,30,40,50,70,100]
Training Function	Levenberg-Marquardt algorithm (trainlm)

Note that each value of the hidden layer size is trained for 1 time. This is done to overcome the variation behavior shown in aspect 1. From the results in Table 5, it can be observed that for the same dataset and settings higher size of the hidden layer is not always useful for the network. Comparing the performance (MSE) values for the test dataset, we can notice that at size 7 the worst network obtained, while the best performance obtained with a size of 3. The tendency to have a better network with smaller hidden layer size indicates that the relationship is strongly linear; given that zero hidden layer size means just a linear relationship.

Table 5. Effect of different values of hidden layer size

Hidden Layer Size	Training Performance	Validation Performance	Training Regression coefficient	Validation Regression coefficient	Test Performance	Test Regression coefficient	Stopping Criteria	#Epochs	Best Epoch
1	4.4797e-05	3.3736e-05	0.90167	0.94308	0.00023087	0.65377	Validation	15	9
2	3.5492e-05	5.5779e-05	0.92415	0.90424	0.00012118	0.75254	Validation	29	23
3	0.00021505	0.00012309	0.49263	0.7856	0.00016401	0.38063	Validation	8	2
4	3.7635e-08	1.2577e-06	0.99993	0.99787	3.537e-05	0.92151	Validation	86	80
5	5.5014e-07	9.0325e-06	0.99892	0.98621	4.3323e-05	0.88726	Validation	37	31
6	2.0001e-05	9.8399e-05	0.95728	0.82861	9.1732e-05	0.74611	Validation	32	26
7	8.9202e-10	9.0773e-07	1	0.99816	1.5529e-05	0.95579	Validation	111	105
8	1.8518e-05	4.0246e-05	0.96986	0.84981	5.5973e-05	0.85245	Validation	26	20
9	5.6209e-06	1.0494e-05	0.98935	0.97837	3.1678e-05	0.92456	Validation	36	30
10	1.1094e-08	9.9194e-06	0.99998	0.98653	2.8237e-05	0.92781	Minimum gradient	73	73
15	7.4451e-07	1.0878e-05	0.99851	0.98191	0.0001381	0.76461	Validation	49	43
20	1.066e-06	9.5245e-06	0.99778	0.98508	2.4596e-05	0.93632	Validation	66	54
25	5.2964e-10	1.3729e-06	1	0.99765	3.5101e-05	0.91515	Minimum gradient	155	155
30	1.2719e-09	2.6812e-07	1	0.99962	1.479e-05	0.95926	Minimum gradient	77	77
40	9.0121e-06	4.72e-05	0.98274	0.91495	6.7694e-05	0.84406	Validation	35	29
50	1.4118e-08	7.0442e-06	0.99997	0.98841	1.8173e-05	0.95269	Validation	62	56
70	7.3678e-09	1.8732e-05	0.99999	0.9635	0.00015692	0.74119	Validation	67	61
100	6.5676e-06	3.5187e-05	0.98578	0.9546	4.6524e-05	0.8761	Validation	23	17

4.3. Effect of different train dataset size

Here we will examine different sizes of training datasets, which actually train and validate datasets [11]. The settings used are given in Table 6.

Table 6. The settings used to examine different sizes of training datasets

Dataset size	[30,40,50,60,100,150,200,250,300]
Variables used:	lp,v,GTT,GTn,GGn,Ts,Tp,T48,T2,P48,P2,Pexh,TIC,mf
Hidden layer size (#neurons)	30
Training Function	Levenberg-Marquardt algorithm (trainlm)

The network is trained for each dataset size for 10 times to overcome the variation in results mentioned in aspect 1. From the results in Table 7, we can observe that by increasing the train dataset

size generally networks improve. Notice that at small dataset size any increase results in improved network performance. In the other hand, by reaching a dataset size of 100 only little improvements is obtained by increasing in the dataset size.

Table 7. The effect of different train dataset size

Dataset Size	Training Performance	Validation Performance	Training Regression coefficient	Validation Regression coefficient	Test Performance	Test Regression coefficient	Stopping Criteria	#Epochs	Best Epoch
30	4.1554e-08	5.3832e-06	0.99994	0.99104	3.2126e-05	0.90781	Validation	64	58
40	3.8476e-09	2.6031e-06	0.99999	0.99621	2.5067e-05	0.94439	Minimum gradient	94	94
50	2.1884e-09	6.3071e-06	1	0.98888	1.2228e-05	0.96515	Minimum gradient	122	122
60	2.32e-06	1.6798e-05	0.99633	0.97331	1.2037e-05	0.96742	Validation	37	31
100	1.0423e-08	2.3211e-07	0.99998	0.99954	1.9465e-07	0.99947	Validation	81	75
150	2.9827e-09	5.4834e-08	0.99999	0.99991	3.787e-08	0.99989	Minimum gradient	85	85
200	1.799e-09	3.0805e-08	1	0.99993	2.2528e-08	0.99994	Minimum gradient	195	195
250	1.7641e-09	2.7389e-08	1	0.99994	1.26e-08	0.99996	Minimum gradient	140	140
300	4.6151e-09	9.6793e-09	0.99999	0.99998	1.1296e-08	0.99997	Minimum gradient	130	130

4.4. Effect of using different training function

In all previous sections we used Levenberg-Marquardt algorithm (trainlm) function. Here we will examine and compare another famous training function Bayesian regularization (trainbr) which is an improved algorithm to the former one [11]. The settings used are shown in Table 8.

Table 8. The settings used to examine and compare Bayesian regularization (trainbr) training function

Dataset size	50
Variables used:	lp,v,GTT,GTn,GGn,Ts,Tp,T48,T2,P48,P2,Pexh,TIC,mf
Hidden layer size (#neurons)	30
Training Function	Levenberg-Marquardt algorithm (trainlm) or Bayesian regularization (Trainbr)

From the result in Table 9 we can notice that for the same settings and dataset Levenberg-Marquardt algorithm (trainlm) is better than Bayesian regularization (trainbr) function. It is also notable that the Bayesian regularization (trainbr) has no validation subset; only training set. Lastly, notice that the number of epochs needed to obtain the network, it is more than of those needed by Bayesian regularization (trainbr) function.

Table 9. The effect of using different training function

Used Function	Training Performance	Validation Performance	Training Regression coefficient	Validation Regression coefficient	Test Performance	Test Regression coefficient	Stopping Criteria	#Epochs	Best Epoch
Trainlm	8.0195e-08	2.9394e-06	0.99984	0.99421	3.0518e-06	0.99191	Validation	50	44
Trainbr	0.00017531	NaN	0.62199	NaN	0.00015315	0.47165	Maximum MU	32	3

4.5. Effect of normalizing dataset before manipulate it to network training

Here dataset is normalized to the range (0.1 0.9) and the quality of the resulted network is compared to a network trained with a not normalized dataset, which is normalized by Matlab Neural Network Toolbox; which has two options for normalization. The first is the standard normalization to the range of (-1 1), using the function (mapminmax) which is the default in the toolbox. Secondly, is the normalization for a range with a specified mean (0) and standard variation (1), using the function (mapstd) [11]. The settings used are shown in Table 10.

Table 10. The settings used to normalize dataset before manipulate it to network training

Dataset size	50 (lp,v,GTT,GTn,GGn,Ts, Tp, T48, T2, P48, P2, Pexh, TIC and mf) with mapminmax normalization (default)
Variables used:	(lp,v,GTT,GTn,GGn,Ts, Tp, T48, T2, P48, P2, Pexh, TIC and mf) with mapstd normalization (lp,v,GTT,GTn,GGn,Ts, Tp, T48, T2, P48, P2, Pexh, TIC and mf) normalized to the range [0.1 0.9]
Hidden layer size (#neurons)	30
Training Function	Levenberg-Marquardt algorithm (trainlm)

From the result in Table 11 notice that performance values of the normalized data are also normalized, so they are here very small values. By comparing the regression (correlation) and the epochs numbers, we could notice that these their methods are equivalent. Using the not normalized data is easier in reading results and more convenient since Matlab Neural Network toolbox does it for us anyway.

Table 11. Effect of normalizing dataset

Dataset used	Training Performance	Validation Performance	Training Regression coefficient	Validation Regression coefficient	Test Performance	Test Regression coefficient	Stopping Criteria	#Epochs	Best Epoch
Matlab normalized (mapminmax)	6.3561e-07	1.0846e-05	0.99875	0.98572	3.0018e-05	0.92551	Validation	53	47
Matlab normalized (mapstd)	2.958e-10	1.1483e-07	1	0.99968	3.8416e-06	0.98944	Minimum gradient	110	110
Normalized to range [0.1 0.9]	2.9215e-05	0.0031949	0.99987	0.98405	0.003383	0.97997	Validation	36	30

5. Test Results

After the factors which affect the learning operation was studied. It is taken some of the data in order to test the best ANN that had been learned by taking 20 random values from all data and compare their results with the actual outputs. The results are illustrated in Figures 2 and 3.

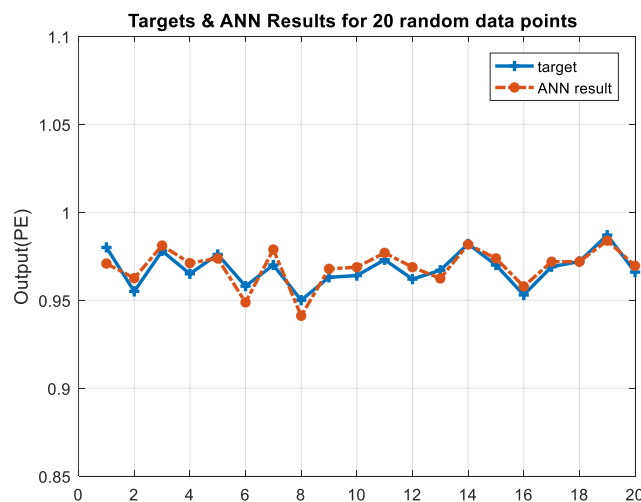


Figure 2. The comparison between the actual results of the GT Compressor decay state coefficient and the test results of the GT Compressor decay state coefficient

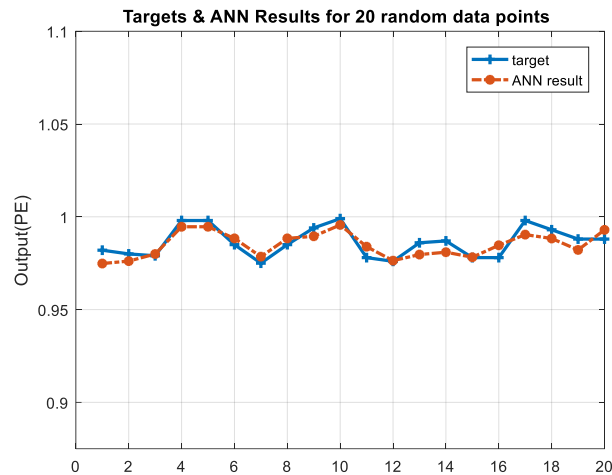


Figure 3. The comparison between the actual results of the GT Turbine decay state coefficient and the test results of the GT Turbine decay state coefficient

6. Conclusion

Many neural networks are created and trained with various settings and sub datasets and then compared to observe the effect of each variation.

It is observed that:

1. The neural network in Matlab with the default setting have randomness in its behavior due to the randomness of the initial weights and bias creation and due to the randomness of dividing the dataset between train, validate and test sets. It can be avoided using given initial weights and bias values, and using (divideind) as the (divideFcn) of the network, which makes the division of dataset explicit to whatever the user decides.
2. Increasing the number of neurons does not always lead to increased quality of the model.
3. Bigger dataset (more data points for the same variables) provides better networks.
4. Different training functions lead to different model quality, in this work Levenberg-Marquardt algorithm better than Bayesian regularization performed for the same setting and dataset.
5. When using Matlab Neural Network toolbox, there is no need to normalize dataset, it is done by the program; in addition, two different normalization types are provided by the toolbox.

References

- [1] Rebizant W, Szafran J, Wiszniewski A (2011) Digital Signal Processing in Power System Protection and Control. Springer-Verlag London
- [2] Cybenko G (1989) Approximation by superposition of a Sigmoidal function. Mathematics of Control, Signals and Systems 2: 303-314.
- [3] Dias FM, Mota AM (2001) Comparison between different control strategies using neural networks. Ninth Mediterranean Conference on Control and Automation, Dubrovnik, Croatia.
- [4] Demuth H, Beale M (2002) Neural Network Toolbox User's Guide. The Mathworks Inc.
- [5] Haykin S (ed) (2001) Kalman Filtering and Neural Networks. Wiley-Interscience.
- [6] Coraddu A, Oneto L, Ghio A, Savio S, Anguita D, Figari M (2016) Machine learning approaches for improving condition-based maintenance of naval propulsion plants. Journal of Engineering for the Maritime Environment 230(1): 136-153.
- [7] Hagan MT, Demuth HB, Beale MH, De Jesus O, Neural Network Design. 2nd Edition ebook.
- [8] Altosole M, Boote D, Brizzolara S, Viviani M (2013) Integration of numerical modeling and simulation techniques for the analysis of towing operations of cargo ships. International Review of Mechanical Engineering (IREME) 7(7): 1236-1245.
- [9] Russell S, Norvig P (1995) Artificial Intelligence: A modern approach. Pearson International.
- [10] Rich E, Knight K (1991) Artificial Intelligence. McGraw-Hill.
- [11] Elfaki E, Ahmed Hassan AH (2018) Prediction of electrical output power of combined cycle power plant using regression ANN model. Int J Comp Science Control Engineering. 6(2): 9-21.

Mechatronics Engineering / Mekatronik Mühendisliđi

Synchronization of Diffusionless Lorenz Chaotic System for Masking Data

Mohammed Mansour*, Sakarya Univ., Dept. of Mechatronics Engineering, Esentepe Campus, Sakarya, Türkiye
*Corresponding author: mohammed.mansour@ogr.sakarya.edu.tr

Keywords: chaos, chaotic system, synchronization, masking
Discipline: Mechatronics Engineering

Abstract

Synchronization is a model that occurs when large number of individuals act or do work together in the same time. Synchronization process appears in different systems and application like oscillators in mechanical systems and chaotic systems. Chaotic systems are a type of nonlinear systems which show unpredictable and complex behavior than other systems. The applications of chaos and chaotic system are available in many areas like management, economic and secure transformation. Chaotic systems can be used for masking data through synchronizing process. Chaotic systems are very sensitive to their initial condition which is the important feature of a chaotic system. So, applying synchronization in chaotic system for secure transforming of analog signal in different applications and especially in industrial application is needed. By this process, a simple way of masking analog signal in some industrial applications can be achieved. In this article, a simulated system for masking an analog signal through synchronization process is proposed. The method and system design ways are shown and analyzed with an example using Diffusion less Lorenz chaotic system. It was clear from the results that the original signal and the signal at the receiver were same.

Introduction

Chaos or chaotic system are non-linear systems which show very high sensitivity to their initial conditions. Chaos is a special case in the non-linearity systems. The definition of chaos can be described in this sentence: chaos represents the irregularity in a regular form. Chaotic systems are completely non-linear systems and they are deterministic nonlinear dynamical systems, so they are complex systems. The earliest observation of chaos in electronics circuits was found in neon bulb oscillator studies by Van der Pol Van der Mark in 1927. Van der Pol Van der Mark described the chaos as noise [1] – [3]. Chaotic systems are dynamical systems which show complex behavior [4]. The following features are seen in chaotic systems: irregular behavior in the time dimension, precision in initial conditions, unlimited number of different periodic oscillation, wide power spectrum like noise, positive Lyapunov [5], [6]. Up to now, various chaotic systems have been introduced such as Lorenz, Rikitake, Rossler, Sprott, Chen, Pehlivan, etc. [7] – [11]. After establishing the mathematical model of chaos, it can be applied in many different areas which are engineering, computers, communications, medicine and biology, management and finance, consumer electronics, etc. [12]. One of the popular practical applications of chaotic systems is secure communication [13] – [16].

Encryption of data is not a new need, since old time people need to use it. The difference is before it was not electronic but now it is. Encryption aims to secure data, so just few people can see them. The high request of saving data in transforming required to find ways for encrypt them. In it is most basic form, encryption is the process of encoding data, making it unintelligible and scrambled [17]. The need of information transmission requires high security to save them from different attacks, this issue was able to be solved using chaos and chaotic system. Since chaos and chaotic systems are very sensitive to their initial conditions, the application of encryption using chaos is important in telecommunication and transmission technology through Synchronization process. Using of Chaos in encrypting data is a very critical method since the chaos systems can be applied together in the same time. This process is defined by synchronization process. Systems are applied together in the same time so, masking of data could be achieved during the process. Different chaotic systems were discovered, using any of them for this process guarantee hiding the information by a mean of masking them. In this article, using Diffusion less Lorenz chaotic System for masking data was proposed based on synchronization process. This proposed work can be used for having secure transferring of analog signals in industrial applications.

Methodology

Synchronization process for any chaotic system can be applied using both identical and cascade methods. These methods have different connection way for the used chaotic system but they both lead to the same mission. Diffusion less Lorenz system equations were used here. For the building of the circuit, using of Both MATLAB Simulink tool or ORCAD Pspice program, simulation of the circuits can be achieved. For the input data, it can be any signal like sine or cosine signal. Chaotic system was applied with its specific initial condition and in the same time, the same system was applied with different initial conditions and inserting the data to be masked, by this way masking process is done.

Before the simulation of the synchronizing circuit, the simulation of the Diffusion Less Lorenz system circuit is given using ORCAD PsPice program. The system equations are given by[18]:

$$\dot{x} = y - x$$

$$\dot{y} = xz$$

$$\dot{z} = -xy + \bar{\alpha}$$

With constant $\bar{\alpha} = 1$ and initial conditions of the system are as follow $X(0) = 1, Y(0) = -1, Z(0) = 0.01$. As mentioned before, any small change in the initial condition changes the system totally. The design of the system using ORCAD Pspice program are as follow. In the circuit below, operation amplifiers with different elements like resistors and capacitors can be used to design analog circuits. The result of these analog circuits is almost like the result of real circuit.

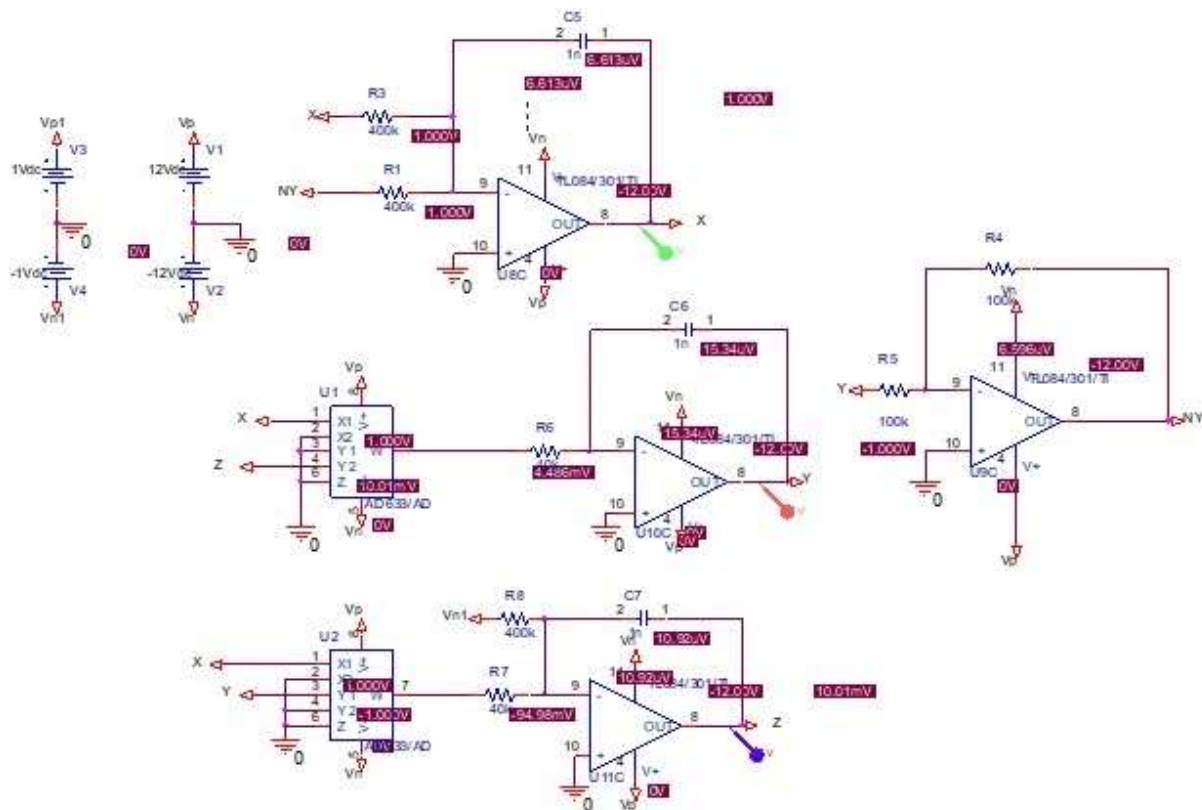


Figure 1. Design of the circuit using Op-Amplifiers

The results of the simulation of the proposed system are given by the figures shown below:

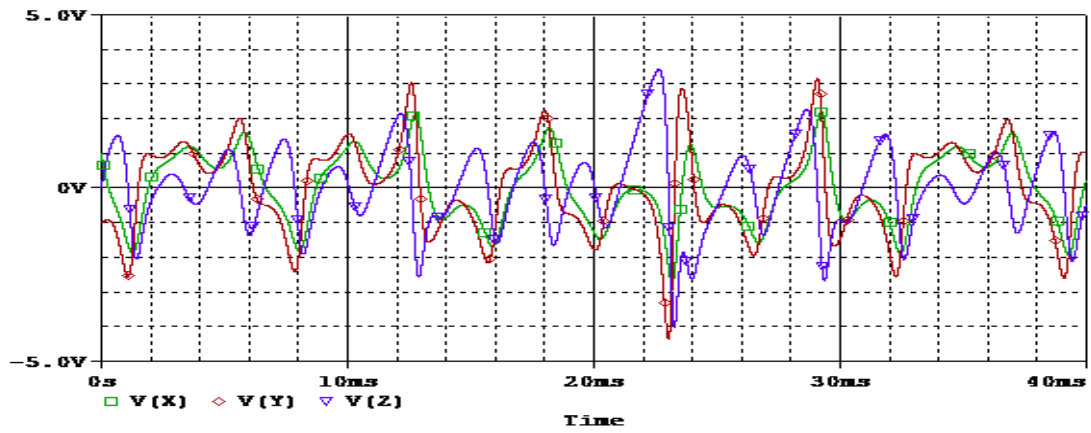


Figure 2. X, Y and Z with time

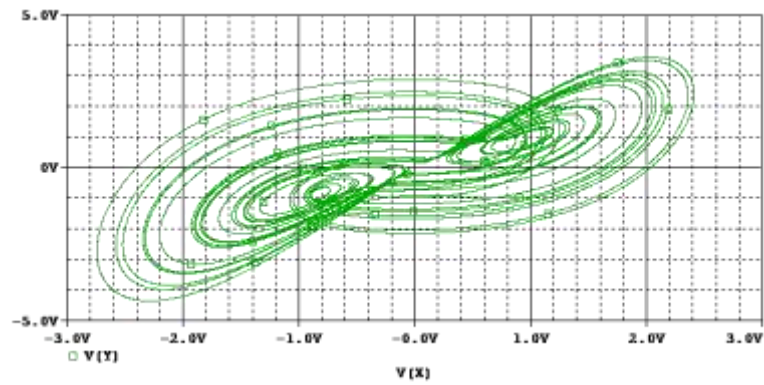


Figure 3. X and Y

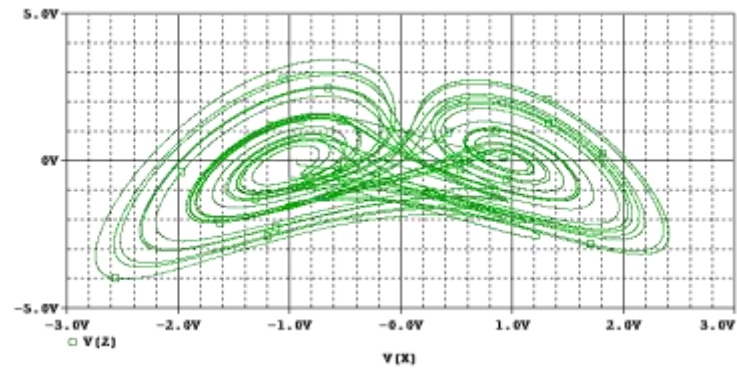


Figure 4. X and Z

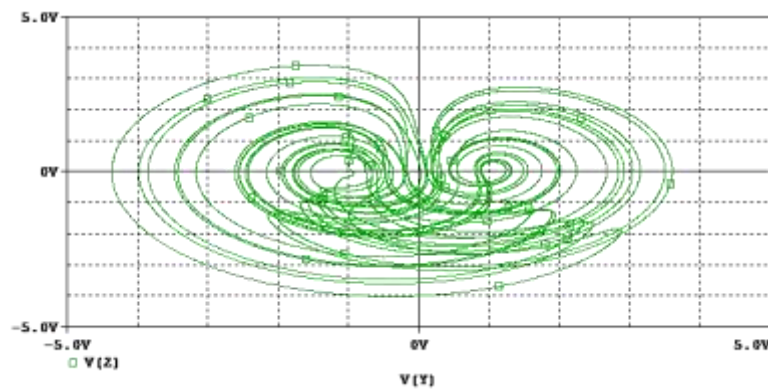


Figure 5. Y and Z

These shapes are called strange attractors which make chaotic system differs from other system. They are used sometime to check whether one system is a chaos system or not. There is other method used for checking the system to decide whether it is chaos or not which is Lyapunov exponents method. This method demands mainly on the initial conditions behavior of a system. It checks the sensitivity of the system to its initial conditions.

As mentioned before, synchronization of the chaotic system can be design using identical or cascade method. In this article, identical method was used. The system design in this case is given by this following figure, the simulation of the system was designed again using ORCAD Pspice program, as mentioned before the results of these simulation give results which is same as real circuit. The other method which called Cascade, use different way of connection but both methods lead to the same result.

Mainly, the system contains two parts, master system (sender) and slave system (receiver). The original in identical method has three inputs which are represented by x, y and z. Using one of these inputs as a main input for the other part of the main system which is the slave system. By this way one can synchronize any signal by adding it to the used input in the slave system which is represented here by x.

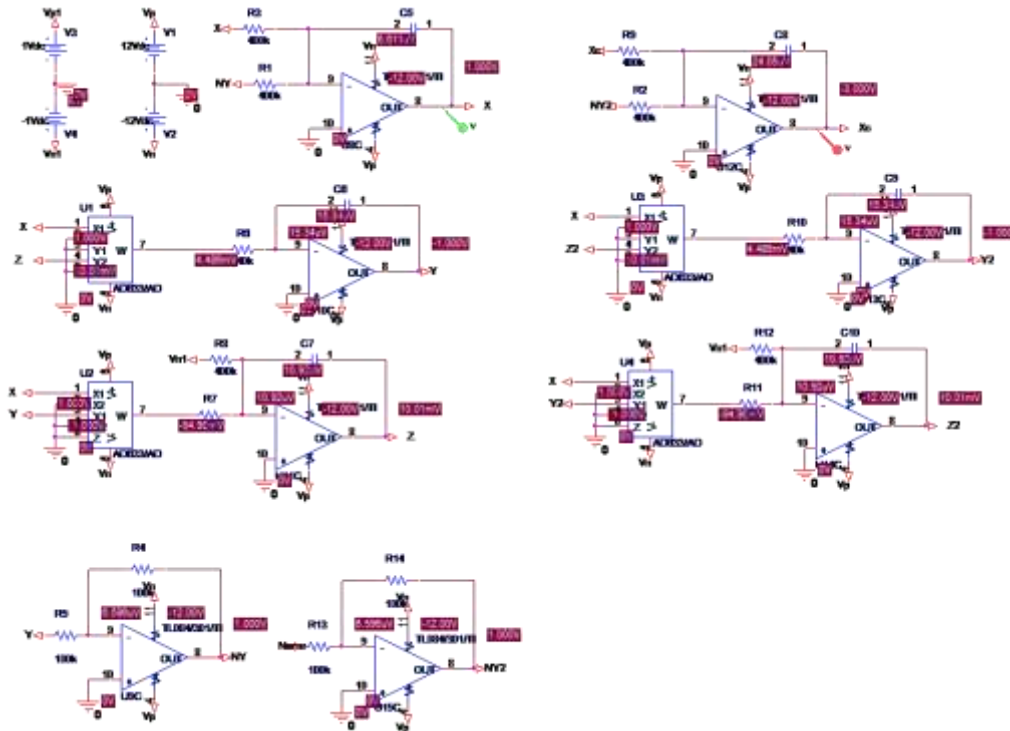


Figure 6. Identical design of the system

The behavior of the system before and after the synchronization process are given in the following figures:

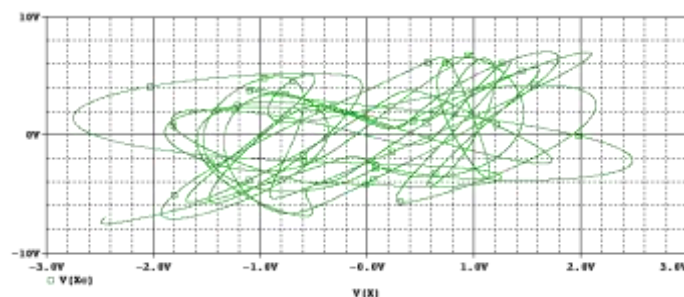


Figure 7. X and Xc before the synchronizing process

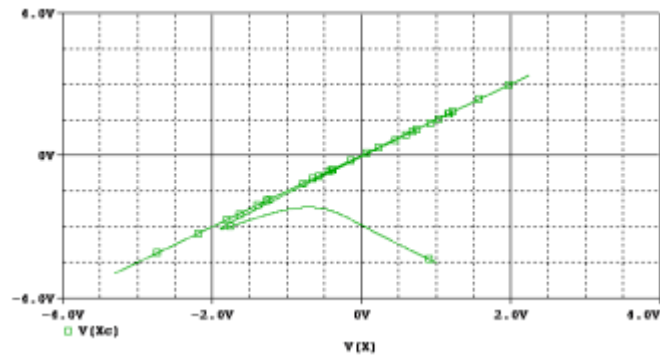


Figure 8. X and Xc after the synchronizing process

Results

The result of synchronizing process is shown below. X of the master system, Xc of the slave system and error are simulated with time. It appears that the difference between X and Xc is zero through the synchronizing process.

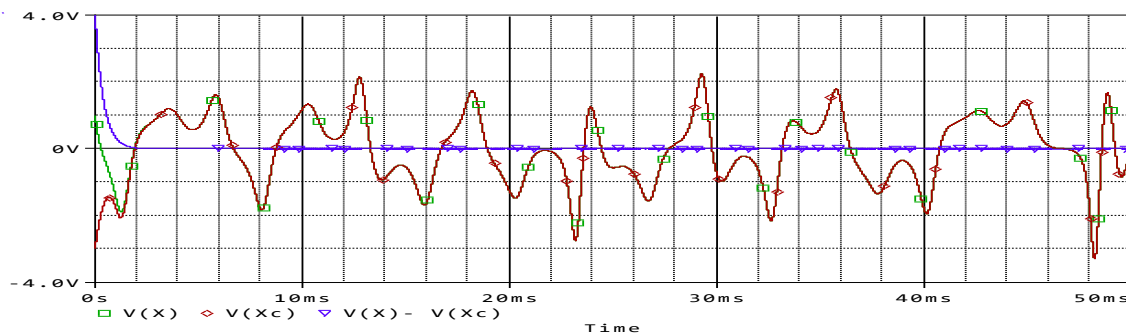


Figure 9. X, Xc and the error after synchronizing process

By this way any analog signal can be added to the X of master system and synchronizing it with X of master system in the slave system. For clear understanding, the result of such a system is given in the following figures. The system design is exactly as given before with just adding the analog signal to the X in the master system.

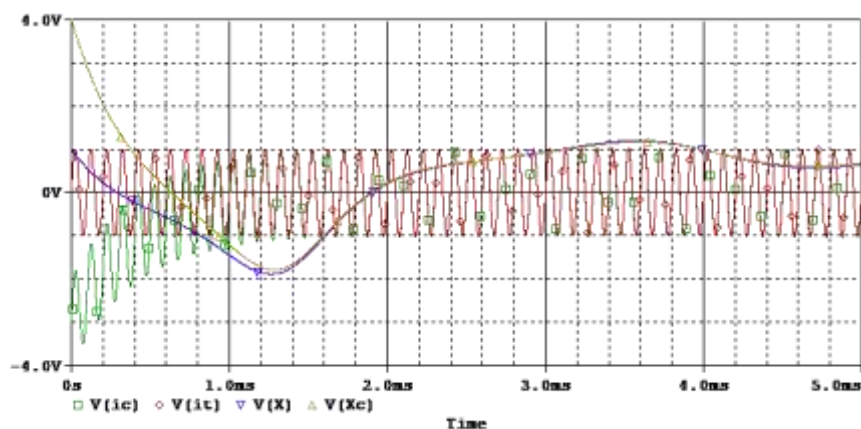


Figure 10. X, Xc, analog signal(it) before and (ic) after synchronizing process

Here in this system, we applied an analog signal which is a sine wave, (it) represents the original signal, (ic) represents the last taken signal at the slave system(receiver). In the next figure, S represents the encrypted signal. It appears from the error that the difference between the original signal and the signal at the receiver are the same ($it = ic$). The original signal in the receiver is given by subtracting the encrypted signal S from Xc in the slave system.

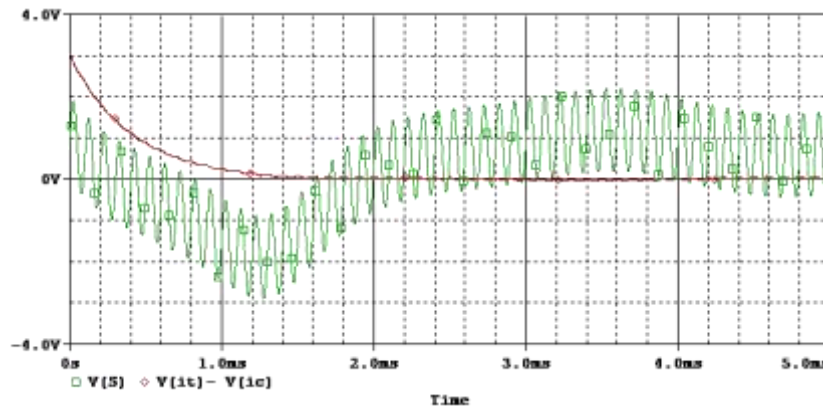


Figure 11. S signal which represents added signal of X and an analog signal, the error between analog signal before and after synchronizing process

Conclusion

In some industrial applications, the need of encrypting data request to design a system which guarantee having a system which can mask data with very high security. Chaos and Chaotic system give the chance for having such system which can mask the analog data with cheap elements. The applications of chaotic systems can be founded in many applications and for different aims. In a secure communication, the application of chaos and chaotic system is important due to high security which can be achieved based on such a system. Since chaotic systems are synchronized in the same time and by this way, a simple and important masking way of analog data can be done.

The applications of chaotic systems in masking and encrypted data is famous topic to study. In a future work, using of chaotic system for encrypting a digital image can be discussed. Another application which can be studied is applying chaotic systems in Artificial Neural Network applications.

References

- [1] Pol BVD, Mark JVD (1924) Frequency DE multiplication. *Nature* 120: 363-364.
- [2] Chua LO, Kennedy MP (1986) Van der Pol and chaos, *IEEE Trans. Circuits Syst.* 33: 97- 980.
- [3] Kennedy MP (1995) Experimental chaos from autonomous electronic circuit, *Phil. Trans.: Phys. Sci. Eng.* 353: 13-32.
- [4] Jost J (2005) *Dynamical Systems: Examples of Complex Behavior*. Springer, New York.
- [5] Kia B (2011) *Chaos computing from theory to application*, Dissertation, Arizona State University.
- [6] de la Fraga LG, Tlelo-Cuautle E, Carbajal-Gomez VH, Munoz-Pacheco JM (2012), On maximizing positive Lyapunov exponents in a chaotic oscillator with heuristics, *Rev. Mex. Fis.* 58: 74-281.
- [7] Rikitake T (1958) Oscillations of a system of disk dynamos, *Math. Proc. Camb. Phil. Soc.* 54: 89-105.
- [8] Rossler OE (1976) An equation for continuous chaos, *Phys. Lett, A*, 57: 397-398.
- [9] Sprott JC(1994) Some simple chaotic ows, *Phys. Rev. E* 50: 647-650.
- [10] Pehlivan, Uyaroglu Y (2010) A new chaotic attractor from general Lorenz system family and its electronic experimental implementation, *Turk. J. Elec. Eng. Comp. Sci.*, 18: 171-184.
- [11] Chen G, Ueta T (1999) Yet another chaotic attractor, *Int. J. Bifurcat. Chaos*: 1465-1466.
- [12] Ditto W, Munakata T (1995) Principles and applications of chaotic systems, *Commun. ACM* 38: 96-102.
- [13] Xing-Yuan W, Ming-Jun W (2009) A chaotic secure communication scheme based on observer, *Commun. Nonlinear Sci. Numer. Simulat.* 14: 1502-1508.
- [14] Xing-Yuan W, Yong-Feng G (2010) A switch-modulated method for chaos digital secure communication based on user dened protocol, *Commun. Nonlinear Sci. Numer. Simulat.* 15: 99-104.
- [15] Liu H, Wang X, Quanlong Z (2011) Asynchronous anti-noise hyper chaotic secure communication system based on dynamic delay and state variables switching, *Phys. Lett. A*, 375: 2828-2835.

3rd International Students Science Congress
3-4 May 2019, İzmir - Turkey

- [16] Xingyuan X, Bing X, Huaguang Z (2010) A multi-ary number communication system based on hyperchaotic system of 6th-order cellular neural network, Commun. Nonlinear Sci. Numer. Simulat 15: 124-133.
- [17] What is encryption (2018) Technology World. <https://www.techworld.com/security/what-is-encryption-3659671>.
- [18] Schrier GVD, Maas Lrm. (2000) The diffusionless Lorenz equations; Shil'nikov bifurcations and reduction to an explicit map, Physica: D,141: 19-36.

Development of a Multi Degrees of Freedom Redundant Reconfigurable Planar Parallel Manipulator with 2 DOF Planar Detachable Serial Dyad

Osman Akın, Basheer Altawil, Adem Candemir, Esra Uçar, Saran Sapmaz
İzmir Kâtip Çelebi Univ, Dept. of Mechatronics Engineering, İzmir, Türkiye
Corresponding author: basheeraltaweel@gmail.com*

Keywords: inverse task, forward task, manipulator, dexterous workspace, Ziegler-Nichols

Discipline: Mechatronics Engineering

Abstract

Nowadays robotic and artificial sciences are the most important area that plays an important role in technology area. The global purpose of the present study is to combine electrical, electronic, mechanical, and programming systems so to end up with a pure Mechatronics system. In order to design such a system, the mechanism with three serial manipulators which can be used separately or synchronized like parallel manipulators must be ready to work manually, and have a compact shape. The mechanism contains both serial and parallel manipulators working principle, direct, and inverse task calculations with their methodologies. The constraint of the machine is to have a maximum dexterous workspace when it is in compact shape within a circle radius 800mm. To solve this problem some software are used, such as Mathematica, SolidWorks, and MATLAB. Thus, we ended up with proper link lengths of robot arms by obeying the constraints. The redundancy of robot mechanism can give us a chance to reach any position from infinite number of kinematic solutions. Another constraint is that the actuators must be DC motors, so Ziegler-Nichols method is carried out. In conclusion, we indicated that by using a suitable controlling algorithm of position and velocity, we could make servo motion of DC motors without having servo motors. In addition, the study adds new features for robot manipulators so that we can control them as serial and parallel manipulator at the same time and in different task configurations. Finally, feedback encoders of the system are the most critical mechanism that may maximize or minimize the system errors with respect to their resolution.

1. Introduction

Serial and parallel manipulators are commonly used in industrial area. A serial manipulator consists of several links connected in series by various types of joints, typically revolute and prismatic joints. One end of the manipulator is attached to the ground and the other end is free to move in space. A parallel manipulator is closed loop kinematic chain mechanism. Both have advantages and disadvantages. Serial manipulator has more workspace than parallel manipulator, on the other side, it is less accurate than parallel manipulator. The main purpose of the study is to design three equal serial manipulators and not only use as serial manipulators but also as parallel one. There is a platform, and one of the gripper endings is always attached to the platform. In this case, gripper design also is important, it should be detectable and attachable in case needed. Plus, the mechanism should have 3 DoF in the end, but with 6 motors which means it is a redundant system. A redundant mechanism is one that contains more degrees of freedom than are needed to perform a given task.

Redundant mechanisms can solve a given primary task in an infinite number of ways. These manipulators have some workspaces. There are two defined workspaces: dexterous and reachable. This information defines the volume of the mechanism, that's why it is a critical criterion. The dexterous workspace can be defined as the area where a manipulator is able to reach with any orientation and the reachable workspace means that the maximum volume that the manipulator can reach. In SolidWorks, these workspaces can be defined as circles that is used as formulas in Mathematica. While choosing the link length there are some important things to take care, such as increasing the link length gives the more workspace but in the other hand it increases the mass of the system which cause also torque increases and so does deflection possibility. The other important point after choosing the lengths is the shape of links. Because when shape is changing, the inertia changes so does torque calculations and force calculations.

2. Methods

2.1. Designing the mechanism

Defining workspaces using Mathematica

In the dexterous area analysis, the algorithm was developed in the Mathematica program in order to find the maximum dexterous area. It was also checked in SolidWorks. Figures 1 and 2 respectively shows the demonstrations.

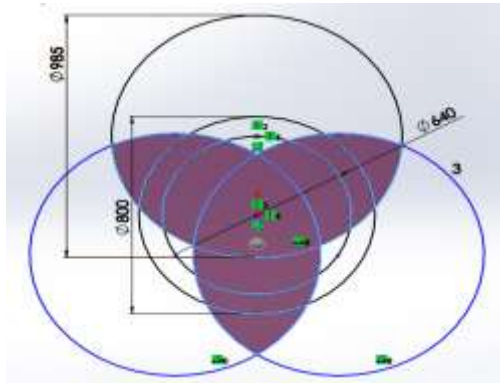


Figure 1. SolidWorks demo

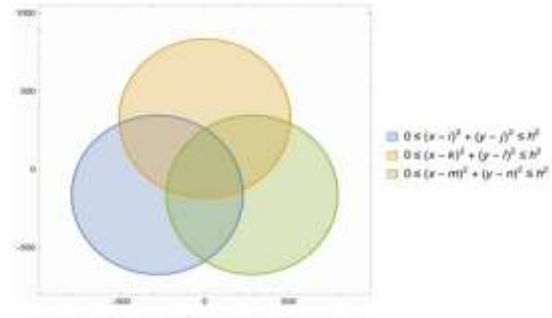


Figure 2. Mathematica demo

Choosing the most optimal link lengths according to workspaces

This data is valid for the link length 220mm.

Dexterous Area: 383438 mm²

Link lengths: $l_1=230$ mm

$l_2=230$ mm

Hexagonal shape dimension: 60 mm

PC1 = Dexterous workspace / (0.8*Footprint Area) = 383438 / (0.8*pi*400²) = 0.95

2.2. Kinematic analysis

D-H convention

D-H analysis is used to define end effector position and orientation. To create those matrices, a table including 4 parameters are filled. Those parameters are, translation, rotation of frame, offset and rotation of the links. First matrices for all links stand for translation along x and y axis. Second and fourth matrices stand for the rotation motion of the links around z axis. The last matrices to define its last position, which is a matrix including the length of link attached to platform.

Forward position, velocity, acceleration, and singularity analysis

For all links, forward kinematics should be done. It is supposed that angles are known and end effector position should be found. Respectively position, velocity and Acceleration analysis are done. By derivation the formulas of position, the velocity formulas are found. And the same, by derivation the velocity formulas, the Acceleration formulas are found. For a robotic arm, there are two possible ways to describe its current position: end-effector and set of joint angles. The Jacobian system relates how movement of the joints causes movement of the elements of joints.

If determinant of Jacob matrix is zero that means the system undergoes singularity, because that means that Jacob matrix cannot be inverted and this causes joints velocity cannot be defined.

$$\begin{bmatrix} \dot{x} \\ \dot{y} \end{bmatrix} = \begin{bmatrix} -a * s\theta_1 - b * s(\theta_1 + \theta_2) & -b * s(\theta_1 + \theta_2) \\ a * c\theta_1 + b * c(\theta_1 + \theta_2) & b * c(\theta_1 + \theta_2) \end{bmatrix} \begin{bmatrix} \dot{\theta}_1 \\ \dot{\theta}_2 \end{bmatrix}$$

$$\begin{bmatrix} \dot{x} \\ \dot{y} \end{bmatrix} = \text{tip velocity matrix}$$

$$\begin{bmatrix} -a * s\theta_1 - b * s(\theta_1 + \theta_2) & -b * s(\theta_1 + \theta_2) \\ a * c\theta_1 + b * c(\theta_1 + \theta_2) & b * c(\theta_1 + \theta_2) \end{bmatrix} = \text{Jacobian matrix}$$

where θ_1 indicates the angle of the first link, θ_2 the angle of the second link, and a and b are the link lengths.

$$\begin{bmatrix} \dot{\theta}_1 \\ \dot{\theta}_2 \end{bmatrix} = \text{joints velocity}$$

Inverse kinematics

This method is used to determine the motors rotation angles by using the information taken from manipulator end effector position and orientation.

Trajectory Analysis

In trajectory analysis, a rejection path is created in SolidWorks as shown in Figure 3. X and Y coordinates of all points on the generated path are determined and shown in Figure 4.

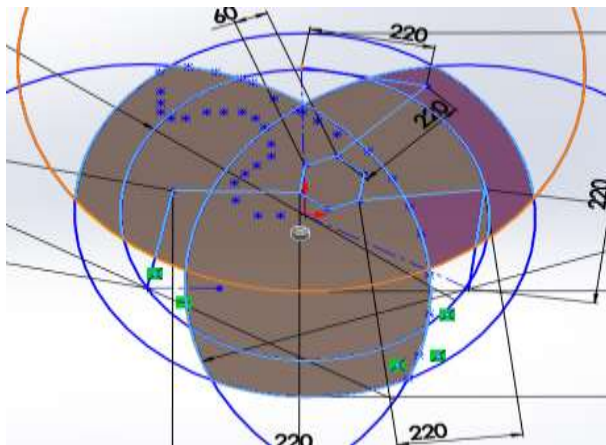


Figure 3. Trajectory using SolidWorks

x	y
246,2	271,6
-246,2	247
-246,2	226
-228	212
-202	212
-166,9	226,32
-136,3	226,3
-103,3	226,3
-81,4	212,9
-66,6	192,1
-55,9	156,6
-55,9	129,9
-81,4	109,11
-103,4	91,4
-120,1	70
-120	32
-81,3	0

Figure 4. Trajectory coordinates

2.3. Torque and Force Analysis, Motor Selection

Dynamic Analysis that can give us feedback for motor selection also carrying out during this study and calculated with Mathematica and SolidWorks programs.

Mathematic program theoretical calculations

Figures 5, 6, 7, 8, 9, 10, 11, and 12 show the orientations, velocity, acceleration, and torque of first and second motor, respectively

In the torque calculations found in the dynamic analysis, the time-dependent x and y equations are put in the appropriate places in the torque equation to obtain the following torque values.

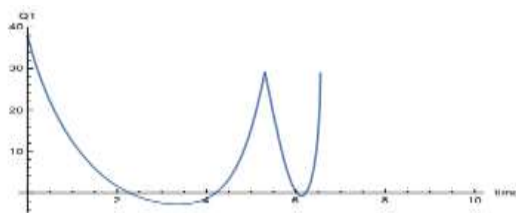


Figure 5. Joints position, first angle

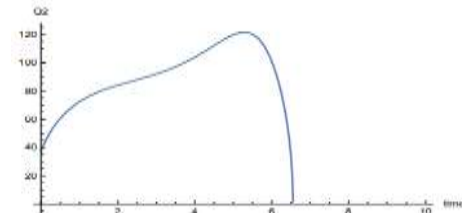


Figure 6. Joints position, second angle

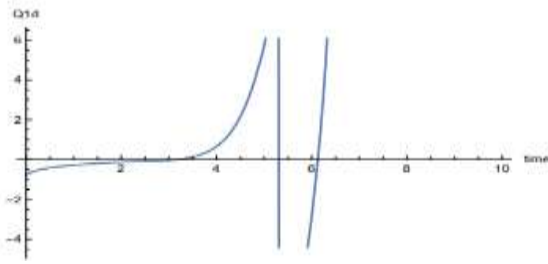


Figure 7. Joints velocity, first angle

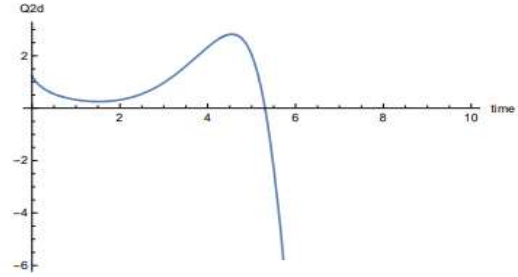


Figure 8. Joints velocity, second angle

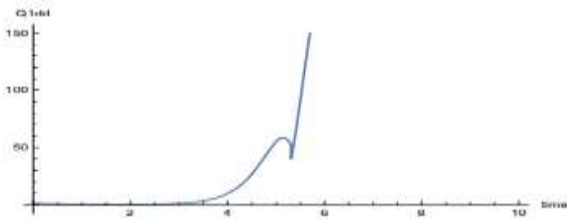


Figure 9. Joints acceleration, first angle

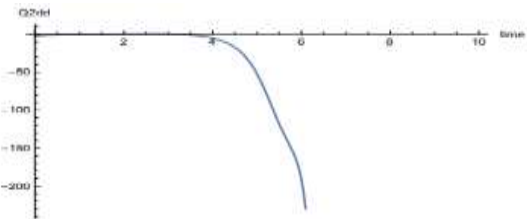


Figure 10. Joints acceleration, second angle

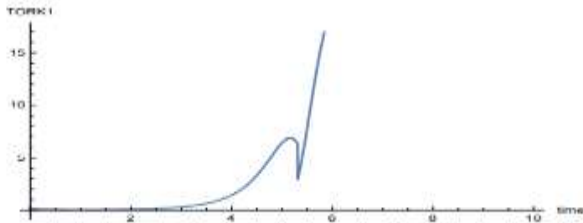


Figure 11. Joints torque, first angle

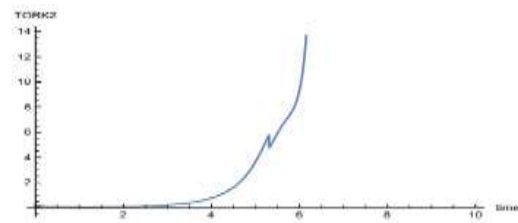


Figure 12. Joints torque, second angle

The accuracy of the code written in the Mathematica is compared and verified with the values obtained from the SolidWorks motion analyze for path generation as shown in above Figures 5-12.

SolidWorks simulation

The motors were fitted to the rotating centers on the assembled series arm in the SolidWorks program and the rotation speed was set at 5 rpm. The path in Figure 13 was created and the points on the path were obtained.

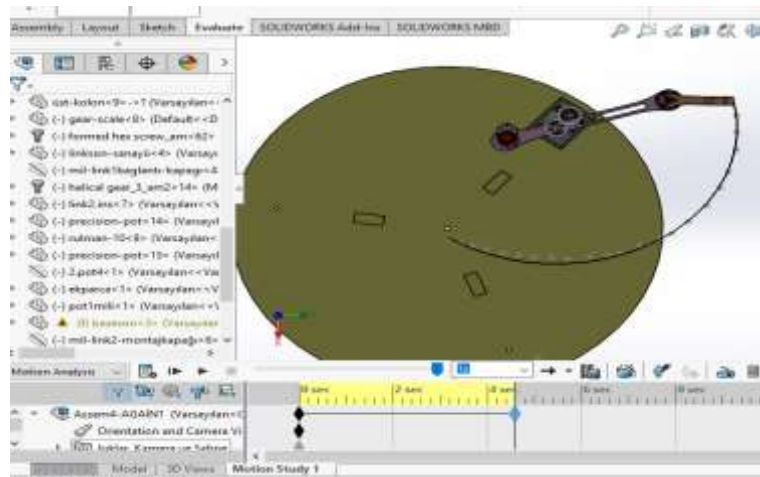


Figure 13. SolidWorks simulation

By substitution of coordinates that we aimed to reach, we could generate the trajectory equation that we insert it into SolidWorks program in order to obtain motors torque then, we could compare that

values with the ones which we got them from Mathematica .Finally the simulated values come to be similar with calculated ones.

2.4. Electrical circuit design

There are lots of ways to drive a motor, such as unidirectional, bidirectional. The most common way to drive a motor is bidirectional, H-bridge is used. Briefly, H-bridge's working principle to forward the input current and define the motor polarization. It is useful to drive the motor in both directions. Figure 14 shows the drive basics of H-Bridge and Figure 15 shows the whole electrical circuit design.

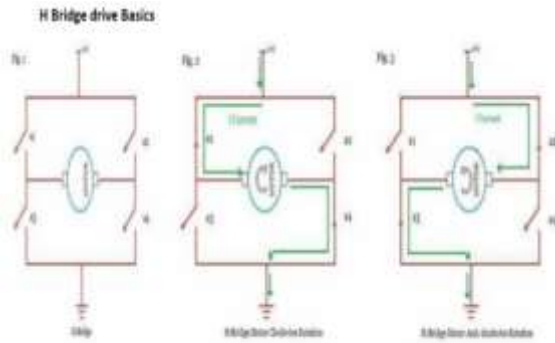


Figure 14. H-Bridge drive basics

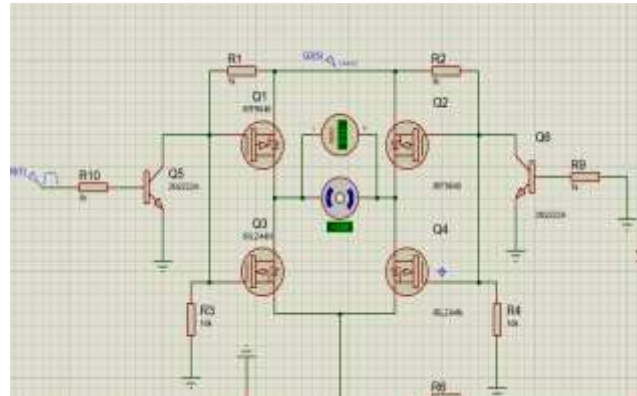


Figure 15. Electrical circuit design

Algorithm of the circuit

H-bridge circuit can be driven on both sides so that to get a velocity feedback for both sides diodes should be used.

- 10k and 22k ohms are used as voltage divider. When 12V comes through 10k,22k, this voltage divider regulates the voltage between 0-5V.
- Because, the feedback is read by a microcontroller, and a microcontroller cannot handle more than 5V.
- Also 22k and 10uF are used as low-pass filter, it cleans the output from noise.

This circuit is designed in Proteus, as a step of PCB circuit. To convert it into ARES, all grounds are held in one terminal block, output of the capacitor, PWM, 12V and motor components are shown as terminal blocks to design in ARES. ISIS is a tool that can be used to simulate circuits in real time. Another usage way of ISIS is to convert the scheme to ARES to have PCB circuit ways.

Then, we convert the type of the circuit to be in PCP version as shown in Figures 16-17.

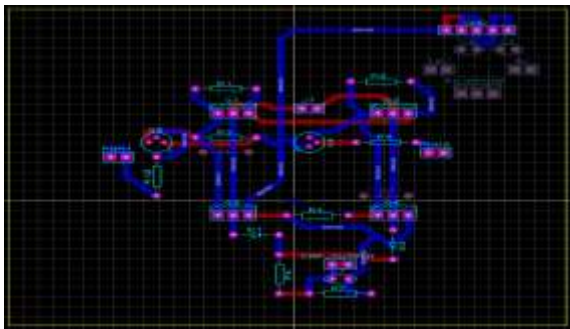


Figure 16. PCB1 circuit

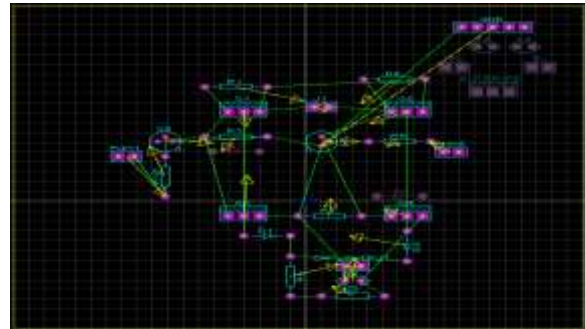


Figure 17. PCB2 circuit

Form of the electric circuit

In this project, ways are good to be thick rather than thin. As a last step in Proteus, this circuit is converted to PDF format, and saved. First step of realizing the circuit is to print it into a glossy paper (Figure 18). Second step is to iron the paper on to copper plate for 10 minutes (Figure 19). Third step is

to let the plate cold down and get rid of paper slowly (Figure 20). If in the ways, there are mistakes, by using an acetate paper they are fixed. Forth step is to have a acid solution which contains 1.5 spoon per hydro, and half cup of a HCl. Then, let the plate's ways are getting seen. With the same solution up to 4 circuits can be made. After 15 minutes, plate is taken out, and cleaned.

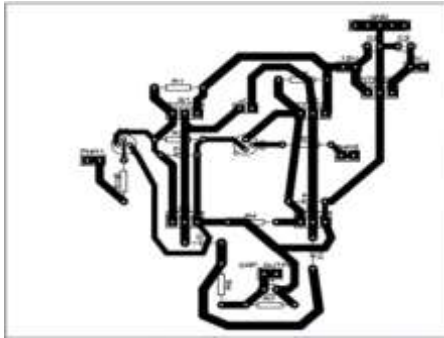


Figure 18. Printed circuit



Figure 19. Ironing onto copper plate



Figure 20. Removing the paper

The logic of PCB to have components' connection via coppers. The only thing to do after that point is to drill the points of components' places and place the component by using solder tool as shown in Figure 21.

MOSFETs and transistors are soldered with headers for the benefit of changing the part easily. Motor outputs are soldered with terminal blocks as shown in Figure 22.



Figure 21. Soldered connections



Figure 22. Terminal blocks

2.5. Control Algorithm

Position control algorithm:

Ziegler Nichols second method of tuning is used to tune the system response. There are three parameters to be tuned: K, Ti, Td, shown in Figures 23-24.

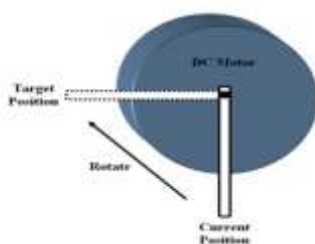


Figure 23. Positions

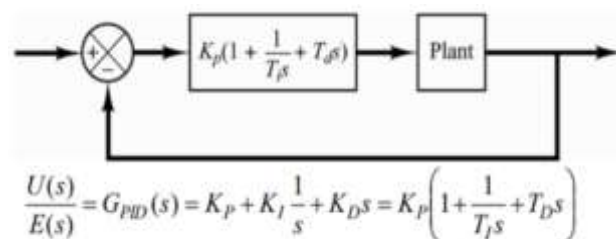


Figure 24. Parameters

Algorithm for selecting proper Kp controlling perimeter

- Set up the H-bridge, and coupling between shafts. (Starting from second step is about coding)
- Have a while (condition==1) loop just before while (TRUE) and after void main ().
- Define an array to collect the values. It will let the Kp value be stored inside an array.
- To finish collecting, make a definition. (For example 100*, the last char will make the condition zero, because it shows that 100 will be used.)
- Here, array is in string form. So, 100 should be converted to int value. Because this value will be multiplied with error, and if it is not converted to int, its anise values will be accounted.
- In this point, Kp is ready, and condition is already zero because of * character.
- With this Kp value, the code gets in a while (TRUE) loop, which means if one wants to change Kp value, microcontroller should be reset, so that the code will start again, condition will become 1 and so on. With Arduino, it is easy to do it. Also with PIC, it only requires a basic button-resistor circuit from its first MCLR leg, or directly shut down the 5V going through MCLR leg.
- There is a desired value that the motor's shaft should arrive, and in the other hand there is actual position of the shaft. The difference between them gives us the "error". As an example, desired value is calculated as 200, but in that instant the shaft's position value is 100. So, error becomes 200-100 = 100.
- Then, Kp value is multiplied with this error. (Kp*100)
- This value defines the pwm, and it is between 0-1023.
- As physical system, an oscillation should be observed to get true Kp value which is called Kc (K critical). If no oscillation, it is not the value that is looked forward to. The microcontroller should be reset and have another Kp value to find

Table 1. Kp, values for the study

Type of Controller	K_p	T_i	T_d
P	$0.5K_c$	∞	0
PI	$0.45K_c$	$\frac{1}{12}P_c$	0
PID	$0.6K_c$	$0.5P_c$	$0.125P_c$

Theoretically, after the proper Kc is found, Pc (period critical: oscillation period in Kc value) should be measured by using a oscillator or counting the oscillation within a time. Table 1 lets us know Kp, Ti and Td values.

2.6. Software

In this study Arduinos are used. Between them, there will be Master-Slave relationship wireless, and with NRF24LN radio module. The Nordic nRF24 is a family of silicon integrated radio transceivers operating in the 2.4GHz band, the most popular one being the nRF24L01. There are three slaves and one master Arduino. As algorithm, given values will be written on the screen, and by using the equations of inverse task, the necessary joint angles will be found. We are supposed to find 6 different values, so if it is stored in an array using the same channel to communicate, slaves can receive this array, and only use the needed one.

3. Results and Conclusion

To manufacture a robot which can have motions smooth and synchronized, some calculations should be taken care of carefully. Using the proper engineering materials is important, such as mathematical calculations including direct-inverse tasks, torque-moment-force, using software to verify all calculations especially While discussing this property of links, it should be chosen with respect to mass and price. The best solution should be found for the most optimized selection. Another property of links

is their shape which effects on inertia, so torque and moment, calculations. When torque and moment change, the selection of motor also may be changed. After deciding the whole design values in SolidWorks since the material types can be also chosen, the final result of torque is found, and a proper motor is chosen. After the motor selection, the connections of this design is concerned, because the bearings and belts are chosen by regarding the motor housing. This is important because it is only manufactured once due to time constraint. If design fails, it should be recreated, and cannot be tried with control. To drive motor, H bridge with MOS-FETs is needed, because MOS-FETs can handle high currents passing through the system, and can drive the motor in both sides. Finally, after the mechanical and electrical parts are done, it is good to go for control parameters, such as Ziegler-Nichols second method of tuning. This work should be precise, that's why controlling the motor parameter is important. To do that, motor characteristic should be found to be tagged as plant, and then PI controller is designed. As conclusion, to design is robot requires lots of knowledge such as mechanical, electric and electronic, mathematical, control algorithm, usage software properly, and the ability of combining all. Finally, as shown in Figure 25 to make any robot manipulator works in a compact shape that may do its job in serial or parallel condition, it is necessary to consider every single component in a critical manner so that you can guarantee your work to go in perfect condition. This figure is shown the work configuration of three serial manipulators that can implement its job in serial or in parallel version, and it can change its physical condition with respect to the required task.

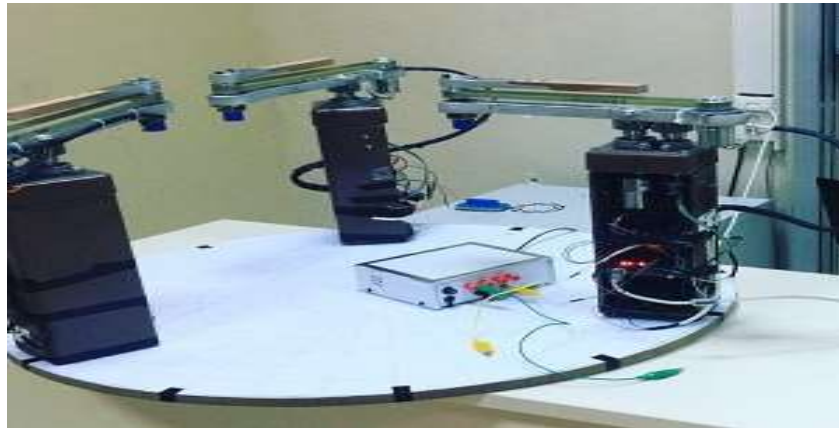


Figure 25. Compact shape of robot manipulators

Acknowledgement

This study was supported by the Presidency for Turks Abroad and Related Communities (YTB) within “International Student Academy” Project.

Material Science and Engineering / Malzeme Bilimi ve Mühendisliği

Optimization of ZnO Nanowires via Hydrothermal Growth

*Elif Simge Turgut, Fethullah Güneş**

İzmir Kâtip Çelebi Univ., Dept. of Materials Science and Engineering, Çiğli Main Campus, İzmir, Türkiye

**Corresponding author: fethullah.gunes@ikc.edu.tr*

Keywords: graphene, hydrothermal synthesis, zinc oxide, transfer process

Discipline: Materials Science and Engineering

Abstract

In this study, zinc oxide nanowire coated on three-dimensional graphene foam was synthesized by a simple hydrothermal method. Aqueous suspension containing ZnO precursors and three-dimensional graphene foam was kept in the hydrothermal process at 90°C and 120°C for 2 hour and 4 hour. As a result, for some parameters, a homogenous distribution of ZnO nanowires on graphene foam is observed. Therefore, this work shows the effects of changing parameters for every step of hydrothermal growth can change the length and diameter distributions.

Introduction

In the last few decades, zinc oxide (ZnO) gained huge attraction due to its superior properties. ZnO is an n-type semiconductor material which has high binding energy (60meV) and wide band gap (3.37 eV) [1-4]. These properties make zinc oxide is useful in many areas especially in electronic applications such sensors, biosensors, transistors and optoelectronics [5].

The zinc oxide have lot of structures which can change the different kind of synthesis methods or changing with the growth parameters. The temperature, solution concentration, type of the substrate, the growth time can directly affect the growth direction and structure. The typical structures of zinc oxides as wire, rod, flake, ellipsoid, and flower-like.

Chen et al [6] used zinc chloride and sodium hydroxide chemicals synthesized nanoparticles by using hydrothermal process. They observed a significant change, in the morphology by changing the temperature. The first report of growing ZnO nanostructure using hydrothermal process is published by Andreas-Vergés et al. [7] But, Vayssieres et al [8] synthesized ZnO nanowire on Si (glass) substrate via controlled synthesis by using HMTA and zinc nitrate attracting more attention than the study of Andres-Vergés et al. The other typical nanostructure of ZnO is flower-like structure that can be synthesized by using hydrothermal synthesis. Wahab et al [9] were also observed the flower-like ZnO nanostructure by using zinc acetate dehydrate and sodium hydroxide in aqueous solutions at 90°C.

The purpose of this study was observing different morphologies and their properties such as diameters and lengths, by changing growth parameters. In this study, hydrothermal growth technique was used for producing zinc oxide nanowires. Firstly, graphene foam substrate was dip coated for development of ZnO nanostructures.

Methodology

As a first stage of this study, graphene foam were used as substrate. Three-dimensional graphene structure which we called graphene foam (GF), synthesized on nickel foam by template-directed chemical vapor deposition (CVD). The reason of GF usage was developing electrical and mechanical properties of samples by combining it with graphene.

After graphene foam synthesis, ZnO nanowires were synthesized with two steps: firstly seeding thin layer of ZnO nanoparticles on graphene foam and secondly growth of ZnO nanowires. For second procedure, hydrothermal method was chosen. Hydrothermal method were occurred in autoclave.

In this study, different methods were used to observe their effect on nanowire diameters and lengths. In order to provide growth of ZnO nanowires graphene foam (GF) was coated with ZnO seeding layer via deep coating method. GF was dipped into seeding layer solution. General process of hydrothermal synthesis of zinc oxide nanostructure growth on substrate can described as listed below:

- I. The ZnO nanoparticles are seeded on a substrate by using sodium hydroxide (NaOH) in ethanol (10mg/10mL) and zinc acetate in ethanol (27.5mg/50mL) mixed solutions with dip coating

- method. The seeding layer improves the nucleation for the growth of nanostructure due to lowering of the thermodynamic barrier.
- II. Hexamethylenetetramine (HMTA) and zinc nitrate di hydrate salt mixture solution is used as a growth solution (5mM, 10mM, and 30mM).
 - III. The zinc oxide seeded onto substrate is kept in the growth solution in autoclave sealed at a certain temperature and time (2h and 4h).
 - IV. The final substrate and growth layer is washed with deionized water and dried in oven at 150°C.

As a first parameter seeding solution concentration were changed. Then dipping times in seeding solution were changed. After that, autoclave concentration (5mM, 10mM, and 30mM), growth time (2h and 4h) and temperature (90°C and 120°C) were changed. After every change in parameter of samples were investigated with scanning electron microscopy (SEM) and X-ray diffraction (XRD).

Table 1. Applied parameters and number of samples

Model No	Parameter	Number of Sample
1	Seeding Solution Concentration	3
2	Dipping Times	3
3	Temperature	2
4	Autoclave Concentration	3

Results and Discussion

XRD patterns of the samples are given in Figure 1. XRD results, the nickel foam were used as substrates for this study, so all XRD patterns contain this peak and marked with (1). Also, ZnO diffraction peaks were observed. The ZnO peaks are marked with (2) and these peaks are in good fit with standard powder diffraction peaks of zinc oxide also known Chinese white JCPDS reference code 36-1451.

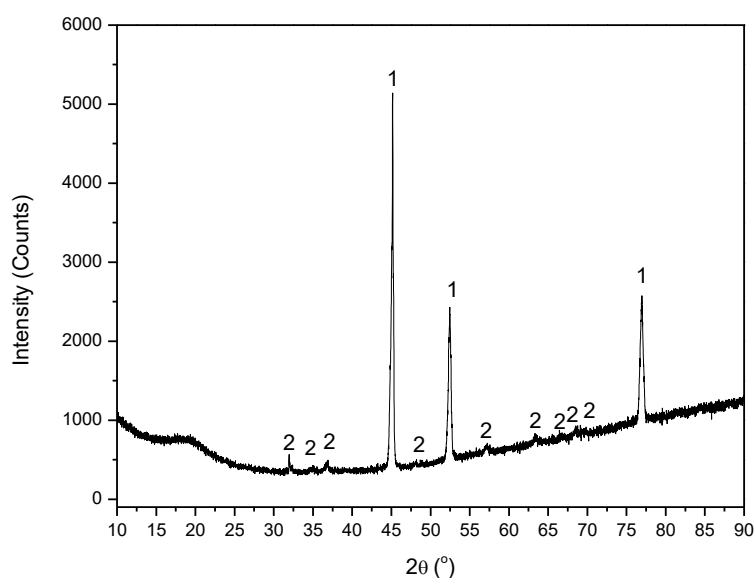


Figure 1. XRD Peaks of graphene foam and ZnO.

Morphology analysis is an important evidence of whether the study was successful and, if so, what parameters are necessary. The ZnO nanowires structures were obtained on GF for some specimens. SEM images of the samples are given in Figure 2.

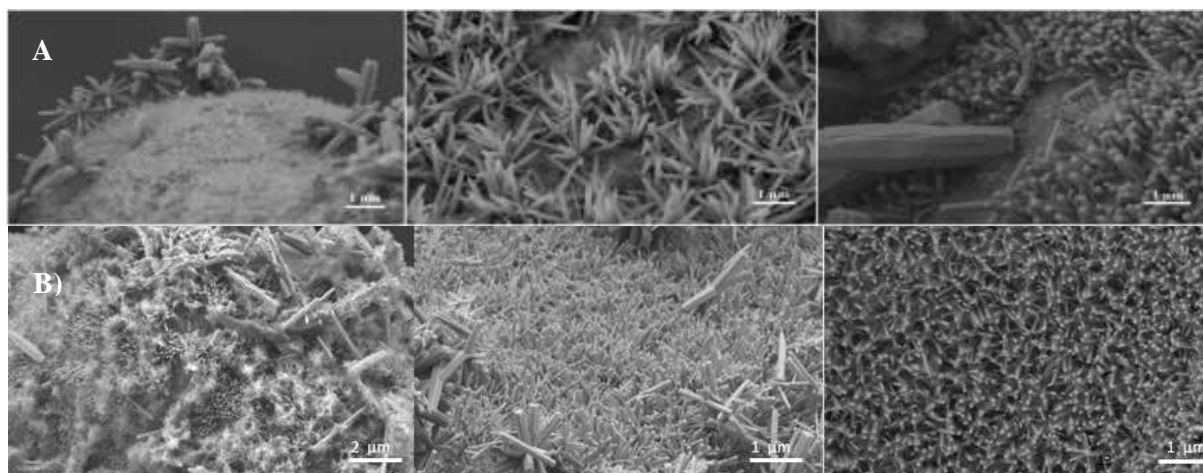


Figure 2. SEM images of ZnO NW-coated on three-dimensional graphene foam.
(A. different dipping times, B. different autoclave concentration.)

Conclusion

In summary, well aligned ZnO NWs deposited on three-dimensional graphene foam by hydrothermal method successfully. The characterization results revealed that ZnO particles with hexagonal zincite phase were distributed over the surface of graphene foam.

SEM images were shown that best results belonged to highest autoclave concentration (30mM), 2 times dip coated, and 4 hours growth time and at 90°C sample.

As a conclusion, this study shows that changing parameters in each step have different types of effect on nanostructure. The parameters of the synthesis and the growth process could be optimized and improved to have better quality ZnO nanowires.

References

- [1] Arya SK, Saha SJE Ramirez-Vick et al (2012) "Recent advances in ZnO nanostructures and thin films for biosensor applications: Review", *Analytica Chimica Acta* 737, 1– 21.
- [2] ZhouJ, Xu N and Wang Z (2006) "Dissolving Behavior and Stability of ZnO Wires in Biofluids: A Study on Biodegradability and Biocompatibility of ZnO Nanostructures". *Adv. Mater.*, 18: 2432-2435. doi:10.1002/adma.200600200
- [3] Lu F, Cai W and Zhang Y (2008) ZnO Hierarchical Micro/Nanoarchitectures: Solvothermal Synthesis and Structurally Enhanced Photocatalytic Performance. *Adv. Funct. Mater.* 18: 1047-1056. doi:10.1002/adfm.200700973.
- [4] Weintraub B, Zhou Z, Li Y, Deng Y (2010) Solution synthesis of one-dimensional ZnO nanomaterials and their applications. *Nanoscale.* 2. 1573-87. 10.1039/c0nr00047g
- [5] Djuricic AB, A.M.C.Ng, Chen XY, (2010) "ZnO nanostructures for optoelectronics: Material Properties and device applications" Dept. of Physics, The University of Hong Kong, 191–259.
- [6] Chen D, Jiao X, and Cheng G, (2000), "Hydrothermal synthesis of zinc oxide powders with different morphologies", *Solid State Commun*, Vol.113, pp. 363-366.
- [7] Andres-Vergés, M., Mifsud, A. and Serna, C. J., (1990), "Formation of rod- like zinc oxide microcrystal in homogeneous solution", *Journal of the Chemical Society, Faraday Transactions*, Vol.86, pp. 959-963.
- [8] Vayssieres, L., Keis, K. and Lindquist, S. E., (2001), "Purpose-Built Anisotropic Metal Oxide Material: 3D Highly Oriented Microrod Array of ZnO", *The Journal of Physical Chemistry*, Vol.105, pp. 3350-3352.
- [9] Wahab R, Ansari SG, Kim YS, Seo HK, Kim GS, Khang G and Shin HS (2007) "Low temperature solution synthesis and characterization of ZnO nanoflowers", *Materials Research Bulletin*, Vol. 42, pp. 1640-1648.

Anotlama Parametrelerinin Ti_6Al_4V Alaşımı Üzerinde Oluşturulan TiO_2 Nanoyapıların Yüzey Özelliklerine Etkisi

Metin Yurddaşkal*, Dokuz Eylül Üniversitesi, Metalurji ve Malzeme Mühendisliği Bölümü, Buca, İzmir, Türkiye
*İletişimden sorumlu yazar: metin.yurddaskal@deu.edu.tr

Anahtar Kelimeler: anotlama, Ti_6Al_4V , TiO_2 , nanoyapılar, yüzey özellikleri
Disiplin: Metalurji ve Malzeme Mühendisliği

Özet

Titanyum alaşımları biyomedikal uygulamaları, çevresel atıkların temizlenmesi, otomotiv ve uçak endüstrisi gibi çok çeşitli alanlarda kullanılmaktadır. Titanyum alaşımı gibi metalik bir malzemenin kaplanması sonucunda da ortaya çıkarılacak yeni yüzey yapılarının sergileyeceği performans da oldukça önem arz etmektedir. Bu kapsamda, farklı anotlama parametreleri kullanılarak Ti_6Al_4V alaşımı üzerinde TiO_2 nanoyapıları elde edilmiştir. Bu çalışmada, anotlama ile edilen nanoyapıların yüzey özelliklerini incelemek amacıyla anotlama süresi sabit tutularak yüzey morfolojisi üzerinde oldukça etkili olan anotlama voltajı 100, 200 300 ve 400 volt olarak seçilmiştir. Elde edilen yüzeylerin, yüzey pürüzlülüğü ve profilleri üç boyutlu yüzey profilometresi, mekanik özellikleri nanoindentasyon cihazı ve su iticilik özellikleri de kontak açısı ölçüm sistemi aracılığıyla karakterize edilmiştir. Anotlama yöntemi ile Ti_6Al_4V alaşımı üzerinde TiO_2 nanoyapıları başarıyla elde edilmiştir. Sonuçlar incelendiğinde anotlama parametrelerinin elde edilen yüzey özelliklerini önemli derecede etkilediği ortaya çıkarılmıştır. Anotlama voltajı arttırıldığında yüzey pürüzlülüğü değerlerinin arttığı ve ayrıca mekanik özellikler olan sertlik ve elastisite modülü gibi değerlerin de arttığı sonucuna varılmıştır.

Giriş

Titanyum alaşımları biyomedikal uygulamaları, çevresel atıkların temizlenmesi, otomotiv ve uçak endüstrisi gibi çok çeşitli alanlarda kullanılmaktadır. Titanyum alaşımı gibi metalik bir malzemenin kaplanması sonucunda da ortaya çıkarılacak yeni yüzey yapılarının sergileyeceği performans da oldukça önem arz etmektedir. Metalik alaşım üzerinde oluşturulacak oksit tabakasının topografyasını ve kompozisyonunu değiştirmek, farklı asit çözeltilerinin içerisinde alaşımın galvanostatik veya potansiyostatik olarak anotlanması ile elde edilmektedir [1].

Bir elektrolit çözeltisinin içerisinde aşırı reaktif asitler kullanıldığı zaman yüzeyde oluşacak oksit tabaka akımın iletimi boyunca çözünecektir ve titanyum alaşımı yüzeyindeki mikro- ve nanoporların olduğu diğer bölgeler içinde kalınlaşacaktır. Bu elektrokimyasal proses TiO_2 tabakasının modifiye olan kristalin yapısına ve artan bir kalınlığa yol açar [2]. Aslında anotlama kompleks bir yöntemdir ve akım yoğunluğu, asitlerin konsantrasyonu, elektrolit kompozisyonu ve sıcaklığı gibi çeşitli parametrelere dayanır. İmplant malzemesi olarak da kullanılan titanyum alaşımlarının kontrollü bir sistemde anotlanması ve farklı anotlama voltajları kullanılması durumunda yüzeyde fiziksel ve kimyasal değişikliklerin meydana geldiği bilinmektedir. Anotlama ile yüzeylerde mikro ve nanoporoz yapıların elde edilmesi, yüksek akım yoğunluğu veya yüksek potansiyellerde aşırı reaktif asitler ile hazırlanan elektrolit içerisinde titanyumun potansiyostatik veya galvanostatik olarak anotlanması ile mümkündür. Bu yüzeylerde ayrıca 100 nm'den daha fazla kalınlıkta oksit tabakaların elde edildiği ve anotlama parametrelerinin yüzeyde oluşan oksit tabakanın yüzey özellikleri üzerinde etkili olduğu görülmüştür [3].

Titanyum ve titanyum alaşımları üzerinde oluşturulan nanoyapılı TiO_2 kaplama yüzeylerinin üstün özellikleri sayesinde son yıllarda yarıiletken malzemeler arasında sıklıkla kullanılmaktadır [4-7]. Metal altlık üzerinde oluşturulan bu tip yarıiletken kaplamalar genellikle plazma sprey teknolojisi, iyon implantasyonu ya da anodik oksitleme tekniği gibi yüzey modifikasyon işlemleriyle gerçekleştirilmektedir. Bu yöntemler arasında anodik oksitleme tekniği basit ve ekonomik olmasının yanı sıra kaplama kalınlığı ile nanotüp/nanopor çaplarının kontrol edilebilmesi sayesinde diğer yöntemlere kıyasla en çok tercih edilen üretim metodudur. Anodik oksitlemenin gerçekleştirilmesinde anotlama parametrelerinin de mikroyapı, yüzey, morfoloji ve mekanik özellikleri doğrudan etkilediğini söylemek mümkündür [8-13].

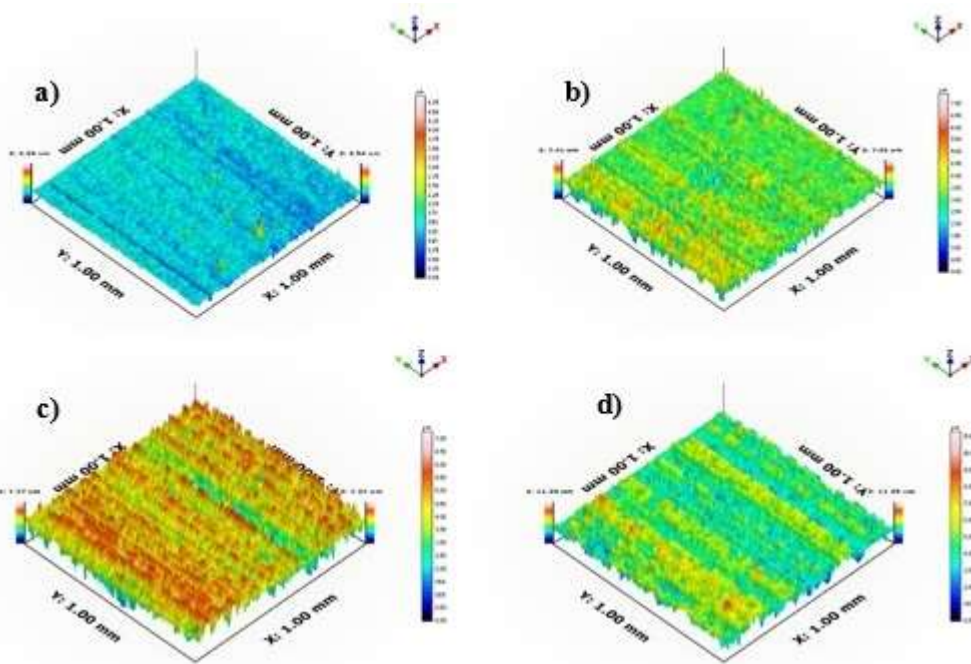
Materyal ve Metot

Numuneler ticari olarak kullanılan Ti6Al4V alaşımından (Gr23) 5 mm kalınlığında ve 16 mm çapında olmak üzere hazırlanmıştır. Kesilmiş bu numuneler zımparalama ve parlatma işlemlerinden geçirilip ardından etanol, aseton ve saf su karışımı ile ultrasonik banyoda 15 dk boyunca yüzeyleri temizlenmiştir. Elde edilen numuneler 1 M H₂SO₄ elektroliti kullanılarak 30 dk boyunca 100, 200, 300 ve 400 V anotlama voltajı altında anotlama işlemine tabi tutulmuştur. Ardından numuneler üzerinde TiO₂ nanoyapıların oluşması amacıyla 500 °C'de 2 saat boyunca hava atmosferinde ısıl işleme tabi tutulmuşlardır.

Ti6Al4V alaşımı üzerinde elde edilen TiO₂ nanoyapıların üç boyutlu yüzey profillerinin incelenmesi amacıyla Ambios marka (XP-2) yüzey profilometresi kullanılmıştır. Farklı anotlama parametreleri ile elde edilen nanoyapıların mekanik özellikleri nanoindentasyon (IBIS) cihazı ile 10 mN yük altında tayin edilmiştir. Ayrıca yüzeyde oluşturulan TiO₂ nanoyapıların temas açıları da belirlenerek anotlama parametrelerinin titanyum alaşımı üzerinde oluşturulmuş TiO₂ nanoyapıların yüzey özelliklerine etkisi araştırılmıştır.

Bulgular ve Tartışma

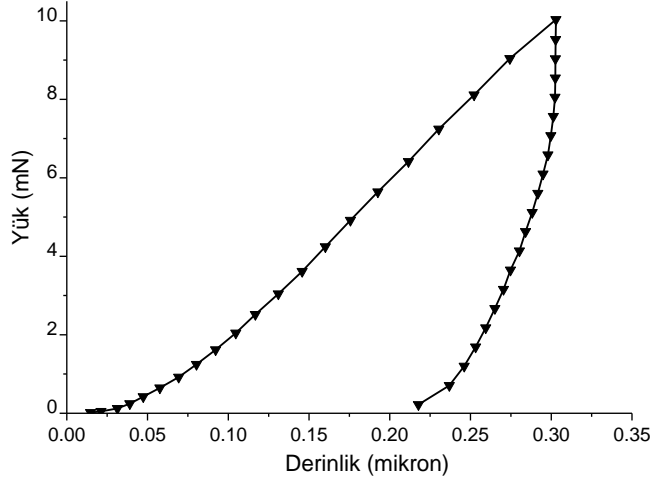
Bu çalışmada, farklı anotlama parametreleri kullanılarak Ti6Al4V alaşımı üzerinde TiO₂ nanoyapıları başarıyla elde edilmiştir. Sonuçlar incelendiğinde anotlama parametrelerinin elde edilen yüzey özelliklerini önemli derecede etkilediği ortaya çıkarılmıştır. Anotlama voltajı arttırıldığında yüzey pürüzlülüğü değerlerinin arttığı ve ayrıca mekanik özellikler olan sertlik ve elastisite modülü gibi değerlerin de arttığı sonucuna varılmıştır. Farklı voltaj değerlerinde elde edilen yüzeylerin Şekil 1'deki üç boyutlu profillerinden de görüleceği üzere anotlama voltajının artmasıyla yüzey pürüzlülüğü değerleri artmıştır. Anotlama voltajının artmasıyla yüzey pürüzlülüğünün artması yapıda oluşan nanotüp benzeri yapıların boyunun uzaması ile ifade etmek mümkün olmaktadır. Literatürde de anotlama voltajının artması ile rutil fazının anataz fazına kıyasla daha baskın olabileceğinden ötürü yüzey pürüzlülüğü değerlerinin de artmış olacağı düşünülmektedir [8].



Şekil 1. Farklı anotlama voltajlarına sahip a) 100 V, b) 200 V, c) 300 V ve d) 400 V yüzeylerin 3 boyutlu profil görüntüleri

Şekil 2'de de elde edilmiş TiO₂ nanoyapıların mekanik özelliklerini göstermek amacıyla 100 V anotlama voltajı altında üretilen numunenin nanoindentasyon sonucu gösterilmektedir. Nanoindentasyon cihazından elde edilen tüm mekanik özellik değerleri Tablo 1'e aktarılmıştır. Tablo 1'den görüleceği üzere tüm numuneler eşit yük (10mN) altında deneye tabi tutularak batma derinliği

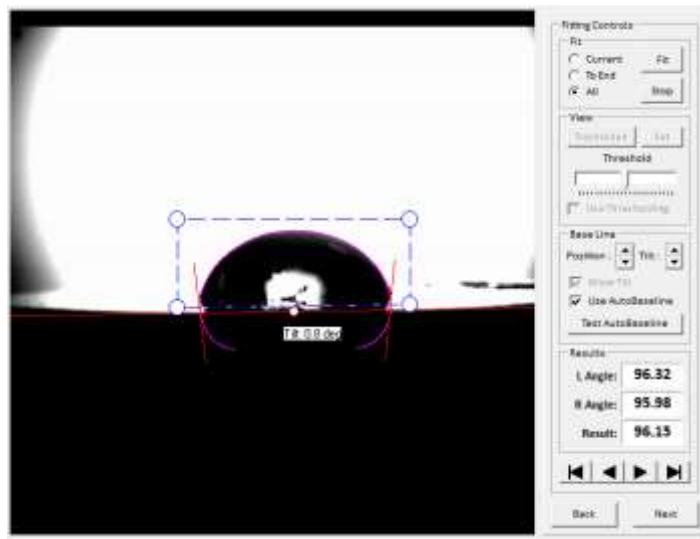
eğrileri elde edilmiştir. Bu analizden elde edilen sonuçlar incelendiğinde sertlik ve elastisite modülü gibi mekanik özellik değerlerinde artışlar meydana gelmiştir. Bu durumun anotlama voltajının artmasıyla daha baskın olan rutil fazından kaynaklandığı düşünülmektedir. Çünkü rutil fazının yoğunluğu anataz fazına göre daha yüksek ve daha rijit olduğundan dolayıdır.



Şekil 2. Anotlama voltajı 100 V olan numune için nanoindentasyon analizi sonucu

Tablo 1. Farklı anotlama voltajı değerlerinde elde edilen yüzeylerin mekanik özellikleri

Anotlama voltajı	100 V	200 V	300 V	400 V
Sertlik (GPa)	3,35	3,42	3,44	3,62
Elastisite modülü (GPa)	96	111	120	137
Batma derinliği (nm)	417	386	376	356
Uygulanan yük (mN)	10	10	10	10



Şekil 3. Anotlama voltajı 100 V olan numune için temas açısı analizi görüntüsü

Farklı anotlama parametreleriyle üretilen TiO₂ nanoyapıların su ıticilik özelliklerinin incelenmesi amacıyla ıslatma (temas) açıları da incelenmiştir. Şekil 3'de 100 V anotlama voltajına sahip numune için ıslatma açısının tespit edildiği analiz görüntüsü verilmiştir. Tüm numuneler için elde edilen ıslatma açısı değerleri Tablo 2'ye aktarılmıştır. Elde edilen ıslatma açısı değerlerine bakıldığında anotlama voltajının artmasıyla birlikte su ıticilik özelliğinin de iyileştiği görülmektedir.

Tablo 2. Farklı anotlama voltajı değerlerinde elde edilen yüzeylerin temas açısı değerleri

Anotlama voltajı	100 V	200 V	300 V	400 V
Temas açısı değeri (°)	96,15	102,64	109,11	118,69

Sonuç

Bu çalışmada, farklı uygulama alanlarında kullanılan Ti6Al4V alaşımı üzerinde TiO₂ nanoyapıları anotlama yöntemiyle başarıyla elde edilmiştir. Anotlama yöntemiyle üretilen oksit nanoyapıların elde edilmesinde elektrolit tipi, anotlama süresi ve anotlama voltajı gibi anotlama parametrelerinden anotlama voltajının yüzey özellikleri üzerine etkisi ortaya çıkarılmıştır. Elde edilen bulgulardan da anlaşılacağı üzere farklı anotlama voltajı değerleriyle üretilmiş numunelerin farklı yüzey özelliklerine sahip olduğu sonucuna varılmıştır. Anotlama voltajının yüzey pürüzlülüğünü artırırken aynı zamanda mekanik özellikleri de iyileştirdiği anlaşılmaktadır. Ayrıca, su iticilik özellikleri de incelendiğinde anotlama voltajının artırılması ile su iticilik özelliklerini geliştirdiği görülmüştür. Sonuç olarak bu çalışmada elde edilen bulgular ile anotlama parametrelerinin yüzey özelliklerini önemli derecede etkilediği ortaya çıkarılmıştır.

Referanslar

- [1] Qin L, Chen Q, Lan R, Jiang R, Quan X, Xu B, Jia Y (2015). Effect of anodization parameters on morphology and photocatalysis properties of TiO₂ nanotube arrays. *Journal of Materials Science & Technology*, 31(10), 1059-1064.
- [2] Krbal M, Sopha H, Pohl D, Benes L, Damm C, Rellinghaus B, (2018) Self-organized TiO₂ nanotubes grown on Ti substrates with different crystallographic preferential orientations: Local structure of TiO₂ nanotubes vs. photo-electrochemical response. *Electrochimica Acta* 264: 393-399.
- [3] Gulati K, Santos A, Findlay D, Losic D (2015). Optimizing anodization conditions for the growth of titania nanotubes on curved surfaces. *J Physical Chemistry C*, 119(28), 16033-16045.
- [4] Roy P, Berger S, Schmuki P (2011). TiO₂ nanotubes: synthesis and applications. *Angewandte Chemie International Edition*, 50(13), 2904-2939.
- [5] Lamberti A, Manfredi D, Calignano F, Pirri CF (2018). TiO₂ nanotube-based smart 3D electrodes by anodic oxidation of additively manufactured Ti6Al4V structures. *Materials Today Communications*, 15, 165-170.
- [6] Xiao H, Li J, He B (2017) Anatase-Titania templated by nanofibrillated cellulose and photocatalytic degradation for methyl orange. *J. Inorganic & Organometallic Polymers & Materials*, 27(4), 1022-1027.
- [7] Sheela JAH, Lakshmanan S, Manikandan A, Antony SA (2018). Preparation and Characterizations of PVP-TiO₂ NPs Calcined at 500, 600 and 700° C by the Hydrothermal Method and Their Properties. *Journal of Inorganic and Organometallic Polymers and Materials*, 28(5), 2036-2045.
- [8] Yurddaskal M (2019) Formation of micro- and nanostructured TiO₂ films by anodic oxidation for enhanced photocatalytic activities. *J. Inorganic and Organometallic Polymers and Materials*, 1-12.
- [9] Yurddaskal M, Dikici T, Yildirim S, Yurddaskal M, Toparli M, Celik E (2015). Fabrication and characterization of nanostructured anatase TiO₂ films prepared by electrochemical anodization and their photocatalytic properties. *Journal of Alloys and Compounds*, 651 : 59-71.
- [10] Grimes CA, Mor GK (2009). TiO₂ nanotube arrays: synthesis, properties, and applications. Springer Science & Business Media.
- [11] Wang J, Ma Y, Guan J, Zhang D (2018). Characterizations of anodic oxide films formed on Ti6Al4V in the silicate electrolyte with sodium polyacrylate as an additive. *Surface and Coatings Technology*, 338, 14-21.
- [12] Kern P, Zinger O (2007). Purified titanium oxide with novel morphologies upon spark anodization of Ti alloys in mixed H₂SO₄/H₃PO₄ electrolytes. *J. Biomedical Materials Res.- A* 80(2), 283-296.
- [13] Zhang ZK, Guo DZ, Xing Y J, Zhang GM (2011). Fabrication of open-ended TiO₂ nanotube arrays by anodizing a thermally evaporated Ti/Au bilayer film. *Applied Surf. Science*, 257(9), 4139-4143.

Preparation and Characterization of Graphene Synthesized by Different Methods

*Ala K. Jehad**, Dokuz Eylül Univ., Dept. of Physics, Tınaztepe Campus, İzmir, Türkiye
Metin Yurddaşkal, Dokuz Eylül Univ., Dept. of Metallurgical and Materials Engineering, Tınaztepe Campus, İzmir, Türkiye
Kemal Kocabaş, Dokuz Eylül Univ., Dept. of Physics, Tınaztepe Campus, İzmir, Türkiye
*Corresponding author: ala.jehad13@gmail.com

Keywords: low-layered graphene, reduced graphene oxide, electrochemical exfoliation

Discipline: Physics, Material Science

Abstract

The exceptional properties of graphene, make it a promising material for boundless applications such as flexible electronics, nanocomposites, sensing, filtration membranes and energy storage. The challenges still exist in technological breakthrough in graphene preparation methods and processes.

In this paper, two different synthesis methods have been used. The first method is modified Hummers' method to produce reduced graphene oxide (rGO) has been showed successful reduction of graphene oxide (GO). The second method is electrochemical liquid phase exfoliation (ELPE) has used with two different inorganic electrolytes, which are sodium sulfate and sulphuric acid to produce low-layered graphene sheets. The characteristics of synthesized graphene sheets and graphene oxide have been estimated using SEM spectroscopy, Raman spectroscopy, FTIR, and XRD.

Introduction

Graphene is a single layer of carbon atoms bonded together in a honeycomb lattice structure; it was isolated from a graphite crystal in 2004 to be the first 2D materials [1]. Graphene has attracted a lot of consideration and has been the subject of countless theoretical and experimental researches due to its own extraordinary physical and chemical properties. Over the past few years, many methods have been used to produce graphene (G) or reduced graphene oxide (rGO), including microchemical cleavage, chemical vapor deposition (CVD), liquid phase exfoliation (LPE), epitaxial growth on SiC substrates, and the reduction of graphene oxide (Hummers' Method). Each method has its own advantages and disadvantages, such as the quality, yield, derived form and the production cost of the graphene.

Modified Hummers' method is one of the notable methods to produce graphene oxide from pure graphite powder (Gr). This chemical method includes both of potassium permanganate ($KMnO_4$), and sulfuric acid (H_2SO_4) addition to the graphite dispersion [2].

The other method is electrochemical liquid phase exfoliation (ELPE) of graphite rods. Electrochemical exfoliation is an effective approach to produce graphene in high scalability and low cost. This method includes graphite rods to work as an anode and cathode electrode. Both with specific electrolyte solution to set an electrochemical cell [3,4].

Experimental

In this study, the following materials have been used: Graphite powder (Gr), Sulphuric Acid (H_2SO_4), Sodium Sulfate (Na_2SO_4), Potassium Permanganate ($KMnO_4$), Hydrogen Peroxide (H_2O_2), Hydrochloric acid (HCl), Hydrazine Hydrate (H_6N_2O), distilled and deionized water (DI water).

Two different methods have been used to synthesize graphene. Reduced graphene oxide (rGO) has been synthesized from graphite powder by modified Hummers' method; and low-layered exfoliated graphene sheets have been synthesized by Electrochemical Liquid Phase Exfoliation (ELPE) with two different electrolyte solutions [4].

a) Hummers' Method

In this method, 100 ml of H_2SO_4 in the ice bath was mixed with 4 g graphite powder and stirred for several minutes. Then 12 g of $KMnO_4$ was added slowly by keeping the temperature less than $20^\circ C$ into the solution. This mixture was stirred for 3 hours; 200 ml of distilled water was added dropwise to the

dispersion with controlling the temperature to be less than 50°C. Then 400 ml of distilled water was added instantly to finish the oxidation process.

To eliminate excess of KMnO_4 , 20 ml of H_2O_2 was dropped slowly and stirred for 10 minutes. To remove any metal impurity during the synthesis of GO, 100 ml of HCl in 900 ml of DI water has been added to wash GO dispersion and centrifuged for several times at 6000 rpm for 10 minutes; then washed again with DI water and centrifuged for six times at 6000 rpm for 10 minutes. The washed GO solution has been left to dry using heater at 80 °C for one night.

For reduction process, 1.5 g of GO in 500 ml of distilled water has been prepared and setup with reflux technique with a proper stirring. Then 0.5 ml of $\text{H}_6\text{N}_2\text{O}$ was added to the GO dispersion and the heater was set to 80°C with stirring at 400 rpm for 16 hours. Next day the reflux setup has been removed, and the sample was washed for 3 times with DI water in centrifuged at 3000 rpm for 15 minutes. Then the sample (rGO) was ready to characterization after being dried again for one night.

b) Electrochemical LPE

Two graphite rods have been made by pressing 3 g of graphite powder with hydraulic press at 10 tons for 5 minutes. The obtained pressed graphite rods have a circular shape with diameter of 30 mm and thickness of 2 mm.

Two electrolyte inorganic solutions have been used for electrochemical exfoliation processes, which are with sodium sulfate solution (Na_2SO_4) has been called (EE1) and sulphuric acid solution (H_2SO_4) has been called (EE2).

In the first Experiment (EE1); 11.36 g of Na_2SO_4 (0.1 M concentration) has been stirred with 800 ml of DI water for 3 min in 13,000 rpm. A constant potential of 10 V was applied to initiate the exfoliation process, which has taken about 2 hours. After the initial exfoliation process, ultra-sonication bath has been applied for 2 hours. Then the exfoliated graphene dispersion washed with DI water for 3 times in centrifuged at 4000 rpm for 15 min. Then the sample has left to dry at 80°C for one night.

In the second Experiment (EE2); 4.26 ml of H_2SO_4 (0.1 M concentration) has been stirred with 800 ml of DI water. A constant potential of 10 V was applied to initiate the exfoliation process, which has taken about 1 hour. After the initial exfoliation process ultra-sonication bath has been applied for 2 hours. Then the exfoliated graphene washed with DI water for 3 times in centrifuged at 4000 rpm for 15 min. Then the sample has left to dry at 80°C for one night.

Results and Discussion

In this study, the obtained samples were all in powder state, which are rGO, EE1, and EE2. The characteristics have been evaluated using Raman spectroscopy, FTIR, XRD, and SEM spectroscopy.

a) Raman Spectroscopy

Raman spectra is used to describe the defects density, doping or functionalization extent, and determining the number of graphene layers. Raman Spectroscopy characteristics have been performed on a RENISHAW in via Raman microscope, with laser monochromatic light at 532nm, with lenses 20x, and 50x. In graphene oxide and reduced graphene oxide samples, two bands are important, the D band is known as defective band which represents the first order scattering of sp^3 hybridized of carbon atoms, while the G band represents the stretching vibration of sp^2 hybridized of carbon bonds.

While in the case of the exfoliated graphene samples, both of D band, G band and the third band 2D are important, where the shape and position of 2D peak is the measure to determine the number of graphene layers per each flake.

Figure 1 shows the Raman spectra of GO before and after reduction process. As can be seen in the figure, the defects on the surface of the rGO decrease which relatively decrease the D band intensity compared to that of GO. The calculated I_D/I_G ratio value of GO and rGO are 0.84 and 0.85, respectively, as seen in Table 1. The increase in the defect density is due to the restoration of sp^2 carbon and decreased in the average sizes of sp^2 domains upon reduction [5,6,9].

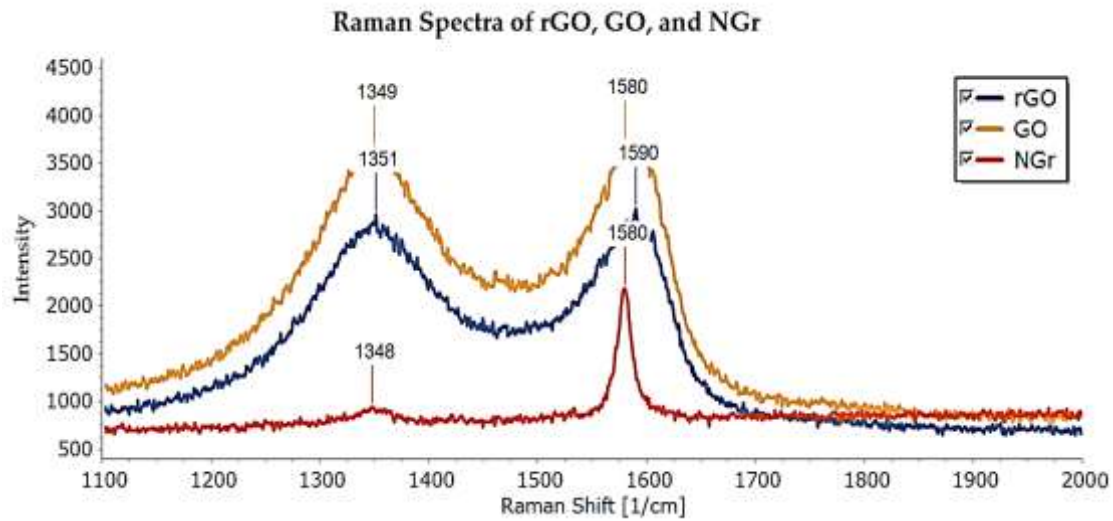


Figure 1. Raman spectra of rGO, GO, and NGr for Hummers' method

Table 1. The defect density in NGr, GO, and rGO

Sample	I_D/I_G
NGr	0.43
GO	0.84
rGO	0.85

Figure 2 shows the Raman spectra of electrochemical exfoliated graphene for both EE1, and EE2. As shown in Table 2. The defect ratio has decreased after the electrochemical exfoliation process in both EE1 and EE2.

While the second important ratio I_{2D}/I_G has showed very interesting results, where the ratio increased by 0.05, and 0.14 after electrochemical exfoliation process for EE1, and EE2 respectively, which has confirmed obtaining low-layered exfoliated graphene sheets [7,9].

Table 2. The defect density I_D/I_G and graphene layer ratio I_{2D}/I_G in NGr, exfoliated graphene EE1 and EE2

Sample	I_D/I_G	I_{2D}/I_G
NGr	0.28	0.55
EE1	0.64	0.60
EE2	0.59	0.64

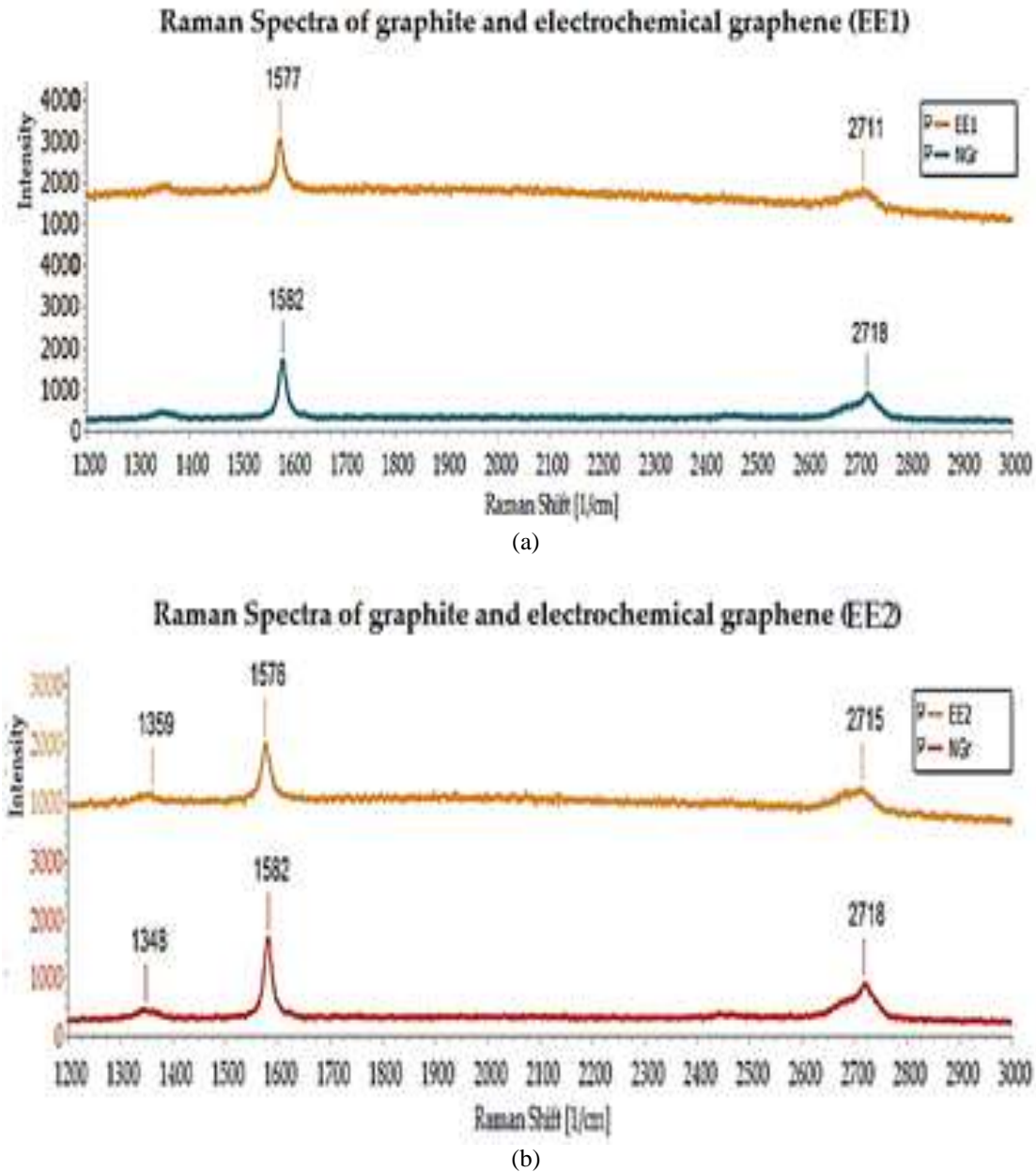


Figure 2. Raman spectra of graphite and electrochemical exfoliation graphene, EE1 with inorganic salts electrolyte, and EE2 with inorganic solvent electrolyte.

b) Fourier-transform infrared spectroscopy (FTIR)

Fourier transform infrared (FTIR) spectroscopy is used to identify the different functional groups in chemical structures of the material. FTIR Spectroscopy characteristic has performed on Thermo scientific NICOLET iS10, with spectrum Range: 4000 - 400 cm^{-1} , and depth: 550 mm.

Figure 3 shows the absorption peaks for rGO, GO, and NGr. For NGr spectra, there was no significant peak found. Furthermore, for GO, the intense and broad peak that appeared at wavelength of 3420 cm^{-1} confirmed the presence of O-H bond, aside C-O stretching can be seen at wavelength of 1340 cm^{-1} .

For RGO, the peak at 3420 cm^{-1} became less broad as compared with GO proving that the hydroxyl group has removed significantly. It is also noticeable that other peaks at 2200 and 3360 cm^{-1} are related to the stretching vibrations of C=C and O-H groups, respectively became less intense than those peaks of GO spectra, which were also due to the removal oxygen by using hydrazine hydrate during the reduction.

The peaks located at 1631 and 1384cm^{-1} are associated with stretching vibration of C-O bond and bending vibration of C-OH groups, respectively. Finally, as can be seen, the reduction of oxygen-containing functional groups has done successfully [6,8].

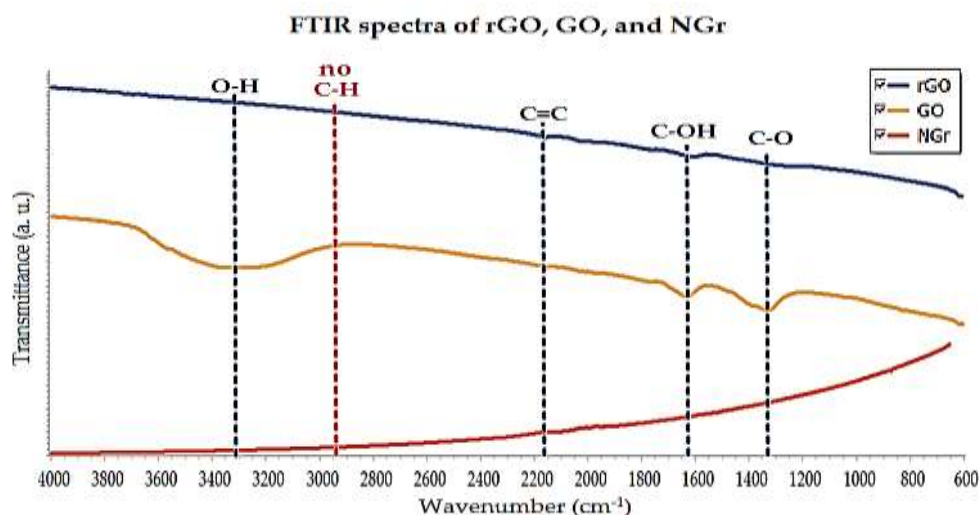


Figure 3. FTIR spectra of GO before and after the reduction process

c) X-ray Powder Diffraction (XRD)

X-ray diffraction is used to examine, determine the crystal structure and the phase change of graphite after oxidation, reduction, and exfoliation processes. X-ray diffraction has employed on Thermo Scientific ARL X'TRA, with Cu- X-ray source, and scanning range ($2\theta = 5 - 60^\circ$)

Figure 4(a) represents the XRD patterns for NGr, GO, and rGO. The yellow curve of GO exhibits an intense diffraction peak at $2\theta = 13.8^\circ$ which is related to the (002) crystalline plane. While in the case of rGO (blue curve), the sharp peak at 13.28° is completely disappeared and a new broad peak appears at $2\theta = 24.24^\circ$, which clearly shows that the oxygen functionalities were significantly reduced and just like that rGO has formed [6,8].

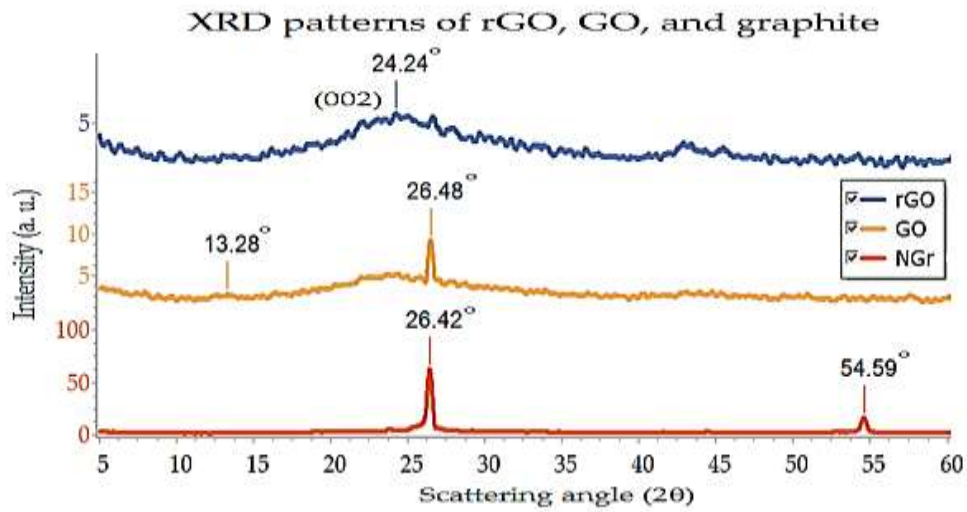
Figures 4(b) and 4(c) represent XRD patterns of electrochemical exfoliation graphene sheets in the peak position of patterns of graphite and exfoliated graphene sheets have not changed in all specimens, where all diffraction peaks at around 26.5° .

The only change has happened after exfoliation process is the peak intensity has weakened from graphite to graphene pattern. The decreased of the intensity is related to the reduction of the number of graphene sheets layers, which has confirmed the successful exfoliation process [7].

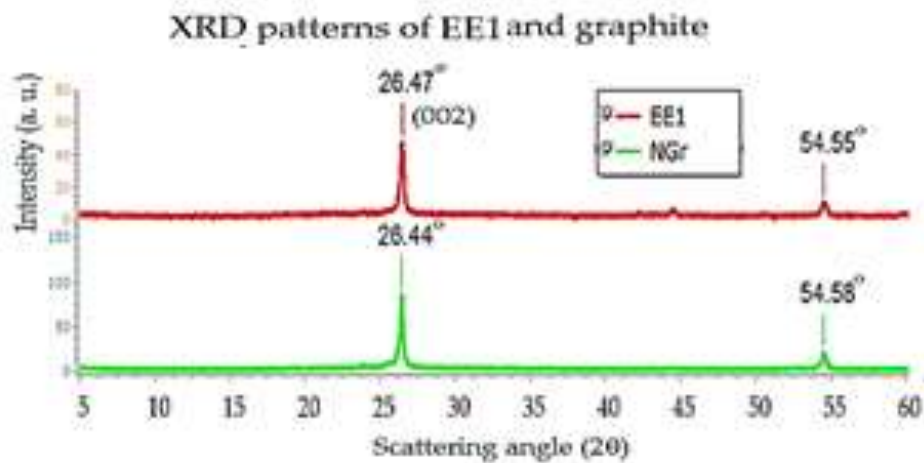
d) Scanning Electron Microscopy (SEM)

SEM (COXEM EM-30 Plus) has been employed with magnification rate 500 - x10k at 20KV to observe the morphology and surface microstructure of the rGO and exfoliated graphene sheets.

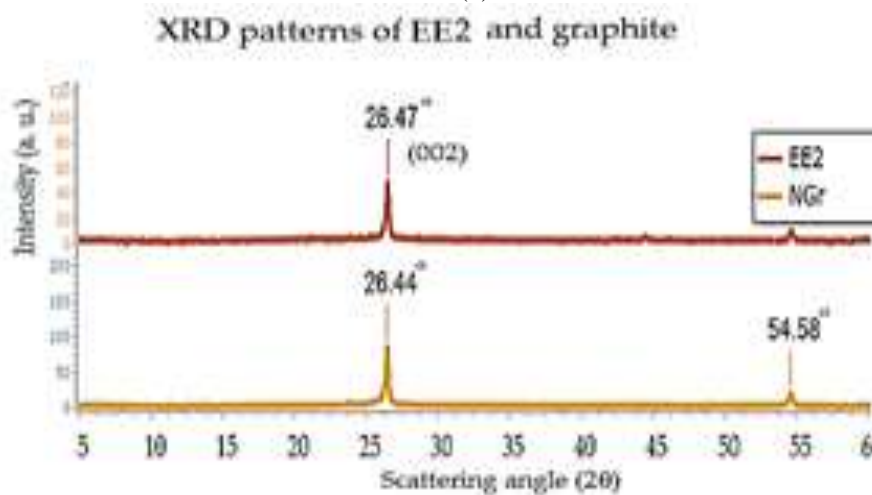
Figures 5(a) and 5(b) show the morphology of natural graphite sheets, as can be seen the aggregation of graphene layers is obvious above each other, with lateral size of is about $\sim 2\text{-}30\ \mu\text{m}$. Figure 5(c) shows the morphology of GO sheets, which are smooth with small wrinkles and folded at the edges, while Figure 5(d) shows SEM image for rGO, which has revealed that the material consists of accumulated and aggregated sheets of reduced graphene oxide [8].



(a)



(b)



(c)

Figure 4. XRD patterns of
(a) GO and rGO, (b) EE1 with NGr, (c) EE2 with NGr

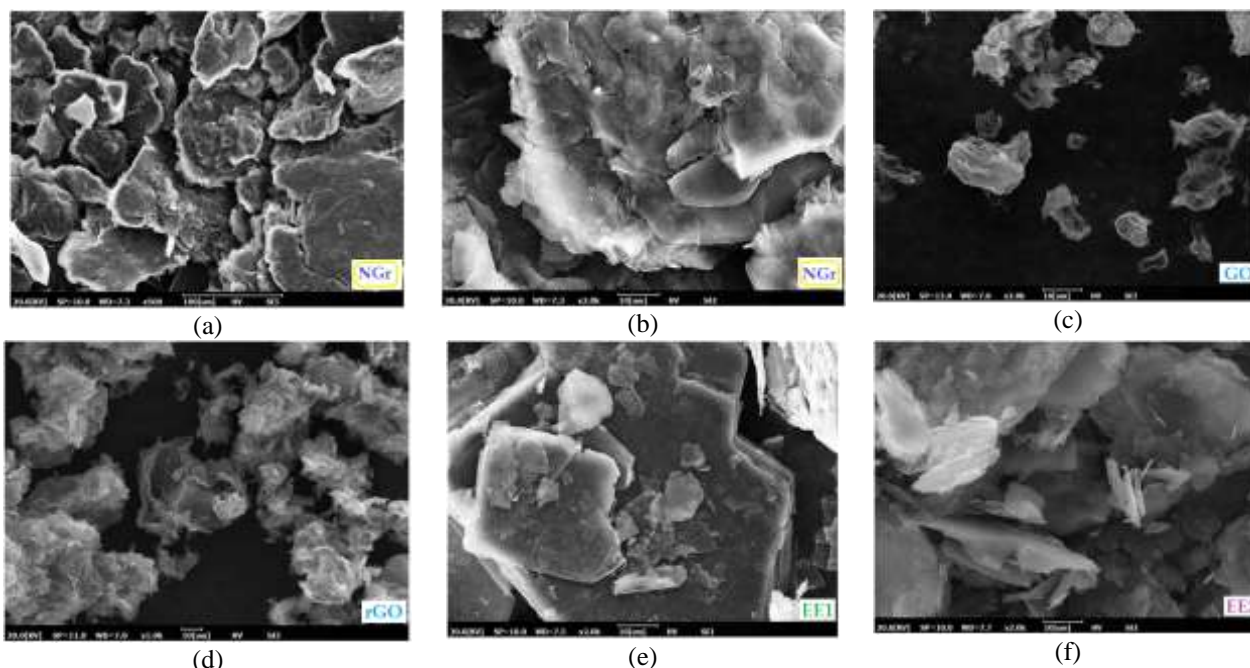


Figure 5. SEM images of (a-b) Natural graphite, (c) GO, (d) rGO, (e) Exfoliated graphene sheets EE1, (f) Exfoliated graphene sheets EE2

The SEM images of synthesized GO, and rGO exhibit well exfoliated layered 2D morphology with the size of few μm [8,9].

Figure 5(e) shows the morphology of electrochemical exfoliation graphene sheets in inorganic salt electrolyte (EE1). As can be seen, the lateral size of sheets have decreased from $\sim 2\text{-}30\ \mu\text{m}$ in the natural graphite sample to $\sim 3\text{-}10\ \mu\text{m}$ after electrochemical exfoliation in Figure 5(e).

Figure 5(f) shows the morphology of electrochemical exfoliated graphene sheets in an inorganic solvent electrolyte (EE2). The same effect has happened to the lateral size of exfoliated graphene sheets, which lateral size of graphene sheets with $\sim 3\text{-}10\ \mu\text{m}$. This result implies the breaking of graphite particles at their weak points, which is confirm the successful exfoliation process [5,9].

Conclusions

In this study, both of rGO and low-layered graphene sheets have been synthesized with modified Hummers' method, and electrochemical liquid phase exfoliation methods respectively. The synthesized rGO powder has been produced successfully, and the reduction process has showed decreasing of the defects on the surface.

A practical and simple electrochemical liquid phase exfoliation approach of graphene based on two different inorganic solutions as electrolytes of graphite into low-layered graphene sheets with sodium sulfate and hydrochloric acid as the intercalation agents has been proposed.

Since all the reagents have been used are not harmful and easily available, it has found that the synthesis of electrochemical exfoliation of graphite rod with hydrochloric acid electrolyte. EE2 has got the best results whence of low-layered graphene and less time.

Acknowledgement

The first author of this study was supported by the Presidency for Turks Abroad and Related Communities (YTB) within "International Student Academy" Project.

References

- [1] Novoselov KS, Geim AK, Morozov SV, Jiang D, Zhang Y, Dubonos, SV, et al. (2004) Electric field effect in atomically thin carbon films. *Science* 306(5696): 666–669.

**3rd International Students Science Congress
3-4 May 2019, İzmir - Turkey**

- [2] Zaaba NI, Foo KL, Hashim U, Tan SJ, Liu W-W, Voon CH (2017). Synthesis of graphene oxide using modified Hummers' method: solvent influence. *Procedia Engineering* 184: 469-477. doi: 10.1016/j.proeng.2017.04.118
- [3] Achee TC, Sun W, Hope JT, Quitzau SG, Sweeney CB, Shah SA, Habib T, Green MJ (2018) High-yield scalable graphene nanosheet production from compressed graphite using electrochemical exfoliation. *Scientific Reports* 8, Article Number: 14525. doi:10.1038/s41598-018-32741-3
- [4] Lin L-S, Westwood AVK, Drummond-Brydson R (2016) Graphene synthesis via electrochemical exfoliation of graphite nanoplatelets in aqueous sulphuric acid. *Carbon* 2016, 10-15 Jul 2016, Pennsylvania State University, Pennsylvania, United States.
- [5] Matsumoto, M., Saito, Y., Park, C., Fukushima, T., & Aida, T. (2015). Ultrahigh-throughput exfoliation of graphite into pristine 'single-layer' graphene using microwaves and molecularly engineered ionic liquids. *Nature Chemistry*, 7(9), 730-736.
- [6] Hidayah NMS, Liu W-W, Lai C-W, Noriman NZ, Khe C-S, Hashim U, Lee HC (2017). Comparison on graphite, graphene oxide and reduced graphene oxide: Synthesis and characterization. *AIP Conference Proceedings* 1892(1) 150002.
- [7] Parvez K, Wu ZS, Li R, Liu X, Graf R, Feng X, Müllen K (2014) Exfoliation of graphite into graphene in aqueous solutions of inorganic salts. *Journal of the American Chemical Society* 136(16): 6083–6091. <https://doi.org/10.1021/ja5017156>.
- [8] Cao N, Zhang Y (2015) Study of reduced graphene oxide preparation by Hummers' method and related characterization. *Journal of Nanomaterials*, Article ID 168125, 5 pp.
- [9] Martins Ferreira EH, Moutinho MVO, Stavale F, Lucchese MM, Capaz RB, Achete CA, Jorio A (2010) Evolution of the Raman spectra from single-, few-, and many-layer graphene with increasing disorder. *Physical Review B*, 82(12) 125429.

Investigation of Mechanical Properties of Al/SiC/nano-FeB Hybrid Composites

Hülya Durmuş*, Nilay Çömez, Canser Gül, Murat Yıldırımkal
Manisa Celal Bayar University, Dept. of Metallurgical and Materials, Manisa, Türkiye.
*Corresponding author: hulya.durmus@cbu.edu.tr

Keywords: aluminum, nano-FeB, SiC, metal matrix composite (MMC), wear

Discipline: Metallurgical and Materials Engineering

Abstract

This study concerned with hardness and wear behavior of Al/SiC/nano-FeB metal matrix composites. These composites which include various weight contents of SiC and nano-FeB (0%, 10%) are produced by powder metallurgy-hot pressing method. Density values of the produced samples measured by Buoyancy Method and calculated by the Archimedes Principle. Then the samples are exposed to wear test at room temperature. Wear tests carried out pin-on-disc wear test machine. A CSM instruments ball-on-disc wear-test unit with an alumina ball was used for the tribological analysis of composites under dry-sliding condition. Contact load was adjusted as 2 N. Sliding speed was set to 15 cm/s along the sliding distance of 100 m. Volumetric material loss was determined by obtaining the profile of the wear track. Material loss tended to increase with increasing sliding distance but it decreases with increasing reinforced materials. The change of material loss between the sliding distance values showed a decreasing trend due to the filling of wear track by the wear debris of alumina ball.

Introduction

For over four decades, aluminum metal matrix composites (AMMC) have been developed to enhance mechanical properties, reduce cost and the weight of parts. AMMC's are used in many fields such as automobile, aerospace and defense industries, because of their high specific modulus, superior wear resistance, great strength when compared to unreinforced materials [1-3].

Ceramic particles such as silicon carbide (SiC), boron carbide (B₄C), iron boride (FeB and Fe₂B) and alumina (Al₂O₃), that have high strength, wear and fatigue resistance are used as a reinforcement to production the particulate reinforced AMMC's. Many different techniques are used for the fabrication of composites such as injection die casting, stir casting and powder metallurgy [4-6].

Reinforced particles can affect mechanical properties, processability, corrosion resistance of composites in different ways. As the type of particle is important, its size and shape are also important [7]. The effects of nano-sized reinforcements on the mechanical or wear properties have not been thoroughly studied.

Materials and Methods

Pure aluminum powder was used as a matrix material. Nano-FeB particles have an average size of 600 nm. Hot pressing was applied for 1 hour at 500 °C and 300 MPa (Figure 1).



Figure 1. Schematic illustration of sample preparation

The produced composite was cut into 16x16x6 mm³ pieces. Densities of the prepared samples were determined by the Archimedes principle.

Microstructural investigations were fulfilled by Nikon Eclipse LV 150 optical microscope using Clemex Software. Hardness measurements were carried out by using Duravision 2000 EMCO Test Brinell hardness tester under 6.25 kg load. Wear performance of the composites was determined by the CSM ball-on disc wear test apparatus under 2 N load for 100 m. Sliding speed was set to 15 cm/s. Schematic illustration of the wear test shown in Figure 2. Wear track profile was obtained by a profilometer at 50m and 100m. Then the volumetric wear loss was calculated using the measurements of the profilometer.

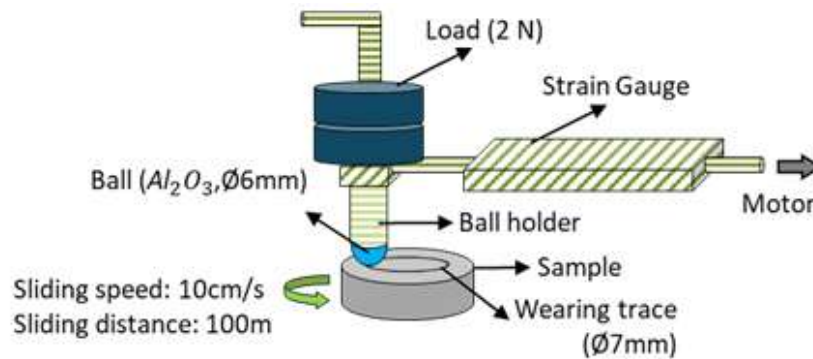


Figure 2. Schematic illustration of wear test

Results and Discussion

The actual density measurements of the produced samples were made, their theoretical densities were calculated and the density-porosity values shown in Table 1 were reached. The density value achieved was at the expected level for the powder metallurgy method in the Al sample. However, the density value obtained for the nFeB-SiC composite was above the expected level and very close to the theoretical density. Al powder particles used contain approximately the same size spherical powder particles. Using the same size of powder prevents the complete removal of voids during sintering the powder metallurgy method, and may cause some porosity [8]. Although the reinforcing elements used were hard, the very small amount of n-FeB particles facilitated the dispersion and reduced porosity by helping to fill in the porosities.

Table 1. Density values of samples

Sample	Theoretical density (g/cm ³)	True density (g/cm ³)	Density value (%)	Porosity (%)
Al	2.70	2.66	98.5	1.5
Al + nFeB/SiC	2.85	2.83	99.3	0.7

The microstructure images of the composite samples produced were shown in Figure 3. The grains were nearly equiaxial. SiC-nano FeB particles showed the almost homogeneous distribution in the aluminum matrix. Some porosities also were observed in the microstructure. These porosities in microstructure are thought to be compatible with the porosity percent values in Table 1.

When the wear traces shown in Figure 5 were examined, a deep and continuous wear trace was observed in the non-reinforced sample. In the reinforced sample, shallow and discontinuous and trace of wear were observed. Width of the wear trace mean value was measured for the unreinforced sample as 2700 μm and for the reinforced hybrid composite 1400 μm . According to the calculations, the width of the wear trace decreased by 47 %. The profile examinations of the worn surfaces were given in Figure 5.e for unreinforced and Figure 5.f for reinforced aluminum. When these figures were examined, it was observed that the unreinforced sample exhibits a wear behavior to form a deep recess. Wear traces were calculated as volumetric with the aid of the data received and were graphically shown in Figure 6. These calculations were repeated for 8 different regions and made based on the average of all values. A decrease in a volumetric loss by 82 percent was observed with the reinforcement.

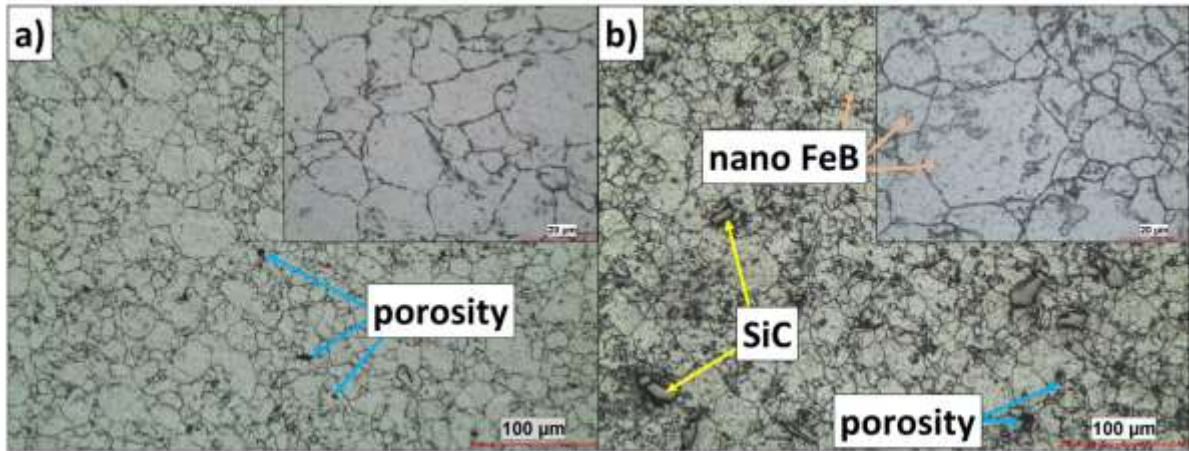


Figure 3. The microstructure of composites a) unreinforced Al, b) n-FeB and SiC reinforced Al

Hard particles reinforcing was affected positively to the Brinell hardness (Figure 4). Particulate reinforcement enhanced the hardness of the composites due to their property of higher hardness than Al, matrix [9].

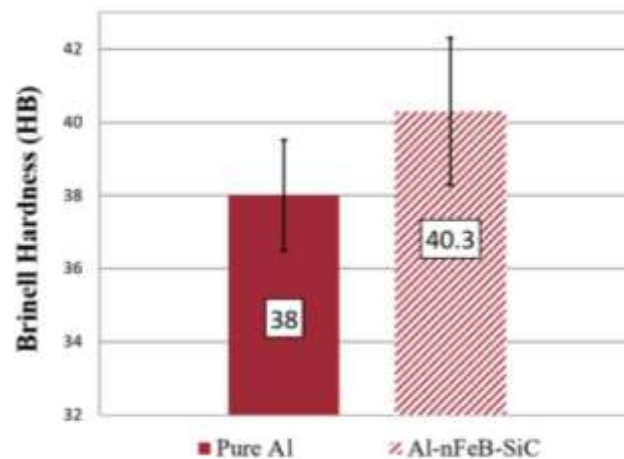


Figure 4. Brinell hardness measurements of the samples

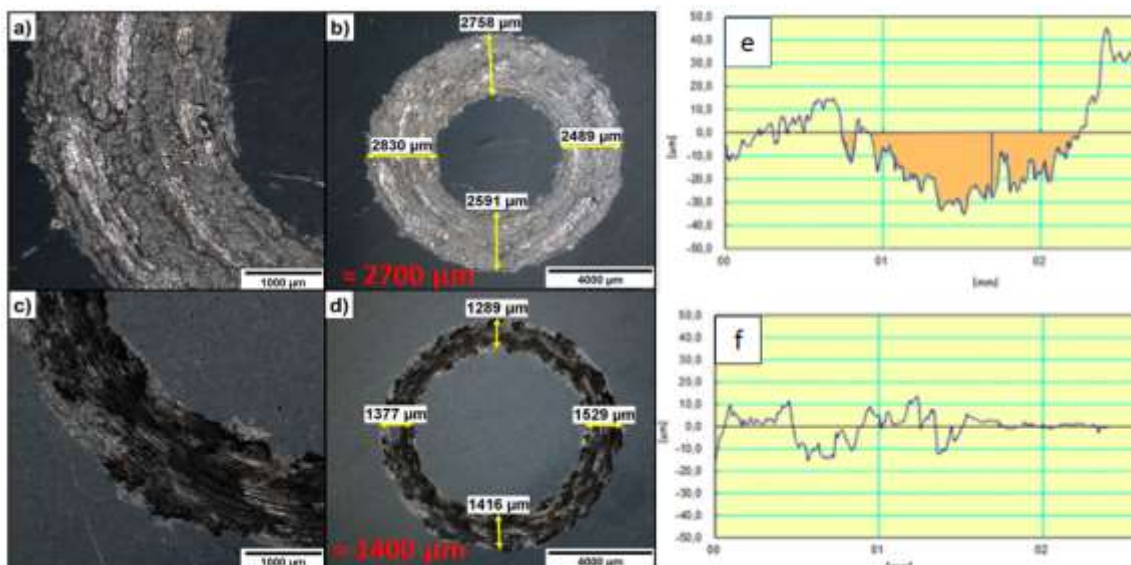


Figure 5. Wear traces of a,b) Al, and c,d) n-FeB and SiC reinforced Al composite

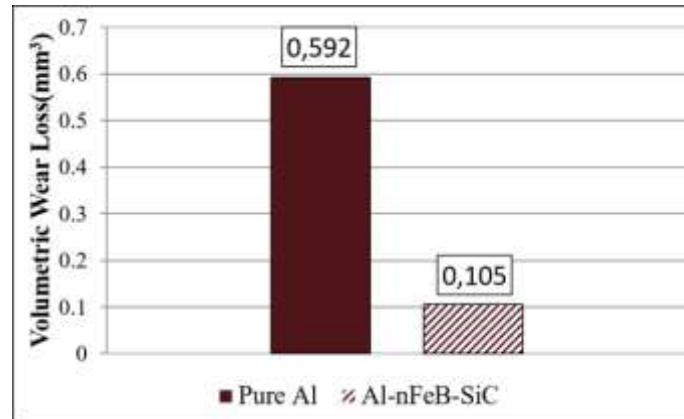


Figure 6. Volumetric wear loss of pure Al and n-FeB and SiC reinforced Al composite

Conclusion

1. SiC particles showed the almost homogeneous distribution in an aluminum matrix.
2. Porosity was found to be less in two samples from density test and microstructure investigations.
3. Brinell hardness of composite increased with the effect of reinforcements. nFeB-SiC particles reinforcing was enhanced the Brinell hardness of composite by 6 %.
4. It was observed stick-slip mechanism from stereo images in Al and Al-nFeB-Si composite.
5. Volumetric wear loss of composite decreased with the effect of reinforcements.

References

- [1] Madeira S, Miranda G, Carneiro VH, Soares D, Silva FS, Carvalho O (2016) The effect of SiCp size on high temperature damping capacity and dynamic Young's modulus of hot-pressed AlSi-SiCpMMCs. *Materials Design* 93:409–417. <https://doi.org/10.1016/j.matdes.2015.12.147>
- [2] Xavier MA and Ajith Kumar JP (2017) Machinability of Hybrid Metal Matrix Composite - A Review. *Procedia Engineering* 174:1110–1118. <https://doi.org/10.1016/j.proeng.2017.01.264>
- [3] Manigandan K, Srivatsan TS, Quick T (2012) Influence of silicon carbide particulates on tensile fracture behavior of an aluminum alloy. *Materials Science and Engineering A* 534:711–715. <https://doi.org/10.1016/j.msea.2011.11.081>
- [4] Xue Y, Shen R, Ni S, Song M, Xiao D (2015) Fabrication, microstructure and mechanical properties of Al-Fe intermetallic particle reinforced Al-based composites. *Journal of Alloys and Compounds* 618:537–544. <http://dx.doi.org/10.1016/j.jallcom.2014.09.009>
- [5] Soltani S, Khosroshahi RA, Mousavian RTi Jiang Z-Y, Boostani AF, Brabazon D (2017) Stir casting process for manufacture of Al-SiC composites. *Rare Metals* 36(7):581–590. <http://doi.org/10.1007/s12598-015-0565-7>
- [6] Darabara M, Papadimitriou GD, Bourithis L (2006) Production of Fe-B-TiB₂ metal matrix composites on steel surface. *Surface and Coatings Technology* 201:2518–3523. <http://doi.org/10.1016/j.surfcoat.2006.08.105>
- [7] Anthony Xavier M, Ajith Kumar JP (2017) Machinability of Hybrid Metal Matrix Composite - A Review. *Procedia Engineering* 174:1110–1118. <http://doi.org/10.1016/j.proeng.2017.01.264>
- [8] Hassani A, Bagherpour E, Qods F (2014) Influence of pores on workability of porous Al/SiC composites fabricated through powder metallurgy + mechanical alloying 591:132–142.
- [9] Annigeri U and Veeresh Kumar G (2018) Effect of Reinforcement on Density, Hardness and Wear Behavior of Aluminum Metal Matrix Composites: A Review. *Materials Today: Proceedings* 5(5):11233–11237. <https://doi.org/10.1016/j.matpr.2018.02.002>

Nanotechnology / Nanoteknoloji

A Study on Improvement of Mechanical Properties of Bone Cement with ZnO Functionalized Carbon Fiber Derivatives

Emine Özge Akkaş, İzmir Kâtip Çelebi Univ. Inst. of Natural & Applied Sciences, Dept. of Nanoscience & Nanotechnology, İzmir, Turkey

Ahmet Aykaç*, İzmir Kâtip Çelebi Univ., Dept. of Engineering Sciences, İzmir, Turkey

*Corresponding author: ahmet.aykac@ikc.edu.tr

Keywords: bone cement, carbon fiber, ZnO-nanowires, interface/interphase, mechanical properties

Discipline: Nanotechnology and Materials Science

Abstract

The aim of this study was to improve the mechanical properties of acrylic bone cement, which is widely used in orthopedics and traumatology. Carbon fiber and modified carbon fibers were added to the acrylic bone cement and the possible effects on the mechanical properties of the bone cement were investigated. Carbon fibers were subjected to galvanic coating and anodizing respectively. Zinc plating was performed on equal surface area of carbon fibers by galvanic coating. ZnO nanowires were then grown on the coated carbon fiber structures by electrowinning. SEM, XRD and FTIR characterizations were used to investigate the size, stability and conductivity of zinc and zinc oxide structures produced on carbon fibers. As a result of the characterization, the most suitable parameters for homogeneity, continuity and coating thickness were determined as 09V10m for galvanic coating and 20V30m for electrowinning. The obtained CF, CF / Zn and CF / ZnO structures were added to the bone cement by 0.1-1% by weight, resulting in polymeric composite materials. These composite materials were subjected to compression and 4 point bending tests and their mechanical properties were examined. As a result of mechanical tests, it can be said that the elastic stress of acrylic bone cement decreases and maximum force increases.

Introduction

In orthopedics, bone cement is commonly used to stabilize the implant by placing it between the implant and the joint and to prevent irregular stress distribution between bone and implant [1]. As an artificial component, PMMA results in the formation of a fibrous layer at the junction between cement and bone, and this particular event can lead to small implants and thus early deterioration. These problems lead to an increase in academic studies to improve the mechanical properties of bone cements [2]. Considering the disadvantages of PMMA, the synthesis of bone cement composites composed of bio-ceramic and carbon-based nanomaterials to improve the mechanical properties of bone cement for biomedical applications has been proposed [3].

Carbon fiber (CF) materials are more widely used than other carbon-based materials with their low cost, strong mechanical properties and are more suitable for mass production than other carbon based nanomaterials. Low fiber strength is a general problem when fully utilizing the excellent physical performance of carbon fiber reinforced polymer composites [4]. Poor fiber-matrix interfacial adhesion may adversely affect the physical and mechanical properties of composites due to surface mismatch between hydrophilic inorganic fillers carbon fiber and non-polar resin [5]. Therefore, it is necessary to support interfacial adhesion and chemical method [6], electrochemical method [7] and so on. In order to improve the properties of composites, various methods have been applied in the carbon fiber surface modification. In some of these methods, the use of biocompatible ZnO-NP has been carried out to increase the adhesion of the carbon oxide doped polymeric composites on carbon fiber surfaces. Zinc oxide nanostructures (ZnO / NP) are more prominent than other metal oxides, such as high specific surface area, biotoxic areas, chemical processes, electrochemical activity and high electron mobility [8, 9].

When literature researches are examined, the number of studies based on the effects of carbon fibers and their modifications on the mechanical behavior of acrylic bone cements is limited. In this study, a new polymeric composite material was added with the addition of 0.1-1% by weight of CF, CF / Zn and CF / ZnO nanocomposite structures to the PMMA bone cement and the changes in the mechanical properties of composite bone cement were investigated.

Methodology

1. Preparation of Carbon Fiber and Modifications

In the first stage to form ZnO nanostructures on carbon fibers, Zn layer was prepared with electrochemical coating on carbon fiber. The electrochemical coating was carried out using an adjustable power supply in the ZnCl₂-based electrolyte. Various parameters such as different potential current, time and temperature were used to obtain the most compatible production methods of the structures in electrochemical coating processes. In the production of ZnO nanostructures, the second stage of the electrochemical anodization process was carried out on the coating experiments which were determined in the appropriate parameters as a result of the characterizations. ZnO nanostructures were grown on carbon fiber using the anodizing method. Anodizing was carried out in a 5mM Potasyumbarbonate (KHCO₃) solution via a DC power source and the distance between the anode cathode was kept about 6 cm for all experiments. For the anodization process, different voltage values and different time studies were performed. The morphology of the Zn and ZnO nanostructures formed on the surface of the carbon fibers as a result of coating and anodization was investigated using a Carl Zeiss 300VP Scanning Electron Microscope (SEM). 1 µm to 10 µm of images were taken for each of the plating and anodizing samples. X-ray diffraction patterns of the samples were determined to determine the phase structure by means of a diffractometer with Cu Ka irradiation. FTIR spectra were recorded using a Thermo Scientific Nicolet iS50 FT-IR Spectrometer in the spectral range 4000-500 cm⁻¹.

2. Preparation of Composite Bone Cement

The bone cement content used in the study was based on the formula of commercial bone cement DePuy CMW1 [10]. In the preparation of composite bone cements, the powder and liquid phases were prepared in a sterile environment by hand mixing with a sterile vessel and a sterile stir bar. The addition of CF, CF / Zn and CF / ZnO structures were obtained by adding 0.1-1% by weight of cement to the powder component. For comparison, 4 different polymeric nanocomposite (PMMA, PMMA / CF, PMMA / CF / Zn, PMMA / CF / ZnO) structures were obtained. The prepared composite bone cements were stored at room temperature and humidity conditions for 1 week. Then, 4 point bending and compression tests were performed to examine the mechanical properties of composite bone cements.

Results

As a result of the experiments, zinc coating process on carbon fiber surfaces has been successful with chemical galvanic coating. The coating results showed that the reaction time, temperature and current directly affected the Zn coating on CF. Characterization of plating experiments with different parameters was performed by scanning electron spectrometer (SEM). The SEM images of the samples formed in different parameters are shown in Figure 1. The most homogeneous and best coating thickness of the galvanized coating process by using the SEM images is the product studied in the 09V10 min parameter. The Zn thickness deposited on the carbon fiber was 1.177 µm.

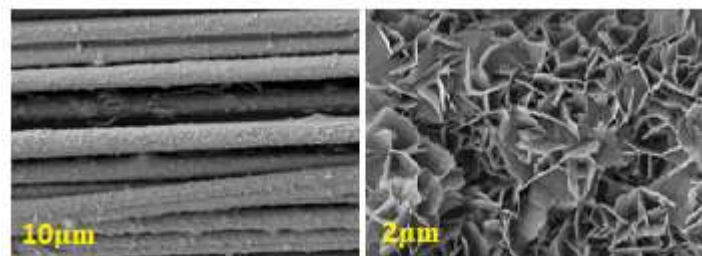


Figure 1. SEM images of CF / Zn composites coated by chemical electroplating method 09V10m.

Based on the results obtained from the electrochemical anodization process, the anodising operations were successful without error. The SEM images of the samples with the best parameters are shown in Figure 2. The thickness of Zn deposited on the carbon fiber was 3.2785 µm.

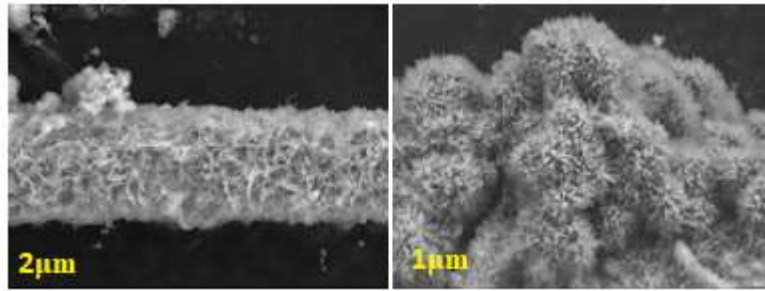


Figure 2. SEM images obtained by electrochemical anodization of zinc coated carbon 20V30m

X-ray diffraction of the Zn and ZnO doped carbon fiber samples obtained after coating and anodization was measured with Panalytical Empyrean XRD using CuK α . Radiation ($K\alpha$ (\AA) = 1.5418 \AA) and $K\beta$ (\AA): 1.392 \AA at a scanning rate of 5. To 90 kayded and 12 / min. After the electrochemical coating and electrochemical anodization, XRD images of the determined parameters were taken. The X-Ray pattern of the sample in the pure carbon fiber and modified determined parameters for comparison purposes is shown in Figure 1. The pattern contains two crystal phases. These phases are zinc (01-087-0713) and carbon (01-075-0444) related to JCPDS numbers. As a result of electroplating, the zinc phase was successfully obtained for the sample.

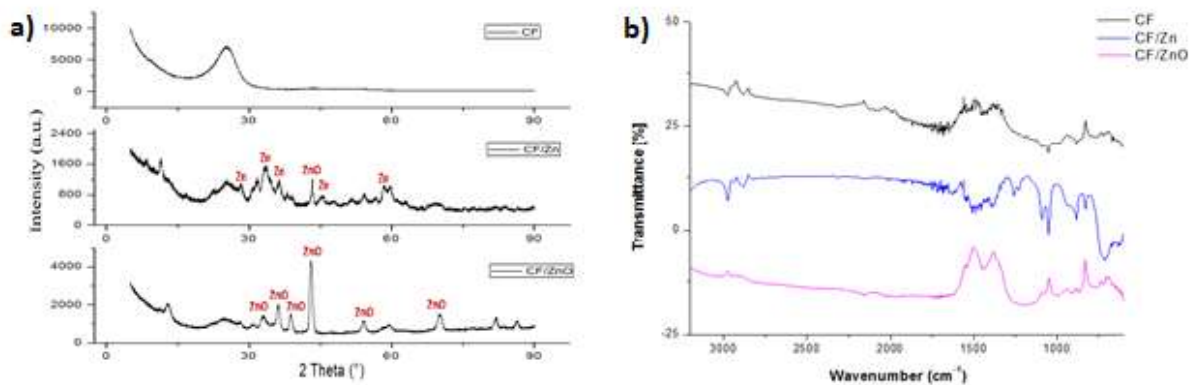


Figure 3. a) XRD results of CF, CF / Zn and CF / ZnO samples b) FTIR results of CF, CF / Zn and CF / ZnO samples

FTIR images of Zn and ZnO doped carbon fiber samples were obtained after plating and anodising. As a result of the images, there were no unwanted functional groups on the samples after coating and anodizing.

The Zn-coated carbon fiber specimen may have a peak value of 1144 cm^{-1} in the Zn metal. The peaks at 1679 cm^{-1} correspond to the Zn-O stretching and deformation vibration. Infrared studies have been conducted to determine the purity and nature of metal nanoparticles. Metal oxides generally provide absorption bands in the fingerprint region resulting from interatomic vibrations, ie below 1000 cm^{-1} .

As a result of all the characterizations, the addition of parameters of the determined carbon fiber, Zn coated carbon fiber and ZnO coated carbon fibers to 0.1-1% by weight will be added to the bone cement. In order to investigate the mechanical properties of composite bone cements prepared with different additives, bending and compression tests will be applied.

Conclusion

In summary, nanostructured ZnO layers were successfully formed on carbon fibers using electrochemical coating and anodization methods in different coating and anodization parameters. New type of composite bone cements will be obtained by the addition of carbon fiber and its modifications to bone cement. The positive or negative effects of the addition of CF, CF / Zn and CF / ZnO nanowires

on bone cement in the mechanical performance of PMMA will be investigated. As a result of the study, new generation composite bone cement which will be the source of new research will be obtained.

References

- [1] Kuhn KD (2005) Properties of Bone Cement: what is Bone Cement?, The Well-cemented Total Hip Arthroplasty. Springer Medizin Verlag, Heidelberg, pp. 52–59.
- [2] Fottner A, Nies, B., Kitanovic, D., Steinbruck, A., Mayer-Wagner, S., Schroder, C., Heinemann, S., Pohl, U., Jansson, V., (2016) Performance of bioactive PMMA-based bone cement under load-bearing conditions: an in vivo evaluation and FE simulation. *J. Mater. Sci. Mater. Med.* 27, 138.
- [3] Puskaa M., Moritza, N., Ahoa, AJ, Vallittu PK (2016) Morphological and mechanical characterization of composite bone cement containing polymethylmethacrylate matrix functionalized with trimethoxysilyl and bioactive glass. *J. Mech. Behav. Biomed. Mater.* 59:11-20
- [4] Sharma M, Gao S, Mäder E., Sharma, H., Wei, L. Y., & Bijwe, J. (2014). Carbon fiber surfaces and composite interphases. *Composites Science and Technology*, 102, 35-50.
- [5] Xie Y, Hill CA, Xiao, Z., Militz, H., Mai, C. (2010). Silane coupling agents used for natural fiber/polymer composites: A review. *Composites Part A: Applied Science and Manufacturing*, 41(7), 806-819.
- [6] Toyoda M, Katoh H, Inagaki M (2001). Intercalation of nitric acid into carbon fibers. *Carbon*, 14(39), 2231-2234.
- [7] Ishifune M, Suzuki, R., Mima, Y., Uchida, K., Yamashita, N., & Kashimura, S. (2005). Novel electrochemical surface modification method of carbon fiber and its utilization to the preparation of functional electrode. *Electrochimica Acta*, 51(1), 14-22.
- [8] Ehlert GJ, Galan U, Sodano HA (2013) Role of surface chemistry in adhesion between ZnO nanowires and carbon fibers in hybrid composites. *ACS Applied Materials & Interfaces*, 5(3), 635-645.
- [9] Drzal LT, Sugiura N, Hook D (1997) The role of chemical bonding and surface topography in adhesion between carbon fibers and epoxy matrices, *Compos. Interfaces* 4 337–354.
- [10] Ormsby R, McNally T, Mitchell C, Dunne N. (2010). Incorporation of multiwalled carbon nanotubes to acrylic based bone cements: Effects on mechanical and thermal properties. *Journal of the mechanical behavior of biomedical materials*, 3(2), 136-145

Development of Glucose Biosensor from Hierarchical Graphene/ α -Fe₂O₃ Nanocomposites

Harun Hano, Ahmet Aykaç*

İzmir Kâtip Çelebi University, Nanoscience and Nanotechnology, Izmir, Turkey

*Corresponding author: ahmet.aykac@ikc.edu.tr

Keywords: chitosan, glucose oxidase, nanobiosensor, graphene foam, nanowires

Discipline: Nano Science and Nano Engineering

Abstract

Biosensors containing biosensing materials and transducers have been tried to be functionalized for years to selectively detect biologically and chemically active components in a fast and precise measurement. Due to the outstanding properties such as electron mobility, high surface area and electrical conductivity, Three-Dimensional Graphene Foam (3D-GF) has been preferred especially in order to produce highly selective glucose biosensor. Moreover, α -Fe₂O₃ nanowire structure is also selected to further increase surface area and the efficiency of the electron transport system. In order to increase the binding mechanism of Glucose Oxidase (GOx) enzyme for measuring glucose level, Chitosan (CS), a biodegradable and biocompatible polymer, will be applied to the surface. The characterization of GF used in this biosensor study has been successfully completed to the desired extent. For the selection of the suitable composite material, the investigation of α -Fe₂O₃ nanowire structure and the determination of appropriate amount of CS is still continued by working on various parameters. The aim of this study is to develop a sensitive and selective glucose biosensor by the formation of GF/ α -Fe₂O₃/CS/GOx composite structure.

Introduction

Diabetes is a disease that occurs when insulin hormone does not work regularly and is out of a certain range of blood glucose. The regular measurement of blood glucose is quite important for the prevention of other diseases in the body. Thus, the production of various functionalized glucose biosensors has an important role. Graphene, a two-dimensional structure, is a carbon allotrope formed by the hybridization of carbon atoms with sp² and formed by layers in the honeycomb structure [1]. GF, one of the graphene derivatives, increases the number of pores in the structure, which further enhances the property of highly conductive graphene in glucose biosensor studies. In particular, it has been reported that glucose oxidase enzyme is expected to be more immobilized as the surface area of the GF increases. Thus, it is expected that measuring the amount of glucose with a material having high loading capacity increases the sensitivity of biosensors and shows excellent immobilization [2].

Moreover, iron-based nanostructures synthesized in the laboratory are used in various studies to improve electrical, optical or catalytic properties. It has been observed that nanocomposite structure, especially iron oxide-graphene based nanocomposites, has an effect on the electrical and electrocatalytic properties in sensors [3]. In particular, α -Fe₂O₃ (Hematite), whose nanowires are planned to be produced in this study, is a n-type semiconductor which is widely located in rocks and soils. This very stable red structure is generally used in photoelectrodes, gas sensors, solar cells and also; medical fields such as drug transport, tissue repair, magnetic resonance (MR) imaging are also used [4].

A material to be used in high efficiency in biosensor applications must have significant properties such as high surface area, electrochemical activity, selectivity, quick response and repeatability. Among all natural polymers, chitosan is commonly preferred because of its film-forming ability, mechanical strength, biocompatibility, biodegradability and non-toxicity [5]. It is especially used in the glucose biosensors to give the molecule higher hydrophilicity because of the amino group it contains and to display a better adhering activity of GOx onto the surface. It is notably considered to increase the bioactivity of the biosensor via covalent bonding of the enzyme to the nanocomposite structure composed of chitosan with metal oxide nanostructure [6]. In this study, GF/ α -Fe₂O₃/CS/GOx composite structure will be formed in order to develop a biosensor which allows the glucose measurement to be more precise and faster. The final biosensor structure is expected to be a material that will stand out with

its large surface area, higher conductivity and selectivity, and superior features compared to other sensor studies.

Methodology

The production of 3D-GF has been accomplished by applying for variable parameters, such as temperature, time and the amount of gases supplied to the chamber etc. Besides, α -Fe₂O₃ nanowire structure will be also enlarged on 3D-GF by selecting Hydrothermal Method. In order to increase the bonding capacity of the enzyme, the surface will be coated with CS. In addition, the selection of the most appropriate structure will be performed by interpreting the characterization results obtained in each step of the study.

Chemical Vapor Deposition method has been selected for the production of GF on a nickel base by releasing argon and hydrogen gases into a closed chamber system. PROTECH-PT-O1200-60IIIIC-4C CVD Furnace in İzmir Kâtip Çelebi University has been used during the implementation of the experiment. In broad terms, carbon atoms decomposed at high temperature by the support of methane gas have been dissolved on the surface of the nickel structure and soon after, diffused to the surface at room temperature. The carbon atoms constitute the honeycomb structure of graphene by enabling sp² hybridization with adjacent atoms so as to be at the lowest energy level. To protect the porous graphene structure, the product has been coated with Polymethyl Methacrylate (PMMA). The nickel structure has been selectively etched to produce only GF and PMMA has been removed by hot acetone. The characterizations of GF has been completed by using X-Ray Diffraction (XRD, Bruker D2 Phaser, IKCU), Raman Spectroscopy (Raman, Renishaw/In Via, IKCU) and Scanning Electron Microscopy (SEM, Carl Zeiss, IKCU).

Furthermore, after the production of GF has been successfully completed, the on-going study is in progress to fabricate α -Fe₂O₃ nanowires via controllable, low cost and environmentally safe Hydrothermal Method. In addition, Sol-Gel Method has been selected to obtain the iron oxide intermediate layer. In this method, GF will be immersed in a solution containing iron and then dried in an oven. The iron oxide film formed on the structure will be placed in the autoclave after the preparation of the appropriate amount of solution. In order to operate the biosensor mechanism within the targeted framework, the most suitable composite material will be found out depending on the characterizations of the nanowires. XRD, SEM and BET will be performed to determine the crystalline structure and surface morphology of GF/ α -Fe₂O₃.

In order to increase the binding capacity of GOx, CS polymer will be put to use due to its biocompatible, biodegradable and non-toxic properties. GF/ α -Fe₂O₃ nanowire structure will be immersed in 1% acetic acid solution containing chitosan and kept in an ultrasonic bath for 2 hours. To remove acetic acid and unbound chitosan molecules, the sample will be washed with ultrapure water in an ultrasonic bath for 5 minutes. Moreover, GF/ α -Fe₂O₃/CS composite material will be subjected to enzyme immobilization by applying for passive coupling without using any chemical agents. The preparation of the enzyme solution will be performed by immersing at 4°C for 24 hours. Moreover, Direct Electron Transfer based on FAD (Flavine Adenine Dinucleotide) coenzyme will occur owing to GF/ α -Fe₂O₃ composite structure which will be developed for the design of the third generation glucose biosensor. SEM and BET will be performed to observe whether CS spreads on the surface as a film and to determine that GOx is retained on the surface. Due to the fact that the sensor planned to be produced in the study is an electrochemical sensor, the measurement which explains the relationship between voltage and current will be measured by Cyclic Voltammetry (CV, CH Instruments, Inc., IKCU). CV tests will be carried out with three electrode system composed of the composite working electrode (GF/ α -Fe₂O₃/CS/GOx), platinum counter electrode and calomel reference electrode. When Phosphate Buffer Solution (PBS) in different glucose concentrations (0.1, 0.3, 0.5, 0.7, 0.9, 1.1, 1.3, 1.5 mM) encounters with GF/ α -Fe₂O₃/CS/GOx composite, calibration curve will be drawn as cathodic current peak responses to the changes of glucose concentration. The expected results are to determine the increase in the peak depending on the amount of glucose. The effect of the immobilization on the response such as binding time on the surface and the enzyme concentration will be investigated.

Results

Raman spectroscopy is the most important characterization method showing sp² hybridization of graphene. According to the results, Figure 1a significantly indicates two sharp peaks. The first one, G

peak, shows sp^2 hybridization on the surface. The another one, 2D peak, is an important indicator of graphene layers, with 2D/G ratio defining the approximate number of layers in the structure. Therefore, the analysis of 2D peak is a critical point to form an estimate of the quality of graphene. 2D/G ratio is approximately 1,41.

Figure 1b shows XRD pattern of 3D-Graphene synthesized on Nickel (Ni) Foam. Ni Foam shows two noticeable peaks at $2\theta = 44,1^\circ$ and $51,5^\circ$ which refer to (111) and (200). In addition that the reflection peak of graphitic carbon leads to a slight increase at $2\theta = 54^\circ$ (004), two sharp peaks also dramatically observed at $2\theta = 26,5^\circ$ and $61,1^\circ$ stating the reflection of graphitic carbon (002) and the reflection of silicon (400), respectively. Even though Ni Foam is etched, Ni peaks is still observed in Figure 1b because GF includes some joint points which make Ni difficult to be removed. Figure 1b has been normalized according to the first graphene peak (002). The comparison proves that Ni (111) diminished 96.38% and Ni (200) diminished 94.38%. The most of Ni has been etched successfully. However, in Figure 1c, SEM image clearly indicates that non-etched Ni structures and 3D-GF structure are detailed. SEM images show the morphology of 3D-Graphene networks with micropores. Transparent graphene layers have been observed after the removal of nickel. SEM images notably prove 3D-Graphene having the flakes of graphene.

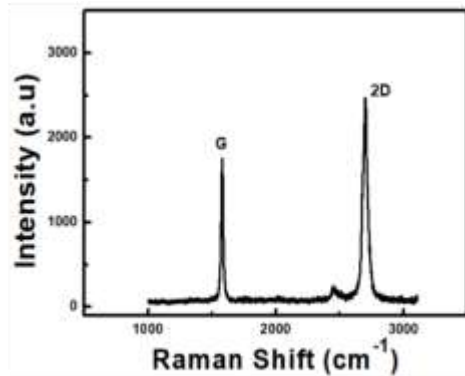


Figure 1a. Raman Spectrum of Graphene

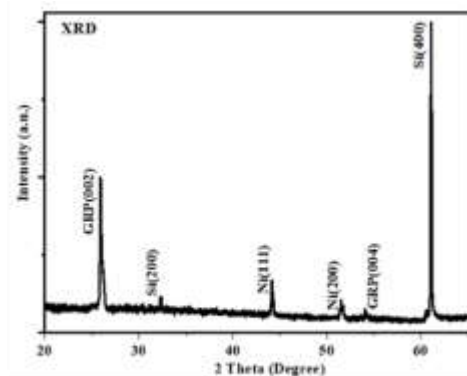


Figure 1b. XRD Spectrum of Graphene

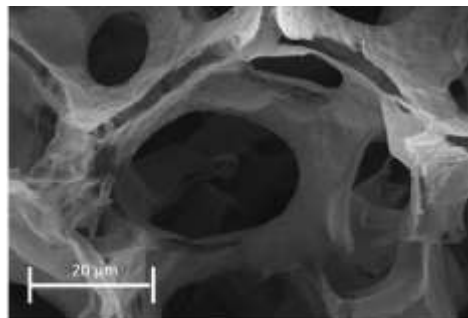


Figure 1c. SEM Image of Graphene

Conclusions

According to the results obtained by Raman Spectrum and XRD Spectrum, the synthesis of GF planned to be used in the biosensor study has been completed as desired. It is clearly understandable that GF, is highly compatible with the biosensor to be produced, will contribute positive effects to its electrochemical activity. However, the synthesis of α -Fe₂O₃ nanowires and the preparation of chitosan in appropriate parameters still continues for the completion of the study.

References

- [1] Celik N, Balachandran W, Manivannan N (2015) Graphene-based biosensors: Methods, analysis and future perspectives. IET Circuits, Devices & Systems. 10.1049/iet-cds.2015.0235.

3rd International Students Science Congress
3-4 May 2019, İzmir - Turkey

- [2] Wang Y, Li H, Kong J (2014). Facile preparation of mesocellular graphene foam for direct glucose oxidase electrochemistry and sensitive glucose sensing. *Sensors and Actuators B: Chemical*. 193 : 708-714. 10.1016/j.snb.2013.11.105.
- [3] Agarwala S, Lim ZH, Nicholson E, Ho GW (2011). Probing the morphology-device relation of Fe₂O₃ nanostructures towards photovoltaic and sensing applications. *Nanoscale*. 4. 194-205. 10.1039/c1nr10856e.
- [4] Movlaee K, Ganjali MR, Norouzi P, Neri G (2017). Iron-Based nanomaterials/graphene composites for advanced electrochemical sensors. *Nanomaterials*. 7. 406. 10.3390/nano7120406.
- [5] Guo J, Zhang T, Hu C, Fu Lei (2014). Three-dimensional nitrogen-doped graphene structure: a high efficient carrier of enzyme for biosensors. *Nanoscale*. 7(4) 10.1039/C4NR05325G.
- [6] Abdul Razak K, Mohamad Nor N, Ridhuan NS (2017). Metal oxide nanostructure-modified electrode for glucose biosensor. *Advanced Materials and their Applications*.

Işığa Duyarlı İlaçların Taşınmasında Kullanılacak PLGA Temeli Polimerik Nanoparçacıkların Sentezi ve Karakterizasyonu

Ahmet Aykaç*, Burcu Topuksal

İzmir Kâtip Çelebi Üniv., Nanobilim ve Nanoteknoloji A.B.D, İzmir, Türkiye

*İletişimden sorumlu yazar: ahmet.aykac@ikc.edu.tr

Anahtar Kelimeler: İlaç taşıma sistemi, polimerik nanoparçacıklar, fotodinamik terapi, siklodekstrinler, PLGA, indosiyenin yeşili.

Disiplin: Nanobilim ve Nanoteknoloji

Özet

Biyo-parçalanabilir polimerlerden elde edilen polimerik nanoparçacıklar bir taşıyıcı sistem olarak proteinlerin, peptidlerin, nükleik asitlerin, küçük ilaç moleküllerinin taşınmasında son yılların en önemli çalışma konularından birisi olmuştur. Günümüzde, multi-disipliner çalışmaların çok organize bir şekilde yürütüldüğü eczacılık, temel bilimler ve tıp alanındaki ortak çalışma alanlarının başında ise yeni nesil ilaç taşıyıcı sistemlerin tasarımı, sentezi ve uygulamaları gelmektedir. Nano ilaçlar ya da yeni nesil ilaçlar olarak bilinen ilaçların eldesinde en çok kullanılan yöntemlerden birisi metalik veya polimerik nanoparçacıkların taşıyıcı olarak kullanılması gelmektedir.

Bu projenin amacı yeni nesil, biyobozunumu (bioparçalanabilir) mümkün olan poly (laktik-ko-glikolik asit) (PLGA) polimeri ile siklodekstrinlerin (CD) türevlendirilmesinden elde edilen PLGA-CD kopolimerlerinden polimerik nanopartiküllerin (P-NPs) sentezi ve karakterizasyonu çalışmalarını kapsamaktadır. Yenilikçi polimerik yapı olan PLGA-CD 'nin sentezi, PLGA' nın alkin formu ile azido CD arasında bakır(I) katalizörlüğünde azide-alkin sikloekleme reaksiyonları ile gerçekleştirilecektir. PLGA-CD polimerik nanopartikülü indosiyenin yeşilinin (ICG) taşınması (enkapsulasyonunu) ve fotodinamik yöntemle ICG salınımını bakterilerin direncini kırma üzerine etkisinin incelenmesini içermektedir. Proje için seçtiğimiz poly (laktik-ko-glikolik asit), polimeri tamamıyla biyobozunur ve biyoparçalanabilir bir polimer olmasının yanısıra, modifikasyonu mümkün olan ticari olarak temin edilebilen, çok pahalı olmayan bir polimerdir. Ayrıca siklodekstrinlerde tamamıyla bioparçalanabilir doğal polimerler olup, ilaç taşıma sistemlerinde çok yaygın bir şekilde kullanılmaktadırlar. Siklodekstrinlerin birçok özelliğine ilaveten, suda çözünürlüğü düşük olan molekülleri enkapsüle etme kapasitelerinin çok yüksek olması bu molekülleri oldukça özel kılmaktadır. Bu çalışmada ICG molekülünün anyonik karakterinin maskelenmesi amacıyla P-NPs içine yüklenmesi ve bunun fotodinamik terapi yöntemi ile birlikte çoklu ilaç direnci geliştiren gram negatif *Pseudomonas aeruginosa* bakterisinin direncini etkin bir şekilde ve daha düşük ilaç konsantrasyonuyla yenmeye yönelik uygulamalar araştırılacaktır.

Giriş

Modern eczacılık biliminin en önemli çalışma konularından birisi; nanoteknolojinin, ilaç tasama sistemlerine entegrasyonu çalışmalarıdır. Nano-ilaç olarak bilinen ilaçların sentezi, kişiselleştirilmiş ilaçlar, akıllı ilaç taşıma sistemleri, enkapsulasyonda nanoteknolojik yaklaşımlar, polimerik ve metalik nanoparçacıkların ilaç hammaddesi ile kaplanması veya ilaçların polimerik ve metalik nanoparçacıklara yüklenmesi yapılan en önemli çalışmaların başında gelmektedir [1]. Bir nanotaşıyıcı sistem dizayn edilirken dikkat edilmesi gereken çok önemli noktalar bulunmaktadır. Aktif ilaç hammaddesinin fiziko-kimyasal ve fizyolojik etkileşimlerden etkilenmesinin engellenmesini göz önünde bulundurmanız gerekir. Spesifik olarak ilaç dağılımlarının göz önünde bulundurulması ve hücreye geçişinin sağlanması gerekir. Örneğin bazı durumlarda ilaç aktif maddesi aniyonik veya katyonik olabilir ve bu bazı durumlarda ilaç hammaddesinin hücre içine geçişini zorlaştırabilir, tasarladığımız nanotaşıyıcının bu engeli aşması amacıyla tasarlanmış olduğunu ve dolayısıyla da hücre içine geçişini kolaylaştırdığımızdan emin olmamız gerekir. Aynı zamanda nanotaşıyıcı sistemlerde boyutun önemli bir parametre olduğunu bilmemiz gerekir. Bazı nanotaşıyıcılar sadece hedeflenen organ, doku veya hücreye spesifik geliştirilebilir ki bu durumda ciddi yan etkisi bulunan ilaçların bu gibi hedefe ilaç taşıyan taşıyıcılarla taşınması hastalıklı olmayan hücrelerde oluşabilecek tahribatların önüne geçer, bu

durumda geliştirilecek nanotaşıyıcıya hangi ilaçların yükleneceği ve bu ilaçların hangi organlarda ne tür yan etkilerinin olduğu iyi bilinmelidir.

İlaç salınımlarının kontrollü salınımı amacıyla tasarlanan ilaç nano-taşıyıcı sistemlerin salınım sürelerinin iyi ayarlanması gerekir. İlaçların tesir değeri, tesir dozu ile tesir sürelerinin göz önünde bulundurulması gerekir. Nano boyuttaki ilaç taşıma sistemleri genel olarak incelendiğinde üç tipten oluştuğu gözlemlenmektedir. Bunlar: Lipozomlar, polimerik nanoparçacıklar (P-NPs) ve misellerdir. Lipozomlar fosfolipidlerin kendi kendine bir araya gelmesi (self-assembly olarak bilinir) ile oluşan yapılardır [2]. Misellerde kendi kendine bir araya gelme sonucunda meydana gelirler fakat farklı olarak farklı tür amfifilik moleküller veya lipid türlerinden oluşurlar [3,4]. Hem lipofilik hem de hidrofilik ilaçların yüklemesinde yardımcı olurlar. Nanoparçacıklar ise genellikle bioparçalanabilir polimerlerden elde edilirler. Bir çok yönden diğer nano boyut ilaç taşıma sistemlerinden daha avantajlı olmalarına karşın formulasyonları diğerlerine oranla daha güçtür. İlaçların korunması, taşınması ve hedefe ulaştırılmasında oldukça etkilidirler. Polimerik nanopartiküller ilaçların kontrollü salınımlarında da etkilidirler [5].

Geçtiğimiz yıllarda sentetik polimerlerden elde edilen nanoparçacık formulasyonları, ilaç etken maddelerinin temel eksikliklerinin giderilmesinde ve hızlı ilaç salınımlarının giderilmesinde kullanılmaya başlandılar. Bu sentetik polimerlerden ilaç taşıma sistemi olarak kullanılacak bioparçalanabilir alifatik zincire sahip poliesterlerden; poli-(ε-kaprolactone, PCL), poli (laktik asit, PLA) [6], poli (glikolik asit, PGA), poli (laktik-ko-glikolik asit, PLGA) [7], en çok ilgi duyulan ve çalışılan polimerlerdendir. Polimerik nanoparçacıkların bazı zayıf noktaları bulunmaktadır, bunların başında ilaç yükleme kapasitelerinin çok iyi olmaması gelir. Bu özelliklerinin geliştirilebilmesi ve ilaç yükleme kapasitelerinin artırılması amacıyla alternatif çözüm yolları bulunmaya çalışılmıştır. Siklodekstrinlerin polimerik yapıyla konjugasyonu sonucu elde edilen kopolimerlerin, ilaç taşıyıcı sistemlerde kullanımı, ilaç yükleme miktarını artırıcı bir yöntem olmuştur [8-10]. Aynı zamanda polimerik nanoparçacıkların yüzeyinde bulunan siklodekstrinler polimerik nanopartiküllerin fonksiyonel hale getirilmesinde ve misafir moleküllere ev sahipliği yapıp bir kompleks oluşturmada yardımcı olacaktır.

Metodoloji

Bu projenin amacı yeni nesil, biobozunumu (bioparçalanabilir) mümkün olan polİ (laktik-ko-glikolik asit) (PLGA) polimeri ile siklodekstrinlerin (CD) türevlendirilmesinden elde edilen PLGA-CD kopolimerlerinden polimerik nanopartiküllerin (P-NPs) sentezi ve karakterizasyonu çalışmalarını kapsamaktadır. Öncelikle beta-siklodekstrini üçlü bağ yapabilmesi ve PLGA ile birleşebilmesi için azidlenme reaksiyonu gerçekleştirilmiştir. PLGA ise propargil reaksiyonu ile sentezlenecektir. Öncelikle Beta-CD 'nin azidlenme reaksiyonunu gerçekleştirmiş olduk ve deneyin ayrıntıları aşağıda anlattığım gibidir.

Su (10 ml) içinde beta-siklodekstrin (2.5 gram 2.0 mmol) ve sodyum azit (1.95g ,30 mmol) karışımı 80 ° C'de 3 gün boyunca karıştırılmıştır. Elde edilen çözelti, hacminin yarısına kadar konsantre edilmiştir ve oda sıcaklığına kadar soğutulmuştur. Çökeltmek için aseton (200 ml) ilave edilmiştir. Elde edilen beyaz katı su (10 ml) içinde yeniden eritilmiştir ve aseton (200 ml) içinde tekrar çökeltmiştir. Bu işlem bir kez daha yapılmıştır. Beyaz katı 2 gün boyunca 60 ° C'de vakum altında kurutulmuştur ve 2,2 g,% 96 elde edilmiştir. Literatür prosedürüne dayanarak, 500 mL'lik yuvarlak bir tabanda şişe β-siklodekstrin (20.0 g, 17.6 mmol) içinde süspansiyon haline getirilmiştir. 250 mL 0.4 M sodyum hidroksit (NaOH) sulu çözeltisi. Şişe buz banyosunda 0 ° C'ye soğutuldu. TsCl (13,4 g, 70,3 mmol) 10 dakika boyunca yavaş porsiyonlar halinde eklenmiştir. 45 dakika sonra 0 ° C'de karıştırıldıktan sonra çökelti süzülerek çıkarılmıştır ve süzütünün pH'ı, HCl sulu çözeltisini bırakarak 8.5'e ayarlanmıştır. Daha sonra karışım 1 saat oda sıcaklığında karıştırılmıştır. Elde edilen beyaz çökelti süzülerek geri kazanılmıştır ve üç kez suyla yıkanmıştır. Nihai ürün, beyaz bir katı verecek şekilde 60 ° C'de vakumlu bir fırında kurutulmuştur. β-CD-OT'ler (8.0 g, 6.2 mmol), 100 ml su içerisinde süspansiyon edilmiştir. 80 ° C'ye ısıtıldıktan sonra NaN₃ (2.0 g, 31.0 mmol) eklenmiştir. Reaksiyon karışımı, 80 ° C'de gece boyunca karıştırılmıştır. Daha sonra reaksiyon çözeltisi oda sıcaklığına soğutuldu ve 800 mL asetonla çökeltmiştir. Nihai beyaz çökelti, süzülerek geri kazanılmıştır ve 50 mL su içerisinde yeniden çözündürülmüş ve tekrar aseton içerisinde çökeltmiştir. Beyaz katı, 2 gün boyunca 60 ° C'de vakum

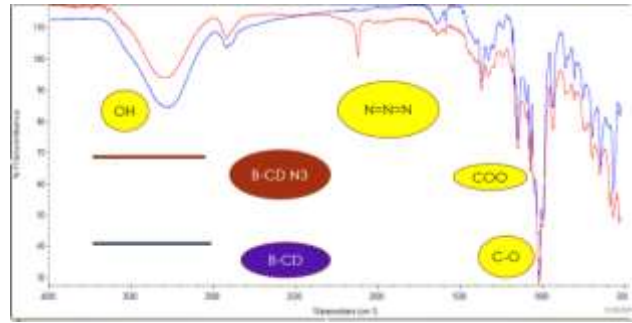
altında kurutulmuştur. Beta siklodekstrini bu şekilde azitlenmiştir. Karakterizasyonu FT-IR da yapılmıştır. Sonuçları ise sonuç kısmında gösterilmiştir.

İkinci aşamada PLGA polimerini propargillenmiştir. Elimizde polietilen glikol (PEG) daha fazla bulunduğu için deneyde PEG polimerini kullanılmıştır. Bir miktar alınan PEG polimeri tetrahidrofuran ve trietilaminle balon jode karıştırılmıştır. Karışımın ağzı kapatılmıştır ve havası alınmıştır. Havası alındıktan sonra azot gazı verilmiştir. Karışıma propargil ve tetrahidrofuran şırınga ile enjekte edilmiştir. Karışım iki saat 0 ° C'de karıştırıldı. Karışım oda sıcaklığına getirilmiştir ve iki gün karıştırılmıştır. Daha sonra eterle karışım süzölmüştür ve iki gün vakumlu fırında bekletilmiştir. Son olarak beyaz toz halinde karışım elde edilmiştir ve karakterizasyon için örnek alınmıştır.

PLGA polimerinden nanopartikül sentezi yapılmıştır. Bir miktar PLGA polimeri aseton ve diklorometan (39/1 ml) ile çözelti hazırlanmıştır. Diğer taraftan polivinil alkolle çözelti hazırlanmıştır. PLGA ile hazırlanan karışım damla damla polivinil alkollü çözeltiye ilave edilmiştir. Renk değişimi gözlenmiştir. Bu karışım bir gün boyunca karıştırılarak aseton uçurulmuştur. Buzlukta bekletilen karışım liyofilizatöre konmuştur. Liyofilize işleminden sonra PLGA nanopartikülleri elde edilmiştir. Nanopartiküller SEM'de (taramalı elektron mikroskobu) gösterilmiştir.

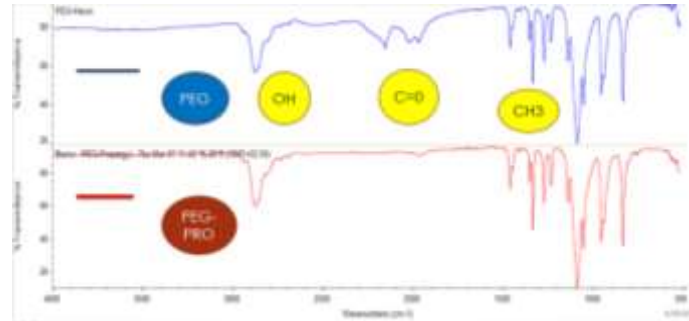
Bulgular

Şekil 1'de beta-siklodekstrinin azitlendiği kanıtlanmıştır. Beta-siklodekstrinin ve beta-siklodekstrin azidonun FT-IR sonuçları karşılaştırmalı olarak gösterilmiştir. Şekildeki azot bağları beta-siklodekstrinin azitlendiğini göstermektedir.



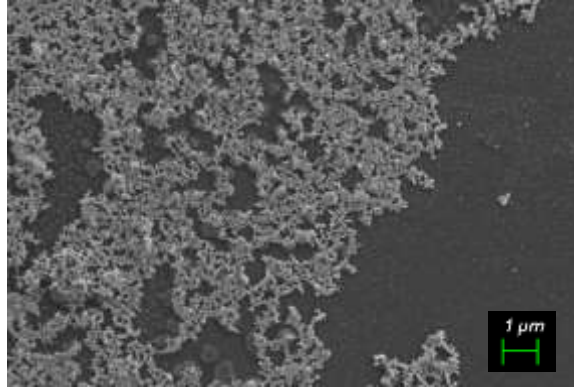
Şekil 1. B-CD Azid FT-IR karakterizasyonu

Şekil 2'de PEG(polietilen glikol) polimerinin propargillendiği FT-IR karakterizasyonunda gösterilmiştir. PEG polimeri ve PEG –propargil karşılaştırmalı olarak gösterilmiştir. PEG-PROPARGİL' de karbon-oksijen bağlarının koaptuğu gözlenmektedir.



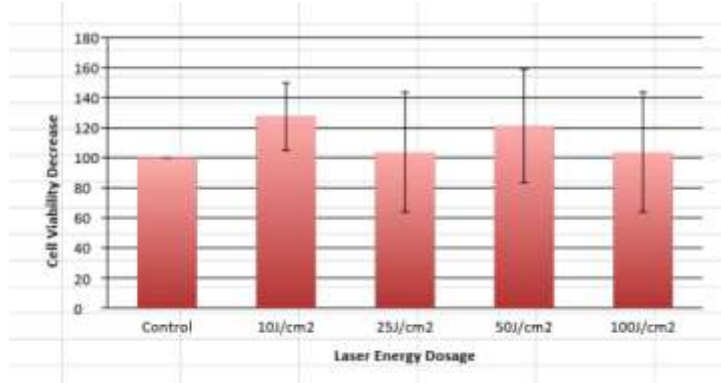
Şekil 2. PEG-Propargil FT-IR Karakterizasyonu

Şekil 3'te PLGA nanopartiküllerinin SEM görüntüsü gösterilmiştir.



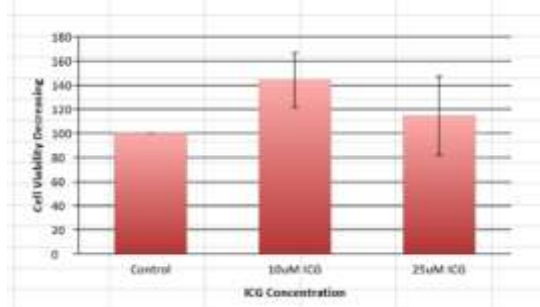
Şekil 3. PLGA Nanopartikülünün SEM Görüntüsü

Şekil 4’te farklı enerji seviyelerinde bakterilere lazerlerle yapılan müdahalelerin sonucu grafikte gösterilmiştir. Bu sonuçlara göre 10 joule, 25 joule, 50 joule ve 100 joule enerji verildiğinde bakteriler strese girerek çoğalmaya başlamıştır. 10 joule enerji verildiğinde bakterilerde daha fazla bir artış görülmüştür.



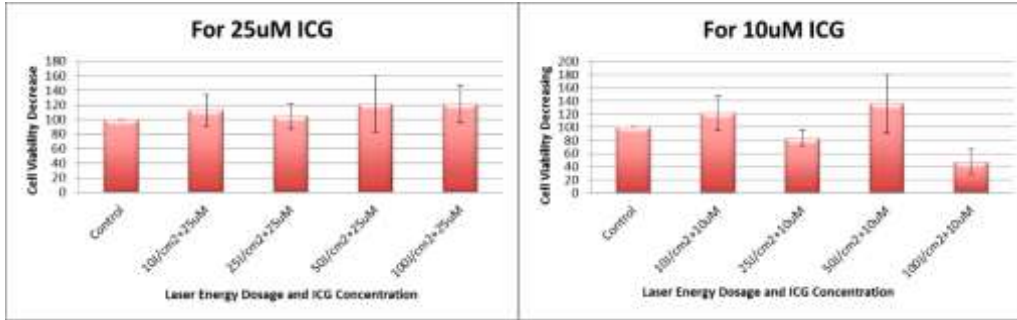
Şekil 4: Bakteriye farklı enerji seviyelerinde yapılan müdahale

Şekil 5’te farklı miktarlarda ICG yeşili bakteriye verilmiştir. Bakteriye 10 mikromolar ICG yeşili verildiğinde daha çok strese girerek çoğalmışlardır.



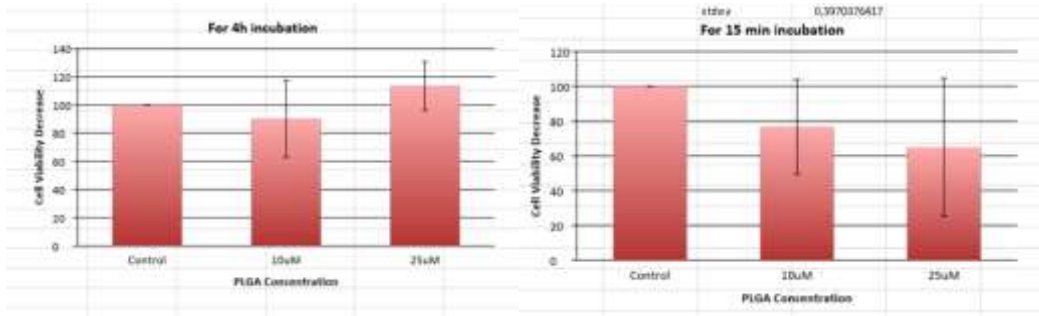
Şekil 5. Bakteriye sadece ICG yeşiliyle müdahale

Şekil 6’ da hem lazer hem de ICG yeşili ile müdahale edilmiştir. 25 mikromolar ve farklı seviyelerde verilen enerji bakterilerin çoğalmasına neden olmuştur. 10 mikromolar, 25 J ve 100 J enerji seviyesinde bakterilerde ölümler gözlenmiştir.



Şekil 6. Laser ve ICG yeşili ile müdahale

Şekil 7’de bakteriyeye PLGA nanopartikülü ile müdahale edilmiştir. Bakteriye ölümler gözlenmiştir fakat bakterilerin tamamında bir etki gözlenmemiştir. Farklı miktarlarda ICG yeşili bakteriyeye verilmiştir. Bakteriye 10 mikromolar ICG yeşili verildiğinde daha çok strese girerek çoğalmışlardır.



Şekil 7: PLGA nanopartikülü ile bakteriyeye yapılan müdahale

Sonuçlar

Bu projede beta-siklodekstrin başarılı bir şekilde azitlenmiştir. FT-IR sonuçlarına göre azot bağları beta siklodekstrin azitte gözlenmiştir. Öte yandan PLGA-Propargil yapısı sentezlenmiştir fakat verimin yükseltilmesi ve optimize edilerek, daha uygun parametrelerde sentezlenmesi için çalışmalar sürmektedir. PLGA dan nanoparçacıklar nanopresipitasyon yönteminde bir miktar türevlendirme yapılarak ve nano emülsiyon yöntemleriyle elde edilmiş ve karakterizasyonu gerçekleştirilmiştir. Ayrıca PLGA nanoparçacıkları SEM’de görüntülenerek yapının topaklanmadığı gözlenmiştir. İlaç salınımı kontrolü için ‘tampon solusyon metodu’ veya ‘dializ membranı metodu’ kullanılacaktır. Kontrol deneyleri kapsamında sadece laser etkisini gözlemek amacıyla farklı enerji seviyelerinde bakterilere müdahale edilmiştir. Bu sonuçlara göre 10 joule, 25 joule, 50 joule ve 100 joule enerji verildiğinde bakteriler strese girerek çoğalmaya başlamıştır. 10 joule enerji verildiğinde bakterilerde daha fazla bir artış görülmüştür. Bu sonuçlardan da görüldüğü gibi tek başına verilen lazer bakteriler üzerinde etkili olmamıştır. Farklı miktarlarda ICG yeşili bakteriyeye verilmiştir. Bakteriye 10 mikromolar ICG yeşili verildiğinde daha çok strese girerek çoğalmışlardır. Hem lazer hem de ICG yeşili ile müdahale edilmiştir. 25 mikromolar ve farklı seviyelerde verilen enerji bakterilerin çoğalmasına neden olmuştur. 10 mikromolar, 25 J ve 100 J enerji seviyesinde bakterilerde ölümler gözlenmiştir. Bakteriye PLGA nanopartikülü ile müdahale edilmiştir. Bakteriye ölümler gözlenmiştir fakat bakterilerin tamamında bir etki gözlenmemiştir. Bu sonuçlar ışığında tek başına uygulanan yöntemlerin yeterli olmadığı gözlenmiştir. Sonuç olarak, *Pseudomonas aeruginosa bakterisi* çok kuvvetli bir direnç mekanizmasına sahip bir bakteri olup, çok hızlı bir direnç mekanizması oluşturabilmektedir. PLGA-CD co-polimeri ile bu olumsuzlukları bertaraf etmeye yönelik yürüttüğümüz çalışmamızda şimdiye kadar elde ettiğimiz sonuçların beklenen sonuçlar olduğunu, tek başına lazer etkisinin, tek başına ICG ilaç etkisinin ve tek başına PLGA nanoparçacıklarının bu bakteriler üzerine etkisinin olmadığını ispatlamış olduk. Projemizin son basamağı olan PLGA-CD co-polimerlerinin eldesi, ICG yüklenmesi ve PDT uygulaması ile proje tamamlanacaktır bu noktada sentez ve analiz çalışmaları yürütülmektedir.

Referanslar

- [1] Aykaç A, Martos-Maldonado MC, Juan M, Casas-Solvas JM, Quesada-Soriano I, García-Maroto F, García-Fuentes L and Vargas-Berenguel A (2014) β -Cyclodextrin-Bearing Gold Glyconanoparticles for the Development of Site Specific Drug Delivery Systems. *Langmuir*, 30, 234–242.
- [2] Couvreur P, Fattal E, Andremont A (1991) Liposomes and Nanoparticles in the treatment of Intracellular Bacterial Infections, *Pharmaceutical Research*, 8 (9), 1079-1086.
- [3] Kataoka K, Harada A, Nagasaki Y (2001) Block copolymer micelles for drug delivery: design, characterization, and biological significance, *Advanced Drug Delivery Reviews* 47, 113-131.
- [4] Lukyanov AN, Torchilin VP (2004) Micelles from lipid derivatives of water-soluble polymers as delivery systems for poorly soluble drugs, *Advanced Drug Delivery Reviews*, 56, 1273-1289.
- [5] Letchford K, Burt H (2007) A review of the formation and classification of amphiphilic block copolymer nanoparticles structures: micelles, nanospheres, nanocapsules, and polymersomes, *European Journal of Pharmaceutics and Biopharmaceutics*, 65, 259-269.

Petroleum and Natural Gas Engineering / Petrol ve Doğalgaz Mühendisliği

Practical Application of Cased Hole Logs in Fluid Movement Detection

Mohamed Issa*

İzmir Kâtip Çelebi Univ., Dept. of Material Science and Engineering, Çiğli Main Campus, İzmir, Türkiye

**Corresponding author: mhed_2020@yahoo.com*

Keywords: cased hole logs, fluid movement detection

Discipline: Petroleum and Natural Gas Engineering

Abstract

Cased hole logs are group of downhole diagnostic tools, that provide many information about the production reservoirs and wells and play an important role in reservoir management and production. Cased hole logs have many applications include formation evaluation (FE), completion efficiency, fluid movement and can be used in new well used to evaluate primary cement around the casing and evaluate top of cement (TOC), and in older wells to detect source of water and gas, identify plugging perforation for treatment or reperforation, casing leaks or split's and cross flow between two perforation or between zones, also are important for secondary and tertiary recovery to track the front and monitoring saturation changes over time "at fixed time". The data obtained from cased hole logs can be used in several application such as maps, plots, logs program or model to describe oil field performance, determine problems and appropriate solution for these problems by workover maintenance.

This work illustrates the application and importance of various logs for recognizing water production problems in oil well (G220-51) field in Libya operated by Arabian Gulf Oil Company (AGOCO). Cased hole logs were run in these wells to diagnose, monitor and determine zonal contribution to detect source of water.

Introduction

The term production logs often used to categorize surveys run for down hole fluid movement detection [1,2]. They are combination of tools which measure the fluid parameters on zone by zone to give information about the type and movement of fluid within and near the well bore and provide the necessary information about water and gas movement inside the well bore (flow between two perforations and flow behind casing in channels) and outside the well bore (contacts movement, breakthrough of water or gas either naturally by encroachment from gas cap or water drive or in case of water or gas injection [3]. production logs can be classified into three major categories [4]. Category one includes tools used to track movement of fluid either inside or immediately outside the casing of the well and response to fluid velocity or fluid type. The logs in this category include temperature survey, mechanical flow meter survey, borehole fluid density, and fluid capacitance devices. Category two includes logs monitor cement placement to locate the cement top to determine whether the cement provides zonal isolation or not [5]. These logs include temperature log and gamma ray log. The third This category includes tools used to assess corrosion, spilt leaks shape in the casing or drill pipe. These tools include mechanical caliper, electromagnetic potential tools current received tools [6].

The of this work is to describe the application of fluid movement cased hole logs in two wells (G220-51, G118-51) in Nafora field with spinner flow meter to monitor producing and diagnose problems in these wells.

Field History

The Nafora Field is located in south eastern part of Libya about 360 km south of Benghazi. There are nineteen producing pools in Nafora field and oil reservoirs are shallow as 1300 ft. and deep as 10000 ft. Oil production is from number of carbonate and clastic reservoirs of different geological age.

As of December 2017, there were 188 wells in Nafora Non-Unit without not including shallow water source wells and wells that were abandoned early in their drilling process due to up hole drilling problems. Cumulative oil production in the field reached 3,108.45 MMSTB by year-end 2017. The average daily oil production rate in 2017 was 135 MSTB/D with an average water cut of 51 % and average reservoir pressure 2600 psig.

Case Study

Well G220-51 is producing from three different formations Khatt, Amal and Bahi. To increase the oil production new perforations were added in Khatt and Amal formations and some intervals were also re-perforated in Bahi and Khatt formations. Significant increase in oil production rate was recorded during production test after the work over. It was important to know the contribution of each formation. Figure 1 shows perforations program, BAHİ (9718-9744 ft), KHATT (9770-9810 ft) and AMAL-L (9820-9840 ft).

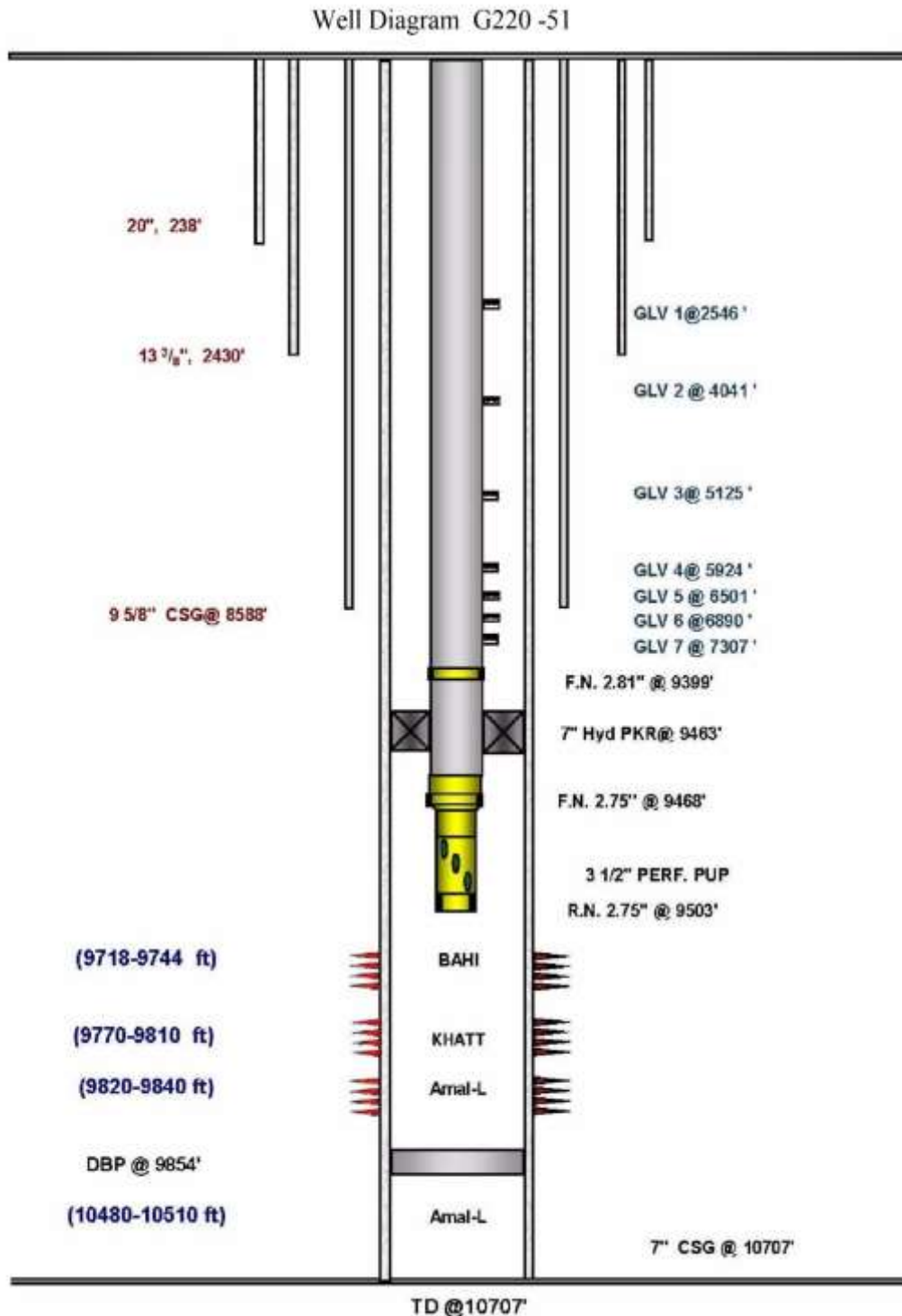


Figure 1. Perforation program well G220-51

Spinner response calibration

The multi pass technique was used to calibrate spinner response by using two up and four down log passes across the production intervals at different cable speed. Figure 2 shows production log profile at different zones. Figure 3 shows the spinner rotation speed correction due to viscous and drag force. Tables 1 and 2 show the spinner response and tool speed (line speed) for up and down passes.

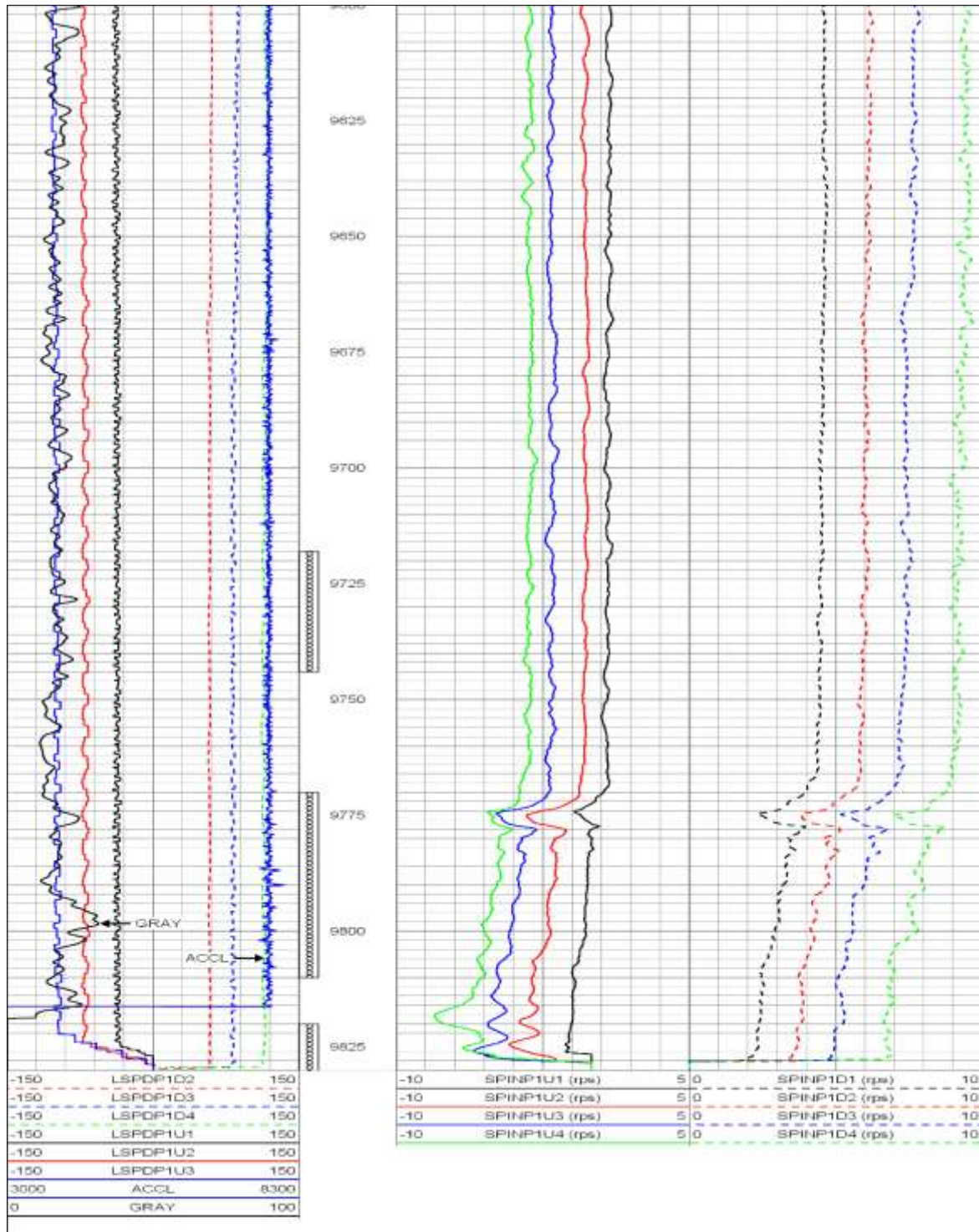


Figure 2. Production log profile spinner and cable speed

3rd International Students Science Congress
3-4 May 2019, İzmir - Turkey

Table 1. Up passes

Spinner (rps)	Tool speed (ft/min)
-1.6	30
-3.5	60

Table 2. Down passes

Spinner (rps)	Tool speed (ft/min)
1.4	35
3.4	63
4.2	82
5.8	114

Fluid viscosity will create offset (spaces) from the straight line (static response) and due to PLs have multiple passes up and down at multiple speed the spinner response should be calibrate to give response slop.

$$\text{Response slope}_{(\text{Up passes})} = \frac{\Delta y (\text{rps})}{\Delta x (\text{ft/min})} = \frac{4.4-2}{90.59-48} = 0.5634 \text{ rps. min/ft}$$

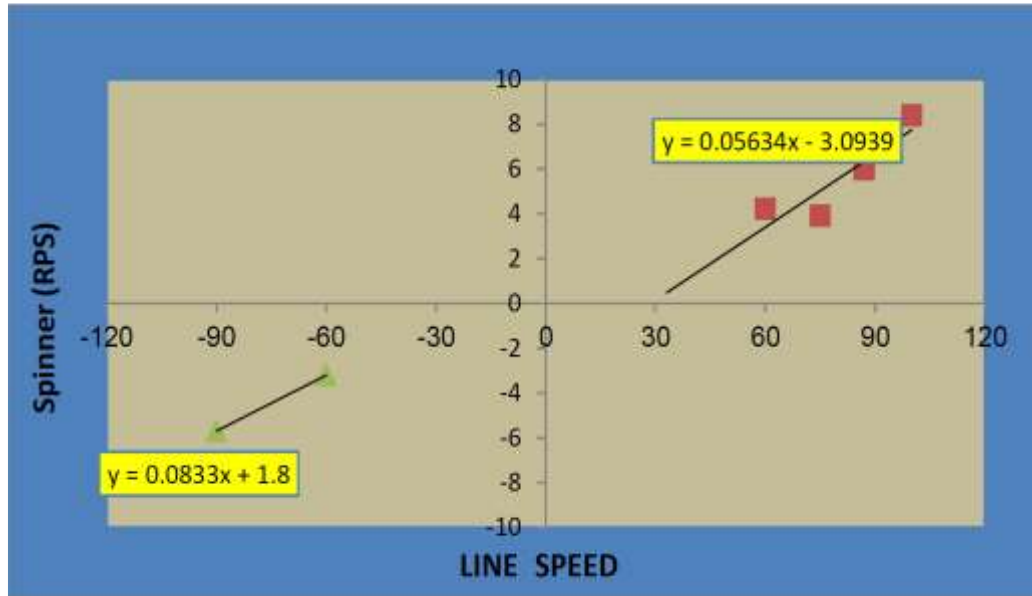


Figure 3. Spinner rotation speed correction due to viscous and drag force

Due to mechanical friction, the blades do not rotate at the slightest flow, so that flow velocity must be increased to overcome mechanical friction. This is the spinner rotational speed or spinner rotational threshold and can be defined as minimum cable speed at which the spinner being to rotate.

$$\text{Threshold} = \frac{\text{Intercept}}{\text{Slope}} = 3.889$$

Apparent fluid velocity for each zone

The velocity measurement from spinner should be corrected to average velocity because the viscosity of the fluid creates velocity profile across the diameter of the pipe. Table 3 shows the calculated apparent velocity for each zone.

$$\text{Apparent velocity} = ((\text{spinner rotational velocity/slope}) + \text{Threshold velocity}) - \text{line speed}$$

3rd International Students Science Congress
3-4 May 2019, İzmir - Turkey

Table 3. Calculated apparent velocity

Depth (ft)	Spinner (rps)	Line speed (fpm)	Slope (rps.min/ft)	Threshold (ft/min)	Apparent velocity (fpm)
9700	7.2	80	0.05634	3.88	59.50
9750	7.4	80	0.05634	3.88	56
9812	4.6	80	0.05634	3.88	10.50
9816	5	80	0.05634	3.88	17.50

Average fluid velocity for each zone

Since the flow rate measured by flow meter at the center of the pipe and consequently greater than the average flow meter; apparent fluid velocity must be calibrated to average fluid velocity by velocity correction factor (Cv). Velocity correction factor for turbulent flow is 0.95. Table 4 shows the corrected apparent velocity for each zone.

Table 4. Corrected apparent velocity

Depth (ft)	Apparent velocity (fpm)	Average velocity (fpm)
9700	59.50	56.525
9750	56.00	53.20
9812	10.50	16.625
9816	17.50	9.976

Down hole phase Holdup from PVT, Fluid Identification, and bulk densities Measurements

The holdup of a fluid phase is the fraction of volume of that phase present in the flowing stream. Fluid identification device in two phase flow mainly density log. Density for water, oil and gas can obtain from density log during shut in condition, or from P.V.T data. Phase holdups are calculated the following equations and shown in Table 5.

Heavy phase holdup (oil) $Y_h = (\text{measured Density} - \text{Density light phase}) / (\text{Density heavy phase} - \text{Density light phase})$

Light phase holdup $Y_L = 1 - Y_h$

Table 5. Calculated hold ups

Depth (ft)	Measured density	Oil density (g/cc)	Gas density (g/cc)	Y_H	Y_L
9700	0.658	0.6974	0.0973	0.934	0.066
9750	0.6619	0.6974	0.0982	0.941	0.059
9816	0.7189	0.6974	0.0984	1.0	0.0

Slip velocity (velocity ratio)

Slip velocity is the relative velocity of the light phase to heavy phase e.g. a standing column of water with gas bubbling up through, the velocity that the gas is move up through the water is the gas slip velocity. There are several various correlation and charts for slip velocity. In this work Smolen and Haliburton correlations were used and the values are shown in Table 6.

Table 6. Calculated slip velocity

Depth (ft)	Apparent velocity (fpm)	Average velocity (fpm)
9700	64.33	59.85
9750	64.55	59.87
9816	66.50	59.88

Downhole superficial phase velocities

The superficial velocity is the velocity of the phase by assuming that occupy the whole pipe and are calculated by using following equations. The results are given in Table 7.

$$Q_h = (Y_h * Q_{total}) - (Y_h * (Y_L * V_{slip \text{ light}}))$$

$$Q_L = Q_{total} - Q_{heavy}$$

Table 7. Superficial phase velocities

Depth (ft)	Q _{total} (fpm)	Y _H	V _s (fpm)	Y _L	Q _H (fpm)	Q _L (fpm)
9700	52.4	0.934	64.33	0.066	46.05	5.46
9750	49.1	0.941	64.55	0.059	43.47	2.02
9816	12.8	1.0	66.50	0.0	13.26	0.0

Superficial velocities should be converted to down hole flow rate by using following equation:

$$Q_i = 1.40 \times C \times V_i \times d^2$$

Table 8. Down hole flow rate

Depth (ft)	Q _H (fpm)	Q _L (fpm)	ID (inch)	Oil (BPD)	Gas (CFPD)
9700	46.05	5.46	6.199	2478	299
9750	43.47	2.02	6.199	2339	109
9816	13.26	0.0	6.199	713	0

Down hole flow rates must be converted to surface flow rates by using following equations

$$\text{Oil}_{STBOP} = \text{down hole oil} / \text{oil formation volume factor}$$

$$\text{Gas}_{Mscf \text{ gas}} = (\text{Down hole gas} / \text{Gas formation volume factor}) + (\text{STBOPD} * (\text{Oil Solution GOR} / 1000))$$

Table 8 shows the cumulative flow rates. Zonal rates can be calculated by subtracting the flow rate below the zone from the flow rate above the zone (Table 9). In this case it is easy to generate percentages.

Table 9. Calculated surface flow rate from down hole flow rate

Depth (ft)	Downhole Oil BPD	Downhole Gas BRD	FVF Oil	FVF Gas	GOR	Surface oil flow rate (STBD)	Surface gas Flow rate (MSCFD)
9700	2478	299	1.333	1.745	480	1859	1073
9750	2339	109	1.333	1.745	480	1755	967
9816	713	0	1.333	1.745	480	535	259

Contributions of each zone are obtained by dividing cumulative flow rate by zonal rate (Table 10).

Table 10. Zonal contribution

Depth (ft)	Cumulative Oil STBD	Zonal Oil STBD	Oil zonal contribution %	Cumulative Oil STBD	Zonal Oil STBD	Oil zonal contribution %
9700	1859	104	6	1073	106	10
9750	1755	1220	67	967	708	70
9816	535	535	27.1	259	259	20

Interpretation

Oil mainly produced from KHATT perforation only mixed with bubble of gas, it appears on temperature friction heating. Most of fluid flow was coming from KHATT and the rest from AMAL and minor flow from BAHİ perforation. Gas is produced mainly from Khatt and Bahi and expands to 1.07 MMscf/d at surface rates. Fluid identifier tool did not detect any water, the whole fluid column was having oil density value, and it was giving smaller reading in flowing because of gas bubble presence.

Conclusion

Many of cased hole logs are termed as production logs since they are run after the well being produced. Production logging is group of diagnostic information on zone by zone. There are three main categories of production logging according to their function. Production logs can easily identify zonal contributions and sources of water production.

Acknowledgement

This study was supported by the Presidency for Turks Abroad and Related Communities (YTB) within “International Student Academy” Project.

References

- [1] Smolen JJ (1994) Cased Hole and Production Log Evaluation. South Sheridan, Pennwell.
- [2] Darling T (2005) Well Logging and Formation Evaluation. Amsterdam, Elsevier.
- [3] Ellis DV, Singer JM (2007) Well Logging for Earth Scientists. 2nd Ed, Dordrecht, Springer.
- [4] Bateman RM (2015) Cased-Hole Log Analysis and Reservoir Performance Monitoring. Boston, Springer.
- [5] Schlumberger (1989) Log Interpretation Principles/Applications. Schlumberger, Houston, TX.
- [6] Serra O (1994) “Fundamentals of Well-Log Interpretation- 1. The acquisition of logging data. Amsterdam, Elsevier.

Physical Therapy and Rehabilitation / Fizyoterapi ve Rehabilitasyon

Using Force-Sensing Resistor – 0.6 Inch Diameter Circle- PI- 1696 to Determine In-Situ Force of Patella

*Heba Aljumaa**, Dokuz Eylül Univ., Dept. of Physiotherapy and Rehabilitation, İzmir, Turkey
Basheer Altawil, İzmir Kâtip Çelebi Univ., Dept. of Mechatronics Engineering, Çiğli Main Campus, İzmir, Turkey

*Corresponding author: heba.jumaa1988@gmail.com

Keywords: patella, knee, force-sensing resistor

Discipline: Physical Therapy and Rehabilitation

Abstract

Knee joint is the biggest joint in the body and carry the most loads of the body. It plays the main role for gait cycle (walking cycle) because the structure of flexion and extension do insertion on this joint. In addition, it is very important for mechanism of knee prosthesis. Patella is important part of this joint and protective cover for joint from any trauma and considered as insertion of quadriceps muscles. Our purpose in this study is to find force points that affect over patella while walking, and it can allow us to know about biomechanics of patella. Furthermore, knee through patella can distribute forces which comes from the muscles through ligaments, in the same topic most of studies were about to determine forces over ligaments of knee. However, in this study, we applied on patella because patella can take important place between big ligaments and we can find the center of forces easily. We used Force-Sensing Resistor – 0.6Inch Diameter Circle- PI- 1696 to determine situ force of patella. Finally, we analyze the results by Arduino program in computer by taking the instantaneous values from serial port and draw them on graphical sketch so that we can observe the changes of the force effecting on person knee during walking.

Introduction

Patella is the largest sesamoid bone in the body. The patella (knee-cap) is located at the front of the knee joint, within the patellofemoral groove of the femur and called knee-cap. The patella has triangular shape and two surface anterior and posterior, it is connected to the tibial tuberosity by the patella ligament, the posterior surface of the patella articulates with the femur.it has two facets medial and lateral. Medial facet articulates with the medial condyle of the femur [1-3] and lateral facet articulates with the medial condyle of femoral.

In physiotherapy there are a variety of studies about biomechanics in the body and how the center of body weight is transmitted. In this study we tried to measure forces applied on patella through gait cycle and from this study we can define mechanical importance of patella for knee. On the other hand, we found studies about measured forces on ligaments, these studies depend on sensors and some of them need surgery to measure to find accurate results [4], but in our study we need just sensor because patella is not deep, it is in surface location. And patella has anatomical importance for ligaments of quadriceps. Figure 1 shows the stimulation of anatomical structures, especially ligaments, of patella. Figure 2 shows the major heads of the quadriceps muscle group.

A balance of muscle mass and geometric angle of insertion (to the anatomic axis of the femur) exert an influence on patellar stability.

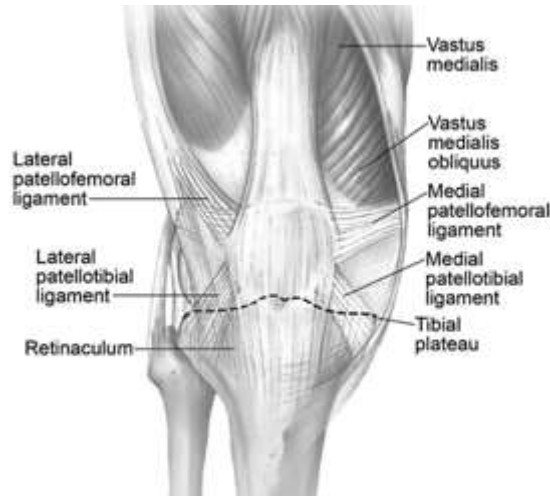


Figure 1. Stimulation of anatomical structures, especially ligaments [1].



Figure 2. The major heads of the quadriceps muscle group [1].

Physical Anatomy of the Knee

The knee has two articulations:

1. Femoraltibia joint: this joint between surface of tibia and two condyles of femur, this joint carries the most weight of body. The length of the femoral joint surface is greater than the tibial joint surface Therefore, the joint surface of the tibia ends before the movement is completed during the flexion and to be able to tolerate this event during knee flexion and extension distal femoral condyles do rotating and sliding [5-8].
2. Patellofemoral joint: between inferior surface of patella and sulcus of femoral, this joint has the main role in mechanism of extension joint and protect the tibiofemoral joint from any direct trauma.

Quadriceps muscle has concentric effect (when the quadriceps contraction) and eccentric effect (when the quadriceps relax) to do mechanism of extension joint. [9-13].

This mechanism like cantilever system when the quadriceps contract the patella tendon become shorter than before. This means arm of force shortens and moment increases, this formed power removes the tibia to occur extension and the end tibia and femur become straight on one. (Moment of force = Moment of resistance). Physical anatomy of the knee is illustrated in Figure 3.

Quadriceps contraction = tibial structures + gravity of earth

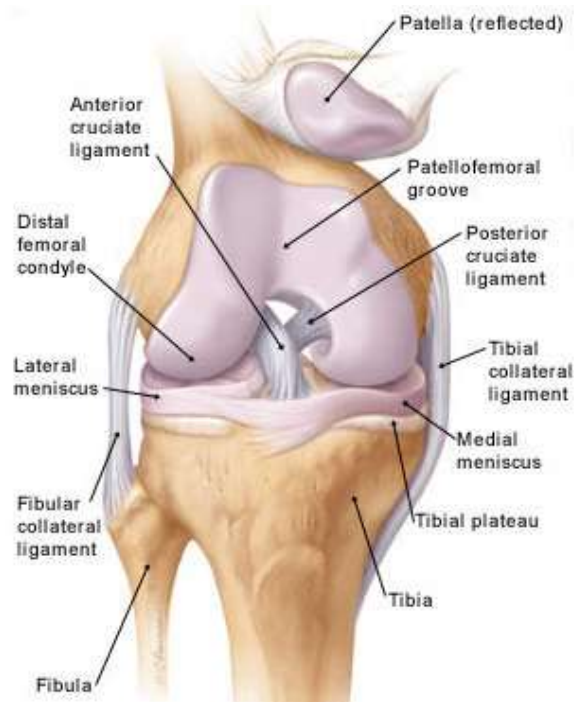


Figure 3. Physical anatomy of the knee [7].

Force of Body Weight Crossed from Patellofemoral Joint:

- When the knee is in flexion 9° position: the knee carries 0.5 of body weight
- When the knee is in flexion 60° position (climbing stairs): the knee carries 3.3 of body weight
- In squat 130° position: the knee carries 7.8 of body weight [14, 15].

In addition Patella problems do not appear just in Patellofemoral joint, it can appear in another place (lower limb, trunk). For example, an anteversion problem in the hip, in clinic it can appear as pain and deviation in the patella [10].

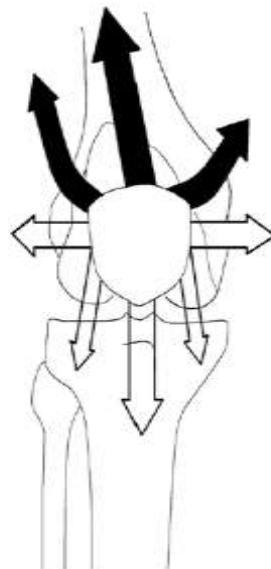


Figure 4. Force of body weight crossed from patellofemoral joint [7].

Figure 4 illustrates the force of body weight crossed from patellofemoral joint. In this figure, black arrows explain active force (later medialis vastus and rectus femoris). White arrows (patella ligament, patellofemoral lig and retinaculum).

Stress Definition

The stress of any mechanical or statical elements totally depends on the external forces that are exerted on that element. By attaching the sensor to the knee we could calculate the contact force between knee itself and holding piece of rubber so that we can decide the behavior of the person from that obtained force, then we can calculate the stress.

Data Limitation to Design Biomechanical Elements

Sensors force limits is between 0 and 120N in electronic devices when we try to take data we have to consider upcoming effects that we are going to obtain and be aware of errors. Applied forces on knee were between 4 and 33N so when we want to design mechanical elements we have to choose its properties with respect to them.

Method

In this study we take 7 healthy people, and put sensors above their patella. Their ages were between 20-23 years, 4 of them are male and 3 are female. The pressure forces above patella are taken during gait cycle (shown in Figure 5) and the data were read by Arduino program. After that we took average values to calculate the percentages.

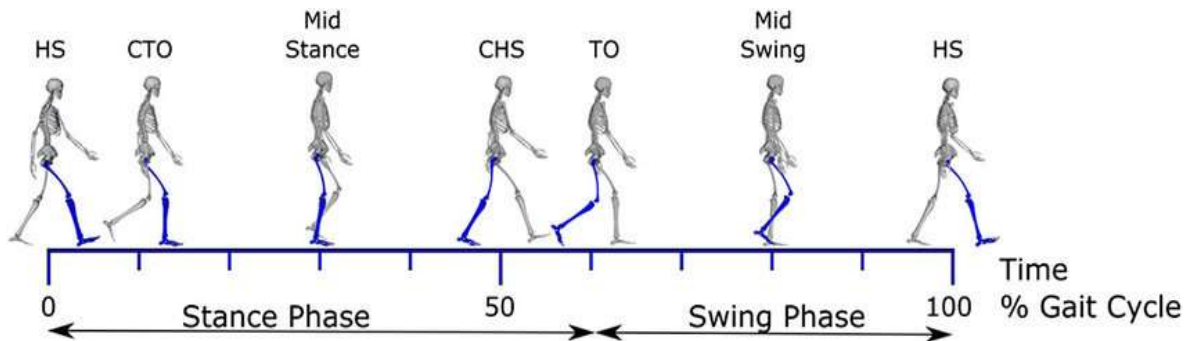


Figure 5. Gait cycle

Elements

In this study, we used a force-sensing resistor – 0.6 Inch Diameter Circle and an electrical circuit compliant to this sensor. A schematic of the sensor and the electrical circuit is shown in Figure 6. Figure 7 shows the location of sensor above patella.

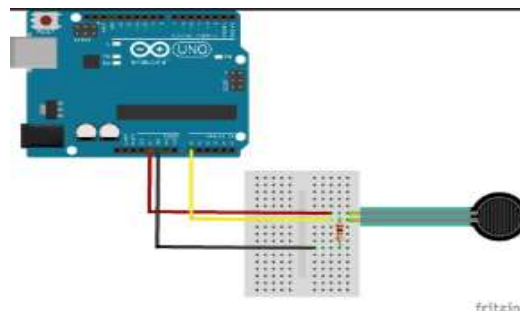


Figure 6. The sensor and the electrical circuit



Figure 7. The location of sensor above patella

Results and Discussion

The forces on patella are measured by our simple system the force values are tabulated in Table 1 according to the leg position. Pressure applied to the patella was in Newton.

Table 1. Data of pressure forces (N) on patella

Leg is outstretched	Tiptoe	Swing	Duck on the heel	Leg is outstretched
6	33	27	26	6
13	4	14	7	13
7	10	9	8	7
12	9	10	8	12
6	10	15	10	11
10	12	10	14	7
7	13	11	11	13

We do not find a significant difference between these pressure forces and this simple difference is because of the different ways of walking from one person to another. The anatomy of the pelvis can change walking type therefore some people can raise them foot more than another one.

During this study we have reached the following results:

- The patella has main role to receive and distribute power.
- The patella takes place in the balance of lower limb.
- Leg is outstretched stage → force = 7.25%
- Tiptoe stage → force = 10.83%
- Swing stage → force = 11.42
- Duck on the heel stage → force = 10%
- Leg is outstretched stage → force = 7.37%

The differences in proportion are due to the difference in pressure strength on the patella during the walking cycle. In leg outstretched stage, there is strength of muscle tension that keep the extension of knee to stand and this strength effect in patella as pressure.

In the tiptoe stage, in addition to the previous strength there are kinetic force that comes from structure surround the patella and start to construction of hamstring muscle. This force causes pressure above patella.

**3rd International Students Science Congress
3-4 May 2019, İzmir - Turkey**

In the swing stage, we can realized kinetic force from structure around the patella but in this stage it is stronger than tiptoe stage because the leg in air and we need energy to swing leg and this needs greater movement, this in turn puts greater pressure on the patella.

In the “duck on the heel” stage, all the structures are tense in the leg to be ready to receive a moment of collision with the ground.

Conclusion

Through this study we founded, by a simple method, that the greatest force been applied over patella was during swing stage and lowest force was during the leg outstretched stage.

Acknowledgement

This study was supported by the Presidency for Turks Abroad and Related Communities (YTB) within “International Student Academy” Project.

Reference

- [1] Karaduman A, Yılmaz ÖT (2016) Fizyoterapi Rehabilitasyon Ortopedik Rehabilitasyon Pediatrik Rehabilitasyon, Pelikan Publishing House.
- [2] Flandry F, Hommel G (2011) Normal anatomy and biomechanics of the knee. *Sports Med Arthrosc Rev.* 19(2):82–92.
- [3] Fredericson, M, Powers CM (2002) Practical management of patellofemoral pain. *Clinical Journal of Sport Medicine* 12(1):36-38.
- [4] Rupert M, Grood E, Byczkowski T, Levy M (1998) Influence of sensor size on the accuracy of in-vivo ligament and tendon force measurements. *J Biomech Eng.* 120(6):764-769.
- [5] Kettelkamp DB, Johnson RJ, Smidt GL, Chao EY, Walker M (1970) An electrogoniometric study of knee motion in normal gait. *J Bone Joint Surg Am.* 52(4):775-790.
- [6] Houglum PA, Bertoti DB (2011) *Brunnstorm's Clinical Kinesiology*, 6th ed. F. A. Davis Company, Philadelphia.
- [7] Lippert LS. (2011) *Clinical Kinesiology and Anatomy*, 5th ed. F. A. Davis Company Philadelphia.
- [8] Kuru İ, Haberal, Avcı Ç (2012) Patellofemoral biomechanics. *TOTBİD Dergisi* 11(4):274-280.
- [9] Kızılay YO (2015) Patellofemoral anatomi ve biyomekanik.
- [10] Fredericson, M, Powers CM (2002) Practical management of patellofemoral pain. *Clinical Journal of Sport Medicine* 12(1):36-38.
- [11] Lavernia C, D'Apuzzo M, Rossi MD, Lee D (2008) Accuracy of knee range of motion assessment after total knee arthroplasty. *J Arthroplasty* 23:85-91.
- [12] Dietz MJ, Sprando D, Hanselman AE, Regier MD, Frye BM (2017) Smartphone assessment of knee flexion compared to radiographic standards. *Knee* 24(2): 224-230
- [13] Chiang CY, Chen KH, Liu KC, Hsu SJ, Chan CT (2017) Data collection and analysis using wearable sensors for monitoring knee range of motion after total knee arthroplasty. *Sensors (Basel)* 17(2) pii: E418. doi: 10.3390/s17020418.
- [14] Greenfield MA, Scott WN (1992) Arthroscopic evaluation and treatment of the patellofemoral joint. *Orthop Clin North Am.* 23(4): 587-600.
- [15] Insall JN (2012) Disorders of the patella. in *Insall & Scott Surgery of the Knee*. Churchill Livingstone.

Congress Photograph Gallery / Kongre Fotoğraf Galerisi

3rd International Students Science Congress
3-4 May 2019, İzmir - Turkey



3rd International Students Science Congress
3-4 May 2019, İzmir - Turkey



**3rd International Students Science Congress
3-4 May 2019, İzmir - Turkey**



3rd International Students Science Congress
3-4 May 2019, İzmir - Turkey



**3rd International Students Science Congress
3-4 May 2019, İzmir - Turkey**



**3rd International Students Science Congress
3-4 May 2019, İzmir - Turkey**



**3rd International Students Science Congress
3-4 May 2019, İzmir - Turkey**



**3rd International Students Science Congress
3-4 May 2019, İzmir - Turkey**



**3rd International Students Science Congress
3-4 May 2019, İzmir - Turkey**



3rd International Students Science Congress
3-4 May 2019, İzmir - Turkey



**3rd International Students Science Congress
3-4 May 2019, İzmir - Turkey**



**3rd International Students Science Congress
3-4 May 2019, İzmir - Turkey**



**3rd International Students Science Congress
3-4 May 2019, İzmir - Turkey**



**3rd International Students Science Congress
3-4 May 2019, İzmir - Turkey**



**3rd International Students Science Congress
3-4 May 2019, İzmir - Turkey**

